Constitutive Models for Rubber VI

Editors:
G. Heinrich, M. Kaliske, A. Lion & S. Reese

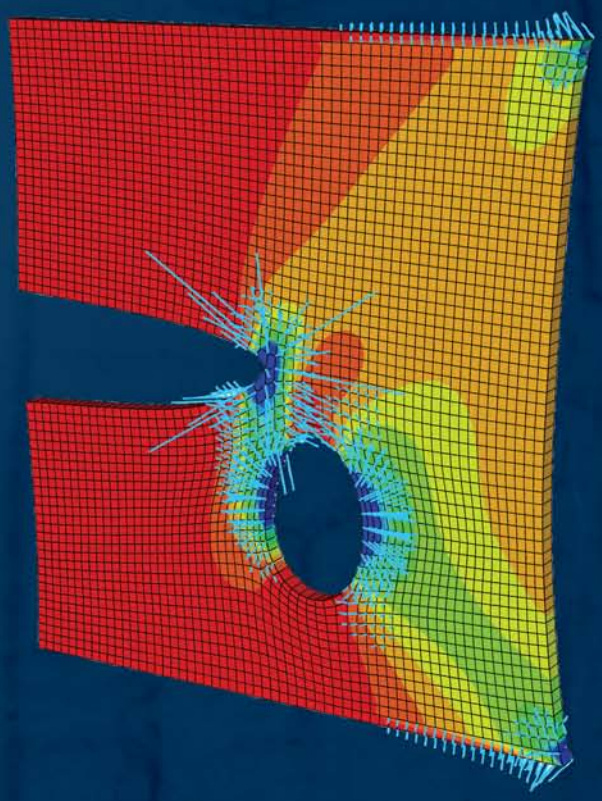

CRC Press
Taylor & Francis Group
A BALKEMA BOOK

CONSTITUTIVE MODELS FOR RUBBER VI

PROCEEDINGS OF THE SIXTH EUROPEAN CONFERENCE ON CONSTITUTIVE MODELS FOR RUBBER, DRESDEN, GERMANY, 7–10 SEPTEMBER 2009

Constitutive Models for Rubber VI

Editors

Gert Heinrich
Leibniz Institute of Polymer Research Dresden, Dresden, Germany

Michael Kaliske
Institute for Structural Analysis, Technische Universität Dresden, Dresden, Germany

Alexander Lion
Institute of Mechanics, University of the Federal Armed Forces Munich, Neubiberg, Germany

Stefanie Reese
Institute of Solid Mechanics, Technische Universität Braunschweig, Braunschweig, Germany

CRC Press
Taylor & Francis Group
Boca Raton London New York Leiden

CRC Press is an imprint of the
Taylor & Francis Group, an **informa** business

A BALKEMA BOOK

CRC Press/Balkema is an imprint of the Taylor & Francis Group, an informa business

Typeset by Vikatan Publishing Solutions (P) Ltd., Chennai, India
Printed and bound in Great Britain by Antony Rowe (A CPI Group Company), Chippenham, Wiltshire

Published by: CRC Press/Balkema
P.O. Box 447, 2300 AK Leiden, The Netherlands
e-mail: Pub.NL@taylorandfrancis.com
www.crcpress.com – www.taylorandfrancis.co.uk – www.balkema.nl

ISBN: 978-0-415-56327-7 (Hbk)
ISBN: 978-0-203-86222-3 (Ebook)

Constitutive Models for Rubber VI – Heinrich et al. (eds)
© 2010 Taylor & Francis Group, London, ISBN 978-0-415-56327-7

Table of contents

Constitutive Models for Rubber VI – Heinrich et al. (eds)
© 2010 Taylor & Francis Group, London, ISBN 978-0-415-56327-7

Foreword

The Sixth European Conference on Constitutive Models for Rubber (ECCMR VI) is hosted in 2009 at the Technische Universität Dresden in Germany and is organized by Gert Heinrich (Dresden), Michael Kaliske (Dresden), Alexander Lion (München) and Stefanie Reese (Braunschweig). In order to reach a high scientific quality and to consider academic as well as industrial aspects, the International Scientific Committee consists of distinguished personalities from universities and industry. Accordingly, the organizing committee would like to thank Herbert Baaser, Paul Buckley, James Busfield, Luis Dorfmann, Sanjay Govindjee, Gerhard Holzapfel, Jörn Ihlemann, Mikhail Itskhov, Manfred Klüppel, Will Mars, Alan Muhr, Ray Ogden, Peter Wriggers and Erwan Verron for their valuable cooperation. We also express our gratitude to the organizers of ECCMR V for their useful support: Adnane Boukamel, Lucien Laiarinandrasana, Stephane Lejeunes, Stephane Meo and Erwan Verron. Since such a conference cannot be realized without external sponsoring, the organizing committee takes this opportunity to thank the sponsors for their massive financial support, in particular with regard to the economical difficult year 2009. Finally, we express our gratitude to Manfred Mahlig and Axel Mittendorf for their exemplary assistance concerning the support of the internet platform and the organisation of the conference proceedings.

In many applications, constitutive models are needed to represent the material properties of filler-reinforced elastomers under quasistatic or dynamic, infinitesimal or finite thermomechanical deformations. Filled rubbers are a typical example, in which multiscale science plays the major role in the structure—property relationship. Elastomers are used for many products like tires, shoes, suspension and engine mounts, seals or shock absorbers, to name a few. In industrial development processes, it is profitable to simulate the behaviour of these parts under realistic operating conditions. This challenge necessitates detailed experimental investigations, the development of constitutive models representing the material behaviour in combination with techniques to identify the material parameters and the development of efficient numerical methods. In the past, great interest was in modelling the quasistatic stress-strain-behaviour of rubber but nowadays, the interests also include the influence of environmental conditions on the material behaviour and estimations of the product lifetime. The latest developments to describe the material behaviour of rubber are presented during this conference.

Thus, the invited keynote lectures come from international universities and industry and are presented by James Busfield (Queen Mary University of London, UK), Will Mars (Cooper Tire & Rubber Company, USA) and Christian Miehe (University of Stuttgart, Germany). Their contributions cover the most challenging fields in the context of constitutive modelling: friction and abrasion, damaging under multiaxial loadings and micromechanical approaches in continuum mechanics.

Besides continuum mechanical modelling approaches and industrial applications, other focal points of the conference are finite element simulations and methods, dynamic material properties, experimental characterization, lifetime prediction, friction, multiphysics and biomechanics, reinforcement, ageing, fracture and fatigue as well as micro- and macromechanical approaches. In these areas, we have about 80 outstanding oral and poster presentations from universities, research institutes, rubber industries and software developers. Although the ECCMR was originally a European conference, the organizers are very delighted since the participants come from all over the world. ECCMR VI is a comprehensive platform, where specialists in constitutive modelling, finite element simulation and experimental testing come together to discuss the state-of-the-art in material modelling of elastomers, to develop new ideas or to create new research networks and projects.

Gert Heinrich
Michael Kaliske
Alexander Lion
Stefanie Reese
September 2009

Constitutive Models for Rubber VI – Heinrich et al. (eds)

Foreword (Volume 1)

The extraordinary stress-strain behavior of rubber has presented an opportunity for inventive engineers and a challenge for scientists since the mid-nineteenth century, and continues to do so today. Major branches of theory, such as the statistical theory of rubber elasticity and finite strain elasticity theory, have been spawned by the properties of rubber. Until recently, however, the theoretical framework for large deformations found little application among rubber engineers because the mathematics rapidly becomes intractable for all but the simplest components. The advent of affordable and powerful computers has changed all this, and brought the challenge of rubber to new sets of people—software engineers and desk-top, as opposed to empirical, designers.

The development of the statistical theory of rubber elasticity in the 1940s, of finite strain elasticity theory in the 1950s, and of convenient forms for the strain energy function in the 1970s, all focused on modelling the elastic characteristics of rubber. Although much literature has appeared in recent years following this theme, the Physics of Rubber Elasticity by L.R.G. Treloar (3rd Edition, Clarendon Press, Oxford, 1975) and the proceedings of a Discussion on Rubber Elasticity (Proc.Roy.Soc.London, 1976, A351, No. 1666, 295–406) remain very valuable reviews.

The treatment of rubber as a 'hyperelastic' material—that is, a material modelled by a strain-energy function for finite strain—was implemented into finite strain element analysis in the 1980s and is now widely available in commercial software packages.

However, only a few engineering elastomers—such as unfilled natural rubber and some grades of polyurethane—really conform to the "hyperelastic" ideal. Most other engineering elastomers incorporate "reinforcing" fillers, needed to confer adequate strength properties and also to improve processing characteristics and to enable adjustment of hardness over a wide range. The stress-strain characteristics of such filled elastomers depart significantly from elasticity. Whileways of thinking about these departures—such as "dynamicto-static ratio" of rubber springs—may have satisfied a previous generation of design engineers, there is now an opportunity to apply more sophisticated models.

One major current challenge is thus to model those aspects of the inelastic behaviour that are relevant to engineers, and to do this in such a way that the models are implementable in finite element analysis.

Although potentially the involvement of representatives of several disciplines should facilitate progress, this is only the case if they talk to each other. In practice, software engineers might rely on the literature and on desktop designers as sources of information about rubber, and fail to achieve as good a balance of understanding as they could if they listened also to experimental rubber scientists and empirical designers. Applied mathematicians might develop phenomenological models which address issues of secondary interest to designers, or which misrepresent important aspects of the experimentally observed behaviour. Experimentalists might develop models without reference to the existing framework of continuum mechanics, resulting in internal inconsistencies and difficulty in implementation in software packages. The First European Conference on Constitutive Models for Rubber sprang from the idea of providing a forum for multi-disciplinary discussion, seeking to bring the fragmented strands of recent research together.

Within the UK a start has been made in this direction—through a workshop on Deformation Modelling for Solid Polymers (Oxford University, 1997) and a seminar on Finite Element Analysis of Elastomers (Institution of Mechanical Engineers, London, 1997). The proceedings of the latter are available as a publication of the same name (Professional Engineering Publications, London, 1999). Similarly, in Germany a workshop of Finite Element Analysis—Basics and FutureTrends was organised by the Deutsche Institute für KautschukTechnology (Hannover, 1998). The interest in these essentially national meetings suggested that further cross-fertilisation should be stimulated by providing a European forum for discussion.

The contributions to this Proceedings cover a wide range of subjects. Consistent with the analysis given above, relatively few authors chose to present hyperelastic models for rubber; however, readers interested in this topic will find ample references to earlier work. Several contributions address inelastic effects

associated with filled elastomers—such as Mullins' effect and quasi-static hysteresis. For others—most obviously in processing uncured rubber—the interest is in modelling viscoelasticity. In addition to stress-strain behaviour, work is presented on frictional contact and on mechanical failure. Looking at the applications side, computational techniques are addressed and applied to a diverse range of components, including tyres, earthquake isolation bearings and intervertebral discs. Overall, the authors have achieved progress in a wide range of areas—including experimental results, theory and practical utility. They raise many questions as well, as one might expect from the first forum of this kind.

We would like to thank our colleagues on the Scientific Committee (R.W. Ogden, Chairman; D. Besdo, R.de Borst, K.N.G. Futler, H.A. Mang, H. Menderez, G. Meschke and H. Rothert) and all the authors who have worked with us to produce this book.

A. Dorfmann
A.H. Muhr
Vienna/Hertford, June 1999

Constitutive Models for Rubber VI – Heinrich et al. (eds)
© 2010 Taylor & Francis Group, London, ISBN 978-0-415-56327-7

Sponsors

The organizing committee gratefully acknowledge the support received from the following sponsors.

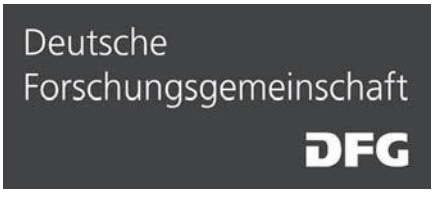

Ageing

Constitutive Models for Rubber VI – Heinrich et al. (eds)
© 2010 Taylor & Francis Group, London, ISBN 978-0-415-56327-7

Accelerated ageing of polychloroprene for marine applications

V. Le Saux, Y. Marco & S. Calloch
Laboratoire Brestois de Mécanique et des Systèmes (EA4325), Brest, France

P.Y. Le Gac
Ifremer—Service Matériaux et Structures, Plouzané, France

N. Ait Hocine
Laboratoire d'Ingénierie des MATériaux de Bretagne (EA4250), Brest, France

ABSTRACT: The accurate evaluation of the lifetime and mechanical properties of rubber-like materials is of particular interest for designers in order to ensure the reliability of such materials and the safety of structures. This is especially true for sensible applications, like offshore pipelines or dry dock seals, needing frequent maintenance operations. The frequency of these operations, and thus their cost, could be reduced by a better understanding of rubber-like materials ageing. To reduce the time cost of this evaluation, accelerated ageing tests using temperature, acid or humid environments as acceleration factors are usually carried out. However, these tests convey unavoidably some artificial phenomena like diffusion limited oxygen, which makes difficult the use of the results. In this study, we focused on a polychloroprene rubber, aged under several accelerated conditions (renewed natural seawater and air ageing both for temperature ranging from 20°C to 80°C). Physical measurements (IR and Raman analysis) are carried out to understand the mechanisms involved in the material degradation. Several mechanical tests are also achieved (uniaxial tension and instrumented micro-hardness tests) in order to observe the consequences of the degradation of the material on its mechanical behaviour.

1 INTRODUCTION

Polychloroprene rubbers are used in various fields thanks to their good constitutive mechanical behaviour, their ability to be effective towards ageing effects and their good resistance to hydrocarbons or aggressive environments such as seawater. For example, they can be found in dry dock seals and offshore applications (pipelines). These structures can spend several years underwater, either continuously or intermittently, and the material selected must be shown to retain its mechanical properties.

Ageing is a complex phenomenon that covers a broad spectrum of multidisciplinary domains from the description of physico-chemistry to the structural analysis with properties gradients (Ofta 2003). To evaluate the durability of a structure, three main requirements are needed:

- the development of experimental techniques that allow the identification of the ageing mechanisms and the main factors controling their kinetics;
- the reduction of studies duration using accelerated ageing experiments whose reliability must be controlled;
- the identification of models for the indicator evolutions identified on samples aged in real or accelerated conditions.

Ageing was for a long time, and still remains nowadays, chemist business. However, lifespan prediction models and relevant end-of-life criteria are based on mechanical concepts. Any ageing study would thus have to contain two aspects. The first one is dedicated to the description of the material microstructure modifications related to the degradation mechanisms occurring at a microscopic scale and to the development of kinetic models in order to predict the microstructure evolution (Gillen et al. 1995) or (Colin et al. 2004). The other one relied on the consequences of these microstructure changes on the macroscopic mechanical properties (Woo and Kim 2006). For both aspects, accelerated ageing experiments to reduce the time characterization are required. An extrapolation to service condition can be realized under certain

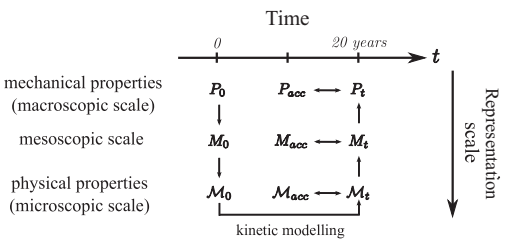

Figure 1. Ideal method for the study of a material ageing.

conditions using for example Arrhenius approach (or any method based on time-temperature superposition principle). The literature shows that most of the studies focus on only one aspect, few studies tried to link these aspects (Celina et al. 2000). This observation can be explained by the gap between the chemical and mechanical scales.

The aim of this study is to reduce the gap between these aspects in order to be more confident in ageing prediction. To reach this goal, the first requierement is to use relevant accelerated ageing conditions. Mechanical and physical experiments are then performed on aged samples. The aim of the first ones is to observe the influence of ageing on classical mechanical macroscopic properties, whereas the aim of the second ones is to identify the ageing mechanisms as a step towards a kinetic model. To make the link between macroscopic and microscopic scales easier, an intermediate scale is added, representative of both approaches. Figure 1 summarizes the method we would like to set-up to predict the evolution of the mechanical behaviour.

2 ACCELERATED AGEING PROTOCOLS

2.1 *Materials*

The samples studied are polychloroprene rubbers afforded by Trelleborg Offshore. For each ageing conditions, a batch of samples is taken from the vessels for several durations. Each batch is composed of one 2 mm-thickness sheet of dimensions 150×150 mm^2, one 8 mm-thickness sheet of dimensions 100×150 mm^2, one compression plot, four AE2 samples and two pure shear specimens.

2.2 *Accelerated ageing conditions*

One key aspect of any ageing studies is the development of relevant accelerated ageing protocols. The aim of these tests is to reduce the characterization time. This is achieved using acceleration factors such as temperature, acid or humid environments. The fundamental aspect of these tests is that they must be representative of natural ageing, *i.e.* only the kinetics of the ageing mechanisms are modified, not the mechanisms themselves. Therefore, the environment in which ageing is realized have to be the same than the natural ageing one. Laboratory ageing was performed in sealed vessels containing renewed natural seawater maintained at different temperatures (20°C, 40°C, 60°C and 80°C) and realized at the Ifremer (center of Brest). A thermo-oxydative ageing in air-circulating oven at 40°C, 60°C, 80°C is also realized in order to compare the effect of the ageing mechanisms on the constitutive mechanical behaviour (these results will not be discussed in this paper).

2.3 *Reference state*

During the ageing, seawater is absorbed into the polymer by a diffusion mechanism. As water is acting as a plasticizer, the mechanical behaviour depends on the ageing degree but also on the amount of absorbed water. In order to be able to compare results and to analyse only the consequence of ageing effects (and not the effect of water), all the experiments were carried out after water loss, *i.e.* after mass stabilization, reached at room temperature.

3 MECHANICAL OBSERVATIONS

3.1 *Uniaxial tension results*

Normalized tensile samples, commonly named H_2 samples, were cut from 2 mm sheets. Experiments were realized on a Lloyd Instruments LR5k+ equipped with a 1 kN loading cell at a displacement speed of 10 mm/min. Deflection was measured using a laser extensometer. Figure 2 shows some experimental curves. The effects of ageing are especially visible for low to mid deformation range (up to 150%), which is the work deformation range, where an important rise fo the initial stiffness is observed. The behaviour afterwhile remains almost unchanged. We can also note a drop of the ultimate properties (elongation and stress at break). Under cyclic loading, we observe an increase of the hysteresis loop (Figure 3), which is also observed for cyclic sollications on massive specimens (AE2). The increase of the hysteresis loop is also related to a higher heat build-up under fatigue sollicitation on AE2 specimen (see the paper of Marco et al. in the present proceedings for more details). Under fatigue sollicitation with a loading ratio equal to zero and a maximum loading corresponding to a maximum principal strain equal to 50%, we observe a decrease of the fatigue life.

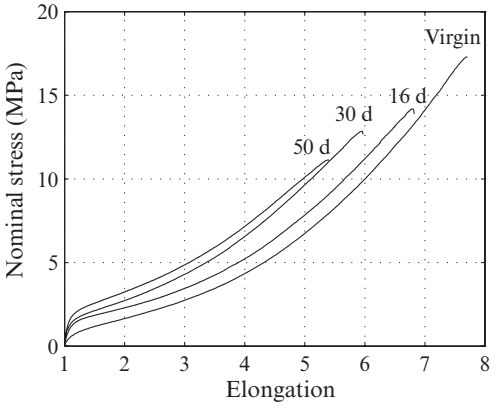

Figure 2. Stress-elongation curves obtained for an ageing temperature of 80°C on H_2 samples.

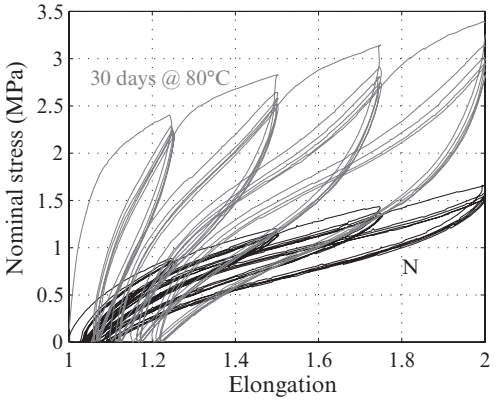

Figure 3. Comparison of cyclic stress-elongation curves for the initial material and an aged one on H_2 samples.

3.2 *DMA results*

Dynamic Mechanical Analysis (DMA) were performed on a 01dB-Metravib DMTA equiped with a loading cell of 150 N. Dynamic strain control tests were realized at 1 Hz. Some results are illustrated on Figure 4. A significant evolution of the conservative modulus E' can be observed, which can be correlated to the initial stiffness rise observed during uniaxial tension test. On the other hand, no significant evolution of the dumping factor tan δ is observed within the dynamic strain rate studied whereas we observed hysteresis loop augmentation during the uniaxial tension tests for larger deformations.

3.3 *Modulus profiling*

Accelerated ageing tests often convey some artificial phenomena. One example is the phenomenom of diffusion limited oxygen observed during thermo-oxydative ageing for high temperatures (Wise et al. 1997). These phenomena make the interpretation of the experimental results difficult because materials are heterogeneous. One appropriate and simple method to mechanically quantify these heterogeneities is to use modulus profiling (Celina et al. 1998). The micro-hardness tester used is developped by CSM, with a Vickers tip. The rubber specimens were cut in cross-section from the 2 mm thickness sheet and encapsulated in epoxy resin to improve sample handling and to insure repetability. The surface was smoothly polished and the modulus profile was obtained by measuring individual modulus data across the cross-sectioned surface of the sample. Each point correspond to the mean of five measurements. One example of modulus profiles is given in Figure 5. The results shows a mean augmentation of the modulus with

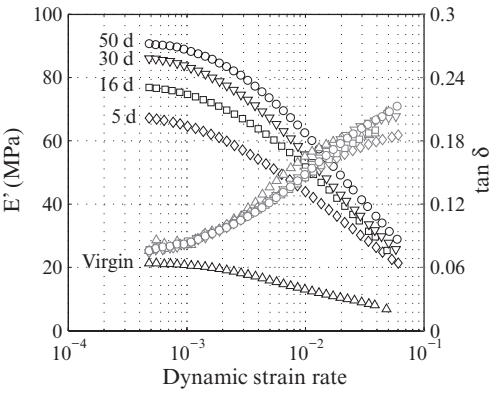

Figure 4. Evolution of the conservative modulus and dumping factor for various ageing conditions at 80°C.

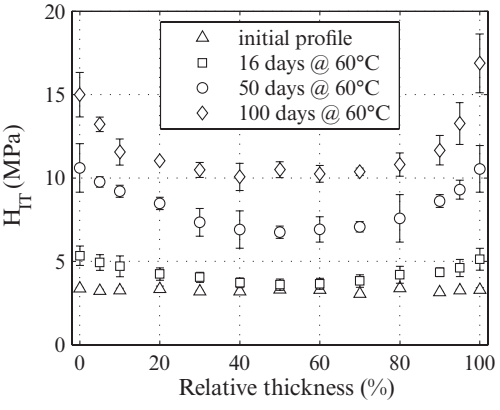

Figure 5. Modulus profiles obtained for various ageing time at 60°C.

increasing ageing duration. This observation can be correlated to the augmentation of the initial modulus observed during uniaxial tension experiments, and to the evolution of the conservative modulus in DMA. Figure 5 also highlights heterogeneities (difference between the surface and the bulk) which are, for the moment, observable only for high temperatures (40°C, 60°C and 80°C) and indicates that accelerated ageing could convey artificial phenomena which are not likely to occur in real ageing conditions. This hypothesis has to be checked by further analysis. One direct consequence of these heterogeneities is that the classical use of mechanical results is false.

4 PHYSICAL OBSERVATIONS

From a mechanical point of view, we have enough informations to set up an Arrhenius-type method to predict the lifetime of the material. But this method can exhibit weaknesses and is to avoid when there is a lack of experimental datas (Celina et al. 2005). For a better understanding of the mechanical behaviour modification and in order to be more predictive, the identification of the ageing mechanisms is needed. We present in this section the analysis achieved and the first conclusions that can be drawn.

4.1 *Gravimetric analysis*

As the ageing is operated in renewed natural seawater, it is important to carry out gravimetric analysis (loss of components, water sorption). They consist in weighting regularly some specimens (here sheets: dimensions 5 cm × 5 cm) during time, the amount of water that have been absorbed by the material is considered equal to the increase in mass of the specimen. Figure 6 gives the results of gravimetric experiments for the four temperatures studied. Weight change is shown as a function of the square root of time of immersion divided by the thickness of the sheet, $t^{1/2}e^{-1}$. This scale is conventional for diffusion data, in order to see if a Fickian model of diffusion can be applied (which is not the case here). From these results, we can observe two main phenomena: an initial weight rise and a weight loss. The weight rise can be attributed to water sorption, whilst the weight loss can be explained by the leaching of low molecular weight components.

4.2 *IR and Raman spectrum*

In order to go further in the investigation of degradation mechanisms, IR spectroscopy have been used. Infra red spectroscopy of organic materials is a widely used technique which provides information on chemical structure. For example, degradation may lead to the formation of additional bands or to the consumption of others. According to some authors (Mott and Roland 2001), ageing of rubber is primarly due to oxydation, even in seawater. To check the validity of this assumption, one sample have been oxydized in an air circulating oven at a temperature of 120°C for 7 days. The comparaison between IR spectrum of this sample and another that has been aged for 130 days at 60°C in seawater is proposed on Figure 7. The C–Cl band at 825 cm^{-1} is used for all the spectrum as internal referencing. During the thermal oxidation of rubbers, a general broad increase in the hydroxyl (~3400 cm^{-1}), carbonyl (~1720 cm^{-1}) and ester (~1175 cm^{-1}) regions of the spectrum is observed. As these regions are not modified for the marine environment aged sample, we can

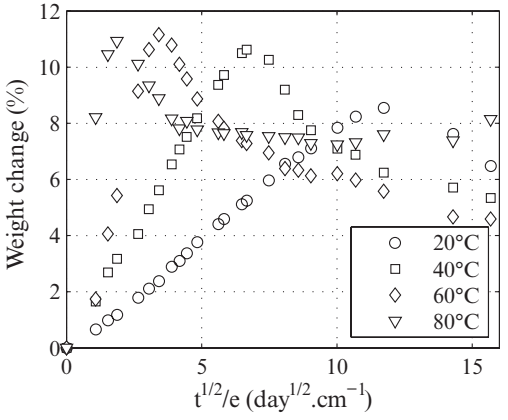

Figure 6. Evolution of the weight change for the different ageing conditions. All these measurements are performed on 2 mm thickness sheets.

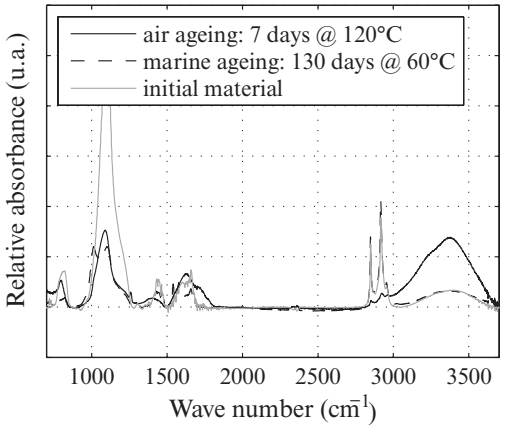

Figure 7. Comparison between the IR spectrum of an oxydized sample and a marine environment one.

say that oxydation of the material is observed. This observation can also be made for all the other ageing conditions, which goes against Mott and Rolland assumption. We have also carried out Raman spectroscopy, which is a technique that complements IR spectroscopy. All Raman spectrum are realized in a water droplet in order to avoid the degradation of the material with the laser during the experiment. One advantage of the Raman spectroscopy is that it is possible to realize a mapping spectrum without cutting the specimens with a microtome. Figure 8 shows some representative results. We can observe different spectrum, which means that the degradation is not homogeneous along the thickness and has also been noticed on the modulus profiles. We note the apparition of a band at 1014 cm^{-1} which can be assigned to a C–O or a C–C band, a reduction of the 1660 cm^{-1} band, attributed to the C=C band, and the apparition of a band at 3500 cm^{-1}, assigned to a O–H band. The degradation could be explained by the degradation of the polychloroprene matrix (deshydrochlorination for example) and a degradation or consumption of the antioxydants. Further testing are running to check theses hypothesis and the firsts results are presented in the next subsections.

4.3 *OIT determination*

Oxydative induction time (OIT) have also been performed on the 8 mm thickness sheets according to ISO 11357-6. OIT is a relative measure of a material's resistance to oxidative decomposition and is determined by the onset of exothermic oxidation in a material at a specified temperature in an oxygen atmosphere (Ginic-Markovic et al. 1998). Therefore, OIT is a global measurement and is not intended to provide the concentration of specific antioxydants. Results are shown on Figure 9. OIT differences are observed along the thickness, which means that the resistance of the material to oxydative decomposition is heterogeneous. We also note a reduction of the resistance to oxydation with the severity of the ageing. This evolution could

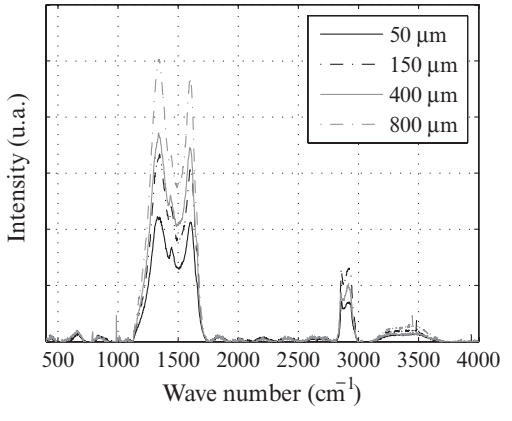

Figure 8. Raman spectrum along the thickness of a 2 mm sheet for the 50 days @ 40°C ageing condition.

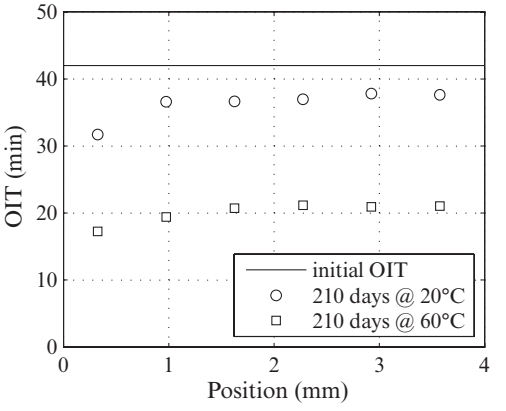

Figure 9. OIT profiling for two ageing conditions.

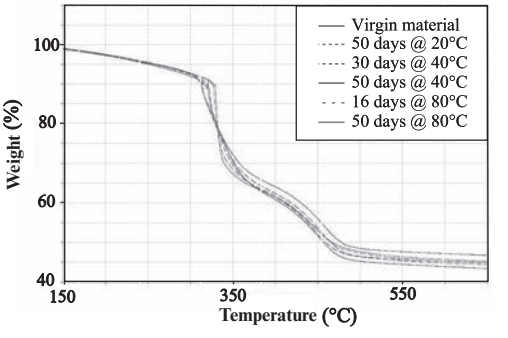

(a) Evolution of the weight

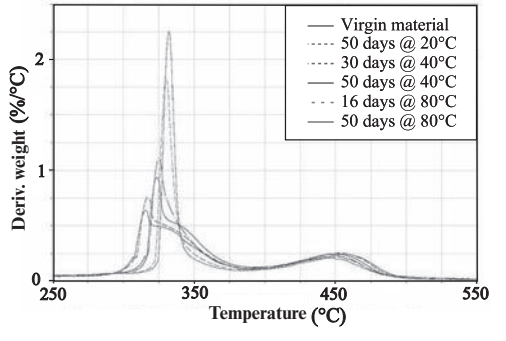

(b) Evolution of the weight derivative

Figure 10. TGA results for different ageing conditions under nitrogen atmosphere.

be explained by the antioxydants consumption, the antioxydants migration or a polychloroprene matrix modification. Further analysis need to be carried out to check these hypothesis.

4.4 *Thermogravimetric analysis*

Thermogravimetric Analysis (TGA) measures the amount and rate of change in the weight of a material as a function of temperature or time in a controlled atmosphere (air or nitrogen). Measurements are used primarily to determine the composition of materials and to predict their thermal stability at temperatures up to 1000°C. This technique can characterize materials that exhibit weight loss or gain due to decomposition, oxidation, or deshydratation. Experiments have been carried out according to NFT46-047 (B procedure). Some results are presented on Figure 10. No components seem to be lost during ageing and only the degradation kinetic of polychloroprene matrix are affected (evolution at 260–275°C), which seems to indicate that the ageing is primarly due to the degradation of the polychloroprene matrix.

5 CONCLUSIONS

In this study, we focused on the ageing of a polychloroprene rubber in a marine environment and presents the first results of a large experimental campaign. Relevant accelerated ageing conditions have been performed in sealed vessels containing renewed natural seawater maintained at different temperatures. Classical mechanical tests have been carried out on aged materials. We have noticed a significant rise of the initial stiffness during uniaxial tests. This observation can also be drawn from DMA and microhardness measurements. Under cyclic sollicitations, a significant rise of the hysteresis loop have been noticed, and correlated to an augmentation of the heat buildup during fatigue test on AE2 specimen. Physical measurements, whose goal was to determine the ageing mechanisms, have been carried out. The first results indicate an heterogeneous degradation along the thickness. The ageing mechanisms could be attributed to the degradation of the polychloroprene matrix, but also to the degradation or consumption of the antioxydants. Some further analyses would let us know whether or not, one phenomenom is dominating. The identification of the ageing mechanisms is the first step leading to the developement of a kinetic model. Finally, modulus profiling seems to be the good tool to extrapolate the observations made at a microscopic scale (ageing mechanisms) to the macroscopic scale (constitutive mechanical behaviour). To validate the method proposed here, some measurements on structures aged in service up to 20 years are planned.

ACKNOWLEDGEMENTS

The authors would like to thank the Britanny region for its financial support and all the actors of the FEMEM project (ENSIETA, Ifremer, Trelleborg Modyn, Trelleborg Offshore, DCNS-Brest, Cesman, UBO, Conseil Général du Finistère, Brest Métropole Océane, Région Pays de la Loire).

REFERENCES

Celina, M., K. Gillen, and R. Assink (2005). Accelerated aging and lifetime prediction: review of non-Arrhenius behaviour due to two competing processes. *Polymer Degradation and Stability* 90, 395–404.

Celina, M., J. Wise, D. Ottesen, K. Gillen, and R. Clough (1998). Oxydation profiles of thermally aged nitrile rubber. *Polymer Degradation and Stability* 60, 493–504.

Celina, M., J. Wise, D. Ottesen, K. Gillen, and R. Clough (2000). Correlation of chemical and mechanical property changes during oxydative degradation of neoprene. *Polymer Degradation and Stability* 68, 171–184.

Colin, X., L. Audouin, and J. Verdu (2004). Determination of thermal oxidation rate constants by an inverse method. Application to polyethylene. *Polymer Degradation and Stability* 86, 309–321.

Gillen, K., J. Wise, and R. Clough (1995). General solution for the basic autoxydation scheme. *Polymer Degradation and Stability* 47, 149–161.

Ginic-Markovic, M., N. Roy Choudhury, M. Dimopoulos, D. Williams, and J. Matisons (1998). Characterization of elastomer compounds by thermal analysis. *Thermochimica Acta* 316, 87–95.

Mott, P. and C. Roland (2001). Aging of natural rubber in air and seawater. *Rubber Chemistry and Technology* 74, 79–88.

Ofta (2003). *Vieillissement et durabilité des matériaux*. Arago 28. OFTA.

Wise, J., K. Gillen, and R. Clough (1997). Quantitative model for the time development of diffusion-limited oxydation profiles. *Polymer* 38(8), 1929–1944.

Woo, C. and W. Kim (2006). Heat-aging on the material properties and fatigue life prediction of vulcanized natural rubber. *e-Journal of Soft Materials* 2, 7–12.

Constitutive Models for Rubber VI – Heinrich et al. (eds)
© 2010 Taylor & Francis Group, London, ISBN 978-0-415-56327-7

Consideration of environmental influences on fatigue tests of elastomer components

J. Spreckels & U. Weltin
Technische Universität Hamburg, Harburg, Germany

M. Flamm & T. Steinweger
Beratende Ingenieure Flamm, Germany

ABSTRACT: This paper proposes a method, which allows a systematical consideration of environmental influences on test-time-reduced fatigue tests of elastomer components. So the damage of the elastomer component caused by the combination of these influences and mechanical loads is nearly equivalent to the damage occurring during the service lifetime of the elastomer component. By means of test results it is shown that due to the consideration of temperature- and ozone-influences, a significant improvement of the consistence of damage effects between tested components and components taken out of practical service can be achieved. Thus, tests based on this method allow an improved judgement of the long-time behaviour and the expected lifetime in service of the tested components.

1 INTRODUCTION

In service, elastomer components used for example as mounts in vehicle engineering, often undergo mechanical loads as well as applicational or environmental influences like temperature or ground-level ozone. These influences may affect the damage occurring in service life and additionally the expected lifetime.

Fatigue tests to predict the expected lifetime normally do not consider environmental influences. Additionally, these tests in most cases are performed with the use of methods for test-time-reduction, which also decreases possible environmental effects caused by the laboratory atmosphere.

To close this gap, a testing method is developed, which allows a systematical consideration of the mentioned environmental influences on test-time-reduced fatigue tests of elastomer components to improve the prediction of lifetime and long-time behaviour of the component in service and also allows an advanced comparison of different components or rubber mixtures.

2 OPERATIONAL AND ENVIRONMENTAL INFLUENCES IN SERVICE AND THEIR EFFECTS

For a reliable prediction of the lifetime of an elastomer component it is necessary to get to know the influences which affect the lifetime in service and their interdependencies to each other. The most important influences for engineering rubber components are described below.

2.1 *Mechanical loads*

Mechanical loadings are of significant importance for the lifetime of an elastomer component. These loads often have a stochastical shape and affect multiaxially.

After sufficient repetitions of load cycles with sufficient levels, mechanical loadings cause—often enhanced by further factors—the development and growth of fatigue cracks which start from flaws

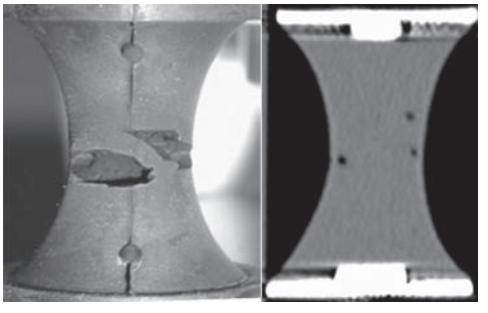

Figure 1. Left: fatigue cracks on an elastomer buffer (made of NR), right: cross-section (computer-tomography scan) with cracks/cavities in material bulk (earlier stage than left).

(Flamm 2005). When the cracks reach a certain size, the elastomer part is no longer able to fulfill its desired function completely, so the lifetime is ended.

Statical loads additionally lead to creep or relaxation processes. Creep describes a progressive increasing of the deformation while stress relaxation means the progressive decrease in stresses (e.g. Gent 2001).

2.2 *Temperature*

A further important factor for the lifetime is the temperature of the elastomer component. This component-temperature is mainly defined by the ambient temperature of the application. Higher temperatures may occur because of the damping of the material due to dynamic loads or may be generated by heat sources near the elastomer part.

In many cases, the temperature varies over time quite a lot due to different service conditions and different ambient temperatures.

Temperature has a great effect on many properties and processes of an elastomer component.

At very low temperatures (typically below –60°C for NR) the material shows a "glassy" behaviour with a relatively high stiffness. The stiffness significantly decreases with increasing temperature (typically up to –30°C for NR), in this region the behaviour seems to be leather-like. In the region above these temperatures (typically –30°C to 100°C for NR) the behaviour is rubber-like, which is desired for most applications. In this region the stiffness is also (but much lower) dependent of the temperature. The amount and direction of this dependency differs due to different applications and materials (Flamm 2003).

Elevated temperatures increase the reaction rates of chemical reactions. Mathematically this can be described with the help of the Arrhenius-equation.

$$V_1 = V_2 \cdot e^{-\frac{E_A}{k}\left[\frac{1}{T_1}-\frac{1}{T_2}\right]} \tag{1}$$

In this equation V_1 and V_2 stand for the reaction rates at the absolute temperatures T_1 and T_2 (in Kelvin) respectively. E_A is the activation energy of the process, k is the Boltzmann constant.

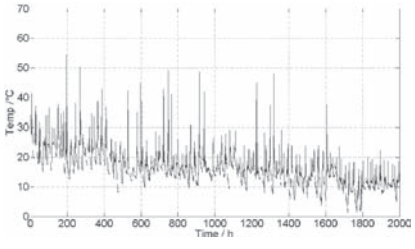

Figure 2. Temperature-time-history (measurement data).

For the rubber material, this means that ageing processes like oxidation and post-curing are significantly accelerated by high temperatures. The chemical part of creep or relaxation processes is also accelerated.

Internal stresses of rubber-metal parts also depend on temperature caused by the distinction of the thermal expansion coefficient of rubber and metal.

Very high temperatures cause effects like chemical degradation which lead to a destruction of the material and so of the component.

The effectivity of the anti-ageing-system of elastomers protected by waxes and chemical ingredients also depends on the temperature (Bhowmick 1991). The wax migrates to the surface to build a protecting film (see next paragraph). The migration rate of the wax undergoes a temperature dependence. At low temperatures, the blooming of the wax only takes places slowly, while at high temperatures the solubility of the wax increases which leads to less thicknesses of the wax layer. Thus, the selection of a wax or wax blend suitable for the occurred temperatures in service is very important for an effective protection. The migration of the wax also supports the migration of additional chemical anti-ageing ingredients, so the temperature dependency also involves the effectivity of the complete anti-ageing-system.

2.3 *Weathering, especially ground-level-ozone*

Weathering is a complex action of different environmental influences.

Of these, a very important influence on elastomers with unsaturated main chains like NR has the ground-level ozone. Ground-level ozone (tri-atomic oxygen O_3) normally only occurs in very low concentrations in low pphm-scale (parts per hundred million), but even these low concentrations often cause damages on elastomer components.

Elastomers with unsaturated main chains are highly susceptible for ozone attack, because ozone reacts with the double bondings of the main chain which results in formation of ozone cracks when the elastomer is strained during ozone attack. Ozone cracks start on the rubber surface and grow perpendicular to the direction of the strain. Below a threshold value for the strain (so called "critical strain"), ozone cracking does not take place. Strains slightly above the critical strain lead to only a few but deep ozone cracks, while with increasing strain the number of cracks increases but the length and depth decreases (e.g. Gent 2001).

Figure 3 shows ozone cracks on a section of a specimen. In the left, there is no cracking compared to the right, possibly because of decreasing strain due to the geometry.

Ozone cracks may grow deep into the material and may act initiating for mechanical crack growth.

To avoid ozone damages, like mentioned before, protecting ingredients are incorporated into the rubber mixture. These are physically working protectors like waxes which only protect at static loads. For protection under dynamic loads chemical antiozonants are used. The most effective chemical antiozonants lead to a staining of the elastomer when acting.

2.4 *Tests to judge the long-time behaviour*

2.4.1 *Fatigue tests*

State of the art is a multiaxial fatigue test which can be used to judge the expected lifetime due to mechanical initiation and propagation of cracks in the elastomer component. As load signal representative load-time histories can be used which can be obtained from service measurements or simulations.

Omission tools like the Rainflow-filtering are used to reduce the usually long time for testing. This method omits load cycles of small amplitudes out of the signal which only have very low influences on the elastomer component's damage (Steinweger 2003).

Beside these tests on components, there are standards for fatigue tests on specimens (overviews e.g. in Brown 2006 and Nagdi 2004).

These tests can be performed to compare different rubber mixtures, to generate fatigue diagrams like Haigh-Diagrams (e.g. for damage calculations) or for fundamental research. In many cases synthetically generated (block) signals are used. Specimens are standarded tensile bars or buffers, for example.

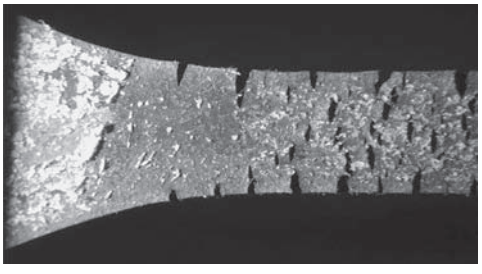

Figure 3. Ozone damage on a section of a tension bar made of NR after 24 h in ozone, strain direction to left/right.

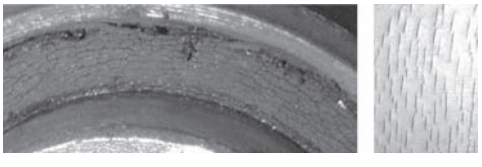

Figure 4. Ozone and fatigue phenomena on a rubber bushing (left) and on a rubber spring (right) respectively.

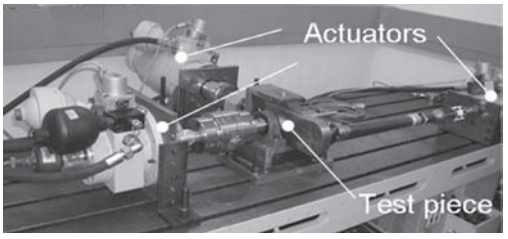

Figure 5. Three-axis test rig.

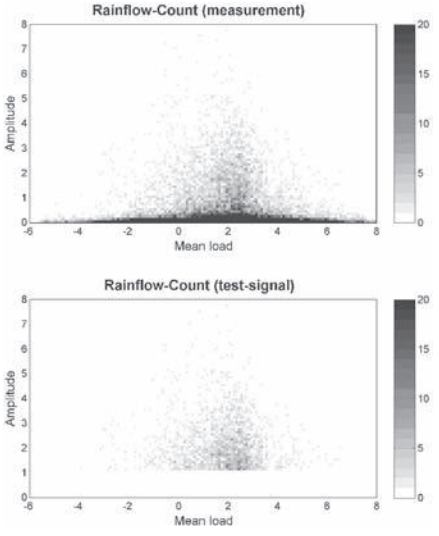

Figure 6. Rainflow-filtering (schematic).

2.4.2 *Temperature tests*

The long-time influence of temperature is often investigated with specimens who are exposed to a high-temperature load over a certain period of time.

Due to the high temperatures, the influence of the temperature is accelerated. After certain time intervals properties (e.g. elongation at break or hardness) of the specimens are investigated and compared to the properties of a non-aged specimen (overviews e.g. in Brown 2006 and Nagdi 2004).

So, different rubber mixtures can be compared to each other. The suitabilty for service has then to be judged with experience and know-how.

2.4.3 *Ozone tests*

The durability against ozone attack is also in many cases investigated via specimen tests.

Therefore specimens get in most cases a static strain and are exposed to an ozoniferous atmosphere. After a certain time the specimens are to be inspected to find out if and to which extend crackings occurred (overviews e.g. in Brown 2006 and Nagdi 2004).

The time reduction compared to the exposition to the real atmosphere is accomplished with a significantly higher ozone concentration.

Like the formerly described methods, this method is mainly suitable to compare different rubber mixtures.

3 SUGGESTED TEST METHOD

The test method described below considers the effects of the former described influences.

The influences appearing in service are to be applied to the test-time-reduced fatigue test so they act in an equivalent amount and cause nearly equivalent damage effects.

3.1 *Test method*

The test method is based on a (if necessary multiaxial) fatigue test. In this test, the elastomer component is exposed to a sequence of loads, which is representative of the loads occurring in service. Test-time can be reduced with the use of omission methods, like described above.

To adjust the ozone attack occurring in service, the elastomer part is additionally exposed to an ozoniferous atmosphere during the fatigue test. It seems necessary to apply the ozone exposition during the test because the mechanical load situation has a significant interdependency to the ozone attack. So, it is assumed that ozone attacks only in the same way as in service, when the service loads are applied. A static exposition could only adjust one strain situation and additionally static ozone protections like waxes would decrease the ozone attack.

As one result of the test time reduction the ageing of the rubber material is reduced compared to the exposition in service. To compensate this, the thermo-oxidative ageing of the material is performed via an exposition of the component to a (relatively) high temperature before the fatigue test (pre-ageing) and/or during certain breaks in the fatigue test which have been arranged for this ageing time (in-between ageing).

3.2 *Test rig*

To validate the proposed method, a test rig has been developed and built up to test elastomer components in the described way. The mechanical loadings (in this application) are applied multiaxially. The temperature of the component can be adjusted with a heating system. To obtain the increased ozone concentration the test rig is equipped with a testing chamber with an external ozone generator and annihilator.

3.3 *Approaches to determine test parameters*

As parameters of the test, there are mechanical loads, the component's temperature during the test, the ozone concentration during the test and the temperature, time and (if needed) intervals for the pre- or in-between ageing, respectively.

3.3.1 *Mechanical loads*

The mechanical test loads are obtained from representative service loads which can be measured or simulated with a multi-body-simulation (MBS) for example. Then a rainflow-filtering follows. With this method, the testing time is reduced due to omission of load cycles with small amplitudes. The remaining damage content of the test signal can be estimated with a numerical damage calculation (Flamm et al. 2003).

3.3.2 *Temperature*

During the testing, the elastomer part should be exposed to the most frequently temperature occurring in service. So it is assured that the most frequently temperature situation out of service is used during the test. To determine the temperature, the most frequently temperature is calculated from the representative measurement data.

If it is not expected that the simplification of the temperature-time history of the measurements in this way does provide suitable results (for example due to very large variations, no distinctive average temperature or frequently non-neglectable periods with high temperatures), the usage of temperature collectives is recommended.

3.3.3 *Ozone concentration*

As a first approach for a calculational estimation of the increased ozone concentration it is used that the ozone crack growth rate is nearly proportional

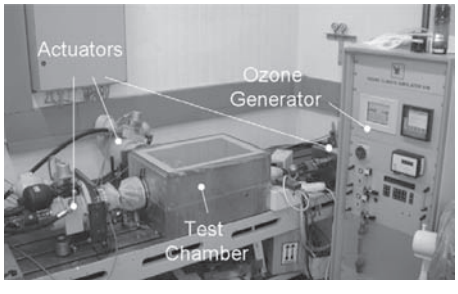

Figure 7. Test rig & chamber.

to the ozone concentration like mentioned in the literature (e.g. Gent 2001, Doležel 1978).

Thus, to get an ozone concentration for the test, an average service concentration is obtained and increased linearly with the factor of test time reduction.

3.3.4 *Accelerated ageing*

For a calculational estimation of the ageing time, a time-temperature-shifting with the use of the Arrhenius equation is used combined with the theory of ageing proceeding (Blaese 2000, Ehrenstein et al. 2007). At this, a span of time at certain temperature is calculated to a (mostly) shorter span of time at the selected ageing temperature of the accelerated exposition.

On the one hand, the exposition temperature should be selected high enough to accelerate the ageing and reduce exposition time, on the other hand, the exposition temperature is limited due to changings in ageing mechanisms and so the validity of the Arrhenius-equation.

The theory of ageing proceeding is used, because the temperature varies while the component is in service. Each temperature causes—according to the time span in which it occurs—a part of the whole material ageing. The whole ageing is obtained in analogy to damage accumulation as the sum of all ageing parts.

So, the temperaure-time-shifting is applied to all of the temperatures that occur in the representative temperature-time history. With the summation, you get an exposition time, during which the material undergoes an equivalent thermo-oxidative ageing like from the temperature-time history.

$$t_{AA} = \sum_{i=1}^{n} t_i \cdot e^{-\frac{E_A}{k}\left[\frac{1}{T_i} - \frac{1}{T_{AA}}\right]} \tag{2}$$

The so calculated ageing time t_{AA} is then multiplied by the expected repetitions of the temperature-time-history in service or in the part for in-between-ageing.

The application of this approach demands the determination of the activation energy for the Arrhenius-equation or the usage of published values (e.g. Mott 2003).

4 TEST RESULTS

Tests with elastomer components were performed using the described test rig. Afterwards these components are compared to components taken out of real service.

As a result the consideration of all mentioned influences causes significant similarities between service and test parts regarding damage effects and the lifetime.

Cracks are caused by ozone and mechanical loads, a distinct differentiation between these two factors seems not always possible.

In many cases, ozone cracks are only or better visible after straining the surface.

Pre-ageing generally decreases the lifetime of the component compared to the lifetime of unaged components. The amount of decrease depends on the exposition time, exposition temperature and the

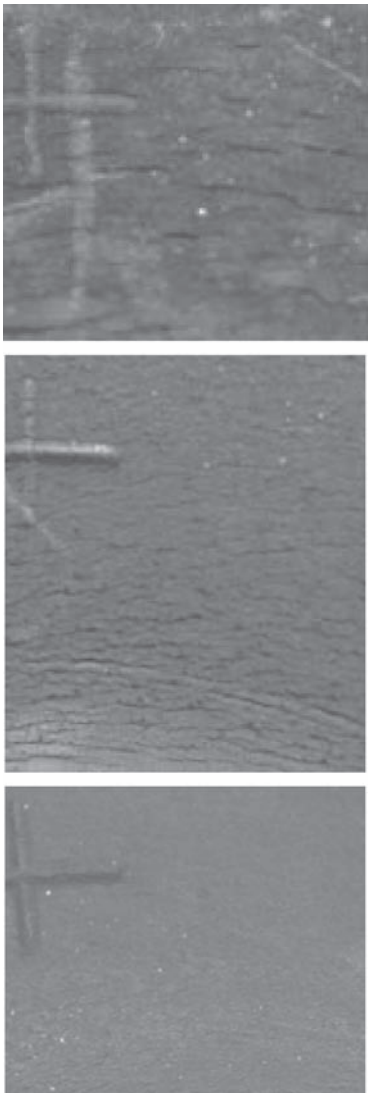

Figure 8. Comparison of component's surface after testing/service: service part (upper picture), tested part with ozone (middle picture) and tested part without ozone (lower picture).

used rubber mixture. The durability against ozone cracking also decreases with increasing ageing. In the investigated case, the pre-ageing has a more important influence on the lifetime than ozone.

The linear approach to determine an equivalent ozone concentration leads to test concentrations that seem to be of suitable regions. Experiments with different concentrations provide that a slight reduction of the calculated concentration seems to improve this approach and so leads to an increased similarity of the damage symptoms of tested components and service components.

5 CONCLUSIONS

The results clarify that with the consideration of environmental and thermal influences for the test, a significant improvement regarding the component's lifetime and the consistence of the damage effects in service and in the test can be achieved, compared to when these effects are neglected.

The observed damages and long-time phenomena are assumed to be caused by a combination of the mentioned mechanical, thermal and ozone influences.

The lifetime is highly dependent on the mechanical loadings and the strength of the material. Thermal ageing decreases this strength and therefore the lifetime.

The approach for a calculational estimation of the ageing time leads to suitable results, comparable to service parts. Whether the effort for an in-between-ageing is endurable and necessary, or the whole ageing can be fulfilled conservatively as pre-ageing before the test, has to be determined in each case.

Ozone has a significant influence on the damage effects. Ozone attack causes cracking that also may decrease the lifetime. To which extent the ozone contributes to a reduction in lifetime depends on the mixture's durability against ozone (also after thermal ageing) and the component itself.

Summing up, a pragmatical method is presented which allows considering ozone and temperature ageing effects on a test-time-reduced fatigue test of elastomer components. The selected approaches to determine testing parameters only need a minimum of material parameters.

The method allows an advanced comparison of different components or rubber materials regarding the long-time behaviour and furthermore allows improved conclusions regarding the service lifetime.

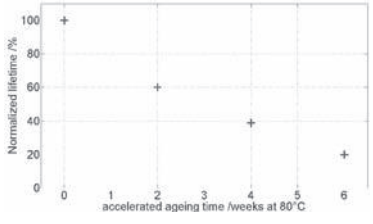

Figure 9. Normalized lifetime as function of ageing time.

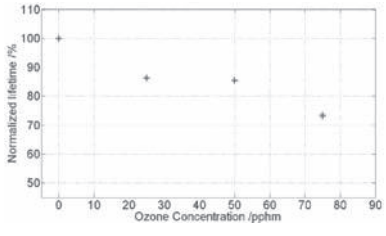

Figure 10. Normalized lifetime as function of ozone concentration.

REFERENCES

Blaese, D. 2000. Methodische Ansätze zur Abschätzung der Lebensdauer von Kunststoffbauteilen bei komplexer Belastung, Shaker, Aachen.

Bhowmick, A. 1991. Fractography of rubbery materials. Elsevier applied science. London.

Brown, R. 2006. Physical Testing of Rubber, Springer.

Doležel, B. 1978. Die Beständigkeit von Kunststoffen und Gummi, Hanser, München Wien.

Ehrenstein, G., Pongratz, S. 2007. Beständigkeit von Kunststoffen, Hanser, München.

Flamm, M. 2003. Ein Beitrag zur Betriebsfestigkeitsvorhersage mehraxial belasteter Elastomerbauteile VDI Düsseldorf.

Flamm, M., Steinweger, T., Weltin, U. 2003. Lifetime prediction of multiaxially loaded rubber springs and bushings. In J.J.C. Busfield & A.H. Muhr, *Constitutive Models for Rubber III, pp. 49–53.* Balkema.

Flamm, M., Steinweger, T., Weltin, U. 2005. Rissbildung und Risswachstum bei Elastomeren, DVM Bericht 237.

Flamm, M., Groß, E., Steinweger, T., Weltin, U. 2005. Creep prognosis for elastomeric parts througt accelerated tests. In P.-E. Austrell & L. Kari (ed.), *Constitutive Models for Rubber IV*; *pp. 445–447*. Rotterdam: Balkema.

Flamm, M., Steinweger, T., Spreckels, J., Brüger, T. 2007. Mechanical Properties of EPDM. In In A. Boukamel, L. Laiarinandrasana, S. Méo & E. Verron (ed.), *Constitutive Models for Rubber V*; *pp. 233–238*. Taylor & Francis/Balkema.

Gent, A. 2001. Engineering with Rubber. 2. Edition. Hanser, München.

Mott, P.H., Roland, C.M. 2003. Alterung von Naturkautschuk in Luft und Meerwasser. in Guimmi, Fasern, Kunststoffe, 11/2003.

Nagdi, K. 2004. Gummiwerkstoffe, Dr. Grupta, Ratingen.

Steinweger, T., Flamm, M., Weltin, U. 2003. A methology for test time reduction in rubber part testing. In J.J.C. Busfield & A.H. Muhr, *Constitutive Models for Rubber III, pp. 27–33.* Balkema.

Constitutive Models for Rubber VI – Heinrich et al. (eds)
© 2010 Taylor & Francis Group, London, ISBN 978-0-415-56327-7

Fatigue life prediction of aged natural rubber material

C.S. Woo, W.D. Kim, B.I. Choi & H.S. Park
Nano Mechanical Systems Research Division, Korea Institute Machinery & Materials, Daejeon, Korea

S.H. Lee & H.C. Cho
Corporate Research & Development Division, Hyundai-Kia Motors, Gyeonggi-do, Korea

ABSTRACT: Aging temperatures play important role in changing the mechanical behavior of rubber, so thermal aging test under different temperatures was carried out to investigate the effect of aging temperatures on the tension, elongation, hardness and fatigue properties of natural rubber. Fatigue life prediction methodology of natural rubber material was proposed by incorporating the finite element analysis and fatigue damage parameter determined from fatigue test. Fatigue life prediction equation effectively represented by a single function using the Green-Lagrange strain and elongation at break. Predicted fatigue lives of the rubber component were in fairly good agreements with the experimental lives within factors of two.

1 INTRODUCTION

The interest of fatigue life evaluation for rubber component such as engine mount was increasing according to the extension of warranty period of the automotive components. A design of rubber components against fatigue failure is one of the critical issues to prevent the failures during the operation. Therefore, fatigue life prediction and evaluation are the key technologies to assure the safety and reliability of mechanical rubber components (Frederick, 1982).

Automotive engine mounts get damaged due to thermal and mechanical loadings. Rubber material was aged during its useful life and the aging phenomena depended upon thermal conditions. Thermal aging under engine room temperature and fluctuating mechanical loading by vehicle dynamic motion have affected the fatigue life of engine mount. When rubber is used for a long period of time, rubber becomes thermal aging, it usually becomes hardened and loses its damping capability. This aging process results mainly from heat due to hysteric loss, and is affects not only the material property but also the fatigue life of rubber.

In this paper, the heat-aging effects on the material properties and fatigue life prediction of natural rubber were experimentally investigated. In order to investigate heat-aging effects on the material properties, the stress-strain curves were obtained from the results of tensile test. The rubber specimens were heat-aged in an oven at the temperature ranging from 50°C to 100°C for a period ranging from 1 to 90 days.

Predictions of fatigue properties of rubber materials and components are currently partly an empiric nature. Fatigue life evaluation of rubber components has hitherto relied mainly on a real load test, road simulator test or bench fatigue test. Although above methods have advantages in accuracy of fatigue life, but cannot be used before the first prototype is made and the fatigue test should be always conducted whenever material or geometry changes are made (Lake, 1997). Fatigue life prediction methodology of vulcanized natural rubber was proposed by incorporating the finite element analysis and fatigue damage parameter determined from fatigue test. Fatigue life tests were performed using the three dimensional dumbbell specimens, which were aged in different amounts. The Green-Lagrange strain at the critical location determined from the FEM was used for evaluating the fatigue damage parameter. Fatigue life prediction equation effectively represented by a single function using the Green-Lagrange.

2 EXPERIMENT

2.1 *Specimen*

Rubber material used in this study is a carbon-filled vulcanized natural rubber, which have the hardness of the International Rubber Hardness Degree 45, 50, 55, 60, 65 (NR45, NR50, NR55, NR60, NR65). Compound recipes, including applied cure conditions, are summarized in Table 1.

Vulcanized rubber sheet about 2 mm thick were pressed and vulcanized with an electrically heated

Table 1. Compound recipes of rubber material.

Ingredient	NR45	NR50	NR55	NR60	NR65
SMR CV60	100	100	100	100	100
C/B FEF	13	22	27	40	40
C/B SRF	–	15	18	20	22
S/A	1	1	1	1	1
ZnO	5	5	5	5	5

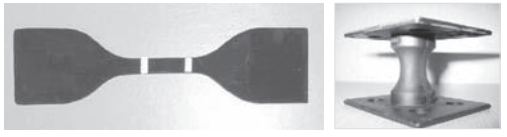

(a) Physical test specimen (b) Fatigue specimen

Figure 1. Geometry of test specimen.

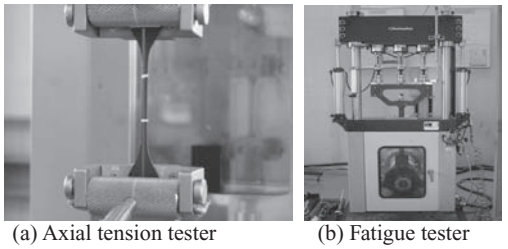

(a) Axial tension tester (b) Fatigue tester

Figure 2. Physical and fatigue tester.

press at 150°C for a given period of time. Dumbbell shaped specimen in Figure 1(a) were cut from vulcanized rubber sheet for the measurement of stress and strain (Brown, 1996). Three-dimensional dumbbell specimen in Figure 1(b) is used for the fatigue damage evaluation of the natural rubber. Three-dimensional dumbbell specimen has an elliptical cross-section and parting lines are located on the minor axis of specimen to avoid undesirable failure at the surface discontinuities (Takeuchi & Nakagawa, 1993).

2.2 *Physical and fatigue test*

To study the ageing property of the rubber materials, samples were aged in an air oven from 50°C to 100°C for 90 day. Then samples were conditioned at ambient temperature for at least 24 h before testing.

Axial tension test was loaded by UTM at a speed of 100 mm/min, and the deflection was measured using a laser extensometer in Figure 2(a). In order to evaluate a fatigue damage parameter of the natural rubber material and the experimental fatigue life, fatigue tests of three-dimensional dumbbell specimen were performed using the fatigue testing system as shown in Figure 2(b). Fatigue tests were conducted in an ambient temperature and heat-aging (70°C) under the stroke-controlled condition with a sine waveform of 5 Hz and the mean displacement is 0, 3, 5, 8, 10 mm at the displacement range is –11 ~ 21 mm.

The fatigue failure was defined as a number of cycles at which the maximum load dropped by 20 percent. As increasing the cycles in initial phase, the maximum load decreased little by little. When the crack grew over the critical size, the maximum load decreased suddenly and the final failure reached.

3 RESULT AND DISCUSSION

3.1 *Physical properties*

The test data of hardness change for specimens heat-aged at different temperatures are shown as symbols in Figure 3 as functions of period. The hardness increases as the heat-aging temperature and/or the heat-aging period increase.

In Figure 4, the stress-strain curves obtained from the tensile test are shown for various temperature and heat aging days. The stiffness increases as the heat-aging temperature and/or the heat-aging period increase. Also, the modulus at 100% increases as hardness increase.

Elongation at break(EB) is very important factor in material properties and fatigue life prediction of rubber components. Test data of elongation change for specimen heat-aged at different temperature are shown as in Figure 5 as functions of period. The elongation decrease as the heat-aging temperature and/or period increase, we known that variation of elongation is a function of period as well as temperature.

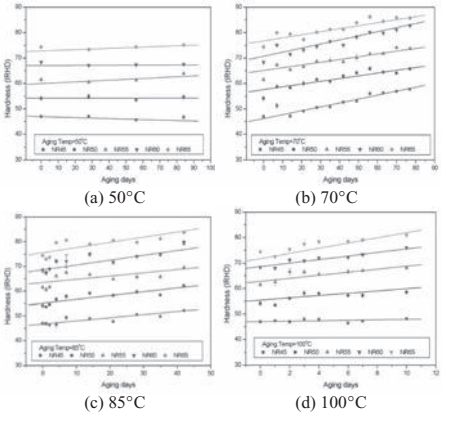

(a) 50°C (b) 70°C

(c) 85°C (d) 100°C

Figure 3. Change of hardness after heat-aging.

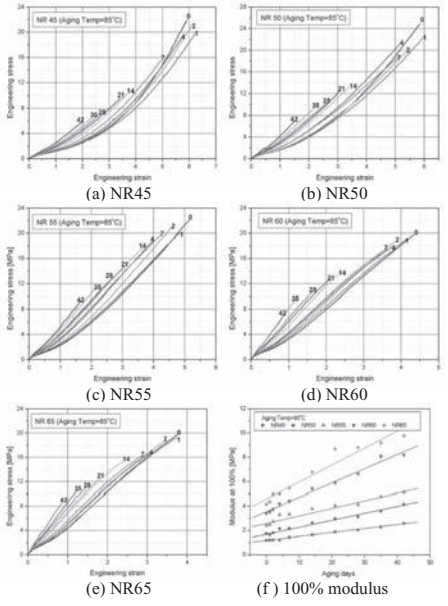

(a) NR45 (b) NR50 (c) NR55 (d) NR60 (e) NR65 (f) 100% modulus

Figure 4. Stress-strain curves and modulus at 85°C.

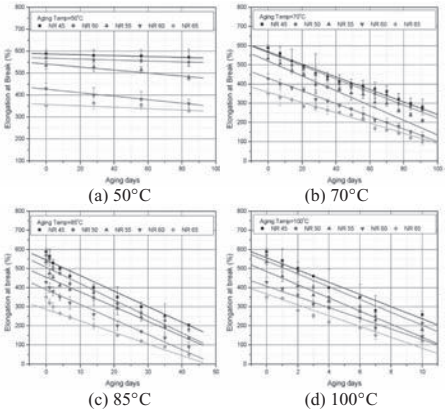

(a) 50°C (b) 70°C (c) 85°C (d) 100°C

Figure 5. Change of elongation after heat-aging.

3.2 *Fatigue life prediction*

Figure 6 shows the relationship between the displacement amplitude and the fatigue life at ambient temperature and 70°C. The fatigue lives decreased according to increasing the mean displacements and hardness. Fatigue life decreased as the tension displacement amplitude and heat aging days increased. It is possible to express the fatigue life with maximum displacement fairly good.

Figure 7(a) shows the Green-Lagrange strain distribution of the three-dimensional dumbbell specimen. The maximum Green-Lagrange strain was found at the surface of the major axis in the

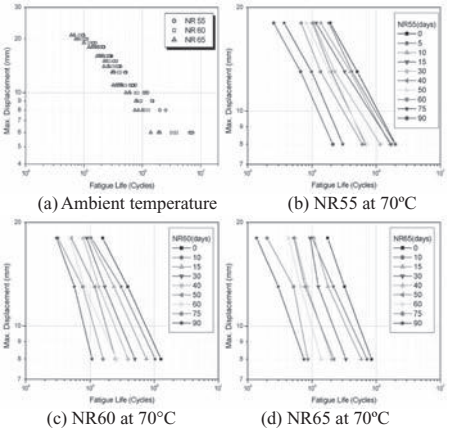

(a) Ambient temperature (b) NR55 at 70ºC (c) NR60 at 70°C (d) NR65 at 70ºC

Figure 6. Fatigue life versus maximum displacement.

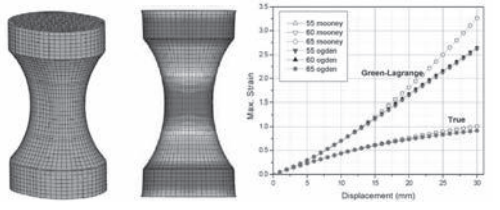

(a) Finite element analysis (b) Strain-displacement

Figure 7. Finite element analysis of three-dimensional specimen.

dumbbell specimen. The Green-Lagrange strain at the critical location determined from the finite element analysis was used for evaluating the fatigue damage parameter of the natural rubber. The displacement and maximum Green-Lagrange strain curve was used for generating a fatigue life equation of the natural rubber expressed by the maximum Green-Lagrange strain as a damage parameter. The maximum Green-Lagrange strain distribution of the three-dimensional dumbbell specimen under displacement was shown in Figure 7(b).

By using the result of the fatigue test and finite element analysis, fatigue life can express the maximum Green-Lagrange strain instead of maximum displacement. Figure 8(a) shows the relation of maximum G-L strain with fatigue life. Fatigue life was effectively represented by the maximum G-L strain, where the G-L strain for each three-dimensional dumbbell specimen is calculated from the displacement versus G-L strain curve in Figure 7(b).

Elongation at break is very important factor in material properties and fatigue life prediction of rubber materials. The test data of elongation at break according to aging days at 70°C are shown as in Figure 8(b). Elongation at break was decrease as the hardness and heat aging day increase.

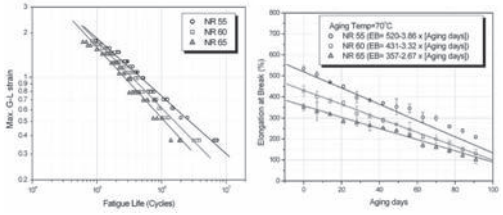

(a) Max. G-L strain-fatigue life (b) Elongation at break

Figure 8. Maximum Green-Lagrange strain and elongation.

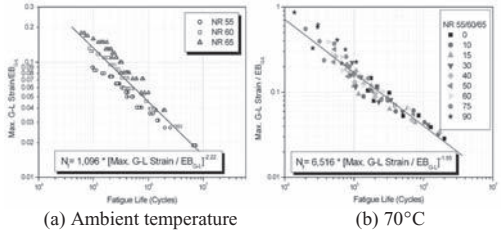

(a) Ambient temperature (b) 70°C

Figure 9. Fatigue life prediction using the normalized strain.

Table 2. Fatigue life prediction of natural rubber.

Condition	Fatigue life prediction equation
Ambient temp.	$N_f = 1{,}096 \cdot [\ \varepsilon_{G\text{-}L} / EB_{G\text{-}L}\ ]^{-2.22}$
Heat-aging (70°C)	$N_f = 6{,}516 \cdot [\ \varepsilon_{G\text{-}L} / EB_{G\text{-}L}\ ]^{-1.55}$

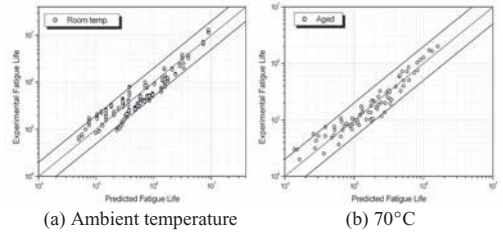

(a) Ambient temperature (b) 70°C

Figure 10. Correlation between experimental and predicted.

Also, normalized strain was defined as dividing by maximum Green-Lagrange strain ($EB_{G\text{-}L}$) at break for the maximum Green-Lagrange strain ($\varepsilon_{G\text{-}L}$). Figure 9(a) and (b) shows relation of normalized strain and fatigue life. Fatigue life prediction equation effectively represented by a single function using the normalized strain. Fatigue life prediction equation (N_f) of natural rubber material was shown in Table 2.

It was observed that the maximum Green-Lagrange strain and normalized strain was a good fatigue damage parameter to account for hardness, amplitude effects. According to fatigue life prediction equation, fatigue life of ambient temperature was longer than at 70°C. Correlation between experimental and predicted fatigue life are shown in Figure 10(a) and (b). Predicted fatigue lives are in a good agreement with experimental lives within a factor of two.

4 CONCLUSION

Fatigue life prediction and evaluation are the key technologies to assure the safety and reliability of automotive rubber components. In this paper, fatigue life prediction methodology of vulcanized natural rubber was proposed by incorporating the finite element analysis and fatigue damage parameter determined from fatigue test. Heat-aging effects on the fatigue life prediction of natural rubber were experimentally investigated.

The Green-Lagrange strain at the critical location determined from the finite element method used for evaluating the fatigue damage parameter. Fatigue life prediction equation effectively represented by a single function using the Green-Lagrange strain. Predicted fatigue lives of the rubber component were in fairly good agreements with the experimental fatigue lives within factors of two. Therefore, fatigue life estimation procedure employed in this study could be used approximately for the fatigue design of the rubber components at the early design stage.

ACKNOWLEDGEMENT

This research has been supported by Development of Materials and Component Program of Ministry of Knowledge Economy, Korea.

REFERENCES

Frederick, R.E. 1982, Science and technology of Rubber, Rubber Division of American Chemical Society.

Lake, G.J. 1997, Fatigue and Fracture of Elastomers, Rubber Chemistry & Technology, 68, 435–460.

Brown, R.P. 1996, Physical Testing of Rubber, Rapra Technology Ltd, Shewbury.

Takeuchi, K. & Nagakawa, M. 1993, Int'l Polymer Sci. Vol. 20, No. 10, pp. 64–69.

Brown, R.P. 2002, Rubber Product Failure, Rapra Review Reports, 13(3).

Brown, R.P. & Butler, T. 2001, Natural Ageing of Rubber-Changes in Physical Properties over 40 Year's, Rapra technology, Shewbury.

Mal, A.K. & Singh, S.J. 1990, Deformation of Elastic Solids, Prentice Fall PTR.

Mullin, L. 1969, Rubber Chemistry & Technology, Vol. 42, pp. 339–362.

Computational methods FEM implementation

Constitutive Models for Rubber VI – Heinrich et al. (eds)
© 2010 Taylor & Francis Group, London, ISBN 978-0-415-56327-7

FE-Implementation of the concept of representative directions

M. Freund
German Institute of Rubber Technology, Hannover, Germany

J. Ihlemann
Chemnitz University of Technology, Chemnitz, Germany

ABSTRACT: The concept of representative directions is intended to generalize one-dimensional material models for uniaxial tension to fully three-dimensional constitutive models for the finite element method. The concept is applicable to each model, which is able to simulate uniaxial loadings, even to those for inelastic material behaviour without knowing the free energy. Material characteristics like nonlinearity, hysteresis and stress softening are generalized in a remarkable similarity to the input model. The concept has been implemented into the finite element programs ABAQUS and MSC. MARC. The implementation requires the computation of the material tangent of the generalized constitutive model. This is achieved by differentiating the stress tensor with respect to the strain tensor almost analytically, which provides a considerable reduction of the simulation runtime. Furthermore there will be shown several methods to increase the numerical efficiency of the algorithm. The FE-implementation enables finite element simulations of inhomogeneous stress conditions, which is finally proved by comparing the original MORPH constitutive model with the uniaxial MORPH model in representative directions.

1 INTRODUCTION

The simulation of industrial components with regard to their mechanical behaviour is basically achieved by means of the finite element method. Thus, for any particular material class a constitutive model is needed, that is able to predict the complete correlation between the given strain condition and the corresponding stress condition, while also considering the loading history. In general, this is equivalent to the input of six independent coefficients of the strain tensor to the user subroutine and the output of six stress values of the corresponding stress tensor. The development of such a three-dimensional constitutive model usually takes a lot of time but often leads to an intermediate stage, that at least enables the prediction of the material behaviour for uniaxial tension. In such a situation it would be a great advantage to find a sufficient approximation of the prospective general behaviour of a constitutive model by describing the uniaxial material behaviour only. This is the idea of the so-called concept of representative directions (Ihlemann 2007).

2 THEORY OF THE CONCEPT

During the deformation of a component there exists an individual strain condition at each material point, that is fully described by the right Cauchy-Green tensor $\underline{\underline{C}}$ (within the framework of idealization of continuum mechanics). By using this symmetrical strain tensor the local elongation $\overset{\alpha}{\lambda}$ of any assumed material line along the associated direction in space $\overset{\alpha}{\underline{e}}$ for each material point can be calculated.

$$\overset{\alpha}{\lambda} = \sqrt{\overset{\alpha}{\underline{e}} \cdot \underline{\underline{C}} \cdot \overset{\alpha}{\underline{e}}} \tag{1}$$

For each of those directions the corresponding uniaxial stress response $\overset{\alpha}{\tilde{T}}$ (2. Piola-Kirchhoff stresses) is identified by the one-dimensional material model, that is to be generalized to a fully three-dimensional constitutive model.

$$\overset{\alpha}{\tilde{T}} = \overset{\alpha}{\tilde{T}}\left(\overset{\alpha}{\lambda}, \dot{\overset{\alpha}{\lambda}}, \ldots \right) \tag{2}$$

The demand, that all the uniaxial stress responses achieve the same stress power as the overall stress tensor concerning the actual deformation, finally leads to an equation for calculating the unknown second Piola-Kirchhoff stress tensor $\underline{\underline{\tilde{T}}}^*$.

$$\underline{\underline{\tilde{T}}}^* = \sum_{\alpha=1}^{n} \overset{\alpha}{w} \overset{\alpha}{\tilde{T}} \overset{\alpha}{\underline{e}} \circ \overset{\alpha}{\underline{e}} \tag{3}$$

From a mathematical point of view this equation describes a type of numerical integration on the surface of a sphere. For an efficient integration the so-called representative directions $\underline{\overset{\alpha}{e}}$ (unit vectors) are selected in such a way, that they are evenly distributed in space. If the distribution is not perfectly even, the uniaxial stress responses are balanced with appropriate weighting factors $\overset{\alpha}{w}$, that depend on the individual orientation of the associated representative direction.

By generalizing one-dimensional material models according to equation (3) the resulting three-dimensional constitutive model is characterized by a compressible material behaviour with a Poisson's ratio of $\nu = 1/4$. To consider the nearly incompressible behaviour of elastomers concerning hydrostatic loads the algorithm is restricted to the deviatoric stress tensor $\underline{\underline{\sigma}}'$. This requires, that the elongations are merely calculated with the isochoric right Cauchy-Green tensor $\overset{G}{\underline{\underline{C}}}$ (with $\overset{G}{\underline{\underline{C}}} = J_3^{-\frac{2}{3}} \underline{\underline{C}}$), which leads to the following relation between $\underline{\underline{\tilde{T}}}^*$ and the final stress tensor $\underline{\underline{\tilde{T}}}$.

$$\underline{\underline{\sigma}} = \left(\underline{\underline{\sigma}}^*\right)' - p\underline{\underline{E}} \Rightarrow \underline{\underline{\tilde{T}}} = \left(\underline{\underline{\tilde{T}}}^* \cdot \overset{G}{\underline{\underline{C}}}\right)' \cdot \underline{\underline{C}}^{-1} - pJ_3\underline{\underline{C}}^{-1} \quad (4)$$

The concept of representative directions can be tested by using well-known constitutive models. In this case the described algorithm is applied to the inelastic MORPH model (Ihlemann 2003), which has been developed to describe the mechanical behaviour of elastomers under large deformations. To identify the eight corresponding material parameters the original MORPH model has been simultaneously adapted to a uniaxial tension and a simple shear measurement of a carbon black filled chloroprene rubber used in air springs while considering the stationary loading cycles only. Figure 1 shows the result of this adaptation for the uniaxial tension test.

Using the same set of material parameters the simulation of a simple shear deformation is still showing a very good agreement with the measurement.

The described parameter optimization was also done with the new concept using the one-dimensional stress-strain behaviour of the original MORPH model within the representative directions. As shown in figures 3 and 4 the resulting generalized constitutive model leads to a very similar material behaviour, which can be adapted to the experiments still very well.

It is to be mentioned, that the adaptation to the same measurements effects a slight difference of the eight optimized material parameters referring to each representative direction compared to the parameters of the original MORPH model. This is caused by the simplified interactions between the representative directions, because in a real material all those material lines are not purely elongated in their own direction but loaded in a more complex manner. But anyway the material characteristics like nonlinearity, hysteresis and stress softening are completeley retained during the process of generalization and are not being lost or falsified.

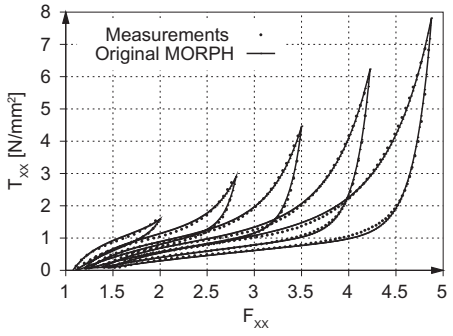

Figure 1. Comparison between uniaxial tension measurements and corresponding simulations with the original MORPH model.

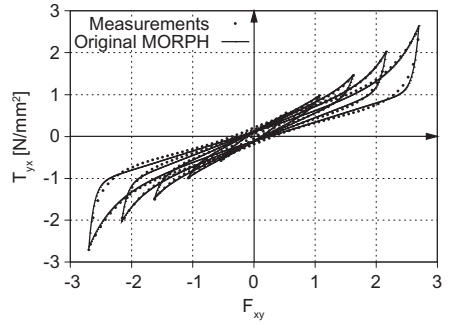

Figure 2. Comparison between simple shear measurements and corresponding simulations with the original MORPH model.

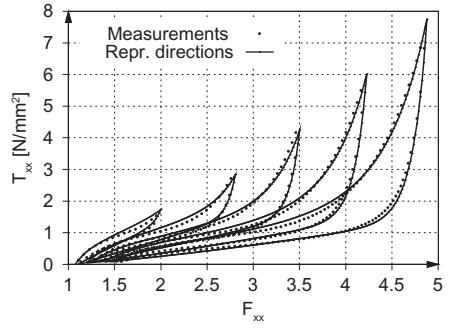

Figure 3. Comparison between uniaxial tension measurements and corresponding simulations with the MORPH model in representative directions.

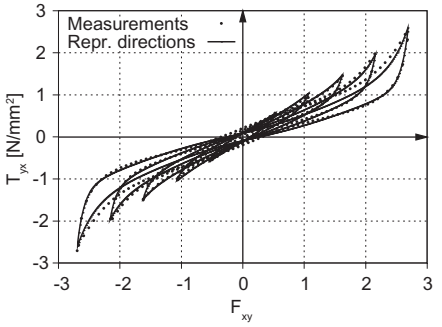

Figure 4. Comparison between simple shear measurements and corresponding simulations with the MORPH model in representative directions.

3 NUMERICAL INTEGRATION

The numerical integration of the uniaxial stress responses causes a dependence of the generalized material behaviour on the orientation of the representative directions. This kind of anisotropy is highly influenced by the number and distribution of those directions. A perfect uniform distribution in space in combination with appropriate weighting factors maximizes the efficiency of the numerical integration for a specific number of directions. An analytical solution for this distribution problem is only given by the five Platonic solids, wheras the icosahedron with its 20 triangles provides the largest number ($n = 10$) of evenly distributed directions in space (s. figure 5).

For $n > 10$ there only exist numerical solutions for this problem, so that the directions are no longer perfectly distributed in space. There are several algorithms for distributing points on the surface of a sphere and calculating the corresponding weighting factors (Sloan & Womersley 2004, Fliege & Maier 1999, Saff & Kuijlaars 1997). Some of the approaches are based on rather mathematical criterions for this optimization problem. In this paper we suggest an algorithm related to the Thomsons problem (Thomson 1904). The idea is to place a given number of points on the surface of a unit sphere, which are modelled as electric charges repelling each other according to Coulombs law while still bonded to the surface of the sphere. The equilibrium of all electric forces finally leads to an almost uniform point distribution, whereas the unit vectors to these points can be used as representative directions (s. figure 6). As corresponding weighting factors for the representative directions it seems to be appropriate to use the surface areas of Voronoi cells constructed around the points on the surface of the sphere.

$$\overset{\alpha}{w} = \frac{\Delta A_{\text{Voronoi}}}{A_{\text{Sphere}}} \quad \text{with} \quad \sum_{\alpha=1}^{n} \overset{\alpha}{w} \overset{!}{=} 1 \tag{5}$$

The motivation for using Voronoi cells as weighting factors results from the fact, that any point within a single Voronoi cell is closer to the associated central point than to the central point of any other Voronoi cell, so that a characteristic region is assigned to each position on the sphere. The construction of the Voronoi diagram shown in figure 6 is based on an algorithm of Sugihara (Sugihara 2002).

For an efficient numerical integration the described algorithm has to be modified in such a way, that two opposite electric charges are permanently coupled during the process of iteration, so that a symmetrical distribution relative to the center of the sphere is secured. This is necessary, because the uniaxial stresses along the representative directions $\overset{\alpha}{\underline{e}}$ always relate to the opposite directions $-\overset{\alpha}{\underline{e}}$ too.

Another possibility to reduce the anisotropy caused by the error of the numerical integration for a specific number of representative directions is to calculate the uniaxial stresses $\overset{\alpha}{\tilde{T}}$ with those elongations $\overset{\alpha}{\lambda}_m$, that are averaged over several elongations $\overset{\alpha\beta}{\lambda}$ within a Voronoi cell.

$$\overset{\alpha}{\lambda}_m = \sum_{\beta=1}^{i} \overset{\alpha\beta}{w}\, \overset{\alpha\beta}{\lambda} \quad \text{with:} \quad \overset{\alpha\beta}{\lambda} = \sqrt{\overset{\alpha\beta}{\underline{e}} \cdot \underline{\underline{C}} \cdot \overset{\alpha\beta}{\underline{e}}} \tag{6}$$

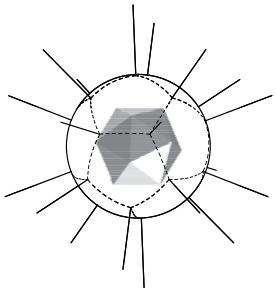

Figure 5. Ten evenly distributed directions in space given by the normals of the surface areas of an icosahedron, respectively by the vertices of a dodecahedron.

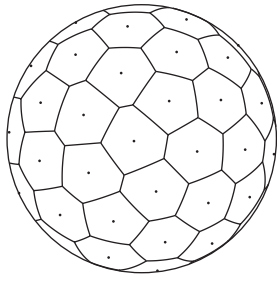

Figure 6. Distribution of 50 points on the surface of a unit sphere with Voronoi cells as corresponding weighting factors.

For this purpose each Voronoi cell α is divided into a certain number of subcells β, whereas the surface areas of these subcells are used as weighting factors for the individually chosen directions of the additional elongations (s. figure 7).

The effect of using averaged elongations is quite similar to the increase of the number of representative directions (respectively the number of calculated stress responses), but the amount of computational cost is much less, because it is comparatively easy to compute elongations than to solve the whole one-dimensional material model for the given number of directions.

The advantage of this method can be proved by simulating a homogeneous uniaxial tension test with a simple Neo-Hooke model in the ten representative directions of the icosahedron. For this purpose the FE-implementation of the concept is used to simulate the deformation of a single finite element. Figure 8a shows the cross-sectional area of the deformed element for an external elongation of $\lambda_x = 3$.

In this case the representative directions of the icosahedron are rotated relative to the direction of the external deformation in order to demonstrate the anisotropy represented by the large shear deformation of the element. For the usage of averaged elongations each triangle of the icosahedron is subdivided into four additional triangles. Figure 8b illustrates the immense effect of this method since the cross-sectional area is nearly quadratic like in case of full isotropy. The shape of the cross-sectional area is highly dependent on the orientation of the system of representative directions. Finally, numerous simulations have shown, that the averaging of elongations results in a reduction of anisotropy in any case.

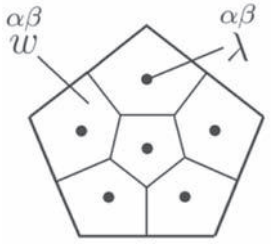

Figure 7. Subdivision of a Voronoi cell for calculating an averaged elongation.

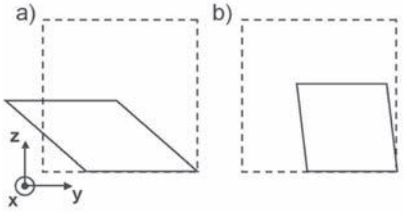

Figure 8. Reduction of the anisotropy by using averaged elongations.

4 FE-IMPLEMENTATION AND SIMULATIONS

The concept of representative directions has been implemented into the finite element programs ABAQUS and MSC. MARC. The user subroutine *HYPELA2* of MSC. MARC relates to the Lagrangian method, while the subroutine *UMAT* of ABAQUS requires the conversion into the Eulerian formulation. In both cases the input of the deformation gradient $\underline{\underline{F}}$ is used to compute the resulting stress tensor.

In the Lagrangian formulation the material tangent is computed by differentiating the second Piola-Kirchhoff stress tensor with respect to the right Cauchy-Green tensor. Because of the symmetry of these tensors, the stiffness matrix can be reduced to 21 independent coefficients K_{AB}.

$$\underline{\underline{\underline{\underline{K}}}} = 2\frac{\partial \underline{\underline{\tilde{T}}}}{\partial \underline{\underline{C}}} \quad \Rightarrow \quad K_{AB} = 2\frac{\partial \tilde{T}_A}{\partial C_B} \tag{7}$$

The second part of the stress tensor (compare equation (4)) is differentiated completely analytically while using the nonlinear function of MSC. MARC for the hydrostatic pressure p.

$$\begin{aligned}\underline{\underline{\underline{\underline{K}}}} &= 2\frac{\partial\left(pJ_3\underline{\underline{C}}^{-1}\right)}{\partial \underline{\underline{C}}} = \left[2KJ_3^{\frac{2}{3}} - KJ_3^{\frac{1}{3}}\right]\underline{\underline{C}}^{-1}\circ\underline{\underline{C}}^{-1} \\ &+ \left[6KJ_3^{\frac{1}{3}} - 6KJ_3^{\frac{2}{3}}\right]\left(\underline{\underline{C}}^{-1}\circ\underline{\underline{C}}^{-1}\right)^{S_{24}} \\ &\text{with } p = 3KJ_3^{-\frac{2}{3}}\left(J_3^{\frac{1}{3}} - 1\right)\end{aligned} \tag{8}$$

The expression $(\underline{\underline{C}}^{-1}\circ\underline{\underline{C}}^{-1})^{S_{24}}$ is defined by Ihlemann (Ihlemann 2006) and means the 1, 2- and 3, 4-symmetrical part of $(\underline{\underline{C}}^{-1}\circ\underline{\underline{C}}^{-1})^{T_{24}}$, which is a tensor, whose second and fourth dyades are changed.

The development of a complete tensorial formulation for differentiating the first part of $\underline{\underline{\tilde{T}}}$ is still in progress, but at least there can be shown the tensorial differentiation of $\underline{\underline{\tilde{T}}}^*$ as a part of it.

$$\frac{\partial \underline{\underline{\tilde{T}}}^*}{\partial \underline{\underline{C}}} = \sum_{\alpha=1}^{n} \frac{\overset{\alpha}{w}}{2}\frac{\partial \overset{\alpha}{\tilde{T}}}{\partial \overset{\alpha}{\lambda}}\frac{1}{\overset{\alpha}{\lambda}}\left[J_3^{-\frac{2}{3}}\,\overset{\alpha}{\underline{e}}\circ\overset{\alpha}{\underline{e}} - \frac{1}{3}\overset{\alpha^2}{\lambda}\,\underline{\underline{C}}^{-1}\right]\circ\overset{\alpha}{\underline{e}}\circ\overset{\alpha}{\underline{e}} \tag{9}$$

For the FE-implementation the differentiation of the uniaxial stress responses $\overset{\alpha}{\tilde{T}}$ with respect to the elongations $\overset{\alpha}{\lambda}$ (stiffness of the one-dimensional material model) is the only part of the generalized constitutive model, that is computed numerically. This enables an efficient extension of the concept with additional one-dimensional material models. For the implementation in ABAQUS the material tangent requires to be calculated according to the Eulerian formulation. This is done by converting the Lagrangian tangent by means of a special matrix developed by Ihlemann (Ihlemann 2006).

The advantage of this almost analytical differentiation over a complete numerical differentiation of the first part of the stress tensor is a considerable reduction of the simulation runtime and of course a certain gain of computational stability. The increase of the efficiency in respect of computational cost is proportional to the number of representative directions. For example a simulation based on an FE-model with 1000 elements including the Ogden material model within 75 representative directions the simulation runtime with the almost analytical material tangent is nearly 3, 5 times less than in case of a complete numerical calculation.

The FE-implementation has been tested by simulating a rubber wheel, which is used by Grosch (Grosch 1996) to measure the friction of elastomers (s. figure 9). In the first loading step a constant force F_y is applied to the axis of the wheel to create a contact with the ground. For this purpose the complete inner area of the wheel is coupled with the axis as if the wheel was mount on a rigid rim. In the next step the axis is moved in x-direction so that the wheel starts to rotate because of the Coulomb friction modelled in the contact area.

In the following there will be shown the results of the original MORPH constitutive model (compare Hohl 2007) as well as the uniaxial MORPH model in representative directions while still using the same optimized material parameters for both models resulting from the adaptations to the measurements (s. figures 1–4). The first result of this simulation can be seen in figure 10, where the vertical displacement of the axis is displayed against the rotation angle.

The similarity of the characteristic of both material models concerning this measurable quantity is quite remarkable, though there remains a certain quantitative difference. During the first revolution the wheel pushes itself back vertically, an effect which cannot explained yet. But at the end of the revolution ($\phi = 360°$) the displacement of the axis increases rapidly, because the current material in the contact area has already been softened at the beginning of the loading process. It can be clearly seen how the stress softening is still continuing after the first revolution until a steady state is reached.

The effect of stress softening during the loading process can be visualized in form of the quantity $C_{T,\max}$ in case of the original MORPH model (s. figure 11). This scalar is defined as the maximum value of the Tresca invariant of the right Cauchy-Green-Tensor $\underline{\underline{C}}$ occurred during the whole loading history at each integration point.

Obviously the distribution of the stress softening is not axissymmetric during the first revolution. This results from the fact, that the wheel pushes itself back, so that the material becomes less softened for increasing rotation angles. In case of the original MORPH constitutive model there exists one scalar value $C_{T,\max}$ for each integration point of the finite element model. But within the concept of representative directions this internal variable is defined for each single direction $\overset{\alpha}{e}$, so that a comparison between these two material models requires an averaging of $\overset{\alpha}{C}_{T,\max}$ over the

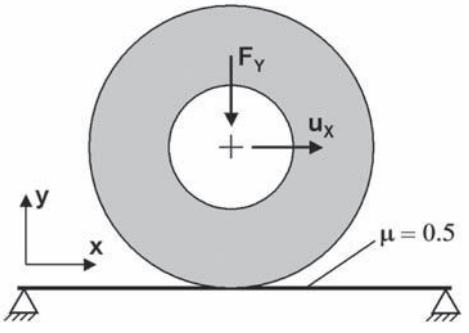

Figure 9. Boundary conditions of the Grosch wheel.

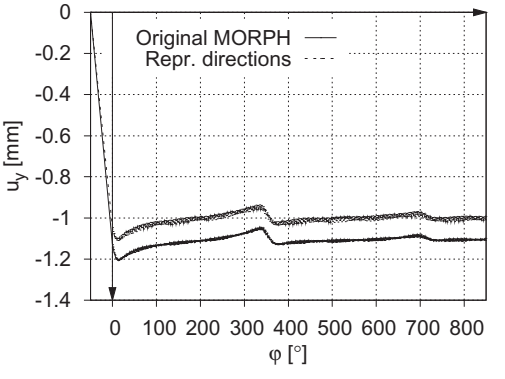

Figure 10. Vertical displacement of the axis of the Grosch wheel during the rotation.

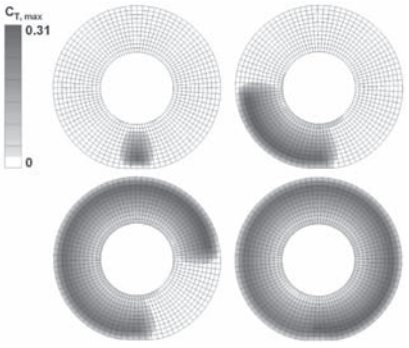

Figure 11. Stress softening in the rotating Grosch wheel simulated with the original MORPH constitutive model ($\varphi = 0°$, 90°, 270°, 360°).

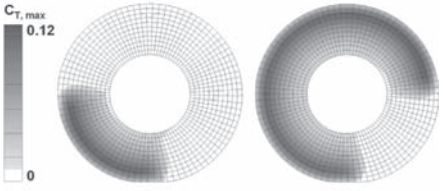

Figure 12. Stress softening in the rotating Grosch wheel simulated with the MORPH model in representative directions ($\varphi = 90°$, 270°).

representative directions for each integration point (s. figure 12).

Obviously the averaging of $\overset{\alpha}{C}_{T,\max}$ enables the visualization of the stress softening in a very similar way as the original MORPH constitutive model. Considering the dependence of the quantity $\overset{\alpha}{C}_{T,\max}$ on the orientation of the representative directions it becomes obvious, that this generalized MORPH material model is characterized by an anisotropic stress softening (in contrast to the original MORPH constitutive model). In this context it should be mentioned, that the effect of anisotropic stress softening in elastomers has already been experimentally proven (Besdo, Ihlemann, Kingston, Muhr 2003).

5 CONCLUSIONS

The concept of representative directions is able to generalize one-dimensional material models for uniaxial tension to fully three-dimensional constitutive models for the finite element method. The algorithm has been implemented into the FE-programs ABAQUS and MSC. MARC. This enables simulations of inhomogeneous stress conditions in complex technical components, though the input models predicts uniaxial material behaviour only.

The computation of the material tangent is based on an almost analytical differentiation of the stress tensor, which results in a remarkable reduction of the simulation runtime compared to a fully numerical differentiation. To increase the efficiancy of the numerical integration for calculating the stress tensor it is necessary to use evenly distributed directions in space which can be generated by simulating repelling charges on the surface of the sphere. Furthermore the anisotropy caused by the discretization can be reduced by calculating the uniaxial stress responses with averaged elongations.

REFERENCES

Besdo, D., Ihlemann, J., Kingston, J.G.R., Muhr, A.H. 2003: Modelling inelastic stress-strain phenomena and a scheme for efficient experimental characterization. In: James Busfield & Alan Muhr (Editors): Constitutive Models for Rubber III, Balkema, Lisse: pp. 309–317.

Fliege, J.; Maier, U. 1999: The distribution of points on the sphere and corresponding cubature formulae. In: IMA Journal of Numerical Analysis, 19 (1999), pp. 317–334.

Grosch, K.A. 1996: Laborbestimmung der Abrieb- und Rutschfestigkeit von Laufflächenmischungen—Teil I: Rutschfestigkeit. In: Kautschuk und Gummi, Kunststoffe 49, 6 (1996), pp. 432–441.

Hohl, C. 2007: Anwendung der Finite-Elemente-Methode zur Parameteridentifikation und Bauteilsimulation bei Elastomeren mit Mullins-Effekt. Dissertation Universität Hannover. Düsseldorf: VDI-Verlag.

Ihlemann, J. 2003: Kontinuumsmechanische Nachbildung hochbelasteter technischer Gummiwerkstoffe. Dissertation Universität Hannover. Düsseldorf: VDI-Verlag.

Ihlemann, J. 2006: Beobachterkonzepte und Darstellungsformen der nichtlinearen Kontinuumsmechanik. Habi-litationsschrift Universitat Hannover.

Ihlemann, J. 2007: Generalization of one-dimensional constitutive models with the concept of representative directions, in: A. Boukamel, L. Laiarinandrasana, S. Méo & E. V (Editors): Constitutive Models for Rubber V, Taylor & Francis, pp. 29–34. London.

Saff, E.B.; Kuijlaars, A.B. 1997: Distributing many points on the sphere, in: Mathematical Intelligencer, 19 (1997), pp. 5–11.

Sloan, I.H.; Womersley, R.S. 2004: Extremal Systems of Points and Numerical Integration on the Sphere, in: Advances in Computational Mathematics, 21 (2004), pp. 102–125.

Sugihara, K. 2002: Laguerre Voronoi Diagram on the Sphere, in: Journal for Geometry and Graphics, Volume 6, No. 1, pp. 69–81.

Thomson, J.J. 1904: On the Structure of the Atom: An Investigation of the Stability and Periods of Oscillation of a number of Corpuscles arranged at equal intervals around the Circumference of a Circle, in: Philosophical Magazine, 6 (1904), pp. 237–265.

Constitutive Models for Rubber VI – Heinrich et al. (eds)

Numerical prediction of mechanical behavior of single walled carbon nanotube/rubber composites

S.K. Georgantzinos, G.I. Giannopoulos & N.K. Anifantis
Mechanical and Aeronautics Engineering Department, University of Patras, Patras, Greece

P.A. Kakavas
Technological Educational Institute of Patras, Department of Renovation and Rehabilitation of Buildings, Patras, Greece

ABSTRACT: The excellent properties of carbon nanotubes have generated technological interests in the development of nanotube/rubber composites. This paper describes a finite element formulation that is appropriate for the numerical prediction of the mechanical behavior of rubber-like materials which are reinforced with single walled carbon nanotubes. The considered composite material consists of continuous aligned carbon nanotubes which are uniformly distributed within the rubber material. It is assumed that the carbon nanutubes are perfectly bonded with the matrix. Based on the micromechanical theory, the mechanical behavior of the composite may be predicted by utilizing a representative volume element. Within the representative volume element, the reinforcement is modeled according to its atomistic microstructure. Therefore, non-linear spring-based line elements are employed to simulate the discrete geometrical structure and behavior of the single-walled carbon nanotube. On the other hand, the matrix is modeled as a continuum medium by utilizing solid elements. In order to describe its behavior an appropriate constitutive material model is adopted. Finally, the interfacial region is simulated via the use of special joint elements of infinite stiffness which interconnect the two materials. Using the proposed model, the stress-strain behavior for various reinforcement volume fractions is extracted. The influence of the single walled carbon nanotube addition within the rubber is clearly illustrated and discussed.

1 INTRODUCTION

Rubber composites can be classified as particulate, laminated, or fibrous depending on their construction. The most commonly available elastomeric composites are reinforced with carbon black particles (Yeo 1990) which range in size from a few hundred to thousand of angstroms. Fillers are added to rubber products as car tires and shock mounts to enhance their stiffness and toughness properties. The unique behavior of carbon black-filled elastomers results due to a rigid, particulate phase and the interaction of the elastomer chains with this phase (Bauer & Crossland 1990). It is well known that such composites usually exhibit highly anisotropic response due to directionality in material properties. Unfortunately, among the existing strain energy functions, both the polynomial as well as Ogden models are unable to capture the sharp decrease in stiffness for filled rubbers at small strains.

As there is a demand in modern technological applications for superior elastomeric composites, innovative reinforcements having superior properties should be introduced. Such reinforcements could be found in the field of nanotechnology. Single walled carbon nanotubes (SWCNTs) are the stiffest and strongest known fibbers, having also remarkable electronic and conductive properties and many other unique characteristics (Thostenson et al. 2001). However, these properties are obviously of limited value in individual tubes. The development of SWCNT based elastomeric composites (Mamedv et al. 2002) could demonstrate both the excellent energy absorption characteristics of the rubber component as well as the advanced structural properties of the nanotubes.

Since it is complicated to introduce appropriate strain energy functions which can effectively represent the complex behavior of SWCNT filled rubbers, the development of an effective numerical tool capable of simulating accurately the behavior of such composites is essential. This study presents a nonlinear, micromechanical, finite element formulation for the evaluation of mechanical behavior of rubber uniformly filled with continuous SWCNTs. Concerning the nanotube modeling (Giannopoulos et al. 2008), the method utilizes the three dimensional atomistic microstructure of the nanotube defining

nodes at the corresponding atomic positions of carbon atoms. Appropriate spring elements, which interconnect the atoms, include directly the potential energies provided by molecular theory and therefore simulate accurately the interatomic interactions (Rappe et al. 1992). In addition, the interactions between the nanotubes and the rubber are simulated via the use of special spring elements of infinite stiffness to model a rigid interface. Various results concerning the stress-strain behavior of the composites are presented and discussed.

2 COMPUTATIONAL MODEL

2.1 *Micromechanical analysis*

Assuming a uniformly reinforced rubber with continuous in length SWCNTs all the computations may be preformed in an appropriate cylindrical representative volume element (RVE). As Figure 1 depicts, the RVE consists of two phases, i.e. a SWCNT and the rubber material.

It is assumed that the two phases are attached via a rigid interface. The radius of the RVE is equal to radius of the matrix material r_m, while r_n is the mean radius of the nanotube around which its nanostructure is assembled. The thickness of nanotube is t_n. Finally, the RVE length is the same with the matrix length and nanotube length ℓ_n. The volume fraction of the SWCNT in the composite with respect to the proposed RVE can be expressed by the following equation

$$V_n = \frac{8 r_n t_n}{4 r_m{}^2 - (2 r_n - t_n)^2} \tag{1}$$

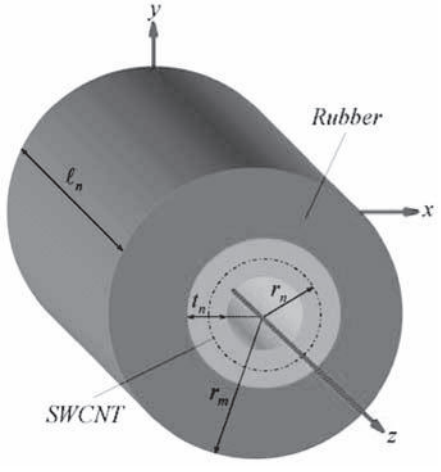

Figure 1. The representative volume element of the SWCNT reinforced rubber.

Small volume fractions are investigated, so that a negligible interaction between adjacent nanotubes could be assumed. The reinforcement used in the analysis is the zigzag armchair (20,0) SWCNT which has a diameter equal to 0.783 nm. Its thickness t_n is typically taken equal to 0.34 nm.

2.2 *Rubber modeling*

The rubber matrix could be modeled discretely by taking into consideration a network of polymeric chains surrounding the reinforcement. However, this would increase significantly the computational cost as well as the complexity of the whole model. Therefore, the matrix is regarded as a continuum medium. This consideration seems valid since the matrix volume is much greater than the SWNT one for the volume fractions considered here. Linear three-dimensional hexahedral isoparametric elements are used for the discretization of the matrix. In order to describe their mechanical behavior the following Mooney Rivlin strain energy density function is utilized (Ogden 1984):

$$W(I_1, I_2, I_3, v) = c_1(I_1 - 3) + c_2(I_2 - 3) + \frac{1}{2}\kappa(I_3 - 1)^2 \tag{2}$$

where I_1, I_2, I_3 define the invariants of the strain tensor, v is the Poisson's ratio and c_1, c_2 are material parameters. These parameters are typically estimated by fitting the stress-strain theoretical equation derived from Equation (2) with corresponding experimental data. In the above equation, parameter κ defines the bulk modulus of the material and is equal to $\kappa = 2(c_1 + c_2)/(1 - 2v)$. The rubber chosen in the present analysis has the material parameters $c_1 = 0.16$ Mpa and $c_2 = 0.035$ Mpa (Kakavas et al. 2007). The bulk modulus is chosen to be $\kappa = 19.5$ Mpa in order to produce a nearly incompressible rubber material ($v = 0.49$). The stress-strain curve that arises for simple tension by using these material parameters is shown in Figure 2 (Kakavas et al. 2007).

Since Equation (2), for small deformations, reduces to Hooke's law, the Young's modulus of the rubber is equal to $E = 6(c_1 + c_2) = 1.17$ Mpa. A two parameter Mooney Rivlin model fails to fit all the experimental data up to break, however, it is suitable for the small strains up to 70% which are tested in the present work.

2.3 *SWCNT modeling*

In contrast with a traditional carbon fiber, the mechanical performance of a SWCNT is strongly dependent on its atomistic nanostructure and therefore it is essential to be implemented into the computational model (Giannopoulos et al. 2008).

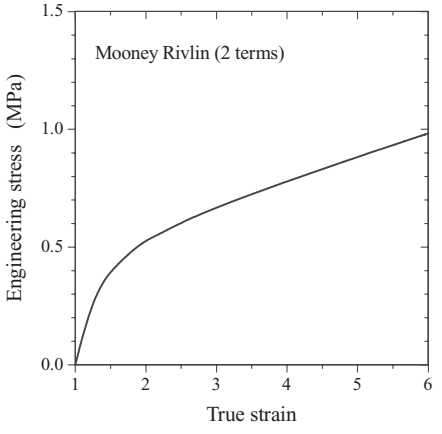

Figure 2. Stress-strain behavior predicted by the Mooney Rivlin model for pure tension.

According to the method adopted the SWCNT is developed around its mean radius r_n. Specifically, the nanotube is considered as a space frame structure in which the carbon atoms are represented by nodes. Their position in three-dimensional space for a particular (n, m) SWCNT is established via the following transformation equation (Kołoczek et al. 2001):

$$(x, y, z) = \left(r_n \cos\left(\frac{x'}{r_n}\right),\ r_n \sin\left(\frac{x'}{r_n}\right),\ y' \right) \tag{3}$$

where (x', y') represents the original coordinate system of a graphene sheet and (x, y, z) represents the new coordinate system of the tube. The nodes that arise by using the above equation are properly connected with nonlinear spring elements in order to represent the potential energy of the interatomic interactions. It is assumed that the specific interactions obey the modified Morse potential (Belytschko et al. 2002):

$$U = U_{stretch} + U_{angle} = D_e\{[1 - e^{-\beta\Delta r}]^2 - 1\} + \frac{1}{2}k_\theta(\Delta\theta)^2[1 + k_{sextic}(\Delta\theta)^4] \tag{4}$$

where $U_{stretch}$ represents the energy due to bond stretching, U_{angle} represents the energy due to bond angle bending, $\Delta r = r - r_0$ represents the bond length variation and $\Delta\theta = \theta - \theta_0$ represents the bond angle variation. The initial bond length and angle are $r_0 = 1.421 \times 10^{-10}$ m and $\theta_0 = 2.094$ rad, respectively. The force parameters of the modified Morse potential are $D_e = 6.03105 \times 10^{-19}$ Nm, $\beta = 2.625 \times 10^{10}$ m^{-1}, $k_\theta = 0.9 \times 10^{-18}$ Nm/rad^2 and $k_{sextic} = 0.754$ rad^{-4} (Belytschko et al. 2002). In the present study, only the bond stretching potential is considered since the bond stretching dominates nanotube strength and the effect of angle-bending potential is small, especially for the uniaxial load investigated here. In order to represent the bond stretching interactions between carbon atoms, nonlinear spring elements are utilized. The force-stretching nonlinear behavior of these spring elements arises by differentiating $U_{stretch}$:

$$F(\Delta r) = 2\beta D_e(e^{-\beta\Delta r} - 1) \tag{5}$$

The above variation is depicted in Figure 3.

The finite element mesh of the SWCNT which is used for the tests is illustrated in Figure 4. In order to ensure that the nanotube length has a negligible effect on the results, the length of the specific tube is chosen to be $\ell_n/r_n > 10$.

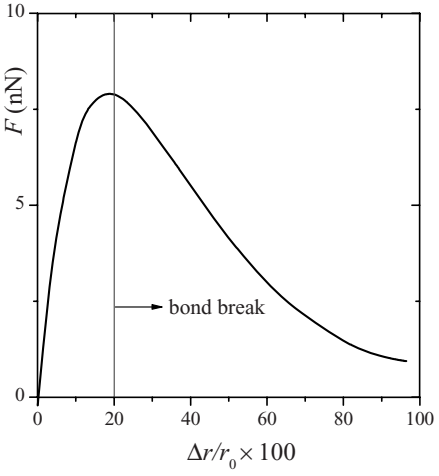

Figure 3. Force-strain curve of the modified Morse potential.

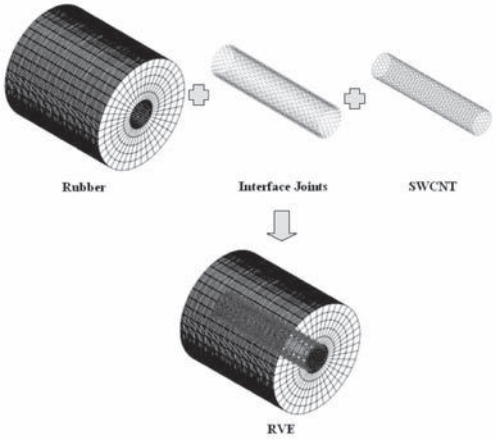

Figure 4. Finite element mesh of the RVE and its components.

2.4 *Interface modeling*

In general, an interface may be described as a region that separates two distinct bodies with different constitutive responses. Interfaces can be modeled either as continuum or as discrete systems, based on the problem of interest and the scale length. Due to the nanoscale dimensions as well as the atomistic modeling of SWCNTs, the discrete modeling of the interfacial region is selected. To realize this idea two-noded interfacial joint elements of infinite stiffness along the three directions of their local coordinate system are employed. These elements connect radially the atoms-nodes of the nanotube with corresponding nodes which belong to the inner cylindrical surface of the matrix which is simulated via the volume elements. As it was previously mentioned, the nanostructure of carbon nanotube is developed around a mean diameter and its thickness is indirectly considered. Therefore, from physical point of view, the length of the joint elements is taken equal to $t_n/2$. Their position inside the RVE can be clearly seen in Figure 4.

2.5 *Solution procedures*

In order to compute the stress-strain uniaxial behavior of the SWCNT reinforced rubber appropriate boundary conditions have to be defined on the RVE. At the one end of the cylindrical RVE only the nodes of the matrix profile are fully restrained, i.e. the degrees of freedom of all nodes of this surface are restricted. In the other end of the RVE, a displacement $u_z = \Delta\ell_m$ is applied uniformly at the nodes of the matrix profile. The corresponding profiles of the nanotube are not supported and loaded, respectively, in order to allow the stiffness of nanotube to be transferred to the matrix exclusively through the interconnection joints, i.e. the interface. The stress σ_z at each strain level $\varepsilon_z = \Delta\ell_n/\ell_n$ is computed via the following equation:

$$\sigma_z = \frac{\sum_{i=1}^{q_m}(-{}^{i}f_z)}{\pi[r_m^2 - (r_n + t_n/2)^2]} \tag{6}$$

where ${}^{i}f_z$ is the computed nodal force in the direction z of node i which belongs on the restrained plane of the matrix and q_m is the total number of nodes which belong to the specific plane.

The problem of the present study is highly characterized by a non-linear nature due to nonlinear behavior of the rubber material and the SWCNT. Thus, the uniform displacement loading $\Delta\ell_n$ is applied according to an incremental manner in order to follow an incremental-iterative procedure. According to this procedure the loading is applied in specified constant increments and an iterative algorithm is utilized to obtain convergence of the solution at each load level. The iterative process is based on the Newton-Raphson method and it is performed until a convergent solution is obtained at a specific step. The monitoring of the convergence is based on displacement and absolute residual norm. After the convergence of the last load increment, the final solution of the problem is achieved.

Table 1. Information about the finite element grids utilized in the analysis.

	Number of elements			Number of nodes		
V_n	Rubber	Tube	Joints	Rubber	Tube	Joints
0.01	35840	2260	1520	40680	1520	3040
0.02	31360	2260	1520	36160	1520	3040
0.03	26880	2260	1520	31640	1520	3040
0.04	27120	2260	1520	22400	1520	3040

Table 1 contains analytical information about the number of elements and nodes used for the computations for all volume fraction cases. The final discretization of all RVE models has been made after convergence tests on mesh density.

The results were computed by using 20 constant load increments. This number of increments was found sufficient to achieve relatively fast and enhanced convergence during Newton-Raphson iterative procedure between sequential increments. The computational cost for extracting the numerical solutions was relatively significant in all cases due to the exclusive usage of three dimensional finite elements. By using a personal computer equipped with a Pentium 4 CPU 3.73 GHz and a RAM 1 GB the computational times have reached 3 h.

3 RESULTS AND DISCUSSION

Using the previously presented numerical formulation, the mechanical uniaxial behavior of the rubber composite for various values of volume fraction V_n may be computed.

Firstly, it is assumed that the carbon-carbon bonds of the SWCNT may be stretched up to 100% without break.

Figure 5 depicts the computed stress-strain behavior of the nanocomposite for various volume fractions. The stress-strain behaviors of the rubber and SWCNT are included in the figure for comparative reasons. Secondly, it is assumed that the carbon-carbon bonds of the SWCNT break (zero spring stiffness) after a 20% strain (Figure 3). The extracted stress-strain behaviors for this case are presented in Figure 6. In this case, the curves present a sharp drop after the SWCNT fracture.

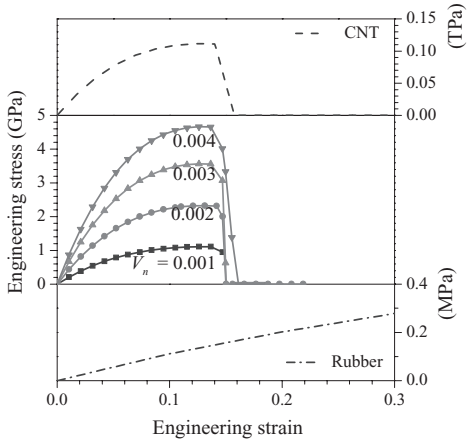

Figure 5. Stress-strain behavior of the composite for several volume fractions without considering SWCNT fracture.

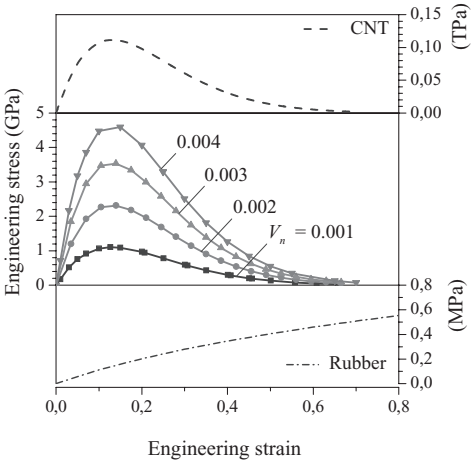

Figure 6. Stress-strain behavior of the composite for several volume fractions considering SWCNT fracture.

As a general conclusion the reinforcement addition in the rubber matrix leads to a very significant increase of its stiffness in all cases. Furthermore, for higher values of volume fraction V_n the toughness of the composite, which is a measure of its capability to absorb energy, is radically improved. Finally, the computations showed that composite Young's modulus seems to obey the rule of mixtures.

4 CONCLUSIONS

A numerical tool capable of predicting the mechanical behavior of SWCNT reinforced rubber has been developed. The formulation is based in a micromechanical, non-linear, finite element approach and utilizes a Mooney Rivlin material model for the rubber and takes into account the atomistic nanostructure of the nanotubes. The computed composite strain-stress behaviors under pure tension show definite advantages that arise by the SWNT reinforcements. The SWNTs improve significantly the composite strength and toughness especially for higher volume fractions. Simultaneously, the absorption energy characteristics of the rubber material are maintained in the composite.

Having as a basis the proposed method the mechanical response of rubber materials filled with SWNTs with more complicated arrangement and nanostructure i.e. nanotextiles and nanocords may be predicted in a future work. Moreover, the discrete nanostructure of the polymeric chains could be incorporated into the model.

REFERENCES

Bauer, R.F. & Crossland, A.H. 1990. The resolution of elastomer blend properties by stress-strain modelling-An extension of the model to carbon-black-loaded elastomers. Rubber Chemistry and Technology 63(5): 779–791.

Belytschko, T., Xiao, S.P., Schatz, G.C. & Ruoff, R.S. 2002. Atomistic simulations of nanotube fracture. Physical Review B 65: 235430.

Giannopoulos, G.I., Kakavas, P.A. & Anifantis, N.K. 2008. Evaluation of the effective mechanical properties of single walled carbon nanotubes using a spring based finite element approach. Computational Materials Science 41(4): 561–569.

Kakavas, P.A., Giannopoulos, G.I. & Anifantis, N.K. 2007. Mixed finite element analysis of elastomeric butt-joints. Journal of Engineering Materials and Technology, Transactions of ASME 129(1): 11–18.

Kołoczek, J., Young-Kyun, K. & Burian, A. 2001. Characterization of spatial correlations in carbon nanotubes-modelling studies. Journal of Alloys and Compounds 28: 222–225.

Mamedv, A.A., Kotov, N.A., Prato, M., Guldi, D.M., Wicksted, J.P. & Hirsch, A. 2002. Molecular design of strong single-wall carbon nanotube/polyelectrolyte multilayer composites. Nature Materials 1: 190–194.

Ogden, R.W. 1984. Nonlinear elastic deformations. New York: John Wiley & Sons.

Rappe, A.K., Casewit, C.J., Colwell, K.S., Goddard, W.A. & Skiff, W.M. 1992. UFF, a full periodic table force-field for molecular mechanics and molecular dynamics simulations. Journal of American Chemical Society 114: 10024–10035.

Thostenson, E.T., Ren, Z. & Chou, T.W. 2001. Advances in the science and technology of carbon nanotubes and their composites: A review. Composites Science and Technology 61: 1899–1912.

Yeoh, O.H. 1990. Characterization of elastic properties of carbon black filled rubber vulcanizates. Rubber Chemistry and Technology 63(5): 792–805.

Constitutive Models for Rubber VI – Heinrich et al. (eds)
© 2010 Taylor & Francis Group, London, ISBN 978-0-415-56327-7

Ansys user defined material implementation of van der Waals model

Heramb Shashikant Pathak
CADFEM GmbH, Graffing b. München, Germany

ABSTRACT: The real chain network is described in terms of a phenomenological modifications of the Gaussian theory. It is shown that by introducing modified invariant $\zeta = \beta\bar{I}_1 + (1-\beta)\bar{I}_2$, van der Waals model describe the multiaxial deformation modes of the chain network. On the basis of van der Waals strain energy function $W(C)$, resulting constitutive equations are derived. van der Waals model is implemented in finite element software like ANSYS. The utility of the approach is demonstrated by comparing the results of stress-strain experiments with numerical and analytical solutions.

Finally, it is shown that non-linear visco-elastic response in stress-strain cycles of natural rubber can be understood within the framework of the classical thermodynamics of irreversible processes.

Keywords: Rubber elasticity, deformation modes, hyperelasticity, van der Waals theory

1 INTRODUCTION

It might be reasonable to take into account the effect of mutual interaction of chain molecules and finite chain length in order to describe the complete physical behavior of the rubber elastic system.

Van der Waals theory of real gas is closely related to the thermomechanical description of the molecular network. By considering mutual interaction between the chain molecules, we arrive at the van der Waals theory of the real conformational gas.

1.1 *Preamble*

The phenomenon of rubber elasticity is associated with micro Brownian motion of the individual elements of long chains in a molecular network. This type of motion is similar to the thermal motion of molecules of an ordinary liquid, with the single difference that the moving units, instead of being entirely independent, are connected together in the form of a macromolecular network. In certain respects, therefore we should expect to find on the local level a close similarity between the properties of rubbers and of liquids.

A rubber is distinguished from a liquid by the presence of long chain molecules, possessing freely rotating links.The molecules are interlocked at few places along their length to form a three dimensional network.

The total number of configurations, hence the entropy of the ideal network, can be calculated by statistical methods. If each junction point is taken to be fixed at its mean position and if the chains have an infinite contour length and if the volume is a strain invariant, the statistical treatment leads to the Gaussian network theory.

The Gaussian theory involves only a single physical parameter, the shear modulus G related to N, the number of chains per unit volume. The elastic properties of the Gaussian are universal because they are independent of the chemical nature of the molecules. The Gaussian network behaves like an ideal conformational gas network comprising chains of infinite contour length. Energy is equipartioned among these chains.

This is easily demonstrated that mechanical equations of state of the ideal gas or of the Gaussian network are analogous.

Ideal gas $P_i = Nk_BT\left(\frac{1}{V}\right)$

Ideal conformational gas network $F_i = Nk_BT\left(\frac{\partial\Psi}{\partial\lambda}\right)$

where, for simple extension test

$$\Psi = \frac{\left(\lambda^2 + \frac{2}{\lambda} - 3\right)}{2}$$

Another interference can be made from the fact that internal energy of the ideal gas or of the Gaussian network are identical.

$$U_{\text{gas}} = U_{\text{network}} = \frac{3Nk_BT}{2}$$

The internal energy U of an ideal gas is given by the kinetic energy of N mass points, equipartitioned amongst these particles. Because there is no interaction, U does not depend on the volume. This is characteristic of an ideal gas. A Gaussian network behaves analogously. Kinetic energy is equipartitioned among the N mass fiber chains. The internal energy does not depend on strain. For this reason we call the Gaussian network an ideal conformational gas network.

In comparing experimental stress-strain curves with formulae derived from the Gaussian theory, one observes serious deviations. It is therefore suggests itself to try to describe real network in terms of phenomenological modification of the Gaussian theory so that fundamental features are preserved. In the van der Waals approach two modifications are put forward, namely, considerations of finite extensibility and global interaction.

2 CONCEPTUAL MODEL

2.1 *Van der Waals model*

Consider incompressible isotropic mechanically stable systems deformed under equilibrium conditions. Since the elastic system is characterized by its strain energy function, it is clear that we have to seek the most general formulation of the elastic potential of a van der Waals network. The system is believed to be represented as a quasi continuum comprised of a defined number of energy equivalent subsystems of deformation, in the case of a perfectly homogeneous network represented by the chains themselves. For an incompressible and isotropic elastic body of this type we led for the principal of material objectivity, to the simplest form of the strain energy function comprising two of the three strain invariants ($\bar{I}_1$, $\bar{I}_2$) of the Cauchy-Green deformation tensor $\bar{C}$. Taking into account the the van der Waals corrections, the universality in the formulation of the strain energy function must necessarily become reduced.

$$W = W(\bar{I}_1, \bar{I}_2; y, a) \tag{1}$$

whereby the strain invariants are written as

$$\bar{I}_1 = tr(\bar{C}) \tag{2}$$

$$\bar{I}_2 = \frac{1}{2}\left\{(tr(\bar{C}))^2 - tr(\bar{C}^2)\right\} \tag{3}$$

The length parameter y is defined as the number of statistical segments per chain while a is the phenomenological fluctuation parameter in the van der Waals version.

2.2 *The van der Waals parameter*

If the chains themselves are not too short, the maximum extensibility of a single entity can be approximated by the use of the Gaussian measure

$$(\lambda_{\text{max-chain}})^2 = y \tag{4}$$

'y' is the number of Kuhn segments.

If the totality of the crosslinks is now transformed according to the law of affinity, we are led to the significant consequence

$$y = (\lambda_{m1})^2 + (\lambda_{m2})^2 + (\lambda_{m3})^2 \tag{5}$$

The maximum strain parameters in the three directions of the coordinate frame, are assumed to be uniquely determined by the single chain structure parameter y. In the mode of simple elongation the maximum strain λ_m^1 is estimated to be roughly identical with

$$\lambda_m^1 \simeq y^{\frac{1}{2}} \tag{6}$$

In the equibiaxial mode the maximum macroscopic strain in both coordinate axes is reduced to the value

$$\lambda_m^2 = \frac{\lambda_m^1}{\sqrt{2}} \tag{7}$$

In swelling a dry network, this process corresponds to the mode of equitriaxial extension, such that the maximum strain in all directions should now become equal to

$$\lambda_m^3 = \frac{\lambda_m^1}{\sqrt{3}} \tag{8}$$

2.3 *Material modeling*

In order to describe the behavior of deformable bodies, we need an additional set of equations in the form of appropriate constitutive laws. A constitutive equations determines the state of stress at any point x of a continuum body at time t

and is necessarily different for different types of continuous bodies. These equations establish an axiomatic or empirical model as the basis for approximating the behavior of a real material. The process of obtaining these constitutive equations is called as **material modelling**.

van der Waals strain energy function W
It is necessary to find infinitely large energy densities when the rubber is strained to its maximum. This singularity has to be met irrespective of the shape the rubber is forced into.

The generalized form of the van der Waals strain energy function is given by

$$\hat{W}(\bar{C}) = G\left[\begin{array}{l} -2y\{\ln(1-\eta)+\eta\} \\ -\left(\frac{2a}{3}\right)\left(\frac{(\zeta-3)}{2}\right)^{\frac{3}{2}} \end{array}\right] \tag{9}$$

where the modified strain invariant ζ is defined by

$$\zeta = \beta\bar{I}_1 + (1-\beta)\bar{I}_2 \tag{10}$$

$$\eta = \left(\frac{(\zeta-3)}{y}\right)^{\frac{1}{2}} = \left(\frac{(\beta\bar{I}_1 + (1-\beta)\bar{I}_2 - 3)}{y}\right)^{\frac{1}{2}} \tag{11}$$

The modulus is explicitly expressed as

$$G = \varrho RT\left(\frac{\xi}{M_c}\right) = \varrho RT\left(\frac{\xi}{yM_s}\right) = \left(\frac{\varrho RT}{yM_0}\right) \tag{12}$$

The molecular weight of the chain M_c can be written as

$$M_c = yM_s \tag{13}$$

with M_s as the molecular weight of the statistical Kuhn segment. But the statistical segment is by no means stretching invariant. To accept strain dependent changes of diffusive conformational freedoms per statistical segment, is equivalent to defining the actual stretching invariant unit with respect to the system's entropy by

$$M_0 = \frac{M_s}{\xi} \tag{14}$$

As system is incompressible, isotropic, there is no change in volume. Hence we will consider only isochoric or volume preserving part of the strain energy. Near incompressibility is often a device by which incompressibility can more readily be enforced within the context of the finite element formulation. This is facilitated by adding a volumetric energy component $U(J)$ to the isochoric (distortional) component $\hat{W}$ to give the total strain energy function $W(\bar{C})$ as follows.

$$W(\bar{C}) = \hat{W}(\bar{C}) + U(J) \tag{15}$$

where the simplest form of a volumetric function $U(J)$ is

$$U(J) = \frac{1}{2}k(J-1)^2 \tag{16}$$

where the penalty number k can represent a true material property, namely the bulk modulus for a compressible material. It will approximately enforce incompressibility. Typical values of k in the region of 10^3–10^4 μ are used for this purpose.

Second Piola-Kirchhoff stress tensor S
The second Piola-Kirchhoff stress tensor (S) is symmetric and parameterized by material coordinates. Therefore, it often represents a very useful stress measure in computational mechanics.

The second Piola-Kirchhoff tensor for a material is obtained in standard manner with the help of relation $\partial III_c / \partial C = J^2 C^{-1}$.

$$S = J^{-\frac{2}{3}}\mathrm{Dev}\left(2\frac{\partial\hat{W}(\bar{C})}{\partial\bar{C}}\right) + U(J)$$

$$S = J^{-\frac{2}{3}}\mathrm{Dev}\left\{2\left[\frac{\partial\hat{W}(\bar{C})}{\partial\bar{I}_1}I + \frac{\partial\hat{W}(\bar{C})}{\partial\bar{I}_2}(\bar{I}_1 I - \bar{C})\right]\right\} + pJC^{-1}$$

Kirchhoff stress tensor τ
The Kirchhoff stress tensor is obtained by performing push forward operation on each second order tensor present in the second Piola-Kirchhoff stress tensor equation.

$$\tau = FS_{\text{isochoric}}F^T + FU(J)F^T$$

Total stress σ
By using the relation $\tau = J\sigma$, we get the expression for total stress. But in order to get it in terms of nearly incompressible form, it is necessary to add isochoric and volumetric part.

Elasticity tensor
The formulation for the elasticity tensor composed of isochoric part $\mathbb{C}_{\text{iso}}$ and volumetric part $\mathbb{C}_{\text{vol}}$.

$$\mathbb{C} = \mathbb{C}_{\text{iso}} + \mathbb{C}_{\text{vol}}$$

The complete expression for the $\mathbb{C}$ takes the following form.

$$\mathbb{C} = \underbrace{\mathbb{P} : \bar{\mathbb{C}} : \mathbb{P}^T}_{A} + \underbrace{\frac{2}{3}\mathrm{Tr}(J^{-\frac{2}{3}}\bar{S})\bar{\mathbb{P}}}_{B} - \underbrace{\frac{2}{3}(C^{-1} \otimes S_{\mathrm{iso}} + S_{\mathrm{iso}} \otimes C^{-1})}_{C} + \underbrace{[pJ[(C^{-1} \otimes C^{-1}) - 2\mathbb{I}] + kJ^2(C^{-1} \otimes C^{-1})]}_{D} \tag{17}$$

3 IMPLEMENTATION AND VALIDATION

3.1 *Co-rotational approach flowchart*

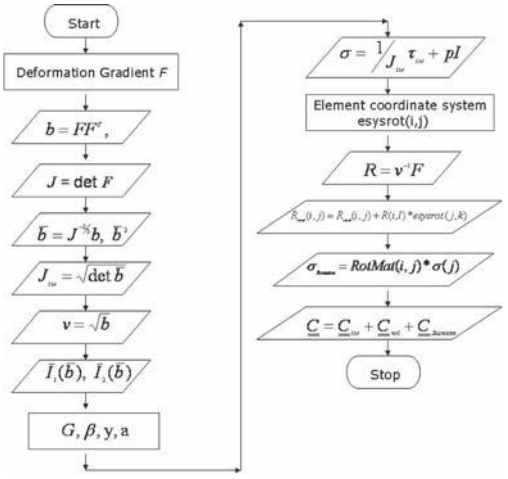

Figure 1. Co-rotational approach.

3.2 *Validation*

In order to validate the implementation material model in finite element software, it is necessary to compare the finite element results with the analytical and simple deformation tests results.

Standard analytical expressions to calculate true stress for different deformation tests are as follows

Uniaxial extension

$$\sigma_1 = 2(\lambda_1^2 - \lambda_1^{-1})\left[\frac{\partial W}{\partial I_1} + \lambda_1^{-1}\frac{\partial W}{\partial I_2}\right] \tag{18}$$

Pure shear

$$\sigma_1 = 2(\lambda_1^2 - \lambda_1^{-2})\left[\frac{\partial W}{\partial I_1} + \frac{\partial W}{\partial I_2}\right] \tag{19}$$

Equibiaxial extension

$$\sigma_1 = 2(\lambda_1^2 - \lambda_1^{-4})\left[\frac{\partial W}{\partial I_1} + \lambda_1^2\frac{\partial W}{\partial I_2}\right] \tag{20}$$

In case of van der Waals material model $\partial\hat{W}/\partial\bar{I}_1$ and $\partial\hat{W}/\partial\bar{I}_2$ are derived by using the following expressions

$$\frac{\partial\hat{W}}{\partial\bar{I}_1} = \beta\frac{\partial\hat{W}}{\partial\varsigma} \tag{21}$$

$$\frac{\partial\hat{W}}{\partial\bar{I}_2} = (1-\beta)\frac{\partial\hat{W}}{\partial\varsigma} \tag{22}$$

where

$$\frac{\partial\hat{W}}{\partial\varsigma} = (1-\eta)^{-1} - a\left\{\frac{(\varsigma-3)}{2}\right\}^{\frac{1}{2}} \tag{23}$$

$$\frac{\partial\hat{W}}{\partial\varsigma} = \left[1-\left(\frac{(\varsigma-3)}{y}\right)\right]^{-1} - a\left[\frac{(\varsigma-3)}{2}\right]^{\frac{1}{2}} \tag{24}$$

$$\frac{\partial\hat{W}}{\partial\varsigma} = \left[1-\left(1-\left(\frac{(\beta\bar{I}_1+(1-\beta)\bar{I}_2-3)}{y}\right)\right)\right] - a\left[\frac{(\beta\bar{I}_1+(1-\beta)\bar{I}_2-3)}{2}\right]^{\frac{1}{2}} \tag{25}$$

3.3 *Comparison with experimental and analytical solution*

In examining the applicability of the stress-strain relations deduced above, it is desirable to work with samples under many types of strain.

Uniaxial extension test

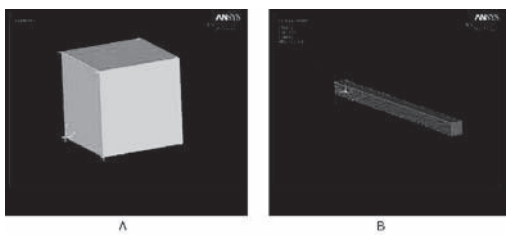

Figure 2. Uniaxial extension test: A) Finite element model B) Deformed shape.

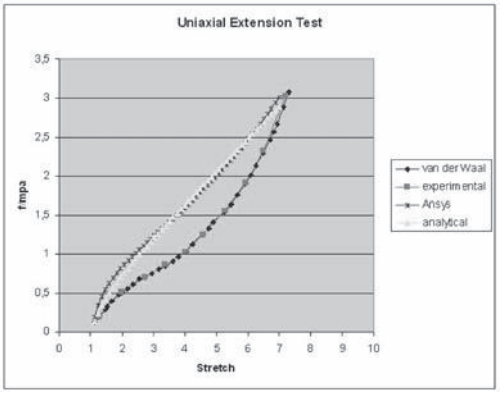

Figure 3. Engineering stress against stretch at T = 295 K for natural rubber according to Treloar. The van der Waals model parameters are G = 0.328, y = 161.29, a = 0.245, beta = 0.50.

The quality of the representation of experiments carried out by Treloar for natural rubber is clearly seen. van der Waals material model result for the uniaxial extension is obtained by using the following formulation for the true stress.

$$f = GD\left\{\frac{1}{(1-\eta)} - a\phi^{\frac{1}{2}}\right\} \tag{26}$$

Use of so called penalty number k will apprximately enforce incompressibility. Typical values of k in the region of 10^3–$10^4\mu$ are used for this purpose. Furthermore, in practical terms, a finite element analysis rarely enforces $J = 1$ in a strict point wise manner, and hence its retention may be important for the evaluation of stresses. As shown in the above figure implementation of the van der Waals material model validate nearly incompressibility condition. In case of simple extension and pure shear the difference between undeformed and deformed volume is nearly equal to one.

Pure shear test

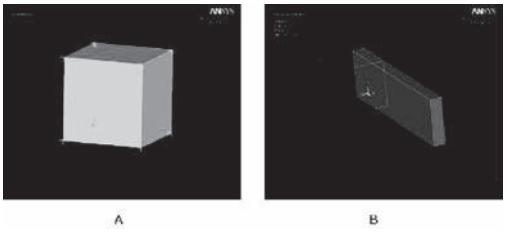

Figure 4. Pure shear test: A) Finite element model B) Deformed shape.

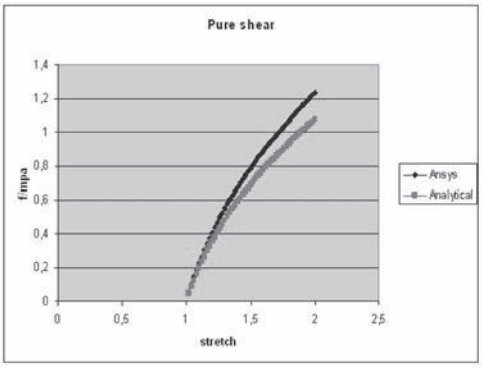

Figure 5. Engineering stress against stretch at T = 295 K for natural rubber according to Treloar. The van der Waals model parameters are G = 0.328, y = 161.29, a = 0.245, beta = 0.50.

Nearly incompressibility condition

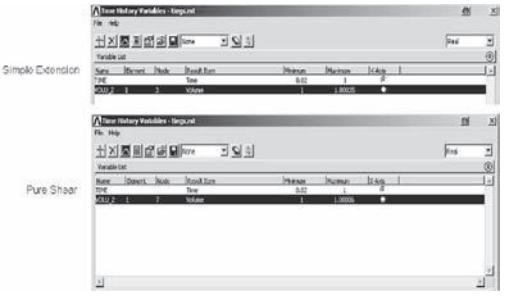

Figure 6. Nearly incompressible hyperelastic material.

4 CONCLUSIONS

A framework has been set up to develop mathematical model for representing the real behavior of matter in which the strains may be the large, i.e. finite. As finite element analysis rarely enforces fully incompressibility, constitutive equations are obtained for nearly incompressible, isotropic hyperelastic material by decoupling it into the volumetric and isochoric parts.

It has been shown that thermomechanical description of van der Waals material model is closely related to the van der Waals theory of real conformational gas. Generalized form of the van der Waals strain energy function Ψ is obtained in terms of modified invariant $\zeta = \beta\bar{I}_1 + (1-\beta)\bar{I}_2$, finite chain extensibility (y) and mutual interaction (a). With the help of phenomenological constitutive equations, stress and strain components are derived from the van der Waals strain energy function. Finally in order to obtain the solution for nonlinear problems in computational

finite elasticity, elasticity tensor is calculated which resembles tangent stiffness matrix arising in a finite element discretization process.

The most general corotational approach is used to implement the material in finite element tool like Ansys. It has been seen that rotation of stress and elasticity tensor from material to spatial coordinate system can be avoided by using Hencky strain formulation. Results of implementation are in agreement with the analytical solution for the deformation tests like simple extension and pure shear.

The conclusion to be drawn from the preceding discussions is that the formulae of the van der Waals modification of the Gaussian network, involving four constants G, β, y, and a, correctly describe the elasto-mechanical properties of real networks. In particular they provide an understanding of the relation between the stress-strain curves for different types of strain.

Future work can include validation of the material model with equibiaxial and volumetric tests results. Validation also must be done by comparing the finite element solution with more and more experimental results for different materials undergoing large deformation. Currently validation is done only for the single element, multielement testing is required. Finally, it is the ultimate aim of this work to implement van der Waals material model in Ansys to make it commercial, as an alternative incompressible, isotropic, hyperelastic material model.

REFERENCES

H.F. Enderle & H.G. Kilian, "General deformation modes of a van der Waals network", Progr Colloid and Polymer Sci 75: 55–61(1987).

H. Ambacher, H.F. Enderle, H.G. Kilian & A. Sauter, "Relaxation in permanent networks" Progr Colloid and Polymer Sci 209: 220–61(1989).

Hanns Georg Kilian, "Equation of state of real networks", November 1979.

"Principles of the van der Waals network concept: Time dependent process", Hanns-Georg Kilian, Markromol. Chem., Macromol. Symp. 30, 169–198(1989).

"A molecular interpretation of the parameters of the van der Waals equation of state for real networks", H.-G. Kilian, Polymer Bulletin 3, 151–158(1980).

"NONLINEAR SOLID MECHANICS"; Gerhard A. Holzapfel.

"Nonlinear Continuum Mechanics for Finite Element Analysis"; Javior Bonet & Richard D. Wood.

"The Physical Testing and Modeling of Hyperelastic Materials for Finite Element Analysis"; Raphael Johannknecht, Esslingen a.N.

"Finite Thermoplastizitat", Dipl-Ing. Armin Fritsch.

"Introduction to Fortran 90 for Engineers and Scientists", Nyhoff and Leestma, Prentice hall.

"Programmer's manual for ANSYS".

Constitutive Models for Rubber VI – Heinrich et al. (eds)
© 2010 Taylor & Francis Group, London, ISBN 978-0-415-56327-7

Filler-reinforced rubber under transient and cyclic loadings: Constitutive modeling and FEM-implementation for time domain simulations

M. Rendek & A. Lion
Institute of Mechanics, Department of Aerospace Engineering University of Federal Armed Forces Munich, Neubiberg, Germany

ABSTRACT: On the basis of comprehensive experimental data, an amplitude dependent constitutive model of finite viscoelasticity based on a rheological Maxwell-chain with process-dependent state variables is developed. The formulation of this thermodynamically consistent model is possible in both the time and the frequency domain. This property is very profitable in the material-parameter identification process for FEM simulations of real parts. This kind of model allows transient FEM simulations of various rubber parts under arbitrary cyclic loading processes. Due to physical and geometrical nonlinearities, these simulations are not possible in the frequency domain. Numerical examples are computed in the context of the transient material behaviour. To this end, deformation processes with dynamic amplitude-changes are prescribed.

1 INTRODUCTION

Cyclically-loaded industrial rubber-parts normally manufactured using complicated filler-reinforced elastomers show many nonlinear viscoelastic effects. Best-known are the frequency- and the amplitude-dependence (Payne-effect) as well as the Mullins-effect. In the context of dynamic material properties in the frequency domain the behaviour of the storage and the loss modulus is generally studied. In order to understand these effects in more detail it is profitable to execute cyclic tests in time domain which allow observing further transients effects. The focus of this paper is concentrated to the amplitude dependence observed already in the 60 s (Payne 1962).

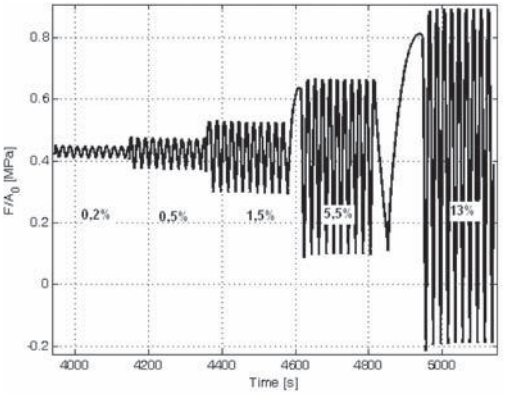

Figure 1. Stress response from cyclic tension test with stepwise changing dynamic amplitude (carbon black filled ESBR).

2 EXPERIMENTAL OBSERVATION OF DYNAMIC MATERIAL BEHAVIOUR

2.1 *Quasistatic tension cyclic tests*

In order to investigate the amplitude dependence, i.e. the reversible softening of the dynamic stiffness with increasing dynamic strain amplitude (Payne 1962), cyclic tension experiments with stepwise changing amplitudes and a frequency of 0.1 Hz were carried out (Fig. 1). Prior to the real test, the rubber specimen was conditioned in order to eliminate the Mullins-effect. It is observed, that the stress amplitudes decrease significantly during a certain time after the amplitude change. The material deformed in such a way becomes softer which corresponds to the Payne-effect in time domain. The observed stress softening and recovery effects can be physically interpreted as process-induced reversible changes in the materials' microstructure.

2.2 *DMA experiments*

As a standard approach to study the Payne-effect and its frequency dependence amplitude sweep

tests with different frequencies were driven (Fig. 2) (Ji-Hyun Cho 2006). The experimental data shows the amplitude dependence of carbon black-filled rubber for different frequencies. With increasing frequency the softening is more pronounced. Corresponding to the smallest amplitude, the frequency dependence is studied with the sweep test in Fig. 4. Typically, the amplitude-dependent storage modulus shows two plateaus regions (Lion et al. 2009) where it is nearly constant. Between them is a pronounced transition area where it decreases with growing amplitudes.

Another method to study the Payne-Effect is the amplitude step test in the time domain which has already been discussed. In this case, the DMA shows the dynamic modulus as a time-dependent function of the dynamic strain amplitude (Fig. 3). The strain amplitude jumps occur every 2700 s.

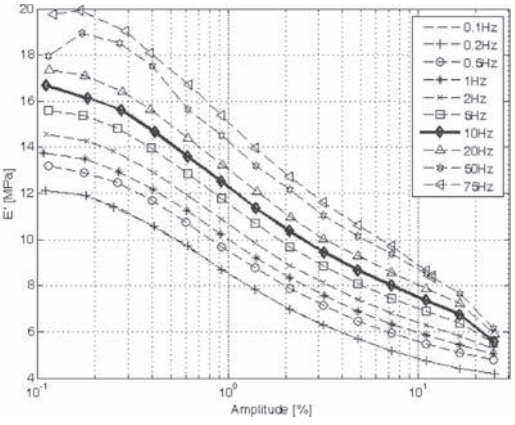

Figure 2. Amplitude sweep (in the transition region) at different frequencies (carbon black filled ESBR, SHORE 75°).

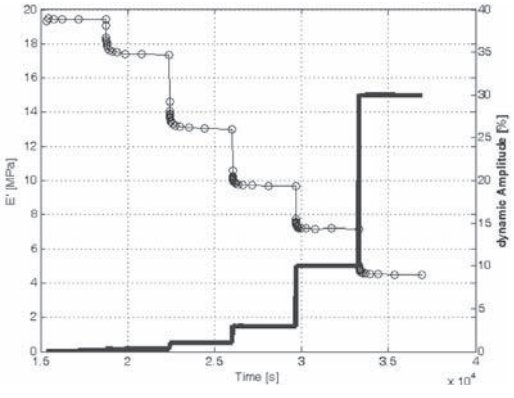

Figure 3. Amplitude step test from DMA at 10 Hz (carbon black filled ESBR, SHORE 75°).

The stationary values of the storage modulus obtained from the amplitude step test (Fig. 3) match with the moduli values belonging to the same strain amplitude and frequency (10 Hz) from the amplitude sweep test (Fig. 2). After the amplitude changes, a pronounced relaxation behaviour is observed.

3 CONSTITUTIVE MODEL

The concept of finite nonlinear viscoelasticity based on Maxwell elements provides a good basis for the representation of the observed phenomena of carbon black-filled rubber (cf. Höfer and Lion 2009 or Lion 2004). The constitutive model describes hyperelastic material behavior, rate- and frequency effects and the amplitude dependence. In the case of transient loading processes, the authors frequently concentrate to the relaxation behavior of the parts (see Holzapfel 1996). As defined in Eq. 1, the total Cauchy stress is decomposed into a rate-independent equilibrium stress and a rate-dependent overstress.

$$\mathbf{T} = \mathbf{T}_{eq} + \sum_{k=1}^{n} \mathbf{T}_{ov_k} \tag{1}$$

The hyperelastic equilibrium stress is modeled by a nearly incompressible model of the Neo-Hookean type with two material parameters (see Eq. 2.). The motivation for this choice is the difference of about three orders of magnitude in the numerical values of the bulk and shear behavior of elastomers.

$$\mathbf{T}_{eq} = \frac{2}{d}(J-1)\mathbf{1} + J^{-\frac{5}{3}}\mu\left(\mathbf{B} - \frac{1}{3}tr(\mathbf{B})\mathbf{1}\right) \tag{2}$$

The overstress is formulated as the sum of partial overstresses belonging to the Maxwell-elements of the chain. The structure of the constitutive equations for the partial overstresses can be motivated from uniaxial Maxwell-elements (Eq. 3) (cf. Haupt 2002). The rate of the partial overstress in Eq. 3 is an Oldroyd derivative and **D** is the well-known strain rate tensor. The scalar functions $H_k(t)/Z_k^0$ can be interpreted as process-dependent relaxation times and the material parameters η_k are the viscosities belonging to the Maxwell elements.

$$\overset{\nabla}{\mathbf{S}}_{ovk} + \frac{H_k(t)}{Z_k^0}\mathbf{S} = 2\frac{\eta_k}{Z_k^0}\mathbf{D} \tag{3}$$

Application of 'pull-back' transformation to Eq. 3, introduction of the internal variables $\mathbf{e}_{\text{plk}}$ of Piola strain type and the definition $c_k = \eta_k/z_k^0$ leads to Eq. 4 for the overstress tensor of Cauchy

type and to Eq. 5 for the inelastic Piola strain. This formulation is equivalent to Eq. 3 and describes the viscoelastic material behaviour in the material configuration.

$$\begin{aligned}\mathbf{T}_{ovk} &= \frac{1}{\det \mathbf{F}} \mathbf{F} \tilde{\mathbf{T}}_{ovk} \mathbf{F} \\ &= -\frac{2c_k}{\det \mathbf{F}} (\mathbf{F} \cdot \mathrm{e}_k \cdot \mathbf{F}^T - \mathbf{F} \cdot \mathrm{e}_{ink} \cdot \mathbf{F}^T)\end{aligned} \tag{4}$$

$$\dot{\mathbf{e}}_{ink}(t) = \frac{H_k(t)}{Z_k^0} (\mathbf{e}(t) - \mathbf{e}_{ink}(t)) \tag{5}$$

The relation between the amplitude dependence and the microstructure relaxation is considered by the function $H_k(t)$. It is defined by Eq. 6 and determined by the internal state variable $q_k(t)$ (Eq. 7) of the corresponding Maxwell element (Rendek and Lion 2009). The rate of the change in the dynamic moduli can be controlled by the gain factors d_k. This allows scaling transient processes and is leading to reduced computation times without loosing information.

$$H_k(t) = 1 + d_k \cdot q_k(t) \tag{6}$$

$$q_k(t) = \frac{1}{\lambda_k} (\|\mathrm{D}\| - q_k(t)) \tag{7}$$

The constants λ_k in the evolution equations for the state variables $q_k(t)$ (Eq. 7) are the relaxation times of the microstructure. However, the experimental data shows that the changes in the dynamic moduli are faster when the strain amplitude increases (Fig. 3) than when it decreases. This implies that the λ_k should depend on the deformation process.

$$\|\mathbf{D}\| = \frac{1}{2} \sqrt{tr((\mathbf{C}^{-1}\dot{\mathbf{C}})^2)} \tag{8}$$

In our model, the amplitude dependence is driven by the norm of strain rate tensor $\|\mathbf{D}\|$ which is very sensitive to amplitude changes (Eq. 8).

4 MATERIAL PARAMETER IDENTIFICATION IN THE FREQUENCY DOMAIN

The above formulated constitutive equations contain a set of material parameters representing the actual material properties. These parameters must be determined by experiments. Since the formulation of the constitutive model is possible in both the time and the frequency domain, the possibility to identify the parameters on the basis of the stress time signals or the curves of the dynamic moduli is provided. The identification according to the dynamic moduli is faster and the identified material constants are valid in wider range of frequencies and amplitudes.

The uniaxial stress response for a sinusoidal deformation process is given by Eq. 9.

$$\frac{\sigma(t) - \sigma_{eq0}}{\Delta\varepsilon} = E' \sin(\omega t) + E'' \cos(\omega t) \tag{9}$$

In Eq. 9, the complex modulus E^* is decomposed into its real part E' describing the dynamic elastic material behavior and its imaginary part E'' which is related to the damping behavior. Due to Fourier analysis of Eq. 4 and Eq. 5 in combination with Eq. 6 and Eq. 7 and some additional assumptions we obtain the first two Fourier coefficients as the frequency-, amplitude- and time-dependent storage and loss modulus (Eq. 10 and Eq. 11).

$$E'(\omega, \Delta\varepsilon, t) = 3\mu + \sum_{n=1}^{k} \frac{\eta_k \omega^2 Z_k^0}{H_k^2(t) + (\omega Z_k^0)^2} \tag{10}$$

$$E''(\omega, \Delta\varepsilon, t) = \sum_{n=1}^{k} \frac{H_k(t) \eta_k \omega}{H_k^2(t) + (\omega Z_k^0)^2} \tag{11}$$

Due to the structure of the model, the identification process is based on two steps. At first, a sufficient small strain amplitude of about 0.1% is applied such that the dynamic moduli are time- and amplitude-independent and we have $H_k = 1$. Thus, the material parameters c_k, η_k and μ can be determined by means of the frequency sweep in Fig. 4.

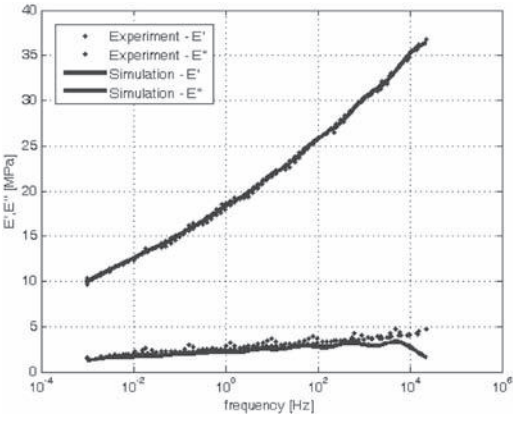

Figure 4. Identification of the material parameters c_k, η_k and μ in the frequency domain, 12 Maxwell Elements were used.

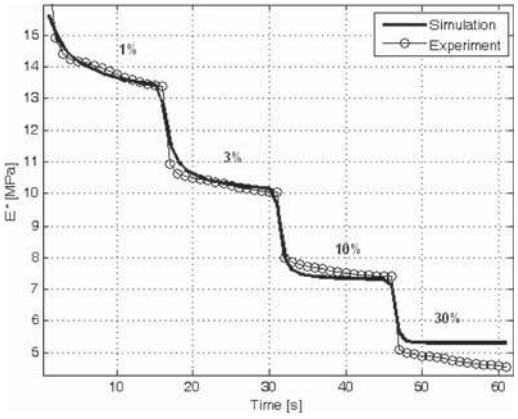

Figure 5. Identification of the amplitude dependent material parameters d_k and λ_k, 12 Maxwell Elements were used.

Table 1. Identified material parameters for 12 Maxwell elements for carbon black filled ESBR (SHORE 75°). The constants c_k are given MPa, the viscosities η_k in MPas, the λ_k in s and the d_k are dimensionless.

	$3\mu = 9.3074$	$d = 0.001$	
$c_1 = 3.2825$	$\eta_1 = 0.0791$	$\lambda_1 = 208.0396$	$d_1 = 9.5834$
$c_2 = 1.4997$	$\eta_2 = 2.3326$	$\lambda_2 = 11.1762$	$d_2 = 28.9479$
$c_3 = 2.4369$	$\eta_3 = 0.4517$	$\lambda_3 = 111.6479$	$d_3 = 11.3158$
$c_4 = 0.7705$	$\eta_4 = 0.1427$	$\lambda_4 = 96.6838$	$d_4 = 6.6054$
$c_5 = 4.5348$	$\eta_5 = 0.0086$	$\lambda_5 = 245.4763$	$d_5 = 11.8292$
$c_6 = 5.6670$	$\eta_6 = 0.0009$	$\lambda_6 = 394.8773$	$d_6 = 25.9584$
$c_7 = 1.7240$	$\eta_7 = 123.57$	$\lambda_7 = 1.1461$	$d_7 = 170.413$
$c_8 = 1.3004$	$\eta_8 = 2.0097$	$\lambda_8 = 3.1922$	$d_8 = 18.3577$
$c_9 = 1.4179$	$\eta_9 = 421.45$	$\lambda_9 = 1.1362$	$d_9 = 703.421$
$c_{10} = 0.988$	$\eta_{10} = 0.011$	$\lambda_{10} = 188.54$	$d_{10} = 8.1464$
$c_{11} = 1.377$	$\eta_{11} = 1265$	$\lambda_{11} = 1.0000$	$d_{11} = 999.99$
$c_{12} = 2.427$	$\eta_{12} = 25.31$	$\lambda_{12} = 2.7444$	$d_{12} = 138.61$

In the second step, the constants d_k and λ_k in Eq. 10 and Eq. 11 describing the amplitude dependence are identified on the basis of the test at 10 Hz (Fig. 5). To compute the time and amplitude dependent modulus it is necessary to solve the evolution equations for the variables q_k (Eq. 7) for the deformation process with stepwise changing amplitude.

To reduce the extremely long simulation times for the parameter identification, the time-axis of the test shown in Fig. 3 was compressed by a factor of 180. Then, the hold times of 2700 s at constant amplitude were reduced to 15 s. The advantage of this scaling is the reduction of the computation times, particularly with regard to long-term transient FEM simulations in the time domain.

In both steps, the parameter identification implies to solve the non-linear least-squares problem with optimization (Eq. 12).

$$\min_{\mu,\eta_k,c_k,d_k,\lambda_k} \frac{1}{2}\left\|E'_{\mathrm{OPT}}\right\|_2^2 = \frac{1}{2}\sum_i \left(E'_{\mathrm{DMA}}(\omega_i) - E'_{\mathrm{SIM}}(\omega_i)\right)^2 \tag{12}$$

For quantitative good parameter identification results with values of the residual norm below 0.1% 12 nonlinear Maxwell elements were needed. The parameters are listed in Table 1. Since the quality of the approximation is sufficient it is not necessary to incorporate more Maxwell-elements or material parameters into the constitutive model.

5 FEM IMPLEMENTATION AND TRANSIENT SIMULATION RESULTS

The developed material model was implemented into the commercial FEM code ANSYS in an updated Lagrangean formulation (Crisfeld 1998). The implementation of user-written constitutive models is possible with the subroutine USERMAT.f which is in the focus of current section. This subroutine is based on a corotational formulation of stresses and strains (cf. Crisfeld 1998 or Simo 2000). All element quantities are initially computed in the reference configuration and then rotated to the current configuration. The polar decomposition of the deformation gradient is needed for large-strain and large-rotation applications. It has been used to compute the rotation tensor R.

$$q_k(n+1) = \frac{\lambda_k}{\lambda_k + \Delta t} q_k(n) + \frac{\Delta t}{\lambda_k + \Delta t}\left\|\mathrm{D}(n+1)\right\| \tag{13}$$

The incremental solution procedure makes the implementation and the integration of the differential equations for the rates of the state variables (Eq. 7) and the rate of inelastic Piola-strains (Eq. 5) very comfortable. Eq. 13 and Eq. 14 are the incremental solutions of Eq. 7 and Eq. 5 with the Euler-Backward algorithm in the recursive form.

$$\mathbf{e}_{plk}(n+1) = \frac{Z_k}{(Z_k + H_k(n+1)\Delta t)}\mathbf{e}_{plk}(n) + \frac{H_k(n+1)\Delta t}{(Z_k + H_k(n+1)\Delta t)}\mathbf{e}(n+1) \tag{14}$$

At every time increment, the stress tensor is computed according the Eq. 4 in the reference configuration. Then, it is rotated to current configuration. The updated total Cauchy stress is the sum of the

rotated total stress from the previous time step and the rotated stress increment (Eq. 15).

$$\mathbf{T}(n+1) = \mathbf{T}(n) + (\Delta\mathbf{R}^T)(\Delta\mathbf{T}(n+1))(\Delta\mathbf{R}) \tag{15}$$

Every incremental solution procedure in the context of finite element analyses needs the tangent stiffness operator matrix. Besides the stiffness matrix, the strain-displacement relationship matrix and the internal force vector are also needed. But in the context of the implementation of material models the material tangent operator is in the focus. Its concrete formulation depends on the formulation of the kinematics in the finite element code. The updated Lagrangean material stiffness matrix, relevant for the FEM code ANSYS, is based on the Jaumann rate of the total Kirchhoff stress tensor and the strain rate tensor (Eq. 16).

$$\overset{\circ}{\mathbf{S}} = \overset{4}{\tilde{\mathbb{C}}}\,\mathbf{D} \tag{16}$$

The stiffness matrix in Eq. 16 can be derived by the pre-transformation of the 4th order material stiffness operator (Eq. 17).

$$\begin{aligned}\overset{4}{\tilde{\mathbb{C}}}(n+1) = {} & [\mathbf{F}^T\otimes\mathbf{F}^T]^{T_{14}}\, 2\frac{\partial\tilde{\mathbf{T}}}{\partial\mathbf{C}}\, [\mathbf{F}\otimes\mathbf{F}]^{T_{14}} \\ & + \det\mathbf{F}([\mathbf{T}\otimes\mathbf{1}]^{T_{14}} + [\mathbf{1}\otimes\mathbf{T}]^{T_{14}})\end{aligned} \tag{17}$$

The additive decomposition of the stress tensor leads to a corresponding decomposition of the material stiffness operator into the sum of equilibrium and overstress parts (Eq. 18).

$$\overset{4}{\tilde{\mathbb{C}}}(n+1) = \overset{4}{\tilde{\mathbb{C}}}_{eq}(n+1) + \sum_{n=1}^{K} \overset{4}{\tilde{\mathbb{C}}}_{ovk}(n+1) \tag{18}$$

The equilibrium part (Eq. 19) can be calculated directly from Eq. 2. The corresponding parts due to the partial overstresses (Eq. 20) were formulated according Eq. 17 and Eq. 4.

$$\begin{aligned}\overset{4}{\tilde{\mathbb{C}}}_{eq}(n+1) = {} & \mu J^{-\frac{2}{3}}([\mathbf{B}\otimes\mathbf{1}^T]^{T14} + [\mathbf{1}\otimes\mathbf{B}^T]^{T14}) \\ & - \frac{2}{3}\mu J^{-\frac{2}{3}}([\mathbf{1}\otimes\mathbf{B}] + [\mathbf{1}\otimes\mathbf{B}]) \\ & + \left(\frac{J\cdot(4J-2)}{d} + \frac{2}{9}\mu J^{-\frac{2}{3}} tr(\mathbf{B})\right) \\ & \times[\mathbf{1}\otimes\mathbf{1}]\end{aligned} \tag{19}$$

Since the overstress (Eq. 4) depends on the variables q_k in order to consider the amplitude dependence, the tangent operator of the overstress depends also on the state variables q_k (Eq. 18). But to compute the tangent operator of the overstress tensor, the partial derivatives with respect to the deformation process-dependent internal variables q_k have been omitted. This negligence has only small influence on the convergence rate.

$$\begin{aligned}&\overset{4}{\tilde{\mathbb{C}}}_{ovk}(n+1) \\ &\quad = [\mathbf{F}^T\otimes\mathbf{F}^T]^{T_{14}}\, 2c_k(\mathbf{C}^{-1}\otimes\mathbf{C}^{-1})^{T23}[\mathbf{F}\otimes\mathbf{F}]^{T_{14}} \\ &\qquad + \det\mathbf{F}([\mathbf{T}_{ovk}\otimes\mathbf{1}]^{T_{14}} + [\mathbf{1}\otimes\mathbf{T}_{ovk}]^{T_{14}})\end{aligned} \tag{20}$$

5.1 *Rubber bloc with hole cyclically loaded with changing dynamic amplitude*

To illustrate the properties and the main benefits of presented material model, transient FEM simulations of a rubber block with a hole in the center were carried out. Such a part could be used, for example, as an engine vibration isolator. The bottom plate is fixed in all directions. The top plate is loaded in the vertical Y-direction with a transient displacement function with changing dynamic amplitudes. The static predeformation is 20% in tension and the excitation frequency is 1 Hz (Fig. 7). The displacement amplitude was switched every 25 s during the computation time (Fig. 7). The material parameters of the 12 nonlinear Maxwell elements for this simulation were identified in chapter 4 (Table 1) and contain all information about the material.

The total computation time of the FEM simulation is reduced by the same scaling factor

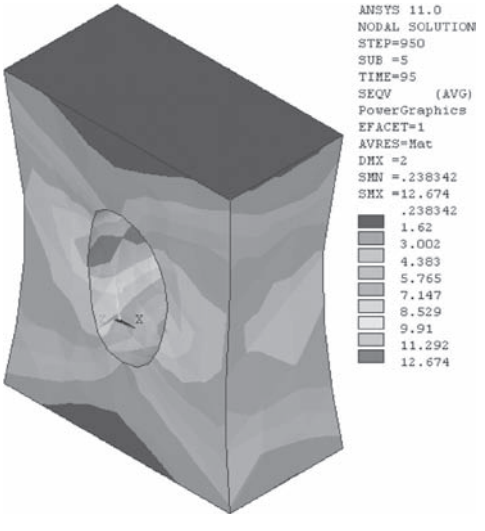

Figure 6. Equivalent stress von Misses at time 95 s (post. 1).

as used in the parameter identification procedure. Thus, the FEM simulation of about 100 s duration corresponds to a real loading process of 180×100 s. Looking at the stress response (Fig. 8) on a given material point of the rubber block with the hole shown in Fig. 6, the experimentally observed softening effect (Fig. 1) is represented by the constitutive model.

For the purpose of an easier post processing and a well-defined physical understanding of the dynamic behavior of the block, the dynamic modulus E^* was computed on the basis of the stress signal $\sigma(t)$ scaled with the amplitude of the local total strains $\Delta\varepsilon$ (Fig. 9). The curve of the time-dependent dynamic modulus shows the expected stepwise decrease in the modulus with increasing dynamic strain amplitude. This result corresponds to the Payne-effect in the time domain and was

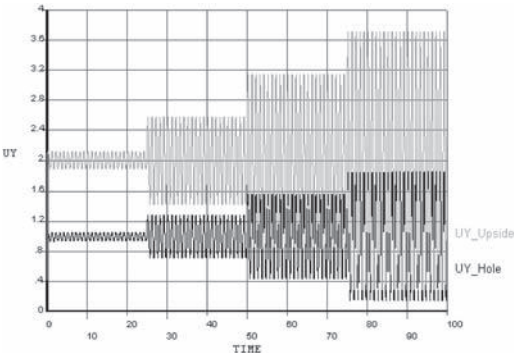

Figure 7. UY_U—Transient loading displacement function with changing dynamic amplitude on the top plate of the model and UY_H—local displacement in hole area.

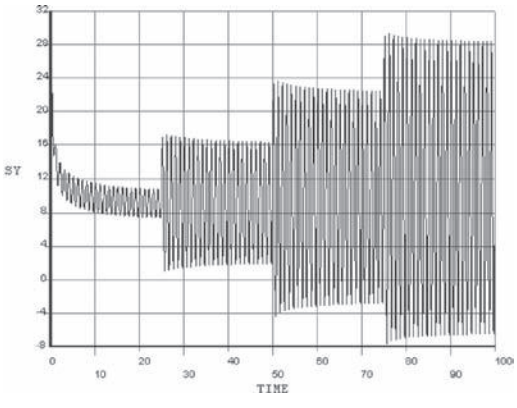

Figure 8. Amplitude dependent stress response in the hole area with microstructure relaxation from FEM simulation.

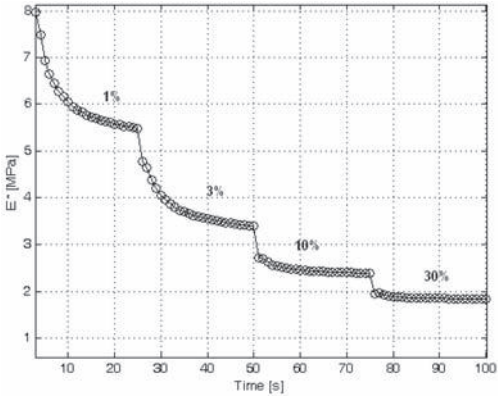

Figure 9. Computed dynamic modulus from the FEM stress response in the area around the hole.

observed in the DMA step-tests plotted in Fig. 3. The effect of different significant microstructure relaxations times during the different deformation amplitudes can be seen in the simulations too.

The positions of critical strains and stresses in the rubber block can be detected directly in the post processor because the local dynamic moduli are influenced by these quantities. As a matter of fact, the area around the hole of the rubber block is the most critical location. According to the computed modulus in Fig. 9, the local stiffness is about four times smaller during large cyclic deformations than during small deformations. This knowledge can be supportively used in the context of material or shape optimizations of bushings or shock absorbers. Further applications of transient simulations can be found in the big area of multibody simulation in the automotive industry. In this context, the dynamic reaction forces from suspension bushings or engine mounts contain basic information for further works, like durability or NVH analyses.

6 CONCLUSIONS

In the present work, a nonlinear constitutive model of finite viscoelasticity which considers the typical amplitude dependence of carbon black reinforced elastomers has been formulated. The basis of the model is a nonlinear Maxwell chain in combination with a hyperelastic equilibrium stress and process relaxation times or viscosities. In order to describe the amplitude dependence a set of additional internal state variables has been introduced which can be attributed to microstructural relaxation phenomena. The developed material model was implemented into the commercial FEM software

ANSYS. The material parameter identification was realized on the basis of comprehensive DMA experiments in both the time and the frequency domain. Already with a fairly small number of 12 nonlinear Maxwell elements the fundamental phenomena of filler-reinforced rubber are qualitatively and quantitatively described. A transient FEM simulation of a simple vibration isolator (rubber block with a hole) was computed as demonstration example.

ACKNOWLEDGEMENT

The authors would like to thank the German research Foundation (DFG) for financial support.

REFERENCES

A. Lion, C.K. (2004). "The Payne effect in finite viscoelasticity: constitutive modeling based on fractional derivatives and intrinsic time scales." International Journal of Plasticity 20: 1313–1345.

A. Lion, J. Retka, M. Rendek (2009). "On the calculation of predeformation-dependent dynamic modulus tensors in finite nonlinear viscoelasticity." Mechanics Research Communications. in print.

M.A. Crisfeld (1998). Non-linear Finite Element Analysis of Solids and Structures. UK, John Wiley & Sons.

G.A. Holzapfel (1996). "On large strain viscoelasticity: continuum formulation and finite element applications to elastomeric structures" International journal for numerical methods in engineering 39(1996): 3903–3926.

J.C. Simo, T.J.R.H. (2000). Computational Inelasticity. New York, Springer-Verlag.

M. Rendek, A. Lion (2009). "Modeling and finite element simulation of filler-reinforced elastomers under dynamic deformations." KGK—Kautschuk Gummi Kunststoffe (2009): 28–35.

P. Haupt, A. Lion (2002). "On finite linear viscoelasticity of incompressible isotropic materials." Acta Mechanica 159(2002): 87–124.

P. Höfer, A. Lion (2009). "Modeling of frequency-and amplitude-dependent material properties of filler-reinforced rubber." Journal of the Mechanics and Physics of Solids 57(2009): 500–520.

A.R. Payne (1962). "The Dynamic Properties of Carbon Black-Loaded Natural Rubber Vulcanisates. Part I*." Journal of Applied Polymer Science VI(19): 57–63.

Constitutive Models for Rubber VI – Heinrich et al. (eds)

A computational contact model for nanoscale rubber adhesion

Roger A. Sauer
Institute for Continuum Mechanics, Leibniz Universität Hannover, Germany

ABSTRACT: We present a continuum mechanical contact model which is capable of describing and simulating rubber adhesion at the nanometer scale. The formulation is based on the coarse-graining of the molecular interaction, like van der Waals attraction, between neighboring solids during contact. A nonlinear finite element implementation of the model is presented which allows the efficient simulation of adhesive contact problems at the range between several nanometers and a few micrometers. The model shows excellent agreement with the analytical JKR theory in the range where the JKR model is applicable. The model behavior is illustrated by several numerical examples. As an application of the contact model the nanoindentation of a thin rubber film is considered.

1 INTRODUCTION

This research is motivated by understanding and analyzing the nanoscale interactions between two contacting bodies. At this scale long-range interaction forces, like van der Waals adhesion, play a crucial role in determining the contact behavior. In many cases molecular adhesion carries over to macroscale problems. Examples include gecko adhesion and rubber adhesion on smooth surfaces. The mechanisms furnishing the transition of adhesion from the nanoscale to the macroscale are a topic of active research. Key factors facilitating the transition are the compliance of the bodies and the surface roughness on the intermediate scales.

In (Sauer and Li 2007b) we have proposed a computational model for nanoscale contact, termed the coarse-grained contact model (CGCM), that offers great flexibility in analyzing general contact problems at the range of a few nanometers to many hundreds of nanometers accurately, and which can be used in computational multiscale techniques to be applied at even larger scales (Sauer 2009).

This paper gives an overview of the coarse grained contact model and discusses its application to rubber adhesion. The overview of the theoretical and computational framework of the CGC model is given in sections 2, 3 and 4. For validation, section 5 presents a comparison between the CGC model and the widely used JKR theory. In section 6 the application of the CGC model to the nanoindentation of a thin rubber film is considered. Section 7 concludes this paper.

2 A CONTINUUM ADHESION MODEL

This section provides an overview of the coarsegrained contact model (Sauer and Li 2007b), which is suitable to model nanoscale rubber adhesion. We consider two interacting bodies, $\mathcal{B}_1$ and $\mathcal{B}_2$, and suppose that the system is governed by the potential energy

$$\Pi = \sum_{k=1}^{2} [\Pi_{\text{int},k} - \Pi_{\text{ext},k}] + \Pi_{\text{c}}, \tag{1}$$

where

$$\Pi_{\text{int},k} = \int_{\mathcal{B}_{0k}} W_k(\boldsymbol{F}_k)\,\mathrm{d}V_k \tag{2}$$

denotes the internal energy of body $\mathcal{B}_k$ ($k = 1, 2$). As an alternative to the integration over the reference configuration $\mathcal{B}_{0k}$, $\Pi_{\text{int},k}$ can also be expressed as an integration over the current configuration $\mathcal{B}_k$. W_k denotes the energy density per reference volume. In general, W_k is a function of the deformation gradient $\boldsymbol{F}_k = \text{grad}\ \boldsymbol{\varphi}_k$.

Adhesive contact is described by the contact interaction energy

$$\Pi_{\text{c}} = \int_{\mathcal{B}_1}\int_{\mathcal{B}_2} \beta_1\beta_2\phi(r)\,\mathrm{d}v_2\,\mathrm{d}v_1, \tag{3}$$

where $\phi(r)$ denotes the interaction energy between the molecules of body $\mathcal{B}_1$ and $\mathcal{B}_2$. Here we use the Lennard Jones potential

$$\phi(r) := \epsilon\left(\frac{r_0}{r}\right)^{12} - 2\epsilon\left(\frac{r_0}{r}\right)^{6}, \tag{4}$$

which is suitable to model van der Waals adhesion. The quantities β_1 and β_2 denote the molecular densities of bodies $\mathcal{B}_1$ and $\mathcal{B}_2$. These densities refer to the current configuration. The transformation

$$\beta_{0k} = J_k \beta_k, \quad J_k = \det \boldsymbol{F}_k, \quad k = 1,2, \tag{5}$$

provides the molecular densities, denoted β_{01} and β_{02}, in the reference configuration.

$\Pi_{\text{ext},k}$ denotes the external energy applied to body $\mathcal{B}_k$ through imposed body forces and surface tractions. The equilibrium configuration of the two interacting bodies is found from setting the variation $\delta\Pi$ equal to zero for all admissible variations of the deformation $\boldsymbol{\varphi}_k$. The variation of the contact energy (3) yields

$$\delta\Pi_{\text{c}} = \sum_{k=1}^{2} \int_{\mathcal{B}_k} \delta\boldsymbol{\varphi}_k \cdot \beta_k \boldsymbol{b}_k \, \mathrm{d}\upsilon_k \tag{6}$$

where

$$\begin{aligned} \boldsymbol{b}_1(x_1) &:= -\frac{\partial \Phi_2}{\partial \boldsymbol{x}_1}, \quad \Phi_2(x_1) := \int_{\mathcal{B}_2} \beta_2 \phi(r) \mathrm{d}\upsilon_2, \\ \boldsymbol{b}_2(x_2) &:= -\frac{\partial \Phi_1}{\partial \boldsymbol{x}_2}, \quad \Phi_1(x_2) := \int_{\mathcal{B}_1} \beta_1 \phi(r) \mathrm{d}\upsilon_1, \end{aligned} \tag{7}$$

denote the interaction forces acting at $x_k \in \mathcal{B}_k$. As seen, they depend on the integration over the neighboring body. Under certain, realistic approximations (Sauer and Wriggers 2009) these forces can be written as

$$\boldsymbol{b}_k(\boldsymbol{x}_k) = \pi \beta_\ell \epsilon r_0^2 \left[\frac{1}{5} \left(\frac{r_0}{r_k} \right)^{10} - \left(\frac{r_0}{r_k} \right)^4 \right] \boldsymbol{n}_{\text{p}}, \tag{8}$$

where r_k denotes the closest distance between point x_k and the surface of the neighboring body $\mathcal{B}_\ell$ ($\ell = 1, 2; \neq k$). Vector $\boldsymbol{n}_{\text{p}}$ denotes the surface normal of $\mathcal{B}_\ell$ at the closest projection point of $\boldsymbol{x}_k$. The material parameters $\mathcal{B}_\ell$ and ϵ can be replaced by Hamaker's constant $A_H = 2\pi^2 \beta_{01} \beta_{02} \epsilon r_0^6$ (Israelachvili 1991). Setting $\delta\Pi = 0$ for all admissible variations $\delta\boldsymbol{\varphi}_k$, we obtain the statement

$$\begin{aligned} \sum_{k=1}^{2} \Big[& \int_{\mathcal{B}_k} \operatorname{grad}(\delta\boldsymbol{\varphi}_k) : \boldsymbol{\sigma}_k \, \mathrm{d}\upsilon_k - \delta\Pi_{\text{ext},k} \\ & - \int_{\mathcal{B}_k} \delta\boldsymbol{\varphi}_k \cdot \beta_k \boldsymbol{b}_k \, \mathrm{d}\upsilon_k \Big] = 0, \quad \forall \delta\boldsymbol{\varphi}_k, \end{aligned} \tag{9}$$

which is the governing weak form of the considered contact problem. Alternatively eq. (9) can also be written as an integration over the reference configuration $\mathcal{B}_{0k}$. Since the contact forces $\boldsymbol{b}_k$, according to eq. (8), vary rapidly, special care is required for the numerical integration of the last term in eq. (9). To improve the numerical integration, an alternative formulation to eq. (9) has been developed in (Sauer and Li 2007b; Sauer and Li 2007a), which is based on surface tractions. We therefore consider

$$\mathrm{d}\upsilon_k = c_\ell(r_k) \mathrm{d}r_k \cos\alpha_k \mathrm{d}a_k, \tag{10}$$

where c_ℓ depends on the surface curvature of the neighboring body $\mathcal{B}_\ell$ (Sauer and Wriggers 2009). For small curvatures $c_\ell \to 1$. With the help of relation (10) we can rewrite statement (9) into

$$\begin{aligned} \sum_{k=1}^{2} \Big[& \int_{\mathcal{B}_k} \operatorname{grad}(\delta\boldsymbol{\varphi}_k) : \boldsymbol{\sigma}_k \, \mathrm{d}\upsilon_k - \delta\Pi_{\text{ext},k} \\ & - \int_{\partial\mathcal{B}_k} \delta\boldsymbol{\varphi}_k \cdot \boldsymbol{t}_k \cos\alpha_k \mathrm{d}a_k \Big] = 0, \quad \forall \delta\boldsymbol{\varphi}_k, \end{aligned} \tag{11}$$

where $\boldsymbol{t}_k$ denotes the contact surface traction defined by

$$\boldsymbol{t}_k := \int_{r_s}^{r_c} c_l(r_k) \beta_k \boldsymbol{b}_k(r_k) \mathrm{d}r_k. \tag{12}$$

Considering β_k constant, the integration of eq. (8) yields

$$\boldsymbol{t}_k = \pi \beta_k \beta_\ell \epsilon r_0^3 \left[\frac{1}{45} \left(\frac{r_0}{r_k} \right)^9 - \frac{1}{3} \left(\frac{r_0}{r_k} \right)^3 \right] \boldsymbol{n}_{\text{p}}. \tag{13}$$

Equation (13), together with eq. (11) provide the basis of the finite element implementation of the CGC model that is discussed in the following section. Further details on the derivation reported above and a careful analysis of the accuracy of this model are presented in (Sauer and Wriggers 2009).

3 NONLINEAR FINITE ELEMENT FORMULATION

This section presents the basic finite element equations of the adhesive contact model governed by weak form (11). The focus here is placed on the treatment of the contact integral (the last term in eq. (11)); the treatment of the internal and external integrals can be found in the nonlinear finite element literature, e.g. (Wriggers 2008).

In order to discretize the contact integral, we consider the usual finite element interpolations for the displacement field $\boldsymbol{u}_k$ and its variation $\delta\boldsymbol{\varphi}_k$. Inside each finite element Γ_e that discretizes the surface of $\mathcal{B}_k$, we have

$$\boldsymbol{u}_\kappa \approx \mathbf{N}_e \mathbf{u}_e, \quad \delta\boldsymbol{\varphi}_\kappa \approx \mathbf{N}_e \mathbf{v}_e \tag{14}$$

with

$$\mathbf{N}_e = [N_1 \boldsymbol{I}, N_2 \boldsymbol{I}, \ldots, N_{n_e} \boldsymbol{I}], \tag{15}$$

where N_I denotes the shape function of node I of element Γ_e. The contact integral over the surface element can thus be written as

$$-\int_{\Gamma_k} \delta\boldsymbol{\varphi}_k \cdot \boldsymbol{t}_k \cos\alpha_k \, \mathrm{d}a_k = \mathbf{v}_\mathrm{e}^T \mathbf{f}_\mathrm{c}^e, \tag{16}$$

where

$$\mathbf{f}_\mathrm{c}^e := -\int_{\Gamma_e} \mathrm{N}_\mathrm{e}^T \boldsymbol{t}_k \cos\alpha_k \, \mathrm{d}a_k \tag{17}$$

defines the contact force vector acting on the nodes of element Γ_e. For practical computations it is convenient to transform this expression to an integration over the reference configuration of the element as is discussed in (Sauer and Wriggers 2009). That paper also gives further details on the finite element derivation and presents the contact algorithm and the linearization of vector $\mathbf{f}_\mathrm{c}^e$.

4 MODEL PARAMETERS

To characterize the size effect and the adhesional strength of a considered problem we introduce the parameters

$$\gamma_L = \frac{R_0}{r_0}, \quad \gamma_W = \frac{W_0}{w_0}. \tag{18}$$

R_0 and r_0 are two length scales that characterize the overall problem geometry and the nanoscale equilibrium spacing of the Lennard-Jones potential (4). Parameter γ_L thus characterizes the size of the problem in relation to the atomic scale. W_0 and w_0 denote two energy densities that correspond to the energy stored in the elastic deformation and in the adhesion. They are defined as

$$W_0 = E, \quad w_0 = \frac{A_H}{2\pi^2 r_0^3}, \tag{19}$$

where E denotes Young's modulus and A_H denotes Hamaker's constant. According to the definition of Hamaker's constant we can also write $w_0 = \beta_{01}\beta_{02}\epsilon r_0^3$. Parameter γ_W characterizes the bulk stiffness of the problem in relation to the strength of adhesion. A large value of γ_W corresponds to relatively stiff bodies and weak adhesion, whereas a low value for γ_W corresponds to relatively soft bodies and strong adhesion. Typical values for the molecular equilibrium spacing and Hamaker's constant are $r_0 = 0.4$ nm and $A_H = 10^{-19}$ J (Israelachvili 1991).

5 COMPARISON WITH THE JKR MODEL

As a validation of the coarse-grained contact model, we compare it with the analytical contact model of (Maugis 1992). This model is a generalization of the widely used JKR model (Johnson, Kendall, and Roberts 1971), which is often applied to rubber adhesion. The comparison presented here extends the comparison reported in (Sauer and Li 2007a). That paper also lists the equations of the analytical Maugis model. The Maugis model is based on linear half-space theory and applies to the adhesive normal contact of two spheres, where the contact area is much smaller than the radius of the spheres. Here we consider contact between a sphere of radius $R_0 = 21$ nm with a flat half-space (i.e. radius ∞). Considering $r_0 = 0.4$ nm, this corresponds to a size parameter of $\gamma_L = 52.5$. In the Maugis model the strength of adhesion is characterized by the parameter $\lambda \in (0, \infty)$. Increasing λ corresponds to increasing adhesion. In fact the limit $\lambda \to \infty$ reproduces the JKR model as a special case. In the present example the adhesion parameter is chosen as $\lambda = 1.3$. Parameter λ is a model specific parameter that has no explicit correspondence to the physically motivated parameter γ_W. It has been found that the value $\gamma_W = 11.55$ produces a remarkable agreement in the following results.

Figure 1 shows the normal contact force P versus the normal contact approach u for the considered problem. For moderate displacements the agreement is excellent. For increasing displacements

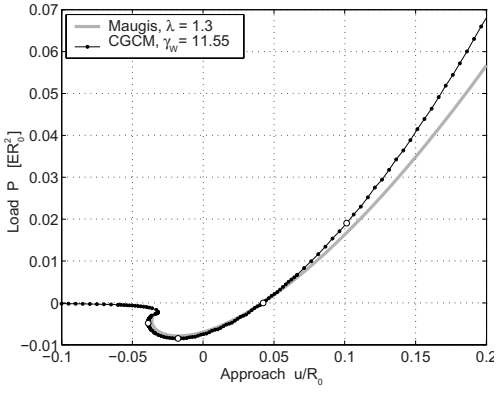

Figure 1. Load displacement curve for a sphere in adhesive contact with a half-space.

the two curves diverge since the small deformation assumption used in the Maugis model is no longer valid. For increasing negative displacements, which correspond to separating the bodies, the Maugis model loses its applicability since it is not defined there. For the considered case a contact instability exists, which is indicated by the S-curve in the load-displacement curve (Sauer and Li 2007b).

To further illustrate the agreement between the two models, we examine the radial contact pressure between the two bodies as is shown in Figure 2. The pressure distribution according to Maugis and the CGC model is shown in the graphs on the right hand side. The agreement between both models is excellent. The vertical axis displays the radial distance from the symmetry axis measured relative to the sphere radius R_0. The horizontal axis measures the pressure in multiples of Young's modulus E. Altogether, four cases are shown, which correspond to the four states at $u = -0.0388\ R_0$, $u = -0.0176\ R_0$, $u = 0.0423\ R_0$ and $u = 0.1013\ R_0$ that are marked by open circles in figure 1. According to the Maugis model these correspond to $a = 0.050\ R_0$, $a = 0.186\ R_0$, $a = 0.329\ R_0$ and $a = 0.420\ R_0$, where a characterizes the radius of the contact area. The graphs on the left hand side display the deformation of the contact partners together with the stress field σ_z, which is the stress component in the vertical direction. The stress coloring chosen in the figure ranges from $-0.12\ E$ (dark blue) to $0.08\ E$ (dark red). Both the stress field, and the pressure distribution show the smooth repulsive compression at the center of contact and the sharp attractive tension at the contact boundary. The agreement between the two models is much better in the repulsive zone than in attractive zone, which is due to the approximation introduced by Maugis in order to describe the adhesive pressure.

Further comparison examples, along with detailed discussions, are given in (Sauer and Li 2007a).

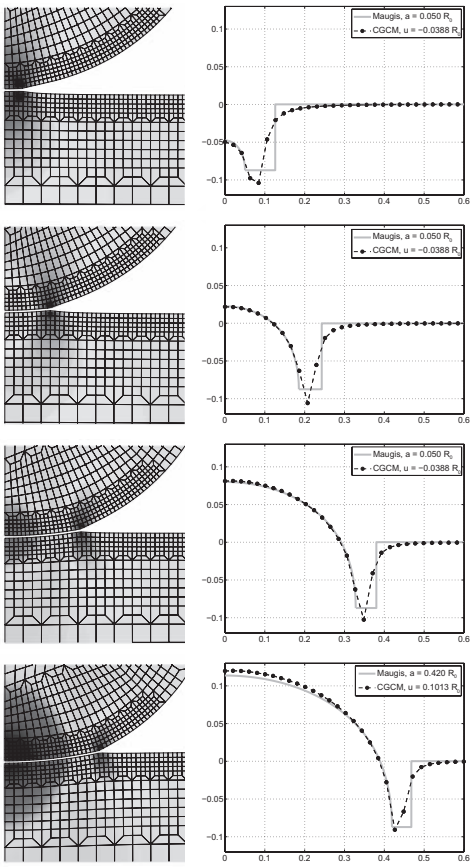

Figure 2. Contact between sphere and half-space: Deformation and stress field (left); contact pressure between the two bodies (right); The four cases correspond to the four states marked in figure 1.

6 NANOINDENTATION EXAMPLE

As a numerical example of the coarse grained contact model we compute the 3D nanoindentation of a thin rubber film. A rigid Vickers indenter is considered, which is a four-sided pyramidal indenter with an opening angle of $2 \times 68°$ between opposing faces. The indenter is pressed into the thin film which has a considered thickness of $R_0 = 10$ nm. Considering $r_0 = 0.4$ nm, this corresponds to a size parameter of $\gamma_L = 25$. Initially a gap of $g_0 = 1.5\ r_0 = 0.06\ R_0$ is chosen between the indenter tip and the film surface. The rubber film is considered perfectly bonded to an underlying rigid substrate. The rubber material is considered nearly incompressible, and is described by the Neo-Hookean material model

$$W(J,\hat{\boldsymbol{C}}) = U(J) + \frac{\mu}{2}(\hat{I}_1 - 3), \tag{20}$$

which is based on a split between the volumetric deformation, described by the determinant of the deformation gradient

$$J = \det \boldsymbol{F}, \tag{21}$$

and the deviatoric deformation, characterized by

$$\hat{I}_1 = \mathrm{tr}\hat{\boldsymbol{C}}, \quad \hat{\boldsymbol{C}} = \hat{\boldsymbol{F}}^T\hat{\boldsymbol{F}}, \quad \hat{\boldsymbol{F}} = J^{-\frac{1}{3}}\boldsymbol{F}. \tag{22}$$

The volumetric strain energy is taken as

$$U(J) = \frac{K}{4}(J^2 - 1) - \frac{K}{2} \ln J. \tag{23}$$

Parameters K and μ denote the bulk and shear modulus which are related to Young's modulus E and Poisson's ratio ν according to

$$K = \frac{E}{3(1-2\nu)}, \quad \mu = \frac{E}{2(1+\nu)}. \tag{24}$$

In the following example Poisson's ratio is chosen as $\nu = 0.499$. E is used for normalization and can thus be left unspecified.

For the following indentation computations a Q1P0 finite element formulation for large deformations is used (Wriggers 2008). Due to symmetry only a quarter segment of the film is modeled. A segment size of $R_0 \times 3R_0 \times 3R_0$ is chosen.

Figure 3 shows the load displacement curves in the range $u \in (-0.1\ R_0,\ 0.5\ R_0)$ for the cases of weak adhesion ($\gamma_W = 1000$) and strong adhesion ($\gamma_W = 10$). The difference between both cases is revealed by the enlargement shown in Figure 4. For $\gamma_W = 10$ considerable attraction ($P < 0$) exists between the bodies prior to contact. For $\gamma_W = 1000$ the attractive forces between the bodies are negligible and the resultant contact load P is positive. Further, Figure 4 shows the results for two different meshes: a coarse mesh with 10 elements along R_0 and a fine mesh with 25 elements along R_0. The figure shows that for $\gamma_W = 1000$ (weak adhesion) the difference between both meshes is very small. For $\gamma_W = 10$ (strong adhesion) however, the coarse mesh causes a large error so that the difference between the coarse and fine mesh is quite large. This shows that for increasing adhesion finer meshes must be used in order to maintain accurate computational results.

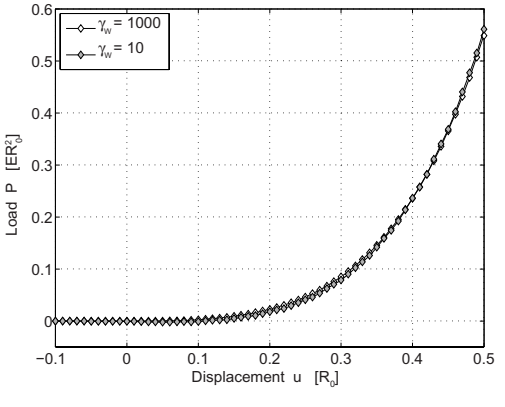

Figure 3. Load displacement curve $P(u)$ for indentation with weak adhesion ($\gamma_W = 1000$) and strong adhesion ($\gamma_W = 10$).

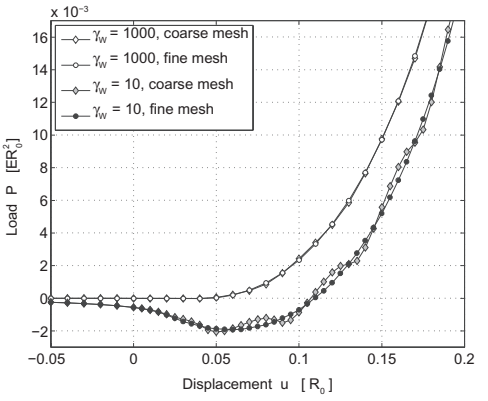

Figure 4. Enlargement of the load displacement curve from figure 3.

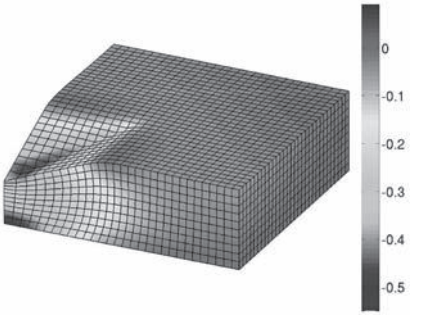

Figure 5. Nanoindentation of a rubber film: deformation and stress field under the indenter for weak adhesion ($\gamma_W = 1000$).

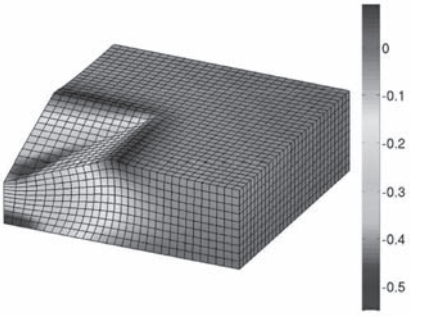

Figure 6. Nanoindentation of a rubber film: deformation and stress field under the indenter for strong adhesion ($\gamma_W = 2.17$).

Figures 5 and 6 display the deformation at $u = 0.5\ R_0$ for $\gamma_W = 1000$, where adhesion is

negligible, and $\gamma_W = 2.17$, where the adhesion is very strong. As can be seen, strong adhesion leads to large tensile contact forces and surface deformations at the contact boundary, which are not present for weak adhesion. The coloring shown in both figures visualizes the stress field σ_r, which is the stress in the radial direction from the indenter tip. For $\gamma_W = 2.17$, the range of σ_r lies between $-0.55\ E$ (blue: compression) and $0.09\ E$ (red: tension). Since the tensile stress region is localized in a narrow band at the contact boundary, a high mesh refinement is needed to capture these forces accurately. The adhesion forces lead to the reduction of the resultant contact force: For $\gamma_W = 1000$ we have $P = 0.549\ ER_0^2$, whereas for $\gamma_W = 2.17$ we only have $P = 0.506\ ER_0^2$.

7 CONCLUSION

The present paper introduces the coarse-grained contact model, a computational nanoscale contact model based on nonlinear continuum mechanics, and applies it to rubber adhesion. The model is validated against the analytical contact model of (Maugis 1992), which is based on the JKR model. The comparison shows an excellent agreement between the models in the range where the JKR theory is applicable. Finally the computational contact model is applied to the analysis of the nanoindentation of a thin rubber film. The different behavior between weak and strong adhesion is illustrated and it is shown that strong adhesion computations require a much larger mesh refinement.

Further validation of the CGC model has been reported in our previous studies: In (Sauer and Li 2007b) the deformation of carbon-nanotubes is computed and compared to related studies in the literature. In (Sauer 2009) a multiscale contact model descibing the gecko adhesion mechanism is presented and it is shown than the computed pull-off forces of a single gecko spatula is in agreement to experimental data. A rigorous numerical analysis of the CGC model as well as details on the 3D finite element equations are discussed in (Sauer and Wriggers 2009).

The continuum mechanical framework gives the CGC model great flexibility and allows the accurate computation of a large class of contact interaction problems at the nanoscale. The CGC model can be applied for length scales down to a few nanometers before the continuum assumption breaks down. At this range the model is still far more efficient than molecular mechanics computations (Sauer and Li 2008).

REFERENCES

Israelachvili, J.N. (1991). *Intermolecular and Surface Forces* (2nd ed.). Academic Press.

Johnson, K.L., K. Kendall, and A.D. Roberts (1971). Surface energy and the contact of elastic solids. *Proc. R. Soc. Lond. A* **324**, 301–313.

Maugis, D. (1992). Adhesion of spheres: The JKR-DMT transition using a Dugdale model. *L. Colloid Interface Sci.* **150**(1), 243–269.

Sauer, R.A. (2009). Multiscale modelling and simulation of the deformation and adhesion of a single gecko seta. *Comp. Meth. Biomech. Biomed. Engng. in press.*

Sauer, R.A. and S. Li (2007a). An atomic interaction-based continuum model for adhesive contact mechanics. *Finite Elem. Anal. Des.* **43**(5), 384–396.

Sauer, R.A. and S. Li (2007b). A contact mechanics model for quasi-continua. *Int. J. Numer. Meth. Engrg.* **71**(8), 931–962.

Sauer, R.A. and S. Li (2008). An atomistically enriched continuum model for nanoscale contact mechanics and its application to contact scaling. *J. Nanosci. Nanotech.* **8**(7), 3757–3773.

Sauer, R.A. and P. Wriggers (2009). Formulation and analysis of a 3D finite element implementation for adhesive contact at the nanoscale. *Comp. Meth. Appl. Mech. Engrg. submitted.*

Wriggers, P. (2008). *Nonlinear Finite Element Methods*. Springer.

Continuum mechanical models

Constitutive Models for Rubber VI – Heinrich et al. (eds)
© 2010 Taylor & Francis Group, London, ISBN 978-0-415-56327-7

Permanent and voluminal strain induced by isotropic ductile damage formulation in forming processes of filled-elastomer materials

Rémi Figueredo & Abel Cherouat
University of Technology of Troyes, ICD/UTT, Troyes, France

ABSTRACT: In this study, we propose to enrich a non-linear coupled damaged hyper-elastic behaviour of rubber like material. In the framework of Continuum Damage Mechanics, the constitutive model takes into account the permanent strain and the volume variation induced by the isotropic damage. The efficiency of the method is validated with some numerical examples and comparison with an experimental data from an uniaxial tensile test.

Keywords: Hyperelasticity, Continuum Damage Mechanics, Permanent Strain, Volume Variation, Filled Elastomers.

1 INTRODUCTION

The rubbery environments present the same mechanical behaviour as hyperelastic or visco-hyperelastic solids. With a wide range of applications in industrial products, and the variety of effects in rubber, the models become more and more sophisticated.

Most of the implementations of constitutive model are done via the free strain-energy function which is modified by introducing variables to take into account the various physical phenomena (Lion 1996; Mullins 1969; Dorfmann and Ogden 2004). For example, the high degree of deformability often generate microscopic and voluminal defects leading to the creation of micro-cracks inside the structure. A first work was done in (Figueredo and Cherouat 2007), where we proposed to enrich a non-linear coupled damaged hyperelastic behaviour of rubber-like materials. This latter reproduce both the Mullins effect in cyclic loading and a permanent degradation effect of the matter noticed as from the primary loading. In addition, the approach has been modified in (Figueredo and Cherouat 2008) considering a permanent strain induced by the degradation effect in the matter.

Now this paper deals with the experimental investigation and constitutive modeling of the mechanical response of filled-elastomer materials. A FE-implementation of a constitutive model for rubber into the programs ABAQUS taking into consideration a permanent and voluminal strain induced by damage is developed and implemented into a general purpose finite element code (ABAQUS via user's subroutine) for forming simulation. In the framework of Continuum Damage Mechanics, the formulation is based on the decomposition of the gradient of deformation into a nearly-incompressible elastic part, which the strain-energy function is depended, and a voluminal damage part induced by an isotropic variable introduced into the same function.

The proposed approach can be used with several examples of the isotropic behaviour filled-elastomer, using classical energy densities, as the Ogden and polynomials models. The local integration is outlined thanks to the Newton iterative scheme applied to a reduced system of one equation after some numerical assumptions. For the equilibrium solution strategy, dynamic explicit method is used. Some numerical examples are presented to discuss the capability of the coupled non linear hyperelastic model to predict isotropic ductile damage initiation and growth during forming processes of filled-elastomer.

2 CONSTITUTIVE MODELING

2.1 *Basics kinematics*

We consider a rubber-like solid regarded as a continuous body. To formulate a three-dimensional constitutive theory to represent the non-linear behaviour of filled-elastomers, the multiplicative

decomposition of the deformation gradient into an elastic and a damage part is used (Sidoroff 1975; Andrieux 1996):

$$\mathbb{F} = \mathbb{F}^e \cdot \mathbb{F}^d \text{ i.e. in determinant: } J = J^e J^d \quad (1)$$

where the elastic ($\mathbb{F}^e$) and the permanent component ($\mathbb{F}^d$) represent respectively the reversible and the irreversible transformation. $\mathbb{F}^d$ is the fictitious intermediate configuration linked to the damage process which is physically interpreted as a unloaded configuration made by the elastic return. Finally, we deduce the elastic left Cauchy-Green tensor and its rate:

$$\mathbb{B}^e = \mathbb{F}^e \cdot \mathbb{F}^{eT} = (\mathbb{V}^e)^2 \quad (2)$$

$$\dot{\mathbb{B}}^e = \mathbb{L} \cdot \mathbb{B}^e + \mathbb{B}^e \cdot \mathbb{L} - 2\mathbb{V}^e \cdot \mathbb{D}^{d*} \cdot \mathbb{V}^e \quad (3)$$

where $\mathbb{V}^e$ is the pure elastic strain tensor (i.e. $\mathbb{F}^e = \mathbb{V}^e \cdot \mathbb{R}^e$). $\mathbb{B}^e$ and $\mathbb{V}^e$ are both Eulerean elastic strain measure. As for $\mathbb{L}\,(= \dot{\mathbb{F}} \cdot \mathbb{F}^{-1})$ and $\mathbb{D}^{d*}(= \mathbb{R}^e \cdot \mathbb{D}^d \cdot \mathbb{R}^{eT})$, they measure the rates strain respectively of the total and the permanent deformation ($\mathbb{D}^d$ being the symmetric part of $\dot{\mathbb{F}}^d \mathbb{F}^{d^{-1}}$).

2.2 *Thermodynamics background*

The pure elastomers are supposed incompressible or almost-incompressible. The deformation due to the carbon chain deployment inside the structure, can not induce variation of volume. This leads us to satisfy the assumption of one elastic transformation isochoric or almost-isochoric. As for the permanent transformation, in the case of filled-elastomers for example, the irreversible formation of micro-cracks and voluminal defects is reflected by an increasing variation of the volume. Thus we should verify during a loading:

$$J^e \approx 1 \text{ and then : } J^d \approx J \quad (4)$$

Under this condition, J increases with the damage's appearance inside the structure. Ones postulate a relation between J and D (D being the scalar internal variable linked with the isotropic damage). For example, from (Saanouni et al. 1998; Andrieux 1996), a potential, depending on J and D, is postulated to satisfy the following internal constraint:

$$\Phi = \Phi\,(J,\, D) = J - g(D) = 0 \quad (5)$$

where $g(D)$ is a differentiable, positive and increasing scalar function of the damage variable D, and $g(D = 0) = 1$ for a classical incompressibility condition.

Within the framework of the laws of isotropic hyper-elastic behaviour, we consider the free strain-energy function W, which depends overall on the elastic motion $\mathbb{F}^e$, and the internal variables Ξ_i associated to physical phenomena inside the material.

We will keep the same notation to express the free strain-energy function W with different mechanics motion elements:

$$W(\mathbb{F}^e, \Xi_i) \simeq W(\mathbb{B}^e, \Xi_i) \simeq W(I_1^e, I_2^e, I_3^e, \Xi_i) \simeq W(\lambda_1^e, \lambda_2^e, \lambda_3^e, \Xi_i)$$

where the I_i^e and the $\lambda_i^e (i \in \{1,2,3\})$ respectively the invariants of the tensor $\mathbb{B}^e$ and the principal elastic elongations (i.e. eigenvalues of $\mathbb{V}^e$).

Finally in an isotherm framework, we write the fundamental inequality of Claudius-Duhem:

$$\mathbf{D} = \tau : \mathbb{D} - \dot{W} \geq 0 \quad (6)$$

where τ is the Kirchhoff stress tensor, and $\mathbb{D}$ the symmetric part of $\mathbb{L}$.

2.3 *The free strain-energy function coupled with damage*

In this work, we propose to couple the Ogden form of strain-energy function with an internal state variable D, which take account the irreversible degradation of the matter following isotropic CDM theory (Lemaitre and Chaboche 1985):

$$W(\bar{\lambda}_i^e, J^e, D) = (1 - D) W_0(\bar{\lambda}_i^e, J^e) \quad (7)$$

with $\bar{\lambda}_i^e = (J^e)^{-1/3} \lambda_i^e$, and:

$$W_0(\bar{\lambda}_i^e, J^e) = \sum_{i=1}^{n} \frac{\mu_i}{\alpha_i} (\bar{\lambda}_1^{e^{\alpha_i}} + \bar{\lambda}_2^{e^{\alpha_i}} + \bar{\lambda}_3^{e^{\alpha_i}} - 3) + \frac{1}{D_1} (J^e - 1)^2$$

This form is decoupled in a deviatoric part (depending on $\bar{\lambda}_i^e$) and a voluminal part (depending on J^e), and μ_i, α_i and D_1 are material parameters.

Just like those form expressed with the invariants of the tensor $\mathbb{B}^e$ (Polynomial form of Mooney), the prediction depends on the development's degree n. The D_1 value determine the compressibility on elastic motion, and it can be considered as almost-incompressible if the value are close to zero (the ABAQUS Software recommends values about 10^{-2}–10^{-3} to satisfy this condition).

Finally the current use of the Ogden form by experimenters (uniaxial-biaxial tensile test, simple

shear) pushes us to make it available on tridimensional simulations.

2.4 *Damage evolution*

In order to describe the damage evolution, we firstly consider W_0 as a function expressed with $\mathbb{B}^e$ and J^e. From the relation (3), we calculate the derivative of W:

$$\dot{W} = 2(1-D)\left[\left(\bar{\mathbb{B}}^e \cdot \frac{\partial W_0}{\partial \bar{\mathbb{B}}^e}\right)^{dev} + \frac{J^e(J^e-1)}{D_1}\mathbb{I}\right] : \mathbb{D} - 2(1-D)\left[\left(\bar{\mathbb{V}}^e \cdot \frac{\partial W_0}{\partial \bar{\mathbb{B}}^e} \cdot \bar{\mathbb{V}}^e\right)^{dev} + \frac{J^e(J^e-1)}{D_1}\mathbb{I}\right] : \mathbb{D}^{d*} + \frac{\partial W}{\partial D}\dot{D}$$

The latter relation is introduced into the inequality of Claudius-Duhem (6), and after some calculations we obtain the folloming relations (the stress-strain relation and the dissipative relation):

$$\begin{cases} \tau = 2(1-D)\left[\left(\bar{\mathbb{B}}^e \cdot \frac{\partial W_0}{\partial \bar{\mathbb{B}}^e}\right)^{dev} + \frac{J^e(J^e-1)}{D_1}\mathbb{I}\right] \\ \mathbf{D} = \mathbf{Y}\dot{D} + \tau : \mathbb{D}^{d*} \geq \mathbf{0} \end{cases} \quad (8)$$

where $\mathbf{Y}$ and τ are the thermodynamic forces respectively associated to the damage D and the permanent rate tensor of deformation $\mathbb{D}^{d*}$ turned, given by:

$$\mathbf{Y} = -\frac{\partial W}{\partial D} = W_0(\bar{\lambda}_i^e, J^e) \quad (9)$$

Following the framework of the Generalised Standard Materials theory in the case of rate-independant flow, a damage criterion is given by (Andrieux 1996):

$$f(\mathbf{Y}; D) = \mathbf{Y} - Q(D) \leq 0 \quad (10)$$

An unloading, neutral loading or loading from a damage state shall be added to this criterion. $Q(D)$ being a differentiable positive and increasing function of D, representing the size of the damage surface in the $\mathbf{Y}$-space and is given by:

$$Q(D) = Q\sqrt[n]{D + D_0} \quad (11)$$

where Q, n and D_0 are the damage parameters. Q is the intensity expressed in term of energy, n is describing the linearity of the damage effect evolution, and D_0 is a positive threshold of non-damage effect (usually $D_0 << 1$). Finally, in the same space, a flow potential is introduced to complete a non-associative damage flow:

$$F_D(\mathbf{Y}, \tau; D) = \mathbf{Y} + \frac{R}{2}\frac{\tau : \tau}{1-D} \quad (12)$$

where R is a parameter describing the intensity of the permanent deformation. Following the standard normality argument the damage and the permanent rate tensor evolution (complementary laws) are given by:

$$\dot{D} = \begin{cases} \dot{\delta}\dfrac{\partial F_D}{\partial \mathbf{Y}} & \text{if } f = 0 \\ 0 & \text{if } f < 0 \end{cases} \quad \mathbb{D}^{d*} = \begin{cases} \dot{\delta}\dfrac{\partial F_D}{\partial \tau} & \text{if } f = 0 \\ 0 & \text{if } f < 0 \end{cases} \quad (13)$$

where $\dot{\delta}$ is the damage multiplier given by the consistency condition $\dot{f} = 0$, i.e.:

$$\dot{\delta} = \frac{(\tau^\circ : \mathbb{D})}{R\tau^\circ : \tau^\circ + Q'(D)} \quad \text{with} \quad \tau^\circ = \frac{\tau}{1-D} \quad (14)$$

3 NUMERICAL APPLICATION

3.1 *Numerical resolution*

After some simplifications, the model is reduced to a scalar equation (damage criterion) and a tensoriel equation (evolution of $\mathbb{B}^e$):

$$\begin{cases} W_0(\bar{\lambda}_i^e, J^e) - Q\sqrt[n]{D + D_0} = 0 \\ \dot{\mathbb{B}}^e - \mathbb{L}\mathbb{B}^e - \mathbb{B}^e\mathbb{L}^T + 2R\dot{D}\mathbb{B}^e \cdot \tau(\mathbb{B}^e) = 0 \end{cases} \quad (15)$$

The Euler-Implicit time discretisation for flow variables and the Newton-Raphson method for non-linear equation resolution are used. The deformation gradient $\mathbb{F}$ is known at the beginning and at the end of the increment and all the other elements are known at the beginning of the increment. ΔD and $\Delta\mathbb{B}^e$ are the principal unknowns. When the systems (17) is resolved, the stress can be calculate from the hyper-elastic behaviour (8) with the new values of $D_{t+\Delta t}$ and $\mathbb{B}^e_{t+\Delta t}$. The proposed model is implemented in ABAQUS Software using user's Subroutine, UMAT and VUMAT, respectively for a global implicit and explicit integration.

3.2 *Identification of material parameters*

Firstly, we propose to identify the material parameters from an experimental uniaxial tensile test of

a filled-elastomer test-tube. The principle of the numerical optimization used for the identification is shown on Table 1. The paramater's values evaluated by the optimization are shown on the Table 2, and the Force-Displacement curve associated to this result are shown on Figure 1. The parameters D_1 and D_0 are not identified in this study, and are fixed respectively to 0.0005 (almost-incompressible condition on the elastic motion) and 10^{-6} (threshold of non-damage condition).

3.3 *Numerical simulations*

3.3.1 *Uniaxial tensile test*

In order to shown the efficiency of the coupled model, we simulate an uniaxial tensile test on a 3D cubic finite element presented on Figure 2. The parameters have the same values shown on table 2.

The comparison of the stress evolution versus the strain, coupled with damage effect and uncoupled, is presented in Figure 3. The stress-softening effect due to the damage processus is observed until the rupture ($D = 1$).

As for the variation of the volume, we present, in Figure 4, the evolution of the different dilations:

Table 1. Numerical optimization method for identification.

Initial parameters	⇒	Stage 1 : ABAQUS SIMULATION (2D test-tube modelled)
		Stage 2 : PYTHON PROGRAM Treatment of the file *.ODB (Force vs Displacement)
Experimental data	⇒	Stage 3 : MATLAB OPTIMIZATION (Simplex method)
		Stage 4 : ERROR PREDICTION
		if true → Optimized parameters else → return to Stage 1

Table 2. Material parameters.

μ_1	–1.6025 MPa	
μ_2	0.2692 MPa	
μ_3	–0.0007 MPa	
α_1	–1.2303	Hyperelastic parameters
α_2	2.8041	
α_3	–4.3190	
D_1	0.0005	
Q	29.2240	
n	2.6468	
D_0	10^{-6}	Damage parameters
R	0.0003	

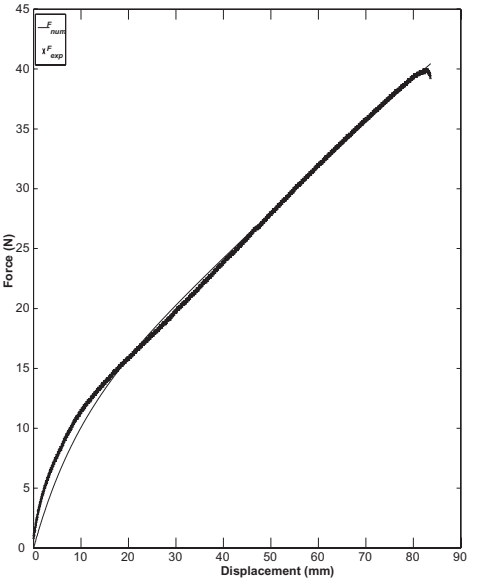

Figure 1. Force vs Displacement.

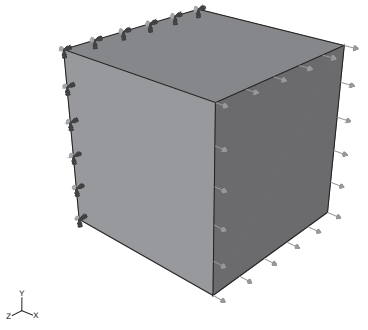

Figure 2. 3D cubic finite element.

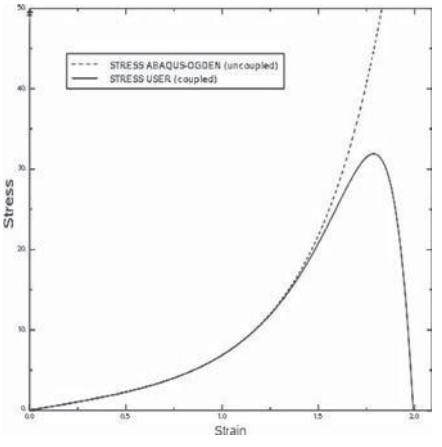

Figure 3. Stress versus Strain.

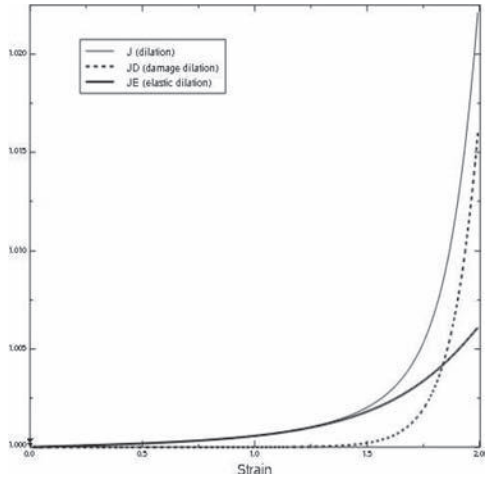

Figure 4. Dilation versus Strain.

J (total), J^e (elastic) and J^d (damage). The total volume has reached approximately 1.022 and we can note an almost-incompressible behaviour for the elastic motion, his value do not exceed approximately 1.005. This latter can be more reduced by the parameter D_1 which can be defined smaller. As for the damage dilation, it reaches approximately 1.015 due to the appearance of the damage during the loading.

3.3.2 *Tensile test of a plate with hole*

We propose to simulate a plate perforated in tensile test. The latter will be modelled in 2D, via the ABAQUS Software, according to the dimensions of the Figure 5.

Only one quarter of the plate will be considered just to reduce the time-calculation. Calculation was carried out with and without damage for the comparison. Another calculation, using it standard model of ABAQUS, was also made to validate our model uncoupled (i.e. $D = 0$ during loading). The distribution of Von-Mises stresses at the hole's edge is shown on the Figure 6. The maximum is reached at the hole's edge on the top. The finite element, whose the stress is maximum, is selected to plot the curves of the Stress versus Strain (see 7) and the variation of volume (see 8).

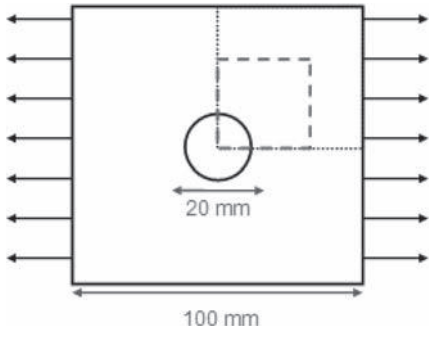

Figure 5. Diagram of the perforated plate.

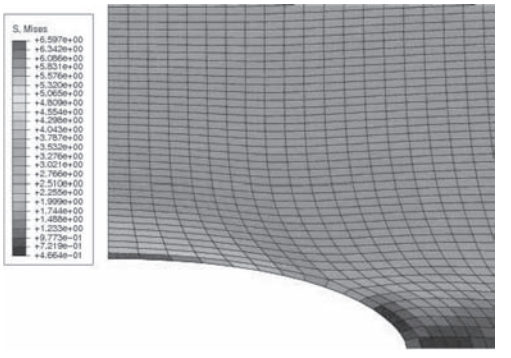

Figure 6. Von-Mises stress at the edge of the hole (MPa).

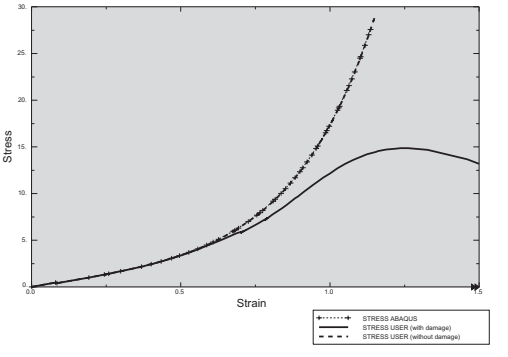

Figure 7. Stress versus Strain.

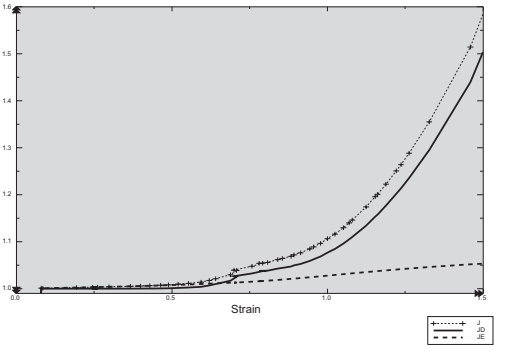

Figure 8. Volume variations.

4 CONCLUSIONS

In this study, we have formulated a rate-independent model that captures the effects of material degradation and a voluminal permanent set for a class of filled-elastomers. In the framework of CDM, an irreversible state variable D model the isotropic damage effect associated to the creation of microcracks inside the structure. The model has been implemented into the finite element code ABAQUS and has been tested in order to shown the efficiency of the method. An optimization script has been developed to identify the different material parameters, hyperelastic and damage, from an uniaxial tensile test. Finally, the softening-stress and the volume variation respectivily induced by damage and the voluminal permanent strain are illustrated with two simulations: An uniaxial tensile test of one 3D finite element, and a tensile test of a plate with hole in 2D. In all cases, the results satisfy the almost-incompressible condition for the elastic motion and a compressible motion for the permanent strain.

REFERENCES

Andrieux, F. (1996). *Sur les milieux visco-hyperélastiques endommageables*. Thèse, Université de Technologie de Compiègne, France.

Dorfmann, A. and R. Ogden (2004). A constitutive model for the mullins effect with permanent set in particle-reinforced rubber. *Solids and Structures 41*, 1855–1878.

Figueredo, R. and A. Cherouat (2007). A new approach to couple a constitutive model for the mullin effect with residual strain and the damage of elastomer materials. In *Proc. ECCMR'07*, pp. 85–90.

Figueredo, R. and A. Cherouat (2008). Permanent strain and damage formulation in forming processes of filled-elastomer materials. In *Proc. ISAFORM'08.*

Lemaitre, J. and J. Chaboche (1985). *Mécanique des matériaux solides*.

Lion, A. (1996). A constitutive model for carbon black filled rubber: Experimental investigations and mathematical representation. *Continuum Mechanics and Thermodynamics 8*(3), 153–169.

Mullins, L. (1969). Softening of rubber by deformation. *Rubber Chemistry and Technology 42*, 339–362.

Saanouni, K., F. Sidoroff, and F. Andrieux (1998). Damaged hyperelastic solid with an induced volume variation. Effect of loading paths.

Sidoroff, F. (1975). Variables interne viscoélasticité: I. variables internes scalaire et tensorielles. *Journal de Mécanique 14*(4), 679–713.

Constitutive Models for Rubber VI – Heinrich et al. (eds)
© 2010 Taylor & Francis Group, London, ISBN 978-0-415-56327-7

An approach to the continuum description of the behavior of particulate elastomeric composites

L.A. Golotina & L.L. Kozhevnikova
Institute of Continuous Media Mechanics UB RAS, Perm, Russia

ABSTRACT: The proposed approach to the macroscopic continuum description of the behavior of particulate polymeric composites consists in prescribing the constitutive relations for tested materials as the dependence of the density of potential strain energy on the finite strain tensor invariants, obtained in studies of deformation and fracture in specialized cells. This relation is represented not analytically but as electronic spreadsheets that involve the results of solving the boundary-value problems of deformation of structural cells. Algorithm of realization of the finite element method is developed to study the stress-strain state of particulate composite products based on the data taken directly from electronic spreadsheets.

1 INTRODUCTION

Dispersion-filled elastomeric composite materials have found wide application in different engineering areas. In coarse-grained elastomeric composites the size of matrix layers between the particles is considerably larger than the typical size of macromolecules. Under such assumption, the mechanical behavior of the material can be described using continuum mechanics approaches. A specified unit cell approach is capable to model fairly well the complicated macroscopic properties of particulate polymer composites. These materials are the systems in which it is possible to stand out the representative structural cells. This allows one to quantitatively estimate the mechanical behavior of cells depending on the governing structural parameters: the volume part of the filler, the properties of the binding polymer and the strength of its coupling with the filler. In this case, it is also possible to investigate the evolution of cells on all stages since the moment of their formation to fracture. Representative structural elements seem to be effective tools for creation macroscopic continuum models of advanced materials. An individual structural element or cell is supposed to be a specific construction capable of reflecting, in principle, macroscopic behaviour of the material. It is supposed, as well, that the construction of the structural cell allows the effective properties of the cell to be determined. The transformation of the stress and strain fields existing inside a cell into the corresponding macroscopic characteristics of the cell is the step in describing a continuous medium.

2 STRUCTURAL CELL

A unit cell of a specified shape under specified loading conditions has been offered earlier as a representative mesoelement for particulate polymeric composites (Moshev & Kozhevnikova 2000). The offered structural unit cell represents an elastomeric cylinder with the height equal to its diameter. A rigid spherical inclusion (filler) is placed at the centre of the cylinder (fig. 1). It is assumed that this element is disposed within a closely packed ensemble. The maximum solid-phase filling of this package reaches 0.64, which coincides with the limiting filling of random structures consisting of identical spherical particles.

The cell is a main carrier of elastomeric composite properties. The tensile strength of the cell is represented by three states: tension without discontinuity, tension with a separating matrix and matrix rupture followed by the loss of strength.

A set of parameters that govern the cell behavior involves: properties of the elastomeric matrix (in the form of neo-Hooke's model) and its rupture

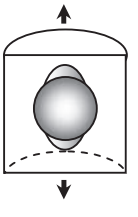

Figure 1. A unit structural cell.

deformation, filler particle size, volume filler concentration, and matrix-filler bond strength. The mechanical behavior of the cell is determined in the solution of the boundary-value continuum problem. It is assumed that the cells, being subjected to tension, compression, or shearing remain cylindrical, and their ends—plane. This provides their dense packing during deformation. Hereinafter the structural cells will be considered as some solid elastic objects possessing the specific behavior. Doing so, we turn from the structural description towards continuum one.

The next step consists in choosing appropriate constitutive relations for the cell's mechanical description. Among numerous alternatives, we have taken the simplest one

$$\sigma_{ij} = 2\,G\,(\varepsilon_1,\,\sigma_0)\,(\varepsilon_{ij} - \theta/3) + \delta_{ij}\,\sigma_0,$$

$$\theta = f(\varepsilon_1,\,\sigma_0).$$

Here, G is the shear modulus, and θ is the volume compressibility. These magnitudes are not constant. They are functions of current magnitudes of the maximum main strain, ε_1, and the mean stress, σ_0.

A number of boundary value problems with various structural input parameters have been solved to get enough data for construction functions, $G\,(\varepsilon_1,\,\sigma_0)$ and $\theta = f(\varepsilon_{ij},\,\sigma_0)$, and ultimate strains at break values of cells.

The analytical description of materials with complicated behaviour, like that of damageable particulate composites, inevitably requires a great number of material parameters for adequate representation. However, as compared with the like descriptions obtained through treatment of physical experiments, it has an advantage of a greater comprehensiveness that can protect from unfounded extrapolations.

3 TABULAR FORM OF CONTINUUM RELATIONS REPRESENTATION

A new method of modeling the mechanical behavior and failure of particulate polymer composites has been developed with the intent to explicitly relate meso- and macroproperties of the material. The proposed approach consists in creating a data base that involves the results achieved in solving the boundary-value problems dealing with deformation of structural cells under different loading conditions up to failure. Calculated results are represented as the dependence of the deformation elastic energy density on the constitutive invariants of the finite strain tensor. The availability of such data base makes it possible to develop the algorithm for the numerical solution of the boundary-value mechanical problems using the finite-element method (or any other numerical method in variational formulation) without the analytical representation of the dependence of the elastic potential on invariants.

A stepwise algorithm has been developed which allows the implementation of the finite element method at large deformations. Also developed are some specialized procedures providing the use of data taken directly from electronic tables in place of physical equations. It allows us to establish a direct connection between discrete tabular data and finite element techniques, based on a commonly used variational equation:

$$\int_V \partial W/\partial\varepsilon \cdot \delta\varepsilon\; dV - \int_V \rho K \cdot \delta u\; dV - \int_S P \cdot \delta u\; dS = 0,$$

where ε is the Cauchy-Green finite strain tensor, $W = W(I_1, I_2, I_3)$ is the potential energy density, I_i are the invariants of tensor ε.

In this case, the task is reduced to: (1) presenting tabular data, emerging from the solution of a set of particular boundary-value problems for unit cells, as a relationship between the potential energy density W and the invariants I_i of the Cauchy-Green finite strain tensor ε; (2) development of an appropriate interpolation procedure allowing rapid search of W-values in the tabular database; (3) the approximation of the relationship $W = W(I_1, I_2, I_3)$ for each finite element in a rather simple form which is suitable for construction of effective numerical algorithms.

The mechanical behavior and conditions for failure of the structural cell of at different volume percent filler fraction were studied under various loading conditions: tension and compression at positive, zero and negative external pressures and shearing. The obtained results were tabulated in electronic form.

Studies performed for discrete models showed that the occurrence of macrocracks in the material is only possible when it is inhomogeneous in properties. This inhomogeneity may be natural (initial) or induced in the course of the lifetime of the material. It produces conditions under which the elastic stability is lost and the macrocrack appears in the most compliant point of the structure. Essential difference in the rigidity of elements comprising particulate composites and stochasticity of their location on structural level give grounds to refer these composites to initially inhomogeneous. As the source of initial inhomogeneity, we consider the variability of local concentration of the filler. First we assume that one cell corresponds to each finite element. To model the inhomogeneity of cells, we

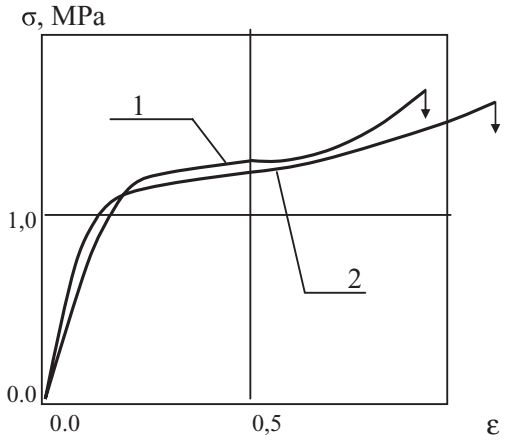

Figure 2. The comparison calculated and experimental stress-strain curves.

use the data obtained by theoretical synthesizing random geometrical figures. For modeling the systems with the prescribed random distribution of properties, we have calculated dependences for cells with different volume filler concentration. The obtained results were tabulated in electronic form. When solving the boundary-value problem, we performed the local approximation W in terms of the data obtained for local concentration that were taken in a random fashion using the distribution function.

The tensile curves were calculated for rectangular specimens. The numerical results were compared with the existing experimental data. It was found that the proposal approach is capable to describe the complicated mechanical behavior of particulate polymer composites. Figure 2 demonstrates the calculated stress-strain curve (2) and experimental data (1) from (Schwarzl et al. 1965). The similarity between the both curves seems to be satisfactory.

4 CONCLUSIONS

As it is demonstrated above, establishing analytical constitutive relations for materials with complicated mechanical behaviour meets considerable difficulties, which originate of necessity to determine and use a great number of material parameters often with unclear physical meaning. Hence, a search of other approaches for describing mechanical behaviour of these materials seems to be justified.

The tabular form of the mechanical description is likely to be a realistic way, when one takes into account that informational resources and the computation time of the modern machinery are considerable and tend to further progressing. However, this approach will require solving some new problems. An algorithm for using such tables is to be developed containing the appropriately selected interpolation procedures and aimed at the incorporation into the well-known finite element techniques.

The transformation of the discrete mechanical description of structural elements into continuum form open the possibility of direct connection between structural specificity and well developed finite element design projects based on utilisation composite materials with complicated mechanical behaviour. This, in essence, means the establishment of a closer contact between material scientists and designers.

Moreover, identifying the behaviour of individual finite elements with the behaviour of individual structural cell we get a unique chance to incorporate into design procedures accounting natural mechanical inhomogeneity that determines the performance variability of the designed macroscopic structures.

REFERENCES

Moshev, V.V. & Kozhevnikova, L.L. 2000 Predictive potentialities of a cylindrical structural cell for particulate elastomeric composites. *Solids Structures.* 37: 1079–1097.

Schwarzl, F.R. et al., Bree, H.W. & Nederveen, C.J. 1965 Mechanical properties of highly filled elastomers. I. Relationship between filler characteristics, shear moduli, and tensile properties, *Proc. 4-th Intern. Congr. Rheolog.* 3: 241–263. Interscience/Wiley, NY.

Constitutive Models for Rubber VI – Heinrich et al. (eds)
© 2010 Taylor & Francis Group, London, ISBN 978-0-415-56327-7

A phenomenological finite strain framework for the simulation of elastic polymer curing

M. Hossain, G. Possart & P. Steinmann
Chair of Applied Mechanics, University of Erlangen-Nuremberg, Erlangen, Germany

ABSTRACT: A phenomenologically motivated small strain model to simulate the curing of thermosets has been developed and discussed in a recently published paper (1). Inspired by the concepts used there, this contribution presents an extension towards the finite strain regime. The thermodynamically consistent framework used here for the simulation of curing polymers is independent of the choice of the free energy density, i.e. any phenomenological or micromechanical approach can be utilised. Both the governing equations for the curing simulation framework and the necessary details for the numerical implementation within the finite element method are derived.

1 INTRODUCTION

There is a vast number of applications in almost every branch of daily life where polymeric materials play an important role. In cases where the very formation of such materials plays a decisive role to meet particular design goals of a structure, e.g. for adhesives in automotive, electronics or aerospace industry, one can observe an increasing demand for constitutive models and simulation methods that consider a time- or degree of cure dependence of the mechanical properties. Apart from adhesives, further applications relevant for such models would be carbon- or glass fibre-reinforced epoxy laminates and (nano-)particle-reinforced polymer structures in general (15; 16).

An uncured polymer usually behaves as a deformable viscous liquid practically incapable of sustaining any load other than hydrostatic. With time evolving, the curing reactions proceed, polymer chains form (and possibly cross-link to each other) and the viscosity of the liquid resin, its molecular weight and the stiffness increase. A number of rheological analogies to such processes have been applied and discussed by several authors (2; 3; 4; 5) and also our previous small strain curing model made extensive use of such assumptions. A physically and chemically sound approach to model polymer curing has been developed in a series of papers by Adolf and co-workers (3; 6; 7; 8; 9), who proposed not only linear constitutive models but also an extension to the large strain regime. Their continuum model, originally devised to describe viscoelastic glassy polymers, is extended towards the curing of polymers by the introduction of an additional dependent variable into the Helmholtz free energy, namely the completion of reaction. The only limitation of this model is that a full derivation of stress tensors and consistent tangent operators, which are essential for the iterative solution of boundary value problems within finite element schemes, is lacking.

Another approach has been published by Lion & Höfer (2) who proposed a phenomenological thermo-viscoelastic curing model for finite strain deformations. It accounts for thermally and chemically induced volume changes via a ternary multiplicative split of the deformation gradient into mechanical, thermal and chemical parts. Similar to Adolf's ansatz, a coordinate of reaction is introduced that corresponds to the degree of cure. The model is mainly based on the assumption of process dependent viscosities as in the previous works of Haupt & Lion (10; 11; 12). The resulting constitutive relation is derived in a thermodynamically consistent manner, i.e. it fulfills the second law of thermodynamics, which is an important issue that many of the earlier curing models did not touch. Detailed algorithmic formulations for the finite element implementation of this model are elaborated in Retka & Höfer (13). The energy density used for the mechanical part of this model is of a phenomenological type.

The main assumption, considered earlier (1) in the development of linear constitutive curing models, is, from the rheological point of view, that a cross-linking or curing process can, for the elastic case, be understood as a continuous increase in stiffness. From a molecular point of view we assumed further that when a step in strain

is applied, the chains between existing cross-links are deformed which is accompanied by some stress distribution in the material. Due to the progress in curing, new cross-links occur which has been conceptualised by the addition of new chains to the network. These fit into the already deformed structure and are not affected by the previous deformation, i.e. new chains do not contribute to the stress until the deformation is changed again. Expressed in rates this behaviour would be described by $\dot{\sigma} = 0$ as long as $\dot{\varepsilon} = 0$. It is noteworthy that this particular behaviour prohibits the simulation of curing materials by just considering an additional time dependence of the material parameters. Since we would like to avoid any initial restriction concerning the choice of constitutive model, we depart from our general equation for the stress update developed in (1) and provide the necessary extensions to capture finite strain deformations. This approach is valid only for materials that have passed the gel point, which is only a weak restriction since the stiffness increase relevant for practical applications takes place mainly after gelation. In particular, we will omit the consideration of the initial polymer solution as a multi-component diffusion mixture.

2 SIMULATION FRAMEWORK

The method introduced here aims at the simulation of materials undergoing finite strain deformations while their elastic properties are simultaneously experiencing a temporal evolution. As a starting point we go back to the general equation for the one-dimensional stress update of our recently published (1) small strain modelling approach for the curing of thermosets:

$$\dot{\sigma}(t) = c(t)\dot{\varepsilon}(t). \tag{1}$$

Thereby, $c(t)$ denotes the time-dependent material stiffness linearly relating stress- and strain-rate. For the case of large strain deformations we transfer this format to

$$\dot{\boldsymbol{S}}(t) = \mathbb{C}(t) : \dot{\boldsymbol{E}}(t) = \frac{1}{2}\mathbb{C}(t) : \dot{\boldsymbol{C}}(t), \tag{2}$$

where $\boldsymbol{S}$, $\boldsymbol{E} = ½[\boldsymbol{C} - \boldsymbol{I}]$ and $\boldsymbol{C}$ denote the 2nd Piola-Kirchhoff stress tensor, the Green-Lagrange strain tensor and the right Cauchy-Green tensor, respectively. By $(\dot{\bullet})$ the material time derivative is expressed and $\mathbb{C}(t)$ describes the time dependent *stiffness operator* as derived from the strain energy density Ψ of an arbitrary, time-dependent material model via

$$\mathbb{C}(t) = 4\frac{\partial^2 \Psi(t)}{\partial \boldsymbol{C}^2(t)}. \tag{3}$$

Stress formulation (2) is of a hypoelastic type, although it differs from the original version proposed by Truesdell & Noll (14). As for any other constitutive assumption, the property of thermodynamical consistency requires special attention. This property is given if a free energy density Φ can be formulated that satisfies the isothermal dissipation inequality

$$\boldsymbol{S} : \dot{\boldsymbol{E}} - \dot{\Phi} \overset{!}{\geq} 0 \tag{4}$$

for all possible processes. The standard Coleman-Noll argumentation then provides the stress formulation (2) if the following ansatz for Φ is chosen:

$$\Phi(t) = \frac{1}{2}\int_0^t [\mathbb{C}'(s) : [\boldsymbol{E}(t) - \boldsymbol{E}(s)]] : [\boldsymbol{E}(t) - \boldsymbol{E}(s)] ds, \tag{5}$$

where $\mathbb{C}'(s) = d\mathbb{C}(s)/ds$ denotes the total differential of the material specific, time dependent stiffness tensor according to Eq. (3) and with respect to the integration variable *s*. In analogy to a linear spring, this convolution integral can be interpreted as the accumulation of elastically stored energy while both the stiffness and the deformation are continuously evolving. Note that definition (5) is physically reasonable if and only if the derivative of the stiffness tensor is positive semi-definite, i.e.

$$[\mathbb{C}' : \boldsymbol{E}] : \boldsymbol{E} \geq 0 \quad \forall \boldsymbol{E}, \tag{6}$$

which is a requirement intrinsically met if $\mathbb{C}$ is derived from an appropriately chosen strain energy density Ψ. To evaluate the dissipation inequality (4) the material time derivative $\dot{\Phi}$ needs to be computed:

$$\dot{\Phi} = \left[\int_0^t \mathbb{C}'(s) : [\boldsymbol{E}(t) - \boldsymbol{E}(s)]\right] : \dot{\boldsymbol{E}}(t) ds. \tag{7}$$

This additionally requires permutability of the double contractions, i.e.

$$\begin{aligned} &[\mathbb{C}' : \boldsymbol{A}] : \boldsymbol{B} = [\mathbb{C}' : \boldsymbol{B}] : \boldsymbol{A} \quad \forall \boldsymbol{A}, \boldsymbol{B} \\ \Leftrightarrow\ &(\mathbb{C}')_{ijkl} A_{kl} B_{ij} = (\mathbb{C}')_{klij} B_{ij} A_{kl}, \end{aligned} \tag{8}$$

which is given since $\mathbb{C}$ stems from a potential and thus possesses major symmetry. Insertion of result (7) into the elastic version of (4) yields

$$\left[\boldsymbol{S}(t)-\int_0^t \mathbb{C}'(s):[\boldsymbol{E}(t)-\boldsymbol{E}(s)]ds\right]:\dot{\boldsymbol{E}}(t)\overset{!}{=}0 \tag{9}$$

and the standard Coleman-Noll procedure provides the following functional for the 2nd Piola-Kirchhoff stress:

$$\boldsymbol{S}(t)=\int_0^t \mathbb{C}'(s):[\boldsymbol{E}(t)-\boldsymbol{E}(s)]ds. \tag{10}$$

Computing the material time derivative finally yields the desired result, i.e. constitutive equation (2):

$$\dot{\boldsymbol{S}}(t)=\mathbb{C}(t):\dot{\boldsymbol{E}}(t)=\frac{1}{2}\mathbb{C}(t):\dot{\boldsymbol{C}}(t). \tag{11}$$

This tensor-valued ordinary differential equation for the stress can be solved iteratively by applying numerical integration schemes like the implicit Euler backward:

$$\boldsymbol{S}^{n+1}=\boldsymbol{S}^{n}+\frac{1}{2}\mathbb{C}^{n+1}:[\boldsymbol{C}^{n+1}-\boldsymbol{C}^{n}], \tag{12}$$

whereas $[\bullet]^n=[\bullet]\,(t_n)$ and $t_{n+1}=t_n+\Delta t$. The main advantage of this stress formulation is that any kind of constitutive (polymer) model—either phenomenologically or micromechanically based—can be inserted. The only ingredients required are the temporal evolutions of the governing material parameters to determine $\mathbb{C}^{n+1}$, which can be parametrised e.g. directly in time or in terms of the degree of cure. In particular, this ansatz is not restricted to hyperelasticity but can also be used for viscoelastic material models. A second important property of relation (12) is its capability to reproduce the physical observation that the stress state of a curing material is changed if and only if its strain state is modified, i.e. $\dot{\boldsymbol{S}}=\boldsymbol{0}$ as long as $\dot{\boldsymbol{C}}=\boldsymbol{0}$. This requirement constitutes a significant design constraint for any model considering curing processes. It assures that the evolution of material properties becomes visible just by the time the deformation state is changed—even though its free energy density evolves permanently.

In order to apply the finite element method for the solution of boundary value problems under certain constitutive assumptions, it is common practice to resort to implicit iterative schemes like the Newton-Raphson method. In particular, a consistent linearisation of stress formulation (12) with respect to changes in strain is required. The computation of this current *tangent operator* introduces a sixth-order tensor $\mathfrak{A}$, namely the derivative of the current material specific stiffness operator with respect to the strain:

$$\begin{aligned}\mathbb{E}^{n+1}&=2\frac{\partial \boldsymbol{S}^{n+1}}{\partial \boldsymbol{C}^{n+1}}\\&=\frac{\partial(2\boldsymbol{S}^{n}+\mathbb{C}^{n+1}:[\boldsymbol{C}^{n+1}-\boldsymbol{C}^{n}])}{\partial \boldsymbol{C}^{n+1}}\\&=\mathbb{C}^{n+1}:\mathbb{I}^{sym}+[\boldsymbol{C}^{n+1}-\boldsymbol{C}^{n}]:\frac{\partial \mathbb{C}^{n+1}}{\partial \boldsymbol{C}^{n+1}}\\&=\mathbb{C}^{n+1}+[\boldsymbol{C}^{n+1}-\boldsymbol{C}^{n}]:\mathfrak{A}^{n+1},\end{aligned} \tag{13}$$

where $\mathbb{I}^{sym}=\frac{1}{2}[\delta_{ik}\delta_{jl}+\delta_{il}\delta_{jk}]$ denotes the symmetric fourth order identity tensor, δ_{ij} is the Kronecker delta and $\mathfrak{A}^{n+1}=\partial\mathbb{C}^{n+1}/\partial\boldsymbol{C}^{n+1}$.

In the following sections, this framework for the simulation of curing materials will be particularised for the Neo-Hooke model. To this end the underlying expressions for free energy density Ψ and stiffness operator $\mathbb{C}$ are recapitulated and the corresponding tangent operators $\mathbb{E}$ are derived.

2.1 *Application: Neo-Hooke model*

We consider a rather simple but frequently used phenomenological constitutive ansatz for polymers, the so-called compressible Neo-Hooke model for which the corresponding free energy density is given by

$$\Psi(\boldsymbol{C},J)=\frac{1}{2}\kappa\,(\ln J)^2-\mu\ln J+\frac{1}{2}\mu\,[I_1-3]. \tag{14}$$

Here, $I_1=\boldsymbol{C}:\boldsymbol{I}$ denotes the first invariant of the right Cauchy-Green tensor while $J=\det\boldsymbol{F}$ is the determinant of the deformation gradient and κ and μ are the Lam parameters. Using Eq. (3) some manipulations provide the corresponding stiffness operator $\mathbb{C}$ which is required in Eqns. (12, 13):

$$\begin{aligned}\mathbb{C}&=4\frac{\partial^2\Psi}{\partial\boldsymbol{C}^2}\\&=\kappa\boldsymbol{C}^{-1}\otimes\boldsymbol{C}^{-1}+2\,[\mu-\kappa\ln J]\,\boldsymbol{C}^{-1}\odot\boldsymbol{C}^{-1}\\&=\kappa\mathbb{A}-2\,[\mu-\kappa\ln J]\,\mathbb{B}.\end{aligned} \tag{15}$$

The fourth-order tensors $\mathbb{A}$ and $\mathbb{B}$ are introduced for the sake of simplicity and can be written componentwise as

$$\begin{aligned}(\mathbb{A})_{ijkl}&=(\boldsymbol{C}^{-1}\otimes\boldsymbol{C}^{-1})_{ijkl}=\boldsymbol{C}^{-1}_{ij}\boldsymbol{C}^{-1}_{kl}\\(\mathbb{B})_{ijkl}&=\left(\frac{\partial\boldsymbol{C}^{-1}}{\partial\boldsymbol{C}}\right)_{ijkl}=-\frac{1}{2}\left[C^{-1}_{ik}C^{-1}_{jl}+C^{-1}_{il}C^{-1}_{jk}\right].\end{aligned}$$

Thus, the current stiffness operator necessary to update the stress according to Eq. (12) is determined by the cure-dependent parameters κ, μ and the strain state included in J, $\mathbb{A}$, $\mathbb{B}$:

$$\mathbb{C}^{n+1}=\kappa^{n+1}\mathbb{A}-2\,[\mu^{n+1}-\kappa^{n+1}\ln J]\,\mathbb{B}. \tag{16}$$

The current tangent operator (13) additionally requires the computation of $\mathfrak{A}^{n+1}$:

$$\begin{aligned}\mathfrak{A}^{n+1} &= \frac{\partial \mathbb{C}^{n+1}}{\partial \boldsymbol{C}} \\ &= \kappa^{n+1}\left[\frac{\partial \mathbb{A}}{\partial \boldsymbol{C}} + 2\ln J \frac{\partial \mathbb{B}}{\partial \boldsymbol{C}} + \mathbb{B}\otimes \boldsymbol{C}^{-1}\right] - 2\mu^{n+1}\frac{\partial \mathbb{B}}{\partial \boldsymbol{C}} \\ &= \kappa^{n+1}[\mathfrak{B} + 2\ln J\mathfrak{C} + \mathbb{B}\otimes \boldsymbol{C}^{-1}] - 2\mu^{n+1}\mathfrak{C}, \end{aligned} \tag{17}$$

which closes the constitutive equations for a Neo-Hookean material undergoing a curing process. For the sake of completeness the sixth-order tensors $\mathfrak{B} = \mathbb{A}$, c and $\mathfrak{C} = \mathbb{B}$, c are given component-wise:

$$\begin{aligned}(\mathfrak{B})_{ijklpq} &= \frac{\partial (C^{-1}_{ij}C^{-1}_{kl})}{\partial C_{pq}} = \frac{\partial C^{-1}_{ij}}{\partial C_{pq}}C^{-1}_{kl} + C^{-1}_{ij}\frac{\partial C^{-1}_{kl}}{\partial C_{pq}} \\ &= -\frac{1}{2}\Big[C^{-1}_{ip}C^{-1}_{jq}C^{-1}_{kl} + C^{-1}_{iq}C^{-1}_{jp}C^{-1}_{kl} \\ &\qquad + C^{-1}_{ij}C^{-1}_{kp}C^{-1}_{lq} + C^{-1}_{ij}C^{-1}_{kq}C^{-1}_{lp}\Big],\end{aligned}$$

$$\begin{aligned}(\mathfrak{C})_{ijklpq} &= -\frac{1}{2}\frac{\partial\,(C^{-1}_{ik}C^{-1}_{jl} + C^{-1}_{il}C^{-1}_{jk})}{\partial C_{pq}} \\ &= \frac{1}{4}\Big[C^{-1}_{ip}C^{-1}_{kq}C^{-1}_{jl} + C^{-1}_{iq}C^{-1}_{kp}C^{-1}_{jl} \\ &\qquad + C^{-1}_{ik}C^{-1}_{jp}C^{-1}_{lq} + C^{-1}_{ik}C^{-1}_{jq}C^{-1}_{lp} \\ &\qquad + C^{-1}_{ip}C^{-1}_{lq}C^{-1}_{jk} + C^{-1}_{iq}C^{-1}_{lp}C^{-1}_{jk} \\ &\qquad + C^{-1}_{il}C^{-1}_{jp}C^{-1}_{kq} + C^{-1}_{il}C^{-1}_{jq}C^{-1}_{kp}\Big].\end{aligned}$$

3 EXAMPLES

A few numerical examples are presented to demonstrate that the proposed simulation framework can reproduce the mechanical behaviour of polymers during isothermal curing. All simulations have been performed using a research-based in-house finite element code that has been extended by the constitutive relations and tangent operators summarised in Section 2.1. First, some one-dimensional examples reflect the behaviour of a single eight-noded brick element for a prescribed uniaxial stretch history and parameter evolution. Next, a three-dimensional simulation is presented to demonstrate the influence of stiffness gain on the material response. For the sake of simplicity, the bulk modulus evolution has always been calculated from the current shear modulus via $\kappa(t) = 2\mu(t)[1+\upsilon]/3[1-\upsilon]$ by assuming a constant Poisson's ratio $\upsilon = 0.35$.

3.1 *One-dimensional example*

First, a simple uniaxial tension test is simulated using a single finite element to check whether the proposed finite strain curing models will predict the gain in stiffness during the advancement of curing and provide a correct behaviour in case the strain rate becomes zero. To this end a three phase deformation is applied consisting of a linear increase to $\lambda = 1.05$ within the first five seconds which is followed by fourty seconds holding and another linear increase to $\lambda = 1.1$ during the last five seconds, cf. Figure 1.

The Neo-Hooke curing model is used with a prescribed exponential saturation function for the evolution of the shear modulus, also depicted in Figure 1. The resulting stress responses versus time and stretch are given in Figure 2. The physical observation that the stiffness increase during curing has no impact on the stress response of a constant deformation state is correctly reproduced, which is reflected by the constant lines between 5 and 45 seconds (left-hand plots) and, implicitly, by the kinks at $\lambda = 1.05$ that stem from the continuous increase of μ (right-hand side curves). Furthermore, the initially fast growing shear modulus leads to a nonlinear stress growth during the first five seconds, whereas the behaviour is almost linear with high stiffness at the end since the saturation value for μ has been reached meanwhile.

3.2 *Three-dimensional example*

A three-dimensional U-shaped geometry is considered to present an example with inhomogeneous

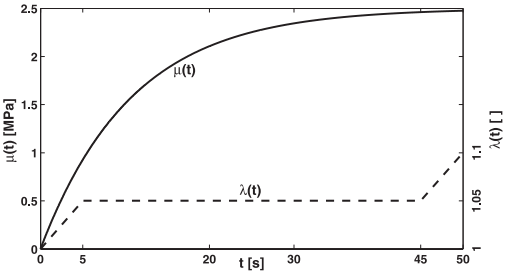

Figure 1. Load history $\lambda(t)$ and shear modulus evolution $\mu(t)$ according to $\mu(t) = \mu_0 + [\mu_\infty - \mu_0]\,[1 - \exp^{-\kappa_\mu t}]$ with $[\mu_0,\ \mu_\infty,\ \kappa_\mu] = [0.0001$ MPa, 2.5 MPa, 0.0925 $s^{-1}]$, applied to the Neo-Hooke curing model.

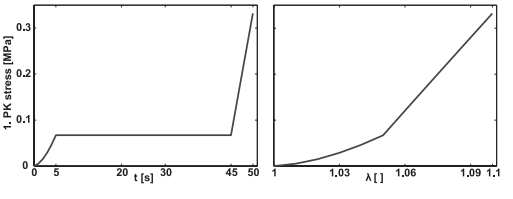

Figure 2. Elastic curing using the Neo-Hooke model, Piola stress vs. time and stretch.

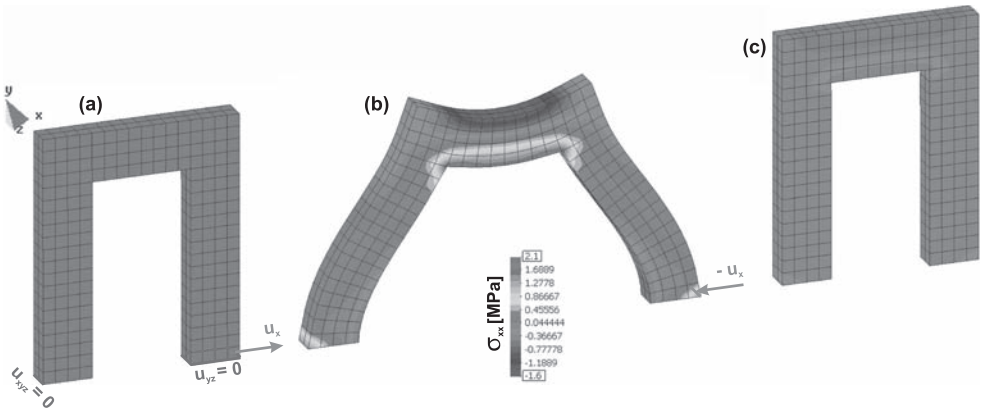

Figure 3. Inhomogeneous 3d-example, Neo-Hooke elastic curing model, (a): initial configuration, bearing and loading, (b): deformation and Cauchy stress after forty displacement loadsteps, $u_x = 16$ mm, (c): deformation-free but still compressively stressed (due to stiffness gain) after forty reverse displacement loadsteps, $u_x = 0.0$.

stress distribution under displacement-driven loading. Its dimensions are $20 \times 16 \times 2$ mm^3. The geometry is discretised by 384 eight-noded hexagonal elements and is supported as depicted in Figure 3(a). Displacement increments $\Delta u_x = 0.4$ mm are applied at the right side leg nodes to achieve elongations in x-direction. While being loaded, the specimen undergoes elastic curing, whereas

$$[\mu_0, \mu_\infty, \kappa_\mu] = [0.0001, 2.5, 0.115]$$

has been chosen for the Neo-Hooke model. Figures 3(b, c) depict the resulting deformations and Cauchy stresses in x-direction after forty tensile and another forty compressive displacement loadsteps. First, tensile stresses and a significant deformation arise, cf. Figure 3(b) while after the second forty displacement loadsteps of equal magnitude but reverse direction, the plate is deformation-free but, due to the interim stiffness increase, still under compressive stresses, cf. Figure 3(c).

4 CONCLUSIONS

This contribution proposes a three-dimensional, thermodynamically consistent framework for the simulation of polymeric materials undergoing curing processes and finite deformations. Based on some elementary rheological considerations the general equations for stress update and tangent operator as required for a finite element implementation are derived. With this at hand, phenomenologically motivated elastic polymer models is utilised. The numerical examples demonstrate that the developed approach is suitable to correctly reproduce the relevant phenomena observable in curing polymers. Nonetheless, some restrictions like the assumption of constant temperature and the purely phenomenological character of the presented approach should and will be subject of further investigation. Especially the extension towards viscoelasticity and the consideration of shrinkage effects is going to be dealt with in the next phase of this work.

REFERENCES

[1] M. Hossain, G. Possart, & P. Steinmann, *A small-strain model to simulate the curing of thermosets*, Computational Mechanics, 43(6): 769–779, 2009.

[2] A. Lion & P. Höfer, *On the phenomenological representation of curing phenomena in contiuum mechanics*, Archive of Mechanics, 59: 59–89, 2007.

[3] D.B. Adolf & R.S. Chambers, *A thermodynamically consistent, nonlinear viscoelastic approach for modeling thermosets during cure*, Journal of Rheology 51: 23–50, 2007.

[4] M. Kiasat, *Curing shrinkage and residual stresses in viscoelastic thermosetting resins and composites*, PhD Thesis, TU Delft, Netherlands, 2000.

[5] C. van't Hof, *Mechanical characterization and modeling of curing thermosets*, PhD Thesis, TU Delft, Netherlands, 2006.

[6] D.B. Adolf & J.E. Martin, *Calculation of stresses in crosslinking polymers,* Journal of Composite Materials 30: 13–34, 1996.

[7] D.B. Adolf & R.S. Chambers, *Verification of the capability for quantitative stress prediction during epoxy cure*, Polymer 38: 5481–5490, 1997.

[8] D.B. Adolf, J.E. Martin, R.S. Chambers, S.N. Burchett, & T.R. Guess, *Stresses during thermoset cure*, Journal of Materials Research 13: 530–550, 1998.

[9] D.B. Adolf, R.S. Chambers, & J.M. Caruthers, *Extensive validation of a thermodynamically consistent, nonlinear viscoelastic model for glassy polymers*, Polymer 45: 4599–4621, 2004.

[10] P. Haupt & A. Lion, *On finite linear viscoelasticity of incompressible isotropic materials*, Acta Mechanica 159: 87–124, 2002.

[11] A. Lion, *Thixotropic behaviour of rubber under dynamic loading histories: experiments and theories*, Journal of the Mechanics and Physics of Solids 46: 895–930, 1998.

[12] A. Lion, *On the large deformation behaviour of reinforced rubber at different temperatures*, Journal of the Mechanics and Physics of Solids 45: 1805–1834, 1997.

[13] J. Retka & P. Höfer, *Numerische Simulation aushrtender Klebstoffe*, Diploma Thesis, Universitt der Bundeswehr Mnchen, 2007.

[14] C. Truesdell & W. Noll, *The non-linear field theories of mechanics.* Springer, Berlin 1992.

[15] E. Ruiz & F. Trochu, *Thermomechanical properties during cure of glass-polyester RTM composites: elastic and viscoelastic modeling*, Journal of Composite Materials 39: 881–916, 2005.

[16] J. Lange, *Viscoelastic properties and transitions during thermal and UV cure of a methacrylate resin*, Polymer Engineering and Science 39: 1651–1660, 1999.

Constitutive Models for Rubber VI – Heinrich et al. (eds)

Experimental and theoretical investigations of the viscoelastic behaviour of cellular rubber

Nadine Koprowski, Michael Johlitz & Stefan Diebels
Chair of Applied Mechanics, Saarland University, Germany

ABSTRACT: In this article the mechanical properties of a porous carbon black-filled rubber are investigated with two different geometries. In this case it is important to mention the porosity and the associated compressibility of this material. In this contribution we focus on the theoretical modelling of the basic elasticity and of the visoelastic behaviour. Therfore, uniaxial tesion tests with different feedrates and different geometries are performed. It is found that the material behaviour is independent of the geometry. The constitutive model for the basic elasticity is based on a polynomial ansatz for an incompressible material which is supplemented by a pressure term to match the compressible behaviour of the structure. Finally, the concepts of finite viscoelasticity with intermediate configuration is applied. Because the material has a strongly nonlinear behaviour with respect to the feedrate nonlinear viscosity functions are introduced. The material parameters of the model are estimated using a stochastic identification algorithm.

1 INTRODUCTION

Rubber materials are used in automotive parts such as tires and gaskets. For the developement of these complex parts the use of simulation tools and therefore an appropriate model of such materials is necessary. The most assemblies are composed of a solid rubber part and a porous rubber part, both carbon black-filled. For the simulation of these complex assemblies, a material model for both kinds of rubbers is required. Porous rubber materials are often called cellular rubber. The investigated cellular rubber is a mixed open- and closed-cell foamed rubber enclosed by a moulding skin. Its mechanical and thermical properties are not yet fully characterized, so research pays a particular attention on it. A worldwide overview on the application of cellular rubber used as gasket in automotive engineering is given by Vroomen, (Vroomen, Choonoo, Odenhamn, and Hatta 2004). Summarizing no correlation between results from experiments on dogbone specimens and the practically applied parts exists for cellular rubber. Therefore an adequate model for cellular rubber does not exist, although there are many material models for incompressible rubber materials.

In this article the developement of a new material model for cellular rubber is proposed. Thus, uniaxial cyclic tests and relaxation tests using different rates are performed. Both the basic elastic and the viscoelastic properties are examined and identified. The particular difficulty of this material is the porosity leading to a structural compressibilty. Hence, a two-phase model is used to represent the experimental data. A compressible material model is developed for the basic elasticity taking into account the structural compressibility. Furthermore the viscoelastic part of the model is obtained. In this context other effects typically observed for rubber materials occure, such as the mullins effect. Another aspect is the high non-linearity with respect to the feedrate. For different feedrates nearly the same stresses and the same hysteresis loops are obtained. To quantify this behaviour a nonlinear viscosity function is established.

2 EXPERIMENTS

2.1 *Samples and measurements*

The experiments are performed using two specimens of different geometries. Both dogbone specimens according to ISO 527, cut from a car door gasket, and cylindrical specimens with a diameter of 9 mm and a length of 110 mm are used.

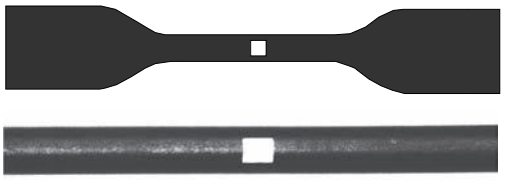

Figure 1. Two geometries of specimens with a silk-screen mark.

To control the deformation, the specimens are marked with silkscreen color as shown in figure 1. Because of the compressibility of the material, the length and width of the mark is recorded by video extensiometry during the deformation. At this connection the stretches λ_1 and λ_2 in tension direction and in transversal direction respectivly can be calculated by

$$\lambda_1 = \frac{l}{l_0}, \quad \lambda_2 = \frac{b}{b_0}, \tag{1}$$

where l, b are the length and width of the mark in the deformed state and l_0, b_0 are the corresponding quantities of the mark in the undeformed state. The material is assumed to be isotropic ($\lambda_2 = \lambda_3$). Hence, the increase of volume during the uniaxial tension test can be calculated by the determinant of the deformation gradient

$$\det \mathbf{F} = \lambda_1 \lambda_2 \lambda_3 = \lambda_1 \lambda_2^2. \tag{2}$$

2.2 *Experiments and analysis*

The following tension tests are performed:

- Preconditioning of the samples by cyclic tests
- Cyclic tests around a medial strain
- Tests at different feedrates to determine the viscoelastic behaviour
- Relaxation tests

The investigated black carbon-filled rubber shows a mullins effect in the first cycle that can be explained with the breakage of some network junction points. Due to this damage process the stress in the second cycle is below the one in the first cycle. Therefore, each specimen has to be preconditioned, which means that the specimen is loaded and unloaded seven times with the highest feedrate of 0.273 s^{-1} until the maximum of deformation (100%). Hence, it can be excluded that the mullins effect influences the behaviour of the material during the test.

Afterwards, the basic elasticity can be examined. In a quasi-static process with a feedrate of 0.000273 s^{-1} the cellular rubber still shows a hysteresis in the stress-strain diagram. Thus, the basic elasticity cannot be investigated with this process. Another possiblity to obtain the basic elastic properties are relaxation tests. Unfortunately relaxation tests cannot be applied for the examined material, because of the long relaxation time. Finally a successful method to obtain the basic elasticity are cyclic tests around a medial strain. In these tests the examined deformation is predetermined and cyclic tests around this deformation are performed as

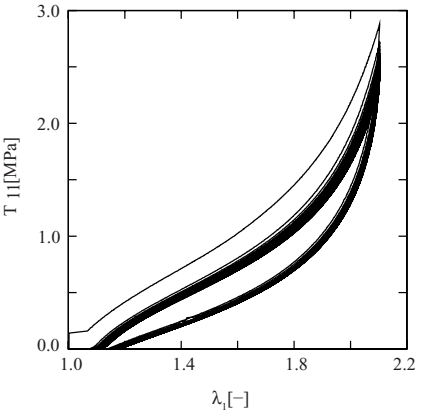

Figure 2. Cyclic tests to get the basic elasticity.

can be seen in figure 2. The maximum peak of the obtained hysteresis in the stress-strain curve begins to fall down to a stationary curve. In figure 2 the first 50 cycles are shown. The stress value in the midpoint of the hysteresis of the medial strain, i.e. a strain of 60% in the example, represents the basic elasticity. By this method, the basic elasticity can be obtained easier and faster than by the other methods. The basic elasticity is recorded for the dogbone and the cylindrical specimens respectivly by the third method and the results are shown in figure 3. The curve of basic elasticity is nearly the same for both geometries. So it can be assumed that the basic elasticity is independent from the geometrical shape of the specimen. For that reason, only the dogbone specimens are investigated. During the basic elasticity tests the behaviour of different feedrates is examined, too. It is found that there is no difference between the both geometries with respect to the visoelastic behaviour. So only the dogbone specimens are used for the following tests. To get more information on the viscoelastic behaviour the stress-strain curve is recorded using three different feedrates in the range from 0.273 s^{-1} to 0.00273 s^{-1} during the first 5 cycles. Figure 4 shows results for the fastest feedrate of 0.273 s^{-1}, figure 5 the medial one and figure 6 the slowest one. It is important to mention that both the degree of the hysteresis and the maximum stress value do not change a lot with respect to the feedrate. Hence, the nonlinearity in time has to be taken into account in the model. The fast softening during the first cycle and the slower softening in the following ones has to be noticed, too.

Finally a relaxation test at a deformation of 60% is performed, figure 7. After a relaxation time of 1800s the obtained stress value is around 10% bigger than the measured basic elasticity.

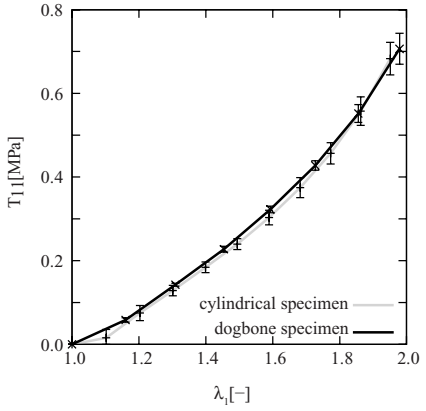

Figure 3. Basic elasticity of cellular rubber for different geometries.

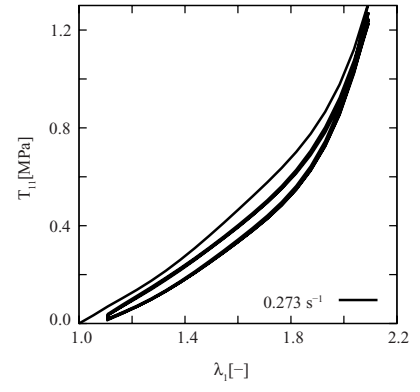

Figure 4. Viscoelastic behaviour at a constant rate of 0.273 s^{-1}.

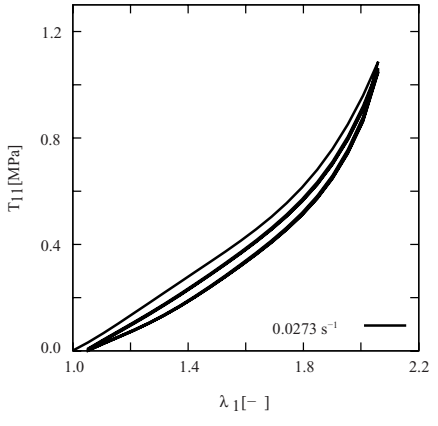

Figure 5. Viscoelastic behaviour at a constant rate of 0.0273 s^{-1}.

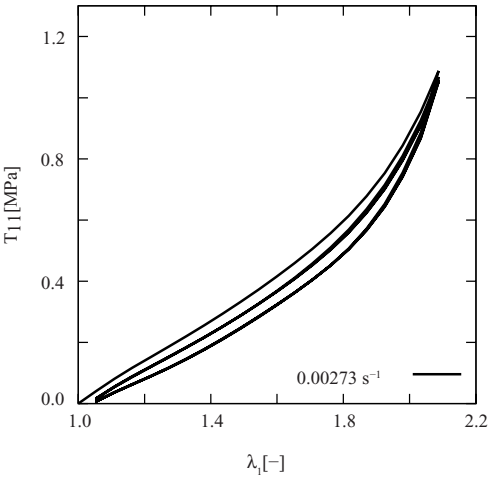

Figure 6. Viscoelastic behaviour at a constant rate of 0.00273 s^{-1}.

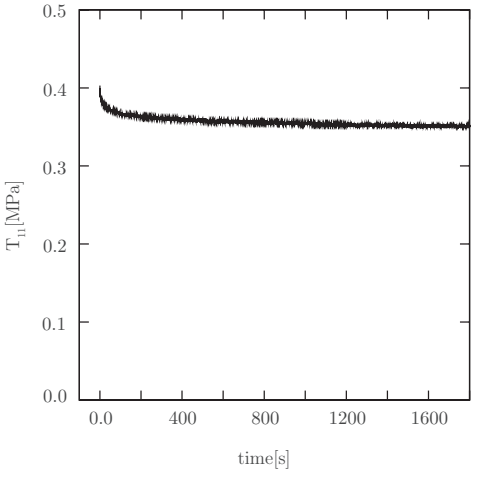

Figure 7. Relaxation tests at a deformation of 60%.

3 MODELLING ASPECTS AND PARAMETER IDENTIFICATION

3.1 *Theoretical modeling*

In this section a phenomenological continuum mechanical model is presented, which is able to adequatly reflect the results observed in the experiments by means of a finite viscoelastic material description including a point of compaction. The required basic theory will be derived and documented, whereby isothermal conditions are assumed and long-range effects are neglected. At this the standard viscoelastic rheological model is used, where a

single spring is connected in parallel to a series of spring-dashpot-elements (Maxwell elements).

The implementation of the finite viscoelasticity is realised on the concept of deformation-valued internal variables, e.g. (Lion 1996; Sedlan 2001; Reese 2001) and others.

In the theory of finite viscoelasticity a multiplicative split of the deformation gradient tensor $\mathbf{F}$ into an elastic part $\mathbf{F}_e$ and an inelastic part $\mathbf{F}_i$ is introduced. In this connection a fictitious intermediate configuration with its own deformation, stress and strain tensors is used. In order to account for the influence of the pore gas the theory of porous media, (Bowen 1980; Bowen 1982; de Boer 2000), is applied, a so-called hybride model, (Ehlers 1993; Diebels 1999).

Additionaly the constitutive equations have to be discussed in a thermodynamically consistent frame. Therefore the Clausius-Planck inequality is recalled. For its derivation, the specific free Helmholtz energy Ψ^S for the solid phase and Ψ^G for the gas phase are introduced. To evaluate the entropy balance, the process variables

$$S = \left\{ \rho^{GR}, \mathbf{B}_S, \mathbf{B}_S^{je} \right\} \tag{3}$$

are choosen where ρ^{GR} stands for the effective gas density, the left Cauchy-Green deformation tensor $\mathbf{B}_S = \mathbf{F}_S \cdot \mathbf{F}_S^T$ and the left Cauchy-Green deformation tensors $\mathbf{B}_S = \mathbf{F}_S^{je} \cdot \mathbf{F}_S^{jeT}$, which describe the Newton elements in the Maxwell elements. The evaluation of the entropy principle, (Coleman and Noll 1963), yields the following form for the Cauchy stress

$$\begin{aligned} \mathbf{T} = &-np^{GR}\mathbf{I} + 2\mathbf{B}_{S\rho^S} \frac{\partial \Psi_{eq}^S}{\partial \mathbf{B}_S} \\ &+ \sum\nolimits_{j=1}^{n} 2\mathbf{B}_{se}^j \rho^S \frac{\partial \Psi_{neq}^S}{\partial \mathbf{B}_{Se}^j}, \end{aligned} \tag{4}$$

with the partial density of the solid ρ^S, the partial density of the gas ρ^G and porosity n. This expression results from the assumption of an inphase motion of the gas and solid phase, i.e. from the assumption that the pores are closed. The pressure term p^{GR} is obtained from the ideal gas law

$$p^{GR} = p_0 \left(\frac{1 - J^S}{J^S - n_0^S} \right), \tag{5}$$

with the Jacobian J^S and the ambient pressure p_0. The basic elasticity is represented by a Yeoh type approach, (Yeoh and Flemming 1997). This law is extended by a volumetrical term which describes the point of compaction, (Ehlers and Eipper 1999). Perhaps a further modification of this term is needed, if the data pool contains results of compression tests. Finally the stress response for the basic elasticity is calculated by

$$\begin{aligned} \mathbf{T}_{eq} = 2J^{-S} \Big[&(c_{10} + c_{20}(\mathrm{I}_{\mathbf{B}_S} - 3) \\ &+ c_{30}(\mathrm{I}_{\mathbf{B}_S}^2 - 9))\mathbf{B}_S - c_{10}\mathbf{I} \\ &- \lambda^S (1 - n_0^S)^2 \left(\frac{J^S}{1 - n_0^S} - \frac{J^S}{J^S - n_0^S} \right) \mathbf{I} \Big]. \end{aligned} \tag{6}$$

Moreover the polynomial ansatz of the Yeoh model is modified to be monotonously. In the case of viscoelastic behaviour a set of Maxwell elements with appropriate evolution equations for the internal variables are established. For the Maxwell elements different models are used. The non-equilibrium stress based on the Neo-Hooke model leads to

$$\mathbf{T}_{neq}^j = 2J^{-S} \left[c_{10}^j \mathbf{B}_{Se}^j - c_{10}^j \mathbf{I} \right] \tag{7}$$

and the modified Yeoh model to

$$\begin{aligned} \mathbf{T}_{neq}^j = 2J^{-S} \Big[&c_{10}^j + c_{20}^j (\mathrm{I}_{\mathbf{B}_{Se}^j} - 3) \\ &+ c_{30}^j (\mathrm{I}_{\mathbf{B}_{Se}^j}^2 - 9) \Big] \mathbf{B}_{Se}^j - 2J^{-S} c_{10}^j \mathbf{I}. \end{aligned} \tag{8}$$

Furthermore the non-linear viscosity is presented by

$$\eta = \eta_0 + \eta_1 k_1^{-\|\mathbf{D}\|} + \eta_2 \exp(-k_2 \|\mathbf{D}\|) \tag{9}$$

with the deformation velocity $\mathbf{D}$ and the parameters η_0, η_1, η_2, k_1 and k_2.

After all, the evolution equations in the deviatoric form result from the dissipation inequality, (Sedlan 2001; Lion 2000). In the case of the Neo-Hookean model the evolution equation is represented by

$$\begin{aligned} \dot{\mathbf{C}}_i^j = \frac{4}{\eta} \Big[&c_{10}^j \mathbf{C} - c_{10}^j \mathbf{C}_i \\ &- \tfrac{1}{3} tr(c_{10}^j \mathbf{C} \cdot \mathbf{C}_i^{j-1} - c_{10}^j \mathbf{I}) \mathbf{C}_i^j \Big] \end{aligned} \tag{10}$$

and for the modified Yeoh model by

$$\begin{aligned} \dot{\mathbf{C}}_i^j = \frac{4}{\eta} \Big[&(c_{10}^j + c_{20}^j (\mathrm{I}_{\mathbf{B}_{Se}^j} - 3) + c_{30}^j (\mathrm{I}_{\mathbf{B}_{Se}^j}^2 - 9)) \mathbf{C} \\ &- c_{10}^j \mathbf{C}_i - \frac{1}{3} \mathrm{tr}((c_{10}^j + c_{20}^j (\mathrm{I}_{\mathbf{B}_{Se}^j} - 3) \\ &+ c_{30}^j (\mathrm{I}_{\mathbf{B}_{Se}^j}^2 - 9)) \mathbf{C} \cdot \mathbf{C}_i^{j-1} - c_{10}^j \mathbf{I}) \mathbf{C}_i^j \Big]. \end{aligned} \tag{11}$$

3.2 *Identification of parameters and simulations*

Based on the obtained data pool the parameters of the presented model have to be determined by a parameter identification. Therefore, the parameters of the basic elasticity are determined. Moreover the viscoelastic parameters are constituted. Three Maxwell elements proved to be sufficient to represent the viscoelastic behaviour of the dogbone specimens in the examined range of feedrates. The first Maxwell element is based on the Neo-Hookean model, the second one on the modified Yeoh model and the third one also on the modified Yeoh model, but using only the last parameter c_{30}^{j}. In this connection the nonlinear viscosity function is only used in the first and third Maxwell element. The second one is responsible for the shape of the curve and the slow decrease of the peak stress in successive cycles.

Figure 8 shows a very good match between the experimental data at feedrate 0.0273 s^{-1} and the numerical simulation. In figure 9 the data of the fastest feedrate is presented. In this case, a good match between the experimental and numerical data is found. There are only small differences at large deformations $\lambda_1 \geq 1.9$. For the smallest feedrate, figure 10, the hysteresis is a bit too small and the characteristic softening after the first cycle cannot be seen. After the cyclic test a relaxation test is simulated to validate the results of the parameter identification. At the beginning of the relaxation there occure some differences between the experimental and the numerical results. After some seconds, the curves converged until the end of experiment. At this point the basic elasticity is not reached as can be seen in logscale, the value is around 10% above the measured basic elasticity, figure. 11.

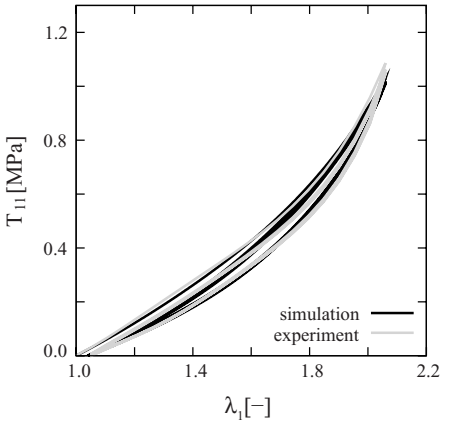

Figure 8. Comparison between experimental and numerical data for a rate of 0.0273 s^{-1}.

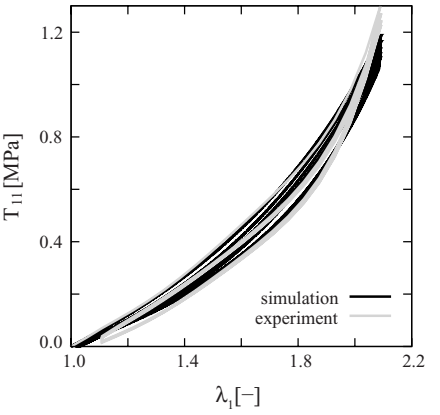

Figure 9. Comparison between experimental and numerical data for a rate of 0.273 s^{-1}.

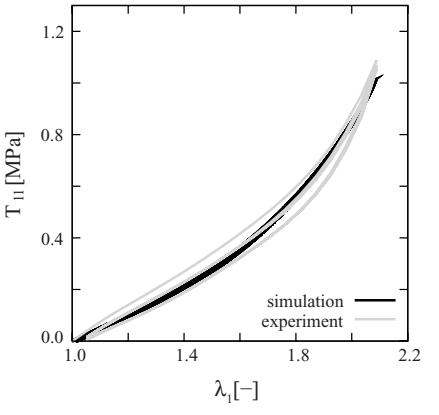

Figure 10. Comparison between experimental and numerical data for a rate of 0.00273 s^{-1}.

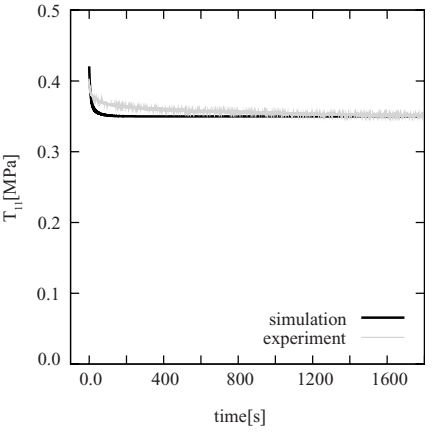

Figure 11. Comparison between experimental and numerical data for a relaxation test.

4 CONCLUSIONS AND OUTLOOK

This study gives an overview of mechanical properties of cellular rubber. Some experiments inform of cyclic tests and relaxation tests are performed. Also a material model based on the theory of porous media is presented. To represent the non linearity with respect to the feedrate a viscosity function is introduced depending on the rate of deformation. The results of cyclic tests show a satisfying agreement with the numerical simulations. The differences between experimental and numerical data are small but they have to be decreased by improving the nonlinear viscosity function. The relaxation test for the used feedrate represents the experimental results very well.

In the further work the material model has to be expanded based on the results of triaxial compression tests. Simulation of real assemblies will also be performed. Taking into account real applications thermical effects should be investigated, too.

REFERENCES

Bowen, R.M. (1980). Incompressible porous media models by use of the theory of mixtures. *Int. J. Engng. Sci. 18*, 1129–1148.

Bowen, R.M. (1982). Compressible porous media models by use of the theory of mixtures. *Int. J. Engng. Sci. 20*, 697–735.

Coleman, B.D. and W. Noll (1963). The thermodynamics of elastic materials with heat conduction and viscosity. *Arch. Rat. Mech. Anal. 13*, 167–178.

de Boer, R. (2000). *Theory of porous media*. Springer-Verlag, Berlin.

Diebels, S. (1999). A micropolar theory of porous media: Constitutive modelling. *Transport Porous Med. 34*, 193–208.

Ehlers, W. (1993). Constitutive equations for granular materials in geomechanical context. In K. Hutter (Ed.), *Continuum mechanics in environmental sciences*, Volume 337 of *CISM International centre for Mechanical Sceinces*, pp. 313–402. Springer-Verlag, Berlin.

Ehlers, W. and G. Eipper (1999). Finite elastic deformations in liquid-saturated and empty porous solids. *Transport Porous Med. 34*, 179–191.

Lion, A. (1996). A constitutive model for carbon black filled rubber, experimental results and mathematical representation. *Continuum Mech. Thermodyn. 8*, 153–169.

Lion, A. (2000). *Thermomechanik von Elastomeren*. Berichte des Instituts für Mechanik der Universität Kassel (Bericht 1/2000).

Reese, S. (2001). *Thermomechanische Modellierung gummiartiger Polymerstrukturen.* Habilitation, Bericht-Nr. F01/4 des Instituts für Baumechanik und Numerische Mechanik, Universität Hannover.

Sedlan, K. (2001). *Viskoelastisches Materialverhalten von Elastomerwerkstoffen, Experimentelle Untersuchung und Modellbildung*. Dissertation, Berichte des Instituts für Mechanik (2/2001), Universität Gesamthochschule Kassel.

Vroomen, G., G. Choonoo, T. Odenhamn, and M. Hatta (2004). EPDM-Moosgummi für die Tür- und Fensterdichtungen von Kraftfahrzeugen. *GAK 3(57)*, 163–176.

Yeoh, O.H. and P.D. Flemming (1997). A new attempt to reconcile the statistical and phenomenological theories of rubber elasticity. *J. Polym. Sci. Part B: Polym. Phys. 35*, 1919–1931.

Constitutive Models for Rubber VI – Heinrich et al. (eds)

A micro-sphere model for rubbery polymers with continuously evolving chain—ODF

Christian Miehe
Institute of Applied Mechanics, University of Stuttgart, Pfaffenwaldring, Germany

ABSTRACT: We outline a micromechanically-based two-scale model for a predictive modeling of finite elasticity, viscoelasticity and damage in rubbery polymers and discuss details of its numerical implementation. The proposed constitutive formulation treats rubbery polymers based on a micro-structure that may be visualized by a micro-sphere. The surface $SO(2)$ of the micro-sphere represents a continuous *orientation continuum* of polymer chains. The key idea of the earlier developed micro-sphere model in rubber elasticity [1] was the combination of (i) micro-mechanism-based constitutive models for the single chain response with (ii) the definition of the macroscopic stress response of the polymer network by a directly evaluated homogenization over the chain orientation space. The setting up of the constitutive models for a single chain of the polymer is performed in an attractive modular format, accounting for non-affine elastic equilibrium response, viscous overstress effects and Mullins-type damage mechanisms. In this work, we modify the micro-sphere model originally proposed in [1, 2, 3] by an additional evolution equation for the *chain orientation distribution function* (codf) defined on the microsphere $SO(2)$. We then define homogenization procedures on $SO(2)$ that exploit the presence of the codf. We outline the continuous formulation of the two-scale model and develop details of its algorithmic implementation. The results obtained by the the proposed *modified micro-sphere model* is compared with the original formulation. The excellent performance and predictive quality of the formulation is demonstrated by means of a representative numerical examples that cover simulations of characteristic experimental results.

REFERENCES

[1] Miehe, C.; Göktepe, S.; Lulei, F. [2004] "A Micro-Macro Approach to Rubber-Like Materials. Part I: The Non-Affine Micro-Sphere Model of Rubber Elasticity", *Journal of the Mechanics and Physics of Solids*, Vol. 52, 2617–2660.

[2] Miehe, C.; Göktepe, S. [2005] "A Micro-Macro Approach to Rubber-Like Materials. Part II: The Micro-Sphere Model of Finite Rubber Viscoelasticity", *Journal of the Mechanics and Physics of Solids*, Vol. 53, 2231–2258.

[3] Göktepe, S.; Miehe, C. [2005] "A Micro-Macro Approach to Rubber-Like Materials. Part III: The Micro-Sphere Model of Anisotropic Mullins-Type Damage". *Journal of the Mechanics and Physics of Solids*, Vol. 53, 2259–2283.

Constitutive Models for Rubber VI – Heinrich et al. (eds)
© 2010 Taylor & Francis Group, London, ISBN 978-0-415-56327-7

Algorithm of constant definition for a visco-elastic rubber model based on cyclic experiments, stress relaxation and creep data

A.G. Pelevin, B. Lauke & G. Heinrich
Leibniz-Institut fur Polymerforschung Dresden e.V., Dresden, Germany

A.L. Svistkov & A.A. Adamov
Institute of continuous media mechanics UB RAS, Perm, Russia

ABSTRACT: A model for simulation of rubber behavior is presented. The equation system is constructed using the scheme illustrating the mechanical behavior of rubbers. The scheme points are connected by elastic, viscous, plastic and transmission elements. To describe the properties of each element, the known equations of the nonlinear theory of elasticity, the theory of nonlinear viscous fluids and the theory of plastic flow under finite deformations are used. A step by step algorithm is proposed to derive the constants of the model. It is shown that the constants of constitutive equations found at earlier steps remain unchanged at subsequent steps. Research experiments (cyclic loading tests including relaxation and creep) provide much useful information concerning the viscoelastic properties of rubbers.

1 INTRODUCTION

1.1 *Model of mechanical behavior of rubbers*

The mechanical behavior of rubbers is described by the model schematically represented in Fig. 1, where each point corresponds to a particular set of constitutive equations. The scheme shows how the tensor nonlinear equations are combined into the system of equations describing the complex viscoelastic behavior of an arbitrarily deformed medium. The algorithm that constructs constitutive equations from separate groups of equations (elastic, viscous, plastic, transmission) is described in detail in this work. The present model uses the approach that is based on the additive decomposition of the strain rate tensor of the medium into the strain rate tensors of the scheme elements. The internal scheme points are required to meet the condition of correlation of Cauchy stress tensors. The scheme for the mechanical behavior of the material has transmission, elastic, viscous and plastic elements, which correspond to the following equations given below.

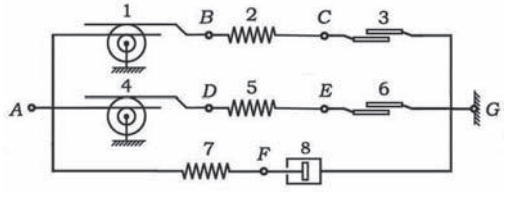

Figure 1. Model for the mechanical behavior of rubber.

2 CONCEPTUAL MODEL

The material under study is assumed to be incompressible. The deviator of the Cauchy stress tensor $\mathbf{T}_i$ of elastic element i is computed using the ordinary formulas of the nonlinear theory of elasticity:

$$\operatorname{dev}\mathbf{T}_i = \operatorname{dev}\left(\rho\sum_{k=1}^{3}\lambda_k^{(i)}\frac{\partial f}{\partial\lambda_k^{(i)}}\mathbf{n}_k^{(i)}\otimes\mathbf{n}_k^{(i)}\right),$$

in which the mass density of the medium free energy f depends on the extension ratio of elastic elements.

$$f = f(\ldots,\lambda_i^{(k)},\ldots),$$

where $k = 1, 2, 3$; $i = 2, 5, 7$; ρ is the mass density of the medium, $\lambda_1^{(i)},\lambda_2^{(i)},\lambda_3^{(i)}$ and $\mathbf{n}_1^{(i)},\mathbf{n}_2^{(i)},\mathbf{n}_3^{(i)}$ are the extension ratios and eigenvectors of the stretch tensor $\mathbf{V}_i$ of the i-th elastic element. Time

variations in the tensor $\mathbf{V}_i$ are calculated by the evolution equation:

$$\frac{2}{\nu_i}\mathbf{Y}_i^{0.5}\mathbf{D}_i\mathbf{Y}_i^{0.5} = \dot{\mathbf{Y}}_i - \mathbf{Y}_i\mathbf{W}_\mathbf{R}^{\mathrm{T}} - \mathbf{W}_\mathbf{R}\mathbf{Y}_i,$$

where $\mathbf{W}_\mathbf{R} = \dot{\mathbf{R}}\mathbf{R}^{\mathrm{T}}$. The formula uses the following notations:

$$\mathbf{Y}_i = \mathbf{V}_i^{\frac{2}{\nu_m}}, \quad \nu_m > 0,$$

where $\mathbf{R}$ is the rotation tensor in the polar decomposition $\mathbf{F} = \mathbf{VR}$ of the strain gradient of the medium $\mathbf{F}$ into the left stretch tensor $\mathbf{V}$ and the rotation $\mathbf{R}$, and ν_m is the ratio of the m-th transmission element, connected on the left to the elastic element under consideration. The rate of work done in the i-th elastic element is determined by the formula:

$$\mathbf{T}_i \cdot \mathbf{D}_i = \rho\sum_{k=1}^{3}\frac{\partial f}{\partial\lambda_k^{(i)}}\dot{\lambda}_k^{(i)} - \frac{\rho\dot{\nu}_m}{\nu_m}\sum_{k=1}^{3}\frac{\partial f}{\partial\lambda_k^{(i)}}\lambda_k^{(i)}\ln(\lambda_k^{(i)}).$$

The rubber used for investigation is a nanocomposite consisting of an elastomeric binder and black carbon aggregated nanoparticles. The structural deformation of the elastomeric binder fraction and the macroscopic deformation of the rubber differ significantly. The difference is taken into account by transmission elements. Application of these elements increases the strain rate tensor at the right point of the transmission element by a factor of ν_m in comparison with the corresponding tensor at the left point and simultaneously decreases the Cauchy stress tensors:

$$\mathbf{D}_m^{\text{left}} = \frac{1}{\nu_m}\mathbf{D}_m^{\text{right}}, \quad \mathbf{T}_m^{\text{left}} = \nu_k\mathbf{T}_m^{\text{right}}.$$

The deviator of the Cauchy stress tensor $\mathbf{T}_j$ of the j-th viscous element is calculated by the equations of the theory of nonlinear viscous fluid using the appropriate strain rate tensor $\mathbf{D}_j$

$$\operatorname{dev}\mathbf{T}_j = 2\eta_j\mathbf{D}_j,$$

For the n-th plastic element, the Cauchy stress tensor deviator is defined by the equations of the theory of plastic flow

$$\mathbf{D}_n = \sqrt{\frac{\mathbf{D}_n\cdot\mathbf{D}_n}{\operatorname{dev}\mathbf{T}_n\cdot\operatorname{dev}\mathbf{T}_n}}\operatorname{dev}\mathbf{T}_n,$$

To complete the system of equations, the proportional relation between the strain rate tensor of the plastic element $\mathbf{D}_n$ and that of the material $\mathbf{D}$ is used.

$$\sqrt{\mathbf{D}_n\cdot\mathbf{D}_n} = \kappa_n\sqrt{\mathbf{D}\cdot\mathbf{D}},$$

where the term κ_n is the nonnegative function prescribed by the relation

$$\kappa_n = \begin{cases}0, & \Phi_n(\mathbf{V},\ldots) < g_n,\\ \zeta_n(g_n), & \Phi_n(\mathbf{V},\ldots) = g_n.\end{cases}$$

The flow function Φ_n that is used to formulate the criterion for the development of plastic deformations in the medium is the function of the stretch tensor $\mathbf{V}$ and other state parameters of the medium. The plastic deformation of the medium takes place only in the case when the flow function Φ_n reaches its maximum value over the entire history of the medium development.

$g_n = \max\Phi_n$.

The material entropy s and the heat flux $\mathbf{h}$ are found using the formulas of nonequilibrium thermodynamics

$$s = -\frac{\partial f}{\partial\theta}, \quad \mathbf{h} = -c_\mathbf{h}\operatorname{grad}\theta,$$

where $c_\mathbf{h} > 0$ is the thermal conductivity.

3 ANALYSIS

Step-by-step technique for determining constants for the model of the mechanical behavior of rubber In order to determine constants for the model, five specimens were tested under cyclic loading conditions. In the first cycle, the specimen was stretched with constant velocity $\dot{\lambda} = 1/60^{-1}$. After that, over the period of 60 minutes one observed the stress relaxation process at a fixed deformation of the medium. Further, the material was unloaded at constant strain rate $\dot{\lambda} = -1/60^{-1}$, and the creep of the material was observed for 30 minutes. Then, other cycles of deformation were started, which differed from the fist cycle by the fact that the stress relaxation was observed for 30 minutes instead of 60 minutes, and the maximum extension ratio was lower than that obtained in the first cycle. Table 1 summarizes extension ratios for each specimen and cycle.

Such experiments provide a great deal of information concerning the mechanical properties of the material. Testing of one specimen during one run gives the data for material softening in the first cycle of deformation (Mullins effect), viscoelastic properties, relaxation and creep processes.

Table 1.

	Specimen				
Cycle	1	2	3	4	5
1	1.5	1.75	2	2.25	2.5
2	1.25	1.25	1.25	1.75	1.25
3	1.5	1.5	1.5	1.75	1.5
4	_	1.75	1.75	1.75	1.75
5	_	_	2	2	2
6	_	_	_	2.25	2.25
7	_	_	_	_	2.5

The constants of the model can be defined in a step-by-step manner based on the data acquired at the previous steps.

$$w = w_2 = c_1^{(2)}\left(\sum_{i=1}^{3}(\lambda_i^{(2)})^2 - 3\right) + c_2^{(2)}\left(\sum_{i=1}^{3}\left(\frac{1}{\lambda_i^{(2)}}\right)^2 - 3\right).$$

FIRST STEP. Consider a simple situation assuming that the volume density of the material free density $w = \rho f$ is the function of extension ratios of the second element only:

$$w = w_2 = c_1^{(2)}\left(\sum_{i=1}^{3}(\lambda_i^{(2)})^2 - 3\right) + c_2^{(2)}\left(\sum_{i=1}^{3}\left(\frac{1}{\lambda_i^{(2)}}\right)^2 - 3\right).$$

This indicates that all elements (between the forth and tenth elements) have no effect on the mechanical behavior of the material. Plastic deformations are accumulated solely in the first cycle of deformation, while in subsequent cycles the material demonstrates elastic behavior. Let us shift the experimental data so that all cycles, excluding the first, leave the origin of coordinates (Fig. 2). Based on the experimental data thus modified, the elastic properties of the second element are defined.

Now we seek the constants $c_1^{(2)}$, $c_2^{(2)}$ of the elastic element and the values of the ratio ν_1 of the first transmission element. The ratio ν_1 is assumed to have its own value for each specimen, while the constants $c_1^{(2)}$, $c_2^{(2)}$ are general for all specimens. The relaxation processes are finished completely. To determine the constants, only the points (equilibrium points) on the experimental curves obtained after the completion of relaxation processes are used. The theoretical curve goes through these points. We consider the points with extension ratios (thick points in Fig. 2) less than the maximum ratio observed in the first cycle of deformation. The case when the theoretical curve passes through other points will be discussed later.

The values of the above quantities are found in the following manner. For the third specimen,

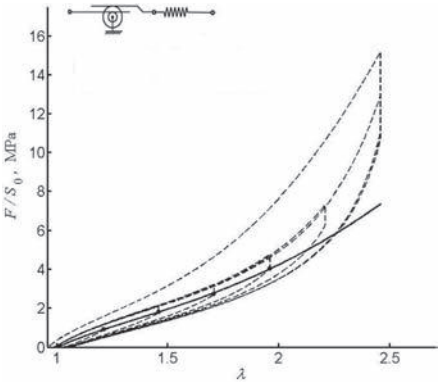

Figure 2. Experimental results obtained by testing the fifth specimen (with shift along the axis λ), and theoretical curve plotted at the first step of determination of constants.

we calculate the values of variables $c_1^{(2)}$, $c_2^{(2)}$ and ν_1 and, for other specimens, only the values of variables ν_1. The values of constants $c_1^{(2)}$ and $c_2^{(2)}$ are used to describe the properties of the elastic element. The third specimen is taken as a basic object for determination of the elastic properties of the medium because it occupies an intermediate position as to the level of maximum deformations. Thus, one may expect to obtain some average values. The model used at the first step and the theoretical curve for the fifth specimen obtained with this model are shown in Fig. 2.

SECOND STEP. Based on the values of the ratio of the first transmission element ν_1 obtained for different specimens, the parameter ν_1 is represented as the function of maximum deformations over the entire strain history of the medium.

$$\nu_1 = \nu_1^{(1)} \exp(-\nu_2^{(1)} \max \mathrm{I_V}), \qquad (1)$$

where the invariant $\mathrm{I_V}$ is obtained by the formula

$$\mathrm{I_V} = \sqrt{3\mathrm{tr}(\mathbf{V}^2) - \mathrm{tr}(\mathbf{V})^2}.$$

Let us now find the other two constants of the model: $\nu_1^{(1)}$ and $\nu_2^{(1)}$. We assume that the first elastic element simulates the relation between the structural stresses in the active part of the binder in the elastomeric nanocomposite and the macroscopic stresses of the material. Clearly, it depends on the fragmentation of aggregates into pieces after the rubber has been stretched. In the model, this process is taken into account by decreasing the ratio of the first transmission element and determined by equation (1).

THIRD STEP. We suggest that the model allows us to take account of irreversible deformation

accumulation. To this end, the scheme is complicated through introducing the third plastic element in it. The properties of this element are defined by the choice of the function $\zeta_3(g_3)$ and $\Phi_3(\mathbf{T})$. Unlike the previous steps, we find it using the real (not shifted) curves of the dependence of the stretching force on the extension ratio of the specimens (Fig. 3).

$$\zeta_3(g_3) = \kappa_0^{(3)} + \kappa_1^{(3)} \exp(\kappa_2^{(3)} g_3),$$

$$\Phi_3 = \sqrt{\text{dev } \mathbf{T} \cdot \text{dev } \mathbf{T}},$$

where $\mathbf{T}$ is the Cauchy stress tensor of the material. Let us now define the values of the constants $\kappa_1^{(3)}$, $\kappa_1^{(3)}$ and $\kappa_2^{(3)}$ so that the model describe accurately the values of the residual extension ratios (after stopping the creep process) for all examined specimens.

FOURTH STEP. To construct the mathematical model of the mechanical behavior of rubbers, the hypothesis for the formation of high-strength fibers in the deformed material is used. The fibers consisting of oriented polymer are formed when the polymeric chains slip off the interface layers of filler particles into the gaps between particle aggregates. We suggest that the fibers appear in the material due to the plastic flow caused by its stretching, and they maintain their elastic properties at any stretch value less than the maximum one. At this step, the elastic properties of the fibers formed in the first cycle of loading are described by elements 4 and 5 (Fig. 1). The properties of plastic element 6 simulating fiber formation are described at step 5. The medium free energy potential is written as a sum $w = w_2 + w_5$, in which

$$w_5 = \begin{cases} 0, & \text{if } \xi_5 < 0, \\ c_5 \xi_5, & \text{if } \xi_5 \geq 0. \end{cases}$$

and

$$\xi_5 = (\lambda_1^{(5)} - 1)(\lambda_2^{(5)} - 1)(\lambda_3^{(5)} - 1).$$

To define the constant c_5 of the fifth elastic element and the ratio ν_4 of the fourth transmission element, all the points on the experimental curve obtained after completion of the relaxation process are used.

FIFTH STEP. At this step, the model takes into account the sixth plastic element that describes fiber formation caused by the motion of polymer chains from the layers into the gaps between inclusions. The properties of this element defined by the choice of the function $\zeta_6(g_6)$ and $\Phi_6(\mathbf{T})$ are found by examining the experimental data points

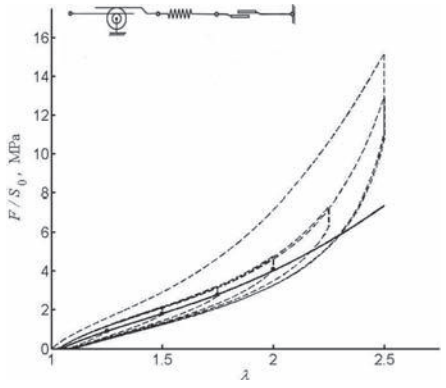

Figure 3. Experimental data obtained by testing the fifth specimen, and theoretical curve plotted at the third step in determining constants.

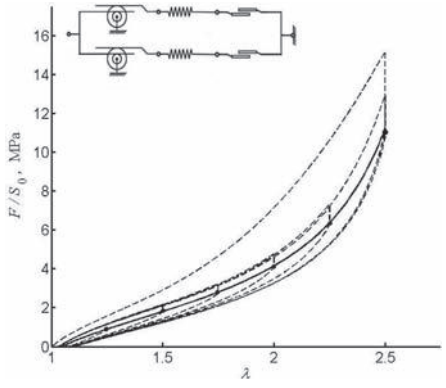

Figure 4. Experimental data obtained by testing the fifth specimen, and theoretical curve plotted at the fourth step of determining constants.

corresponding to the moments of completion of the relaxation process in the first cycles of deformation of all specimens (Fig. 5).

$$\zeta_6(g_6) = \kappa_0^{(6)} + \kappa_1^{(6)} \exp(\kappa_2^{(6)} g_6),$$

$$\Phi_6 = \sqrt{\text{dev } \mathbf{T} \cdot \text{dev } \mathbf{T}},$$

where $\mathbf{T}$ is the Cauchy stress tensor defining stresses in the material. Let us select the values of constants $\kappa_0^{(6)}$, $\kappa_1^{(6)}$ and $\kappa_2^{(6)}$ so that the calculation curve for first-cycle loading passes through the chosen points.

SIXTH STEP. Let introduce in the model elements describing the viscoelastic behavior of the material. This procedure can be realized in two ways, of which one suggests insertion of several Maxwell elements with simple dependences for viscosity coefficients, and the other by insertion of only one

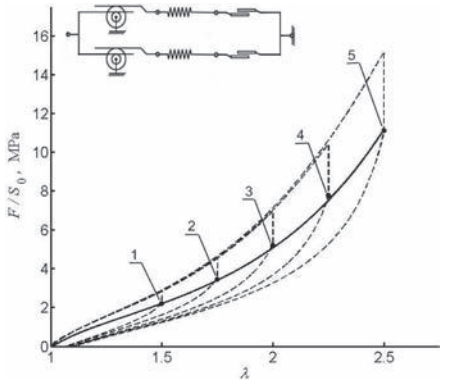

Figure 5. Experimental results for the first cycles of deformation of the specimen. The dot-and-dash curve refers to the first specimen, the dot curve to the third specimen, and the dash curve to the fifth specimen. The solid curve shows theoretical data determined for material stretching with consideration of increasing plastic deformations.

of these elements with non-linear expression for viscosity coefficient. We have chosen the second variant and used the seventh elastic and eighth viscous element to describe the peculiarities of the material behavior (Fig. 1). The medium free energy potential is written as a sum $w = w_2 + w_5 + w_7$, in which

$$w_7 = c_1^{(7)}\left(\sum_{i=1}^{3}(\lambda_i^{(7)})^2 - 3\right).$$

The viscous element properties are determined by the following shear viscosity function:

$$\eta_8 = \eta_0^{(8)} \exp\left(\eta_1^{(8)}\mathbf{I}_V\right).$$

The constants $c_1^{(7)}, \eta_0^{(8)}\ \eta_1^{(8)}$ chosen such that the theoretical curve coincides with the experimental data at the stretched parts of the material obtained in all cycles of deformation, excluding the first cycle.

SEVENTH STEP. The mathematical expression for the viscosity function η_8 is complicated to get an adequate description of the experimental results collected both during the stretch of the material and during the removal of external loads. For this purpose, one more term is added to the mathematical expression η_8.

The constants $\eta_2^{(8)}, \eta_3^{(8)}$ and $\eta_4^{(8)}$ are chosen such that the theoretical curves coincide with the experimental curves both when stretching the specimen and on its unloading in all cycles of deformation, excluding the first cycle.

$$\eta_8 = \eta_0^{(8)} \exp\left(\eta_1^{(8)}\mathbf{I}_V\right) + \eta_2^{(8)}\left(\exp\left(-\eta_3^{(8)}\mathbf{V}\cdot\mathbf{D}\right) + \exp\left(-\eta_4^{(8)}\mathbf{V}\cdot\mathbf{D}\right)\right)$$

EIGHTH STEP. During the two previous steps, fast processes have been modeled. Now, it is necessary to verify theoretical calculations, which allows us to describe accurately stress relaxation processes. To this end, the numerical value of viscosity in the process of relaxation must be essentially larger than the viscosity of the material underwent loading and unloading cycles. Consider this process in detail. First, let us forget for some time the expression found for η_8. For each specimen, we have several segments of stress relaxation that occurred during deformation of the specimens (Fig. 7). Under relaxation, the values of stretch of the specimen remain unchanged, only the extension ratios of the seventh elastic element change. The viscosity values η_8 are approximated by the formula:

$$\eta_8 = \eta_6^{(8)} \exp\left(b\mathbf{I}_{V7}\right),$$

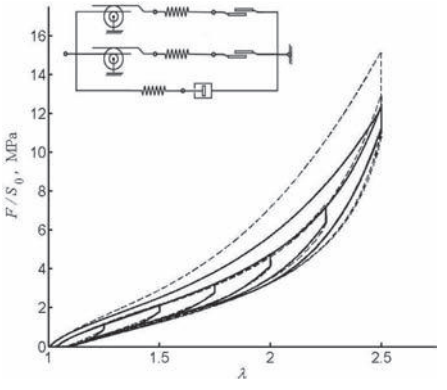

Figure 6. Experimental data obtained by testing the fifth specimen, and theoretical curve plotted at the seventh step of determining constants.

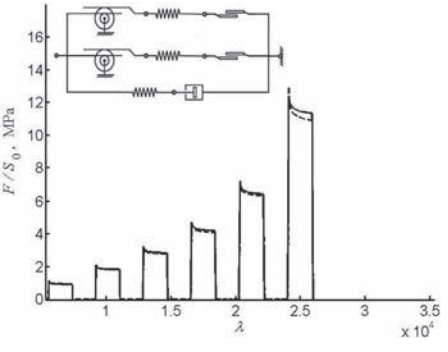

Figure 7. Experimental data obtained by testing the fifth specimen, and theoretical curve plotted at the eighth step of determining constants.

where $\mathbf{I}_{V7} = \sqrt{3\mathrm{tr}(\mathbf{V}_7^2) - \mathrm{tr}(\mathbf{V}_7)^2}$. The value of parameter b depends on the stretch tensor of the specimen. The value of each extension ratio is defined, and then its strain dependence is described by the following mathematical expression:

$$b = -\frac{\eta_6^{(8)}}{\exp\left(\eta_7^{(8)}\mathbf{I}_\mathrm{V}\right)},$$

where $\eta_6^{(8)}, \eta_7^{(8)}$ are constants. The viscosity function takes the form

$$\eta_8 = \eta_5^{(8)} \exp\left(-\frac{\eta_6^{(8)}\mathbf{I}_{V7}}{\exp\left(\eta_7^{(5)}\mathbf{I}_\mathrm{V}\right)} \right)$$

TENTH STEP. Let us comSbine fast and slow relaxation times of viscosity

$$\begin{aligned}\eta_8 = {} & \eta_0^{(8)} \exp\left(\eta_1^{(8)}\mathbf{I}_\mathrm{V}\right) \\ & + \eta_2^{(8)}\left(\exp\left(-\eta_3^{(8)}\mathbf{V}\cdot\mathbf{D}\right) + \exp\left(-\eta_4^{(8)}\mathbf{V}\cdot\mathbf{D}\right)\right) \\ & + \eta_5^{(8)} \exp\left(\frac{-\eta_6^{(8)}\mathbf{I}_{V7}}{\exp\left(\eta_7^{(8)}\mathbf{I}_\mathrm{V}\right)} \right) \exp\left(-\eta_8^{(8)}\mathbf{I}_\mathrm{D}\right)\end{aligned}$$

where $\mathrm{I}_\mathrm{D} = \sqrt{3\mathrm{tr}(\mathbf{D}^2) - \mathrm{tr}(\mathbf{D})^2}$, and the constant $\eta_8^{(8)}$ is defined by examining the points where the loading regime changes from loading to relaxation and from relaxation to unloading.

ELEVENTH STEP. To describe the experiment in the first cycle of loading, the following term is added to the obtained dependence of viscosity:

$$\begin{aligned}\eta_8 = {} & \eta_0^{(8)} \exp\left(\eta_1^{(8)}\mathbf{I}_\mathrm{V}\right) \\ & + \eta_2^{(8)}\left(\exp\left(-\eta_3^{(8)}\mathbf{V}\cdot\mathbf{D}\right) + \exp\left(-\eta_4^{(8)}\mathbf{V}\cdot\mathbf{D}\right)\right) \\ & + \eta_5^{(8)} \exp\left(\frac{-\eta_6^{(8)}\mathbf{I}_{V7}}{\exp\left(\eta_7^{(8)}\mathbf{I}_\mathrm{V}\right)} \right) \exp\left(-\eta_8^{(8)}\mathbf{I}_\mathrm{D}\right) \\ & + \eta_9^{(8)} \exp\left(\eta_{10}^{(8)}\mathbf{I}_\mathrm{V}\right) \exp\left(\eta_{11}^{(8)} \frac{\mathbf{I}_\mathrm{v} - \max(\mathbf{I}_\mathrm{V})}{\max(\mathbf{I}_\mathrm{V})} \right),\end{aligned}$$

where the constants $\eta_9^{(8)}, \eta_{10}^{(8)}$ are defined in the first cycle of loading, since the current and maximum values of stretch of the specimen coincide. The analysis of the remaining cycles of deformation yields the constant $\eta_{11}^{(8)}$.

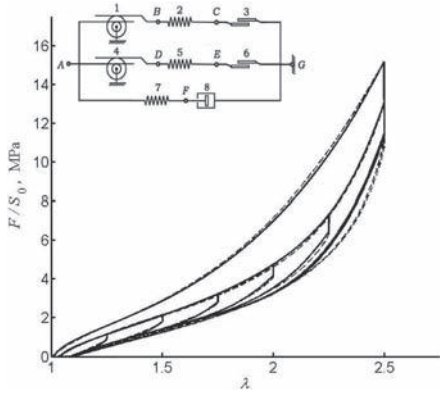

Figure 8. Experimental data obtained by testing the fifth specimen, and theoretical curve plotted at the eleventh step of determining constants.

4 CONCLUSIONS

The step-by-step approach has been developed to determine the constants of the model describing the viscoelastic properties of rubbers. The system of constitutive equations takes into account the peculiarities of the material behavior at the structural level. The theoretical results describe accurately the behavior of rubbers.

ACKNOWLEDGEMENT

The work was supported by Russian Foundation for Basic Research (Grant 09-08-00530) and DFG-FOR 597.

Constitutive Models for Rubber VI – Heinrich et al. (eds)
© 2010 Taylor & Francis Group, London, ISBN 978-0-415-56327-7

Structural-phenomenological modelling of softening and recovery of mechanical properties of elastomer nanocomposite

A.L. Svistkov, A.G. Pelevin & A.A. Adamov
Institute of Continuous Media Mechanics, Ural Branch of Russian Academy of Sciences, Perm, Russia
Leibniz-Institut fur Polymerforschung Dresden e.V., Dresden, Germany

B. Lauke & G. Heinrich
Leibniz-Institut fur Polymerforschung Dresden e.V., Dresden, Germany

ABSTRACT: A general method of constructing the system of constitutive equations was applied to develop the model describing the behaviour of rubber compounds. The effect of softening of the material after the first stretching (Mullins effect), viscoelastic properties and recovery of mechanical behavior after the long rest and thermostating is simulated.

INTRODUCTION

Rubbers are elastomeric nanocomposites that have long been used in industry and are of great practical importance. The incorporation of active fillers in rubber compounds increases by an order of magnitude the strength of the material compared to the unfilled elastomer and increases breaking deformations (Kraus, 1971). These materials have a number of features essential for the understanding of their behavior. In particular, near filler particles there appear polymer layers with special characteristics. During the failure of rubber compounds, at the tip of a macrorupture there occur fibers joining the edges of this macrorupture (Le Cam et al., 2004), where the polymer chains are in the oriented state (Trabelsi et al., 2003). The formation and disappearance of the oriented regions explain the hysteresis phenomena in the material subject to cyclic loading (Toki et al. 2003; Toki et al. 2004). On this basis, we put forward the following hypothesis: during deformation, between the aggregates of filler particles there appear uniaxially oriented fibers caused by the slippage of polymers chains from the layers near the active filler into the gaps between particles. In the present paper, we offer the structural-phenomenological model able to accurately describe the mechanical behavior of the medium taking into account the process of fiber formation at the nano-level of the material.

The mathematical model describing the mechanical behavior of the material is schematically represented in Figure 1. The system of constitutive

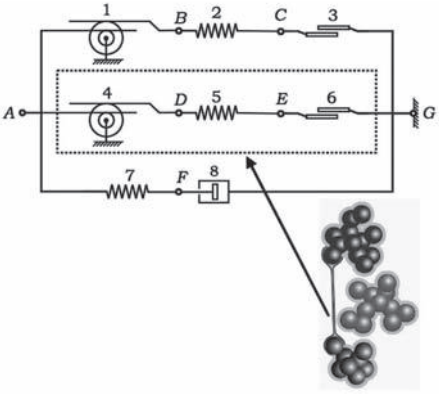

Figure 1. Scheme of mechanical behavior of rubber compound. Elements in dashed box simulate mechanical properties of high-strength fibers.

equations is constructed in correspondence with following rules:

1. To each point of the scheme the rate of deformation tensor of this point is assigned, which plays the role of a tensor parameter necessary for construction of the mathematical model.
2. The Cauchy stress tensor and the rate of deformation tensors are assigned to the elastic, viscous and plastic elements of the scheme.
3. For each transmission element the Cauchy stress tensor for the left and right points are used.
4. It is assumed that the rate of deformation tensor of the left point of the scheme coincides

with the rate of deformation tensor **D** of the medium, and the rate of deformation tensor of the right point of the scheme is equal to zero.

5. The rate of deformation tensor of elastic, viscous and plastic elements is calculated as the difference between the rate of deformation tensors of the left and right points of these elements.
6. The material is assumed to be incompressible. The trace of any rate of deformation tensor in the model is equal to zero.
7. The Cauchy stress tensor **T** of the medium is equal to the sum of the Cauchy stress tensors of elastic elements and the left points of transmission elements connected with the left point of the scheme.
8. The sum of the Cauchy stress tensors of elastic, viscous and plastic elements and the right points of transmission elements connected on the left with any inner point of the scheme is equal to the sum of the Cauchy stress tensors of elastic, viscous and plastic elements and the left points of transmission elements connected on the right with this point of the scheme.

Our investigation focuses on the study of isothermal processes. To describe the properties of elements shown in the scheme, the known formulas from continuum mechanics are used. For calculation of the Cauchy stress tensors $\mathbf{T}_i$ of elastic elements, we take the mass density of free energy f, which is the function of stretch ratios of all elastic elements

$$f = f(\theta,...,\lambda_1^{(i)},\lambda_2^{(i)},\lambda_3^{(i)},...),$$

where $\lambda_1^{(i)},\lambda_2^{(i)},\lambda_3^{(i)}$ are the stretch ratios for the i-th elastic element. This means that the deviator of the Cauchy stress tensor of the i-th elastic element should be calculated by the formula of the nonlinear elasticity theory

$$\operatorname{dev}\mathbf{T}_i = \operatorname{dev}\left(\rho\sum_{\kappa=1}^{3}\lambda_\kappa^{(i)}\frac{\partial f}{\partial\lambda_\kappa^{(i)}}\mathbf{n}_\kappa^{(i)}\otimes\mathbf{n}_\kappa^{(i)}\right),$$
$$\operatorname{dev}(\cdot) = (\cdot) - \frac{1}{3}\operatorname{tr}(\cdot),$$

where ρ is the mass density of the material, and $\mathbf{n}_1^{(i)},\mathbf{n}_2^{(i)},\mathbf{n}_3^{(i)}$ form an orthonormal triple of eigenvectors of the stretch tensor $\mathbf{V}_i$ of the elastic element. $\mathbf{V}_i = \lambda_1^{(i)}\mathbf{n}_1^{(i)}\otimes\mathbf{n} + \lambda_2^{(i)}\mathbf{n}_2^{(i)}\otimes\mathbf{n}_2^{(i)} + \lambda_3^{(i)}\mathbf{n}_3^{(i)}\otimes\mathbf{n}_3^{(i)}$.

For the i-th elastic element, the material time derivative of the stretch tensor $\dot{\mathbf{V}}_i$ is calculated by equation:

$$\frac{2}{\nu_m}\mathbf{Y}_i^{0.5}\mathbf{D}_i\mathbf{Y}_i^{0.5} = \dot{\mathbf{Y}}_i - \mathbf{Y}_i\mathbf{W}_\mathbf{R}^{\mathrm{T}} - \mathbf{W}_\mathbf{R}\mathbf{Y}_i, \qquad (1)$$
$$\mathbf{W}_\mathbf{R} = \dot{\mathbf{R}}\mathbf{R}^{\mathrm{T}},$$

where

$$\mathbf{Y}_i = \mathbf{V}_i^{\frac{2}{\nu_m}}, \quad \nu_m > 0,$$

R is the rotation tensor in the polar decomposition $\mathbf{F} = \mathbf{VR}$ of the deformation gradient of the medium **F** into the left stretch tensor **V** and the rotation **R**; ν_m is the transmission ratio of the m-th transmission element connected on the left with the considered elastic element. If the left point of the elastic element coincides with the left point of the scheme then transmission ratio ν_m is equal to unity.

The known equations of the nonlinear elastic theory describing the time variation of stretch ratios of the i-th elastic element

$$\dot{\lambda}_k^{(i)} = \lambda_k^{(i)}\mathbf{n}_k^{(i)}\otimes\mathbf{n}_k^{(i)}\cdot\mathbf{D}_i, \quad k = 1,2,3$$

and the rate of work in this element

$$\mathbf{T}_i\cdot\mathbf{D}_i = \rho\sum_{k=1}^{3}\frac{\partial f}{\partial\lambda_k^{(i)}}\dot{\lambda}_k^{(i)}$$

are the consequences of equation (1) in the case when the parameter ν_m is a constant

$$\nu_m = \text{const}.$$

In the general case, parameters ν_k can be the time decreasing functions. They are convenient to use for modeling the growth of damages in the medium.

The deviator of the Cauchy stress tensor of the j-th viscous element is calculated by the formula from the theory of nonlinear viscous fluids

$$\operatorname{dev}\mathbf{T}_j = 2\eta_j\mathbf{D}_j,$$

where the shear viscosity coefficient is the non-negative function of state parameters $\eta_j \geq 0$.

The deviator of the Cauchy stress tensor of the plastic element is calculated by the formula of the plastic flow theory

$$\mathbf{D}_n = \sqrt{\frac{\mathbf{D}_n\cdot\mathbf{D}_n}{\operatorname{dev}\mathbf{T}_n\cdot\operatorname{dev}\mathbf{T}_n}}\operatorname{dev}\mathbf{T}_n, \qquad (2)$$

where n is the number of the plastic element. For modeling the plastic flow process, it is necessary to exclude the ambiguity in expression (2). To this end, it is offered to use the mathematical expression which links the rate of deformation tensor of the plastic element with the rate of deformation tensor of the medium:

The symbol k_n designates the non-negative function of state parameters. When calculating,

we assume that plastic flow is possible under the following condition:

$$\max \text{inv}\,(\mathbf{T}_n) = \text{inv}\,(\mathbf{T}_n), \tag{3}$$

where

$$\text{inv}\,(\mathbf{T}_n) = \sqrt{\text{dev}\mathbf{T}_n \cdot \text{dev}\mathbf{T}_n},$$

i.e., when the invariant of stresses in the appropriate plastic element is equal to the maximum of this invariant in the considered element during the whole deformation history of the medium.

The transmission element in the model serves to increase the rate of deformation tensor by ν_m times and to decrease simultaneously the Cachy stress tensor by ν_m times

$$\mathbf{T}_m^{\text{left}} = \nu_m \mathbf{T}_m^{\text{right}}, \quad \mathbf{D}_m^{\text{left}} = \frac{1}{\nu_m}\mathbf{D}_m^{\text{right}},$$

where ν_m is the non-negative function of the state parameters (the transmission ratio), and k is the number of the transmission element.

The necessity to introduce transmission elements into the model stems from the following.

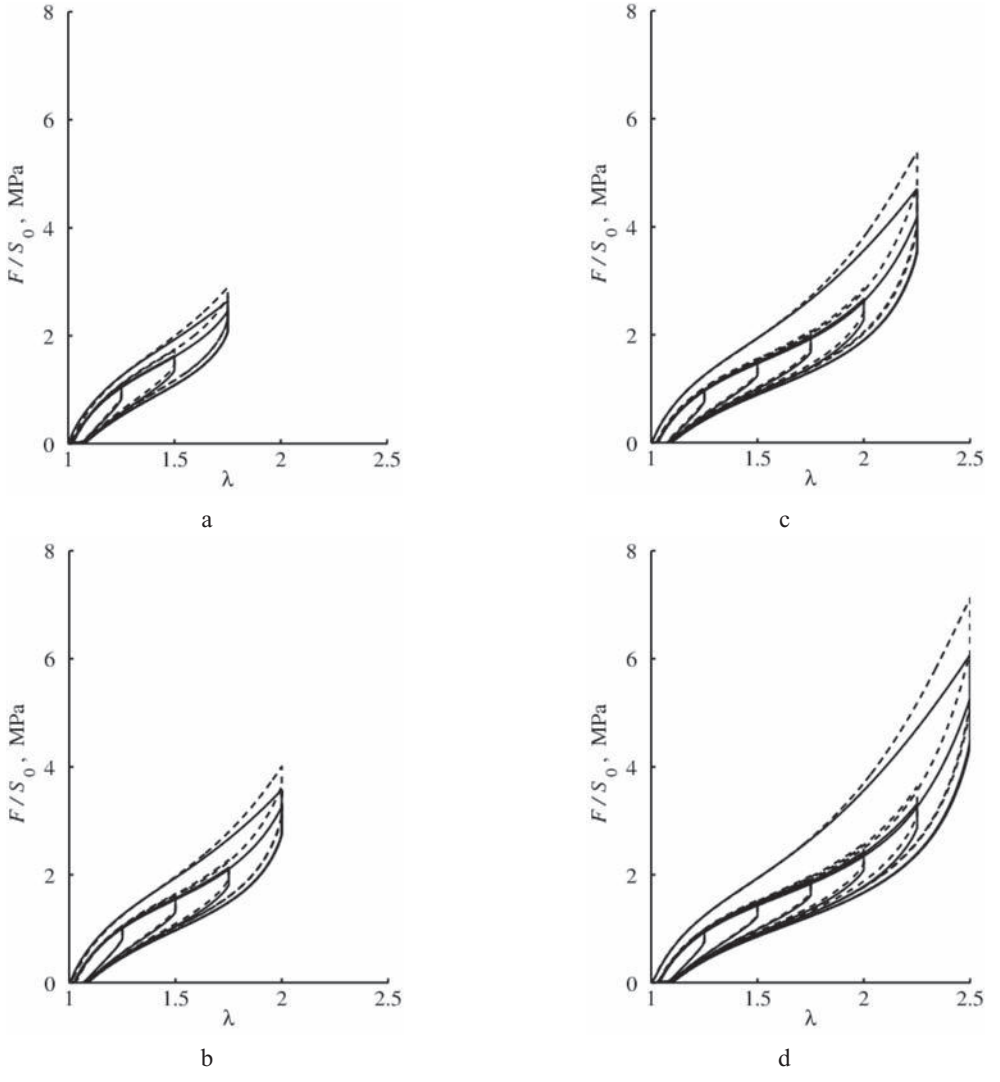

Figure 2. Difference in mechanical behavior of rubber compound in first experiment after thermostating (continuous lines) and in second experiment after long rest and new thermostating (dashed lines). Maximum stretch ratio in experiment equal to 1.75 (a), 2 (b), 2.25 (c) and 2.5 (d).

In the initial state, the particle aggregates of carbon black in rubbers touch each other, forming a filler network. We put forth a hypothesis that during deformation the polymer chains slipped off from the polymer layers near the filler particles into the gaps between aggregates, where high-strength fibers are formed as a polymer in the uniaxially oriented state (Figure 1). The strength of these fibers is a thousandfold higher than the strength of the elastomeric material without a filler (binder strength). This increases the macroscopic strength of rubbers (filled elastomers) by an order of magnitude. For example, the strength of spider cobweb is 2000–4000 MPa and the strength of non-crystallizing elastomeric materials is 4–10 MPa. We reason that such a relationship between strengths will also appear when comparing the strengths of oriented fibers and the binder.

The fact that during deformation polymer chains slipped off into the gaps between aggregates clarifies the deformation growth at the moment of rupture of filled elastomers compared to the unfilled material. In the course of deformation, the neighboring particle aggregates of carbon black move away at a large distance from each other, and other aggregates come into the gaps between them. However, the material is not destroyed in this case. After removing the external load, the material reverts to

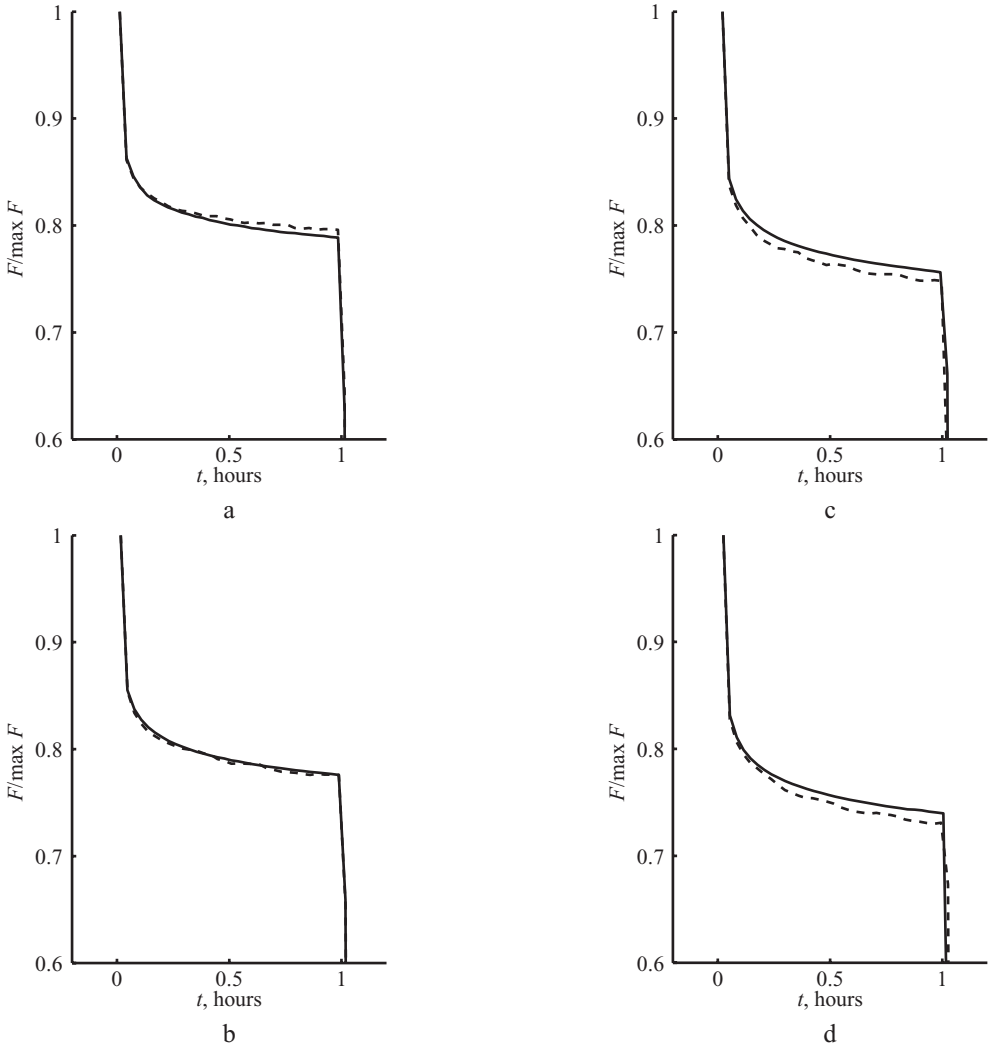

Figure 3. Relaxation curves of samples in the first experiments (continuous lines) and in the second experiment (dashed lines). Maximum stretch ratio in experiment equal to 1.75 (a), 2 (b), 2.25 (c) and 2.5 (d).

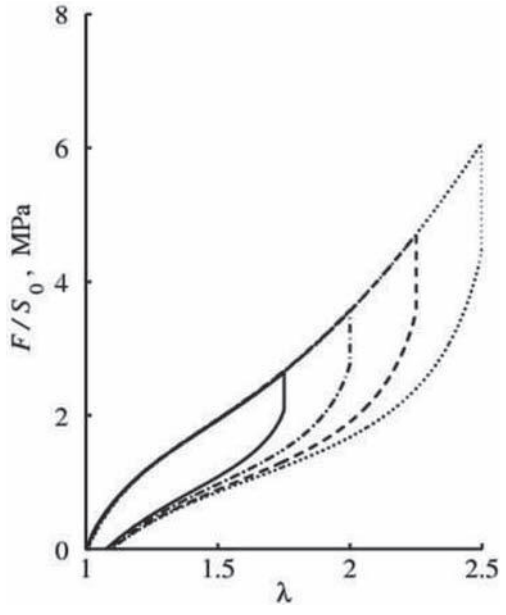

Figure 4. First cycles of deformation of samples in the first experiments after thermostating.

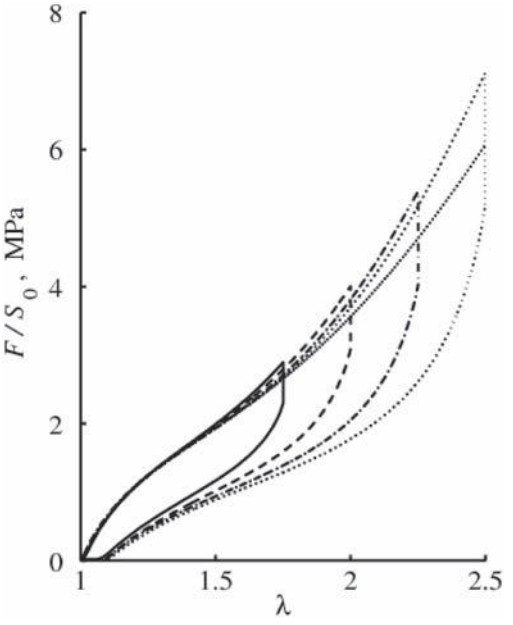

Figure 5. First cycles of deformation of samples in the second experiment after long rest and new thermostating (right plot).

its primary state. This may take place only in the case when fibers are able to elongate by several tens of times. The macroscopic deformations of the material do not exceed the stretch ratios of 4–7. This distinction between the macroscopic deformations and the deformation of separate elements of the material on structural level can be taken into account by the transmission elements introduced in the model.

We simulated the effect of softening of the material after the first stretching (Mullins effect), viscoelastic properties and recovery of mechanical behavior after the long rest and thermostating (Figure 2–Figure 5). We found that all difference in mechanical behavior of rubber compound in first experiment after thermostating and in second experiment after long rest and new termostating was produced by plastic element with number six. It means from our viewpoint that only hight-strength fibers remember the long history of deformation of the material.

ACKNOWLEDGEMENT

The research was supported by Russian Foundation for Basic Research and the Ministry of Industry, Innovation and Science of the Perm Region (Grant 07-08-96017, 09-08-00530) and DFG-FOR 597.

REFERENCES

Kraus, G. 1971. Reinforcement of elastomers by Carbon Black. *Advance of Polymer Science* 8: 155–237.

Le Cam, J.-B. Huneau, B. Verron, E. Gornet L. 2004. Mechanism of Fatigue Crack Growth in Carbon Black Filled Natural Rubber. *Macromolecules* 37: 5011–5017.

Trabelsi, S. Albouy, P.-A. Rault, J. 2003. Stress-Induced Crystallization around a Crack Tip in Natural Rubber. *Macromolecules* 36: 9093–9099.

Toki, S. Sics, I. Ran, S. Liu, L. Hsiao, B.S. 2003. Molecular orientation and structural development in vulcanized polyisoprene rubbers during uniaxial deformation by in situ synchrotron X-ray diffraction. *Polymer* 44: 6003–6011.

Toki, S. Sics, I. Ran, S. Liu, L. Hsiao, B.S. Murakami, S. Tosaka, M. Kohjiya, S. Poompradub, S. Ikeda, Y. Tsou, A.H. 2004. Strain induced molecular orientation and crystallization in natural and synthetic rubbers under uniaxial deformation by in-situ synchrotronv X-ray study. *Rubber Chemistry and Technology* 77: 317–335.

Constitutive Models for Rubber VI – Heinrich et al. (eds)
© 2010 Taylor & Francis Group, London, ISBN 978-0-415-56327-7

A phenomenological model for the material behaviour of elastomers due to multi network chains

Christian Ziegler
Hochschule Offenburg, Offenburg, Germany
Freudenberg Forschungsdienste KG, Computer Aided Engineering, Weinheim, Germany

ABSTRACT: Multi network theory is a suitable framework for describing the material behaviour of elastomer components. It has been shown in former works that these models are able to predict the changes in mechanical behaviour due to ageing effects like stress relaxation and set, respectively. In that case the number of chain segments of the original polymer network is reduced due to chain scission while new chain populations are generated in a non-deformed state due to post curing processes. This concept of multiple competing network chains can be generalized to simulate the viscous material behaviour of elastomers and the Payne effect, respectively. In this framework viscous behaviour can be interpreted on one hand as a reduction of the number of chain segments of the original polymer network coinciding on the other hand with the generation of an equal number of chain segments of a new chain population. Additionally, the interaction of polymer and filler which is responsible for the Payne effect, the dependence of the dynamic modulus on strain amplitude, might also be interpreted as scission and creation of new polymer chains at filler particles. A thorough phenomenological visco-elastic model is presented which might easily be implemented in FEM codes.

1 MATERIAL MODEL FOR RUBBER

1.1 *Introduction*

The mechanical behaviour of elastomeric materials typically is described within the framework of non-linear thermo-elasticity or visco-elasticity on the basis of the formulation of a strain energy density function, Ogden (1984). Many models are based upon the assumption of entropy-elastic behaviour of a network of macro-molecules. For the simplest material model, the Neo-Hookean model, the stiffness is directly proportional to the density of polymer chains. In this context it is important to distinguish between the terms of 'macro-molecule' and 'polymer chain'. While the former represents the realistic item of the chemical molecule, the 'polymer chain' only represents a fraction of the molecule between two constraints which can be defined by cross-links and additional entanglements between two macro-molecules, respectively. For a static material model these constraints are assumed to remain constant in time which yields a constant number of polymer chains and constant stiffness, respectively. For a rubber material the cross-links can be considered in a first approximation as fixed constraints and constant in time. The entanglements of molecules in contrast change in time due to polymer slippage. This might be interpreted as a reduction of polymer chains leading to a reduction of stiffness and gives rise to stress relaxation. By all means a change in micro-structure of the polymer network occurs.

There are additional long-term effects which also change the micro-structure of the polymer network and consequently the effective number of polymer chains in the material. These effects are summarized by ageing processes and will be used in the following to explain the basic assumptions of the model which can be generalized to simulate the viscous behaviour of the material. An implementation of these concepts into FEM codes is straightforward and has been carried out to the solver ABAQUS, Baaser & Ziegler (2006), Baaser et al. (2009).

1.2 *Ageing processes*

For a chemical description of the ageing processes there are endless possible reactions which all can be summarized for a mechanical description by two basic mechanisms: the scission and recombination of polymer chains. If a polymer backbone breaks due to a chemical reaction it is obvious that the appropriate polymer chain no longer contributes to the stiffness of the material. But even when a cross-link between two macro-molecules breaks the formerly constrained polymer chains are released which also results in a reduction of effective polymer chains. Chain ends are able to

recombine creating new cross-links. Additionally a radical attack on the polymer backbone might result in a generation of new bonds between two molecules, both processes increase the effective number of polymer chains and the overall stiffness of the material, respectively. It is important to note, that these new polymer chains are generated in a relaxed state, i.e. stress- and strain-free. Their contribution to the strain energy density must be related to their strain-free configuration and therefore to the configuration at the time of creation. A new population of polymer chains was created which competes with the original one. Whenever the deformation changes a new population of polymer chains is created with its own strain-free configuration where the contribution of the strain energy density must be referred to. This finally leads to a large number of competing populations of polymer chains. The competitive situation of two populations is obvious when unloading the material after a long ageing period. In Figure 1(a) the original population of polymer chains in a reference volume is shown in an unloaded state. The particular polymer chains are indicated as springs. Theses springs are stretched when loaded by a constant strain (b). If this load remains constant for a long time new polymer chains can be created stress-free (c). When the load finally is removed (d) the original polymer chains seek to reach their unloaded configuration which is hindered to a certain amount by the new created population finally yielding a remnant deformation, usually referred as permanent set.

1.3 *Generalization to viscous behaviour*

Within the framework of competing polymer chain populations a generalization to viscous rubber behaviour is apparent with the description of so-called physical relaxation processes in mind. In a micro-mechanical view physical relaxation at a certain constant deformation can be understood as the change of entanglements due to polymer slippage. A single polymer chain originally belonging to the initial population no longer contributes to the stiffness, which has the same effect as the scission of this polymer chain. But the chain is not really split, it is rather relaxed in the actual configuration and has to be assigned to a new population of polymer chains which are strain-free in the actual deformation state. It is important to note that—in contrast to the ageing model—the total number of polymer chains remains constant. It is not the number of polymer chains that alters but the affiliation to different populations of polymer chains. When the load changes again the number of polymer chains in both populations decrease in favor of a third population similar to the ageing model. The only difference to the ageing model concerns the evolution rate of the number of polymer chains of the new population.

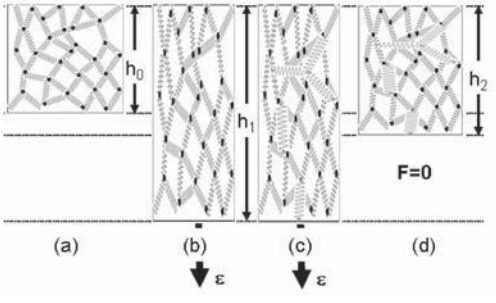

Figure 1. Origin of permanent set due to competing polymer populations.

2 VISCOUS BEHAVIOR IN THE FRAMEWORK OF MULTI NETWORK THEORY

2.1 *Constitutive model*

For the simplest hyperelastic material model, the Neo-Hookean model, the strain energy density w is given by

$$w = G/2 \cdot (I_1 - 3), \tag{1}$$

where $I_1 = \mathrm{tr}\{\mathbf{B}\}$ denotes the first invariant of the left Cauchy-Green strain tensor $\mathbf{B} = \mathbf{F}\mathbf{F}^{\mathrm{T}}$ ($\mathbf{F}$ denotes the deformation gradient) and G is the shear modulus, Ogden (1984). Within the framework of statistical mechanics G is proportional to the initial density of polymer chains N_0 and yields

$$G = N_0 kT, \tag{2}$$

with k the Boltzmann constant an T the absolute temperature. For a uniaxial load with constant stretch ratio λ the Cauchy stress equals

$$\sigma = N_0 kT \cdot \left(\lambda^2 - \frac{1}{\lambda}\right). \tag{3}$$

Due to polymer slippage N_0 is no longer constant but decreases with time. So equation (3) is able to describe physical relaxation in a phenomenological way. Assuming a new population of polymer chains with density N_{NC} has been created at a stretch ratio of λ_{C} their contribution to the strain energy density must be referred to this deformation λ_{C}. A description of general multi-axial

loads requires the use of tensor formulation. The relevant deformation gradients are shown in Figure 2, where B_0 and B_t denote the reference and the actual configuration, respectively. The ordinary deformation gradient $\mathbf{F}_0(t)$ maps the reference configuration on the actual configuration. B_ξ denotes the intermediate configuration at time ξ where the new population is created and $\mathbf{F}_\xi(t)$ is the deformation gradient which maps this intermediate configuration on the actual one. For the sake of simplicity a Neo-Hookean law is assumed for the new population, too. Due to the Neo-Hookean behaviour and according to equations (1) and (2) the contribution of the new population to strain energy density is

$$w = \frac{1}{2} \cdot N_{\mathrm{NC}} kT \cdot (\mathrm{Tr}\{\mathbf{F}_\zeta^{\mathrm{T}}(t)\mathbf{F}_\zeta(t)\} - 3). \tag{4}$$

It is obvious from Figure 2 that the intermediate deformation gradient can be expressed via the ordinary deformation gradient

$$\mathbf{F}_\zeta(t) = \mathbf{F}_0(t)\mathbf{F}_0^{-1}(\xi). \tag{5}$$

For a uniaxial load at stretch ratio λ equations (4) and (5) result in the Cauchy stress of

$$\sigma = N_{\mathrm{NC}} kT \cdot \left(\left(\frac{\lambda}{\lambda_C} \right)^2 - \frac{\lambda_C}{\lambda} \right) \tag{6}$$

with λ_C the stretch ratio of the intermediate configuration where the new population was created. When the load varies with time a new population of polymer chains is created for each deformation state and each population contributes to Cauchy stress by a term comparable to equation (6). Thus, the strain energy function becomes a functional of the deformation history and the density of polymer chains has to be replaced by its evolution rate $\dot{N}_{\mathrm{NC}}$.

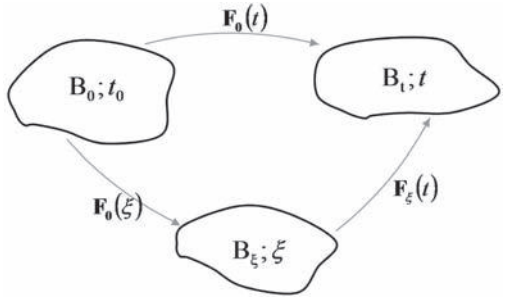

Figure 2. Different configurations for constitutive model.

2.2 *Evolution rate for the new population of polymer chains*

It has been stated above that the number of new created polymer chains in a new deformation state equals the total number of the polymer chains which has been broken in all former populations within the same time period. Therefore the decay law of the original population is a crucial quantity. Since it is more intuitive to argue with the number of polymer chains instead of the density of polymer chains we use the former expression in the following although being well aware that it should be the density to be argued with. Let us assume that the polymer chains of the original population consist of permanent chains that do not break and variable chains that are able to break at a certain configuration and finally are attached to a new population. The number/density of polymer chains at the beginning $t = 0$ can be specified by

$$N_0 = N_p^{(0)} + N_v^{(0)}, \tag{7}$$

where $N_p^{(0)}$ and $N_v^{(0)}$ are the permanent and variable number of polymer chains, respectively. For a constant load only the permanent polymer chains remain to the original population when time goes to infinity, the variable ones have been broken. When $N^{(0)}(t)$ denotes the number of polymer chains of the original population with respect to time this quantity can be written as

$$N^{(0)}(t) = N_p^{(0)} + g(t) \cdot N_v^{(0)} \tag{8}$$

with $g(0) = 1$ and $g(\infty) = 0$. Very often the function g is parameterized by a series of exponential decays called Prony series. For a constant deformation the relaxation modulus of the material is given via equation (2) by

$$G(t) = N^{(0)}(t)kT. \tag{9}$$

When a new population of polymer chains is created these chains are able to break. There are no permanent chains belonging to the new population and for the sake of simplicity the decay of the population is assumed to be governed by the same function g as the original population. Consider a constant deformation for a short time period Δt. There is a certain number of polymer chains of each existing population that break within Δt and the total number of these chains form the new population strain-free in the actual configuration. With this assumption the rate of increase for the new created polymer chains $\dot{N}_{\mathrm{NC}}$ is governed by a Volterra integral equation of the second kind

$$\dot{N}_{\mathrm{NC}}(t) + \int_0^t \dot{N}_{\mathrm{NC}}(\xi) \cdot \dot{g}(t - \xi)\mathrm{d}\xi = -N_v^{(0)} \cdot \dot{g}(t). \tag{10}$$

If the function g is parameterized by a Prony series

$$g(t) = \sum_{i=1}^{n} g_i \cdot \mathrm{e}^{-t/\tau_i} \tag{11}$$

with g_i and τ_i the various relaxation strengths and relaxation times, respectively, the integral equation (10) can be solved more or less analytically and in combination with the multi-axial constitutive model introduced in the last section this formulation is able to be implemented into a FEM code, e.g. ABAQUS using the UMAT interface.

2.3 *Verification of the model*

Since the FEM implementation of the material model has not done yet we present the predictions of the model for some simple deformation modes and compare them to the results of well-known models like the generalized Maxwell element in linear visco-elasticity. In each case we start with the relaxation modulus $G(t)$ or equivalent to that the function $g(t)$ in equation (8). As mentioned above $g(t)$ is parameterized by a certain number of exponential decay functions which is called the Prony series in this context. Both the number of Prony elements and the loading mode are diversified whereas we use simple shear and uniaxial tension for loading mode. It is important to note that both functions $G(t)$ and $g(t)$ do not show any strain dependence. This means that the characteristics of the relaxation process stay the same no matter how large the deformation is. But anyway the model is applicable to large deformations without any restrictions.

2.3.1 *Harmonic shear loads*

First we apply a harmonic shear load of constant amplitude

$$\varepsilon(t) = \hat{\varepsilon} \cdot \sin \omega t. \tag{12}$$

The simplest relaxation behaviour consists of a single Prony element

$$g(t) = \mathrm{e}^{-t/\tau}, \tag{13}$$

which is able to describe in connection with the distinction of the number of polymer chains by permanent and variable ones (cf. equation (8)) a Maxwell element. For a relaxation time $\tau = 0.1$ s, the stress strain behaviour for a frequency of $f = 1$ Hz and a shear amplitude of 0.01 is shown in Figure 3. The fraction of permanent polymer chains was determined at 10% of the total number of initial polymer chains for this test example. Starting from zero load a stationary state in stress-strain-curve is reached after a very few cycles. The dynamic modulus of this stationary state is shown in Figure 4 for different frequencies.

Both, the Maxwell element in linear visco-elasticity and our model result in exactly the same relation for storage and loss modulus, respectively. But already the next less simple relaxation model with two relaxation times which is equivalent to two Prony elements results in different shape of the dynamic modulus which is shown in Figure 5 and Figure 6. For this example the relaxation times have been determined $\tau_1 = 0.1$ s and $\tau_2 = 10$ s, respectively. Since τ_2 is ten times larger than the period of the load the stationary state is not reached as fast as in the former example (cf. Figure 3).

2.3.2 *Uniaxial tension*

In the framework of non-linear visco-elasticity it is more enlightening to analyze the stress-strain behaviour of materials when loaded by a uniaxial tension since many of the commonly used material models are only valid for small strain amplitudes and differences between the models become apparent for large strains. In addition to that the notion of dynamic modulus is ambiguous since different definitions which are equivalent for small strains

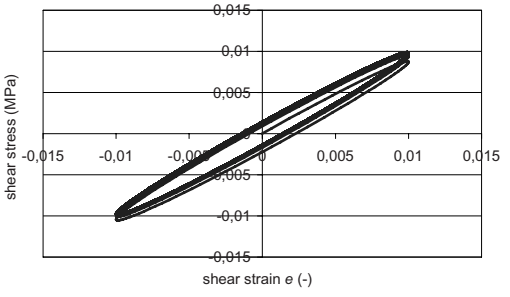

Figure 3. Stress strain behavior for harmonic shear load.

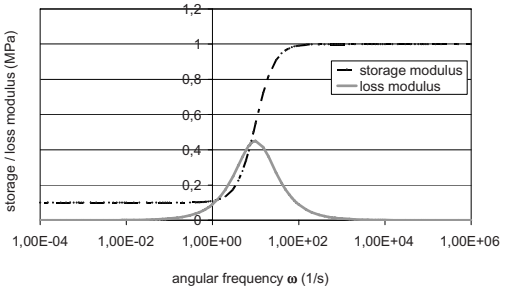

Figure 4. Dynamic modulus for one Prony element with angular frequency.

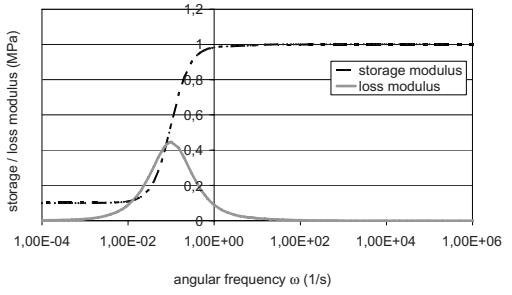

Figure 5. Dynamic modulus for 2 Prony elements in our model.

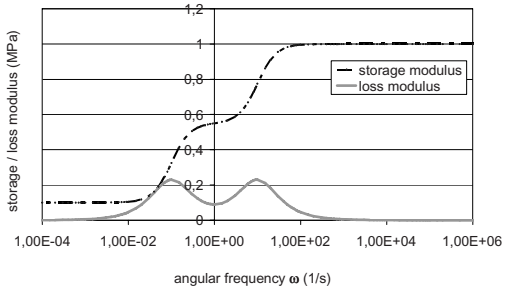

Figure 6. Dynamic modulus for 2 Prony elements for linear visco-elasticity.

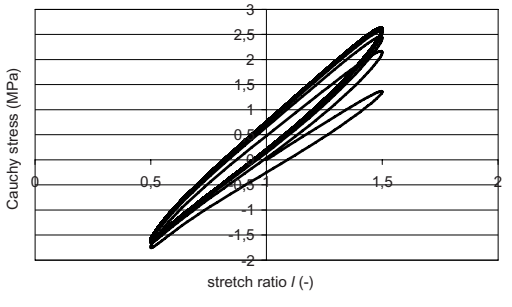

Figure 7. Stress strain behavior for uniaxial tension with strain amplitude of 50%.

have different results for large strains. The tensor formulation of our model ensures the applicability of large strains without any restrictions. Starting analogous to section 2.3.1 with only one relaxation step with a relaxation time $\tau = 0.1$ s, the stress strain behaviour for a frequency of $f = 1$ Hz is shown in Figure 7. If the results of the stress are expanded in powers of the strain amplitude the small strain approximation is obtained by neglecting the higher orders in strain amplitude. For this approximation the dynamic modulus is well-defined and yields—except for a factor 3—the same result compared to harmonic shear loads. The same holds true when two Prony elements and therefore two relaxation times are considered.

3 MODELLING THE PAYNE EFFECT—AN OUTLOOK

In addition to those non-linear effects whose origin is the non-linear kinematics for large strains there is another source of non-linearity for realistic elastomer materials: due to the weak bond energy between polymer chains and filler particles these bonds are able to break and rearrange. In a microscopic view the bond is released when the external energy on the polymer chain exceeds the binding energy of the polymer filler bond. These circumstances might also be described by scission and new generation of polymer chains. In contrast to the analysis in the former chapters the amount of the broken chains is no longer a function of time but depends on the deformation history of the polymer chains. For multi-axial loads a strain measure is necessary which governs the scission or rearrangement of polymer and filler. When the deformation exceeds a critical value, the polymer chain is assumed to disconnect from the filler particle. Subsequently the chain is unloaded and relaxed and can adsorb again on any filler particle. When a polymer chain disconnects from a filler particle the number of polymer chains of the initial population of polymer chains is reduced by one. Since this chain is able to absorb at the filler in a relaxed state, this can be interpreted as a creation of a new population of polymer chains that are unloaded in the configuration at their time of creation. So for every population the strain must be referred to the strain at the time of its creation. To evaluate the evolution rate for the new populations of polymer chains the whole load history has to be taken into account since the actual strain tensor has to be referred to the strain tensor at the time of the creation of the population. For that reason a FEM implementation is hardly successful at the moment since the stress tensor has to be stored for each material point at each time increment.

3.1 *Prediction for harmonic shear load*

According to the decay law $g(t)$ (cf. equation (8)) of polymer chains at a relaxation experiment a decay function has to be defined which governs the break and rearrange of the polymer at filler particles. In a first approximation the decay law has been selected as an exponential decay with respect to the strain $\Delta\varepsilon$ referred to the strain at the time of creation. Similar to equation (8) the number

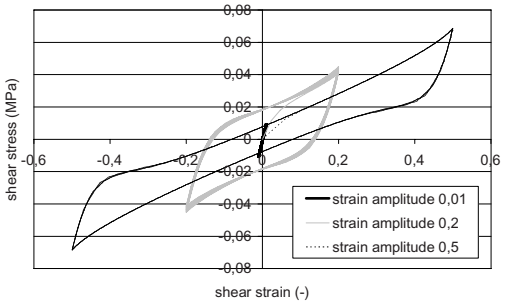

Figure 8. Stress-strain curve for harmonic shear load with different strain amplitudes.

of polymer chains of the initial population can be written

$$N^{(0)}(\varepsilon) = N_p^{(0)} + g(\varepsilon) \cdot N_v^{(0)} = N_p^{(0)} + N_v^{(0)} \cdot \mathrm{e}^{-\frac{\Delta\varepsilon}{\varepsilon_v}}. \tag{14}$$

With a fraction of 10% for the number of the permanent polymer chains and a parameter $\varepsilon_v = 0.02$ in the decay law (cf. equation (14)), a harmonic shear load with strain amplitude 0.2 shows a stress-strain behavior which has no longer the shape of an ellipse but has pronounced corners at maximum strain. The stress-strain curve for different strain amplitudes is shown in Figure 8. Starting for small strain amplitudes with a high slope and hardly any hysteresis both the slope of the end-to-end diagonal and the hysteresis depend on the strain amplitude. When the slope of the end-to-end diagonal is defined as the size of the storage modulus this means that the dynamic modulus is a decreasing function of the strain amplitude which commonly is referred to the Payne effect.

4 CONCLUSIONS

A flexible constitutive material model is presented that can be applied to describe different elastomer material properties like the ageing behaviour, the viscous behaviour and the dependence of the dynamic modulus on strain amplitude most commonly called the Payne effect, respectively, starting from the relaxation modulus of the material. The viscous material behaviour is evaluated analytically even for finite strains, when the relaxation modulus consists of a Prony series, a sum of exponential decay functions. It is shown that the dynamic modulus in the small strain approximation equals the result of the three parameter model of linear visco-elasticity. For two or more Prony elements already the differences to the results of the generalized Maxwell model are specified. In an outlook a description of the Payne effect within the framework of this model is shown which will be able to simulate strain amplitude dependence in time-domain calculations. While the modelling of the ageing behaviour has already been implemented in FEA code, both, the viscous behaviour and the simulation of the Payne effect has to be done in future while there are some restrictions especially for the last mentioned Payne effect that might prevent the implementation for general load cases.

REFERENCES

Baaser, H. & Ziegler, C. 2006: Simulation von Setz- und Relaxationsvorgängen von Elastomerbauteilen mit Hilfe des mehrachsig formulierten Freudenberg-Alterungsmodells; *14. Internationale Dichtungstagung, Stuttgart*, ISBN 978-3-00-019913-4, 537–546.

Baaser, H & Häusler. O & Mehling V. & Ziegler C. 2009: Simulation of Relaxation and Set in Elastomer Components using the multi-axial Freudenberg-Ageing model; *IRC 2009, Nürnberg* (in press).

Ogden, R.W. 1984: *Non-linear elastic Deformations*; Ellis Horwood Ltd.

Dynamic properties and vibration

Constitutive Models for Rubber VI – Heinrich et al. (eds)

An experimental study of magneto-sensitive natural rubber components applied in a vibration isolation system

A. Alberdi, N. Gil-Negrete & F.J. Nieto
CEIT and Tecnun (University of Navarra), Department of Applied Mechanics, San Sebastian, Spain

L. Kari
The Marcus Wallenberg Laboratory for Sound and Vibration Research, Royal Institute of Technology, Stockholm, Sweden

ABSTRACT: The effectiveness of magneto-sensitive natural rubber components applied in a vibration isolation system is experimentally investigated, where influences of excitation position, amplitude, frequency and magnetic field are examined. The magneto-sensitive elastomer consists of micron-sized, irregularly shaped iron particles blended in soft natural rubber at a concentration close to the critical particle volume fraction, shown to be the most favorable composition for optimum behaviour. A rigid aluminium mass supported on four vibration isolators is excited by an electro-dynamic shaker. Each component of this vibration isolation system is composed of two thin, square shaped, symmetrically positioned magneto-sensitive elements excited in simple shear with a magnetic field applied perpendicularly to the motion by an electromagnet. The magnetic field is varied by applying different intensities through the coil. The excitation position is either on the centre or on the edge of the surface of the mass, using step-sine excitation of various amplitudes in the frequency range of 0 to 300 Hz. The results show that it is possible to use magneto-sensitive rubber for vibration control purposes.

1 INTRODUCTION

Vibration isolators usually require a combination of stiffness and damping to provide a proper connection between two parts of a structure and a proper isolation from unwanted vibrations. Most of them are made of rubber, which means that once installed in an application their dynamic behaviour in frequency cannot be adjusted to avoid critical frequencies.

Different solutions (see, i.e., Carlson & Jolly 2000, Yu et al. 2001, Gil-Negrete et al. 2005) such as passive fluid mounts, adaptive tuned vibration absorbers (TVA), stiffness tunable mounts and suspensions or variable impedance surfaces have been proposed in order to reach more tunable characteristics.

Magneto-sensitive (MS) elastomers constitute a new kind of smart material that offer an alternative approach to the problem (Carlson & Jolly 2000). They consist of magnetically polarisable particles embedded in an elastomer matrix, and their properties can be modified rapidly, continuously and reversibly when applying an external magnetic field.

Iron particles are usually selected as polarisable particles due to their high permeability, low remanent magnetisation and high saturation magnetisation. The distribution of these particles in the elastomer can be anisotropic or isotropic, depending on whether they have been aligned by an applied magnetic field before curing.

Research on dynamic properties of magneto-sensitive elastomers has been performed of late. Most studied isotropic and anisotropic distributions of carbonyl iron, spherical particle filled elastomer matrix. For example, Bellan & Bossis (2002) studied the amplitude dependence and magnetic sensitivity of the Young modulus at very low frequencies; Boczkowska et al. (2007) focused on urethane magneto-rheological elastomers, varying particle volume concentration up to 33% and measuring storage modulus in the 0–100 Hz range at a deformation amplitude of 0.1%; Chen et al. (2007) introduced natural rubber as matrix material, focusing on the different shear modulus and loss factor at low frequencies (5 Hz) that could be obtained by varying magnetic field and temperature when vulcanising the mixture; Varga et al. (2006) and Schrittesser et al. (2008) went up to 100 Hz, comparing dynamic properties of compounds with and without application of magnetic field during vulcanisation. The influence of the magnetic field was more pronounced for anisotropic specimens.

Nevertheless, from the point of view of manufacturing MS rubbers it would make the process easier if the application of a magnetic field before curing could be avoided. Lokander & Stenberg (2003a, b) observed that high magneto-rheological (MR) effects can be also reached with isotropic MS elastomers with larger irregularly shaped iron particles if the particle concentration is close to the critical particle volume concentration (CPVC). Furthermore, they showed that the MR effect is independent of the elastomer matrix.

Following this research line, Blom & Kari (2005a, b) worked with irregularly shaped iron particles in silicone and natural rubber. They explored the frequency and amplitude dependence of the shear modulus in the audible frequency range, and Lejon & Kari (2008) included the influence of the preload.

Theoretical applications based on experimental results show how the performance of vibration isolators is greatly improved by adopting magneto-sensitive rubbers (Blom & Kari 2005b, c).

In this project, the potential applications of magneto-sensitive rubber in noise and vibration control need to be studied experimentally. Natural rubber was thus selected as matrix material, due to its appropriate characteristics in vibration isolation. The iron particles were irregularly shaped and in a concentration close to the CPVC. Curing of MS rubber was conducted in absence of magnetic field, thus leading to an isotropic distribution of particles within rubber matrix. The frequency range was restricted to the low structure-borne vibration transmission range.

On the one hand, characterisation of dynamic properties was performed in the frequency range of interest in simple shear MS natural rubber components, varying amplitude and magnetic field. On the other hand, laboratory measurements were conducted in a vibration isolation system, which consisted of aluminium mass mounted upon four MS components and excited by an electro-dynamic shaker. The influences of excitation position, amplitude, frequency and magnetic field were analysed.

2 DYNAMIC TESTS ON MS COMPONENTS

2.1 *Materials and methods*

The raw matrix material was natural rubber (SMR GP) containing 100 phr rubber, 6 phr zinc oxide, 0´5 phr stearine, 3´5 phr sulphur, 0´5 phr mercaptobenzothiazole and 40 phr plasticisers. The iron particles were irregularly shaped with a particle size distribution of 77´7% of 0–38 µm, 15´6% of 38–45 µm and 6´7% of 45–63 µm. The iron particles were mixed into the natural rubber at a particle concentration of 33% during the vulcanisation process, which was conducted in the absence of a magnetic field and thus led to an isotropic ground state.

Simple shear MS rubber samples (half of the standardised quadruple simple shear specimen) were created from two MS rubber elements $25 \times 25 \times 2$ mm in dimension and symmetrically positioned, as shown in Figure 1. The elements were glued to the steel plates using Loctite 406. The magnetic field was applied to the samples perpendicularly to the motion by an electromagnet.

Dynamic stiffness measurements of the MS components were conducted in an Instron MHF400 dynamic testing machine. The components were subjected to shear displacement of constant amplitude. The excitation signal frequency varied from 50 Hz to 300 Hz with a constant frequency step of 10 Hz. The magnetic field was generated by a home-made electromagnet, consisting of a power-supplied coil wired round an iron C-frame directing a magnetic flux perpendicular to the shear direction. The magnetic field was controlled by the electric current through the coil, which ranged from 0 A to 2 A, where the saturation of the samples was reached. All these tests were performed at the excitation amplitudes of 0.01, 0.025, 0.05, 0.075 and 0.1 mm.

2.2 *Results and discussion*

The dynamic shear modulus magnitude and loss angle are shown in Figure 2 in the absence of

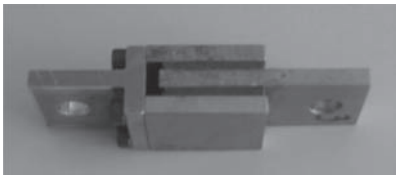

Figure 1. Simple shear MS rubber sample.

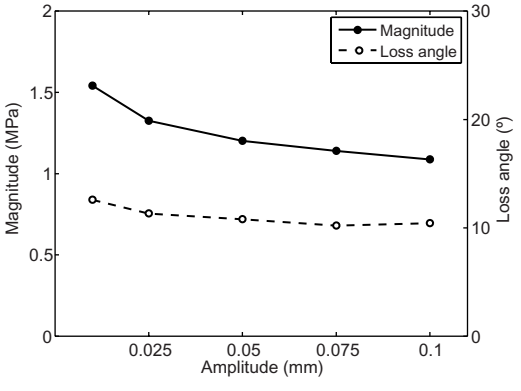

Figure 2. Shear modulus magnitude and loss angle versus amplitude at 100 Hz and no magnetic field.

magnetic field for the five tested amplitudes, at the excitation frequency of 100 Hz. The loss angle is between 10–12° and the magnitude shows an amplitude dependence characteristic of any filled rubber, decreasing from 1.5 MPa at 0.01 mm to 1 MPa at 0.1 mm.

Figures 3, 4 show the dynamic shear modulus magnitude and loss angle respectively over the frequency range of interest of the MS components for an excitation amplitude of 0.01 mm. It can be observed how the magnitude increases with the applied magnetic field while the loss angle remains unaffected. When an intensity of 2 A is applied to the electromagnet the MS component is said to be magnetically saturated since the magnitude does not increase significantly for higher intensities.

The relative magneto-rheological effect (MR effect) is depicted in Figure 5 for the five tested amplitudes, corresponding to an excitation frequency of 100 Hz. The MR effect is defined as the increase in magnitude of the dynamic shear modulus in the presence of magnetic field compared to that in the absence of magnetic field. Figure 5 indicates that the MR effect increases with decreasing excitation amplitude. The largest MR effect recorded corresponds to the amplitude of 0.01 mm with an increase of almost 28% when the samples are saturated.

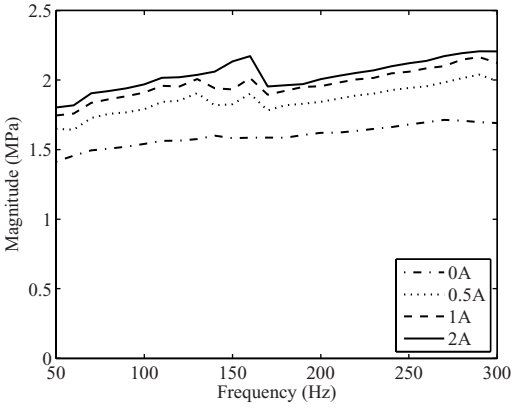

Figure 3. Shear modulus magnitude versus frequency for different intensities at 0.01 mm.

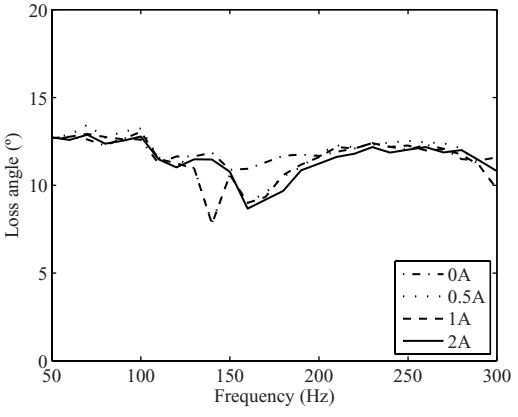

Figure 4. Shear modulus loss angle versus frequency for different intensities at 0.01 mm.

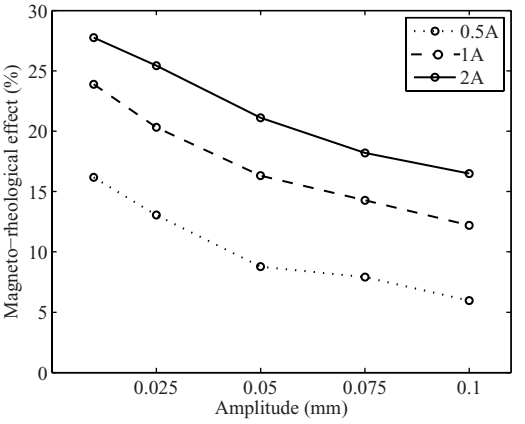

Figure 5. Relative magneto-rheological effect versus amplitude at 100 Hz.

3 APPLICATION CASE

3.1 *Procedure*

A vibration isolation system was mounted in the laboratory in order to study the effectiveness of using magneto-sensitive natural rubber components as isolators. It consisted of a rigid aluminium mass of 13 kg and dimensions of 220 × 180 × 120 mm supported on four MS rubber samples placed at the four corners of the block (Fig. 6).

The magnetic field was applied to each component perpendicular to the shear direction by an electromagnet. The four electromagnets were connected in parallel and fed by a single source. The electric current through each coil was varied from 0 A to 2 A, the point at which the saturation of the components is attained.

The mass was excited by an electro-dynamic shaker. The excitation force signal was a step-sine of constant amplitude starting at 10 Hz and increased with a constant frequency step of 2 Hz up to the maximum frequency of interest, not over 300 Hz.

Excitation amplitudes of 1, 5, 10 and 50 N were applied. The response of the system in vertical direction was captured with an ICP accelerometer.

Frequency response functions were obtained between different excitation and response positions; when the shaker was applied to the center of the top surface of the mass. The acceleration was measured at an adjacent position (point inertance), and when the excitation position was on the mid point of one edge of the top surface, the accelerometer was placed at the mid point of the opposite edge (transfer inertance), as illustrated in Figure 6. Instruments used for measurements are shown in Table 1.

3.2 *Results and discussion*

The influence of the excitation level is shown in Figure 7 when no magnetic field is applied to the samples. These frequency response functions were measured by exciting and measuring the response in the center of the upper surface of the block, and thus the vertical mode was captured. As the excitation force increases, the MS components are subjected to larger displacements. This causes lower dynamic stiffness and hence the decrease of the natural frequency of the vertical mode, as it is observed in Figure 7.

In Figure 8 the influence of the magnetic field is depicted for an excitation force amplitude of 10 N. The magnetic field makes the components stiffer and therefore, it causes a shift of the resonances towards higher frequencies. The natural frequency

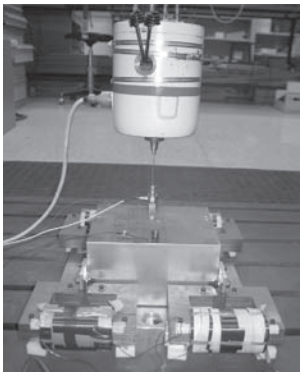

Figure 6. Measurement set-up of the aluminium mass supported on four MS components.

Table 1. Measurement instruments.

Instrument	Model
Electro-dynamic shaker	LDS 409
Force trasducer	DYTRAN 1051V4
ICP accelerometer	PCB 333A31
Power-supply	VD 310
Frequency analyzer	I-DEAS TEST

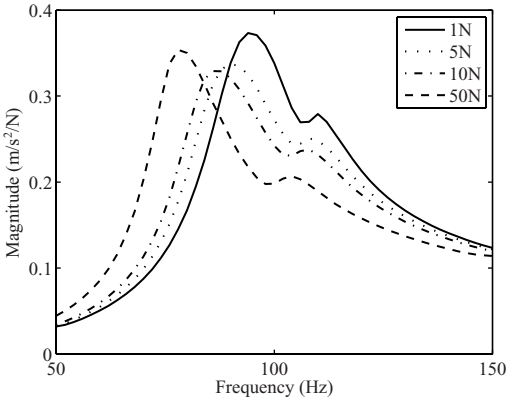

Figure 7. Point inertance for different excitation levels with no magnetic fields.

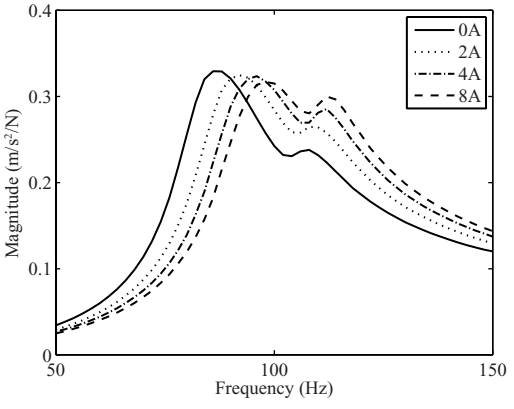

Figure 8. Point inertance for different intensities with excitation amplitude of 10 N.

of the system without any applied magnetic field is 88 Hz and moves to 100 Hz when an electrical current of 2 A goes through each electromagnet, that is, when the components are magnetically saturated.

From the resonance frequencies of the vertical mode the magnitude of the dynamic shear modulus can be estimated using Equation 1:

$$f = \frac{1}{2\pi}\sqrt{\frac{4K}{m}} = \frac{1}{2\pi}\sqrt{\frac{8AG}{me}} \qquad (1)$$

where f = natural frequency of the vertical mode; m = mass of the block; K = magnitude of dynamic stiffness; A = area of MS elements; e = thickness of MS elements; G = magnitude of dynamic shear modulus.

Looking at the results obtained from the dynamic tests on the MS components used as isolators (Figs. 2, 3), it might be concluded that an excitation force of 10 N leads to a displacement close to 0.01 mm on the samples.

Regarding the magneto-rheological effect, it may be obtained from these FRF measurements since it is directly related to the frequency shift:

$$f_2 / f_0 = \sqrt{\mathrm{MR} + 1} \tag{2}$$

where f_2 = natural frequency with 2 A; f_0 = natural frequency with 0 A; MR = relative MR effect.

In Table 2 the variation of the resonances from zero-field to saturation is shown for excitation forces of 1, 10 and 50 N, and the corresponding MR effects (calculated using Equation 2). Comparing these results to the MR effect shown in Figure 5, displacements of less than 0.01, 0.01 and 0.05 mm could be estimated for the considered excitation levels respectively.

Finally, Figure 9 shows the effect of changing the excitation and measurement positions, where a rotation mode was also excited apart from the vertical mode that was present in the previous measurements. Curves corresponding to zero-field and saturated states are displayed, when the excitation force amplitude was 10 N. The resonance frequency shifts from 92 Hz with zero-field to 102 Hz in saturation for the vertical mode, and from 176 Hz to 196 Hz for the rotation mode.

The original resonance peak can be avoided and reduced in 26.1% for the first mode and in 37.6% for the second, if the magnetic field is applied. A control strategy that consisted on turning on and off the magnetic field manually was followed in order to elude those peaks. The test started with an intensity of 2 A applied to the coils. At 98 Hz the magnetic field was turned off up to 128 Hz, where it was switched on again. The saturated curve was followed up to 184 Hz, where the MS components were again back at its original properties until the end of the test. The frequency response function acquired in this test is tagged as "controlled FRF" in Figure 9.

Table 2. Frequency shift and magneto-rheological effect.

	Excitation force (N)		
Intensity (A)	1	10	50
0	98 Hz	88 Hz	78 Hz
2	114 Hz	100 Hz	86 Hz
MR effect (%)	44	29	21.5

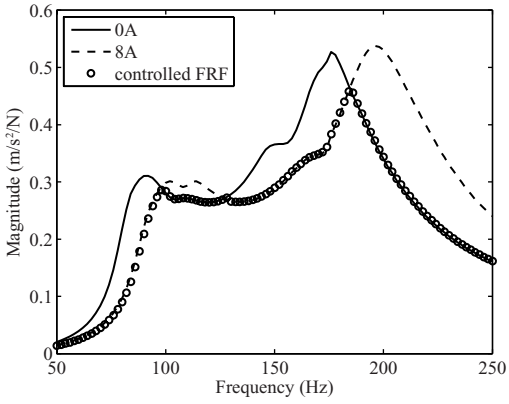

Figure 9. Transfer inertance for zero-field and saturated states with excitation amplitude of 10 N.

4 CONCLUSIONS

A vibration isolation system was experimentally investigated in order to study the effectiveness of using magneto-sensitive natural rubber components as isolators. Laboratory measurements were conducted in the low structure-borne vibration transmission frequency range of interest in a rigid mass support on four MS components and excited by an electro-dynamic shaker. The natural frequencies of the system were shifted approximately 10% when the magnetic field was applied since the MS samples became stiffer. By manually controlling the magnetic field through the samples, resonance peaks could be avoided, reducing the level of the frequency response functions. These results demonstrate the potential of using magneto-sensitive rubber in noise and vibration control in real applications.

ACKNOWLEDGEMENTS

The Basque Government is gratefully acknowledged for the financial support through an aid of the Research Personnel Training Program of the Department of Education, Universities and Research. This research is also supported in part by the Department of Education of the Spanish Government.

REFERENCES

Bellan, C. & Bossis, G. 2002. Field dependence of viscoelastic properties of MR elastomers. *International Journal of Modern Physics B* 10(17 & 18): 2447–2453.

Blom, P. & Kari, L. 2005a. Amplitude and frequency dependence of magneto-sensitive rubber in a wide frequency range. *Polymer Testing* 23: 656–662.

Blom, P. & Kari, L. 2005b. Magneto-sensitive rubber in the audible frequency range. *Constitutive Models for Rubber IV*: 553–556. Netherlands: Balkema.

Blom, P. & Kari, L. 2005c. Smart audio frequency energy flow control by magneto-sensitive rubber isolators. *Smart Materials & Structures* 17(1).

Boczkowska, A., Awietjan, S.F. & Wroblewski, R. 2007. Microstructure-property relationships of urethane magnetorheological elastomers. *Smart Materials & Structures* 16: 1924–1930.

Carlson, J.D. & Jolly M.R. 2000. MR fluid, foam and elastomer devices. *Mechatronics* 10: 555–569.

Chen, L., Gong, X., Jiang, W., Yao, J., Deng, H. & Li, W. 2007. Investigation on magnetorheological elastomers based on natural rubber. *Journal of Materials Science* 42: 5483–5489.

Gil-Negrete, N., Rivas, A. & Vinolas, J. 2005. Predicting the dynamic behaviour of hydrobushings. *Shock and Vibration* 12: 91–107.

Lejon, J. & Kari, L. 2008. The frequency-dependent behaviour of natural rubber based magneto-sensitive rubber with respect to preload, vibrational amplitude and magnetic field strength. *Proceedings of Time Dependent Behaviour of Rubber, London, 30 October 2008*: 1–7.

Lokander, M. & Stenberg, B. 2003a. Performance of isotropic magnetorheological rubber materials. *Polymer Testing* 22: 245–251.

Lokander, M. & Stenberg, B. 2003b. Improving the magnetorheological effect in isotropic magnetorheological rubber materials. *Polymer Testing* 22: 677–680.

Schrittesser, B., Major, Z. & Filipcsei, G. 2008. Dynamic mechanical behaviour of polydimethylsiloxane based magneto rheological elastomers. *Proceedings of Time Dependent Behaviour of Rubber, London, 30 October 2008*: 9–14.

Varga, Z., Filipcsei, G. & Zrinyi, M. 2006. Magnetic field sensitive functional elastomers with tuneable elastic modulus. *Polymer* 47: 227–233.

Yu, Y., Naganathan, N.G. & Dukkipati, R.V. 2001. A literature review of automotive vehicle engine mounting systems. *Mechanism and Machine Theory* 36: 123–142.

Constitutive Models for Rubber VI – Heinrich et al. (eds)
© 2010 Taylor & Francis Group, London, ISBN 978-0-415-56327-7

Representation of dynamic elastomer behavior with focus on amplitude dependency

Herbert Baaser & Guido Hohmann
Freudenberg Forschungsdienste KG, Weinheim, Germany

ABSTRACT: In this article, we present a description and FE implementation of a phenomenological material model incorporating the time-dependent (viscous, dynamic) behaviour of elastomers for industrial applications such as seals and dampers. In particular, we focus on a numerical representation of amplitude dependency in the time domain in addition to the classic viscous descriptions. This PAYNE or FLETCHER-GENT effect results in a decrease in dynamic stiffness with increasing strain amplitude and therefore influences all experimental observations on elastomer materials. In our formulation, the hyperelastic (static) part of the material response is defined on the basis of any freely selected function of strain energy (density), where the branch of time domain viscoelasticity is realised by using a hereditary integral and a PRONY series formulation. In addition, we modify each of the resulting modules in order to account for the amplitude dependency. This approach is based on a factorisation of experimental results and culminates in a scalar weighting of the modules of the PRONY series. An examples from automotive bushing application shows the capability and numerical efficiency of that constitutive description.

1 INTRODUCTION

In this article, we describe a phenomenological material model which simulates the static and dynamic behaviour of elastomers for industrial applications such as seals and dampers. In this connection, we consider viscous, i.e. time-dependent, behaviour in which dynamic stiffness decreases with increasing strain amplitude (PAYNE effect) in addition to frequency dependency. Viscosity is modelled in the time domain by means of a PRONY series whose parameters are determined by a dynamic-mechanical analysis (DMA). In addition, the resulting characteristic modules are modified in order to simulate the influence of the excitation amplitude, see also (Baaser 2007). A similar formulation also results in (Höfer and Lion 2007) due to an expansion of the KRAUS model. We adjust the above-referenced formulation to data which is also gained from these measurements. As shown in Fig. 2, these measurement results indicate an additional dependency on the applied shear angle given as dynamic strain. In Fig. 3, we demonstrate the same results with the reference module $|G|_{\text{ref}}$ at 1% shear, standardised as a function of this equivalent shear. We suggest here to calculate the equivalent shear γ_{eqv} in line with

$$\gamma_{eqv} = \sqrt{\frac{1}{2}(I_1 + I_2) - 3}, \qquad (1)$$

where the first and second invariant of the right or left CAUCHY-GREEN deformation tensor, **C** or **b**, are designated with I_1 and I_2. The core element of this modification for the representation of amplitude dependency is the determination of this typical deformation measurement for the purpose of comparing the local component strain with the shear stress of a DMA measurement, see also Fig. 1. The presented model approach is implemented using the ABAQUS finite-element system by way of the UMAT interface. Consistent derivation of the material tangent ensures the optimum convergence of the equilibrium iteration of the non-linear problem and can thus be used for all element types in simulation. This signifies a gain in efficiency specifically for industrial applications. Taking an example from automotive technology, the efficiency of the model and its implementation are demonstrated.

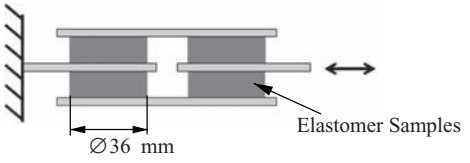

Figure 1. DMA-test specimen under harmonic load applying a "best practice" simple shear mode.

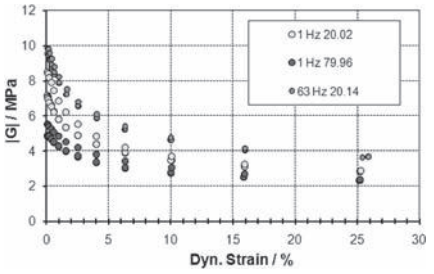

Figure 2. Amplitude dependency: stiffness decrease for increasing amplitudes at 1 hz and 63 hz excitation for temperatures of about 20°C and 80°C.

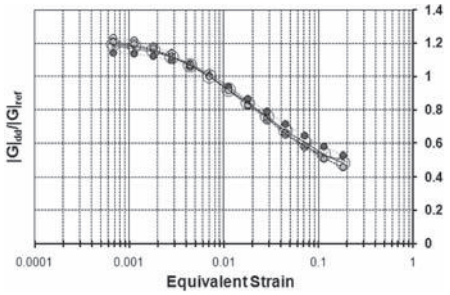

Figure 3. Normalized results of fig. 2 at 1% shear.

2 MECHANICAL MODEL FOR TIME-DEPENDENT BEHAVIOUR

This mechanical model is very largely based on formulations known from technical literature for rate-dependent inelasticity in the case of major deformations. More details can, for example, be found in (Kaliske and Rothert 1998) or (Holzapfel 2000). The key focus here is a three-dimensional extension of the rheological model depicted in Fig. 4. The one-dimensional formulation of response of the situation in Fig. 4 yields in differential equations for each string α. Their 3D generalization is given by

$$\dot{\mathrm{Q}}_\alpha + \frac{\mathrm{Q}_\alpha}{\tau_\alpha} = \dot{\mathrm{S}}_{iso,\alpha}, \tag{2}$$

where the $\mathbf{S}_{iso,\alpha}$ indicate the isochoric parts of the (possibly nonlinear) responses of the springs, and τ_α is the relaxation time of the α'th string. A closed form solution of (2) is given by the time-related convolution of the individual tension rates of a MAXWELL string responses in the stress

$$\mathrm{Q}_\alpha = \mathrm{e}^{-T/\tau_\alpha}\mathrm{Q}_{\alpha 0} + \int_0^T \mathrm{e}^{-(T-t)/\tau_\alpha}\dot{\mathrm{S}}_{iso,\alpha}(t)\mathrm{d}t, \tag{3}$$

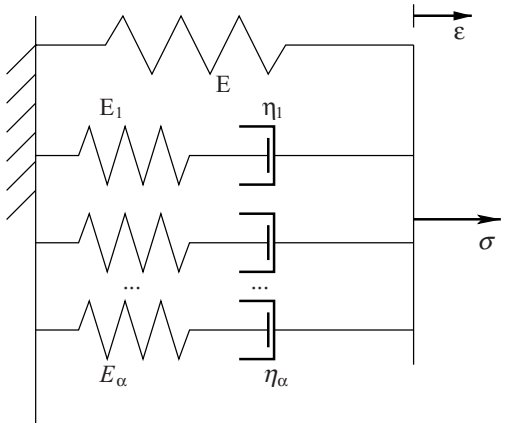

Figure 4. Uniaxial model of viscoelastic behavior by a spring element in parallel to MAXWELL elements (generalized POYNTING-THOMPSON-structure).

for each string. For the numerical implementation of this formulation, (Holzapfel 2000) contains appropriate details and information about implementation, specifically for treatment of the history variables. Within this context, the benefit of the modular structure and thus the flexibility for the treatment of any hyperelastic formulations are shown here. An expanded model with a formulation of the YEOH type is depicted which, in the static case, is adjusted to measurement data from uni-axial tensile tests, see (Baaser et al. 2006) and thus reflects the basic elasticity of the model in the infinite string in Fig. 4.

3 CONSIDERATION OF AMPLITUDE EFFECT BY "BEST DISTANCE" APPROXIMATON

As indicated by experimental findings in Fig. 2, elastomeric materials also demonstrate a distinct decrease in stiffness with increasing amplitude (PAYNE or FLETCHER-GENT effect) due to the polymer-filler interaction, in addition to frequency dependency. In the procedure shown here, we modify the stiffnesses assumed in Fig. 4 with a factor which we obtain from an adjustment using an exponential function, see Fig. 3 and later in (10). Thus, we additionally include an amplitude dependency in the constitutive law as a function of the equivalent shear suggested in (1).

In order to define such "equivalent shear", we are searching for a measure to compare a general deformation **b** to a standardized shear state e.g. given by $\mathbf{b}_{SiSh} = \mathbf{F}_{SiSh} \cdot \mathbf{F}^{\mathrm{T}}_{SiSh}$ in the sense of a "best distance". Assuming a "best practice" simple shear situation realized by a sample in Fig. 1, we characterize that by the deformation gradient

$$\mathrm{F}_{SiSh} = \begin{bmatrix} 1 & \gamma & 0 \\ 0 & 1 & 0 \\ 0 & 0 & 1 \end{bmatrix} \tag{4}$$

with the typical shear angle γ. So, the question arise, how to find an "equivalent shear" γ_{eqv} characterizing the shear portion in an arbitrary state **b**.

Defining a "distance measure"

$$a^2 = (I_1 - I_1^{SiSh})^2 + (I_2 - I_2^{SiSh})^2 \tag{5}$$

of the invariants I_1 and I_2 of **b** compared to them of $\mathbf{b}_{SiSh}$, we can minimize a^2 in (5) in order to obtain γ in (4), because

$$I_{1,2}^{SiSh} = I_{1,2}^{SiSh}(\gamma) = 3 + \gamma^2. \tag{6}$$

Minimization of (5) with respect to γ,

$$\frac{\partial a^2}{\partial \gamma} = -4\gamma(I_1 + I_2) + 8\gamma(3 + \gamma^2) \stackrel{!}{=} 0 \tag{7}$$

gives us $\gamma = \pm\sqrt{1/2(I_1 + I_2) - 3}$, where we define the positve solution as γ_{eqv} as already given in (1).

In the following, we give some examples for that proposal. Given (a) an uniaxial deformation defined by the uniaxial stretch λ_{1ax}, we obtain

$$\gamma_{eqv}^{1ax} = \sqrt{\frac{1}{2}\left(\lambda_{1ax}^2 + \frac{2}{\lambda_{1ax}} 2\lambda_{1ax} + \frac{1}{\lambda_{1ax}^2}\right) - 3}; \tag{8}$$

and (b) a biaxial deformation defined by the stretch λ_{biax}, we obtain

$$\gamma_{eqv}^{biax} = \sqrt{\lambda_{biax}^2 + \frac{1}{2\lambda_{biax}^4} + \frac{\lambda_{biax}^4}{2} + \frac{1}{\lambda_{biax}^2} - 3} \tag{9}$$

All arbitrary deformation modes lie in between these extrem values of uniaxial and biaxial stretch given in Tab. 1 in the case of ideal incompressible material such as elastomeric products in that range of observation. In adddition, to visualize these results, we give (1) plotted as surface over the plane of invariants $I_1 - I_2$ in Fig. 5. So, one can easily get an impression of that proposal for γ_{eqv} in order to determine the shear portion of an arbitrary deformation by the draft computation in (1).

Table 1. Examples for γ_{eqv}.

λ_{1ax}	γ_{eqv}^{1ax}	λ_{biax}	γ_{eqv}^{biax}
1.0	0.0000	1.0	0.0000
1.5	0.7169	1.5	1.5246
2.0	1.2748	2.0	3.0465
2.5	1.7621	2.5	4.7910
3.0	2.2111	3.0	6.8277

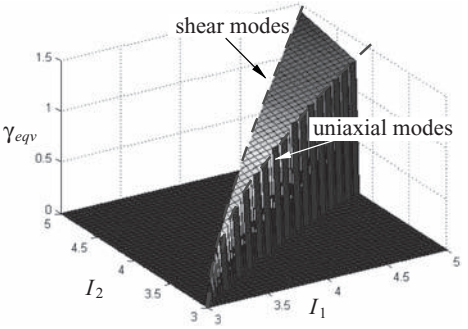

Figure 5. The equivalent shear γ_{eqv} as function of I_1 and I_2 visualized as surface in between arbitrary uniaxial and shear states. The biaxial states can be given in that diagram by mirroring the uniaxial case on the shear line.

4 REALIZATION & IMPLEMENTATION

The formulations described here are implemented in the ABAQUS finite-element system by way of the UMAT interface in FORTRAN77. In accordance with the convention provided there, in this routine, based on the current deformation gradient **F** and on the history data, the CAUCHY stress tensor $\boldsymbol{\sigma}$ and the consistent module $\mathbb{D}$ with respect to the logarithmic deformation value $\varepsilon = \ln(\mathbf{v})$ of the left stretch tensor **v** are calculated in the current configuration and returned. Due to the nonlinearities in the constitutive law, the local solution of an equation system as an integration during the time interval $[t,\mathrm{t} + \Delta t]$ is necessary at the level of the UMAT interface, i.e. each integration point of any element formulation, see (Tsakmakis and Willuweit 2003). We perform this integration using an implicit EULER method, which, as is generally known, is not per se isochoric, see (Baaser 2004). For this reason, an additional constraint condition is included in this equation to obtain material incompressibility.

5 MATERIAL CHARACTERIZATION & PARAMETER CALIBRATION

The material model presented here is adjusted to materials by means of a dynamic-mechanical

analysis (DMA) using defined specimens (see Fig. 1) which are run through by way of a broad temperature window within a frequency range. This means that a master curve of the material is obtained using a temperature-frequency correspondence (WLF shift), see also (Kaliske and Rothert 1998). This curve (see Fig. 6) can be depicted by a PRONY series through the parameter set G_α^{Prony} and τ_α^{Prony} for each string, signifying a direct analogy to the MAXWELL elements in Fig. 4.

As mentioned above, we modify the resulting modules G_α^{Prony} for the purpose of describing the storage and loss portion in addition by factorisation in order to obtain an influence of the strain amplitude in the model. For this purpose, the curve depicted in Fig. 3 is applied to the modules as

$$G_\alpha^{mod}(\gamma_{eqv}) = \frac{A}{1 + B\exp(-k\gamma_{eqv})} G_\alpha^{Prony} \tag{10}$$

permitting an adjustment by means of an exponential function with three parameters A, B, k and, thus, modifying the modules of the MAXWELL strings, see Fig. 4.

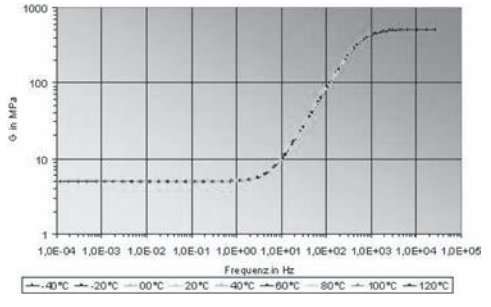

Figure 6. Master curve—storage modulus.

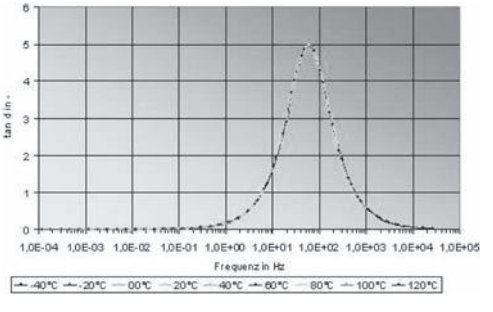

Figure 7. Master curve—loss angle at reference temperature.

6 EXAMPLE & RESULT

Within this context, we consider a typical chassis bushing from an automotive application in a 3D model as depicted in Fig. 8. In order to investigate the influence of amplitude dependency, we use this model to consider torsional stiffness at different torsional angles of up to 7° at a constant excitation frequency. Material properties have been determined for this component by the adjustment described above. As a model response, we analyse the resulting reaction moment as a function of excitation, see Fig. 9. In addition to hysteresis for this strain mode, the quality of simulation is demonstrated there in concurrence with the measurement results. Whereas a simulation with the ABAQUS standard without modification provides an excessively stiff behaviour with regard to amplitude dependency, the amplitude dependency of the material considered in this model is seen as a result. This amplitude dependency is also visible in the structural response and demonstrates a decrease with regard to the standard formulation at a given frequency and amplitude.

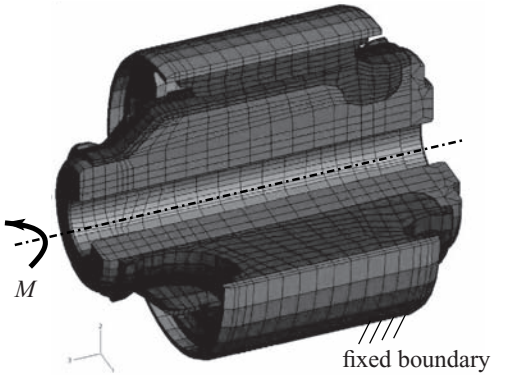

Figure 8. 3D-FEM-Model (cut section) of a bushing from automotive application and depicted torsional moment about z-axis.

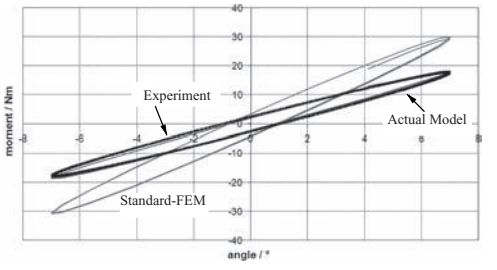

Figure 9. Torsional stiffness about z-axis—7°.

7 SUMMARY & CONCLUSIONS

The numerical implementation of a time-dependent material model in the commercial ABAQUS FE program package is presented here. This material model is also capable of taking into consideration the amplitude dependency of the material response which is known for elastomers. This is achieved by modifying the stiffnesses of the MAXWELL elements in the representation by means of a PRONY series ("factorisation"). The necessary material parameters are calibrated from a dynamic-mechanical analysis. In this way, in addition to the semi-realistic simulation of static elastomer properties, the viscous, i.e. time-dependent, characteristics can be integrated in the numerical model. This now also permits dynamic simulations of overall components which, as indicated here taking the example of a chassis bushing, result in statements about stiffness behaviour depending on the excitation amplitude.

REFERENCES

Baaser, H. (2004). The PADÉ-approximation for matrix exponentials applied to an integration algorithm preserving plastic incompressibility. *Comp. Mechanics* **34**(3), 237–245.

Baaser, H. (2007, Dec). Representation of Elastomers in Industrial Applications. *PAMM 7(1),* 4060011–4060012. online: Mar 31 2008.

Baaser, H., O. Häusler. and C. Ziegler (2006). Ein Materialmodell zur Abbildung von Inelastizitat in Elastomeren. In *ISC.* Stuttgart.

Höfer, P. and A. Lion (2007). Amplitude-dependent phenomena of filler-reinforced rubber: Experiments, modelling and simulation. *PAMM 7(1)*, 4060029–4060030.

Holzapfel, G. (2000). *Nonlinear Solid Mechanics.* Number ISBN 0-471-82304. Wiley.

Kaliske, M. and H. Rothert (1998). Constitutive approach to rate-independent properties of filled elastomers. *International Journal of Solids and Structures 35(17)*, 2057–2071.

Tsakmakis, C. and A. Willuweit (2003). Use of the elastic predictor-plastic corrector method for integrating finite deformation plasticity laws. In K. Hutter and H. Baaser (Eds.), *Deformation and Failure in Metallic Materials.* Springer.

Constitutive Models for Rubber VI – Heinrich et al. (eds)
© 2010 Taylor & Francis Group, London, ISBN 978-0-415-56327-7

Viscoelastic properties of filler reinforced elastomers

M. Klüppel & J. Fritzsche
Deutsches Institut für Kautschuktechnologie e.V. Hannover, Germany

ABSTRACT: For a better understanding and for getting a deeper insight into structure and dynamics of filler reinforced elastomers, it is important to investigate the relations between filler network morphology, interphase dynamics and bulk viscoelastic properties on a broad frequency scale. In the present work, dynamic-mechanical and dielectric spectra of silica and carbon black filled S-SBR samples are studied in a wide frequency and temperature range. For the creation of dynamic-mechanical master curves frequency dependent measurements at different temperatures are applied to cover a larger frequency range. It is demonstrated that the time-temperature-superposition (TTS)-principle is not fulfilled for filled elastomers and the introduction of vertical shift factors is necessary to obtain viscoelastic master curves. The changes in the dynamic-mechanical properties by the incorporation of fillers and the failure of the TTS-principle in the low frequency (high temperature) regime are shown to be related to the superimposed dynamics of the filler network. It is governed by the viscoelastic response of glassy-like polymer bridges between adjacent filler particles, which differs from that of the polymer matrix. The reduced chain mobility close to the filler interface becomes apparent by a broadening of the glass transition on the low frequency side.

1 INTRODUCTION

Traditional filler like carbon black or silica have long been used for reinforcement of elastomers especially in mechanical purposes. Recently the physical improvement of polymers using nanoparticles like silicate nanoparticles, organoclays or nanotubes became more and more important. The employment of these nanoparticles remains in an increasing interest in understanding the changes in dynamic and structural properties caused by fillers and nanoparticles. In particular, the use of the traditional fillers results in improved resistance to wear and tear, decreasing heat build up, increased stiffness as well as increased fatigue resistance and abrasion resistance (Kraus 1965). But up to now the origin of this reinforcement effects is only partly known. Years ago it was suggested that the reinforcement of polymers is accompanied by the formation of immobilized polymer layers due to the interfacial interaction between the polymer matrix and filler, which leads to a general change in thermodynamic properties of the system. The existence of glassy-like polymer layers was proposed by different authors based on results obtained by NMR- and dielectric spectroscopy and mechanical analysis. Additionally various authors reported measurements on thin polymer films showing that the measured glass transition temperature of these films strongly depends on the thickness of the polymer layer. In dependence of the substrate causing an attractive or repulsive interaction with the polymer an increase or a decrease of the glass transition temperature with decreasing layer thickness could be found (Hartmann et al. 2003, Soles et al. 2004, Grohens et al. 2002). These results have been confirmed by simulations and analytical studies concerning the change of dynamics next to filler surfaces (Starr et al. 2002, Douglas & Freed 1997).

Recently (Long & Lequeux 2001) developed a thermodynamic model giving an interpretation of these phenomena. They proposed that the viscosity close to the glass transition is determined by slow dynamic domains resulting from thermally induced density fluctuations and the glass transition process originates in the percolation of these slow domains. They found that the percolation threshold depends on the interaction between polymer and substrate. For strongly interacting polymer films the threshold is lower due to the emergence of additional rigid paths through the substrate. Thus, the dynamics are modified near the surface resulting in a dependence of the glass transition temperature $T_g(\omega)$ on the distance from the surface. This implies a glassy-like polymer shell with temperature and frequency dependent thickness surrounding the filler particles. In various investigations (Berriot et al. 2002, Berriot et al. 2003) were able to show that this concept allows to describe quantitatively some typical effects on the dynamic-mechanical modulus with the

incorporation of filler. However, with a certain amount of filler additionally the influence of the filler network has to be taken into account which was not considered by (Long & Lequeux 2001). The role of filler networking in different aspects of rubber reinforcement has been investigated by several authors. A review is given in (Heinrich & Klüppel 2002, Klüppel 2003). In particular, it has been demonstrated that, driven by osmotic depletion forces, filler networking takes place during heat treatment or vulcanization. Due to strong polymer-filler couplings the polymer between adjacent filler particles is not squeezed out totally and characteristic gaps remain. The confined polymer in these gaps is strongly immobilized and forms glassy-like bridges between adjacent filler particles transmitting the stress through the filler network (Klüppel 2003, Klüppel & Heinrich 2005, Le Gal et al. 2005). Since viscoelastic response of the filler network results from the stiffness and viscose losses of the immobilized polymer bridges the small strain elastic modulus of highly filled composites can be traced back to the specific viscoelastic properties of the glassy bridges, i.e. the filler-filler bonds (Klüppel 2003, Meier & Klüppel 2008.

The viscoelastic properties are important entities for several rubber technological applications like friction and fracture mechanics. It was demonstrated by (Le Gal et al. 2005, Le Gal & Klüppel 2008) how viscoelastic master curves can be used for modeling the dry and wet friction behavior of elastomers on rough surfaces. In addition, it has been shown by (Klüppel 2009) how viscoelasticity impacts the fracture mechanical properties as the crack growth rate of elastomers under cyclic loading.

In the present paper we will address some open questions related to micro-mechanical mechanisms affecting the viscoelastic properties of filled elastomers. Therefore we will analyze a solution styrene butadiene rubber filled with different loadings of silica and carbon black, respectively. The silica is silanized with silane as a coupling agent to provide a chemical bonding between filler and polymer. We will focus on the investigation of the dynamic-mechanical behavior using horizontal shift factors determined by dielectric-relaxation spectroscopy for creation of dynamic-mechanical master curves based on the time-temperature-superposition principle. The results will be discussed by referring to a thermal activation of filler-filler bonds and the viscoelastic response of the filler network together with the glass transition gradient model introduced by (Long & Lequeux 2001) focusing on a qualitative understanding of the filler induced changes in the dynamic-mechanical properties.

2 EXPERIMENTAL

2.1 *Sample preparation*

The samples have been prepared with the styrene-butadiene rubber (VSL 2525-0, 25% styrene content, 25% vinyl content, Lanxess, Germany), which was filled with different loadings of silica (Ultrasil GR 7000, Evonik Degussa GmbH, BET surface area) and carbon black (N339). For the silica filled samples the content of silane TESPT (Bis-(triethoxy-silylpropyl) tetrasulfane) was varied between 1.7 and 6.7 phr in dependence of the filler content due to the changing amount of reactive silanole groups with increasing filler content. Furtheremore, 3 phr zinc oxide, 1 phr stearic acid, 2 phr N-isopropyl-N'-phenyl-p-phenylendiamine (IPPD), 2,5 phr n-cyclohexyl-2-benzothiazole-sulfenamide (CBS) and 1,7 phr soluble sulfur were used as vulcanisation system.

The composites were prepared in an internal mixer rotating at 50 rpm in a multi-step-mixing procedure. At first the rubber and the silica were mixed in the internal mixer at 140°C. The silane was added for in-situ-silanisation at 150°C and the silanisation reaction was performed during 10 min. In second step after 24 hours the masterbatch was again mixed in the internal mixer at 130°C for 8 min to ensure the silanization reaction is completed. In a third step the rest of anti aging additives and curatives was added at 40°C on the two-roll mill. The curing study was carried out with the help of a rheometer (Monsanto ME 2000) at 160°C. The samples were cured under pressure at 160°C to 2 mm plates in dependence of the determined t_{90} vulcanization time.

2.2 *Dielectric and DMA measurements*

Dielectric investigations have been carried out in a wide temperature range (–100°C to +100°C) and at frequencies from 0.1 Hz to 10 MHz using a broadband dielectric spectrometer BDS 40 (Novocontrol GmbH, Germany). The temperature was varied in five-degree steps using the temperature control system Novocool. The temperature uncertainty amounts to ±0.5°C. The measured geometry was a disc shaped plate capacitor with a diameter of 40 mm. The sample with a thickness of 2 mm was placed between two gold-plated electrodes. To provide an excellent contact between sample and electrodes thin gold layers have been sputtered onto the flat surface of the sample plate. A force-limiting spring was used to ensure that always the same clamping force was exerted onto the test-capacitor keeping thickness and electrical contact as comparable as possible between different samples. The dielectric permittivity and the dielectric loss have been recorded for each sample in dependence of temperature and frequency.

The dynamic-mechanical measurements were performed in the torsion-rectangular mode with strip specimen of 2 mm thickness and 30 mm length with an ARES rheometer (Rheometrix). The dynamic moduli were measured over a wide temperature range (–80°C to +80°C) at a frequency of 1 Hz and 0.5% strain amplitude for temperature dependent measurements. For creating dynamic-mechanical master curves frequency dependent measurements have been performed at different temperatures between +60°C and –60°C in five degree steps varying the frequency between 0,01 Hz and 16 Hz. The strain amplitude was kept constant at 0.5%.

3 RESULTS AND DISCUSSION

Dynamic-mechanical measurements have been performed by varying the frequency at various constant temperatures. By applying the time-temperature superposition principle for the unfilled polymer the different branches have been shifted horizontally to obtain viscoelastic master curves. The horizontal shift factors obtained in this way for the unfilled sample are plotted as a function of temperature in Fig. 1.

As reference temperature $T_{ref} = 293.5\ K$ is chosen. In addition, the horizontal shift factors for the unfilled and filled samples have been determined using dielectric relaxation spectroscopy by extracting the local maxima of the dielectric loss of the glass transition process. Previous investigations have shown that this procedure is successful since the underlying cooperative processes causing the glass transition process are identical in both investigation measurement methods (Le Gal et al. 2005). The resulting shift factors for the unfilled sample and the samples filled with 40 phr and 80 phr of Silica are also included in Fig. 1.

Obviously, the location of the glass transition of the matrix, indicated by the loss maxima, is not affected by the presence of filler. Accordingly, all samples can be described by a single set of horizontal shift factors. The solid line in Fig. 1 demonstrates that all samples can be fitted by the well known WLF equation:

$$\log a_T = \frac{-C_1\ (T - T_{ref})}{C_2 + T - T_{ref}} \tag{1}$$

The horizontal shift factor is defined as the ratio of relaxation times $a_T = \tau\,(T)\,/\tau\,(T_{ref})$. The resulting WLF-constants are found as $C_1 = 5.15$ and $C_2 = 126.57$°C. We point out that the identical set of horizontal shift factors for the unfilled and filled samples does not mean that the whole dynamics of the polymer matrix remains unchanged, since a broadening of the glass transition loss maximum is generally observed with increasing filler loading.

Figure 2 shows the constructed master curves for unfilled and filled samples by applying the single set of horizontal shifting factors obtained in Fig. 1 by the adaptation to Equ. (1). It demonstrates explicitly that the horizontal shifting leads to a well matching master curve for the unfilled samples. For the filled samples with increasing filler content a increasing discontinuity of the single branches at low frequencies is observed. Obviously in these cases the time-temperature superposition is not fulfilled. The data in Fig. 2 show that master curves for unfilled polymer networks or melts can be constructed on a broad frequency scale by applying

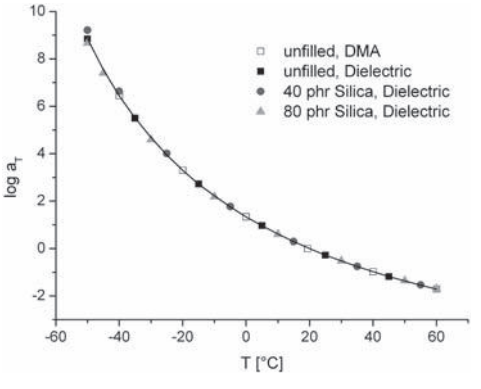

Figure 1. Horizontal shift factors determined by dynamic-mechanical spectroscopy (open symbol) and dielectric spectroscopy (filled symbols); The solid line represents a fit according to the WLF-Equ. (1).

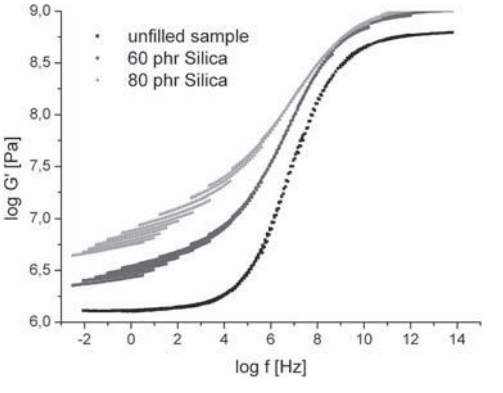

Figure 2. Master curve of the unfilled sample and the samples filled with 60 phr and 80 phr of silica created with horizontal shift factors from Fig 1.

the time-temperature superposition principle. This is based on the fact that all characteristic relaxation times, as e.g. Rouse relaxation- or tube reptation time, can be traced back to the temperature dependent diffusion time of the monomer units on a molecular length scale. For polymer blends with different glass transition temperatures or filled elastomers with interpenetrating networks this is no longer the case, since the mechanical response results from additive network contributions with different dynamics. This kind of superposition of interpenetrating networks with different relaxation behavior implies that one network component is governing the mechanical response of the whole system in a certain temperatures or frequency regime and the other component in another.

In the case of filler reinforced elastomers the low temperature (high frequency) mechanical response mainly results from the glassy polymer matrix, while the high temperature (low frequency) response is dominated by the filler network, provided the filler network is significantly stiffer than the polymer matrix (Klüppel 2003). Accordingly, at low frequencies the Arrhenius like thermal activation of the filler network, resulting from the immobilized polymer bridges between adjacent filler particles, can not be compensated by the WLF-like horizontal shifting factors of the polymer matrix and discontinuous branches are found for the filled samples in Fig. 2. Fair overlapping of the branches can only be obtained at high frequencies beyond the glass transition of the matrix, which then dominates the mechanical response of the system.

Since it was demonstrated that the horizontal shift factors are independent of the filler content it was necessary to use vertical shift factors to compensate the mismatches. An Arrhenius-plot of the vertical shift factors necessary to obtain G' master-curves for the silica filled samples is shown in Fig. 3. For all filled samples a fair linear behavior of the vertical shift factors is found in the temperature range above the glass transition of the matrix indicating a thermally activated process causes the deviation in the master curves. The slope can be interpreted as an apparent activation energy of the filler network, resulting from glassy-like polymer bridges between adjacent filler particles which form the filler-filler bonds (Klüppel 2003, Heinrich & Klüppel 2004, Klüppel & Heinrich 2005, Meier et al. 2007, Meier & Klüppel 2008).

The so obtained activation energies are summarized in Table 1. They increase almost linearly with increasing filler loading, indicating that there is a change of the dynamics of the glassy bridges resulting either from an decreasing gap size of filler-filler bonds or from an increasing influence of overlapping regions of adjacent filler particles

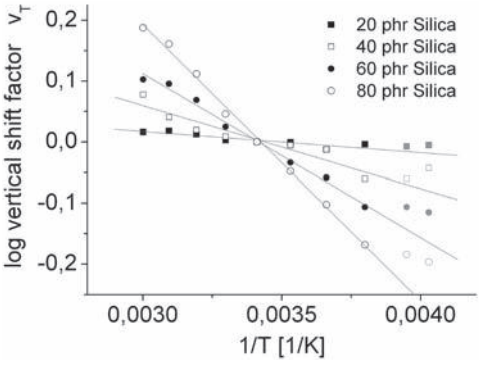

Figure 3. Arrhenius dependence of the vertical shift factors necessary to obtain G' master-curves for the silica filled samples.

Table 1. Comparison of the activation energies determined by temperature dependent measurements of G' (Fig. 6) and vertical shifting to obtain G' master-curves for the silica filled samples depicted in Fig. 3.

	Temperature sweeps	Vertical shifting
0 phr	0.03 ± 0.02 kJ/mol	0 kJ/mol
20 phr	0.93 ± 0.10 kJ/mol	0.66 ± 0.12 kJ/mol
40 phr	3.26 ± 0.06 kJ/mol	2.62 ± 0.36 kJ/mol
60 phr	6.66 ± 0.18 kJ/mol	5.15 ± 0.2 kJ/mol
80 phr	11.22 ± 0.20 kJ/mol	8.67 ± 0.2 kJ/mol

with rising filler concentration. This correlates with the experimental observation that the glass transition temperature of ultra-thin films between attractive walls decreases strongly with film thickness if the thickness falls below 20 nm (Hartmann et al. 2003, Soles et al. 2004, Grohens et al. 2002). The gap size between adjacent filler particles of the filler network typically lies in the range of a few nm (Meier et al. 2007, Meier & Klüppel 2008), implying strong effects of the gap spacing on mechanical properties of filler-filler bonds, e.g. stiffness, strength or activation energy.

The final dynamic-mechanical G' master curves of the silica filled samples after applying horizontal and vertical shifting are shown in Fig. 4. An increasing frequency dependence of the master curves at low frequencies is observable with increasing filler loading. Since the filler network is dominating the mechanical response in the low frequency regime we can conclude that this behavior is due to an increasing stiffness of the filler network. Accordingly, the observed frequency dependence is due to the frequency response of the glassy-like polymer bridges between adjacent filler particles forming the filler-filler bonds. Nevertheless, with rising

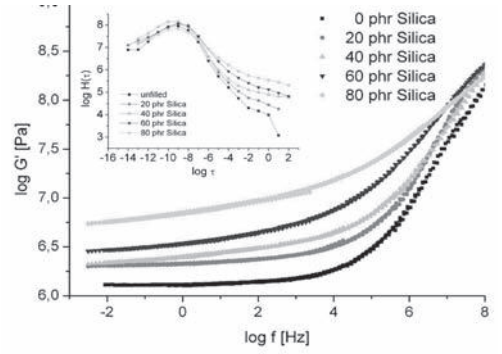

Figure 4. G' master curves of the silica filled samples after application of horizontal and vertical shifting; Inset: Relaxation time spectra of the samples calculated according to Equ. (2).

frequency just below the glass transition frequency an additional effect results from the growing polymer shells with slowed-down dynamics around the filler particles. This effect becomes more pronounced for large loadings, since the amount of polymer matrix forming a gradient of reduced mobility in the vicinity of the filler surface is increasing with filler concentration. Furthermore, for large filler loadings an overlap of regions with slowed down dynamics of different filler particles has to be taken into account. The sum of these effects can be related to the observed broadening of the glass transition regime on the low frequency side with increasing filler loading.

The role of filler-filler bonds, on the one side, and the slowed-down dynamics close to filler particles, on the other side, in dynamic-mechanical properties can be analyzed on different time scales by referring to the relaxation time spectra depicted in the inset of Fig. 4. They have been calculated from the master curves of G' according to the iterative approximation method of Williams and Ferry (Williams & Ferry 1953, Ferry 1980):

$$H(\tau) = AG'd\log G'/d\log\omega\big|_{1/\omega=\tau} \quad \text{for } p<1$$

$$\text{with } A=(2-p)\Big/2\Gamma\left(2-\frac{p}{2}\right)\Gamma\left(1+\frac{p}{2}\right) \qquad (2)$$

Here p is the local slope of H at $\tau = 1/\omega$, which must be smaller than one, and Γ is the gamma function. The inset of Fig. 4 demonstrates that the presence of fillers modifies the behavior of the relaxation time spectrum during the glass transition, i.e. a less pronounced drop of relaxation time contributions is found. On time scales 10^{-8} to 10^{-3} s a power law behavior $H \sim \tau^{-m}$ is more or less realized and the scaling exponent increases from about $m = 0.6$ to 0.4 with increasing filler loading. This is related to the observed broadening of the glass transition in Fig. 4. It is expected to result from the slowed-down dynamics close to filler particles. Nevertheless, a full theoretical understanding of the modified power law exponent due to confined polymer shells around filler particles is outstanding so far. Furthermore, one observes a considerable contribution of relaxation times larger than 10^{-3} s which also increases with filler loading. This relaxation at longer time scales is attributed to the filler network.

The dynamic-mechanical master curves of both, G' and G'', for the carbon black filled samples after applying horizontal and vertical shifting are depicted in Figs. 5a and 5b, respectively. Fig. 5c

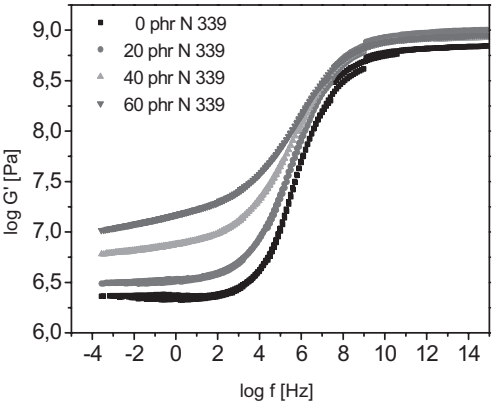

Figure 5a. G' master curves of the carbon black filled samples after application of horizontal and vertical shifting.

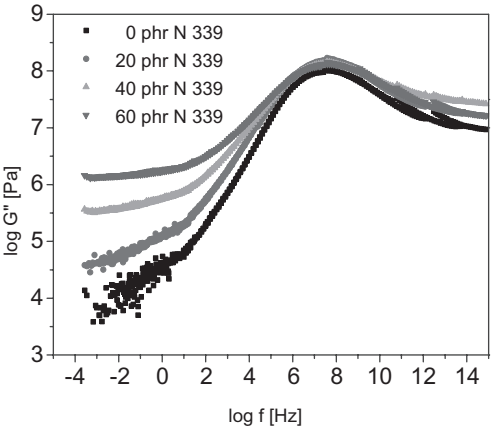

Figure 5b. G'' master curves of the carbon black filled samples after application of horizontal and vertical shifting.

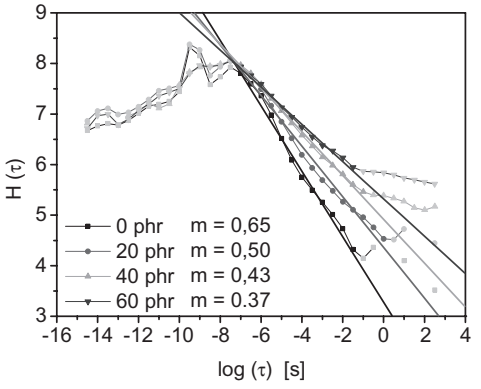

Figure 5c. Relaxation time spectra of the carbon black filled samples calculated according to Equ. (2). The inserted regression lines correspond to a power law behavior $H \sim \tau^{-m}$.

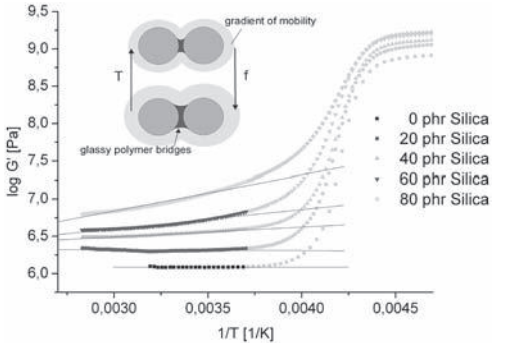

Figure 6. Arrhenius plot of the temperature dependent measurements of the storage modulus of the silica filled samples; Inset: Schematic view of modified polymer dynamics in the vicinity of filler particles.

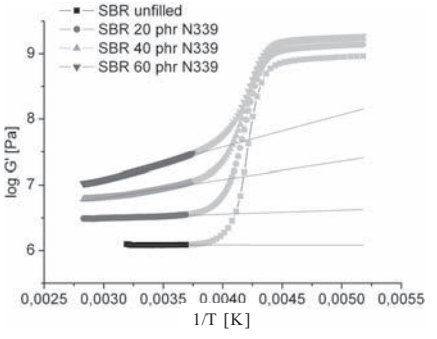

Figure 7. Arrhenius plot of the temperature dependent measurements of the storage modulus of the carbon black filled samples.

shows the relaxation time spectra obtained with Equ. (2) from the G' master curves at various filler content. The results are similar to the behavior of the silica filled samples depicted in Fig. 4. Again, the observed frequency dependence in the low frequency regime can be related to the frequency response of the filler network or more precisely the filler-filler bonds, consisting of glassy-like polymer bridges between adjacent filler particles (primary carbon black aggregates). At intermediate frequencies, a broadening of the glass transition regime with increasing filler loading is observed due to the growing polymer shells with slowed-down dynamics around the filler particles. This effect results in a less pronounced drop of the relaxation time spectra during the glass transition on time scales 10^{-8} to 10^{-1} s, where a power law behavior $H \sim \tau^{-m}$ is observed. As depicted in Fig. 5c, the slope m decreases systematically with filler loading due to the increasing amount of interphase. The additional contribution at relaxation times larger than 10^{-1} s is attributed to the filler network.

The impact of the filler network with thermally activated filler-filler bonds can also be observed for the temperature dependent viscoelastic data. An Arrhenius-plot of the storage modulus G' measured at 1 Hz is shown in Figs. 6 and 7 for the silica and carbon black filled samples, respectively. As indicated by the inserted regression lines one observes a thermal activation of G' in the high temperature range, which becomes more pronounced with increasing filler content. This effect is typical for elastomers filled with highly reinforcing fillers (Heinrich & Klüppel 2002, Heinrich & Klüppel 2004). In a plot of log G' as a function of the inverse temperature the differences in this behavior with increasing filler content can be quantified calculating the value for the slope n in a defined temperature range following an Arrhenius like behavior. The slope $n = -E_A/R$, where R is the gas constant, corresponds to an activation energy which is physically related to the thermal activation of the filler-filler bonds. In analogy to the vertical shifting factors depicted in Fig. 3, this slope is increasing with increasing filler content, resulting in an increasing activation energy of the glassy bridges. But as slightly visible in Figs. 6 and 7, the linear function dominates the behavior of log G' in dependence of the inverse temperature but do not describe the behavior of G' completely. An underlying potential function, introduced in (Berriot et al. 2002, Berriot et al. 2003) describes the change of the elastical modulus due to the increase of the thickness of a glassy shell around the filler particles with decreasing temperature (Long & Lequeux 2001). Both effects are difficult to separate, though the most

significant contribution of the growing shells results close to the glass transition temperature T_g leading to the observed broadening of the glass transition on the high temperature side. For temperatures higher than about T_g + 30°C the Arrhenius-fits in Figs. 6 and 7 represent a reasonable description of the experimental data, confirming the conclusion from the frequency dependent data (Fig. 3) that the filler network is dominating the behavior of G' in the low frequency or high temperature regime. The systematic deviations from the Arrhenius behavior at higher temperatures can be explained by an increase of the cross-section of the glassy-like polymer bridges (filler-filler bonds) with decreasing temperature as indicated in the inset of Fig. 6.

A comparison of the activation energies resulting from vertical shifting and temperature dependent measurements of the silica filled samples is shown in Tab. 1, giving slightly higher values for the activation energies obtained by temperature dependent measurements. Furthermore, with increasing filler content the difference between the activation energies is increasing. This can be related to the stronger incline of the frequency dependent modulus with increasing filler content observed in Fig. 4, indicating a more pronounced stiffening of filler-filler bonds. Accordingly, the horizontal shifting compensates larger parts of the thermal activation of filler-filler bonds as derived from the temperature dependent measurements in Figs. 6 and 7. We finally point out that the detected characteristic load dependence, i.e. the increase of the activation energy and the stronger frequency response of glassy-like polymer bridges indicate that the bond length or gap distance decreases slightly with increasing filler concentration leading to filler-filler bonds with different mechanical properties and relaxation dynamics.

4 CONCLUSIONS

It has been shown that the viscoelastic response of the viscoelastic moduli, G' and G'', of filler reinforced elastomers at high temperatures (low frequencies) is due to a combination of two effects: On the one hand side, the slowing down of the dynamics of the polymer matrix close to the filler surface leads to a broadening of the glass transition on the high temperature (low frequency) side. This may be considered by an underlying potential function, which describes the thickness of a glassy layer around filler particles. On the other hand side, due to its higher stiffness compared to the polymer matrix, the filler network governs the dynamic-mechanical properties of the composites in the high temperatures (low frequency) regime. Accordingly, the viscoelastic response is due to glassy-like polymer bridges between adjacent filler particles. In a plot of log G' against the inverse temperature an Arrhenius like behavior is obtained, which describes the thermal activation of filler-filler bonds (Figs. 6 and 7).

Since the viscoelastic response of the filler network, i.e. glassy-like polymer bridges, differs from that of the polymer matrix, the time-temperature superposition principle is not fulfilled. This implies a failure of the master procedure making the introduction of vertical shift factors necessary (Fig. 2). The vertical shift factors show an Arrhenius like behavior, which can again be related to the activation energy of glassy-like polymer bridges (Fig. 3). At low frequencies, the resulting master curves of the storage modulus reflect the increasing stiffness of filler-filler bonds with rising frequency. At intermediate frequencies just below the glass transition, an additional stiffening of the composite results due to an increasing thickness of the glassy polymer layers around filler particles (Figs. 4 and 5).

ACKNOWLEDGEMENTS

This work was supported by the Deutsche Forschungsgemeinschaft (SPP 1369) and the Bundesministerium für Bildung und Forschung (BMBF, 03X0002D).

REFERENCES

Berriot, J., Montes H., Lequeux, F., Long, D. & Sotta, P. 2002 *Macromolecules* 35:9756.

Berriot, J., Montes H., Lequeux, F., Long, D. & Sotta, P. 2003 *Europhysics Letters* 64(1):50.

Douglas, J.F. & Freed, K.F. 1997. *Macromolecules* 30:1813.

Ferry, J.D. 1980. *Viscoelastic Properties of Polymers*, J.Wiley & Sons, 3rd Edition.

Grohens, Y., Hamon, L., Reiter, G., Soldera, A. & Holl, Y. 2002. *Eur. Phys. J. E*, 8: 217.

Hartmann, L., Fukao, K. & Kremer, F. 2003. Molecular dynamics in thin polymer films. In Kremer, F., Schönhals, A. (eds.) *Broadband dielectric spectroscopy*, Springer: Berlin, Heidelberg, New York.

Heinrich, G. & Klüppel, M. 2002. Recent Advances in the Theory of Filler Networking in Elastomers. *Adv. Polym. Sci.* 160: 1.

Heinrich, G. & Klüppel, M. 2004. *Kautschuk Gummi Kunststoffe* 57: 452.

Klüppel, M. 2003. The Role of Disorder in Filler Reinforcement of Elastomers on Various Length Scales. *Adv. Polym. Sci.* 164: 1.

Klüppel, M. 2009. Evaluation of viscoelastic master curves of filled elastomers and applications to fracture mechanics. *J. Phys.: Condens. Matter* 21:035104.

Klüppel, M. & Heinrich, G. 2005. *Kautschuk Gummi Kunstst.* 58:217.

Klüppel, M. & Meier, J. 2001. Modeling of Soft Matter Viscoelasticity for FE-Applications. In D. Besdo, R.H. Schuster & J. Ihlemann (eds), *Constitutive Models for Rubber II*, Lisse: Balkema.

Klüppel, M., Meier, J. & Heinrich, G. 2003. Impact of Pre-Strain on Dynamic-Mechanical Properties of Carbon Black an Silica Filled Rubbers. In J.J.C. Busfield & G.A.H. Muhr (eds), *Constitutive Models for Rubber III*. Lisse: Balkema.

Kraus, G. (ed.) 1965. *Reinforcement of elastomers*. N.Y. London Sydney: Wiley, Interscience Publ.

Le Gal, A., Yang, Y. & Klüppel, M. 2005. *J. Chem. Phys.* 123: 014704.

Le Gal, A. & Klüppel, M. 2008. Investigation and Modelling of Rubber Stationary Friction on Rough Surfaces *J. Phys.: Condens. Matter* 20:015007.

Long, D. & Lequeux, F. 2001. *Eur. Phys. J. E* 4:371.

Meier, J.G., Mani, J.W. & Klüppel, M. 2007. *Phys. Rev. B* 75: 054202.

Meier, J.G. & Klüppel, M. 2008. *Macromol. Mater. Eng.* 293:12.

Starr, F.W., Schrøder, T.B. & Glotzer, S.C. 2002. *Macromolecules* 35:4481.

Soles, C.L., Douglas, J.F. & Wu, W.-L. 2004. *J. Polym. Sci, Part B* 42:3218–3234.

Williams, M.L. & Ferry, J.D. 1953. *J. Polym. Sci.* 11:169.

Constitutive Models for Rubber VI – Heinrich et al. (eds)
© 2010 Taylor & Francis Group, London, ISBN 978-0-415-56327-7

Simulation of self-heating of dynamically loaded elastomer components

Volkmar Mehling & Herbert Baaser
Freudenberg Forschungsdienste KG, Computer Aided Engineering, Weinheim, Germany

ABSTRACT: Heat generated by internal dissipative processes results in high temperatures within thick-walled rubber components, because of the low heat conductivity of elastomeric materials. However, temperature strongly influences the mechanical properties and is a crucial factor for lifetime and fatigue. It is therefore of vital interest, to predict operating temperatures inside of dynamically loaded elastomer components as well as their mechanical response at operating temperature. We present a method to simulate the stationary temperature distribution within elastomeric components on the basis of a weak coupling of a stationary heat-transfer with a visco-elastic loading analysis. It takes into account the temperature dependency of the material properties on one hand and the inhomogeneous heat generation by visco-elastic dissipation on the other. An iterative scheme is implemented, utilizing ABAQUS as Finite-Element-Solver for the mechanical and thermal problems. The simulation is compared to an analytical solution and the application to an inhomogeneous loading of a rubber component is presented.

1 INTRODUCTION

Rubber is a living material of high complexity. Todays applications however demand for high accuracy in the estimation of the behavior of elastomeric components by numerical simulation through the whole life-cycle. Therefore, a large number of models deals with the description of the mechanical behavior of rubber under different loading conditions, and their change in time due to fatigue and ageing. Even when the focus is set on the mechanical properties, it must not be forgotten, that the underlying mechanisms are driven by physical as well as chemical processes. This is why all properties of rubber are highly temperature dependent and constitutive models for rubber are either temperature dependent, or only valid for certain constant temperatures. Therefore, the knowledge of the temperature and its distribution throughout the volume of a component is essential for a highly accurate prediction of its behavior. Examples of test specimen have shown, that the self-heating can change from uncritical to destructive in the same experimental setup, when the rubber hardness is changed by only 5 ShA.

There are three possible sources of temperature development in rubber components: First, heat flowing through the surface of the rubber volume, i.e. by convection or radiation from the environment or by heat flow to or from attached parts. Second, heat can be generated by external radiation in the bulk. Both heat sources are controlled externally. In a heat-transfer analysis they appear as boundary or loading conditions. This is different for the third source, which is the heat production by internal dissipation. This dissipation is due to viscous hysteresis and internal friction in the material. It couples mechanical and thermal processes and cannot be captured as easily as the other sources of heat mentioned above. High temperatures result from heat production on the one hand and from low heat conductivity on the other. Rubber materials are known for their low heat conductivity. Therefore, in the case of dynamical loading, this can lead to considerably high temperatures, especially in components with large rubber bulk volume, even when the dissipation is held at a low level.

This work is dealing with the estimation of the selfheating by dynamical loading in a visco-elastic framework. The focus is set on the evaluation of stationary temperature distributions in the case of periodic deformation. The presented method provides a tool for the practical analysis of temperature distributions in elastomer components as precondition for a more efficient use of all temperature-dependent mechanical material models and a further reduction of product development time and costs.

2 SELF-HEATING MODEL

2.1 *Coupling of mechanics and heat-transfer*

The description of self-heating requires the consideration of mechanical and thermal fields and the coupling between both. The mechanical part of the problem deals with motion and deformation and

the connected forces. The second field concerns the flow of heat within a volume by heat-transfer. There are many constitutive models for the mechanical behavior of various materials. Their application in numerical simulation by the finite element method (FEM) is state of the art. Similarly, the theory of heat-transfer is well established (Baehr & Stephan, 1994). Our interest is aimed at the combination of both in a coupled analysis.

There are two mechanisms of coupling: During mechanical processes energy is lost due to dissipation. Dissipated energy is transformed into heat and must therefore appear in the heat-transfer problem as local power of heat. On the other hand, the mechanical properties of materials—especially of rubber—depend on the temperature. Therefore, the temperature distribution within the structure influences the mechanical response.

A possible strategy for the solution of the coupled problem could be the simultaneous solution of the complete set of equations. This would require a numerical tool that provides all necessary interfaces. This is not straight forward and possible only with deeper involvement in the architecture of the numerical tool. A different approach is a so-called weak coupling of both types of analysis. It has the advantage to combine the perfectly well established solutions of the two related subproblems, provided by most FEM-software packages. The mechanical and the heat-transfer problems are solved separately from each other. However, they are coupled by an iterative scheme, where the average power of dissipation is taken from the mechanical simulation result and entered into the heat-transfer analysis as local power of heating. On the other hand, the temperature distribution resulting from the latter is introduced into a new mechanical simulation in the next iteration step as initial condition, allowing for a correct description of the mechanical material behavior at every point of the model due to the local temperature and thermal expansion. The result is a new distribution of power of dissipation, and so on. This scheme is repeated in a loop until all fields have converged, see Figure 1.

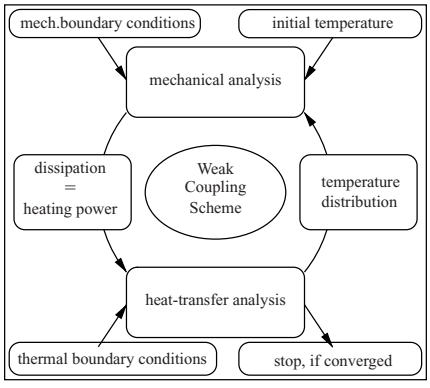

Figure 1. Iteration scheme—weak coupling of mechanical and heat-transfer analysis.

2.2 *Mechanical constitutive model*

The dynamical material properties are often measured by dynamic-mechanical analysis (DMA) for a fixed amplitude and a range of temperatures and frequencies. The results of this analysis e.g. in the form of master-curves for storage and loss moduli, G' and G'' resp., and temperature-frequency shift-functions describe a combination of viscous and frictional dissipative effects. The latter are often associated to the fracture and recombination of filler-clusters, while the former are assumed to trace back to the gliding of polymer chains in the rubber compound. It is difficult to distinguish both from each other. Therefore it is common practice to model the dynamical constitutive behavior of rubber as linear visco-elastic—well aware of the fact, that certain effects like amplitude-dependency (Payne) or static hysteresis cannot be reproduced by such a model and that limits of linearity must be checked in the specific case, see e.g. (Schwarzl, 1990).

We follow this simplified approach, assuming, that the viscous dissipation predicted by the visco-elastic model is representative for the total dissipation in the material. Then, the average local dissipation density can be calculated by a visco-elastic analysis of a complete stationary loading cycle from time t_0 to t_1 as

$$d = \frac{1}{t_1 - t_0} \int_{t_0}^{t_1} \sigma \cdot \dot{\varepsilon} \, \mathrm{d}t \tag{1}$$

In a uniaxial loading situation the integral in equation (1) yields the area inside one stationary hysteresis loop in the σ over ε plot.

2.3 *Heat-transfer problem*

The thermal subproblem is described by Fouriers law

$$q_i = -\lambda \frac{\partial T}{\partial x_i}, \tag{2}$$

where q_i are the components of the heat flux vector, $\vec{q}, \partial T / \partial x_i$ is the temperature gradient, and λ is the heat conductivity of the material under consideration. The connected boundary conditions are

$$q_n = \lambda \frac{\partial T}{\partial x_i} \cdot n_i = \alpha (T_s - T_\alpha), \tag{3}$$

$$T = \bar{T}_s, \tag{4}$$

with the heat-transfer coefficient α, the surface and ambient temperatures, T_s and T_a, respectively and the prescribed surface temperature, T_s. The component of the heat flux vector, along the surface normal, $\bar{n}$, i.e. the heat flux through the surface, is denoted by q_n. It must be mentioned that the heat-transfer coefficient is an unknown that is usually difficult to catch because it depends not only on the material and surface but also on the ventilation. Additionally, the ambient temperature is generally inhomogeneous and often influenced by the temperature of the component itself. If radiative heat-transfer on the surface is to be considered, it follows the STEFAN-BOLTZMANN law

$$q_n = \lambda \frac{\partial T}{\partial x_i} \cdot n_i = \varsigma \in [(T_s - T_0)^4 - (T_\alpha - T_0)^4] \cdot \tag{5}$$

The absolute zero temperature is denoted by T_0, ς is the STEFAN-BOLTZMANN constant and $\in$ is the emissivity of the surface. For rubber it can be set to one in a first estimate, which is the emissivity of a full radiator. For simplicity, in the examples shown in this paper, all thermal constants as well as the ambient temperature are assumed to be constant.

3 IMPLEMENTATION

The proposed scheme has been implemented using ABAQUS/STANDARD as solver (VISCO and HEAT-TRANSFER, STEADY STATE analysis) and ABAQUS/VIEWER as post-processor. The iterative scheme is realized by a number of user-implemented shell-, and Python scripts, including load step regulation, job and convergence-control and results-processing. Note, that the representation of master-curves by PRONY-series, as used by ABAQUS, may differ significantly from the original ones. Great care must be taken, to keep this error small. However, these issues will not be presented in detail here. Convergence is defined to be reached, when the maximum change of temperature in the model between two following iteration steps remains below a threshold value of one percent.

4 CYLINDRICAL SPECIMEN UNDER UNIAXIAL CYCLIC LOADING

For a demonstration of the methods capability to predict the temperature development within a component, we turn to a simple example, where a largely analytical solution is possible. This solution is then compared to the results of the proposed method. Furthermore, the influence of additional features not present in the analytical solution, like surface radiation and inhomogeneous heating is shown.

4.1 *Analytical solution*

A cylindrical rubber specimen of Radius R and length l is subjected to cyclic tension/compression loading. Viscous dissipation in the volume causes a rise in temperature. The ends of the cylinder in axial directions are assumed to be perfectly insulated. Then heat flux is possible only in radial direction and in the stationary case, all heat generated in the interior leaves the specimen as flux through the outer surface. In other words, the heat-transfer problem becomes one-dimensional and the model resembles an infinitely long cylinder. The average dissipation density during one loading cycle Δt can be roughly estimated from DMA-data for a temperature $\bar{T}$ and the loading frequency f by

$$d \approx \frac{\hat{u}\hat{F}}{lR^2\Delta t} \sin\delta. \tag{6}$$

Here, $\hat{u}$ and $\hat{F}$ are the displacement and force amplitudes and δ denotes the loss angle according to $\tan\delta = G''/G'$. For the deformation-controlled setup considered here, the force can be approximated from the master-curve data as a function of the displacement, using the storage modulus G' at the current temperature $\bar{T}$ and frequency f in a NEO-HOOKE an hyper-elastic constitutive law

$$F \approx G' A_0 \left(1 \pm \hat{\varepsilon} - \frac{1}{(1 \pm \hat{\varepsilon})^2}\right) \tag{7}$$

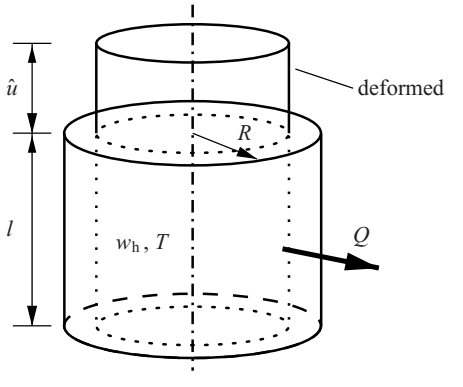

Figure 2. Cylindrical rubber specimen—geometry and boundary conditions.

in tension and compression, where A_0 is the undeformed crossection area of the cylinder and $\hat{\varepsilon} = \hat{u}/l$ denotes the nominal strain amplitude. A force amplitude can be defined accordingly.

To make things as simple as possible, the visco-elastic material properties—and therefore the power of heating w_h—are assumed to be constant in the whole volume. Because of the temperature dependency of the visco-elastic law, this is in contradiction to the expected result of an inhomogeneous temperature distribution T. The error resulting from this inconsistency is proportional to the maximum temperature deviation $|\bar{T} - T|$. It is shown below, that in the special case of the infinite cylinder, this error remains very small. To minimize it, $\bar{T}$ must be chosen close to the volume average of T. This can be done by trial and error or by a simple optimization scheme.

In the case of the simplified cylinder model problem with constant power of heating w_h, the total amount of heat generated within the specimen of outer radius R and length l per unit time is

$$Q_{tot} = \pi R^2 l w_h. \tag{8}$$

Accordingly, the amount of heat produced inside a smaller cylindrical sub-volume of radius r is

$$Q(r) = \pi r^2 l w_h. \tag{9}$$

In the stationary case, it is equal to the amount of heat flux leaving this volume in radial direction through its respective surface of $A(r) = 2rl\pi$. Thus, the flux density at every point inside of the specimen is

$$q(r) = \frac{1}{2} r w_h. \tag{10}$$

with this result, integration of (2) yields the temperature distribution

$$T(r) = \frac{1}{4}\frac{w_h}{\lambda}(R^2 - r^2) + T_s, \tag{11}$$

where T_s is determined from the convection boundary condition (3) and (8) as

$$T_s = T_0 + \frac{2Rw_h}{\alpha}. \tag{12}$$

Again, for the sake of simplicity, surface flux due to radiation is not considered here. The mechanical properties used for the calculation are those of a natural rubber compound with a hardness of 55 ShA. The model parameters are given in Table 1. The model is loaded by a relative displacement of the cylinders ends by a sine-function in time.

The results of different iteration steps of the calculation are given in Table 2 and shown in Figure 3(a). The temperatures in the center and on the surface and the average temperature in the cylinder volume are denoted by T_c, T_s and T_v, respectively. Initially, a temperature of $\bar{T} = 50$°C is assumed in order to estimate the power of heating by (6) to be 0.368 mW/mm^3. Then, the surface temperature is 112°C and the temperature at the core is 121°C. Clearly, the first 'guess' of 50°C was much too low. Because of this, the dissipation is overestimated and high temperatures are the result. For the second try, the volume average temperature from the first solution, 116°C, is taken as new value of $\bar{T}$. After repetition of this procedure a converged solution is achieved. The resulting core-temperature of the cylinder is 93°C with a power of heating of 0.267 mW/mm^3.

For this example, the analytical solution works very well. There is a maximum temperature difference of 3.9 K between the assumed temperature $\bar{T}$ and the result, such that the visco-elastic properties do not vary strongly in the volume and the assumption of constant heating power is in acceptable agreement with the result. Because of this, the result is very close to the numerical one presented below. This cannot be expected, when the range of temperatures in a component is much larger.

4.2 *Numerical solution*

The above analytical solution describes the simplified cylinder model problem discussed here very

Table 1. Model parameters.

Parameter	Dimension	Symbol	Value
Radius	mm	R	5
Length	mm	I	20
Displacement amplitude	mm	$\hat{u}$	1
Frequency	Hz	f	50
Heat-transfer coefficient	mW/mm^2/K	α	0.01
Heat conductivity	mW/mm/K	λ	0.26
Ambient temperature	°C	T_a	20

Table 2. Analytical solution, compare to Figure 3(a).

Step	T °C	w_h mW/mm^3	T_c °C	T_s °C	T_v °C
1	50	0.368	121	112	116
2	116	0.237	84.8	79.2	81.7
3	81.7	0.287	98.6	91.7	94.8
4	94.8	0.258	90.7	84.5	87.3
8	90.1	0.267	93.0	86.7	89.5

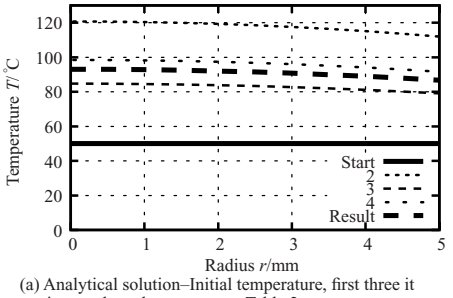

(a) Analytical solution–Initial temperature, first three it erations and result; compare to Table 2.

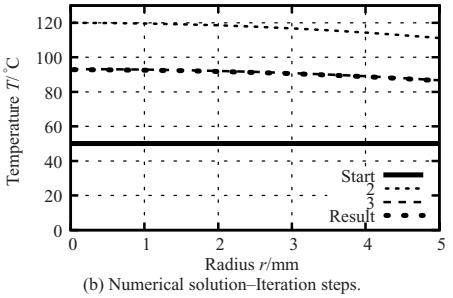

(b) Numerical solution–Iteration steps.

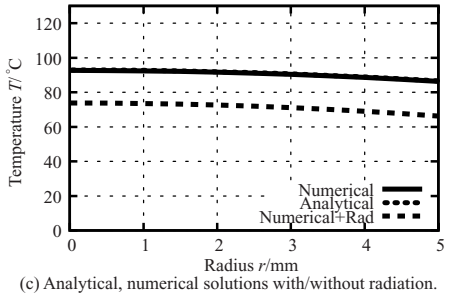

(c) Analytical, numerical solutions with/without radiation.

Figure 3. Self-heating of infinitely long cylinder.

well. However, for general geometries, multiaxial loading and heat transport, and when more complex boundary conditions are required, the need for a numerical scheme becomes evident. In this section, the numerical solution is presented. In addition to this, the influence of radiative heat transport will be discussed. For the FEM-solution, an axial-symmetric model with ten linear elements in radial direction is used.

In Figure 3(b), the results of the different iteration steps of the numerical scheme are shown. Iteration starts with an initial temperature of 50°C. There is a rapid convergence of the solution, see Figure 4. The iteration is terminated after the third step, when the maximum change in temperature is less than one percent. The maximum and minimum temperatures in the center and on the surface of

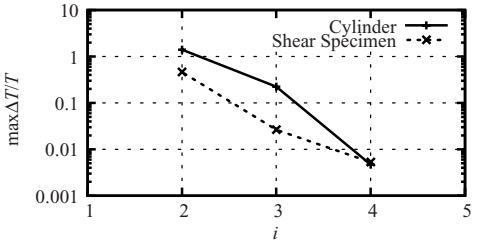

Figure 4. Convergence of solution.

the cylinder, respectively, in the converged solution are 92.7°C and 86.4°C. A comparison of the first iteration steps of the analytical and the numerical solutions is worthwhile because the power of heating is homogeneous for both. However, its value is estimated from the master-curve by (6) in the former and it is calculated by the FEM-solver and post-processing in the latter. The numerical simulation yields a value of 0.364 mW/mm^3. The deviation between both solutions is below 1%. The direct comparison of the analytical and numerical results is given in Figure 3(c). The difference between both solutions is negligible.

For the simulation with radiative surface heat transport, an emissivity of the surface of $\varepsilon = 1$ has been chosen. This results in a drop of the temperature by about 19.5°C. This may seem a comparably large drop. However, the current model problem is dominated by the heat flux through the surface. The heat loss due to radiation in the presented case is about one third less than the heat loss due to convective heat transfer.

5 EXAMPLE: SHEAR TEST-SPECIMEN

For the demonstration of the application of the presented method to a non-homogeneous, multi-axial loading situation we consider a comparably massive test specimen, used for fatigue experiments at Freudenberg Schwingungstechnik Industrie, GmbH & Co. KG, Velten. The axisymmetric design has an elastomer volume of a hight of 7.5 cm and an approximate diameter of 15 cm. The material parameters used in the simulation are those of a 55 ShA natural rubber compound. Loading is applied by displacement-controlled relative shearing of the metal plates with an amplitude of ±10 mm and a frequency of 5 Hz. Thermal boundary conditions are chosen as for the cylindrical specimen above, including radiative and convective heat-transfer. Temperatures are prescribed on the outside surfaces of the metal plates to be 30°C and 41°C. Using symmetries, the component is discretized as half-model.

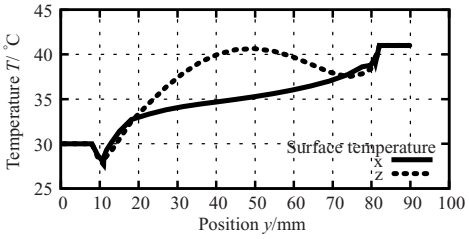

Figure 5. Surface temperature of shear test-specimen.

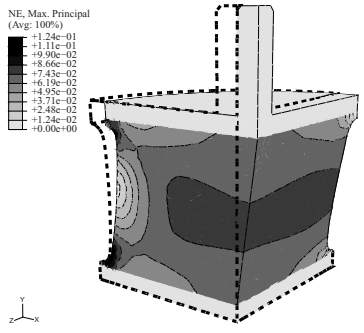

(a) Deformation and max. nominal strain(–)

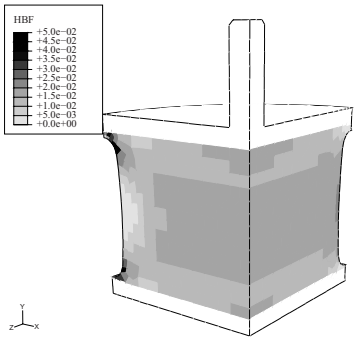

(b) Power of heating (mW/mm³)

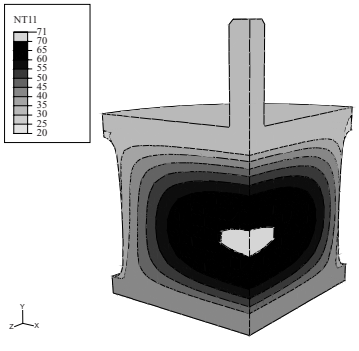

(c) Resulting temperature (°C)

Figure 6. Shear test-specimen—Results.

Convergence of the solution is achieved in three steps. The rate of convergence is similar to the one observed in the cylinder-simulation presented in the previous chapter, see Figure 4. The maximum resulting temperature in the inside of the specimen is found to be approximately 70°C, while the surface temperatures remain in a moderate range. In Figure 5, the surface temperatures are plotted along the y-axis for two paths which resemble the edges of the quarter-model depicted in Figure 6.

6 CONCLUSIONS

A scheme for a coupled analysis of visco-elastic material behavior including the effect of self-heating due to internal dissipation is presented. The method is compared to the analytical solution of the model problem of an infinite cylinder with homogeneous heating, and found to be in excellent agreement. Furthermore the application to general inhomogeneous and multi-axial loading situations is demonstrated for the example of a massive shear test specimen, known to exhibit very high temperatures in the experiment. The uncertainties of the method lie in the linear visco-elastic description of the mechanical material behavior and in the representation of the master-curves in terms of PRONY-series. The validity of temperature-shift function must be checked. Furthermore the thermal boundary conditions are difficult to handle and may call for inverse engineering methods. For this reason, the comparison to experimental results is not straight forward and subject to ongoing research at FREUDENBERG FORSCHUNGSDIENSTE KG.

ACKNOWLEDGMENTS

This work has been realized in co-operation with our partners FREUDENBERG DICHTUNGS - UND SCHWINGUNGSTECHNIK GMBH & CO KG and VI-BRACOUSTIC GMBH & CO KG.

REFERENCES

Hans Dieter Baehr & Karl Stephan. Wärme- und Stoffübertragung. Springer-Verlag, Berlin, 1994.

Friedrich Rudolf Schwarzl. Polymermechanik. Springer-Verlag, Berlin, 1990.

Constitutive Models for Rubber VI – Heinrich et al. (eds)
© 2010 Taylor & Francis Group, London, ISBN 978-0-415-56327-7

Efficient dynamic modeling of rolling tyre tread blocks

P. Moldenhauer & M. Kröger
Institute of Machine Elements, Design and Manufacturing, Technical University Freiberg, Germany

ABSTRACT: The dynamic behaviour of a tyre tread block is described by a modularly arranged model with a high numerical efficiency. Special emphasis is laid on the interaction between structural dynamics and contact mechanics. Furthermore, the model includes the rolling process of the tyre: The tread block follows a trajectory which is obtained from the deformation of the tyre belt. The results from simulations with a single tread block provide a deeper insight into highly dynamic processes that occur in the contact patch such as tyre squeal, run-in or snap-out effects.

1 INTRODUCTION

Tyre tread blocks are permanently subjected to different driving states such as acceleration or ABS braking as well as cornering. Even for a constant vehicle velocity the tread blocks experience an excitation resulting from the tyre deformation in the contact patch and from friction induced vibrations. The contact time of a tread block for a vehicle velocity of 100 km/h takes about 10 ms. During this contact the tread block passes a sticking and a sliding phase and finally snaps out. This leads to an unsteady dynamic behaviour of the tread blocks which has to be covered in models to achieve a realistic simulation.

On the one hand present tread block models usually show a high grade of complexity. For example, in (Hofstetter 2004) a three-dimensional finite element approach with non-linear material description and thermo-mechanical coupling is applied. Such models are only applicable within limits for dynamic calculations because of the computational effort. On the other hand there are models that treat the tread block as a simple elastic beam (Bschorr et al. 1981) or a time-dependent viscoelastic spring model (Liu et al. 2008). Here, the block geometry or important structural effects are neglected.

The aim of this approach is to compromise between these concepts to calculate dynamic processes and vibrations of tyre tread blocks. This means to model the geometric and dynamic properties of the tread block and its interaction with the road surface including the frictional contact as well as the rolling contact without the loss of numerical efficiency.

2 TREAD BLOCK MODEL

The basic idea is to model the structural dynamics and the complex contact mechanics at first separately, see Figure 1. Each mechanical or physical effect is described by one module whereas the single modules are linked and interact with each other during the simulation. At present the model consists of four modules:

- Dynamic description of tread block
- Friction characteristic
- Non-linear contact stiffness
- Wear

The single modules are described in the following subsections.

2.1 *Dynamic description of tread block*

This module considers the tread block geometry and mechanical properties e.g. density, elasticity or damping.

For this purpose a finite element model of the tread block has to be generated in advance. The

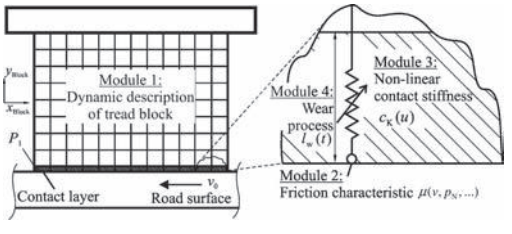

Figure 1. Modular tread block model.

model includes velocity dependent damping which is assumed to be proportional to the stiffness matrix. In order to achieve a high numerical efficiency it is necessary to reduce the model with respect to its degrees of freedom by an adequate method.

Here, the Craig/Bampton transformation is applied, cp. (Craig & Bampton 1968). The system equation with the mass, stiffness and damping matrix of the system is subjected to this reduction method. It has originally been developed for applications in the field of structural dynamics and can be interpreted as the combination of a static and a modal condensation. Important degrees of freedom, which are here the contact nodes, are explicitly retained in the reduced system.

Therefore, point contact elements can be coupled to the contact nodes of the reduced model which represent the contact layer where the contact mechanics are considered.

2.2 *Friction characteristic*

Rubber friction can be divided according to different effects: Hysteresis, adhesion, cohesion and viscous friction, see (Kummer 1966). In technical applications these effects always occur in combination resulting in a complex friction characteristic. It depends on many parameters like relative velocity, normal pressure, temperature, surface roughness, lubrication and wear. As a consequence many types of friction characteristics can be observed for rubber contacts. To determine a local friction characteristic it is possible to use mathematical models (Persson 2004), (Heinrich 2007), simulations or experiments. The adequacy of the single methods for a given application depends on the respective problem. The advantage of an experimental investigation is that all physical effects of rubber friction are considered with their interactions.

A friction characteristic of a local rubber sample made of tread material on a corundum surface grit 400 has been measured in dependence of the relative velocity and the normal pressure on a tribometer test rig, cp. Figure 2.

The local friction characteristic shows a maximum with respect to the relative velocity and a decreasing friction coefficient with increasing normal pressure which is typical also for real road surfaces such as asphalt or concrete. The measured friction characteristic has been approximated with a function that consists of an exponentially decreasing velocity dependent term and an exponentially decreasing pressure dependent term. For numerical reasons the friction characteristic is smoothed by an arc tangent function to avoid the distinction between sticking and sliding and to comprise the maximum at low sliding velocities. The approximated friction characteristic is shown in Figure 2

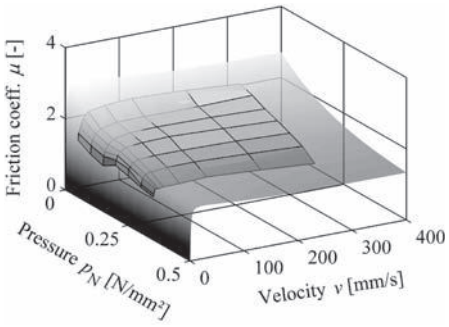

Figure 2. Measured (grid) and approximated (semi-transparent) local friction characteristic.

and is applied to every point contact element. The input parameters relative velocity and normal contact pressure at the respective point contact elements are calculated within the simulation for each time step.

2.3 *Non-linear contact stiffness*

The non-linear contact stiffness covers the normal contact properties between the soft rubber block and the rough solid surface. When both bodies contact each other only the highest asperities of the rough surface penetrate the rubber leading to a small contact stiffness. With increasing penetration depth the contact stiffness increases because of the larger number of contact points, cp. (Gäbel 2008).

This non-linearity is considered by non-linear springs that are coupled to the reduced finite element model. Figure 3 depicts the comparison between measurement and simulation for the static normal force-displacement characteristic of the whole tread block on the same corundum surface grit 400 which has been used for the experimental identification of the friction characteristic.

The experimental investigation is described in detail in (Kröger 2007). Because the friction characteristic and the properties of the rough surfaces

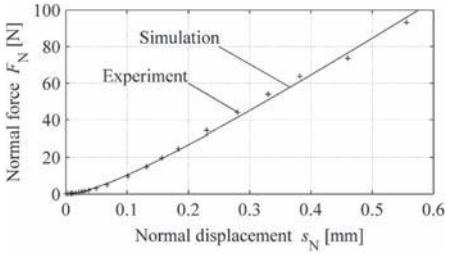

Figure 3. Measured and simulated normal force-displacement characteristic.

are described with the point contact elements of the contact layer it is now possible to model the road surface as smooth. This approach and a fast contact algorithm lead to a further reduction of the computational effort.

2.4 *Wear*

Rubber wear which occurs due the sliding friction in the tyre contact patch changes the tread block shape. Although a significant tread wear does not appear after one single revolution the shape generally influences the frictional and dynamic behaviour, see (Moldenhauer 2008). The effect of wear is covered in the model by allowing the lengths of the non-linear springs from the contact layer to decrease. The reduction of the spring lengths, which represent a certain rubber wear volume, obeys a wear law, see (Kröger 2007).

The present wear law depends linearly on the relative velocity, the normal pressure and the friction coefficient. The implementation of a non-linear wear can easily be realised but usually many coefficients have to be identified with a high experimental effort to realistically to simulate rubber wear, see e.g. (Viswanath 1994). Wear effects are neglected in this work because the focus is laid on the rolling contact.

3 ROLLING CONTACT

For the implementation of rolling contact some assumptions are made: The stiff steel belt determines the kinematics of the soft rubber tyre tread. Hence, the single tread block passes a displacement-controlled trajectory within the simulation.

Gyroscopic and centrifugal forces acting on a single tread block are neglected because they are small compared to the normal and tangential contact forces. Furthermore, they act evenly on the whole tread block and therefore only marginally influence processes in the contact area and dynamic effects.

With these assumptions the rolling motion can be applied to the tread block model without losing numerical efficiency which is one of the basic requirements. The tread block is then still simulated with a fixed support. However, the contact forces of a tread block performing the rolling motion of the tyre are applied to the model.

This approach has the advantage that the above described model with the reduced system matrices as well as the nodal coordinates remain unchanged. Figure 4 depicts the concept of the rolling contact implementation: The fixed system gets as input parameter the trajectory $y_{\mathrm{Tr}}(x_{\mathrm{Tr}})$ of the tyre belt for the translatory motion of the tread block.

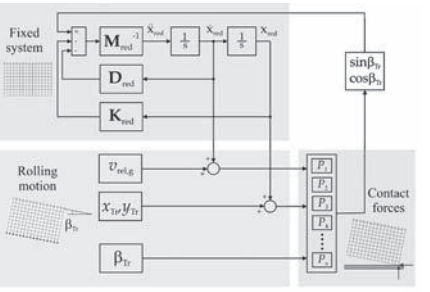

Figure 4. Rolling contact algorithm.

The angle $\beta(x_{\mathrm{Tr}})$ describes the gradient of the trajectory and considers the rotatory motion of the tread block. The combined motion of translation and rotation is superposed with the system coordinates x_{red} of the reduced system. Therefore, also the algorithm for the detection of contact is the same. The point contact elements P_i provide the normal and tangential contact forces which are transformed in the fixed tread block system and act on the respective contact nodes.

Additionally, the relative velocity $v_{\mathrm{rel,g}}$ between tyre belt and road enters the simulation and significantly influences the frictional behaviour due to the velocity and pressure dependent friction characteristic. This relative velocity has to be defined prior to the simulation and represents the tyre slip velocity.

The distance between steel belt trajectory and road surface defines the normal load due to the displacement-controlled motion of the tread block on the steel belt trajectory. This distance has to be adjusted according to the respective tyre load conditions. The steel belt deformation is calculated in advance by finite element calculations of a whole tyre.

Here, FE calculations for a truck tyre under stationary rolling conditions are used in the following, see (Näser 2005). In order to conform the 3D FE tyre data to the 2D tread block model the centerline in circumferential direction of the outermost belt layer has been extracted.

Due to the discretisation of the FE model it is necessary to smooth the belt data in order to obtain a continuous rolling motion. A polynomial approximation leads to good fitting results in the vicinity of the contact patch, cp. Figure 5. The approximated function directly enters the simulation as trajectory coordinates, see Figure 4.

4 SIMULATION RESULTS

4.1 *Instationary effects*

The following simulations are conducted with the contact parameters and the friction characteristic

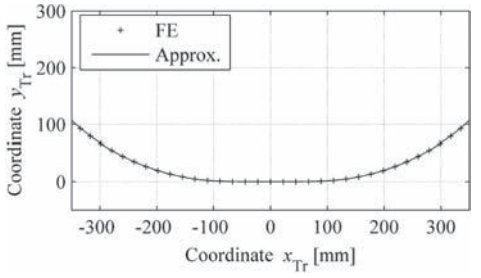

Figure 5. Polynomial approximation of finite element tyre belt deformation.

shown in Figure 2 and Figure 3 and represent a corundum surface as contact partner.

The relative velocity between tread block and rough surface is $v_{rel,g} = 1$ m/s which is a typical slip velocity for braking conditions. The distance between the steel belt trajectory and the surface has been adjusted so that a nominal normal pressure of $p_N = 0.8$ N/mm² is applied to the tread block in the middle of the contact patch ($x = 350$ mm). This normal load corresponds to truck tyre conditions.

The tread block has a length and width of 15 mm and a height of 10 mm. The elasticity modulus is $E = 12$ N/mm² and Poisson's ratio has been set to $\nu = 0.49$ according to the incompressibility of the rubber material. The damping matrix is assumed to be proportional to the stiffness matrix. The proportionality factor β has been determined by an experiment of free vibration decay of the tread block to $\beta = 1.5\ 10^{-4}$ 1/s.

During the run-in phase, the tread block contacts the surface with the leading edge which is depicted in Figure 6 with the corresponding contact pressure distribution. In this state the leading edge experiences a high contact pressure peak whereas the trailing edge lifts off and is not in contact with the rough surface. Here the tread block is stressed at most.

Then a sticking phase follows where the leading edge has no relative velocity to the surface. The tread block shears until the structural restoring forces exceed the friction forces and the tread block comes to the sliding phase. Here, the tread block performs a pure translatory motion where

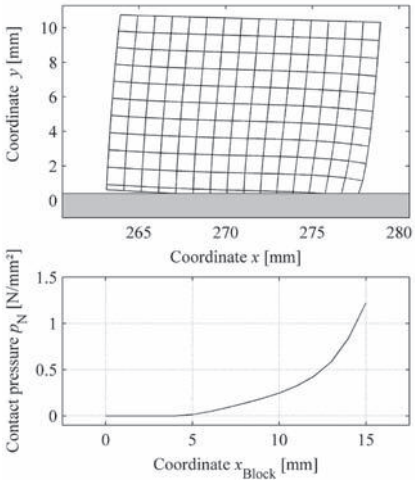

Figure 6. Deformation of tread block entering the contact patch and corresponding contact pressure distribution.

the normal pressure still shows a peak at the leading edge which is lower than in the run-in phase. Finally the block snaps out and returns to its undeformed configuration. A chronological view of the deformation behaviour during passage of the contact page depicts Figure 7.

For further investigations the relative velocity of the leading edge is shown in Figure 8 where the different phases with sticking; sliding and snap-out can be identified. At the transition from sticking to sliding the tread block is dynamically excited.

4.2 *Vibrational effects*

Within a second simulation the nominal pressure is reduced to $p_N = 0.25$ N/mm² which is a typical value for passenger cars. All other parameters are unchanged. Then another phenomenon is observed: Due to the decreasing friction characteristic with respect to the relative velocity friction induced vibrations occur in this parameter range. The displacement of the leading and the trailing edge show the typical saw tooth behaviour, see Figure 9. The whole tread block performs oscillations which

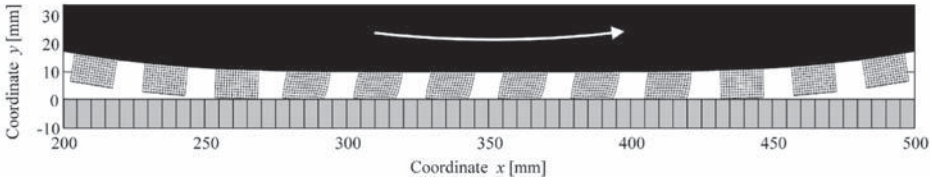

Figure 7. Chronological view of tread block deformation.

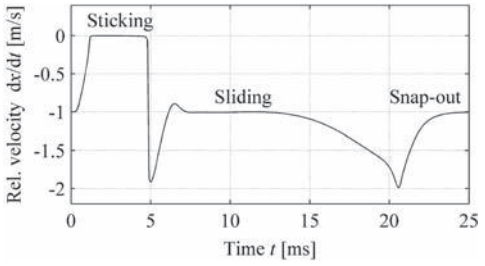

Figure 8. Relative velocity of leading edge.

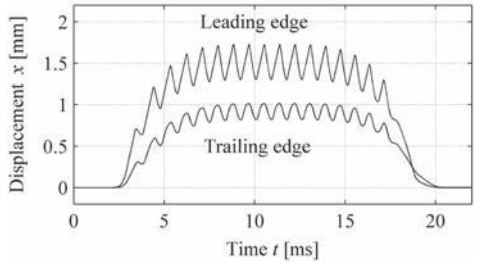

Figure 9. Stick-slip vibrations of leading and trailing edge.

are known as stick-slip vibrations. For these conditions there is only a very short sticking phase at the beginning of the contact zone which can be explained by the comparably small nominal normal contact pressure.

The stick-slip frequency is at 3500 Hz which is in the squeal regime. From a safety-related point of view these vibrations are unwanted. They lead to changing contact conditions that influence with a high frequency the contact area of the tread block and the frictional behaviour. This reduces the braking deceleration and the potential cornering forces.

5 CONCLUSIONS

The presented model covers the dynamics of a tyre tread block with a focus on numerical efficiency. The computational time for one passage of the contact zone on a standard personal computer is about 30 seconds including backward transformation of the reduced degrees of freedom into the original finite element degrees of freedom. The modularly arranged model considers structural effects, the local friction characteristic, the nonlinear contact stiffness and wear effects.

To include the rolling contact the tread block model follows the trajectory of a steel belt. Simulations show four different phases during passage of the contact patch: run-in, sticking, sliding and snap-out. The model simulates tyre tread block squeal effects in a certain contact parameter range which result from friction induced vibrations.

The model furthermore delivers the reaction forces to the fixed support which represents the coupling to the tyre belt. The results can be used in global tyre models as excitation forces from the tread blocks without modeling them. This concept allows the realistic and numerically efficient calculation of tyre dynamics.

ACKNOWLEDGEMENT

The investigations received financial support from the German Research Foundation DFG within the research group FOR492 “Dynamic contact problems with friction of elastomers”.

REFERENCES

Bschorr, O.; Wolf, A. & Mittmann, J. 1981. *Theoretische und experimentelle Untersuchungen zur Abstrahlung von Reifenlärm.* MBB-Bericht Nr. BB-48381-Ö *(in German)*.

Craig, R. & Bampton, M. 1968. *Coupling of Structures for Dynamic Analyses.* AIAA Journal 6(7): 1313–1319.

Gäbel, G.; Moldenhauer, P. & Kröger, M. 2008. *Local Effects Between Tire and Road.* In ATZautotechnology 4: 48–53.

Heinrich, G. & Klüppel, M. 2007. *Rubber Friction and Tire Traction.* In VDI-Berichte 2014: 341–360.

Hofstetter, K. 2004. *Thermo-mechanical Simulation of Rubber Tread Blocks During Frictional Sliding.* PhD Thesis, Vienna University of Technology.

Kröger, M.; Moldenhauer, P. & Gäbel, G. 2007. *Modular Modelling of Dynamic Systems with Elastomer Contacts.* In IUTAM Symposium on Computational Methods in Contact Mechanics, IUTAM Bookseries 3: 277–290.

Kummer, H.W. 1966. *Unified Theory of Rubber and Tire Friction.* Pennsylvania State University Engineering Research Bulletin B-94.

Liu, F.; Sutcliffe, M.P.F. & Graham, W.R. 2008. *Modeling of Tread Block Contact Mechanics Using Linear Viscoelastic Theory.* In Tire Science and Technology 36(3): 211–226.

Moldenhauer, P.; Ripka, S.; Gäbel, G. & Kröger, M. 2008. *Tire Tread Block Dynamics: Investigating Sliding Friction*. In Tire Technology International 2008, The Annual Review of Tire Materials and Tire Manufacturing: 96–100.

Näser, B.; Kaliske, M.; André, M. 2005. *Durability Simulations of Elastomeric Structures*, In Constitutive Models for Rubber IV (ECCMR): 45–50 *and personal communication.*

Persson, B.N.J.; Albohr, O.; Tartaglino, U.; Volokitin, A.I. & Tosatti, E. 2004. *On the Nature of Surface Roughness with Application to Contact Mechanics.* In Journal of Physics: Condensed Matter 16: R1–R62.

Viswanath, N. & Bellow, D.G. 1995. *Development of an Equation for the Wear of Polymers.* In Wear 181–183: 42–49.

Constitutive Models for Rubber VI – Heinrich et al. (eds)

Fitting a viscoplastic time-domain model to equivalent viscoelastic materials data

A.H. Muhr
TARRC, Hertford, UK

ABSTRACT: An attempt is made to capture comprehensive "dynamic properties" data, including effects of filler loading, amplitude, frequency and temperature, using a simple viscoelastic-elastoplastic overlay model with a small number of parameters. The source of the data is the values of dynamic shear modulus and phase angle for a range of natural rubber formulations, most including carbon black as a filler, tabulated in TARRC's Natural Rubber Engineering Data Sheets.

1 INTRODUCTION

Traditionally, the "equivalent viscoelastic approach" has been used to characterise the "dynamic properties" of filled rubber. This characterisation is done in the frequency domain by subjecting the rubber to a series of forced sinusoidal strain tests covering a range of amplitudes, frequencies and temperatures, and tabulating the linearised dynamic properties, ie the storage G' and loss G'' moduli (or alternatively, dynamic modulus G^* and phase angle δ). Although the dependence of the data on amplitude, ie the Fletcher-Gent or Payne effect, is in conflict with the linear viscoelastic assumption in the interpretation, the approach has served many designers of rubber components very well in the achievement of appropriate response to quasi-periodic excitations. For this reason, comprehensive data on material properties are available in this form.

Progress has been described elsewhere on devising time-domain models that can capture the amplitude effect and are compatible with 3D non-linear finite element packages (Ahmadi et al, 2005–2009; Austrell et al. 2001; Lion & Kardelky, 2004).

This paper addresses the further challenge of capturing all of the tabulated "dynamic properties" using a small number of parameters for one such model, being a simple viscoelastic-elastoplastic overlay. The emphasis is on covering a wide range of temperatures, as tabulated in TARRC's Natural Rubber Engineering Data Sheets (EDS; TARRC, 1979–1986), but the dependence of the parameters on the volume fraction of reinforcing black is also considered.

2 MODEL

Filled rubber is modelled here as a linear hyperviscoelastic matrix (the crosslinked polymer) in parallel with a load-bearing filler "structure" that exhibits partial breakdown and healing during each deformation cycle. The total stress τ is the sum of hyperviscoelastic (hve) and elastoplastic (ep) terms:

$$\tau = \tau_{hve} + \tau_{ep} \tag{1}$$

Only simple shear will be considered here. The proposed model has full time-domain capability but is fitted to the frequency-domain EDS data. It does not cover the Mullins effect, and the data also refer to the scragged material. In the EDS, and here, the harmonic method is used to express G' and G'' in terms of Fourier integrals of the stress response to a forced sinusoidal strain history:

$$\begin{aligned} \gamma &= \tilde{\gamma}\sin\omega t \\ G' &= \frac{\omega}{\pi\tilde{\gamma}}\oint \tau(t)\tilde{\gamma}\sin(\omega t)dt \\ G'' &= \frac{\omega}{\pi\tilde{\gamma}}\oint \tau(t)\tilde{\gamma}\cos(\omega t)dt \end{aligned} \tag{2}$$

This has the advantage over secant and skeleton linearisations (Ahmadi & Muhr, 1997) that the modulus functionals are linear, so that

$$\begin{aligned} G' &= G'_{hve} + G'_{ep} \\ G'' &= G''_{hve} + G''_{ep} \end{aligned} \tag{3}$$

The hyperviscoelastic time-domain model is

$$\tau_{hve}(t) = \int_0^t G(t-s)\dot{\gamma}(s)ds \tag{4}$$

where the relaxation modulus $G(t)$ has four parameters being G_∞, H_0, H_m and m:

$$G(t)-G_\infty = -\frac{H_0}{\log_{10}(e)}\log_{10}\left(\frac{t}{t_{\max}}\right) + \Gamma(1+m)\left[H_m\left(\frac{t}{t_0}\right)^{-m} - H_m\left(\frac{t_{\max}}{t_0}\right)^{-m}\right] \quad (5)$$

where Γ, the gamma function, is a generalization of the factorial function to non-integer arguments, and t_0 = 1 s, and $t_{\max}$ sets the upper time limit of applicability of the model.

For numerical evaluation, Equation 4 was discretised as a Prony series, and this latter form also enables the effect of time-temperature correspondence to be incorporated:

$$G(t,T) = G_\infty(T_{ref})\frac{T}{T_{ref}} + \sum G_i(T_{ref})\frac{T}{T_{ref}}\exp(-t/a_T\tau_i) \quad (6)$$

ie G_∞ and the G_i are proportional to absolute temperature T and all the relaxation times τ_i are subject to the same temperature dependent shift factor a_T, which could for example be estimated from the empirical WLF equation

$$\log_{10}(a_T) \approx -\frac{8.86(T-T_s)}{101.6+T-T_s} \quad T_s \approx T_g + 50\,\mathrm{K} \quad (7)$$

where T_g is the glass transition temperature. If T_{ref} is some value other than T_s, then a_T in Equation 5 needs to be replaced by $a_T / a_{T_{ref}}$. The same principles were used to plot experimental data for unfilled NR on a mastercurve using a value of T_s = 253 K (see Muhr, 2009). Values of G' and G'' were calculated from the model using the standard expressions derived from Equations 3 and 5.

The elastoplastic stress contribution, in simple shear, is calculated (Ahmadi et al, 2007; Ahmadi & Muhr, 2009), after the first loading cycle, from an incremental relationship:

$$\Delta\tau \equiv \Delta\tau_{epR}(\gamma) = 2\tau_{epL}\left(\frac{\Delta\gamma}{2}\right) \quad (8)$$

where R stands for retraction and $\tau_{epL}(\gamma)$ is the stress for the primary loading. Equation 7 is valid until the next reversal in the direction of straining, when the increments are rezeroed. As a working hypothesis, it may be generalised to 3D general deformations by using a suitable elasto-plastic model. A start has been made to show that this provides at least a fair description of the multiaxial behaviour of filled rubber (Ahmadi et al, 2005); appropriate plasticity models in ABAQUS are discussed by Ahmadi et al. (2009). For the present purposes a 3-parameter expression for the loading function in simple shear is used:

$$\tau_{epL}(\gamma) = A\,\gamma(\gamma^2+c^2)^{-b/2} \equiv G_{ep,0}\gamma\left(\frac{\gamma^2}{c^2}+1\right)^{-b/2} \quad (9)$$

where $G_{ep,0} \equiv Ac^{-b}$ is the elastoplastic shear modulus contribution in the small strain limit. Alternative expressions may be used, and one possibility is to use the Kraus equation, designed to fit the strain-dependence of the dynamic modulus, for the elastoplastic loading curve.

An Arrhenius temperature dependence may be incorporated into the elastoplastic contribution, following Kraus and Payne:

$$A(T) = A(296\,\mathrm{K})\exp\left(\frac{E}{RT}-\frac{E}{296R}\right) \quad (10)$$

where R is the gas constant and it has been assumed that b and c are independent of T.

A spreadsheet was written to implement the models; for the elastoplastic contribution the trapezium rule was used to evaluate Equations 1. Details are given elsewhere (Muhr, 2009).

3 MATERIALS

Attention is focused on the set of NR-based materials summarised in Table 1. Their full formulations and many Standard properties are provided in the original publication (TARRC, 1979–1986); the cure system is the same for all these materials. The unfilled NR, designated EDS19, is assumed to contribute the hyperviscoelastic contribution, augmented by the strain amplification factor 1 + 2.5φ from Einstein's equation, to the models used for the materials filled with different loadings of N330 carbon black. The filler loading is quantified on the basis of parts per hundred of rubber (phr) and volume fraction $\varphi = (\mathrm{phr}/\rho_f)/(100/\rho_r + \mathrm{phr}/\rho_f)$ where ρ_f and ρ_r are the densities 1820 and 966 kgm^{-3} of filler and rubber respectively.

Table 1. Selected natural rubber materials from the EDS.

Material	N330/[phr]	φ	1 + 2.5φ
EDS19	0	0	1
EDS14	15	0.074	1.185
EDS15	30	0.137	1.318
EDS16	45	0.193	1.483

4 FITTING THE PARAMETERS

Figure 1 shows the fit achieved to the data set at 10% amplitude for EDS19 using the 4-parameter viscohyperelastic model; values of the parameters used to achieve this fit are shown in Table 2.

To fit the data for the filled materials to Equation 9 we need first to subtract off the contribution of the unfilled NR matrix from the measurements for the filled rubber to give G'_{ep}, and then seek to find E from a plot of $\log(G'_{ep})$ versus $1/T$, as shown in Figure 2. It was found possible to achieve a good fit to the EDS15 and EDS16 data using a common value of E, and the same value of E could be used

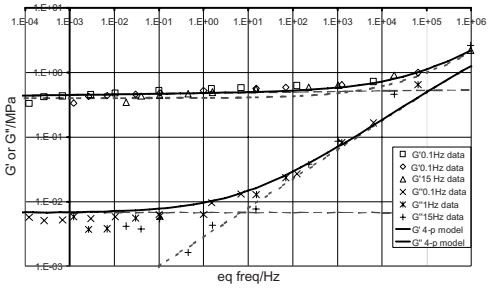

Figure 1. Fit to EDS19 data for all temperatures and frequencies (shear amplitude 10%) presented as a mastercurve at 296 K; see Table 2 for parameters. · · · · model with H_0 set to zero; - - - model with H_m set to zero.

Table 2. Parameters for the EDS19 matrix.

Hyperviscoelastic parameters				WLF parameter
G_∞/MPa	H_0/MPa	H_m/MPa	m	T_s/K
0.4	0.0043	0.0002	0.57	203

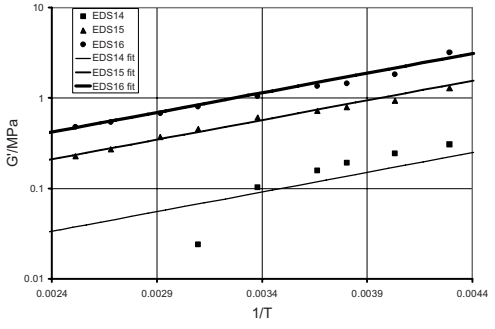

Figure 2. Arrhenius plot of G'(1 Hz, 10%) data minus (G'_{hve}) calculated according to the 4-parameter model for EDS19, amplified by factors 1 + 2.5φ; fits according to Equation 9; parameters are given in Tables 2 and 3.

Table 3. Fitting parameters used for the elastoplastic contribution.

Material	E/R (K)	$A(0.01 + c^2)^{-b/2}$ (MPa)	A(296 K) (MPa)	b	c
EDS14	1000	0.003052	0.04	0.35	0.006
EDS15	1000	0.019075	0.25	0.35	0.006
EDS16	1000	0.03815	0.50	0.35	0.006

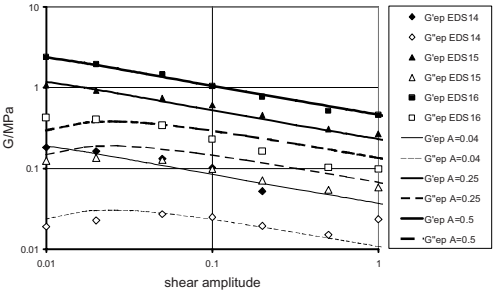

Figure 3. Fitting of elastoplastic parameters to $G_{ep} = G$(1 Hz, 296 K) where G_{hve} is calculated from $(1+2.5\varphi)G$(model, EDS19), the latter being the fit from Figure 1. In all cases, $b = 0.35$, $c = 0.006$.

to give a fair fit to the EDS14 data, taking the view that the filler loading for it is rather low so the resolution of the magnitude of the reinforcement is poor. Values of E and $A(296\text{ K})(0.1^2 + c^2)^{-b/2}$, obtained from the straight line fits in Figure 2, are given in Table 3.

b and c were chosen, using Figure 3, to fit the amplitude dependence of the moduli, and this fit also provides an additional check on the value of A(296 K). In fact, the same values of A were used in both Figures 2 and 3, resulting in a slight compromise on fits that might have been made independently. A reasonable fit was achieved using the same values of b and c for all the loadings of filler. Values of A, b and c are given in Table 3.

5 DISCUSSION

The individual parameters used in the model have distinctive effects and their physical significance will be explored here.

The behaviour of the matrix material, EDS19, at higher temperatures (the "rubbery plateau"—ambient and above, for natural rubber) is dominated by two parameters: the shear modulus G_∞, which may be estimated from the crosslink density using the statistical theory of rubber elasticity, and the relaxation parameter H_0 which may be estimated

from the rate of stress relaxation, expressed as % reduction per tenfold increase in time.

The shear moduli of EDS19 show a stronger dependence on temperature (or high equivalent rate), below ambient, than expected from the modest viscoelasticity quantified by H_0. However, by introducing the two viscoelastic power law parameters, H_m and m, this effect can be fitted reasonably well. These two parameters are needed to model the region of the viscoelastic master curve at temperatures (or frequencies) between those corresponding to the rubbery plateau and the transition to a glass. Referring to the portions of mastercurve given in Figure 1, G_∞ only affects the low frequency G' fit, and H_m and m only affect the high frequency end of the two master curves. The 2-parameter rubbery plateau model (dashed lines) fits the data quite well at low equivalent frequency, and the power law model (dotted lines) fits quite well at high equivalent frequency, but only by using the 4-parameter combination (thick solid lines) can a good fit be achieved over the entire range of the results.

Figures 4 and 5 assess the quality of fit achieved over a wide range of temperature and frequency for the full set of materials. G' is quite well captured as a function of amplitude, but the capture of G'' is less satisfactory (Figure 4). The filled rubbers show a much greater effect of frequency than described by the model (Figure 5).

The "matrix" model for EDS19 was augmented using the hydrodynamic reinforcing factor due to Einstein to account for the basic stiffening effect of non-interacting rigid spherical inclusions. Extensions of the hydrodynamic theory to include

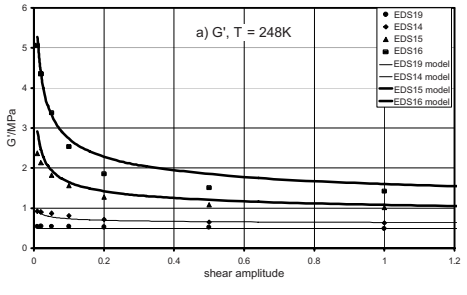

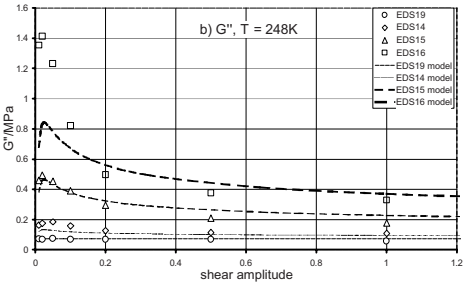

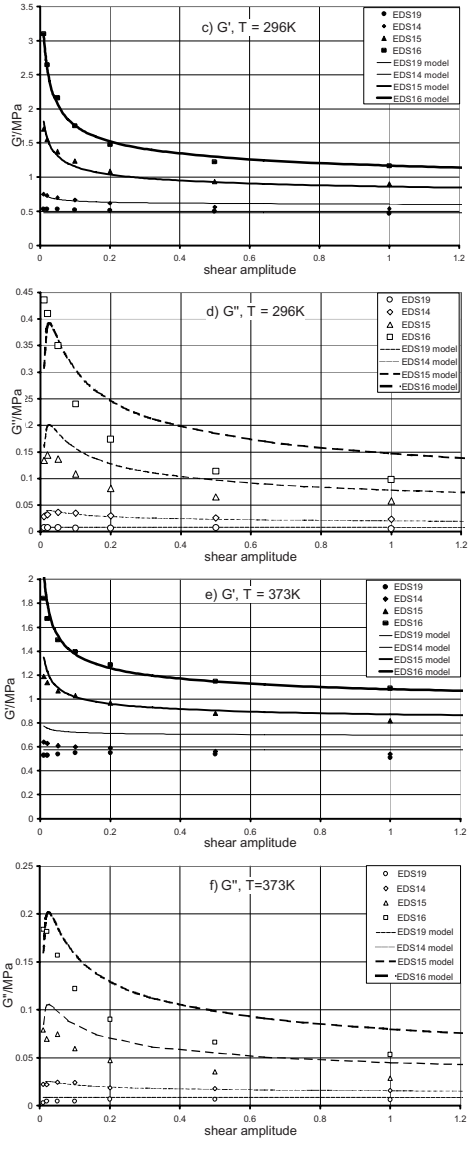

Figure 4. Amplitude dependence of shear moduli (shear strain 10%) a) G'(248 K) b) G''(248 K) c) G'(296 K) d) G''(296 K) e) G'(373 K) f) G''(373 K).

effects of interaction and departure from spherical shape exist and may be justified, but will not capture the additional mechanism (breakage and recovery) needed to explain the hysteresis introduced by reinforcing filler.

As details of geometry and dispersion of the filler are at best complicated, if known at all, it seems more appropriate to retain the simplest possible hydrodynamic modulus enhancement and add to it a phenomenological extra mechanism,

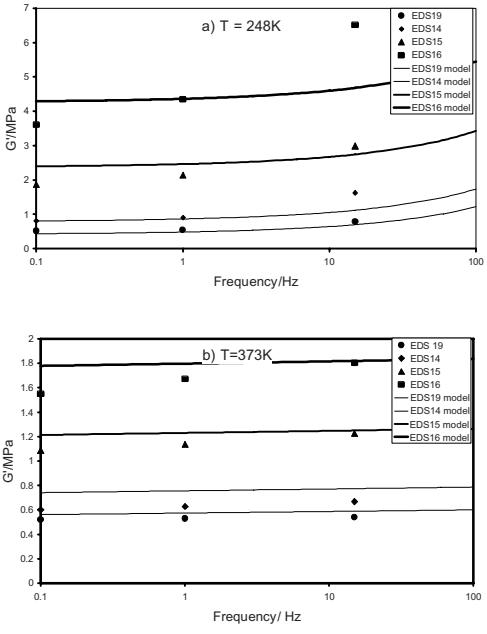

Figure 5. Frequency dependence of storage moduli (shear strain 2%) a) 248 K b) 373 K.

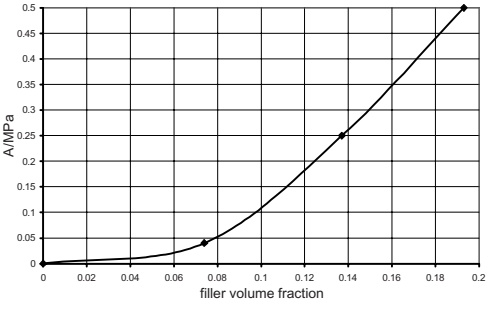

Figure 6. Dependence of elastoplastic modulus A on filler volume fraction. The line is just a guide for the eye.

given by Equations 7 to 9, which we will refer to as the "extra effect of reinforcement".

Two of the parameters needed to model the extra effect of reinforcement, *b* and *c*, describe the effectiveness of strain to break it down, and *A*, the third, describes the magnitude of the effect. It appears to be justified on the basis of the EDS results in Figure 3 to regard *b* and *c* as independent of filler loading; the dependence of *A* is shown in Figure 6.

The extra reinforcing effect depends non-linearly on the filler volume fraction, and is very small until a threshold loading is reached that corresponds approximately to that used in EDS14. This may relate to the percolation phenomenon: above a threshold volume fraction the electrical conductivity of rubber loaded with carbon black rises sharply, suggesting formation of a carbon black "structure" at higher loadings. Payne (1965), though, pointed out that the extra reinforcing effect depends on degree of dispersion of the black, not just on its loading; this too seems consistent with the idea that *A* measures the effectiveness of black-black interaction in a "structure" embedded in the rubber matrix.

The activation energy *E* describes the effectiveness of increased temperature in reducing the magnitude of the extra reinforcing effect. A single value, independent of filler loading, enables a reasonable fit to be made for all the materials over the range of temperatures. However, Equations 7 to 9 do not incorporate any effect of rate, or temperature-rate

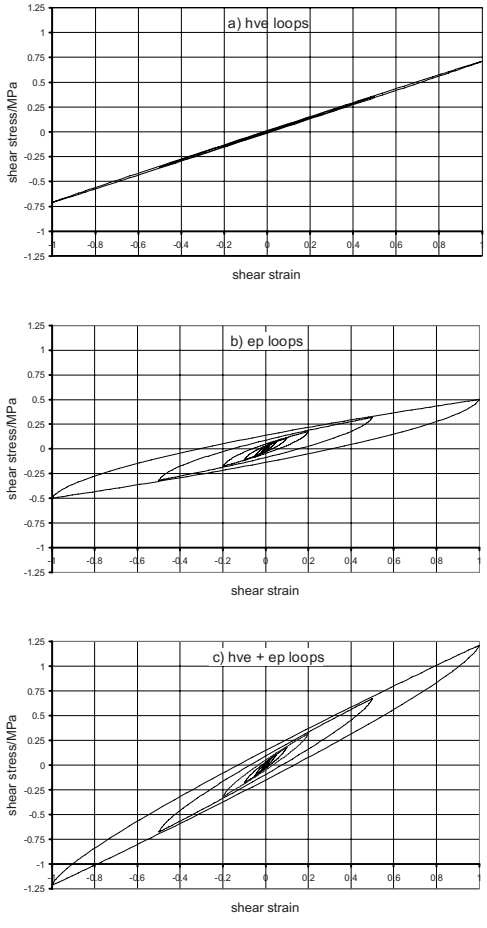

Figure 7. Hysteresis loops (EDS16, 296 K, 1 Hz) according to the model. a) hve term only b) ep term only c) complete model (hve + ep).

correspondence. This is a major weakness of the model, as seen in the relatively poor fits to the effect of frequency on the dynamic properties of filled rubber (Figures 5). It may also be seen in Figures 5 that even if the EDS19 results for G'' versus frequency were scaled up to reach a similar magnitude to that for EDS15 or EDS16, the effect of frequency would still be too weak. It thus appears that the extra reinforcing effect introduces higher frequency and temperature dependences to the material. The time-domain model used cannot include rate dependence of the extra effect of reinforcement, although in a frequency domain form such dependence could be imparted to A, eg by fitting it to the WLF equation, using a higher value of T_s than used for the matrix rubber. Such a frequency domain model could be implemented in FE software using the methodology developed by Rabkin (2007).

Figures 7 serve to emphasise that the proposed model is time-domain; and used as such to create the hysteresis loops, to which Equations 1 are applied to find the equivalent viscoelastic dynamic properties parameters. Thus we have gone behind the EDS data, to resurrect a general stress-strain behaviour that is broadly consistent with the tables of dynamic properties.

6 CONCLUSIONS

For each material, EDS tabulates the results of 117 dynamic tests, each test delivering two values, G^* and δ. The fit has been achieved using all data for EDS19 (Figure 1) to fit the four parameters for the hyperviscoelastic contribution (G_∞, H_0, H_m and m), 27 datapoints to fit the activation energy E for the elastoplastic contributions (Figure 2) and 39 additional datapoints to fit the 5 remaining elastoplastic parameters, A(EDS14), A(EDS15), A(EDS16), b and c; 300 datpoints in all. Since both the hyperviscoelastic model and the elastoplastic contributions are modeled in such a way that the parameters yield both G' and G'', the fit would have differed little if made only on the basis of the subset of 162 G' datapoints. The final model, using 8 parameters, only one of which depends on the filler loading, gives a reasonable capability of regenerating all 936 datapoints from the EDS.

The model thus seems to be a reasonably efficient way to capture all the data. The approach of applying it to a set of materials differing only in the quantity of filler has the merit that it has emerged as reasonably justifiable that only A, the magnitude of the extra reinforcing effect, need be varied, and it must, from a physical point of view, vary smoothly and systematically with the filler loading. The process of fixing values to the parameters may thus also serve to identify imperfections in the data, as judged by physical implausibility.

REFERENCES

Ahmadi H.R, Ihlemann J & Muhr A.H, 2007. "Time dependent effects in dynamic tests of filled rubber" pp 305–310 in Boukamel, Laiarinandrasana, Meo & Verron, eds, Constitutive Models for Rubber V, Leiden: Taylor & Francis/Balkema.

Ahmadi H.R, Kingston J.G.R & Muhr A.H, 2005. "Modelling dynamic properties of filled rubber in uniaxial and biaxial stress configurations" in Austrell P-E & Kari L, eds. Constitutive Models for Rubber IV, Leiden: Balkema.

Ahmadi H.R, Kingston J.G.R & Muhr A.H, 2008. "Dynamic properties of filled rubber. I—Experimental data and FE simulated results", Rubber Chem & Tech 81: 1–18.

Ahmadi H.R. & Muhr A.H. 1997. Modelling dynamic properties of filled rubber. Plastic, Rubber and Composites Processing and Applications 26: 451–461.

Ahmadi H.R & Muhr A.H, 2009. "Dynamic properties of filled rubber. II—Physical basis of contributions", submitted to Rubber Chem & Tech.

Ahmadi H.R, Muhr A.H, Dalrymple T & Govindrajan 2009. "Appraisal of nonlinear plasticity models for filled rubber using benchmark tests" to be presented at ECCMRVI.

Austrell P-E, Olsson A.K & Jönsson 2001. "A method to analyse the non-linear behaviour of carbon-black filled rubber using standard FE-codes" in Besdo D, Schuster R.H & Ihlemann J, eds, Constitutive Models for Rubber II, Lisse: Balkema.

Lion A, Kardelky C & Haupt P 2003. "The frequency and amplitude dependence of the Payne effect: Theory and experiments" Rubber Chem & Tech, 76: 533.

Lion A, Kardelky C, 2004. "The Payne effect in finite viscoelasticity: Constitutive modelling based on fractional derivatives and intrinsic time scales" J Plasticity, 20, 1313.

Muhr A.H 2009. "Dynamic properties of filled rubber. IV The effect of temperature" submitted to J Rubber Research.

Payne A.R 1965. "Effect of dispersion on the dynamic properties of filler-loaded rubbers" J Appl Polym Sci, 9: 2273–2284

Rabkin M 2007. "Simulation of the Fletcher-Gent effect by using the subroutine UPHI MSC/MARC" pp 263–268 in Boukamel, Laiarinandrasana, Meo & Verron, eds, Constitutive Models for Rubber V, Leiden: Taylor & Francis/Balkema.

TARRC, Natural Rubber Engineering Data Sheets, 1979–1986, www.tarrc.co.uk

Constitutive Models for Rubber VI – Heinrich et al. (eds)
© 2010 Taylor & Francis Group, London, ISBN 978-0-415-56327-7

On the modelling of the frequency dependence of the material behaviour of elastomers with emphasis on the coefficient of thermal expansion

J. Peters & O. von Estorff
Institute of Modelling and Computation, Hamburg University of Technology, Germany

M. Achenbach
Parker Hannifin GmbH & Co. KG, Packing Division Europe, Bietigheim-Bissingen, Germany

ABSTRACT: The material behaviour of elastomers is characterized by a frequency dependence and therefore a glass transition not only in its mechanical but also in its thermal properties. In this contribution an approach is presented, by which not only the frequency dependence in the mechanical properties in the sense of linear viscoelasticity can be described but also in addition in the coefficient of thermal expansion. For this purpose, the state space known from thermostatics is enlarged by internal variables to allow for the description of non-equilibrium states as well. The free energy function is chosen as thermodynamic potential. It is expanded into a Taylor-series of 2nd order. A set of contained material parameters is identified as contribution of each internal variable to the effective coefficient of thermal expansion. The results obtained from the numerical simulation agree with observations made in experimental investigations.

1 INTRODUCTION

The frequency dependence of the coefficient of thermal expansion can be investigated in experiments in which a sinusoidal temperature load is applied. As a result, a complex coefficient of thermal expansion is obtained. In Figure 1 results are shown from an investigation of Bauer & Boehmer (2000) in which capacitive scanning dilatometry was employed. A thin film made of polystyrene was subjected to a harmonic temperature loading with an amplitude of less than 1 K at a frequency of 4 mHz in the temperature range depicted. While in the in-phase response α' a transition from a lower "glassy" value to a higher "relaxed" value occurs as the temperature is increased, the out-of-phase response α'' runs through a maximum as the transition in α' occurs. Thus the results are similar to the ones obtained in a dynamic-mechanical analysis in which the storage and loss modulus are determined. Just as there exists a shift property in the mechanical case, by which the data obtained for one temperature can be related to that at another temperature by the well known time-temperature shift principle (Ferry 1980), the same is true for the thermal properties, as can be seen from Figure 2. Here, results from a harmonic experiment with polybutadiene are depicted for two different frequencies of the sinusoidal temperature input.

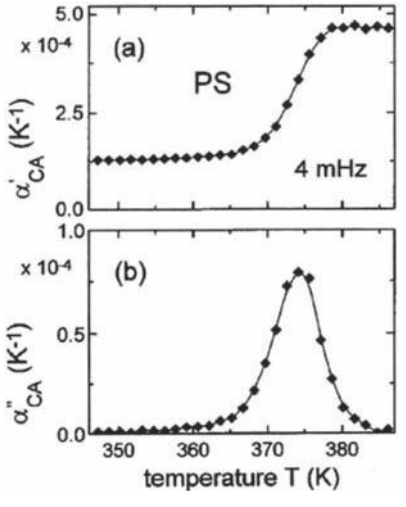

Figure 1. In-phase and out-of-phase response α' and α'' of the coefficient of thermal expansion in a harmonic experiment with polystyrene (from Bauer & Boehmer 2000).

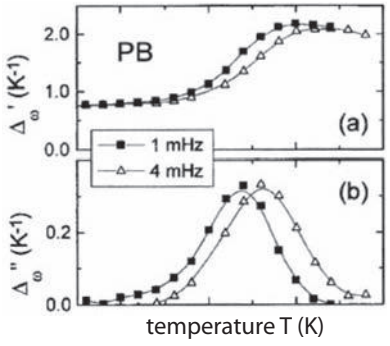

Figure 2. In-phase and out-of-phase response Δ' and Δ'' of the coefficient of thermal expansion in a harmonic experiment with polybutadiene for two different frequencies (from Bauer & Boehmer 2000).

2 BASIC EQUATIONS

For the derivation of constitutive equations describing the frequency and hence temperature-dependent material behaviour of polymeric materials, the specific free energy function ψ is an adequate thermodynamic potential (e.g. Haupt 2002, Mueller 1985). It is related to the internal energy u and the entropy s, both given as quantities per unit mass, by

$$\psi = u - \theta s, \tag{1}$$

where θ is the thermodynamic temperature. Substituting the material time derivative of u obtained from (1) into the first law of thermodynamics

$$\rho \dot{u} = \mathbf{T} : \dot{\mathbf{E}} - \mathrm{div}\mathbf{q}, \tag{2}$$

where ρ is the mass density, $\mathbf{T}$ the Cauchy stress tensor, $\dot{\mathbf{E}}$ the time rate of change of the infinitesimal strain tensor, and $\mathbf{q}$ the heat flux vector,

$$\rho\theta\dot{s} = -\rho\dot{\psi} + \mathbf{T} : \dot{\mathbf{E}} - \rho s\dot{\theta} - \mathrm{div}\mathbf{q} \tag{3}$$

is obtained as the local form of the energy balance. With the balance equation for the specific entropy s

$$\rho\theta\dot{s} = -\theta \mathrm{div}\frac{\mathbf{q}}{\theta} + \rho\theta\gamma, \tag{4}$$

where γ is the specific entropy production, and the equality

$$\theta \mathrm{div}\frac{\mathbf{q}}{\theta} = \mathrm{div}\mathbf{q} - \frac{1}{\theta}\mathrm{grad}\theta \cdot \mathbf{q}, \tag{5}$$

an equation for the entropy production γ in the form

$$\rho\theta\gamma = -\rho\dot{\psi} + \mathbf{T} : \dot{\mathbf{E}} - \rho s\dot{\theta} - \frac{1}{\theta}\mathrm{grad}\theta \cdot \mathbf{q} \tag{6}$$

is obtained. The second law of thermodynamics states, that the entropy production γ has to be non-negative. Hence, from (6) the so-called Clausius-Duhem inequality results

$$-\rho\dot{\psi} + \mathbf{T} : \dot{\mathbf{E}} - \rho s\dot{\theta} - \frac{1}{\theta}\mathrm{grad}\theta \cdot \mathbf{q} \geq 0. \tag{7}$$

As in the following the derivation of the constitutive equations is restricted to the one-dimensional case to reduce mathematical complexity and focus on the general ideas, the one-dimensional form of (7) is stated as well. In this case $\mathbf{T}$ reduces to the scalar Cauchy stress σ and $\mathbf{E}$ to the strain ε in the corresponding direction:

$$-\rho\dot{\psi} + \sigma\dot{\varepsilon} - \rho s\dot{\theta} - \frac{1}{\theta}\mathrm{grad}\theta \cdot \mathbf{q} \geq 0. \tag{8}$$

3 CONSTITUTIVE MODEL

The first constitutive assumption posed in this model is taken from irreversible thermodynamics (e.g. Keller 1977). The free energy ψ is said to not only depend on deformation ε and temperature θ, but also a set of so-called internal variables ξ_k

$$\psi = \psi(\varepsilon, \theta, \xi) \quad \text{with } \xi = (\xi_1, \ldots, \xi_k, \ldots, \xi_n). \tag{9}$$

The internal variables are to describe the deviation from equilibrium. Hence, in equilibrium their value depends on the independent variables ε and θ known from thermostatics, while in the non-equilibrium case their time evolution is governed by a set of differential equations still to be specified.

From (9) the material time derivative $\dot{\psi}$ is obtained as

$$\dot{\psi} = \frac{\partial\psi}{\partial\varepsilon}\dot{\varepsilon} + \frac{\partial\psi}{\partial\theta}\dot{\theta} + \sum_{k=1}^{n}\frac{\partial\psi}{\partial\xi_k}\dot{\xi}_k \tag{10}$$

and with (8)

$$\left(\sigma - \rho\frac{\partial\psi}{\partial\varepsilon}\right)\dot{\varepsilon} - \rho\left(s + \frac{\partial\psi}{\partial\theta}\right)\dot{\theta} - \rho\sum_{k=1}^{n}\frac{\partial\psi}{\partial\xi_k}\dot{\xi}_k - \frac{1}{\theta}\mathrm{grad}\theta \cdot \mathbf{q} \geq 0. \tag{11}$$

Just to avoid any misunderstanding: The summation convention according to Einstein is not made use of in this paper. A product between two parameters with matching indices therefore does not imply a summation. Equation (11) has to be

satisfied for arbitrary thermo-mechanical processes such that two potential relations and a remaining inequality result

$$\sigma = \rho \frac{\partial \psi}{\partial \varepsilon}, \tag{12}$$

$$s = -\frac{\partial \psi}{\partial \theta}, \tag{13}$$

$$-\rho \sum_{k=1}^{n} \frac{\partial \psi}{\partial \xi_k} \dot{\xi}_k - \frac{1}{\theta} \operatorname{grad}\theta \cdot \mathbf{q} \geq 0. \tag{14}$$

If the free energy ψ is independent of $\operatorname{grad}\theta$ and a special process with $\operatorname{grad}\theta = \mathbf{0}$ is assumed,

$$-\rho \sum_{k=1}^{n} \frac{\partial \psi}{\partial \xi_k} \dot{\xi}_k \geq 0 \tag{15}$$

alone must hold. If further the internal variables are taken to be independent,

$$-\rho \frac{\partial \psi}{\partial \xi_k} \dot{\xi}_k = A_K \dot{\xi}_k \geq 0 \quad \text{with } A_k = -\rho \frac{\partial \psi}{\partial \xi_k}, \tag{16}$$

where A_k is the affinity associated with each internal variable k, must hold for any of the k internal variables. The simplest ansatz for the evolution equations of the internal variables fulfilling (16) is

$$\dot{\xi}_k = \frac{1}{z_k(\varepsilon, \theta, \xi_k)} A_k \quad \text{with } z_k(\varepsilon_k, \theta, \xi_k) > 0. \tag{17}$$

Hence, the second law of thermodynamics poses a restriction on the choice of the evolution equations for the internal variables.

For the explicit form of the free energy function ψ in (9) the following approach is used. It is expanded into a Taylor-series of 2nd order about the undeformed ($\varepsilon_0 = 0$) and hence stress-free state as a reference state with a reference temperature of θ_{ref}, such that

$$\begin{aligned} &\Delta\varepsilon = \varepsilon - \varepsilon_0 = \varepsilon, \quad \Delta\theta = \theta - \theta_0 = \vartheta, \\ &\Delta\xi = \xi - \xi_{ref} = \xi, \quad k = 1 \ldots n, \end{aligned} \tag{18}$$

where $\xi_{ref} = 0$ has been set for all k internal variables. Performing the Taylor-series expansion, the following expression is obtained

$$\begin{aligned} \rho\psi = \rho\psi_{ref} &+ \frac{1}{2} a\varepsilon^2 + b\varepsilon\vartheta + \frac{1}{2} c\vartheta^2 + d\varepsilon + e\vartheta \\ &+ \frac{1}{2} \xi \cdot \mathbf{f}\xi + \mathbf{g} \cdot \xi\varepsilon + \mathbf{h} \cdot \xi\vartheta + \mathbf{k} \cdot \xi. \end{aligned} \tag{19}$$

The $n \times n$ matrix $\mathbf{f}$ with $\mathbf{f} = \mathbf{f}^T$ contains the second-order derivatives of ψ with respect to the internal variables and in its most general form allows for a coupling between internal variables. This aspect is not made use of in the following such that $\mathbf{f}$ is taken as a diagonal matrix. Evaluation of (12), (13) and (17) yields

$$\sigma = a\varepsilon + b\vartheta + \sum_{k=1}^{n} g_k \xi_k, \tag{20}$$

$$\rho s = -b\varepsilon - c\vartheta + \rho s_0 - \sum_{k=1}^{n} h_k \xi_k, \tag{21}$$

$$\dot{\xi}_k = -\frac{1}{z_k}(f_{kk}\xi_k + g_k\varepsilon + h_k\vartheta), \tag{22}$$

where $\sigma(0,0,\mathbf{0}) = 0$ and $\rho s(0,0,\mathbf{0}) = \rho s_0$ have been applied. Equations (20) to (22) resemble the complete set of constitutive equations for this model. Before the determination of the material parameters is discussed, the internal variables are rescaled according to

$$\tilde{\xi} = -\frac{f_{kk}}{g_k} \xi_k \tag{23}$$

to give

$$\begin{aligned} \sigma &= a\left[\varepsilon - \sum_{k=1}^{n} \frac{g_k^2}{a f_{kk}} \tilde{\xi}_k + \frac{b}{a}\right] \\ &= a\left[\varepsilon - \sum_{k=1}^{n} e_k \tilde{\xi}_k + \frac{b}{a}\vartheta\right], \end{aligned} \tag{24}$$

$$\rho s = -b\varepsilon - \sum_{k=1}^{n} \frac{h_k g_k}{f_{kk}} \tilde{\xi}_k - c\vartheta + \rho s_0, \tag{25}$$

$$\begin{aligned} \dot{\tilde{\xi}}_k &= -\frac{1}{\dfrac{z_k(\theta)}{f_{kk}}}\left(\tilde{\xi}_k - \varepsilon - \frac{h_k}{g_k}\vartheta\right) \\ &= -\frac{1}{\tau_k(\theta)}(\tilde{\xi}_k - \varepsilon + \alpha_k\vartheta). \end{aligned} \tag{26}$$

4 PARAMETER IDENTIFICATION

In order to start with the identification of the material parameters contained in the constitutive equations, (24) and (26) are considered for the case of $\theta = \theta_{ref}$, hence $\vartheta = 0$, first. It turns out that in this case the equations correspond with the equations obtained for the standard linear-viscoelastic solid. Therefore, a can be identified as the modulus in the glassy state E_0, and e_k and τ_k as relaxations strengths and corresponding relaxation times. As z_k according to (17) can be a function of the absolute temperature θ, the temperature dependence of the relaxation times $\tau_k(\theta)$ is inherent in the model.

It can be included by the standard procedure of invoking a shift-factor according to WLF- or Arrhenius-type equations (Ferry 1980).

It remains to identify a set of parameters (b/a; $\alpha_k = -h_k/g_k$, $k = 1\ldots,n$) which, looking at the units, are of a type of a coefficient of thermal expansion. Hence, it suggests itself to obtain these parameters from dilatometric experiments. For the case of an unrestricted thermal expansion the thermal strain ε_{th} can be obtained from the constitutive equations by setting $\sigma = 0$

$$\varepsilon_{th} = \sum_{k=1}^{n} e_k \tilde{\xi}_k - \frac{b}{a}\vartheta, \tag{27}$$

$$\dot{\tilde{\xi}}_k = -\frac{1}{\tau_k(\theta)}(\tilde{\xi}_k - \varepsilon_{th} + \alpha_k \vartheta). \tag{28}$$

If in a thought experiment a temperature step is applied starting from the reference state with $\tilde{\xi}_{ref} = 0$ for all k, the internal variables at first remain zero such that

$$\varepsilon_{th} = -\frac{b}{a}\vartheta = \alpha_0 \vartheta \tag{29}$$

is the initial response. Since the system is expected to react with the value of the coefficient of thermal expansion in the glassy state α_0, the factor $-b/a$ can be identified as α_0.

In order to identify the remaining parameters α_k, it is instructive to evaluate the model response again for a dilatometric experiment, this time with a harmonic temperature input in the form

$$\vartheta = \hat{\vartheta} e^{iwt}. \tag{30}$$

Here, ω is the angular frequency, $i = \sqrt{-1}$ the imaginary unit, and $\hat{\vartheta}$ the amplitude of the excitation. The system responds with the same frequency but shifted in phase such that

$$\varepsilon_{th}(\omega) = \hat{\varepsilon}_{th}(\omega) e^{iwt}, \tag{31}$$

$$\tilde{\xi}_k = \hat{\tilde{\xi}}_k(\omega) e^{iwt} \tag{32}$$

hold, where $\hat{\varepsilon}_{th}(\omega)$ and $\hat{\tilde{\xi}}_k(\omega)$ are the complex amplitudes of thermal strain and internal variables, respectively. Substituting equation (30) through (32) into the constitutive equations (27) and (28), a relation between strain amplitude and temperature amplitude can be established

$$\frac{\varepsilon_{th}(\omega)}{\hat{\vartheta}} = \frac{\alpha_0 - \sum_{k=1}^{n} \alpha_k \frac{e_k}{1 + i\tau_k\omega}}{1 - \sum_{k=1}^{n} \frac{e_k}{1 + i\tau_k\omega}} = \alpha^*(\omega), \tag{33}$$

which can be interpreted as complex coefficient of thermal expansion $\alpha^*(\omega)$. Hence, the model indeed shows a frequency dependence of the coefficient of thermal expansion. Splitting up (33) into real and imaginary part according to $\alpha^*(\omega) = \alpha'(\omega) - i\alpha''(\omega)$, the following results are obtained

$$\alpha'(\omega) = \frac{\left(\alpha_0 - \sum_{k=1}^{n} \alpha_k \frac{e_k}{1+(\omega\tau_k)^2}\right)\left(1 - \sum_{k=1}^{n} \frac{e_k}{1+(\omega\tau_k)^2}\right)}{\left(1 - \sum_{k=1}^{n} \frac{e_k}{1+(\omega\tau_k)^2}\right)^2 + \left(\sum_{k=1}^{n} \frac{e_k\tau_k\omega}{1+(\omega\tau_k)^2}\right)^2} + \frac{\left(\sum_{k=1}^{n} \alpha_k \frac{e_k\tau_k\omega}{1+(\omega\tau_k)^2}\right)\left(\sum_{k=1}^{n} \frac{e_k\tau_k\omega}{1+(\omega\tau_k)^2}\right)}{\left(1 - \sum_{k=1}^{n} \frac{e_k}{1+(\omega\tau_k)^2}\right)^2 + \left(\sum_{k=1}^{n} \frac{e_k\tau_k\omega}{1+(\omega\tau_k)^2}\right)^2} \tag{34}$$

$$\alpha''(\omega) = \frac{\left(\alpha_0 - \sum_{k=1}^{n} \alpha_k \frac{e_k}{1+(\omega\tau_k)^2}\right)\left(\sum_{k=1}^{n} \frac{e_k\tau_k\omega}{1+(\omega\tau_k)^2}\right)}{\left(1 - \sum_{k=1}^{n} \frac{e_k}{1+(\omega\tau_k)^2}\right)^2 + \left(\sum_{k=1}^{n} \frac{e_k\tau_k\omega}{1+(\omega\tau_k)^2}\right)^2} + \frac{\left(1 - \sum_{k=1}^{n} \alpha_k \frac{e_k}{1+(\omega\tau_k)^2}\right)\left(\sum_{k=1}^{n} \alpha_k \frac{e_k\tau_k\omega}{1+(\omega\tau_k)^2}\right)}{\left(1 - \sum_{k=1}^{n} \frac{e_k}{1+(\omega\tau_k)^2}\right)^2 + \left(\sum_{k=1}^{n} \frac{e_k\tau_k\omega}{1+(\omega\tau_k)^2}\right)^2} \tag{35}$$

The α_k therefore can be interpreted as individual contribution of each relaxation process, characterized by one of the k evolution equations of the internal variables, to the total thermal expansion. Evaluating (34) and (35) for high frequencies

$$\alpha'(\omega \to \infty) = \alpha_0, \quad \alpha''(\omega \to \infty) = 0 \tag{36}$$

are obtained as can be expected. For low frequencies the same result is obtained for α'' while with the relation for α' a connection between the coefficient of thermal expansion in the glassy state α_0 and the coefficient in the relaxed state α_∞ is obtained

$$\alpha'(\omega \to 0) = \frac{\left(\alpha_0 - \sum_{k=1}^{n} \alpha_k e_k\right)}{\left(1 - \sum_{k=1}^{n} e_k\right)} = \alpha_\infty \tag{37}$$

It should be noted at this point, that with the approach presented, a frequency dependence of

the heat capacity at constant deformation can also be established and that the material parameters not yet discussed are associated with this heat capacity. For the case of the heat capacity at constant stress a corresponding investigation was published by Lion & Yagimli (2009).

5 NUMERICAL RESULTS

In order to illustrate the capability of the model presented, some results from simulations, in which only on internal variable is used, are collected in this section. Numerical values have been assigned to the material parameters on the basis of typical values for rubber materials. The value of the coefficient of thermal expansion in the glassy state α_0 has been set to $100 \cdot 10^{-6}$ 1/K, the modulus in the relaxed state to $\alpha_\infty = 200 \cdot 10^{-6}$ 1/K such that with a value of $e_1 = 0.998$ for the relaxation strength, a values of $\alpha_1 = 99.86 \cdot 10^{-6}$ 1/K is obtained according to (37). The relaxation time τ_1 has been set to a value of 1.2 s for the glass transition temperature of $\theta_g = -20°C$. The temperature dependence of the relaxation time is included by evaluating the shift factor $a(\theta,\theta_g)$, relating the relaxation time at the glass transition temperature to another temperature, via

$$\tau_1(\theta) = a(\theta,\theta_g)\,\tau_1(\theta_g) \tag{38}$$

according to the WLF-equation (Williams, Landel & Ferry 1955)

$$\log a(\theta,\theta_g) = \frac{-C_1(\theta-\theta_g)}{C_2+\theta-\theta_g}. \tag{39}$$

C_1 and C_2 have been set to the universal values of 17.44 and 51.6 K, respectively.

5.1 *Frequency domain*

With the established material parameters, the real and the complex part of the coefficient of thermal expansion can be calculated over a range of temperature as a function of frequency employing (34) and (35). The results are depicted in Figure 3. The real part passes from the value in the glassy state $\alpha_0 = 100 \cdot 10^{-6}$ 1/K to the value in the relaxed state $\alpha_\infty = 200 \cdot 10^{-6}$ 1/K as the temperature is increased. The imaginary part runs through a maximum as the glass transition occurs in the real part. Hence, the numerical results qualitatively depict the results obtained from measurements as depicted in Figure 1. As the frequency at which the temperature sweep is performed is increased, the transition shifts to higher temperatures just as in the experimental data depicted in Figure 2.

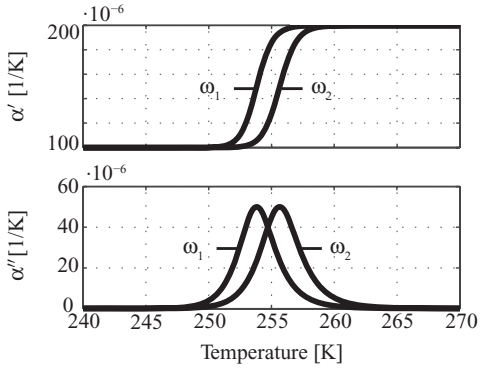

Figure 3. Temperature dependence of the real and the imaginary part α' and α'' of the complex coefficient of thermal expansion α^* for two frequencies with $\omega_1 = 1$ mHz, $\omega_2 = 4$ mHz, hence $\omega_2 > \omega_1$.

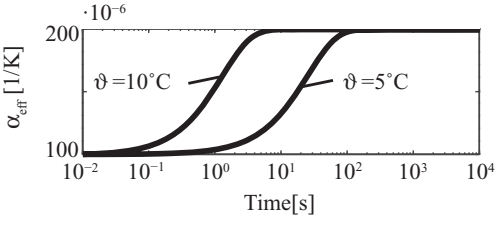

Figure 4. Time evolution of the effective coefficient of thermal expansion α_{eff} after a temperature step ϑ with two magnitudes has been applied.

5.2 *Time domain*

With the derived model, simulations in the time domain can be performed as well. As an example for a time domain simulation, the step response of the system is calculated employing equations (27) and (28). If a temperature step is applied starting from the glass transition temperature θ_g as reference temperature, the results depicted in Figure 4 are obtained.

Here, the effective coefficient of thermal expansion $\alpha_{\text{eff}}(t)$ is plotted as a function of time. It is defined as

$$\alpha_{\text{eff}}(t) = \frac{\varepsilon_{th}(t)}{\vartheta}. \tag{40}$$

At first, the value of the effective coefficient of thermal expansion α_{eff} corresponds with the value in the glassy state, such that $\alpha_{\text{eff}} = \alpha_0 = 100 \cdot 10^{-6}$ 1/K. Later, as the simulation time reaches the order of the effective relaxation time, the transition to the

relaxed value of $\alpha_{\text{eff}} = \alpha_{\infty} = 200 \cdot 10^{-6}$ 1/K occurs. As the effective relaxation time is smaller with higher temperature, the transition occurs earlier in the case where the higher temperature step is applied.

6 CONCLUSION

It could be shown that with the approach presented in this paper not only the glass transition in the mechanical properties of polymeric media but also in thermal properties such as the coefficient of thermal expansion can be modelled. For this purpose, the state space known from thermostatics, which consists of a measure for deformation and the absolute temperature, was enlarged by so-called internal variables to also allow for a consideration of non-equilibrium states. The free energy was chosen as the thermodynamic potential and expanded into a Taylor-series. It remains to validate the derived relations and the numerical results, which could 'only' show, that the experimentally observed behaviour can be depicted qualitatively by the model, as there is a lack of experimental data which resemble the glass transition in the mechanical *and* the thermal properties of single rubber compounds.

REFERENCES

Bauer, C. and R. Boehmer (2000). Capacitative scanning dilatometry and frequency-dependent thermal expansion of polymer films. *Physical Review E 61*(*2*), 1755–1764.

Ferry, J. (1980). *Viscoelastic properties of polymers.* New York: John Wiley.

Haupt, P. (2002). *Continuum mechanics and theory of materials*. Berlin: Springer.

Keller, J. (1977). *Thermodynamik der irreversiblen Prozesse*. Berlin: de Gruyter.

Lion, A. and B. Yagimli (2009). On the frequency-dependent specific heat and TMDSC: constitutive modelling based on thermodynamics with internal state variables. *Thermochimica Acta 490*, 64–74.

Mueller, I. (1985). *Thermodynamics.* London: Pitman.

Williams, M., R. Landel. and J. Ferry (1955). The temperature dependence of relaxation mechanisms in amorphous polymers and other glass-forming liquids. *Journal of the American Chemical Society* 77(14), 3701–3707.

Constitutive Models for Rubber VI – Heinrich et al. (eds)

Experimental determination of the mechanical properties of naturally aged rubber

I. Petrikova & B. Marvalová
Technical University of Liberec, Czech Republic

ABSTRACT: The aging effects on the dynamical and tribological properties of naturally aged segments of Polyisoprene/Polybutadiene Rubber Blend (IR/BR) with a different service history were investigated experimentally. Specimens sliced from segments were subjected to a series of static and relaxation tests, to dynamic mechanical analysis, and to hardness and friction measurements. Rubber becomes harder in the course of aging, loses its damping capability, and the properties determining its friction behaviour change and friction coefficient are reduced in comparison with the virgin state.

1 INTRODUCTION

Isoprene/Butadiene rubber segments used in resilient wheels effectively reduce vibrations and noise in transportation. Beside their damping function, the rubber segments have to transmit considerable alternating shear force and to sustain a large cyclic compressive load superposed on large static prestrain. Their material is degraded owing to severe operational conditions such as heavy mechanical loading, thermal loading due to the internal dissipative heating and to external temperature variation. In addition, permeation of oxidative, photolytic and hydrolytic agents causes deterioration in the material properties particularly of the outside surface. Rubber ages and becomes harder, it loses its damping capability and those properties determining its friction behaviour change. A long-lasting compressive load changes the segment shape and dimensions and produces a permanent set. After a certain period, slips between the wheel and rubber segments occur and the segments fail to perform their function without any apparent damage. The aging effects on the dynamical and tribological properties of naturally aged segments with different service history were experimentally investigated. Estimates of service life can then be made by extrapolating the degree of degradation after a given time of functioning.

Samples sliced by water jet from segments were subjected to a series of static and relaxation tests, to dynamic mechanical analysis, as well as to hardness and friction testing.

The experimental measurement of the time dependent response and of damping properties of viscoelastic materials consists of performing uniaxial creep and stress relaxation tests which are suitable for studying the material response over a long period of time.

We previously investigated the quasistatic rate-dependent behaviour of virgin segments of isoprene-butadiene rubber in compression regimes. The behaviour at different strain levels was examined in detail through quasistatic cyclic tests and in simple and multistep relaxation tests. The viscosity-induced rate-dependent effects were described and parameters of the material model were determined. The model was implemented into FE code (Marvalova 2007). The present paper is focused on the dynamic mechanical analysis of virgin and aged segments.

The dynamic mechanical analysis (DMA) is well suited for the identification of the short-time range of polymer response. DMA consists of dynamic tests, in which the force resulting from a sinusoidal strain controlled loading is measured.

The dynamic behaviour of filler-reinforced rubber has been investigated by many material scientists. The dependence of the storage and dissipation modulus on the temperature, the predeformation, the deformation amplitude and the frequency were all investigated. It was demonstrated that the moduli also depend on the type of filler material. Payne (1965) first pointed out that the moduli of carbon black filled rubber lessen with increasing deformation amplitudes. By means of further tests he reached the conclusion that this behaviour must be attributed to a thixotropic change. Lion (1998) observed that both the storage and the dissipation modulus depend on the frequency of the deformation process. This variation is weakly pronounced and in a good approximation of power-law type. In terms of the theory of linear viscoelasticity this behaviour corresponds to a continuous relaxation

time distribution. With increasing temperatures, he observed both a decrease in moduli and a lessening of the frequency dependence. The dependence of the dynamic moduli on the filler content and the static predeformation has been investigated in detail by Namboodiri and Tripathy (1994). When a viscoelastic material is subjected to a sinusoidally varying strain, after some initial transients the stationary stress-response will be reached in which the resulting stress is also sinusoidal, having the same angular frequency but advanced in phase by an angle δ. Then the strain lags the stress by the phase angle δ. The axial displacement $u(t)$ consists of a static predeformation u_0 under compression which is superimposed by small sinusoidal oscillations:

$$u(t) = u_0 + \Delta u \sin(2\pi f t). \tag{1}$$

Stresses and strains are calculated with respect to the reference geometry of the pre-deformed specimen:

$$\varepsilon_0 = u_0/(L_0 + u_0), \quad \Delta\varepsilon = \Delta u/(L_0 + u_0), \tag{2}$$

where L_0 is the undeformed length of the specimen. The force response $F(t)$ of the specimen is a harmonic function and can be written as:

$$F(t) = F_0 + \Delta F \sin(2\pi f t + \delta). \tag{3}$$

F_0 is the static force depending only on the pre-deformation u_0. The force amplitude ΔF and the phase angle δ depend, in general, on the predeformation, the frequency and the strain amplitude (Lion & Kardelky 2004, Hofer & Lion 2009). If the incompressibility of the rubber is assumed $A_0 L_0 = A(L_0 + u_0)$, where A_0 is the cross-sectional area of the undeformed specimen, we can relate the force to the cross-sectional area A of the predeformed specimen:

$$\sigma(t) = \frac{F(t)}{A} = \sigma_0 + \Delta\sigma[\cos(\delta)\sin(2\pi f t) + \sin(\delta)\cos(2\pi f t)]. \tag{4}$$

The dynamic stress-response $\sigma(t)$ normalised by the deformation amplitude $\Delta\varepsilon$ can be written:

$$\sigma(t) = \sigma_0 + \Delta\varepsilon[G'(\varepsilon_0, f, \Delta\varepsilon)\sin(2\pi f t) + G''(\varepsilon_0, f, \Delta\varepsilon)\cos(2\pi f t)], \tag{5}$$

where

$$G'(\varepsilon_0, f, \Delta\varepsilon) = \frac{\Delta\sigma}{\Delta\varepsilon}\cos(\delta), \tag{6a}$$

and

$$G''(\varepsilon_0, f, \Delta\varepsilon) = \frac{\Delta\sigma}{\Delta\varepsilon}\sin(\delta) \tag{6b}$$

are the storage and dissipation moduli respectively, and δ is the phase angle. In general, carbon black-reinforced rubber has fairly a weak frequency dependence in conjunction with a pronounced amplitude dependence (Hofer & Lion 2009). If the strain amplitude $\Delta\varepsilon$ increases, the storage modulus G' lessens and the dissipation modulus G'' shows a more or less pronounced sigmoidal behaviour-Payne effect. If the material is linear viscoelastic, then these two moduli depend neither on the deformation amplitude nor on the static predeformation. The damping factor or loss tangent (tan δ) which is the ratio G''/G' is the measure of mechanical energy dissipated as heat during the dynamic cycle. If the dynamic strain amplitude is constant in time, we can observe time-independent moduli (Lion 1998). These phenomena are frequently interpreted as a dynamic state of equilibrium between breakage and recovery of physical bonds linking adjacent filler clusters. The most common model of this state is the Kraus model (Kraus 1984, Ulmer 1996) which describes the amplitude dependence of dynamic moduli. The influence of static pre-deformation ε_0 is included in the models of Kim et al. (2004), Cho & Youn (2006) and the uniaxial form of the frequency, amplitude and pre-strain dependent dynamical moduli are proposed by Lion (2004).

The purpose of this present paper is to summarise the results of experimental research into the behaviour of rubber samples with different service history under dynamic loading conditions. We carried out harmonic strain-controlled tests under compression and studied the dependence of the storage and dissipation moduli on the frequency, on the deformation amplitude and on the static pre-strain.

2 EXPERIMENTAL

The sample is a rectangular parallelepiped whose width, depth, and height are 15, 15, and 20 mm respectively. The specimens were cut by water jet from segments that have been in operation for different times. Since the operating conditions are not known, the only measure of segment fatigue is the number of kilometres travelled. This number, in thousands of kilometres is shown in Table 1, together with the hardness values. Specimens marked R are all from one producer, the specimen marked G is of unknown provenance.

Table 1. Hardness of samples and the path in thousands of km.

Sample	0 R	1 R	2 R	3 G	4 R	5 R	6 R
[km]	0	175	255	172	75	473	146
ShoreA	70.3	82.4	86.1	85.4	83.6	83.5	88.3

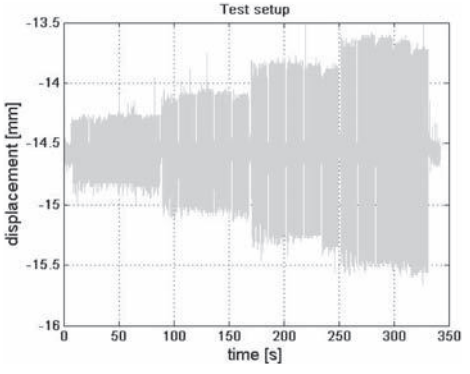

Figure 1. Dynamic mechanical analysis test setup.

The tests are performed at room temperature using an electrodynamic Instron testing machine. In the preconditioning process applied, the pre-strain was about $\lambda_0 = 0.65$ under compression and the amplitude $\Delta\varepsilon$ about 0.08.

Subsequent to this preconditioning process, three different constant compressive pre-strains $\lambda_0 = 0.85$, 0.75 and 0.65 were applied, and for each of them, five ascending amplitudes of the superimposed harmonic strain varied between 0.01 and 0.06. The frequencies varied in 5 steps between 1 and 10 Hz for all of strain amplitude. The process was strain-controlled. The test setup repeated for every static pre-strain is obvious from Figure 1.

Raw test data sampled at 1 KHz were recorded by PC and evaluated in the Matlab Signal Processing Toolbox. The discrete Fourier transform was used to determine the frequency content of force and head displacement signals and to calculate the phase lag between them.

Furthermore, we determined the complex dynamic modulus as the ratio between the amplitudes of stress and strain and dynamic moduli were calculated according to the relation (6).

3 RESULTS OF MEASUREMENT

3.1 *Dynamic properties of virgin samples*

The influence of the static pre-deformation (λ_0 increasing from 0.85 over 0.75 to 0.65) on the loss angle and dynamic moduli were monitored for virgin samples.

The evolution of loss angle δ of virgin material for the three compressive pre-deformations is evident from the Figure 2. The loss angle decreases markedly with increasing pre-strain and the storage modulus increases as is evident from the Figure 3.

In the measured range of amplitudes and frequencies the graph of the loss angle resembles a horse saddle. The frequency dependence of the loss angle δ is weak; it passes through a moderate minimum between 1 and 3 Hz.

By contrast, the amplitude dependency is pronounced, the loss angle reaches its maximum approximately in the middle of the interval of amplitude.

The storage modulus of virgin specimens on Figure 3 increases notably with increasing static pre-stretch λ_0. The storage modulus increases slightly with increasin g frequency and significantly decreases with increasing amplitude. Both dependencies are monotonous in the range of frequencies and amplitudes applied.

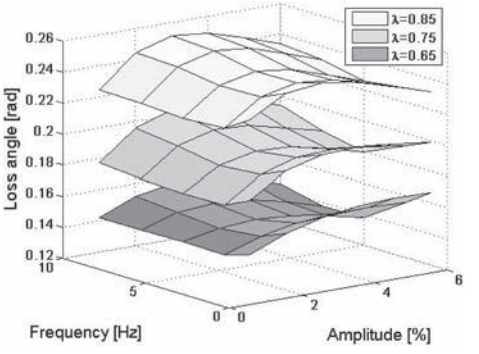

Figure 2. Variation of loss angle of virgin specimens with amplitude and frequency at different pre-strains λ.

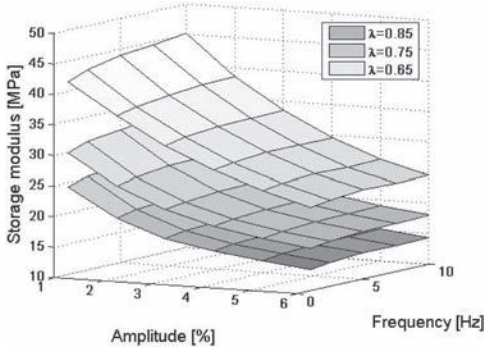

Figure 3. Variation of storage modulus of virgin specimens with amplitude and frequency at different pre-strains λ.

The loss modulus of virgin specimens on the Figure 4 follows similar trends with the difference that it does not depend significantly on the static pre-stretch λ_0.

3.2 *Dynamic properties of aged samples*

The main task of this experimental work was to investigate how the natural aging and fatigue affect mechanical properties of rubber segments.

Dynamic properties were measured by means of the DMA on 6 sets of aged samples. In each set, there were 5 samples with the same operational history which is evident from the Table 1.

3.2.1 *Loss angle* δ

Comparison of loss angles of samples with a different service history is on the Figure 5. The graph represents the dependency on amplitudes at the static pre-strain $\lambda_0 = 0.75$ and the frequency 5 Hz.

We see that the loss angles of aged and virgin samples have a similar trend. The loss angle values of aged specimens are lower than the loss angle of virgin specimens. The only exception is the set of samples G172, which is from a different producer.

3.2.2 *Storage modulus*

Comparison of storage moduli of specimens with different service history is on Figure 6. We see a considerable fall of storage moduli of all samples with increasing values of amplitude. An analysis of the measured data shows that the dependence of storage moduli on frequency is weak for all samples in the applied frequency interval.

The majority of the storage moduli of aged samples are bigger than the storage modulus of virgin material. The sample R473 that has been in the longest operation shows the largest storage modulus.

3.2.3 *Loss modulus*

A comparison of loss moduli of aged and virgin samples is on Figure 7. Loss moduli diminish with increasing amplitude. The difference of their values is small, nevertheless, the loss modulus of virgin material is lower than most of the other values.

3.3 *Hardness of segments and permanent set*

The permanent set and the hardness of all aged segments were measured prior to being sliced into samples by water jet.

3.3.1 *Permanent set*

The average thickness reducing permanent set in the direction of main compressive working load is about 11.5%. The extending permanent set is about 16.2% in the circumferential direction of the wheel. In this direction the segments are subjected to shear due to the torque transmission, and they are also enlarged owing to the compression in a perpendicular direction.

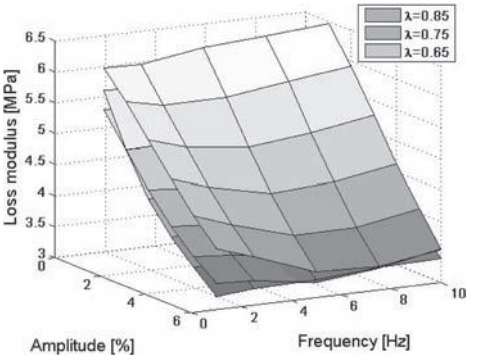

Figure 4. Variation of loss modulus of virgin specimens with amplitude and frequency at different pre-strains λ.

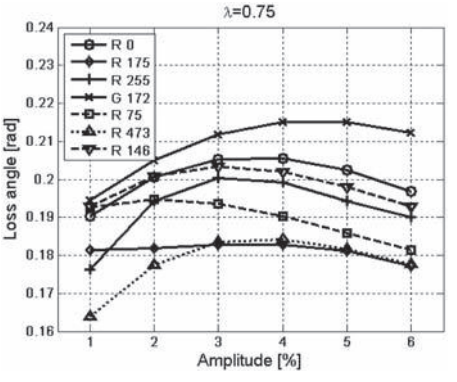

Figure 5. Comparison of loss angles of specimens with different service history at $\lambda_0 = 0.75$ and at frequency 5 Hz.

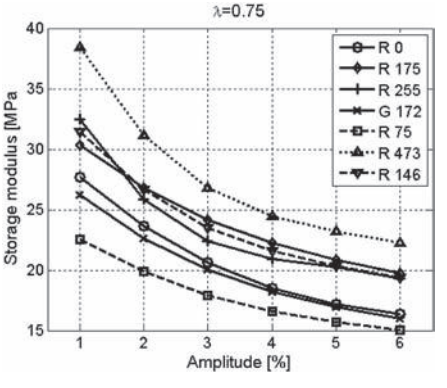

Figure 6. Comparison of storage moduli of specimens with different service history at $\lambda_0 = 0.75$ and at frequency 5 Hz.

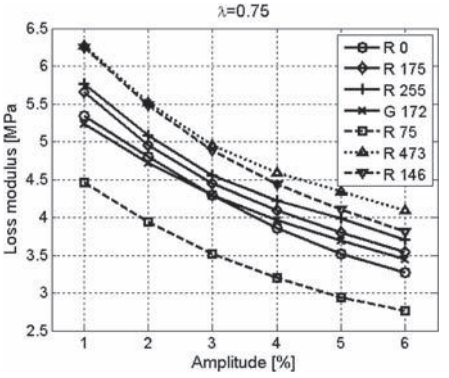

Figure 7. Comparison of loss moduli of specimens with different service history at $\lambda_0 = 0.75$ and at frequency 5 Hz.

3.3.2 *Hardness*

Hardness Shore A of rubber segments is listed in the Table 1. The hardness on the surface of the worn segments is 10–15 ShA more than hardness of virgin segments. The reason for such a difference is probably the enhanced degradation of surface layers.

4 CONCLUSION

DMA tests were conducted under strain-controlled loading condition at room temperature to prove assumed difference of dynamical properties amongst IR/BR samples prepared from naturally aged segments with a different service history. Based on the test results we can draw some conclusions:

- All samples show the Payne effect—as the strain amplitudes of the load increase, storage and loss moduli decrease.
- The frequency dependence of observed dynamic quantities is weak in the experimental frequency range.
- The loss angle decreases and the storage modulus increases with the increasing static pre-strain.
- The loss angles of virgin rubber samples are larger than of worn ones.
- Storage moduli of samples from worn segments are greater than storage moduli of virgin samples.
- The segments become harder and stiffer during their service life and lose their damping capability.
- Dimensions of segment change markedly due to the permanent set.

For all these reasons segments can fail to perform their function which is quite unusual for a rubber element. In addition to the vibration damping they have to transmit the driving torque by means of friction. Usually the slip between the wheel disc and rim put an end to segment life. The main purpose of this study was to examine this one aspect of the segment failing. An exhaustive study of segment reliability remains a future endeavour.

ACKNOWLEDGEMENT

This work was supported by a grant from Ministry of Education of Czech Republic under Contract Code MSM 4674788501.

REFERENCES

Cho, J.-H., Youn, S.-K., 2006, A viscoelastic constitutive model of rubber under small oscillatory load superimposed on large static deformation considering the Payne effect, *Arch. Appl. Mech.*, 75, pp. 275–288.

Hofer, P., Lion, A., 2009, Modelling of frequency- and amplitude-dependent material properties of filler-reinforced rubber, *J. Mech. Phys. Solids*, Vol. 57, pp. 500–520.

Kim, B.K., Youn, S.K., Lee, W.S., 2004, A constitutive model and FEA of rubber under small oscillatory load superimposed on large static deformation, *Arch. Appl. Mech.*, 73, pp. 781–798.

Kraus, G., 1984, Mechanical losses in carbon black filled rubbers, *J. Appl. Polym. Sci.*, Vol. 39, pp. 75–92.

Lion, A., 1998, Thixotropic behaviour of rubber under dynamic loading histories: experiments and theory, *J. Mech. Phys. Solids*, Vol. 46, No. 5, pp. 895–930.

Lion, A., Kardelky, C., 2004, The Payne effect in finite viscoelasticity: constitutive modelling based on fractional derivatives and intrinsic time scales, *Int. J. Plasticity*, Vol. 20, pp. 1313–1345.

Lion, A., 2004, Phenomenological modelling of the material behaviour of carbon black-filled rubber, *Kautschuk Gummi Kunststoffe*, Vol. 57, No. 4, pp. 184–190.

Lion, A., 2005, Phenomenological modelling of strain induced changes in filler-reinforced elastomers, *Kautschuk Gummi Kunststoffe*, Vol. 58, No. 4, pp. 157–162.

Marvalova, B., Viscoelastic properties of filled rubber—Experimental observations and material modelling, *Constitutive Models for Rubber V*, Eds. A. Boukamel, L. Laiarinandrasana, S. Meo & E. Verron, pp. 79–84.

Namboodiri, C., Tripathy, D., 1994, Static and dynamic strain-dependent viscoelastic behaviour of black-filled EPDM vulkanisates, *J. Appl. Polymer Sci.*, Vol. 53, pp. 877–889.

Payne, A.R.,1965, Dynamic properties of natural rubber containing heat treated carbon black, *J. Appl. Polymer Sci.*, Vol. 9, pp. 3245–54.

Ulmer, J.D., 1996, Strain dependence of dynamic mechanical properties of carbon black-filled rubber compounds, *Rubber chem. technol.*, Vol. 69, No. 1, pp. 15–47.

Wang, M.J., 1998, The role of filler networking in dynamic properties of filled rubber, *Proceedings of conf. of Rubber Division of Am. Chemical Soc.*, Indianapolis, Indiana, May 1998, Paper No. 48, pp. 1–35.

Constitutive Models for Rubber VI – Heinrich et al. (eds)

Modelling and simulation of dynamically loaded elastomer-mounts under predeformation

J. Retka & A. Lion
University of the Federal Armed Forces, Neubiberg, Germany

ABSTRACT: The article deals with the formulation of a frequency-dependent material model in order to describe the combined static and dynamic load of elastomer-mounts. First the authors outline the requirements on the model and second deduce an appropriate description of the process. The proceeding results in a frequency-dependent constitutive model. Finally a proposal to implement the model is discussed.

1 INTRODUCTION

In the course of further development of computational predictions of component properties the demand for predictions of the material-response to dynamic loads is increasing. The mounting of vibrant structures is realized by elastomer-materials on a big scale. Examples are engine mounts in the automotive industry. The vibration behaviour and the resulting acoustic emissions affect directly the driving comfort. Current methods to construct such mounts are based upon experiences and possible malfunctions are assessed late. Therefore a computational simulation is useful to influence the development as early as possible.

At the beginning this article motivates the description of the material properties in the frequency domain. The considered load case is divided into two parts: First a static finite predeformation results from the weight of the mounted structure. Second the structure superimposes vibrations which are small in comparison with the predeformation.

The presented approach bases on an existing constitutive model of finite viscoelasticity, described at first by Haupt and Lion (2002), which is enhanced to describe the material behaviour in the frequency domain as proposed by Lion, Retka and Rendek (2009). The used constitutive model is characterized by its variability based on a thermomechanical consistent theory. In addition this procedure is applicable to arbitrary constitutive models.

With the derived frequency-domain formulation the implementation in a FE-program is possible following a proposal by Morman und Nagtegaal (1983). In this case the constitutive equations are implemented in the program MSC.Marc and the results are discussed.

2 MATERIAL BEHAVIOUR

The used material is normally a nonlinear viscoelastic elastomer and therefore it is necessary to discuss the influence of the four parameters frequency, temperature, predeformation and amplitude of the harmonic excitation. With respect to the mentioned load case it is necessary to describe the material in the frequency domain. Hence the experiments have to be carried out in the frequency domain. Elastomers show typically a frequency-dependent behaviour as shown in Figure 1. In this context, the concept of thermo-rheological simplicity is used, in order to generate the master curve.

During the entire loading process the temperature is assumed to be constant at room temperature. Due to the low glass transition temperature of the tested material an exponential relation can be used to describe the technical interesting range of frequency from 1–1000 Hz. The dependences of the

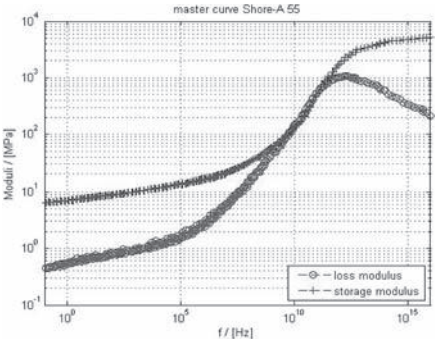

Figure 1. Master curve of an elastomer with the shore hardness shore-A 55.

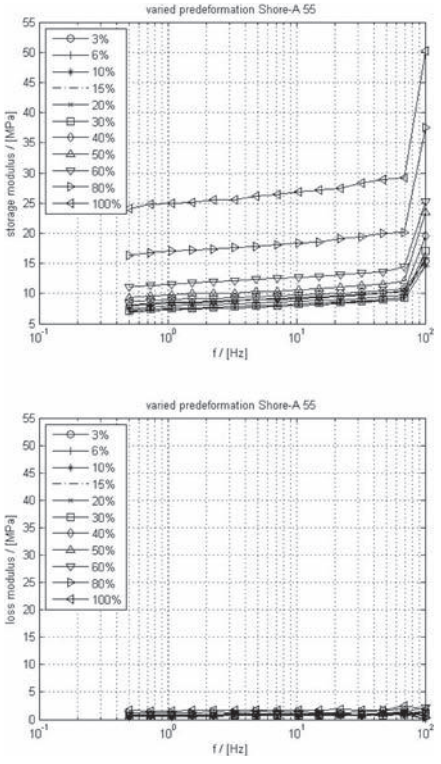

Figure 2. Storage and loss modulus as function of the frequency and different predeformations at room temperature.

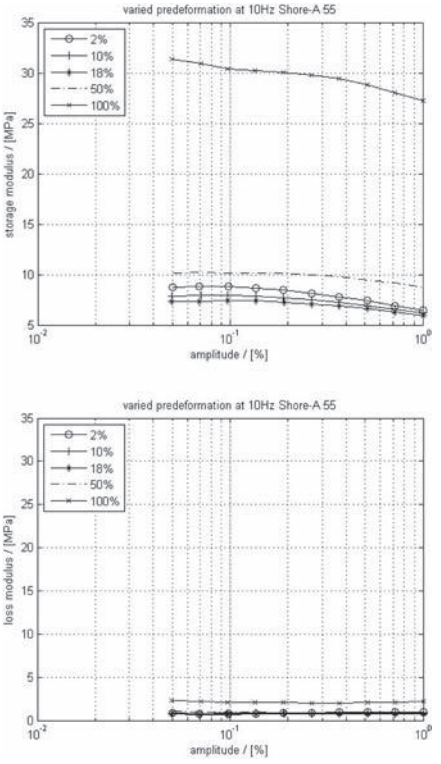

Figure 3. Storage and loss modulus as function of the amplitude of the harmonic excitation at a frequency of 10 Hz and room temperature.

storage and the loss modulus on the predeformation and on the amplitude of the harmonic excitation are shown in Figure 2 and Figure 3. Thereby one can see the pronounced dependence on the predeformation. For small amplitudes in comparison with the predeformation $\Delta\varepsilon << \varepsilon_0$ and $\Delta\varepsilon < 0{,}1\%$ the influence on the material behaviour is negligible as diagrammed in Figure 3.

If the amplitude-dependence of the material should be considered, time-domain simulations must be carried out.

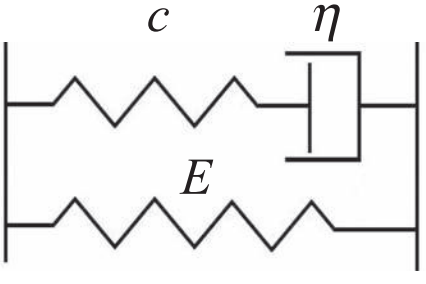

Figure 4. Maxwell-model.

3 MODELLING

A proved model to describe viscoelasticity is the Maxwell-model.

A one dimensional model is shown in Figure 4. The model consists of a spring with the elasticity modulus E and one or more Maxwell-elements which are connected in parallel. If the structure is deformed, e.g. one pulls an end, the model generates a stress which is composed of two parts. The spring with the modulus E adds an equilibrium part and the Maxwell-elements result in a rate-dependent overstress. Subject to the viscosities η_k of the dashpots, the springs with the elasticities C_k show relaxation until the equilibrium stress remains on its own.

This approach can be enhanced to a three dimensional model. The proceeding consists of three parts: development of kinematic relations, evaluation of the balance principles and derivation of constitutive equations.

First of all the kinematics will be considered. The deformation gradient $\mathbf{F}$ maps the reference configuration R to the current configuration C and is decomposed into a volume deformation $\bar{\mathbf{F}}$ and an isochoric part $\hat{\mathbf{F}}$ (Figure 5).

$$\mathbf{F} = \bar{\mathbf{F}}\hat{\mathbf{F}} \quad \begin{cases} \bar{\mathbf{F}} = J^{1/3}\mathbf{1} \\ \hat{\mathbf{F}} = J^{-1/3}\mathbf{F} \\ J = \det \mathbf{F} \end{cases} \tag{1}$$

For the further calculation only the history of the isochoric deformation is taken into account. For this reason a relative isochoric deformation gradient $\hat{\mathbf{F}}_{t(s)}$ is introduced. It maps tangent vectors from the current isochoric configuration at the time t to a previous isochoric configuration at the time s. Further introduced measures for the deformation are the Right Cauchy Green tensor $\mathbf{C} = \mathbf{F}^T\mathbf{F}$ and the Piola strain tensor $\mathbf{e} = 1/2(\mathbf{C}^{-1}-\mathbf{1})$ which can be calculated for each configuration.

The next step is the selection of an appropriate ansatz for the free energy density which satisfies the dissipation principle. With respect to the conception of the Maxwell-model the free energy density functional consists of a hyperelastic equilibrium part and a rate-dependent non-equilibrium part. The second part is a functional of the history of the isochoric relative Piola strain tensor. In comparison with the Maxwell-model the free energy represents the elastic energy stored in the springs.

$$\rho_R \psi_{(t)} = w_{eq(\mathbf{C})} - \int_{-\infty}^{t} G_{(t-s)} \frac{d}{ds} tr(\hat{\mathbf{e}}_{t(s)}) ds$$
$$\text{with} \quad G_{(t)} = \sum_{k=1}^{n} \mu_k e^{-\frac{t}{z_k}} \tag{2}$$

ρ_R is the mass density of the material in the reference configuration and $G_{(t)}$ is a scalar-valued relaxation function which is the sum of decreasing exponentials.

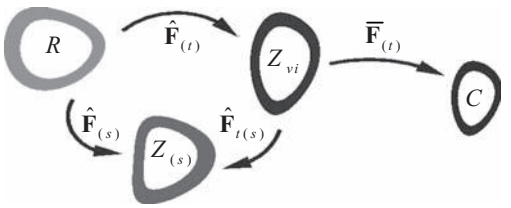

Figure 5. Volumetric-isochoric split of the deformation gradient.

The evaluation of the dissipation principle

$$-\rho_R \dot{\psi}_{(t)} + \frac{1}{2}\tilde{\mathbf{T}} \cdot \dot{\mathbf{C}} \geq 0 \tag{3}$$

in case of isothermal conditions and in the material description results in the constitutive equations and leads to the following stress-strain relation

$$\tilde{\mathbf{T}} = \tilde{\mathbf{T}}_{eq} + \tilde{\mathbf{T}}_{ov} = 2\frac{\partial w_{eq}}{\partial \mathbf{C}} - 2\overset{4}{\mathbf{P}} \int_{-\infty}^{t} G_{(t-s)} \hat{\mathbf{e}}'_{(s)} ds \tag{4}$$

with the time-dependent fourth order projection tensor

$$\overset{4}{\mathbf{P}}_{(t)} = (\det \mathbf{C})^{-1/3} \left[\overset{4}{\mathbf{1}} - \frac{1}{3}\mathbf{C}^{-1} \otimes \mathbf{C} \right] \tag{5}$$

which follows from the kinematics.

Analogous to the Maxwell-model the 2nd Piola Kirchhoff stress tensor contains an equilibrium stress and an overstress.

In order to linearize the relation geometrically around a predeformation $\mathbf{F}_0$ the ansatz

$$\begin{aligned} &\mathbf{F}_{(t)} = \mathbf{f}_{(t)}\mathbf{F}_0, \\ &\mathbf{f}_{(t)} = \mathbf{1} + \mathbf{h}_{(t)}, \quad \|\mathbf{h}\| << 1 \end{aligned} \tag{6}$$

is chosen and the incremental strain tensor

$$\mathbf{E}_{\text{lin(t)}} = \frac{1}{2}(\mathbf{h}_{(t)} + \mathbf{h}^T_{(t)}) \tag{7}$$

is defined. Now the geometrically linearized version of the stress-strain relation can be calculated.

$$\begin{aligned} \tilde{\mathbf{T}} = 2\left.\frac{\partial w_{eq}}{\partial \mathbf{C}}\right|_{\mathbf{C}_0} + 4\left.\frac{\partial^2 w_{eq}}{\partial \mathbf{C}^2}\right|_{\mathbf{C}_0} \mathbf{F}_0^T \mathbf{E}_{\text{lin}} \mathbf{F}_0 \\ + 2\overset{4}{\mathbf{R}}_0 \sum_{k=1}^{n} \int_0^t \mu_k e^{-\frac{t-s}{z_k}} \mathbf{F}_0^T \dot{\mathbf{E}}_{\text{lin(s)}} \mathbf{F}_0 ds \end{aligned} \tag{8}$$

with the predeformation-dependent fourth order projection tensor

$$\overset{4}{\mathbf{R}}_0 = \left[\mathbf{C}_0^{-1} \otimes \mathbf{C}_0^{-1} \right]^{\overset{23}{T}} - \frac{1}{3}\mathbf{C}_0^{-1} \otimes \mathbf{C}_0^{-1} \tag{9}$$

Finally it is necessary to deduce the dynamic modulus tensor. The assumption of harmonic incremental deformations is represented by the incremental strain tensor

$$\mathbf{E}_{\text{lin(t)}} = \frac{1}{2}(\mathbf{h}_{(t)} + \mathbf{h}^T_{(t)}) = \Delta \mathbf{E}_{\text{lin}} e^{i\omega t} \tag{10}$$

with the amplitude $\Delta\mathbf{E}_{\text{lin}}$ and the angular frequency ω of the harmonic excitation.

The evaluation of equation (8) for large times respectively the stationary solution results in the following expression for the 2nd Piola Kirchhoff stress tensor

$$\begin{aligned}\tilde{\mathbf{T}} &= 2\left.\frac{\partial w_{eq}}{\partial \mathbf{C}}\right|_{\mathbf{C}_0} + \left(4\left.\frac{\partial^2 w_{eq}}{\partial \mathbf{C}^2}\right|_{\mathbf{C}_0} + \sum_{k=1}^{n} \frac{2i\omega\mu_k z_k}{1+i\omega z_k} \overset{4}{\mathbf{R}}_0 \right) \\ &\quad \times \mathbf{F}_0^T \Delta\mathbf{E}_{\text{lin}} \mathbf{F}_0 e^{i\omega t} \\ &= 2\left.\frac{\partial w_{eq}}{\partial \mathbf{C}}\right|_{\mathbf{C}_0} + \overset{4}{\mathbf{G}}_{(\omega)}\, \mathbf{F}_0^T \Delta\mathbf{E}_{\text{lin}} \mathbf{F}_0 e^{i\omega t}\end{aligned} \tag{11}$$

with the frequency-dependent dynamic modulus tensor of fourth order $\overset{4}{\mathbf{G}}_{(\omega)}$ which is related to the reference configuration.

4 IMPLEMENTATION

Based on the mentioned proposal by Morman und Nagtegaal (1983) the FE-program MSC.Marc has an interface for the implementation of constitutive models and its frequency-range formulations.

Provided that the material is incompressible and under isothermal conditions one can enter a dynamic modulus tensor referred to the predeformed configuration.

With the push forward transformation $\mathbf{F}_0 \tilde{\mathbf{T}} \mathbf{F}_0^T$ of equation (11) and the assumption of incompressibility the predeformed stress-strain relation

$$\mathbf{T}_0 = 2\mathbf{F}_0 \left.\frac{\partial w_{eq}}{\partial \mathbf{C}}\right|_{\mathbf{C}_0} \mathbf{F}_0^T + \overset{4}{\mathbf{G}}_{0(\omega)}\, \Delta\mathbf{E}_{\text{lin}} e^{i\omega t} \tag{12}$$

is obtained and the associated fourth order dynamic modulus tensor is

$$\begin{aligned}\overset{4}{\mathbf{G}}_0(\omega) &= 4(\mathbf{F}_0 \otimes \mathbf{F}_0)^{\overset{23}{T}} \left.\frac{\partial^2 w_{eq}}{\partial \mathbf{C}^2}\right|_{\mathbf{C}_0} (\mathbf{F}_0^T \otimes \mathbf{F}_0^T)^{\overset{23}{T}} \\ &\quad + \sum_{k=1}^{n} \frac{2i\omega\mu_k z_k}{1+i\omega z_k} \left(\overset{4}{\mathbf{1}} - \frac{1}{3}\mathbf{1}\otimes\mathbf{1} \right).\end{aligned} \tag{13}$$

This is the required form for the interface. It is possible to implement the derived fourth order dynamic modulus tensor completely at the program. The simulation is carried out analogue to the proceeding shown above. First the predeformation is calculated in the time-domain and thereafter linearized in the neighbourhood of the predeformation. At the end the material response to incremental harmonic excitations is calculated in the frequency-domain.

The hyperelastic material behaviour can be described for example with a Mooney-Rivlin-model. Furthermore the use of other constitutive models of viscoelasticity seems to be possible.

5 OUTLOOK

It is intended to introduce the results in industrial processes. The aim is the prediction of the behaviour of elastomer-mounts at the beginning of the development process. With respect to this certain elastomers are analysed and first calculations are carried out.

Further steps are the enhancement of the constitutive model to different environmental influences. Of particular interest are the temperature and aging phenomena generated by different effects.

REFERENCES

Haupt, P. & Lion, A. 2002. On Finite Linear Viscoelasticity Of Incompressible Isotropic Materials. *Acta Mechanica* 159: 87–124.

Lion, A.; Retka, J.; Rendek, M. 2009. On the Calculation of predeformation-dependent dynamic modulus tensors in finite nonlinear viscoelasticity. Accepted by: *Mechanics Research Communications.*

Morman, K.N. & Nagtegaal, J.C. 1983. Finite Element Analysis of Sinusoidal Small-Amplitude Vibrations in Deformed Viscoelastic Solids. Part 1: Theoretical Development. *Int. J. for Numerical Methods in Engineering* 19: 1079–1103.

Constitutive Models for Rubber VI – Heinrich et al. (eds)

The visco-elastic behaviour of elastomers at large pre-strains

N. Suphadon, A.G. Thomas & J.J.C. Busfield
Department of Materials, Queen Mary University of London, London, UK

ABSTRACT: Kuhn and Kunzle (1955) explained that the reduction in loss angle for small oscillations with increasing pre-strain resulted from the molecular rearrangement of the polymer. In contrast, Suphadon et al. (2009) showed that the loss angle decreased due to changes in geometry alone and that the loss modulus was constant for a wide range of unfilled materials up to quite large strains. They also found that for a range of unfilled rubbers that a pre-strain, of up to 100% strain, did not induce any anisotropy in the loss modulus behaviour when measured using small strain oscillations superimposed on the larger pre-strain. From this work it was clear that the energy dissipation depended only on the geometric shape of the sample and not on the pre-strain. This paper extends the previous work to larger pre-strains for SBR (styrene butadiene rubber) and NR (natural rubber) compounds some of which incorporate fillers. The results show for materials that with 25 phr of carbon black filler, the loss modulus is still independent of the pre-strain for normal working strains but at filler contents of 50 phr, the loss modulus increases with pre-strain at extension ratios lower than 2. This probably results from the significant effect of the strain amplification which arises at higher filler volume fraction. Additional experiments to investigate the effect of the load history and anisotropy in the loss modulus with pre-strain are also described.

1 INTRODUCTION

In engineering applications rubber materials are often subjected to a combination of complex dynamic loads. Hence, the viscoelastic behaviour of the materials under complex loading is important. Busfield et al. (1999), Busfield et al. (2000) and Davies et al. (1996) studied the dynamic behaviour of pre-strained strips of rubber subjected to a tensile oscillation. Suphadon et al. (2009) used a similar approach to study anisotropy in the viscoelastic behaviour. For a range of unfilled rubbers, at pre-extension ratios below 2 the loss modulus is independent of the pre-strain and the energy dissipation depends upon the change in geometry only. In this work larger prestrains to an extension ratio above 2 are observed using both unfilled and filled rubbers. The anisotropy in the loss modulus with strain can be examined by loading a pre-strained rubber sample with a superimposed torsion oscillation or a additional tension oscillation.

2 EXPERIMENTAL

Styrene-butadiene (SBR) and natural rubber (NR) compounds were used in this experiment. A compression moulded rectangular rubber strip was used to examine a tension superimposed with small tensile oscillation. The dimensions were 80 mm in length, 5 mm in width and 2 mm in thickness. A compression moulded rubber cylinder was used to examine a tension superimposed with a small torsional oscillation. The bonded cylindrical rod had a diameter of 12.2 mm and a length of 75 mm. Table 1 summarises all the different rubber compositions and the processing conditions.

The dynamic behaviour of rubber can be represented by a complex shear modulus, G^*.

$$G^* = G' + \mathrm{i}G'' \tag{1}$$

Here G' is the storage shear modulus (elastic component) and G'' is the loss shear modulus (dissipated energy component). All experiments in this work have been conducted using a free vibration set up, where the dissipated energy is expressed in terms of the log decrement, Δ,

$$\Delta = \frac{1}{n}\ln\left(\frac{x_i}{x_{i+n}}\right), \tag{2}$$

where x_i is the amplitude of cycle and n is the number of free oscillations being measured.

The elastic behaviour of each material was also measured using dumbbell shaped specimens of 2 mm thickness and 3 mm width in the gauge length

Table 1. Rubber formulations and processing conditions.

	SBR0	SBR25	SBR50	NR0	NR25	NR50
Ingredient						
NR (SMR CV-60)	0	0	0	100	100	100
SBR (JSR 1500)	100	100	100	0	0	0
Carbon black (HAF*)	0	25	50	0	25	50
Stearic acid	2	2	2	2	2	2
Zinc oxide	5	5	5	5	5	5
HPPD* (antioxidant)	1	1	1	1	1	1
CBS* (accelerator)	0	0	0	1.5	1.5	1.5
DPG* (accelerator)	1	1	1	0	0	0
Sulfur	1.5	1.5	1.5	0.5	0.5	0.5
Moulding condition						
Curing time	70	70	70	15	15	15
Temperature	160	160	160	160	160	160

HPPD* = N-(1, 3-dimethyl butyl)-N-phenyl-p-phenylenediamine
CBS* = N-Cyclohexy-2-benzothiazole sulfenamide
DPG* = diphenyl guanidine
HAF* = High abrasion furnace

which were tested in a screw driven Instron 5550 using an optical strain measuring device. Each specimen was loading at the rate 500 mm/minute until break.

The pre-strained sample superimposed with a torsion oscillation has been examined previously by several researchers (Kuhn and Kunzle 1955), (Mason 1959), (Mohsin 1987), (Mooney and Gerke 1941) and has more recently been adopted by Suphadon et al. (2009). A suitable schematic for the test is shown in Figure 1. The base of the rubber cylinder was fixed and the top was mounted to a torsion inertia bar. The cylinder was pre-strained by pulling an inelastic string attached above the inertia bar. After each pre-strain has been applied the sample was allowed to relax for 3 minutes to reduce the effects of stress relaxation on the measurements. A torsion oscillation was established by tapping the torsion bar. The period of oscillation and the decay in the oscillation amplitude were measured using a non-contacting displacement sensor and recorded on PC oscilloscope.

In our case the definitions of G' and G'' are expressed in terms of the undeformed geometry (Suphadon et al. 2009)

$$G' = \left(\frac{2I\omega^2}{\pi}\right)\left(\frac{l_0}{r_0^4}\right)\lambda^3 \tag{3}$$

$$G'' = \left(\frac{2I\omega^2\Delta}{\pi^2}\right)\left(\frac{l_0}{r_0^4}\right)\lambda^3 \tag{4}$$

where I is moment of inertia of the rectangular bar, ω is angular frequency, l_0 is the length of the specimen, r_0 is the radius of the specimen and λ is extension ratio.

A schematic for the apparatus used for the static tensile tests superimposed with an additional tensile oscillation is given in Figure 2. The inertia bar in this case was supported by a knife-edge and was also clamped at the centre of a rubber specimen. The specimen was extended to a specified pre-strain and then also kept in this extension for 3 minutes. The beam was set in motion by releasing an electromagnet. As the beam oscillates, the reduction in the oscillation amplitude was measured using the same method as during the torsion-tension experiment. In this case, G' and G'' are also expressed in terms of the undeformed geometry as defined by Busfield et al. (1999), Busfield et al. (2000) and Davies et al. (1996) as,

$$G' = \left(\frac{I\omega^2}{6a^2}\right)\left(\frac{l_0}{A_0}\right)\lambda^2, \tag{5}$$

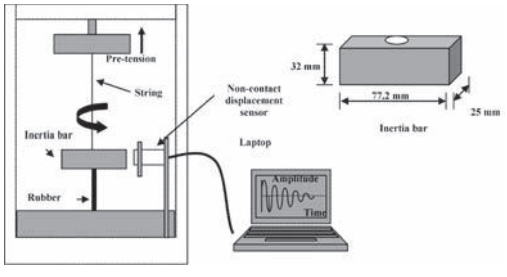

Figure 1. A schematic for a prestrain superimposed with a torsion oscillation.

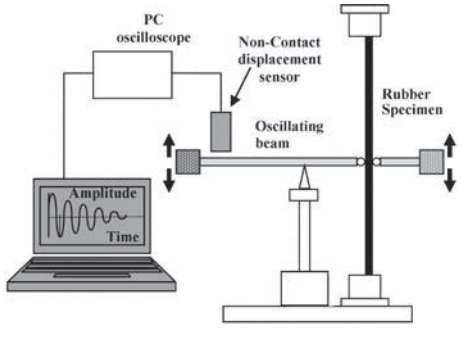

Figure 2. A schematic for a pre-strain superimposed tension oscillation.

$$G'' = \left(\frac{I\omega^2\Delta}{6\pi a^2}\right)\left(\frac{l_0}{A_0}\right)\lambda^2 . \quad (6)$$

I is the moment inertia of the beam, a is the distance from the knife edge to the clamped rubber, l_0 is the original test piece length and A_0 is the undeformed cross-sectional area of the test piece.

3 RESULTS AND DISCUSSION

Suphadon et al. (2009) found for unfilled rubbers the loss modulus was independent of pre-strain for pre-strains below 2 and the loss modulus was the same whether measured using the torsion oscillation (out of plane with the pre-strain) or the tension oscillation (in plane with the pre-strain). This work extends this work to larger pre-strains greater than 2 and also to filled rubbers.

The incorporation of fillers made the materials much stiffer and stronger as shown in Figures 3(a) and 3(b). All the rubbers showed an elongation at break above 400% strains which meant that all the tests were done up to a maximum extension ratio of 3.8 for all the compounds. Equations 3 and 4 were used to determine G' and G'' respectively for the static pre-strain superimposed with torsion oscillation. Equations 5 and 6 were used to calculate G' and G'' respectively for the static pre-strain superimposed with a tension oscillation.

Figures 4 and 5 show the graph of the loss modulus as a function of a large pre-strain measured using both experiments. The dependence of loss modulus with pre-strain is modest at extension ratios below 3.0 for NR0 and SBR0 but above

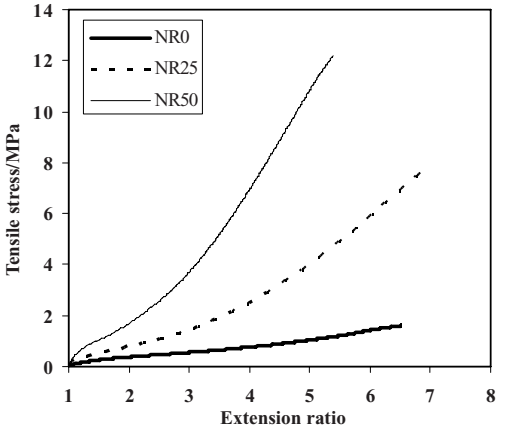

Figure 3(a). Tensile stress against extension ratio for different NR compounds.

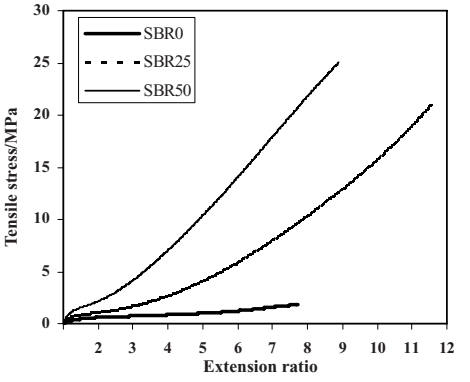

Figure 3(b). Tensile stress against extension ratio for different SBR compounds.

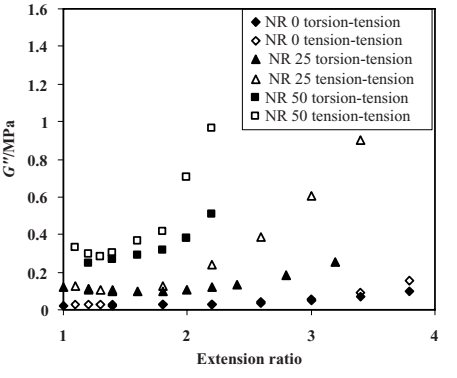

Figure 4. Comparison of G'' measured from pre-tension superimposed torsion oscillation and pre-tension superimposed tension oscillation test, plotted as a function of pre-strain for the NR compounds.

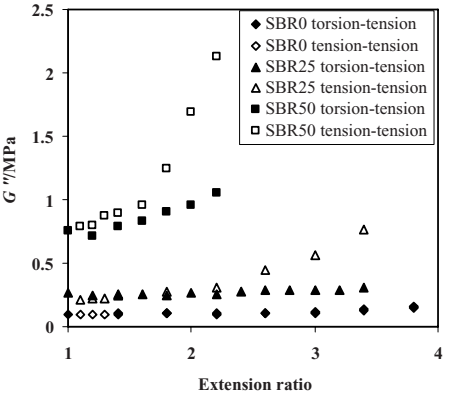

Figure 5. Comparison of G'' measured from pre-tension superimposed torsion oscillation and pre-tension superimposed tension oscillation test, plotted as a function of pre-strain for the SBR compounds.

that an upturn is observed. Suphadon et al. (2009) suggested at these large extensions molecular orientation and finite extensibility might have started to have an effect on the viscoelastic behaviour. The orientation of the monomer units, as distinct from the chain segments between crosslink, is probably the controlling factor in any change in G'' with strain. The statistical theory suggests that the orientation of the chain segments between crosslink is modest until the polymer chains are extended by a substantial fraction of their contour length. For SBR25 and NR25 the change in loss modulus with pre-extension is modest up to extension ratio of 2, but the upturn is clearly more marked than was the case for the unfilled rubber. This is probably due to the effect of strain amplification (Busfield et al. 2005), (Guth and Gold 1938). For highly filled rubber, the loss modulus of SBR50 and NR50 is clearly dependent on the pre-stain. The graphs upturn when the pre-extension ratios are lower than 2. These clearly show the significant effect of the strain amplification on G''.

Figure 4 for the SBR and Figure 5 for the NR compare the loss modulus measured using both tests. The loss modulus measured using both torsion and tension oscillations give the same result for the loss modulus for the unfilled NR and SBR compounds. Over a very wide range of strains it is clear that the loss modulus is isotropic with strain. For the filled materials the loss modulus was isotropic at smaller pre-strains, but at larger pre-strains the loss modulus diverges indicating an anisotropy in the behaviour.

One possible explanation for this is that one viscoelastic dissipation mechanism frequently attributed to filled elastomers typically occurs as a result of frictional sliding of the polymer over the filler interface. In this case a small oscillation in the direction of pre-strain may more readily result in slippage and hence more energy dissipation in the loading direction.

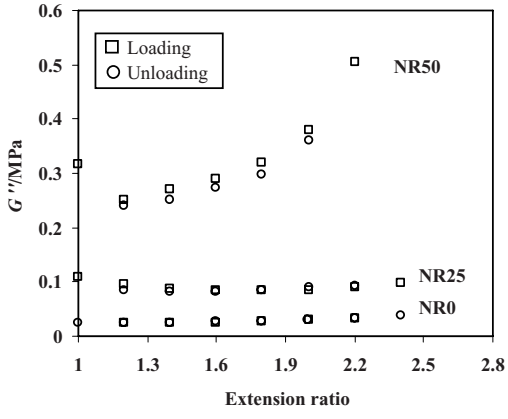

Figure 6. Comparison of G'' measured from pre-tension superimposed torsion oscillation and pre-tension superimposed tension oscillation test, plotted as a function of pre-strain for the NR compounds.

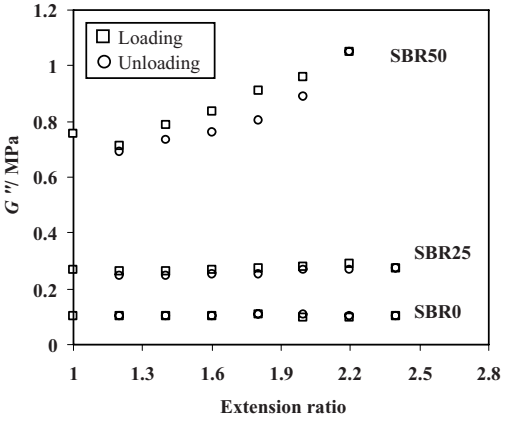

Figure 7. Comparison of G'' measured from pre-tension superimposed torsion oscillation and pre-tension superimposed tension oscillation test, plotted as a function of pre-strain for the SBR compounds.

Figures 6 and 7 show that the loss modulus of unfilled and lightly filled rubber is virtually independent from the loading history of the pre-strain. With the difference between the data being measured when the pre-strain is increased and the data measured when the pre-strain is reduced being only modest, with the loss modulus in the loading direction being higher than during unloading (Asare et al. 2009).

4 CONCLUSIONS

The effect of a large pre-strain on the dynamic behaviour of the rubber has been investigated using both in-plane and out-of-plane oscillations. At lower pre-strains the loss modulus is independent of pre-strain in contrast to larger pre-strains there is a slight dependence with pre-strain. The pre-strain did not induce any anisotropy in G'' at a lower pre-strain. However at larger pre-strains it is possible that the constraint in the monomer units in the rubber network might effect the viscoelastic behaviour. Unfilled rubbers show that the independence of the loss modulus with pre-strain is present to a greater pre-strain than is the case for the filled rubber, probably as a result of strain amplification effects of the filler. Also the loss modulus of both experiments is isotropic for unfilled rubber but the incorporation of filler introduces an anisotropy at larger pre-strains.

This probably being due the frictional sliding at the filler boundaries being dependent upon the direction of the stress field around the filler. Additionally, these experiments confirm that all compounds tested are independent of the loading history. The results in this work are useful for general engineering applications such as rubber using in vibration damping where a complex loading is applied to a component and the designer wishes to predict the energy dissipation per cycle. The introduction of a single term for the loss modulus for a range of geometries, pre-strains and loading cycle means that it should be much easier to design components using finite element analysis.

ACKNOWLEDGEMENT

One of the authors, Nutthanun Suphadon, would like to express his gratitude to the Royal Thai Government Scholarship Scheme for funding this research.

REFERENCES

Asare, S., Thomas, A.G. and Busfield, J.J.C. (2009). "Cyclic stress softening in elastomer components." *Rubber Chemistry and Technology* (in press).

Busfield, J.J.C., Deeprasertkul, C. and Thomas, A.G. (1999). "Effect of liquid on the dynamic properties of carbon black filled natural rubber as a fuction of pre-strain." Constistutive Models for Rubber, Dorfmann and Muhr, eds., 87–94.

Busfield, J.J.C., Deeprasertkul, C. and Thomas, A.G. (2000). "The effect of liquids on the dynamic properties of carbon black filled natural rubber as function of pre-strain." *Polymer*, 41, 9219–9225.

Busfield, J.J.C., Thomas, A.G. and Yamaguchi, K. (2005). "Electrical and Mechanical Behaviour of Filled Rubber III." *journal of polymer Science: Part B: Polymer physics*, 43(1469–1661).

Davies, C.K.L., Thomas, A.G. and Akutagawa, K. (1996). "The Effect of Low Molar Mass Liquids on the Dynamic Mechanical Properties of Elastomers Under Strain." *Prog Rubber Plastics Technol*, 12, 174.

Guth, E. and Gold, O. (1938). *Phys. Rev*, 53, 322.

Kuhn, W. and Kunzle, O. (1955). "Experiment determination of the dynamic viscosity and elasticity and also the relaxation time spectrum of rubber III." *Rubber Chemistry and Technology*, 28, 694.

Mason, P. (1959). "The viscoelastic behaviour of rubber in extension." *Journal of Applied Polymer Science*, 1(1), 63.

Mohsin, M.A and Treolar, L.R.G. (1987). "Thermoelastic measurements of some elastomers under extension and torsion." *Polymer*, 28, 1893.

Mooney, M. and Gerke, R.H. (1941). "A torsional Hysteresis test for rubber." *Rubber Chemistry and Technology*, 14, 35–45.

Suphadon, N., Thomas, A.G. and Busfield, J.J.C. (2009). "Viscoelastic Behaviour of Rubber Under a Complex Loading." *Journal of Applied Polymer Science*, 113, 693–699.

Experiments and characterisation

Constitutive Models for Rubber VI – Heinrich et al. (eds)
© 2010 Taylor & Francis Group, London, ISBN 978-0-415-56327-7

Dynamic characterization of elastomers using impact testing

P.-E. Austrell
Lund University, Lund, Sweden

A.K. Olsson
AREVA NP Uddcomb, Helsingborg, Sweden

ABSTRACT: Dynamic characterization of elastomers, i.e. laboratory testing and fitting of constitutive models, is quite complicated. The demands on the laboratory equipment and the skill of the personal handling the test equipment are high. Stationary harmonic testing is an established method for evaluating dynamic properties of elastomers. However, it is demanding experimentally when it comes to high frequencies. The purpose of this investigation is to evaluate theoretically if impact testing can be an alternative to the harmonic test method. The impact behavior of an elastomer showing both rate and amplitude dependence is evaluated numerically. It is shown that the stress-strain behavior during impact show similarities to the stationary harmonic behavior of the material. Quantities comparable to the dynamic stiffness and phase angle can be derived from the impact behavior. It is also shown that amplitudes of 1–15% strain and frequency/rate dependence in the range 30–200 Hz, can be resolved with velocity and mass of the impacting body having realistic values. Moreover, a schematic experimental setup is also discussed. Impact testing has a potential to be a very simple method to obtain dynamic data for elastomers, to use in calibration of constitutive models. Alternatively it can be used as a simple quality control of dynamic properties in various elastomeric materials.

1 INTRODUCTION

This theoretical study investigates the possibilities and limitations of using impacting bodies of different velocity and mass as a means to characterize the dynamic behavior of elastomers.

Using the harmonic test method in a fixed rig is quite complicated and demanding. This method imposes extreme requirements on the stiffness and stability of the test equipment for high frequencies and the equipment is very expensive. Also, heat generation by hysteresis work might be a problem. The question assessed here is, if the impact test method can be used to replace the more common stationary dynamic testing method. The impact test method is much less demanding experimentally. It is easy to achieve high strain rates without using a very stiff rig. Also, for testing at varying temperatures a climate chamber built round the test rig is not necessary. The specimen is simply heated to the required temperature and tested by impacting weights. Moreover, pre straining of the specimen can also be obtained, as schematically discussed in Section 5.

Impact testing is used as a standard test for determination of rebound resilience (ISO 1767 for example) using a pendulum hammer. The initial and final position of the pendulum is measured and the losses during the contact with the rubber is taken from the difference in potential energy of the impacting mass. This can be used to give a rough estimate of the stiffness and damping properties of the tested elastomer. However, the purpose here is to look at the dynamics of the impact with higher resolution. The method proposed here requires the displacement of the mass and the force in the rubber to be measured as functions of time during the contact (which is in the order of 10 ms).

Other applications where impact testing can be used is for obtaining hyper-elastic properties in FE-analysis of rubber components at high strain rates. As for example in development of shock absorbers (Austrell et al, 2004) and in the ongoing work (Centeno Gil O.J. 2009) on rubber bushings in car crash simulations.

Impact testing for the purpose of obtaining constitutive models has been done before by other researchers for example (Hoo Fatt & Al-Quraishi 2007) and (Yang et al, 2000). They used impact testing to model hyper-viscoelastic behavior.

Impact testing is particularly useful when it comes to simultaneous high strains and high strain rates.

This was explored in a previous work concerning a so called "bump stop" in a car suspension

(Austrell P-E. & Wirje A. 2007). However, the main purpose here is to compare the impact test method with the more established method of using stationary dynamic harmonic testing in a range of moderate strain levels where the amplitude dependence of many elastomers is pronounced.

Two possible specimens are considered in the next section; impact on a double shear specimen, or impact on a lubricated compression test specimen. Using both covers the two fundamental load cases for rubber units. In Section 3 concerning values of mass and velocity and in Section 4 where the numerical simulation of the impact is discussed, a compression specimen is assumed. In practise the impact can be accomplished by free falling weights, an impact pendulum, or similar arrangements. In section 5 a schematic experimental setup is discussed. It is assumed that corresponding values of force and displacement versus time can be measured.

2 PRELIMINARIES

In this section, some basic equations are presented using the assumption that the material is purely elastic. A simple linear spring model is used for basic understanding of how parameters such as maximum compression and pulse time depends on the impacting velocity and mass in connection to the modulus of the rubber.

The purpose here is as mentioned, to compare the impact test method with the stationary harmonic test. This involves comparing the pulse duration time t_p with the period time T. Figure 1 shows schematically the displacement versus time for the two cases.

In order to get approximately the same loading rate and level in the two methods it should hold that $t_p = T/2$ and that the maximum displacement u_{max} and the amplitude u_0 is of the same value, according to Figure 1.

For the purpose of obtaining some basic approximate formulas, the rubber specimen to be tested is as mentioned simply considered as a linear spring with stiffness k. At time $t = 0$ a mass m hits the specimen at a certain velocity. In this simple linear elastic case the pulse according to Figure 1 will be a half period sine function according to

$$u(t) = u_{max} \sin\left(\sqrt{\frac{k}{m}}t\right) \tag{1}$$

giving the pulse time t_p dependent on the impacting mass m and the stiffness as

$$t_p = \pi\sqrt{\frac{m}{k}}. \tag{2}$$

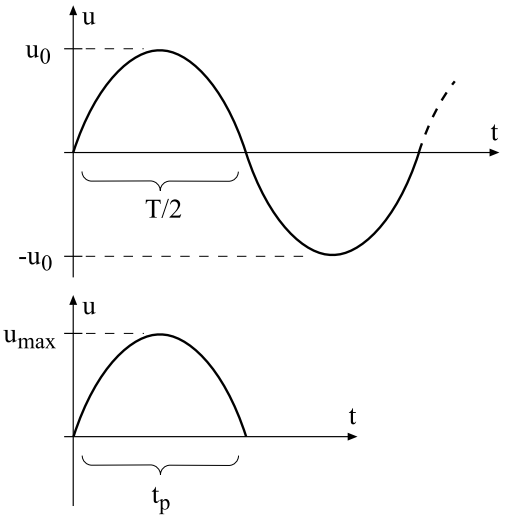

Figure 1. Comparison of displacement versus time for the harmonic and the impact test method. Pulse time t_p and the period time T are shown.

In the linear elastic case the deformation histories are completely equal in shape for the impact test and for the stationary harmonic test (looking at comparable time intervals).

The maximum deformation u_{max}, according to Figure 1, of the spring can be found by a simple energy balance where the kinetic energy of the impacting mass is put equal to the strain energy in the maximum deformed position of the specimen, giving

$$u_{max} = v_0\sqrt{\frac{m}{k}} \tag{3}$$

where v_0 is the velocity of the impacting mass.

Now, if the impact test specimen is of the double shear type the stiffness can be expressed as

$$k_s = 2\frac{G_{dyn}A}{H} \tag{4}$$

because two rubber parts are being sheared. G_{dyn} is some dynamic shear modulus of the material, A is the area of one part exposed to shear stress, and H is the thickness of one part. For the compression specimen the stiffness is

$$k_c = \frac{3G_{dyn}A}{H} \tag{5}$$

for "small" strains in the range of say 0 to 15%, because the initial elastic modulus $E = 3G$ for an

incompressible material. A is the area exposed to compressive stress, and H is the height of the specimen. In order to obtain a homogeneous compressive stress it is assumed that the contacting surfaces are lubricated.

From these expressions some important basic relationships can be derived. First the pulse duration time can be found by putting Eq. (4) or Eq. (5) into Eq. (2) giving the expression

$$t_p = \pi \sqrt{\frac{mH}{3G_{dyn}A}} \tag{6}$$

for the compression specimen and similar for the shear specimen. It can be seen that the pulse duration time (corresponding to half the period time in stationary harmonic testing) is only dependent on the mass of the impacting body for a given test specimen.

The maximum strain in the test specimen can be derived from Eq. (3) and Eq. (2), giving

$$\varepsilon_{max} = \frac{u_{max}}{H} = v_0 \frac{t_p}{\pi H} \tag{7}$$

for both specimens. The conclusion here is that for a given impacting mass (yielding constant t_p) the maximum strain will be dependent only on the velocity of the impacting body.

3 RANGE OF APPLICATION

This section considers the possibilities and limitations with the impact method compared to the harmonic method. A typical (medium stiff) rubber material of about 60 Shore units will be considered as a reference for estimating roughly values of impacting masses and velocities.

In a previous work (Olsson A.K., Austrell P.-E. 2001) several materials were characterized using harmonic shear test data in the range 1–12% shear strain and frequencies from 1 to 180 Hz. The dynamic modulus of some materials varied a lot with amplitude, but a rough mean value for the given range of frequencies and amplitudes can be estimated for use in the approximate expressions derived in the previous section. For this purpose the dynamic modulus of the example material used here is set to $G_{dyn} = 3$ MPa.

Moreover, a compression specimen in form of a cylinder with equal diameter and height $D = \mathrm{H} = 25$ mm will be considered here. However, the ordinary double shear specimen with 25×6 mm rubber discs will have approximately the same stiffness as the compression specimen considered and the values below are therefore approximately valid also for the shear test.

The purpose here is to investigate if the same range of amplitudes and strain rates as the ones mentioned above can be covered by using the impact test method. The connection between the frequency in the harmonic test and the pulse duration time in the impact test is $f = 1/T = 1/(2t_p)$ giving the translation between pulse time and frequency as $t_p = 1/(2f)$. This is used to obtain the required mass from Eq. (6) giving the connection

$$m = \frac{3G_{dyn}A}{4\pi^2 H} \frac{1}{f^2}. \tag{8}$$

Numerical values of the impacting mass using this equation are shown in Figure 2.

The velocity required to reach a certain strain level is according to Eq. (7). By using $t_p = 1/(2f)$ the velocity is expressed as

$$v_0 = \varepsilon_{max} \pi H 2 f. \tag{9}$$

By using Eq. (9), values of velocity corresponding to frequency are shown in Figure 3 as straight lines for some selected strain levels.

From these two figures it can be seen that frequencies below say 30 Hz are hard to evaluate with this particular specimen. The mass is increasing asymptotically and the velocity of the impacting body is getting impractically low. In the other end of the frequency rang e it is seen that increasing the corresponding frequency causes the impacting mass to become very small.

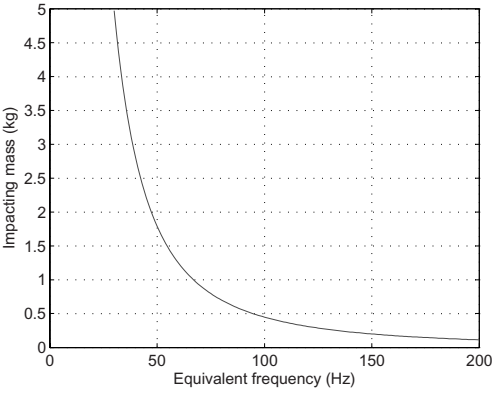

Figure 2. Impacting mass vs equivalent frequency $f = 1/2t_p$ in an harmonic test.

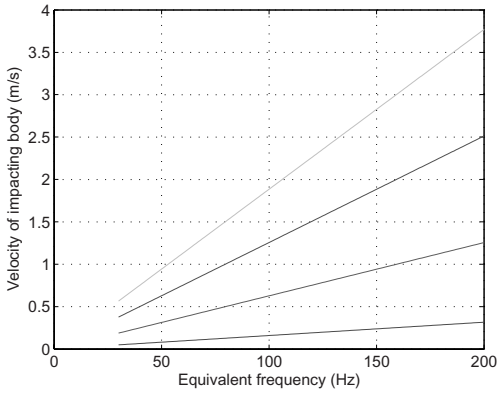

Figure 3. Velocity of impacting body vs equivalent frequency. Maximum strain ε_{max} from below 1, 4, 8, and 12%.

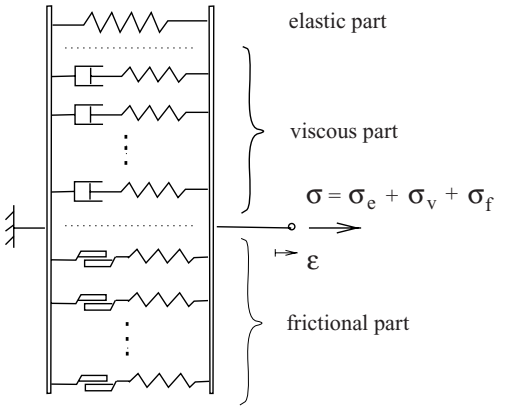

Figure 4. Visco-elastic elasto-plastic model used in the evaluation.

4 EVALUATION BY NUMERICAL EXPERIMENTS

The similarities between the impact test and the stationary harmonic test are explored further in this section. The motivation for pursuing this is that if the material is purely elastic, the stress and the strain pulse are both sinusoidal for impact loading as was mentioned in the introduction and shown in Eq. (1).

Here the impact test method is numerically evaluated using a material with three main branches having elastic, visco-elastic, and elasto-plastic properties. The model used is the same as in (Olsson & Austrell 2001). The material is fictive but it is arranged to be realistic for a material with an overall modulus corresponding roughly to a 60 Shore material having both amplitude and frequency dependence of dynamic modulus and phase angle.

A Matlab program was developed to evaluate the effects of a mass impacting on a compression specimen. The rectilinear motion of the mass is obtained from Newton's second law by using a contact force generated by the visco-elastic elasto-plastic model cited above, also shown in Figure 4.

In Figure 5 the impact strain and stress histories are shown together with the composed stress strain curve. The dashed line in the strain history is the part where the mass loses contact with the test specimen (the contact force is zero) and bounces of. Moreover, an extension of the pulse to a full loop is also shown in the figure (with a dashed line). By using the full loop in the figure, quantities that are comparable to the stationary harmonic test can be derived as

$$E_{dyn}^{eq} = \frac{\sigma_{max}}{\varepsilon_{max}} \quad \delta^{eq} = \pi \frac{\Delta t}{t_p} \quad f^{eq} = \frac{1}{2t_p} \tag{10}$$

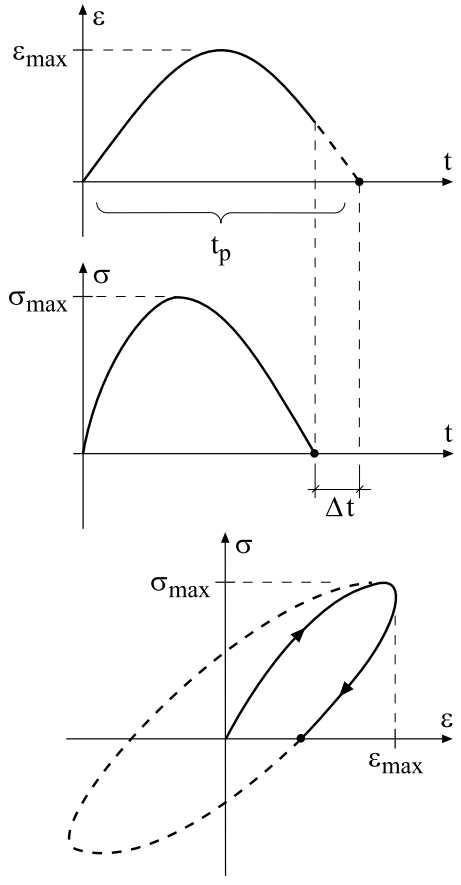

Figure 5. Evaluation of dynamic properties comparable to the harmonic test method.

The dynamic modulus is simply the quota between maximum stress and maximum strain. The damping properties are assessed by the comparable phase angle δ^{eq}, also obtained from the same figure by extension to a full loop. The comparable frequency is found from the extrapolated strain history in the figure.

Using the Matlab program and choosing mass and velocity according to the previous section, a comparison to the harmonic behavior was obtained using the expressions in Eq. (10). In Figures 6 and 7 the impact version of dynamic modulus and phase angle are shown together with actual modulus and phase. In the evaluation, Δt in Figure 5 was estimated using a linear extrapolation in the force free part of the strain history. This gave an overestimation of the phase angle δ^{eq}. By using 75% of the linearly extrapolated Δt the values according to Figure 7 was obtained. The resemblance is quite good, indicating that by the simple comparison proposed here the stationary dynamic properties can be estimated.

The simulations show that frequency/rate and amplitude dependence in the considered range can be resolved by use of impacting bodies with easy achievable masses and velocities. Although no fitting routine for the constitutive parameters has yet been established for the impact test, it is clear that it is equally possible to distinguish between rate and amplitude effects as in the harmonic test method.

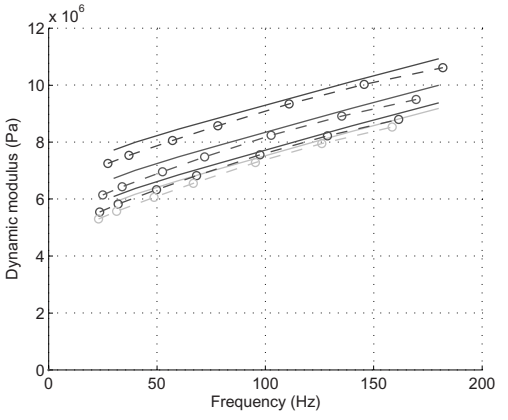

Figure 6. Comparison of dynamic modulus evaluated by sinusoidal loading (solid lines) and evaluation with impacting mass (dotted lines). Maximum strain amplitude from above 1,4, 10, and 15%.

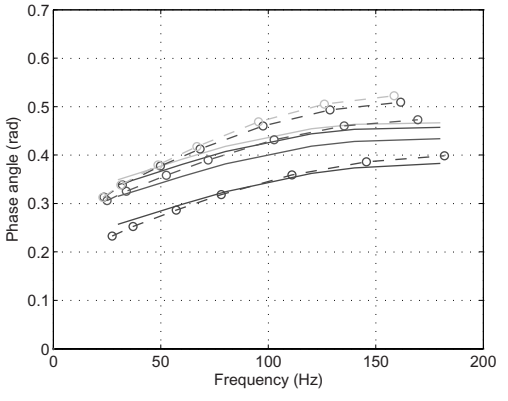

Figure 7. Comparison of phase angle evaluated by sinusoidal loading (solid lines) and evaluation with impacting mass (dotted lines). Maximum strain amplitude from below 1,4, 10, and 15%.

5 SCHEMATIC LABORATORY SETUP

Impact testing can be arranged in several ways as discussed in the introduction. A simple way is to use free falling weights of different mass, falling from different heights. In the range of amplitudes and equivalent frequencies considered (1–15% and 30–200 Hz), the velocities are from 0.05 m/s to 5 m/s and the masses are from 0.2 kg to 5 kg roughly. The highest velocity (5 m/s) corresponds to a weight falling from about 1.3 m. For the lowest velocities an arrangement with free falling masses may be impractical due to the very small heights required.

A test setup making it possible to control the velocity of the impacting mass is shown in Figure 8 a). A motor with weights hanging in a light

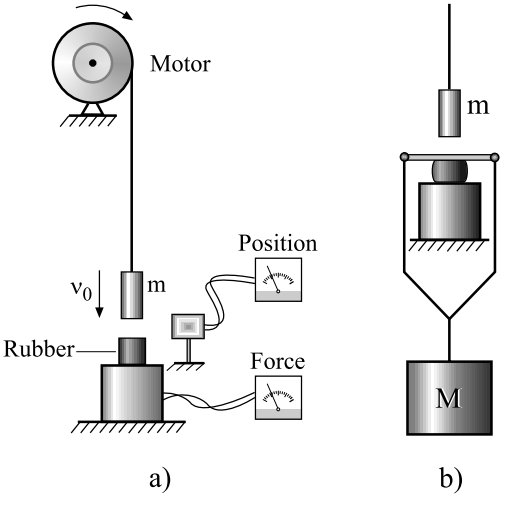

Figure 8. a) Possible experimental setup for impact testing b) also including pre-strain.

flexible wire sets the speed of impact. The force is measured by a load cell and the displacement is measured by some form of contact free device. It is assumed that stress and strain can be measured synchronously with good resolution (as functions of time).

In many cases it is desirable to be able to include pre-strain. Schematically this can be accomplished by hanging a weight according to Figure 8 b). In practice one might use a light plate connected to flexible wires that can be tightened to obtain the pre strain.

6 CONCLUSIONS

The impact method is, as mentioned in the introduction, very useful for evaluating high strain rates and large strain levels occurring simultaneously. However, this theoretical evaluation of the impact test focused on smaller strain levels. It was shown that the impact method can be a much simpler and less costly alternative to stationary harmonic testing for frequencies above say 30 Hz. It was shown that dynamic rubber properties can be evaluated with the same resolution as in the harmonic method. Other advantages is that testing at different temperatures is easy to accomplish, without interference of heating by hysteresis work.

A schematic experimental setup including the possibility to include pre-straining of the specimen, was also proposed.

Apart from being used as a means to produce data for calibration of constitutive models it could also be used as a quality control for dynamic properties of various rubber materials.

REFERENCES

Austrell P-E. and Wirje A. 2007, A viscoelastic bump stop model for multi-body simulations, *Proceedings of the fifth European conference on constitutive models for rubber* (*ECCMR*), Paris.

Austrell P-E. et al, 2004, Utveckling av ändläges-dämpare for Bosch Rexroth teknik AB (in Swedish), Development of a Shock absorber för Bosch Rexroth, *TVSM-7140, Division of Structural Mechanics,* Lund.

Centeno Gil O.J. 2009 (to be published), Crash CAE modelling of rubber bushings. *Volvo Car corp. and Lund University, Master thesis report, Division of Structural Mechanics,* Lund, Sweden.

Hoo Fatt M.S. and Al-Quraishi A.A. 2007, High strain rate constitutive modeling for natural rubber, *Proceedings of the fifth European conference on constitutive models for rubber* (*ECCMR*), Paris.

Olsson A.K. and Austrell P.-E. 2001, A fitting procedure for a viscoelastic-elastoplastic material model. *Proceedings of the second European Conference on Constitutive Models for Rubber*, Germany.

Yang L.M., et al, 2000, A visco-hyperelastic approach to modelling the constitutive behaviour of rubber, *International Journal of Impact Engineering 24, 545–560.*

Constitutive Models for Rubber VI – Heinrich et al. (eds)

Dynamic mechanical analysis of prestrained highly-filled elastomers

A. Azoug, R.M. Pradeilles-Duval & A. Constantinescu
Laboratoire de Mécanique des Solides – CNRS UMR 7649, Ecole Polytechnique, Palaiseau, France

R. Nevière
SNPE Matériaux Energétiques, Centre de Recherches du Bouchet, Vert-le-Petit, France

ABSTRACT: The viscoelastic behavior of an industrial solid propellant, belonging to the class of highly-filled elastomers containing nonreinforcing fillers, is compared with propellants with modified sol fraction. The sol fraction is the part of the binder which is unlinked to the global network and therefore not contributing to elastic response. Dynamic Mechanical Analysis (DMA) tests are performed, superimposing a static tensile strain with small oscillating deformations. The percentage and the chemical composition of the sol fraction influence significantly the observed nonlinearity, corresponding to an increase in complex modulus and a decrease in loss tangent beyond a deformation threshold. Mathematical formulae are proposed to model the observed non linear behaviour. This behaviour could be explained assuming that the applied static deformation stretches the network until maximum extensibility is reached, leading to an important increase in complex modulus with increasing deformation. Elongation and orientation of the network constrains the sol fraction, reducing its molecular mobility and modifying measured loss tangent.

1 INTRODUCTION

Adding fillers to a polymer fundamentally modifies its viscoelastic properties. Highly-filled polymers have a filler volumic fraction up to 80%, implying that a small quantity of binder ensures cohesion. The modelling of the nonlinear viscoelastic mechanical behavior exhibited by these materials is hardly accessible. Local deformation mechanisms are not clearly determined because of complex binder-fillers interactions. The aim of this work is to understand the links between solid propellant microstructure and its macroscopic mechanical properties.

Molecular mobility of polymer chains in the binder appears to be directly dependent on the microstructure and strongly influences mechanical properties. Molecular mobility is defined as the ability of a polymer chain to diffuse in the viscous medium consisting of the surrounding polymer molecules. As segments of a chain molecule move in response to an applied stress, viscous forces from the medium delay the motion and some energy is dissipated as heat. The global motion delay in the sample is directly measured by the phase angle δ in a Dynamic Mechanical Analysis (DMA) experiment. Therefore, the study focuses on DMA tests.

A particular procedure is used, superimposing a tensile static strain with small strain oscillations. This procedure has been previously discussed on unfilled rubber in tensile mode, (Mason 1959, Davies et al. 1996), on filled elastomers with carbon black or silica fillers in tensile and shear mode, (Meinecke and Maksin 1981, Sullivan and Demery 1982, Arai and Ferry 1986, Voet and Morawski 1974, Dutta and Tri-pathy 1990, Busfield et al. 2000, Warley et al. 2007) and on highly-filled elastomers in torsion mode (Adi-coff and Lepie 1970). The results highlight new aspects of the nonlinear viscoelasticity exhibited by these materials.

It is important to point out that in these studied materials, the binder/filler systems are either reinforcing or nonreinforcing, depending on whether or not the fillers strongly interact with the binder and improve the system rupture strength (Stacer et al. 1990). Nonreinforcing fillers, while supposedly weakly interacting with the binder, strongly influence the viscous properties of the material. The previous observations of the dynamic properties of filled elastomers, containing reinforcing fillers, according to temperature, frequency and strain amplitude were attributed to an evolution of a filler network within the material (Payne and Whittaker 1971, Medalia 1978, Wang 1998). In nonreinforcing systems, the non linearity of viscoelastic properties appears to depend on binder behaviour and filler-binder interactions (Stacer et al. 1990).

The DMA test is achieved on solid propellants with modified sol fraction. The sol fraction is the part of the binder unlinked to the global network and not contributing to the elastic response. The comparison between these propellants behaviour demonstrates that the observed non linearities can not be solely attributed to the fillers. The work focuses on understanding the role of the sol fraction in the macroscopic deformation of the composite.

The tested materials are presented in section 2. Section 3 describes the experimental procedure. In section 4, the results of DSC and prestrained DMA are reported and a mathematical model is considered. The discussion in section 5 suggests a local deformation mechanism explaining the test results.

2 MATERIALS

All samples are prepared from the same propellant formulation consisting of ammonium perchlorate and aluminium fillers and a hydroxy-terminated polybuta-diene (HTPB) based binder. The total filler mass fraction is 88%wt. The polyurethane rubber is made by curing a HTPB prepolymer with a methylene diicy-clohexyl isocyanate (MDCI). NCO/OH ratio is 0.8, which implies that part of the HTPB molecules remains unlinked to the network. Plasticizer dioctyl aze-late (DOZ) is also added. The sol fraction contains the plasticizer and the unlinked HTPB molecules. More precisely, unlinked HTPB molecules are partially cross-linked between them but not connected to the global network. The material is then thermally cured for 2 weeks at 50°C.

Extraction of sol fraction by swelling in a solvent allows its substitution by swelling again in different blends. Weight loss after extraction indicates the quantity of sol fraction in the initial formulation and weight gain after swelling measures the quantity of substituted blend in the final sample. The modified compositions are described in the following paragraph.

1. *Sample I*: Reference material, non modified propellant,
2. *Sample E*: extraction of sol fraction, no substitution,
3. *Sample P*: substitution by HTPB prepolymer,
4. *Sample PC*: substitution by cross-linked HTPB,
5. *Sample D*: substitution by plasticizer DOZ,
6. *Sample PD*: substitution by a blend of HTPB and DOZ.

The composition and percentage of each sample sol fraction is given in Table 1.

Table 1. Sol fraction composition and mass fraction.

	Sol fraction	
Sample	Nature	Mass fraction
I (Reference)	HTPB DOZ	6.8%wt
E	–	0.0%wt
P	HTPB prepolymer	2.4%wt
PC	cross-linked HTPB	2.5%wt
D	DOZ	29.5%wt
PD	HTPB DOZ blend	2.6%wt

Several difficulties arise from this procedure. First the diffusion of HTPB molecules in the sample is not possible unless the temperature is elevated at 60°C during a month. The swelling into plasticizer causes the sample to inflate and end up with a sol fraction about four times superior to the initial one. Finally swelling into a mixture of HTPB molecules and plasticizer implies the ratio of each constituent into the added sol fraction is unknown.

3 EXPERIMENTAL PROCEDURE

The glass transition temperature T_g is determined by a Differential Scanning Calorimetry test (DSC). DSC studies are performed using a Mettler Toledo DSC 30. The samples are submitted to two cycles of temperature, cooling from 20°C to –120°C with a cooling rate of –20°C/min and heating from –120°C to 100°C with a heating rate of 5°C/min. T_g temperature is measured on each cycle in the heating phase. Measurement takes place in nitrogen atmosphere, with a flow rate of 40 ml/min. Reported T_g values are the mean values at inflexion points.

Dynamic Mechanical Analysis (DMA) experiments are achieved using a Metravib Viscoanaly-seur VA3000 at room temperature. The frequency is 5 Hz. Different levels of static strain are applied, from 0.0001% to 10% or sample break. At each static level (Fig. 1), a sinusoidal strain of single strain amplitude (SSA) 0.01% is superimposed and complex modulus E^* and loss tangent $\tan\delta$ are measured.

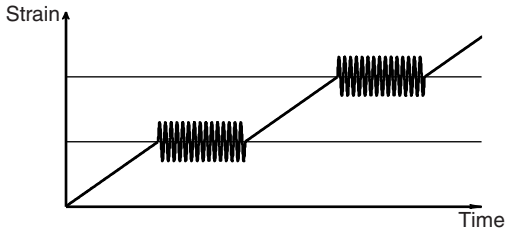

Figure 1. Strain versus time during a prestrained DMA test.

4 RESULTS

4.1 *Glass transition temperature*

The results of DSC experiments are given in Table 2. The glass transition temperature of each material is compared with the ones of the HTPB prepolymer and of the plasticizer.

4.2 *Prestrained DMA*

The results of DMA experiments are given on Figures 2 and 3. Complex modulus E^* and loss tangent $\tan\delta$ are found to evolve according to mathematical functions (1) and (2).

$$E^* = A + B(-log\epsilon)^m, \tag{1}$$

$$\tan\delta = C - D(-log\epsilon)^n. \tag{2}$$

The constants A, B, C, D, m and n are obtained thanks to a leastsquares optimization algorithm in Matlab®. Samples E and D present respectively a different material behaviour and a highly scattered loss tangent measurement. Except for these samples, global error for each sample is less than 10% of measured value.

For each material, value at low static strain is directly given by parameters A and C. Non linearity threshold and slope can be determined from constants B, C, m and n according to equations (3), (4), (5) and (6). ϵ_t and p represent deformation threshold and nonlinearity slope. Exponents e and δ stand for complex modulus and loss tangent. Results for each sample are given in Table 3.

$$log\epsilon_t^e = -(0.05A/B)^{1/m} \tag{3}$$

$$p^e = -Bm(-log\epsilon)^{(m-1)}/\epsilon ln10 \tag{4}$$

Table 2. Glass transition temperatures.

Sample	T_g
P	–347.3 K
E	–348.7 K
PC	–348.7 K
HTPB	–353.6 K
I	–356.8 K
PD	–358.3 K
D	–376.6 K
DOZ	–379.2 K

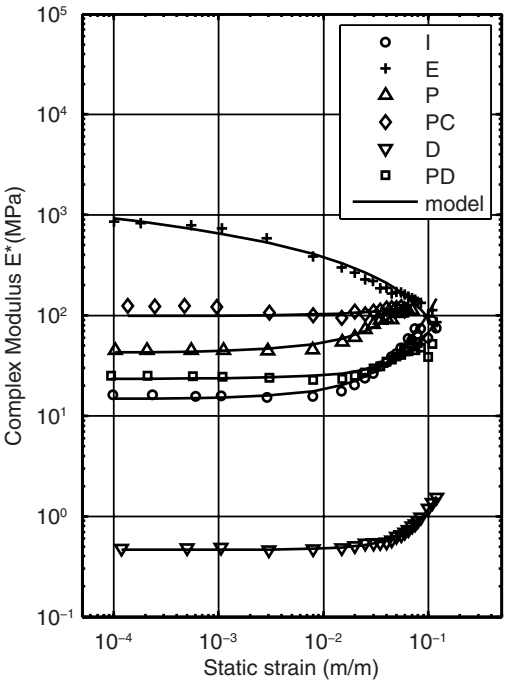

Figure 2. Complex modulus according to static strain, at room temperature, frequency of 5 Hz and SSA of 0.01%.

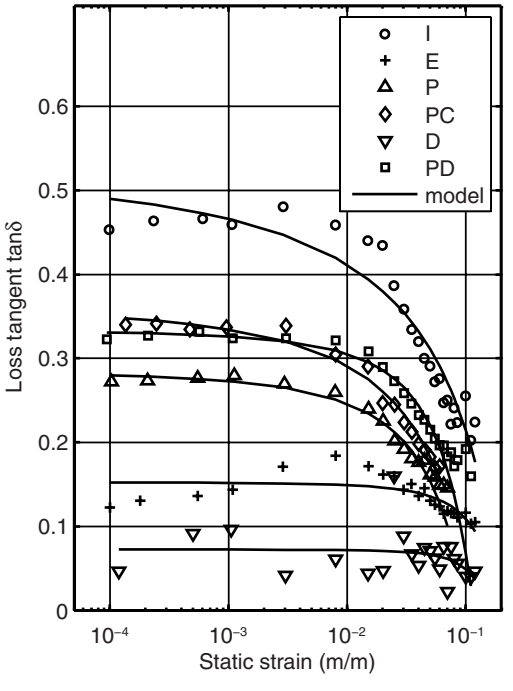

Figure 3. Loss tangent according to static strain, at room temperature, frequency of 5 Hz and SSA of 0.01%.

Table 3. Optimization results.

	Low static		Threshold		Slope	
	A MPa	C –	ε_t^e %	ε_t^δ %	p^e MPa	p^δ –
I	15	0.54	0.2	0.02	850	–2.1
E	854	0.15	–	–	–190	–0.5
P	42	0.29	0.1	0.13	1800	–2.5
PC	98	0.37	1.2	0.01	420	–2.6
D	0.5	0.07	1.3	3.65	8	–0.4
PD	23	0.33	0.5	0.43	450	–2.5

$$log\varepsilon_t^\delta = -(0.05C/D)^{1/n} \tag{5}$$

$$p^\delta Dn(-log\varepsilon)^{(n-1)/\varepsilon ln10} \tag{6}$$

A nonlinearity threshold has not been found for sample E complex modulus. As noticed on Figure 2, this particular material undergoes damage at very low static strain and the test ends with sample break at strain inferior to 10%.

Measured material D loss tangent is particularly scattered (Figs. 3 and 4). Loss tangent value is too low to enable a clear measure and the strain amplitude is not high enough. At a single strain amplitude of 0.1%, the measure gets less scattered (Fig. 4). Test is still achieved at 0.01% single strain amplitude because sample E could not bear a larger strain amplitude without break.

5 ANALYSIS

5.1 *Glass transition temperature*

The glass transition temperature T_g is an indicator of mobility of polymer molecules into the microstructure, therefore these results highlight the influence of sol fraction. The binder of the sample E is composed of cross-linked HTPB only. Its T_g is then 5 K superior to the one of the HTPB prepolymer (Table 2). Addition of cross-linked or non cross-linked HTPB molecules to the microstructure appears to leave T_g in the same range. This can be caused by the low amount of sol fraction added due to the difficult diffusion of HTPB molecules into the material.

The similarity between materials I and PD indicates that ratio of HTPB and DOZ in sol fraction of sample PD could be close to ratio in the initial sol fraction of material I. It will be considered in this work that the ratio between HTPB and DOZ molecules in materials PD and I are identical.

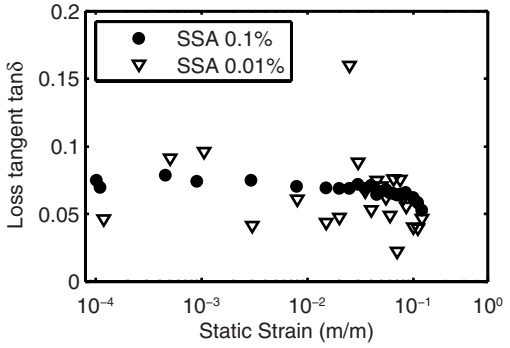

Figure 4. Sample D loss tangent according to single strain amplitude (SSA).

Finally, material D exhibits a very low T_g, confirming that the quantity of plasticizer absorbed was very large compared to initial sol fraction.

5.2 *Prestrained DMA—value at low static strain*

As shown in previous work (Azoug et al. 2009), the complex modulus value at low static strain, A, depends on the filler fraction, the polymer network and the quantity of plasticizer in the sol fraction whereas the loss tangent value at low static strain, C, depends on the composition and quantity of sol fraction. All studied materials contain the same amount of filler and the same polymer network, the sol fraction is the only variation.

These considerations are confirmed by the evolution of the complex modulus value A according to sol fraction content. Indeed, the materials containing plasticizer, D, I and PD, present the lowest values, respectively 0.46, 15 and 23 MPa (Table 3). Nevertheless, sol fraction quantity and interactions between sol fraction and polymer network seem to significantly influence the complex modulus value. Complex modulus variation from 23 to 15 MPa between materials PD and I is explained by the raise in sol fraction content from 2.6 to 6.8%wt (Table 1).

In non plasticized systems, complex modulus differences directly depend on molecular mobility in the substituted sol fraction. Since there is no sol fraction in material E, the mobility is low and A is the highest, 854 MPa (Table 3). In material PC, sol fraction mobility is improved but still low in consequence of HTPB molecules cross-linking. As mobility increases, A is lowered to 98 MPa. Finally, in material P, molecular mobility is considerably enhanced by the introduction of sol fraction and A decreases to 42 MPa.

Likewise, the evolution of loss tangent value at low static strain C can be explained by the differences

of microstructure. It appears that loss tangent value is null when the molecules are extremely mobile or totally immobile. Hence the loss tangent evolves with the amount of friction between the polymer chains.

Material D contains 29%wt of plasticizer (Table 1), molecules are extremely mobile and loss tangent value of 0.07 is low (Table 3). Contrary to material D, material E contains no sol fraction, mobility is extremely low, however C value is 0.15.

Materials P and PC sol fractions contain HTPB chains. Combination of absence of plasticizer and cross-linking of HTPB molecules (for material PC only) limits the mobility and causes friction between polymer chains. Loss tangent values are respectiveley 0.29 and 0.37 (Table 3). Material PD contains HTPB molecules and plasticizer. Although the role of plasti-cizer is to diminish friction between chains, it seems the quantity introduced is not sufficient to stop the phenomenon since loss tangent value is still 0.33. Finally, material I sol fraction represents 6.8%wt of the composite (Table 1) and its composition is similar to material PD sol fraction. Consequently C equals 0.54.

5.3 *Prestrained DMA—nonlinearity threshold*

The threshold is an indication of the macroscopic state of deformation which has to be reached to engage the nonlinear mechanism. The first point is the extremely low threshold values at which nonlinear effects appear. Indeed, high filler content leads to high strain amplification (Mullins 1969). The same type of nonlinearity has been discussed in carbon black filled rubber systems at a threshold depending on the filler volume fraction (Meinecke and Maksin 1981).

The threshold value depends on filler content and extensibility of the polymer network. Maximum extensibility of the network is supposed to be reached at the threshold, explaining the complex modulus increase beyond this value. Since, in this study, all materials have the same polymer network, the sol fraction composition appears to influence the threshold.

First, material PC thresholds ε_t^e and ε_t^δ are very distant, respectively 1.2% and 0.01% (Table 3). The high value of ε_t^e and low value of ε_t^δ are not explained yet. Material D exhibits thresholds for complex modulus ε_t^e as well as for loss tangent ε_t^δ particularly superior to other materials, respectively 1.3% and 3.65%. This is a consequence of network swelling by plasticizer molecules. There is no friction within the network. Moreover, plasticizer molecules being very mobile, they are able to move quickly according to network deformation.

Materials P, I and PD show that threshold value depends on sol fraction percentage and mobility. Indeed, the low mobility of HTPB molecules in material P makes them a constraint on the network and reduces the network maximum extensibility. Threshold is 0.1% for complex modulus and 0.13% for loss tangent. The more mobile the chains are, the less they take up space into the network. Material I and PD thresholds should then be equal or superior to those found for material P. It is the case with one notable exception for material I ε_t^δ, which is 0.02%. Comparing the results (Fig. 3), it can be seen that the obtained low value is due to differences between model and experiment results at low static strain. Considering only experimental values, material I loss tangent threshold appears to be about 0.3%.

Furthermore, a lower sol fraction quantity limits the constraint on the network and raises maximum extensibility. Hence material PD thresholds are higher than material I, respectively 0.5% and 0.2% for ε_t^e and 0.43% and 0.02% for ε_t^δ.

5.4 *Prestrained DMA—nonlinearity slope*

The supposed mechanism is that the polymer network reaches maximum extensibility at the threshold, although this extensibility depends on composition and quantity of sol fraction. Nonlinearity slopes p^e and p^δ give information about local deformation mechanisms beyond threshold and indicates that the sol fraction behaviour is part of the nonlinear mechanism.

The increase in complex modulus could be the consequence of maximum extensibility of polymer network due to strain amplification. However, loss tangent decrease suggests a diminution of friction between chains within the microstructure. It was shown in 5.2 that loss tangent value is a direct consequence of sol fraction percentage and composition. Hence, although deformations are not transmitted to sol fraction, it suffers mobility loss as a result of static strain application. These considerations lead to the following supposed mechanism. Beyond threshold, the sol fraction, which is embedded in polymer network, is increasingly constrained and its molecular mobility is reduced. Sol fraction composition and percentage affect its ability to be hindered by the network. For instance, plasticizer allows the sol fraction to keep mobility in spite of increasing static strain whereas a lack of mobility in sol fraction in the absence of static strain makes the impact of deformation more limited.

Material P has the highest nonlinearity slope p^e, 1800 MPa (Table 3), because of the absence of plasticizer and the relatively high molecular mobility of sol fraction HTPB chains, as discussed in 5.2. Materials PD and I exhibit a weaker slope p^e, respectively 450 and 850 MPa. Plasticizer molecules in the formulation are limiting mobility loss.

The difference in slope between materials PD and I is attributed to variations in sol fraction quantity, implying variations in network extensibility and sol fraction constraints. In material PC, the impact of static strain is restricted by reduced sol fraction mobility due to cross-linking of HTPB molecules. Consequently the slope p^e, 420 MPa, is also weaker than material P slope. Eventually, material D contains a great quantity of plasticizer and the influence of static strain is weak. The slope p^e is 8 MPa.

The results for p^δ are less accurate. Slopes p^δ of materials P, PC and PD are close and differences are within the model error, respectively –2.5, –2.6, –2.5 (Table 3). It is supposed that the low quantity of sol fraction prevents differentiation between the three materials regarding diminution rate of friction into the microstructure.

Comparing them with material I shows that, as discussed in 5.3, a large quantity of sol fraction constitutes an obstacle for the network. So while the slope p^e increases with increasing sol fraction, the slope p^δ decreases in the same case. p^δ value is –2.1 for material I and represents the capacity of the network to constrain the sol fraction and hence decrease friction. The more sol fraction there is, the larger network deformation is needed to achieve sol fraction constraining.

Eventually, slopes p^δ of materials E and D are extremely low, respectively –0.5 and –0.4. This is easily explained by the absence of friction at low static strain. In addition, material E does not contain any sol fraction and the loss tangent decrease is probably a consequence of network stretching and orientation. Material D sol fraction is too mobile to be significantly constrained in the explored strain range.

6 CONCLUSIONS

In this study, we discussed DSC and prestrained DMA experiments performed on solid propellants with substituted sol fractions and proposed a mathematical functions to model the nonlinear behaviour. Although DSC results do not emphasize sol fraction differences between materials containing only HTPB molecules, prestrained DMA experiments are extremely sensitive to sol fraction composition. Results from DMA test and modelling allow to propose a local mechanism explaining the observed nonlinearity.

One can assume that at strain threshold, the polymer network reaches maximum extensibility, as previously (Mason 1959, Voet and Morawski 1974, Davies et al. 1996). However, it is important to retain that the maximal extensibility depends on composition and quantity of sol fraction. Increasing chains mobility decreases their ability to form obstacle to network deformation.

Beyond the strain threshold, the sol fraction, which is embedded in the polymer network, is increasingly constrained and its molecular mobility reduces. The mobility loss rate is proportional to loss tangent non-linearity slope and depends on (i) filler fraction leading to strain amplification, (ii) polymer network since the cross-link density directly impacts sol fraction mobility, (iii) sol fraction composition and quantity as they affect its initial mobility and its ability to be hindered by the network.

While this local mechanism has not yet been proven, for example by using direct molecular mobility measurements, its ability to explain experimental macroscopic behaviour is satisfying. A better understanding of these mechanisms could lead to a physically-based constitutive law in order to simulate dynamic behaviour of highly-filled elastomers.

ACKNOWLEDGEMENT

The work of AA is financially supported by DGA, Délégation Générale pour l'Armement (France). The authors would like to thank M^me^ Amiet (DGA) for support of this project and M^me^ Vallat (ICSI, Mul-house) for fruitful discussions regarding the sol fraction.

REFERENCES

Adicoff, A. and A. Lepie (1970). *J. Appl. Polym. Sci. 14*, 953–966.

Arai, K. and J. Ferry (1986). *Rubber Chem. Technol. 59*, 605–614.

Azoug, A., R. Pradeilles-Duval, A. Constan-tinescu, and R. Nevière (2009). *submitted to XIX^ème^ Congrès Français de Mécanique CFM'2009, Marseille.*

Busfield, J., C. Deeprasertkul, and A. Thomas (2000). *Polymer 41*, 9219–9225.

Davies, J., A. Thomas, and K. Akutagawa (1996). *Prog. Rubber Plastics Technol. 12*(3), 174–190.

Dutta, N. and D. Tripathy (1990). *Polym. Test. 9*, 3–13.

Mason, P. (1959). *J. Appl. Polym. Sci. 1*(1), 63–69.

Medalia, A. (1978). *Rubber Chem. Technol. 51*, 437–523.

Meinecke, E. and S. Maksin (1981). *Rubber Chem. Technol. 54*, 857–870.

Mullins, L. (1969). *Rubber Chem. Technol. 42*, 339–.

Payne, A. and R. Whittaker (1971). *Rubber Chem. Technol. 44*, 440–478.

Stacer, R., C. Hubner, and D. Husband (1990). *Rubber Chem. Technol. 63*, 488–502.

Sullivan, J. and V. Demery (1982). *J. Polym. Sci. Pol. Phys. Ed. 20*, 2083–2101.

Voet, A. and J. Morawski (1974). *Rubber Chem. Technol. 47*, 765–777.

Wang, M. (1998). *Rubber Chem. Technol. 71*, 520–589.

Warley, R., D. Feke, and I. Manas-Zloczower (2007). *J. Appl. Polym. Sci. 104*, 2197–2204.

Constitutive Models for Rubber VI – Heinrich et al. (eds)
© 2010 Taylor & Francis Group, London, ISBN 978-0-415-56327-7

Volume change in stretched crystallisable rubbers

J.-B. Le Cam & E. Toussaint
French Institute for Advanced Mechanics (IFMA) Campus de Clermont-Ferrand/les Cézeaux, Aubiére Cedex, France
Fédération de Recherche—TIMS CNRS FR 2856, Complexe Scientifique des Cézeaux, Aubiére Cedex, France

ABSTRACT: The present study deals with change in volume of stretched crystallizable cis-1,4 polyisoprene rubber. During deformation, natural rubber exhibits volume variation induced by both cavitation and stress-induced crystallization. In this work, we propose to measure this volume variation by an original full-field measurement technique. The high resolution of this technique allows us to identify characteristic stretch ratios during mechanical cycles. More especially, the competition between cavitation and stress-induced crystallization is discussed related to stretch ratios at the beginning of crystallization and at the end of crystallite melting. Moreover, the addition of fillers significantly influences the volume variation response. They amplify the cavitation/decohesion phenomenon and allow the crystallization to begin at a lower stretch ratio. Results obtained with filled compound under cyclic loading conditions show that relative volume change is stabilized for a lower number of cycles than the stress-stretch response and that the crystallinity seems to be lower than for unfilled natural rubber. Finally, for the applied strain rate, the Mullins effect is found to have no influence on the value of stretch ratios at the beginning of crystallization and at the end of crystallite melting.

1 INTRODUCTION

Elastomeric materials are subjected to significant change in volume during their deformation. The first record of this phenomenon dates back as far as 1884 in the works of Joule (1884). The author observed that the specific gravity of natural rubber decreased upon stretching it (about 0.15 per cent for a 100 per cent stretch). Later, while studying the nature of the stress-strain curves for natural rubber containing different pigments in varying quantities, Schippel (1920) considered that possibly when the rubber was sufficiently stretched that it might pull away from the particles of pigment in their axes of stress and cause vacua to be formed on both sides of each particle and a considerable increase in the rubber body might therefore be observed. Moreover, at large deformations, the polymer chain network evolves and stress-induced crystallization can occur (Feuchter 1925; Acken et al. 1932; Long et al. 1934; Thiessen and Wittstadt 1936). As fillers are added, the strain is amplified locally and the strain concentration in the filler vicinity is favorable to crystallization. These previous results seem to indicate that the occurrence and growth of cavities and stress-induced crystallization are the main phenomena involved in the deformation of crystallizable rubbers. The aim of the present study is therefore to investigate the competition between these two phenomena and to highlight the influence of fillers and repeated cycles on it. In the first section, the experimental set-up is precisely detailed and in the second section the results obtained are presented by distinguishing filled and unfilled natural rubbers.

2 EXPERIMENTAL SET-UP

2.1 *Materials and sample*

All the samples contain 3 g stearic acid, 9.85 g zinc oxide, and 3 g sulphur, per 100 g of natural rubber. Some of them are filled with carbon black (34 g per 100 g of natural rubber). The unfilled compound is heated to 160°C for 10 min, the filled compound is heated to 160°C for 7 min. In the following, unfilled and filled compounds will be referred to as NR and F-NR respectively. The degree of crosslinking, characterized by the number ν of moles of crosslinks per g, was estimated using the Mooney elastic coefficient C_1, determined from experimental relations between tensile nominal stress π (force per unit of unstrained cross-sectional area) and stretch ratio λ:

$$\frac{\pi}{2(\lambda - \lambda^{-2})} = C_1 + \frac{C_2}{\lambda} \tag{1}$$

From the simple kinetic theory of rubber elasticity (Treloar 1975):

$$\nu = 2\frac{C_1}{RT} \tag{2}$$

where R is the gas constant and T is absolute temperature. In the case of unfilled compound, ν is found to be equal to 11.3 mol/g $\times$ 10^{-5}. To overcome aging problems, samples are frozen at −18°C 48 h after their molding. They are then thawed out 24 hours before testing. The sample dimensions are 30×4 mm^2 and 2 mm thick.

2.2 *Loading conditions*

Mechanical cycles are performed under prescribed uniaxial displacement with a 50 N Instron 5543 testing machine. Hygrometry is equal to 34% and the temperature of the room is set at 23°C. The corresponding stretch ratio varies between 1 and 4.7 for unfilled NR samples and between 1 and 2.55 for filled NR samples. The strain rate is set to 1.3 min^{-1} for each test.

2.3 *Volume variation measurement*

The change in volume is deduced from the displacement fields on the sample surface obtained by the digital image correlation technique. It consists in correlating the grey levels between two different images of a given zone. Each image corresponds to different stretch ratio levels. To improve the image contrast, suitable white paint is sprayed on the surface before testing samples. This leads to a black and white random gray field. This optical technique allows us to reach a resolution of 0.1 pixel corresponding to 5.9 µm and a spatial resolution (defined as the smallest distance between two independent points) of 10 pixels corresponding to 590 µm. The software used for the correlation process is SeptD (Vacher et al. 1999).

Figure 1 presents the overall view of the optical setup. It consists in a cooled 12-bit dynamic Sensicam camera connected to a personal computer in order to process image acquisition and data treatment with the SeptD software. A uniform light at the sample's surface is ensured by lamps. The charge-coupled device (CCD) of the camera has $1.4 \cdot 10^6$ joined pixels (1376×1040). The camera is fixed on a multidirectional adjustable support and the distance between the sample and the CCD matrix is about 60 cm. In this configuration, an area of 4×81 mm^2 is within shot of the digital camera. The size of this zone is sufficient to calculate global displacement slopes in both horizontal and vertical directions.

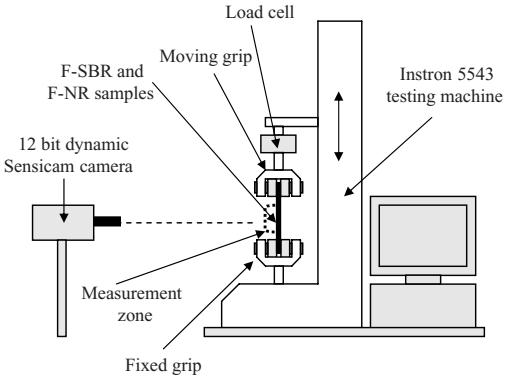

Figure 1. Overall view of the optical setup.

The previous full-field measurements are then considered to calculate the volume variation of the samples at each step of loading. For each mechanical cycle test, 36 and 28 images are stored for NR and F-NR respectively. The first image is the reference one and corresponds to the undeformed state. The other images correspond to successive deformed states. Because of the large deformations undergone by the material, the displacement fields for each deformed state cannot be calculated by correlating images from the reference image. Thus, the following method has been developed:

1. two successive images are correlated and the relative displacement fields are calculated with SeptD software. Between two images, a displacement of 3 mm is imposed by the moving grip. Then, relative displacement slopes in the horizontal and vertical directions are determined from Matlab software. In the present work, the material behavior is assumed to be transversely isotropic. This assumption has been checked from displacement calculated on the front and the side faces of the samples. So, relative stretch ratios and relative volume change can be calculated;
2. finally, stretch ratios and volume variations are obtained by successive multiplications of the relative ones. This method has been validated by correlating the reference image and the last image of the cycle.

3 RESULTS

First, volume variation measurements are presented for NR during the first mechanical cycle. Second, similar measurements are carried out with F-NR to determine the influence of carbon black fillers on volume variation, i.e. on cavitation/decohesion and on stress-induced crystallization.

Finally, volume variations in the filled compound obtained under three cycles are presented and discussed in relation with the well-known stress softening occurring during the first cycles in such a material (Mullins 1948). It should be noted that each result presented in the present section has been validated by two other tests.

3.1 *Volume variation in NR*

Figure 2(a) presents the stress-stretch response of the material obtained during the first mechanical cycle and Figure 2(b) the corresponding volume variation. Figure 2(b) shows that the relative volume variation does not exceed 6.10^{-2} during the cycle. Here, the curve obtained can be modeled by four segments ([OA], [AB], [BC] and [CD]). The competition between cavitation and stress-induced crystallization can be described in relation with each segment:

1. segment [OA]: the volume increases due to the occurrence and growth of cavities. As already reported in the literature, cavitation takes place around zinc oxide particles and at the poles of metallic oxide inclusions (Le Cam et al. 2004). The higher the stretch level, the higher the size of cavities;

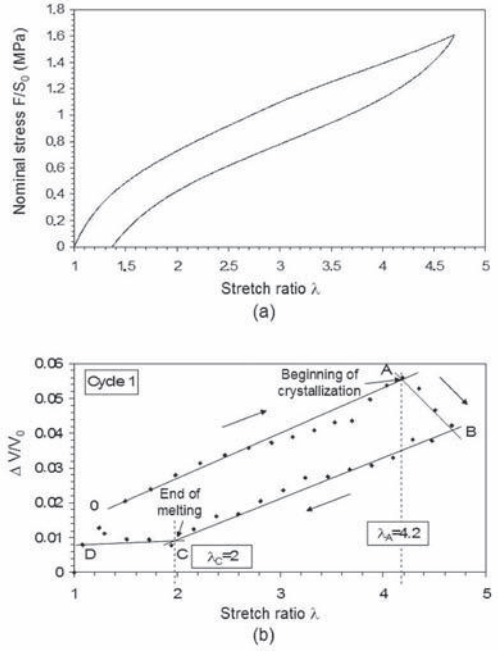

Figure 2. The first mechanical cycle in NR: (a) stress-stretch response, (b) volume variation.

2. segment [AB]: from λ_A, the volume begins to decrease. Even if cavities continue to appear and grow, another phenomenon tends to reduce the volume. In fact, volume decrease in NR is well-known to be due to the reorganization of the polymer chain under stress, namely stress-induced crystallization (Flory and Rehner 1943; Gent et al. 1998). This phenomenon is of the first order compared to cavitation;
3. segment [BC]: during the unloading, the sample volume at a given stretch ratio is smaller than during loading. This can be due to either the difference between the kinetics of crystallization and of crystallite melting or the anelas-tic deformation of cavities. To investigate the deformation processus of cavities, volume change is measured over one cycle for which the maximum stretch ratio is still inferior to λ_A, i.e. the stretch ratio at which crystallization is initiated. Figure 3(a) presents the stress-stretch curve obtained. The fact that the hysteresis loop is very small indicates that no crystallization occurs in the bulk material (Trabelsi et al. 2002). Figure 3(b) shows that the volume change is the same for loading and unloading. This indicates that the nucleation, the growth and the closure of cavities can be considered as an elastic process at the macroscopic scale.

   The kinetics of crystallization and crystallite melting can be studied by stopping the displacement of the moving grip during the mechanical cycle. Here, the moving grip is stopped for 1 min every 3 mm during the third mechanical cycle, i.e. a stabilized mechanical cycle. The results are presented in Figure 4. During the stops, stress relaxes for the loading but does not increase for unloading. That proves that contrary to crystallization, crystallite melting is instantaneous. Thus, crystallization initiated at a given stretch ratio continues during the extension test at a greater stretch ratio. This is in good agreement with the recent works of Trabelsi et al. (2002). These results prove that the hysteresis loop obtained for volume change curves is only due to chain crystallization. To finish, point C corresponds to the melting of the last crystallites;
4. segment [CD]: the volume slightly decreases when the cavities close.

To summarize the previous results, relative volume variation does not exceed $6 \cdot 10^{-2}$ in NR. No significant residual volume change is observed. This indicates that the deformation of cavities can be considered as an elastic process for uniaxial tensile loading. This in turn shows that cavitation, i.e. volume increase, does not take part into the

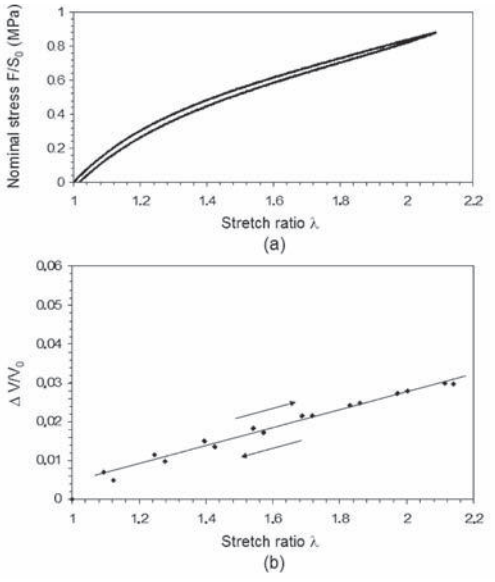

Figure 3. The first mechanical cycle in NR for prescribed stretch ratio inferior to A: (a) stress-stretch response, (b) volume variation.

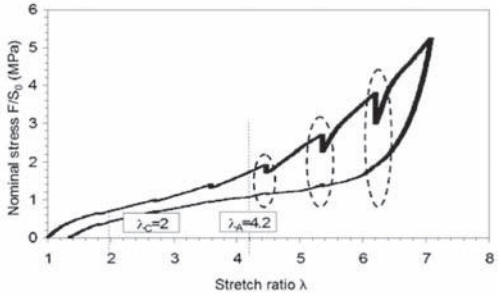

Figure 4. Tensile test stopped 1 min every 3 mm.

residual stretch obtained after the first mechanical cycle. Competition between cavitation and crystallization has been highlighted. More particularly, crystallization is a first order phenomenon and tends to reduce the volume of the material even though cavities continue to grow. The difference in kinetics between crystallization and crystallite melting, more particularly, the fact that, contrary to crystallization, crystallite melting is an instantaneous phenomenon, explains that for a given stretch ratio, the volume variation is lower during unloading than during loading. The elongation at the beginning of crystallization and at the end of crystallite melting are found to be equal to 4.2 and 2, respectively.

3.2 *Influence of fillers*

The previous material has been filled with 34 g of carbon black (N326) per 100 g of natural rubber. The sample's geometry remains the same as for NR. One cycle is performed under prescribed displacement. The maximum stretch ratio reached during the cycle is equal to 2.55.

The stress-stretch response of the material obtained during the first mechanical cycle is presented in Figure 5(a). As expected, fillers increase the material rigidity. Figure 5(b) gives the corresponding volume variation. In this figure, the relative volume variation reaches $24 \cdot 10^{-2}$ at a maximum stretch ratio equal to 2.55. As explained above, fillers amplify the cavitation and the decohesion phenomena. They also amplify the strain (Trabelsi et al. 2003). The obtained volume variation curve can be modeled by five segments ([OA], [AB], [BG], [GC] and [CD]). Similarly to the previous result, characteristic stretch ratios (A and C) are observed in this curve and a new characteristic stretch ratio G is also observed. Thus, it is possible to describe the competition between cavitation and stress-induced crystallization related to each segment:

1. segment [OA]: from zero deformation, the volume increases due to the occurring and growth of cavities;

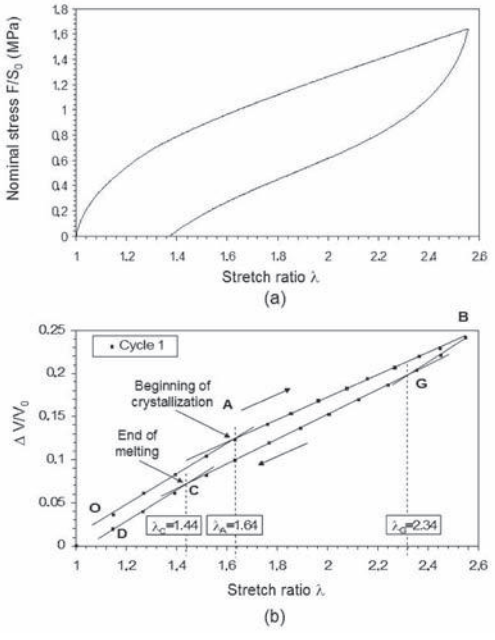

Figure 5. The first mechanical cycle in F-NR: (a) stress-stretch response, (b) volume variation.

2. segment [AB]: from A = 1.64 the curve slope is lower than for segment [OA]. In fact, even if cavities grow continuously, cavitation is still a first order phenomenon due to the addition of fillers, crystallization begins and is opposite to the volume increase. The fact that crystallization occurs at a lower stretch ratio than for NR is explained by the presence of fillers which amplify the local deformation;
3. segment [BG]: at the beginning of the unloading, the volume decreases as the cavity size decreases and the melting of crystallites starts. Similarly to the unfilled compound, the crystallinity level obtained during unloading is superior to the one obtained in loading for a given stretch ratio and the volume variation is inferior during unloading;
4. segment [GC]: the volume of cavities continues to decrease, and crystallites continue to melt, but with a higher rate. Consequently, the rate of volume variation is inferior;
5. segment [CD]: melting of crystallites is complete, and the volume decrease is only due to cavities closing.

To summarize, the addition of fillers increases the volume variation. The fact that from $\lambda = 1.64$, the volume variation does not decrease as in NR indicates that, even if the elongation at crystallization is lower than in NR, the addition of fillers tends to minimize the level of crystallinity for a given stretch ratio. This is the reason why the hysteresis loop is smaller in F-NR than in NR. This is in good agreement with the results of Trabelsi et al. (2003). Finally, the influence of the kinetics of stress-induced crystallization on volume variation in both NR and F-NR can be summarized by the diagram in Figure 6.

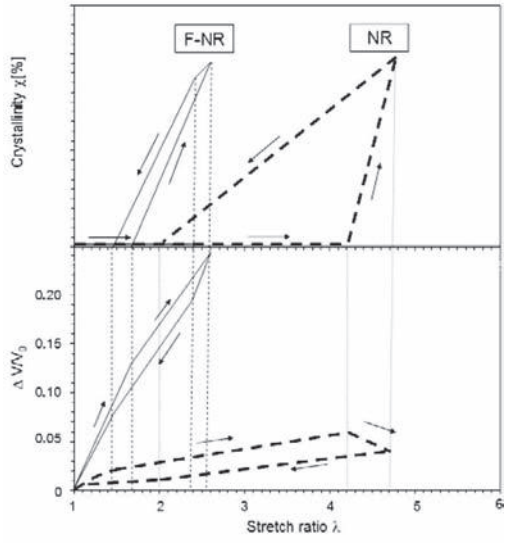

Figure 6. Influence of the kinetics of stress-induced crystallization on volume variation in both NR and F-NR.

3.3 *Volume variation during cyclic loadings*

To investigate the volume variation obtained during cyclic loading, three mechanical cycles were performed. Figure 7(a) presents the stress-stretch response and Figure 7(b) the corresponding volume

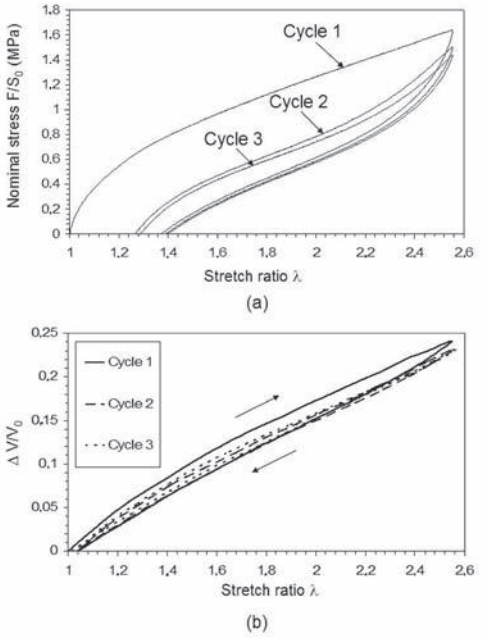

Figure 7. The first three mechanical cycles in F-NR: (a) stress-stretch response, (b) volume variation.

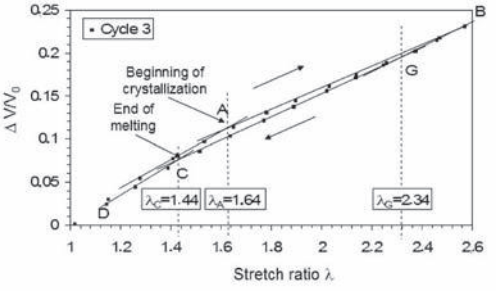

Figure 8. The third mechanical cycle presented in Figure 7(b).

variation. The second figure shows that the highest of the relative volume change and of the hysteresis area are reached during the first cycle. During the second and the third cycles, these quantities are lower. Contrary to the stress-stretch response, the volume variation is stabilized after the first cycle. This result shows that cavitation and decohesion are not preponderant phenomena involved in the Mullins effect (Mullins 1948). Moreover, from the third cycle presented in Figure 8, the same characteristic stretch ratios as those of the first cycle are observed: crystallization starts at $A = 1.64$ and the last crystallites melt at $\lambda = 1.44$.

4 CONCLUSION

Volume variation measurements performed in both unfilled and filled natural rubber highlight the competition between cavitation and stress-induced crystallization. Results show that the relative volume change does not exceed $6 \cdot 10^{-2}$ in NR whereas it reaches $24 \cdot 10^{-2}$ in F-NR. This is explained by the fact that fillers, which concentrate stress, are favorable to cavitation. The fact that no significant residual volume change is observed indicates that the mechanisms involved in volume variation are different from those that induce residual stretch. The full-field measurement method used in this study allows us to identify characteristic stretch ratios at the beginning of crystallization and at the end of crystallite melting. The difference in the kinetics of crystallization and crystallite melting explains the volume variation hysteresis loop observed during cyclic loading. The higher the hysteresis loop, the higher the difference in crystallization and melting kinetics. Here, fillers are found to minimize this difference. Finally, volume variation is stabilized after the second cycle and cyclic loadings do not influence the characteristic stretch ratios. The present work leaves some issues of importance unanswered, one of which is the comparison between the volume variation in crystallizable and uncrystallizable rubbers, especially under cyclic loadings. Further work in this field is currently being envisaged by the authors of this paper.

REFERENCES

Acken, M.F., W.E. Singer, and W.P. Davey (1932). X-ray study of rubber structure. *Ind. Eng. Chem. 24*, 54–57.

Feuchter, H. (1925). The volume contraction with the formation of anisotropic rubber systems by stretching. *Gummi-Ztg 39*, 1167–1168.

Flory, P.J. and J. Rehner (1943). Statistical mechanics of cross-linked polymer networks. *J. Chem. Phys. 11*(11), 512–520.

Gent, A.N., S. Kawahara, and J. Zhao (1998). Crystallization and strength of natural rubber and synthetic cis-1, 4-polyisoprene. *Rubber Chem. Technol. 71*, 668–678.

Long, J.D., W.E. Singer and W.P. Davey (1934). Fibering of rubber. time lag and its relation to structure. *Ind. Eng. Chem. 26*, 543–547.

Joule, J.P. (1884). *India-rubber, §33 in: The Scientific Papers of James Prescott Joule*, Volume 1. Taylor and Francis, red lion court, fleet street: The Physical Society of London.

Le Cam, J.-B., B. Huneau, E. Verron, and L. Gornet (2004). Mechanism of fatigue crack growth in carbon black filled natural rubber. *Macromolecules 37*, 5011–5017.

Mullins, L. (1948). Effect of stretching on the properties of rubber. *Rubber Chem. Technol. 21*, 281–300.

Schippel, H. F. (1920). Volume increase of compounded rubber under strain. *J. Ind. Eng. Chem. 12*, 33–37.

Thiessen, P.A. and W. Wittstadt (1936). Crystals and fused substance in stretched rubber (a preliminary communication). *Rubber Chemistry and Technology 9*, 52–54.

Trabelsi, S., P.-A. Albouy, and J. Rault (2002). Stress-induced crystallization around a crack tip in natural rubber. *Macromolecules 35,* 10054–10061.

Trabelsi, S., P.-A. Albouy, and J. Rault (2003). Effective local deformation in stretched filled rubber. *Macromolecules 36,* 9093–9099.

Treloar, L.R.G. (1975). *The Physics of Rubber Elasticity.* Oxford: Oxford University Press.

Vacher, P., S. Dumoulin, F. Morestin, and S. Mguil-Touchal (1999). Bidimensional strain measurement using digital images. *Instn Mech Engrs Part C ImechE 213.*

Constitutive Models for Rubber VI – Heinrich et al. (eds)
© 2010 Taylor & Francis Group, London, ISBN 978-0-415-56327-7

Influence of temperature on durability behavior of carbon black filled natural rubber

P. Charrier, T. Ramade & D. Taveau
Modyn Trelleborg, Zone ind. de Carquefou, Carquefou Cedex, France

Y. Marco & S. Calloch
ENSIETA, Laboratoire LBMS (EA 4325), Brest Cedex, France

ABSTRACT: Despite numerous studies dealing with rubber durability prediction, information about fatigue behavior versus temperature are still scarce. This could be explained by the difficulty to perform reliable tests at different temperatures. In this study, relaxing Wöhler curves have been achieved for a standard carbon black filled NR with a skin temperature ranging from 10°C to 102°C. During the setting of the experimental protocol, a so-called "thermal accommodation" was observed during the first thermal cycle. Creep and relaxation levels are well above the classical expected ones if the sample is clamped before starting the thermal cycles. Moreover, at high temperatures both thermal and ageing brittle failures have been observed. The upper limit of the temperature range was therefore defined according to the cyclic stiffness evolution to set apart the results disturbed by an ageing induced during the tests. A continuous decrease of the duration life with the increase of the test temperature was finally observed, which is not a classical result.

1 INTRODUCTION

1.1 *Industrial motivation*

Even if the design of anti-vibration parts for automotive industry becomes easier thanks to recent improvements in durability prediction (Ostoja-Kuczynski et al. 2003, Ostoja-Kuczynski et al. 2005 for example), some key issues still have to be faced. According to the authors, the highest priority to enhance the predictions reliability is to take into account the temperature influence on elastomers durability properties.

It is well-known that some of the anti-vibration parts on vehicle are exposed to ambient temperature (the temperature variation could go roughly from –20°C to +40°C). However, other parts are close to heat sources like engine or exhaust line. For that parts, the maximum continuous temperature can reach 80°C or more and this maximum temperature will even increase according to new European anti-pollution norms. Measuring the Wöhler curve of one compound at room temperature is consequently no more sufficient. It is mandatory to evaluate its durability properties for various temperatures, without knowing in advance what will be the temperature profile indicated in the oncoming carmaker specifications.

One strategy could be to measure the Wöhler curves of the compound every 10°C going from 0°C to 100°C or more. Another approach would be to understand the effect of the temperature on the elastomer durability properties. The present paper deals with this second proposal.

1.2 *Scientific background*

Till now, scientific papers dealing with the variation of durability with temperature are few (we focus here on small cracks initiations, not on crack propagation). However, some interesting results have to be highlighted.

As usual for rubber durability, we first have to report the great work of Cadwell et al. (1940). The authors performed cyclic tests with enforced displacements on dumbbell samples made out of natural rubber. On Figure 1, X-axis gives the rubber temperature (from approximately –30°C to +60°C). Y-axis is the ratio of the duration life measured for a given rubber temperature and the one at 37°C. The two curves in black stand for the dispersion observed by the authors using different "stocks". Does it correspond to different storage conditions or different batches, it is not so clear. One can observe that the durability dependence versus temperature is not continuously decreasing and presents a maximum. According to the authors, in region A (low temperatures), the duration life decreases with a slope depending on

the "freezing characteristics of stock". One can assume that quiescent crystallisation without loading (about 20°C) is involved in this process. The authors analysed region B (high temperatures) taking into account ageing of the rubber coupled with a pure temperature effect on duration life.

Other important results were proposed by Lake & Lindley (1964). The plots of Figure 2 are very similar to the ones of Cadwell et al. (1940). In addition to NR results (the crosses), SBR duration lives are also available (circles). The ratio between the maximum and the minimum duration lives for the tested temperature range (from about 0°C to 100°C) is equal to 4 for the NR and 10.000 for the SBR.

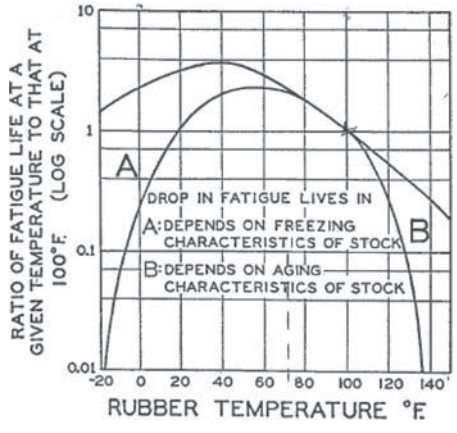

Figure 1. Rubber temperature effect on NR durability according to Cadwell et al. (1940).

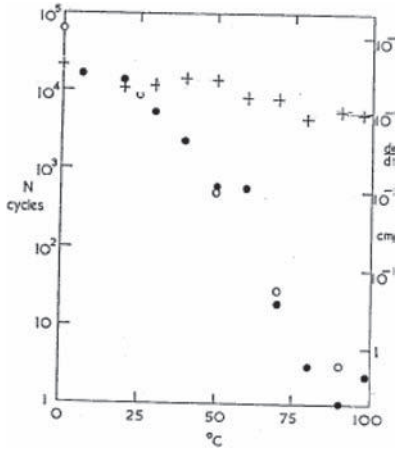

Figure 2. Temperature influence on fatigue duration life according to Lake & Lindley (1964). Crosses stand for NR results and circles for SBR one.

The "low" temperature sensitivity of the NR is linked to its ability to crystallize. As demonstrated by Le Cam et al. (2005), the strain induced crystallization generates hard ligaments in the crack tip (cf. Figure 3) that limit the crack propagation. In the contrary, for SBR (cf. Figure 4), there is no "matrix reinforcement", and the durability properties are strongly linked to the polymer visco-elasticity.

Looking carefully at the NR results in Figure 2, we can also observe that the "duration life versus temperature" curve exhibits a maximum close to 30–40°C, which is similar to the results of Cadwell et al. (1940). Finally, a sudden decrease of the duration life is noticeable at 75°C. Lake & Lindley do not provide any explanations about these variations.

To sum-up, for high temperatures, heat ageing and strain induced crystallization (cf. Figure 5), coupled with the visco-elasticity of the polymer, seem to be among the main factors influencing the durability. For lower temperatures, the durability decreases with temperature even if the matrix is

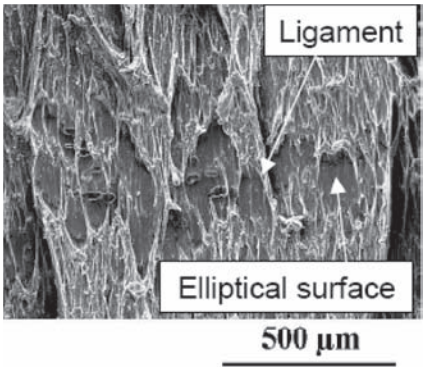

Figure 3. NR crack tip observed by Le Cam et al. (2005) during fatigue crack propagation.

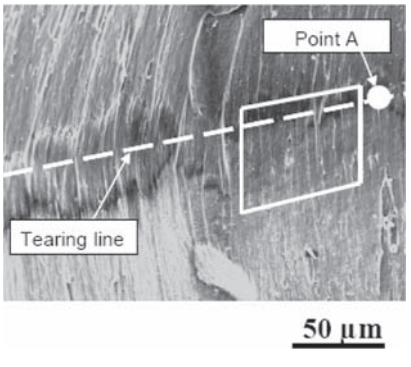

Figure 4. SBR crack tip observed by Le Cam et al. (2005) during fatigue crack propagation.

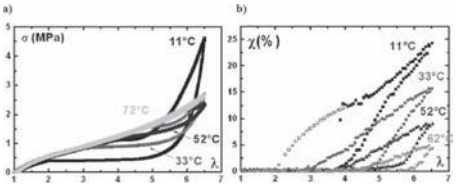

Figure 5. Stress and crystallinity ratio versus elongation at various temperatures for an unfilled NR (Marchal 2006).

less visco-elastic. This could be linked to quiescent crystallization but still has to be investigated.

2 EXPERIMENTAL CONTEXT

2.1 *Test rig and sample*

The compound, the test rig and the samples used in this study are the ones already mentioned in the former papers presented at the ECCRM (Ostoja-Kuczynski et al. 2003, Ostoja-Kuczynski et al. 2005). We will only remind here that the oven temperature ranges from 0°C to 100°C. The shapes of the two kind of samples used are presented in Figure 6.

A schematic outlook of the testing device is proposed in Figure 7. During the tests, at least three temperatures are measured:

- The oven temperature;
- The rubber skin temperature using Infra-Red sensor pointing out at the sample skin;
- The device temperature using a classical thermal-sensor.

To take into account the thermal losses is crucial for tests achieved under several temperatures. A special care was taken here to assert that the aluminum inserts glued to the rubber sample and clamped on the device have the same temperature than the oven.

Moreover, it is important to underline that, during cyclic tests, the sample temperature increases due to heat build-up. Hysteresic losses depend on test amplitude and rubber temperature and the temperature rise is also directly linked to the test frequency. In order to measure Wöhler curves with several fixed targeted rubber skin temperatures and for a large strain amplitude range, we have used FEA simulations to define the testing frequencies (Le Chenadec 2007). We can therefore ensure that the skin temperature of the sample for a given Wöhler curve at a chosen rubber temperature, does not depend on the load level. It is also worth noting that the small cross-section of the chosen sample (cf. Figure 6-b) leads to a limited temperature gradient from skin to core (less than 7°C).

2.2 *Test protocol and "thermal accommodation"*

Starting the test campaign, a basic question arose: the samples have to be screwed on the device but "when?" and "how?". Some surprising results were obtained which lead to achieve specific preliminary tests. In the current section, we will present some of the obtained results without being able to explain all of them.

The test procedure consists in going from 20°C to 100°C two times with pauses of about 20 minutes at various intermediate temperatures. The mechanical load is either displacement or force controlled, imposing constant or cyclic values:

- First of all, we have enforced a constant 0 N force and measured the displacement reaction during the two thermal cycles (cf. Figure 8). When the temperature increases, the global displacement also rises due to thermal dilatation. Using a thermal dilation coefficient of $200 \cdot 10^{-6}$ K^{-1} for the rubber and $25 \cdot 10^{-6}$ K^{-1} for the aluminum device, we were able to predict the measured global dilation during both thermal cycles including the device and the sample (cf. Figure 8);

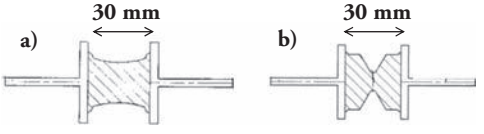

Figure 6. Test samples used in the present study.

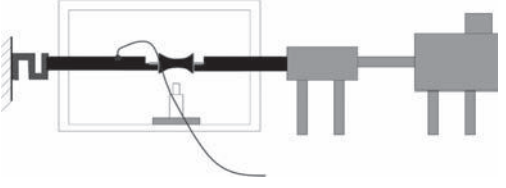

Figure 7. Schematic outlook of the testing device.

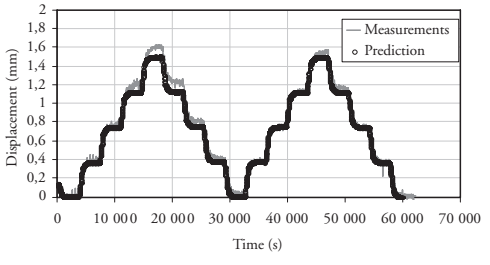

Figure 8. Displacement evolution during a 0 N force controlled test and two thermal cycles going from 20°C to 100°C.

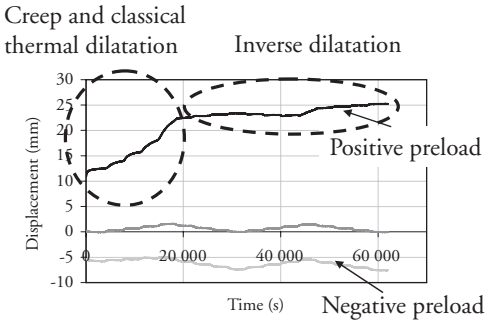

Figure 9. Displacement evolution during enforced constant force tests (positive, null and negative) and two thermal cycles going from 20°C to 100°C.

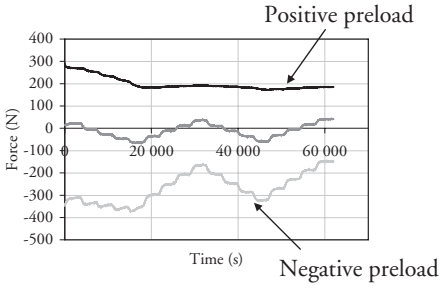

Figure 10. Force evolution during enforced constant displacement tests (positive, null and negative) and two thermal cycles going from 20°C to 100°C.

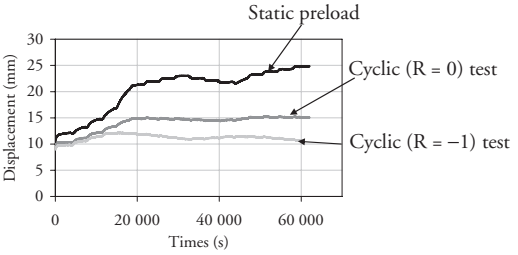

Figure 11. Displacement evolution during enforced force tests (cyclic and static) for two thermal cycles going from 20°C to 100°C.

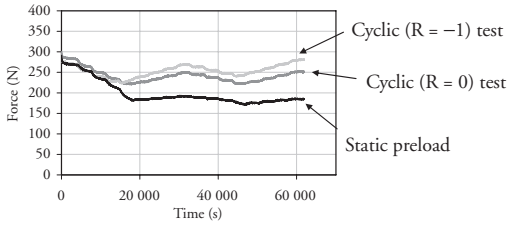

Figure 12. Displacement evolution during enforced displacement tests (cyclic and static) and for two thermal cycles going from 20°C to 100°C.

– The same tests were performed with a positive and a negative force preloads (cf. Figure 9). During the first thermal cycle with a positive preload, we have observed a very important creep and then a "thermal inversion" (i.e. the thermal dilatation coefficient switched to a negative value). The second thermal cycle provides a much more stable evolution of the displacement (i.e. at the end of the second thermal cycle, we nearly recover the measured displacement at the beginning of this cycle). First of all, we conclude that, both for compressive and tensile conditions, a "thermal accommodation" during the first thermal cycle arises—with the positive preload, the reaction displacement is multiplied by 2 in less than 6 hours—that can not only be explained by classical visco-elasticity. Secondly, when the displacement is high enough, the expected classical thermal inversion is clearly visible;
– Similar tests were performed with enforced positive, null and negative displacements (cf. Figure 10). Load levels were chosen to ensure that the displacements were equivalent to the ones used in the previous tests at the beginning of the first thermal cycle. Once again, we observe an important relaxation step during the first thermal cycle. The second one is more stable, highlighting, there again, a "thermal accommodation". During these tests, the enforced displacements were not high enough to reach the thermal inversion elongation;
– The level of variation of the force/displacement was so surprising with constant preload that we have performed similar tests with cyclic loadings (both repeated and alternated tests were conducted). We can notice that the cyclic "thermal accommodation" level is well below the static one with enforced forces (Figure 11) or displacements (Figure 12).

All these results obtained with a fatigue device have been confirmed using TMA apparatus, so that we can say the Gough-Joule effect is evidenced but only after a "first thermal accommodation" which level depends on the kind of loading (static, repeated, alternated…). For us, it is an important issue that has to be explained.

Moreover, using the TMA apparatus, the thermal dilatation coefficient was measured as a function of the preload both in tension and in compression (cf. Figure 13). It is important to note that this thermal dilatation coefficient is the one measured during the second thermal cycle, i.e. after "thermal accommodation". Our results

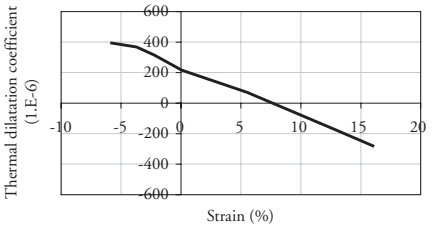

Figure 13. Thermal dilatation coefficient versus strain obtained after a first thermal accommodation cycle.

are conformed to classical ones showing that, at a preload of about 10%, the thermal dilatation coefficient becomes negative.

Regarding the present study, it was decided to let the sample unscrewed during 2 hours in the oven at the testing temperature before clamping it. It was then checked that there was no unexpected evolution of the force during the cyclic tests.

3 TEST RESULTS ANALYSIS

3.1 *Temperature range*

Based on this preliminary study on both the test rig and the test procedure, the aimed temperature range for the skin sample was set to [10°C; 102°C]. Frequency was then used as a tuning parameter to balance heat build-up and test duration.

3.2 *Failure surface analysis*

Before talking about crack initiation results (depending on the local skin temperature), it must be mentioned that the shape of the fracture surface depends on temperature (cf. Figure 14).

As the temperature increases, brittle failure zones can be observed on the failure surface (increasing areas with a low rugosity shown on Figure 14). These zones can be related to the failure history which exhibits two steps (cf. Figure 15): first a classical mechanical initiation and propagation step, giving a failure surface with a roughness equivalent or smaller than the one at room temperature. During that stage, the sample stiffness regularly and continuously decreases (combination of visco-elasticity, damage cumulation and crack growth). Then, in a second stage, the sample breaks in one cycle and the associated zone of the failure surface is smooth. When the temperature increases, this brittle failure appears sooner and the size of the smooth area increases. For the studied material, brittle failures appear for skin temperatures higher then approximatively 83°C. However, the crack tip temperature has to be accurately evaluated in order to define this transition temperature (this is a still on-going work).

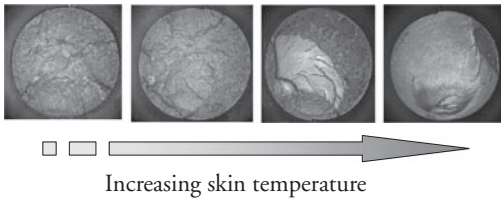

Figure 14. Failed surface as a function of the skin temperature during fatigue test in the studied temperature range.

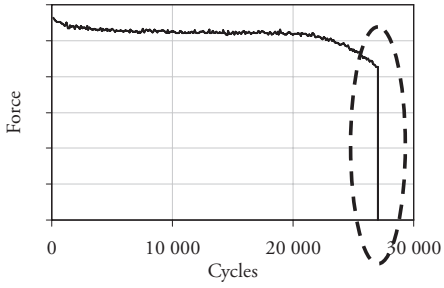

Figure 15. Evolution of the reaction force during high temperature fatigue test (102°C) highlighting "thermal brittle failure" after a mechanical propagation stage.

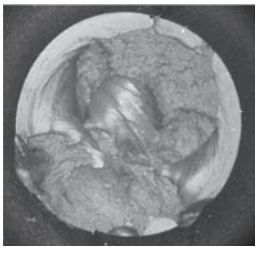

Figure 16. Failed surface for a temperature of 120°C, i.e. higher than the studied temperature range.

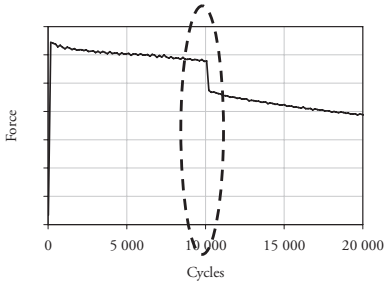

Figure 17. Reaction force evolution during a very high temperature fatigue test (120°C) highlighting "ageing brittle failure" preceding a mechanical propagation stage.

When performing tests out of the previous temperature range (using another test device), a new type of failure was observed (cf. Figure 16). Before any mechanical propagation, a brittle failure appears and the corresponding failed area is a smooth ring located at the skin of the sample (cf. Figure 17). In that precise case, we can assume that the heat ageing during the test is so important that it drives the ageing of the sample cross-section threw the so-called D.L.O. (Diffusion Limited Oxygen) effect. It leads the skin to become so brittle that it breaks after some cycles.

3.3 *Heat ageing during the tests*

It is well known that heat ageing can be detected for NR compounds by a stiffness increase along the test. So, we have chosen to follow the stiffness during cyclic test ignoring the two hours spent in the oven before starting the test. For our analysis we used the full range stiffness, dividing the measured force range by the enforced displacement range.

As demonstrated in Figure 18, for the highest skin temperature tested, the cyclic stiffness increases during the fatigue test and we can assume that our rubber ages during the test. This is not the case (or less visible) at lowest temperatures.

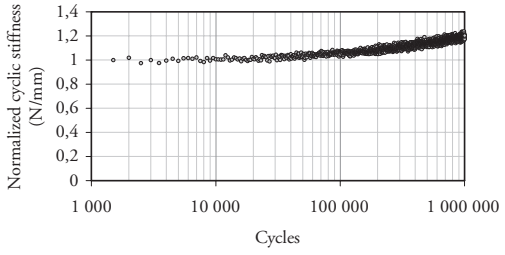

Figure 18. Normalized cyclic stiffness versus the number of cycles during a fatigue test with a skin temperature of 102°C.

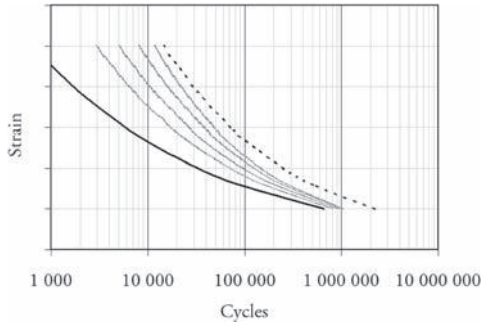

Figure 19. Measured strain Wöhler curves (R = 0) for different temperatures. Doted line corresponds to 10°C. Dashed ones correspond to 30°C, 44°C, 62°C and 83°C. Finally, the black one corresponds to 102°C.

3.4 *Measured Wöhler curves*

Let's see now how the relaxing (R = 0) Wöhler curves for the tested compound are modified by the temperature, measured at the skin of the sample (cf. Figure 19).

First of all, the Wöhler curve measured at 102°C is quite clearly far from the others. This can be explained by the previously mentioned heat ageing during test that weakens the NR compound.

The Wöhler curve measured at 10°C is also far from the others demonstrating a higher resistance of the compound at low temperatures. This is not what have been observed by Cadwell et al. (1940) or Lake & Lindley (1964), but is expected if we think about the reinforcement due to the strain induced crystallization.

The plots of the duration life and of the Wöhlers curves slopes versus the skin temperature of the sample both confirm that (cf. Figures 20 & 21):

– Above a threshold temperature, the material becomes weaker, and we assume that this is due to thermal ageing;

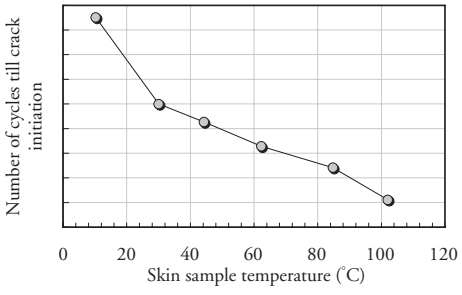

Figure 20. Measured duration life evolution versus sample skin temperature at a constant level of enforced strain.

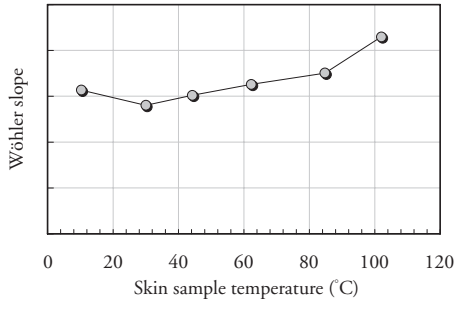

Figure 21. Measured Wöhler slope evolution versus sample skin temperature.

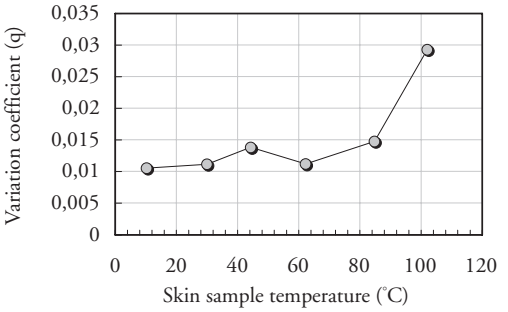

Figure 22. Durability scattering evolution versus sample skin temperature.

– Below another threshold temperature, the material becomes stronger (which is different from previous results of the literature) due to strain induced crystallization.

3.5 *Durability scattering*

Another approach to visualize the effect of the heat ageing during fatigue test consists in focusing on the durability scattering. Figure 22 shows that, at 102°C, the variation coefficient (i.e. standard deviation divided by mean value) grows in an unexpected manner unless heat ageing is involved.

4 CONCLUSION

To conclude about this on-going study, authors would like to mention that:

1 Performing fatigue test at various temperatures requires numerous cautions, among which the "thermal accommodation" presented here is not the least;
2 Heat ageing can disturb fatigue test at high temperatures so that special care have to be used to restrict the studied temperature range in order to dissociate the pure thermal effect from the thermal ageing;
3 At low temperatures, it seems that there is a divergence between the already published results and the ones proposed here. Room temperature (about 20°C) corresponds to the melt temperature of NR crystals without any preload. We can suppose that below this temperature, the fatigue behavior will be enhanced. It corresponds to our experimental results but not to the former ones. Maybe experimental protocol could explain these variations but it still has to be demonstrated.

Authors would like to thank Renault and PSA-Peugeot-Citroën for the participation to this study.

REFERENCES

Cadwell, S.M., Merril, R.A., Sloman, C.M & Yost, F.L. 1940. Dynamic Fatigue Life of Rubber. *Industrial and Engineering Chemistry, 12, n°1: 19–23.*

Lake, G.J. & Lindley, P.B. 1964. Cut growth and fatigue of rubbers. II. Experiments on a noncrystallizing rubber. *Journal of Applied Polymer Science, –8, 707–721.*

Le Chenadec, Y., Stolz, C., Raoult, I. Nguyen T., M.-L., Delattre, B. & Charrier, P. 2007. A novel approach to the heat build-up problem of rubber. *Proceedings 5th European Conference on Constitutive Models for Rubber, Paris, September-2007.*

Le Cam, J.-B., Verron, E., Huneau, B., Gornet, L. & Pérocheau, F. 2005. Micro-mechanism of fatigue crack growth: comparison between carbon black filled NR and SBR. *Proceedings Fourth European Conference on Constitutive Models for Rubber, Stockholm, June-2005.*

Marchal, J. 2006. *Cristallisation des caoutchoucs chargés et non chargés sous contrainte: Effet sur les chaînes amorphes*. Ph-D Dissertation, University of Paris XI.

Ostoja-Kuczynski, E., Charrier, P., Verron, E., Marckmann, G., Gornet, L. & Chagnon, G. 2003. Crack initiation in filled natural rubber: experimental database and macroscopic observations. *Proceedings Third European Conference on Constitutive Models for Rubber, London, September-2003.*

Ostoja-Kuczynski, E., Charrier, P., Verron, E., Gornet, L. & Marckmann, G. 2005. Influence of mean stress and mean strain on fatigue life of carbon black filled natural rubber. *Proceedings Fourth European Conference on Constitutive Models for Rubber, Stockholm, June-2005.*

Constitutive Models for Rubber VI – Heinrich et al. (eds)

Multi-axial viscoelastic deformation of carbon-black filled EPDM rubber

D.S.A. De Focatiis
Department of Chemical and Environmental Engineering, University of Nottingham, UK

F. Abraham
Mechanical & Design Engineering, University of Portsmouth, UK

C.P. Buckley
Department of Engineering Science, University of Oxford, UK

ABSTRACT: Cyclic tensile stress-strain data for a cross-linked EPDM rubber in uniaxial, biaxial and constant width modes of deformation are presented. After extraction of the rubbery and viscous contributions, the rubbery data is modelled using the Edwards-Vilgis strain energy function with parameters evolving with the maximum stretch. It is found that the cross-link density reduces with increasing stretch, but the slip-link density is invariant. The viscous contribution is a strong function of stretch but invariant of maximum stretch. This presents an opportunity to model the behavior using a strain energy function with evolving parameters in parallel with viscoelastic anisotropic flow units.

1 INTRODUCTION

Filled elastomers are increasingly important industrial materials because of their unique flexibility and damping properties, and are used in a range of applications such as seals, dampers, transmission belts and automotive tyres. They exhibit a range of complex phenomena when subjected to repeated loadings: (1) the stress-softening phenomenon known as the Mullins effect (Mullins & Tobin 1957); (2) complex pre-conditioning dependent viscoelasticity; and (3) a small degree of permanent set.

The generation of constitutive models able to accurately predict the mechanical response of such components forms an essential part of their design, and can also contribute to the understanding of the mechanisms underpinning such a response.

In this paper we present a series of experimental observations aimed at shedding light on these phenomena. We propose a means of separating the rubbery and viscous contributions to the stress. The rubbery stress is then used to identify the evolution of a set of strain energy function parameters with the amount of pre-deformation. The viscous stress can then be examined, and is found to be both a unique function of stretch in the rubber, and invariant of pre-deformation.

These findings are aimed at supporting the implementation and validation of a new constitutive model able to capture the complex multiaxial viscoelastic deformation of this type of elastomers.

2 EXPERIMENTAL METHOD

The material studied in this work is an accelerated sulphur cross-linked carbon-black filled (50phr) oil extended ethylene-propylene-diene (EPDM) rubber. Sheets of material approximately 0.5 mm thick were compression-moulded for 13 minutes at 160°C using a heated press. Specimens for tensile testing were cut from the sheet using a dog-bone cutter. 70 mm square specimens were cut from the sheet for biaxial testing.

Uniaxial tensile testing was performed in an In-stron tensile testing machine fitted with a counterbalanced elastomer extensometer, at room temperature at a constant true strain rate of 0.03 s^{-1}, as measured in the gauge length by the extensometer, imposed using a feedback loop.

Biaxial testing was performed using the Oxford flexible biaxial stretcher (Buckley & Turner 1999) at room temperature at a constant nominal strain rate of 0.03 s^{-1}. Strain was measured by non-contact video tracking of small markers placed near the centre of the specimen.

All tests consisted of 4 load-unload cycles, loading to a specified maximum stretch, and unloading

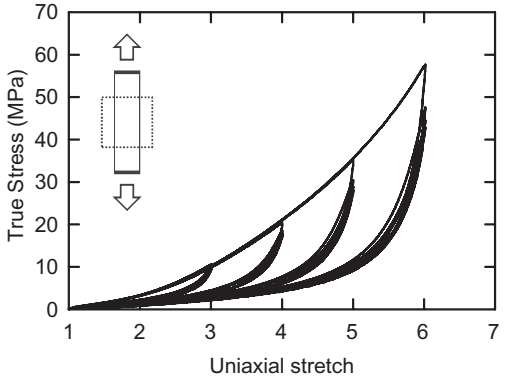

Figure 1. Representative uniaxial stress-strain cycles to different levels of pre-deformation.

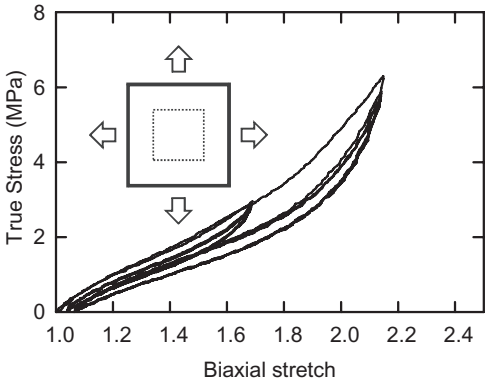

Figure 2. Representative equibiaxial stress-strain cycles to different levels of pre-deformation.

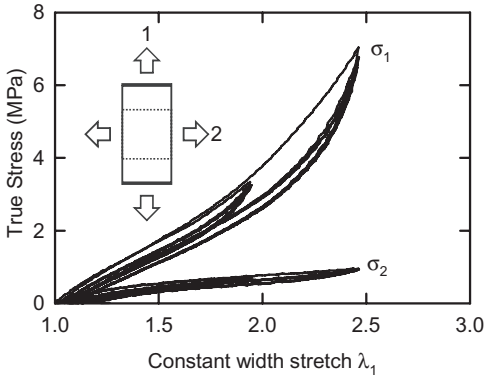

Figure 3. Representative constant width stress-strain cycles to different levels of pre-deformation.

to a tensile force of 0.1 N to avoid buckling. In uniaxial deformation experiments a range of 10 maximum stretches from $\lambda = 1.5$ to $\lambda = 6$ were used. A range of grip displacements corresponding to maximum stretches from $\lambda = 1.5$ to $\lambda = 2.25$ were used in equibiaxial deformation, and from $\lambda = 1.5$ to $\lambda = 3$ in constant width deformation, Representative stress-strain curves for the cycles in the three modes of deformation are shown in Figures 1–3.

3 ANALYSIS

The premise for this work is provided by the ideas of Haward and Thackray (1968) for the modelling of polymeric materials. Two contributions are ascribed to the stress, arising from: (a) an underlying entropy-elastic network with connectivity provided by chemical cross-links, including bonding at the rubber and carbon-black interface, and entanglements; and (b) viscoelastic inter-molecular interactions. In the case of the simple deformation sequences presented here the behaviour of the network is assumed to depend only on the maximum stretch previously reached. Therefore unloading-reloading loops following the first loading to the maximum stretch can be used to determine separately the contributions from (a) the network, and (b) viscoelasticity, following a procedure similar to that suggested previously by Prisaca-riu et al. (2005).

The network stress was calculated as the mean of the unloading and reloading stress at a given strain, and the viscous stress as half of the difference between the unloading and reloading stress, as illustrated in Figure 4. In order to remain clear of viscoelastic transients, data from the first and final 0.33 strain of any loading and unloading cycle is not used for this purpose.

The physically based Edwards-Vilgis (EV) strain energy function (Edwards & Vilgis 1986) was used

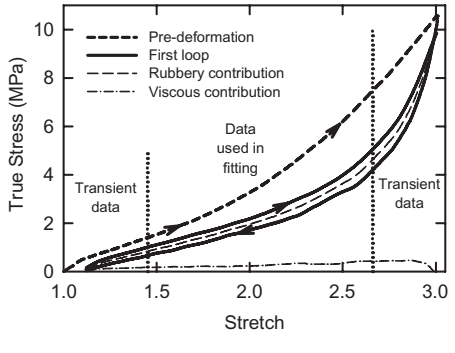

Figure 4. Extraction of a rubbery contribution and a viscous contribution from a stress-strain loop.

to model the rubbery contribution, and was implemented in Matlab. An in-house minimisation routine was used to find the best set of EV parameters for the rubbery stress obtained from each loop, minimising the rms error in stress. The parameters are N_s and N_c, the number densities of slip-links and cross-links respectively, α, a measure of finite chain extensibility, and η, the slip-link mobility factor. In order to account for the relatively small amount of permanent set ε_{set} exhibited by this material, the permanent set stretch $\lambda_{set} = 1 + \varepsilon_{set}$ is used as a further parameter. Thus the effective stretch λ_{eff} seen by the material after permanent set can be related to the measured stretch λ through $\ln \lambda = \ln \lambda_{set} + \ln \lambda_{eff}$.

4 RESULTS

For the case of uniaxial deformation, the set of fitted parameters N_s and N_c, α and η, and ε_{set} are shown in Figures 5–7 respectively as functions of the maximum pre-deformation. Figures 8–9 and 10–11 illustrate parameters N_s and N_c, and α and η, for equibiaxial and constant width deformation respectively. The amount of permanent set under equibiaxial and constant width deformations (not shown) was small. Remarkably, the rms error in stress from the fitting routine remains below 0.5% of the maximum stress in all the uniaxial loops, and below 1.5% of the maximum stress in all the equibiaxial and constant width loops, indicating that the EV function is appropriate for capturing the particular shape of the rubbery part of these curves.

The evolution of the rubbery parameters with increasing number of cycles was investigated experimentally in all three modes of deformation for up to 100 cycles (not shown). Although there is a limited amount of evolution in the parameters with cycle number, this is small relative to the evolution of the same parameters with pre-deformation.

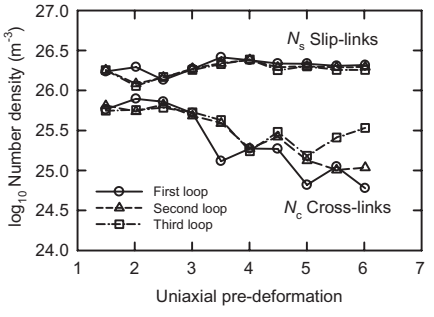

Figure 5. The evolution of the number density of slip-links and cross-links in the rubbery stress with uniaxial pre-deformation.

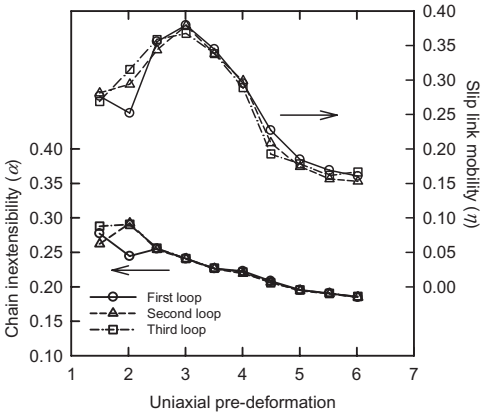

Figure 6. The evolution of the chain inextensibility parameter α and the slip-link mobility parameter η with uniaxial pre-deformation.

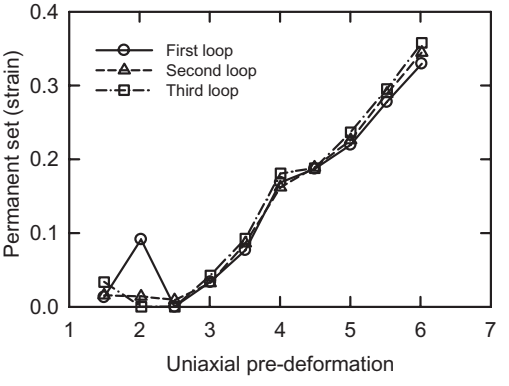

Figure 7. The evolution of the strain at permanent set (evaluated as a fitting parameter for the rubbery contribution) with uniaxial pre-deformation.

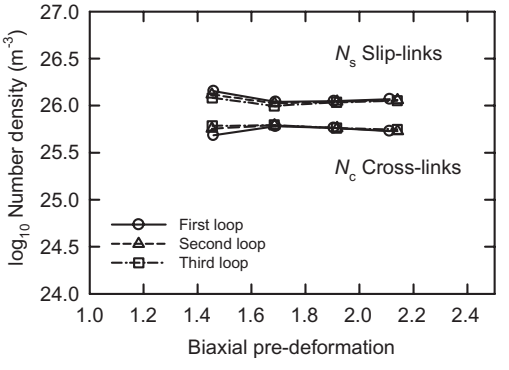

Figure 8. The evolution of the number density of slip-links and cross-links in the rubbery stress with equibiaxial pre-deformation.

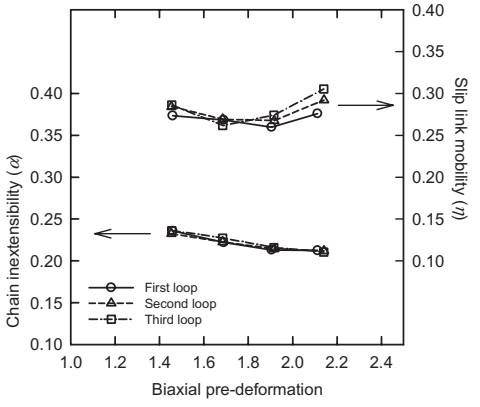

Figure 9. The evolution of the chain inextensibility parameter α and the slip-link mobility parameter η with equibiaxial pre-deformation.

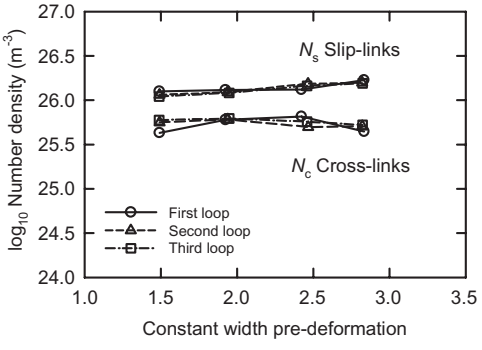

Figure 10. The evolution of the number density of slip-links and cross-links in the rubbery stress with constant width pre-deformation.

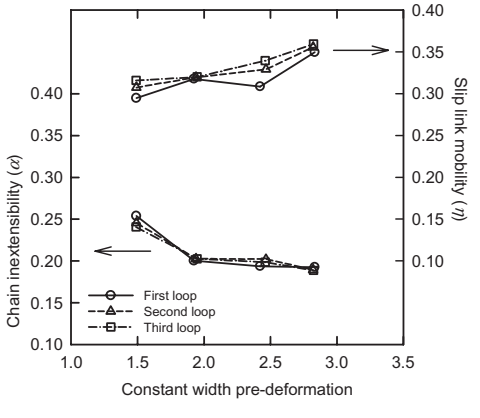

Figure 11. The evolution of the chain inextensibility parameter α and the slip-link mobility parameter η with constant width pre-deformation.

In the first phase of this work it is not our intention to investigate this evolution. Thus we pursue with the assumption that the above parameters depend only on the maximum stretch previously reached.

The strain rate dependence of the response was also investigated experimentally in all three modes of deformation at rates from 0.01 to 0.1 s^{-1} (not shown). The effect of strain rate on the rubbery parameters was also found to be small relative to the other effects.

5 DISCUSSION

5.1 *Entropic contribution*

As can be seen from Figure 5 for uniaxial deformation, although the slip-link density as found from fitting remains approximately constant with pre-deformation, the cross-link density appears to decrease. At the same time, Figure 6 shows that the chain inextensibility parameter α is also decreasing. α is related to the limiting (asymptotic) value of the stretch λ_{max} in the EV model through $\alpha = 1/\lambda_{max}$. A possible physical interpretation is that, with increasing pre-deformation, some polymer chains are becoming too tightly stretched, and breaking loose from bonding at the polymer carbon-black interface. Thus, there is a reduction in apparent cross-link density, and chains can reach a larger limiting λ_{max}. However, the entanglements (represented by slip-links) are a topological feature of the network and therefore their number density is unaffected by strain.

In the equibiaxial and constant width deformation modes, there is evidence of a similar decrease in the value of α (Figs. 9, 11), but the deformations are not large enough to be able to discern with any certainty whether the same trends are present in N_s and N_c (Figs. 8, 10).

The presence of carbon black in a system such as the EPDM used here leads to a strain amplification in the rubber network. This is at present not specifically accounted for in the parameters N_s, N_c, α, η and λ_{set}.

The entropy-elastic part of the stress, evaluated from the fitted parameters, is shown in Figure 12 as a function of the effective stretch seen by the rubber (corrected for permanent set) for all 10 uniaxial tests.

5.2 *Viscoelastic contribution*

The viscoelastic contribution to the stress was obtained from all the loops using the procedure described above. Figure 13 shows the computed viscosity from the first unloading-reloading loop (away from transients) as a function of the effective stretch seen by the rubber, for all 10 uniaxial tests

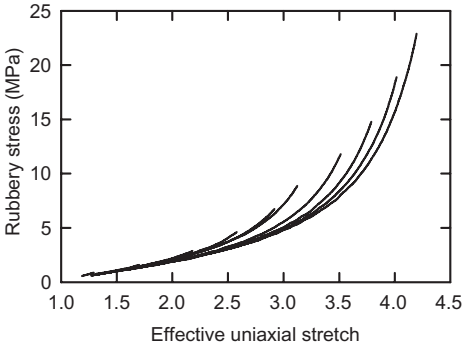

Figure 12. The rubbery contributions to the stress as functions of the effective stretch for different uniaxial pre-deformation levels (first loop).

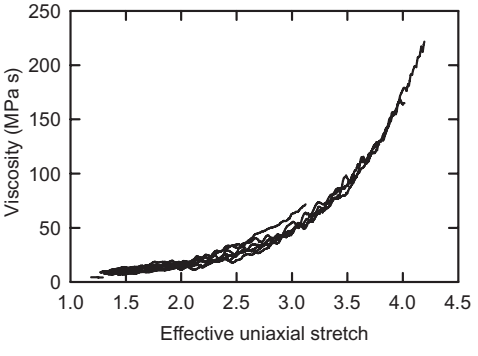

Figure 13. The viscosity, calculated as viscous stress/strain rate, as a function of the effective stretch, for different uniaxial pre-deformation levels (first loop).

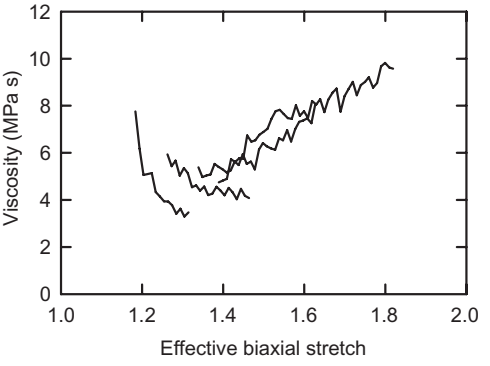

Figure 14. The viscosity, calculated as viscous stress/strain rate, as a function of the effective stretch, for different equibiaxial pre-deformation levels (first loop).

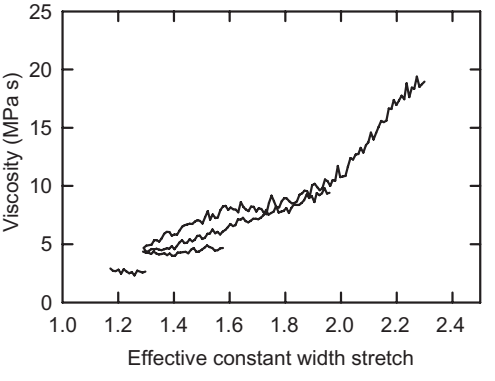

Figure 15. The viscosity, calculated as viscous stress in the stretching direction/strain rate, as a function of the effective stretch, for different constant width pre-deformation levels (first loop).

to different degrees of pre-deformation. Figures 14 and 15 show the computed viscosities from the first unloading-reloading loop for the four equibiaxial and four constant width tests respectively. Although there is considerable noise in the data due to the small values of viscous stress relative to the rubbery stress, after due correction for permanent set there appears to be a unique viscosity 'master curve' in each mode of deformation. The viscosity is invariant of the levels of pre-deformation, but in all cases increases with stretch in the rubbery network. This increase is particularly noticeable in the uniaxial data where it changes from ~5 MPa s at low stretch to beyond 200 MPa s at large stretches. This implies that the viscoelastic contribution can be represented as a unique function of strain in the rubbery network, but is independent of pre-deformation and rubbery network parameter evolution.

A possible explanation for this observation is that the viscous contribution arises from intermolecular interactions that are unaffected by the breakdown in polymer-filler bonding, but where the flow units are intrinsically anisotropic. With increasing strain, the combined effect of such flow units becomes increasingly anisotropic as a result of molecular alignment at a local (sub-entanglement) length scale. One approach to incorporate this phenomenon is to model the flow as a spectrum of units that are intrinsically anisotropic, and whose anisotropy evolves with network stretch (Buckley 2006).

It must be emphasized that the 'master curve' can be obtained only after accounting for the permanent set in the rubbery stress, which is not a direct experimental measurement, but obtained as a parameter in the fitting of the EV strain energy function to the rubbery stress. Although the viscosity is strictly speaking pre-conditioning dependent, this is only because of the dependence

of permanent set on pre-deformation. Once the permanent set is accounted for, the viscosity reduces to a 'master curve' and becomes independent of pre-deformation.

5.3 *Constitutive model development*

The experimental findings presented here offer a range of insights into the necessary features of a constitutive model able to cope with combined multi-axial viscoelastivity and the Mullins effect in filled elastomers.

The main features to be accounted for are: (1) a small, but not insignificant amount of permanent set as a result of pre-deformation; (2) an underlying rubbery network whose parameters evolve with increasing pre-deformation (the Mullins effect); and (3) a viscosity that is invariant of pre-deformation once permanent set is accounted for, but that exhibits a strong dependence on current network stretch.

A range of phenomenological and microstructural models have been proposed to describe the Mullins effect (see for example Marckmann et al. 2002, Hor-gan et al. 2004, Qi & Boyce 2004), and some models have included viscoelastic effects (Bergstrom & Boyce 2000), but to our knowledge no model presently captures the complex pre-deformation invariant but strongly stretch-dependent viscosity.

Incorporating the anisotropic flow mdel proposed previously by Buckley (2006) to account for strain hardening phenomena of glassy polymers near the glass transition into a constitutive model for filled elastomers presents a possible means of capturing this phenomenon.

Further developments of a constitutive model should account for the anisotropic nature of the Mullins effect, the small strain rate dependence, and the evolution of network parameters with increasing number of cycles.

6 CONCLUSIONS

This study has presented cyclic tensile stress-strain curves for a cross-linked carbon-black filled EPDM rubber in three modes of deformation: uniaxial, equibiaxial and constant width. A technique has been proposed for extracting the rubbery and viscous contributions to the stress and their dependence on the extent of pre-deformation. The rubbery contribution from each loop was fitted to the Edwards-Vilgis strain energy function, and the evolution of the strain energy function parameters determined.

In uniaxial deformation this procedure revealed that the apparent cross-link density reduced with increasing pre-deformation, but that the slip-link, or entanglement density was constant. In equibiaxial and constant width deformation the results are not inconsistent with the findings under uniaxial deformation. The finite extensibility of the network was found to increase with increasing pre-deformation in all three modes of deformation.

The viscoelastic contribution to the stress was extracted using the same procedure. In each mode of deformation the viscosity was found to be invariant with respect to the amount of pre-deformation once permanent set is accounted for, but to increase with increasing stretch in the rubber, possibly revealing anisotropy of flow.

ACKNOWLEDGEMENT

The authors wish to acknowledge the contribution of Dr. T. Alshuth of the German Institute of Rubber Technology (DIK) in supplying the EPDM rubber material.

REFERENCES

Bergstrom, J.S. & Boyce, M.C. 2000. Large strain time-dependent behavior of filled elastomers. *Mechanics of Materials* 32: 627–644.

Buckley, C.P. 2006. Viscoplastic flow in solid polymers as an intrinsically anisotropic Eyring process. In *13th International Conference on Deformation, Yield and Fracture of polymers,* Kerkrade, The Netherlands.

Buckley, C.P. & Turner, D.M. 1999. Application of flexible biaxial testing in the development of constitutive models for elastomers. In Dorfmann, A. & Muhr, A.H. (eds), *Constitutive Models for Rubber.* Rotterdam: Balkema.

Edwards, S.F. & Vilgis, T. 1986. The effect of entanglements in rubber elasticity. *Polymer* 27 (4): 483–492.

Haward, R.N. & Thackray, G. 1968. The use of a mathematical model to describe isothermal stress-strain curves in glassy thermoplastics. *Proceedings of the Royal Society of London Series A* 302: 453–472.

Horgan, C.O., Ogden, R.W. & Saccomandi, G. 2004. A theory of stress softening of elastomers based on finite chain extensibility. *Proceedings of the Royal Society of London Series A* 460: 1737–1754.

Marckmann, G., Verron, E., Gornet, L., Chagnon, G., Charrier, P. & Fort, P. 2002. A theory of network alteration for the Mullins effect. *Journal of the Mechanics and Physics of Solids* 50 (9): 2011–2028.

Mullins, L. & Tobin, N.R. 1957. Theoretical model for the elastic behavior of filler-reinforced vulcanized rubber. *Rubber Chemistry and Technology* 30: 551.

Prisacariu, C, Buckley, C.P. & Caraculacu, A.A. 2005. Mechanical response of dibenzyl-based polyurethanes with diol chain extension. *Polymer* 46 (11): 3884–3894.

Qi, H.J. & Boyce, M.C. 2004. Constitutive model for stretch-induced softening of the stress-stretch behavior of elastomeric materials. *Journal of the Mechanics and Physics of Solids* 52: 2187–2205.

Constitutive Models for Rubber VI – Heinrich et al. (eds)
© 2010 Taylor & Francis Group, London, ISBN 978-0-415-56327-7

Mechanical characterization of rubber from one heterogeneous test

T. Guélon*
Laboratoire d'Ingénierie pour les Systèmes Complexes (LISC), Aubière cedex, France

E. Toussaint* & J.-B. Le Cam*

Laboratoire de Mécanique et Ingénieries (LaMI) Blaise Pascal University (UBP), French Institute for Advanced Mechanics (IFMA), Campus de Clermont-Ferrand / les Cézeaux, Aubière Cedex, France

* *Fédération de Recherche TIMS CNRS FR 2856, Aubière Cedex, France*

ABSTRACT: The present study deals with the mechanical characterization of elastomeric materials. Classically, three homogeneous tests are considered to identify constitutive parameters, namely Uniaxial Tensile (UT), Pure Shear (PS) and Equibiaxial Tensile (ET) tests. Here, a new method is proposed: it consists in inducing the three previous homogeneous tests from only one heterogeneous mechanical test. For this purpose, a conventional tensile machine is used and a new apparatus is designed to be adapted on the machine. The test-induced heterogeneity is discussed related to two criteria based on the existence of UT, PS and ET and on the distribution of the maximal principal elongation at each material points of the sample surface. Experimentally, kinematic fields are provided on the sample surface by an image correlation code suitable for large deformations. Finally, an inverse technique, so-called Virtual Field Method, is used to identify the material parameters in the framework of the Mooney hyperelasticity.

1 INTRODUCTION

The behaviour of rubber-like materials is generally modelled in the framework of hyperelasticity. Numerous constitutive relations are available in the literature (Marckmann and Verron 2006). The identification of the material parameters that govern the constitutive equations is still a difficult task. Classically, three homogeneous tests are considered to identify constitutive parameters, namely uniaxial tensile (UT), pure shear (PS) and equibiaxial tensile (ET) (Ward and Hadley 1993), (Sasso et al. 2008) and a trade-off between the different sets of values obtained for each type of test must be found. These tests are based on the strong assumption of homogeneity of the kinematic fields induced by each test.

In the present work, a new approach based on a heterogeneous test that simultaneously generates the three types of strain states abovementioned is pro-posed. For that purpose, the authors propose to design and adapt a new apparatus on a conventional uniaxial tensile machine that generates a heterogeneous strain state. The sample geometry and the loading conditions are defined beforehand by numerical investigations. Two criteria are defined to discuss the heterogeneity induced by the test. Kinematic fields are provided by a Digital Image Correlation software suitable for large deformations: *Correli*^{LMT} (Hild 2002). Constitutive parameters are identified using an inverse method called the virtual field method.

2 CHOICE OF THE SAMPLE GEOMETRY AND THE LOADING CONDITIONS

In this section, a heterogeneous test that combines UT, PS and ET from a conventional tensile machine is presented. A numerical approach is used to choose the sample geometry and the loading conditions in order to generate sufficient heterogeneity of the kinematic fields. Criteria used to estimate Test-Induced Heterogenity (TIH) are defined and the chosen sample geometry and loading conditions are presented.

2.1 *Test-induced heterogenity*

We analyse the heterogenity induced by the test using the $I_1 - I_2$ diagram where I_1 and I_2 are the first and second invariants of the right Cauchy-Green tensor $\mathbf{C}$ (Holzapfel 2000). This diagram allow us to determine the loading condition applied at

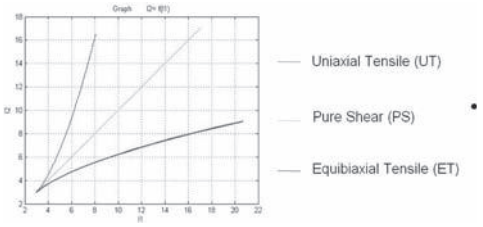

Figure 1. Three basic loading cases.

each material point of the kinematic fields. In this diagram (see Fig. 1), the three curves UT, PS and ET are plotted. The localization of any point in this diagram indicates the corresponding loading condition: it can be only one of the three previous loadings or a combination of two of them.

In order to characterize TIH, we propose two criteria. Firstly, the test has to generate the three homogeneous loading conditions, namely UT, PS and ET. Secondly, for each loading condition, i.e. UT, PS and ET, a distribution of the maximal principal stretch ratio (defined as the ratio between actual and initial lengths) has to be observed and must be sufficiently large considering the chosen constitutive equations and its field of validity. In the following, these criteria are used to choose both sample geometry and loading conditions.

2.2 *Sample geometry and loading conditions*

In the present study, a uniaxial tensile machine is used. In order to generate heterogeneity in the kinelatic fields, a change in geometry (for instance by adding notches or holes) could be considered. However, because of large deformations, the strain state obtain in an elastomer tends to be homogeneous, i.e. TU, whatever the geometry. So, numerical investigations are carried out to choose both sample geometry and biaxial loading conditions that generate a high heterogeneity level. The sample geometry and the loading conditions applied are presented in Figure 2. The sample geometry, which corresponds to a three branch sample, is 2 mm thick, 60 mm high and the branches are 20 mm in width. The bottom branch is clamped, the loading is carried out by applying prescribed displacement following the axis of the two other perpendicular branches.

A Finite Element Analysis is performed using the Ansys 10.0 package to discuss the TIH. Element type plane 182 is used to ensure the incompressibility assumption. The mesh is composed of 640 elements. For the sake of simplicity, we have chosen the Mooney strain energy density (Mooney 1940):

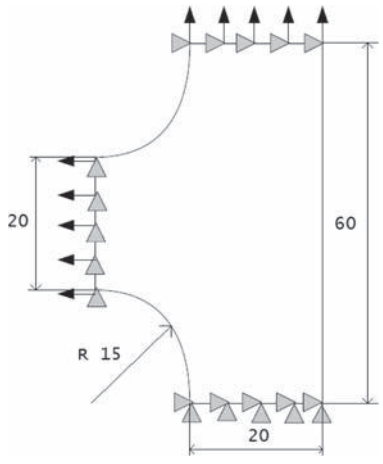

Figure 2. Sample geometry and loading conditions.

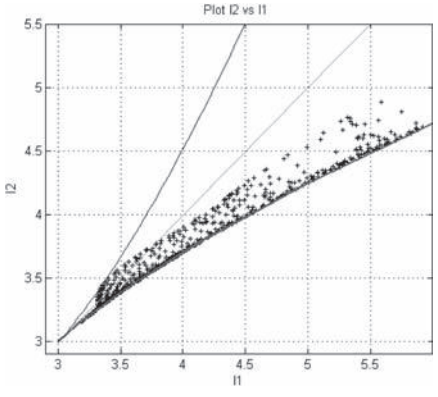

Figure 3. Loading cases in the ($I_1 - I_2$) plane.

$$W = C_1(I_1 - 3) + C_2(I_2 - 3) \tag{1}$$

where C_1 and C_2 are the material parameters. Their values are chosen equal to 0.4 MPa and 0.04 MPa, respectively, which are typical values for carbon black filled natural rubber.

Figure 3 shows that in the ($I_1 - I_2$) diagram, the three homogeneous tests are satisfactorily represented and distributed. The corresponding maximum principal elongation (see Fig. 4) of each loading case at the sample surface is deduced from Figure 3.

Global stretch ratios (defined as the ratio between actual and initial sample lengths) of 1.71 and 1.42 are prescribed following the horizontal and the vertical axes, respectively. The equivalent maximum stretch ratio is higher for UT than

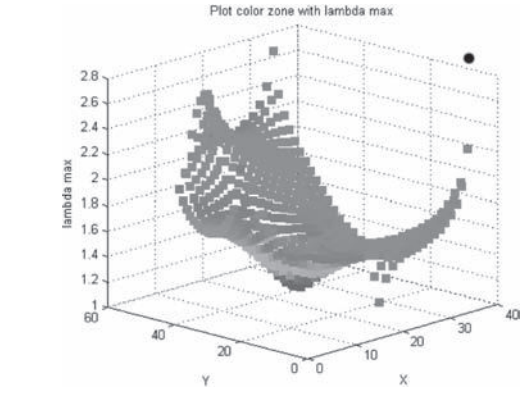

Figure 4. Numerical TIH visualization: maximum value of the principal stretch ratio.

for PS and ET. This is explained by the fact that PS and ET are obtained by the extension of the branches. From Figure 4, one can conclude that each loading case is satisfactorily represented in terms of distribution of the maximum principal stretch ratio.

3 EXPERIMENTAL SET-UP

The numerical configuration is now used to perform the test with a conventional uniaxial testing machine. To prescribe a biaxial loading condition, a new apparatus is designed. It is presented in the first part of this section. Then, the measurement of the displacement fields is precisely described.

3.1 *New apparatus*

The testing machine, referred to as MTS 858 Elastomer Test System, has a loading capacity of 15 kN. The loading cell is 1 kN capacity. A new tensile apparatus is designed to be adapted to the uniaxial tensile machine. It allows to generate ET at the sample centre. This apparatus is mounted on the left testing machine column (see Fig. 5).

Figure 6 presents a picture of the apparatus. It is composed of four parts:

- part A allows the apparatus to be fixed on one of the two columns;
- part B is a grip in which the horizontal branch of the sample is fixed;
- part C corresponds to a helical slide that ensures the horizontal branch of the sample to be stretched;
- part D is a ruler used to measure the horizontal displacement of the grip.

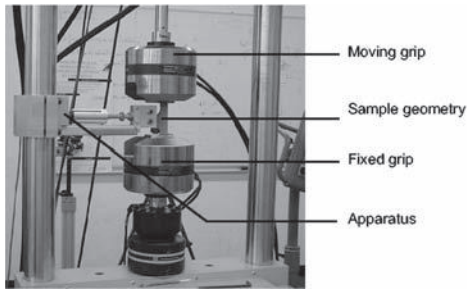

Figure 5. Experimental set-up.

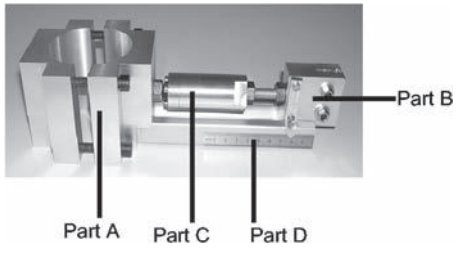

Figure 6. Proposed apparatus.

In practise, the two vertical branches of the sample are fastened on the grips of the conventional testing machine, then the branch perpendicular to the previous ones is fastened on the apparatus grip.

3.2 *Measurement of the kinematic fields*

Digital Image Correlation (DIC) technique is used to measure the displacement fields at the sample surface. For that purpose, images are shot with a cooled 12-bit dynamic CCD camera with 1376×1040 squared pixels and *CORRELI*^{LMT} software is used. The DIC technique is well-suited for measuring large strains and has already been used in the case of elastomeric materials (Chevalier et al. 2001). To determine the displacement field of a given image with respect to a reference image, one considers a set of sub-images (i.e., a square region that contains $N \times N$ pixels). This set is referred to as Zone of Interest (ZOI). A suitable correlation function is used to calculate the displacement of the centre of a given ZOI in two images captured at different stages of an experiment. In the present work, special attention is paid to the choice of the size of the ZOIs that define the region of interest (ROI). Here, the size of the ZOI is equal to 16 pixels with a shift of 16 pixels. This parameter characterises the measurement grid. To improve the image contrast, white paint is sprayed on the sample surface before testing.

4 IDENTIFICATION OF THE MATERIAL PARAMETERS

In this section, we present the method used to identify the material parameters of a given model from one heterogeneous test. It must be emphasized that no closed-form solution generally exists for such a problem, thereby meaning that no simple relation between local measurements, load, specimen geometry and unknown parameters is available. Extracting constitutive parameters in this case is a major issue which must be tackled using relevant tools. We propose here to use the so-called Virtual Fields Method (VFM) which has recently be used for characterizing elastomeric materials within the framework of large deformations (Promma et al. 2009).

The VFM relies on the Principle of Virtual Work (PVW) which can be regarded as the global equilibrium of the specimen under study or the weak form of the local equations of equilibrium (Dym and Shames 1973). In case of large deformations, assuming a plane state of stress and neglecting body forces such as weight, the PVW can be written as follows:

$$\int_{S_0} \Pi : \frac{\partial U^*}{\partial X} dS_0 + \int_{\partial S_0} (\Pi.n).U^* dl = 0 \forall U^* K.A. \quad (2)$$

where Π is the first Piola-Kirchhoff stress tensor (PK1), the X s are the Lagrangian coordinates, U^* is a kinematically admissible virtual field, S_0 is the surface of the specimen in the initial configuration the boundary of S_0 and n the unit vector perpendicular to this boundary. Considering the Mooney strain energy density, one can express the stress components as functions of the actual strain components. This leads to the following equation:

$$\begin{aligned} C_1 \int_{S_0} A : \frac{\partial U^*}{\partial X} dS_0 + C_2 \int_{S_0} B : \frac{\partial U^*}{\partial X} dS_0 \\ = \int_{\partial S_0} (\Pi.n).U^* dl = 0 \forall U^* K.A. \end{aligned} \quad (3)$$

where A and B are quantities depending on the components of the deformation gradient tensor F. This equation is linear with respect to the unknown parameters C_1 and C_2. In the integrands above, there are two types of terms: A and B on one hand, $\partial U^*/\partial X$ on the other hand. A and B are directly deduced from the full-field measurements whereas $\partial U^*/\partial X$ is derived from the virtual field U^*. At this stage, the idea consists in writing the PVW with two different virtual fields U^*. Since actual strain fields are heterogeneous, this leads to two independent equations where C_1 and C_2 are unknown. They are obtained by inverting the linear system.

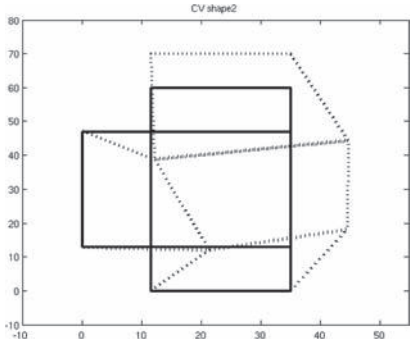

Figure 7. Example of one optimized virtual fields (dotted line) used for identifying C_1 and C_2. The maximum global stretch ratios is superimposed with the virtual mesh (solid line).

Choosing at best the two virtual fields is a key issue in the method. In the present case of large deformations and hyperelasticity, it has been decided to use the following heuristic method. A large number of virtual fields is first randomly generated. Then, the set of two virtual fields that leads to the best conditioning of the linear system (assessed with the condition number) is finally chosen for identification purposes. Those two virtual fields provide parameters less sensitive to noisy data. In the present work, virtual fields have been defined piecewise (Toussaint et al. 2006) because of the particular shape of the specimen. Four subregions are used to mesh the specimen because of its particular shape. The virtual displacement defined in each of the four sub-regions is described by polynomial shape functions multiplied by the virtual displacement of the nodes defining the corners of the sub-regions. These shape functions are similar to those employed in the finite element method. Figure 7 presents an example of optimized initial fields used for identifying C_1 and C_2 for the maximum global stretch ratios.

5 RESULTS

5.1 *Experimental kinematic fields*

The biaxial tensile test is carried out by prescribing a 25 mm displacement along both the x- and y- directions shown in Figure 2. The corresponding global stretch ratios are 1.71 and 1.42 along the x- and y-directions, respectively. In order to avoid the well-known stress accommodation (Mullins 1948; Meunier et al. 2008; Godin et al. 2009)

over the first mechanical cycles, three cycles are first carried out with the same maximum stretch ratio, thereby partially stabilizing the mechanical response of the specimen. Images are stored for every 1 mm of prescribed displacement in both directions. The material considered here is a carbon black filled natural rubber. Its composition and some of its mechanical properties are given in Table 1.

A typical view of the horizontal and vertical displacement fields obtained for the maximum prescribed global stretch ratios is shown in Figure 8.

Differentiating these fields provides the four components of the displacement gradient. They are obtained by using a centered finite differences scheme. In the present case, 740 experimental points are processed. This number is close to the number of elements used for numerical simulations and makes it easier to compare numerical and experimental TIH visualizations (see Figs. 3 and 9).

The states of strain of the three homogeneous tests (UT, PS and ET) are represented and the equivalent maximum stretch ratio is higher for UT than for PS and ET. Figure 10 presents the maximum principal stretch ratio for each ZOI.

Here, each loading case is satisfactorily represented in terms of maximum stretch ratio distribution. With regard to the previous analysis and numerical prediction, the TIH satisfies the two criteria used to define a sufficient level of TIH. Some points are encircled in Figures 9 and 10. They correspond to points taht are located at the border of the sample i.e. to zones for which there are insufficient measurement points to obtain an efficient image correlation. To summarize, these experimental results are in good agreement with the numerical prediction in terms of TIH.

Table 1. Material formulation (parts per hundred rubber) and mechanical properties.

Components	NR
Rubber	100
Zinc oxide	9.85
Oil	3
Carbon black	34
Sulfur	3
Stearic acid	3
Antioxidant	2
Accelerators	4
Density	1.13
Shore A hardness	58
Stress at break (MPa)	22.9
Elongation at failure	635

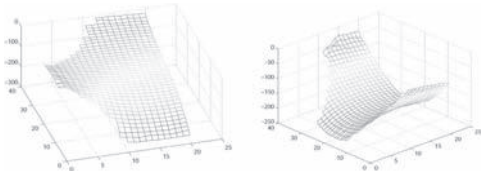

Figure 8. Displacement fields.

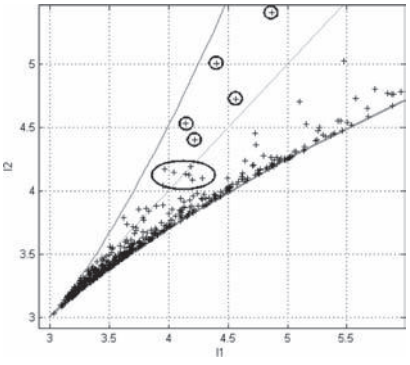

Figure 9. Loading cases in the ($I_1 - I_2$) plane.

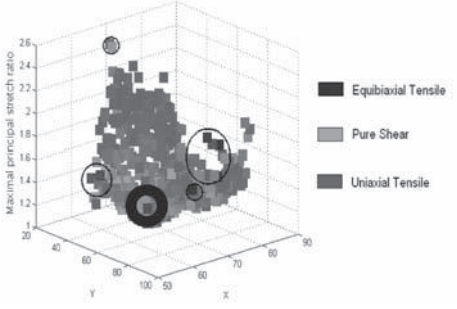

Figure 10. Experimental TIH visualization: maximum value of the principal stretch ratio.

5.2 *Identification results*

Identification results are presented in Figure 11 for each step of the loading. This step is equal to 1 mm along both the x- and y- directions. C_1 and C_2 are calculated at each loading step. The global stretch ratio reported along the horizontal axis in Figure 11 is that prescribed along the y- direction.

Apart from stretch ratios inferior to 1.05, both C_1 and C_2 remain approximately constant while the global stretch ratio increases, thereby showing that the Mooney strain energy density presently used correctly describes the actual mechanical response

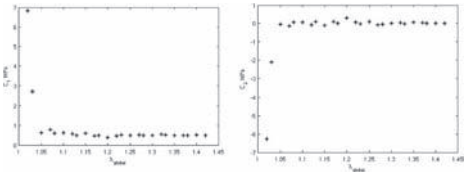

Figure 11. Identification of the material parameters C_1 and C_2.

of the specimen. The mean values of C_1 and C_2 deduced from these curves are 0.509 MPa and 0.012 MPa, respectively. These values are acceptable with regard to thermodynamic considerations (Ball 1977). It should be noted that only the loading steps corresponding to a global stretch ratio along the y- direction ranging between 1.05 and 1.42 are considered here. In fact, identifying C_1 and C_2 in the domain of low stretch ratio leads to unreliable results. This is explained by the fact that the material parameters are not sufficiently activated in this domain. It should be noted that this observation is valid whatever the law considered.

6 CONCLUSION

The aim of the present paper is to propose an alternative to the classical method of identifying constitutive parameters of rubber. For that purpose, only one heterogeneous test is performed. Sample geometry and loading conditions are chosen using numerical simulations in order to involve UT, PS and ET at the sample surface. The test-induced heterogeneity is discussed related to two criteria. To perform the heterogeneous test, a new apparatus is designed and is adapted on a conventional tensile machine. Displacement fields are measured on the specimen surface using the DIC technique.

Unknown constitutive parameters are then deduced from these fields using a suitable identification procedure: the Virtual Fields Method extended to hyperelasticity. Results obtained are in agreement with theoretical and numerical expectations, thus confirming the feasibility of the present approach. An interesting perspective would be to identify parameters governing more complicated constitutive models. For instance, it could be interesting to take into account the significant change in volume observed under extension in such a material (Le Cam and Toussaint 2008).

REFERENCES

Ball, J. (1977). Convexity conditions and existence theorems in nonlinear elasticity. *Arch. for Ration. Mech. An. 63*, 337–403.

Chevalier, L., S. Calloch, F. Hild, and Y. Marco (2001). Digital image correlation used to analyze the multiaxial behavior of rubber-like materials. *Eur. J of Mech. A-Solid 20*(2), 169–187.

Dym, C.L. and I.H. Shames (1973). *Solid Mechanics A Variational Approach.* McGraw-Hill Book Company.

Godin, N., S. Chaki, J. Courbon, S. Deschanel, S. Gillet, and B. Gautier (2009). Acoustic emission potentialities for characterization of mullins effect in natural rubber materials filled with carbon black. *Polymer Testing 28*, 103–105.

Hild, F. (2002). Correlilmt: a software for displacement field measurements by digital image correlation. Technical Report 254, LMT. Internal report.

Holzapfel, G.A. (2000). *Nonlinear Solid Mechanics. A continuum approach for engineering.* J. Wiley and Sons.

Le Cam, J.-B. and E. Toussaint (2008). Volume variation in stretched natural rubber: competition between cavitation and stress-induced crystallization. *Macromolecules 41*(20), 7579–7583.

Marckmann, G. and E. Verron (2006). Comparison of hyperelastic models for rubberlike materials. *Rubber Chem. Technol. 79*, 835–858.

Meunier, L., G. Chagnon, D. Favier, L. Orgéas, and P. Vacher (2008). Mechanical experimental characterization and numerical modelling of an unfilled silicone rubber. *Polymer Testing 27*, 765–777.

Mooney, M. (1940). A theory of large elastic deformation. *J. Appl. Phys. 11*, 582–592.

Mullins, L. (1948). Effect of stretching on the properties of rubber. *Rubber Chem. Technol.* 21, 281–300.

Promma, N., B. Raka, M. Grédiac, E. Toussaint, J.-B. Le Cam, X. Balandraud, and F. Hild (2009). Application of the virtual fields method to mechanical characterization of elastomeric materials. *Int. J. Solids Struct. 46*, 698–715.

Sasso, M., G. Palmieri, G. Chiappini, and D. Amodio (2008). Characterization of hyperelastic rubber-like materials by biaxial and uniaxial stretching tests based on optical methods. *Polymer Testing 27*, 999–1004.

Toussaint, E., M. Grédiac, and F. Pierron (2006). The virtual fields method with piecewise virtual fields. *Int. J Mech. Sci. 48*, 256–264.

Ward, I.M. and D.W. Hadley (1993). *An Introduction to the Mechanical Properties of Solid Polymers.* John Wiley and Sons Ltd.

Constitutive Models for Rubber VI – Heinrich et al. (eds)
© 2010 Taylor & Francis Group, London, ISBN 978-0-415-56327-7

Experimental characterization and parameter identification of inelastic effects in filled rubber materials

S. Hoffmann, M. André & T. Schmidt
Robert Bosch GmbH, Waiblingen, Germany

E. Haberstroh
RWTH Aachen University, Aachen, Germany

ABSTRACT: Rubber materials are used in many engineering applications mainly because of their elastic properties. Nevertheless, inelastic effects often must not be neglected during the predictive design process which is commonly supported by numerical methods. A crucial point in simulation of rubber parts is the selection of a suitable material model and the reliable determination of material parameters. This work is focussed on the experimental characterization of the quasi-static Mullins effect and residual plastic strains in filled rubber materials due to uniaxial loading. A common problem during rubber material testing is how to avoid visco-elastic contributions to the test results. Thus, a special test sequence and an appropriate evaluation scheme have been developed. This method allows the identification of purely quasi-static contributions to the material response. Afterwards, the achieved test data is used to identify the parameters for the Mullins model as introduced by Ogden and Roxburgh in 1999 in combination with an elasto-plastic approach. Finally, the quality and the limitations of this approach, as provided by the finite element software ABAQUS, are investigated.

1 INTRODUCTION

Very often hyperelastic material models for rubber are calibrated from simple uniaxial tension tests. Although very low strain rates might be used, the stress-strain data will suffer from the influence of visco-elastic effects, i.e. the data and the calibrated material model will not represent the quasi-static material behavior.

The same problem arises when the Mullins effect is investigated. A standard tension test will not allow to determine the stress softening properly, since the measured virgin stress-strain curve is never quasi-static.

In this work a new test sequence and evaluation scheme are proposed which avoid these problems. The provided quasi-static test data is then used to calibrate a material model describing the Mullins effect and plastic strains.

In Section 2 of this work the material models for hyperelasticity, plasticity and stress softening are introduced. Afterwards a special test sequence for uniaxial tension tests and an evaluation scheme, which eliminate visco-elastic effects and deliver a pure quasi-static response, are presented (Section 3). Third, the calibration of the three material models based on the evaluated test data is explained (Section 4).

Finally, in Section 5 the quality and the limitations of the presented approach, consisting of the test sequence, the evaluation scheme and the calibration process, are investigated.

2 CONSTITUTIVE MODELS

The non-linear elastic behavior of Elastomers is usually modeled by hyperelastic constitutive models. These are defined through a strain energy function

$$W = W(\lambda_1, \lambda_2, \lambda_3) \tag{1}$$

where λ_i, with $i = 1, 2, 3$, denote the principal stretches (Holzapfel 2008).

Most experimental tests are based on a uniaxial stress state with stretch

$$\lambda = \frac{l}{l_0} = 1 + \varepsilon, \tag{2}$$

where l and l_0 denote the specimen lengths in the deformed and undeformed state, respectively. Since rubber material can be assumed to be

incompressible ($\lambda_1 \cdot \lambda_2 \cdot \lambda_3 = 1$), in this case the deformation can be simplified to

$$\lambda_1 = \lambda \tag{3}$$

and

$$\lambda_2 = \lambda_3 = \frac{1}{\sqrt{\lambda}}. \tag{4}$$

The nominal principal stresses $\hat{S}_i$ are derived from the strain energy function by

$$\hat{S}_i = \frac{\partial W}{\partial \lambda_i} = \sum_{j=1}^{3} \frac{\partial W}{\partial I_j} \frac{\partial I_j}{\partial \lambda_i}, \; i = 1, 2, 3, \tag{5}$$

where $I_j, j = 1, 2, 3$ represent the three strain invariants. If a uniaxial stress state is applied, these are

$$I_1 = \lambda^2 + \frac{2}{\lambda}, \tag{6}$$

$$I_2 = \frac{1}{\lambda^2} + 2\lambda \tag{7}$$

and

$$I_3 = 1. \tag{8}$$

While the nominal stresses are related to the undeformed state, the Cauchy stresses (also called true stresses) are related to the deformed state of the material. In the uniaxial stress state the conversion is done by

$$\sigma = \lambda \cdot S. \tag{9}$$

2.1 *Hyperelasticity—Kilian model*

The model proposed by Kilian (1981) is based on an analogues behavior of polymer chains and ideal gas. In contrast to models like Neo-Hooke and Mooney-Rivlin it is able to represent the entire hyperelastic stress-strain curve, even the stiffening in the range of large strains, quite well.

Considering volumetric incompressibility and neglecting the dependency of the second strain invariant the strain energy function of the Kilian-Model can be reduced to

$$W = \mu \left[-(\lambda_m^2 - 3) \left[\ln(1 - \xi) + \xi \right] - \frac{2}{3} \alpha \left(\frac{I_1 - 3}{2} \right)^{\frac{3}{2}} \right] \tag{10}$$

with

$$\xi = \sqrt{\frac{I_1 - 3}{\lambda_m^2 - 3}}, \tag{11}$$

where the parameter μ determines the shear modulus in the origin of the stress-strain curve, α denotes the gradient in the inflection point and λ_m the locking stretch.

From Equation (10) the Cauchy stress in the uniaxial stress state is

$$\sigma(\lambda) = \mu \left(\frac{1}{1 - \xi} - \alpha \left(\frac{I_1 - 3}{2} \right)^{\frac{1}{2}} \right) (\lambda^2 - \lambda^{-1}). \tag{12}$$

2.2 *Plasticity—isotropic hardening*

In this work plastic material behavior is considered by the von-Mises plasticity model with isotropic hardening (Simo & Hughes 1989).

The initial yield stress σ_F marks the beginning of plastic deformation. Stresses which exceed the yield stress lead to the evolution of plastic strains, while loadings below the yield stress result in pure elastic deformation.

The isotropic hardening approach causes the yield stress to increase with rising plastic deformation.

Stress computation is based on the elastic part of stresses only, while the plastic strains do not contribute to the stresses. Hence, the total strain needs to be split into an elastic and a plastic part. In this work we use logarithmic strains according to

$$\varepsilon^{\ln} = \varepsilon_{el}^{\ln} + \varepsilon_{pl}^{\ln} \tag{13}$$

with

$$\varepsilon^{\ln} = \ln(\lambda) \tag{14}$$

in order to be in agreement with the approaches used in the finite element software ABAQUS (Dassault Systèmes 2008).

2.3 *Mullins effect—pseudoelasticity*

Here we use the phenomenological model of pseudoelasticity proposed by Ogden and Roxburgh (1999) in order to describe the Mullins effect. This model represents the idealized, quasi-static Mullins effect (Fig. 2) and, thus, neglects any viscous effects.

The Mullins effect describes a stress-softening of filled rubber materials, which is induced by the maximum strain in total strain history (Mullins

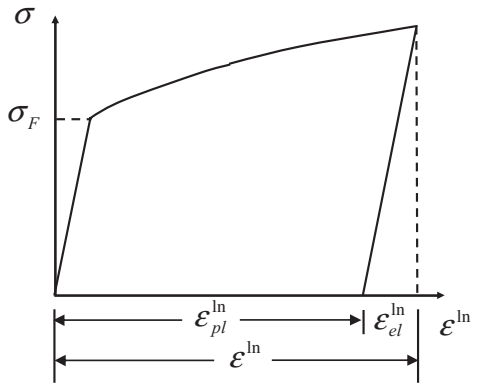

Figure 1. Plastic deformation with isotropic hardening.

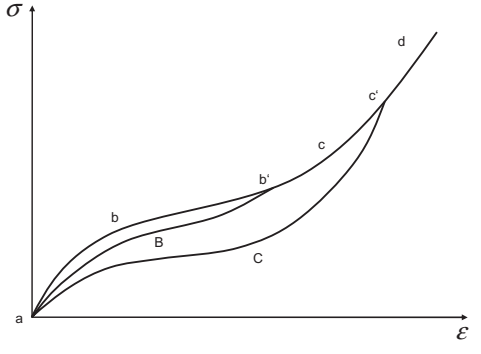

Figure 2. Idealized Mullins effect proposed by Ogden and Roxburgh (1999).

1959). If a deformation exceeds the former maximum strain, the stress response will first follow the virgin curve (b-c-d), but during unloading the softening effect will be visible (curve B or C). According to this model, the amount of softening depends only on the maximum strain that has ever been achieved in history. Consequently, further load cycles that do not exceed this strain maximum (b′ or c′) will be observed as purely elastic, following the softened curves B or C, respectively.

The modified strain energy function W_{Mul} according to Ogden and Roxburgh is defined as

$$W_{Mul}(\lambda_i, \eta) = \eta \cdot W(\lambda_i) + \phi(\eta) \tag{15}$$

where η is the damage variable, $\phi(\eta)$ the damage function and W represents the virgin material's strain energy function.

The evolution approach of the damage variable η uses the Gaussian error function

$$erf(x) = \frac{2}{\sqrt{\pi}} \int_0^x e^{-t^2} \mathrm{d}t. \tag{16}$$

Within the finite element software ABAQUS it is implemented as

$$\eta = 1 - \frac{1}{r} \cdot erf\left(\frac{W^{\max} - W}{m + \beta \cdot W^{\max}} \right), \tag{17}$$

where $W^{\max}$ is the maximum strain energy that has ever been achieved and r, m, β are material dependent parameters (Govindarajan et al. 2008).

During first time loading the strain energy W is equal to $W^{\max}$ and so the damage variable becomes $\eta = 1$. This is also true for further loads that exceed $W^{\max}$. During unloading or for loads smaller than $W^{\max}$ the value of the damage variable is smaller than 1 and the stress response is softened according to Equation (15).

Considering stress softening, the uniaxial true stress σ is calculated by

$$\sigma(\lambda, \eta) = \eta \cdot \lambda \cdot S(\lambda). \tag{18}$$

3 EXPERIMENTAL SETUP AND EVALUATION SCHEME

The goal of the presented test sequence is the elimination of visco-elastic effects from the quasi-static response. Uniaxial tension tests are used for this purpose.

A full separation can only be achieved by an infinitely low strain rate. Thus, the quasi-static response is often approximated by a reduction of the strain rate. However, this yields increased test durations and often still delivers bad results.

The test sequence proposed in this work avoids these problems by a determination of the quasi-static response through an averaging approach. The test sequence basically consists of a loading and an unloading cycle. Each half cycle is interrupted by some relaxation phases which are carried out at certain strains $\varepsilon_{r,j}$ where j denotes the number of the sampling point. This yields partially relaxed stress values $\sigma_{load,j}$ and $\sigma_{unload,j}$ which correspond to the strains $\varepsilon_{r,j}$, where a relaxation process is carried out (Figure 3).

The assumed quasi-static stress response $\sigma_{s,j}$ at the applied strains $\varepsilon_{r,j}$ is defined by the average of these two stress values

$$\sigma_{s,j} = \frac{1}{2}(\sigma_{load,j} + \sigma_{unload,j}). \tag{19}$$

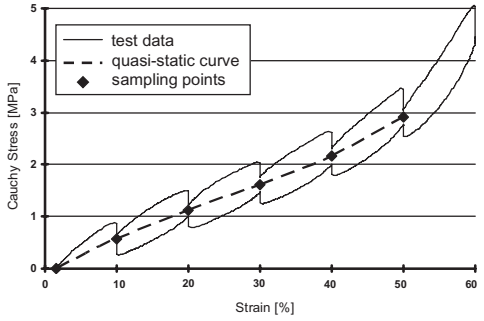

Figure 3. Relaxation test: Stress-strain response of the softened material (EPDM, 78 Shore A) with $\varepsilon_{max} = 60\%$.

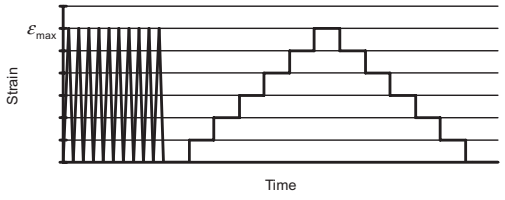

Figure 4. Single *Mullins test* sequence with $\varepsilon_{max} = 60\%$.

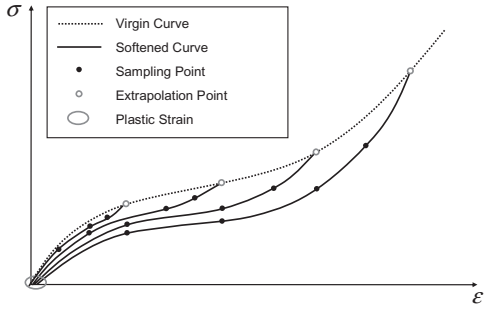

Figure 5. Quasi-static Mullins effect.

This finally yields several sampling points ($\varepsilon_{r,j}$, $\sigma_{s,j}$) of the quasi-static stress-strain-curve that can be used for parameter identification.

A consequence of this approach is that at maximum strain ε_{max} the quasi-static stress cannot be determined properly, because there is only one stress value $\sigma_{load,max}$ from the loading half cycle available. Therefore, we use an extrapolation of the sampling points at lower strains to determine the quasi-static response at the maximum strain ε_{max}. The Kilian model is used for this purpose. It is mentionable that this stress value at maximum strain ε_{max} corresponds to the stress in the virgin material state σ_v, since $W = W^{\max}$.

In Figure 4 the strain applied to the rubber sample during the test sequence is illustrated. This sequence provides the required data to determine the sampling points ($\varepsilon_{r,j}$, $\sigma_{s,j}$) of a quasi-static stress-strain curve valid for a certain maximum strain ε_{max}. It is divided into three sub-sequences. First, ten preconditioning cycles are applied in order to achieve the stress softening and plastic deformation corresponding to the maximum strain ε_{max}. Then a relaxation phase is carried out, that allows to determine the plastic strain ε_{pl}. Finally, the quasi-static stress response $\sigma_{s,j}$ of the softened material is determined by the relaxation test described above.

Adopting this approach for analyzing the stress softening, several of these test sequences with increasing maximum strain are successively carried out at the same rubber specimen. The whole procedure is referred to as *Mullins test* (Hoffmann 2008) in this paper.

Figure 5 summarizes the results of the *Mullins test*. It also shows the extrapolation of each quasi-static stress curve to the stress value in the virgin material state σ_v^i, where i denotes the number of the test sequence with the maximum applied strain ε_{max}^i.

4 PARAMETER IDENTIFICATION

In order to represent the quasi-static material behavior that is shown in Figure 5, three constitutive approaches are combined in this work: the Kilian-Model for hyperelasticity, the model of isotropic hardening for plasticity and the model of pseudoelasticity for stress softening. These constitutive models are supported by the finite element software ABAQUS through the commands: *HYPERELASTIC, *PLASTIC and *MULLINS EFFECT (Dassault Systèmes 2008).

The plastic flow criterion is simply defined in tabular form by the yield stress σ_v^i and a corresponding plastic strain ε_{pl}^i. This data is extracted from the test data, where the plastic strain ε_{pl}^i is measured after sub-sequence 2 of the test sequence, and the extrapolated virgin stress σ_v^i is taken as the corresponding yield stress. The parameters defining the hyperelastic Kilian model are determined by approaching the sampling points of the virgin curve σ_v^i through this model. Finally the parameters of the model of pseudoelasticity are determined from the sampling points of the quasi-static response $\sigma_{s,j}^i$.

5 RESULTS

5.1 *Examples*

The capability of this approach is shown by a comparison of evaluated experimental data and

simulation results. The comparison is conducted for two different materials and two temperatures.

The experimental data is provided by the evaluated Mullins test as described in Section 3. For the quasi-static finite element analysis a cube model with only one element is used. The applied boundary conditions represent the uniaxial tension test state.

Figures 6–8 show a comparison of the simulation results and the experimental data. It is obvious, that the material models represent the stress response qualitatively correct. Nevertheless, a deviation can be observed in the range of small strains, what will be discussed in detail in the next sub-section.

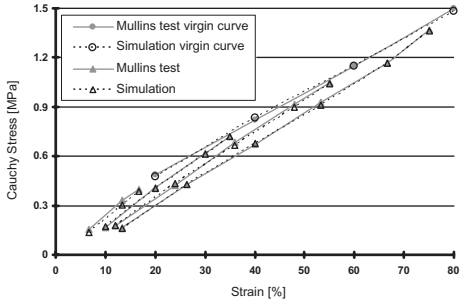

Figure 6. *Mullins test* results and simulation results for HNBR (50 Shore A) at 23°C and 80% maximum strain.

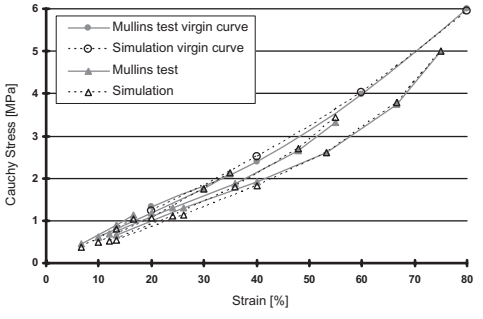

Figure 7. *Mullins test* results and simulation results for EPDM (78 Shore A) at 23°C and 80% maximum strain.

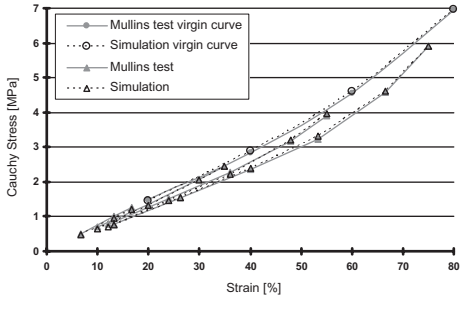

Figure 8. *Mullins test* results and simulation results for EPDM (78 Shore A) at 100°C and 80% maximum strain.

5.2 *Limitations of the model of pseudoelasticity*

The limitations of the model proposed by Ogden and Roxburgh (1999) have been subject of other publications before, see e.g. Kazakeviciute-Makovska (2007). The main limitation is that the damage approach according to Equation (17) is not able to model the measured evolution of the stress softening. In this work this is clarified by a comparison of the measured relative damage values

$$a^i_{rel,j} = \frac{\sigma^i_v - \sigma^i_{s,j}}{\sigma^i_v} \tag{20}$$

with the values computed from the model of pseudoelasticity.

The measured relative damage (Fig. 9) shows a maximum that is increasing with rising maximum strain ε^i_{max}. Within Ogden's model of pseudoelasticity, the reduced stress is computed from the virgin stress by

$$\tilde{\sigma}^i_{s,j} = \eta^i_j \cdot \tilde{\sigma}^i_v. \tag{21}$$

Here, the symbol '~' denotes values that are computed from the investigated material model. Hence, the relative damage $\tilde{a}^i_{rel,j}$ predicted by the model of pseudoelasticity becomes

$$\tilde{a}^i_{rel,j} = \frac{\tilde{\sigma}^i_v - \eta^i_j \cdot \tilde{\sigma}^i_v}{\tilde{\sigma}^i_v} = 1 - \eta^i_j$$

$$= \frac{1}{r} \cdot erf\left(\frac{\tilde{W}^{\max}_j - \tilde{W}^i_j}{m + \beta \cdot \tilde{W}^{\max}_j} \right). \tag{22}$$

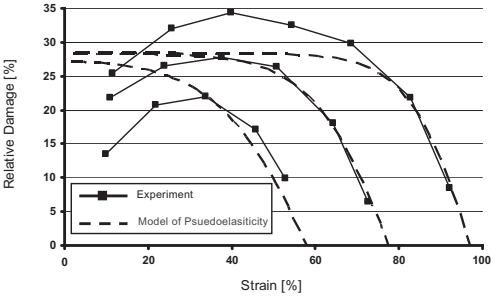

Figure 9. Relative damage progression of EPDM (78 Shore A) softened curves at 23°C and different maximum strains (60%, 80% and 100%).

The computed damage (Fig. 9) does not show a maximum. Thus, the model of pseudoelasticity is not able to represent the stress softening for small strains within a softened curve qualitatively correct.

Nevertheless, at large strains the model yields very good results.

6 CONCLUSIONS

A new test sequence and evaluation scheme for the identification of the Mullins effect was presented, that allow to determine a purely quasi-static response from uniaxial test data. Instead of sufficiently low strain rates, relaxation phases at specific strains and an averaging approach were used in order to determine the quasi-static response. Furthermore, the virgin material behavior was approximated by an extrapolation approach.

The quasi-static Mullins effect, determined by the new test sequence, was represented by using the Kilian model for hyperelasticity, an isotropic hardening approach for plastic effects and Ogden's model of pseudoelasticity for stress softening. Based on these material models numerical simulations were carried out. The comparison of test data and numerical results showed that the quasi-static Mullins effect is described qualitatively correct for different materials and temperatures. Nevertheless, there were some mentionable deviations in the damage evolution at small strains.

Besides the characterization of the Mullins effect the approach represented an effective way of considering quasi-static inelastic effects in numerical simulations of filled rubber materials.

REFERENCES

Dassault Systèmes Simulia Corp. 2008. ABAQUS Version 6.8 Documentation. Providence, Rhode Island, USA.

Govindarajan, S.M.; Hurtado, J.A. & Mars, W.V. 2007. Simulation of Mullins Effect and Permanent Set in Filled Elastomers Using Multiplicative Decomposition. *5th European Conference on Constitutive Models for Rubber, Paris, 4–7 September 2007*.

Hoffmann, S. 2008. Modellierung des Mullins-Effekts von Elastomeren mit der FEM-Software ABAQUS. *Diploma Thesis, RWTH Aachen University, Aachen*.

Holzapfel, G.A. 2000. *Nonlinear Solid Mechanics*. Weinheim: WILEY-VCH Verlag.

Kazakeviciute-Makovska, R. 2007. Experimentally Determined Properties of Functions in Pseudo-Elasticsoftening Models of the Mullins Effect. *International Journal of Solids and Structures* 44(11–12): 4145–4157.

Kilian, H.G. 1981. Equation of state of real networks. *Polymer* 22: 209–217.

Mullins, L. 1959. Effect of Stretching on the Properties of Rubber. *Journal of Rubber Research* 16(12): 275–289.

Mullins, L. 1969. Softening of Rubber by Deformation. Rubber. *Chemistry and Technology* 42(1): 339–362.

Ogden, R.W. & Roxburgh, D.G. 1999. A pseudo-elastic Model for the Mullins Effect in Filled Rubber. *Proceedings of the Royal Society of London*. 455: 2861–2877.

Saccomandi, G. & Ogden, R.W. 2004. *Mechanics and Thermomechanics of Rubberlike Solids*. Wien: Springer.

Simo, J.C. & Hughes, T.J.R. 1989. *Computational Inelasticity*. Springer.

Constitutive Models for Rubber VI – Heinrich et al. (eds)
© 2010 Taylor & Francis Group, London, ISBN 978-0-415-56327-7

Flocculation kinetics in the light of jamming physics: New insights into the Payne-effect in filled rubbers

Sven Richter, Marina Saphiannikova & Gert Heinrich
Leibniz-Institut für Polymerforschung Dresden e. V., Dresden, Germany

ABSTRACT: After an introduction into the general characteristics of the jamming behavior, two filler flocculation experiments on a silica-filled ethylene propylene diene monomer elastomer and on a polycarbonate melt filled with multi-walled carbon nanotubes are presented. We propose that these experiments can be regarded as jamming phenomena. The experimental data are successfully modeled using the stress superposition approach.

1 INTRODUCTION

Jamming processes, which exhibit non-equilibrium transitions from a fluid-like to a solid-like state, are characterized solely by the sudden arrest of the particle dynamics (Liu and Nagel 1998; Trappe et al. 2001; Robertson and Wang 2005; Biroli 2007). This arrest may happen either due to the crowding of non-interacting particles at high loadings or due to the presence of strong attractive (repulsive) interactions between the particles at low loadings. Jamming processes can occur in a variety of systems of diverse characteristic length scales, e.g. molecular structures, colloidal suspensions, polymer-filler composites, granular materials, and even automobile traffic (Liu and Nagel 1998).

Jamming and glass-formation processes appear to have interrelated physics. The idea of jamming is that perhaps all of these amorphous solids are solid-like for the same reason: a universal jammed state, and by understanding it, we understand all of these materials simultaneously. Moreover, in each case, there are control parameters that allow the system to be changed from jammed to unjammed (fluidized) state, e.g. by applying an external stress (or external strain) that exceeds a critical yield stress (a critical strain).

Recently, for filled rubbers it has been found that the spectral density of fluctuations of the storage modulus around the mean value exhibits a power law behaviour with an exponent of two, similar to the exponent reported in jamming process (Wang & Rackaitis 2006).

To gain insight into the physics of the jamming process in filled polymer systems, we have undertaken a relatively simple nonlinear viscoelastic investigation, herein after referred to as the "flocculation" experiment. In this experiment the structural changes in the filler phase are followed by measuring the time evolution of storage modulus after application different strain amplitudes to the sample, below and above the critical strain. We already reported on the flocculation experiment in our previous paper (Costa et al. 2008) about low density polyethylene nanocomposites filled with layered double hydroxide particles. Here, we make a step further and try to reproduce the measured data theoretically, with the help of a superposition approach in which the contributions from the polymer matrix and the filler phase are accounted for separately.

Here we show, that the filler agglomerates in a polymer melt and in an elastomer matrix can be ruptured under application of the nonlinear shearing and re-agglomerate again in the quiescent state, when the shearing is stopped.

2 RESULTS AND DISCUSSION

It is well known that mechanical reinforcement in filled polymer systems can be achieved without a network between the filler particles (Einstein's or Smallwood's formula, (Smallwood 1944; Larson 1999) mechanical mixing laws (Torquato 2001)). At the same time attractive interactions between the filler particles as well as depletion interactions with the polymer matrix lead to the appearance of filler-enriched spatial regions (fractal agglomerates) which can come to a contact and form a micron-scale filler network. These large-scale soft agglomerates may be ineffective in the reinforcement of hard materials, since the modulus of a fractal cluster falls below that of the matrix for large cluster sizes (Witten et al. 1993). Contrary, a dramatic mechanical reinforcement due to the presence of large-scale agglomerates can be achieved in soft materials, that is in elastomers and polymer melts, already at low filler loadings (Schaefer and Justice 2007).

If the polymer matrix is filled with attractively interacting nanoparticles, its mechanical behaviour can be described in the framework of superposition approach. In this approach the total stress tensor, $\boldsymbol{\sigma}$, is represented by a sum of two stresses

$$\boldsymbol{\sigma} = X\boldsymbol{\sigma}_m + \boldsymbol{\sigma}_f^{net} \tag{1}$$

where $\boldsymbol{\sigma}_m$ is the viscoelastic stress arising in the matrix due to stretching and orientation of polymer strands. To describe the polymer stress in this equation, one can probe any of appropriate constitutive models proposed for the elastomer matrix (polymer melt). The second component on the right site of equation (1), $\boldsymbol{\sigma}_f^{net}$, arises due to attractive interactions between the particles and will be described later.

Hydrodynamic reinforcement of the polymer matrix is taken into account by multiplying $\boldsymbol{\sigma}_m$ by the hydrodynamic amplification factor, X. In the case of hard spherical particles such as carbon black and silica, X can be estimated using the Batchelor formula (Larson 1999)

$$X = 1 + 2.5\phi + 6.2\phi^2, \tag{2}$$

where ϕ is the volume fraction of the filler particles. Equation (2) reduces to $X = 1 + 2.5\phi$, i.e. the Einstein's (Smallwood's (Smallwood 1944)) formula in the limit of small loadings. In the case of highly elongated particles, X is given by (Thomasset et al. 2005)

$$X = 1 + 2\phi\left(1 + \frac{A}{15}\right), \tag{3}$$

where A is the stress-shape coefficient

$$A = \frac{r^2}{2\ln r}, \qquad r >> 1 \tag{4}$$

which depends only on the particle aspect ratio $r = L/d$ (L is the particle length and d is its diameter). Equation (3) can be also used in the case of semi-flexible particles such as carbon nanotubes, only one should take the persistence length instead of the particle length for estimation of the aspect ratio. Thus, we consider only hydrodynamic interactions between filler particles and the polymer matrix and neglect possible attractive interactions between them.

2.1 *Filled elastomer*

Let us probe the superposition approach on a silica-filled ethylene propylene diene monomer (EPDM) elastomer. Figure 1 presents the results of flocculation experiment at $f = 1.67$ *Hz* for the EPDM matrix filled with 40 phr Aerosil particles. The sample was pre-treated at the strain amplitude

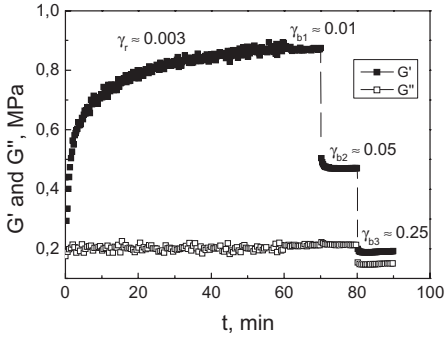

Figure 1. Flocculation kinetics (jamming experiment) of the silica particles in the EPDM elastomer.

$\gamma_0 \approx 0.25$ to cause a considerable damage of the filler clusters. At the first stage of the flocculation experiment the silica-EPDM elastomer is subjected to the oscillatory shearing with a strain amplitude $\gamma_r \approx 0.003$. It is chosen to be so low that the sample at this stage can be considered to be in the quasi-quiescent state. The slight oscillatory perturbation is only necessary to detect the changes in G' and G'' with time. Thus, at the first stage one is able to follow in-situ re-agglomeration of the silica clusters destroyed previously in the process of pre-treatment. When the stationary state is nearly attained after 60 minutes, the sample is subjected to shearing with slightly higher strain amplitude $\gamma_{b1} \approx 0.01$. At this strain amplitude the storage modulus of the filled sample stays nearly unchanged. However, if the silica-EPDM elastomer is subjected to considerably stronger shearing, first at $\gamma_{b2} \approx 0.05$ and then at $\gamma_{b3} \approx 0.25$, the storage modulus falls in both cases abruptly reaching at the end of flocculation experiment the reinforced matrix value. Interestingly, the loss modulus of the silica-EPDM elastomer stays nearly unchanged up to $\gamma = 0.25$: $G'' \approx 0.21$ *MPa*.

The similar flocculation experiment (not shown here) reveals that the storage and loss moduli of the unfilled EPDM elastomer can be considered to be constant till $\gamma = 1.0$: $G'_m = 0.07$ *MPa* and $G''_m = 0.06$ *MPa*. Thus, we can re-write the superposition equation (1) for the case of oscillatory shearing at different strain amplitudes as follows

$$G'(t) = XG'_m + G'_f(t), \tag{5a}$$

$$G'' = XG''_m + G''_f(t). \tag{5b}$$

Further, to simplify our analysis, let us neglect viscose effects in the filler network, i.e. assume that $G''_f = 0$. This gives a value of $X \approx 3.5$ which corresponds to the volume fraction of about 45% (it is overestimated compared to 20% at the 40 phr

Aerosil loading). Time evolution of the pure elastic filler network can be described using the modified Hooke's model

$$\sigma_f^{Net} = G_f(1-\xi_b)\gamma, \tag{6}$$

where G_f is the effective elastic modulus of the filler network and $0 \le \xi_b \le 1$ is a structural parameter that reflects the state of the particle network at particular shear conditions (Leonov 1990).

In the absence of shear, time evolution of the structural parameter is usually described by a single kinetic equation

$$\frac{d}{dt}\xi_b = -\lambda_0^{-1}\xi_b^n \tag{7}$$

with the relaxation time λ_0. The value of exponent n defines what kind of cluster growth is expected during the recovery process: for example, $n = 1$ corresponds to the first-order kinetics and $n = 2$ to the second-order kinetics. However, we found out that it is impossible to reproduce the recovery branch of the flocculation experiment, $\gamma_r = 0.003$, using a single kinetic equation (7) with a constant value of the kinetic exponent, i.e. using a pure rate law. So, only the middle part of the recovery branch can be described using the second-order kinetics law (Richter et al.).

Initially, the growth of clusters is very fast obeying the kinetic law with $2 \le n \le 3$, whereas it slows down considerably at the final stage of recovery process when n takes the values around 1. Such complex behavior can be interpreted assuming different kinds of the agglomeration process: first, in the very beginning, when a lot of single particles are provided, the multi-particle agglomeration, which gradually changes to the cluster-cluster agglomeration at the middle flocculation stages, followed by addition of the rest of particles to a well-formed network at the late stages (see Figure 2).

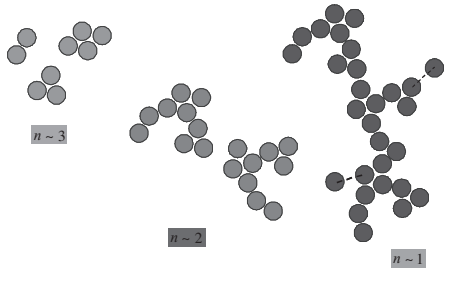

Figure 2. Schematic representation of filler agglomeration: multi-particle aggregation (left) into clusters with $2 \le n \le 3$; cluster-cluster aggregation into the filler network with $n \sim 2$ (middle); addition of single particles to a well-formed network $n \sim 1$ (right).

Interestingly, this complex behavior can be very well described (see the recovery branch in Fig. 3) using the superposition of three kinetic equations of the first order with the same weight, i.e.

$$\xi_b(t) = \frac{1}{l}\sum_{i=1}^{l} e^{-t/\lambda_i}, \quad l = 3 \tag{8}$$

The recovery times λ_i are found to be equal to 60, 310 and 2160 sec.

In the presence of shear, time evolution of the structural parameter is usually described by another kinetic equation

$$\frac{d}{dt}\xi_b = a\dot{\gamma}_{eff}^m(1-\xi_b) - \lambda_0^{-1}\xi_b \tag{9}$$

where a is the rupture parameter and $\dot{\gamma}_{eff} = (2/\pi)\gamma_0\omega$ is the effective shear rate. The value of exponent m depends on whether the breakage of structure is caused by the elastic strain accumulated in the filler structure, $m = 1$, or by the dissipated energy, $m = 2$ (Yziquel et al. 1999). As the recovery branch has been fitted with three exponents, one may assume that it is necessary to follow the same approach for description of shear-induced breakage. However, we found out that it is not the case: two longest recovery processes play no role in the presence of oscillatory shear. Only the fastest recovery process with $\lambda_1 = 60\ s$ manifests itself in the all three breakage steps. Hence, one should take λ_0 in equation (9) equal to the shortest recovery time, $\lambda_0 = \lambda_1$. Further, equation (9) with $m = 1$ overpredicts the breakage of filler structure at the small strain amplitude $\gamma_{b1} = 0.01$ and underpredicts it at the high strain amplitude $\gamma_{b3} = 0.25$ (not shown here). However, the use of $m = 2$ provides an excellent fit of all breakage steps (Figure 3, $a = 0.2\ s$). This shows that the process of structure damage is governed not by the accumulated strain but rather by the energy dissipated during this process.

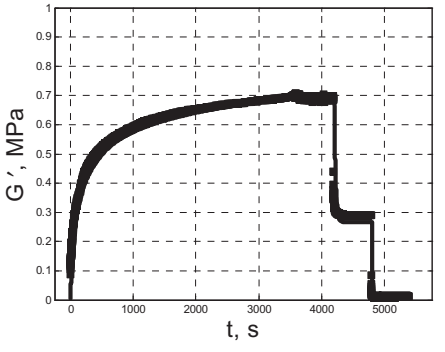

Figure 3. Time evolution of storage modulus in the flocculation experiment on the silica-filled EPDM elastomer: experiment (squares), fit (dashed line).

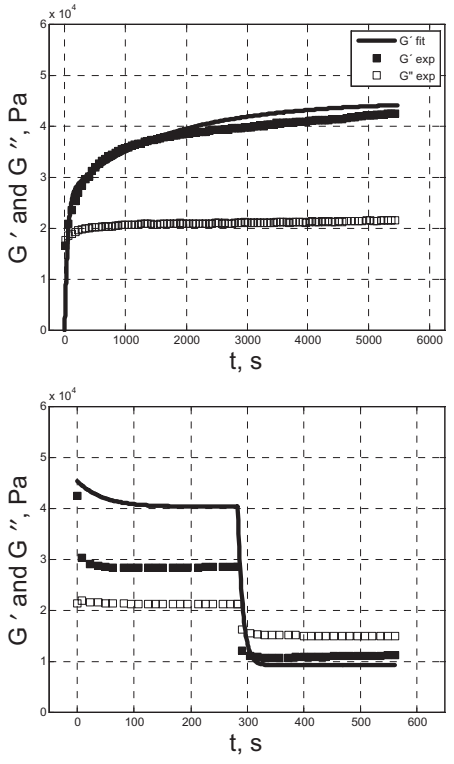

Figure 4. Flocculation kinetics (jamming experiment) of the CNT particles in the PC melt. Recovery branch (above), breakage branch (below).

2.2 *Filled polymer melt*

Let us now probe the superposition approach on a polycarbonate (PC) melt filled with multi-walled carbon nanotubes (CNTs). Figure 4 presents the results of flocculation experiment at $\omega = 1$ *rad/s* for the PC matrix filled with 5 wt% CNTs. These composites were produced by injection molding which causes a considerable damage of the CNT clusters because of very high shear rates. At the first state of the flocculation experiment the CNT-PC melt is subjected to the oscillatory shearing with a very low strain amplitude $\gamma_t = 0.005$ (Figure 4 above).

Thus, the sample is in the quasi-quiescent state stage, and one is able to follow in-situ the re-agglomeration of the CNT clusters destroyed previously in the process of injection molding. The reagglomeration (recovery) process is found to be extremely slow without a sign of saturation even after two hours. It can be seen that both moduli considerably increase with time: G' approximately three times and G'' approximately 25% compared to their initial values.

After application of the oscillatory shearing with $\gamma_{b1} = 0.05$, the storage modulus drops immediately staying however higher than its initial value measured in the beginning of flocculation experiment (Figure 4 below). The loss modulus stays nearly unchanged. The next shearing step with $\gamma_{b2} = 0.25$ leads to a drop in both moduli. One observes a solid-liquid transition as at this breakage step the loss modulus attains a higher value than the storage modulus.

The similar flocculation experiment (not shown here) reveals that the storage and loss moduli of the unfilled PC melt can be considered to be nearly constant (compared to the moduli of filled PC melt): $G'_m = 0.2\,kPa$ and $G''_m = 3.5\,kPa$. Thus, we can use the same superposition equations (5) for description of oscillatory shearing of CNT-PC melt at different strain amplitudes. The main difference with the filled elastomer is that one cannot neglect viscose effects in the filler network in the case of polymer melt. Therefore, the stress experienced by the filler structure will be described by a modified viscoelastic Maxwell model

$$(\boldsymbol{\sigma}_f^{Net})_{(1)} + \tau^{-1}(\xi_b)\boldsymbol{\sigma}_f^{Net} = G_f\dot{\gamma}, \tag{10}$$

where $\dot{\gamma}$ is the rate-of-strain tensor and $(\boldsymbol{\sigma}_f^{Net})_{(1)}$ denotes the upper-convected time derivative of a tensor $\boldsymbol{\sigma}_f^{Net}$ (Bird et al. 1987). Equation (10) implies a process-dependent relaxation time, $\tau(\xi_b)$, which is an intrinsic feature of the thixotropic systems (Barnes 1997; Dullaert and Mewis 2006)

$$\tau(\xi_b) = \frac{\tau_f}{m(\xi_b)}. \tag{11}$$

Here τ_f is the characteristic time of filler structure and

$$m(\xi_b) = \alpha + \frac{(1-\xi_b)^{-d} - 1}{d}, \tag{12}$$

is the phenomenological mobility function. The latter is constructed in such a way that it describes the transition to the solid-like behavior in the limit of vanishing shear rates and the shear-thinning behaviour with the exponent $d > 0$ at high shear rates. Additionally, the residual parameter $\alpha < 1$ describes a non-vanishing G''_f at small frequencies. Time evolution of the structural parameter ξ_b will be again described by equations (8) and (9).

To extract a set of six parameters, $\{a, \lambda_0, G_f, \tau_f, \alpha, d\}$, we measured first the strain sweep for the CNT-PC melt at $\omega = 1$ *rad/s*. The dynamic oscillatory shearing at this frequency shows that at low strain amplitudes both storage and loss moduli of the CNT-PC composite remain constant and independent of the applied strain (Figure 5 above), whereas above a critical strain $\gamma_{cr} \sim 0.01$ both moduli

decrease with increasing strain. As G' decreases faster than G'', it is possible to observe the solid-liquid transition, i.e. considerable damage of the filler structure, around the strain amplitude of 0.1. At this amplitude the structural parameter ξ_b increases to about 0.5 (Figure 5 below). Using the values of storage and loss moduli at the lowest strain amplitude, it is possible to extract the values of two parameters: $X = 1.5$ and $G_f = 57.1\ kPa$. To extract the rest of parameter set, we performed the shear growth experiments for the unfilled and filled polycarbonate at shear rates up to $1s^{-1}$ (not shown here). The polycarbonate melt does not exhibit the shear-thinning behaviour at these shear rates having the zero-shear viscosity $\eta_0 = 8000\ Pa \cdot s$.

The stationary viscosity, η_{st}, for the the PC matrix filled with 5 wt% CNTs is presented in Figure 6 (circles). One can observe a strong shear-thinning behavior which can be fitted (dashed line) using the stationary solutions of equations (1) and (10) for the case of constant shearing

$$\eta_{st} = X\eta_0 + \frac{G_f \tau_f}{\alpha + \dfrac{(1+a\lambda_0\dot{\gamma}_0^2)^d - 1}{d}} \tag{13}$$

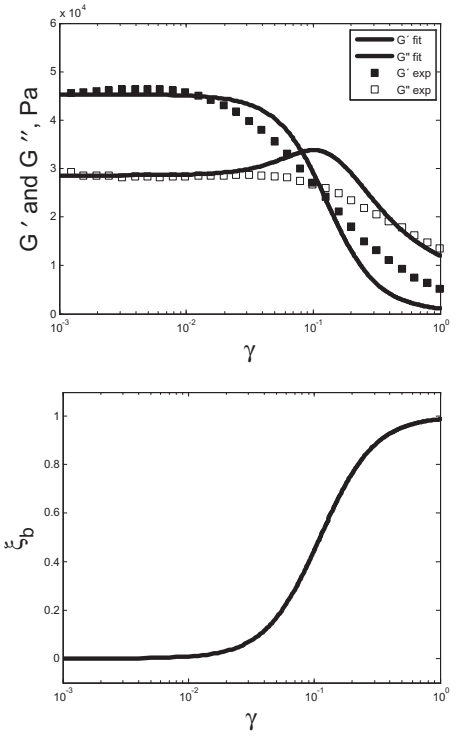

Figure 5. Strain sweeps of the storage and loss moduli (above) and corresponding changes of the structural parameter (below) for the CNT-PC melt at $\omega = 1$ rad/s.

with the following parameters: $\alpha = 0.329$, $\tau_f = 1.41$ s and $a\lambda_0 = 200\ s^2$. Note, that the rupture parameter a and the short recovery time λ_0 appear in equation (13) in the combination and can be only separated using the fit of an additional experiment.

For control, we calculated the dependence of complex viscosity on the effective shear rate (solid line) using the extracted parameter set

$$\left|\eta^*\right| = \omega^{-1}\sqrt{(G_f')^2 + (G_f'')^2}. \tag{14}$$

Here we used the solution of equation (10)

$$G_f' = G_f \frac{(\omega\tau(\xi_b))^2}{1+(\omega\tau(\xi_b))^2},\ G_f'' = G_f \frac{\omega\tau(\xi_b)}{1+(\omega\tau(\xi_b))^2} \tag{15}$$

valid for $\lambda_0 >> 2\pi/\omega$ (Lion 2008). In this case the storage and loss moduli are given by usual Maxwell expressions, only the time is not anymore constant but depends on the structural parameter according to equation (11). Comparison with the corresponding experimental data for the complex viscosity (diamonds) reveals a very good agreement between both dependencies.

The recovery branch of the flocculation experiment can be well described using the superposition of two kinetic equations of the first order with the same weight, i.e. $l = 2$ in equation (8). This gives the shortest time $\lambda_1 = 50\ s$ and the longest time $\lambda_2 = 2000\ s$ (Figure 4 above). The fast recovery process corresponds presumably to the formation of carbon nanotubes agglomerates, while the extremely slow process is very likely caused by the gradual rearrangement of a whole network structure. To obtain a best fit, we should use a slightly different value of the residual parameter: $\alpha = 0.52\tau_f$. We found out that only this choice of α provides a reasonable

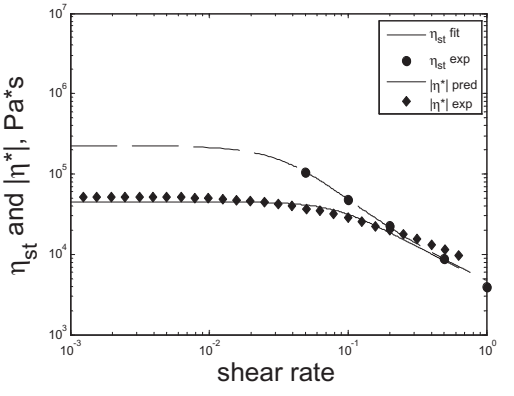

Figure 6. Dependencies of the stationary viscosity, η_{st}, and complex viscosity, $|\eta^*|$, on the (effective) shear rate.

fit of the strain sweeps (Figure 5 above). The theory however predicts a maximum of the loss modulus which is not observed in the experiment, presumably due to the use of only one relaxation mode.

Similar to the filled elastomer, only the fastest recovery process with $\lambda_1 = 50\ s$ manifests itself in the two breakage steps. Unfortunately, in the case of filled polymer melt we could not achieve a high quality of the fit for the breakage branch in the flocculation experiment. The first breakage step with $\gamma_{b1} = 0.05$ stays considerably underestimated (Figure 4 below, $a = 4\ s$). The observed discrepancy has presumably two reasons: 1) Description of flocculation experiment in the filled polymer melts needs a much longer parameter set than in the filled elastomers; 2) The samples used were produced by the injection molding technique which inevitably leads to a different filler microstructure in different probes.

3 CONCLUSIONS

In this study we carried out dynamic oscillatory shearing experiments on two, on the first sight quite different, filled polymer systems. In spite of different matrices (elastomer—polymer melt) and different fillers (silica particles—multi-walled carbon nanotubes), these experiments reveal more similarities than discrepancies between the two systems. In particular, a dramatic increase of the storage modulus has been found during recovery of the filler structure in the flocculation experiment for both systems. This recovery process cannot be described by a pure rate law which presumes a single type of the particle agglomeration. Contrary, analysis of the experimental data reveals a multistage agglomeration process: first, fast organization of particles into clusters, then much slower agglomeration of clusters into the filler network, finally, extremely slow addition of single particles to a well-developed network. Each stage can be characterized by its own rate law (or recovery time). During the process of shear-induced breakage only the shortest recovery time plays a role.

Thus, similar to other jammed systems, the filled polymer systems demonstrate an asymmetric behaviour upon approaching the steady state depending on whether the system was initially at higher or lower shear strain. In particular, the recovery time of filler structure in the quiescent state is found to be one-two orders of magnitude larger than a characteristic recovery time in the nonlinear shear regime.

ACKNOWLEDGEMENTS

This work was carried out with the support of the BMBF Project "CarboNet" No. 03X0504E. Bayer Technology Services GmbH (Leverkusen, Germany) is greatly acknowledged for providing the samples for rheological measurements. We thank René Jurk and Klaus Werner Stöckelhuber for providing the data on filled elastomer samples.

REFERENCES

Barnes HA (1997). Thixotropy—a review. *J Non-Newt Fluid Mech* 70: 1–33.

Bird RB, Armstrong RC, et al. (1987). *Dynamics of polymeric fluids*. John Wiley & Sons, New York.

Biroli G (2007). Jamming—A new kind of phase transition? *Nature Physics* 3: 222.

Costa FR, Saphiannikova M, et al. (2008). Layered double hydroxide based polymer nanocomposites. *Adv Polym Sci* 210: 101–168.

Dullaert K and Mewis J (2006). A structural kinetics model for thixotropy. *J Non-Newt Fluid Mech* 139: 21–30.

Larson RG (1999). *The structure and rheology of complex fluids*. Oxford University Press, New York, Oxford.

Leonov AI (1990). On the rheology of filled polymer melts. *J Rheol* 34: 1039–1068.

Lion A (2008). Constitutive modeling of the dynamic properties of elastomers. In "Constitutive models for rubber V". Taylor & Francis, London.

Liu AJ and Nagel SR (1998). Jamming is not just cool any more. *Nature* 396: 21–22.

Richter S, Saphiannikova M, et al. (2009). Jamming in filled polymer systems. *Macromol Symp* submitted.

Robertson CG and Wang X (2005). Isoenergetic jamming transition in particle-filled systems. *Phys Rev Lett* 95: 075703, 1–4.

Schaefer DW and Justice RS (2007). How nano are nanocomposites? *Macromolecules* 40: 8501–8517.

Smallwood HM (1944) Limiting law of the reinforcement of rubber. *J Appl Phys* 15: 758–766.

Thomasset J, Carreau PJ, et al. (2005). Rheological properties of long glass fiber filled polypropylene. *J Non-Newt Fluid Mech* 125: 25–34.

Torquato S (2001). Random Heterogeneous Materials: Microstructure and Macroscopic Properties, Interdisciplinary Applied Mathematics. Springer, USA.

Trappe V, Prasad V, et al. (2001). Jamming phase diagram for attractive particles. *Nature* 411: 772–775.

Wang XR, Rackaitis M (2006). Fluctuations and critical phenomena of a filled elastomer under deformation. *Europhys Lett* 75: 590–596.

Witten TA, Rubinstein M, et al. (1993). Reinforcement of rubber by fractal aggregates. *J Phys II* 3: 367–383.

Yziquel F, Carreau PJ, et al. (1999). Rheological modelling of concentrated colloidal suspension. *J Non-Newt Fluid Mech* 86: 133–155.

Constitutive Models for Rubber VI – Heinrich et al. (eds)
© 2010 Taylor & Francis Group, London, ISBN 978-0-415-56327-7

Mechanical and structural characterization of rubber under one-, two- and three-dimensional load

K. Schneider & A. Schöne
Leibniz Institute of Polymer Research Dresden, Dresden, Germany

ABSTRACT: Structural changes of elastomer composites during load/deformation, fatigue and crack propagation shall be investigated by online x-ray scattering, using time resolved as well as scanning techniques. Main attention will be paid to the beginning of cavitation and changes in phase morphology. Due to the large ratio between compression to tensile or shear modulus the cavitation which is relevant for damage will happen mainly under local 3-axial load. Therefore it is also necessary to perform the experiments under a comparable loading situation. A special test arrangement for 3-axial tensile tests will be presented which enables simultaneous x-ray scattering.

By Online-X-ray scattering with synchrotron radiation a time resolution in the order of seconds and a spatial resolution in the order of microns can be achieved. A combination of WAXS and SAXS enables to characterize the crystalline state or changes within it as well variations within the amorphous phase and cavitation processes.

1 INTRODUCTION

For a constitutive modeling of rubber it is necessary to understand the mechanisms of mechanical deformation in the whole deformation range as well as under different load.

While in the case of uni- and biaxial tension of rubber quite high deformation is possible, under three-dimensional loading due to the relative high compression modulus the situation is rather different. Mainly under three-axial tension cavitation is expected as pre-stage of failure.

By online-SAXS and -WAXS it is possible to throw light on the underlying mechanisms of deformation and failure. While SAXS enables to detect structural units with different electron density and with sizes in the range to about 100 nanometer WAXS enables to recognize strain induced crystallization, crystalline units, and their orientation.

2 EXPERIMENTAL

2.1 *Materials*

Within the current project different natural and synthetic rubber materials were produced with well-defined composition and filler. The details of the material are summarized in Table 1.

2.2 *Mechanical characterization*

For mechanical testing different experiments were established. To get a comprehensive information of mechanical properties the materials under investigation must be tested under quite different load. So it is convenient to use unidirectional tension and if necessary compression, the pure shear geometry (tension with specimen with a high width compared with length and thickness) or biaxial tension. On the other side fracture mechanical experiments are of interest, where the structure in the crack tip is investigated scanning this region with a small x-ray beam.

The used fracture mechanical sample forms are MDB (micro-dumbbell; or MDB-H: in some cases with an additional hole in the middle of the sample) and DENT (double edge notched tensile specimen).

To estimate true strain over the whole specimen grating techniques were used. In the easiest case a

Table 1. Investigated rubber specimen.

Rubber	Filler	Additives	Form
NR (Natural rubber, Polyisoprene)	None or 50 phr carbon black N220	ZnO, stearic acid, sulphur, accelerator	MDB, DENT
SBR (Styrene-Butadiene-Rubber)	60 phr carbon black N115 and N339 resp.	ZnO, stearic acid, sulphur, accelerator	MDB, MDB-H
XNBR (Carboxylated Acrylnitrile-Butadiene-Rubber)	0 and 5 phr Nanofil 15	ZnO, stearic acid, sulphur, accelerator	MDB, DENT

regular pattern was applied by a flexible dye and the deformation of the meshes followed during the experiment.

To realize that the highest stress and so also the highest strain is in the middle of the specimen a waisted sample geometry was used. The geometry of these specimen is shown in Figure 1.

Typical stress-strain-curves for uniaxial tension estimated via the force-displacement-curves using the grating technique are shown in Figure 2.

To get information about the behavior under 3-axial load a new specimen form is developed, which is shown in Figure 3.

These specimen are loaded simultaneously in 8 directions by the supporting metal blocks. Again the estimation of local deformation of the rubber-core of the specimen is planned to be estimated by optical measurement. On the basis of this measurements by FE-modeling the loading situation must be estimated. Within the gap between the blocks is sufficient space for SAXS- and WAXS-measurements.

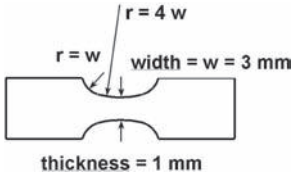

Figure 1. Geometry of the waisted specimen, the dimensions can be scaled.

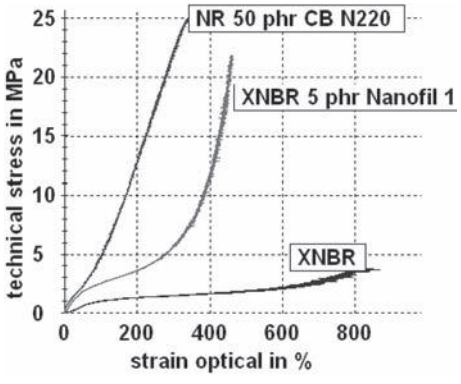

Figure 2. Stress-strain-curve of different rubbers, strain optically estimated.

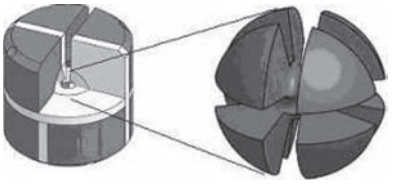

Figure 3. Geometry for a specimen for 3-axial tensile test.

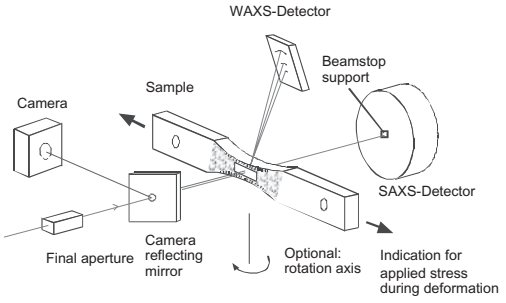

Figure 4. Experimental arrangement for Online-SAXS and -WAXS during deformation.

2.3 *Scattering experiments*

The finally used experimental arrangement was described in some detail by Davies et al. (2004), see Figure 4.

While a waisted specimen is stretched horizontally, SAXS and WAXS in equatorial direction are measured simultaneously. Following a regular or random surface structure with a camera via a mirror with a pin-hole enables to estimate simultaneously locally the 2d strain field at the beam position. Similarly also pre-damaged or fracture mechanical samples can be brought into the beam and scanned over a region of interest.

The proposed arrangement was used successfully investigating semi-crystalline polymers during deformation (Schneider et al. 2006, Schneider et al.) and fracture (Schneider 2008).

3 FIRST RESULTS AND DISCUSSION

According to the amorphous structure of rubber networks there is no representative scattering. The situation becomes different, if there are fillers or additives within the material, which are active in scattering, like ZnO or layered silicates. Their anisotropic orientation can be followed by scattering.

In the case of natural rubber strain-induced crystallization can be observed. This allows on the one hand the estimation of local internal strain within the material. On the other hand it enables to estimate the amount of crystallizable chains within the network.

Scanning fracture mechanical samples shows, that the structural changes near the crack tip are very similar the homogeneous deformed sample with comparable strain.

a b c

Figure 5. WAXS pattern of NR DENT specimen, scan near the crack tip (a) as well as its decomposition into an amorphous (b) and a crystalline contribution (c).

Figure 5 shows the pattern of stretched natural rubber of a DENT specimen near the crack tip with a high local strain and its decomposition into the contributions of the amorphous and the crystalline parts.

Unloading the strain-crystallizes rubber there is a remarkable hysteresis.

While by WAXS the orientation and deformation of crystallites can be followed, SAXS enables to follow variations within the amorphous phase and cavitation processes. The first indication of cavitation is a strong increase of scattering intensity due to the high difference of electron density within the rubber and the cavities.

A strategy to find model-free characteristic dimensions within a material under the condition of cylindrical symmetry within the structure is presented by Stribeck 2007. By image processing the 2-dimensional pattern were transformed into 2-dimensional slices across the (electron density) autocorrelation function and further by edge enhancement characteristic lengths can be extracted from the cord distribution function.

Unfortunately it is not straight forward possible to identify the underlying structures. Therefore it is desirable to complement the scattering investigations with methods, which verify the estimated structures, e.g. by electron microscopy.

4 CONCLUSIONS

The experiments presented here enable the monitoring of the continuously changing mechanisms of deformation and energy dissipation in rubber. Due to the high number of parallel processes, the use of structure characterisation by X-ray scattering techniques should be complemented by further independent investigations. This combination of methods is likely to provide a well-founded basis for material development and optimisation.

ACKNOWLEDGEMENT

The authors are grateful to the ESRF and ID13 staff for the provision of beamtime under the project MA170, particular thanks are due to R. Davies for the support during the experiments, as well as HASYLAB and BW4 staff for the provision of beamtime under the project 20060086, particular thanks to A. Timmann and St. Roth for the supporting the experiments. Special thank to N. Stribeck (University of Hamburg) for the support in the course of data evaluation.

REFERENCES

Davies, R.J., Zafeiropoulos, N.E., K. Schneider, et al. 2004. Colloid. Polym. Sci, 2004 (282), 854.

Schneider, K. et al. 2006. The study of Cavitation in HDPE Using Time Resolved Synchrotron X-ray Scattering During Tensile Deformation, *Macromolecular Symposia*, 2006 (236), 241–248.

Schneider, K. 2008. Online-structure characterisation of polymers during deformation and relaxation by Synchrotron-SAXS and -WAXS. In Kaliske, M., Heinrich, G., Verron, E (Eds.): *EUROMECH Colloquium 502 Reinforced Elastomers: Fracture Mechanics, Statistical Physics and Numerical Simulations; Proc. internat. Symp. Dresden, 08–10 September 2008*, Dresden.

Stribeck, N. 2007. *X-Ray Scattering of Soft Matter*, Heidelberg, Springer.

Constitutive Models for Rubber VI – Heinrich et al. (eds)

Stress relaxation behaviors of filled rubbers under various deformations

T. Tada, T. Mabuchi & K. Muraoka
Sumitomo Rubber Industries, LTD. Kobe, Hyogo, Japan

K. Urayama & T. Takigawa
Faculty of Engineering, Kyoto University Kyoto, Kyoto, Japan

ABSTRACT: Stress relaxation behaviors under various types of deformation have been investigated for carbon black filled and unfilled styrene butadiene rubbers. We discuss the separability of the time(t)–and deformation(λ)-dependent terms on the stress relaxation component, i.e, $\Delta\sigma_i(\lambda_x, \lambda_y, t)$ $(= \sigma_i(\lambda_x, \lambda_y, t) - \sigma_{i,\infty}(\lambda_x, \lambda_y)$ where $\sigma_{i,\infty}$ is the equilibrium stress) along each principal axis ($i = x, y$). The $\Delta\sigma_i(\lambda_x, \lambda_y, t)$–$t$ curves obtained under various deformations are reduced to a single curve, when $\Delta\sigma_i(\lambda_x, \lambda_y, t)$ is normalized by the total relaxation strength, $\Delta\sigma_{i,\infty}(\lambda_x, \lambda_y) = \sigma_{i,0}(\lambda_x, \lambda_y) - \sigma_{i,\infty}(\lambda_x, \lambda_y)$, where $\sigma_{i,0}$ is the initial stress. This result indicates that the separability of interest works for $\Delta\sigma_i$, i.e., $\Delta\sigma_i(\lambda_x, \lambda_y, t) = \Delta\sigma_{i,\infty}(\lambda_x, \lambda_y)\psi(t)$ where the time-dependent term $\psi(t)$ is common to all types of deformation. Interestingly, $\psi(t)$ for carbon black filled rubber well agrees with that for SBR without filler. This indicates that the time constants of stress relaxation in the filled rubbers are similar to those in the rubber matrix, although the filled and unfilled rubbers differ in $\Delta\sigma_{i,\infty}$.

1 INTRODUCTION

The finite element method (FEM) simulation is a strong and important tool to design the industrial rubber products because in many cases, they are subjected to complex deformations in use. The FEM analysis requires the constitutive equations which accurately describe the stress-strain behaviors under all types of deformation. Many types of phenomenological constitutive equation for rubbers have been proposed (For a review, Beda 2005). The determination of the model parameters or the assessment of the models has often been made using the uniaxial deformation (stretching and/or compression) data due to the experimental simplicity. The analysis relying on only uniaxial deformation often leads to incorrect results because the uniaxial deformation is only a particular one among all accessible deformations of rubbers (Treloar 1949, Urayama 2006). Evidently, the stress-strain data under various deformations provide unambiguous basis to establish the reliable constitutive equations. In principle, general biaxial strains with varying independently the principal strains in the two orthogonal directions cover the whole range of accessible deformations of incompressible rubbers. We demonstrated that the stress–strain data of the silicone rubbers under general biaxial deformations provided a definite basis to deduce a phenomenological form of strain energy density function (W) as well as to assess various molecular theories of rubber elasticity (Kawamura et al. 2001, Urayama et al. 2001).

The FEM analysis of filled rubbers is practically very important because the filler reinforcement markedly improves the mechanical properties of rubbers. Compared to the unfilled rubbers, the filled rubbers exhibit a pronounced viscoelastic effect together with the remarkable improvements of fracture properties. The stress of the filled rubbers is considerably time dependent, and it shows large relaxation toward the equilibrium one at fixed strains. This stress relaxation effect complicates the establishments of the constitutive equations for filled rubbers. An important key on this issue is whether the separability of the time and strain effects on stress(σ)—which is well known for uncrosslinked polymer melts (Doi & Edwards 1986)—works for crosslinked rubbers. Several researchers attacked this issue but the conclusion remains unsettled: There exist both types of results that supported the success and failure of the separability (Kawabata & Kawai 1977, Sullivan 1986, Quigley et al. 1995, Roland et al. 1989). It should be noted that most of the earlier studies discussed the separability regarding σ. For polymer melts without crosslinks, σ resulting from imposed deformation vanishes after a finite

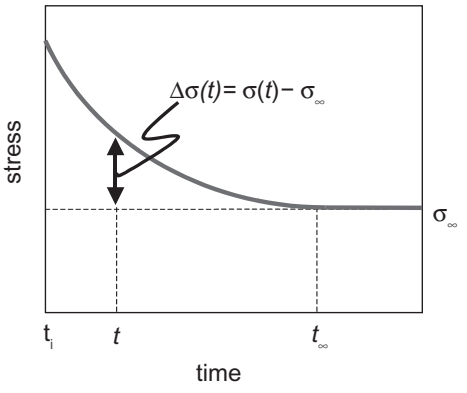

Figure 1. Schematic illustration of the stress relaxation at a fixed strain for rubbers. σ_∞ represents the equilibrium stress.

time because they are essentially liquids. In the case of rubbers with crosslinks, σ exhibits decay but stays finite even in the long time limit. In the present study, we emphasize that we should discuss the separability regarding the stress relaxation component ($\Delta\sigma$), instead of σ itself: $\Delta\sigma$ is given by $\Delta\sigma = \sigma - \sigma_\infty$ where σ_∞ is the equilibrium stress (Figure 1). It should be noticed that $\Delta\sigma$ becomes zero at equilibrium as in the case of σ in uncrosslinked polymer melts. A major reason of the puzzling conclusions for the separability in the earlier studies is that they employed σ –which does not vanish in the equilibrium-for discussion. We investigate the stress relaxation behavior of the filled rubbers under several deformation modes (equi-biaxial, pure shear and uniaxial stretching) with various degrees of deformation. We assess the validity of the time-strain separability for $\Delta\sigma$ under various deformations. We also point out the similarity in the stress relaxation behavior between the filled and unfilled rubbers. The results in the present study provide an important basis of the full description of the nonlinear viscoelastic behaviors of filled rubbers.

2 EXPERIMENTAL

2.1 *Sample preparation*

The carbon-black filled and unfilled rubber vulcanizates were prepared using Nipol SBR 1503 (ZEON Co.) and the ISAF grade of carbon black (N222 Mitsubishi Chemical Corporation). The sample sheets with a thickness of ca. 1 mm were made by the vulcanization of the mixtures of SBR and additives. The mixing process consisted of the two steps. Firstly, 100 phr of SBR was mixed with 2 phr of stearic acid and 3 phr of zinc oxide by 1.7 litters Banbury mixer at 140°C for 5 minutes. For the filled samples, 47.2 phr of carbon black (corresponding to the volume fraction of 0.2) was also added. Next, the resultant SBR compound was mixed with 1.5 phr of sulfur and 1.0 phr of the two kinds of accelerator (N-tert-butyl-2-benzothiazolesulphenamide and N,N′-diphenyl guanidine) by two roll mixing mill at 80°C. The obtained green rubber was vulcanized in a press mold at 170°C. The vulcanization times for the filled and unfilled samples were 12 and 14 minutes, respectively. The vulcanization time was determined from the results of curelastmeter at 170°C.

2.2 *Biaxial stress relaxation measurements*

Biaxial stress relaxation measurements were carried out with a biaxial stretching apparatus (IS-GIKEN KOGYO Co.)(Figure 2). A square-shaped sample sheet was clumped by totally twenty chucks, that is, four chucks at each side and one chuck at each corner. The detailed mechanism of the instrument is similar to that of the biaxial tester in a literature (Kawamura et al. 2001), although the maximum load of the present apparatus (980 N) is larger. The principal ratios in the two orthogonal axes (λ_x and λ_y) are variable independently. The present investigation employed the three deformation modes, i.e., uniaxial stretching ($\lambda_y = \lambda_z = \lambda_x^{-1/2}$), pure shear ($\lambda_z = \lambda_x^{-1}$ and $\lambda_y = 1$), and equi-biaxial stretching ($\lambda_x = \lambda_y$, $\lambda_z = \lambda_x^{-2}$). Prior to the collection of the stress relaxation data, the equi-biaxial pre-tension of $\lambda_x = \lambda_y = 2$ was applied for 20 minutes to eliminate the undesirable initial effects such as the deformation history.

The stress relaxation measurements were conducted 5 minutes after the full release of the pre-tension. The measurements were carried out at –20°C, 0°C, and 23°C within the accuracy of 0.5°C.

The stress relaxation was measured at various λ_x in each deformation mode. The ratio λ_x was

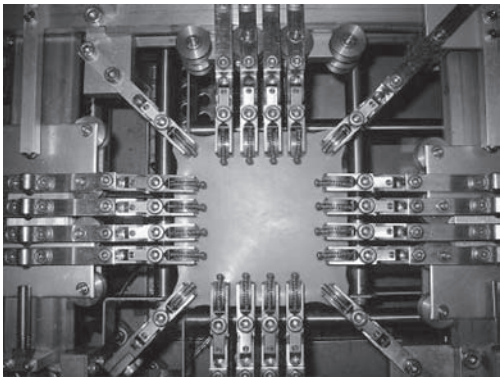

Figure 2. Photograph of the biaxial stretching instrument.

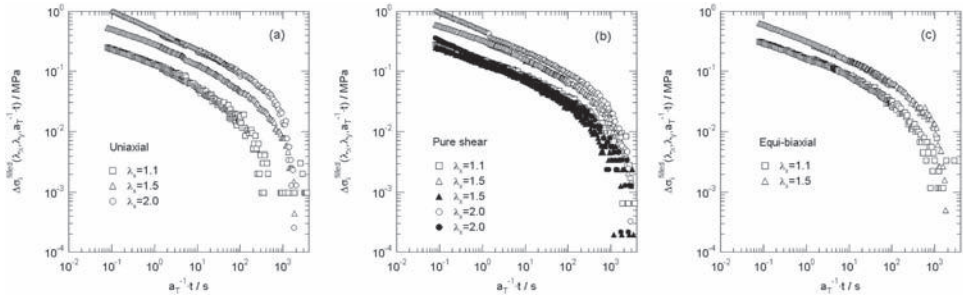

Figure 3. Double logarithmic plots of $\Delta\sigma_i^{filled}(\lambda_x, \lambda_y, a_T^{-1}t)$ versus reduced time, $a_T^{-1} \cdot t$, under (a) uniaxial stretching, (b) pure shear, and (c) equi-biaxial stretching for the filled SBR. The filled symbols in (b) represent the data in the y-direction.

varied from 1.1 to 2.0 for the filled SBR, and from 1.1 to 1.5 for the unfilled SBR. The sample sheets were stretched to a target principal ratio with a crosshead speed of 8.3×10^{-3} m/s. The time dependence of the force was measured after the imposition of λ_x of interest. About 6 seconds was required to reach $\lambda_x = 2$ (the maximum λ_x in the present study) from the undeformed state. Accordingly, the data for the first 10 seconds after reaching the target elongation were excluded in the analysis of stress relaxation because they include the delay effect. The force at each deformation reached the quasi-equilibrium state at $t > 2{,}500$ s at 23°C. The quasi-equilibrium stress was estimated by averaging the data in the region of 2,500 s < t < 3,600 s.

3 RESULTS AND DISCUSSION

In the beginning, the master curve of the stress relaxation [i.e., σ_i–log($a_T^{-1}t$) curve] at each deformation was made using the corresponding σ–log(t) curves at different T on the basis of the conventional time-temperature superposition principle in order to extend the accessible time scale. The master curves were successfully constructed by a horizontal shift without vertical shift. It should be noted that the horizontal shift factor (a_T) depends on only T, and it is independent of the deformation mode as well as λ.

$$a_T(\lambda_x, \lambda_y, T) \equiv a_T(T) \tag{1}$$

More interestingly, a_T at each T for the filled elastomers was identical with that for the unfilled ones.

$$a_T^{filled}(T) = a_T^{unfilled}(T) \tag{2}$$

We obtain the time dependence of $\Delta\sigma_i$ for each deformation from the corresponding master curve of stress relaxation. Figure 3 shows the double logarithmic plots of $\Delta\sigma_i(\lambda_x, \lambda_y, a_T^{-1}t)$ vs. $a_T^{-1}t$-where the reference temperature is 23°C–for the filled elastomers. The time-temperature superposition considerably extends the available time window. The resultant time scale covers from 10^{-1} s to the equilibrium (4×10^3 s).

The total relaxation strength ($\Delta\sigma_{i,\infty}$; $\Delta\sigma_{i,\infty} = \sigma_i(t) - \sigma_{i,\infty}$) depends on both deformation mode and λ, the details of which will be discussed later. We can compare only the time dependence of $\Delta\sigma_i$, between various deformations by using the reduced quantity ψ:

$$\psi(\lambda_x, \lambda_y, t) = \frac{\Delta\sigma_i(\lambda_x, \lambda_y, t)}{\Delta\sigma_{i,\infty}(\lambda_x, \lambda_y)} \tag{3}$$

Figures 4 and 5 show the time dependence of $\psi(\lambda_x,\lambda_y,t)$ for various deformations for the filled

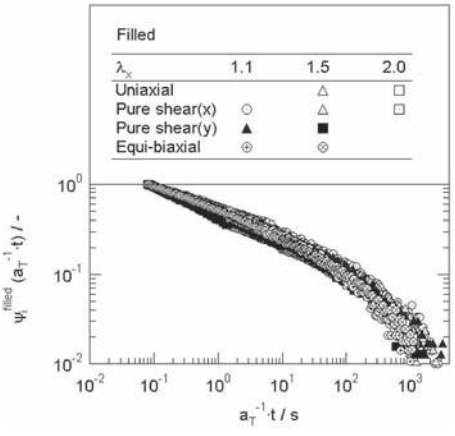

Figure 4. Double logarithmic plot of $\psi_i^{filled}(\lambda_x, \lambda_y, a_T^{-1}t)$ versus reduced time, $a_T^{-1}t$, under equi-biaxial stretching, pure shear, and uniaxial stretching for the filled SBR. The principal ratio was varied from 1.1 to 2.0.

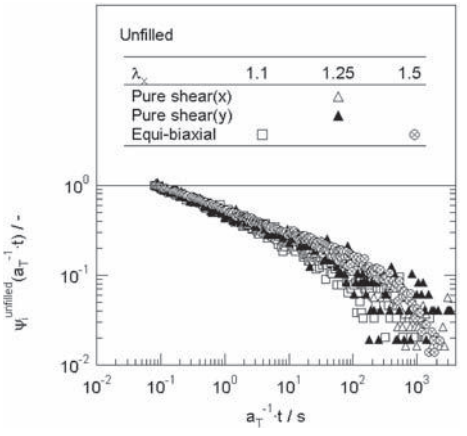

Figure 5. Double logarithmic plot of $\psi_i^{unfilled}(\lambda_x, \lambda_y, a_T^{-1}t)$ versus reduced time, $a_T^{-1}t$, under equi-biaxial stretching, pure shear for the unfilled SBR. The principal ratio was varied from 1.1 to 1.5.

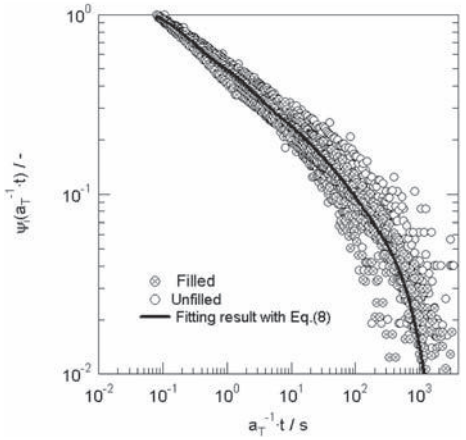

Figure 6. Double logarithmic plot of $\psi_i(\lambda_x, \lambda_y, a_T^{-1}t)$ versus, $a_T^{-1}t$ under equi-biaxial stretching, pure shear, and uniaxial stretching for black filled and unfilled elastomers solid line represents the fitting result of Eq. (8).

and unfilled elastomers, respectively. In each figure, all the curves appear to fall on a single master curve in the entire time range investigated here. An appreciable data scattering in Figure 5 is due to the small degree of $\Delta\sigma_{i,\infty}$ for the unfilled rubber. The results in Figures 4 and 5 are also expected from the fact that all $\Delta\sigma_i(\lambda_x, \lambda_y, a_T^{-1}t)$-$a_T^{-1}t$ curves -which for the filled rubber are shown in Figure 3- have a similar shape. The quantity of vertical shift of each curve needed for the superposition in Figure 3 is proportional to $\Delta\sigma_{i,\infty}$ for the corresponding deformation. The result in Figures 4 and 5 clearly indicates that ψ is common to all types of deformation independently of the degree of deformation, i.e.,

$$\psi(\lambda_x, \lambda_y, t) \equiv \Delta\psi(t) \tag{4}$$

This means that $\Delta\sigma$ is separable into the time- and strain-dependent terms for the filled and unfilled elastomers, respectively:

$$\Delta\sigma_i^{filled}(\lambda_x, \lambda_y, t) = \Delta\sigma_{i,\infty}^{filled}(\lambda_x, \lambda_y)\psi^{filled}(t) \tag{5}$$

$$\Delta\sigma_i^{unfilled}(\lambda_x, \lambda_y, t) = \Delta\sigma_{i,\infty}^{unfilled}(\lambda_x, \lambda_y)\psi^{unfilled}(t) \tag{6}$$

As in the case of $\sigma(t)$ for uncrosslinked polymer melts, the time-strain separability works for $\Delta\sigma_i$ of the unfilled and filled rubbers.

Figure 6 is the merger of the data in Figures 4 and 5, i.e., the comparison of $\psi^{filled}(t)$ and $\psi^{unfilled}(t)$. The data of the filled and unfilled elastomers are highly overlapped with each other in the whole time region. This indicates that $\psi(t)$ for the filled elastomers is the same as that for the unfilled ones:

$$\psi^{filled}(t) = \psi^{unfilled}(t) \tag{7}$$

Equation (7) means that the relaxation process in the filled elastomers is governed by that in the rubber matrix. This is also supported by no difference in a_T between the filled and unfilled elastomers (Eq. 2). Isono et al. investigated the T dependence of dynamic viscoelasticity of the rubbers filled with silica and carbon black (Wu. et al. 2007). They showed that the glass transition temperatures (T_g) of the filled and unfilled elastomers are similar, and that it is almost independent of filler content. They concluded that the thermal motion of fillers and rubber molecules are governed by segmental friction constant of the matrix polymer. Our results confirm that this conclusion is valid even when the filled elastomers are subjected to large and complicated deformations.

The separability of the time-dependent and strain-dependent terms for $\Delta\sigma$ facilitates to formulate the constitutive equations describing the viscoelastic effects under large strains in various deformation modes, because the time dependence of $\Delta\sigma$ at various deformations can be described by only a time function $\psi(t)$. The function $\psi(t)$ in Figure 6 is well approximated by a sum of the five exponential functions:

$$\psi(t) = \sum_{j=1}^{5} A_j \exp\left(-\frac{t}{\tau_j}\right) \tag{8}$$

where A_j and, τ_j used for fitting are listed in Table 1. The fitted curve by Eq. (8) is shown by the solid line in the figure.

As mentioned before, the total relaxation strength $\Delta\sigma_{i,\infty}$ considerably depends on the deformation mode and λ. Figure 7 shows the dependence of $\Delta\sigma_{i,\infty}$ on $(I_1 + I_2 - 6)$ for the filled and unfilled elastomers where I_1 $(= \lambda_x^2 + \lambda_y^2 + \lambda_z^2)$ and I_2 $(= \lambda_x^2 \lambda_y^2 + \lambda_y^2 \lambda_z^2 + \lambda_z^2 \lambda_z^2)$ represent the first and second invariants of the deformation gradient tensor. The relaxation strengths $\Delta\sigma_{i,\infty}$ for both the filled and unfilled elastomers appear to increase with the degrees of deformation. However, this tendency may be simply because σ increases with strain. This effect can be eliminated by reducing $\Delta\sigma_{i,\infty}$ by the initial stress (σ_0) at each deformation. Figure 8 shows this reduced quantity $(\Delta\sigma_{i,\infty}/\sigma_0)$ as a function of $(I_1 + I_2 - 6)$. The reduced relaxation strength seems to be almost constant independently of the degree of deformation, although the data are scattered: $\Delta\sigma_{i,\infty}/\sigma_0 = C^{\text{filled}} \approx 0.40$ for the filled elastomer, and $\Delta\sigma_{i,\infty}/\sigma_0 = C^{\text{unfilled}} \approx 0.25$ for the unfilled elastomer. The constancy of the reduced relaxation strength significantly simplifies the deformation-dependent terms in Eqs. (5) and (6):

$$\Delta\sigma_{i,\infty}^{\text{filled}}(\lambda_x, \lambda_y) = C^{\text{filled}} \sigma_{i,0}^{\text{filled}}(\lambda_x, \lambda_y) \tag{9}$$

Table 1. Parameters of Eq(8) used for fitting.

j	1	2	3	4	5
A_j	0.093	0.114	0.125	0.298	0.541
τ_j	535	56.4	11.3	1.81	0.198

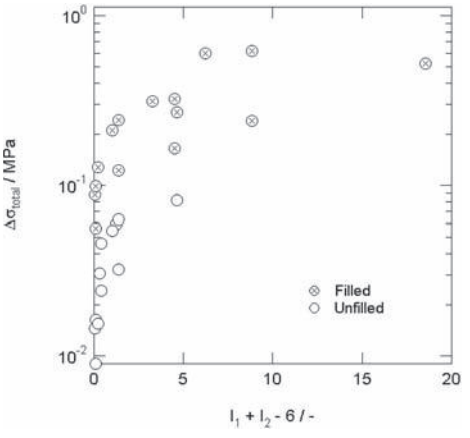

Figure 7. Logarithm of $\Delta\sigma_{i,\infty}$ plotted versus $(I_1 + I_2 - 6)$ under various deformations where I_1 and I_2 represent the first and second invariants of deformation gradient tensor.

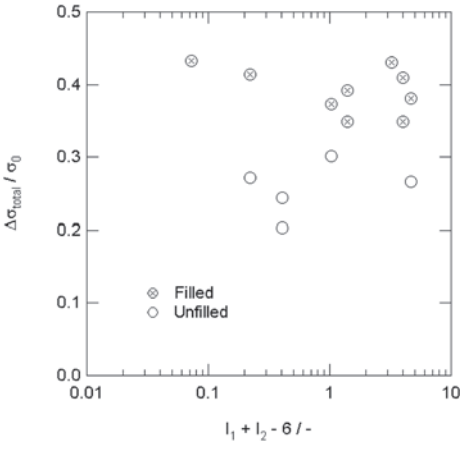

Figure 8. $\Delta\sigma_{i,\infty}/\sigma_0$ logarithmically potted versus $(I_1 + I_2 - 6)$ at different deformation mode where I_1 and I_2 represent first and second order invariants.

$$\Delta\sigma_{i,\infty}^{\text{filled}}(\lambda_x, \lambda_y) = C^{\text{unfilled}} \sigma_{i,0}^{\text{unfilled}}(\lambda_x, \lambda_y) \tag{10}$$

On the basis of the separability of the time and strain terms for $\Delta\sigma$, a form of W including the time effect may be expressed by

$$W(\lambda_x, \lambda_y, t) = (W_0 - W_\infty)\psi(t) + W_\infty \tag{11}$$

where W_0 and W_∞ are the strain energy density functions in the short time limit ($a_T^{-1} t \approx 10^{-1}$ s in the present study) and equilibrium, respectively. The functions W_0 and W_∞ can be determined on the basis of the stress-strain data under various deformations in the short and long time limits, respectively. The existing phenomenological forms of W may be available as W_0 and W_∞. The total relaxation strength of stress $(\Delta\sigma_{i,\infty})$ corresponds to $\partial(W_0 - W_\infty)/\partial\lambda_i$. If the constancy of the reduced relaxation strength [Eqs. (9) and (10)] is valid, W_∞ is simply related to W_0 with the constant C^{filled}. It means that we need only the form of W_0. The evaluation of the forms of $W(\lambda_x, \lambda_y, t)$ along this line, i.e., the full description of the nonlinear viscoelastic effects under various deformations will be conducted in our separate study.

REFERENCES

Beda, T. 2005. Reconciling the Fundamental Phenomenological Expression of the Strain Energy of Rubber with Established Experimental Facts. *J. Polym. Sci.* Part B: Polym. Phys. 43, Issue 2,: 125–134.

Doi, M. & Edwards, S.F. 1986. *"The Theory of Polymer Dynamics"*. New York: Clarendon press, pp. 249–255.

Kawabata, S. & Kawai, H. 1977, *"Strain Energy Density Functions of Rubber vulcanizates from Biaxial Extension"*. Berlin Heidelberg: Springer-Verlag, 24, pp. 89–124.

Kawamura, K., Urayama, K., & Kohjiya, S. 2001. Multiaxial Deformation of End-Linked Poly (dimethylsiloxane) Networks. 1. Phenomenological Approach to Strain Energy Density Function. *Macromolecules* 34: 8252–8260.

Quigley, C.J., Mead, J. & Johnson, A.R., 1995. Large Strain Viscoelastic Constitutive Models For Rubber, Part II: Determination of Material Constants. *Rubber Chem. Tech*. 68: 230–247.

Roland, C. The Mullins Effect in Crosslinked Rubber. 1989. *J. Rheol.* 33(4): 659–670.

Sullivan, J.L. 1986. The Relaxation and Deformational Properties of a Carbon-Black Filled Rlastomer in Biaxial Tension. *J. Appl. Polym. Sci* 24: 161–173.

Tralor, L.R.G. 1949. *The Physics of Rubber Elasticity*. London: Oxford at the Clarendon Press. pp. 114–128.

Urayama, K., Kawamura, T., & Kohjiya, S. 2001. Multiaxial Deformations of End-linked Poly (dimethylsiloxane) Networks. 2. Experimental tests of Macromolecular Entanglement Models of Rubber Elasticity. *Macromolecules* 34: 8261–8269.

Urayama, K. 2006. An Experimentalist's View of the Physics of Rubber Elasticity. *J. Polym. Sci.* Part B: Polym. Phys. 44: 3440–3444.

Wu, J., Fujii, S. Kawahara, S., & Isono, Y. 2007. Filler Effects on Temperature Dependence of Viscoelastic Properties of Filled Rubbers. *e-Journal of Soft Materials* 3: 41–48.

Fatigue and lifetime

Constitutive Models for Rubber VI – Heinrich et al. (eds)

Beyond Miner's rule for the fatigue of elastomers: Experiments and modelling

Audrey Jardin
Michelin, Research and Technology Center, Clermont-Ferrand, France
Université Pierre et Marie Curie Paris 06, UMR 7190, Institut Jean Le Rond d'Alembert, Paris, France

Jean-Baptiste Leblond
Université Pierre et Marie Curie Paris 06, UMR 7190, Institut Jean Le Rond d'Alembert, Paris, France

Daniel Berghezan
Michelin, Research and Technology Center, Clermont-Ferrand, France

ABSTRACT: A series of uniaxial fatigue experiments carried out on diabolo-shaped specimens made of elastomers shows many discrepancies with Miner's cumulative damage rule predictions. A new heuristic model is then established, introducing a continuum damage mechanics model which describes fatigue by means of a damage parameter D and an evolution equation for this parameter. This law involves an empirical parameter representing the discrepancies to Miner's law. The results obtained using this model give a better representation of the experiments than Miner's rule's predictions.

1 INTRODUCTION

Miner's cumulative damage rule is still the most commonly used to predict the fatigue of elastomers, thanks to its simplicity which makes it one of the easiest to use. Many researches (D. Klenke and A. Beste 1987) (L. Lemaitre and J.L. Chaboche 1978) (F. Ellyin and D. Kujawski 1984) (F. Ellyin and D.Kuhawski 1988) have been carried out in order to improve Miner's law. This rule predicts that the total damage is the sum of the damages obtained for each loading. This sum is equal to one when the sample breaks. This rule does not take into account the load sequence effects or interactions between the cycles: for a given number of cycles, it states that the damage is the same, regardless of the order in which the different loadings are applied.

The aim of the present work is firstly to test this cumulative damage rule on rubber. A series of uniaxial fatigue experiments have been carried out on two specimens of Styrene-Butadiene-Rubber (SBR). The force loading conditions are specific to each sample, due to different carbon black contents: 30 and 60 "Per Hundred of Rubber" (PHR) in each SBR specimen. The results obtained show many discrepancies with Miner's cumulative damage rule predictions.

The second aim of this work is therefore to propose a new heuristic model which takes into account these discrepancies. Consequently, we have introduced (i) a continuum damage mechanics model which describes fatigue by means of a damage parameter D and (ii) a damage law for the evolution of this parameter. This damage law represents the discrepancies to Miner's rule and thus gives a total Miner's cumulated damage which can be lower or greater than unity. The discrepancies to Miner's rule are represented by means of a parameter α which depends on the applied loading and the value of which is determined from the experiments by the least square method.

The results obtained using the proposed model give a better representation of the experiments than Miner's rule.

2 MINER'S CUMULATIVE DAMAGE RULE

Miner's cumulative linear damage rule (M.A. Mine 1945) is a damage function predicting failure after a sequence of different loadings, by calculating the damage of the specimen for each loading.

In case of a unique cyclic loading, the damage (noted D_{Miner}) is the ratio of the number of cycles realized n over the number of cycles required to cause the failure N_f of the sample at a given loading level:

$$D_{Miner} = \frac{n}{N_f} \tag{1}$$

If a cyclic solicitation is composed of p different loadings, the total damage is expressed as follows:

$$D_{Miner} = \sum_{i=1}^{p} D_{Miner\,i} = \sum_{i=1}^{p} \frac{n_i}{N_{fi}} \tag{2}$$

where

- p is the number of distinct loadings levels,
- $D_{Miner\,i}$ is the fraction of sample life consumed at load level i,
- n_i is the number of cycles at loading level i,
- N_{fi} is the number of cycles required to cause the failure at the level i.

Furthermore when the sum of damages is equal to one, the sample is expected to break.

Among the many drawbacks of Miner's law, we recall that it does not take into account the load sequence effects or interactions between the cycles: for a given number of cycles, it states that the damage is the same, regardless of the order in which the different loadings are applied.

In order to test Miner's law, a series of uniaxial fatigue experiments have been carried out and the results are presented in the following section.

3 EXPERIMENTS AND RESULTS

All the fatigue experiments have been carried out at room temperature on diabolo-shaped specimens (Fig. 1) made of Styrene-Butadiene-Rubber (SBR) with different carbon black contents: 30 "Per Hundred of Rubber" (PHR) for the specimen A and 60 PHR for the specimen B.

These diabolo-shaped specimens are subjected to cyclic loadings with a frequency of 3 Hz. Due to the different carbon black contents in the two specimens, different maximum loads are applied in each, in order to limit the duration of each experiment.

Miner's cumulative damage rule has been tested for only two loadings in the present paper. The loadings 1 and 2 for sample A are respectively set to 60 N and 90 N, while for sample B, they are set to 110 N and 130 N.

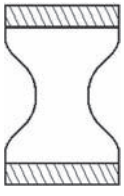

Figure 1. Diabolo-shaped specimens.

According to the equation (3), Miner's total damage is written as follows:

$$D_{Miner} = \frac{n_1}{N_{f1}} + \frac{n_2}{N_{f2}} = D_{Miner1} + D_{Miner2} \tag{3}$$

and this quantity is equal to one at failure.

In order to test this cumulative law, the numbers of cycles at which a diabolo-shaped specimen fails at a given loading is first determined using a uniaxial tensile machine. For each loading, three trials are made to ensure the validity of the results.

Figure 2 shows that three phases can be distinguished during the fatigue experiments.

Thanks to figure 2, we observe that during our fatigue experiments, we have three phases. The first is the phase of accomodation (noted 1 on figure 2), it corresponds to a sudden drop of the rigidity of the material. The second phase is the phase of stabilisation (noted 2 on the figure 2), where we can observe that the displacement becomes stable. This phase takes a very long time and corresponds to the greatest part of the specimen's total lifetime. The last phase (noted 3 on the figure 2), corresponds to the sudden growth of the minimum and maximum displacements, it occurs just before the failure of the specimen.

The loading sequence carried out for the two specimens to test Miner's cumulative law are:

- 66% of the number of cycles to failure for loading 1 then until the failure for loading 2,
- 33% of the number of cycles to failure for loading 1 then until the failure for loading 2,
- 66% of the number of cycles to failure for loading 2 then until the failure for loading 1,
- 33% of the number of cycles to failure for loading 2 then until the failure for loading 1.

For each loading sequence, the experiments have been repeated three times in order to verify

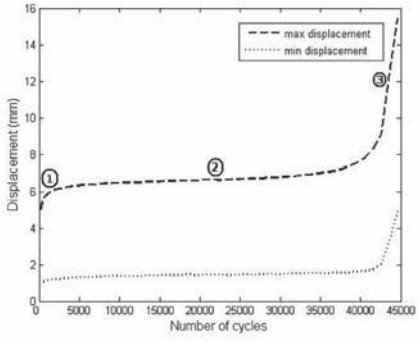

Figure 2. Variation of the minimum and maximum displacements for sample B loaded at 130 N.

the reproducibility of the tests. Miner's cumulative damage rule has thus been tested twelve times for each material.

The fatigue experiments show in some cases, a Miner's total damage higher than 1 which can be due to a material reinforcement after the first solicitation. In the same manner for others experiments, we obtain the contrary, that is a very fast damaging of the material which generates a total damage of Miner smaller than 1. These observations don't allow to use Miner's cumulative damage rule. The aim of the new model introduced in the next part is to overcome the limitations of Miner's cumulative law.

4 A NEW HEURISTIC MODEL

For a given loading resulting in a failure in N_f cycles, we proposed the following damage evolution law:

$$\frac{dD}{dN} = \frac{g(D, N_f)}{N_f} \tag{4}$$

The function $g(D, N_f)$ has to verify the following conditions:

- the necessary condition: $\int_0^1 \frac{dD}{g(D, N_f)} = 1 \forall N_f$; (because at a constant loading amplitude, D has to be equal to 1 when $N = N_f$)
- the function g cannot be the product of two functions which depend respectively on D and N_f, in order to predict the discrepancies to Miner's linear law.

A particular form of $g(D, N_f)$, the simplest possible which verifies these conditions, is:

$$g(D, N_f) = \frac{1}{1 + 2\alpha\,(D - 1/2)} \tag{5}$$

where $\alpha \equiv \alpha\,(N_f)$.

$\alpha\,(N_f)$ means that α depends on the applied loading level (and thus ultimately of N_f).

After having specified the form of the function g, we can explain how to determine the parameters α_1 and α_2 corresponding to the two loadings. We then define:

$$G(D, N_f) = \int_0^D \frac{dD'}{g(D', N_f)} = \alpha D^2 + (1 - \alpha) D \tag{6}$$

For a loading sequence (C_1, C_2), the total damage of Miner is:

$$D_{Miner} = \frac{N_1}{N_{f1}} + \frac{N_2}{N_{f2}} \tag{7}$$

with

$$\begin{cases} \dfrac{N_1}{N_{f1}} = G(D, N_{f1}) \\ \dfrac{N_2}{N_{f2}} = 1 - G(D, N_{f2}) \end{cases} \tag{8}$$

where D represents the damage of the sample after the first cyclic loading.

Using equations 6 and 8, D^2 is eliminated and an expression for the damage D is obtained:

$$D = \frac{\alpha_1(-1 + N_2 / N_{f2}) + \alpha_2(N_1 / N_{f1})}{\alpha_2 - \alpha_1} \tag{9}$$

Replacing D in equation (7), we obtain a relation between the experimental data and the numerical parameters α_1 and α_2 of the form

$$f_1(N_1/N_{f1},\, N_2/N_{f2},\, \alpha_1,\, \alpha_2) = 0$$

In the same manner, for a loading sequence (C_2, C_1), we obtain a relation of the form $f_2(N_1'/N_{f1},\, N_2'/N_{f2},\, \alpha_1,\, \alpha_2) = 0$.

For a succession of two loadings, like for our fatigue experiments, we have to determine α_1 and α_2 by the least square method. It's necessary for that to have at least two equations, thus at least two experiments.

5 COMPARISON BETWEEN EXPERIMENTAL RESULTS AND THE NEW MODEL

This section compares the results obtained with the new model and the results obtained during our twelve fatigue experiments on diabolo-shaped specimens. The lifetime computed with the model and during our experiments are grouped in tables 1 and 2 for the specimen A and in tables 3 and 4 for the specimen B.

$D_{Miner\ 1exp}$ and $D_{Miner\ 1model}$ represent the damage obtained experimentally and numerically for loading 1, and $D_{Miner\ 2exp}$ and $D_{Miner\ 2model}$ for loading 2.

The loading orders (C_1,C_2) or (C_2,C_1) indicate the first loading applied to the sample. Indeed, if this is (C_2,C_1) (line 8 in the tables 1 and 2), then the first loading applied is loading 2 until a Miner's damage of 0.66 then loading 1 until the failure.

The comparison between the experimental and numerical results shows for the sample A (tables 1 and 2), a better prediction than Miner's cumulative rule, even when observing a damage for one loading greater than 1 (line 12 in the tables 1 and 2). Indeed, the experiments give $D_{Miner\ 1exp}$ equal to 1.10, the model gives $D_{Miner\ 1model} = 0.90$,

Table 1. Damages obtained with the experiments for the sample A.

Loadings order	$D_{Miner\ 1exp}$	$D_{Miner\ 2exp}$	$D_{Miner\ total\ exp}$
(C_1, C_2)	0.33	0.81	1.14
	0.33	0.31	0.64
	0.33	0.13	0.46
	0.66	0.01	0.67
	0.66	0.43	1.09
	0.66	0.23	0.89
(C_2, C_1)	0.40	0.66	1.06
	0.62	0.66	1.28
	0.63	0.66	1.29
	0.57	0.33	0.90
	0.64	0.33	0.97
	1.10	0.33	1.43

Table 2. Damages obtained with the model for the sample A.

Loadings order	$D_{Miner\ 1model}$	$D_{Miner\ 2model}$	$D_{Miner\ total\ model}$
(C_1, C_2)	0.17	0.70	0.87
	0.44	0.38	0.82
	0.55	0.28	0.83
	0.80	0.11	0.91
	0.50	0.32	0.82
	0.64	0.22	0.86
(C_2, C_1)	0.46	0.70	1.16
	0.56	0.62	1.18
	0.57	0.62	1.19
	0.73	0.44	1.17
	0.75	0.41	1.16
	0.90	0.19	1.09

Table 3. Damages obtained with the experiments for the sample B.

Loadings order	$D_{Miner\ 1exp}$	$D_{Miner\ 2exp}$	$D_{Miner\ total\ exp}$
(C_1, C_2)	0.33	1.66	1.99
	0.33	2.08	2.41
	0.33	1.56	1.89
	0.66	1.47	2.13
	0.66	0.40	1.06
	0.66	0.74	1.40
(C_2, C_1)	0.12	0.66	0.78
	0.05	0.66	0.71
	0.04	0.66	0.70
	0.15	0.33	0.48
	0.11	0.33	0.44
	0.08	0.33	0.41

Table 4. Damages obtained with the model for the sample B.

Loadings order	$D_{Miner\ 1model}$	$D_{Miner\ 2model}$	$D_{Miner\ total\ model}$
(C_1, C_2)	0.27	0.94	1.21
	0.23	0.96	1.19
	0.27	0.94	1.21
	0.59	0.68	1.27
	0.68	0.57	1.25
	0.64	0.61	1.25
(C_2, C_1)	0.13	0.74	0.87
	0.07	0.86	0.93
	0.06	0.87	0.93
	0.18	0.65	0.83
	0.14	0.71	0.85
	0.12	0.76	0.88

that is an error of 18% and the Miner's law gives $D_{pred\ 1Miner} = 0.67$, that is an error of 39%.

For these loading sequences, the model computes $\alpha_1 = 0.430$ and $\alpha_2 = -0.300$ corresponding respectively to the loadings 1 and 2.

For the sample B, the experimental total damages (Tables 3 and 4) are greater than 1 when loading 1 is applied first and lesser than 1 when loading 2 is applied first. The model gives a better representation of the experiments than Miner's cumulative rule when the damage for a unique loading is much higher than 1 like in line 7. Indeed, $D_{Miner\ 2exp}$ is equal to 1.66, the model gives $D_{Miner\ 2model} = 0.94$, which is an error of 43% and Miner's law gives $D_{pred\ 2Miner} = 0.67$ that is an error of 60%. For these loading sequences, the model computes $\alpha_1 = -0.09$ and $\alpha_2 = 1$ corresponding respectively to the loadings 1 and 2. Even if our model gives less satisfactory results for fatigue experiments for the sample B than for the sample A, the aim of this work to give a better prediction of the experiments than Miner's cumulative damage rule, is fulfilled.

6 CONCLUSIONS

A fatigue experimental compaign carried out on diabolo-shaped specimens made of elastomers with different carbon black contents: 30 and 60 PHR in each SBR specimen, has allowed to test Miner's cumulative damage rule and to conclude that Miner's law predictions in term of lifetime are not very accurate. In order to overcome the limitations of Miner's cumulative law, we have proposed a particular model. This one has permitted

to obtain values of Miner's damage closer to the experimental results than Miner's law predictions.

REFERENCES

D. Klenke and A. Beste (1987). Ensurance of the fatigue life of metal-rubber component. *Kautschuk Gummi Kunstoffe 40*, 1067–1071.

F. Ellyin and D. Kujawski (1984). A cumulative damage theory for fatigue crack initiation and propagation. *International Journal of Fatigue 6*, 83–88.

F. Ellyin and D. Kujawski (1988). On the concept of cumulative fatigue damage. *International Journal of Fatigue 37*, 263–278.

L. Lemaitre and J.L. Chaboche (1978). Aspect phénoménologique de la rupture par endom-magement. *Journal de Mécanique Appliquée 2*, 317–363.

M.A. Miner (1945). Cumulative damage in fatigue. *Journal of Applied Mechanics 67*, A159–A164.

Constitutive Models for Rubber VI – Heinrich et al. (eds)

Constitutive and numerical modeling of the fatigue behavior of a filled rubber

J. Grandcoin
Laboratoire de Mécanique et d'Acoustique UPR7051-CNRS, Marseille, France

A. Boukamel
Ecole Centrale de Marseille, Marseille, France
Laboratoire de Mécanique et d'Acoustique UPR7051-CNRS, Marseille, France

S. Lejeunes
Laboratoire de Mécanique et d'Acoustique UPR7051-CNRS, Marseille, France

ABSTRACT: This paper presents a hyper-vico-plastic constitutive model with damage, which is based both on the generalization of rheological models to finite strain and on a micro-physically motivated statistical approach. An experimental campaign of fatigue was realized and has allowed to study the fatigue behavior with respect to amplitude and frequency of the mechanical sollicitation. A model of fatigue based on cumulative damage is proposed. Finally, a numerical implementation has permitted to confront the experimental results to the numerical ones.

1 INTRODUCTION

Elastomeric material are widely used by many industries: automotive, aeronautic … In many applications, elastomeric parts are closely linked to security and require reliability properties. That is why a perfect knowledge of the mechanical behavior is needed, both for static and dynamic loadings, and furthermore for the life time prevision. These goals require a modeling of the behavior which takes into account material and geometrical non-linearities, entropic processes and fatigue influence.

The present work is concerned with the constitutive modeling of the dissipative and fatigue behavior of a silicon elastomer filled with silica. The constitutive model is based on an micro-physically motivated hyper-visco-plastic behavior associated with statistical concepts as already presented in previous ECCMR (Boukamel et al. 2005; Boukamel et al. 2007). This statistical aspect allows the model to cover a wide range of frequency with few parameters.

The fatigue behavior is investigated from an experimental campaign which was realized on cyclic traction and shear tests with various amplitudes, frequencies and pre-loadings. From the experimental results an evolution of material parameters upon the number of fatigue cycles has been determined. Starting from these observations and with the hypothesis of a cumulative and isotropic damage, a damage fatigue model has been developed that takes into account the positive part of the free energy rate both on the interface fillers/matrix and inside the matrix when an energetic criteria has been reached (Grandcoin 2008; Mars 2001). The model has been implemented in a finite element software to confront the experimental fatigue configurations to numerical ones.

2 A STATISTICAL HYPER-VICO-PLASTIC MODEL

2.1 *Micro-physical hypothesis*

Elastomers belong to the family of flexible high polymers. They consist in macromolecular chains with ramifications and exhibit high deformability and a dissipative dynamical behavior. Furthermore, this dissipative behavior depends on the vulcanization, the industrial process and moreover on the fillers which are incorporated.

By taking into account the heterogeneity of the material at a microscopical scale, it is proposed to adopt a simple representation of the Representative Elementary Volume (REV). It is supposed to be composed by a filler agglomerate into an elastomeric matrix with an intermediate zone called interphase (see figure 1(a)). The behavior of each component is supposed as follow (see figure 1(b)):

- a hyper-viscoelastic behavior of Poynting-Thomson for the matrix;

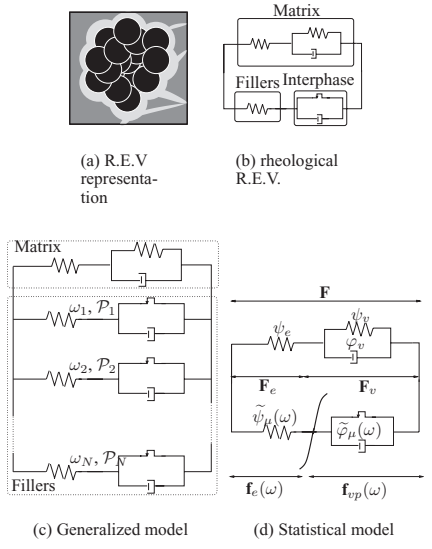

(a) R.E.V representation

(b) rheological R.E.V.

(c) Generalized model

(d) Statistical model

Figure 1. Hyper-visco-plastic statistical model.

- an hyperelastic behavior for the filler aggregate;
- a visco-plastic behavior for the interphase.

It is also supposed that the affinity hypothesis is verified (VOIGT hypothesis).

2.2 *The statistical approach*

The main idea of this approach consist in a combination of the simple rheological behavior of each different population of R.E.V which could be present in the material. The statistical approach allows the generalization of a parallel assembly of a finite number of rheological branches to an infinite one. The interest of this approach resides in the cover of different characteristic times and different yield stress at the interphase. Furthermore, this approach presents the advantage of a multi-branches model (generalized model) without an increase of the number of material parameters (Martinez 2005; Boukamel 2006).

Starting from the rheological representation of the R.E.V. and the concept of a multi-branches model (or multi R.E.V) each family of aggregates can be associated with a random variable ω. This variable can be linked to the yield stress at the interphase which is closely related to the physical properties of the aggregates. It is also defined a probability of presence: $\mathcal{P}(\omega)d\omega$ of each family in the material.

The constitutive model is based on the concept of multiplicative decompositions or intermediate states as early proposed in (Sidoroff 1974). The deformation gradient $\mathbf{F}$ is decomposed as: $\mathbf{F} = \mathbf{F}_e \cdot \mathbf{F}_v = \mathbf{f}_e(\omega) \cdot \mathbf{f}_p(\omega)$, and it is defined the left CAUCHY-GREEN deformation tensors: $\mathbf{B}_e = \mathbf{F}_e \cdot \mathbf{F}_e^T$ for the elastic part in the matrix and $\mathbf{B}_v = \mathbf{F}_v \cdot \mathbf{F}_v^T$ for the viscous part in the matrix. The elastic deformation in the filler is represented by $\mathbf{b}_e(\omega) = \mathbf{f}_e(\omega) \cdot \mathbf{f}_e^T(\omega)$. It is also defined the specific free energy and a pseudo-potential of dissipation as follow:

$$\begin{cases} \psi = \psi_e(\mathbf{B}_e) + \psi_v(\mathbf{B}_v) + \int_0^\infty \tilde{\psi}_\mu(\omega, \mathbf{b}_e(\omega))\mathcal{P}(\omega)d\omega \\ \varphi = \varphi_v(\mathbf{D}_v^o) + \int_0^\infty \tilde{\varphi}_\mu(\omega, \mathbf{d}_{vp}^o(\omega))\mathcal{P}(\omega)d\omega \end{cases} \quad (1)$$

where $\mathbf{D}_v^o$ and $\mathbf{d}_p^o(\omega)$ are objective Eulerian rates of deformation, respectively in the matrix and in the filler.[1] Using the so-called internal dissipation inequality and the normality principle, equation (1) gives us the following state and complementary laws:

$$\begin{cases} \sigma = \sigma_m + \int_0^\infty \tilde{\sigma}(\omega)P(\omega)d\omega - p\mathbf{1} \\ \sigma_m = 2\rho[\psi_{e,1}\mathbf{B}_e - \psi_{e,2}\mathbf{B}_e^{-1}]^D \\ \tilde{\sigma}(\omega) = 2\rho[\tilde{\psi}_{\mu,1}(\omega)\mathbf{b}_e(\omega) - \tilde{\psi}_{\mu,2}(\omega)\mathbf{b}_e^{-1}(\omega)]^D \end{cases} \quad (2)$$

$$\begin{cases} 2\rho[\psi_{e,1}\mathbf{B}_e - \psi_{e,2}\mathbf{B}_e^{-1} + 2\psi_{v,1}\mathbf{V}^{-1}\mathbf{B}\mathbf{V}^{-1}]^D = \dfrac{\partial \varphi_v}{\partial \mathbf{D}_v^o} \\ 2\rho[\tilde{\psi}_{\mu,1}(\omega)\mathbf{b}_e(\omega) - \tilde{\psi}_{\mu,2}(\omega)\mathbf{b}_e^{-1}(\omega)]^D = \dfrac{\partial \tilde{\varphi}_\mu(\omega)}{\partial \mathbf{d}_{vp}^o(\omega)} \end{cases}$$

It has been taken into account in these equations of the incompressibility condition: $Tr(\mathbf{D}) = Tr(\mathbf{D}_v^o) = Tr(\mathbf{d}_{vp}^o(\omega)) = 0$. To proceed further, it is adopted a GENT-THOMAS and a NEO-HOOKE free energy types together with a quadratic form of the pseudo-potential for the viscosity and a classical VON-MISES yield function for the plastic part:

$$\begin{cases} \rho_0\psi_e = C_1(I_1(\mathbf{B}_e) - 3) + C_2 Ln\left(\dfrac{I_2(\mathbf{B}_e)}{3}\right) \\ \psi_v = A(I_1(\mathbf{B}_v) - 3 \\ \varphi_v = \dfrac{H}{2}\mathbf{D}_v^o : \mathbf{D}_v^o \\ \tilde{\psi}_\mu(\omega) = a(\omega)(I_1(\mathbf{b}_e(\omega)) - 3), \quad \forall \omega \geq 0 \\ \tilde{\varphi}_\mu(\omega) = \dfrac{\eta(\omega)}{2}\mathbf{d}_{vp}^o(\omega) : \mathbf{d}_{vp}^o(\omega) + \chi(\omega) \| \mathbf{d}_{vp}^o(\omega) \| \end{cases} \quad (3)$$

According to the previous choices, the behavior of the matrix is defined from the material parameters C_1 and C_2 of the Gent-Thomas hyperelastic model, from A the modulus of the viscous part and from

[1] By using the polar decomposition $\mathbf{F}_e = \mathbf{V}_e \cdot \mathbf{R}$ and $\mathbf{f}_e(\omega) = \mathbf{v}_e(\omega) \cdot \mathbf{r}(\omega)$, these objective tensors are defined from the Eulerian rates of deformation: $\mathbf{D}_v^o = \mathbf{R} \cdot \mathbf{D}_v \cdot \mathbf{R}^T$ and $\mathbf{d}_{vp}^o(\omega) = \mathbf{r}(\omega) \cdot \mathbf{d}_{vp}(\omega) \cdot \mathbf{r}(\omega)^T$.

H the viscosity parameter. The behavior of a filler is characterised by the hyperelastic coefficient $a(\omega)$, by the viscosity $\eta(\omega)$ and by the yield stress $\chi(\omega)$. Finally, the following statistical functions are retained:

$$\begin{cases} P(\omega) = \dfrac{1}{P_0}\exp\left(-\left(\dfrac{\omega}{\Omega}\right)^2\right), \quad \forall \omega \geq 0 \\ \text{with } P_0 = \displaystyle\int_0^\infty \exp\left[-\left(\frac{\omega}{\Omega}\right)^2\right] d\omega \\ \chi(\omega) = \bar{\chi}\dfrac{\omega}{\omega_0}, a(\omega) = a_0 \exp\left(-\dfrac{\omega}{\omega_0}\right), \eta(\omega) = \bar{\eta}\dfrac{\omega}{\omega_0} \end{cases} \quad (4)$$

There are **9** material parameters to be identified, **7** are determinist ($C_1, C_2, A, H, a_0, \bar{\eta}$ and $\bar{\chi}$) and **2** are statistical (Ω et ω_0).

3 EXPERIMENTAL TESTS AND PARAMETERS IDENTIFICATION

3.1 *Identification strategy*

Due to the complexity of the model and to the number and the interdependency of the material parameters, it has been necessary to develop a specific identification strategy to distinguish typical plastic effects from viscous effects. The proposed strategy is based on the following steps:

1. Starting from quasi-static experimental tests (shear and traction)
   - Identification of C_1 and C_2,
   - Estimation of $A, a_0, \bar{\chi}, \Omega$ and ω_0.
2. Relaxation tests allow to:
   - Identify A, H and ω_0,
   - Correct $a_0, \bar{\chi}, \bar{\eta}, \Omega$ and ω_0.
3. Triangular cyclic tests (at different rates) allow to correct the prediction of $a_0, \bar{\chi}, \bar{\eta}$, and Ω

3.2 *Experimental campaign*

According to the previously defined strategy, the experimental campaign has been realized at a controlled temperature $T = 25°C$ on a silicon elastomer filled with silica. This campaign has been consisted in:

- Uniaxial traction tests on tension specimens, with quasi-static loadings, triangular cyclic loadings and relaxation.
- Shearing test on double-shearing specimens, with quasi-static loadings, triangular cyclic loadings at various rates and various amplitudes of strain.

The figures 2 and 3 illustrate some results of the identified model compared to experimental tests.

3.3 *Evaluation of fatigue*

To analyze the effect of fatigue on the material behavior, it has been realized a specific experimental campaign on tension specimens (traction) and double shearing specimens with a specific shape at

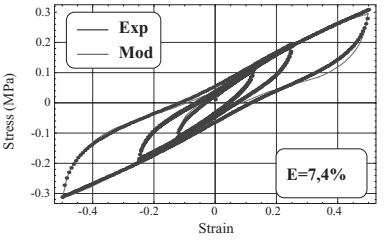

(a) Quasi-static shearing

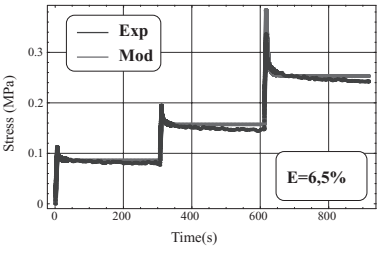

(b) Shearing relaxation test

Figure 2. Identification of the material parameters.

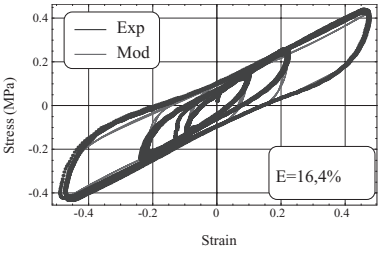

(a) Shearing cyclic test

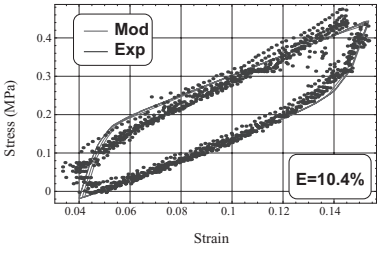

(b) Traction cyclic test

Figure 3. Identification of the material parameters.

the outer surface (figure 4(a)). This campaign has consisted in:

- Cyclic fatigue test for various cycle numbers, frequency and amplitudes of loading;
- Characterization tests, as described in the previous section, for each level of fatigue (from 1000 to 50000 cycles for traction and 1000 to 7000000 for shearing, depending on the amplitude of fatigue).

The preliminary results of this campaign has shown that the visible damages are initiated near the center of the outer faces of the double shearing specimen. Furthermore, the principal effects of fatigue on the material behavior are a softening response and a diminution of the dissipation.

(a) Double shearing specimen for fatigue

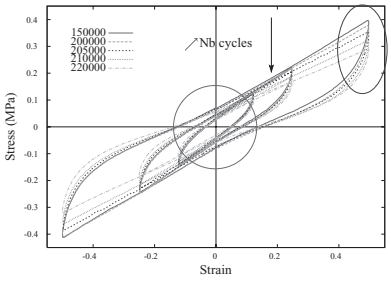

(b) Evolution of the behavior with fatigue

Figure 4. Fatigue tests.

4 TOWARDS A MODILISATION OF FATIGUE

In the aim of a better understanding of the interaction between the matrix and the agglomerates of fillers, it was realized microscopical observation with a SEM in collaboration with the *Centre des Matériaux, Mines de Paris*. This observations were done on traction specimen which were previously subjected to fatigue test. The principal micro-damage mechanism observed was a decohesion at the interphase matrix/fillers. Furthermore, observations had shown the permanent aspect of this decohesion.

These earlier observations has conduced to analyse the influence of the material parameters of the statistical model on the cyclic response in shearing. It has been observed that the more influent parameters are the hyperelastic parameter of the matrix (C_1, C_2) and the statistical yield stress at the interphases Ω (see figures 4). From these phenomenologic observations, it can be postulated that the damage of the material can be described by a decrease of the hyperelastic parameters of the matrix leading to a softening effect together with a reduction of the yield stress at the interphase. So, to model the damage behavior in fatigue, it must be take into account of the two previous aspect and by considering an isotropy hypothesis, one has:

- A damage at the interphase matrix/fillers which can be described by a decrease of the yield stress

$$d = 1 - \frac{\Omega}{\Omega^0}$$

where Ω_0 is defined from the initial behavior (non-damaged material).

- A damage of the matrix with a softening effect

$$D = 1 - \frac{\Delta\sigma_0}{\Delta\sigma_0^0}$$

where $\Delta\sigma_0^0$ and $\Delta\sigma_0$ are respectively the maximum variation upon a stabilised cycle of the stress response of the matrix branch at the initial state and the damaged state.

The evolution of theses two damage variables upon the number of loading cycles was obtained through the identification of the parameters C_1, C_2 and Ω at various level of fatigue (see figure 6). The damage of the material seems to initiate during the first cycles into the interphase and it is propagated into the matrix in the next cycles. Using the hypothesis of a linear cumulative model, it can be postulated the following evolution equations for the two damage variables with respect to the number of cycles[2]:

$$\begin{cases} \dfrac{\delta d}{\delta N} = \dfrac{d^\alpha}{1-\alpha}\left(\dfrac{R_\mu}{R_\mu^0}\right) \\ \dfrac{\delta D}{\delta N} = \mathcal{H}(d-d_0)\dfrac{D^A}{1-A}\left(\dfrac{R_M}{R_M^0}\right) \end{cases} \tag{5}$$

with

$$\begin{cases} R_\mu = \displaystyle\int_0^\infty \left(\int_0^T \left\langle \rho\dot{\tilde{\psi}}(t,\omega)\right\rangle dt\right) P(\omega)d\omega \\ R_M = \displaystyle\int_0^T \left\langle \rho\dot{\psi}_e + \rho\dot{\psi}_v \right\rangle dt \end{cases} \tag{6}$$

In the previous expressions, R_M and R_μ represent *returnable cyclic energies* which can be defined as the difference between the given energy and the

[2] $\mathcal{H}(\cdot)$ and $\langle X\rangle$ are respectively the HEAVISIDE function and the positive part of X.

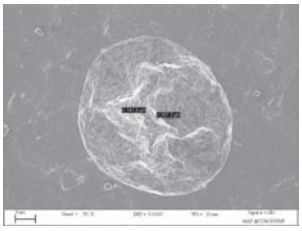

(a) Before fatigue

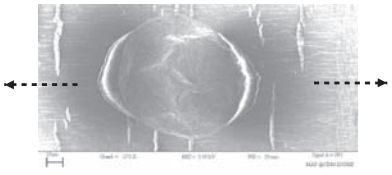

(b) After fatigue, 100% of strain amplitude

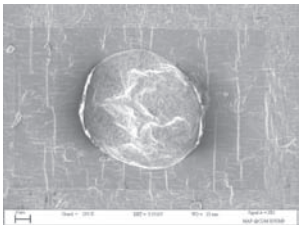

(c) Permanent decohesion

Figure 5. Microscopic observation of the damage mechanism in fatigue.

dissipated one, and such respectively in the matrix branch and the statistical branch. This model requires the identification of 5 material parameters: α, A, R_μ^0, R_M^0 and d_0. The last one can be viewed as a yield damage of the interphase from which the damage is initiated into the matrix. R_μ^0, R_M^0, are the fracture energies during a static test.

5 FINITE ELEMENT SIMULATION

5.1 *Numerical implementation*

The proposed statistical hyper-visco-plastic model was implemented in the finite element software Ze-BuLoN, by using a discretization that consist in three level: spatial, statistic and temporal. These developments are based on a perturbed

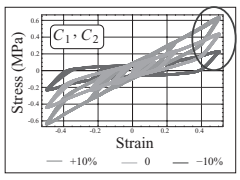

(a) Material parameters analysis of the matrix

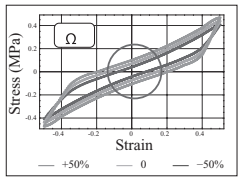

(b) Analysis of the inter-phase parameter

Figure 6. Phenomenologic observations of damage on the behavior.

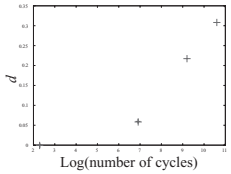

(a) Damage at the inter-phace

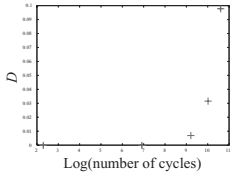

(b) number of cycles

Figure 7. Evolution of the damage variable upon fatigue.

Lagrangian formulation to take into account of the incompressibility. They are integrated in a NEWTON-RAPHSON algorithm with an elementary static condensation of the pressure dof. The integration of the evolution equations is based on a specific exponential mapping scheme which will be described in a paper to appear (Lejeunes et al. 2009). The damage evolution laws has been taken into account using a week coupling scheme, that can be sum up as follow

- A preliminary post-treatment step is provided to calculate R_M and R_μ on the first fatigue cycles,
- A simulation of characteristic tests at N number of cycles is realized using the fields R_M and R_μ which were calculated from the first step to finally obtain d and D,
- A simulation of characteristic tests by taking into account the previously evaluated damage variables.

5.2 *Simulation of the shearing test*

It has been realised a simulation of some shearing tests made on the specific shaped specimen (figure 4(a)). The amplitude of the strain loading is 25% and the frequency of the cyclic signal is 6 *Hz*. The global and local results of the finite element simulation show:

- a good prediction of the fracture initiation location (fig. 8),
- a good accordance of the numerical and the experimental results of a characteristic test

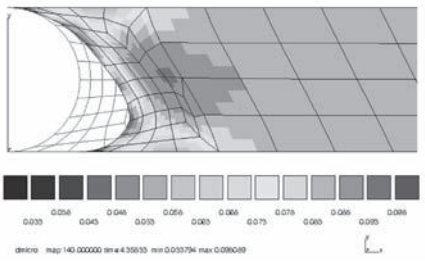

(a) Damage variable d

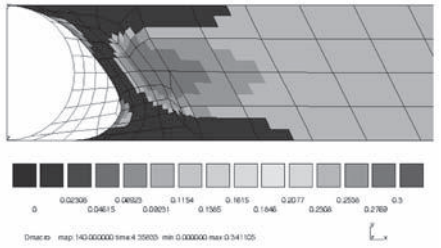

(b) Damage variable D

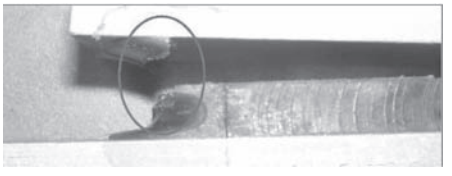

(c) Fracture initiation location

Figure 8. Damage fields after 180000 cycles of fatigue and fracture initiation.

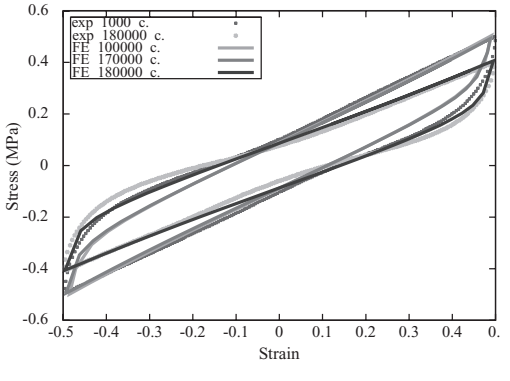

Figure 9. Numerical and experimental results of a shearing test after fatigue.

realized after 170000 and 180000 cycles of fatigue, under a triangular cyclic loading at 50% of strain amplitude (fig. 9).

6 CONCLUSION

With the goal to model the behavior of filled elastomer in fatigue, it has been proposed a microphysically motivated statistical model that can take into account different family of aggregates. This model is derivated from a rheological view of a R.E.V., which consists of a filler aggregate inside an elastomeric matrix with an interphase at the frontier of the two first phases. A damage law by fatigue as been integrated into the proposed model, with two specific mechanism: decohesion of the interphase matrix/fillers following by a propagation into the matrix.

From the experimental point of view, it has been realized an experimental campaign that has consisted both in cyclic fatigue tests and characterisation tests. This campaign has allowed to quantify the evolution of the material parameters upon fatigue.

Finally, the finite element implementation and the numerical simulation of some experimental tests have shown a good agreement between the proposed model and the experiments.

REFERENCES

Boukamel, A. 2006. *Mechanical and numerical modelisation of elastomeric materials and structures.* Mémoire HDR, Université de la Méditerranée.

Boukamel, A., J.M. Martinez. & S. Méo 2005. A statistical approach for a hyper-visco-elasto-plastic model for a filled elastomer. In *Constitutive Models for Rubber IV*, pp. 191–196.

Boukamel, A., S. Méo. & S. Lejeunes 2007. Fe-implementation of a statistical hyper-visco-plastic model. In *Constitutive Models for Rubber V*, pp. 255–261.

Grandcoin, J. 2008. *A tribute to the modelisation of the disipative behavior of filled elastomers: From a microphysical modelisation towards the caracterisation of fatigue.* Ph.D. thesis, Université d'Aix-Mareille II.

Lejeunes, S., A. Boukamel. & S. Méo 2009. Some numerical integrators for rheological models at finite strain based on multiplicative decompositions. *To appear.*

Mars, W. 2001. *Multiaxial fatigue of rubber.* Ph.D. thesis, University of Toledo.

Martinez, J. 2005. *Modelisation and caracterisation of the hyperviscoplastic behavior of an elastomer under multiharmonic loadings and various temperatures.* Ph.D. thesis, Université d'Aix-Mareille II.

Sidoroff, F. 1974. Un modèle viscoélastique non linéaire avec configuration intermédiaire. *J. Méc.,* 679–713.

Constitutive Models for Rubber VI – Heinrich et al. (eds)
© 2010 Taylor & Francis Group, London, ISBN 978-0-415-56327-7

Lifetime prediction of rubber products under simple-shear loads with rotary axes

R. Klauke & T. Alshuth
German Institute of Rubber Technology (DIK), Hannover, Germany

J. Ihlemann
Chemnitz University of Technology, Chemnitz, Germany

ABSTRACT: Lifetime predictions of technical rubber products in most cases are based on long time fatigue experiments. During those experiments the samples are cyclically loaded till failure. Usually the loading is initiated with an uniaxial deformation whereby the amplitude and the mean value of the load is varied in the course of the test series. However, in the majority of cases the dominant loading condition in rubber-parts is a mixture of many different loading conditions. Moreover, the loading direction in a material point does not remain constant but often changes throughout the deformation process. Therefore, a lifetime prediction with conventional approaches, based on data from equidirectional experiments leads to an error for inelastic and anisotropic materials under the described loading conditions. For the decoupling on the laboratory scale of the dependencies of the lifetime on the loading amplitude on the one hand and on the change of the loading direction on the other hand, an experimental rig according to (Gent 1960) has been developed, which is used in a new way for lifetime investigations under simple shear loads with rotary axes.

1 INTRODUCTION

There are many different approaches to evaluate the lifetime of rubber parts. What they all have in common is the fact, that the prediction is based on data which results from equidirectional experiments. In those cases a lifetime prediction can lead only to satisfactory results, when it is made for an isotropic and elastic material or for a loadcase with constant loading directions. Under those conditions the equidirectional experiments provide sufficient information for the prognosis of the lifetime. Typical rubber products usually are not loaded equidirectionally and the material itself is inelastic. Therefore, not taking the change of the loading direction into account, the common lifetime predictions are not complete. In this paper a new experimental approach is presented, which allows a split of the lifetime analysis into experiments which are based on tests with varying amplitudes and constant loading directions on the one side and tests with a constant amplitude and rotating loading directions on the other side. A common known example for changing loading directions throughout a deformation is the simple shear process, which is outlined in Figure 1. As can be observed, the directions of the connecting lines between the edges of the square change throughout the simple shear process. The lines in the undeformed square can be regarded as a representation for the directions of the lagrangian eigenvectors. When the inscribed square reaches a configuration where it is rectangular again, its edges represent the directions of the eulerian eigenvectors. As simple shear is often a dominant deformation in complex deformed structures, the influence of changing loading directions on the lifetime of rubber parts must be taken into consideration.

Figure 1. Outline of a simple shear process.

2 EXPERIMENTAL SETUP

2.1 *Simple shear with rotating axes*

The basis of the new experimental approach is a simple shear deformation process with rotating axes, which is outlined in Figure 2. The process is initiated by a simple shear deformation with the

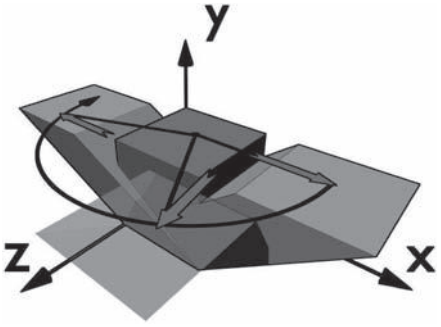

Figure 2. Simple shear with rotating axes.

shear strain s according to the coefficients of the deformation gradient $\underline{\underline{F}}$.

$$\left[F_{ab}\right] = \begin{bmatrix} 1 & s & 0 \\ 0 & 1 & 0 \\ 0 & 0 & 1 \end{bmatrix} \tag{1}$$

The deformation process continues with the translatoric shift of the undeformed material planes on a circular track around the y-direction. Hereby, all planes maintain their orientation to each other. Equation 2 shows the coefficients of the corresponding deformation gradient.

$$\left[F_{ab}\right] = \begin{bmatrix} 1 & f(\varphi) & 0 \\ 0 & 1 & 0 \\ 0 & g(\varphi) & 1 \end{bmatrix} \tag{2}$$

with

$$\varphi = \omega t \tag{3}$$

$$f(\varphi) = s \cdot \cos(\omega t) \tag{4}$$

$$g(\varphi) = s \cdot \sin(\omega t) \tag{5}$$

With the beginning of the rotational phase of the experiment, it can be observed that the resulting force $\underline{F}$ and the shear deformation do not have the same direction anymore. This phenomenon is based on the fact that, in comparison to elastic materials, the resulting forces in inelastic materials do not necessarily have to be in the same direction, as the principle eigenvector of the deformation. Moreover they can vary in the course of the deformation process due to effects like energy dissipation and stress-softening. For a simple shear process with rotating axes the resulting force vector can be regarded in a configuration, where the direction of the first component is the same, as the direction of the translatoric displacement in radial direction.

$$\underline{F} = \begin{bmatrix} F_R \\ F_U \\ 0 \end{bmatrix} \underline{e_a} \tag{6}$$

In this configuration $\underline{F}_R$ always stands in a right angle to the actual movement of the deformation process. It therefore has no contribution to the energybalance, except for the initial simple shear deformation. On the contrary, the circumferential force $\underline{F}_U$ only has a contribution to the energybalance during the rotational phase, because its direction is always the same as the direction of the movement. As there is no change in the momentary configuration of the deformation, it stays a simple shear deformation throughout the whole process, the circumferential force must be originated in dissipative effects, which occur only due to the change of the direction of the deformation.

The energy, which is dissipated per revolution of the simple shear process with rotating axes, can be computed with the value of the circumferential component of the force vector $\underline{F}$ according to equation 7.

$$\Phi = \int_0^{2\pi} F_R r d\varphi \tag{7}$$

Hereby, Φ stands for the amount of dissipated energy during one revolution, φ for the actual angular position and r for the displacement of the initial simple shear deformation. Regarding the fact, that a mere change of the direction of deformation is connected with energy dissipation, it can be concluded that this process induces damage in the material and therefore the material itself has a limited lifetime under those conditions. The angle between the direction of the translatoric displacement of the simple shear deformation and the resulting force is the so called phase angle ψ. It can be computed directly via the two components of the resulting force, as shown in equation 8.

$$\psi = arctan\left(\frac{F_U}{F_R}\right) \tag{8}$$

First simulations of a simple shear process with rotating axes have been made by (Ihlemann 2003), where the existence of the phase angle for this deformation process could be accounted for theoretically.

2.2 *Experimental rig*

For the realization of a simple shear deformation with rotating axes, a testing machine according to (Gent 1960) has been constructed. It can be used for the mechanical characterization of materials as well as for lifetime measurements, of which the second is the main purpose of the rig. A principle outline of the machine is given in Figure 3, which shows the procedure of an experiment in four steps.

The machine consists of three parts, whereby, during a measurement, the outer parts stay fixed in their position. The middle part has a degree of freedom in radial direction. In the first step, two rotationally symmetric samples are clamped into the rig in a double-sandwich-arrangement, each between one outer and the middle part. The experiment is initiated with the radial displacement of the middle part. In that way, a simple shear deformation is realized in the samples. The geometry of the samples is optimized in a way, that with the radial displacement of the middle part, simple shear is the predominating deformation throughout the whole volume of the samples. This is necessary to realize a nearly homogenous deformation and to be able to correlate between the measured forces and the observed phenomena. At the same time, the maximum load is located within the sample, far away from contact- and surface areas, so that a failure is most probable in the interior. After initiating a simple shear deformation, one of the shafts of the outer parts is rotated to start a simple shear deformation with rotating axes. For inelastic materials, the middle part would move sideways due to energy-dissipation, as is shown in Figure 3 in the third image. If the resulting movement is restricted as shown in the fourth image, the circumferential force could be measured instead. The radial force due to the simple shear deformation and the circumferential force due to dissipation effects both are the measurement quantities of the new testing device. With those two measurands and the computed phase angle the lifetime behavior of rubber-materials under simple shear loads with rotary axes can be characterized. Hereby it is a major advantage,that in spite of the dynamic characteristics of the experiment, the measurands stay constant in short-term-observation. A theoretical discussion on this kind of loading can be found in (Ahmadi 1999).

2.3 *Long time fatigue experiments under simple-shear-loads with rotating axes*

The first experiments with the new testing device have shown, that rubberlike materials have a limited lifetime under simple-shear loads with rotating axes. Figure 4 shows the results of a long time fatigue experiment with the testing machine, whereby the course of the radial force and the circumferential force during the experiment are plot against the revolutions of the samples. The experiment has been carried out till failure of one of the samples in the double-sandwich-arrangement.

During the first 10000 cycles, stress softening effects can be observed in the curve progression of the two measured forces. The material becomes weaker and both forces decrease in the course of the experiment. After that, both quantities stay constant in short-terms. In long-term-observation, the radial force decreases with an increasing number of revolutions, but the circumferential force stays constant. The diminution of the radial force in the course of the experiment shows, that a modulation of the loading direction leads to a weakening of the material which can be grounded on

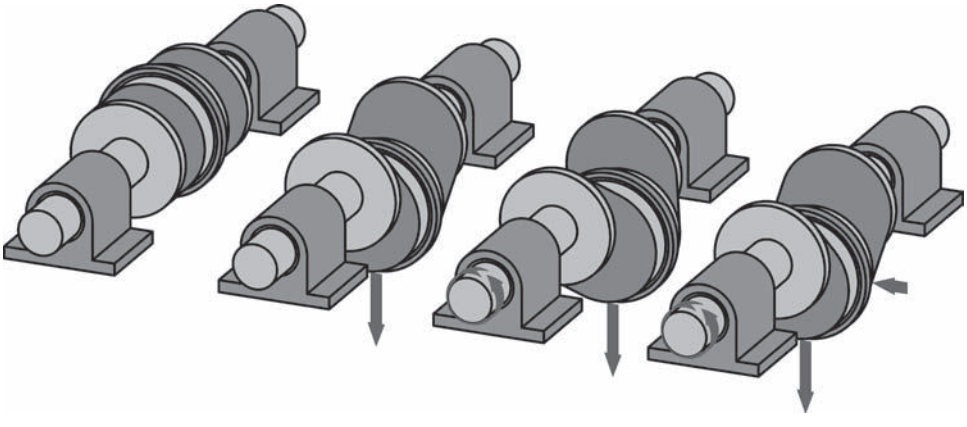

Figure 3. Outline of experimental rig.

accumulated damage within the samples. Figure 5 shows the course of the appropriate phase angle. It can be calculated according to equation 7 with the absolute values of the measured forces. For presentation purposes the results in Figure 5 have been filtered to suppress noise effects.

As the radial force decreases and the circumferential force stays constant over the lifetime of the material it can be concluded, that the phase angle increases slightly. But this is hardly to detect until catastrophic crack growth due to the comparatively small changes in the radial force. Physically, an increasing phase angle is equivalent to an increasing relative energy dissipation, which can be explained with friction in microscopic cracks throughout the volume of the sample material. Those cracks can be found with the help of computer tomography inside the samples or with a REM-analysis on the crack-surfaces of a broken sample. As a result of the rotational symmetry of the deformation process, the cracks also have a circular shape. An example for such a crack is shown in Figure 6.

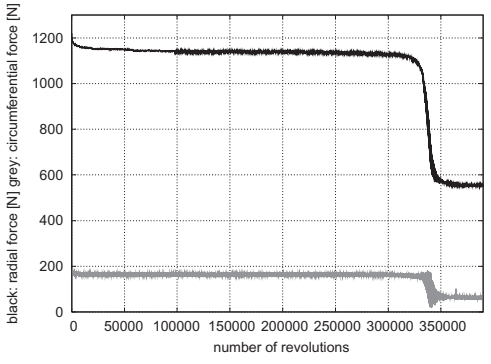

Figure 4. Examplatory measurement with EPDM.

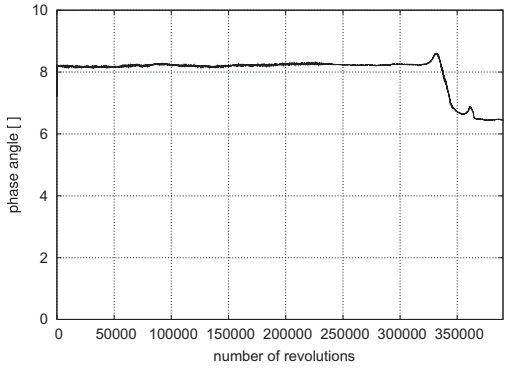

Figure 5. Phase angle in dependence of revolutions.

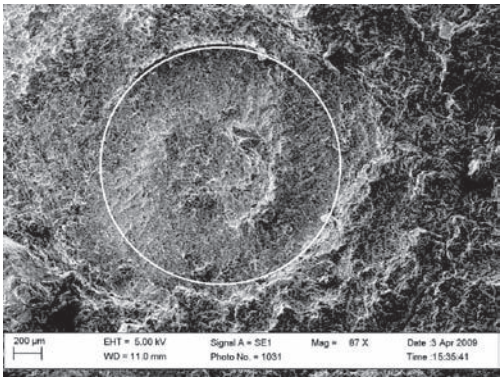

Figure 6. REM-Analysis of microscopic cracks at the crack surface.

For visualization purposes, the crack has been marked with a white circle. The catastrophic crack growth can be observed in the course of both forces as well as in the course of the phase angle. Due to the decreasing stiffness of the material, the radial force decreases significantly. At the same time, the energy-dissipation increases due to cracks within the sample which is resulting in a higher amount of friction at the surfaces of the cracks. This effect is represented in the course of the circumferential force, which first slightly increases and then decreases significantly before the complete failure of the sample. As there is an increase and a decrease in the course of the circumferential force, it is probable that there are two effects taking place at the same time: increasing energy-dissipation due to crack-induced friction and decreasing energy-dissipation due to increasing damage in the filler-network. To confirm this hypothesis, further investigations are necessary.

Analyzing the course of the phase angle, there is also a slight increase observable, which is at a maximum shortly before the complete failure of the sample. It also indicates the occurrence of friction within the material due to microscopic cracks, as already has been mentioned in respect to the circumferential force. When the phase angle reaches its maximum value after approximately 330000 revolutions the the energy dissipation due to friction on the crack surfaces of the samples is at a maximum, too. The following decrease of the phase angle shows the continued crack growth and the involved damage in the structure of the material. However, when the phase angle decreases to a value, which is significantly below the value before the catastrophic crack growth, this behavior cannot only be explained by effects from the sample geometry or the material itself. In fact, the phase angle has to stay constant independently

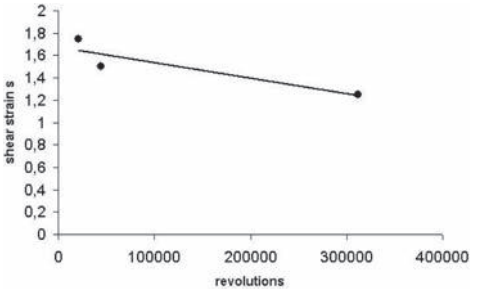

Figure 7. Lifetime behavior of sulfur crosslinked EPDM.

of the number of samples because it represents a material property. As both samples in the double-sandwich-arrangement consist of the same material and the change of the phase angle after the failure of one sample is always a decrease, it is improbable, that the difference in the phase angle can be explained with varying material properties due to processing effects. Therefore, the decrease has to have other reasons. A possible explanation for the difference in the course of the calculated phase angle before and after the failure of one sample is the influence of friction from the bearings. With the failure of one sample, the reaction forces and therefore the friction in the bearings decrease. To confirm this theory, further investigations are necessary. For an overview of the general lifetime behavior of EPDM under simple shear load with rotating axes, measurements with varying amplitudes have been realized. Figure 7 shows the results of long time fatigue experiments with shear strains of $s_1 = 1.25$, $s_2 = 1.5$ and $s_3 = 1.75$. Each point represents the mean of the results from two experiments. As can be seen in Figure 7, the lifetime of the material decreases with an increasing shear strain.

The axis of abscissae shows the number of revolutions till failure, the ordinate shows the shear strain.

The criterion for failure is defined with the complete break of one sample in the double-sandwich-arrangement. The state of the other sample has not been taken into account.

2.4 *Mechanical characterization*

With the help of the simple shear deformation with rotating axes, a mechanical characterization of rubberlike material is possible. For this purpose, a loadcase according to Figure 8 is put into practice.

The principle is to drive the shear strain towards determined positions and keep the loading for a certain time. In the example, shear strains from 0 to 1.75 in steps of 0.25 have been realized one after another. Each strain level has been kept for ten minutes of time. After reaching the maximum strain level, the procedure is repeated in reversed order and the samples are unloaded. Again, each strain level is kept for ten minutes. Figure 8 shows an exemplary measurement with sulfur cross linked NR.

The sinusoidal behavior of the curve can be attributed to minor inhomogeneities in the samples, which are expanded due to beating effects. Those beating effects are caused by the superposition of the rotational speed of the testing machine and the measurement frequency. Regarding the radial force, stress softening effects can be observed. Especially for the higher amplitudes it can be seen, that the radial force decreases over the time with an increasing number of revolutions. Moreover, the stress softening effects can be shown with the help of a direct comparison of the values for the radial force in the loading and in the unloading process. It can be observed, that during the unloading process the

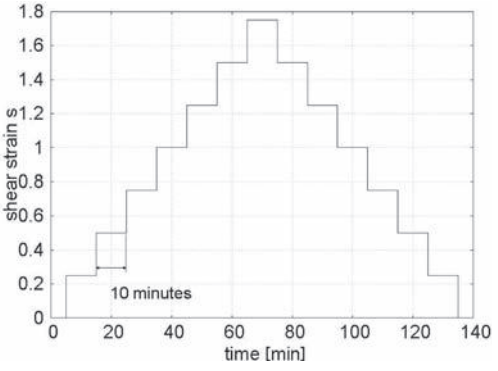

Figure 8. Loadcase for a mechanical characterization under simple shear load with rotating axes.

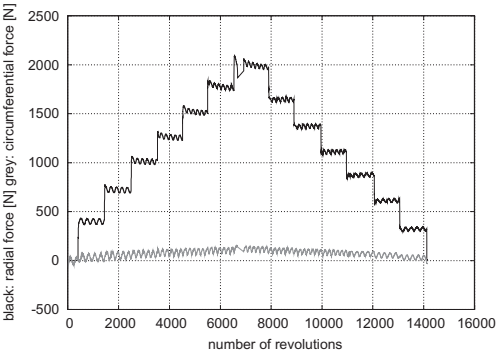

Figure 9. Example measurement for the characterization of NR.

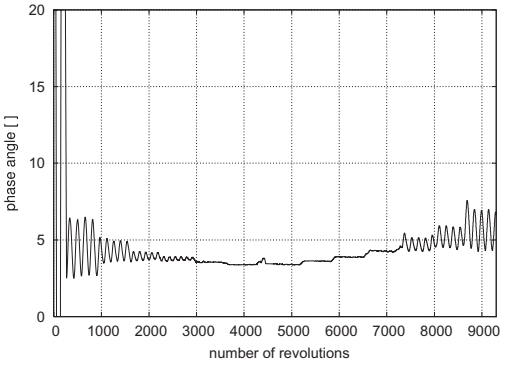

Figure 10. Phase angle of a NR during the mechanical characterization.

resulting force for a certain loading level is significantly lower, than in the loading process, although the samples have been deformed with the same shear strain amplitude. This behavior represents the Mullins-Effect (Mullins 1948). Analyzing the behavior of the radial force, it can be found that it increases with an increasing loading level.

With the help of the radial and the circumferential force, the phase angle can be determined to show its dependence on the shear strain amplitude. For a better interpretation of the behavior of the phase angle, the calculated results have been filtered to suppress the influence of the beating effects. As can be seen in Figure 10, the phase angle is dependent on the shear strain amplitude. With an increasing shear strain the phase angle decreases.

At the beginning of the experiment the measured forces are comparatively small so that the quotient of those two values, which is according to equation 7 necessary to compute the phase angle, magnifies the beating effects. Therefore, the scattering is at a maximum for small deformations, which can be found at the beginning and at the end of the experiment and small for the larger deformations, which are situated in the middle.

3 CONCLUSIONS

First investigations, using the experimental rig for long time fatigue experiments under simple shear load with rotating axes show, that in contrast to elastic materials, a pure modulation of the loading direction has a significant effect on the lifetime of rubberlike materials. In that context, rotational symmetric cracks have been found and analyzed. In dependence of still unknown parameters, which will be identified in future investigations, the induced damage for the simple shear process with rotating axes can be even more pronounced than for comparable loadcases like simple shear or uniaxial deformations. Hereby, the life time experiments under the described loading conditions are not a substitute for the common lifetime investigations, but an extension for the characterization of the lifetime of inelastic materials. It is a major advantage of the new testing device, that in spite of the dynamic characteristic of the experiment, the mesurands stay constant in short-term-observation.

Beside the long time fatigue experiments, the simple shear deformation with rotating axes is suitable for the mechanical characterization of rubber. Especially effects like stress-softening and the determination of the phase angle can be realized easily. Hereby it could be shown, that the phase angle is dependent on the shear strain amplitude under the described loading conditions.

ACKNOWLEDGEMENTS

We like to thank the following consortiums of companies for the support of our project.

1. Adam Opel GmbH
2. Continental AG, Contitech AG, PHOENIX Traffic Technology GmbH
3. Freudenberg Forschungsdienste KG, Vibracoustic GmbH & Co. KG
4. GMT GmbH
5. Henniges Automotive GmbH & Co. KG
6. REMA TIP TOP
7. Veritas AG
8. ZF Boge Elastmetall

REFERENCES

Ahmadi, H.R., J. Gough, A.H. Muhr & A.G. Thomas (1999). *Bi-axial experimental techniques highlighting the limitations of a strain-energy description for rubber. *Dorfmann, A., Muhr, A. (eds.), Constitutive Models for Rubber, Balkema, Rotterdam 21.*

Gent, A.N. (1960). Simple rotary testing machine. *British Journal of Applied Physics 11.*

Ihlemann, J. (2003). Kontinuumsmechanische Nachbildung hochbelasteter technischer Gummiwerkstoffe. *Düsseldorf: VDI.*

Mullins, L. (1948). Effect of stretching on the properties of rubber. *Rubber Chem. Tech. 21.*

Constitutive Models for Rubber VI – Heinrich et al. (eds)
© 2010 Taylor & Francis Group, London, ISBN 978-0-415-56327-7

Rubber component fatigue life evaluation based on FE-modelling and material testing

R. Lillbacka
SP Technical Research Institute of Sweden, Building Technology and Mechanics, Borås, Sweden
FS Dynamics Sweden AB, Göteborg, Sweden

E. Johnson
SP Technical Research Institute of Sweden, Building Technology and Mechanics, Borås, Sweden

M. Bellander
Scania CV AB, Södertälje, Sweden

ABSTRACT: Rubber components are used extensively in, e.g., the automotive industry for vibration absorbtion whereby they are subjected to cyclic mechanical loading that can lead to fatigue failure. Therefore, it is vital that the fatigue life of the component can be estimated a-priori based on the knowledge of its service condition. In this paper an approach based on FE-modelling, in combination with fatigue material testing, is evaluated and compared to fatigue testing of the component. The studied component is a standard damper made of carbon black filled natural rubber (NR). Monotonic material tests are used for choosing the appropriate constitutive model and to determine the material parameters for the NR material. Moreover, the FE model of the component is verified using the digital image correlation system ARAMIS™. Based on the results from the FE calculations, and material fatigue testing, the fatigue life of the component is estimated using different fatigue measures, i.e., the maximum engineering strain, strain energy density and cracking energy density. The results show that the estimated fatigue lives of the component from the calculation approaches are similar. However, the comparison with the fatigue testing of the component shows that the fatigue life estimates are quite poor and that they are non-conservative. Some probable causes for this are also discussed.

1 INTRODUCTION

Rubber components are used extensively in, e.g., the automotive industry for vibration absorbtion whereby they are subjected to cyclic mechanical loading that can lead to fatigue failure. Therefore, it is vital that the fatigue life of the component can be estimated a-priori based on the knowledge of its service condition. Due to heat generation and the sensitivity of rubber material to increased temperature, fatigue evaluation of rubber components with testing must be undertaken at very low frequencies, often around 1 Hz. This makes fatigue testing of rubber time consuming and expensive which motivates the use of modelling and simulations to estimate the fatigue life.

In similarity with metals, the fatigue life is not only controlled by the loading range but also by the mean load (or R-ratio), by the multiaxial loading state and the sequence of loading cycles at variable amplitude loading. Compared to metals, rubber is more sensitive to environmental conditions such as temperature, ozone and oxygen. Rubber also shows a more complicated constitutive behaviour with initial transient softening of the stress-strain-curve (Mullin's effect), strain-crystallization in some rubber materials, hysteresis effects and viscous effects. Among these, fatigue life is especially affected by the strain-crystallizing effect. A strain-crystallizing rubber material will actually show a reversed influence on the R-ratio than what is found in other rubber materials and in metals in general. For a thorough discussion of the factors affecting fatigue life, cf. Mars (2001) and the references therein.

The fatigue failure process for rubber materials is generally divided into the crack nucleation and crack propagation parts, cf. Mars & Fatemi (2002). As a consequence of this, the different approaches used to predict the fatigue life of rubber components are also divided between those who consider the nucleation, Wang et al. (2002), Luo & Wu (2006), Kim et al. (2004) and Saintier et al. (2006)

or propagation, Busfield et al. (2005) of the cracks. In this paper, the crack nucleation approach will be pursued. More specifically, the maximum engineering strain, maximum strain energy density and maximum cracking energy density, cf. Mars (2001), will be used as measures of the fatigue damage.

The fatigue life of a standard damper used in the automotive industry, made of carbon black filled natural rubber (NR) having a hardness of 60 shore A, is analyzed using both FE calculations and testing. Monotonic material tests are used for choosing the appropriate constitutive model for the NR material and to determine the material model parameters. Moreover, the FE model of the component is verified using the digital image correlation system ARAMIS™ in monotonic component tests. Based on the results from the FE calculations, and material fatigue testing, the fatigue life of the component is estimated using the different measures of the fatigue damage and compared with the fatigue life obtained from component testing.

2 MATERIAL AND COMPONENT TESTING

2.1 *Material*

The studied component is made of a commercially formulated carbon black filled natural rubber (NR). The NR material is viscous, incompressible, isotropic and is able to withstand very large elastic deformations. During cyclic loading the NR material will soften initially, hence, for compressive load control this means that the measured compression of the component will increase during the loading. Furthermore, NR is a material that exhibits strain crystallisation, i.e., the stiffness of the material increases in the high loading end of each cycle due to the fact that the polymer chains become highly ordered. As a consequence of this there is a reversed dependence on the R-ratio as compared to metals. Hence, increasing the R-ratio with constant load range increases the fatigue life.

2.2 *Monotonic material tests*

Uniaxial tension and compression material tests, with prescribed deformation, were performed with the aim to evaluate different hyperelastic material models and choose the most appropriate. The tension and compression tests were performed according to the standards ASTM D412 and ISO 7743, respectively. The environment during the tests was a standard laboratory environment with room temperature and humidity. A total of 10 tensile and 2 compressive tests were done and a mean curve was fitted to the results by visually picking values, cf. Figure 4. The resulting curve shows the typical sigmoidal shape associated with rubber materials.

2.3 *Cyclic material tests*

Fatigue testing, according to the standard ASTM D 4482–99, was also performed on the NR material using Dumbell test specimens. The test material was delivered as sheets $300 \times 300 \times 2$ mm, from which the Dumbell test specimens were die cut. A Die C, but with 5 mm shorter waist section, was used in order to maximize the deformation (strain level).

The specimens were cycled between a maximum and minimum tensile strain at a frequency of 1.67 Hz. Two different R ratios, were considered; $R = 0$ and $R = 0.2$ where $R = \varepsilon_{\min}/\varepsilon_{\max}$. Different levels of maximum strain were also applied; 40, 50, 75, 100, 150, 200 and 250%. The number of cycles to failure (N_f), as a function of the applied maximum engineering strain ($\varepsilon^E_{\max}$), were recorded for the tests and also the load-deflection curves for the initial cycles. The number of cycles to failure is defined as the number of cycles until the specimen was completely ruptured. However, this coincides almost identically with the number of cycles until the first crack appears since the crack propagation time is very short compared to the initiation time. Since the load-deflection curve was recorded for the tests it was also possible to calculate the maximum strain energy density ($\mathrm{SED}_{\max}$) and maximum cracking energy density ($\mathrm{CED}_{\max}$) from the tests. These are defined as the maximum value of the SED and CED respectively in a cycle where these are defined as

$$\mathrm{SED} = \int_0^t \sigma_{ij}\dot{\varepsilon}_{ij}dt \quad \text{and} \quad \mathrm{CED} = \int_0^t r^T\sigma_{ij}\dot{\varepsilon}_{ij}rdt \qquad (1)$$

where σ_{ij} is the Cauchy stress, $\dot{\varepsilon}_{ij}$ is the symmetric part of the velocity gradient and the vector r is the normal to the crack plane. Thus, the SED is the area beneath the stress-strain curve and the CED is the part of the SED that is available for crack growth in different directions defined by r, cf. Mars (2001). It can be shown that, cf. Mars (2001), for a uniaxial tensile test SED = CED. This is based on the fact that the crack plane normal is parallel to the direction of stretching. Hence, the crack initiates and propagates perpendicular to the direction of stretching. It should be noted that the maximum engineering strain, strain energy density and cracking energy density are all independent of the R ratio since it is the maximum value during the cycle that is used. The results from the cyclic material tests were used to obtain equations relating the number of cycles to failure, N_f, to the applied

Table 1. Obtained parameter values from the curve fit using the test data from cyclic material tests.

	R = 0	R = 0.2
$N^f(\varepsilon^E_{\max})$	$A = 6.1*10^{10}$	$A = 2.4*10^{13}$
	$B = -2.95$	$B = -4.06$
$N^f(\mathrm{SED}_{\max})$	$C = 5.8*10^4$	$C = 1.3*10^5$
	$D = -1.78$	$D = -2.14$
$N^f(\mathrm{CED}_{\max})$	$E = 5.8*10^4$	$E = 1.3*10^5$
	$F = -1.78$	$F = -2.14$

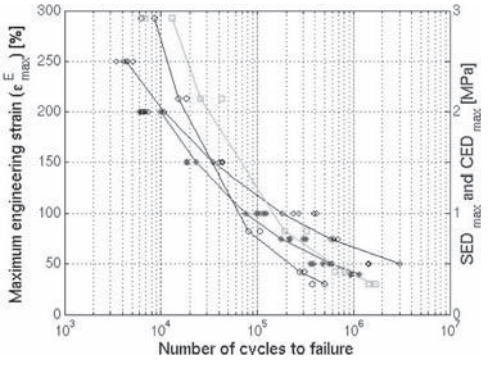

Figure 1. Experimental fatigue lifes for Dumbell test specimens and fitted curves as a function of: Maximum engineering strain ($\varepsilon^E_{\max}$) R = 0 [asterisk], Maximum engineering strain ($\varepsilon^E_{\max}$) R = 0.2 [diamonds], $\mathrm{SED}_{\max}$ and $\mathrm{CED}_{\max}$ R = 0 [circles], $\mathrm{SED}_{\max}$ and $\mathrm{CED}_{\max}$ R = 0.2 [squares].

maximum engineering strain, SED and CED. This was done using a curve fitting procedure in Matlab. The equations that were fitted are

$$N^f = A(\varepsilon^E_{\max})^B,\ N^f = C(\mathrm{SED}_{\max})^D \text{ and}$$
$$N^f = E(\mathrm{CED}_{\max})^F \qquad (2a, b, c)$$

for the different measures. The parameter values obtained from the curve fitting procedure are presented in Table 1 and the results from the tests and curve fit are presented in Figure 1.

2.4 *Monotonic component tests*

Compression tests in room temperature were done on the NR component in order to obtain input to the validation of the FE model. The component consists of a homogeneous rubber cylinder with an actual diameter of 47.5 mm and a length of 38 mm. The compression load was ramped to 7.0 kN with a velocity of 10 mm/min and thereafter the component was unloaded. The test-setup can be seen in Figure 2. The figure shows the load actuator at the top of the picture and the steel plates used to distribute the applied load to the component. During the tests the axial deformation was measured via the testing machine.

Moreover, the radial and tangential deformations and engineering strains were measured by the optical measuring system ARAMIS™. This system uses digital image correlation (DIC), with an arbitrary screen pattern that is applied with a spray bottle, to obtain point-wise deformations and strains at the surface of the component. The results from the component tests are given in Figures 6–7 and in Figure 8 where also the point at which the point-wise measures are taken is indicated. Note that, due to the large strains developed during the tests, the applied screen pattern was corrupted above 3.0 kN. This leads to missing parts in the load-strain curve, especially for the axial and major (tangential) engineering strains, which can be seen in Figure 7. The tangential and largest principal strain (major strain) coincide for the specific loading condition considered.

2.5 *Cyclic component tests*

The components were loaded using load control in an Instron 8501-machine with a control system MAX V5.2 and a sinusoidal wave form at a frequency of 1 Hz. The frequency was chosen such that the heating of the rubber material was kept low during the loading. The temperature increase of the rubber material was also measured during one of the tests and it was confirmed that the heating of the rubber could be neglected. Furthermore, the applied loading was compressive with maximum compressive loads ($\mathrm{P}_{\max}$) of: 3, 3.5, 4 and 5 kN. Moreover, two different R-ratios were used: R = 0 and R = 0.2 where the R-ratio is defined

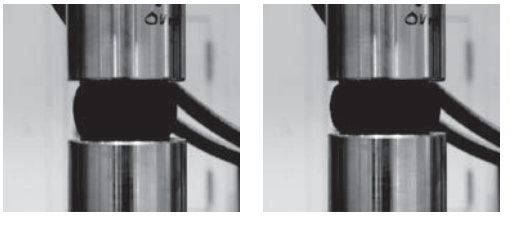

Figure 2. Test setup and load application. The rubber component, i.e. rubber cylinder and steel plates, is in the middle and the parts at the top and bottom are the fixtures used for controlling the rotations at load application. Load: 3 kN left and 5 kN right.

as $|P_{min}|/|P_{max}|$. Figure 4 shows the component at different load levels.

In order to avoid that the component was tilted, as cracks appeared, a guided fixture that eliminated rotations at load application was manufactured. Ocular observation of the component under testing was made, at least once per 24-hour period, with the main purpose to identify cracks. With a frequency of 1 Hz this means that the initiation time could be missed with a maximum of 86400 cycles ($60 * 60 * 24$). From the observations it was seen that the cracks initiated and propagated preferentially in the partition plane, i.e. the plane that occurs where the two halves of the mould used for moulding the rubber component meet. Further investigations, using microscopy, also revealed that the cracks start at the surface of the component. The propagation direction was parallel to the direction of the applied loading. Some cracks initiated at other locations than in the partition plane and these were also perpendicular to the applied loading. Finally it was seen that several cracks appeared and that crack coalescence was occurring. Figure 3 shows an example of a crack occurring in the partition plane.

The fatigue life of the component was recorded for the different applied maximum loads and R-ratios. The definition of fatigue life, used here, corresponds to the number of cycles for a crack to initiate (i.e. become visible). In Figure 10, the tested fatigue life as a function of the maximum applied compressive loading is shown for both $R = 0$ and $R = 0.2$. Furthermore, the same curve fitting procedure in Matlab, as for the cyclic material tests, was used to obtain curve fits to the data for $R = 0$ from the tests. The function that was fitted is

$$N^f = G_{\exp}\left(P_{\max}\right)^{H_{\exp}} \tag{3}$$

and the obtained parameter values are: $G_{exp} = 1.6509 * 10^9$ and $H_{exp} = -6.90$ No curve fit was done for $R = 0.2$ since the discrepancy in the recorded fatigue lives for this case is so large that this is not meaningful.

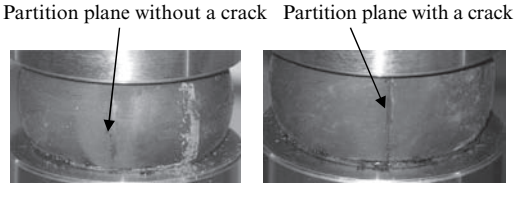

Figure 3. A crack is found at one side of the partition plane (right part of figure). The test is conducted at $R = 0$ and a maximum compressive loading of 5 kN.

3 FINITE ELEMENT CALCULATIONS

3.1 *Material model*

The studied component is made of natural rubber (NR) which is a viscous, isotropic and incompressible material that is able to deform elastically to very large strains. Therefore, the behaviour of the NR is modelled using an isotropic hyperelastic material model, whereby the large strains and the nonlinear elastic behaviour can be accounted for. Furthermore, the incompressibility of the NR is enforced by the addition of a pressure term in the finite element formulation (cf. below). Note that, since the unloading of the component was not considered, no attempt to incorporate the softening into the material model was done. Different hyperelastic material models were evaluated by comparing the calculated results with the experimental results for the uniaxial tension and compression tests described above. The material parameters for the different models were determined using the experimental results and a built in curve fitting procedure in the commercial FE-code Abaqus. The final result from the evaluation can be seen in Figure 4 below. Hence, most of the evaluated models give good predictions for compression and tension up to 100%, however, for larger tensile strains the Yeoh and Ogden models give the best predictions. Therefore, these two models were chosen for the calculations on the component.

3.2 *Geometry and mesh*

The NR cylinder (with diameter of 47.5 mm and a length of 38 mm, cf. above) was meshed by approximately 30 000 C3D8H elements. The C3D8H elements in ABAQUS are 8-node linear hybrid brick elements with constant pressure. These elements can be seen in Figure 5, where a half of the actual

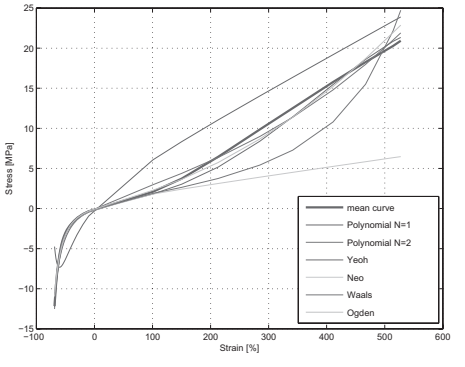

Figure 4. Experimental and calculated nominal (engineering) stress-strain curves for tension and compression.

meshed component is shown, coloured lilac. The constant pressure term is added, in the elements, in order to fulfil the incompressibility of the NR material. Furthermore, M3D4R membrane elements were added as a skin to the NR cylinder. These elements do not contribute to the stiffness of the NR cylinder and are only used to better resolve the strains in the surface, since the cracks initiate there. The NR cylinder is bonded to the steel plates at both the top and bottom and there is a steel pin at the centre of each plate. All steel parts are modelled as rigid since steel is much stiffer than NR.

The steel plates in the FE-model are modelled with a flat surface. In reality, the pin will stick out from the plate with 3 mm into the rubber cylinder. Another simplification that has been introduced is that the curve of the corner between the NR cylinder and the steel plate is neglected. However, since the cracks initiate at the surface of the component and preferably in the centre plane, between the upper and lower edges of the NR cylinder, these simplifications are deemed to not have any significant effect on the results.

The loading of the component was applied at the centre of the top end of the steel pin. Note that the unloading was not considered since it is the maximum strain that is of interest considering the different fatigue measures. All degrees of freedom for the opposite lower pin were locked. The considered output from the FE-model, i.e., strains, stresses, deformations and energies are integration point values corresponding to the point specified in Figure 8. This point is chosen due to the fact that the tangential (tensile) strain is maximized at this location and therefore the cracks should initiate at this location.

3.3 *Verification of the FE model*

The results from the verification of the FE-model, regarding axial and radial deformation and major engineering strain, are given in Figures 6 and 7 below. The results show that both of the calculated results using the Ogden or the Yeoh hyperelastic models correlate quite well with the experimental results. Furthermore, the distribution of the major (tangential) engineering strain from the tests and the FE calculations, with the Ogden hyperelastic model, are compared in Figure 8. These results also show that the measured and calculated results correlate quite well.

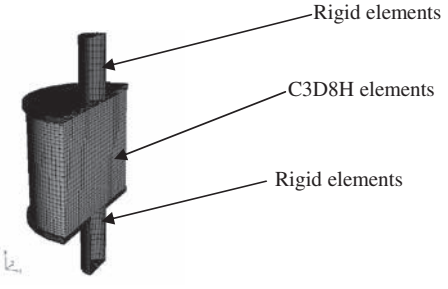

Figure 5. FE model of the component.

3.4 *Fatigue life estimation using FE modeling and material tests*

The finite element model (that is described above) for the component, with the Ogden hyperelastic material model, was used to calculate values for the different fatigue measures. During the compression, large tensile tangential strains develop at the surface of the component. These are maximized in the centre plane, between the upper and lower steel plates, according to Figure 8. Therefore, the point specified in Figure 8 was used for calculating

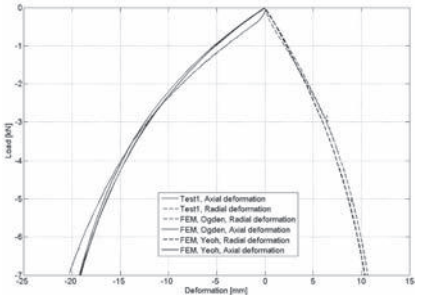

Figure 6. Measured and calculated axial and radial deformations for the Ogden and Yeoh hyperelastic models. Both the tested and calculated values are taken in the point specified in Figure 8.

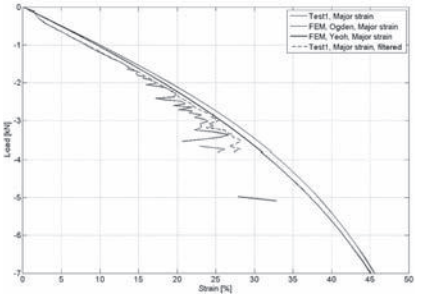

Figure 7. Measured and calculated major (tangential) engineering strain for the Ogden and Yeoh hyperelastic models. Both the tested and calculated values are taken in the point specified in Figure 8.

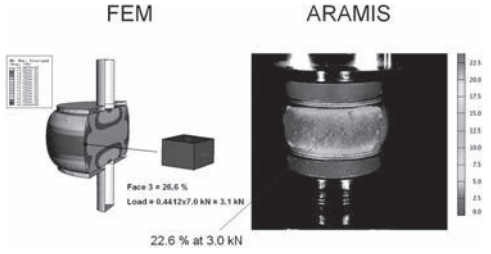

Figure 8. Measured and calculated major (tangential) engineering strain distributions for the Ogden hyperelastic model.

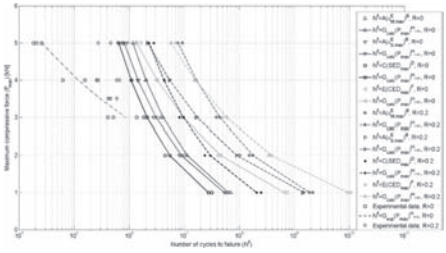

Figure 9. Calculated and tested fatigue life for the rubber component and fitted curves as a function of the maximum applied compressive force.

the different fatigue measures. More specifically, the different output that was needed from the FE-calculations, were obtained as integration point values corresponding to the point specified in Figure 8. The values of the maximum engineering strain and also the maximum SED (according to Eq. (1)) were obtained directly as output from Abaqus. Two different values for the maximum engineering strain were used, $\varepsilon^E_{S,\max}$ and $\varepsilon^E_{M,\max}$ where the S and the M corresponds to values obtained in the C3D8H solid and M3D4R membrane elements, respectively (cf. above). Note that the energy in the membrane elements is zero since they have no stiffness. The maximum CED is not available as output from ABAQUS. This has to be calculated from the integration point values of the Cauchy stress and the logarithmic strain, that are a part of the output from Abaqus. Furthermore, in order to calculate the maximum CED (according to Eq. (1)) the direction of the crack propagation has to be defined. The crack will propagate perpendicular to the direction of the largest principal strain, i.e. in the axial direction of the component, and hence, the vector r will coincide with the tangential direction of the component, i.e., $r = (1,0,0)$. An in-house Matlab program was written and used to calculate the value of the CED based on the output from Abaqus (Cauchy stress and logarithmic strain) and specified vector r.

All three fatigue measures, as a function of the load applied to the component, are presented in Table 2. The life of the component is obtained by using the calculated values of the different fatigue measures and the fatigue testing results for the NR material. Hence, we are able to insert the values of the different fatigue measures into Eq. (2a, b, c) and calculate the number of cycles to failure. Note that these calculations were performed for both R = 0 and R = 0.2 whereby the different parameter values in Table 1 have been used. The results are presented in Figure 9. Thus, the maximum compressive load, applied to the component, and the logarithm of the number of cycles to failure are plotted against

Table 2. Maximum engineering strain ($\varepsilon^E_{*,\max}$), strain energy density (SED) and cracking energy density (CED) as a function of the applied compressive loading on the component.

Load [kN]	1	2	3	4	5
$\varepsilon^E_{M,\max}$ [%]	9.9	19.0	26.7	33.0	37.8
$\varepsilon^E_{S,\max}$ [%]	11.0	21.0	33.0	43.0	54.4
$\mathrm{SED}_{\max}$ [MPa]	0.029	0.087	0.143	0.192	0.236
$\mathrm{CED}_{\max}$ [MPa]	0.005	0.025	0.061	0.107	0.154

Table 3. Parameter values for Eq.(4) obtained from the curve fit using the calculated fatigue life for the component for the different fatigue measures.

Data based on	G_{calc}	H_{calc}
$N^f(\varepsilon^E_{S,\max})$, R = 0	$6.36 * 10^7$	–2.48
$N^f(\varepsilon^E_{S,\max})$, R = 0	$5.40 * 10^7$	–2.94
$N^f(\mathrm{SED}_{\max})$, R = 0	$2.75 * 10^7$	–2.33
$N^f(\mathrm{CED}_{\max})$, R = 0	$6.57 * 10^8$	–3.83
$N^f(\varepsilon^E_{M,\max})$, R = 0.2	$1.90 * 10^9$	–3.42
$N^f(\varepsilon^E_{S,\max})$, R = 0.2	$1.52 * 10^9$	–4.05
$N^f(\mathrm{SED}_{\max})$, R = 0.2	$2.07 * 10^8$	–2.79
$N^f(\mathrm{CED}_{\max})$, R = 0.2	$9.30 * 10^9$	–4.60

each other. Furthermore, the same curve fitting procedure as for the experimental data can be utilized to give an equation relating the number of cycles to failure to the maximum applied compressive force to the component ($P_{\max}$)

$$N^f = G_{calc}(P_{\max})^{H_{calc}} \tag{4}$$

Note that the different fatigue measures and also the different R ratios will lead to different values

of the parameters G_{calc} and H_{calc}. These values are tabulated in Table 3.

4 DISCUSSION AND CONCLUSIONS

The first conclusion that can be drawn from Figure 9 is that there is a large difference between the calculated fatigue lives for the different fatigue measures. Furthermore, the difference is dependent on the applied maximum compressive load such that it is greater for smaller loads. This is a manifestation of the fact that the slopes obtained from the curve fits are different. The SED is the most conservative of the different fatigue measures whereas the CED and the maximum engineering strain from the membrane elements are the most non-conservative measures depending on the applied load.

From Figure 9 it is also evident that there is large difference in the calculated and tested fatigue lives for the component. More specifically, all of the calculated fatigue life estimates are non-conservative, hence, the estimated fatigue lives are much longer than the actual tested fatigue lives. This behaviour has also been reported by Kim et al. (2004) where they have compared tests and calculated fatigue lives of an engine rubber mount. Moreover, the parameters from the curve fits, using the tested or calculated fatigue lives, are different, cf. Eq. (3) and Table 3. Table 4, shows the quotient between the calculated fatigue life and the mean value of the tested fatigue life for the different applied maximum compressive loads. The smallest difference between the calculated and the tested fatigue life is obtained for a load of 3 kN, R = 0 and a fatigue life estimate based on the maximum SED (quotient 2.42) whereas the largest difference is obtained for a load of 5 kN, R = 0 and a fatigue life estimate based on the maximum engineering strain from the membrane elements (quotient 62.0).

Some probable causes for the differences in the calculated and tested fatigue lives are: (i) errors in the FE calculations that lead to erroneous values for the fatigue measures. However, these results have been verified using digital image correlation and it seems that the strains at the surface of the component are captured correctly. Further analysis of the initiation sites of the cracks have revealed that the cracks start at the surface and thus, the errors introduced by the FE calculations should be small, (ii) differences in the NR materials used for the material and component tests. Hence, the calculated fatigue lives are based on cyclic material tests using test specimens cut from a 2 mm thick NR sheet whereas the component has been moulded. Swelling tests revealed that there is a small difference in crosslink density between these two. However, the difference is so small that it can not explain the difference in the calculated and tested fatigue lives, (iii) there is a difference in the surface finish between the NR sheets and the component. Hence, the fact that both the slope of the curve fit and the fatigue life for the test and the calculations are different indicates that two different mechanisms are involved in the fatigue crack initiation in the component and material tests. A preliminary test that indicates the influence of the surface roughness has been performed. In this test the surface of the component was grinded such that the notch at the partition plane disappeared. Microscopy pictures of the grinded and original component are shown in Figure 10. Hence, the surface of the original component appears to be quite rough, especially near the partition plane. The component was then loaded with a maximum compressive load of 5 kN and R = 0. The recorded fatigue life for this test was 244 000 cycles which is a factor 10 more than for the components with a rough surface finish, (iv) the fact that monotonic stress strain data was used may have a significant impact on the results. As rubber shows stress softening, the material was characterised as being a little too soft compared to reality. Thus, when

Table 4. Quotient between calculated and tested fatigue lives as a function of the applied loading and R-ratio.

Load [kN]	3	4	5
$N^f(\varepsilon^E_{M,\max})/N^f_{\exp,mean}$, R = 0	4.9	12.2	62.0
$N^f(\varepsilon^E_{M,\max})/N^f_{\exp,mean}$, R = 0	3.6	8.7	43.1
$N^f(\mathrm{SED}_{\max})/N^f_{\exp,mean}$, R = 0	2.4	6.7	35.3
$N^f(\mathrm{CED}_{\max})/N^f_{\exp,mean}$, R = 0	11.0	19.0	53.6
$N^f(\varepsilon^E_{M,\max})/N^f_{\exp,mean}$, R = 0.2		32.0	20.5
$N^f(\varepsilon^E_{M,\max})/N^f_{\exp,mean}$, R = 0.2		20.0	12.4
$N^f(\mathrm{SED}_{\max})/N^f_{\exp,mean}$, R = 0.2		8.6	6.1
$N^f(\mathrm{CED}_{\max})/N^f_{\exp,mean}$, R = 0.2		29	15.3

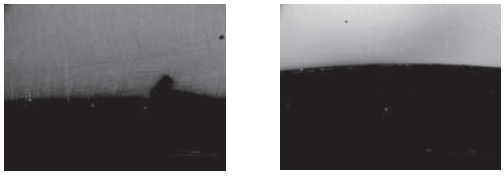

Figure 10. Microscopy pictures of the non-grinded (original) and grinded component in the left and right figure, respectively.

components were tested for their fatigue life, they were deformed more (higher strains) than what the models predicted.

ACKNOWLEDGEMENT

This work has been performed as a part of the RUBFAT project. Therefore we would like to acknowledge the companies that have provided valuable input and also partly funded the project and Swerea IVF which has been a research partner in the project.

REFERENCES

J.J.C. Busfield, V. Jha, H. Liang, I.C. Papadopoulos & A.G. Thomas. 2005. Prediction of fatigue crack growth using finite element analysis techniques applied to three-dimensional elastomeric components. *Rubber and Composites*, 34(8).

W.D. Kim, H.J. Lee, J.Y. Kim & S.-K. Ko. 2004. Fatigue failure life estimation of an engine rubber mount. *Int. J. Fatigue*, 26, 553–560.

R.K. Luo & W.X. Wu. 2006. Fatigue failure analysis of anti-vibration rubber spring. *Engng Failure Analysis*, 13, 110–116.

W.V. Mars, Multiaxial fatigue of rubber. 2001. *PhD Dissertation*, University of Toledo.

W.V. Mars & A. Fatemi. 2002. A literature survey on fatigue analysis approaches for rubber. *Int. J. Fatigue*, 24, 949–961.

N. Saintier, G. Cailletaud & R. Piques. 2006. Crack initiation and propagation under multiaxial fatigue in a natural rubber. *Int. J. Fatigue*, 28, 61–72.

B. Wang, H. Lu & G. Kim. 2002. A damage model for the fatigue life of elastomeric materials. *Mech. Of Materials*, 34, 475–483.

Constitutive Models for Rubber VI – Heinrich et al. (eds)
© 2010 Taylor & Francis Group, London, ISBN 978-0-415-56327-7

Fatigue design and test on Chevron rubber springs used in rail vehicles

R.K. Luo, W.J. Mortel & A.D. Spinks
Department of Engineering and Technology, Trelleborg Industrial AVS, UK

X.P. Wu
School of Civil Engineering and Architecture, Central South University, Changsha, China

ABSTRACT: This paper is about the fatigue design issues on rubber-to-metal bonded springs used in railway industry. The investigation, based on the actual fatigue loads, is carried out on these failed and modified products using a method of continuum mechanics. To simplify the simulation, a non-linear quasi-static analysis is carried out and then the residual stresses are superimposed to obtain the effective stress range to predict the metal crack initiation. For the rubber parts of the spring a three-dimensional effective stress criterion is employed to predict the fatigue crack initiation. The fatigue crack initiation for the metal parts of the failed component is predicted at 225 K cycles under specified fatigue load against total metal broken at 700 K cycles from the test. For the rubber spring, subsequently modified and optimised, the total fatigue life for the metal parts of the component, is 8.0 million cycles against 1.75 million cycles from the test without any crack observed. The rubber fatigue crack initiation is predicted at 90 K cycles against crack onset around 79 K cycles and crack length 40 mm at 145 K cycles from the test. From the design point of view it is important to optimize the rubber profile under this very tight allowable space to provide the maximum support of the metal interleaves and at the same time to meet the minimum requirements of the manufacture process.

1 INTRODUCTION

The Chevron Springs are operating worldwide in a diversity of service applications including LRV, Metro, Freight wagons, High Speed Passenger Coaches and Locomotives. This paper is about the fatigue design issues on rubber-to-metal bonded springs used in railway industry. The spring, as shown in Figure 1 during a fatigue test, consist of metal plates (cold-bent to a V shape) and bonded with four rubber layers through a moulding process. There are residual stresses left in the metal plate during the manufacture process. Recently a need to improve time and cost efficiencies to meet customer's requirement(1.25 million cycles) has caused an unexpected early fatigue failure (0.7 million cycles) of the component with no immediate explanation(see figure 2), which leads to an integrated fatigue evaluation project involving a number of departments. Previous dynamic analyses has produced excellent fatigue predictions for a railway vehicle bogie frame under actual operating environment without residual stresses, see Luo etc. But in this situation there are very high residual stresses involved. It is well know that residual stresses can play a key role on the fatigue lives of engineering components.

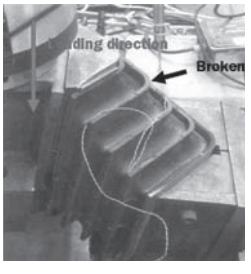

Figure 1. The Chevron rubber springs on the test rig.

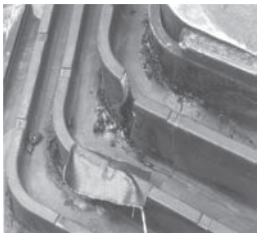

Figure 2. A metal failure of the Chevron rubber spring (after 0.7 million cycles).

1.1 *Metal fatigue with residual stress*

There are several experimental methods available to determine residual stresses. They include magnetic field, boring, slicing, surface and deep hole drilling, X-ray diffraction and neutron diffraction method etc. Webster etc.used the neutron strain scanning technique to measure the internal residual stress distributions of rails and compared with conventional destructive strain gauge results and theoretical predictions. Theoretical work has also done by many researchers. Chien etc. employed both linear elastic mechanics and linear fracture mechanics approaches to investigate the fatigue influence of residual stresses induced by the fillet rolling process on a ductile cast iron crankshaft section under bending loads. Their results have shown that it can only determine the crack initiation life for small cracks initiated on the surface, but cannot indicate whether cracks can propagate through or arrest in the compressive residual stress zone. Larue and Daniewicz used the crack closure-based methodology to simulate fatigue crack growth from a hole with a pre-existing compressive residual stress via two-dimensional elastic–plastic finite element analyses. They pointed out that predictions from the closure-based method are highly dependent on the constitutive relationship between the crack growth rate and the effective stress intensify factor range used, highlighting the need for experimental methods to reliably measure this correlation. The influence on residual stresses by heat treatment is also conducted. Williams etc. investigated the fatigue behaviour of a low-alloy powder metallurgy (P/M) sintered steel. Significant compressive surface stresses were generated during the machining of the fatigue specimens. A heat-treatment at 175°C after machining had no effect on these residual stresses, but polishing the surface resulted in a 20% reduction in compressive stresses. Webster and Ezeilo have concluded that reliable predictions of fatigue performance is possible as long as the accurate profile of the stresses is available. For the accurate assessment of fatigue lifetimes a detailed knowledge of the residual stress profile is required.

1.2 *Rubber fatigue*

In parallel with the metal fatigue it is also necessary to evaluate the rubber performance. Similar to the metal fatigue analysis there are two methods to deal with the rubber fatigue caused by mechanical failure: continuum mechanics (total life) and fracture mechanics (defect-tolerant). Roughly speaking the total fatigue life in continuum mechanics is defined as the sum of the number of cycles to initiate a fatigue crack to some predefined size. The defect-tolerant in fracture mechanics is based on that there are inherent flaws in all engineering products. The useful fatigue life is defined as the number of cycles to propagate the dominate crack from this initial size to some critical dimension. The principal differences may be dependent on how the crack initiation and the crack propagation stages of fatigue are quantitatively defined.

For the fracture mechanics approach it has been found that the most appropriate formulation is in terms of the strain energy release rate and there is a limiting tearing energy below which no crack propagation occurs, see Lake and Thomas. Gent etc. analysed bonded rubber cylinders, linking the crack propagation to the tearing energy. They obtained a life prediction equation in the form of power law. Busfield etc. used energy release rate to predict fatigue crack growth in three modes of deformation and validated with the experiment results. It is shown that the maximum strain energy release rate can be used to predict the direction of crack growth. The fatigue crack growth for one of the applications (a gearbox mount) under investigation was predicted within a factor of 2 at different displacements for all three modes of deformation. Timbrell and Muhr etc. used the strain energy release rate to investigate the failure of the "O" ring and provided some guidance to use this approach. Mars and Fatemi have reviewed the development of analysis approaches for predicting fatigue life in rubber. They concluded that the crack initiation has received less attention and an adequate multiaxial nucleation life approach is needed to accurately predict fatigue life in rubber component. Luo and Wu etc. used a three-dimensional effective stress criterion, taking all principal stress tensors into consideration, to predict fatigue crack initiation and validated against several engineering applications of anti-vibration rubber components. Charrier and Verron etc. suggested that the crack initiation method should be preferred at the early design stage for anti-vibration components.

In a summary instead of conducting detailed fatigue crack growth analysis the best approach here is to target the fatigue crack initiation on both metal and rubber parts of the component. The investigation, based on the actual fatigue loads, was carried out on these failed and modified products using a method of continuum mechanics. It was assumed that the residual stresses were well kept in the metal part. To simplify the simulation, a non-linear quasi-static analysis was carried out and then the residual stresses were superimposed to obtain the effective stress range to predict the metal crack initiation. For the rubber parts a three-dimensional effective stress criterion was employed to predict the fatigue crack initiation. The fatigue failure was taken as visual crack observation (normally 1–2 mm).

2 MATERIAL FATIGUE PROPERTIES

2.1 *Metal fatigue resistance*

The metal part is made from steel with yielding stress 355 MPa. The fatigue life of the metal part of the Chevron rubber spring can be estimated from the principal stress histories in the critical area in the structure using a duration curve from a design code. The current British Standard design code of practice for fatigue design and assessment of steel structures is BS7608. In BS7608, the material properties, the S-N relationships, have been established from statistical analysis of available experimental data (using linear regression analysis of log S and log N) with minor empirical adjustments to ensure compatibility of results between the various classes. The equations for the S-N curve relationship may be written in a basic form as

$$N\sigma_r^m = k_0 H^d \tag{1}$$

where N is the number of cycles to failure, σ_r is the stress range, m, k_0 and H are constants, and d is the number of the standard deviations below the mean. The standard basic design S-N curves (mean minus two standard deviations) are shown in Figure 3.

2.2 *Rubber fatigue resistance*

The material properties used are associated with a moderately filled (nominal 59IRHD) synthetic polyisoprene with good low creep performance.

Fatigue resistance can be represented by a curve which indicates a component failure at constant dynamic amplitude under a certain number of cycles. Normally a stress range against a cycle number forms a curve (S-N) to characterise the resistance of the material. Here the fatigue life estimation method was based on previously-obtained data for the rubber material used and on an effective stress (σ_f). σ_f was a function of the principal Cauchy stress ranges (σ_1, σ_2 and σ_3 are the maximum, middle and minimum principal stresses respectively) taking multi-axial loading effect.

$$\sigma_f = \sqrt{\sigma_1^2 + A\sigma_2^2 + B\sigma_3^2}$$

$$\sigma_1 > 0, \quad \sigma_1 \geq \sigma_2 \geq \sigma_3, \quad -1 < A\,(\text{or } B) \leq 1 \tag{2}$$

Here A and B are weightings and the following assumptions are made.

a. There is no fatigue damage when a point is under compression in all directions.
b. A (or B) is taken as positive when σ_2 (or σ_3) is positive (ie tensile).
c. The fatigue damage caused by any one of the other two principal directions will not exceed that caused by σ_1.

General speaking Equation (2) describes an ellipsoidal failure envelope, as shown in Figure 4. Under this definition any point on the ellipsoidal surface gives the same fatigue damage caused by a repeated cyclic loading.

There are now some procedures under consideration to give A and B. In one of the procedures, A (or B) is given the maximum value (1) for safety, provided that σ_2 (or σ_3) > 0 and the value 0 if σ_2 (or σ_3) ≤ 0. That is

$$A\,(\text{or } B) = 1, \quad \text{when } \sigma_2\,(\text{or } \sigma_3) > 0 \tag{3}$$

$$A\,(\text{or } B) = 0, \quad \text{when } \sigma_2\,(\text{or } \sigma_3) \leq 0 \tag{4}$$

The worst case is

$$\sigma_f = \sqrt{\sigma_1^2 + \sigma_2^2 + \sigma_3^2} \quad \sigma_1 \geq \sigma_2 \geq \sigma_3 > 0 \tag{5}$$

This criterion has all characteristics of a stress tensor and can be easily integrated with finite element codes (for example, Abaqus) and used in engineering applications. Under uniaxial loading

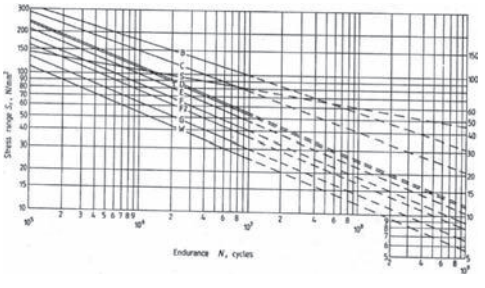

Figure 3. The S-N curve of the metal.

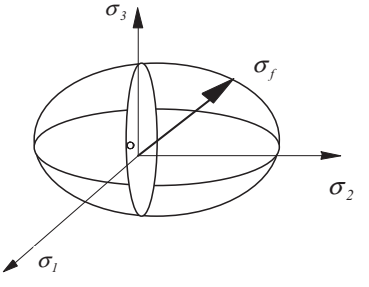

Figure 4. Illustration of the effective stress criterion.

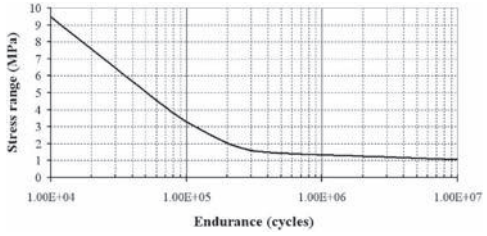

Figure 5. S-N curve of the rubber material.

condition ($\sigma_2 = \sigma_3 = 0$), the criterion is degenerated as $\sigma_f = \sigma_1$, which is the maximum tensile stress criterion. More details and definitions can be seen in Luo etc.

The rubber crack initiation is a result of the cumulative damage when visual cracks appeared (normally 1–2 mm). The fatigue resistance curve of the rubber material is shown in Figure 5.

3 FINITE ELEMENT MODELS AND FATIGUE LOAD

Finite element analysis has been used to predict the stress distributions and evaluate the fatigue behaviour. During fatigue tests a pair of the components has been arranged as a whole unit. The two parts have been fixed on a frame with 22 degrees apart, formed as a Vee shape. The nominal loading range is 60 kN.

3.1 *Two-dimensional finite element models*

In order to quickly evaluate the effects on stress values due to bending moment. A pair of two-finite element models of a cross section of the rubber springs, one was for failed component and the other was for a modified component, were generated. The difference between the two models is that the lengths of the rubber layers of the modified component are several millimetres longer than those of the failed component. A typical fatigue load was applied to both models. The results are shown in Figure 6 and Figure 7 respectively. It is clear that the stress value was dropped by 5.5% (from 600 MPa to 576 MPa) when adding extra rubber. It is possible that the excessive bending moment caused the earlier fatigue failure. The principle for the service life extension lies on the reduction of the stress range. Therefore having more rubber support on the metal interleaf can reduce the dynamic bending stresses. Further two three- dimensional-model (half of the part) have been used to evaluate the failed part and modified part respectively. The two models have used similar finite element mesh to form a comparable base

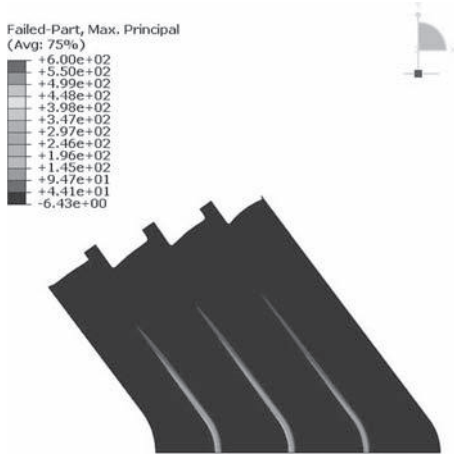

Figure 6. Stress profile of the failed component.

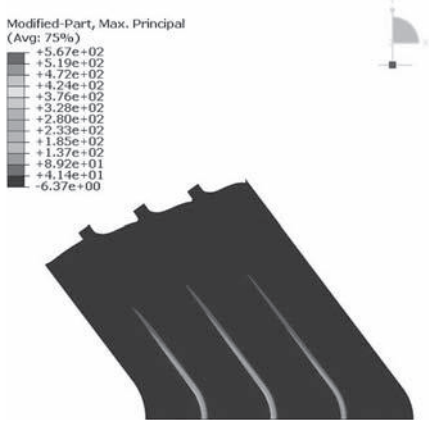

Figure 7. Stress profile of the modified component.

and have approximately 160,000 degrees of freedom each. The modified component has more rubbers between each layer than does the failed component. At the same time it is also necessary to meet the minimum clearance requirement for the manufacture process to improve time and cost efficiencies.

4 METAL FATIGUE VERIFICATION

The simulation of fatigue loading was carried out on both failed and modified Chevron rubber springs. The stress profiles of the failed part is shown in Figure 8. The stress ranges are valued at 613 MPa at first interleaf of the failed component and 460 Mpa, also at the first interleaf, for the modified component respectively. The critical areas

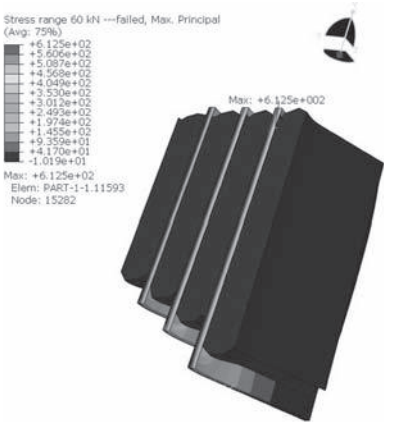

Figure 8. Stress profile of the failed part (the maximum value is 612.5 MPa).

are at the apex of the first interleaf from the back plate. The interleaf broken from the fatigue test for the failed part has validated the location predicted, see Figure 2. There is also a second highest stress area at the middle interleaf of the failed component but there is no failure observed.

The location of the early failure has been identified and validated. The next one is to validate the duration of the fatigue life based on the following approach.

As said before, the fatigue duration curves from BS7608 were used for the fatigue evaluation. The curves can be applied to both weld and non-welded structures. When it is used to estimate a service life, the result is the cumulative damage and hence the time taken for crack initiation to occur. The life derived from this standard is dependent not only upon stress ranges and the number of cycles encountered, but also upon the acceptable probability of failure. Here the class B with a 2.3 per cent probability of failure is used to validate the fatigue analysis. The steel has minimum yield stress 355 MPa. After the metal was bent to the required shape, a 355 MPa compression residual stress was generated on the inner surface. Therefore the stress range can be reduced to 258 MPa (from 613 MPa) for the failed part and 105 MPa (from 460 MPa) and the modified part respectively. Based on the duration curve (Figure 3) the fatigue life for the failed part is about 225 K cycles against test result about 700 K cycles (total metal interleaf fracture, see Figure 2). This is a reasonable estimation. It indicates a good agreement between the simulation and the test from the failed part. From the design point of view it is clearly explained that the unexpected early failure was due to the less rubber support for the metal interleaves. For the modified component, when the same principle was applied, a fatigue crack initiation of 8 million cycles was obtained. The prediction would meet the 1.25 million cycle requirement.

Based on the above prediction, it was decided to start the prototype manufacture and test procedure. Finally the modified component successfully completed 1.25 million cycles without metal broken, more requirement kept this test moving towards 1.75 million cycles. After the test finished all the metal parts have been carefully examined and no fatigue cracks found.

5 RUBBER FATIGUE VERIFICATION

In parallel with the metal fatigue prediction the rubber fatigue evaluation for the modified component was also carried out based on the three-dimensional effective stress method. Figure 9 shows the effective stress profile of the modified component. The critical area is at the second layer of the rubber from the back and located about 10 mm below the rubber top free surface. The value of the effective stress σ_f is 3.55 MPa. From the rubber design curve in Figure 5 the corresponded cycle number for 3.55 MPa is about 90 K.

Figure 10. shows the top part of the rubber spring after 79 K fatigue loading cycles. The blisters at the apex of the second layer of the rubber part can be clearly seen on the enlarged photo. There are no other sites showing the blisters. The fatigue crack appeared on the same area after the fatigue test passed 145 K cycles. The length of the crack is about 40 mm long.

6 DISCUSSIONS

For the fatigue design of the anti-vibration component it is important to optimize the rubber profile under this very tight allowable space to provide the

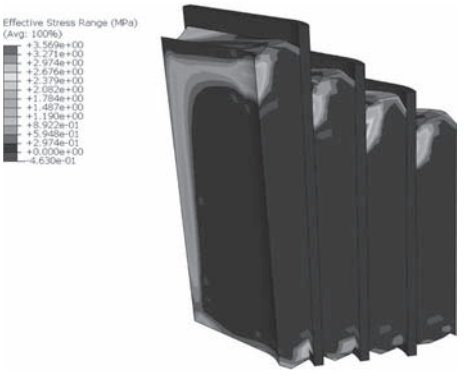

Figure 9. Effective stress profile (the red colour showing the critical area).

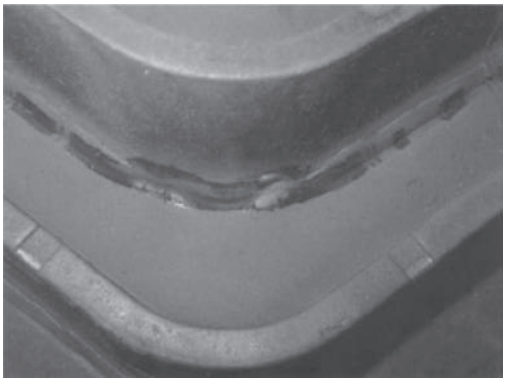

Figure 10. Rubber blisters in the Chvron rubber spring after 79 K cycles, the position of the blister is the same location as FEA indicated.

maximum support of the metal interleaves and at the same time to meet the need for time and cost saving requirements of the manufacture process. It is indicated that when a component is subjected to a bending dominated fatigue loading it may have significant influence on the service life even by a small change of the supporting areas.

The modified component has now manufactured and successfully entered the service. It is demonstrated that this approach can be employed at a suitable design stage for both metal and rubber fatigue evaluation on anti-vibration springs.

ACKNOWLEDGEMENTS

The authors thank Trelleborg IAVS allowing to publish this paper. Also the authors are very grateful to Mr. Foster and Mr. Crewe in Product Test Laboratory, Mr. Livingston in Engineering Support Department, Mr. Booth from Tooling Department, Mr. Edgar from Material Test Laboratory and Mr. Kenney from Quality Department for their support. X.P. Wu, one of the authors, would like to thank the support from National Natural Science Foundation of China(50578160/50878214);the Key Grant Science and Technology Research Planning Projects of The Ministry of Railway of Peoples Republic of China (2008G032-12;2008G017-C).

REFERENCES

Luo, R.K., Gabbitas B.L. & Brickle B.V., 1994, Fatigue life evaluation of a railway vehicle bogie using an integrated dynamic simulation, Journal of Rail and Rapid Transit, 208, 123–132.

Luo, R.K., Gabbitas B.L. & Brickle B.V., 1994, An integrated dynamic simulation of metro vehicles in a real operating environment, Vehicle System Dynamics, 23, 334–345.

Luo, R.K., Gabbitas B.L. & Brickle B.V., 1996, Fatigue design in railway vehicle bogies based on dynamic simulation, Vehicle System Dynamics, 25, 449–459.

Luo, R.K., Gabbitas B.L. & Brickle B.V., 1996, Dynamic stress analysis of an open-shaped railway bogie frame, Engineering Failure Analysis, 1(3), 53–64.

Webster P.J., Wang X., Mills G., Webster G.A., 2 June 1992, Residual stress changes in railway rails, Physica B: Condensed Matter, Volumes 180–181, Part 2, 1029–1031.

Chien W.Y., Pan J., Close D., Ho S., January 2005, Fatigue analysis of crankshaft sections under bending with consideration of residual stresses, International Journal of Fatigue, Volume 27, Issue 1, 1–19.

LaRue J.E., Daniewicz S.R., March 2007, Predicting the effect of residual stress on fatigue crack growth, International Journal of Fatigue, Volume 29, Issue 3, 508–515.

Williams J.J., Deng X., Chawla N., September-November 2007, Effect of residual surface stress on the fatigue behaviour of a low-alloy powder metallurgy steel, International Journal of Fatigue, Volume 29, Issues 9–11, 1978–1984.

Webste G.A., Ezeilo A.N., Supplement 1, 2001, Residual stress distributions and their influence on fatigue lifetimes, International Journal of Fatigue, Volume 23, pp. 375–383.

Lake, G.J., Thomas, A.G., 1982, Mechanics of fracture of rubber-like materials, Finite elasticity (A83-34326 15-39). The Hague, Martinus Nijhoff Publishers, 25–45.

Gent A.N., Chang T.Y.P., Leung M.B., April 1993, Fracture and fatigue of bonded rubber blocks under compression,Engineering Fracture Mechanics, Volume 44, Issue 6, 843–855.

Busfield, J.J.C., Jha, V., Liang H., Papadopoulos, I.C., Thomas, A.G., Oct 2005, Plastics, Prediction of fatigue crack growth using finite element analysis techniques applied to three-dimensional elastomeric components, Rubber and Composites, 34 (8), 349–356.

Mars W.V., Fatemi A., September 2002, A literature survey on fatigue analysis approaches for rubber, International Journal of Fatigue, Volume 24, Issue 9, 949–961.

Wu W.X., Cook P.W., Luo R.K. & Mortel W.J., 2004, Fatigue Life Investigation in the Design Process of Metacone Rubber Springs, Elastomers and Components: Service Life Prediction—Progress and Challenges, edited by V. Coveney, 189–201.

Luo R.K., Wu W.X., Cook P.W., & Mortel W.J., 2004, An approach to evaluate the service life of rubber springs used in rail vehicle suspensions, Journal of Rail and Rapid Transit, 218, 173–177.

Luo R.K. and Wu W.X., 2006, Fatigue failure analysis of anti-vibration rubber spring, Engineering Failure Analysis, Vol. 13, No. 1, 110–116.

Charrier P., Verron E., Ostoja-Kuczynski E., Marckmann G., Gornet L. & Chagnon G., 2003, Theoretical and numerical limitations for the simulation of crack propagation in natural rubber components, Constitutive Models for Rubber III, (Proceedings of the Third European Conference on Constitutive Models for Rubber), A.A. Balkema, 3–10.

BS7608, 1993, Code of practice for Fatigue design and assessment of steel structures, UK.

ABAQUS User Manual, 2008, Dassult Systems, USA.

Constitutive Models for Rubber VI – Heinrich et al. (eds)
© 2010 Taylor & Francis Group, London, ISBN 978-0-415-56327-7

Towards a new fatigue life characterization based on heat build-up measurements?

Y. Marco, V. Le Saux, S. Calloch & C. Doudard
Laboratoire Brestois de Mécanique et des Systèmes (EA4325), Brest, France

P. Charrier
Trelleborg Modyn, Carquefou, France

N. Ait Hocine
Laboratoire d'Ingénierie des MATériaux de Bretagne (EA4250), Brest, France

ABSTRACT: The temperature of rubber-like materials increases under cyclic loadings, due to its dissipative behaviour and low thermal conductivity. This well-known phenomenon, called heat build-up, has attracted the attention of researchers for a long time. But, to our knowledge, no published studies have tried to link this temperature rise to the fatigue life behaviour, as it can be done for many metallic materials. Three main points are discussed in this study. Firstly, a specific experimental protocol has been developed to capture the instantaneous heat build up. Based on this protocol, a "heat build-up test" is denned in order to link the temperature rise to the principal maximum strain, which is a commonly used variable for fatigue life criterion. Secondly, a discussion on the correlation between these results and the fatigue life behaviour will be opened, illustrated for several industrial materials by a comparison between heat build-up measurements and fatigue life duration. Finally, X-ray tomography measurements have been achieved on specimens used for fatigue tests.

1 INTRODUCTION

Rubber-like materials are extensively used in industrial applications because of their ability to undergo large deformations and their damping behaviour. Elastomeric components used in the automotive industry, such as engine mounts or torque rod, are submitted to cyclic loadings and a good conception towards fatigue phenomenon is therefore a necessity to insure the safety of these structures.

Fatigue life properties are usually studied by submitting a specimen to a given cyclic load and measuring the number of cycles needed to reach an end-of-life criterion (crack of a given length, fracture of the specimen, stiffness loss). From these results, the so-called Wöhler curve, or "S-N" curve (Stress–Number of cycles) is built. This classical method presents at least two main disadvantages to be *reliable*: it requires long duration tests and a large number of specimens (at least 50 specimens) in order to have a good estimation of the phenomenon intrinsic dispersion. These two disadvantages obviously limit the study of fatigue life properties and the determination of the influence of some parameters (i.e. mean load, amplitude load, etc.) on these properties. To reduce this cost (in time and money), other methods have to be developed. For several years, different methods for the rapid estimation of mean fatigue limit of metallic materials based on temperature measurements have been developed. The aim of this paper is to investigate the opportunity to use these methods for rubber-like materials. In a first part, a heat build-up experiment and the associate analysis suitable for metallic materials is reminded. Based on this protocol, a heat build up experiment suitable for rubber-like materials is proposed. Taking into account the specific aspects of this kind of materials, the experiment relates the temperature rise to the maximum principal strain. In a third part, the relevance of a link between thermal measurements and fatigue life properties is discussed from results measured on fifteen industrial materials. Finally, X-ray microtomography measurements are carried out on specimens used for fatigue life characterization in order to compare the population of cavities to the thermal rise.

2 HEAT BUILD-UP MEASUREMENTS ON METALLIC MATERIALS

For several years, different methods for the rapid estimation of mean fatigue limit of metallic materials based on temperature measurements have been developed. The method is to apply successive series of given number of cycles for different increasing stress levels (figure 1a). For each stress level, the change of the temperature variation $\theta = T - T_0$ (where T is the current temperature of the sample during the test measured by a thermocouple or an infrared camera and T_0 its initial value) is recorded and the steady-state temperature $\bar{\theta}$ determined (figure 1b). Beyond a given limit it is observed that the steady-state temperature $\bar{\theta}$ starts to increase significantly (figure 1c). This change is correlated with a state where the fatigue limit is exceeded and can be related to the apparition of microplasticity, *i.e.* plasticity at a microscopic scale, that occurs in the material. A correlation between the mean fatigue limit and the stress level leading to the temperature increase can be empirically proposed (figure 1c). From a unique value on the Wöhler curve, which can be obtained by letting the last amplitude step runs until the sample breaks, and using an energetic approach based on a critical dissipated energy, it is also possible to reproduce the mean Wöhler curve (figure 1d). The main advantage of this technique is that it is possible to characterize the mean HCF (High Cycle Fatigue) behaviour using a single specimen in only half a day.

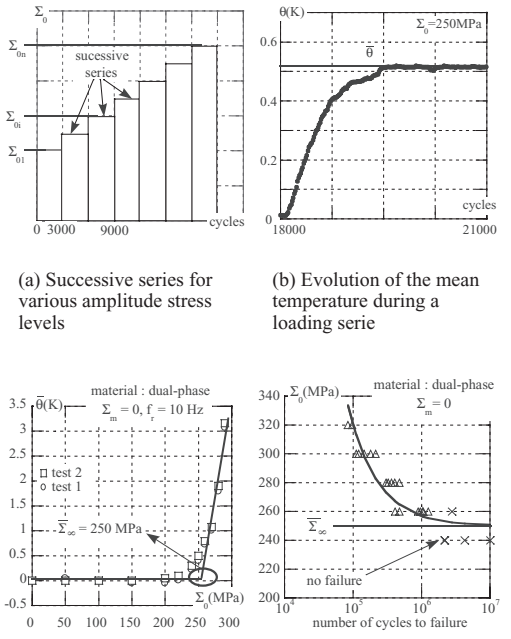

(a) Successive series for various amplitude stress levels

(b) Evolution of the mean temperature during a loading serie

(c) Evolution of the heat build up

(d) Mean Wöhler curve

Figure 1. Empirical method to correlate heat build-up measurements to fatigue life mean behaviour (Doudard et al. 2005).

3 DEVELOPMENT OF A HEAT BUILD-UP EXPERIMENT

3.1 *Temperature measurements*

A heat build-up experiment can be defined as a cyclic test during which the temperature of the specimen is measured. The number of cycles used is are the number of cycles needed for the temperature to stabilize. The first difficulty encountered to measure the temperature is linked to the large displacements of the specimen during a fatigue test. The use of thermocouples is to be avoided since this technology presents some limitations (fixation on the specimen, response time). We have chosen to use an infrared camera, which gives access to a 2-D measurements with an interesting acquisition rate (50 frames/seconds), even if it will only be a surface measurement.

The experimental protocol proposed is using a sequence of movies which allows temperature measurements whatever the deformation of the specimen (figure 2). One convenient approach is to consider the extremal positions of the specimen. As all experiments were carried out with a loading ratio equal to zero with displacement control, the non deformed and maximum deformed geometry are considered, as shown on figures 2b and 2c. With this processing, we get an envelope of the temperature variation and we are able to evaluate the coupling contribution (difference between the temperature measured in the maximum deformed position and non-deformed position).

3.2 *Heat build-up curve construction*

From the successive loads carried out on a AE2 specimen, we can generate a heat build-up curve by associating a fatigue life parameter to the steady-state temperatures. This parameter could be the maximum principal strain ε^I_{max} (Ostoja Kuczynski 2005), the maximum principal Cauchy stress σ^I_{max} or an equivalent stress (Saintier et al. 2006), the strain energy density W, the cracking energy density W_e (Mars 2001), or the minimum principal configurational stress Σ^* (Verron and Andriyana 2008). We have chosen to use the maximum principal strain as fatigue life parameter, which seems to

be the most natural parameter since our experiments are displacement controled. A heat build-up curve is therefore built from the steady-state temperature as a function of ε^I_{max} as illustrated on figure 3.

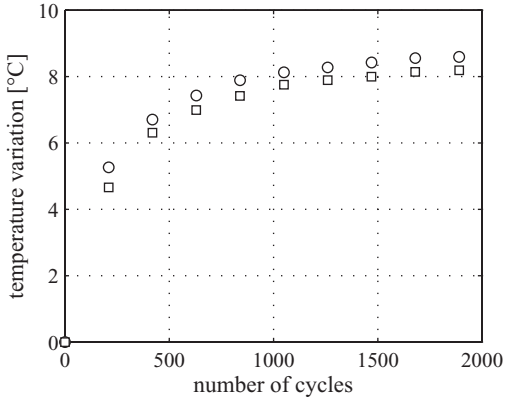

(a) Evolution of the temperature variation

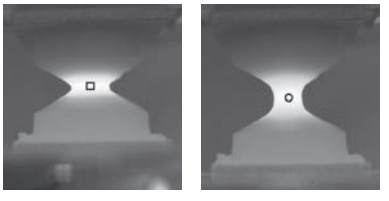

(b) non deformed position

(c) maximum deformed position

Figure 2. Evolution of the temperature envelope for one value of displacement amplitude.

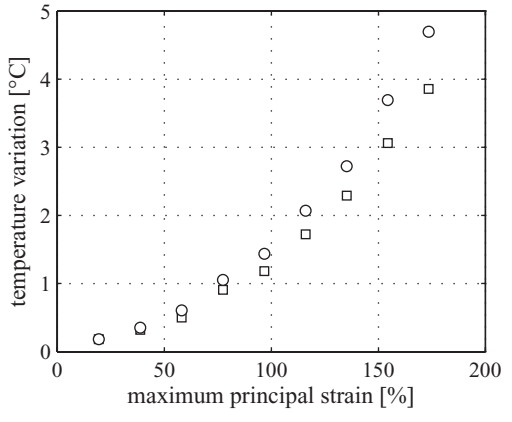

Figure 3. Heat build-up curve example.

4 A LINK WITH FATIGUE LIFE BEHAVIOUR?

4.1 *Is there an obvious correlation between heat build-up and fatigue life duration?*

Fifteen indutrial materials (with known tan δ and fatigue lifetime for a given amplitude) have been tested according to the test described previously, in order to compare the thermal response to their fatigue resistance. A few curves obtained during this campaign are plotted on figure 4. The main difference with the curves obtained for metallic materials is that none of the tested materials exhibits a brutal temperature rise. It is therefore difficult to determine a clear switch from non damaging loads (that is to say under a fatigue limit) to damaging ones. It is not very surprising, though, as the Wöhler curves obtained for elastomers usually show no clear fatigue limit and are still decreasing. Nevertheless, the classification of the curves are good for both fatigue resistance and tan δ. As this fact was observed for the other ten tested materials, a not yet resolved question is: what is really measured during a heat build up test? To give some clues on that question, other tests have been achieved on well chosen materials either showing the same tan δ but with different fatigue resistance, either having the same fatigue resistance but with different tan δ. These results are detailed in the next section.

4.2 *What stands behind heat build-up?*

Rubber-like materials are known to be hysteretic materials at a macroscopic scale, which means that some energy is dissipated or stored during a mechanical cycle. This hysteresis is not well

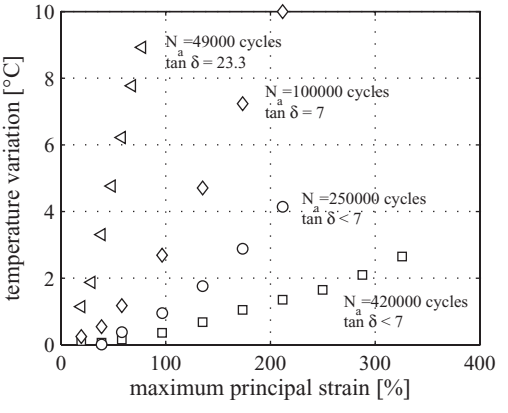

Figure 4. Heat build-up curves examples for various industrial materials. Only the temperature variations associated to the minimal position of the specimen are plotted.

explained and can be justified by several manners (Miehe and Keck 2000), ranging from interacting fillers, crystallization, viscosity, plasticity, damage, … The contribution of each of these sources are not clearly identified but it is usually assumed that viscosity is one of the most important. Figure 5 presents the curves obtained for three materials that have the same tan δ and different fatigue lifetime. We observe that for a first range of deformation (i.e. up to 80%), no clear differences in the temperature rises are to be seen but as the strain imposed increases, the three curves separates with significant differences (the precision on the temperature measurement is about 3/100°C), and the curves of the tested materials are ranking well according to their fatigue resistance. Nevertheless, it is difficult to propose a clear way to analyse these tests and one can see that a gap of 100 000 cycles in the initiation lifetime induce only a slight difference in the temperature curves. Other tests have been performed on materials that have the same fatigue lifetime (at a given amplitude of strain) but different tan δ. Figure 6 presents the results obtained and, there again, the curves are different and ordered according to their viscous properties. These results clearly show that a split between viscous dissipation and a dissipation related to the fatigue resistance is far less easy to identify for elastomers than for metallic materials. What should be noted is that the curves presented here are a not complete and have to be continued by letting the last amplitude step runs until the sample breaks. These curves will consequently be different even if the first steps are the same. Still, these tests afford interesting data and we wish to go further in their analysis by the use of modeling and physical measurements.

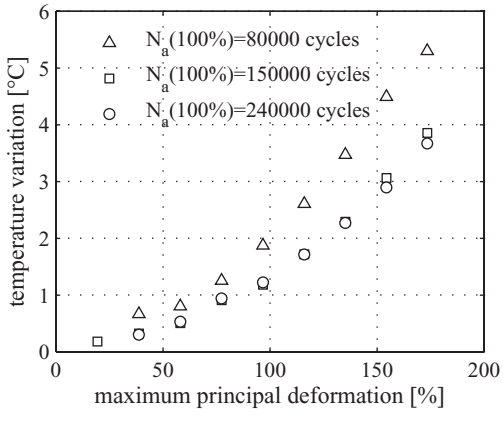

Figure 5. Heat build-up curves for materials having comparable tan δ, but different fatigue life behaviours.

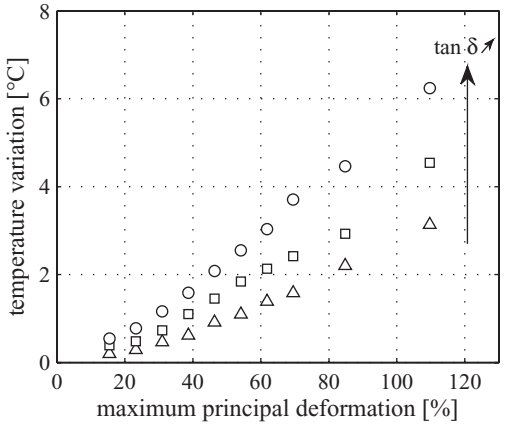

Figure 6. Heat build-up curves for materials having different tan δ, and same fatigue life behaviour.

4.3 *How can we use these tests?*

The first way to use these tests is to take advantage of the stabilization of the temperature rise under cyclic loadings to identify the parameters of a thermo-visco-hyperelastic constitutive model. As the final goal of this study is to try to quickly identify a fatigue indicator, the link could be done using two different approachs:

- the developement of a local criterion for fatigue crack initiation based on a dissipation approach, in a similar manner to (Lacroix et al. 2005)
- the proposal of a damage value that depends both on the dissipation given by the model and the number of cycles (Grandcoin 2008)

The second way implies to be able to follow the damage of the sample along the fatigue or heat build-up tests. One of the most useful techniques is X-ray microtomography (Le Gorgu Jago 2007). As an illustration, we present in the next section some results obtained during a fatigue campaign on a polychloroprene rubber.

5 EVOLUTION OF FATIGUE DAMAGE USING X-RAY TOMOGRAPHY

X-ray microtomography is a non destructive technique allowing investigating the density differences in a material. It is very useful for organic materials because their low density allows measurements on massive specimens with a reasonable time of exposition. The spatial resolution is about 5 µm and the use of a specific software allows the visualisation of the cavities and the quantification of the porosity (see figure 7) The figure 8 presents the fatigue campaign: several AE2 specimens were

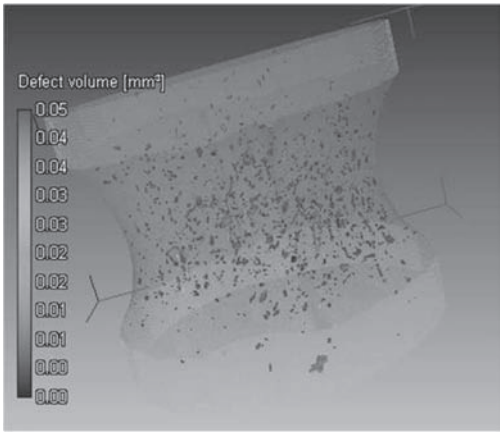

Figure 7. Example of cavities mapping in the central zone of a AE2 specimen.

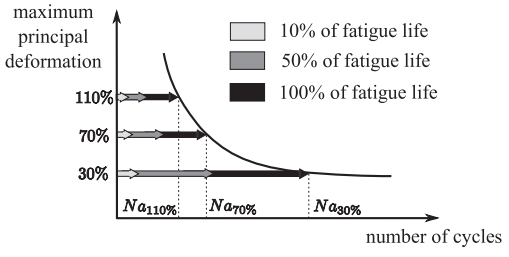

Figure 8. Evolution of the volumic density of cavities as a function of the number of cavities for the different discus.

submitted to cyclic solicitation with different levels of local maximal strain. For the three imposed strain levels, the tests were stopped for different fatigue lifetime (10, 50 and 100% of initiation lifetime, previously evaluated on another specimen). As shown on figure 9 and 10, the scale is representative of the fatigue mechanisms and very helpful to understand what happens during fatigue crack initiation and propagation. As the samples used present a section that evolves, it is possible to study several discus of the sample (see figure 11) and to associate (as a first approximation), the mean principal strain with the cavities populations measured. The figure 12 shows an example of that kind of analysis for a sample submitted to a high strain level and stopped at 10% of the initiation lifetime. Figure 13 shows the evolution of the cavities populations in the central zone for several strain level and lifetime percentages. We can observe that both the size and the number of the cavities are evolving with the strain level and the number of cycles.

The analysis of these results will afford very valuable data for the identification of damage evolution laws and fatigue criterion, based either on maximal dissipated energy or critical size or porosity. The application of this technique to heat build up

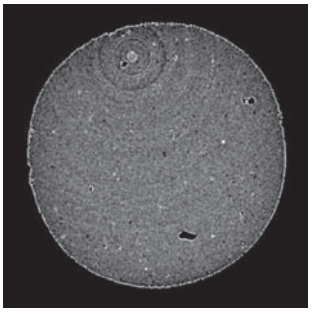

Figure 9. Population of cavities across a section.

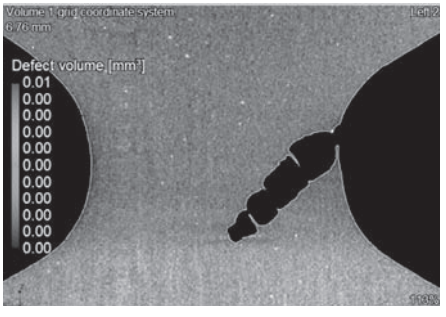

Figure 10. Representative picture of crack propagation mechanism: cavities coalescence behind the crack tip.

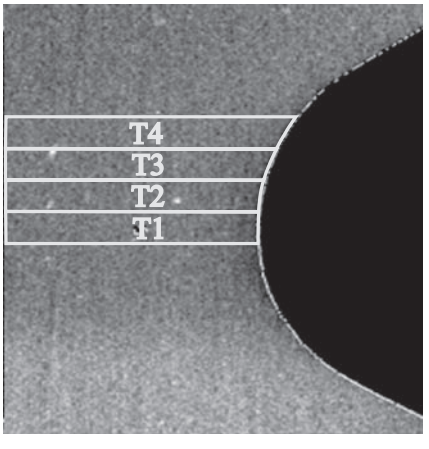

Figure 11. Decomposition of the central zone of the AE2 specimen into several discus.

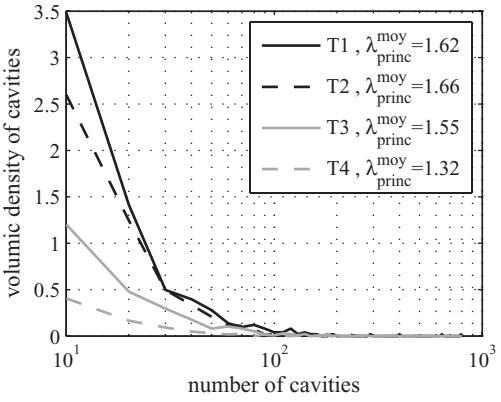

Figure 12. Evolution of the volumic density of cavities as a function of the number of cavities for the different discus.

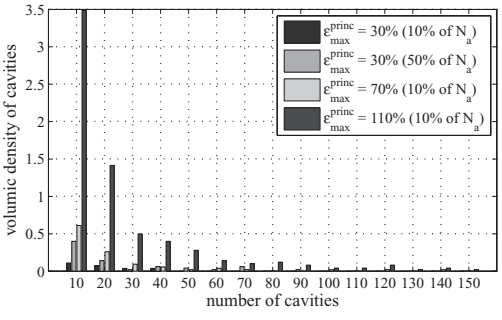

Figure 13. Evolution of the volumic density of cavities for different loadings and percentages of the lifetime expectancy in the T1 discus for a polychloro-prene rubber.

measurements is also scheduled and should be very helpful to discriminate viscous and cyclic damage contributions to the temperature rise.

6 CONCLUSIONS

In this study we focused on the development of a heat build-up test, which relates the maximum principal strain to the temperature rise. A first step was to propose an accurate measurement protocol allowing taking large displacements into account and that allowed discriminating the temperature rise induced by cumulative dissipation from the thermo-elastic contribution. More than twenty industrial materials were consequently tested in order to test the ability of that kind of test to be representative of the fatigue resistance of elastomers. These tests provided promising results but the highly viscous nature of these materials prevents any quick analysis and it will be necessary to use a dissipative hyperelastic model in order to dissociate the viscous contribution from what comes from microscopic damage. An important point is that the heat build-up test seems to be a very appropriate tool to identify the parameters of such a model since both mechanical and thermal responses are analysed. As illustrated in this paper for a fatigue study, microtomography measurements will be very valuable to help the understanding of what is seen during the heat build up tests and to feed the model with damage kinetics.

ACKNOWLEDGEMENT

The authors would like to thank the Britanny region for its financial support and all the actors of the FEMEM project (ENSIETA, Ifremer, Trelleborg Modyn, Trelleborg Offshore, DCNS-Brest, Cesman, UBO, Conseil Général du Finistére, Brest Métropole Océane, Région Pays de la Loire).

REFERENCES

Grandcoin, J. (2008). *Contribution à la modélisation du comportement dissipatif des élastomères chargés: d'une modélisation micro-physiquement motivée vers la caractérisation de la fatigue*. Ph.D. thesis, Université d'Aix-Marseille II.

Lacroix, F., S. Méo, G. Berton, F. Chalon, A. Tougui, and N. Ranganathan (2005, June 27–29th). A local criterion for fatigue crack initiation on chloroprene rubber: approach in dissipation. In *ECCMR IV*, Stockholm (Sweden).

Le Gorgu Jago, K. (2007, September 4–7th). Fatigue life of rubber components: 3D damage evolution from X-ray computed microtomography. In *ECCMR V*, Paris (France).

Mars, W. (2001). *Multiaxial fatigue of rubber*. Ph.D. thesis, University of Toledo.

Miehe, C. and J. Keck (2000). Superimposed finite elastic-viscoelastic-plastoelastic stress response with damage in filled rubbery polymers. Experiments, modelling and algorithmic implementation. *Journal of the Mechanics and Physics of Solids 48*, 323–365.

Ostoja Kuczynski, E. (2005). *Comportement en fatigue des élastomères: application aux structures antivibratoires pour l'automobile*. Ph.D. thesis, Ecole Centrale de Nantes, Université de Nantes.

Saintier, N., G. Cailletaud, and R. Piques (2006). Multiaxial fatigue life prediction for a natural rubber. *International Journal of Fatigue 28*, 530–539.

Verron, E. and A. Andriyana (2008). Definition of a new predictor for fatigue crack nucleation in rubber. *Journal of the Mechanics and Physics of Solids 56*, 417–443.

Constitutive Models for Rubber VI – Heinrich et al. (eds)
© 2010 Taylor & Francis Group, London, ISBN 978-0-415-56327-7

Identifying the damaging events in a multiaxial duty cycle

W.V. Mars
Cooper Tire & Rubber Company, Findlay, Ohio, USA

ABSTRACT: The duty cycle of a rubber component in field service often involves time-varying loads applied simultaneously from several directions—ie multiaxial loading. This contribution demonstrates an analysis whereby events occurring in a multiaxial duty cycle can be ranked according to their contribution to the overall damage rate. In order to account for the transformation of multiaxial loading into the experience of localized flaws, the duty cycle on each material plane is considered, along with its corresponding damage rate. Once the damaging events have been identified and ranked, the original duty cycle can then be simplified by constructing a new duty cycle composed from a number of the most damaging events in the original cycle. Calculations are made for a series of duty cycles reconstituted via this procedure, illustrating the degree to which minor cycles influence the overall damage rate, and the selection of the failure plane.

1 INTRODUCTION

Under dynamic loads, elastomeric components can fail due to the nucleation and growth of cracks, even when the loads remain always below the static strength of the material. Although much has been learned about the physics and phenomenology of such fatigue failures, there remains a great demand to integrate that knowledge into tools capable to address the materials and duty cycles that occur in everyday use. Consider, for example, that of all product design criteria, fitness for a given service life is often the most costly criterion to evaluate: 1) it is inherently destructive of expensive prototypes, 2) it calls for extended running times, and 3) it requires elaborate systems to apply loading history and collect measurements.

This contribution describes the application of a new tool—the Endurica™ fatigue life prediction code (www.endurica.com)—to a common task: the transformation of a long multi-axial, aperiodic duty cycle (perhaps a direct recording of service conditions) into an abbreviated duty cycle (perhaps suitable for use as an accelerated product development test). It is often not initially obvious which events contribute most to the fatigue failure process, and which events may be dropped from consideration. It is desired that the shorter duty cycle retain those features of the original cycle that produce the original mode of failure.

2 HISTORICAL CONTEXT

Systematic study of fatigue failure in rubber was made as early as 1940 (Cadwell et al.). Since then, a great deal of knowledge about fatigue in rubber has developed. Available reviews cover: the physics of strength and fatigue (Lake 2003, Persson et al. 2005), available approaches for fatigue analysis (Mars and Fatemi 2002, Mars 2007), the historical development of Fracture Mechanics (Thomas 1994), and factors that affect fatigue (Mars and Fatemi 2004).

The Fracture Mechanics approach has gained wide recognition, and has matured into well-accepted methods and tools. Rivlin and Thomas (1953) and Thomas (1955) proposed the tearing energy as a criterion for characterizing mechanical conditions at a crack tip. The criterion found immediate application in studies of what magnitude of loading would cause a crack to tear, and what would be its rate of tearing (Greensmith and Thomas 1955). It was also applied to cases involving dynamic loading (Thomas 1958). Early studies focused on fatigue crack growth occurring with the load fully relaxed between each application. Later, Lindley (1973) looked into the effects of non-relaxing cycles. The advent of Finite Element Analysis enabled the energy release rate to be evaluated for real components and structures under complex loading (Lindley 1972), and the approach has been implemented through a variety of schemes (Parks 1977, Shih et al. 1986, Shivakumar et al. 1988, Steinmann 2000, Mueller and Maugin 2002), and is commercially offered in several finite element codes.

A complementary paradigm, the Crack Nucleation approach, is also available. It consists in the idealization that cracks may appear at each point in a material, in any orientation, and that they do so according to a criterion defined in terms of parameters describing the loading state from a continuum viewpoint. In this approach, cracks are said to

"nucleate" or "initiate". Gent, Lindley, & Thomas (1964) showed that the fatigue lives of apparently uncracked tension specimens could be computed from the crack growth characteristics, along with assumptions that 1) microscopic flaws were present initially and grew according to a known rate law, and 2) the loading state of the crack was related to the far-field strain energy density (the continuum mechanical parameter) in the test specimen. Several workers (Mars 2002, Mars & Fatemi 2006a & b, Andriyana et al. 2008, Saintier et al. 2006a & b, Yeoh 2002, Gough & Muhr 2005) have further explored the continuum mechanical parameterization required to account for the mapping between far-field loading state and the crack loading state under multiaxial conditions. In this work, we apply the cracking energy density parameter introduced by Mars (2002). The cracking energy density represents approximately the portion of the strain energy density that is available for release by crack growth on a given material plane. It is worth noting that further efforts are currently underway with the aim to achieve a more exact connection between the fracture mechanics and crack nucleation approaches (Ait-Bachir et al. 2009).

Either the Crack Nucleation or the Fracture Mechanics approach may be used to determine how loads applied to a component are transformed into the localized experience of a given failure site. Once the localized experience is known, then an account can be made of how each individual loading event contributes to the overall development of the fatigue failure process. Procedures for identifying individual events have been developed for materials other than rubber (Downing and Socie 1982). They have been investigated and applied successfully to rubber (Harbour et al. 2007a, 2008a), taking care to account for rubber's unique dependence on time and R ratio.

3 PROBLEM STATEMENT

3.1 *Objectives*

Given:

- a strain-crystallizing elastomer with known elastic and fatigue properties.
- a duty cycle satisfying the plane stress condition, and consisting of 3 independent strain channels, each containing a range of low- and high-frequency variations.

Find:

- the Haigh and Cadwell diagrams corresponding to the specified material properties
- the loading history experienced by the most critical plane
- a listing of individual cycles in the history, ranked according to their relative contribution to the overall damage rate
- an abbreviated strain history reconstituted from the most damaging events, and retaining approximately the same failure plane as the original

Method:

- All calculations presented here were made with the version 2.17 Endurica fatigue life prediction code.

3.2 *Material properties*

The chosen material for this analysis represents a filled NR. The hyperelastic behavior is given via the Arruda-Boyce law (Boyce and Arruda 2000), with shear modulus $G = 3$ MPa, and locking stretch $\lambda_L = 4$, as shown in Figure 1.

Fatigue behavior is given via a fracture mechanical description. The efficiency of this approach lies in the fact that each test specimen produces observations of fatigue behavior over a range of conditions.

The crack growth properties under fully relaxing conditions are defined by the classical rate laws:

$$\frac{dc}{dN} = A(T_{\max} - T_0) \tag{1}$$

$$\frac{dc}{dN} = r_c \left(\frac{T_{\max}}{T_c} \right)^F \tag{2}$$

$$A = \frac{r_c T_t^F}{T_c^F (T_t - T_0)} \tag{3}$$

Here, $r = dc/dN$ is the rate of crack growth, and $T_{\max}$ is the peak crack driving force. When $T_{\max}$ is greater than a transition value T_t, equation (1) is

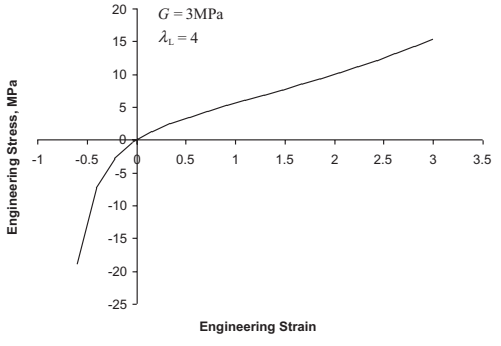

Figure 1. Simple tension/compression stress-strain behavior assumed in this analysis.

used, and when T_{max} is less than T_t equation (2) is used. T_0 is the mechanical threshold, below which no growth occurs. T_c is the strength of the material, r_c is the rate of fatigue crack growth occurring when the crack driving force reaches T_c. F is the power-law slope. We used the values given in Table 1.

The crack growth behavior under non-relaxing conditions is defined by a strain-crystallization function $F(R)$ (Mars 2009), which follows the Mars-Fatemi model (Mars and Fatemi 2003) in regarding that crystallization is implicitly represented in the relationship of power-law slope to the ratio $R = T_{min}/T_{max}$. The effect of the strain crystallization function is to retard crack growth under non-relaxing conditions, as illustrated in Figure 2.

3.3 *Duty cycle*

The original duty cycle is plotted in Figure 3. The cycle is defined in terms of three components of the nominal strain tensor (the remaining 3 components being completely determined by incompressibility, and by the plane stress condition), with each component given as a series of 1000 instants of time.

Table 1. Parameter values for fatigue crack growth rate law.

Parameter	Units	Value
r_c	m/cyc	10^{-6}
T_c	J/m^2	10^4
F	–	2
T_t	J/m^2	450
T_0	J/m^2	50

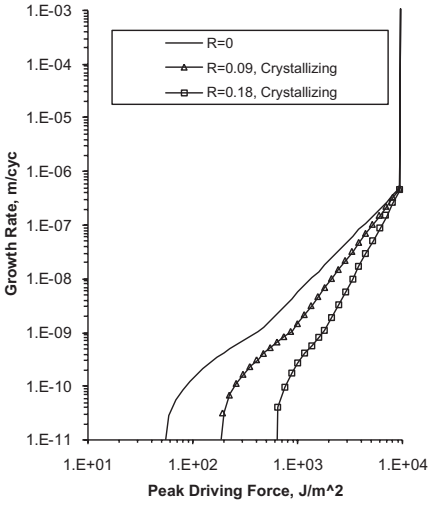

Figure 2. Fatigue crack growth behavior. Note the crack retardation effect afforded by strain crystallization.

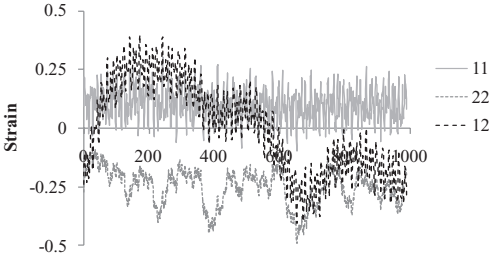

Figure 3. Original duty cycle in terms of nominal strain.

4 ANALYSIS

The basis of the calculation is integration of the damage law $da/dN = r(T,R)$. The integration starts at the naturally occurring flaw size a_0, and proceeds to the critical crack size a_f. We have used here $a_0 = 20 \times 10^{-3}$ mm, and $a_f = 1$ mm.

$$N = \int_{a_0}^{a_f} \frac{1}{r(T,R)} da \tag{4}$$

For purposes of evaluating the damage rate of variable amplitude histories, the linear rule studied in the work of Harbour et al. (2007b, 2008b) has been applied. That is, if a duty cycle is composed of M individual cycle events, then the rate of crack growth per application of the entire duty cycle is equal to the sum of the rates of the M individual cycles.

$$r = \sum_{i=1}^{M} r(T_{\max,i}, R_i) \tag{5}$$

As shown in Figure 4, the damage law is evaluated for each plane on which a crack might initiate, and the plane is then selected which minimizes the total life.

The loading history on the plane, which is used for evaluating equations (4) and (5), is determined through the cracking energy density W_c, obtained by integrating the definition

$$dW_c = \vec{S} \cdot d\vec{\varepsilon} \tag{6}$$

where $\vec{S}$ is the traction vector on the specified material plane tending to open and shear the crack faces, and $d\vec{\varepsilon}$ is the strain increment vector on the specified material plane. The energy release rate T

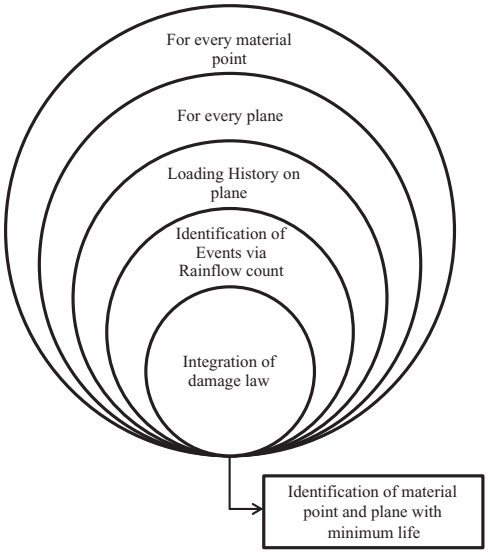

Figure 4. Fatigue life prediction algorithm.

was estimated through its postulated relation to the cracking energy density:

$$T = 2\pi W_c a \tag{7}$$

5 RESULTS AND DISCUSSION

5.1 *Haigh and Cadwell diagrams*

Representing constant amplitude crack nucleation behavior over a sufficient range of conditions is a prerequisite to the analysis of variable amplitude duty cycles. In our analysis, the specification of nucleation behavior is implicit through the definition of crack growth behavior and initial flaw size. As a check, we have computed crack nucleation behavior in two formats well-known to fatigue practitioners: the Haigh diagram and the Cadwell diagram.

The Haigh diagram, sometimes also called a 'constant life diagram', is essentially a contour plot in which lines of equal fatigue life are plotted in a space with axes representing the mean strain and the strain amplitude of the constant amplitude cycle. Figure 6 shows the results of our calculation. Contours are labeled according to their base 10 logarithm (so that 2 = 100 cycles, 3 = 1000 cycles, etc). Our computed results for the shape of the Haigh contours are consistent with experimental observations made by others (Andre et al. 1999, Oshima et al. 2007), especially in regards to the beneficial effects of large mean tension. For example, see Figure 5. Note that the computed results cover a wider range of operating conditions than has been reported in experimental studies to date. The difficulty of testing such a large experimental range is formidable.

The Cadwell diagram is an alternative format, first generated by its namesake (Cadwell et al. 1940), which also summarizes the dependence of the crack nucleation life on the oscillation limits of the constant amplitude cycle. In the Cadwell diagram, the base 10 logarithm of the fatigue life is plotted as a function of the minimum strain, with the strain amplitude held constant. A family of curves is then constructed by varying the strain amplitude. For a strain-crystallizing material, typical features include a local minimum of the crack nucleation life at a minimum strain of zero, and dual life maxima for compressive and tensile minimum strain. Our computed results are shown in Figure 7. Contours are labeled according to the

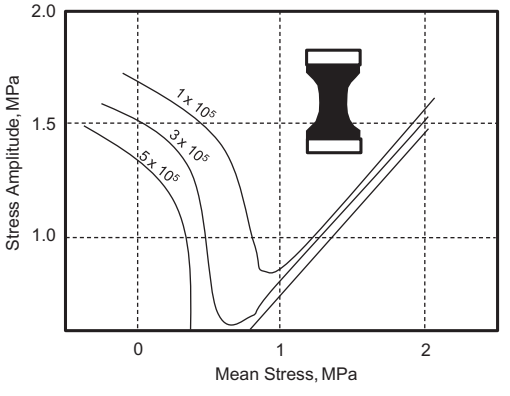

Figure 5. Partial Haigh diagram derived from crack nucleation experiments (Andre et al. 1999).

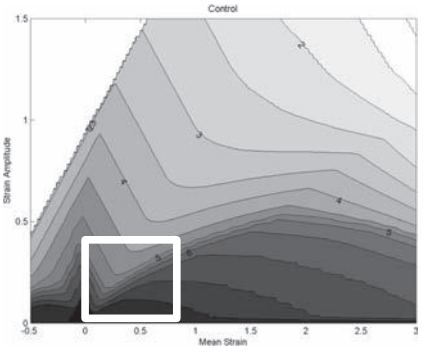

Figure 6. Computed Haigh diagram for the material studied. The white box highlights the region which may be compared to results in the previous Figure.

strain amplitude. Cadwell's results for a filled NR are shown in Figure 8.

5.2 *Loading history on the critical plane*

The failure plane was selected from among all possible planes to minimize fatigue life. The dependence of fatigue life on plane orientation is given in Figure 9. The failure plane is predicted to occur at an orientation of 4 deg.

The history of cracking energy density depends on the plane selected. The history corresponding to the plane of minimum life is shown in Figure 10. It can be appreciated that, on the selected plane, many of the individual loading cycles are non-relaxing, but the largest cycles are fully relaxing. The instant of most severe loading (at $t = 653$ sec) is also easily identified in this view.

5.3 *Contribution of events to the damage rate*

By applying a rainflow counting algorithm, the loading history from Figure 10 can be parsed into a list of individual events, and the damage contribution from each can be computed. Figure 11 plots T_{max} and R for each of the 253 events identified. The events are sorted in order from most damaging to least. Not surprisingly, the events contributing the most damage on the critical plane tend to be fully relaxing cycles with large peak values.

Figure 12 plots the initial crack growth rates of the sorted events, for a crack with the given initial flaw size.

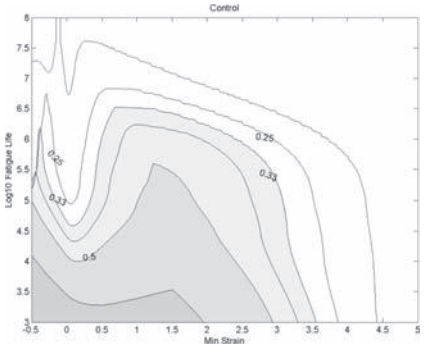

Figure 7. Computed Cadwell diagram for the material studied.

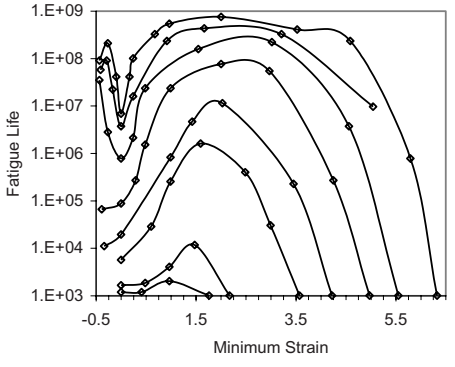

Figure 8. Cadwell's original results (Cadwell et al. 1940) for filled NR. Results are shown for amplitudes of 25, 33, 50, 125, 250, and 350%.

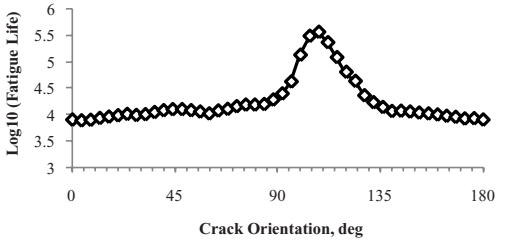

Figure 9. Dependence of fatigue life on crack plane orientation, for the original duty cycle.

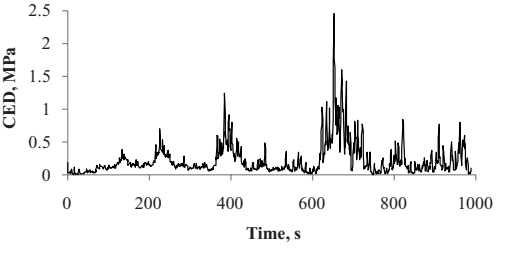

Figure 10. History of cracking energy density on the critical plane.

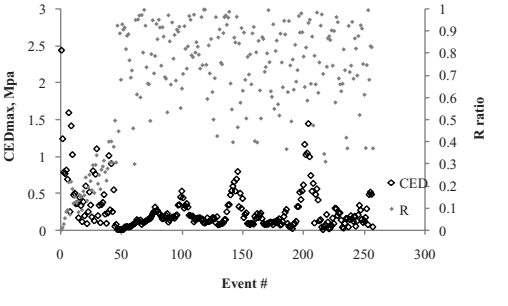

Figure 11. Identified events, ordered by contribution to damage rate. The peak CED and the R ratio are plotted for each event.

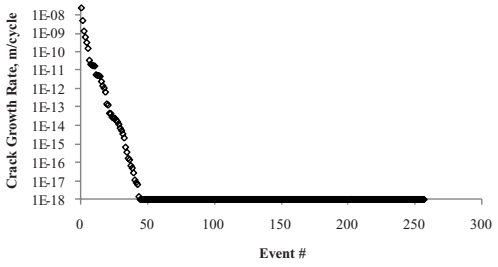

Figure 12. Initial damage rate associated with each event in the original duty cycle.

5.4 *Abbreviated strain history*

For each individual event considered, the rainflow algorithm returns indices enabling the instants of maximum and minimum loading to be identified in the original duty cycle. Knowing which events account for the largest damage contributions, the loading states at the corresponding times can be extracted, and used to reconstitute an abbreviated duty cycle. The abbreviated cycle can then be run through the life analysis to compare the failure plane and the computed fatigue life. Figure 13 shows how the life depends on the number of events retained.

Depending on the number of events retained, the distribution of damage among potential failure planes may vary considerably. Figure 14 compares the damage distributions for several different scenarios. The best approximation to the full cycle occurs when 64 events are retained. The life is only a factor of two longer, and the damage distribution is quite similar. The duty cycle corresponding to $M = 64$ events is shown in Figure 15. By removing $253 - 64 = 189$ events from the cycle, and their associated heating effects, an opportunity is created to shorten the time scale of the test.

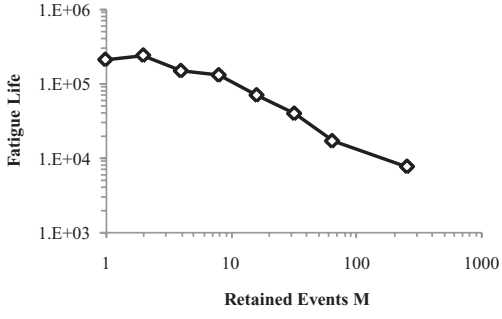

Figure 13. Computed life as a function of the number of events retained from the original duty cycle. The full cycle contains 1000 points, which produce 253 events on the critical plane.

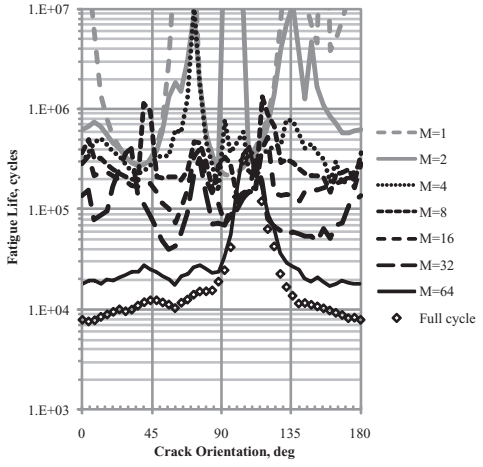

Figure 14. Influence of duty cycle abbreviation on the damage distribution among potential crack orientations. M is the number of retained events.

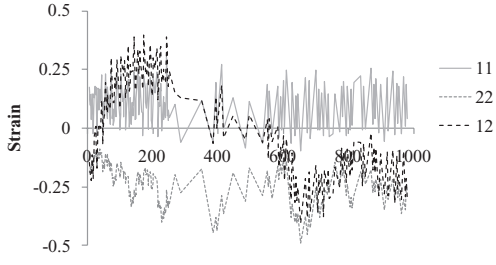

Figure 15. Abbreviated duty cycle, with $M = 64$ retained events.

6 CONCLUSIONS

A sufficient representation of fatigue behavior can now be made computationally to enable the completion of important fatigue design and evaluation tasks for rubber components. We have demonstrated, for example, that the Haigh and Cadwell diagrams can be computed, and that the damaging effects of a multiaxial, variable amplitude duty cycle can be traced to the most critical plane(s), and to the particular events that contribute most to the damage. This knowledge can be used to mitigate design deficiencies, and to construct abbreviated duty cycles that have nearly the same damage effects as the original.

REFERENCES

Ait-Bachir, M.A., Verron, E., Mars, W.V. 2009. Energy release rate of small cracks under finite, multiaxial straining, ECCMR Dresden, Germany.

Andre N., Cailletaud G., Piques R., 1999. Haigh diagram for fatigue crack initiation prediction of natural rubber components, *Kautschuk Gummi Kunstoffe*, 52(2): 120–123.

Andriyana A., Saintier N., Verron, E. 2008. Multiaxial fatigue life prediction of rubber using configurational mechanics and critical plane approaches: a comparative study. Constitutive Models for Rubber V: 191–196. Boukamel, Laiarinandrasana, Meo, Verron (eds), Taylor & Francis, London, ISBN 978 0 415 45442 1.

Boyce, M.C., Arruda, E.M. 2000. Constitutive models of rubber elasticity: a review, *Rubber Chemistry and Technology,* 73(3): 504–523.

Cadwell S.M., Merrill R.A., Sloman C.M., Yost F.L. 1940. Dynamic fatigue life of rubber, *Rubber Chemistry and Technology*, 13(2): 304–315.

Downing S.D., Socie D.F. 1982. Simple Rainflow Counting Algorithms, *International Journal of Fatigue*, 4(1): 31–40.

Gent A.N., Lindley P.B., Thomas A.G. 1964. Cut growth and fatigue of rubbers. I. The relationship between cut growth and fatigue, *Journal of Applied Polymer Science*, 8(1): 455–466.

Greensmith, H.W., Thomas, A.G. 1955. Rupture of rubber. III. Determination of tear properties, *Journal of Polymer Science*, Volume 18(88): 189–200.

Gough, J., Muhr, A.H. 2005. Energy release rates for small cracks in rubber components, Constitutive Models for Rubber IV: 51–57. Austrell & Kari (eds), Taylor & Francis, London, ISBN 0 415 38346 3.

Harbour, R.J., Fatemi, A., Mars, W.V. 2007a. The effect of a dwell period on fatigue crack growth rates in filled SBR, *Rubber Chemistry and Technology*, 80(5): 838–853.

Harbour, R.J., Fatemi, A., Mars, W.V. 2007b. Fatigue crack growth of filled rubber under constant and variable amplitude loading conditions, *Fatigue & Fracture of Engineering Materials & Structures,* 30(7): 640–652.

Harbour, R.J., Fatemi, A., Mars, W.V. 2008a. Fatigue crack orientation in NR and SBR under variable amplitude and multiaxial loading conditions, *Journal of Material Science*, 43(6): 1783–1794.

Harbour, R.J., Fatemi, A., Mars, W.V. 2008b, Fatigue life analysis and predictions for NR and SBR under variable amplitude and multiaxial loading conditions, *International Journal of Fatigue*, 30(7): 1231–1247.

Lake, G.J. 2003, Fracture mechanics and its application to failure in rubber articles, *Rubber Chemistry and Technology*, 76(3): 567–591.

Lindley, P.B. 1972. Energy for crack growth in model rubber components, *Journal of Strain Analysis*, 7(2): 132–140.

Lindley P.B. 1973. Relation between hysteresis and the dynamic crack growth resistance of natural rubber, *International Journal of Fracture*, 9(4): 449–462.

Mars, W.V. 2002. Cracking energy density as a predictor of fatigue life under multiaxial conditions, *Rubber Chemistry and Technology*, 75(1): 1–17.

Mars, W.V. 2007. Fatigue life prediction for elastomer structures, *Rubber Chemistry and Technology*, 80(3): 481–503.

Mars, W.V. 2009. Computed Dependence of Rubber's Fatigue Behavior on Strain Crystallization, *Rubber Chemistry and Technology*, 82(1): 1–11.

Mars, W.V., Fatemi, A. 2002. A literature survey on fatigue analysis approaches for rubber, *International Journal of Fatigue*, 24(9): 949–961.

Mars, W.V., Fatemi, A. 2003. A phenomenological model for the effect of R ratio on fatigue of strain crystallizing rubbers, *Rubber Chemistry and Technology*, 76(5): 1241–1258.

Mars, W.V., Fatemi, A. 2004. Factors that affect the fatigue life of rubber: A literature survey, *Rubber Chemistry and Technology*, 77(3): 391–412.

Mars, W.V., Fatemi, A. 2006a. Nucleation and Growth of Small Fatigue Cracks in Filled Natural Rubber Under Multiaxial Loading, *Journal of Materials Science*, 41: 7324–7332.

Mars, W.V., Fatemi, A. 2006b. Analysis of Fatigue Life Under Complex Loading: Revisiting Cadwell, Merill, Sloman, and Yost, *Rubber Chemistry and Technology*, 79(4): 589–601.

Mueller, R., Maugin, G.A. 2002. On material forces and finite element discretizations. *Computational Mechanics* 29: 52–60.

Oshima H., Aono Y., Noguchi H., Shibata S. 2007. Fatigue Characteristics of Vulcanized Natural Rubber for Automotive Engine Mounting (Characteristics of Composition and Mechanical Properties) *Memoirs of the Faculty of Engineering, Kyushu University*, 67(2): 75–83.

Parks, D.M. 1977. The Virtual Crack Extension Method for Nonlinear Material Behavior, *Computer Methods in Applied Mechanics and Engineering*, 12: 353–364.

Persson B.N.J., Albohr O., Heinrich G., Ueba H., 2005. Crack propagation in rubber-like materials, *Journal of Phyics: Condensed Matter*, 17: R1071–R1142.

Rivlin, R.S., Thomas, A.G., 1953. Rupture of rubber. I. Characteristic energy for tearing, *Journal of Polymer Science*, 10(3): 291–318.

Saintier N., Cailletaud G., Piques R. 2006a. Crack initiation and propagation under multiaxial fatigue in a natural rubber, *International Journal of Fatigue*, 28(1): 61–72.

Saintier N., Cailletaud G., Piques R. 2006b. Multiaxial fatigue life prediction for a natural rubber, *International Journal of Fatigue*, 28(1): 530–539.

Shih, C.F., Moran, B., Nakamura, T. 1986. Energy Release Rate along a Three-Dimensional Crack Front in a Thermally Stressed Body, *International Journal of Fracture*, 30: 79–102.

Shivakumar, K.N., Tan P.W., Newman, J.C. 1988. A virtual crack-closure technique for calculating stress intensity factors for cracked three dimensional bodies, *International Journal of Fracture*, 36(3): R34–R50.

Steinmann, P. 2000. Application of material forces to hyperelastic fracture mechanics. Continuum mechanical setting. *International Journal of Solids and Structures* 37: 7371–7391.

Thomas, A.G., 1955. Rupture of rubber. II. The strain concentration at an incision, *Journal of Polymer Science*, 18(88): 177–188.

Thomas, A.G. 1958. Rupture of rubber. V. Cut growth in natural rubber vulcanizates, *Journal of Polymer Science*, 31(123): 467–480.

Thomas A.G. 1994. Development of fracture mechanics for elastomers, *Rubber Chemistry and Technology*. 67(3): G50–G60.

Yeoh, O.H. 2002. Relation between crack surface displacements and strain energy release rate in thin rubber sheets, *Mechanics of Materials*, 34(8): 459–474.

Constitutive Models for Rubber VI – Heinrich et al. (eds)

The effect of pre-stressing on the equi-biaxial fatigue life of EPDM

N. Murphy
School of Manufacturing and Design Engineering, Dublin Institute of Technology, Dublin, Ireland

J. Hanley
Centre for Elastomer Research, Dublin Institute of Technology, Dublin, Ireland

S. Jerrams
Directorate of Research and Enterprise, Dublin Institute of Technology, Dublin, Ireland

ABSTRACT: Previous papers presented by the authors at ECCMR in 2003–2007 outlined the development of a dynamic equi-biaxial fatigue testing system for elastomers. The design iterations to achieve synchronisation of image capture with pressure measurement, instantaneous adjustment of parameters to allow constant stress amplitudes throughout testing and influence of test sample geometry were amongst the topics discussed. In the research presented in this paper, initially samples were fatigued at a constant engineering stress amplitude and a zero minimum engineering stress, allowing full relaxation of the samples between cycles, but comparative tests were then produced for samples subjected to the same engineering stress amplitude, but with non-relaxing conditions, i.e. a constant pre-stress, applied throughout the test. Results are presented showing that there is an increase in the fatigue life of the EPDM specimens when a pre-stress is applied to the samples within a specific range of peak engineering stresses. The results from these tests will be analysed in a further study to determine if failure occurs within a predictable range of complex elastic modulus and if this can provide a reliable basis for fatigue life prediction.

1 INTRODUCTION

Most rubber parts fail in fatigue and as a result establishing what the fatigue life of an elastomeric component will be has become a topic of increasing interest to materials scientists in recent years. Fatigue testing to date has generated results using equipment which loaded the specimens in uniaxial tension, combined tension and torsion or in shear. While these methods provide much useful insight into the fatigue behaviour of elastomers, they do not describe the full spectrum of elastomeric material behaviour under cyclic loading. It is desirable to test rubber cyclically in a variety of stress-strain modes to fully define dynamic material properties.

Dynamic bubble inflation is capable of loading test-pieces in equi-biaxial tension for any stress or strain amplitude and can record the total cycles to failure. This test method allows specimens to be fatigued to failure equi-biaxially and facilitates completion of the characterisation of fatigue life for all loading cases for a particular elastomer.

A fundamental question posed is the manner in which pre-stressing affects the fatigue behaviour of the rubber, where it is subjected to equi-biaxial dynamic loading. This is the motivation for this section of the research programme.

2 THEORY

Bubble inflation is assumed to comply with theory for applying pressure to a thin spherical shell structure possessing negligible bending stiffness, alternatively described as membrane theory.

Pressure p is applied to one side of a thin sheet with thickness t to cause it to inflate and produce a bubble-like shell. From the measurement of pressure p and the radius of curvature r the equation for stress at the pole can be determined from Equation 1.

$$\sigma = p \cdot \frac{r}{2t} \tag{1}$$

3 OBJECTIVES

Previous work carried out in the Centre for Elastomer Research (CER) at Dublin Institute of Technology showed that control of equi-biaxial dynamic tests by bubble inflation required cycling at constant controlled stress amplitudes.

Abraham et al. found that the fatigue life of a uni-axially dynamically loaded sample could be increased by pre-stressing (Abraham *et al*, 2001).

The uni-axial tests conducted on filled EPDM resulted in large increases in fatigue life when tensile pre-loads were applied.

The tests presented in this paper were carried out in order to establish if pre-stressing an equi-biaxially fatigued sample would result in increases in fatigue life for similar stress amplitudes.

4 MATERIALS

EPDM rubber of 70 Shore A hardness, cross-linked with sulphur and containing low activity carbon black was chosen for this investigation.

5 METHODOLOGY

Specimens of 50 mm original diameter and 2 mm original thickness were used. For the bubble inflation tests, these samples were clamped and dynamically inflated and deflated through a 35 mm diameter orifice. Prepared specimens had a pattern of dots applied to their surface. The deformation of this pattern during inflation and deflation was recorded by an optical system, allowing correlation to a specific stress value at the bubble pole for each image captured. Equi-biaxial testing of EPDM was carried out between constant stress limits of $\sigma = PR/2t_0$, as defined by Johannknecht et al for cyclic bubble inflation (Johannknecht *et al*, 2002) where t_0 is the original specimen thickness. These tests were intended to establish if the effect of pre-stressing was similar to that found by Abraham et al for the uni-axial case.

Illustrative results of the equi-biaxial fatigue tests are shown in the form of plots of $\sigma = PR/2t_0$ versus Stretch Ratio for specimens that have both pre-stressing and no pre-stressing (Figure 1).

The DYNAMET system used to carry out these tests was developed by the CER at Dublin Institute of Technology. DYNAMET enabled the specimens to be cycled between controlled stress limits. The bubble volume and pressure were monitored during cycling.

6 TEST RESULTS AND DISCUSSION

6.1 *Analysis of the effect of pre-stress on fatigue life*

A series of fatigue tests were carried out using the DYNAMET system, where samples were fatigued to failure with a minimum pre-stress applied. The fatigue lives of these samples were compared to those of samples fatigued without pre-stressing. These results are shown in the S-N curve in Figure 2 below.

As Figure 2 illustrates, pre-stressing for the dynamic equi-biaxial case under these conditions did not result in definitive increases in fatigue life for the EPDM samples. However, the outcome of these tests led to further investigation into the parameters used for stress control in cyclic bubble inflation.

6.2 *Stress-strain considerations*

Figure 3 shows the geometric relationships for the bubble inflation case.

Looking at the case of engineering stress in the inflated bubble case gives:

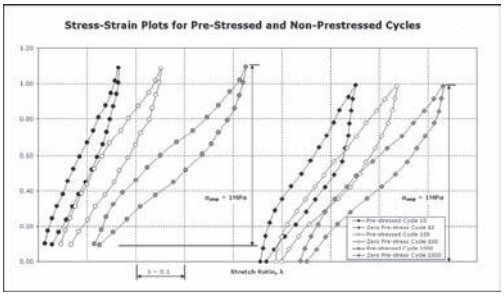

Figure 1. $\sigma = PR/2t_0$ versus Stretch Ratio for specimens that have both pre-stressing and no pre-stressing.

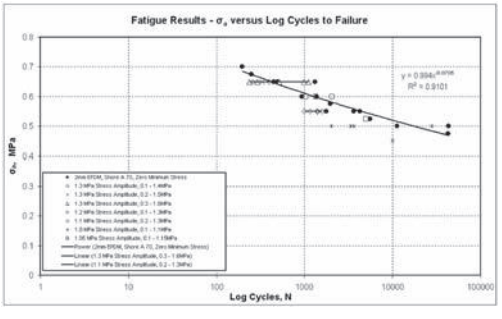

Figure 2. S-N curve for EPDM samples with and without pre-stressing.

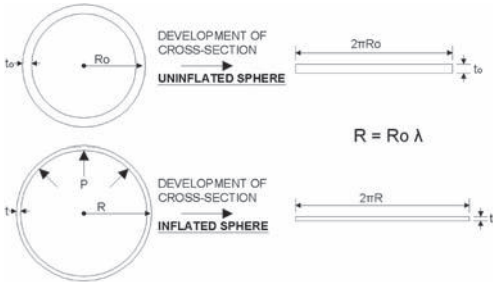

Figure 3. Geometric relationships for the bubble inflation loading case.

$$\sigma_{eng} = F/A_0 \quad (2)$$

$$F = \text{Applied Force} \quad (3)$$

$$A_0 = \text{Original Area} = 2 \pi R_0 t_0 \quad (4)$$

$$\text{Force} = \text{Pressure} \cdot \text{Resisting Area} \quad (5)$$

In terms of the resisting area of the bubble, this can be described by:

$$\text{Resisting Area} = \pi R^2 \quad (6)$$

$$\text{Force} = P \pi R^2 \quad (7)$$

It should be noted that the radius of the bubble can be described by:

$$R = \text{Radius of Inflated Bubble} = R_0 \lambda_1 \quad (8)$$

$$\text{Force} = P \pi R_0 2 \lambda_1^2 \quad (9)$$

$$\sigma_{eng} = F/A_0 \quad (10)$$

$$\sigma_{eng} = P \pi R_0^2 \lambda_1^2/2 \pi R_0 t_0 \quad (11)$$

By rearranging and with reference to equation (8),

$$\sigma_{eng} = PR \lambda_1/2 t_0 \quad (12)$$

When this relationship is compared to the standard method of calculating stress for the bubble inflation case (Equation 1), as shown in Figure 4, the changes in peak engineering stress with cycling using $\sigma = PR/2t$ as a control parameter are apparent.

This problem illustrates the effect of the principal stretch ratio $\lambda_{1,2}$ on the peak engineering stress value. When the value of λ at peak stress is analysed with respect to cycles, the relationship changes with the accumulation of cycles. To account for this change in λ over the duration of a test, compensation in the control system was included with respect to the change in λ versus the number of cycles accumulated during the test.

This alteration was incorporated into the DYNAMET control system. Figure 5 below shows the $\sigma_{eng} = PR \lambda_1/2t_0$ control for a series of inflation and deflation cycles.

6.3 *Analysis of fatigue results with pre-stressing*

A set of fatigue tests were again carried out where samples were fatigued to failure, again with one set being subjected to a minimum pre-stress and the other set being fatigued without pre-stressing.

In this case, $\sigma_{eng} = P R \lambda_1/2 t_0$ control was used in the dynamic testing of all specimens.

The results of these tests are shown in the S-N curve in Figure 6 below.

At values of peak engineering stress just below the rupture stress of the material, the samples are being subjected to fatigue cycles which induce high levels of damage into the sample, resulting in early failure due to rapid rupture of the specimen. Once the material is subject to loading below this region, in this case 2.0 MPa for non pre-stressed samples, the degree of damage incurred in loading cycles is reduced and crack growth conditions manifest until failure of the sample occurs.

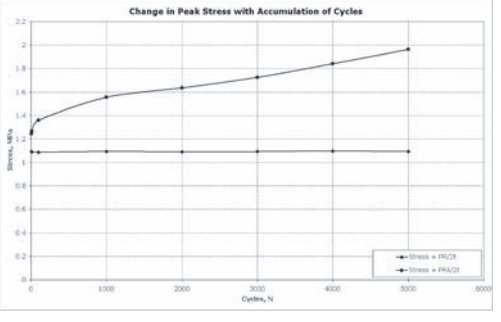

Figure 4. Changes in peak engineering stress with cycling using $\sigma = PR/2t$ as a control parameter.

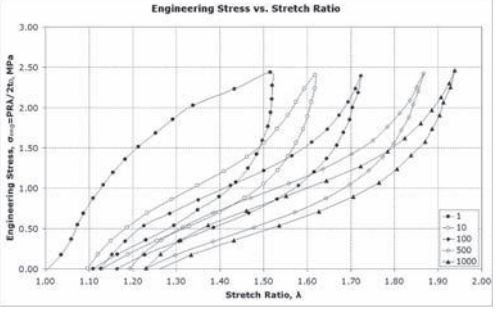

Figure 5. Plot of first 1000 cycles of a fatigue test, using $\sigma_{eng} = PR \lambda_1/2t_0$ control.

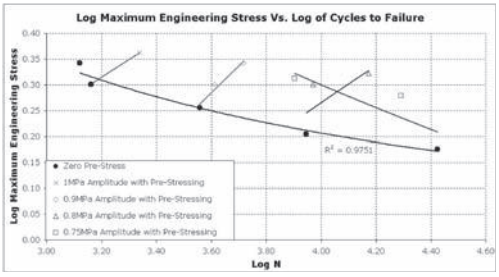

Figure 6. S-N curve for EPDM samples with and without pre-stressing, using $\sigma_{eng} = PR\ \lambda_1/2\ t_0$ control.

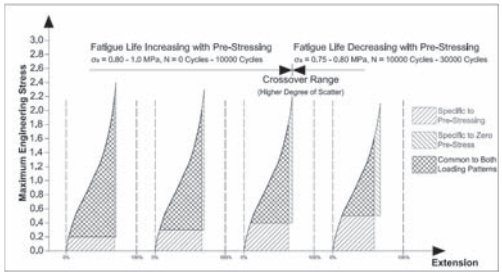

Figure 7. Effect of dynamic stored energy due to pre-stressing on fatigue life.

As shown in Figure 6, the fatigue life for pre-stressed samples increased over a specific range of stress amplitudes. However in this case, for stress amplitudes below $\sigma_a = 0.8$ MPa, pre-stressing did not show definite increases in fatigue lives and in fact reductions in fatigue life were recorded for lower stress amplitudes.

7 CONCLUSIONS

A method of controlling the upper engineering stress values in an equi-biaxial fatigue test has been developed and the results are presented. By monitoring the change in stretch ratio with accumulation of cycles, the peak engineering stress throughout a fatigue test can be controlled, allowing constant engineering stress equi-biaxial fatigue tests to be carried out for an elastomer. Using this method of loading, S-N curves for an elastomer can be generated which exhibit lower levels of scatter than those typically associated with uni-axial results.

The effect of pre-stressing in dynamic equi-biaxial fatigue of EPDM shows that below the high damage region of loading, increases in fatigue life have been recorded.

It is apparent from the results presented that the fatigue lives of samples cycled to a controlled equi-biaxial stress amplitude with pre-stressing is greater than that of samples cycled to the same stress amplitude with zero pre-stressing.

However, this effect is only apparent for very high maximum stress levels in the pre-stressed cycles. Figure 7 illustrates the variation in the effect of pre-stressing with changing engineering stress amplitudes.

The reduction in dynamic stored energy due to pre-stressing during any loading cycle is less influential on the total dynamic stored energy with decreasing peak stress limits and increases in the R_{ratio} for the material being tested where,

$$R_{ratio} = \sigma_{min}/\sigma_{max} \tag{13}$$

A point is reached below which the contribution of the stored energy solely attributable to the pre-stressing is not sufficient to increase fatigue life and in fact as the test programme continued, reduced fatigue lives of the samples tested were recorded for pre-stressed conditions with lower maximum engineering stresses.

Similar tests in uni-axial fatigue testing of filled EPDM (Abraham *et al*, 2001) have shown increases in fatigue life of EPDM with tensile pre-stressing. However, the range over which pre-stressing increased fatigue life was larger and pre-stressing results were not shown for samples in excess of 60,000 cycles. This may explain why the phenomenon shown in the equi-biaxial case has not been demonstrated for the uni-axial case. If uni-axial testing with pre-stressing for very high cycle lives does demonstrate a reduction in the effect of pre-stressing, it is postulated that equi-biaxial cyclic testing can demonstrate material characteristics common to both methods in a shorter period of time.

Another aspect to be examined is the possibility that pre-loading of EPDM does not give increased life across the full service load range in the uni-axial case. The authors intend to verify this and compare the results with equi-biaxial tests on similar compounds. This will determine conclusively if the effect is relevant within the normal service conditions of rubber components.

The results presented in this paper will also be investigated in further detail to determine if there is a limiting value of elastic modulus (E*) for the material at failure. This will determine if failure occurs within a predictable range of complex elastic modulus regardless of loading methods and can therefore provide a reliable basis for fatigue life prediction.

ACKNOWLEDGEMENTS

The authors would like to thank the Faculty of Engineering and the Directorate of Research and Enterprise in the Dublin Institute of Technology.

REFERENCES

Abraham, F., Alshuth, T., Jerrams, S., 2001. "Parameter Dependence and Prediction of Fatigue Properties of Elastomer Products". Rubber Chemistry and Technology Journal, Vol. 75, Issue 4, p 365, September/October 2002.

Hanley, J., Ph.D. thesis, Dublin Institute of Technology, Dublin, Ireland, 2008.

Jerrams, S., Hanley, J., Murphy, N., Ali, H., Equi-Biaxial Fatigue of Elastomers: The Effect of Oil Swelling on Fatigue Life, Rubber Chemistry and Technology Journal, Vol. 81, Issue 4, p 638–649, September/October 2008.

Johannknecht, R., Jerrams, S., Clauss, G. 2002. "Determination of non-linear, large equal bi-axial stresses and strains in thin elastomeric sheets by bubble inflation". Proceedings of the Institute of Mechanical Engineers, Vol. 216 Part L, No L4, (ISSN 1464-4207) Journal of Materials, Design and Applications.

Mars, W., Fatemi, A., RUBBER CHEM. TECHNOL. 77, 391 (2004).

Murphy, N., Hanley, J., McCartin, J., Lanigan, B, McLoughlin, S., Jerrams, S., Clauss, G., Johannknecht R. Determining multiaxial fatigue in elastomers using bubble inflation. In Constitutive Models for Rubber; Austrell, P.E., Kari, L., Ed.; Balkema, 2005; Vol. 4; p 65.

Murphy, N., Hanley, J., Ali H., Jerrams, S,. The Effect of Specimen Geometry on the Multiaxial Deformation of Elastomers. In Constitutive Models for Rubber; Boukamel, A., Laiarinandrasana, L., Méo, S., Verron, E., Taylor & Francis, 2007; Vol. 5; p 61.

Constitutive Models for Rubber VI – Heinrich et al. (eds)

Extended Wöhler curve to predict fatigue life of elastomeric components

M. Rabkin & Th. Brüger
Vibracoustic GmbH & Co. KG, Hamburg, Germany

ABSTRACT: An extension of the celebrated Wöhler curve in order to take into account the mean loading effect is presented. This extension describes the fatigue life of elastomeric parts as a function of two parameters of the damage variable: the amplitude and the R-ratio. The damage variable is defined on basis of the Green-Lagrange strain and can take positive as well as negative values. The parameters of the extended Wöhler curve characterise the material properties regarding the fatigue life under cycle loading. The experimental program to identify these parameters in a simple manner using a rubber specimen is developed. The different output form of the results of the fatigue life analysis is discussed. The comparison of the obtained extended Wöhler curves for NR and CR elastomers is given. An example of fatigue life prediction for real elastomeric components is demonstrated.

1 INTRODUCTION

The fatigue behaviour of natural rubber (NR) is commonly characterised by a Wöhler curve, which describe the relationship between the amplitude of the damage variable and the fatigue life under cyclic loading. The damage variable (e.g. stress, strain, strain energy density etc.) represents the response of the material with respect to its fatigue life. It is well-known fact that not only the damage variable amplitude but its mean value as well can have very significant influence on fatigue behaviour of rubber materials (mean loading effect). Neglecting this effect in fatigue life estimations can completely invalidate the predictions of the cycles-to-failure. The goal of this work is the development of an analytical description of the material fatigue behaviour under cyclic loading in order to incorporate the mean loading effect.

2 BASIC TERMS AND DEFINITIONS

2.1 *Strain state*

In the presented work the material response on the cyclic loading will be characterise only by means of the strain approach. This seems to be more appropriate for rubber parts (Eckwert et al. 2003).

Then there can be selected four different basic strain states: uniaxial (tensile and compression), plane strain and hydrostatic state (Holzapfel 2000). Assume the material is incompressible, i.e. for the stretches $\lambda_i\,(i = 1, 2, 3)$ is valid:

$$\lambda_1\lambda_2\lambda_3 = 1$$

In this case each of this basic strain states can be well-defined using only two stretches, for example λ_1 (maximal principal value) and λ_3 (minimal principal value). Note that the so called equibiaxial tensile strain state is, in strain view, identical to the compression state and in the case of the hydrostatic state all stretches are equal 1.

2.2 *Damage variable and damage parameters*

Here the damage variable is defined based on the Green-Lagrange strain. Consider the hyperelastic incompressible body under displacement controlled cyclic load w. It can be introduced two different combined damage variables, which react to the direction change of the displacement w during a loading period:

$$\varepsilon_{3\_1} = \begin{cases} \varepsilon_3, w < 0 \\ \varepsilon_1, w \geq 0 \end{cases} \quad \text{and} \quad \varepsilon_{1\_3} = \begin{cases} \varepsilon_1, w < 0 \\ \varepsilon_3, w \geq 0 \end{cases}$$

where ε_1 and ε_3 are the principal maximum and minimum values of the Green-Lagrange tensor strain respectively.

The difference between both of the introduced combined variables can be demonstrated on the example of the uniaxial tensile-compression state in a rod of length L under alternating load w (Figure 1).

In the following the damage variable ε_D is defined as

$$\varepsilon_D = \varepsilon_D(w) = \begin{cases} \varepsilon_{1\_3}, \max\limits_w(\varepsilon_{1\_3}) > \max\limits_w(\varepsilon_{3\_1}) \\ \varepsilon_{3\_1}, \text{otherwise} \end{cases} \tag{1}$$

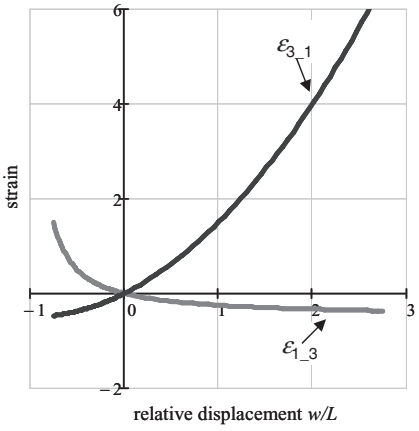

Figure 1. Two combined damage variables in case of the uniaxial strain state.

The damage variable ε_D (1) depends on the displacement w, on the local space coordinate and is as well as w a cyclic time function.

Three parameters of the damage variable function can be used for the fatigue life estimation: the amplitude ε_a, the mean value ε_m and the fatigue ratio R_ε. They are calculated as follows:

$$\varepsilon_a = \frac{1}{2}(\varepsilon_{\max} - \varepsilon_{\min})\,\varepsilon_m = \frac{1}{2}(\varepsilon_{\max} + \varepsilon_{\min})\,R_\varepsilon = \frac{\varepsilon_{\max}}{\varepsilon_{\min}}$$

where $\varepsilon_{\max}$ and $\varepsilon_{\min}$ are the maximum and minimum values of the damage variable ε_D during a loading period. Note that only two parameters, for example, ε_a and R_ε, are sufficient to describe definitely this damage variable.

2.3 *Loading state*

The loading state is characterised by means of the R_ε-ratio, namely:

$$\text{loading state} = \begin{cases} \text{tensile}, & 0 < R_\varepsilon < 1 \\ \text{compression}, & 1 < R_\varepsilon < \infty \\ \text{static}, & R_\varepsilon = 1 \\ \text{alternating}, & -\infty < R_\varepsilon \le 0 \end{cases}$$

The changing of the loading state depending on R_ε can be illustrated with the following diagram:

Notes:

1. There is not direct relationship between the loading and the strain states. For example, in case of the plane strain state it can be realized all loading states, depicted in Figure 2.
2. The normally used damage variables as principal maximal strain (or stress), strain energy density etc. cannot describe the alternating loading state because they only take the positive values.

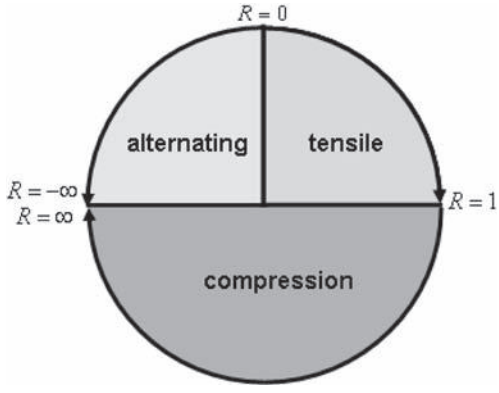

Figure 2. Loading states.

3 EXPERIMENT TESTING AND ANALYTICAL MODEL

The fatigue life test was performed at room temperature on a NR-blend rubber specimen in the form of a buffer (Figure 3). The measurements were carried out under uniaxial displacement controlled sinusoidal loading w in direction of the buffer axis at three fixed displacement amplitudes (6 mm, 8 mm and 11 mm) and different mean values (preloads) with the frequency 3 Hz.

The lifetime was defined as a number N of cycles-to-failure, at which the specimen stiffness (the quotient force amplitude/displacement amplitude) gets lower then 10% of a reference value. Furthermore the test was limited by $N = 3 \cdot 10^6$ cycles.

The damage variable (1) as a function of the displacement w was calculated in the critical point (Figure 3) using the FE-simulation program MSC. MARC with the Mooney-Rivlin hyperelastic material model. The material model parameters were identified from quasi static measurements by means of a specially developed technique of a uniaxial approximation. The values of the fatigue ratio R_ε were varied for each value of the displacement amplitude in the range $-0.3 < R_\varepsilon \le 0.3$.

The proposed analytical approach exhibits the generalisation of the known power law equation for the Wöhler curve (ε-N-diagram). Whereby the

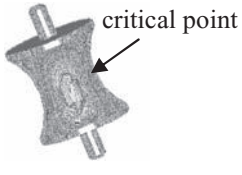

Figure 3. Rubber buffer specimen: height = 36 mm, maximum radius = 20 mm, minimum radius = 12.8 mm.

life time N can be expressed as a function of two arguments, ε_a and R_ε, in the form

$$N = N(\varepsilon_a, R_\varepsilon), \tag{2}$$

whereas the dependence on R_ε is piecewise described for the tensile and alternating parts of the loading state. The fatigue life model (2) has four parameters for each of the loading state parts. These parameters were determined from obtained test results using a fit-procedure.

4 SOME RESULTS AND DISCUSSION

The fatigue life test data and the fitted—according to (2)—curves are presented in Figure 4 in the form of the R-N-diagram, which indicate the relationship between fatigue life N and fatigue ratio R_ε at fixed amplitudes ε_a.

The presented fatigue life model (2) provides the possibility to plot the iso-lifetime lines: the curves with constant fatigue life values. These lines in the plane ε_a–R_ε (ε-R-diagram) are depicted in Figure 5.

An alternative output form of the iso-lifetime lines is the well known Haigh-diagram (André et al. 1999): the plot in the plane ε_a–ε_m. The ε-R-diagram can be converted into the Haigh-diagram, but the proposed visualization form has the advantage that the fatigue life depends directly on R_ε.

The presented analytical approach and experimental program were reviewed by several elastomeric blends and for all of them have been obtained similar results.

For comparison is shown in Figure 6 the R-N-diagram for a Polychloroprene Rubber (CR).

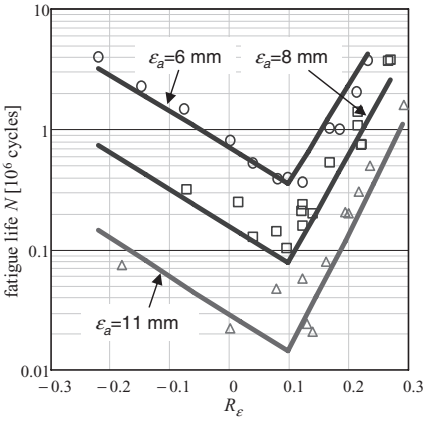

Figure 4. R-N-diagram for a NR blend: experiment (symbols) and model (solid lines).

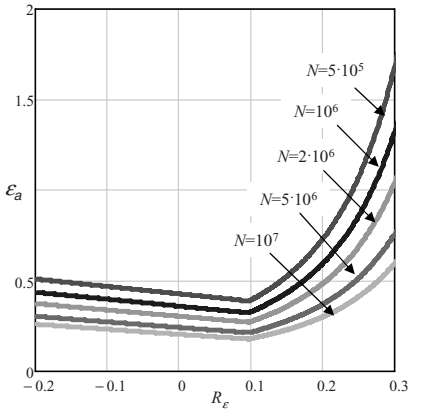

Figure 5. Iso-lifetime lines (ε-R-diagram).

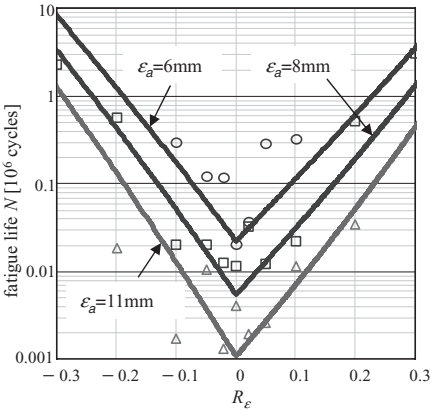

Figure 6. R-N-diagram for a CR blend: experiment (symbols) and model (solid lines).

5 FATIGUE LIFE ESTIMATION

The fatigue life with regards to the mean effect can be estimated in case of a non-periodic (stochastic) load $w_s(t)$ by means of the rainflow counting method in combination with the famous Palmgren-Miner rule.

The process of the fatigue life estimation can be performed as follows:

1. Calculation of the damage response

$$\varepsilon_D(t)_s = \varepsilon_D(w_s(t)) \tag{3}$$

(1) as a time history signal using FE-analysis. If the non-periodic load is given as a force $F_s(t)$ it can be converted to the corresponded displacement load $w_s(t)$ by means of the force-displacement-diagram $F = F(w)$.

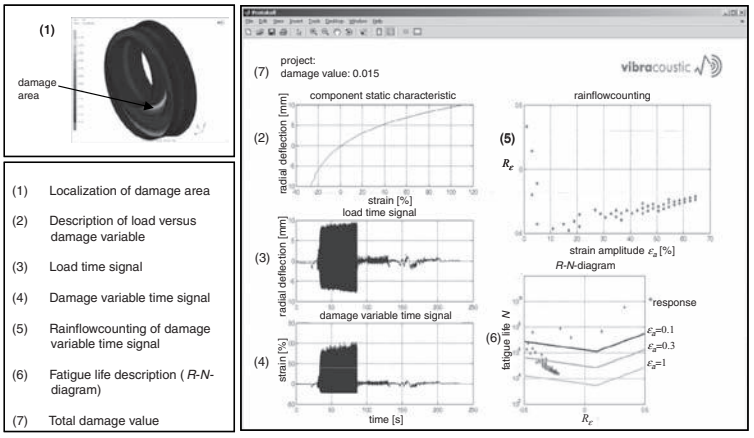

Figure 7. Fatigue life estimation for a rubber mounting using the Vibracoustic MATLAB-tool LDSIM.

2. Rainflow counting: decomposition of the time history signal (2) into single cycles (oscillations) with amplitudes ε_{a_i} and R-ratios R_{ε_i} and counting of those cycles. This procedure can be symbolically expressed in the form

$$\varepsilon_D(t)_s \rightarrow \left\{\varepsilon_{a_i}, R_{\varepsilon_i}, n_i\right\}_{i=1}^{K_s}$$

where n_i = Number of the repetitions of the single cycle s_i

$$s_i = \left\{\varepsilon_{a_i}, R_{\varepsilon_i}\right\}$$

K_s = total Number of the single cycles.

3. Calculation of the accumulated total damage D on the basis of the Palmgren-Miner rule as a sum of the contributions from the single oscillations s_i:

$$D = \sum_{i=1}^{K_s} \frac{n_i}{N(\varepsilon_{a_i}, R_{\varepsilon_i})}$$

Note that the event of total failure is defined by $D \geq 1$.

The described process of the fatigue life estimation is realized and developed by the company Vibracoustic in the MATLAB-tool "LDSIM". One example of the using of this tool for a rubber component is shown in Figure 7.

6 CONCLUSION

In this study, a new approach to describe the fatigue behavior of natural rubber under cyclic loading is presented. The proposed fatigue life model is based on the extension of the Wöhler curve and involves the mean loading effect. There are two important aspects of the new approach:

1. use of a damage variable, which is based on the Green-Lagrange strain and can take positive or negative values depending on the time history load,
2. analytical description of the fatigue behaviour as a function of the two arguments, damage variable amplitude and corresponded R-ratio.

The test program to identify the fatigue life model parameters is curried out using a rubber buffer specimen. The experimental data is evaluated by means of the FE-analysis and is represented in the form of the R-N-diagram at different damage variable amplitudes. A comparison of the R-N-diagrams for two different rubbers—NR and CR—is given. The fatigue life estimation of the rubber parts under arbitrary time history load is performed using the rainflow counting method and subsequent the Palmgren Miner rule taking into account the mean loading effect. The proposed approach is developed by Vibracoustic and implemented in the MATLAB-tool "LDSIM". An application of the developed tool for a rubber mounting is demonstrated.

REFERENCES

Eckwert, P, Meyer R. & Neitzel E. 2003. Life prediction for rubber springs. *ZEV rail Glasers Annalen* 127(3–4): 140–148.

Holzapfel, G. 2000. *Nonlinear Solid Mechanic: A Continuum Approach for Engineering.* Chichester: John Wiley Ltd.

André, N, Gailletaud, G. & Piques, R. 1999. Haigh diagram for fatigue crack initiation prediction of natural rubber components. *Kautsch. Gummi Kunstst 5*: 120–123.

Constitutive Models for Rubber VI – Heinrich et al. (eds)
© 2010 Taylor & Francis Group, London, ISBN 978-0-415-56327-7

Hyperelasticity with volumetric damage

E. Verron
Institut de Recherche en Génie Civil et Mécanique UMR CNRS 618,
École Centrale de Nantes, Nantes Cedex, France

G. Chagnon
Université de Grenoble/CNRS, Laboratoire Sols, Solides Structures - Risques (3S-R),
Grenoble Cedex, France

J.-B. Le Cam
Laboratoire de Mécanique et Ingénieries - IFMA/UBP, Aubière Cedex, France

ABSTRACT: The present paper presents a simple framework to model continuous volumetric damage in elastomers. The formulation predicts phenomenologically the growth of microscopic cavities, and can be applied to both static and fatigue loading conditions. This first version of the approach cannot handle cavitation and is limited to small values of porosities. The derivation is based on the use of a simple scalar damage parameter, the irreversible volume change, and takes naturally into account the change in stiffness through the explicit dependence of the material parameters on the damage variable. The thermodynamic force which drives the volume change contains the hydrostatic stress and also a contribution due to stiffness evolution. As a first application, a damage compressible neo-Hookean constitutive equation is derived and a simple example is studied.

1 INTRODUCTION

Rubber-like materials are usually considered as incompressible. However, under multiaxial or fatigue loading conditions, cavitation and cavities growth take place, and lead to damage and finally to fracture (Farris 1968; Le Cam et al. 2004; Le Gorju 2007). Special experiments can be carried out to exhibit this behaviour as proposed by Gent and Thomas (1958), Gent and Wang (1991) or Legorju-Jago and Bathias (2002). For modelling, on the one hand the cavitation phenomenon under hydrostatic loading conditions is studied considering the stability conditions for the sudden growth of microscopic cavities in the incompressible bulk (see Ball (1982), Horgan and Abeyaratne (1986) for example). On the other hand, several phenomenological approaches have been proposed to predict the growth of pre-existing cavities; the corresponding models incorporate damage variables into compressible hyperelastic approaches (see Boyce and Arruda (2000) for a short review) to quantify the irreversible change of porosity (Andrieux et al. 1997; Dorfmann et al. 2002; Layouni et al. 2003; Li et al. 2007). These models can also be extended to cavitation by adapting the rate equation of the damage variable (Dorfmann 2003). Nevertheless, they are limited to small values of the porosity.

In the present paper, similarly to Andrieux et al. (1997), we propose a simple theoretical framework to model the compressibility induced by damage in hyperelastic materials. Our approach is phenomenological and is restricted to small values of porosity, such that the growing cavities do not interfere. The scalar damage variable is the irreversible volume change and its influence on the stiffness of the material is taken into account through the material parameters. The rate equation chosen here is not adapted to sudden volume change (cavitation) but only to continuous volume change (damage by continuous growth of cavities).

The derivation of the model is described in the next section, the emphasize being laid on the determination of the thermodynamic force which drives the volume change. Then, a very simple constitutive equation which generalizes the compressible neo-Hookean model is considered to illustrate the relevance of the method.

2 DERIVATION OF THE CONSTITUTIVE EQUATION

2.1 *General formulation*

2.1.1 *Kinematics*

It is considered here that under loading, the body exhibits an irreversible volume change due to what

can be called *a volumetric damage*. In the general framework of large strain, the material is supposed homogeneous, isotropic and hyperelastic. Moreover, we assume that it initially contains small flaws that can be considered as holes. To simplify the derivation, the RVE is assumed to deform as sketched in Figure 1; the deformation gradient $\mathbf{F}$ is separated into two parts:

- an irreversible volume change between the initial configuration (C_0) and the intermediate configuration (C_i). It is defined by the deformation gradient $J_c^{1/3}\mathbf{I}$, in which J_c is the ratio of irreversible volume change between the two configurations. In the figure, this volume change is illustrated by the irreversible growth of small holes; nevertheless, we do not consider their microscopic evolution: interaction, coalescence, …
- a classical elastic deformation, which gradient is denoted $\mathbf{f}$, between the intermediate configuration (C_i) and the deformed configuration (C).

The well-established multiplicative decomposition of the deformation gradient is adopted:

$$\mathbf{F} = \mathbf{f}\, J_c^{1/3}\mathbf{I} = J_c^{1/3}\mathbf{f}. \tag{1}$$

Indeed, the deformation process can be described by the two following variables: the observable strain (through $\mathbf{F}$) and the internal variable J_c which describes damage.

2.1.2 *Constitutive equations*

First, the reversible deformation between configurations (C_i) and (C) is considered hyperelastic: it exists a strain energy function $w_{J_c}(\mathbf{f})$ per unit of volume in (C_i). It is highly important to note that this strain energy function depends on J_c in two ways: through $\mathbf{f}$, recalling Eq. (1), and through the material parameters which *explicitly* depend on the irreversible volume change, as notified by the subscript $\cdot_{J_c}$. Second, the deformation between (C_0) and (C_i) being totally irreversible, no elastic strain energy is involved. Then, the total strain energy of the material is simply the strain energy w_{J_c} written per unit of undeformed volume, i.e. unit of volume in (C_0):

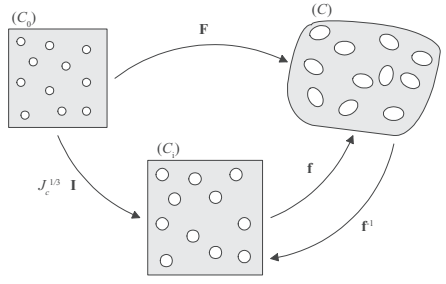

Figure 1. Deformation of the RVE.

$$W(\mathbf{F}, J_c) = J_c\, w_{J_c}(\mathbf{f}). \tag{2}$$

Once the strain energy function defined, one can easily derive the constitutive equations. Restricting the problem to a purely mechanical theory, i.e. ignoring thermal effects, the Clausius-Planck inequality is

$$\mathcal{D}_{\text{int}} = \mathbf{P} : \dot{\mathbf{F}} - \dot{W} \geq 0, \tag{3}$$

where $\mathcal{D}_{\text{int}}$ is the internal dissipation and $\mathbf{P}$ is the first Piola-Kirchhoff stress tensor. Recalling that W depends on both the deformation gradient $\mathbf{F}$ and the internal variable J_c,

$$\mathcal{D}_{\text{int}} = \mathbf{P} : \dot{\mathbf{F}} - \left.\frac{\partial W}{\partial \mathbf{F}}\right|_{J_c} : \dot{\mathbf{F}} - \left.\frac{\partial W}{\partial J_c}\right|_{\mathbf{F}} \dot{J}_c \geq 0. \tag{4}$$

Following Coleman and Noll (1963), $\dot{\mathbf{F}}$ and $\dot{J}_c$ can be chosen arbitrarily and then the constitutive equation for $\mathbf{F}$, i.e. the stress-strain relationship, is

$$\mathbf{P} = \left.\frac{\partial W}{\partial \mathbf{F}}\right|_{J_c}, \tag{5}$$

and the internal dissipation reduces to

$$\mathcal{D}_{\text{int}} = G\,\dot{J}_c \geq 0 \quad \text{with} \quad G = -\left.\frac{\partial W}{\partial J_c}\right|_{\mathbf{F}} \tag{6}$$

where G is the thermodynamic force which drives the irreversible change in volume. Eq. $(6)_2$ is the constitutive equation for J_c.

Stress-strain relationship. One can now derive Eq. (5):

$$\mathbf{P} = \left.\frac{\partial W}{\partial \mathbf{F}}\right|_{J_c} = \frac{\partial J_c w_{J_c}(\mathbf{f})}{\partial \mathbf{F}} = J_c \frac{\partial w_{J_c}}{\partial \mathbf{f}} : \frac{\partial \mathbf{f}}{\partial \mathbf{F}}. \tag{7}$$

Introducing $\mathbf{p} = \partial w_{J_c}/\partial \mathbf{f}$ the first Piola-Kirchhoff stress tensor with respect to the intermediate configuration (C_i), and after some algebraic manipulations, the nominal stress reduces to (see for example Holzapfel (2000) for such derivation)

$$\mathbf{P} = J_c^{2/3} \frac{\partial w_{J_c}(\mathbf{f})}{\partial \mathbf{f}}. \tag{8}$$

Note that the derivation of $\mathbf{p}$ is straightforward: once the strain energy function w_{J_c} is chosen, the classical hyperelastic theory applies.

Thermodynamic force for change in volume. The thermodynamic force which drives the irreversible change in volume is

$$G = -\left.\frac{\partial W}{\partial J_c}\right|_{\mathbf{F}} = -w_{J_c} - J_c \left.\frac{\partial w_{J_c}(\mathbf{f})}{\partial J_c}\right|_{\mathbf{F}}. \tag{9}$$

The second right-hand side term can be calculated as follow

$$\left.\frac{\partial w_{J_c}(\mathbf{f})}{\partial J_c}\right|_{\mathbf{F}} = \left.\frac{\partial w_{J_c}}{\partial J_c}\right|_{\text{expl}} + \frac{\partial w_{J_c}}{\partial \mathbf{f}} : \frac{\partial \mathbf{f}}{\partial J_c}, \tag{10}$$

where the subscript $\cdot_{\text{expl}}$ denotes the explicit differentiation with respect to J_c, which involves the differentiation of the material parameters. Considering again the intermediate engineering stress tensor $\mathbf{p}$, we have

$$\frac{\partial w_{J_c}}{\partial \mathbf{f}} : \frac{\partial \mathbf{f}}{\partial J_c} = \mathbf{p} : \left(-\frac{1}{3} J_c^{-4/3} \mathbf{F}\right). \tag{11}$$

So, invoking Eqs. (1) and (8), the thermodynamic force is

$$G = -J_c \left.\frac{\partial w_{J_c}}{\partial J_c}\right|_{\text{expl}} - \left(w_{J_c} - \frac{1}{3}\mathbf{p} : \mathbf{f}\right). \tag{12}$$

This equation can be transformed by introducing the Eshelby stress tensor $\Sigma = W\mathbf{I} - \mathbf{F}^T\mathbf{P}$:

$$G = -J_c \left.\frac{\partial w_{J_c}}{\partial J_c}\right|_{\text{expl}} - J_c^{-1}\Sigma : \frac{\mathbf{I}}{3}. \tag{13}$$

Moreover, considering the velocity gradient associated with the irreversible volume change $\mathbf{L}_c$, which is simply $J_c^{-1}\dot{J}_c\mathbf{I}/3$ here, and its symmetric part, the rate of deformation tensor $\mathbf{D}_c$ (equal to $\mathbf{L}_c$ in the present case), the internal dissipation can be written as

$$\mathcal{D}_{\text{int}} = -J_c \left.\frac{\partial w_{J_c}}{\partial J_c}\right|_{\text{expl}} \dot{J}_c - \Sigma : \mathbf{D}_c, \tag{14}$$

and the thermodynamic force is then

$$G = -J_c \left.\frac{\partial w_{J_c}}{\partial J_c}\right|_{\text{expl}} - J_c^{-1}\text{tr}\left(\frac{\Sigma}{3}\right). \tag{15}$$

Finally, this expression can be simplified by rewriting the Eshelby stress tensor as proposed by Verron and Andriyana (2008): noting $(\mathbf{N}_i)_{i=1,2,3}$ the principal strain directions in the reference configuration and recalling that the Eshelby stress tensor is symmetric for isotropic elastic materials, Σ becomes

$$\Sigma = \sum_{i=1}^{3} (W - \lambda_i^2 S_i)\mathbf{N}_i \otimes \mathbf{N}_i, \tag{16}$$

where $(\lambda_i)_{i=1,2,3}$ are the principal stretch ratio and $(S_i)_{i=1,2,3}$ the eigenvalues of the second Piola-Kirchhoff stress tensor. Introducing the relationship between these principal stresses and the principal Cauchy stresses

$$\sigma_i = J^{-1}\lambda_i^2 S_i \quad i = 1,2,3 \tag{17}$$

where $J = \det \mathbf{F}$ characterizes the total change in volume between (C_0) and C, i.e. reversible and irreversible, the Eshelby stress tensor can be written as

$$\Sigma = \sum_{i=1}^{3} (W - J\sigma_i)\mathbf{N}_i \otimes \mathbf{N}_i, \tag{18}$$

and

$$\text{tr}\left(\frac{\Sigma}{3}\right) = W - J\sigma_s \tag{19}$$

where σ_s is the spherical part of the Cauchy stress tensor, i.e. the hydrostatic stress. So, the thermodynamic force reduces to

$$G = -\left.\frac{\partial W}{\partial J_c}\right|_{\text{expl}} + \frac{J}{J_c}\sigma_s. \tag{20}$$

2.1.3 *Evolution equation*

To close the general formulation of the model, we should precise the rate equation for the internal variable J_c. Such equation can be written as:

$$\dot{J}_c = f(G, \mathbf{F}) \tag{21}$$

where the function f must be positive to ensure the positivity of the dissipation. In order to simplify the model, we simply choose a very simple "damage-like" evolution equation under the following form:

$$\dot{J}_c = \begin{cases} kG & \text{if } G < G_{\max} \\ 0 & \text{otherwise.} \end{cases} \tag{22}$$

In this equation, the parameter k is a positive real scalar value which depends on the material and $G_{\max}$ stands for the maximum value of the thermodynamic force G previously endured by the material.

2.2 *A particular model*

Once the general theory derived, particular models can be proposed by specifying the strain energy density w_{J_c}. We consider the case where the elastic deformation (from (C_i) to (C)) is compressible and we adopt one of the simplest strain energy densities for compressible hyperelastic materials: the generalization of the incompressible neo-Hookean

model proposed by Simo and Pister (1984) and adopted later by both Ehlers and Elipper (1998) and Bischoff et al. (2001). So the complete strain energy density is

$$W(\mathbf{F},J_c) = J_c \underbrace{[C(i_1-3-\ln i_3)+D(\ln i_3)^2]}_{w_{J_c}(\mathbf{f})} = CJ_c\left(J_c^{-2/3}I_1-3+2\ln\frac{J_c}{J}\right) + 4DJ_c\left(\ln\frac{J_C}{J}\right)^2, \quad (23)$$

where i_1 and i_3 are the invariants of the right Cauchy-Green elastic strain tensor $\mathbf{f}^T\mathbf{f}$, i.e. its trace and determinant respectively. Note that for the deformation gradient $\mathbf{f}$, the spherical-deviatoric split is not considered. In this equation the material parameter C is twice the shear modulus, and the material parameter D is proportional to the compressibility modulus.

Two cases are now considered.

- The first one for which there is no stiffness decrease due to damage, i.e. material parameters are constant, $C = C_0$ and $D = D_0$. In that case, the engineering stress tensor $\mathbf{P}$ and the thermodynamic force G are respectively

$$\mathbf{P} = 2C_0J_c^{1/3}\mathbf{F} - \left(2C_0 + 8D_0\ln\frac{J_c}{J}\right)J_c\mathbf{F}^{-T} \quad (24)$$

and

$$G = -C_0\left(J_c^{-2/3}\frac{I_1}{3}-1\right) + \ln\frac{J_c}{J}\left(-2C_0-8D_0-4D_0\ln\frac{J_c}{J}\right). \quad (25)$$

- The second one for which the stiffness decreases, i.e. C and D depends on J_c. To specify the dependence of these parameters on J_c, we invoke the statistical theory of rubber elasticity which states that

$$C = \frac{1}{2}nkT, \quad (26)$$

with n being the number of active polymer chains per unit of volume, k the Boltzmann constant and T the temperature. Considering the mass conservation equation between configurations (C_0) and (C_i),

$$n_0 dV_0 m_{\text{chain}} = n_i dV_i m_{\text{chain}} \quad (27)$$

where n_0 and n_i are the chain densities per unit of volume in (C_0) and (C_i), dV_0 and dV_i the infinitesimal volumes in (C_0) and (C_i), and m_{chain} is the mean mass of the chains, and recalling that $dV_i = J_c dV_0$, one can state that

$$C(J_c) = C_0/J_c. \quad (28)$$

The second parameter D is not directly related to the chain density; nevertheless, we consider the same relationship with the initial compressibility modulus

$$D(J_c) = D_0/J_c \quad (29)$$

In that case, the engineering stress tensor $\mathbf{P}$ and the thermodynamic force G are respectively

$$\mathbf{P} = 2C_0J_c^{-2/3}\mathbf{F} - \left(2C_0 + 8D_0\ln\frac{J_c}{J}\right)\mathbf{F}^{-T} \quad (30)$$

and

$$G = 2C_0\left(J_c^{-5/3}\frac{I_1}{3}-\frac{1}{J_c}\right) - 8\frac{D_0}{J_c}\ln\frac{J_c}{J}. \quad (31)$$

3 FIRST RESULTS

In order to illustrate the previous theory, we consider a very simple problem: a sample is first subjected to cyclic triaxial loading conditions, then it is uniaxially stretched. More precisely, the loading conditions are

- Four equi-triaxial cycles under prescribed stretch ratio λ: from $\lambda = 1$ to $\lambda = 1.25$, then from $\lambda = 1$ to $\lambda = 1.5$, then from $\lambda = 1$ to $\lambda = 1.75$, and finally from $\lambda = 1$ to $\lambda = 2$. The deformation gradient and the engineering stress tensor are respectively

$$\mathbf{F} = \lambda(\mathbf{e}_1\otimes\mathbf{e}_1 + \mathbf{e}_2\otimes\mathbf{e}_2 + \mathbf{e}_3\otimes\mathbf{e}_3), \quad (32)$$

$$\mathbf{P} = P(\mathbf{e}_1\otimes\mathbf{e}_1 + \mathbf{e}_2\otimes\mathbf{e}_2 + \mathbf{e}_3\otimes\mathbf{e}_3). \quad (33)$$

- One uniaxial loading path under prescribed stretch ratio from $\lambda = 1$ to $\lambda = 3$ with

$$\mathbf{F} = \lambda\mathbf{e}_1\otimes\mathbf{e}_1 + \mu(\mathbf{e}_2\otimes\mathbf{e}_2 + \mathbf{e}_3\otimes\mathbf{e}_3), \quad (34)$$

$$\mathbf{P} = P\mathbf{e}_1\otimes\mathbf{e}_1. \quad (35)$$

The following values of the material parameters are adopted: $C_0 = 1$ MPa, $D_0 = 10$ MPa and $k = 0.01$.

First, for both models, we present the evolution of J_c as a function of the loading time and the stress-strain response during the triaxial loading phase: in Figures 2 and 3 for the first model without change in material parameters (Eqs. (24–25)),

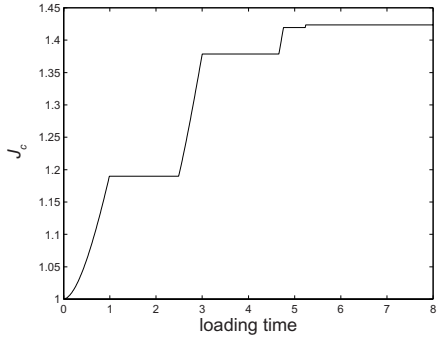

Figure 2. Model without change in material parameters: evolution of the volumetric damage during the four triaxial cycles.

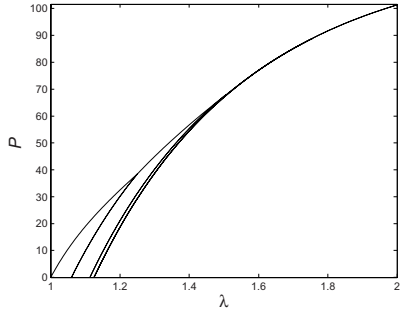

Figure 3. Model without change in material parameters: stress-strain response during the four triaxial cycles.

and in Figures 4 and 5 for the second model with change in material parameters (Eqs. (30–31)). The comparison of the volumetric damage evolution in Figs. 2 and 4 exhibits that ignoring the induced change in material parameters leads to a limit in the irreversible change in volume (see the two final constant steps in Fig. 2), whereas if this change is taken into account the volumetric damage evolves continuously during triaxial cyclic loading. This mechanical response can be also observed with the stress-strain responses in Figs. 3 and 5: for the former model a unique curve is reached for about $\lambda = 1.5$ and unloading parts of the response become closer and closer as depicted in Fig. 3. For the latter model, Fig. 5 shows that the material stiffness evolves in a regular manner and the resulting cyclic response is similar to the one encountered with damage-like constitutive equations, see for example Chagnon et al. (2004).

Finally, we examine the mechanical response obtained during the final uniaxial extension in Figures 6 and 7. For both models, J_c does not change under loading (the curves are not shown here). Nevertheless, the first model exhibits a "strange" behaviour: the stiffness of the material

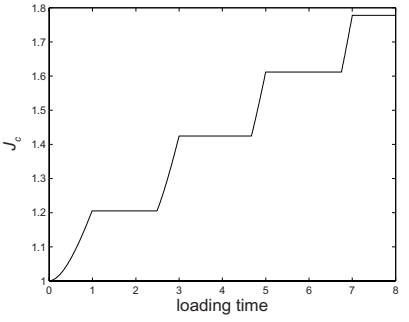

Figure 4. Model with change in material parameters: evolution of the volumetric damage during the four triaxial cycles.

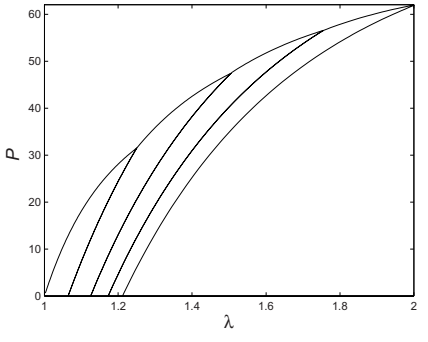

Figure 5. Model with change in material parameters: stress-strain response during the four triaxial cycles.

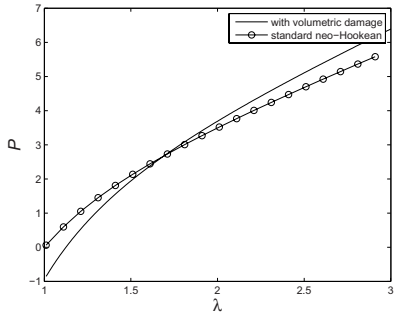

Figure 6. Model without change in material parameters: uniaxial stress-strain response.

is revealed always greater than its initial stiffness (before damage), and the undamaged and damaged curves intersect which means that for stretch ratios greater than 1.75 the stress is greater in the damaged material than in the undamaged one; this behaviour is physically irrelevant. For the second model, the stiffness of the damaged material is always lower than the initial stiffness and the curves never intersect.

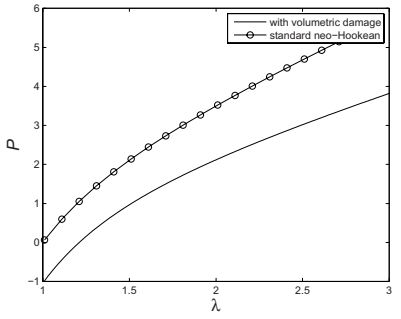

Figure 7. Model with change in material parameters: uniaxial stress-strain response.

4 CONCLUSION

In this paper, a new method has been proposed to consider irreversible growth of cavities in rubber-like materials. The general framework consists in introducing a scalar damage variable J_c which represents the irreversible volume change at a material point; then, the constitutive equations are derived with in the framework of Thermodynamics or Irreversible Processes. The originality of the present approach consists in taking into account the stiffness change induced by damage through the explicit dependence of the material parameters on the damage variable. Moreover, considering the statistical rubber elasticity theory, the extension of the neo-Hookean model has been derived and the dependence of the shear modulus on J_c has been easily established. Finally, a first proof of the model relevance has been proposed by considering a very simple loading history.

Further work will be carried out first to extend the model to cavitation through the choice of a more complex rate equation for J_c and second to implement the model in the finite element context.

REFERENCES

Andrieux, F., K. Saanouni, and F. Sidoroff (1997). Sur les solides hyperélastiques à compressibilité in-duite par 1'endommagement. *Comptes Rendus de l'Académie des Sciences—Series IIB 324(5)*, 281–288.

Ball, J.M. (1982). Discontinuous equilibrium solutions and cavitation in nonlinear elasticity. *Phil. Trans. R. Soc. Lond A 306*, 557–611.

Bischoff, J.E., E.M. Arruda, and K. Grosh (2001). A new constitutive model for the compressibility of elastomers at finite deformations. *Rubber Chem. technol. 74*, 541–559.

Boyce, M.C. and E.M. Arruda (2000). Constitutive models of rubber elasticity: a review. *Rubber Chem. Technol. 73*, 505–523.

Chagnon, G., E. Verron, L. Gornet, G. Marckmann, and P. Charrier (2004). On the relevance of continuum damage mechanics for the Mullins effect in elas tomers. *J. Mech. Phys. Solids 52*, 1627–1650.

Coleman, B.D. and W. Noll (1963). The thermodynam ics of elastic materials with heat conduction and vis cosity. *Arch. Rational Mech. Analysis 13*, 167–178.

Dorfmann, A. (2003). Stress-softening of elastomers in hydrostatic tension. *Acta Mechanica 165*, 117–137.

Dorfmann, A., K.N.G. Fuller. and R.W. Ogden (2002). Shear, compressive and dilatational response of rubberlike solids subject to cavitation damage. *Int. J. Solids Struct. 39*, 1845–1861.

Ehlers, W. and G. Eipper (1998). The simple tension problem at large volumetric strains computed from finite hyperelastic material laws. *Acta Mechanica 130*, 17–27.

Farris, R.J. (1968). The influence of vacuole formation on the response and failure of filled elastomers. *Trans. Soc. Rheol. 12*, 315–334.

Gent, A.N. and A.G. Thomas (1958). Forms of the stored (strain) energy function for vulcanized rubber. *J. Polym. Sci. 28*, 625–637.

Gent, A.N. and C. Wang (1991). Fracture mechanics and cavitation in rubber-like solids. *J. Mater. Sci. 26*, 3392–3395.

Holzapfel, G.A. (2000). *Nonlinear Solid Mechanics. A continuum approach for engineering.* Chichester: J. Wiley and Sons.

Horgan, C.O. and R. Abeyaratne (1986). A bifurcation problem for a compressible nonlinearly elastic medium: growth of a micro-void. *J. Elast. 16*, 189–200.

Layouni, K., L. Laiarinandrasana, and R. Piques (2003, 15–17 September). Compressibility induced by damage in carbon black reinforced natural rubber. In J. Busfield and A. Muhr (Eds.), *Constitutive Models for Rubber III*, pp. 273–281. A.A. Balkema.

Le Cam, J.-B., B. Huneau, E. Verron, and L. Gornet (2004). Mechanism of fatigue crack growth in carbon black filled natural rubber. *Macromolecules 37*, 5011–5017.

Le Gorju, K. (2007). Fatigue life of rubber components: 3d damage evolution from x-ray computed microtomography. In A. Boukamel, L. Laiarinandrasana, S. Méo, and E. Verron (Eds.), *Constitutive Models for Rubber V*, pp. 173–177. Taylor & Francis.

Legorju-Jago, K. and C. Bathias (2002). Fatigue initiation and propagation in natural and synthetic rubbers. *Int. J. Fatigue 24*, 85–92.

Li, J., D. Mayau. and F. Song (2007). A constitutive model for cavitation and cavity growth in rubber-like materials under arbitrary tri-axial loading. *Int. J. Solids Struct. 44*, 6080–6100.

Simo, J.C. and K.S. Pister (1984). Remarks on rate constitutive equations for finite deformation problems: computational implications. *Comput. Methods Appl. Mech. Engng. 46*, 201–215.

Verron, E. and A. Andriyana (2008). Definition of a new predictor for multiaxial fatigue crack nucleation in rubber. *J. Mech. Phys. Solids 56*, 417–443.

Friction

Constitutive Models for Rubber VI – Heinrich et al. (eds)

Modelling friction and abrasion in rubber

J.J.C. Busfield
Department of Materials, Queen Mary University of London, London, UK

ABSTRACT: The exact mechanisms present during frictional sliding and abrasion of an elastomer over a hard asperity are discussed. It is widely accepted that the two principal factors in rubber friction result from the adhesion and hysteresis behaviour of the elastomer. Through modelling and measurement it has been shown an additional geometric factor contributes significantly to the frictional force. This geometric term is thought likely to make a contribution to friction experienced in applications such as the sliding of tyres over a road surface. Also, the abrasion process has been measured and modelled using a calculated strain energy release rate for a specific type of sliding contact and this has been used to compare both measured and calculated abrasion rates. The correlation is good for a wide range of conditions and different materials and this analysis helps explain why some materials are more abrasion resistant than others.

1 INTRODUCTION

It has been shown (Champ et al. 1974 & Gent and Pulford, 1984) that the abrasion of rubber by a blade in a single direction leads to the formation of a characteristic surface abrasion pattern consisting of periodic parallel ridges perpendicular to the sliding direction. The size and shape of the ridges characterise the specific abrasion processes. The abrasion mechanisms proposed by Southern & Thomas (1979) have the rate determining abrasion process being concentrated at the root of these ridges. Crack growth takes place in this region and the abrasion pattern is observed to move into the surface at an angle to the rubber surface that is specific to the loading geometry, the load conditions and the material properties.

This crack growth problem can be tackled using a fatigue analysis approach (Busfield et al. 2005), where a geometrically independent characteristic relationship exists between the cyclic crack growth rate versus the maximum strain energy release rate attained during the loading cycle for a specific rubber.

The process of rubber abrasion based on a line contact has been investigated by several others including Gent & Pulford (1983) and Liang et al. (2009a, 2009b). The wear rate during steady state abrasion is calculated from the rate of mass lost per cycle from the wheel and by measuring the rate of advancement of individual ridges over the surface.

The early fracture mechanics based research on rubber abrasion only considered the horizontal frictional force using an analysis such as that given by Southern & Thomas (1979). They proposed an equation to correlate the measured horizontal friction force, F with the strain energy release rate, T:

$$T = \frac{F}{h}(1+\cos\theta) \tag{1}$$

where h is the width of the contact line between the blade and the surface, and θ is the angle at which the crack penetrates into the surface. This equation assumes the entire horizontal force is available to drive the crack. Liang et al. (2009a) showed the friction at the various interfaces also has a significant effect on the amount of energy available to drive the crack. This limits the accuracy of equation 1 in determining the strain energy release rate for a wide range of different asperity geometries and sliding conditions. An alternative approach proposed by Liang et al. (2009a) is used to calculate the strain energy release rate using a finite element analysis approach. The method chosen to do this is the virtual crack extension method used by Busfield et al. (2005). Here the relation between the strain energy release rate and the fatigue crack growth rate measured on a pure shear fully relaxing fatigue crack growth experiment is used to predict the rate of abrasion for four different elastomeric materials. This can be compared to the experimentally observed wear rates.

The frictional behaviour is an important parameter in determining the strain energy release rate but as Gabriel et al. (2009) showed, modelling friction in elastomers is not a simple task and using just a simple Coulomb friction term ignores additional contributions to sliding friction due to geometric effects. This is discussed next.

2 MODELLING FRICTION

Persson (2001) states the adhesion contribution to friction is negligible in a tyre/road contact, and the major contribution to friction is from a hysteresis term alone. This is examined using the two different test configurations shown in Figure 1 and Figure 2 respectively. In configuration 1 the rubber is deformed and wraps around the rigid indenter. In configuration 2 the rubber becomes plane under deformation. Unfilled NR samples were made in each configuration as detailed by Gabriel et al. (2009). Finite element models were made of each configuration and to eliminate time dependent behaviour and the effects of energy losses in the model, the behaviour is described by the elastic properties alone using a Mooney strain energy function.

A Plint friction tester was used here to investigate the two different geometrical configurations. The tests were operated at a low velocity of 0.0001 ms^{-1} in order to minimise the effect of viscous energy dissipation through hysteresis, so an almost static friction measurement could be assumed. The remaining hysteretic contribution was only indirect through adhesion effects and was assumed to be negligible. Further the adhesion contribution was decreased by coating the surface with a thin layer of talcum powder. The experiments used a polished 12 mm spherical steel slider on a rubber block or a rubber hemisphere, having a 12 mm diameter, on a polished steel track.

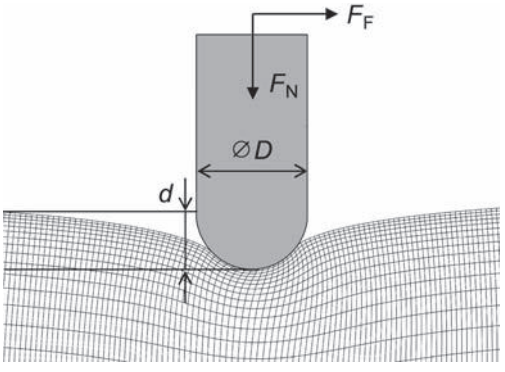

Figure 1. A flat rubber sheet with a rigid indenter sliding over the surface.

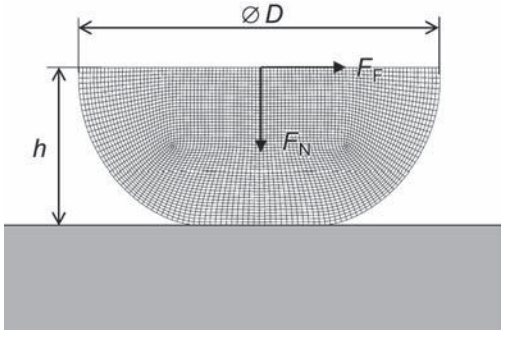

Figure 2. A rubber sphere sliding over a flat rigid surface.

The FEA models have two basic geometrical parameters. For configuration 1 this includes the diameter of the rigid slider D, and the depth of deformation d. For configuration 2, D is now the diameter of the rubber hemisphere, the depth of deformation d is defined as:

$$d = \frac{D}{2} - h \tag{2}$$

where h defines the height of the deformed hemisphere. The experiments and FEA models use a rubber block thickness of 5.5 mm, with a maximum indentation of around 1.5 mm at the highest normal load (20 N). Earlier work by Busfield and Thomas (1999) showed how to account for a ratio of rubber thickness to the diameter of circular contact less than 10:1, to account for complications arising due to the supporting (rigid) boundary conditions underneath the rubber block. A similar approach was seen to work well here.

Amontons' friction model (Amontons, 1699), also known as Coulomb friction, is employed at the interface in the analysis, where a single parameter, the (input) coefficient of friction μ_I, is defined as the ratio between the frictional force at the surface divided by the resulting normal force during sliding. Even though Amontons' friction model, originally designed for metals, is thought to be not applicable for rubber friction it is still used by many engineers and scientists (Smith, 2008).

The standard way of inputting the coefficient of friction μ_I in the FEA model is to define it as the ratio of the frictional force divided by the normal force. The resulting coefficient of friction μ_R calculated from the FEA model is therefore the result of dividing the calculated output frictional sliding force, RF_F, by the calculated output normal force RF_N. At first sight, it would appear, the resulting calculated output friction ratio μ_R should be the same as the input coefficient of friction μ_I, however, this is not borne out for test configuration 1 by examining the results shown in Figure 3, where the ratio of μ_R divided by μ_I is plotted against the normalised depth of penetration d/D for the NR compound.

For configuration 2, where a rubber sphere comes into contact with a flat rigid surface, the

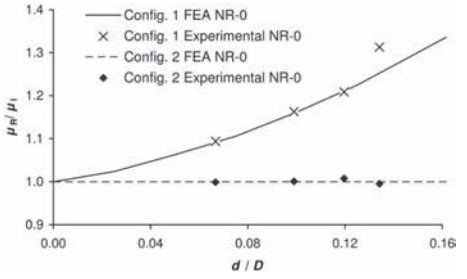

Figure 3. The ratio of μ_R/μ_I plotted against the depth of penetration/indenter diameter for NR-0.

resulting contact is over a plane interface, the ratio between μ_I to μ_R is an approximately constant value of 1 for both the measured data and the predicted behaviour irrespective of the extent of deformation. The apparent increase in friction of test configuration 1 can not easily be attributed to the increase in contact area or change in normal stress, as in both configurations the contact area increases with increasing normal load. It appears that a geometric effect of deforming the rubber surface onto the curved rigid profile has the effect of adding an additional contribution to rubber friction. This is considered to be attributed to an increase in the wrapping angle of the rubber around the rigid indenter. This behaviour can be considered similar to the increase in friction resulting from a rope being wrapped around a capstan (Schallamach, 1969). The increase in indentation depth creates an increase in the angle of contact even when the imposed friction coefficient remains the same at the interface. This factor can be of considerable practical significance for example in explaining the increased friction experienced with certain types of road surface containing sharp asperities or during blade abrasion experiments. In addition, it is of interest that the coefficient of friction measured in many instances might be higher than if the friction had been measured using a plane surface contact.

3 MODELLING ABRASION

Due to the difficulties described the actual friction parameter chosen in the abrasion models was selected to ensure the average sliding frictional force measured during the abrasion experiments was reproduced in the finite element model.

In the current work, the abrasion rate was measured in the bulk at steady state for a range of normal loads (4 N, 8 N, 12 N, 16 N & 20 N) by weight loss. Also, the rate and angle of the crack growth was measured several times for each different loading condition for all four rubber compounds. The average observed crack growth angle at the root of the asperity was used to create a model which could be used to calculate the strain energy release rate.

Four materials were chosen for this study. Three were unfilled NR0, unfilled SBR0 and unfilled BR0. An additional filled SBR25 compound was also investigated. The formulations for these materials are given in Table 1.

The fatigue crack growth rate per cycle dc/dn versus strain energy release rate, T for each for the four materials is plotted over the range of experimental significance as the best fit line to represent the data shown in Figure 4. The ranking makes NR0 as the

Table 1. The compound formulations, curing conditions and strain energy function coefficients for the different materials used in this work.

Ingredients	SBR0	SBR25	NR0	BR0
SBR	100	100	–	–
NR	–	–	100	–
BR	–	–	–	100
Carbon Black (N330)	–	25	–	–
Zinc Oxide	3.0	3.0	5.0	3.5
Stearic acid	1.0	1.0	2.0	2.0
Antioxidant (HPPD)	1.0	1.0	3.0	1.0
Accelerator (CBS)	–	–	1.5	1.0
Accelerator (DPG)	1.0	1.0	–	0.15
Sulphur	3.0	3.0	1.5	1.0
Curing time/ minute	60	60	60	50
Curing temperature/°C	160	160	145	150
Mooney SEF Coefficients	C1 = 0.128 C2 = 0.167		C1 = 0.188 C2 = 0.072	C1 = 0.136 MPa C2 = 0.167 MPa
Yeoh SEF Coefficients		C10 = 0.337 C20 = 0.0053 C30 = 0.00053		

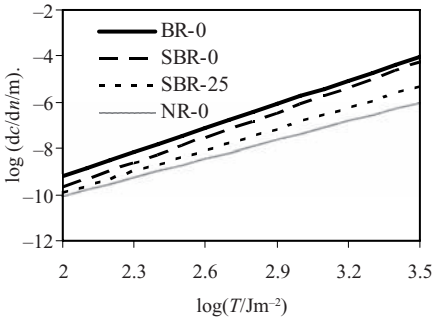

Figure 4. The crack growth rate versus strain energy release rate for the different materials examined in this work.

most crack resistant and BR0 as the weakest with the SBR0 somewhere in between with the inclusion of the filler greatly improving the crack resistance for SBR25. The reason for this comparative weakness of SBR0 to NR0 (Busfield et al. 2002) results from the fatigue behaviour in SBR exhibiting predominantly a time dependent behaviour with a strain induced crystallisation arising in the NR materials introducing a cyclic component in that improves the fatigue properties of NR. The introduction of fillers make SBR useful in comercial applications but the behaviour is still not as good as NR filled elastomers (Tsunoda et al. 2000).

Different materials and different abrasion processes are seen to create different abrasion patterns. What is attempted here is to examine experimentally the markedly different patterns developed on abrasion wheels during blade abrasion to see how the development of the asperity alters the level of the strain energy release rate attained during frictional sliding and to see how this might alter the wear rate.

3.1 *Experimental techniques and results*

A Mooney strain energy function (SEF) was used to characterise the three unfilled materials and a Yeoh SEF was used to characterise the filled rubber in the finite element models (Kumar et al. 2007). The detail of these models is given in Liang et al. (2009a, 2009b). The coefficients for use in the finite element model were derived from a tensile test up to a principle extension ratio of 3. The coefficients thus derived are given in Table 1.

The relationship between the crack growth rate per cycle dc/dn is a simple function of strain energy release rate T, which can be defined in the range of interest as:

$$\frac{\mathrm{d}c}{\mathrm{d}n} = X\left(\frac{T}{T^*}\right)^{\psi} \tag{3}$$

where c is the crack length, n is the number of cycles and X and ψ are rubber crack growth parameters determined from an independent pure shear fatigue crack growth rate test and the strain energy release rate T. T* is introduced in Equation 3 in order to make the part of the equation raised to a power dimensionless. It is given a value of 1 Jm^{-2}. The measurements follow the procedure described by Tsunoda et al. (2000). All of the experiments in this paper were carried out at room temperature, which was observed to range from 20° to 25°C. The measured crack growth parameters are shown in Table 2 and are plotted in Figure 4.

All the abrasion experiments were carried out using equipment described by Fukahori et al. (2008).

Table 2. Values of the crack growth properties ψ and X measured using a pure shear crack growth fatigue test piece for all the compounds.

Materials	ψ	$X \times 10^{-17}$/m
BR0	2.97	398
NR0	2.92	7.88
SBR0	3.61	1.16
SBR25	3.06	9.14

Solid cylindrical rubber wheels were prepared for all four materials. The wheels were initially 68 mm in external diameter, 12.4 mm in internal diameter and 12.5 mm wide. They were held in a clamp and were abraded by rotating against a stationary razor blade edge. The wheels were rotated at an average sliding speed of 70 mm/s. The normal load was applied directly on the abrasion blade using weights of 4 N, 8 N, 12 N, 16 N and 20 N on each material. The weight of the specimen was monitored regularly by removing the specimens from the machine and weighing them. Once the abrasion processes reached steady state, the average rate of weight loss dw/dn was constant. The different rate of weight loss per cycle was measured for all the materials and all the loading conditions. The method to convert this weight loss into an average rate of crack growth is described in detail in Liang et al. (2009a). It requires the careful examination of micrographs of the abrasion surface which in combination with knowledge of the weight loss allows the rate of advancement of the crack at the root of the asperity to be calculated as well as the angle at which the abrasion pattern is advancing into the rubber. Thus the actual crack growth rate per cycle dc/dn can be calculated for each point and this is plotted in Figure 5. Each of the wheels is sectioned perpendicular to the abraded surface to allow the abrasion pattern to be more easily observed and to allow representative models to be derived for the

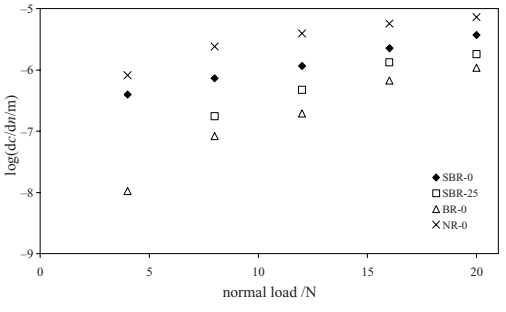

Figure 5. The resolved crack growth rate per cycle during wear versus the normal load.

finite element work. These representative patterns are shown in Figure 6 for a 12 N abrasion force.

All the finite element models used the explicit dynamics finite element package ABAQUS/Explicit, version 6.4. A representative single ridge photograph of a steady state condition is shown in Figure 7 for SBR0 developed under a 12 N normal load and in Figure 8 for BR0 developed under a 12 N normal load. The FEA model dimensions being taken directly from measured abrasion patterns. In order to simplify the structure of the models, the ridge was assumed uniform through its thickness and therefore a plane strain model was appropriate. Two dimensional plane strain reduced integration elements with hourglass control (CPE4R) were used.

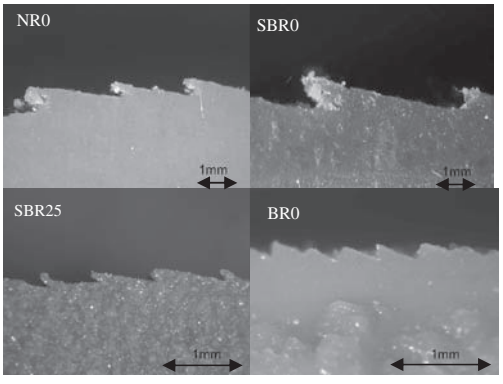

Figure 6. Sectioned profiles of the saw tooth abrasion pattern for each rubber material.

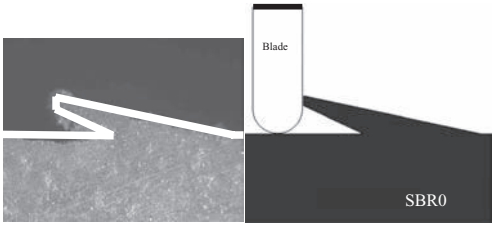

Figure 7. The sample geometry for SBR0 developed at steady state using a 12 N force and a schematic of the finite element model adopted in the analysis.

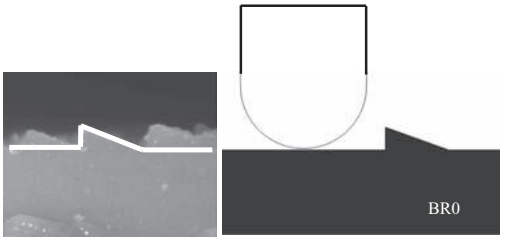

Figure 8. The sample geometry for BR0 developed at steady state using a 12 N force and a schematic of the finite element model adopted in the analysis.

The same approach was used to calculate the strain energy release rate as was described by Liang et al. (2009a). The velocity of the abrader in the explicit dynamics finite element model was the same as the average wheel surface rotation speed at 70 mm/s. The abrader was initially moved down vertically to compress the rubber until the required normal load was achieved. This vertical displacement was maintained throughout the analysis and the abrader was moved horizontally to abrade the ridge until the ridge had been completely passed over and had been released. The virtual crack extension technique was used to calculate the strain energy release rate. The configuration was modelled and the total strain energy in the rubber as the asperity is deformed monitored. It is then remodelled with the length of the cut at the root of the asperity increased slightly in length and in the direction measured during the wear measurement. This has the effect of slightly increasing the length of the tongue of the abrasion pattern. The difference between the two energies at equivalent displacements defines the energy released as the cut length is increased. The strain energy release rate being the change in energy divided by the increase in the crack surface area.

The role of friction in these models is very important. To ensure an appropriate coefficient was used in each case the friction was altered until the measured horizontal force matched that calculated by the finite element model.

The value of the strain energy release rate calculated for a set of conditions is shown in Figure 9

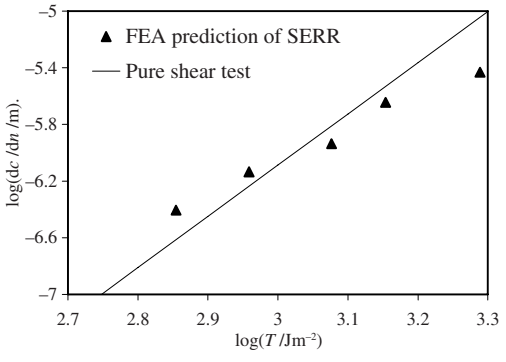

Figure 9. The crack growth rate plotted versus strain energy release rate (SERR) measured from the abrasion test shown as the data points for SBR0 compared with that measured from the cyclic fatigue crack growth test shown as the line.

against the measured crack growth rate measured during the abrasion. Also plotted on the line is the independently measured crack growth rate from a fully relaxing cyclic fatigue test measured using a pure shear crack growth test geometry. For the case of SBR0 shown in Figure 9 the prediction is excellent as was shown by Liang et al. (2009a).

3.2 *Abrasion discussion*

Figure 5 shows the rate of advancement of individual asperities. BR0 has the slowest rate and NR0 is the fastest with SBR25 showing some improvement in the wear rate when compared to SBR0. The size of the abrasion asperities are largest for NR0 and they are much smaller for BR0. Also the spacing between the asperities is smallest for BR0. The abrasion patterns for the SBR0 and SBR25 are broadly similar to each other and the pattern for BR0 is by far the smallest in size, with virtually no tongue being developed at the asperity.

The virtual crack extension method allows the strain energy release rate to be calculated under exceptionally challenging conditions. The calculated strain energy release rate for a given asperity and a given normal force of 12 N is used to look up the crack growth rate in Figure 4 and the data compared to the measured abrasion rate in Table 3. The abrasion rate predictions are good for SBR0 and SBR25. The rate calculated from the BR0 is also of the correct order of magnitude, which is typically considered a good fit for this type of calculation. The calculated rate is about five times faster than the measured rate. This difference may be due to an increased significance of rate effects. From both the measured results and the predicted results the abrasion processes for BR0 are slower than for NR0 and SBR0.

Table 3 shows for NR0 the measured abrasion is about thirty times faster than expected from the fracture mechanics prediction alone. It is likely strain induced crystallisation improves the cyclic fatigue crack test results measured at 5 Hz to a much higher degree than the much faster abrasion process. This theory has been checked previously by Southern and Thomas (1979) using isomerised NR, which by virtue of suppressing the crystallisation in NR repositioned the NR back into the correct ranking. This would suggest the speed of loading during abrasion is fast enough to beat the rate of crystallisation.

Table 3. Calculated wear rate and the measured wear rate under for a 12 N normal force.

Materials	Rate from FEA & PS	From abrasion test
BR0	0.3×10^{-7} m	1.6×10^{-7} m
NR0	1.3×10^{-7} m	39.8×10^{-7} m
SBR0	4.4×10^{-7} m	11.7×10^{-7} m
SBR25	2.7×10^{-7} m	4.8×10^{-7} m

Even without the complications of strain induced crystallisation, the materials do not rank in the same order for the abrasion data as they do using the fatigue behaviour measured at 5 Hz. One possible thought is that in the weaker materials the asperities are torn off easily and the resulting tongue is on average much shorter. This results in a much lower strain energy release rate being available to drive the wear process at the root of the asperity. This lower strain energy release rate dominates the behaviour and therefore results in a lower abrasion rate than for the other materials.

This finding helps explain why weak materials are sometimes surprisingly good in abrasion. There are however some significant problems left still to tackle in abrasion of rubber. What determines the average asperity length and the angle at which the cut advances into the rubber surface? Also, how might a dramatic rise in the rate of loading, in particular if we could beat the crystallisation, change the predictions using this technique?

4 CONCLUSIONS

Friction is typically attributed to both adhesion forces that are related to the intermolecular process taking place on the interface surface and hysteresis, being the viscoelastic energy lost in a certain volume of deformed rubber. This work reveals an additional geometrical factor also exists. This contribution is dependent on the depth of penetration of the rigid surface into the elastomer, changing the angle of contact between both surfaces. In contrast, tests using a different geometry (rubber hemisphere) did not show this effect. The entirely geometric contribution considerably increases the actual coefficient of friction in comparison to the input value and is anticipated to make a significant contribution to many everyday frictional sliding applications.

The strain energy release rate when combined with an independent measure of the rate of crack growth measured using a fatigue crack growth test gives a reasonable prediction of the abrasion rate for SBR0, SBR25 and BR0. However, NR0 appears to be about 30 times worse in abrasion than would be expected from the cyclic fatigue crack growth measurements. This is most likely to result from the strain induced crystallisation being suppressed by the very rapid loading rates encountered during blade abrasion.

It is apparent the low strength of BR0 results in much smaller asperities being formed under steady state abrasion. When these asperities are modelled they create low values of strain energy release rate which result in a much slower abrasion rate. Conversely the strongest material NR0 has the longest tongue on the asperity and this in turn generates much larger values for the strain energy release rate at the root of the asperity and this contributes to the poor abrasion resistance.

ACKNOWLEDGEMENTS

I would like to thank my collaborators on these topics: Hancheng Liang and Philip Gabriel for their hard work in measuring and modelling the behaviour described; Alan Thomas for his unwavering guidance and Yoshihide Fukahori for his thought provoking discussions. In addition I would like to thank Tun Abdul Razak Research Centre (TARRC) for the extensive use of their friction testing facilities and the loan of the abrasion testing facilities. Finally Bridgestone are thanked for financially supporting the research students.

REFERENCES

Amontons, G., Mémoires de l'acadèmie royale, Histoire de l'Académie Royale des Sciences avec les Mémoires de Mathématique et de Physique (1699) 206.

Busfield, J.J.C. and Thomas, A.G. (1999) Rubber Chemistry and Technology, **72,** 876–894.

Busfield, J.J.C., Jha, V., Liang, H., Papadopoulos, I.C. and Thomas, A.G. (2005) Plastics, Rubbers and Composites, **34**, 349–356.

Busfield, J.J.C., Tsunoda, K., Davies, C.K.L. and Thomas, A.G. (2002) Rubber Chemistry and Technology, **75**, 643–666.

Champ, D.H., Southern, E. and Thomas, A.G. (1974) Coatings and Plastics preprints, **34**, 237–243.

Fukahori, Y., Liang, H., Busfield, J.J.C., (2008) Wear, **265,** 387–395.

Gabriel, P., Thomas, A.G. and Busfield, J.J.C. (2009) submitted to Wear.

Gent, A.N. and Pulford, C.T.R. (1983) Journal of Applied Polymer Science, **28**, 943–960.

Kumar, P., Fukahori, Y., Thomas, A.G. and Busfield, J.J.C., (2007) Polymer Science Part B: Polymer Physics, **45,** 3169–3180.

Liang, H., Fukahori, Y., Thomas A.G., and Busfield, J.J.C. (2009a) Wear, **266**, 288–296.

Liang, H., Fukahori, Y., Thomas A.G., and Busfield, J.J.C. (2009b) submitted to Wear.

Persson, B.N.J. (2001) Journal of Chemical Physics, **118,** 3840–3861.

Schallamach, A. (1969) Wear, **13,** 13–25.

Smith, R.H., (2008) Analyzing friction in the design of rubber products and their paired surfaces, CRC Press, London.

Southern E. and Thomas, A.G. (1979) Rubber Chemistry and Technology, **52**, 1008–1018.

Tsunoda, K., Busfield, J.J.C., Davies, C.K.L. and Thomas, A.G. (2000) Journal of Materials Science, **35**, 5187–5198.

Constitutive Models for Rubber VI – Heinrich et al. (eds)

Wet and dry friction of elastomers in advanced simulation compared to experiment

L. Busse & M. Klüppel
Deutsches Institut für Kautschuktechnologie (DIK), Germany

ABSTRACT: Friction is an elemental process in any mechanical system. Understanding the parameters is vital for controlling friction, either to maximize or to minimize it. We investigate the influence of silica filler content in SBR rubber on the friction behaviour on wet and dry surfaces (rough granite and asphalt) at different velocities by tribologic experiments and by simulation. We present an advanced method based on a recently developed friction model for rough fractal surfaces, which can also predict other friction parameters, like the true contact area, by knowing the surface descriptors of the substrate and the viscoelastic behaviour of the elastomer. It is shown that by calculating relaxation time spectra, the number of free fit parameters can be reduced. Still, the results of simulations can well be adapted to the measurements. Generally, friction increases with filler concentration on wet substrates. The dry (adhesion) friction turns out to establish a high velocity plateau that becomes lower but more pronounced with increasing filler amount.

1 INTRODUCTION

Understanding Friction means understanding the interaction of material properties, surface properties and lubricant. Surfaces can be regarded as fractal in many cases (Mandelbrot 1982) as prerequisite of a mathematical description of friction phenomena.

Based on a fractal analysis, Klüppel & Heinrich (2000) developed a friction model for rubber on rough surfaces that can be expanded to any number of scaling ranges (Le Gal 2007). Originally used for wet friction systems described by Kummer (1986), dry systems became accessable with additional fit parameters (Le Gal & Klüppel 2005). The next logical task is to reduce the number of free fit parameters by material constants.

This shall be done by investigating how different amounts of filler in elastomers change the wet and dry friction on granite and asphalt with a silica amount up to 80 phr. Parameters gained from bifractal surface profile analysis and relaxation time spectra gained from viscoelastic properties are used to simulate friction and other features with a minimum of free fit parameters.

2 THEORY

2.1 *Self-affine surfaces*

The granite and asphalt of our experiments both are self-affine in surface, so a magnification α in the lateral xy-plane corresponds to a magnification α^H in vertical z-direction (Mandelbrot 1982). The implied Hurst coefficient H gives the fractal dimension $D = 3 - H$. This self-affinity is true only below the macroscopic scale denoted by the lateral cut-off length $\xi_{\|}$ and its corresponding vertical length $\xi_{\perp}$. They can be calculated with the height-difference correlation function:

$$C_z(\lambda) = < (z(x+\lambda) - z(x))^2 > \tag{1}$$

which describes the correspondence of two points separated laterally by the distance λ with heights $z(x)$ and $z(x+\lambda)$. Applied over the complete surface profiles, "< >" denotes the average operator.

Above $\xi_{\|}$ and $\xi_{\perp}$, the flat surface shows no correlation between the analyzed points whereas below these cut-off length, self similar surfaces display in the correlation function a graph with slope H. When two self similar structures superpose on the surface, the graph can be described by two linear parts separated at the cross over lengths λ_2, λ_3 etc. and corresponding Hurst coefficients and thus fractal dimensions. The linear relationship between C_z and the surface descriptors $\xi_{\perp}$, $\xi_{\|}$, λ_2, D_1 and D_2, for two self similar structures for $\lambda > \lambda_2$ is (Le Gal et al. 2006)

$$C_Z(\lambda) = \xi_{\perp}^2 \cdot \left(\frac{\lambda}{\xi_{\|}} \right)^{2H_1} \tag{2}$$

and for $\lambda < \lambda_2$

$$C_Z(\lambda) = \xi_\perp^2 \cdot \left(\frac{\lambda}{\lambda_2}\right)^{2H_2} \cdot \left(\frac{\lambda_2}{\xi_{\|}}\right)^{2H_1} \tag{3}$$

If more than two scaling ranges should be necessary, these formulas can be expanded to any wanted number of multifractality (Le Gal et al. 2007).

2.2 *Hysteresis friction simulation*

The total friction $\mu_{tot} = \mu_{Adh} + \mu_{Hys}$ consists of the adhesion friction μ_{Adh} and hysteresis friction μ_{Hys}. The latter appears when local asperities deform the rubber sample and cause energy dissipations. According to our model the hysteresis friction under normal force F_N is for two scaling ranges depending on velocity v (Müller et al. 2002)

$$\mu_{Hys}(v) \equiv \frac{F_{Hys}}{F_N} = \frac{<\delta>}{2\,\sigma_0 v} \cdot \left(\int_{\omega_{\min}}^{\omega_2} \omega \cdot \mathrm{E}''(\omega) \cdot S_1(\omega)\, d\omega + \int_{\omega_2}^{\omega_{\max}} \omega \cdot \mathrm{E}''(\omega) \cdot S_2(\omega)\, d\omega \right) \tag{4}$$

using the Fourier transformed power spectrum densities $S(\omega)$ (Meyer et al. 2008) with $\omega_{\min} = 2\pi v/\xi_{\|}$ and $\omega_2 = 2\pi v/\lambda_2$

$$S_1(\omega) = \frac{(3 - D_1) \cdot \xi_\perp^2}{2\pi v \xi_{\|}} \cdot \left(\frac{\omega}{\omega_{\min}}\right)^{-\beta_1} \tag{5}$$

for $\omega_{\min} < \omega < \omega_2$ or

$$S_2(\omega) = \frac{(3 - D_1) \cdot \xi_\perp^2}{2\pi v \xi_{\|}} \cdot \left(\frac{\omega_{\min}}{\omega_c}\right)^{\beta_1} \cdot \left(\frac{\omega}{\omega_c}\right)^{-\beta_2} \tag{6}$$

for $\omega_2 < \omega$, with $\beta_1 = 7 - 2D_1$ and $\beta_2 = 7 - 2D_2$.

E'' is the loss modulus of the elastomer, σ_0 is the applied pressure and $<\delta> = b < z_p >$ is the mean excitation depth inside the rubber with the mean penetration depth z_p of the asperities into the rubber, scaled by the factor b.

The true contact area A_c in contrast to the nominal contact area A_0 is (Le Gal et al. 2007)

$$\frac{A_c}{A_0} \approx \left(\frac{\xi_{\mathrm{II}} \cdot F_0^2(t) \cdot F_{3/2}(t_s) \cdot \left|E(2\pi v/\xi_{\mathrm{II}})\right| \tilde{n}_s^{\,2}}{808\pi \cdot s^{3/2} \cdot \xi_\perp \cdot \left|E(2\pi v/\lambda_{\min})\right|} \right)^{\frac{1}{3}} \tag{7}$$

$$F_0 = \int_t^\infty \phi(x)\,dx \quad \text{and} \quad F_{3/2} = \int_t^\infty (x-t)^{3/2} \cdot \phi(x)\,dx \tag{8}$$

are the Greenwood-Williams functions (Greenwood & Williamson 1966) with the normalized distances $t = d/\sigma_{HD}$ and $t_s = d/\sigma_{SHD}$ with the gap distance d and the standard deviations σ_{HD} of the height distribution and σ_{SHD} of the summit height distribution.

2.3 *Adhesion friction simulation*

On dry systems, adhesion has to be considered additionally to hysteresis friction, because molecular interactions with the force F_{Adh} appear, leading to the adhesion friction coefficient (Le Gal & Klüppel 2005)

$$\mu_{Adh} = \frac{F_{Adh}}{F_N} = \frac{\tau_s \cdot A_c}{\sigma_0 \cdot A_0} \tag{9}$$

with the applied pressure σ_0 and the interfacial shear stress τ_s (Le Gal & Klüppel 2006)

$$\tau_s = \tau_0 \cdot \left(1 + \frac{E_\infty/E_0}{(1 + (v_c/v))^n}\right) \tag{10}$$

The static shear stress τ_0 and the critical velocity v_c, where the τ_s converges to a maximum (De Gennes 1996), are free fit parameters. E_∞/E_0 and n (Persson & Brener 2005) are material parameters.

$$n = \frac{1-m}{2-m} \tag{11}$$

is gained from the linear part $H = \tau^{-m}$ of the exponent $m(\tau) < 1$ in the glass transition range of the relaxation time spectra $H(\tau)$ (Williams & Ferry 1953)

$$H(\tau) = \frac{\left(1 - \frac{\alpha}{2}\right)}{\Gamma\left(2 - \frac{\alpha}{2}\right) \cdot \Gamma\left(1 + \frac{\alpha}{2}\right)} \cdot G' \cdot \frac{d\log(G')}{d\log(\omega)} \tag{12}$$

which can be evaluated from master curves of the storage modulus G' with the relaxation time $\tau = 1/\omega$, applying the local slope α to the gamma function Γ.

3 EXPERIMENTS & RESULTS

3.1 *Surfaces*

Two substrates are involved in our experiments: granite and asphalt. For both, height distributions $\Phi(z)$ were achieved from surface profiles. The granite distribution is more symmetric and steeper than asphalt. Height-difference correlations were calculated according to equation (1) and their surface parameters found for two scaling ranges, summarized in Table 1.

Table 1. Surface descriptors for granite and asphalt.

Surface descriptors	Granite	Asphalt
D_1	2.37	2.39
D_2	2.14	2.09
λ_2 [μm]	93.0	332
$\xi_\parallel$ [μm]	2490	1440
$\xi_\perp$ [μm]	310	430
$\xi_\parallel/\xi_\perp$	7.96	3.35

Both surfaces have similar fractal dimensions and their vertical roughnesses are only slightly different. Their horizontal cut-off lengths differ and make a higher parallel-orthogonal ratio on granite, which is less sharp. The cross-over length on asphalt is larger due to the grain size.

3.2 *Material*

Samples with a thickness of 2 mm consist of S-SBR 2525 unfilled and with 20, 40, 60 and 80 phr silica Ultrasil GR7000. To find their viscoelastic behaviour, dynamic-mechanical analysis has been performed and extracted into master curves for functions of the shear moduli G' and G''. Frequency sweeps give discrete branches for every temperature, which can according to the time-temperature-superposition principle be shifted horizontally in order to form a continuous curve with a fix branch at 20°C. Above the glass transition temperature, the shift factors obey the WLF relationship with WLF constants $C_1 = -3.85$ and $C_2 = 91.2$°C, for the unfilled sample. Though filled samples also apply these factors, vertical shifting is necessary as well.

The master curves in Figure 1 show how the glass transition is broadened with rising filler content and how the filler increases G' monotonously in the low frequency range and leaves the high frequencies unchanged, so the ratio $E'_\infty/E'_0 = G'_\infty/G'_0$ as used in equation (11) decreases (Table 2).

The loss modulus G'' in Figure 2 also increases monotonously with filler content at low frequencies, whereas its maximum and the higher frequencies keep their position.

The maximum of $\tan\delta = G''/G'$ decreases strongly when filler is added but does not change frequency (Figure 3).

Relaxation time spectra with can be calculated from DMA measurements with equation (12) using the Ferry method with two iteration steps. The linear negative slope $m < 1$ in Figure 4 between absolute maximum at $\tau < 10^{-7}$ s and beginning minimum at $\tau > 10^{-3}$ s, is flattened by increasing filler, thus increasing n as given in equation (11). Values

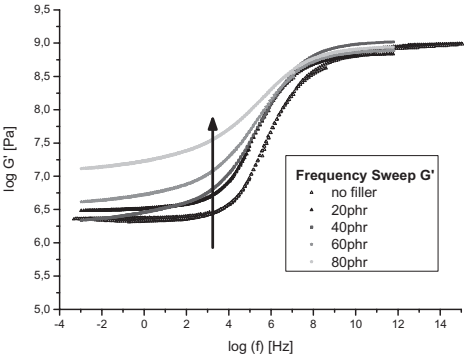

Figure 1. Master curves for G'.

Table 2. Material fit parameters.

phr Silca	E_∞/E_0 (f)	Slope m	Exponent n
0	473.2	0.714	0.209
20	298.2	0.711	0.211
40	541.1	0.594	0.283
60	389.2	0.441	0.357
80	177.8	0.358	0.390

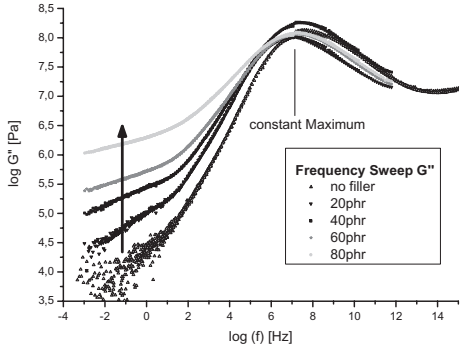

Figure 2. Master curves for G''.

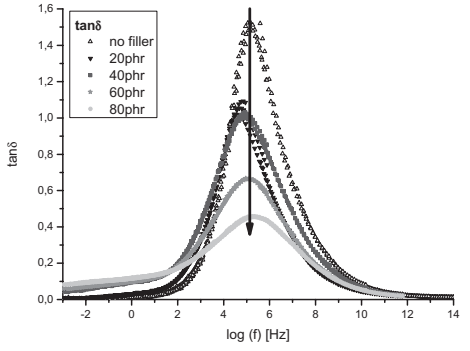

Figure 3. Master curves for $\tan\delta$.

for it are noted in Table 2. We use these exponents to fit simulation to adhesion measurements.

3.3 *Friction*

Friction has been measured with 50 mm ∗ 50 mm samples sliding stationary between 0,01 mm/s and 30 mm/s on dry and wet surfaces with a pressure of 12.3 kPa at room temperature. To validate our model, simulations based on material and surface parameters have been conducted and fit to the experiments with parameters from Table 2 and Table 3.

To exclude adhesion, the substrate has been covered with a 5% vol tenside in water solution. These wet systems result in hysteresis friction solely, as shown in Figure 5: Friction increases with velocity. This holds over the whole investigated range, though on asphalt the increase is diminished when sliding fast because of its smoother surface. In general, friction is augmented by applying more filler to the samples as the filler increases the shear moduli of the elastomer and thus hysteresis. Both substrates establish comparable friction coefficients. The measured curves can be simulated well for low and moderate velocities, but less accurate when sliding faster than a few mm/s. Simulations for high fillings are less steep and thus less dependent on velocity because their elasticity depends less on temperature and thus less on frequency than for weak filling. The scaling factor b drops from high to constant values as soon as 40 phr silica is reached, and is higher on asphalt where penetrating asperities propagate more deeply.

Even in dry state, substrates do not differ much in friction. Here, an adhesion part is added to the hysteresis part, which drastically increases friction, as seen in Figure 6. Growing filler content does not necessarily increase total friction but establishes a plateau at higher velocities, like it was observed by Le Gal & Klüppel (2008) and Grosch (1963) in similar systems. The reason is that the adhesion friction contrarily to hysteresis decreases above moderate velocity (some mm/s) and also with filler amount because the true contact areas decreases with velocity. The higher hardness of filled elastomers prevents the rubber from intense contact, too. The paramount friction for 40 phr filling corresponds well to the maximum of the fitted critical velocity. The simulation is excellent for all samples on both substrates, even though the number of free fit parameters has been reduced by deriving n from material properties, except

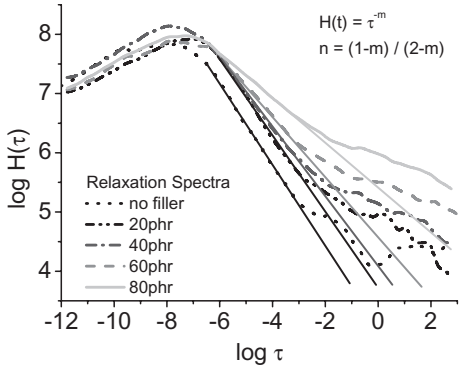

Figure 4. Relaxation time spectra of the sample pool.

Table 3. Free fit parameters.

	Granite			Asphalt		
phr Silica	b –	τ_0 kPa	v_c mm/s	b –	τ_0 kPa	v_c mm/s
0	70	5.91	0.020	–	–	–
20	27	6.56	0.045	10	64	0.62
40	7	15.4	1.90	4.5	150	9.00
60	6.8	18.8	0.90	5.5	110	0.60
80	7.5	48.8	0.33	7	420	1.00

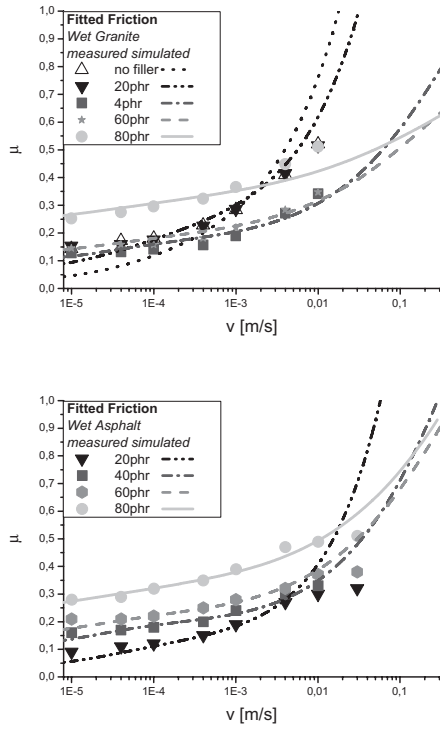

Figure 5. Wet friction for granite (top) and asphalt (bottom).

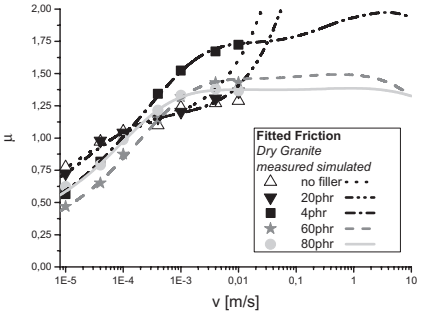

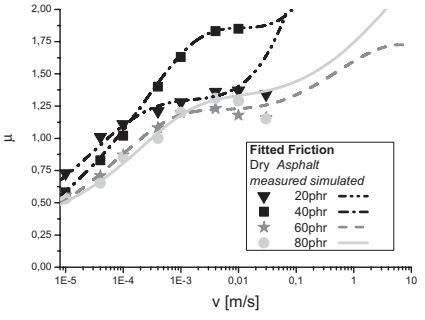

Figure 6. Dry friction for granite (top) and asphalt (bottom).

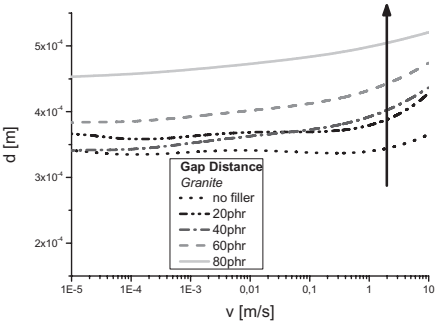

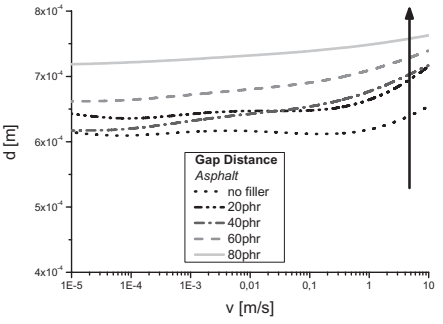

Figure 7. Gap distance for granite (top) and asphalt (bottom).

for the fast velocities on asphalt. Temperature effects by friction heating may not be ruled out on dry substrates when the sliding speed is high enough, resulting in increased elasticity and thus in decreased hysteresis as part of total friction.

3.4 *Contact simulation*

The gap distance d between the rubber bottom and the mean substrate height $< z >$ can directly be predicted by simulation. It increases with velocity (Figure 7), as the time for the elastomer to enter the cavities of the substrate is reduced. Filler increases the gap distance as decreasing the elasticity prevents the rubber to fill cavities. On asphalt the distance is a bit higher due to the slightly higher $\xi_\perp$.

The true contact area in Figure 8 decreases to the per mille range with filler content and velocity, caused by the vanishing ability of rubber to fill the gaps and thus get in contact with its interface when either the elasticity or the contact time is diminished. Contact on granite is larger than on asphalt because the larger ratio $\xi_\parallel/\xi_\perp$, meaning a flatter surface, allows more contact, even for high velocities.

The shear stress τ_s as free adhesion fit parameter in equation (10) rises and converges with velocity, as seen in Figure 9. It also rises with filler amount due to a decrease in elasticity for both granite and asphalt, just like its starting values τ_0. Shear stress is definitely higher on asphalt and rises about one decade later. The exponent n distorts the curves with increasing filler. Increasing n, decreasing E_∞/E_0 and increasing τ_0 let the critical velocities v_c reach a maximum at 40 phr, indicated by dots in the graph.

4 CONCLUSIONS

Silica in steps of 0, 20, 40, 60, 80 phr has been mixed in SBR252. Surface, material and friction experiments have been conducted and compared to simulations on wet and dry granite and asphalt, based on a model for fractal surfaces. Master curves for G′ and G″ show a low frequency increase, a tan δ decrease with filler and a rising n for the relaxation time spectra.

Hysteresis friction increases with velocity quite similarly on both substrates, and is increased by filler. On dry substrates friction is augmented for low velocities, then converges to higher velocity with rising filler amount, especially on granite, which can well be confirmed by simulations for all substrates and lubrications. Accuracy is not limited by reducing the number of free parameters when regarding n as a given material parameter.

Further simulation results with increasing filler include a higher gap distance, a decreasing true contact area and a rising shear stress, which is much higher on asphalt.

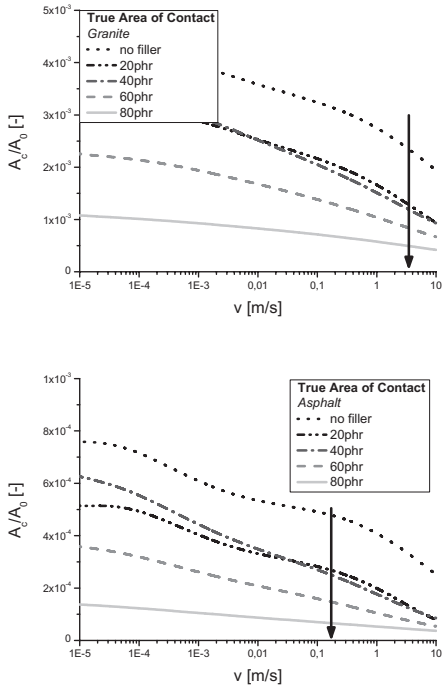

Figure 8. True contact area for granite (top), asphalt (bottom).

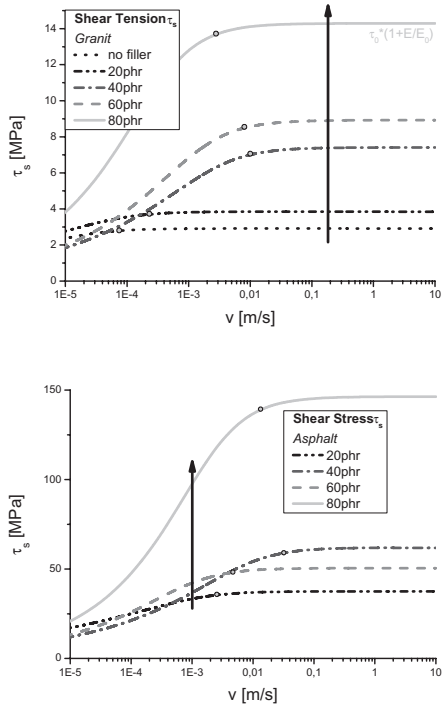

Figure 9. Shear stress for granite (top) and asphalt (bottom).

ACKNOWLEDGEMENTS

We would like to thank A. Le Gal and N. Zhang for their valuable contributions and the DFG for financial support in FOR492.

REFERENCES

De Gennes, P. 1996. Soft Adhesives. *Langmuir* 12, 4497.

Greenwood, J. & Williamson 1966. *J., Proc. R. Soc.* London, A295, 300.

Grosch, K. 1963. The relation between the friction and visco-elastic properties of rubber. *Proc. R. Soc. London A* 274, 21.

Klüppel, M. & Heinrich, G. 2000. Rubber Friction on Self-Affine Road Tracks. *Rubber Chem. Technol.* 73, 578.

Kummer, H. 1986. *Rubber Chem. Technol.* 41, 895.

Le Gal, A. & Klüppel, M. 2005. Modelling of rubber friction: A quantitative description of the hysteresis and adhesion contribution. *Constitutive Models for Rubber IV*, Tabor & Francis Group, London.

Le Gal, A., Yang, X. & Klüppel, M. 2005. Evaluation of sliding friction and contact mechanics of elastomers based on dynamic mechanical analysis. *J. Chem. Phys.* 123, 014704.

Le Gal, A. & Klüppel, M. 2006. Investigation and Modelling of Adhesion Friction on Rough Surfaces. *Kautschuk Gummi Kunstst.* 59, 308.

Le Gal, A., Yang, X. & Klüppel, M. 2006. Sliding friction and contact mechanics of elastomers on rough surfaces. *Analysis and Simulation of Contact Problems*, Springer, 253.

Le Gal, A. 2007. Investigation and Modelling of Rubber Stationary Friction on Rough Surfaces. *(PhD Thesis)* University of Hannover.

Le Gal, A., Guy, L., Orange, G., Bomal, Y. & Klüppel, M. 2007. Modelling of sliding friction for carbon black and silica filled elastomers on road tracks. *Wear* 264, 606.

Le Gal, A. & M. Klüppel 2008. Investigation and Modelling of Rubber Stationary Friction on Rough Surfaces. *J. Phys. Condens. Matter* 20, 015007.

Mandelbrot, B. 1982. *The fractal geometry of nature*. W.H. Freeman, N.Y.

Meyer, T., Busse, L., Le Gal, A. & Klüppel, M. 2008. Simulations of hysteresis friction and temperature effects between elastomers and rough or microscopically smooth interfaces. *Constitutive Models for Rubber V*, Tabor & Francis Group, London.

Müller, A., Schramm, J. & Klüppel, M. 2002. Ein neues Modell der Hysteresereibung von Elastomeren auf fraktalen Oberflächen. *Kautschuk Gummi Kunstst.* 55, 432.

Persson, B. & Brener, E. 2005. Crack propagation in viscoelastic solids. *Phys. Rev. E* 71; 036123.

Williams, M. & Ferry, J. 1953. Second Approximation Calculations of Mechanical and Electrical Relaxation and Retardation Distributions. *J. Polym. Sci.* 11, 169.

Constitutive Models for Rubber VI – Heinrich et al. (eds)
© 2010 Taylor & Francis Group, London, ISBN 978-0-415-56327-7

Compression of rubber disks between frictional surfaces

A.N. Gent, F.M. Discenzo & J.B. Suh
Departments of Mechanical Engineering & Polymer Science, University of Akron, Akron, Ohio, USA

ABSTRACT: A review is given of the compression of a rubber disk sandwiched between two rigid surfaces and either bonded to them or held by friction. Distributions of normal and shear stress are determined in both cases, and the overall compressive stiffness is evaluated as a function of disk aspect ratio a/h, where a is the radius and h is the thickness. Force-displacement relations during retraction are also derived, and the total energy expended in frictional sliding is calculated. A large fraction (about one-half) of the input energy is found to be dissipated against friction for disks of large aspect ratio, compressed between low-friction surfaces. Finite Element Analysis (FEA) was also carried out. The stress distributions and force-displacement relations were generally quite similar to the analytical results, even though the stress singularity at the edge of the disk is ignored in the analysis.

1 INTRODUCTION

Rubber blocks are widely used as compression springs and cushioning devices. Frictional constraints at the loaded surfaces prevent a block from expanding freely outwards, and the apparent compression modulus is therefore greater than the actual modulus. Approximate solutions are given for blocks of circular cross-section, sandwiched between rigid frictional surfaces. The compressive strains are assumed to be small and the rubber is taken to be linearly-elastic and incompressible in bulk. Coulomb's frictional law is assumed to hold.

Finite element (FE) calculations of the interfacial stress distributions were also made, using ABAQUS software. The ratio a/h of radius to thickness was given values between 1 and 12. The compressive strain was increased from zero to 2% in increments of 0.1%, and then decreased back to zero. The friction coefficient μ was assigned values between 0.1 and 1.

2 SMALL COMPRESSIONS OF BONDED BLOCKS (GENT 1994)

The deformation is regarded as the superposition of a homogeneous compression and shear deformations that restore points in the planes of the bonded surfaces to their original positions. An originally-vertical plane becomes parabolic, with a maximum outwards displacement k, obtained from the conservation of volume as $3er/4$ at a radial distance r and a compressive strain of e. Both FE calculations and direct observation show that the outwards displacement of the free surface of a thin block is quite close to a parabolic shape (Fleischman & Gurvich 2003). The outwards deformation is assumed to be maintained by an internal pressure P, given by:

$$P/Ee = (a^2 - r^2)/h^2 \tag{1}$$

where E is Young's modulus of the rubber and h is the block thickness. Shear stresses t set up at the bonded interfaces are given by

$$t = Eer/h. \tag{2}$$

Measurements of the interfacial stresses for bonded blocks under small compressions were in good agreement with Eqs. 1 and 2 (Gent et al 1974).

The contribution F_1 to the compressive force arising from restraints at the bonded surfaces is obtained by integrating Eq. 1 over the loaded area. Adding the contribution from simple compression, the total force F is obtained as:

$$F/\pi a^2 Ee = 1 + (1/2)(a/h)^2. \tag{3}$$

Constraints due to bonding thus raise the apparent modulus for thin bonded blocks by a large factor.

3 COMPRESSION OF A DISK BETWEEN FRICTIONAL SURFACES (DISCENZO, 1975, THORNTON ET AL. 1988, 1989)

Slipping outwards will occur when the shear stress t reaches the maximum permitted by friction. The amount k of lateral bulging is then reduced

to $3(er - 2u)/4$, where u is the slip distance at a radial distance r. The corresponding shear stress t becomes $-\mu(P + Ee)$, and P in the slip region is obtained as

$$P(r \geq r_1) = Ee \{\exp [2\mu(a - r)/h] - 1\} \quad (4)$$

where r_1 is the radial distance at which slipping starts. On equating dP/dr from Eq. 4 and Eq. 1, r_1 is obtained as $\mu h \exp [2\mu(a - r_1)/h]$. Note that this result does not include the amount of compression. Thus the size of the slip zone is predicted to be independent of the applied load.

4 COMPARISON WITH FE RESULTS

Calculated shear stresses t are shown in Figure 1 for a disk of aspect ratio $a/h = 12$. Corresponding curves from FEA are included. They are quite similar. Initially, the stress increases linearly from the disk center up to r_1. Then a sharp transition occurs; the stress decreasing exponentially with r to the edge of the disk.

5 APPARENT MODULUS E_A AND ENERGY DISSIPATED IN SLIDING

The compressive force F can be obtained by integration as before, yielding:

$$F/\pi a^2 Ee = [(R_1^4\, a^2/2h^2) + (R_1^3\, a/\mu h)) + (R_1^2/\mu^2) + (R_1\, h/2a\mu^3) - (h/a\mu) - (h^2/2a^2\mu^2)] \quad (5)$$

where $R_1 = r_1/a$. The right-hand side of Eq. 5 is the ratio of the apparent modulus E_a to the actual modulus E. Values are plotted in Figure 2 against a/h for selected values of μ. Even small amounts of slipping are seen to cause large reductions in apparent modulus.

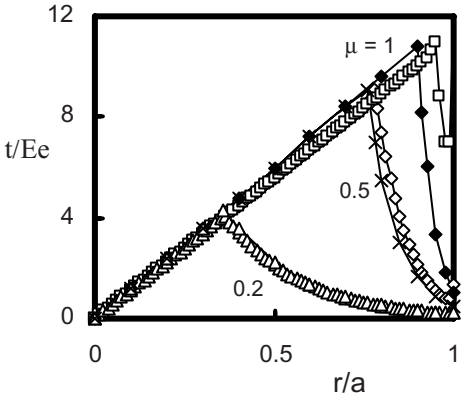

Figure 1. Shear stresses from analysis and FEA for a disk of aspect ratio $a/h = 12$.

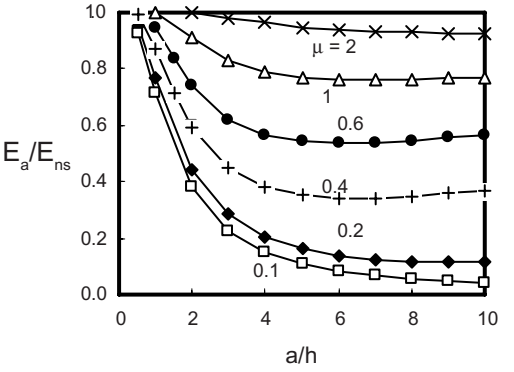

Figure 2. Effective compression modulus E_a vs aspect ratio a/h of disks compressed between surfaces with friction coefficient μ. E_{ns} denotes the effective modulus for a bonded disk, from Eq. 3.

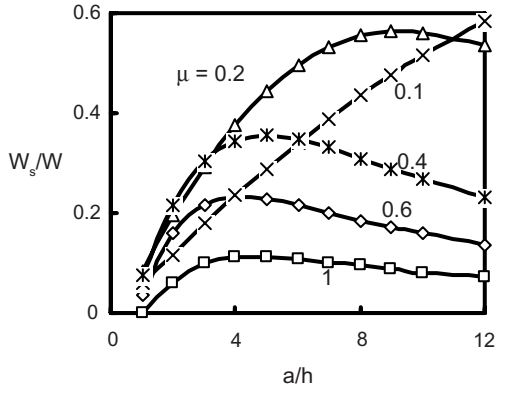

Figure 3. Energy W_s dissipated in frictional sliding as a fraction of input energy W vs aspect ratio a/h for disks compressed between frictional surfaces.

The energy W_s expended against friction can be calculated by integrating contributions from sliding motions at corresponding shear stresses t. Values are plotted in Figure 3. They are seen to approach 50% for blocks of high aspect ratio compressed between low-friction surface.

ACKNOWLEDGEMENTS

This work forms part of a program of research supported by the Lord Corporation. A fuller account of it is given elsewhere (Gent et al, 2009).

REFERENCES

Discenzo, F.M. 1975. Compression and retraction of a circular disk between flat parallel rigid surfaces. M.S. Thesis, University of Akron (1975).

Fleischman, T. & Gurvich, M.R. 2003. A simple approach to characterize finite compressibility of elastomers. *Rubb. Chem. Technol.* 76: 912–922.

Gent, A.N. 1994. Compression of rubber blocks. *Rubb. Chem. Technol.* 67: 549–558.

Gent, A.N., Henry, R.L. & Roxbury, M.L. 1974. Interfacial stresses for bonded rubber blocks in compression and shear. *ASME J. Appl. Mech*. 41: 855–859.

Thornton, J.S., Montgomery, R.E.,Thompson, C.M. & Dillard, D.A. 1988, 1989. Analysis of interfacial stresses for elastomeric disks in compression. *Polymer Eng. Sci.* 28: 655–659; 29: 432 (1989).

Constitutive Models for Rubber VI – Heinrich et al. (eds)

The mechanics of sliding friction between a rigid indenter and a rubber surface

P. Gabriel, Y. Fukahori, A.G. Thomas & J.J.C. Busfield
Department of Materials, Queen Mary University of London, UK

ABSTRACT: The frictional behaviour of rubber is explored in this paper. Two principal factors, adhesion and hysteresis, are commonly considered to make the greatest contribution to rubber friction. Gabriel et al. (submitted) also highlighted the contribution from an additional geometric factor. The geometrical influence for a range of different indenters on rubber friction is investigated further here using finite element analysis. The frictional force resulting from the dynamic contact between a rigid cylinder and rubber can be considered in several ways: the first defined as rolling where the cylinder roles over the surface, which is believed to have a significant hysteresis term; the second where a cylinder is rotated in a fixed position relative to the sheet, where the geometry does not change and hence the adhesion term would be the dominant contribution. The third situation requires a locked cylinder to be dragged without rotation over a rubber surface. In this case there will be a contribution from adhesion and hysteresis. The detailed relationship between these terms is explored here for a rubber with a high glass transition temperature and hence large viscoelasticity at room temperature.

1 INTRODUCTION

Different contributions to rubber friction are investigated in this paper. The main sources for the frictional force arise when an elastomer is slid over a rigid surface are described as a combination of both an adhesional and a hysteresis term. The adhesional term is a surface effect resulting from the intermolecular interaction between two surfaces (Roberts & Thomas 1975). The hysteresis term, also sometimes known as the deformation contribution, results from the energy lost through the deformation process of a certain volume of rubber (Roberts 1992). Gabriel et al. (submitted) showed the geometry of the contacting surfaces can also make an additional contribution. Two cases were compared, in which a rubber was in sliding contact with a flat or hemispherical shaped surface. In the former case, the rubber stays in plane contact, whereas in the latter, the rubber conforms to the hemisphere, resulting in an increase in the frictional force. As shown in Figure 1 the contact area between a tyre and a road surface is governed by the geometry of the individual surface asperities. The arising frictional force is, therefore, influenced by the typical average shape and sharpness of individual asperities.

Extending the investigations on geometric effects, the influence of different interface geometries (conical and hemispherical) on the resulting frictional force is investigated to examine how both very smooth, as well as extremely rough surfaces can have a high coefficient of friction. In addition,

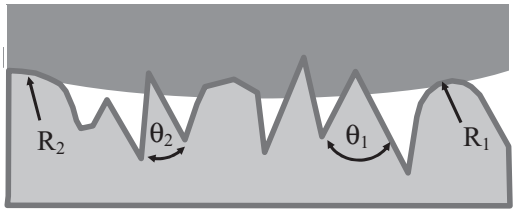

Figure 1. Schematic drawing of tyre and road contact. The different angles, θ, and radii, R, show the different idealised asperities.

three different frictional contact situations have been monitored experimentally: The first case uses a cylinder that rolls over a flat rubber surface where the frictional force results predominantly from the hysteresis contribution alone (Moore & Geyer 1972). The second case arises when a cylinder rotates in a fixed position, so there is no change in the deformed rubber state and hence the hysteresis term does not significantly contribute to the friction, once sliding is established. A third scenario arises when a cylinder slides over the rubber surface without rotation. In this third case both adhesional and hysteresis friction contribute to the overall behaviour. An experimental setup has been developed to investigate the different frictional forces arising during these rolling/sliding/rotation contact situations. It is often assumed the frictional forces from the three different frictional setups can

be expressed in a simple summation where the frictional force from sliding alone is expected to be the combination of the other two terms:

$$F_{SLIDING} = F_{ROTATION} + F_{ROLLING} \quad (1)$$

2 EXPERIMENTAL

The formulation, processing conditions and essential mechanical properties for the investigated rubbers are all shown in Table 1.

A number of steel cones from angles of 10° to 170° and polished steel hemispheres with diameters ranging from 6 mm to 240 mm were manufactured and tested on SBR. A pin-on-plane friction tester, developed by Roberts (1994), was used to measure the Coulomb coefficient of friction, which results from the frictional sliding force as the normal load F_N is varied from 1 N to 20 N. The sliding velocity was kept slow and constant at 0.0001 m/s in order to avoid flash temperature effects as investigated by Persson (2006). All experimental investigations throughout this work have been done at ambient temperature (23°C). Since the surface finish of bodies in contact has a significant influence on frictional force output the rubber was vulcanised in a grit blasted mould. This procedure diminishes the stick-slip effect often observed when two smooth, mirror-like surfaces are in contact. This rougher moulded surface produced more reproducible results than abrading the rubber surface manually with sand paper, as adopted previously (Grosch 1963). In a tyre/road contact the adhesional contribution to rubber friction is often neglected (Persson 1999), however, in a laboratory experiment without contaminations such as wear and dust particles, the adhesional term can make a significant contribution to the frictional force. The measured frictional force results, therefore, from a combination of hysteresis as well as adhesion components.

Table 1. Details of the two rubber compounds used in this work.

	SBR	IR
Ingredients [phr]		
SBR-0 Type 1500	100	0
3,4 Polyisoprene	0	100
Stearic Acid	2	1.5
Zinc Oxide	5	3
Antioxidant 6-PPD	3	1.5
Accelerator DPG	1.3	0
Accelerator MBTS	1	0
Accelerator CBS	0	2
Sulphur	1.5	1
Processing conditions		
Vulcanisation temp/°C	160	160
Vulcanisation time/min	60	60
Key properties		
Glass transition temp/°C	–45	–8
Young's modulus/MPa*	1.8	1

*10% strain chord modulus at 22°C.

For the finite element analysis (FEA), ABAQUS Explicit (Version 6.7, by Simulia) was employed to investigate changes in geometry and maximum principal stresses. Two-dimensional (axis-symmetric) models (Busfield & Thomas, 1999) as well as three-dimensional models have been used in indentation and friction simulation. As suggested by Jha et al. (2008) a Mooney stored energy function was used to model the elastic behaviour.

In the second experimental series rolling, sliding and rotation have all been investigated. Three friction testers, shown schematically in Figure 2 have

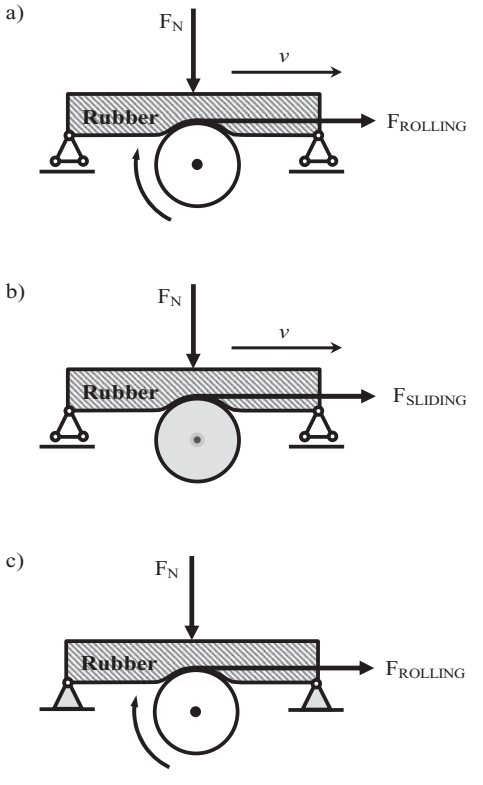

Figure 2. a) Setup to investigate rolling: Cylinder rotates due to moving rubber block with velocity *v*, while in position b) sliding is measured as the cylinder centre is fixed c) Setup to investigate rotational forces, where a screw driven cylinder rotates on a fixed rubber block.

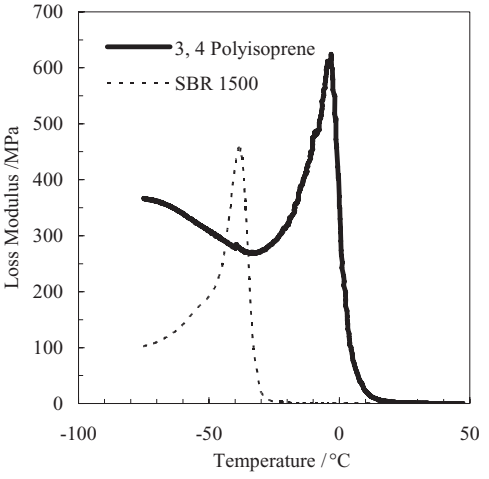

Figure 3. Temperature dependence of the loss modulus E″ measured for both rubbers via dynamic mechanical analysis (DMA) in tension mode. The maximum peak of E″ is located in the region of the glass transition temperature.

been developed in order to measure the force output of each of the above named states individually. Each uses geometrically identical contact situations, where a rubber block contacts a steel cylinder (the outer race of ball bearing, ∅ = 13 mm) under a given normal load ranging from 1 N to 10 N. Both $F_{ROLLING}$ or $F_{SLIDING}$ were measured directly whilst the rubber block is moved over the rubber roller. In contrast, the screw-driven roller in friction tester was rotated in a stationary position on the fixed rubber block to measure $F_{ROTATION}$.

As the force due to rolling is known to be small, a high loss 3, 4 polyisoprene rubber (with a high Tg of –8°C) was used, since the losses due to deformation in the rubber are higher and will be easier to measure than in a normal SBR-0 (with a lower Tg of –45°C) as shown in Figure 3.

Furthermore, the rubber surface was vulcanised with a mirror-like, smooth finish, resulting in an increase in the adhesional term of the total friction force. Similarly, the cylinder has a polished surface. The velocity (either sliding or rolling) at the point of contact of each system was kept constant at 0.01 m/s.

3 DISCUSSION AND RESULTS

While the indentation for hemispheres (Timoshenko & Goodier 1973) and conical indenters (Sneddon 1975) on infinite rubber blocks can be predicted mathematically, in case of finite block thicknesses (here 5.5 mm) these formulae fail to predict the indentation behaviour well. Therefore, the indentation of all the indenters was experimentally measured and confirmed using FEA (Busfield & Thomas, 1999). Whereas the hemispheres indent little into the rubber block, as shown in Figure 4, the indentation level of the cones increases rapidly with load. In the analytical approach the square of the penetration depth is proportional to the normal load. So the figure is plotted as depth squared versus load.

Figure 5 shows the influence of cone angle on dry rubber friction. Both, blunt cones and needle-like, sharp cones result in higher friction. From a cone angle of 160° up to 50°, the coefficient of friction was almost independent of the normal load and no scratch patterns were observed within the test range. With increasing cone sharpness a fracture pattern on the surface was observed even with just a single pass.

When the indenting cone is moved horizontally over the rubber, elastic energy is stored in the system and sliding occurs when the shear forces are exceeded by the horizontal frictional force. According to Gent (2001) the stored energy can be the driving force for propagating cracks, and, as described by Fukahori et al. (2008), cracks propagate in abrasion processes if the local stresses are bigger than the tensile stresses. The sharper the cone, the higher the stress concentration underneath the tip in the rubber creating a higher

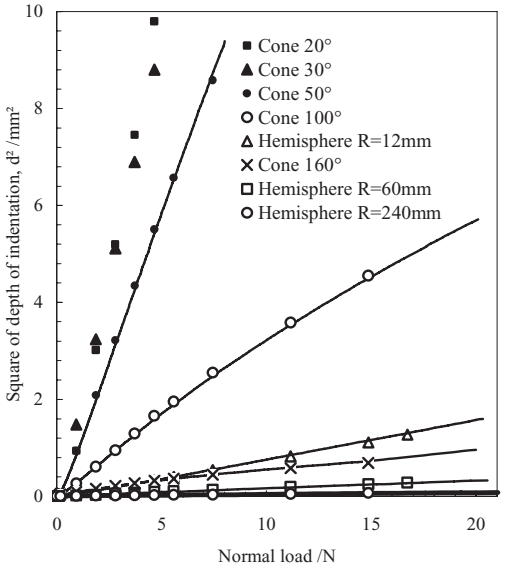

Figure 4. The indentation behaviour of cones and hemispheres on SBR can be predicted well using FEA code. Data points reflect experimental data, whereas lines show FEA calculation.

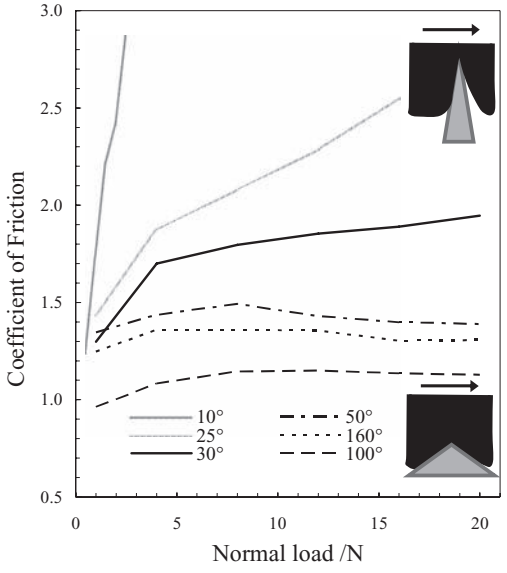

Figure 5. Frictional sliding of conical indenters over SBR. The resulting frictional force broadly increases with increasing cone sharpness.

probability tearing can be established. In addition to adhesional and hysteresis losses, the energy lost due to fracture of rubber contributes to the total frictional force, resulting in an increase of the coefficient of friction with normal load for the sharper cones. With increasing cone sharpness the depth of indentation increases under similar normal loads, so a volume of rubber is deformed to a larger extent horizontally by a sliding indenter, increasing the energy losses due to deformation. In the extreme case of needle-like cones, the indentation can lead to penetration into the rubber, leading to an infinite coefficient of friction due to large horizontal deformation of rubber. When the cone angle increases to say a 160° cone angle the friction force is again seen to increase. While the maximum stresses at the tip of each cone increase with cone sharpness, for blunt cones the contact area increases, increasing the adhesional friction term. A flat surface with a cone angle of 180° would give in theory, a further increase in friction, as shear forces become greater for the two flat surfaces. Supporting this, as shown in Figure 6, with an increase in the radius of curvature producing a flatter profile, the friction increases. In contrast to cones, it decreases with load. These hemispheres under these normal loads did not generate abrasion, as the pressure distribution underneath the slider was lower.

It is shown, depending on the geometric contact situation, the frictional force differs significantly. For sharp, needle-like, asperities, the frictional force is a contribution from the deformation term (a well as a contribution from a tearing term), whereas with blunt asperities the influence in friction is more commonly due to the adhesional term. In order to replicate the friction behaviour different FEA models such as those suggested by Liang et al. (2009) are required.

The frictional forces in the three measured states of friction: rolling, sliding and rotation are shown in Figure 7. As expected the frictional sliding force $F_{SLIDING}$ is greater than the values for $F_{ROTATION}$ and $F_{ROLLING,}$ as both, adhesion and hysteresis contribute during sliding. The force from rotation has a lower contribution from hysteresis as the rubber is just

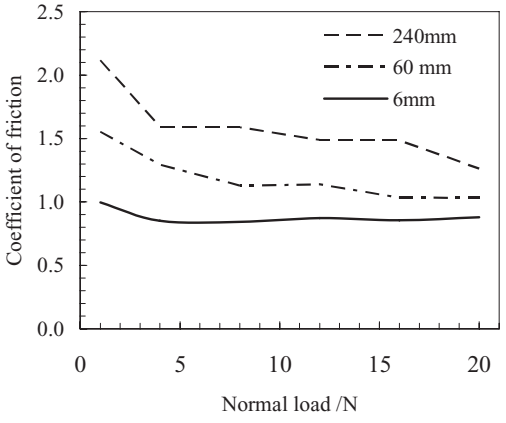

Figure 6. The coefficient of friction versus normal load for hemispherical indenters on SBR.

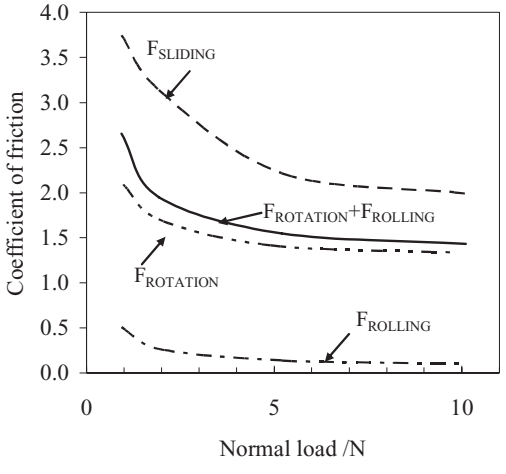

Figure 7. Three different states of rolling measured on IR. The frictional forces from rotation and rolling are insufficient to explain the sliding force output.

deformed at the start and a smaller force is required to maintain deformation once sliding is established. The rolling force is considered to result from a single hysteresis term alone. This could only be measured using a high loss, high T_g rubber, since similar tests on unfilled SBR and natural rubber compounds generated horizontal force outputs in the rolling state that were too small to measure. However, from Figure 7 it is clear, a simple summation of $F_{ROTATION}$ and $F_{ROLLING}$ would not express $F_{SLIDING}$ satisfactorily. Reasons for this can be the different amounts of deformation of rubber between sliding and rotation. Furthermore, as the rubber block conforms to the cylindrical indenter, wrapping of the rubber contributes to sliding, whereas less wrapping occurs for rolling and rotation contact. Further tests have to be undertaken to separate the different influences.

4 CONCLUSIONS

The frictional force for two different indenter geometries, conical and hemispherical, representing idealised asperities, in contact with a rubber block has been investigated. Two effects can be observed from different cones in contact with a rubber block: While the frictional force arising from nearly flat cones has a contribution due to a combination of adhesion and hysteresis, with increasing cone sharpness the frictional force results from additional tearing and a larger contribution from the deformation of a rubber volume. Furthermore, three different frictional contact conditions, namely rolling, sliding and rotation under the same geometric conditions have been investigated. The common assumption that a simple summation of the frictional rolling and rotational forces can express the frictional sliding force is shown to be not entirely valid. Further work is required to understand this behaviour further.

ACKNOWLEDGEMENTS

The authors gratefully acknowledge the access to research facilities at the Tun Abdul Razak Research Centre (TARRC), UK, as well as the rubber supplied by the Marangoni Group, Italy. One of the authors, P. Gabriel, would like to thank Bridgestone and the Engineering and Physical Sciences Research Council (EPSRC) for financial support.

REFERENCES

Busfield, J.J.C. and Thomas, A.G., 1999, Indentation tests on elastomer blocks, *Rubber Chemistry and Technology*, 72, 876–894.

Fukahori, Y., Liang, H. and Busfield, J.J.C., 2008, Criteria for Crack Initiation during Rubber Abrasion, *Wear*, 265, 387–395.

Gabriel, P., Thomas, A.G. and Busfield, J.J.C., Influence of interface geometry on rubber friction, submitted to *Wear*.

Grosch, K.A., 1963, The Relation between the Friction and Visco-Elastic Properties of Rubber, *Proceedings of the Royal Society of London. Series A* 274(1356), 21–39.

Jha, V., Hon, A.A., Thomas, A.G. and Busfield, J.J.C., 2008, Modelling of the effect of fillers on the stiffness of rubbers, *Journal of Applied Polymer Science*, 107, 2572–2577.

Liang, H., Fukahori, Y., Thomas, A.G. and Busfield, J.J.C., 2009, Rubber Abrasion at steady state, *Wear*, 266, 288–296.

Moore, D.F. and Geyer, W., 1972, A review of adhesion theories for elastomers, *Wear*, 22, 113–141.

Persson, B.N.J., 1999, Sliding Friction, *Surface Science Reports*, 33, 83–119.

Persson, B.N.J., 2006, Rubber friction: role of the flash temperature, *Journal of Physics: Condensed Matter*, 18, 7789–7823.

Roberts, A.D., 1992, A guide to estimating the friction of rubber, *Rubber Chemistry and Technology*, 65, 673–686.

Roberts, A.D., 1994, New rubber friction testing machine, *Rubber World*, 209(4).

Roberts, A.D. and Thomas, A.G., 1975, The Adhesion and Friction of smooth surfaces, *Wear*, 33, 46–64.

Sneddon, I., 1975, *Applications of Integral Transforms in the Theory of Elasticity*, New York, Springer-Verlag, Chapter A, Section 111.

Timoshenko, S.P. and Goddier, J.N., 1973, *Mathematical theory of elasticity*, New York, McGraw-Hill, Chapter 9, Section 108.

Fracture and crack propagation

Constitutive Models for Rubber VI – Heinrich et al. (eds)
© 2010 Taylor & Francis Group, London, ISBN 978-0-415-56327-7

Energy release rate of small cracks under finite multiaxial straining

M. Aït-Bachir & E. Verron
Institut de Recherche en Génie Civil et Mécanique UMR CNRS 6183, École Centrale de Nantes, Nantes Cedex, France

W.V. Mars
Cooper Tire and Rubber Company, Findlay, USA

ABSTRACT: The energy release rate of small cracks governs fatigue crack nucleation. A method is presented here to efficiently and accurately evaluate the energy release rate of such cracks, arbitrarily oriented, under general conditions of finite multiaxial loading. As a motivation, the dependence on crack length is then investigated. It is demonstrated that the energy release rate of small cracks is proportional to the crack length and that the proportionality factor is a function of the far-field parameters only. An attempt is then made to search for a general expression of this proportionality factor under simple loading conditions.

1 INTRODUCTION

Studies carried out in the recent years have brought to light the physical phenomena governing fatigue life of rubber (Cam et al. 2004; Le Gorju 2007). It turns out to be driven by the growth of small cavities transforming then into small cracks and propagating throughout the material up to a critical size that leads to a major loss of material properties. The propagation of these small cracks represents the main stage of fatigue life.

Regarding small crack growth prediction two distinct approaches are usually considered. The crack initiation approach is based on the evaluation of the mechanical fields of a crack-free material in order to study how a small flaw would propagate when subjected to these mechanical conditions; this approach lies thus within the framework of continuum mechanics. Some predictors have already been developed to predict crack initiation (Mars 2002; Verron and Andriyana 2008). To the contrary, the crack propagation approach studies the propagation of an existing small crack embedded in the material (Gent et al. 1964; Lake and Lindley 1965).

Actually, in some simple cases it is possible to reconcile these two approaches. Indeed, considering a small crack of length c under plane stress uniaxial tension, Rivlin and Thomas have been able to factorize the energy release rate T (Rivlin and Thomas 1953):

$$T = 2kWc \tag{1}$$

where W stands for the strain energy density of the far-field region and k is a factor that depends only on the far-field loading conditions. This result has later been extended to both pure shear and equibiaxial tension (Yeoh 2002). Thus, it turns out that for a small crack subjected to simple loading conditions, the energy release rate is proportional to the crack length and the proportionality factor is a function of the far-field parameters only.

In this paper we aim at developping a method to easily estimate the energy relase rate of small cracks under arbitrary plane stress loading conditions and then at investigating the factorization of the energy release rate with respect to the crack length.

2 METHODS

2.1 *A simple tool to model a small crack under arbitrary loading conditions*

A method is needed first to model a small crack, arbitrarily oriented, under general conditions of far-field multiaxial loading.

2.1.1 *Present definition of a small crack*

In order to define the concept of small crack we introduce first the notion of "boundary" as a circular region drawn around the crack, on which we compare solutions for the "body" and the "crack neighbourhood" (see Figure 1):

- "body" refers to the solution obtained for a deformed body without considering the effects of a crack. As we move away form the edge, the gradients induced by edge effects get smaller and imply an upper limit on the size of the "boundary".
- "crack neighbourhood" refers to the solution obtained for a crack embedded in an infinite medium, with specified far-field loading conditions. As we move away from the crack, the gradients induced by the crack get smaller and imply a lower limit on the size of the "boundary".

A crack is then said to be small when one can draw a boundary around it such that the solution on the boundary, in both the "body" and in the "crack neighbourhood", is constant to within a given tolerance.

Note here that this definition is very general because edge effect is considered. However, in the present study, the body is made up of an isotropic hyperelastic material and is subjected to multiaxial homogeneous loading conditions; thus gradients of the mechanical fields in the body are nul. The body-crack neighbourhood boundary is then chosen at a location where gradients tend to zero.

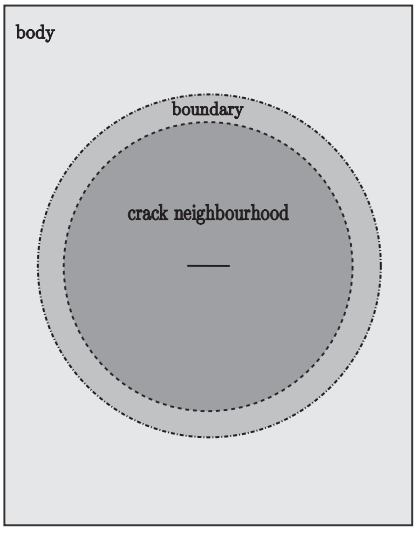

Figure 1. Body (whitish grey), crack neighbourhood (dark grey) and boundary (grey).

2.1.2 *Modelling boundary displacements under plane stress multiaxial straining*

The small crack assumption permits us to impose the far-field state of stress directly via the displacement at the boundary. Indeed, except in a very small region around the crack, the stress and strain fields are homogeneous and are the same as in the crack-free model for which the analytical expressions of strain and stress fields along with the strain energy density are completely known.

The original model consists of a small through-crack with orientation θ (in the undeformed configuration) under a far-field equibiaxial straining (λ_1, λ_2) in the frame of reference $(\vec{e}_1, \vec{e}_2)$ (see Figure 2). Throughout the deformation the crack rotates and ends up with an orientation ψ with respect to its orientation in the undeformed configuration. The problem with this method is that a new geometry is required whenever the crack orientation θ is to be changed.

However, from the perspective of the crack, changing the crack orientation boils down to changing the far-field loading (or equivalently the far-field straining) (see Figure 3). Thus, by performing first a change of basis and then a pull-back to maintain the crack orientation fixed throughout the deformation, we can express the associated far-field strain in the crack-based frame and capture the same range of conditions with a single FE model. Moreover, no restriction is made on the geometry of the far-field boundary which requires working out a very general expression of the displacement to be imposed to a node at the boundary. In order to conveniently study the effect of biaxiality, far-field loading parameters (λ_1, λ_2) are replaced by (λ, B) with $\lambda_2 = \lambda$ and $\lambda_1 = \lambda^B$. Thus $B = \log \lambda_2 / \log \lambda_1$ quantifies the biaxiality and can be called the biaxiality

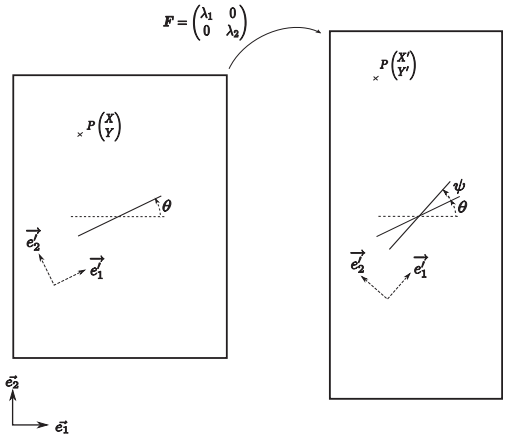

Figure 2. Small through-crack under finite biaxial straining with arbitrary orientation.

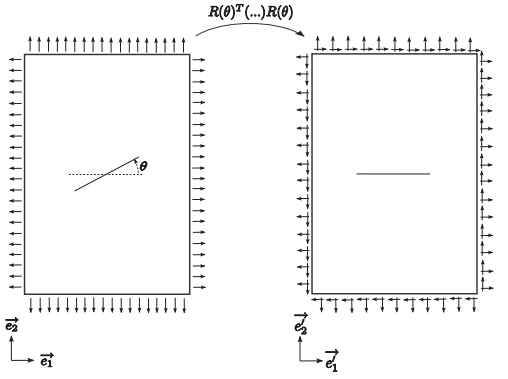

Figure 3. Original and new models after performing the appropriate change of basis (undeformed configuration).

factor (Mars 2002). The relationship between the undeformed coordinates (X, Y) and the deformed coordinates (X', Y') of a point P in the crack-based frame ($\vec{e_1'}$, $\vec{e_2'}$) (see Figure 2) under the far-field loading conditions described above is given by:

$$\begin{pmatrix} X' \\ Y' \end{pmatrix} = R(\psi)^T R(\theta)^T \begin{pmatrix} \lambda^B & 0 \\ 0 & \lambda \end{pmatrix} R(\theta) \begin{pmatrix} X \\ Y \end{pmatrix} \tag{2}$$

where

$$R(\theta) = \begin{pmatrix} \cos\theta & -\sin\theta \\ \sin\theta & \cos\theta \end{pmatrix} \tag{3}$$

and

$$R(\psi) = \begin{pmatrix} \cos\psi & -\sin\psi \\ \sin\psi & \cos\psi \end{pmatrix} \tag{4}$$

It should be pointed out that the implementation of the previous calculation (Eq. 2) and further computations carried out in this study were all obtained with the finite element software Abaqus in which the displacement of a node at the far-field boundary was imposed via a DISP subroutine.

2.2 *Basic validations*

First we have validated the calculations described in 2.1.2 by verifying that a crack-free model gives homogeneous loading for all B, λ and θ.

We then focused our attention on the "small crack" requirement. Indeed, far from the crack, it is desired to get a homogeneous stress field. This condition can never be met rigorously because of the finite dimension of the model and the presence of the crack. However, on using the method presented in section 2.1.1 a criterion was set to check accuracy of the approximation. The latter was considered acceptable when the relative error on the far-field stress when compared to the crack free model was less than 1%. From the experience a crack length 40 times smaller than the dimension of the model fits well into this criterion.

Note here that an additional satisfactory way to validate the calculations is to compare the energy release rate computed by Abaqus (J-integral) with the fracture mechanics solutions and from some studies carried out in finite strain (Yeoh 2002).

2.3 *Energy release rates of small cracks and their factorization*

It is first desired to develop a method that enables us to capture the influence of the presence of a small crack on the variation of the mechanical fields in the crack neighbourhood and that reveals how that variation makes up for the energy release rate. Using this method, the factorization of the latter with respect to the crack length is then investigated. Finally, on the basis of the numerical results obtained via finite element analysis, we examine the dependence of the energy release rate of small cracks on the farfield parameters B, λ and θ.

2.3.1 *J-integral*

The J-integral represents a way to calculate the energy release rate. It was first introduced within the framework of planar small strain as a contour path integral around the crack tip (Rice 1968). Thereafter, it was extended to planar finite strain. Indeed, on considering a contour Γ surrounding the crack tip and leaning on both faces of the crack in the undeformed configuration, the J-integral writes:

$$J = \vec{q} \cdot \int_\Gamma \sum \vec{N} dS \tag{5}$$

where $\sum$ stands for the Eshelby stress tensor, $\vec{q}$ is the crack direction vector and $\vec{N}$ is the outward normal vector to the surface element dS in the under formed configuration.

We remind the reader that, for an elastic material, the J-integral is path-independent which permits the arbitrary choice of the contour surrounding the crack tip to calculate the energy release rate (Rice 1968). For the sake of simplicity, the far-field Eshelby stress tensor is denoted $\sum^\infty$ throughout the rest of this paper.

Let us focus now our attention on the contour. A rectangular contour of characteristic dimension R has been chosen (see Figure 4). On choosing R such that $R/c \to \infty$ the evaluation gets highly simplified (see Table 1). Indeed, Γ_A, Γ_B and Γ_C lie then in the far-field region wherein the Eshelby stress tensor is uniform and is equal to $\sum^\infty$.

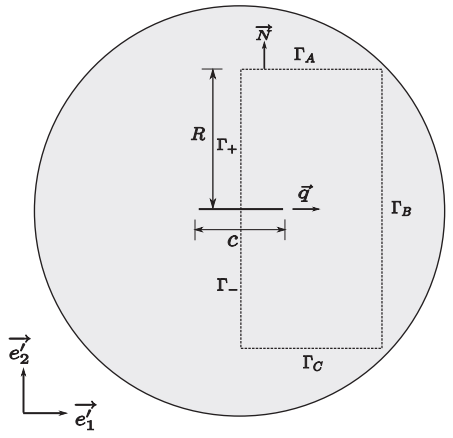

Figure 4. Contour for the evaluation of the *J*-integral.

Hence we have:

Table 1. Contributions to the energy release rate.

Segment	$\vec{N}$	$\vec{q}\cdot\int_\Gamma \Sigma\vec{N}d\Gamma$
Γ_+	$-\vec{e_1'}$	$-\int_0^R \Sigma_{11}(l)dl$
Γ_A	$\vec{e_2'}$	$\Sigma_{12}^{\infty} R$
Γ_B	$\vec{e_1'}$	$2\Sigma_{11}^{\infty} R$
Γ_C	$-\vec{e_2'}$	$-\Sigma_{12}^{\infty} R$
Γ_-	$-\vec{e_1'}$	$-\int_{-R}^0 \Sigma_{11}(l)dl$

It follows that

$$J = \lim_{R\to+\infty} \int_{-R}^{R}\left(\sum_{11}^{\infty} - \sum_{11}(l)\right)dl \tag{6}$$

Using the symmetry with respect to the crack line, we deduce that:

$$J = 2\int_0^{+\infty}\left(\sum_{11}^{\infty} - \sum_{11}(l)\right)dl \tag{7}$$

Note here that the expression above is not an approximation but the exact formula of the energy release rate. However, because the model has finite dimension, the upper bound for the integral is necessarily $< +\infty$. Thus, we can only compute an approximation of the energy release rate:

$$J \cong 2\int_0^{L}\left(\sum_{11}^{\infty} - \sum_{11}(l)\right)dl \tag{8}$$

where L is the maximum distance to the crack face in the $\vec{e_2'}$-direction.

2.3.2 *Proportionality of J with respect to the crack length*

Let us consider two different small cracks: one with length cand the other one with length kc where k is a real number. Both are subjected to the same far-field loading conditions. Using Eq. (7), the energy release rate of a crack of length cwrites:

$$J(c) = 2\int_0^{+\infty}\left(\sum_{11}^{\infty} - \sum_{11}^{c}(l)\right)dl \tag{9}$$

while the energy release rate of a crack of length kc writes:

$$J(kc) = 2\int_0^{+\infty}\left(\sum_{11}^{\infty} - \sum_{11}^{kc}(l)\right)dl \tag{10}$$

where Σ_{11}^{c} (respectively Σ_{11}^{kc}) denotes the Eshelby stress associated with the crack of length c (respectively of length kc).

By using the substitution $l = kl'$, we obtain that $dl = kdl'$. It follows that:

$$J(kc) = 2k\int_0^{+\infty}\left(\sum_{11}^{\infty} - \sum_{11}^{kc}(kl')\right)dl' \tag{11}$$

Let us focus now on the effect of multiplying the crack length by a factor k on the transformation of the mechanical fields with respect to the original problem of a crack of length c. We recall that the latter consists in a small crack embedded in a medium that has infinite dimension; thus changing the crack length by a factor k boils down to performing a homothetic transformation with a scale factor k and where the homothetic center is the center of the crack. And as the segment Γ_+ goes by the center of the crack, the mechanical fields along its length obey the homothetic transformation with respect to the crack length. Hence we have:

$$\sum_{11}^{kc}(kl) = \sum_{11}^{c}(l) \text{ on } \Gamma_+ \tag{12}$$

and we deduce that:

$$J(kc) = 2k\int_0^{+\infty}\left(\sum_{11}^{\infty} - \sum_{11}^{kc}(kl)\right)dl \tag{13}$$

$$= 2k\int_0^{+\infty}\left(\sum_{11}^{\infty} - \sum_{11}^{c}(kl)\right)dl \tag{14}$$

$$= kJ(c) \tag{15}$$

Note here that no limits were placed on the particular plane stress loading condition. Thus, the argument we have just made is completely general and is valid for all λ, B and θ.

This result implies that it is sufficient to work out the energy release rates for one crack size, and

that the energy release rate of all other crack sizes are then determined.

3 NUMERICAL RESULTS

The behaviour of the isotropic hyperelastic material was modeled by an incompressible neo-Hookean model.

3.1 *Variation of the energy release rate versus crack length*

In order to validate the proportionality law demon strated previously (see Eq. (15)), the dependence of the energy release rate on the crack length has been investigated for various far-field loading conditions (B ranging from –0.5 to 1, λ ranging from 1 to 5 and θ ranging from 0° to 90°). Indeed, for each and every far-field state of stress, the energy release rate has been computed twice for two different crack lengths: c and $2c$. All the results obtained so far show that, for Bincreasing from –0.5 to 1 with an increment of 0.25, for λ increasing from 1.1 to 5.0 with an increment of 0.1 and θ increasing from 0° to 90° with an increment of 15°, we always verify:

$$\frac{J(B,\lambda,\theta,2c)}{J(B,\lambda,\theta,c)} = 2 \tag{16}$$

3.2 *Variation of the energy release rate versus crack orientation*

For various biaxiality factors (B ranging from –0.5 to 1), the influence of λ on the variation of the energy release rate versus the crack orientation has been investigated.

As we can observe (see Figure 5 and Figure 6), for B in [–0.5, 1] the energy release rate strictly decreases as the crack orientation increases in both small and finite strain: the maximum is reached at $\theta = 0°$ and the minimum is reached at $\theta = 90°$. However, under equibiaxial tension (B = 1), the energy release rate is independent from the crack orientation in both small and finite strain and thus only depends on λ.

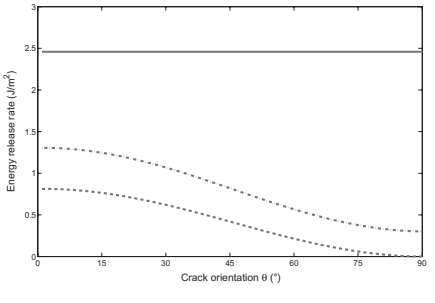

Figure 5. Energy release rate under simple loading conditions (uniaxial tension ---, pure shear – - – and equibiaxial tension —) in small strain (λ = 1.1).

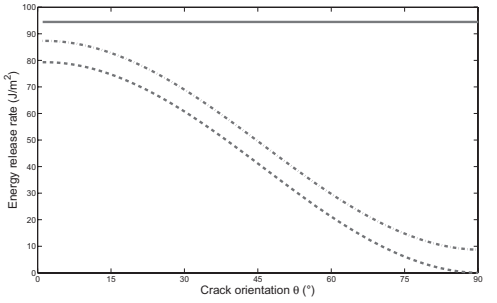

Figure 6. Energy release rate under simple loading conditions (uniaxial tension ---, pure shear – -– and equibiaxial tension —) in large strain (λ = 2.5).

4 DISCUSSION: FAR-FIELD PARAMETER OF THE SCALE LAW

The proportionality of the energy release rate with respect to the crack length (section 2.3.2) permits the following factorization:

$$J(\lambda, B, \theta, c) = f(\lambda, B, \theta)\, c \tag{17}$$

where f is a function of the far-field parameters only.

4.1 *Comparison with linear elastic fracture mechanics (LEFM)*

From the solution of LEFM for a rubberlike material (Mars 2006), f can be factorized into:

$$f(\lambda, B, \theta) = f^0(\lambda, B)\,(\cos^2\theta + \beta^2 \sin^2\theta) \tag{18}$$

where

$$\beta = \frac{2B+1}{B+2} \tag{19}$$

and f^0 is a function of λ and B only. $f^0(\lambda, B)$ is basically the value of $f(\lambda, B, \theta)$ at $\theta = 0°$. Thus, regarding the original problem (see Figure 2), f^0 depends only on the far-field state of stress.

Note here that all the energy release rates computed in small strain for B ranging from –0.5 to 1 and θ ranging from 0° to 90° completely match this theoretical factorization.

4.2 *Factorization of the energy release rate in finite strain under simple loading cases*

Under equibiaxial tension, because the energy release rate is independent from the crack orientation, the previous factorization of f remains obviously valid. Under uniaxial tension, we can draw the same conclusion from the numerical results. Indeed, on comparing the factorization with the energy release rate values computed for λ ranging from 1.1 to 5, we always have:

$$f(\lambda, -0.5, \theta) = f(\lambda, -0.5, 0°) \cos^2 \theta \tag{20}$$

However, under pure shear and actually for all B in [–0.5, 1.0], a simple comparison with numerical results clearly shows that the previous factorization (Eq. 18) cannot be extended to finite strain.

As for now, all the arguments that we made in this subsection are based only on finite element results but they have the benefit to guide us towards the simplification of the expression of f under simple loading cases. From the remarks above we deduce that:

$$J(\lambda, -0.5, \theta, c) = (f^0(\lambda, -0.5) \cos^2 \theta)\, c \tag{21}$$

and

$$J(\lambda, 1, \theta, c) = f^0(\lambda, 1)\, c \tag{22}$$

wherein the general expression of f^0 still needs to be determined.

5 CONCLUSIONS

A new method for modelling small cracks under arbitrary loading states and finite straining has been presented. The latter was successfully tested against the most known cases (uniaxial tension, equibiaxial tension and pure shear).

We have also investigated how the energy release rate is balanced by the distribution of configurational stresses. It has then been proved that the energy release rate of a small crack (suitably defined) always follows a linear scale law with respect to crack size, regardless of loading state.

Finally some progress has been made towards a general-purpose expression for energy release rate under arbitrary loading.

REFERENCES

Cam, J.-B.L., B. Huneau, E. Verron, and L. Gornet (2004). Mechanism of fatigue crack growth in carbon black filled natural rubber. *Macromolecules 37*, 5011–5017.

Gent, A.N., P.B. Lindley, and A.G. Thomas (1964). Cut growth and fatigue of rubbers. i-the relationship between cut growth and fatigue. *Journal of Applied Polymer Science 8*, 455–466.

Lake, G.J. and P.B. Lindley (1965). The mechanical fatigue limit for rubber. *Journal of Applied Polymer Science 9*, 1233–1251.

Le Gorju, K. (2007). Fatigue life of rubber components: 3d damage evolution from x-ray computed microtomography. In *Constitutive Models for Rubber V*.

Mars, W.V. (2002). Cracking energy density as a predictor of fatigue life under multiaxial conditions. *Rubber Chem. Technol. 75*, 1–17.

Mars, W.V. (2006). *Heuristic approach for approximating energy release rates of small cracks under finite strain, multiaxial loading*. Gresham Books, Abington.

Rice, J.R. (1968). A path independent integral and the approximate analysis of strain concentration by notches and cracks. *Journal of Applied Mechanics 35*, 379–386.

Rivlin, R. and A. Thomas (1953). Rupture of rubber. *Journal of Polymer Sciences 10*, 291.

Verron, E. and A. Andriyana (2008). Definition of new predictor for multiaxial fatigue crack nucleation in rubber. *J. Mech. Phys. Solids 56*, 417–443.

Yeoh, O.H. (2002). Relation between crack surface displacements and strain energy release rate in thin rubber sheets. *Mechanics of Material 34*(8), 459–478.

Constitutive Models for Rubber VI – Heinrich et al. (eds)
© 2010 Taylor & Francis Group, London, ISBN 978-0-415-56327-7

In-situ SEM study of fatigue crack growth mechanism in carbon black-filled natural rubber

S. Beurrot, B. Huneau & E. Verron
Institut de Recherche en Génie Civil et Mécanique UMR CNRS 6183,
École Centrale de Nantes, Nantes Cedex, France

ABSTRACT: A micro-tensile testing machine placed in the chamber of a scanning electron microscope is used to perform in-situ fatigue tests on a 43 phr carbon black-filled *cis*-1,4-polyisoprene rubber; the crack tip is observed in realtime during crack propagation. These observations lead to a detailed description of the crack tip morphology, to the understanding of the fatigue crack growth mechanism and to the microstructural explanation of crack branching phenomenon. Finally these results are related to the great fatigue properties of natural rubber and to strain-induced crystallization.

1 INTRODUCTION

Carbon Black-filled Natural Rubber (CB-NR) exhibits longer fatigue life than other elastomeric materials (Beatty 1964). Number of mechanical studies have been proposed to quantify the long-term durability of this material (see Lake (1995, Mars and Fatemi (2002) and the references herein). Nevertheless, only few recent papers investigate the microstructural aspects of fatigue crack growth in rubber (Le Cam et al. 2004; Hainsworth 2007); in these studies, fatigue tests are first conducted until a sufficiently long fatigue crack develops in the sample, then this sample is stretched and the open crack is observed in a Scanning Electron Microscope (SEM). Moreover, Le Cam et al. develop an original "microcutting" technique which permits to observe fatigue damage behind the crack tip and then to propose a scenario of fatigue crack growth in NR (Le Cam et al. 2004).

The aim of the present paper is to verify this previously proposed mechanism and to enrich the understanding of the phenomena involved during fatigue crack growth at the microstructural scale. In this purpose, in-situ SEM fatigue experiments are conducted and crack propagation is observed in real-time. Indeed, we believe that only such observations enable to unquestionably establish the scenario.

The experimental procedure is first described in details. Then, the next section presents the thorough description of the crack tip, clarifies the scenario of crack propagation and explains how secondary cracks appear. Finally, these results are discussed in the light of both macroscopic fatigue properties and straininduced crystallization of natural rubber.

2 EXPERIMENTAL

The aim of the present experiments is to observe the evolution of the crack tip during rubber fatigue crack propagation, in *real-time*. The experiments are conducted in three steps: i. the specimen is precut with a scalpel, ii. a classical fatigue experiment is then conducted in a standard machine until a fatigue crack propagates and iii. the experiment is continued in a micro-tensile testing machine placed in a SEM.

2.1 *Apparatus*

The micro-tensile testing machine used for this study is sufficiently small-sized to be placed in the chamber of a SEM and the double screw driving system leads to easy observation because the centre of the sample, i.e. the position of the crack tip, does not change during loading. Nevertheless, two major difficulties are due to the characteristics of the machine. First, its size and the limited distance between the clamps (from 20 mm to 40 mm) constrain both size and shape of the samples. Indeed, a special design of samples is needed to induce large strain in the vicinity of the crack. Second, as the relative speed of the clamps can vary from 0.1 mm/min to 2 mm/min, the maximum frequency of a fatigue test is 0.83 mHz, such value leading to days-long experiments. This is the reason why samples are pre-cut and the fatigue crack is first propagated in a classical tensile-testing machine.

2.2 *Material and design of the sample*

The material considered here is an industrial 43 phr CB-NR, provided in 2 mm thick calendered sheets.

As mentioned above, a special shape of sample was chosen in order to achieve large strain in crack vicinity and to propagate it; the corresponding geometry is shown in Figure 1.

2.3 *Procedure*

i. The first step consists in pre-cutting the sample to localize the crack in its centre. This cut is made with a scalpel and the resulting crack is less than 1 mm deep and between 1 and 2 mm long.
ii. To reduce the duration of the fatigue experiment, a fatigue crack is initiated from the precut in a standard fatigue machine. Fully relaxing cycles of stretch amplitude 200% are considered and the frequency is chosen to limit self-heating, i.e. less than 1 Hz. This first part of the fatigue test is stopped after the crack has propagated of about 50% of precut deepness.
iii. Finally, the experiment is continued in the small scale tensile machine. Loading conditions are identical to those of ii. except the frequency which is 0.83 mHz. Observation is made in a Jeol 6060LA SEM using secondary electrons imaging. Note that if a too high power electron beam is used, crack tip is damaged: microscopic cracks develop perpendicular to the loading direction. To overcome this difficulty, four parameters need to be lowered to reduce the energy of the electron beam per unit area: the probe current, the accelerating voltage, the magnification and the exposure time. Once these parameters set, the fatigue experiment is stopped once per cycle at maximum stretch to photograph the crack tip.

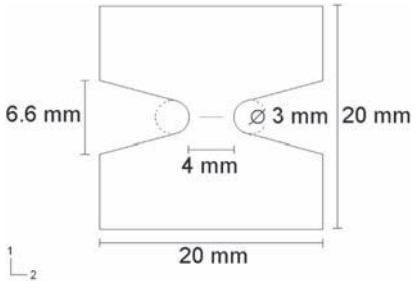

Figure 1. Geometry of samples.

3 MECHANISM OF FATIGUE CRACK PROPAGATION

3.1 *Description of the crack tip*

Figure 2 presents the front view of the fatigue crack tip. In the former figure, tensile direction is indicated by white arrows and the propagation direction is normal to the photomicrograph. As observed previously (Le Cam et al. 2004; Hainsworth 2007), the crack tip is composed of number of diamond-shaped zones separated by ligaments. The pattern of ligaments and diamond-shaped zones can be described as multi-scaled as large diamond-shaped zones delimited by large ligaments are themselves made up of smaller zones delimited by smaller ligaments. The diamond-shaped zones are flat and smooth compared to the ligaments, and those ligaments emerge from the smooth surfaces. The most noticeable characteristic of the crack tip is the pattern regularity. Surprisingly, the ligaments are not parallel to the tensile direction. In fact, they are parallel to two directions which are symmetric with respect to the tensile direction. The angle between the direction of ligaments and the loading direction decreases with the extension of the sample. Consequently, at a given deformation even if the size of diamond-shaped zones varies, all of them have the same length-width ratio. For instance, in Fig. 2, this ratio is 4 to 1. Nevertheless, the size of the diamond-shaped zones is not uniform; indeed the knots of the pattern are not regularly located. Finally, the crack tip also contains another relief feature: as it will be established in

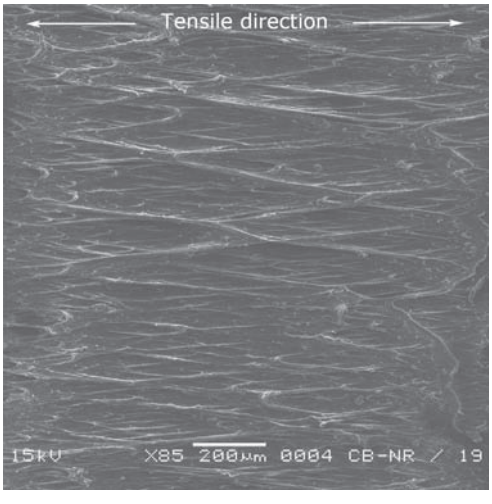

Figure 2. Top view of a representative crack tip.

Figure 3. Open crack tip (top view and section).

the following, it corresponds to previously broken and then shrunk ligaments. They are located at the knots of the pattern, i.e. at the intersection of the ligaments.

The previous description was devoted to rubber matrix, but as the material considered in this study is an industrial CB-NR, it contains a lot of different inclusions. Most of them are zinc oxides or carbon black agglomerates. In most of the cases, they are contained in elliptical cavities.

Finally, Figure 3 summarizes the description of the crack tip microstructure: the left-hand drawing shows the front view and presents the different elements described above, and the right-hand drawing is a side view which highlights the relief of the crack front.

3.2 *How does the crack propagate?*

Figure 4 shows six SEM images of a 0.5 mm^2 area of the crack tip taken respectively for the maximum stretch of in-situ fatigue cycles 1, 10, 21, 31 and 41. The micromechanism of fatigue crack growth in rubber can be established thanks to this figure. From one SEM image to another, it clearly appears that all the crack tip zones are affected by crack growth: positions of ligaments change with loading as shown by the white lines drawn on images. It means that the crack front is a surface rather than a line. Moreover, the evolution of the diamond-shaped zones suggests a three-step mechanism for crack propagation as emphasized in Figure 5. In order to describe this evolution, we choose Fig. 5 (a) as the reference state of the zones. Under loading, zones become larger (see changes between Fig. 5 (a), (b) and (c)), and cavities and inclusions appear on the surface (see Fig. 5 (c)). It means that the matter tears and the zone grows deeper in the direction normal to the crack surface, i.e. the direction of crack growth (it cannot be seen in the figure). The more the zone goes deeper, the more the ligaments which delimit it are stretched. Then after a few number of cycles, one of these ligaments breaks (see Fig. 5 (d)) and shrinks (see Fig. 5 (e)). Two different evolutions of the microstructure are observed: a new ligament may emerge or the two diamond-shaped zones

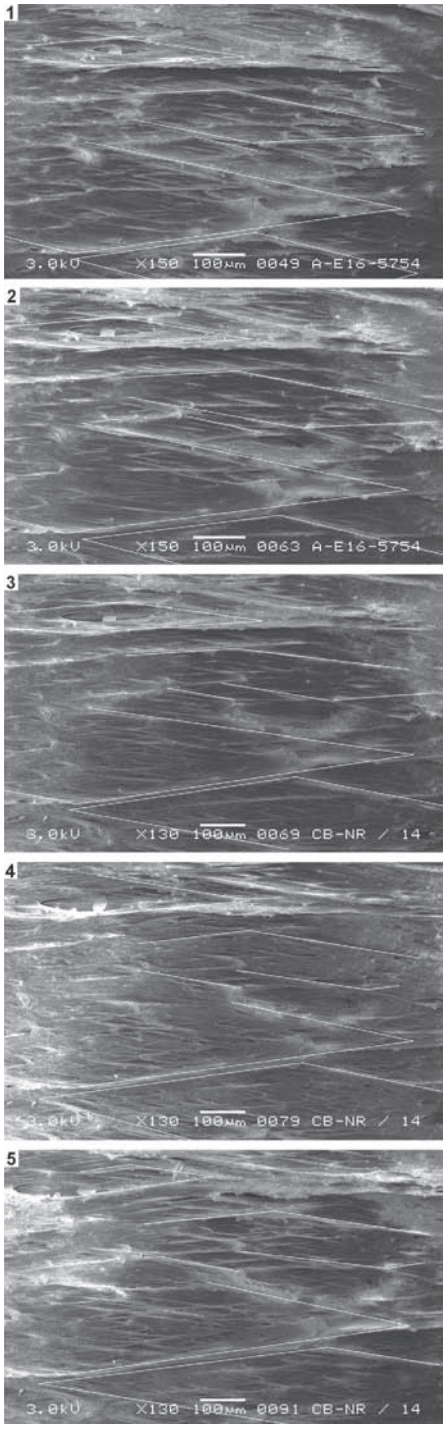

Figure 4. Evolution of a crack tip during cyclic loading after respectively 1, 10, 21, 31 and 41 in-situ cycles.

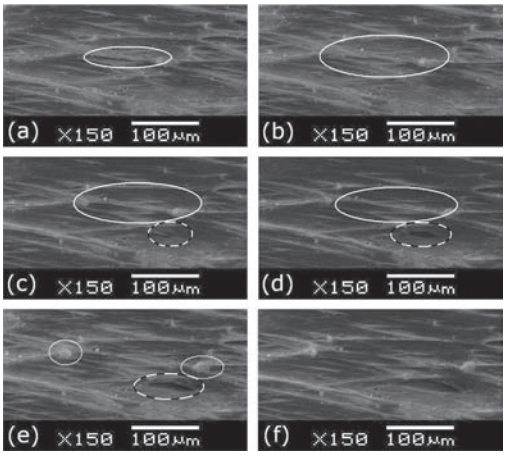

Figure 5. Successive photographs of the same detail of a crack tip during the rupture of a ligament after respectively 1, 3, 4, 5, 6 and 8 in-situ cycles.

separated by the broken ligament may coalesce as shown in Fig. 5 (f). In both cases, the matter reorganizes itself in a large vicinity of the broken ligament through the displacement of ligaments and diamond-shaped zones. In fact, this mechanism repeats itself in every diamond-shaped zone of the crack front. From a temporal point of view, this phenomenon occurs in a continuous manner with different velocities in each point. From a spatial point of view, it can happen simultaneously in different locations of the crack front.

To close this section, we summarize the main elements of the previous mechanism with the help of a five-step scenario as depicted in Figure 6.

a. Fig. 6 (a) presents the initial state of a diamond-shaped zone and its delimiting ligaments; it is a detail of the drawing of the crack tip in Fig. 3,
b. the diamond-shaped zone grows larger and deeper, showing new inclusions and ligaments (see Fig. 6 (b)),
c. as a consequence, ligaments which delimit the zone are stretched and one of them gets thinner than in the previous cycle (see Fig. 6 (c)),
d. eventually, this ligament breaks (see Fig. 6 (d)),
e. finally, the matter reorganizes itself through coalescence of the diamond-shaped zone with one of its neighbours (see Fig. 6 (e)).

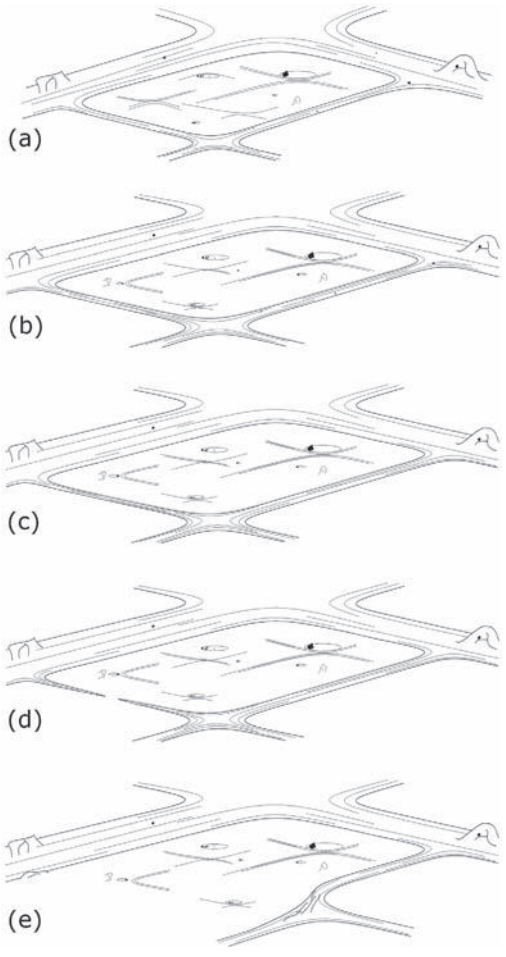

Figure 6. Fatigue crack propagation mechanism.

3.3 *How do secondary cracks appear?*

In the previous sections, the crack was observed only when opened. However, the study of the closed crack exhibits the path of a fatigue crack in natural rubber. To perform these observations, samples are cut in two with a scalpel along the plane defined by the tensile and propagation directions in the middle of the crack. Figure 7 presents the side view of the crack which is slightly open to observe more easily the crack path. It highlights the main crack path which is normal to the tensile direction and several secondary cracks. Similarly to (Hamed 1994), the term "secondary crack" refers to short deviated cracks developed from the main one. Their length varies from 10 μm to 100 μm. In order to establish the scenario of secondary cracks formation also called "crack branching phenomenon", it is necessary to determine how diamond-shaped zones evolve relatively to the others. In this purpose, the crack tip is observed with a different orientation from the previous images (Figs. 4 and 5): samples are rotated 90° in the SEM chamber to change the orientation of the ligaments with respect to the

secondary electron detector. The obtained image is presented in Figure 8; it emphasizes the relief of the crack tip due to the shadow contrast. It shows that all diamond-shaped zones are not in the same plane: some of them are deeper than others (see those indicated by white arrows in Fig. 8).

The crack propagation mechanism proposed in Section 3.2 does not take into account kinetics. The presence of diamond-shaped zones of different deepness in Fig. 8 suggests that even though the diamond-shaped zones evolve in a continuous manner, they do not grow deeper at the same speed. Moreover, recalling that the crack front is a surface rather than a line, the crack branching scenario will be established with the help of Figure 9. It shows the evolution under fatigue loading of three contiguous diamond-shaped zones (*a*, *b*, *c*) located at the crack front surface. It is a simplified representation of the crack tip cross-section: the right-hand drawings describe the close crack with the same view as in Fig. 7 and the left-hand drawings show the same crack but opened. To simplify the discussion, the scenario is established by considering three successive steps:

1. Initially, the three diamond-shaped zones *a*, *b* and *c* are separated by ligaments (grey in the figure) and have the same depth. When the crack is closed, there is only one branch.
2. Later on, when the crack has propagated, zones *a* and *c* have grown deeper than zone *b*. So, the close crack presents two similar branches. The main crack will develop from one or the other (*a* or *c*).

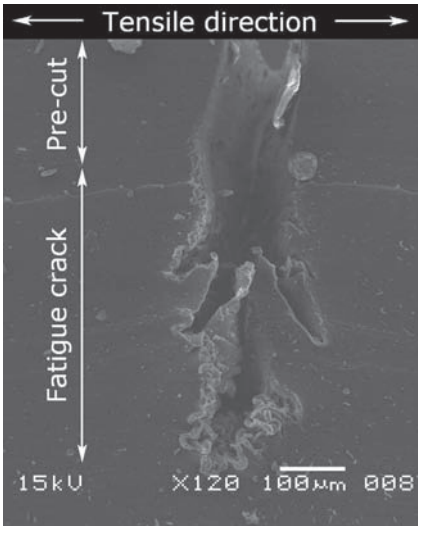

Figure 7. Crack path observed in a cut sample.

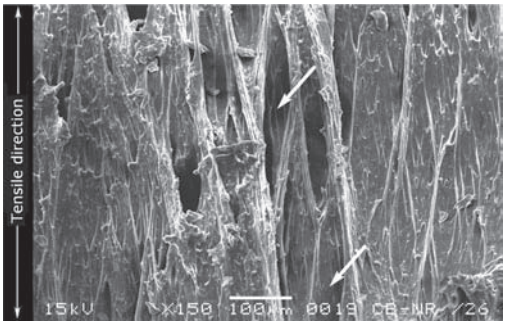

Figure 8. Top view of a crack tip –90° rotated specimen in the chamber of the specimen.

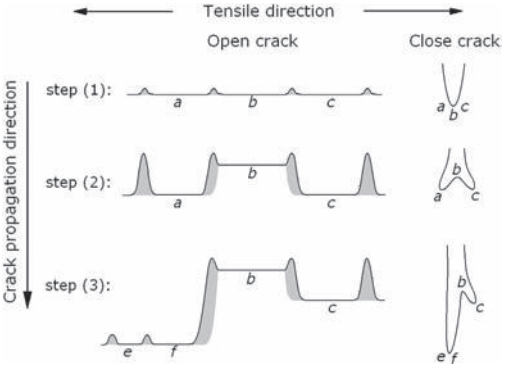

Figure 9. Branching phenomenon mechanism.

3. As the crack continues to propagate, one of the two previous branches will become the main crack due to both local mechanical conditions and microstructure. In the figure, zone *a* has become the main crack, and turned into two new diamond-shaped zones *e* and *f* because the former ligaments which delimited zone *a* broke and new ones appeared; zone *b* does not evolve anymore because it is partially relaxed; and zone *c* forms a secondary crack.

During crack propagation, the elementaryscenario described above repeats: zones *e* and *f* will evolve in the same manner as zones *a*, *b* and *c* in step (1). It is to note, that zones *a*, *b*, *c* can be three single diamond-shaped zones or three groups of several zones.

4 DISCUSSION

Recently, some authors performed interrupted fatigue tests and observed stretched samples in SEM (Le Cam et al. 2004; Hainsworth 2007).

Le Cam et al. observed the damage induced by fatigue and proposed the mechanism of crack propagation in natural rubber. Nevertheless, only observations performed during crack propagation enable to unquestionably establish this mechanism. Here, in-situ SEM experiments have been conducted to observe fatigue crack propagation in rubber in real-time. If such experiments have been already conducted for metallic materials (Crepin et al. 2000), to our knowledge, the present work is the first attempt to apply this technique to rubber materials.

With the careful procedure used during this study, we are able to highly improve the description of both crack tip morphology and propagation mechanism we previously published (Le Cam et al. 2004). First, the crack tip description is enriched: ligaments morphology and orientation were thoroughly investigated. Second, the present mechanism of crack propagation is in good agreement with the previous one, except for the perpendicular micro-cracks and the cavities which were observed by Le Cam et al. and not here. In fact, those micro-cracks were due to the electron beam; moreover, we believe that what was called a cavity in our previous study was only a smooth hollow which deepness was overestimated. Third, additional experiments allow to explain crack branching in NR under fatigue loading conditions.

The microscopic mechanism presented above explains the great fatigue properties of NR at the macroscopic scale: long fatigue life (Mark et al. 2005) and low crack growth rate (Lake 1995; Papadopoulos et al. 2008). Indeed, the ligaments of the crack tip resistto crack propagation in two ways: they induce a surface crack front rather than a tearing line as well as branched cracks which both help to dissipate energy and then hold up crack advance as previously argued by Hamed (Hamed 1994).

The great fatigue properties of NR are usually correlated with its ability to crystallize under deformation. In order to relate this property to our results, we now compare NR to Styrene Butadiene Rubber (SBR), an elastomer which does not exhibit strain-induced crystallization. More precisely, a similar study has been conducted for a SBR material with the same amount of carbon black fillers than in the NR considered here. It highlights three main differences between NR and SBR fatigue crack growth mechanisms:

- SBR crack tip does not present ligaments. Even though we observe sort of filaments parallel to tensile direction, the crack tip is very smooth and experiments reveal that those filaments do not resist to crack propagation as ligaments do in NR,
- the in-situ crack propagation observation also shows that in SBR the crack front is a line rather than a surface as in NR,
- crack branching does not occur in SBR contrary to what is observed in NR.

This comparison demonstrates that the heterogeneity of the microstructure at the crack tip (ligaments, diamond-shaped zones) is a consequence of strain-induced crystallization in NR.

At the close of this study, the mechanism of fatigue crack propagation in NR is qualitatively well-established; further investigations are now required to quantify the heterogeneity of some physical quantities, for example crystallinity and strain, at thecrack tip.

REFERENCES

Beatty, J.R. (1964). Fatigue of rubber. *Rubber Chemistry and Technology 37*, 1341–1364.

Crepin, J., T. Bretheau, D. Caldemaison, and F. Ferrer (2000). Low cycle fatigue behaviour of beta treated zirconium: Partial irreversibility of twinning and consequences for damage. *ActaMaterialia 48*, 505–516.

Hainsworth, S.V. (2007). An environmental scanning electron microscopy investigation of fatigue crack initiation and propagation in elastomers. *Polymer Testing 26*, 60–70.

Hamed, G.R. (1994). Molecular aspects of the fatigue and fracture of rubber. *Rubber Chemistry and Technology 67*, 529–536.

Lake, G.J. (1995). Fatigue and fracture of elastomers. *Rubber Chemistry and Technology 68*, 435–460.

Le Cam, J.B., B. Huneau, E. Verron, and L. Gornet (2004). Mechanism of fatigue crack growth in carbon black filled natural rubber. *Macromolecules 37*, 5011–5017.

Mark, J.E., B. Erman, and F.R. Eirinch (2005). *The Science and Technoloy of Rubber.* Elsevier Inc.

Mars, W.V. and A. Fatemi (2002). A literature survey on fatigue analysis approaches for rubber. *International Journal of Fatigue 24*, 949–961.

Papadopoulos, I.C., A.G. Thomas, and J.J.C. Busfield (2008). Rate transitions in the fatigue crack growth of elastomers. *Journal of Applied Polymer Science 109*, 1900–1910.

Constitutive Models for Rubber VI – Heinrich et al. (eds)
© 2010 Taylor & Francis Group, London, ISBN 978-0-415-56327-7

Applying infrared thermography to determine heat sources at the crack tip of rubber specimens

J.B. Le Cam, X. Balandraud, M. Grédiac & M.P. Moutrille
Laboratoire de Mécanique et Ingénieries (LaMI, EA 3867 - FR TIMS/CNRS 2856), Université Blaise Pascal (UBP), Institut Français de Mécanique Avancée (IFMA), Campus de Clermont-Ferrand/Les Cézeaux, Aubière Cedex, France

T. Pottier
Laboratoire SYMME, Polytech'Savoie, Annecy le Vieux Cedex, France

ABSTRACT: This study deals with the thermal response of elastomeric materials subjected to cyclic mechanical loading. An infrared camera is used to measure the temperature fields at the surface of a notched specimen. Rather than analyzing temperature fields, which depend on the heat diffusion within the specimen and the heat exchanges with the outside of the specimen, heat sources produced by the material are calculated by using the heat diffusion equation. Because of large displacements that occur during the tests, a motion compensation technique is performed in order to track the material points during the stretching of the specimen. The results obtained enable us to highlight the well-known thermoelastic inversion phenomenon and to observe a strong localization of heat sources close to the crack tip.

1 INTRODUCTION

The study deals with the thermal response of notched elastomeric materials. Studying the crack propagation in elastomeric materials is a critical issue which has been thoroughly studied in the past (see for instance, Lindley et al. 1964 and Thomas 1958). Different experimental techniques can be used to investigate physical phenomena involved during crack propagation, such as scanning electron microscopy or X-rays microtomography. In the present study, the authors propose to use infrared (IR) thermography. To date, infrared thermography has proved to be a relevant technique for non-destructive analysis of materials and structures, as well as for studying the thermomechanical response of materials subjected to mechanical loading. The so-called thermoelastic stress analysis is classically used for the measurement of stress fields: a high-frequency cyclic loading is applied to elastic structures, leading to a temperature oscillation due to the thermoelastic (isentropic) coupling. Another approach consists in estimating the heat sources produced by the material (Chrysochoos et al. 1989). Indeed, temperature fields are sometimes difficult to analyze because of the heat conduction within the specimen and the heat exchange with the outside of the specimen. Heat source fields can be obtained by processing the thermal data with the heat diffusion equation. This approach, which has been successfully applied to various materials, is applied in the present study to analyze the thermomechanical response at the crack tip of elastomeric materials. The large deformations undergone by this kind of material lead to large displacements of the material points. Consequently, the tools usually developed for processing temperature maps for small deformation are no longer suitable, especially in case of heterogeneous temperature fields. The objective of the present work is first to develop a motion compensation technique to process the temperature fields provided by an IR camera, before calculating and analyzing heat source fields at the crack tip.

2 THERMOMECHANICAL BACKGROUND

In this section, the thermomechanical framework to analyze temperature maps is briefly recalled.

2.1 *Heat diffusion equation*

The thermodynamic process involved in the material deformation is considered as quasi-static. Any material volume element is defined by n state variables: temperature T, a strain tensor denoted E and some internal variables V_1, V_2,… , V_{n-2} such as plastic strain or volume fractions of phases existing in the material. The specific free energy potential is denoted $\psi(T, E, V_k)$.

Assuming the Fourier's law to model the heat conduction, the heat diffusion equation can be written as follows (Chrysochoos & Louche 2001):

$$\rho C_{E,Vk}\dot{T} - div\,(K\ grad\ T) - r = s \tag{1}$$

where ρ is the density, $C_{E,Vk}$ is the specific heat at constant values of E and V_k, K is the thermal conductivity tensor and r the external heat source. The quantity s is the heat source produced by the material. It is composed of different terms:

$$s = d_1 + \rho T \frac{\partial^2 \psi}{\partial T \partial E}\dot{E} + \rho T \frac{\partial^2 \psi}{\partial T \partial V_k}\dot{V}_k \tag{2}$$

where:

- the first term d_1 is the mechanical dissipation (or intrinsic dissipation). This positive quantity corresponds to the heat production due to mechanical irreversibilities such as internal friction or plasticity;
- the second term is the thermomechanical coupling between temperature and strain. It is called thermoelastic coupling (or isentropic coupling). It is negative for a positive strain rate, and conversely.
- the third term corresponds to the thermomechanical couplings between temperature and the state variables V_k. They correspond for instance to latent heat production in case of first-order phase transformation phenomenon.

2.2 *Hypothesis for heat source assessment*

The classical approach used to assess the heat sources from the temperature fields provided by an IR camera (Chrysochoos & Louche 2001) is now recalled. For the sake of simplicity, the heat conduction is considered isotropic. Equation 1 can be then rewritten using the laplacian operator and k. The latter is the conductivity coefficient that replaces the thermal conductivity tensor K. As temperatures are obtained by an IR camera on the specimen surface, it is assumed that the problem is a bidimensional one if the specimen is flat and thin. Let us now consider the z-direction perpendicular to the (x, y) plane of the problem. The specimen is assumed to be thin, so the through-thickness temperature T is assumed to be almost constant. However, the temperature gradient $\partial T/\partial z$ is different from zero near the front and back sides of the specimen because of heat exchanges with ambient air. Averaging Equation 1 through the thickness of the specimen leads to:

$$\rho C_{E,Vk}\left(\dot{T}\frac{T - T_{amb}}{\tau}\right) - k\Delta_{2D}T - r = s \tag{3}$$

where Δ_{2D} is the 2D-dimensional laplacian operator in the (x, y) plane, T_{amb} is the ambient temperature and τ a time constant which characterizes the heat exchanges with the ambient air on the external surfaces of the specimen.

As the external heat source field r is difficult to assess, this quantity is removed from Equation 3 by subtracting a so-called reference temperature field T_0. This field corresponds to any temperature distribution when the specimen does not produce heat source s. It is obtained in practice just before loading the specimen for instance.

Let θ be the temperature variation from the reference temperature field T_0:

$$\theta = T - T_0 \tag{4}$$

One can deduce from Equation 3:

$$\rho C_{E,Vk}\left(\dot{\theta} + \frac{\theta + T_0 + T_{amb}}{\tau}\right) - k\Delta_{2D}\theta = s \tag{5}$$

3 EXPERIMENTAL SET-UP

3.1 *Material*

The material under test is a 34 part per hundred of rubber in weight (phr) carbon black filled natural rubber (CB-NR). It is obtained from a compound that is allowed to cure for 7 minutes at 160 degree C. The chemical composition and some of its mechanical properties are given in (Le Cam et al. 2004). Thermophysical properties involved in Equation 5 are given in Table 1.

3.2 *Specimen geometry*

Figure 1 presents the geometry of the specimens. The thickness is equal to 4 mm. A 2 mm long crack is initiated with a razor blade at the center of the specimen before testing. Two metallic inserts have been bonded at the top and bottom of the elastomeric material to be able to grip the specimen in the testing machine.

3.3 *Specimen preparation for thermal analysis*

The surfaces of the specimens are slightly polished and cleaned. Carbon black fillers make surfaces

Table 1. Thermophysical properties.

Property	Value
Density	1.13
Specific heat (J/Kg.K)*	2100
Thermal conductivity (W/m.K)*	0.8

*(Granta 2006).

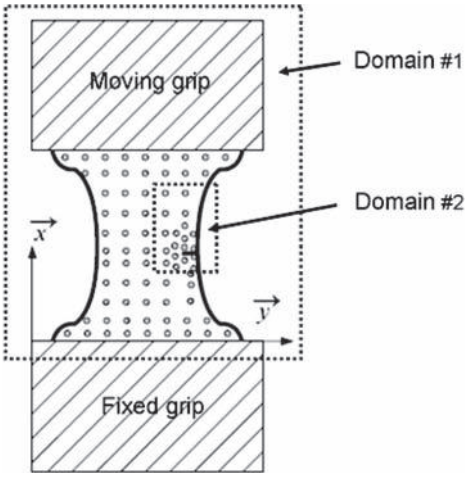

Figure 1. Specimen geometry and zones observed by the IR camera.

naturally black, so no specific surface preparation is required. Thermal emissivity is supposed to be close to one.

For the motion compensation technique detailed in Section 4.2 below, a limited number of material points are chosen on the specimen surface (see Figure 1). Reflective spots are plotted on the rubber surface before testing. Due to the difference of emissivity between ink and plain elastomer, reflective spots appear on the temperature maps.

The spot density is adjusted in such a way that more spots are placed in the vicinity of the crack. Far away from the crack, the distance between the reflective spots is about 4 mm.

3.4 *Loadings*

A 15 kN MTS testing machine is used to test specimens under uniaxial cyclic loading. The signal is sinusoidal with a loading frequency f_L equal to 0.5 Hz. The stretch ratio λ is defined by the ratio between the maximum and the initial lengths. It oscillates between 1.03 and 1.67. In order to avoid the Mullins effect, specimens are previously tested under the same loading conditions and over 10 cycles.

3.5 *Measurement*

Temperature measurements are performed at room temperature with a Cedip Jade III-MWIR infrared camera which features a local plane array of 320×240 pixels and detectors with a wavelength range of 3.5–5 µm. The integration time is 1500 µs and the acquisition frequency f_a is 150 Hz. The thermal resolution (Noise Equivalent Temperature Difference) is equal to 20 mK around 20 degree C.

Two zones are investigated in this study. Their location and size are shown in Figure 1:

- Domain #1: this zone enables us to observe the whole surface of the specimen, even for the maximum stretch ratio (1.67).
- Domain #2: this zone focuses on the area around the crack.

For the IR camera used, the spatial resolution is the size of the surface observed by any pixel. The value depends on the magnification of the objective, and therefore on the size of the zone under investigation. For domains #1 (the whole surface) and #2 (the zone surrounding the crack), it is equal to 219 and 131 µm, respectively.

In order to ensure that the internal temperature of the camera is optimal for performing the measurements, it is set up and switched on for one hour before the experiment. The stabilization of the camera temperature is necessary to avoid any drift of the measurements during the test.

3.6 *Characterization of the time constant*

Time constant τ involved in Equation 5 is determined experimentally. This constant mainly depends on the convection phenomenon that defines the heat exchange at the interface with ambient air. Its value is expected to vary on the specimen surface as the convection depends on the velocity. As a first approach, the value is here supposed to be a constant. It is obtained when the specimen temperature returns to ambient temperature after heating. The mean experimental temperature evolution is fitted with the solution of Equation 5 (where $s = 0$) and τ is deduced. The following value is obtained: $\tau = 345$ s. It must be noted later that the heat exchanged by convection is in fact negligible compared to the absorption term $\rho C_{E,Vk}\, \partial\theta/\partial t$ for the loading conditions defined in the present experiments.

4 DATA PROCESSING FOR HEAT SOURCE ASSESSMENT

4.1 *Problem*

The objective of the post-processing technique is to calculate the left-hand side of Equation 5 by processing the experimental data. In case of large displacements, a given pixel of the IR detector matrix does not correspond to the same material point while loading. The objective is then to track the material points before processing the temperatures. It seems that constructing a suitable motion compensation technique in the context of mechanical testing and temperature measurement using an IR camera has only seldom been addressed in the literature (Sakagami et al. 2006).

4.2 *Motion compensation technique*

A "reference geometry" is defined. In the present case, it corresponds to the sample geometry when a slight initial displacement is applied to avoid any local buckling. Calculations will be carried out in the current configuration, but results will be displayed in the reference one.

A suitable algorithm is developed using the Matlab package and a 'reshaping' operation of the temperature maps is performed. Full details concerning the numerical implementation can be found in (Pottier et al. 2009). From a practical point of view, the co-ordinates of the reflective spots are localized. The spots are tracked during the cyclic load. The displacement fields are then interpolated between the spots using the shape functions of the elements of a mesh whose nodes are the spot centers. Temperature maps are then 'reshaped' in the reference geometry. Finally, the heat sources (in the current configuration) are calculated and displayed in this reference geometry.

It must be noted that a specific procedure when subtracting the reference temperature T_0 (see Equation 4) must be used because the IR detectors of any matrix array camera feature a slight non-uniformity for instance due to the Narcissus effect. Full details are given in (Pottier et al. 2009).

5 APPLICATION TO A RIGID BODY MOTION

Before applying the technique to a notched elastomeric specimen, a first test is performed with a simple motion: a rigid-body translation. One side of the specimen is fixed in the moving grip and the other side remains free. The moving grip describes a cyclic linear translation whose amplitude is 29.45 mm. A temperature gradient of about 6 degrees C is generated within the specimen using a frozen steel block placed on the free side. The temperature field is measured by the IR camera for a few seconds (the temperature field in the specimen does not change during this short acquisition time).

The motion compensation technique is applied to obtain the temperature evolution at each material point. No heat is produced by the material during this rigid-body motion. Thus, no temperature variation is expected to appear once the post-processing method is applied. The results obtained for a given material point are shown in Figure 2. The efficiency of the motion compensation technique is verified for this motion of the specimen. In particular, it clearly appears that taking into account the IR detector non-uniformity is important for a correct analysis of temperature fields.

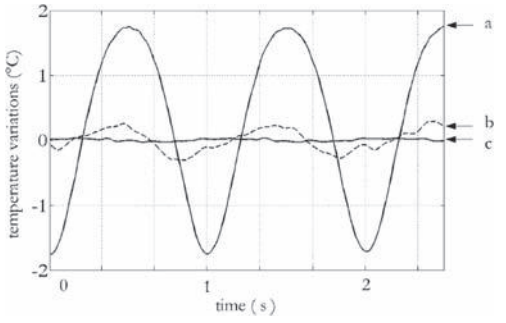

Figure 2. Temperature variation of a given material point in a specimen subjected to a rigid body motion. Curve a: without motion compensation; curve b: with motion compensation but without taking into account the IR detector non-uniformity; curve c: with complete motion compensation technique.

6 RESULTS ON STRETCHED ELASTOMERIC SPECIMENS

6.1 *Analysis on the whole surface (domain #1)*

Figure 3 presents the seven material points considered here for the analysis.

Figure 4 presents their temperature evolutions. Several points are worth noting:

- The thermal response of the material is not strictly sinusoidal. Indeed, the thermal response is caused by two types of coupling, namely the thermoelastic and the entropic couplings. For a small deformation increase from the undeformed state, heat sources are negative (first order effect of the thermoelastic coupling). If the deformation is large enough, the entropic coupling becomes greater than the thermoelastic coupling; so a positive heat source is produced. A minimum is obtained in the thermal response curve when the two coupling phenomena exhibit the same order of magnitude. This phenomenon is usually referred to as thermoelastic inversion.
- The temperature variations in zones 3, 4 and 5 are always greater than the temperature variations in zones 1, 2, 6 and 7. The maximum temperature is obtained for zone 4. Indeed, the gauge section is more stretched, thus leading to more heat production and consequently to highest temperature variation in the specimen.
- The temperature in zones 1 and 7 on the one hand, and the temperature in zones 2 and 6 on the other hand, are different. This is simply due to the temperature difference between the fixed grip and the moving grip.

Heat sources calculated using the procedure above are presented in Figure 5. For the sake of simplicity, only results obtained for zone 3 are plotted.

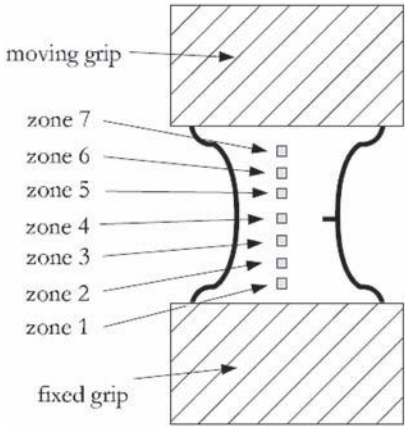

Figure 3. Seven zones considered along the specimen.

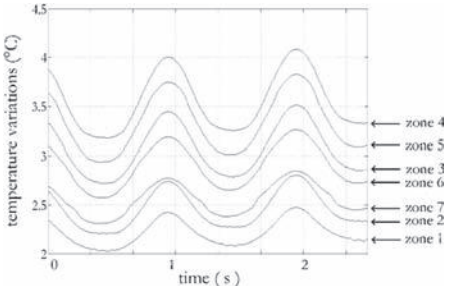

Figure 4. Temperature evolutions.

Other zones exhibit a similar response. In this figure, the stretch ratio, the temperature variations and the heat sources are plotted versus time. It must be noted that the stretch ratio considered here is a macroscopic quantity (λ_{macro}), i.e. it is calculated from the displacement of the moving grip. Calculation performed by the Finite Element Method has shown that the microscopic stretch ratio (λ_{micro}) reaches 1.14 and 5 at the crack tip when λ_{macro} is equal to 1.03 and 1.67, respectively.

The following conclusions can be drawn:

- As expected, the heat sources are almost equal to zero when the strain rate $d\lambda/dt$ is null.
- As already explained above, temperature variations in Figure 5b are not strictly sinusoidal. For small strain amplitudes ($\lambda < 1.1$), a short plateau is observed. It is related to the thermoelastic inversion that takes place when both the thermoelastic and the entropic phenomena exhibit the same order of magnitude. The thermoelastic inversion does not clearly appear in the curve plotted in Figure 5b, but a significant change in slope is observed in Figure 5c, at about $\lambda_{macro} = 1.1$.

However, with such an analysis of the whole specimen surface, the spatial resolution is not sufficient to perform a correct calculation near the crack.

6.2 *Analysis near the crack (domain #2)*

The same method as above is now applied in the domain #2 (see Figure 1) where significant strain gradients are expected. Figure 6 presents the seven material points considered here for the analysis.

Figure 7 presents the temperature evolutions of these material points. The following conclusions can be drawn:

- The temperature variations in zones 1 and 7 as well as zones 2 and 6 are quite similar. This can

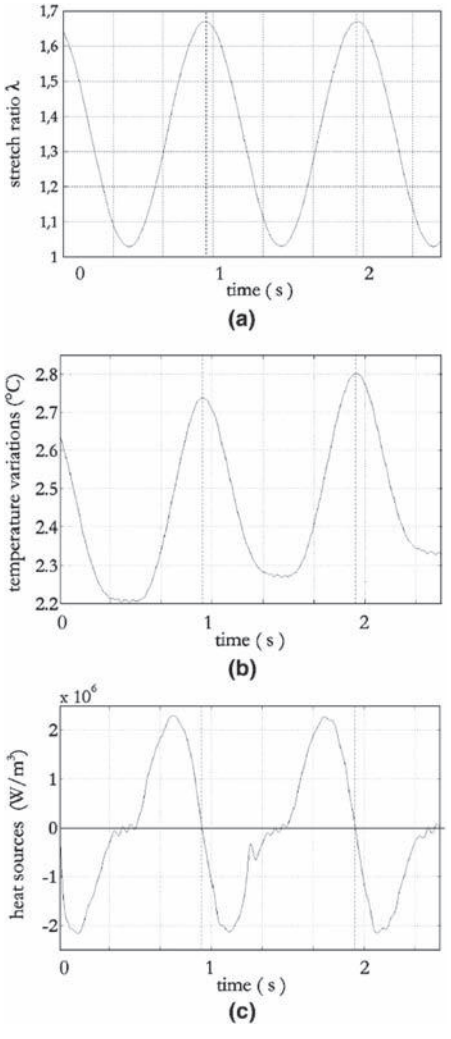

Figure 5. Evolutions of the stretch ratio, temperature variations and heat sources for zone 3 in the specimen.

be explained by the symmetry of the crack and by the fact that these zones are close to each other.

- The temperature evolution in zones 1 and 7 (i.e. the less stretched zones) clearly highlights the thermoelastic effects discussed above.
- The thermoelastic effect does not appear in zones 3, 4 and 5 in which the minimum strain level is higher. As explained above, as λ_{macro} between 1.03 and 1.67 at the macroscopic scale, λ_{micro} varies between 1.14 and 5 at the crack tip.

Finally, Figure 8 shows an example of heat sources map in the zone surrounding the crack tip ($\lambda_{macro} = 1.3$, during unloading). As may be seen, the crack is slightly open because of the preloading. In this figure, it clearly appears that the maximum value in terms of heat source is obtained at the crack tip. A high gradient of heat sources is observed when moving from the crack tip to the bulk material. Note also that no heat sources are detected along the crack lips, close to the free boundary.

7 CONCLUSION

A motion compensation technique has been developed to process the temperature fields provided by an infrared camera when large displacements exist in the specimen under test. The technique enables us to track the material points while the specimen stretches. So the heat sources produced by the material can be calculated. The relevancy of the motion compensation technique has been first shown using a simple displacement field: a translation. Notched elastomeric specimens have then been tested at room temperature. Temperature evolutions have been analyzed using two different scales: a large scale corresponding to the whole sample surface and a refined scale around the crack. Finally, heat sources have been assessed and analyzed. The competition between thermoelastic and entropic couplings is observed at low elongations. A strong localization of the heat sources at the crack tip has been clearly evidenced.

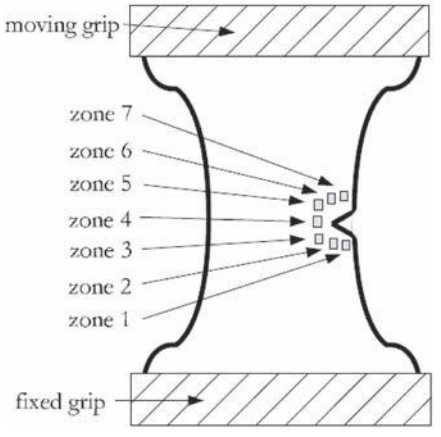

Figure 6. Zones considered near the crack.

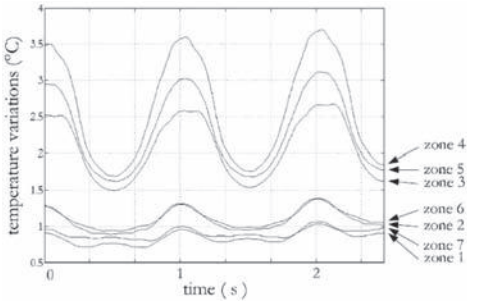

Figure 7. Temperature evolutions in the vicinity of the crack.

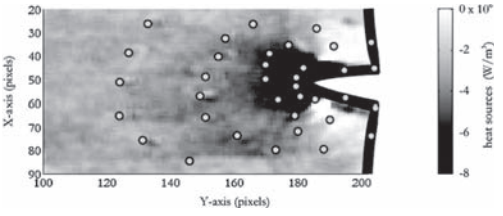

Figure 8. Example of heat source map in the zone surrounding the crack tip.

REFERENCES

Chrysochoos A & Louche H. 2001. Thermal and dissipative effects accompanying luders band propagation. *Mater Sci Eng A Struct* 307: 15–22.

Chrysochoos A, Maisonneuve O, Martin G, Caumon H & Chezeau JC. 1989. Plastic and dissipated work and stored energy. *Nucl Eng Des* 114: 323–333.

Granta. 2006. CES selector. http://www.grantadesign.com/products/ces/

Le Cam JB, Huneau B, Verron E & Gornet L. 2004. Mechanism of fatigue crack growth in carbon black filled natural rubber. *Macromolecules* 37: 5011–5017.

Lindley PB, Gent AN & Lake GJ. 1964. Cut growth and fatigue of rubbers. I. The relationship between cut growth and fatigue. *J Appl Polym Sci* 8: 455–466.

Pottier T, Moutrille MP, Le Cam JB, Balandraud X & Grédiac M. 2009. Study on the use of motion compensation techniques to determine heat sources. Application to large deformations on cracked rubber specimens. *Exp Mech* In press. DOI 10.1007/s11340-008-9138-0.

Sakagami T, Nishimura T, Yamaguchi T & Kubo N. 2006. Development of a new motion compensation technique in infrared stress measurement based on digital image correlation method. *Nihon Kikai Gakkai Ronbunshu A/Trans Jpn Soc Mec Eng* 72: 1853–1859.

Thomas AG. 1958. Rupture of rubber. V. Cut growth in natural rubber vulcanizates. *J Polym Sci* 31: 467–480.

Constitutive Models for Rubber VI – Heinrich et al. (eds)
© 2010 Taylor & Francis Group, London, ISBN 978-0-415-56327-7

Structural influence on crack propagation behaviour in elastomeric materials

T. Horst & G. Heinrich
Leibniz Institute of Polymer Research Dresden, Dresden, Germany

ABSTRACT: The tearing energy, defined as the total amount of energy required to advance a fracture plane by one unit area, is generally used for the characterisation of crack propagation in elastomeric materials. This quantity is highly affected by the various dissipative processes in elastomeric compounds. Modifying the structure of elastomers influences both the energy dissipation outside of the fracture process zone and the fracture process itself. Energy dissipation mechanisms outside of the fracture process are mainly due to viscoelasticity of the polymeric network characterised by the relaxation time spectrum and due to the breakdown and re-aggregation of filler clusters when the material is reinforced with hard fillers such as carbon black. The dissipative processes in the vicinity of the crack front within the fracture process zone are influenced e.g. by the the crack velocity. In order to study its influence, steady crack tip fields were calculated at various crack tip velocities within the linear viscoelastic theory. Results will be discussed qualitatively with respect to possible fracture mechanisms. Beside the crack velocity, the inhomogeneous structure of the material influences the fracture process as well. Structural modifications lead to different fracture surface morphologies, as it can be seen mostly with the naked eye. A statistical analysis of a particular fracture surface topography by means of height-height correlation functions allows for an estimation of corresponding length scales of the fracture process.

1 INTRODUCTION

Elastomeric materials are widely used in industry e.g. for tyres, seals and print rollers. The required service life of such components is usually decreased due to the formation and propagation of cracks. Hence, the modification of material structure in order to increase the resistance against crack initiation and crack propagation is an important branch of materials science. The fracture of a material generally involves a number of complex processes on multiple length scales. An increased fracture toughness can be achieved by modifying the structure of the material by way of inducing dissipative processes on various lexngth scales, which result in increasing the energy adsorption accompanying the process of crack propagation through this material.

Elastomeric materials are weakly cross-linked polymers. Above the glass transition temperature, even weak external forces can cause large deformations of these materials, owing to the high internal flexibility of network chains. These materials are typically blended with fillers in order to enhance their mechanical properties such as hardness, stiffness or abrasion resistance. Because of the large deformations in the vicinity of the crack front, the stress and strain fields are not known, neither quantitatively nor qualitatively. Hence, the use of local fracture mechanical parameters is not appropriate for the characterisation of cracks in elastomeric materials. The global energy balance in a specimen undergoing crack propagation seems to be the only candidate for the characterisation of fracture in these materials. Therefore, the tearing energy defined as the total amount of energy to advance a fracture plane by one unit area for charactersiation of crack propagation in elastomeric materials was introduced in order to characterise fracture in elastomeric materials (Rivlin and Thomas 1953). However, such a quantity does not contain information about the nature and the interplay of the accompanying dissipative processes.

2 STRUCTURAL MODIFICATION AND ITS INFLUENCE ON TEARING ENERGY

In elastomeric materials there are at least two main dissipative processes in the bulk. The first is related to the Brownian dynamics of network chains at temperatures above the glass transition. As a consequence, elastomeric materials show a viscoelastic deformation behaviour characterised by the relaxation time spectrum. Hence, the external loading rate is important for the way the material deforms and the amount of viscelastic energy dissipation

which shows a maximum at charactersitic loading times that are comparable to the relaxation times (Strobl 2007). The second dissipative mechanism is related to the blended filler especially at higher filler concentrations. Above the percolation threshold a weakly bonded superstructure is formed from the interpenetrating filler clusters as a result of the flocculation of primary filler aggregates. Mechanical connectivity between the filler particles that belong to different primary aggregates is provided by a flexible, nanoscopic bridge of glassy polymers, formed due to the immobilization of the rubber chains close to the gap between different primary aggregates (Klüppel 2003). With increasing strain, the stress-induced breakdown of rigid filler clusters occurs due to destroying nansocopic bridges connecting them. This leads to a filler induced energy dissipation, that can be observed as hysteretic stress-strain cycles during quasistatic harmonic loading of an elastomeric specimen. If an elastomeric specimen or component contains a crack then a third source of dissipation must be taken into account. The so-called small scale dissipation contains all the complex dissipative processes changing the material from an intact to a broken state. This separation process is located in the immediate vicinity of the crack front within the fracture process zone.

As a consequence, the locations of the processes of energy dissipation in elastomeric materials are not restricted to the immediate surrounding of the crack front and they are caused not only by the propagating crack, but also by the specific loading conditions and the loading history. Modification of the structure of elastomers influences both the energy dissipation far from the crack front and the fracture process leading to different crack propagation behaviour. A crack can propagate mainly either in a slow stable or in a fast unstable manner. To study the influence of crack velocity and the reasons for the change between both propagation regimes is therefore of high interest. The increase of tearing energy with increasing crack velocity can be ascribed to the viscoelastic losses in the vicinity of the crack front but outside the fracture process zone due the huge change of shear modulus accompanying the dynamic glass transition (Persson et al. 2005). However, stable and unstable crack propagation leave different marks on the fracture surface of elastomeric materials, as it can be seen with the naked eye. Though, the fracture process in the immediate vicinity of the crack front, where the material is extensively stretched and the inhomogeneous structure of the material has a pronounced influence on it, has not been investigated well so far. Fracture surfaces as a result of stable crack propagation show generally higher roughness than those created by unstable crack propagation. In order to explore the reasons for these differences, the influence of crack velocity on the stress and strain field in the vicinity of the crack front was studied qualitatively within linear viscoelastic theory in section 3 where beside the shear also the dilatational behaviour was taken into account. Analysing the fracture surface has been prooven to be an important tool to draw conclusions from the fracture process. On the basis of a particular fracture surface it will be shown in section 4 by means of statistical analysis how characteristic length scales of the fracture process can be estimated.

3 STATIONARY VISCOELASTIC CRACK TIP FIELDS

Due to viscoelasticity the deformation behaviour of elastomeric materials depends on the time scale of external loading with respect to the relaxation times of the material. In the case of crack propagation, the local loading rate of a material point in the vicinity of the crack tip is not only controlled by the external loading rate but also by the crack tip velocity. Even though the change of bulk behaviour from uncompressible to compressible does not contribute to a large extent into the viscoelastic energy dissipation, its influence on the fracture process must be taken into account. In order to find a hint for the fact that fracture surfaces are generally smoother when the crack has propagated in an unstable than in a stable manner, viscoelastic fields were analysed as a function of crack velocity. Due to the fact that growth of existing voids are a consequence of a critical hydrostatic stress (Gent and Wang 1991), shear and dilatational contributions will be considered separately.

For an isotropic linear viscoelastic deformational behaviour, the relation between the strain and the stress tensor is given by

$$\epsilon_{ij}(t) = \frac{1}{2}\int_{-\infty}^{t} J(t-\tau)\frac{d\sigma_{ij}^{dev}}{d\tau}d\tau + \frac{1}{9}\delta_{ij}\int_{-\infty}^{t} B(t-\tau)\frac{d\sigma^{tr}}{d\tau}d\tau \tag{1}$$

where the trace and the deviator of a second order tensor are defined by

$$(\cdot)^{tr} = (\cdot)_{kk}$$

and

$$(\cdot)_{ij}^{dev} = (\cdot)_{ij} - \tfrac{1}{3}\delta_{ij}(\cdot)_{kk}.$$

splitting shape change from volume dilatation contributions. Hence, the shear compliance function $J(t)$ and the compressibility function $B(t)$ characterise the shape change and the dilational behaviour of a linear viscoelastic material.

For the study, the specific case of a thin plane viscoelastic specimen loaded in tension mode (Mode I) was considered. Then, by means of the correspondence principle of linear viscoelasticity (Kanninen and Popelar) the viscoelastic fields can be derived from the solution of a corresponding elastic boundary value problem by inverse Laplace-Transformation. Hence, the viscoelastic plane near tip stress field is given by

$$\begin{bmatrix}\sigma_{11}\\ \sigma_{22}\\ \sigma_{12}\end{bmatrix} = \frac{K_I}{\sqrt{2\pi r}}\cos\frac{\varphi}{2}\begin{bmatrix}1-\sin\frac{\varphi}{2}\sin\frac{3}{2}\varphi\\ 1+\sin\frac{\varphi}{2}\sin\frac{3}{2}\varphi\\ \sin\frac{\varphi}{2}\cos\frac{3}{2}\varphi\end{bmatrix} \tag{2}$$

and the corresponding plane near tip displacement field is

$$u_i = \int_{-\infty}^{t} J(t-\tau)\frac{du_i^J(\tau)}{d\tau}d\tau + \int_{-\infty}^{t} B(t-\tau)\frac{du_i^B(\tau)}{d\tau}d\tau \tag{3}$$

with

$$\begin{bmatrix}u_1^J\\ u_2^J\end{bmatrix} = K_I\sqrt{\frac{r}{2\pi}}\left(\frac{5}{6}-\frac{1}{2}\cos\varphi\right)\begin{bmatrix}\cos\frac{\varphi}{2}\\ \sin\frac{\varphi}{2}\end{bmatrix}$$

and $$\begin{bmatrix}u_1^B\\ u_2^B\end{bmatrix} = \frac{4}{9}K_I\sqrt{\frac{r}{2\pi}}\begin{bmatrix}\cos\frac{\varphi}{2}\\ \sin\frac{\varphi}{2}\end{bmatrix}$$

in a Cartesian frame with its origin attached to the crack tip moving with velocity υ in direction $\vec{e}_1$ (Horst and Heinrich 2008). It can be seen in Equation (3), that not only the actual value but also the history of the stress intensity factor K_I and the polar coordinates (r,φ) of a material point influence the near tip displacement and consequently the near tip strain field.

In order to study the steady linear viscoelastic crack tip fields qualitatively, the stress intensity factor was assumed to be nearly constant and only the crack velocity determines the position vector of a material point in the moving frame. The viscoelastic material parameters were chosen of the same order of magnitude as that of a real rubber material. The shear compliance, that describes the shape change behaviour, increases at long times to a thousandfold of the short time value. The bulk compliance, that describes the dilatational behaviour, decreases from a finite value at short times to zero at long times. For both transitions we used the same retardation time. Hence, the transition from a glassy and compressible material at short times to a rubbery and uncompressible material was described.

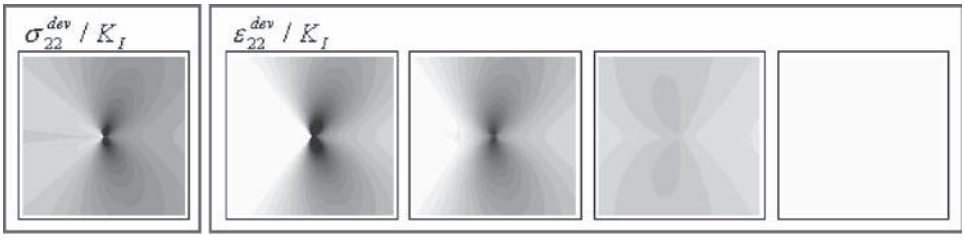

(a) Deviatoric fields

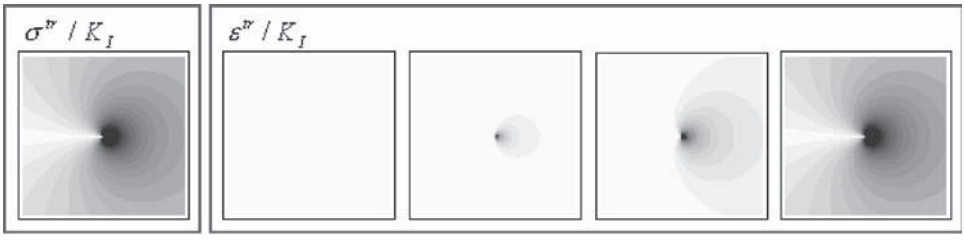

(b) Dilatational fields

Figure 1. Normalised stress and strain field in the vicinity of the crack tip at various crack tip velocities, velocity is increasing from left to right, same scale used (a) σ_{22}^{dev}/K_I and $\varepsilon_{22}^{dev}/K_I$, (b) σ^{tr}/K_I and ε^{tr}/K_I.

Results of the characteristic near tip fields at various crack tip velocities can be seen in Figure 1 where it can be shown that a transition from a rubbery to a glassy material behaviour occurs in the vicinity of the crack tip with increasing crack tip velocity. The increase of tearing energy at higher crack tip velocities is due to the dissipation of viscoelastic energy in the vicinity of the crack tip outside of the fracture process zone that can be ascribed to the dramatic decrease of the shear modulus in glass transition (Persson et al. 2005). The change of bulk behaviour in the vicinity of the crack tip from uncompressible to compressible does not contribute to a large extent in the viscoelastic dissipation. However, it can be seen that the dilatational behaviour influences the fracture process. At low crack tip velocities the volume of the material cannot increase due to a positive hydrostatic stress unless cavities are formed or existent cavities has grown. Whereas at higher crack tip velocities cavity formation is suppressed at macroscopic length scales.

The investigation of fracture surfaces of non-crystallising SBR compounds confirms this result that in the low crack tip velocity range the surfaces are rather rough, at least on the macroscopic scale. In contrast, in the high velocity range the fracture surfaces are much smoother. We postulated that the surface roughness originates from cavitations ahead of the crack tip due to a critical hydrostatic stress state.

4 FRACTURE SURFACE ANALYSIS

The morphology of the fracture surfaces is a signature of the complex fracture process on the scale of microstructure of the material. Even though roughness varies with different microstructures, it was found that roughness scaling properties are comparable for many materials. Recent studies reveal that these fracture surfaces are anisotropic objects that show self-affine scaling characterised by different roughness exponents for profiles extracted across and along the crack propagation direction, see Equation (6) for the definition of the roughness exponent. For a wide range of materials including glass, mortar, wood, quasi-crystals and metallic alloys, roughness exponents determined across and along the crack propagation direction are found to be $\zeta \approx 0.8$ and $\beta \approx 0.6$, respectively. However, it was found that the fracture surface roughness exponents in glassy ceramics and sandstone are significantly lower: $\zeta \approx 0.4$ and $\beta \approx 0.5$, respectively, which put the universality of the higher roughness exponents in question. Furthermore, it is found that higher roughness exponents describe the scaling behaviour on the length scales of the fracture process zone, where a ductile mechanism prevails. On length scales that are larger than the size of the fracture process zone, the morphology proves to be well described by the smaller roughness exponents, see (Ponson 2007) and references herein.

As an example, fracture surfaces created by unstable crack propagation in an emulsion styrene-butadiene rubber (SBR) vulcanisate, which was reinforced with 50 phr carbon black N330 (Reincke 2005), were analysed by height-height correlation functions (Horst et al.). Fracture surfaces were obtained from single edge notched tension specimens (SENT) under quasi-static tensile loading at room temperature. The surfaces were scanned in several areas with 1024×1024 data points by means of an AFM Q-Scope 250 (Quesant Instrument Corporation, USA) using intermitting mode. Scanning was carried out in both directions, i.e. across and along the crack propagation direction.

Profiles along the crack propagation direction $\vec{e}_1$ and across the crack propagation direction $\vec{e}_3$ of the scanned surface were analysed by means of height-height correlation functions

$$C_k(\Delta r) = \left\langle \left| h(r+\Delta r) - h(r) \right|^k \right\rangle_r^{\frac{1}{k}} \tag{4}$$

based on the k-th moment of the height fluctuations

$$\Delta h(\Delta r) = \left| h(r+\Delta r) - h(r) \right| \tag{5}$$

on a scale Δr. The angular brackets in Equation (4) denote the average over the profile coordinate r.

In the case of height fluctuations Δh obeying a Gaussian distribution with a self-affine scaling of the variance with Δr, the height-height correlation functions become

$$C_k^G = \left(2\Delta r^{2\xi}\right)^{1/2} \left(\frac{\Gamma\left(\frac{k+1}{2}\right)}{\sqrt{\pi}} \right)^{1/k} \tag{6}$$

with ξ being the roughness exponent, which is denoted as β and ζ for fracture surface profiles along and across the crack propagation direction, respectively. The ratio defined by

$$R_k = \frac{C_k(\Delta r)}{C_2(\Delta r)} \tag{7}$$

yields

$$R_k^G = \sqrt{2} \left(\frac{\Gamma\left(\frac{k+1}{2}\right)}{\sqrt{\pi}} \right)^{\frac{1}{k}} \tag{8}$$

for the Gaussian case and as a consequence, the height-height correlation functions (6) normalised by (8) collapse for all k (Santucci et al. 2007). Deviations from the Gaussian distribution of height fluctuations result in multi-affine scaling regime, i.e. a k-dependent roughness exponent caused by vertical jump discontinuities in the roughness profile.

Typical results of the height-height correlation functions (4) normalised by the Gaussian ratio (8) for profiles along and across the crack propagation direction are plotted in Figure 2. It can be seen, that there exist a self-affine regime within a certain range of length scales. The upper cut-off length of the indicated scaling regime is about 400 nm for profiles extracted along the crack front and along the propagation direction. The lower cut-off is about 80 nm for profiles along the crack propagation direction, determined by the observed

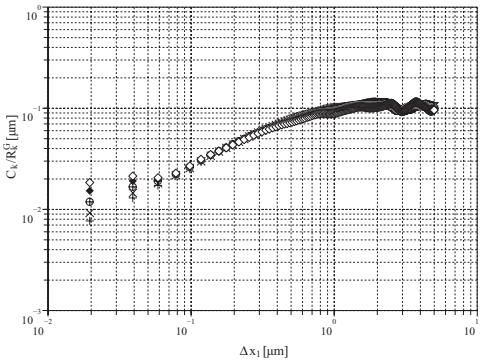

(a) profile along the crack propagation direction

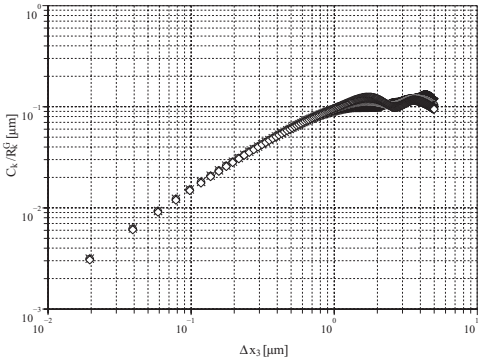

(b) profile along the crack front

Figure 2. Typical height-height correlation functions C_k normalised by R_k^G for $k = 1\ldots5$.

deviation of the height fluctuation distribution from the Gaussian law that results in a multi-affine scaling regime. In the case of the profiles along the crack front, height fluctuations obey a Gaussian distribution, at least on the scales exceeding that of the lateral resolution of the measurements, which leads to a self-affine scaling. Jump discontinuities can also take place, but their influence is limited to the length scales that are smaller than the lateral resolution of the measurements. A power law fit within the range of self-affine roughness scaling for every profile of seven measured topographic AFM images leads to the roughness exponents $\zeta = 87 \pm 0.03$ for profiles across the crack propagation direction and $\beta = 0.70 \pm 0.06$ for profiles along the crack propagation direction. These values determined for the fracture surfaces formed in the considered highly filled rubber material as a result of fast crack propagation are found to be close to those determined for other materials, on the length scales where a ductile fracture process prevails, i.e. on length scales where the coalescence of voids or microcracks is the dominant mechanism. Hence, the upper cut-off length of about 400 nm can be used as a rough estimate of the dimension of the fracture process zone within the fracture plane.

It is interesting to note that the lower cut-off length of about 80 nm for profiles along the crack propagation direction is slightly smaller than the size of the carbon black aggregate, i.e. 130 nm. The large strains in the ligament developed during quasistatic loading of the sample before final fast crack propagation induce a total breakdown of the filler network implying cluster sizes of the order of the aggregate size. Consequently, the concentration of destroyed nanoscopic bridges between filler aggregates is quite high due to the high filler content. The multi-affine scaling regime on the scales smaller than 80 nm for profiles along the crack propagation direction can therefore be attributed to profile overhangs due to voids developed from destroyed nanoscopic bridges between different filler aggregates.

5 CONCLUSIONS

It was shown that structural modification of an elastomeric material modifies the tearing energy in such a way that both energy dissipating contributions outside and within the fracture process zone are generally affected. In order to understand especially the influence of viscoelastic energy dissipation on the tearing energy and the fracture process, steady viscoelastic crack tip fields were calculated for various crack tip velocities. It was shown that a transition from a rubbery to a glassy material behaviour takes place with increasing crack

tip velocities. Whereas the increase of tearing energy can be ascibed to the shear behaviour, the transistion from a (nearly) incompressible to an compressible behaviour influence the fracture process. Thus, a damage mechansim in form of formation, growth and coalescence of cavities is favoured in slow crack growth leading to a rougher fracture surface compared to the case of fast crack propagation, where the damage mechanism is prevented at least on macroscopic length scales.

In order to show how relevant length scales of the fracture process can be estimated, a particulate fracture surface of an highly filled SBR compound was analysed by means of height-height correlation functions. For a specific range of length scales, a self-affine regime with characteristic roughness exponents along and across the crack propagation direction was determined. The values of these roughness exponents are close to those observed for fracture surfaces of non-rubber materials where the roughness exponents characterise the scaling behaviour at length scales within the fracture process zone. Consequently, the upper cut-off length scale of this regime was used to estimate the size of the fracture process zone. Furthermore, multiscaling features on the smallest length scales indicate steep height discontinuities on the roughness profiles. These are the result of poor measurement of profile overhangs caused by the damage process. The corresponding range of length scales up to lenght scales comparable to the size of filler aggregates give further insight into the fracture process in highly filled elastomeric compounds.

ACKNOWLEDGEMENT

The authors express their gratitude to the Deutsche Forschungsgemeinschaft (German Research Foundation, DFG) for financial support within the Research Unit "Fracture Mechanics and Statistical Mechanics of Reinforced Elastomeric Blends" (FOR 597). The fruitful collabaration with Katrin Reincke, Sybill Ilisch and Wolfgang Grellmann (MLU Halle-Wittenberg) is highly appreciated.

REFERENCES

Gent, A. and C. Wang (1991). Fracture mechanics and cavitation in rubber-like solids. *Journal of Materials Science 26*(12), 3392–3395.

Horst, T. and G. Heinrich (2008). Crack propagation behavior in rubber materials. *Polymer Science Series A 50*(5), 583–590.

Horst, T., K. Reincke, S. Ilisch, G. Heinrich, and W. Grellmann. Fracture surface statistics of filled elastomers, *submitted to Physical Review E.*

Kanninen, M. and C. Popelar (1985). *Advanced Fracture Mechanics.* Oxford University Press, USA.

Klüppel, M. (2003). The role of disorder in filler reinforcement of elastomers on various length scales. *Advances in Polymer Science 164*, 1–86.

Persson, B., O. Albohr, G. Heinrich, and H. Ueba (2005). Crack propagation in rubber-like materials. *JOURNAL OF PHYSICS CONDENSED MATTER 17*(44), 1071.

Ponson, L. (2007). Crack propagation in disordered materials: how to decipher fracture surfaces. *Ann. Phys. Fr 32*(1), 1–120.

Reincke, K. (2005). *Bruchmechanische Bewertung von ungefullten und gefullten Elastomerwerk-stoffen*. Mensch-und-Buch-Verlag.

Rivlin, R. and A. Thomas (1953). Rupture of rubber. *Journal of Polymer Sciences 10*, 291.

Santucci, S., K. Maloy, A. Delaplace, J. Math-iesen, A. Hansen, J. Haavig Bakke, J. Schmit-tbuhl, L. Vanel, and P. Ray (2007). Interdisciplinary physics-Statistics of fracture surfaces (6 pages). *Physical Review E* 75(1), 16104–16104.

Strobl, G. (2007). *The Physics of Polymers Concepts for Understanding Their Structures and Behavior: Concepts for Understanding Their Structures and Behavior*. Springer.

Constitutive Models for Rubber VI – Heinrich et al. (eds)

Discrete modelling of fracture processes in rubber material

Christiane Morgner, Michael Kaliske & Gordon Geißler
Institut für Statik und Dynamik der Tragwerke, Technische Universität Dresden, Germany

ABSTRACT: The consideration of the fracture mechanical sensitivity and the failure process is of substantial significance in order to gain reliable simulation results with regard to the safety and durability of rubber components. A novel adaptive implementation of the cohesive finite element method is presented which allows a discrete modelling of the fracture process by inserting cohesive elements into the initial discretization of the structure depending on a crack growth criterion. Instead of the stress-strain-dependencies used for the bulk material, the behaviour of the opening crack faces is described by an initially rigid traction-separation-law. The new adaptive modification of node coordinates and element boundaries on basis of the anticipated crack propagation direction suggested by the failure criterion allows furthermore the representation of arbitrary crack patterns. It is shown how different crack growth criteria affect the predicted crack path.

1 INTRODUCTION

Fracture mechanical investigations are of special importance for rubber materials. In order to predict the safety and durability of a component by a finite element simulation, the fracture mechanical sensitivity as well as the potential crack path have to be investigated. Common approaches to simulate the propagation of cracks include the application of softening material formulations to continuum elements leading to a smeared representation of the crack path or the application of adaptive crack propagation algorithms. However, these strategies are not able to represent the process of crack growth within the process zone. In contrast, the implementation of cohesive surfaces between the continuum finite elements in order to model discrete cracks provides a mesh independent framework to represent failure processes.

First discrete crack models on basis of cohesive finite elements were proposed by Dugdale (1960), who investigated steel sheets, and by Barenblatt (1962), who conducted theoretical studies on an atomistic scale. First numerical implementations of cohesive process zones by Hillerborg et al. (1976) featured a staggered substitution of the symmetric supports with equilibrium forces related to the crack opening displacement to simulate the localized failure of the structure. Needleman (1987) introduced a formulation with coincident nodal points in the initial configuration and stated the now common representation of the cohesive constitutive relations in terms of a traction separation law providing so a first representation of a crack and interface delamination in the framework of the finite element method. This separate description of the cohesive zone and the spatial bulk material, which is represented by stress-strain-dependencies, allows to account for a realistic modelling of the crack opening process zone.

Since the cohesive elements can only be located at the bulk elements' boundaries, a priori considered cohesive surfaces are usually integrated in the original finite element mesh. This conventional method is well suited if the crack path is known in advance, e.g. in case of the delamination of composite materials or glued structures. For computations with unknown crack paths, cohesive surfaces must be provided between all internal continuum element boundaries, as shown in Xu & Needleman (1994) as well as in Tijssens et al. (2000). The second technique suffers from two main disadvantages: Firstly, it leads to an exorbitant increase of the system's degrees of freedom and, secondly, the effective stiffness of the structure is seriously decreased. In case of a one-dimensional analysis, the effective stiffness yields

$$E_{eff} = E_0 - \frac{E_0}{1 + K_0 h_e / E_0} = \frac{E_0 K_0}{E_0 n_e + K_0} \tag{1}$$

depending on the bulk material's modulus E_0, the initial stiffness of the traction separation law K_0, and the uniform cohesive element spacing h_e or the number of surfaces n_e, respectively.

In this contribution, a new approach is presented which does not rely on an initial implementation of cohesive surfaces but uses instead an adaptive insertion of these elements in dependence on a crack growth criterion.

2 THE INITIALLY RIGID COHESIVE ZONE MODEL

The conventional method of a priori considered cohesive elements is based on an initially elastic traction separation law, as shown in Figure 1a). Due to the failure criterion as an inherent component of the cohesive phase, it is also referred to as an intrinsic model (cf. Kubair & Geubelle (2003)).

In contrast, the proposed approach is based on an initially rigid traction separation law as shown in Figure 1b). Such initially rigid descriptions of the cohesive constitutive relations have been used for example by Hillerborg et al. (1976) or Carpinteri & Colombo (1989) who proposed an algorithm to model the prescribed state of a certain crack extension with the help of an equilibrium iteration based on the crack tip opening δ and the corresponding cohesive forces F_c. The first application of an initially rigid traction separation law in the context of a general finite element framework was presendet by Camacho & Ortiz (1996). Recent publications covering three-dimensional investigations (Pandolfi & Ortiz (2002)) as well as several applications (e.g. Pandolfi et al. (1999), Ruiz et al. (2001)) are so far limited to short time dynamics in an explicit time integration scheme.

Since in case of most real fracture processes the crack will evolve slowly and stably, the initially rigid description of the cohesive zones was therefore derived and implemented for a quasi-static implicit finite element code. While procedures basing on an initially elastic traction separation law involve only a cohesive element formulation at an appropriate programming interface, the initially rigid approach requires an additional consistent modification of the global data structure in every time step associated with crack growth. Based on the boundary representation update procedure proposed by Pandolfi & Ortiz (2002) for tetrahedral elements with quadratic interpolation for explicit dynamical applications, a model adaptive discrete fracture simulation on basis of hexahedron elements with linear interpolation was derived for an implicit finite element framework. Following a constitutive analysis of the structure, where the non-linear system of equations has to be solved by a Newton iteration accounting for the residual vector and the stiffness matrix, a modification of the finite element system depending on the extrinsic crack growth criterion is carried out.

If the value of the particular failure criterion (cf. Section 3) at one element point exceeds the critical value (encircled nodes in Figure 2a)), a separate boundary update routine is applied. According to the anticipated crack propagation direction suggested by the failure criterion, the relevant corresponding surface is selected for further system modification. In this surface, all nodes which exceed the critical value are duplicated and new cohesive faces are created between them (Fig. 2b)). The nodal connectivity is modified for one of the two associated volume elements. In further crack propagation steps, an additional modification of the nodal connectivity for the preceding cohesive elements is required (Fig. 2c)). In order to ensure robustness and convergence of the proposed solution procedure, the equilibrium state of a duplicated nodal point before and after the boundary update has to be preserved, i.e. the initial traction in the cohesive elements has to adopt the forces released by the separation of the bulk elements. Considering the equilibrium state of the assembled structure

$$\mathbf{K}_{ji}^{E1}\mathbf{u}_i + \mathbf{K}_{ji}^{E2}\mathbf{u}_i = \boldsymbol{F}_1 + \boldsymbol{F}_2 = \mathbf{0} \tag{2}$$

where $\mathbf{u}_i$ represent the current deformations and $\mathbf{K}_{ji}$ the corresponding element stiffness contributions, the opposite forces $\boldsymbol{F}_1$ and $\boldsymbol{F}_2$ have to be mapped by an affine initial traction of the particular traction separation law. Detailed information regarding the so-called time continuity task of initially rigid implementations can be found in the publications of Papoulia & Vavasis (2003) and Sam et al. (2005) where the demand for an initial stress state resulting in individual parameters for each cohesive softening function is thoroughly discussed. The correct initial traction vector $\boldsymbol{T}$ can be computed from the equation of the resultant nodal forces of the volume and the cohesive element at the time of node duplication, which is given as

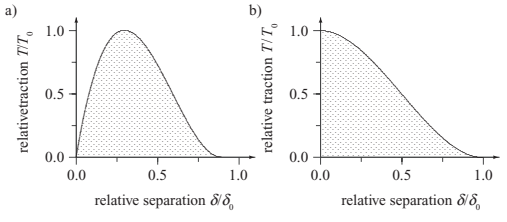

Figure 1. Comparison of a) initially elastic and b) initially rigid traction separation law.

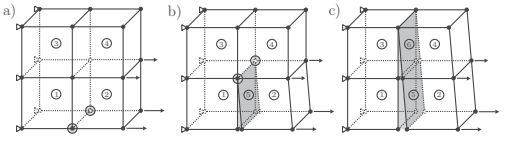

Figure 2. Adaptive implementation of cohesive elements.

$$\boldsymbol{F}_i = \int_{\Gamma_c} N^T \boldsymbol{T}\, \mathrm{d}\Gamma_c = \mathbf{K}^E_{ji}\mathbf{u}_i = \int_\Omega \sigma \frac{\partial \boldsymbol{u}}{\partial \boldsymbol{x}} \mathrm{d}\Omega \tag{3}$$

without consideration of inertia effects. The reaction force of the volume element can be computed from the decomposed stiffness **K** and the displacement **u** of node *i*, respectively, from the integration over the element domain Ω. The resultant material description of one cohesive surface consists of different material models for each node. In this context, a numerical integration scheme of the Newton-Cotes type for the element matrix computation is used.

3 CRACK PROPAGATION DIRECTION

The discrete modelling of crack growth under realistic loading conditions requires a crack growth criterion which provides information on the crack propagation itself as well as on the direction of crack growth. While the use of crack intensity factors is limited to problems with specified geometry, loading and crack configuration, the application of energy or stress criteria offers the possibility to model arbitrary crack propagation. In order to evaluate the capability of stress criteria to provide reliable information regarding the crack propagation direction, an averaged stress criterion and a criterion of averaged principal stress directions are examined.

3.1 *Crack growth criteria*

The averaged principal stress criterion (e.g. Wells & Sluys (2001) and Dumstorff & Meschke (2004)) allows a realistic evaluation of the stress field around the crack tip by analysing not only the stress at the crack tip but in the crack tip vicinity. In order to average the stresses around the crack tip, a weight function is used

$$\bar{\sigma}_{ij} = \frac{\sum \omega(R,L)\sigma_{ij}}{\sum \omega(R,L)}. \tag{4}$$

The anticipated crack propagation direction can be determined as the normal vector of the principal stress direction calculated from the averaged stresses.

In contrast, the averaged principal stress direction criterion is based on an averaging of the field of the prinicipal stress eigenvectors in the vicinity of the crack tip.

The weight function $\omega(R, L)$ can be for example of the Gaussian type (e.g. Wells & Sluys (2001) and Dumstorff & Meschke (2004))

$$\omega(R,L) = \frac{1}{(2\pi)^{3/2}L^3}\exp\left(-\frac{R^2}{2L^2}\right) \tag{5}$$

or linear

$$\omega(R,L) = \begin{cases} -\dfrac{R}{L}+1 & \text{for } R < L \\ 0 & \text{for } R \geq L \end{cases} \tag{6}$$

depending on the distance from the crack tip R, and the form parameter L. Figures 3 and 4 show the influence of both parameters on the area around the crack tip affected by averaging for both types of weight function.

3.2 *Adaptive mesh modification*

In order to represent the arbitrary crack paths within the finite element model, an adaptive

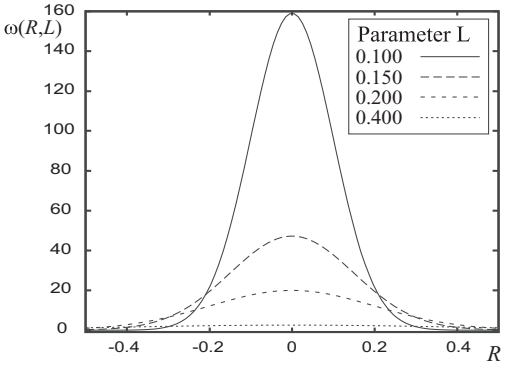

Figure 3. Gaussian weight function.

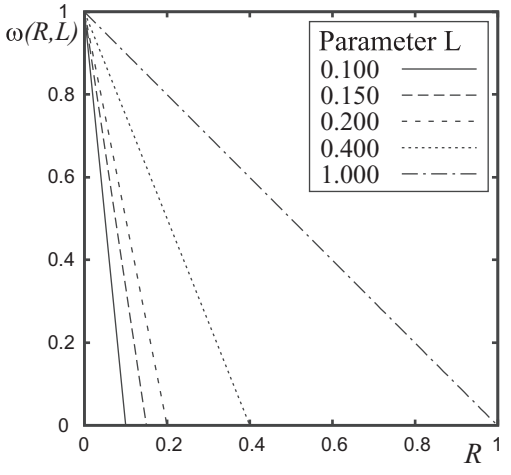

Figure 4. Linear weight function.

modification of the initial disretization with respect to the location of nodes and element boundaries on basis of the anticipated crack propagation direction suggested by the failure criterion is additionally required. The relocation of the new crack tip dx from the original to the modified nodal coordinates x and x′, respectively, is obtained from the interpretation of the crack growth criterion (Fig. 5). The remaining mesh is then modified subsequently for each crack propagation step. Considering constant nodal locations in normal direction, the external boundaries of the numerical model as well as restrictions regarding the shape of the continuum elements are taken into account by weight functions N_x and N_y set for each individual relocation of a node in x- and y-direction depending on the distance from the crack tip.

4 EXAMPLES

4.1 *Rubber plate*

The application of the averaged stress criterion is shown for a square rubber plate under tension and shear loading leading to Mode I and Mode II fracture, respectively. The plate features an initial notch with a horizontal orientation starting at the left edge and ending with a sharp crack tip at the midpoint of the specimen, which has a uniform side length of $l = 1$ mm. The geometry and the FE mesh are shown in Figure 6. The Neo-Hooke material has a Young's modulus of $E = 2$ MPa and a Poisson's ratio of $\nu = 0.49$. Tension opening loading conditions are realised by vertical displacements (Fig. 7) and for the pure shear mode by a horizontal load pair (Fig. 8). The system is fixed in the third direction to represent plane strain boundary conditions. In order to assess the influence of the weight function on the predicted crack propagation direction, different values of the parameter L are investigated for the Gaussian weight function.

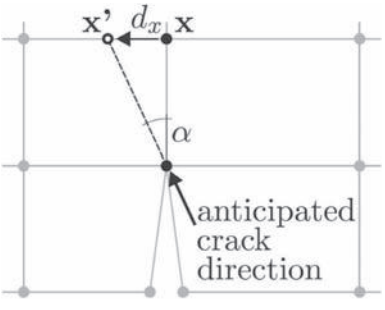

Figure 5. Anticipated crack propagation angle α.

For Mode I, all values of L lead to straight crack paths in accordance with the anticipated Mode I crack direction (Fig. 7).

In case of Mode II, all investigated values of L yield reasonable results which correspond to the anticipated crack path of 45° under pure shear loading. Figure 8 shows that the simulated crack paths for $L \leq 0{,}075$ mm deviate from the anticipated direction but that the consideration of a sufficient large part of the stress field around the crack tip will lead to good accordance. The same effects could also be observed for linear weighting functions and for different variations of the finite element discretization.

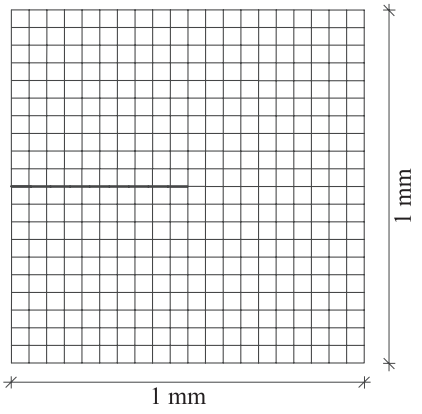

Figure 6. Rubber plate: Geometry and mesh.

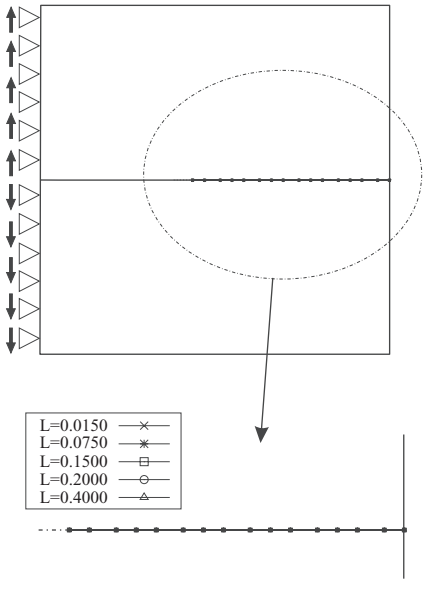

Figure 7. Rubber plate, simulated crack paths for Mode I.

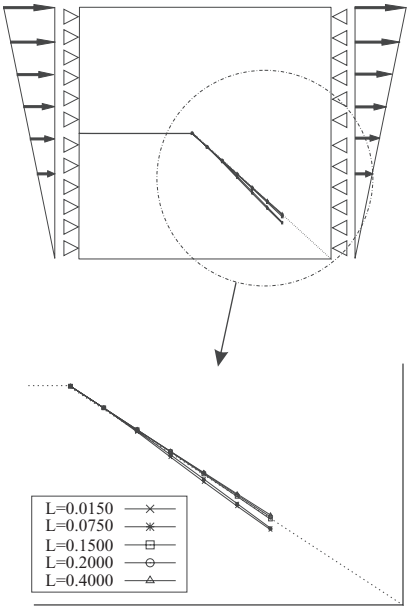

Figure 8. Rubber plate, simulated crack paths for Mode II.

4.2 *L-panel specimen*

In order to assess the reliability of the proposed mesh adaptive cohesive finite element model for arbitrary crack growth, a L-panel specimen is studied in addition to the rubber plate. On the basis of the experiments of Winkler (2001), who investigated a concrete L-panel specimen, the proposed method is validated with regard to the predicted crack shape as well as the comparison of the experimental and the numerical global response of the system during ongoing crack propagation.

The dimensions of the experimental setup and the applied boundary conditions are shown in Figure 9. The lower horizontal edge is fixed by a compact reinforcement construction within the concrete. This reinforcement construction is welded on a massive steel plate with a thickness of 50 mm to eliminate deformation effects from the specimen's support. The vertical load at the horizontal leg is applied uniformly at the lower horizontal surface with a distance of 30 mm from the right vertical end. The applied load-control is changed to a displacement-driven experiment, shortly before the maximum load is reached. The global response of the system until complete failure is characterised by a vertical displacement value over the applied load. The vertical displacement is measured at the position indicated in Figure 9.

The average values of the characteristic material parameters are given by a Young's modulus of $E = 25850$ MPa and a Poisson's ratio of $\nu = 0.18$. The axial tensile strength of the concrete material has a value of $f_t = 2.70$ MPa and, for the fracture energy, a value of $G_c = \Gamma_0 = 0.09$ N/mm is determined experimentally. A structured mesh with eight node linear displacement bulk elements is used for the finite element discretization. The finite element model depicted in Figure 10 consists of a regular part with 20×20 elements in the upper left corner (zone A). The resultant element size is $l_m = 12.5$ mm in the zone of expected crack propagation. For the remaining area, a structured mesh with a constant size of the bulk elements is defined (zone B). For the lower left part, a discretization with a coarse mesh at the support and a finer mesh in the upper region is used to provide smaller elements close to the

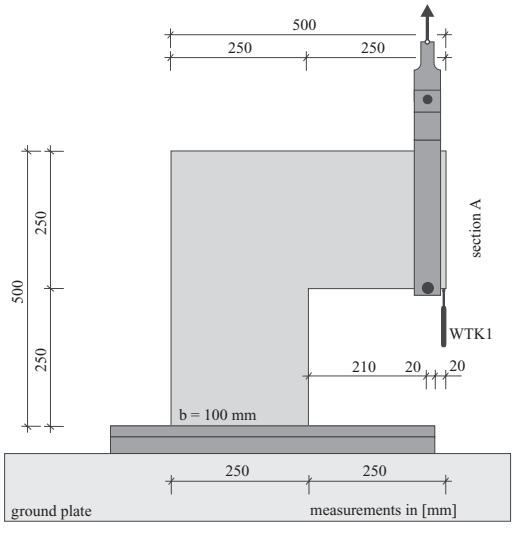

Figure 9. L-panel specimen, experimental setup.

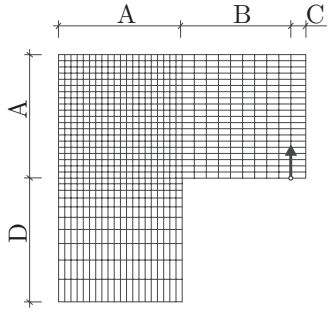

Figure 10. L-panel specimen, finite element model.

zone of crack propagation (zone D). Along the constant thickness of $b = 100$ mm, one element is used.

The specimen fails in the test with a single crack starting at the internal corner and moving upwards with a decreasing gradient. The gray lines in Figure 11 show the experimental results of both the front and the back surface for three investigations. The black line represents the result of the predicted crack path of the numerical simulation for an applied vertical displacement of $u_v = 0.4$ mm and shows a good agreement with the experimental results. The computed crack is found mainly within the area of the experimental investigations. The application of the mesh adaptive algorithm results in the final discretization of Figure 12.

The relationship between the applied vertical load and a characteristic displacement value is used to describe the global response of the fracture specimen. The load F is depicted with respect to the vertical displacement u_v at the position of load application (measured by WTK 1 as depicted in Figure 9). The load-displacement dependencies for the experimental investigation of three identical panels is shown in the diagram of Figure 13 as dotted lines. In oder to evaluate the computational model as well as the specified material parameters, a computation without any crack consideration was carried out. It was observed that the computed initial stiffness is not able to represent the elastic behaviour of the experiment and that the reaction forces for the early deformation states are too large. The difference between the determined Young's modulus and the value of the fracture specimen or a small rigid body motion with resultant larger deformation values are seen as possible reason. Apart from the initial deviation, the numerical simulation agree well with the observed characteristics of the experiment.

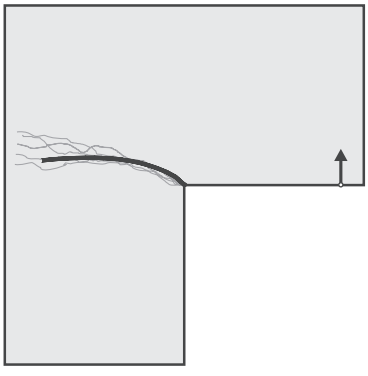

Figure 11. L-panel specimen, experimental and computed crack path.

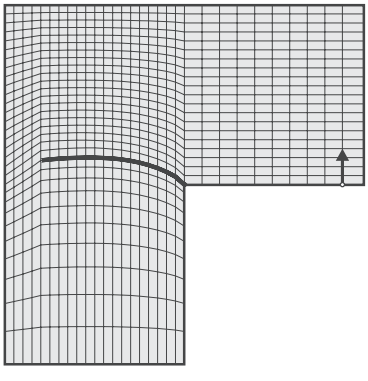

Figure 12. L-panel specimen, final mesh configuration.

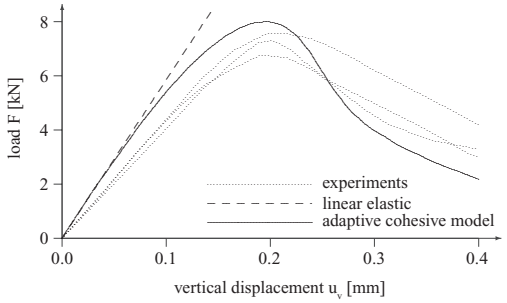

Figure 13. L-shaped specimen, load-vertical displacement curve.

5 CONCLUSIONS

A unique implementation of the cohesive zone model within the finite element method was presented. Based on an adaptive system modification and the evaluation of the preferred crack direction, the model also allows the representation of arbitrary curvilinear crack propagation independent of the initial discretization. The simulations of a rubber plate and of an L-panel specimen in comparison with experimental results validated the applicability of the proposed method to classical fracture modes as well as to realistic loading conditions.

ACKNOWLEDGEMENT

The support of this work by the research group "Fracture Mechanics and Statistical Mechanics

of Reinforced Elastomeric Blends" and by the Deutsche Forschungsgemeinschaft under contract KA1163/3-2 is gratefully acknowledged.

REFERENCES

Barenblatt, G.I. 1962. The mathematical theory of equilibrium cracks in brittle fracture. *Advances in Applied Mechanics 7*, 55–129.

Camacho, G.T. & M. Ortiz 1996. Computational modelling of impact damage in brittle materials. *International Journal of Solids and Structures 33*, 2899–2938.

Carpinteri, A. & G. Colombo 1989. Numerical analysis of catastrophic softening behaviour (snap-back instability). *Computers and Structures 31*, 607–636.

Dugdale, D.S. 1960. Yielding of steel sheets containing slits. *Journal of the Mechanics and Physics of Solids 8*, 100–104.

Dumstorff, P. & G. Meschke 2004. Investigation of crack growth criteria in the context of the extended finite element method. In *European Conference on Computational Mechancis in Applied Sciences and Engineering (ECCOMAS)*.

Hillerborg, A., M. Modeer, & P.E. Petersson 1976. Analysis of crack formation and crack growth in concrete by means of fracture mechanics and finite elements. *Cement and Concrete Research 6*, 773–781.

Kubair, D.V. & P.H. Geubelle 2003. Comparative analysis of extrinsic and intrinsic cohesive models of dynamic fracture. *International Journal of Solids and Structures 40*, 3853–3868.

Needleman, A. 1987. A continuum model for void nucleation by inclusion debonding. *Journal of Applied Mechanics 54*, 525–531.

Pandolfi, A., P. Krysl, & M. Ortiz 1999. Finite element simulation of ring expansion and fragmentation. *International Journal of Fracture 95*, 279–297.

Pandolfi, A. & M. Ortiz 2002. An efficient adaptive procedure for three-dimensional fragmentation simulations. *Engineering with Computers 18*, 148–159.

Papoulia, K.D. & S.A. Vavasis 2003. Time continuity in cohesive finite element modeling. *International Journal for Numerical Methods in Engineering 58*, 679–701.

Ruiz, G., A. Pandolfi, & M. Ortiz 2001. Three-dimensional cohesive modeling of dynamic mixed-mode fracture. *International Journal for Numerical Methods in Engineering 52*, 97–120.

Sam, C.-H., K.D. Papoulia, & S.A. Vavasis 2005. Obtaining initially rigid cohesive finite element models that are temporally convergent. *Engineering Fracture Mechanics 72*, 2247–2267.

Tijssens, M.G., B.L. Sluys, & E. Van der Giessen 2000. Numerical simulation of quasi-brittle fracture using damaging cohesive surfaces. *European Journal of Mechanics, A/Solids 19*, 761–780.

Wells, G.N. & L.J. Sluys 2001. A new method for modelling cohesive cracks using finite elements. *International Journal for Numerical Methods in Engineering 50*, 2667–2682.

Winkler, B.J. 2001. *Traglastuntersuchungen von un-bewehrten und bewehrten Betonstrukturen auf der Grundlage eines objektiven Werkstoffgesetzes fur Beton*. Ph.D. thesis, Universität Innsbruck.

Xu, X.-P. & A. Needleman 1994. Numerical simulations of fast crack growth in brittle solids. *Journal of the Mechanics and Physics of Solids 9*, 1397–1434.

Constitutive Models for Rubber VI – Heinrich et al. (eds)
© 2010 Taylor & Francis Group, London, ISBN 978-0-415-56327-7

The influence of the test properties on dynamic crack propagation in filled rubbers by simultaneous tensile- and pure-shear-mode testing

R. Stoček & G. Heinrich
Leibniz Institute of Polymer Research Dresden, Dresden, Germany

M. Gehde
Chemnitz University of Technology, Chemnitz, Germany

ABSTRACT: Crack growth characteristics of rubber materials are important for determination of strength and durability of the materials. In classical studies of fracture mechanics of rubber, it was featured tensile- and prominently pure-shear-test pieces. In this paper a fatigue crack growth of rubber materials is determined by using a method of simultaneous Tensile- and Pure-shear-Mode Testing. Measurement were made in order to characterize the fatigue crack growth behavior as a function of the tearing energy, determined by strain energy density in test piece of tensile- and pure-shear geometry. Measurements were made to observe the effects of loading frequency and amplitude. Comparison of the fatigue crack growth behavior between tensile- and pure-shear-test pieces was observed for verification of experimental data measured by simultaneous tensile- and pure-shear-mode testing.

1 INTRODUCTION

An important criterion for determination of dynamically loaded rubber materials is their resistance to fatigue crack growth. The problem of crack growth in rubber materials was first studied by work of Rivlin & Thomas (1953) and they determined a critical value of the tearing energy. It was demonstrated (Lake 1983, Lake 1987), that the critical tearing energy is independent of the geometry of test piece and can be formulated as a material property.

The important parameters are also test conditions such as loading method, load mode (sine-, triangle-waveform, pulse-loading), frequency, temperature and amplitude. The loading methods are the most important tensile- and pure-shear-method. With the pure-shear-method it is amenable to a simple fracture mechanics analysis provided the crack length c is long relative to its high H (distance between the clamps in the undeformed state). With the data from the pure-shear-method, it is possible exactly to describe the fatigue behaviours of rubber materials. The geometry of test piece is the base for the selecting of test method. For the tensile-mode, it is required the test piece with the geometry H >> W (high >> width) (Fig. 1). The pure-shear-test piece consists of a thin, rectangular strip of rubber held by rigid clamps along its long edges. The requirement from the geometry criterion is H << W for the pure-shear-test piece (Fig. 2).

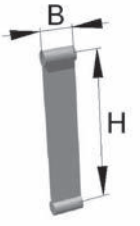

Figure 1. Tensile test piece.

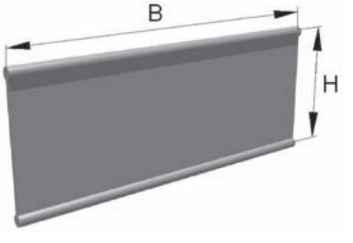

Figure 2. Pure-shear test piece.

Measurements used in the study was a new method for analysis of dynamic crack propagation in filled rubber by simultaneous tensile- and pure-shear-mode testing based on a theoretical approach of fracture mechanic of rubber.

In the present work the crack growth behavior and tearing energy in pure-shear-test pieces in comparison with tensile-test pieces were investigated. Measurements were made to observe the effects of different loading conditions (amplitude, frequency) to demonstrate the simultaneous testing of two different methods and comparison of the different theoretical background.

2 THEORETICAL BACKGROUND

2.1 *Tearing energy*

Tearing energy is defined as the energy released per unit area of crack surface growth (Rivlin & Thomas 1953)

$$T = -\left(\frac{\partial W}{\partial A}\right)_l = -\frac{1}{t}\left(\frac{\partial W}{\partial c}\right)_l \tag{1}$$

where T = tearing energy; W = elastic energy stored in specimen; A = area of fracture surface of the crack; c = crack length; t = thickness of sample; l = sample length.

The tearing energy (Eq. (1)) represents the energy input at which catastrophically progressive crack growth that is initiated. Experimental measurements show that, when crack propagation is expressed in terms of the tearing energy, the relation is independent of specimen type and geometry. Rivlin and Thomas (1953) gave the expression for tearing energy for a test pieces with tensile- and pure-shear-geometry.

2.2 *Tearing energy for tensile-test piece*

$$T_t = 2 \cdot k \cdot w \cdot c \tag{2}$$

where w = strain energy density per unit volume; c = crack length; k = strain-dependent term.

An approximate relation for k was determined by Lake (1995)

$$k = \frac{\pi}{\sqrt{\lambda}} = \frac{\pi}{\sqrt{1+\varepsilon}} \tag{3}$$

where λ = extension ratio; ε = strain, and thus, the Eq. (2) takes the form

$$T_t = \frac{2 \cdot \pi}{\sqrt{\lambda}} \cdot w \cdot c = \frac{2 \cdot \pi}{\sqrt{1+\varepsilon}} \cdot w \cdot c \tag{4}$$

The strain energy density term w can be determined from measurement of the tensile stress-strain curve, where the area under the curve is the strain energy density.

2.3 *Tearing energy for pure-shear-test piece*

The next type of test piece that was used in this work is pure-shear-specimen (Fig. 3).

Pure-shear-test piece is characterized as following: crack c is sufficiently long and wide to high ratio that is sufficiently great. The specimen could be divided into different regions. Region A is unstrained and region B is in pure-shear. Furthermore there is an area of complicated strain around the crack tip in region C, and a region of edge effect shown as D. If the maximum cyclic deformation remains constant and the crack length is increased by dc, the region of complicated strain C moves along by dc, but the pattern of strain, and hence the energy stored, remains unaltered. The net effect is, therefore, to decrease region B and increase region C by a volume $H \cdot D \cdot dc$ and thus decrease the total elastic energy $w \cdot H \cdot D \cdot dc$, where w is the elastic energy density in the pure-shear region B. The most important equitation for characterization of pure-shear mode is:

$$T_p = w \cdot H \tag{5}$$

The value w can be found from the strain in the pure-shear region and knowledge of the pure-shear stress versus strain relationship.

2.4 *Determination of fatigue crack propagation*

Fatigue crack growth behavior under the applied dynamic stress is expressed as the length of crack growth per each repeating cycle as a function of tearing energy

$$\frac{dc}{dn} = f(T) = B \cdot T_{t,p}^{\beta} \tag{6}$$

where the value of dc/dn is the rate of fatigue crack growth and B and β are polymer-specific constants (Lake 1983). If the cut length c changes only slightly, the quantity actually determining crack growth in the equation is the elastically stored energy T_t in tensile- and T_p in pure-shear-test piece.

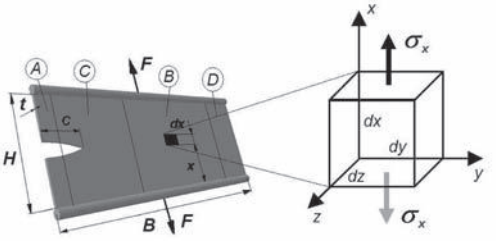

Figure 3. Model of strained Pure-shear-test piece.

3 EXPERIMENTS

3.1 *Realisation of crack propagation measurement by simultaneous tensile- and pure-shear-mode testing*

Figure 4 show a schematic diagram of a machine for investigating the fatigue crack growth of rubber materials by simultaneous tensile- and pure-shear-mode testing. It is possible to measure four tensile- and simultaneous three pure-shear-test pieces. Each bottom clamp attachment of samples is fixed to the traverse. The traverse is connected to the piston, whereby dynamically powers a hydropulser. The hydropulser is driven by a frequency sweep generator through sinusoidal waveform, within the frequency range of 0,1–20 Hz. Each upper clamp attachment of samples is fixed to the load cell and its corresponding sample clamp attachment is connected to a separate computer-controlled stepping motor to ensure constant pre-stress during the whole time of testing.

The crack growth of each rubber test piece is monitored through an image process system with high-speed CCD monochrome camera mounted on the linear motion axis system. The camera moves along the x-axis from test piece to test piece and takes a picture of involved sample. After that the picture has been digitalized and then the software localizes the crack position and determines the crack length.

3.2 *Preparation of rubber test pieces and conditions of fatigue crack growth measurement*

For measurement, SBR rubber material was filled with 50 phr waste rubber powder as well as silica and carbon black. The material was vulcanised at 180°C and 190 bar. The vulcanisation time was

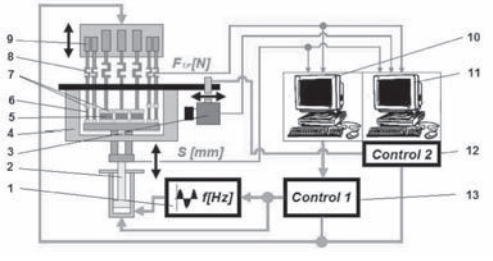

Figure 4. Schematic diagram of the test machine: 1-frequency generator; 2-hydropulser; 3-CCD monochrome camera; 4-isolated chamber; 5-pure-shear test piece; 6-tensile test piece; 7-clamps; 8-load cells; 9-stepper motors; 10-PC1; 11-PC2; 12-control unit 2; 13-control unit 1.

Table 1. Test pieces geometry.

Type of test piece	Height mm	Width mm	Thickness mm	Crack length mm
Tensile 1	15.0	15.0	1.6	2.5
Tensile 2	25.0	15.0	1.6	2.5
Tensile 3	43.0	15.0	1.6	2.5
Pure-shear 1	15.0	120.0	1.6	20.0
Pure-shear 2	25.0	120.0	1.6	20.0
Pure-shear 3	43.0	120.0	1.6	20.0

obtained using Rheometer AR 2000 ex and assessed at 30 min. Fatigue tests were conducted on three types of tensile- and three types of pure-shear-test pieces.

The test pieces were subjected to isolated chamber of test machine and tested with three different test conditions.

1. The first measurement was done for analyses of influence of height of pure-shear-test piece under the identical loading amplitude and frequency. The amplitude of test pieces was 10 mm. Thus, the extension ratio varied from 1.23 to 1.67 for test pieces. The frequency was 10 Hz.
2. The second measurement was done by identical extension ratio of 1.67 for test pieces 1 and 2 with the frequency of 10 Hz.
3. The third measurement was done by identical extension ratio of 1.67 for test pieces No. 2 and reduced frequency of 5 Hz.

The waveform of the fatigue tests for all loading conditions was sinusoidal. Tests were conducted at room temperature and at atmospheric pressure.

4 RESULTS

4.1 *Influence of different extension ratio on crack growth*

Figure 5 shows the dynamic crack growth curve for test pieces of various high of geometry tested under the identical loading amplitude. Thus, the each of test piece was loaded under different extension ratio (1.23–1.67). As it can be expected, the higher the extension ratio uses, the higher the crack growth obtain. Thus, all of test pieces displayed in this plot follow different trend. With the lower extension ratio, the curves are characterized by trends, where the crack lengths are slow. Comparing tensile- and pure-shear-test pieces, the trends are roughly the same. Because of the extension

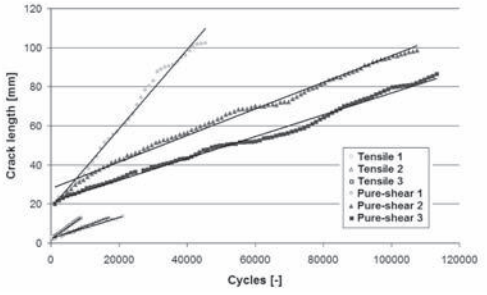

Figure 5. Dynamic crack growth curve for test pieces at various extension ratio.

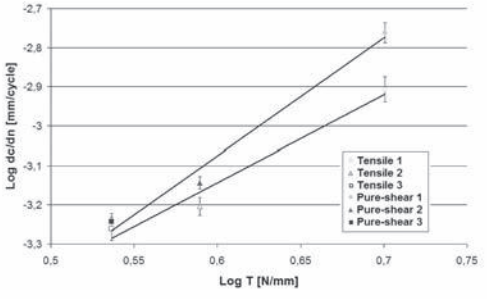

Figure 6. Crack growth rate as a function of tearing energy for tensile- and pure-shear-test pieces at various extension ratio.

ratio of similarity, the same trend can be measured in the range of the crack growth for width of different test pieces.

The crack growth rate dc/dn of tensile- and pure-shear-test pieces for different extension ratio are plotted as a function of the tearing energy $T_{t,p}$ using a log-log scale. The experimental results are shown in Figure 6. Over the range of tearing energy the range of crack propagation increased. These results are dependent upon the power law as indicated in Eq. (6). The lower value of the exponent β for lower extension ratio denotes more resistance to crack growth at a given tearing energy.

4.2 *Identical extension ratio for all test pieces*

Figure 7, the dynamic crack growth plot for test pieces strained under the identical extension ratio of 1.67, shows in comparison with Figure 5. As it can be expected, all test pieces displayed in this plot follow roughly the same trend.

The cracks growth rates dc/dn of tensile- and pure-shear-test pieces for identical extension ratio, plotted as a function of the tearing energy $T_{t,p}$ in a log-log scale show roughly identical values (Figure 8). The differences depend on complicated

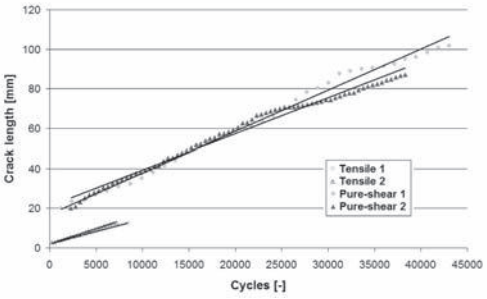

Figure 7. Dynamic crack growth curve for test pieces at identical extension ratio.

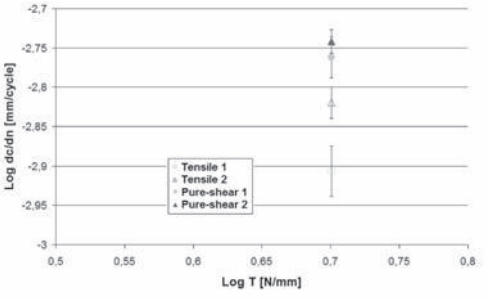

Figure 8. Crack growth rate as a function of tearing energy for tensile- and pure-shear-test pieces at identical extension ratio.

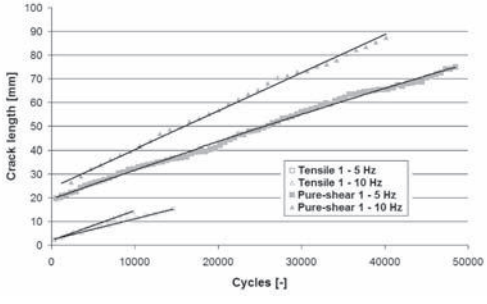

Figure 9. Dynamic crack growth curve for test pieces at various frequency and identical extension ratio.

rubber matrix consisting of rubber and waster rubber powder.

4.3 *Influence of loading frequency on crack growth*

In Figure 9, it can be seen the experimental results showed the dynamic crack growth curve as the effect of variable frequency. The effect of frequency up to 10 Hz on the crack growth behavior was evident

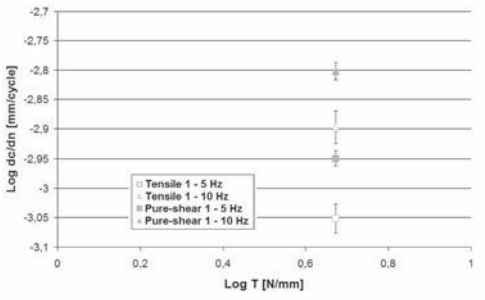

Figure 10. Crack growth rate as a function of tearing energy for tensile- and pure-shear-test pieces at various frequency and identical extension ratio.

but it is not significant. As the frequency increased from 5 to 10 Hz, the rate of crack growth increased to about 29% of the rate at a given tearing energy for tensile- and pure-shear-test piece.

5 CONCLUSION

A study of the fatigue behavior of filled rubber by simultaneous tensile- and pure-shear-mode testing was undertaken using a new concept of testing machine Tear Fatigue Analyzers. An advanced test method was successfully applied to determine fatigue crack growth characteristics by variable test conditions (extension ratio, frequency). The test method makes it possible to measure simultaneous two different modes and to observe in situ the length of the crack growth.

Some measurements were made of fatigue crack growth for simultaneous tested tensile- and pure-shear-test pieces by different loading conditions. The fatigue data were presented as power law relations between the crack growth rate and tearing energy. The experimental data verified the theoretical background for the determination of crack propagation in filled rubber by simultaneous tensile- and pure-shear-mode testing.

ACKNOWLEDGEMENT

This work was financially supported by German Research Foundation (DFG-Research FOR 597).

REFERENCES

Rivlin, R.S.; Thomas, A.G.: Rupture of rubber. I. Characteristic energy for tearing. Journal of Polymer Science, **10** (1953) 291–318.

Lake, G.J.: Aspects of fatigue and fracture of rubber, Prog. Rubber Technol. **45** (1983) 89.

Lake, G.J.: Effect of Crack Tip Sharpness on the Strength of Vulcanized Rubbers, Journal of Polymer Science, Part B, Polymers Physics, **25** (1987), 1157–1190.

Lake, G.J.: Fatigue and Fracture of Elastomers, Rubber Chemistry and Technology, **68** (1995), 435–460.

Griffith, A.A.: The phenomena of rupture and flow in solids, Philos. Trans. R. Soc. Lond., Ser. A **221** (1920), 163.

Industrial applications

Constitutive Models for Rubber VI – Heinrich et al. (eds)

Appraisal of nonlinear plasticity models for filled rubber using benchmark tests

H.R. Ahmadi & A.H. Muhr
Tun Abdul Razak Research Centre-TARRC, UK

T. Dalrymple
SIMULIA, Great Lakes Region, USA

S. Govindarajan
SIMULIA, Providence, RI, USA

ABSTRACT: The paper describes the desired hardening rule for a proposed viscoplastic model for filled rubber. The suitability of plasticity models currently available in a commercial FE code for this purpose is then examined. It is concluded that a recently implemented Multilinear Kinematic Hardening Plasticity (MKHP) material model is capable of providing the desired Masing rule for filled rubber and is indistinguishable from a previously proposed overlay approach by Austrell, leading to a significant reduction in computation time. In addition, results are presented for the overlaid model where a newly offered finite strain plasticity model is used to calculate the response of hyperelastic-perfectly-plastic materials. The model uses multiplicative decomposition of deformation gradient and has been used to show that finite yield strains may also be used in the viscoplastic model with additive decomposition after all without significant problem.

1 INTRODUCTION

Examination of Harris' results (1987), and others has led to the suggestion that a dissipative process is responsible for both the amplitude effect and the hysteresis in filled rubber (Ahmadi, Gough, Muhr & Thomas 1999 and Gough 2000). Therefore any generalized 3 dimensional model for filled rubber should exhibit a dissipative process that follows the "retraction rule" observed during Harris' uniaxial simple shear tests. The exact nature of the micro-mechanical processes responsible for this dissipative behavior in filled rubber is not well understood. However, in the absence of this knowledge the computational mechanics community can either model filled rubber using a phenomenological approach or use models based on physical processes that exhibit such behavior. Plasticity models are one possible candidate material model that do exhibit a "retraction rule" which may provide an approach to modeling the phenomena studied by Fletcher & Gent, Payne and Harris mentioned above. The two major advantages of using such models are a) the existence of extensive scientific theories, developed primarily for steel industry, in the form of plasticity literature and b) the availability of a large number of plasticity material models in commercial FE codes.

The aim of this paper is to examine plasticity models currently available in commercial codes such as Abaqus, and establish their merits and possible limitations for modeling the inelastic behavior of filled rubber.

2 BACKGROUND

In previous publications, (Ahmadi, Kingston & Muhr, 2008 and Ahmadi & Muhr, 2007), a simple "viscoplastic" model was proposed, capable of implementation in existing commercial FEA packages, with the scope to capture those aspects of the stress-strain behaviour of filled rubber that are most significant in engineering application, in particular the Payne or Fletcher-Gent effect. Attention was given to assembling the model from separately identified physical contributions, so that not only are the number of parameters small but also they may be at least semi-quantitatively related to the formulation of the elastomer. It was confirmed that the proposed "viscoplastic" approach captured the essence of the behaviour when examined in several

modes of deformation and for two materials, one filled NR and the other filled SBR.

However, the hardening rules for the plasticity models available in commercial packages, required for predicting the elastoplastic contribution to the stress response, appear to be unsuitable for producing the unloading stress-strain paths observed with filled rubber. This was overcome by decomposing the elastoplastic component into a number of elastic-perfectly-plastic components in parallel, each represented as a separate FE mesh in an overlay (Austrell, 2001). Although this approach has been successful, it led to an increase in the computation time compared to using a single plasticity model with an appropriate hardening rule.

3 CHARACTERISTICS OF THE BASIC MODEL

The basic model, consisting of hyperelastic, viscoelastic and elastoplastic contributions in parallel, is described in Ahmadi, Kingston & Muhr (2005, 2008), where it was also shown that the model is cast in a suitably general form for 3-D implementation in finite element analysis. According to the model the shear stress τ is given by:

$$\tau = \tau_{he} + \tau_{ep} + \tau_{ve} \quad (1)$$

where the subscripts *he*, *ep* and *ve* stand for hyperelastic, viscoelastic and elastoplastic respectively.

For filled rubber the elastoplastic stress contribution is considered to be governed by two curves (Ahmadi & Muhr, 2007)- see Figure 1.

From the knowledge of the loading curve, the retraction curves can be constructed using dilation transformation with a magnification factor of two about the origin. This is known as Masing approximation (Masing, 1926).

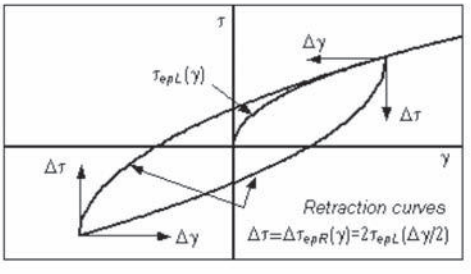

Figure 1. Schematic diagram showing hysteresis loop for a "Viscoplastic" material having a loading curve of $\tau_{epL}(\gamma)$. The relationship between the retraction curves $\tau_{epL}(\gamma)$ and loading curve is also shown.

4 PLASTICITY MODELS

4.1 *Elastic-perfectly-plastic models*

A number of simulations were carried out to predict the response of a unit length cube modeled using one C3D8 element subjected to sinusoidal tensile-compressive deformation at 1 Hz. The material model was elastic-perfectly-plastic with Young's modulus 3.655 MPa and Poisson's ratio 0.49999. The tensile yield strain was varied for each run over a range of 0.0029 to 0.29. Table 1 shows the comparison between the set yield strain and true stress values in tension and those obtained by simulation.

The simulated hysteresis loops are also shown in Figure 2 for four dynamic strain amplitudes. The first loading and retraction curves depart from linearity as the yield strain is increased. Austrell (1997) reported theory for such behaviour. This departure from linearity is also shown in Table 1.

Further simulations were carried out to predict the response of a unit length 2D plane strain element to sinusoidal simple shear deformation at 1 Hz.

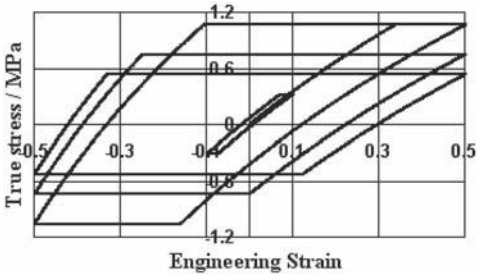

Figure 2. Hysteresis loops for tension-compression response of elastic-perfectly-plastic material model. Yield strains set at 8.7, 14.5, 20.3 and 29%, elastic modulus set at 3.665 MPa and Poisson's ratio of 0.49999.

Table 1. Comparison between the set yield true stress and engineering strain in tension and those found from a simulation using a single element cube.

Set	Simulated	Set	Simulated
σ_y	σ_y	ε_y	ε_y
0.0106	0.0106	0.0029	0.0030
0.0212	0.0212	0.0058	0.0060
0.1060	0.1060	0.0290	0.0296
0.2120	0.2120	0.0580	0.0598
0.3180	0.3180	0.0870	0.0909
0.5300	0.5300	0.1450	0.1575
0.7420	0.7420	0.2030	0.2256
0.8480	0.8480	0.2320	0.2639
1.0600	1.0600	0.2900	0.3365

The material model was similar to that used for the tensile simulations. Table 2 shows the corresponding yield stress and strain response of the material in simple shear at a defined tensile yield stress and strain value. The theoretical values in the table are the relationship between the tensile and shear yield stress and strains using infinitesimal elasticity theory (Ahmadi & Muhr, 2008). The basic assumption here is that yield occurs when the distortional strain energy density reaches a critical value. For an incompressible material with an infinitesimal tensile yield strain ε_y this results in a yield strain in simple shear of: $\tau_y = \sigma_y/\sqrt{3}$. It appears that the agreement between infinitesimal theory predictions and the simulated results is reasonable up to tensile strains of 14.5%, corresponding to yield strains in shear of 25%. The last column of table 2 gives the post yield slope of shear stress-strain curve. It is interesting that the slope begins to become negative above 12% yield strain in shear.

Figure 3 shows the hysteresis loops for the cyclic simple shear deformations for values of tensile yield strains of 2.9, 5.8, 14.5 and 29%, corresponding to yield strains in shear at 5, 10, 25 and 50%. The largest loop for the 50% yield strain case clearly shows the negative slope beyond yield and exhibits non-closed loop not expected from such a model.

Table 2. The simulated and infinitesimal theory predictions for the yield strain and stress in simple shear.

		Sim.	Theory	Sim.	Theory	Sim.
σ_y	ε_y	τ_y	$\tau_y = \sigma_y/\sqrt{3}$	γ_y	$\gamma_y = (\sqrt{3})\varepsilon_y$	Slope
0.011	0.003	0.006	0.006	0.005	0.005	0.000
0.021	0.006	0.012	0.010	0.010	0.012	0.000
0.053	0.015	0.031	0.031	0.025	0.025	−0.001
0.106	0.029	0.061	0.061	0.050	0.050	−0.001
0.212	0.058	0.122	0.122	0.102	0.100	−0.003
0.318	0.087	0.183	0.184	0.152	0.151	−0.006
0.530	0.145	0.304	0.306	0.253	0.251	−0.019
0.742	0.203	0.422	0.428	0.353	0.352	−0.038
0.848	0.232	0.480	0.490	0.406	0.402	−0.049
1.060	0.290	0.592	0.612	0.509	0.502	−0.077

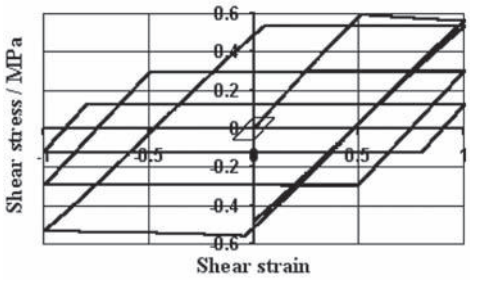

Figure 3. Hysteresis loops for simple shear response of elastic-perfectly-plastic material model. Yield strains in shear set at 5, 10, 25 and 50% corresponding to similar values to those shown in Figure 2 for the tensile compression simulations.

4.2 *Overlay of elastic-perfectly-plastic models*

Three simulations were carried out on a single element plane strain model. In the first simulation the material model was an elastic-perfectly-plastic material with Young Modulus of 1.232 MPa and tensile yield stress of 0.0724 giving a yield strain of 0.0589. These values are appropriate to the elastic-perfectly-plastic part of a viscoplastic model for a filled natural rubber vulcanizate. The model was subjected to cyclic deformation in shear of strain amplitude of 0.12. The second simulation was identical to the first but the material model had a Young's Modulus of 2.6493 MPa and tensile yield stress of 0.02527 giving a yield strain of 0.0095. The third simulation involved overlaying these two models as described in Austrell (2001) and Ahmadi, Kingston & Muhr (2008). The simulated shear response of the overlaid model, described in section 4.2, when subjected to 1¼ cycles of dynamic strain amplitude 0.1, is shown in Figure 4.

Table 3 shows the dynamic properties of the three models described in Figure 4 analy-zed using the Secant method (Ahmadi & Muhr 1997). The data in Figure 5 shows that overlaying elastic-perfectly-

Table 3. Dynamic properties of elastoplastic models.

Material	Shear modulus	Energy in the loop
E = 1.232	0.348	0.003
E = 2.6394	0.122	0.006
Overlay	0.470	0.009

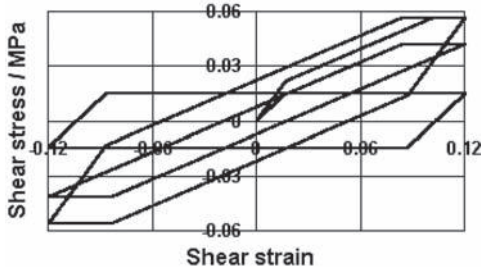

Figure 4. Hysteresis loops in shear for two elastic-perfectly-plastic materials each subjected to cyclic shear deformation with amplitude of 0.12. The largest loop shows the response when the two models are overlaid.

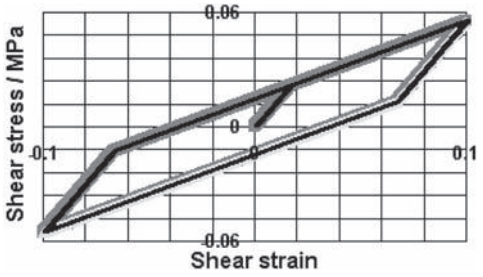

Figure 5. One and quarter cycle hysteresis loop for two overlaid elastic-perfectly-plastic materials, with properties described in section 4.2, dark line: simulated results for overlaid model. Half cycle light shaded line (top right of the plot to bottom left): Masing transformation of the first quarter cycle. Thick dark shaded line: simulated results using MKHP model.

plastic models exhibits Masing's "retraction" rule desired for modeling filled rubber.

4.3 *Overlay models for filled rubber*

In a previous publication a viscoplastic material model for filled rubbers based on an overlay of hyperelastic, viscoelastic and elastic-perfectly plastic materials was fitted to a filled natural rubber vulcanizate (Ahmadi, Kingston & Muhr 2008). A methodology for fitting the model to the quasi-static response of the material was also described. The aim in this section is to present the simulated response to cyclic simple shear deformation for such a model, using a 2D plane strain single element mesh and a full 3D multi-element mesh. These results were then analyzed, using the secant method, to obtain equivalent linear dynamic shear properties for the viscoplastic material. The parameters of the model are those given in Ahmadi, Dalrymple, Kingston and Muhr (2008).

Figure 6 shows the hysteresis loops for the material model when subjected to amplitudes from 5 to 50% shear strain at 1 Hz. The FE model was an overlay of one hyper-viscoelastic and 6 elastic-perfectly-plastic materials each represented by one 2D plane strain element. Figure 7 shows the hysteresis loop for 20% strain together with the loop corresponding to the elastoplastic contribution on its own. As with Figure 5, the desired "retraction rule" is obeyed, shown by the light shaded line in the figure. Figure 8 shows a 3D FE model for a disc of rubber using 2040 (340 by 6 layers) brick elements. (C3D8). The same material model as that for figures 6 and 7 was used for the analysis.

Figures 9a & b show the dynamic properties for the single 2D element model and the 3D overlaid multi brick element models. Also shown are the

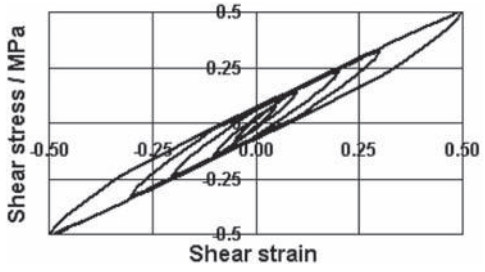

Figure 6. Simulated loops for an overlay of 1 hyper-viscoelastic and 6 elastic-perfectly-plastic materials.

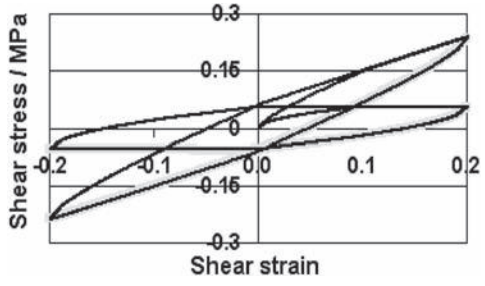

Figure 7. One and quarter loop for the 20% dynamic strain amplitude shown in figure 6. Also shown is the loop only for the contribution of the 6 elastic-perfectly-plastic materials where the stress is constant beyond 10.6% shear strain corresponding to the point at which all 6 elements have undergone yield.

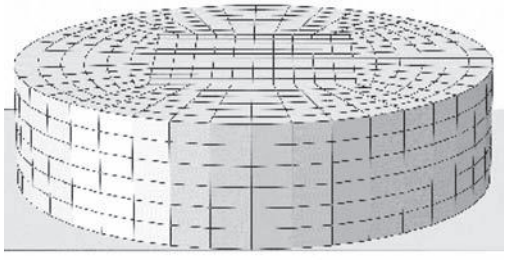

Figure 8. 3D model for rubber disc.

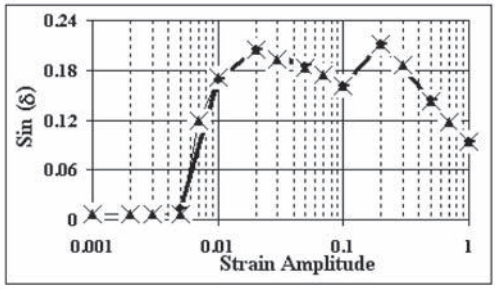

Figure 9a. Variation of Sin (δ) with shear strain amplitude.

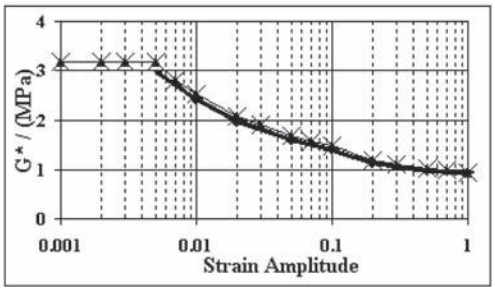

Figure 9b. Variation of G* with shear strain amplitude, triangles- 2D single element overlaid model, solid line- 3D disc overlaid model, circles- similar to solid line, but multiplicative decomposition was used to calculate the response of the elastic-perfectly-plastic materials, crosses- 2D single elements using MKHP model.

results for the 3D disc overlaid model where a new finite strain plasticity model is used to calculate the response of the elastic-perfectly-plastic material.

This new material model allows the use of hyperelasticity for nonlinear elasticity to be combined with plasticity model. It is based on a multiplicative decomposition of the deformation gradient into elastic and plastic parts, rather than the traditional additive decomposition of the total strain (Weber & Anand, 1990 and Simo, 1992).

This is discussed in detail in section 4.5. In addition, Figures 9a & b show the simulated results for the 2D model using a Multilinear Kinematic Hardening Plasticity model, discussed in the next section. These procedures have recently been implemented in Abaqus.

4.4 *Multilinear Kinematic Hardening Plasticity (MKHP) model for filled rubber*

This material model was implemented in Abaqus version 6.8 and is provided in the form of a built-in UMAT user subroutine, using the USER MATERIAL and DEPVAR option. It uses an overlay of elastic-perfectly-plastic materials; in principle, very similar to the model described by Austrell, Olsson & Jonsson, (2001) and Ahmadi, Kingston & Muhr, (2008) but with the exception that only one set of FE mesh is required, hence the size of the FE model and the computation time is reduced.

This new model is not described fully in current Abaqus documentation and is therefore briefly described here and a previous publication, Ahmadi, Dalrymple, Kingston & Muhr (2008).

The material is assumed to have up to N subvolumes, each with elastic-perfectly-plastic behaviour, which have different yield strengths, σ_{yi} in tension but the same elastic modulus, E and are subjected to the same total strain. When multiple subvolumes are combined together, complex material behaviour, such as multilinear hardening can be modeled; Crisfield (1997) and Chen & Han (1936). The Multilinear Kinematic Hardening Plasticity (MKHP) model takes piece-wise linear stress-plastic strain (σ_i, ε_i^{pl}) curves as input (see Figure 2 of Ahmadi, Dalrymple, Kingston & Muhr, 2008). The number of subvolumes used in the model is equal to the number of stress-plastic strain (σ_i, ε_i^{pl}) pairs given on the curve. The yield strength σ_{yi} of the ith subvolume can be shown to be:

$$\sigma_{yi} = \sigma_i + \boldsymbol{E}\varepsilon_i^{pl} \tag{2}$$

The "weight" to each subvolume is equal to:

$$\omega_i = \frac{1}{\left(1+\dfrac{\boldsymbol{H}_i}{\boldsymbol{E}}\right)} - \sum_{k=1}^{k=i-1} \omega_k \tag{3}$$

where H_i is the slope of the hardening curve, known as hardening modulus, i.e. the slope of each (σ_i, ε_i^{pl}) chord in the stress-plastic strain plot (see Figure 2 of Ahmadi, Dalrymple, Kingston & Muhr, (2008)). It is assumed that the hardening modulus beyond the last data point is zero; equation (3) therefore ensures that the sum of all subvolume weights is one.

In a given solution (time) increment, all subvolume, the increment in plastic strain and the total stress at the end of the increment are computed using a von Mises yield criterion with the associated flow rule. The total stress and total plastic strain for the entire volume is then calculated as:

$$\{\sigma\} = \sum_{1}^{N} \omega_i \{\sigma_i\} \tag{4}$$

and

$$\{\varepsilon^p\} = \{\varepsilon^p\}_0 + \sum_{i=1}^{N} \omega_i \{\Delta\varepsilon_i^p\} \tag{5}$$

where $\{\varepsilon^p\}_0$ is the plastic strain at the beginning of the increment.

The procedure for fitting the parameters for the MKHP material used as the elastoplastic part of the "viscoplastic" model is given in Ahmadi, Dalrymple, Kingston & Muhr (2008). However, equation 2 was mistyped in their paper. The predictions of the two viscoplastic models using in one case a MKHP material and in another an overlay of

elastic-perfectly-plastic materials for the case of cyclic simple shear deformation of filled rubber using one 2D plane strain model for a disc of rubber has also been presented in Ahmadi, Dalrymple, Kingston & Muhr (2008). For comparison these 2D element results are also presented in figures 9a & b.

4.5 *Multiplicative versus additive decomposition*

The classical plasticity models assume that the total strain in the material is an additive combination of elastic and plastic strains i.e. $\varepsilon = \varepsilon_e + \varepsilon_p$, the elastic strain ε_e is much smaller than the subsequent plastic strain ε_p; this is also known as *E-P* model. This assumption seems inappropriate for rubber as the yield strain may be required to be large. The multiplicative decomposition theory, (Lee, 1969, Weber & Anand, 1990 and Simo, 1992) is based on the assumption that the deformation gradient $\boldsymbol{F}$ in the material is expressed as the multiplication of an elastic deformation gradient $\boldsymbol{F}^e$ and the plastic deformation gradient $\boldsymbol{F}^p$ i.e. $\boldsymbol{F} = \boldsymbol{F}^e \boldsymbol{F}^p$. the convention is that the rigid body rotation part of the deformation is contained in $\boldsymbol{F}^p$, whereas $\boldsymbol{F}^e$ contains only the stretch component of the deformation. It can be shown that the velocity gradient $\boldsymbol{L} = \dot{\boldsymbol{F}}\boldsymbol{F}^{-1}$ for such a deformation has also elastic and plastic components $\boldsymbol{L}^e$ and $\boldsymbol{L}^p$. These are given by:

$$\begin{aligned} \boldsymbol{L}^e &= \dot{\boldsymbol{V}}^e \boldsymbol{V}^{e-1} = \boldsymbol{D}^e + \boldsymbol{W}^e \\ \boldsymbol{L}^p &= \dot{\boldsymbol{F}}^p \boldsymbol{F}^{p-1} = \boldsymbol{D}^p + \boldsymbol{W}^p \end{aligned} \tag{6}$$

where $\boldsymbol{V}^e$ is the elastic stretch tensor and $\boldsymbol{D}$ and $\boldsymbol{W}$ are the symmetric and asymmetric components of the elastic and plastic velocity gradient. It can be shown that for such deformation $\boldsymbol{D} \neq \boldsymbol{D}^e + \boldsymbol{D}^p$ and similarly $\boldsymbol{W} \neq \boldsymbol{W}^e + \boldsymbol{W}^p$ unless $\boldsymbol{V}^e$ is small i.e. the elastic strains are small.

Abaqus offers finite strain elastic-plastic deformation for elastic-perfectly plastic and isotropic hardening models, but the model cannot be combined with kinematic hardening model. The elastic part of the model may be defined using strain energy density functions offered under the hyperelastic materials. In this paper a comparison has been made between the results of the analysis using the overlay approach in which for one case additive and for another multiplicative decomposition were used. The hyperelastic part of the model was an incompressible neo-Hookean material with the coefficient C_1 set equal to $E/6$. Comparison of the two analyses is important in order to establish whether the magnitude of the tensile yield strain set in overlay model using additive decomposition approach would violate the small strain assumption of this theory. The results of the two models for the 3D multi-element model are also included in figures 9a & b. The hysteresis loops for these two models, not shown here due to lack of space, are very similar, which is why the equivalent viscoelastic dynamic properties data shown in figures 9a & b are coincident. This may suggest that in the additive decomposition analysis the yield strain for the elastic-perfectly-plastic components do not violate the assumptions in the model.

5 BRIEF DISCUSSION AND CONCLUSIONS

- Overlaying elastic-perfectly-plastic materials gives the Masing's rule, as desired for modelling filled rubber. This is not possible with the classical kinematic hardening plasticity.
- Overlay gave additive results for a single element, suggesting appropriate implementation of the plasticity model in Abaqus.
- Results for single element and 3D disc agree well. The 3D disc model predicts slightly lower values for the shear modulus due to the effect of the free edge. However, all sets of data show an unexpected double peak in the sin (δ) results. This is due to the particular and coarse discretisation into elastic-perfectly-plastic materials. The chosen shear strains at yield for these materials were 0.50, 0.91, 1.7, 3.0, 5.5 and 10.2% with the corresponding shear moduli of 1.21, 0.25, 0.19, 0.14, 0.11 and 0.34 MPa. The last element has the second highest shear modulus and yields at the highest strain of 10.2%. Hence, it dissipates the largest energy when it yields, resulting in the sin (δ) value rapidly increasing beyond this point. Finer discretisation of the elasto-plastic part would eliminate this numerical artefact.
- The MKHP model is indistinguishable from the Overlay model. This provides much lower computational time.
- Multiplicative decomposition analysis of the 2D and 3D disc models agree with the additive decomposition results, suggesting that using additive decomposition, despite the small strain assumption in yield strain of the plastic model, gives reasonable results.
- Abaqus offers finite strain elasticity for the elastic part of the elastic-perfectly plastic model. Hence different strain energy density functions may be used to model this part of the model. This is not as yet provided for MKHP material models.

REFERENCES

Ahmadi, H.R., Dalrymple, T., Kingston, J.G.R. & Muhr A.H. 2008. Dynamic properties of filled rubber.

III—Use Nonlinear Kinematic Hardening Plasticity Material Models. *Paper 78 of Fall 174th Technical Meeting of the Rubber Division of the American Chemical Society, Louisville, Kentucky.*

Ahmadi, H.R., Gough, J., Muhr, A.H. & Thomas, A.G. (1999). Bi-axial experimental techniques highlighting the limitations of a strain-energy description of rubber, Dorfmann, A.L., and Muhr, A.H. (eds.) *Constitutive Models for Rubber I,* 65–71 Rotterdam: Balkema.

Ahmadi, H.R., Kingston, J.G.R. & Muhr, A.H, 2008. Dynamic properties of filled rubber. I—Simple model, experimental data and simulated results. *Rubber Chemistry and Technology*, 81: 1–18.

Ahmadi, H.R. & Muhr, A.H. 1997. Modelling dynamic properties of filled rubber. *Plastic, Rubber and Composites Processing and Applications* 26: 451–461.

Ahmadi, H.R. & Muhr A.H. 2007. Dynamic properties of filled rubber. II—physical basis of contributions to the model. *Paper 39 of Fall 172nd Technical Meeting of the Rubber Division of the American Chemical Society, Cleveland, Ohio.*

Austrell, P.E., Olsson, A.K. & Jonsson, M. 2001. A method to analyze the non-linear dynamic behaviour of carbon-black filled rubber components using standard FE codes, D. Besdo, R.H. Schuster and J. Ihlemann (eds.) *Constitutive Models for Rubber II*, 231–237 Rotterdam: Balkema.

Chen, W.F. & Han, D.J. 1988. Plasticity for Structural Engineers, Springer-Verlag, New York, USA.

Crisfield, M.A. 1997. Nonlinear Finite Element Analysis of Solids and Structures, Volume 2: Advanced Topics, John Willey & sons, Chichester, England.

Gough, J. 2000. Stress-strain behaviour of rubber, PhD thesis submitted to Queen Mary and Westfield College-University of London.

Harris, J. 1987. Dynamic testing under non-sinusoidal conditions and the consequences of nonlinearity for service performance. *Rubber Chemistry and Technology*, 60: 870–887.

Lee, E.H. 1969. Elastic-Plastic Deformation at Finite Strains, Transactions of ASME, Journal of Applied Mechanics, Vol. 36, Part 16, pp. 1–6.

Masing, G. 1926. "Eigenspannungen and verfertigung beim messing." *Proc., 2nd Int. Congress on Applied Mech.*, Zurich, Switzerland.

Simo, J.C. 1992. Algorithms for Static and Dynamic Multiplicative Plasticity that Preserve the Classical Return Mapping Schemes of the Infinitesimal Theory, *Computer Methods in Applied Mechanics and Engineering*, vol. 99, 61–112.

Weber, G. & Anand, L. 1990. Finite Deformation Constitutive Equations and a Time Integration Procedure for Isotropic, Hyperelastic-Viscoplastic Solids, *Computer Methods in Applied Mechanics and Engineering*, vol. 79, pp. 173–202.

Constitutive Models for Rubber VI – Heinrich et al. (eds)
© 2010 Taylor & Francis Group, London, ISBN 978-0-415-56327-7

Temperature dependence of midsole materials

K. Brückner & S. Odenwald
Institute of Mechanical and Polymer Engineering, Sports Equipment and Technology, Chemnitz University of Technology, Germany

J. Heidenfelder
Department of Human Locomotion, Chemnitz University of Technology, Germany

ABSTRACT: The purpose of this study was to investigate the temperature influence on the mechanical properties of midsole materials. The board materials were tested by an adapted hydraulic impact test of running shoes and the dynamic mechanical analysis (DMA) as a standard test method for polymers within a certain temperature range. The results show that the absorbed energy and the stiffness II of board materials decrease with an increase of temperature as investigated for running shoes. Furthermore, the hydraulic impact test is adequate for characterising midsole materials due to the frequency and stroke dependency of foam materials under different temperatures.

1 INTRODUCTION

The load sequence of running is characterised by an impact peak in which the heel area of the shoe is, within few milliseconds, loaded with twice the runner's bodyweight. Thereby, the shoe midsole, usually made of flexible foam, reduces this impact to a physiological harmless level by absorbing energy while being deformed up to 45% of the initial thickness. It is assumed that a portion of this energy as a result of compression by the pressure of the foot is dissipated as heat. This heat would influence the properties of the midsole material due to the temperature dependency of flexible foams. According to Heidenfelder (2004) energy absorption and functional stiffness of running footwear decrease while temperature increases.

2 METHOD

Midsole materials were tested with an adapted hydraulic impact test HIT under different temperatures conditions. Thereafter, results were compared with dynamic mechanical properties of the dynamic mechanical analysis (DMA) as a standard test method for identifying temperature dependent dynamic properties of polymers.

2.1 *Hydraulic impact test*

2.1.1 *Testing device*

Determination of cushioning abilities of foam materials was tested according to the mechanical cushioning test applied to complete running shoes. The test normally is performed by using a servo-hydraulic testing device (Figure 1) equipped with a heel-like shaped stamp which is oriented perpendicular to the base of the sample.

2.1.2 *Load spectrum*

The design of the mechanical test method is derived from biomechanical test results of biomechanical analyses of ground reaction forces (GRF) (continuous line in Figure 2). Analysis of the resulting curve shows that the tested heel area is loaded with twice the runner's bodyweight while running at a speed of 3.5 ms (Heidenfelder et al., 2005). GRF in vertical direction shows two peaks: the initial impact peak and the subsequent active peak where leg muscles push the body from the ground (Swigart et al., 1993). The load rises within 35 ms to the first impact peak, and decreases to zero after another 35 ms in the heel area. This load cycle is repeated every 700 ms corresponding to a frequency of 1.4 Hz. The testing machine imitates this load-time-characteristic (dashed line in Figure 2) while punching the heel area of the shoe with a ball-shaped stamp.

2.1.3 *Test results and analysis*

100 load cycles were collected in short-time tests and data was collected from the 100th cycle. The first cycles are used to create a steady material state and to bring up the required force by the machine. The analysed parameters of the test are (Heidenfelder et al., 2005):

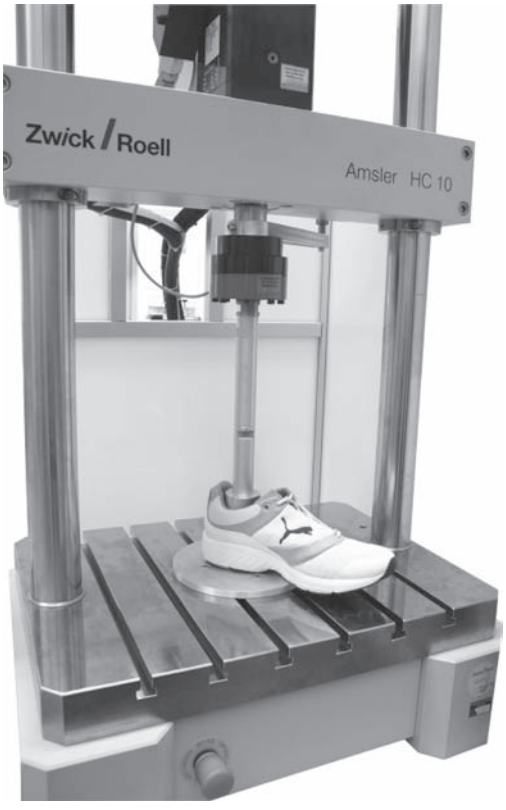

Figure 1. Hydraulic impact test of running footwear.

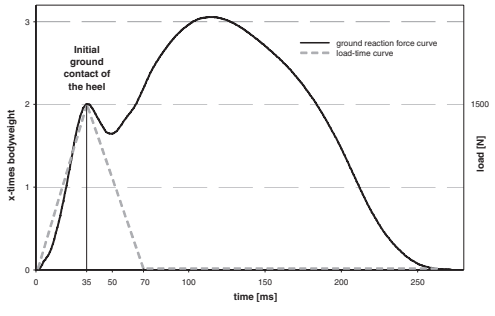

Figure 2. Ground reaction force; load-time characteristic of the testing device.

– energy loss: energy which was absorbed by the material and dissipates to thermal energy,
– stiffness II/functional stiffness (compression stiffness at high deformation between 1000–1500 N): represents the load of the footwear during the initial ground contact of the heel.

2.1.4 *Adapted test method with 45% deformation*

The test setup with a load of 1500 N—being used for the test of complete shoes—would cause disproportional high deformation of the foam materials. With respect to this fact, the test of foam material has to be adapted for receiving results comparable to real shoe conditions. An internal database from a mechanical hydraulic impact tests of 42 running shoes sums up a mean deformation of 45% by the hydraulic impact test. For this reason the pure foam material was tested deformation-controlled with a stroke of 45% of the materials thickness. According to the coplanar board material the test was performed with a flat stamp. Stiffness II was analysed at high deformation between 67–100% of the maximal force. A heat gun was used for tempering the sample while controlling the temperature by a temperature sensor—centrically integrated in the sample (Figure 3). The load-deformation data and the temperature were collected from every 100th cycle.

2.2 *Temperature range*

The temperature range was determined between 25 and 55°C according to the results of long term hydraulic impact test of running shoes (Heidenfelder, 2004). The results show that midsole temperature increases up to approximately 55°C within the first 15 min. After 15 min. temperature stays on a constant level.

2.3 *Dynamic mechanical analysis DMA*

For measuring the dynamic mechanical properties of the foam material a DMA Q800—Module by TA Instruments Ltd. equipped with a compression clamp was used. In order to obtain the properties as a function of temperature, the test was performed with an amplitude of 100 µm at 1 Hz

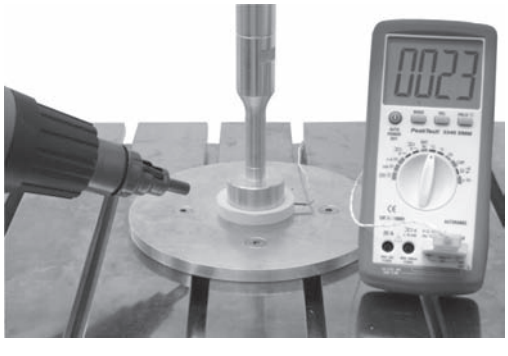

Figure 3. Adapted hydraulic impact test with heat gun and temperature sensor.

Table 1. Properties of the tested midsole materials.

	Hardness [Asker C]	Density [g/cm³]	Rebound elasticity [%]
EVA-H: *Hardness*	58	0,21	39
EVA-A: *AbsorbShock*	51	0,21	21
EVA-L: *Light*	51	0,16	38
EVA-R: *Resilient*	53	0,22	53

frequency between 20 and 65°C, with a heating rate of 3°C/min. The samples with a mean height of 9.52 ± 0.02 mm were prepared in a cylindrical shape with a diameter of 10 mm corresponding to the plate diameter of the compression clamp. The properties of the foam material were measured in the same direction as loaded in running shoes. The analysed DMA parameters are the loss factor tan δ which characterises the mechanical damping and the stiffness (Ehrenstein, 1999).

2.4 *Materials*

The tested materials (Table 1) were boards of flexible foam material of Ethylen/Vinylacetat with hardnesses and densities in the usual range of midsole properties (Boyer et al., 2004 & Verdejo et al., 2004).

3 RESULTS AND DISCUSSION

3.1 *Energy loss and loss factor tan δ*

The data points of the hydraulic impact test are bonded by a potential trend line.

The results (Figure 4) show that the energy loss of the hydraulic impact test decreases for all of the tested EVA- board materials with increasing temperature. This confirms the ascertainment of shoes of Kenoshita et al. (1996) and Heidenfelder (2004) who reveal a decreasing energy loss by an increasing temperature for the tested shoes.

The results of the loss factor (Figure 5) point out only a slight increase of tan δ with increasing temperature for three of the tested materials. This suggests a low temperature dependency of the loss factor except for EVA-A. The amount of changing for the loss factor is lower than for the energy loss which decreases within approximately 20°C to half the initial value.

The EVA-R corresponding to the highest rebound elasticity presents the lowest tan δ as well as the lowest energy loss. According to the lowest rebound elasticity the EVA-A sums up the highest energy loss and loss factor but admittedly at lower temperature (up to approximately 40°C), indicating that a material with a high rebound elasticity presents a lower energy loss and loss factor respectively.

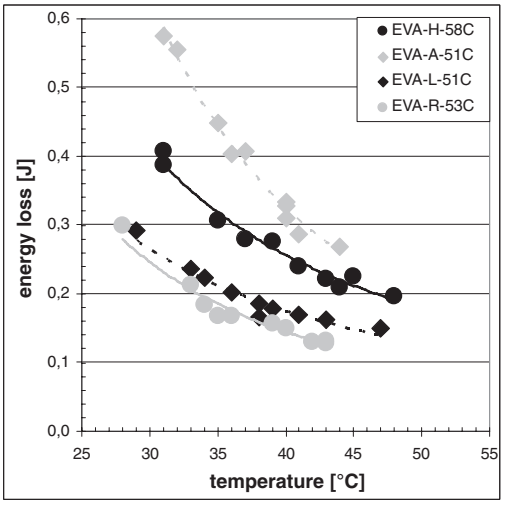

Figure 4. Dependence of energy loss on the temperature.

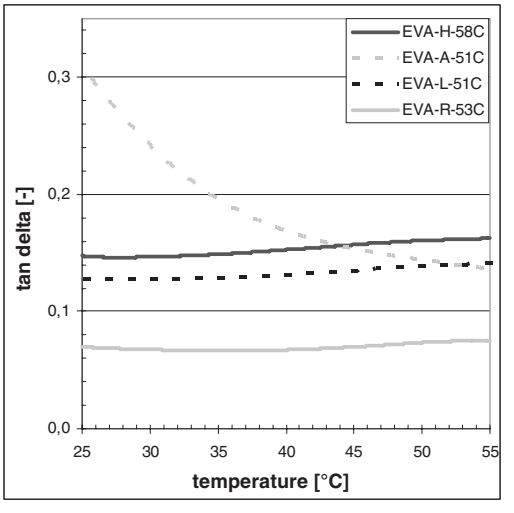

Figure 5. Dependence of tan δ on the temperature.

3.2 *Stiffness*

In Figures 6–7 stiffnesses in both tests present an increase of the data by decreasing temperature. This confirms the temperature characteristics of shoes described by Kleindienst et al. (2001) and Heidenfelder (2004).

The amount of changing is higher for the stiffness than for stiffness II.

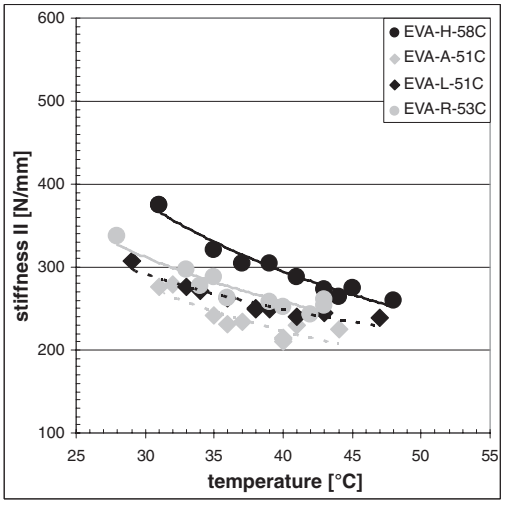

Figure 6. Stiffness II of the HIT test at different temperatures.

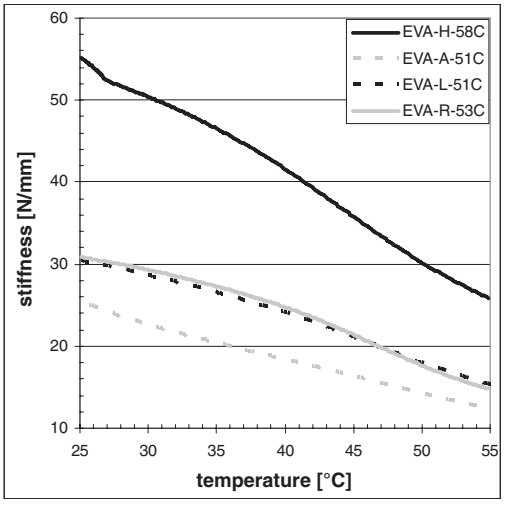

Figure 7. Stiffness of the DMA at different temperatures.

Obviously, DMA and HIT test differ in the amplitude of stroke (HIT: 3.6 mm; DMA: 100 µm). With respect to this fact it is assumed that DMA only measures the surface and respectively the matrix properties of the material (Rodriguez- Perez et al. 2000). The important fact is that there is no correlation of HIT and DMA test. Therefore, the hydraulic impact test is adequate for characterising midsole materials due to the frequency and stroke dependency of foam materials.

4 CONCLUSION AND OUTLOOK

The results of the hydraulic impact test of the pure midsole material show a comparable temperature behaviour as the results of complete shoes (the lower the temperature, the higher the energy loss and the stiffness II). Furthermore, the HIT test is adequate for characterising midsole materials.

To keep the cooling of the sample by the bearing plate and the stamp during the hydraulic impact test sequence in mind, a heating cabinet would provide a constant ambient temperature.

The presented results were measured only on one sample per material. With respect to this fact further materials have to be tested to validate these results.

ACKNOWLEDGEMENT

Special thanks to Puma Inc., Herzogenaurach, Germany for supplying the tested foam materials and TA Instruments Ltd., Eschborn, Germany for borrowing the compression clamp.

REFERENCES

Boyer, K.A. & Nigg, B.M. 2004. Muscle activity in the leg is tuned in response to impact force characteristics. *Journal of Biomechanics* 37: 1583–1588.

Ehrenstein, G.W. 1999. *Polymer- Werkstoffe: Struktur—Eigenschaften—Anwendungen*. München: Hanser Fachbuch.

Heidenfelder, J. 2004. Temperaturabhängigkeit von Zwischensohlenmaterialien in Laufschuhen, M.A. thesis. Chemnitz University of Technology.

Heidenfelder, J., & Odenwald, S. 2005. Mechanische Prüfung von Laufschuhen. DIVERS Workshop „Wechselwirkung zwischen Materialtechnologie & Bewegungs- Analyse im Sport". 127–136.

Kinoshita, H. & Bates, B.T. 1996. The Effect of Environmental Temperature on the Properties of Running Shoes. *Journal of Applied Biomechanics* 12: 258–268.

Kleindienst, F., Krabbe, B. & Westphal, K. 2001. Temperature influence of varying midsole hardness on functional properties. *Proc. of the 5th Symp. on Footwear Biomechanics*: 54–55.

Rodriguez-Perez, M.A. & de Saja, J.A. 2000. Dynamic mechanical analysis applied to the characterisation of closed cell polyolefin foams. *Polymer Testing* 19: 831–848.

Swigart, J.F., Erdmann, A.G. & Cain P.J. 1993. An energy based method for testing cushioning durability of running shoes. *Journal of Applied Biomechanics* 9: 26–47.

Verdejo, R. & Mills, N.J. 2004. Heel- shoe interactions and durability of EVA foam running shoe midsoles. *Journal of Biomechanics* 37: 1379–1386.

Constitutive Models for Rubber VI – Heinrich et al. (eds)

Anisotropic hyperelastic models in Abaqus

S.M. Govindarajan & J.A. Hurtado
DS SIMULIA Corporation, Rising Sun Mills, Providence, USA

ABSTRACT: The authors have implemented two distinct formulations in Abaqus for modeling anisotropic hyperelastic materials: strain-based and invariant-based. In the strain-based formulation, the strain energy function is expressed in terms of the components of the Green-strain tensor, assuming that the preferred material directions in the reference configuration are orthogonal. Generalized Fung models, which are widely used in bio-mechanics and bio-medical applications, have been implemented using this formulation. In the invariant-based formulation, the strain energy function is expressed in terms of an irreducible set of invariants of the right-Cauchy Green tensor and the preferred material directions (which may be non-orthogonal) in the reference configuration. A strain energy function proposed by Holzapfel-Gasser-Ogden for arterial walls has been implemented using the invariant-based formulation in Abaqus. The user may implement a general form of the strain energy function through a user-defined subroutine for both the formulations. Two examples that demonstrate the usefulness of the anisotropic hyperelasticity capability in Abaqus are shown.

1 INTRODUCTION

Many materials of technological interest exhibit anisotropic elastic behavior due to the presence of preferred directions in their microstructure. Examples of such materials include common engineering materials such as fiber-reinforced composites, reinforced rubber, wood, etc. as well as soft biological tissues such as arterial walls, heart tissues, etc. When these materials are subjected to small strains (less than 2–5%), their mechanical behavior can generally be modeled using conventional anisotropic linear elasticity. Under large deformations, however, these materials exhibit highly anisotropic and nonlinear elastic behavior due to rearrangements in the microstructure, such as reorientation of the fiber directions with deformation. The accurate simulation of these nonlinear large-strain effects requires the use of constitutive models formulated within the framework of anisotropic hyperelasticity.

The work presented in this paper is concerned with modeling of anisotropic hyperelastic materials such as reinforced rubber and soft biological tissues, under arbitrarily large strains. The plan of the paper is as follows. The formulations of the anisotropic hyperelastic models in Abaqus are discussed in Section 2, followed by examples in Section 3 and conclusions in Section 4.

2 FORMULATION

Hyperelastic materials are described in terms of a strain energy potential, U, which defines the strain energy stored in the material per unit of volume in the reference configuration as a function of the deformation at that point in the material. Strain-based and invariant-based formulations have been implemented in Abaqus for the representation of the strain energy potential of anisotropic hyperelastic materials. These formulations are described in some detail below.

2.1 *Strain-based formulation*

In the strain-based formulation, the strain energy function is expressed directly in terms of the components of the Green strain tensor, $U = U(\boldsymbol{\varepsilon}^G)$.The Green strain is defined as $\boldsymbol{\varepsilon}^G = (\mathbf{C} - \mathbf{I})/2$, where $\boldsymbol{C} = \mathbf{F}^T$. $\mathbf{F}$ is the right Cauchy-Green tensor; and $\mathbf{I}$ is the identity matrix. Without loss of generality, the strain energy function can be written in the form

$$U = U(\bar{\boldsymbol{\varepsilon}}^G, J) \tag{1}$$

where $\bar{\boldsymbol{\varepsilon}}^G = (\bar{\mathbf{C}} - \mathbf{I})/2$ is the modified Green strain tensor; $\bar{\mathbf{C}} = J^{-2/3}\mathrm{C}$ is the modified right Cauchy-Green tensor; and $J = \det(\mathbf{F})$ is the volume change.

An underlying assumption in the models based on the strain-based formulation is that the preferred material directions are initially aligned with an orthogonal coordinate system in the reference configuration. These directions may become non-orthogonal only after deformation. Examples of strain-based energy functions include the Fung model which has been implemented

directly in Abaqus. This model is commonly used for simulation of soft biological tissues and is described below. Other forms are also supported via a dedicated user-subroutine where the strain energy function (Equation 1) and the derivatives with respect to the Green-strain must be defined by the user.

2.1.1 *Generalized Fung model*

The generalized Fung strain energy potential in Abaqus is based on the two-dimensional exponential form proposed by Fung (1979, 1993), suitably generalized to arbitrary three-dimensional stress states (Humphrey, 1995), and has the following form:

$$U = \frac{1}{2}c(e^{Q}-1) + \frac{1}{D}\left[\tfrac{1}{2}(J^2-1) - \ln J\right] \tag{2}$$

where c and D are the material properties corresponding to deviatoric and volumetric behavior, and Q is defined as

$$Q = \overline{\boldsymbol{\varepsilon}}^{G} : \mathbf{b} : \overline{\boldsymbol{\varepsilon}}^{G} = \overline{\varepsilon}^{G}_{ij} b_{ijkl} \overline{\varepsilon}^{G}_{kl} \tag{3}$$

where $\mathbf{b}$ is a dimensionless symmetric fourth-order tensor of anisotropic material constants. In Abaqus this tensor can be fully anisotropic (21 constants) or orthotropic (9 constants).

2.2 *Invariant-based formulation*

Using the continuum theory of fiber-reinforced composites (Spencer, 1984) the strain energy function can be expressed directly in terms of the invariants of the deformation tensor and the fiber directions. For example, consider a composite material that consists of an isotropic hyperelastic matrix reinforced with N families of fibers. The fiber directions in the reference configuration are characterized by a set of unit vectors $\mathbf{A}_\alpha$, $\alpha = 1,\ldots,N$. Then the most general form of the strain energy function is $U = U(\mathbf{C}, \mathbf{A}_\alpha)$, $\alpha = 1,\ldots,N$. Using isotropic representation functions, the strain energy can be expressed in terms of an irreducible set of invariants that form the integrity basis of the tensor $\mathbf{C}$ and the vectors $\mathbf{A}_\alpha$:

$$\begin{aligned} U(\mathbf{C}, \mathbf{A}_\alpha) &= U(\overline{I}_1, \overline{I}_2, J, \overline{I}_{4(\alpha\beta)}, \overline{I}_{5(\alpha\beta)}; \zeta_{\alpha\beta}) \\ &\alpha = 1,\ldots,N; \beta = 1,\ldots,\alpha \end{aligned} \tag{4}$$

where $\overline{I}_1 = \operatorname{tr} \overline{\mathbf{C}}$ and $\overline{I}_2 = \frac{1}{2}(\overline{I}_1^2 - \operatorname{tr} \overline{\mathbf{C}}^2)$ are the first and second invariants of $\overline{\mathbf{C}}$, and $\overline{I}_{4(\alpha\beta)}$ and $\overline{I}_{5(\alpha\beta)}$ are the *pseudo-invariants* of $\overline{\mathbf{C}}$, $\mathbf{A}_\alpha$ and $\mathbf{A}_\beta$ given as:

$$\overline{I}_{4(\alpha\beta)} = \mathbf{A}_\alpha \cdot \overline{\mathbf{C}} \cdot \mathbf{A}_\beta; \qquad \overline{I}_{5(\alpha\beta)} = \mathbf{A}_\alpha \cdot \overline{\mathbf{C}}^2 \cdot \mathbf{A}_\beta \tag{5}$$

It should be pointed out that the pseudo-invariant notation used above differs slightly from the notation commonly used in the literature. The authors advocate this notation because it is independent of the number of family of fibers. The terms $\zeta_{\alpha\beta} = \mathbf{A}_\alpha \cdot \mathbf{A}_\beta$ are geometrical constants (independent of deformation) equal to the cosine of the angle between the directions of any two families of fibers in the reference configuration. The fiber directions need not be orthogonal in the reference configuration.

An example of the invariant-based energy function which is directly supported in Abaqus is the form proposed by Holzapfel, Gasser, and Ogden (2000, 2006) for arterial walls, and is described below. Other forms of the strain energy function are supported via a dedicated user-subroutine where the function (Equation 4) and its derivatives with respect to the invariants must be defined by the user. For example, the form proposed by Kaliske et al. (2005) can be easily implemented in this user subroutine as shown in Dassault Systèmes, 2008a.

2.2.1 *Holzapfel-Gasser-Ogden (HGO) form*

The Holzapfel-Gasser-Ogden energy potential for incompressible arterial layers with distributed collagen fibers is written as:

$$\begin{aligned} U &= C_{10}(\overline{I}_1 - 3) + \frac{k_1}{2k_2}\sum_{\alpha=1}^{N}\left\{\exp(k_2\langle \overline{E}_\alpha\rangle^2)\right\} \\ \overline{E}_\alpha &= \kappa(\overline{I}_1 - 3) + (1-3\kappa)(\overline{I}_{4(\alpha\alpha)} - 1) \end{aligned} \tag{6}$$

In the above, C_{10}, k_1 and k_2 are material parameters. The model assumes that the directions of the collagen fibers within each family are dispersed (with rotational symmetry) about a mean preferred direction. The structure parameter κ $(0 \le \kappa \le \frac{1}{3})$ characterizes the level of dispersion of the collagen orientations. When $\kappa = 0$, the fibers are perfectly aligned (no dispersion). When, $\kappa = \frac{1}{3}$ the fibers are randomly distributed and the material becomes isotropic.

3 EXAMPLES: ARTERIAL LAYERS AND REINFORCED RUBBER

We now present two examples that demonstrate the usage of anisotropic hyperelastic capability in Abaqus. The first example uses the built-in HGO strain energy potential to model the passive response of the adventitial layer of human iliac arteries. The second example employs the user defined anisotropic hyperelastic strain energy function to model a class of reinforced rubbers.

3.1 *Passive response of arterial layers*

This problem has been analyzed numerically by Gasser et al. (2006).

3.1.1 *Problem description*

We carried out numerical analyses of simple tensile tests of adventitial strips cut along the axial and circumferential directions of the artery, as illustrated in Figures 1–2. Following Gasser et al. (2006), the adventitial strips considered in this study have referential dimensions of 0.01 m length × 0.003 m width × 5×10^{-3} m thickness and are assumed to be stress free in the reference configuration.

The mechanical response of the adventitial layer is modeled using the HGO anisotropic hyperelastic strain energy function described previously. It is assumed that two families of collagen fibers are embedded in the specimens, symmetrically arranged with respect to the axial and circumferential directions of the artery and with no component in the thickness direction (Fig. 1). The families of fibers have mean orientations $\mathbf{A}_1$ and $\mathbf{A}_2$ in the reference configuration. The angle between the mean orientation of the fibers and the circumferential direction is $\gamma = 49.98°$. A value of the dispersion parameter $\kappa = 0.226$ is used in the numerical simulations. For comparison, numerical tests are also carried out assuming ideal alignment of the collagen fibers ($\kappa = 0$). The following material parameters are used: $C_{10} = 7.64$ kPa, $k_1 = 999.6$ kPa, and $k_2 = 524.6$. The specimens are loaded in the longitudinal direction, and their end faces are not allowed to deform. The numerical analyses are conducted using the static analysis procedure in Abaqus/Standard. Linear solid hybrid elements (C3D8H) are used to model the incompressible deformation of the arterial layers. Additional details of the model description can be found in Dassault Systèmes, 2008b.

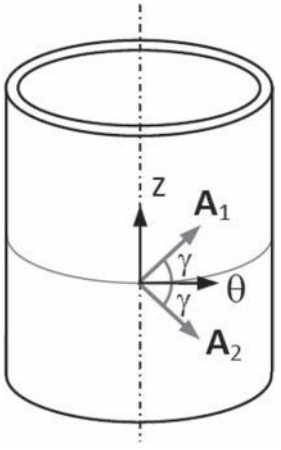

Figure 1. Adventitial layer with two embedded families of fibers with mean orientations $\mathbf{A}_1$ and $\mathbf{A}_2$.

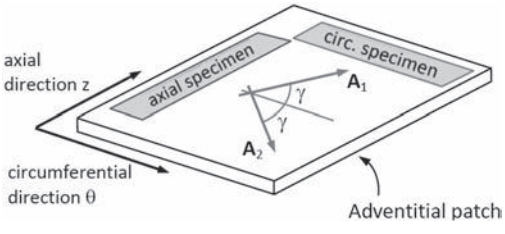

Figure 2. Definition of circumferential and axial specimens for the tensile tests.

3.1.2 *Results*

Figure 3a shows the computed stress in the tensile direction for the axial specimen with distributed fibers ($\kappa = 0.226$) for a tensile load of 2.0 N. The thickness of the specimen remains approximately constant during loading, with small transition zones at the ends of the strips. The corresponding results for the case of perfectly aligned fibers ($\kappa = 0$) are shown in Figure 3b. In this case the embedded collagen fibers need to rotate significantly toward the loading direction before they can carry substantial load. The combined effect of the large rotation of the fibers and the incompressibility constraint causes the thickness of the specimen to increase (and the width to decrease) in the middle region of the strip, away from the restrained boundaries. The transition zones at the end of the strip resemble the deformation patterns observed in woven fabrics.

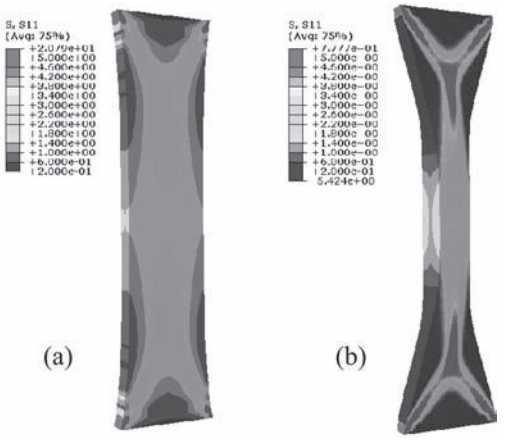

Figure 3. Stress in the direction of applied load for iliac adventitial strips cut in the axial direction with (a) dispersed collagen fibers ($\kappa = 0.226$) and (b) perfectly aligned fibers ($\kappa = 0$). Results correspond to an applied load of 2.0 N.

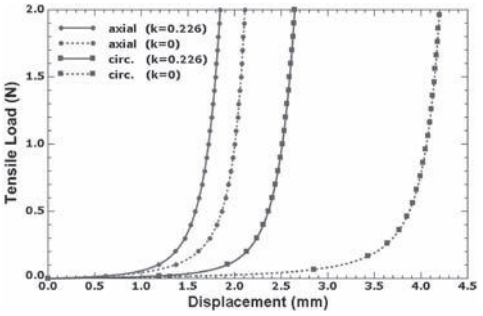

Figure 4. Load-displacement response of circumferential and axial specimens.

The results for the circumferential specimens are reported in Dassault Systèmes, 2008b.

Figure 4 shows the computed load versus displacement curves for the circumferential and axial specimens. The dashed curves correspond to the simulations with ideally aligned fibers, and the continuous curves correspond to the simulations that include dispersion. The material response is very soft at low stretches; only a small force is needed to achieve significant extension. Once the collagen fibers are approximately aligned with the loading direction, the material stiffens rapidly. This is particularly evident in the case of the circumferential specimen with $\kappa = 0$; the alignment requires very large average stretches, and the specimen stiffens at a displacement of about 4 mm. In contrast, when dispersion is included in the simulation, the collagen fibers need to rotate less before they carry load compared with the ideally aligned case. Therefore, the dispersion of the collagen fibers leads to a stiffer macroscopic response of the specimens. Specifically, the dispersion parameter κ controls the elongation at which the specimen stiffens. These numerical results for axial and circumferential specimens are in agreement with the results reported in Gasser et al. 2006.

3.2 *Anisotropic response of reinforced rubber*

Abaqus provides a general framework to define Equation 4 through a user defined subroutine. In this example we employ this user subroutine to model the anisotropic response of reinforced rubber.

3.2.1 *Reinforced rubbers*

In some industrial applications of rubbers, it is desirable to have differing mechanical properties along different directions. This is typically achieved during the manufacturing process of rubber through either a pattern of reinforcing particles, or a pattern of ply-lay-up of reinforcing fibers. A schematic of one such material is show in Figure 5. In this case, the manufacturing process involves rolling a

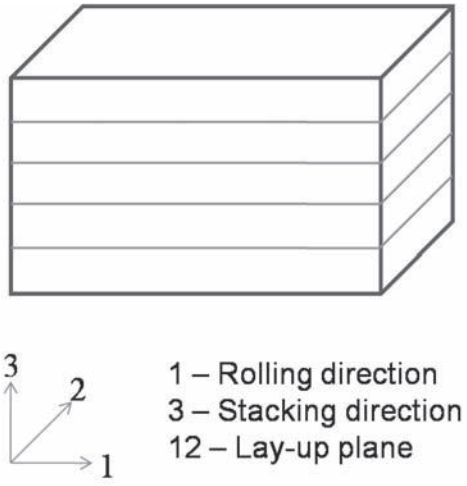

Figure 5. Schematic of reinforced rubber specimen.

ply of the reinforcements along direction 1, and then stacking them up in direction 3, in a matrix of rubber.

The anisotropic response of the reinforced rubber specimen is known from experiments. Then a certain form of the invariant-strain energy function is chosen, and an optimal set of the coefficients that minimizes the square of the error between the test data and theoretically predicted results is obtained. Once this is done, the user can then easily program this strain energy function into a user-defined subroutine. In the following, we present one such strain energy potential for the above material and show the corresponding results.

We conceived the form of the strain energy function based on the construction of the material, and the experimental data, which of course is influenced by the manufacturing process. Since the underlying rubber material is isotropic, we chose a neo-Hookean term that depends on the first invariant; then we added terms to capture the anisotropic response of the ply of reinforcements in direct and shear behavior. Assuming the material to be incompressible, one form of the strain energy potential is:

$$U = a_1(\bar{I}_1 - 3) + b_1(\bar{I}_{4(11)} - 1)^2 + c_1(\bar{I}_{4(22)} - 1)^2 + d_1\bar{I}_{4(12)}^2 + e_1\bar{I}_{4(23)}^2 + f_1\bar{I}_{4(13)}^2 \quad (7)$$

The coefficients in Equation 7 were obtained after curve fitting the theoretical stress responses of the above-mentioned energy potential to test data; these coefficients have units of stress.

$$a_1 = 1,\ b_1 = 44,\ c_1 = 7 \qquad d_1 = 45,\ e_1 = 10,\ f_1 = 17 \quad (8)$$

For confidentiality reasons, we do not present the experimental data and the corresponding coefficients. A representative set of coefficients is listed in Equation 8. The strain energy potential (Equation 7), and its first- and second-order derivatives with respect to all the invariants were then programmed into the user subroutine UANISOHYPER_INV.

3.2.2 *Results*

Figure 6 shows the response of the above-mentioned material under uniaxial tension in different directions, up to the strain levels provided in the test data. The stiffness in direction 1, which is the dominant fiber direction, is about 6 times that of the stiffness in direction 2, and is about 18 times that of the stiffness in direction 3.

In this material, based on the manufacturing process described earlier, we expect that the stiffness in direction 1 to be higher than that of 2, and 2 higher than that of 3. The supplied test data reflects that. Our choice of the strain energy potential (Equations 7–8), and consequently the simulation results matched the test data very well.

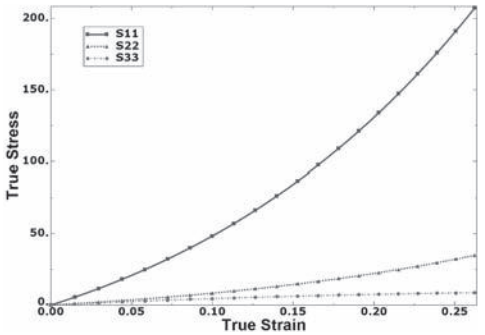

Figure 6. Uniaxial response of reinforced-rubber (characterized by Equation 7) in different directions.

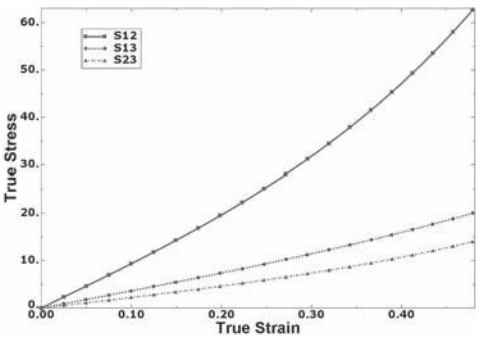

Figure 7. Response in simple shear of reinforced-rubber (characterized by Equation 7) in different planes.

Figure 7 shows the response of the material in simple shear in different planes. Once again the simulation results agreed very well with the test data.

4 CONCLUDING REMARKS

We have implemented a general framework for simulation of anisotropic hyperelastic materials using two different approaches: strain-based and invariant-based strain energy potentials. The value of this model has been demonstrated by studying the mechanical behavior of a human iliac artery and using the general anisotropic hyperelastic framework to model a class of reinforced-rubber materials. The authors envision extension of this general framework to include nonlinear rate effects.

ACKNOWLEDGEMENTS

The authors would like to thank Ian Stevenson for sharing the data for reinforced rubber, and Fengbin Xu for his help in characterizing the material for simulation.

REFERENCES

Dassault Systèmes. 2008. *ABAQUS User Subroutines Reference Manual*, Version 6.8.

Dassault Systèmes. 2008. *ABAQUS Benchmark Manual*, Version 6.8.

Fung, Y.C., Fronek, K. & Patitucci, P. 1979. Pseudoelasticity of arteries and the choice of its mathematical expressions. *American Journal of Physiology* 237: H620–H631.

Fung, Y.C. 1993. Biomechanics—mechanical properties of living tissues. New York: Springer.

Gasser, T.C., Ogden, R.W. & Holzapfel, G.A. 2006. Hyperelastic modeling of arterial layers with distributed collagen fiber orientation. *Journal of the Royal Society Interface*, 3: 15–35.

Holzapfel, G.A., Gasser, T.C. & Ogden, R.W. 2000. A New Constitutive Framework for Arterial Wall Mechanics and a Comparative Study of Material Models. *Journal of Elasticity*, 61: 1–48.

Humphrey, J.D. 1995. Mechanics of arterial wall: review and directions. *Critical Reviews in Biomedical Engineering* 23: 1–162.

Kaliske, M. & Schmidt, J. 2005. Formulation of Finite Nonlinear Anisotropic Elasticity. *CADFEM GmbH Infoplaner* 2: 22–23.

Spencer, A.J.M. 1984. Constitutive Theory for Strongly Anisotropic Solids. In A.J.M. Spencer (ed), *Continuum Theory of the Mechanics of Fiber-Reinforced Composites, CISM Courses and Lectures No. 282, International Centre for Mechanical Sciences*: 1–32. Wien: Springer-Verlag.

Constitutive Models for Rubber VI – Heinrich et al. (eds)
© 2010 Taylor & Francis Group, London, ISBN 978-0-415-56327-7

Investigation on the optimal specimen design for planar-biaxial materials testing of soft materials

J. Helfenstein & M. Hollenstein
Institute for Mechanical Systems, ETH Zurich, Zurich, Switzerland

E. Mazza
Institute for Mechanical Systems, ETH Zurich, Zurich, Switzerland;
EMPA, Swiss Federal Laboratories for Materials Testing and Research,
Dübendorf, Switzerland

ABSTRACT: Planar biaxial tests have become popular to complement classic uniaxial tests on soft materials. For their ease of handle cruciform shaped specimen geometries are often used. So far little research was done in the soft tissue community to improve the specimen geometry with respect to materials parameter determination. Following the idea of Mönch and Galster (1963) we present a numerical method to maximize the area of homogeneous equibiaxial loading. Our findings suggest that already a low number of slots in the cruciform sample limbs help to increase the area significantly.

1 INTRODUCTION

In order to characterize soft materials like rubbers or biological tissues, planar-biaxial tests have become popular to complement classic uniaxial materials tests. It is known that the latter only are not sufficient to fully characterize the materials response (Bass et al. 2004).

A first planar-biaxial test setup for soft biological tissues was presented by Lanir & Fung (1974). Ever since the interest in biaxial materials testing was growing in the soft tissue community (Sacks 2000). An especially appealing feature of planar-biaxial testing is that a typical setup (i.e. independent control of the two principal test axes) allows for an elastic, isotropic and (nearly) incompressible material to assess its complete specific strain energy potential, i.e. to test over the complete strain-space.

Starting in the field of metals testing, planar biaxial materials tests often use cruciform shaped specimen geometries for their ease of handle (e.g. clamping). Unlike in other scientific communities (Hardacker 1981; Demmerle and Boehler 1993; Abdul-Aziz and Krause 2006; Smits et al. 2006, and others), so far little research was done in the soft tissue community to improve the specimen geometry with respect to the model parameter determination (Waldman and Lee 2005).

Section 2 explains the importance of having a homogeneous loading at the center part of the specimen where the local strains and stresses are known.

To maximize the biaxially loaded area it helps to slot the limbs of the cruciform specimen (Mönch and Galster 1963). In this light, we optimize the specimen geometry along with the force transmission into the specimen towards uniformity of the induced strain-and stress-field in the test region by use of a numerical optimization scheme.

2 MOTIVATION

In classic materials testing the forces and displacements at the clamp interfaces to the specimen are measured. Based on these global measurements the local stress and strain state in test region of the specimen must be assessed in order to calibrate constitutive models by means of regression analyses. This in turn implies that the states of strain and stress in the test region must be compatible with the nominal stress and strain values obtained from the global measurements, i.e. the clamp force divided by the corresponding cross-sectional area and the displacement divided through the clamp to clamp initial free gauge length, respectively. Therefore, appropriate design of the test setup and specimen geometry is a fundamental prerequisite to materials testing in order to establish the required well-defined state of strain and stress in the test region.

In contrast, one could argue that once the interface forces, displacements and the probe geometry are known, the setup can be modeled within a finite element framework and the material

parameters determined from solving the inverse problem. In what follows, we demonstrate that this generally is not a suitable approach. To this end we perform an in silico planar biaxial test on two non-slotted cruciform specimen geometries with different limb lengths, where we have prescribed the material behavior as an Ogden-type (ABAQUS 2006). A nominal stretch of 1.3 is applied equally to both cruciform axes (equibiaxial tension) and the resulting reaction forces are computed at the virtual clamp interfaces. The prescribed clamp displacements and the computed reaction forces are then used to calibrate a third order reduced polynomial (ABAQUS 2006) to the test data by solving the inverse problem. The results are shown in Figure 1.

When plotting the equibiaxial characteristic of the in silico material against the reduced polynomial fit for the short and long limbs, two observations become apparent: (i) the results obtained from the planar biaxial tests on an regular cruciform specimen do not predict the true equibiaxial material behavior, i.e. the obtained material parameters are not associated with an equibiaxial state of deformation, and (ii) the results are specimen geometry dependent.

The observations can be explained, as the specimen test region is in a mixed deformation mode; there exits no relation between the nominal stress and strain values and the prevailing stress and strain fields. Thus a similar error is to be expected if the constitutive parameters were estimated from the nominal measurements. Concluding, this demonstrates the importance of the specimen geometry and the requirement for explicit assignment of the model parameters to the mode of deformation in nonlinear materials testing. These observations motivate appropriate design of specimens and the general test setup such that the state of strain and the associated state of stress in the test region become accessible by means of the available measuring data.

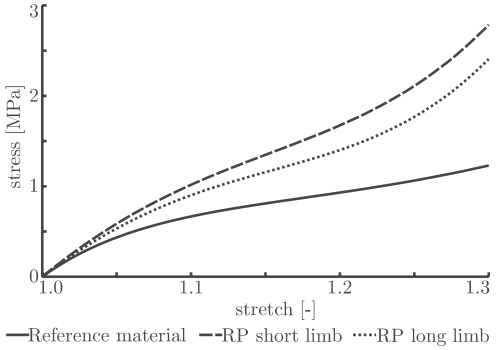

Material parameters		
Ogden	$\mu_1 = 4.62\,\text{MPa}$,	$\alpha_1 = 3.95$,
	$\mu_2 = -2.65\,\text{MPa}$,	$\alpha_2 = -0.8$.
RP, short limbs	$C_{10} = 1.02\,\text{MPa}$,	$C_{20} = -0.51\,\text{MPa}$,
	$C_{30} = 0.55\,\text{MPa}$.	
RP, long limbs	$C_{10} = 1.12\,\text{MPa}$,	$C_{20} = -0.35\,\text{MPa}$,
	$C_{30} = 0.46\,\text{MPa}$.	

Figure 1. Comparison between the equibiaxial characteristics of the in silico reference material and the fitted reduced polynomials (RP).

Typically, in planar biaxial test setups in-plane deformations are measured by means of optical methods; the full kinematics is well-defined if incompressible material behavior can be assumed. In order to obtain a significant relation between the global force measurements and the local stress state, the homogeneous biaxial test region in the mid-section of the cruciform needs to be maximized.

3 METHODS

The problem of biaxial stretch in a homogeneous isotropic probe can be simplified by several means: (i) the symmetries of the problem can be used such that only one quarter of the specimen has to be considered, (ii) far away from the clamping the loading case can be considered as a plane stress situation. In addition to these two general assumptions we restrict our study to the case of *equi-biaxial* loading.

3.1 *Definition of the biaxial area*

We assume a point to be under equibiaxial and homogeneous load if

- its principal stresses do not differ for more than τ_1 from each other and
- the mean principal stress does not differ for more than τ_2 from the mean principal stress at the center point.

The side length L of the maximum square that is inscribed to this set of points, without including any other points, we call the *size* of the *biaxial area* (Fig. 2).

3.2 *Simulations*

For the maximization of the biaxial areas size we use the optimization toolbox from Matlab (R2006a, The MathWorks, Inc., Natick, MA). Two algorithms are used: an unconstrained nonlinear optimization (*fminsearch*) that uses a Nelder-Mead simplex method and a constrained genetic algorithm (*ga*). The genetic algorithm allows to define an initial population consisting of parameter sets and the corresponding fitness values (errors). To do

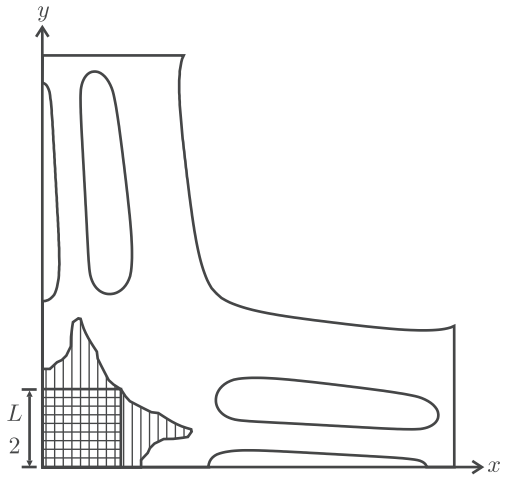

Figure 2. Quarter of a deformed specimen. Points under equibiaxial and homogeneous load are hatched vertically. The maximum inscribed square, the biaxial area, is hatched horizontally.

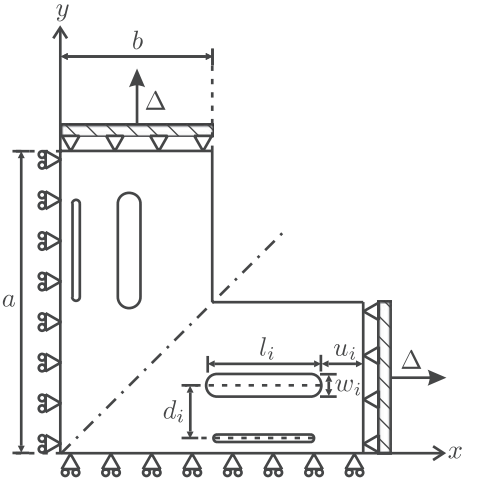

Figure 3. Implemented geometry with its parametrization, boundary conditions and imposed displacments.

so we previously define parameter sets that cover a large portion of the design space and compute their respective errors $1/L$. From the results we take the twenty best ones (corresponding to the size of the initial population). The length L is computed at the deformed state with a global stretch of 1.5. For all error calculations we set the two tolerances $\tau_1 = 5\%$ and $\tau_2 = 1\%$.

Both algorithms call a function that starts the finite element software ABAQUS (SIMULIA, Providence, RI) and that, after termination of the simulation, computes the error defined as $1/L$. After being called ABAQUS starts a Python script that generates the geometry, assigns the material properties, meshes the geometry and initiates the FE-computation. In order to transfer the trial parameter set to ABAQUS, our Matlab code writes them in a text file that is read by the Python script. Vice versa, the results from ABAQUS (coordinates and principal stresses of all nodes) are written to a text file that is read by the Matlab routine.

Figure 3 shows the parametrization of the geometry with slots in the specimen limbs. The symmetries with respect to the principal axes of the specimen are exploited and only one quarter is simulated. The end of the limbs are clamped, displacements (Δ) are applied such that global stretches of 1.5 are obtained. The fixed dimensions $a = 40$ mm and $b = 20$ mm are half of the total size of the cruciform specimen and half of the limb width, respectively. The set $\{w_i, l_i, u_i, d_i\}$, $i = 1,\ldots, n$, parameterizes one single slot. n is the total number of slots in a half limb. w_i designates the width, l_i the length, u_i the distance from the slot to the limbs end and d_i the distance from the centerline of the $i-1$ slot to the centerline of the ith slot. d_1 is the distance from the limbs centerline to the centerline of the first slot.

Table 1. Constraints that are used with the genetic algorithm.

$w_i > 0.2$ C1	$\sum_i^n w_i < 20$ C2
$l_i > 0.2$ C3	$l_i > w_i$ C4
$u_i > 0.2$ C5	$d_1 \geq 0$ C6
$d_i > 0.5 \times (w_{i-1} + w_i) + 1.0$ for $i > 2$	C7

Table 1 summarizes the constraints that are used for the parameters in the case of the genetic algorithm. Condition C7 ensures that there is a ligament of atleast 1.0 mm between two slots.

Simulations are done with quadrilateral two dimensional eight node biquadratic plane stress elements (CPS8). The typical element size is set to 0.5 mm. Incompressibility is assumed for the material, a typical assumption often made for soft biological tissues and rubbers. The elastic properties are modeled as Neo-Hookean with an initial shear modulus of 2 MPa.

4 RESULTS

First optimizations were done using the Nelder-Mead simplex method but it turns out that the solutions of this optimization procedure stay in the very same region as defined by the initial parameter set. Therefore we changed to a genetic algorithm.

Table 2. Results of the optimizations. The first column (#) indicates the number of slots per limb.

#	L [mm]	w_i [mm]	l_i [mm]	u_i [mm]	d_i [mm]
0	9.966				
2	34.058	2.938	15.569	5.306	5.722
4	36.066	1.133, 3.000	15.750, 18.000	4.000, 2.000	0.000, 7.000
6	38.000	1.214, 1.402, 1.862	18.427, 1.815, 18.013	1.977, 18.250, 2.328	2.488, 3.326, 4.088

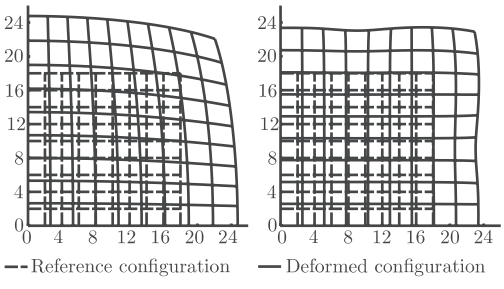

Figure 4. Simulated displacements at the center of the cruciform specimen: left) specimen without any slots, right) specimen with 4 slots per limb.

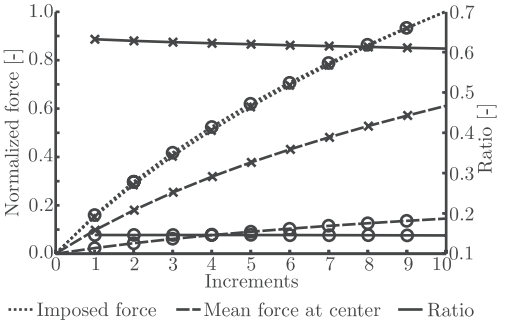

Figure 5. Time evolution (increments) of the imposed force, the mean force that goes through the biaxial area and the ratio thereof. (o: specimen without slots, ×: specimen with 4 slots per limb).

Table 2 summarizes our best solutions with no, two, four and six slots per limb. When no slots are present the size of the biaxial area is equal to 9.966 mm. Already two slots give a significant increase of 242%, L = 34.058 mm. Including more and more slots the size of the biaxial area increases as well. In the solution with four cuts the innermost slots (d_1 = 0 mm) do coincide such that in fact only three cuts are present. The best solution obtained with six slots raises L up to 38 mm. The second slot in this solution is very short compared to the others (l_2 = 1.815 mm) but neglecting this slots degrades the length L to 23.292 mm (–39%).

Figure 4 shows the displacement fields at the central part of two configurations with slots (only on quarter is shown). On the left the displacement field where no slots are used: it can be seen, that only a rather small area with a side length of approximately the above mentioned 5 mm can be considered as equibiaxially loaded. In contrast to the case where four (three) slots per limb are simulated, here the homogeneity of the deformation increases significantly.

Since the stiffness of the limbs is smaller than the stiffness of the central part, the global stretch of 1.5 is not fully regained at the center part where local stretches in the order of 1.3 are obtained.

Figure 5 shows the results of a study of the force flux in the specimen without and with four slots per limb (the forces are normalized with the maximum value of the respective applied total force). The imposed force at the clamping is partially transferred to the biaxial area. Without any slots 14% of the total force are transferred, using four slots increases the ratio up to 62%. This ratios are not constant and change, in the case with four slots, for approximately 4% over the whole deformation process (1% in the case without any slots). The standard deviation of the force acting on different sections in the biaxial area is in the range of 0.7% of the mean force amplitude.

5 DISCUSSION

We consider a point under equibiaxial and homogeneous load if its principal stresses do not differ for more than τ_1 = 5% and the mean stress at that point do not differ for more than τ_2 = 1% from the mean stress at the center point of the probe. The size of the biaxial area is measured by the side length L of the largest square inscribed to that area that contains no other points. The homogeneous equibiaxial deformation of a square can be described analytically such that an analytical regression analysis can be envisaged.

In our study we use a cruciform specimen geometry with a total width of 80 mm and a limb length of 20 mm each, such that the central region of 40 × 40 mm results. The arms ends are clamped and displacements of 20 mm are applied to each (such that global stretches up to 1.5 result).

For a non-slotted specimen the biaxial area has a size of $L = 9.966$ mm at that stretch. A consequence of this small biaxial area is that only little of the specimen is under biaxial and the global response is dominated by other load cases. Only 14% of the global force goes through the sections of the biaxial area.

In order to increase the size of the biaxially loaded area Mönch & Galster (1963) proposed to cut slots in the specimen limbs. Adapting their idea to numerical optimization methods allows to search for non intuitive optimal solutions for the positioning and size of the slots. The best solution found with two slots per limb increases the size of the biaxial area by 242%. This means that a larger portion of the specimen is effectively under biaxial load. Including up to four more slots increases the size of the biaxial area by another 11%. The solution with six slots shows that rather small changes influence the solution significantly. Omission of the two smallest slots with a length of only 10% of the next longer slots degrades the solution by 39%.

Figure 4 shows the computed displacement fields for the two configurations with no and with four slots per limb. As expected from the computed sizes L the deformation field for the latter configuration is much more homogeneous for a larger area.

In case of the geometry with four slots the ratio between the global force and the force acting on the sections of the biaxial area is significantly increased compared with the situation without any slots (62% vs. 14%). This finding suggests that most of the global force is held by the biaxial area and that the influence of modes other than equibiaxial is reduced.

6 CONCLUSIONS

Material parameters determination from planar biaxial materials testing needs knowledge of the local strains and stresses at the biaxially loaded part in the specimen. As we show in Section 2 fitting only global displacements and forces acting on cruciform specimens can lead to significant errors. Local strains can be measured by optical methods and are therefore directly accessible. This is different for the local stresses, their value has to be estimated from the global forces measured at the clampings.

The ratio between global forces and local stresses depends on the geometry of the specimens and, for the case of nonlinear material behavior as well, on the material parameters. Linear elastic materials are a special case, where the latter dependency does not hold. For such materials Demmerle & Boehler (1993) presented a specimen shape for which the local stress equals the nominal stress.

For soft biological materials that have generally a nonlinear mechanical behavior this dependency of the ratio between global and local forces can be minimized by enlarging the biaxial area. A large area under biaxial load ensures that most of the force flux passes it and therefore the dependency of the ratio gets smaller. If, in addition, the stress field in the biaxial area is homogeneous the stresses can be determined from the globally acting forces.

Following the idea of Mönch and Galster (1963) we present a numerical method to maximize the area of homogeneous (equi-) biaxial loading in cruciform shaped specimens undergoing biaxial materials testing. Our findings suggest that already a low number of slots helps to increase the biaxial area significantly.

Using three slots in an optimal arrangement the ratio between global and local forces varies for only 4% with ongoing deformations. This variation can be neglected considering other imprecisions that occur during soft tissue testing. Using this geometry around 60% of the total force goes through the biaxial area instead of only 14% in the case with no slots. Thus the dependency of the ratio on the material parameters is reduced.

Our results need to be validated experimentally but we can conclude that the uncertainties in material parameters determinations can be minimized using an optimized specimen geometry.

The possibility of creating slotted specimens from soft biological materials may sometimes be restricted. Therefore we will focus in a next step on cruciform specimens with cuts in the limbs.

REFERENCES

ABAQUS (2006). *Online documentation, version 6.6.* ABAQUS Inc.©.

Abdul-Aziz, A. and D. Krause (2006). Cruciform specimen design for testing advanced aeropropulsion materials under dyclic in-plane biaxial loading. In *Proceedings of SPIE,* Volume 6176, pp. 617609-1-617609-10.

Bass, E.C., F.A. Ashford, M.R. Segal. and J.C. Lotz (2004). Biaxial testing of human annulus fibrosus and its implications for a constitutive formulation. *Annals of Biomedical Engineering 32*(9), 1231–1242.

Demmerle, S. and J.P. Boehler (1993). Optimal design of biaxial tensile cruciform specimens. *Journal of the Mechanics and Physics of Solids 41*, 143–181.

Hardacker, K. (1981). Instrument and specimen shape for biaxial testing of paper. *Journal of Physics E: Scientific Instruments 14*, 593–596.

Lanir, Y. and Y.C. Fung (1974). Two dimensional mechanical properties of rabbit skin i. experimental system. *Journal of Biomechanics 7*, 29–34.

Mönch, E. and D. Galster (1963). A method for producing a defined uniform biaxial tensile stress field. *British Journal of Applied Physics 14*(11), 810–812.

Sacks, M.S. (2000). Biaxial mechanical evaluation of planar biological materials. *Journal of Elasticity 61*, 199–246.

Smits, A., D. Van Hemelrijck, P.T.P., and A. Cardon (2006). Design of a cruciform specimen for biaxial testing of fibre reinforced composite laminates. *Composites Science and Technology 66*, 964–975.

Waldman, S.D. and J.M. Lee (2005). Effect of sample geometry on the apparent biaxial mechanical behaviour of planar connective tissues. *Biomaterials 26*(35), 7504–7513.

Constitutive Models for Rubber VI – Heinrich et al. (eds)
© 2010 Taylor & Francis Group, London, ISBN 978-0-415-56327-7

Layout process of pre-stressed rubber suspension bushings

J. Jagusch & A. Firla
ContiTech AG & ContiTech Vibration Control GmbH, Hannover, Germany

ABSTRACT: Rubber suspension bushings are well tuned components of a complex dynamic system. Thus a good achievement of the demanded specification is very important. Numerical methods like FEM are common tools to forecast the elastic characteristics. Besides the geometry of the final component some essential steps like shrinkage and swaging within the manufacturing procedure have to be considered. A simulation of the inverse processes is applied for the definition of the mold geometry of the rubber component. These inverse steps allow a direct shape determination of the mold design which will meet the specifications of the finished part.

1 INTRODUCTION

1.1 *Framework*

In the automotive industry rubber suspension bushings are essential for technical and safety reasons. A suspension bushing generally has requirements to the stiffness in 3 translational and 3 rotational directions. The stiffness in this context is the slope of the quasi static force-deflection curve which is describing the applied force or torque as a function of the associated deformation. These so called characteristic curves are typically starting softly almost linear and are strongly progressive at higher deformations.

2 DESIGN CONSIDERATIONS

The design of the suspension bushing has to consider the demands of stiffness and others like durability for the assembly-ready component. This article will focus on the quasi static elastic behavior of the suspension bushing.

2.1 *Layout demands*

The main layout properties for a suspension bushing are the geometry, i.e. the thickness and shape of the elastic springs and the gap sizes and shape of the bump stops. While the thickness and shape of the elastic springs define the initial characteristic of the suspension bushing, the gaps to the bump stops are a feature which is controlling the upturn of the characteristic curve, i.e. starting the progressive branch of the suspension bushing.

Furthermore the material hardness which determines the elasticity can be adopted by the portion of carbon black. The range of hardness is usually limited by acoustic and comfort demands.

2.2 *Process demands*

Manufacturing of rubber components comprises several steps like vulcanization and in case of suspension bushings, swaging is a common forming process for pre-stressing, thus more stiffness and enhanced durability is provided. These steps pose a challenge for the designer who has to develop the mold geometry such a way that the suspension bushing in the final state meets the requirements.

For small gap sizes additional restrictions have to be considered since gaps are limited by the mold

Figure 1. Typical suspension bushing with elastic springs and bump stops, outer sleeve and inner part.

geometry which needs a minimum wall thickness for a stable molding.

In case of radial swaging and non cyclic symmetric layout the shrinkage and swaging procedure will change eccentricity of the inner part, gap sizes and all other geometric properties.

3 INVERSE PROCESS SIMULATION

The analysis of suspension bushings by means of the Finite Element Method is common practice. In the usual design process the design engineer sets up an initial draft which will be analyzed in order to determine the characteristic quasi static force-deflection curves.

This task is extended in this presentation by requesting the initial geometry of the mold design which shall meet the specifications of the finished part. Therefore the Finite Element analysis is extended by the inverse process of shrinkage and swaging. The approach is illustrated by means of a typical example of a suspension bushing.

3.1 *Initial model geometry*

A draft design based on experience and analytical tools for the layout of the finished suspension part is created. It considers the elastic requirements of the rubber springs and the gaps of the bump stops. Pre-stressing due to swaging and shrinkage is not considered in this stage. Figure 2 shows one quarter of the created CAD model with initial top gap g_t = 0.0 mm and bottom gap g_b = 3.0 mm. The position of the inner part is referenced to be 1.20 mm, which is the initial distance of the inner part's axis to the centerline of the outer cylindrical surface.

A Finite Element model is set up out of this geometric draft design. The inner metal and the outer sleeve are modeled by rigid conditions on the respective interfaces.

The material properties are selected as incompressible hyper-elastic description. For simplicity a Neo-Hooke formulation with $C_{10} = 0.747$ N/mm^2 was applied. The value of C_{10} was determined by measurement of the stiffness at an early stage prototype and comparison to a FEM-Simulation. For the contour determination the material parameters and the hyper-elastic approach are of minor influence.

3.2 *Mold geometry*

The shrinkage and the swaging are applied in an inverse sense. This way the expected mold geometry will be approximated. The provisional swaging is applied as a radial deformation at the outer surface of the rubber component. Figure 3 illustrates the swaging in radial direction which is outward in this inverse step and symbolized by outward arrows. An extension of the outer radius of c = 1.85 mm

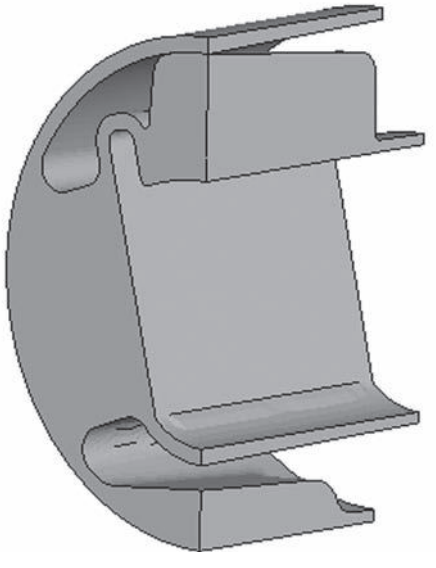

Figure 2. Initial guess geometry of finished part (quarter model due to symmetry).

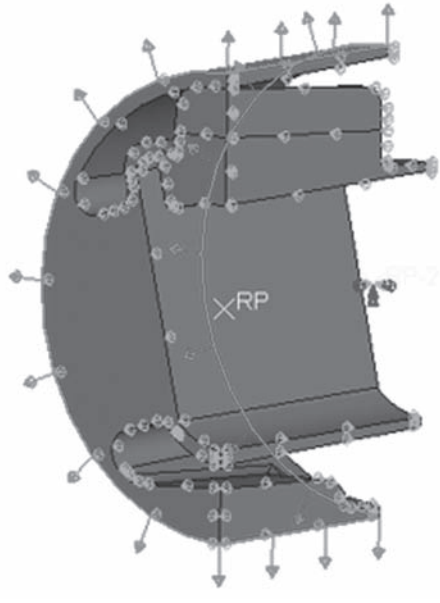

Figure 3. Boundary conditions for inverse swaging and symmetry.

was applied. Additional boundary definitions are the symmetry conditions. The inner part can move up- and downwards. A total movement of the inner part of 1.87 mm downwards with respect to the cylindrical centerline was computed. Therefore the positioning of the inner part will be

1.20 mm – 1.87 mm = –0.67 mm

below the centerline of the outer cylinder in the mold geometry.

The inverse shrinkage by an amount of 1.5% is modeled by a temperature dependent expansion ratio of $\alpha_t = 0.01\ K^{-1}$ and a related fictive temperature field of $\Delta\theta = 1.5$ K applied to the rubber. This way a rubber growth or swelling of 1.5% is modeled.

As a result the movement of the inner rigid part and the gap sizes in the mold geometry are determined. The final deformed shape of the FEM-model is interpreted as the mold geometry. The deformed shape can be transferred to the CAD-System and is the bases for the mold design. Furthermore the resulting FEM-state can be used for the simulation of the swaging and shrinkage process, but has to be released from stresses for the initial configuration of the following step.

Figure 4 shows the computed mold geometry after application of inverse processes. The growth of the top gap compared to figure 1 is obvious, while the bottom gap is almost unchanged. Also the position of the inner part can be observed and a relative displacement of 1.87 mm downwards is stated. All gap sizes and the displacements of the inner part are summarized in Table 1.

3.3 *Process steps*

In a second step a new FEM-model is set up starting from the before computed mold design as an initial, unstrained state. The swaging and shrinkage is applied in the order according to the real process. First shrinkage of 1.5% is applied to the rubber material by a fictive temperature analogously to the first FEM-analysis.

In the following step the swaging of 1.85 mm radial deformation is applied to the outer surface of the rubber suspension bushing. The resulting shape with gaps and the deflection of the inner part are again computed and the deformed shape is depicted in Figure 5.

The initial gap at the top side is closed after swaging. In case of an abandonment of the swaging procedure a mold with a closed gap was not producible since the mold needs a minimum of substance thickness.

4 MEASUREMENTS

4.1 *Geometric properties*

The main geometric properties, i.e. the gap to the vertical blocking positions and the movement of the inner part are tracked in the states of production and compared to the results of the FEM analysis.

Table 1 summarizes the measurements and compares it to the FEM results.

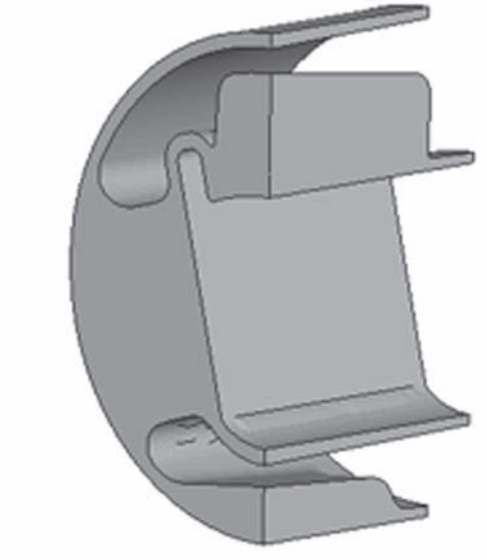

Figure 4. Mold geometry after inverse swaging and swelling.

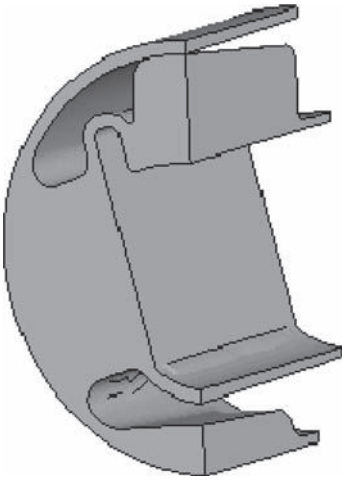

Figure 5. Geometry of the finished part after swaging and shrinkage.

Table 1. Deformation of rubber component during the design and manufacturing process.

State model	Top gap mm	Bottom gap mm	Center* mm
Initial design finished part (only virtually designed)			
FEM	0.0	3.0	1.20
Mold geometry			
Prototype mold	3.28	2.83	–0.67
FEM	3.28	2.83	–0.67
Non-swaged part			
Prototype	5.65	2.60	–1.70
FEM	4.40	2.40	–1.32
Finished part after swaging			
Prototype	0.30	3.00	0.90
FEM	0.00	3.22	1.40

* Center means vertical position of a reference point at the inner part with respect to the centerline of outer cylinder of the outer rubber surface. The initial value is according to the specification. Upwards is positive for this value.

The dimension "Center" is the position of the initial axis of the inner part. The differences of the positions yield the deflection of the inner part for each production step.

4.2 *Elasto-static properties*

For the final evaluation of the suspension bushing the characteristic vertical load-deflection curve is compared to the specified curve. A vertical preload of 430 N has to be considered when evaluating the initial stiffness, which is calculated to be c_f = 375 N/mm whereas the measured value is c_f = 368 N/mm.

The graph in Figure 6 shows the characteristic deflection curve of the prototype and the computed curve after shrinkage and swaging compared to the specification. The operating point is the position of the inner part with pre-load applied. The initial stiffness is calculated at this position.

The following Figures 7 and 8 show overlays of photographs of the prototype and front views of the FEM-model in a translucent plot. These illustrations allow a comparison of the geometric properties of the prototypes and the results of the FEM-model. The translucent part of the deformed FEM-model comprises only the front section. This view allows a better comparison of the elastic springs' width.

Figure 7 is an overlay plot of the non-swaged state. The prototype on the picture includes the outer sleeve which has to be considered. The outer circle of the FEM-section is scaled and positioned over of the photograph in such a way that the

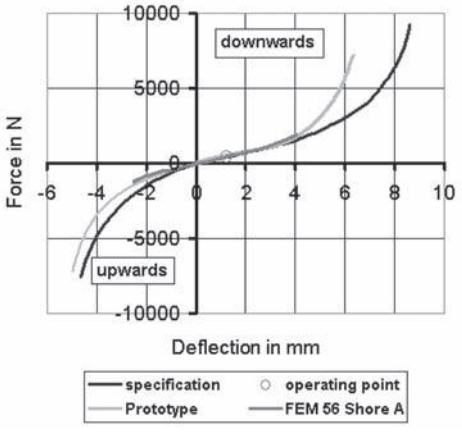

Figure 6. Characteristic curves compared to specification.

Figure 7. Suspension bushing before swaging. Front section of the FEM-model over the prototype.

outer rubber surface of the prototype fits the outer diameter of the FEM-section as well as possible.

The prototype has smaller sizes of the elastic springs while the slope angle agrees well. Also the upper bump stop is smaller in the prototype than in the FEM-model. The minimum gap sizes at the bump stops of the prototype cannot be seen from this picture because the perspective in the photograph does not allow a view to the closest gap location. The front section view of the FEM-model does not show this size either due to the mold incline. This is even more obvious at the lower bump stop, which is not included in the front section of the FEM-model, because it is positioned more to the middle of the suspension bushing.

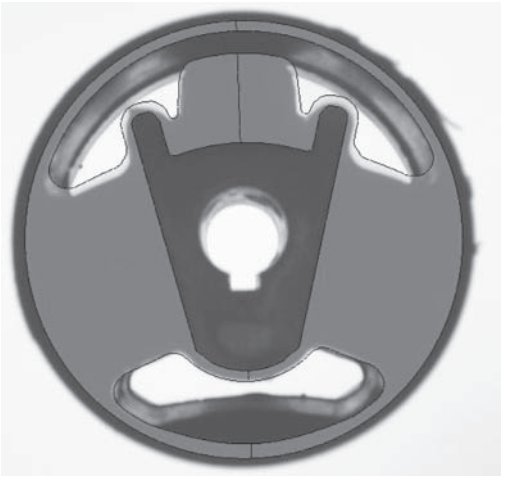

Figure 8. Suspension bushing after swaging. Front section of the FEM-model over the prototype.

Figure 8 shows the same comparison of the prototype and the computed FEM-model shape for the swaged state. The adjustment of the scaling and position is performed analogously to figure 7.

Also in this state the elastic springs keep a bit smaller in width at the prototype than in the FEM-model and the slope angle of the springs agrees well. Concerning the gap views the deficiencies of figure 7 apply also for figure 8. The photographs of the prototypes do not allow a direct view to the top and bottom gap of the bump stops. The minimum gap sizes are listed in table 1.

5 DISCUSSION

The overall situation looks well fitted by the prototype and the FEM-model respectively.

Concerning the geometric properties the slope angle of the elastic springs is acceptable, but the width of the elastic springs is smaller in the prototype than in the FEM-model. Deviations in the assumed shrinkage may be one reason for this difference. The comparison of the contour is somewhat difficult, since the mold incline and the perspective in the photograph distort the shape of the prototype. The perspective influence can be well seen from the bore hole in figure 8 at the inner part, which looks to be squeezed, but is straight in reality.

The stiffness demands agree well with the requirements in the initial range. For higher load levels the FEM-model was not able to converge. The measured curve is too progressive for high deformation levels. Some corrections in the design-shape of the bump stops will be necessary for a better fit in the high deformation range. At least the fitting of the characteristic curve for high deformations was not the focus of the presented procedure. The most important goal is to meet the initial stiffness, which was very good achieved.

The computed geometric measures of the gaps and the deformation of the inner part are close to the specified values. The final position of the inner part is forecasted by the FEM model to be 1.4 mm above the centerline of the suspension bushing. The intended positioning of 1.2 mm was not achieved in the FEM model. The prototype shows a position of 0.9 mm of the inner part which deviates 0.3 mm from the intended value of 1.2 mm. This can easily be adjusted by the positioning of the bore hole at the inner part.

The specific situation of the presented suspension bushing is the nonlinear effect due to contact condition during the swaging procedure. Without contact the inverse process should be identical to the reversed original process. In that case all measures were identical but changed in sign. With contact appearance the process is not just the negative mapping of the reversed shrinkage and swaging steps.

Furthermore the position of the centerline is uncertain since the part is out of roundness at the outer diameter. Especially the swaging process yields a non circular outer shape when the swaging die is removed. This leads to deviations between simulated model which is ideally circular and the prototype. The model can be extended to consider this effect, but was not investigated so far. Nevertheless at least the characteristic of the bushing in the assembled state is of interest. In the vehicle the bushing is enclosed by the lug of the strut where it will be operating. The lug will enforce the roundness of the suspension bushing.

6 CONCLUSIONS

The presented procedure is an effective process to determine the shape necessary for a mold which meets the specifications for the finished part. An iterative development process is shortened and less prototyping loops will be needed. The designer yields a robust and reproducible process to easily accomplish his tasks.

Constitutive Models for Rubber VI – Heinrich et al. (eds)

Effect of plate technology and orientation on flexographic line deformation

T.V. Korochkina, J.A. Cherry, T.C. Claypole & D.T. Gethin
Welsh Centre for Printing and Coating, School of Engineering, University of Wales Swansea, Swansea, UK

ABSTRACT: This paper describes both experiments and constitutive models to predict the response of a photopolymer plate during ink transfer cycle. Two, commercially available, plate making technologies have been compared to identify their limits. The two plates were produced with the same image which included fine line features. The lines were measured using white light interferometry to obtain line profile. Varying results have been observed between the two plates, and overall it would appear that plate A produces the widest lines at all nominal values and the greatest line height at the majority of nominal values. A nonlinear numerical model of the individual line has been developed and used to examine the deformation of the plates under a range of printing conditions and image characteristics. Three hyperelastic constitutive models were fitted with the experimental data (Mooney, Ogden and Yeoh). Numerical results and comparisons show that both Mooney and Ogden constitutive models are applicable to multiaxial states of stress and strain. The numerical results agree well with the experimental data in both simple tension and pure shear. Numerical models have been used to determine the change in line profile, as the deformations occur on a microscopic level. The simulations yield information on contact parameters. The results are reported and discussed.

1 INTRODUCTION

Flexography is mainly used for packaging applications, but also is a potential technology for the micro manufacture of electronic devices and biosensors. The behaviour of a flexographic plate as it passes through the printing nip is a key parameter in controlling quality of the printed feature. A modern flexographic plate is made of a photopolymer material, which is subjected to back exposure to UV light to achieve a desired relief depth, followed by front exposure to UV light through a mask to harden the image regions. Soft non-image areas are subsequently washed away leaving the raised image area on the plate. Geometry of the raised feature on the plate will affect their deformation as they are subjected to the engagement and therefore the final printed feature size and its quality.

To assess the feasibility of using flexography for the printing of fine features for electronics and biosensors a comparison of two, commercially available, plate making technologies have been compared to identify their limits. Both plates were made under standard processing conditions. There were subtle differences to the way the plates were imaged. The two plates were produced with the same image. The image included microscopic line features as well as various track and gaps.

Prior to modelling the two plates were measured using white-light interferometry to identify the true line size and profile produced for the nominal value.

2 EXPERIMENTAL

2.1 *Material characterization*

It is broadly accepted that at least two different modes of deformation are required to derive the material constants that define the stress strain relationship accurately for input into a FEA model. Two photopolymer sheets were cast at 1.7 mm thickness for mechanical tests. Test samples 25 mm wide for tensile test and 40 mm wide for pure shear tests were prepared. The tests were carried out using an Instron 4301 universal test machine at TARRC, UK at 23°C in laboratory air.

To determine the material parameters, two different sets of physical test data, namely, uniaxial tension and pure shear were used. Experimental data points were from the 25% strain loading path of the third cycle, where a stable equilibrium stress-strain curve was obtained.

2.2 *Printing plates*

2.2.1 *Plate image*

The two plates used will be referred to as A and B. Each plate was produced with the same

image, Figure 1. The image included line features varying from 10 µm to 300 µm at 0° (referred to as 'horizontal'), 45° (referred to as 'diagonal') and 90° (referred to as 'vertical') to print direction as well as various track and gaps.

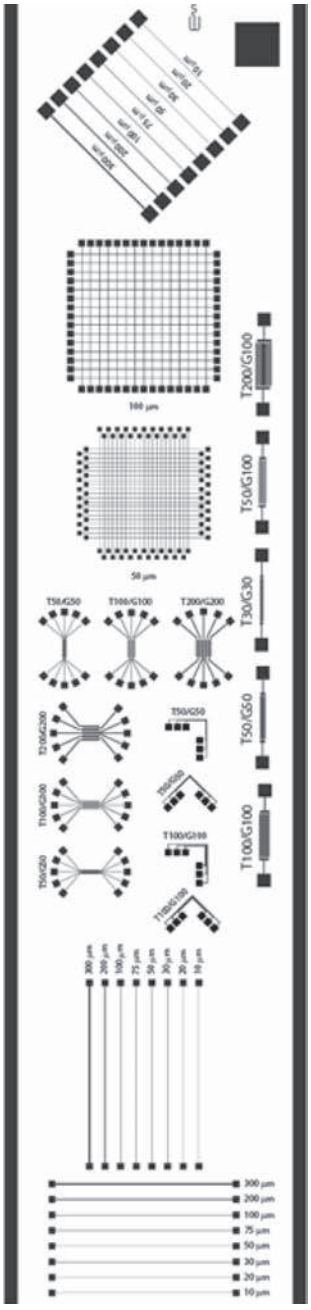

Figure 1. Plate image.

2.2.2 *Line profile*

The lines were measured using white light interferometry which allows accurate measurement of three-dimensional profile of the line, Figure 2. An example of two-dimensional profile of the same line is shown in Figure 3. In this paper 300 µm individual line results in the vertical, horizontal and diagonal directions are presented.

The measured line width has been compared against the nominal value of 300 µm for two plates for all line directions. A large variation was observed in the horizontal line widths for the two plates. Plate A produces wider lines than plate B. Line gain for plate A was approximately 1%. Unlike the plate A, plate B produces the line loss of approximately 11%. As with the results displayed for the horizontal line width, plate A produces the widest vertical lines. Line gain/loss is still observed for the plates. Once again plate A produces wider diagonal lines than plate B (see Figure 4). The line gain for diagonal lines for plate A is considerably larger than for the horizontal and vertical lines, whereas for plate B it is similar to the loss seen for the horizontal and vertical lines.

The measured line height has been compared for two plates for all line directions. Plate A displays the greater line height than plate B, approximately 670 µm for diagonal lines, Figure 4. The results for vertical line height show similar trends to those for the diagonal lines. The results for horizontal line

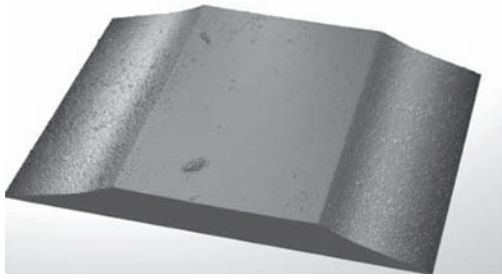

Figure 2. Three-dimensional line profile.

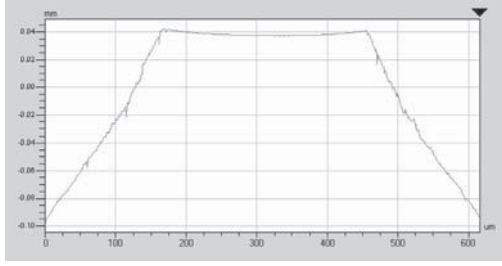

Figure 3. Two-dimensional line profile.

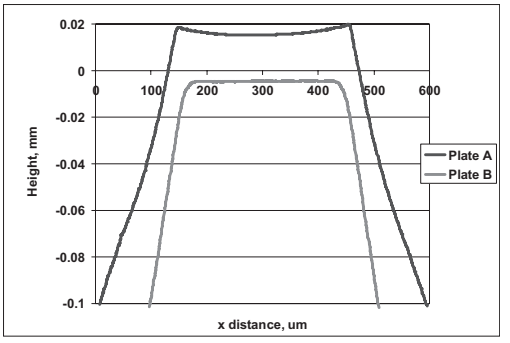

Figure 4. Comparison of two-dimensional line profiles in diagonal direction.

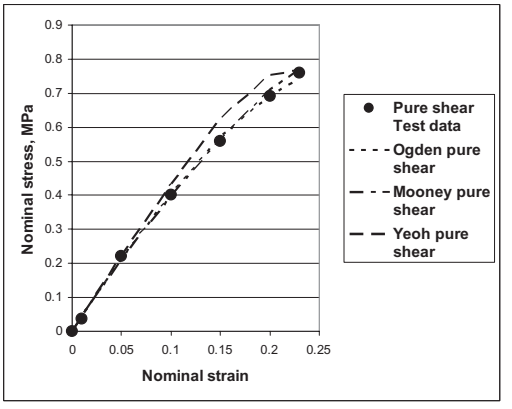

Figure 5. Pure shear comparison.

height show similar trends to those for the diagonal and vertical lines. However both plates display a slight increase in the line height. Plate B shows the line height closer to the nominal value of 635 μm.

3 MODEL DEVELOPMENT

3.1 *Software*

ABAQUS with extended capabilities necessary to analyse the mechanical behaviour of elastomer materials was used as the simulation system. Non-linear FEA was employed since the line geometry changes as the load is applied and contact evolves. An incremental implicit scheme was applied to simulate the progressive engagement and to facilitate capture of the consequent deformation of the line and contact evolution through iteration.

3.2 *Model verification*

The experimental data of the uniaxial tension and pure shear tests were used to curve fit the Mooney (Mooney 1940), Ogden (Ogden 1972) and Yeoh (Yeoh 1990) laws. A comparison of the experimental and fitted data is plotted in Figure 5 from low to high strain levels. Results show that the Yeoh model can only describe the photopolymer behaviour accurately at low strains because it does not allow representation of the finite extensibility of real networks. The predicted and experimental results for both tests match within ±5%. It is important to underline that this is a global error; the specific accuracy at a given point of the model could differ. Both the Mooney and Ogden models have better results over the whole characteristic. Nevertheless, the Mooney model exhibits an error of about ±3% which is slightly higher than that of the Ogden model. This is possibly due to Ogden model dependence on the second invariant. The Ogden

Table 1. Values of the Mooney material parameters.

Plate	C_{10} (MPa)	C_{01} (MPa)
A	1.174	–0.662
B	0.431	0.059

Table 2. Values of the third order Ogden material parameters.

Plate	μ_1 (MPa)	μ_2 (MPa)	μ_3 (MPa)	α_1	α_2	α_3
A	36.698	–17.503	20.069	6.819	8.320	5.264
B	0.559	8.313E–6	0.421	2.433	20.299	–1.058

computational and experimental results for both tests match very well within ±2.5% error for both plates and will now be used in numerical simulations of line deformation.

The material parameters for Mooney and Ogden models for plate A and B are summarised in Tables 1 and 2 respectively. The material parameters were determined through an appropriate least-squares-fit procedure, which minimizes the relative error in stress.

3.3 *Finite element modelling*

Six numerical models of the line were constructed depending on plate technology and line orientation. When building each model, the geometry was constructed to mach the plate, measured with the white-light interferometer (section 2.2.2). The line shapes used for the two model types that represent the concave (plate A) and flat (plate B) surface areas of the lines, are shown in Figure 4. Only

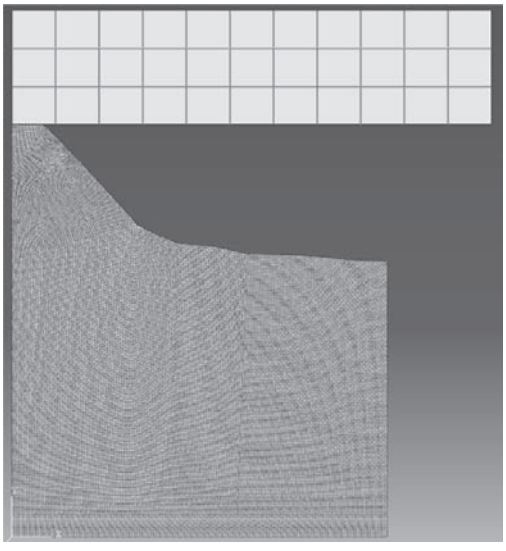

Figure 6. Mesh of full model.

half of the line was used for numerical modelling (Figure 6) due to symmetry. The mesh of the whole model is shown, illustrating the increased mesh resolution of the line.

Engagement was simulated by displacing a plain flat rigid surface on to the lines on the flexographic plate. The plate was assumed to be flat, as the radius of the impression cylinder is large in comparison with the size of the line. The engagement was then applied normal to the line surface instead of a rolling engagement. The engagement between the plate and substrate was varied for each plate at 1, 2, 3, 4 and 5thou.

For the purpose of the numerical study, the models assumed negligible friction in the contact to simulate the lubricating effect of the ink when printing on to a non-absorbent substrate. A low friction coefficient is likely to lead to more image distortion due to a tendency for a sliding behaviour and this represents the worst case condition. The entire plate thickness was included as well as the mounting tape used during printing.

4 RESULTS AND DISCUSSION

Figure 7 shows a typical contact pressure distribution during contact evolution. The legend on the right hand side of the graphs represents the amount of vertical displacement of the impression cylinder in mm. As expected, by increasing the vertical displacement, the contact pressure is increased. The graphs also show an impact on the contact area, in that the increase in engagement increases the contact area. There is a significant increase in contact pressure towards the edge of the line. Figure 8 shows the corresponding results for the effective stress. The high stress near the line edge of the printing plate means that this is the point where the plate will experience significant initial wear. This will degrade the plate and will be critical for print registration and reproducibility.

The combined effect of engagement and plate technology on contact pressure distribution for vertical lines is shown in Figure 9, plotted against actual contact area on the plate. A large variation was observed in the contact pressure distribution for the two plates. Plate A displays significantly lower contact pressure for first half of the contact area than plate B. The opposite is observed for the second half of the contact area. This

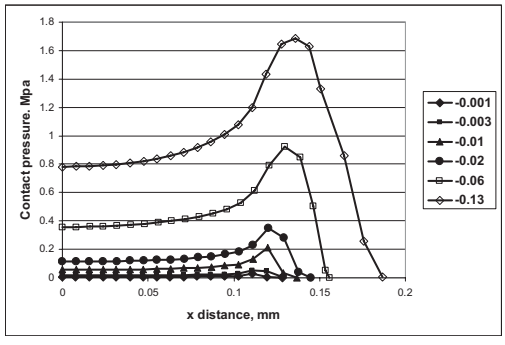

Figure 7. Typical contact pressure distribution along contact area for horizontal line of the plate B for different vertical displacements.

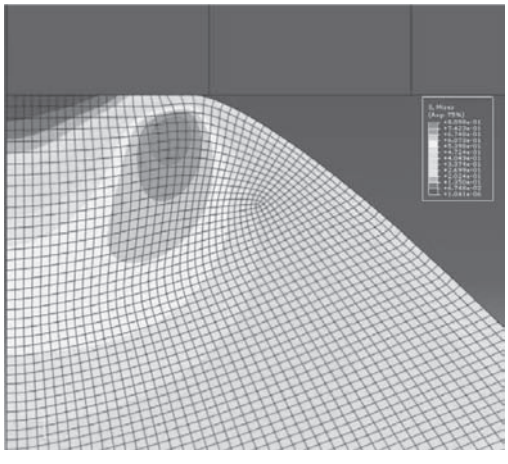

Figure 8. Effective stress field in horizontal line for the plate B.

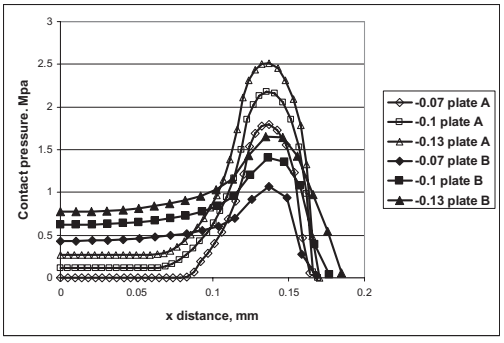

Figure 9. Contact pressure distribution along contact area for vertical lines for two plates for different engagements.

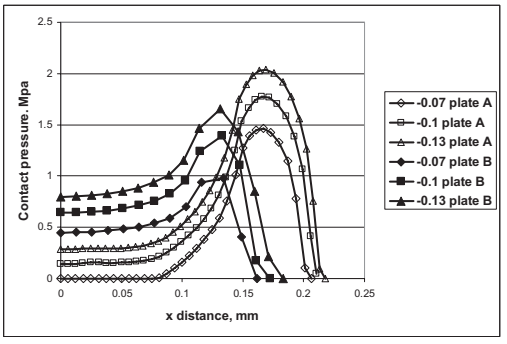

Figure 10. Contact pressure distribution along contact area for diagonal lines for two plates for different engagements.

was attributed to one point initial contact due to the concave shape of the line top for plate A, Figure 4. As engagement increased, contact pressure increased, with similar differences between consecutive engagements for both plates. For plate A, the contact area for all engagements remains almost constant. For plate B, the contact area increased slightly by ca. 0.02 mm.

The results for horizontal line contact pressure distribution show similar trends to those for the vertical lines for both plates.

Figure 10 shows contact pressure distribution for diagonal lines. Once more, a large variation was observed in the contact pressure distribution for the two plates. Unlike the results for vertical and horizontal lines, plate A produces a greater contact area than plate B. This resulted in reduction of maximum contact pressure by approximately 0.5 MPa for all engagements.

Figure 11 displays the plate lateral displacement for vertical lines as a function of position from the centre line of the line (x distance). This has been computed by noting the displacement of nodes on the line surface. With the increase in engagement, the X-displacement increases along the half contact area, remains constant at low engagement or decreases at higher engagement at the beginning of the second half and reaches its maximum at the end. As shown plate deformation occurs when it is brought into contact with either the anilox roller or impression cylinder. Plate A produces greater X-displacement than plate B at all engagements. The results for horizontal line X-displacements show similar trends to those for the vertical lines for both plates. The results for diagonal line X-displacements show similar trends to those for the vertical and horizontal lines for both plates, Figure 12. The crossover between the curves reflects an increase in contact area for plate A.

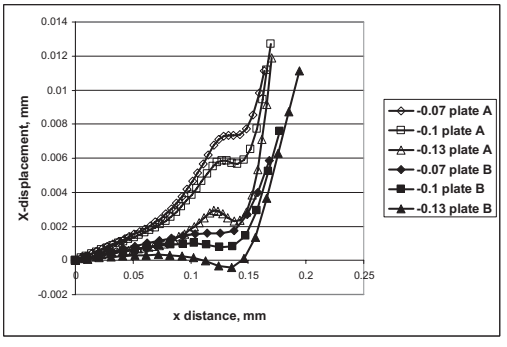

Figure 11. X-displacement along the contact area for vertical lines for two plates for different engagements.

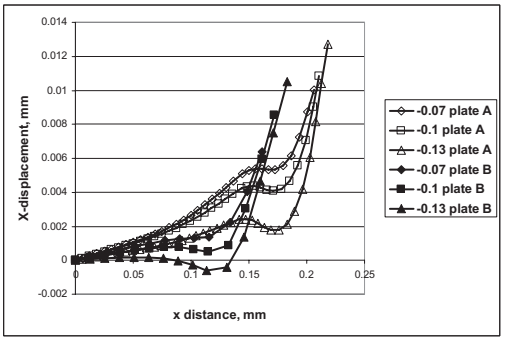

Figure 12. X-displacement along the contact area for diagonal lines for two plates for different engagements.

Image distortion occurs due to differences that are present in this contact, for example as a consequence of different frictional behaviour. This will be addressed in a later study.

5 CONCLUSIONS

A combined experimental and numerical investigation into the detailed behaviour of the flexographic plate line during ink transfer has been described. A numerical two-dimensional model has been developed and tested against experimental data. The numerical model yielded detailed information about the line deformation during ink transfer including the contact pressure distribution, the size of the contact area and X,Y-displacements as well as stress and strain fields in the flexographic plate. The effect of the engagement (vertical displacement), plate technology and line orientation was studied.

It was found that increasing engagement increases the pressure in contact between the plate and impression cylinder for both plates. The plate B showed a marked reduction in contact pressure for a given vertical displacement. This resulted in significant reduction of the effective stresses at the contact surface of the plate and under it.

The effect of line direction was investigated for two commercially available plates. The results obtained show that the vertical and horizontal lines show similar trends in terms of contact pressure distribution and contact area. It was discovered that, the diagonal lines on the other hand show an increase in contact area for plate A and a reduction in contact area for plate B in comparison to both vertical and horizontal lines.

X-displacements on the line have been calculated. Plate B showed a significant reduction in X-displacements for a given vertical displacement. These may be compared with the printed line width. This will be explored in future studies.

ACKNOWLEDGEMENT

The authors gratefully acknowledge EPSRC for funding the research and Dr. A.H. Murh of TARRC, UK for his kind support and valuable discussions.

REFERENCES

Bould, D.C., Claypole, T.C. & Bohan, M.F.J. 2004. An investigation into plate deformation in flexographic printing. Proc. Instn Mech. Engrs. Part B (218): 1499–1511.

Ogden, R.W. 1972. Large deformation isotropic elasticity I: on the correlation of theory and experiment for incompressible rubberlike solids. *Proceedings of the royal society of London, Series A,* Vol 326, 565–584.

Rivlin, R.S. 1948. Large elastic deformations of isotropic materials. I. *Phil. Trans. R.Soc.Lond. Series A,* Vol. 240, 459–490.

Yeoh, O.H. 1990. Characterization of elastic properties of carbon black filled rubber vulcanizates. *Rubber Chemistry and Technology* 63: 792–805.

Constitutive Models for Rubber VI – Heinrich et al. (eds)
© 2010 Taylor & Francis Group, London, ISBN 978-0-415-56327-7

Thermo-mechanical finite element analysis of a viscoelastic model

A. Matsuda
University of Tsukuba, Ibaraki, Japan

Y. Mizutani & H. Shinkai
Central Research Institute of Electric Power Industry, Kanagawa, Japan

ABSTRACT: In this paper, 3-dimentional finite strain analysis of thermo-mechanical viscoelastic material was discussed to predict the permanent deformation of natural rubber (NR). Relaxation times for viscous characteristics of this model were calculated by the Arrhenius equation and temperature of rubber. Furthermore, uniaxial loading tests by loading test machine and the stress-relaxation tests in the thermal chamber were conducted to evaluate the mechanical and thermal characteristics and effect of temperature on the stress relaxation to confirm the applicability of the simulation code. From the simulated results, the developed code shows enough accuracy to predict the stress reduction of natural rubber parts under the long-term compression.

1 INTRODUCTION

1.1 *Lifetime of rubber parts*

The prediction of the lifetime of rubber parts such as elastomer O-rings and sealing elements is an important issue for all mechanical devices used for electricity. Radiated and chemical gases and/or fluids, and mechanical oil leakages, even in small amounts, are not desirable for the transmission or generation of electricity. Therefore replacement and maintenance schedules for O-rings and sealing elements should be appropriately set.

The Japanese Industry Standards (JIS K 6262) and other standards describe aging tests for O-rings. In the JIS, permanent strain that defines the ratio of elastic and plastic deformation of O-rings is used to determine replacement time. Permanent strain is given by the following expression:

$$\varepsilon_p = \frac{d_0 - d_1}{d_0 - d_2} \times 100\ (\%) \tag{1}$$

where, d_0 and d_1 are section diameter before and after deterioration, respectively. The depth of the O-ring ditch is d_2. Generally, O-rings are exchanged when permanent strain ε_p is larger than 80%.

1.2 *Gas-insulated switchgear (GIS)*

The gas-insulated switchgear (GIS: see Fig. 1) is a piece of electric insulation equipment used to seal aggressive gas (sulfur hexafluoride: SF_6) from the environment. The SF_6 gases used produce a global warming coefficient of about 24,000 times that of carbon dioxide, though electric insulation functions have improved in efficiency. Naturally, many O-rings are used between the GIS main body and the aluminum flange to seal in the SF_6 gas.

The degradation rate of rubber is known to follow the Arrhenius equation (Arrhenius 1889). Therefore accelerated aging tests that apply compression on O-rings at a higher temperature than normal environmental conditions can be used to estimate permanent strain in a short amount of time. Once the activation energy for thermal degradation is obtained, estimation of exchange time is possible using the Arrhenius equation.

However, for the replacement period obtained from the Arrhenius equation, the temperature is assumed to be constant. Moreover, it is difficult to apply to O-rings under temperatures that vary greatly.

In this paper, we show the finite element analysis of a thermo-mechanical viscoelastic model that allows the prediction of permanent strain of rubber-like materials. Experimental results of stress reduction tests of natural rubber (NR) under various temperatures are also shown. From these test results, thermal and mechanical coefficients for numerical simulation were approximated.

2 SIMULATION METHOD

2.1 *Viscoelastic model*

In this section, we introduce the volumetric and deviatoric multiplicative split first suggested by

Figure 1. Gas-insulated switchgear (GIS).

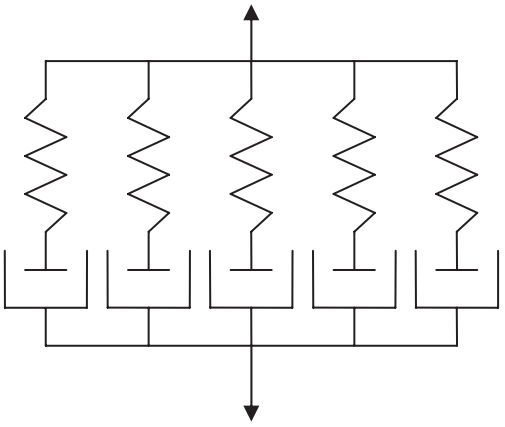

Figure 2. Maxwell viscoelastic model.

Flory (1961). The deviatoric part of the deformation gradient tensor is given as

$$\bar{F} = J^{-\frac{1}{3}} F, \tag{2}$$

where J is the determinant of the deformation gradient tensor $\boldsymbol{F}$. The second Piola-Kirchhoff stress tensor $\boldsymbol{S}$ of the viscoelastic material is given by (Simo 1987, Simo & Hughes 1997):

$$S = 2\frac{\partial W(\bar{\boldsymbol{C}})}{\partial \boldsymbol{C}} - \frac{\partial \bar{\boldsymbol{C}}}{\partial \boldsymbol{C}} \sum_{i=1}^{N} \boldsymbol{Q}_i + Jp\boldsymbol{C}^{-1}, \tag{3}$$

where $\boldsymbol{C}$ and $\bar{\boldsymbol{C}}$ are the right Cauchy-Green tensor and volume-preserving of the right Cauchy-Green tensor, respectively. W and p are the strain energy function of elastic deformation and hydrostatic pressure, respectively. $\boldsymbol{Q}_i$ and N are the viscous stress tensor and the number of dashpots in Figure 2, respectively. The viscoelastic stress $\boldsymbol{Q}_i$ satisfies the following evolution equations including material temperature $\theta(K)$ as follows:

$$\begin{aligned} &\dot{\boldsymbol{Q}}_i(t) + \frac{1}{\tau_i(\theta)} \boldsymbol{Q}_i(t) = \frac{\gamma_i}{\tau_i(\theta)} DEV\left\{ 2\frac{\partial W}{\partial \boldsymbol{C}} \right\}, \\ &\lim_{t \to -\infty} \boldsymbol{Q}_i(t) = 0, \end{aligned} \tag{4}$$

where $\tau_i(\theta)$ is the relaxation time of a dashpot and the notation DEV is given by

$$DEV[\bullet] = (\bullet) - \frac{1}{3}[(\bullet) : \boldsymbol{C}]\boldsymbol{C}^{-1}. \tag{5}$$

From the results of the stress relaxation tests on NR block specimens, we applied the following relationships to the temperature-dependent stress relaxation behavior of rubber materials using the Arrhenius equation.

$$\begin{aligned} \tau_i(\theta) &= \frac{\tau_i(\theta_0)}{\alpha} \\ &= \frac{\tau_i(\theta_0)}{A exp\left(\frac{-E}{R\theta}\right)}, \end{aligned} \tag{6}$$

where α is the rate constant of the chemical reaction depending on the temperature of the rubber, R is the gas constant (= 8.31447 J/K/mol), θ_0 is the referenced temperature, E is the activation energy, and A is the prefactor. Equation (6) means that the relaxation time $\tau_i(\theta)$ of all dashpots shortens uniformly with an increasing temperature.

3 EXPERIMENTS AND MODELING

3.1 *Static loading test of NR*

The NR specimens used for the static loading test and relaxation test were cube-shaped, with height, width, and depth all equal to 51 mm (Fig. 3).

The shear modulus of the NR was 0.6 MPa, and Seki et al., obtained the strain energy function W of the NR using a biaxial test of the NR sheet specimen as follows (Fukahori et al., 1993):

$$\begin{aligned} \frac{\partial W(\bar{I}_A)}{\partial \bar{I}_A} &= C_{A1} + C_{A2}(\bar{I}_A - 3) + C_{A3}(\bar{I}_A - 3)^2 \\ &\quad + C_{A4} exp\{ C_{A5}(\bar{I}_A - 3) \} \end{aligned}, \tag{7}$$

where $\bar{I}_1$ and $\bar{I}_2$ are the first and second invariants of the volume-preserved right Cauchy-Green tensor. Coefficients of equation (7) are shown in Table 1.

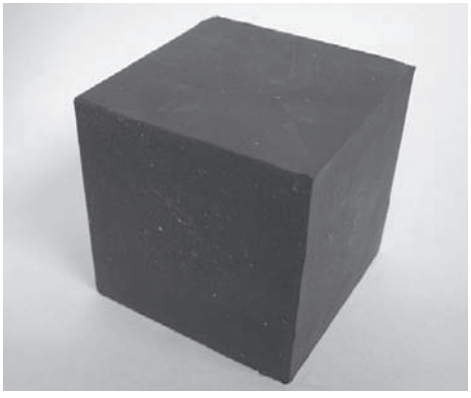

Figure 3. NR specimen.

Table 1. Coefficients of strain energy function.

A	C_{A1}	C_{A2}	C_{A3}	C_{A4}	C_{A5}
1	2.05E-01	1.32E-02	2.35E-04	0.171	–2.12
2	1.35E-02	–1.61E-03	6.32E-05	–6.87E-02	–6.44

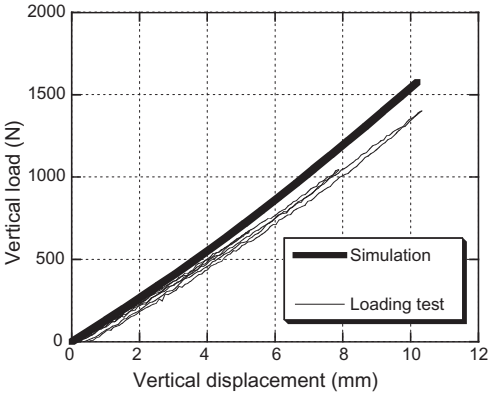

Figure 4. Relationships between vertical load and displacement of NR block.

A uni-axial loading test machine was used for the static compression test. The compressional deformations corresponding to 10% and 20% of height were applied to the NR specimens at room temperature. The relationships between vertical load and displacement resulting from the loading test and 3-dimensional Finite Elemental Method analysis are shown in Figure 4.

For numerical simulation, 1,000 ($10 \times 10 \times 10$) displacement/pressure mixed elements (Hughes 2000) were used for FEM modeling. The mean stress distribution resulting from the numerical simulation of the loading test is shown in Figure 5.

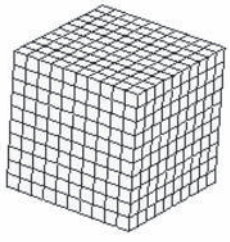

(a) Initial shape

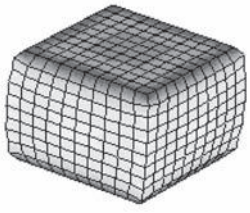

(b) 10 mm of compression

Figure 5. Mean stress distribution of 3-dimentional FEM simulation.

Table 2. Test conditions of relaxation tests.

Temperature (K)	Days	Vertical deformation
333 K	10	10 mm
353 K	10, 16, 30	10 mm
373 K	10	10 mm

Although the stiffness calculated using the numerical simulation was slightly larger than that of the loading test, their tendencies correspond well.

3.2 *Stress relaxation test for NR*

The stress relaxation tests for NR were conducted in a thermal chamber under three constant temperature conditions. The test conditions are shown in Table 2. The test specimens were kept at 333 K, 353 K, and 373 K constantly after applying a compressional deformation of 10 mm (20% of height) using SUS jigs. The surface temperature of a specimen was measured with a thermocouple, and the vertical load was measured using the heat-resistant load cell.

Figure 6 shows 30-day results at the 353 K condition, and 10-day results at the 333 K and 373 K conditions. Test results are normalized by dividing the maximum load.

3.3 *Modeling of stress relaxation*

The viscoelastic stress reduction under a constant temperature and deformation is given as the

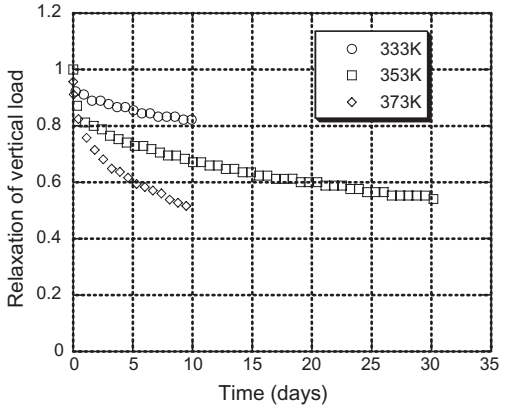

Figure 6. Relationships between relaxation of compressional load and time.

following relationship when the deformation is applied at $t = 0$:

$$\frac{\sigma(t)}{\sigma(0)} = \sum_{i=1}^{N} \gamma_i \exp\left(-t/\tau_i(\theta)\right) \tag{8}$$

We introduced 7 spring and dashpot connections in parallel to approximate the relaxation times $\tau_i(\theta_0)$ and material parameters γ_i from the 30-day test results under the referenced temperature θ_0 (353 K). Here the relaxation times $\tau_i(\theta_0)$ were assumed as follows:

$$\sum_{i=1}^{N} \tau_i(\theta_0) = 10^{(i+2)}\ [s] \tag{9}$$

It was then possible to calculate the acceleration rate α as 0.092 at the 333 K condition, and 4.53 at the 373 K condition.

In Figure 7, the logarithm of α and the reciprocal of absolute temperature ($1/\theta$) were plotted on the vertical and horizontal axes, respectively. The relationship between the logarithm of α and the reciprocal of absolute temperature shows good linearity. This indicates that the stress relaxation of NR follows the Arrhenius equation.

From the linear approximation of the test, we obtain A = exp (34.16) and E/R = 12,135.

The viscous characteristics calculated with a referenced relaxation curve ($\theta_0 = 353$ K) and the Arrhenius equation were shown in Figure 8.

3.4 *FEM simulation of permanent strain*

Material parameters were introduced to the FEM simulation code and numerical simulations of stress relaxation tests were conducted.

Table 3. Relaxation time $\tau_i(\theta_0)$ and material parameter γ_i for numerical simulation.

i	$\tau_i(\theta_0)$	γ_i
1	1.00E+03	0.009511
2	1.00E+04	0.10817
3	1.00E+05	0.077811
4	1.00E+06	0.14764
5	1.00E+07	0.561931
6	1.00E+08	0
7	1.00E+09	0.094937

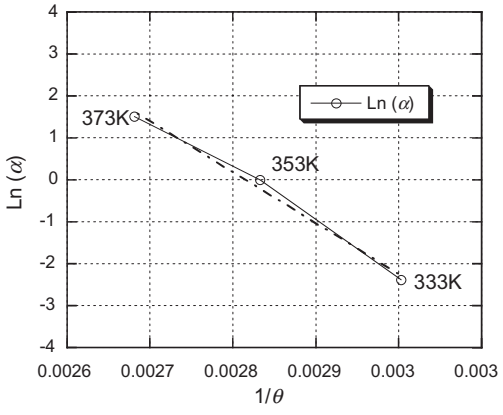

Figure 7. Arrhenius plot of stress relaxation rate.

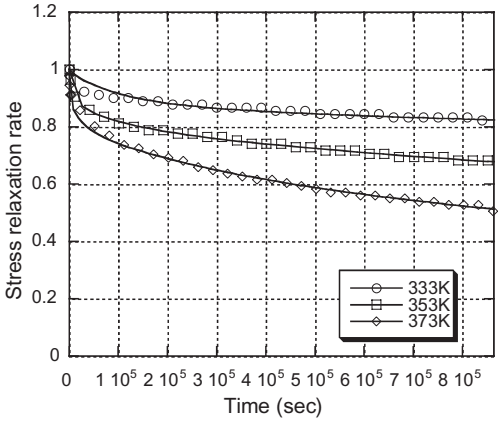

Figure 8. Stress relaxation curves ($\theta = 333$ K, 373 K) calculated by the Arrhenius equation and referenced relaxation curve ($\theta_0 = 353$ K).

In the numerical analysis of stress relaxation, the heat transfer was calculated at the same times and temperatures as each integration point were fed to the viscosity.

Figure 9. NR specimen after relaxation test (30 days at 353 K).

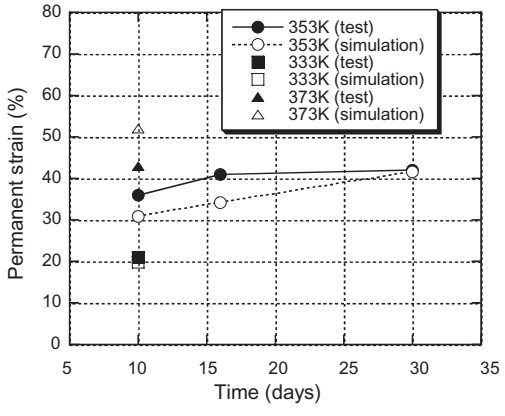

Figure 10. Comparison of permanent strain given by test and simulation.

For the boundary condition in the numerical simulation, the initial compressional deformation was applied to the top surface and the specimen's viscosity and thermal conductivity were calculated while maintaining the deformation.

The shape of the NR specimen after the relaxation test is shown in Figure 9. Permanent deformation remained.

In Figure 10, permanent strain resulting from the relaxation test and the numerical simulation were plotted. The permanent strain was calculated by using the following equation:

$$\varepsilon_p = \frac{H - h}{H - H_0}, \tag{10}$$

where H is the height of the initial test, and h is the height of the central body after the relaxation test. H_0 represents the height of the specimen during the relaxation test.

4 CONCLUSION

To estimate the permanent strain of a rubber material dependant on the environmental temperature, a nonlinear viscoelastic model for rubber-like material was proposed.

In this model, the relaxation time of a dashpot was calculated using the Arrhenius equation with temperatures of each FEM element.

The viscous parameters for the model were obtained using a relaxation test on NR.

The relaxation tests were simulated numerically, and the permanent strain resulting from the relaxation tests and numerical simulation show good agreement.

REFERENCES

Arrhenius, S.A. 1889. On rates of inversion reaction in cane-sugar under the action of acids, *Z. Phys. Chem.* 4:226–248.

Flory, R.J. 1961. Thermodynamic relations for highly elastic materials, *Transactions of the Faraday Society* 57:829–838.

Fukahori, Y., & Seki, W. 1993. Stress analysis of elastomeric materials at large extensions using the finite element method. *Journal of matelial science* 28:4143–4152.

Hughes, T.J.R. 2000. The finite element method. New York: Dover.

Simo J.C. 1987. On a fully three-dimensional finite-strain viscoelastic damage model: Formulation and computational aspects, *Computer methods in applies mechanics and engineering* 60:153–173.

Simo, J.C., & Hughes, T.J.R. 1997. *Computational Inelasticity* New York: Springer.

Micro- and macromechanical approaches

Constitutive Models for Rubber VI – Heinrich et al. (eds)

Simulation of phantom elastomeric polymer networks

V. Galiatsatos
Leibniz Institute of Polymer Research, Dresden, Germany

ABSTRACT: Mechanical properties of elastomeric polymer networks depend on variables such their crosslink functionality and density, functionality distribution, presence of diluents and others. Simulation of elastomers is one very useful way to study the effect of those variables on properties such as the shear modulus of the network. In our contribution we study the structure of phantom polymer networks that are produced after successive random chain and crosslink removal. We decode the network structure by inspecting their connectivity, separating the soluble fraction from the gel fraction and calculating the cycle rank of the gel. We report the cycle rank which is related to the shear modulus of the network. Additionally we report structural details of those networks, such as dangling ends and crosslink functionality distribution.

1 INTRODUCTION

Molecular theories of rubberlike elasticity are a valuable tool that aids in the understanding and development of rubber compounds for a multitude of useful applications. The connection of course is through the development and application of constitutive equations.

Simulation tools are also very useful in complementing and guiding the development of molecular theories by providing information that is either difficult or impossible to obtain by experimentation. Simulations are also very effective in studying network structures that are too complicated for analytical theories. In that respect simulation and theory can work together in resolving outstanding issues in this fascinating area of technology. (Galiatsatos 1995, Galiatsatos 2005).

Simulation tools range from the quantum mechanical level through all the way up to finite element analysis and continuum mechanics. Due to the various limitations of each individual method it is advisable to employ methods that address various length and time scales.

In this contribution we employ connectivity algorithms and develop simulation tools to study the structure of model elastomeric systems as they degrade. We focus on phantom networks, where interchain interactions are set to zero. The systems under consideration have tetrafunctional crosslinks and they are perfect, i.e., no dangling ends or double strands or any inelastic loops are present.

2 METHOD DEVELOPMENT

One of the most fundamental properties of a polymer network is its cycle rank, ξ, as defined by Flory. (Flory 1982, Flory 1985) The cycle rank is defined as the number of independent circuits contained in a network. These circuits may be assumed to be long, each having many chains in them. The elastic response of a network is uniquely determined by the cycle rank. According to Flory the cycle rank may be calculated by subtracting the total number of crosslinks μ of the network from the total number of network chains ν plus one, i.e.:

$$\xi = \nu - \mu + 1 \tag{1}$$

Qualitatively the cycle rank is the number of "cuts" required to reduce the network to a tree. In the simulation we implement formula (1) exactly. To accomplish that, we rely on a Breadth-First Search (BFS) traversal to inspect the network structure. BFS returns the breadth-first search (BFS) tree. A BFS of a network explores all crosslinks adjacent to the current crosslink before moving on. We rely on a queue data structure to keep track of the order in which crosslinks are to be explored. The next crosslink to be explored sits at the front of the queue while newly discovered crosslinks get inserted in the back. The search ends when the queue is empty. Since we rely on Flory's definition of the cycle rank we need to further modify the BFS search and delete all chains from the network that are not tree chains.

Given the adjacency list A(v) for each crosslink v of the network the following algorithm conducts a BFS. On completion of the search each vertex has acquired a breadth first index (BFI) indicating the order in which the vertex was visited. Vertex u is visited first and BFI(u) = 0. In a queue items are removed in the same order that they are added.

1. for all v ∈ do BFI(v) ← 0
2. i ← 1; BFI(u) ← 0
3. add u to the queue
4. while the queue is not empty do
   a. begin
   b. remove a vertex from the queue, call it w
   c. For all v ∈ A(w) do
      i. if BFI(v) = 0 then
         1. begin
         2. BFI(v) ←i + 1
         3. i ← i + 1
         4. add v to the queue
         5. end
   d. end

The last step in our calculation for the cycle rank is to subtract the number of edges that is the output of the BFS (network to tree) routine from the total number of elastically active chains in the network.

Having developed a method to calculate the cycle rank we proceed to construct a perfect tetrafunctional network, which will serve as the starting point of our simulations. In order to avoid edge effects we embed the network on the surface of a torus. This allows all crosslinks to have the same functionality initially. We should also mention that at this point we deal with two dimensional networks. However the method described here applies to three-dimensional networks as well.

We confirm that all crosslinks of the created network have the same prescribed functionality by inspecting the Degrees of the Graph representing the network.

The degradation process is simulated by randomly deleting network chains. The process simply inspects a List containing network chain information and removes chains form that List in a random fashion.

The next step in the simulation is to separate the largest component from the rest of the system, which was created by the degradation process. The system besides containing this largest component (i.e., the gel) now also contains a variety of small structures ranging from isolated crosslinks to structures containing micro-gels (i.e., few crosslinks and few chains connected together). To accomplish the separation we first partition the Graph G that represents the degraded network system into connected components. We then construct a List containing all subgraphs of G induced by the appropriate number of vertices for each subgraph. The largest component is chosen simply by sorting the List. The Cycle Rank of the gel is calculated by invoking the procedure described at the beginning of this Section.

Typical results besides the Cycle Rank, which is normalized per network chain, included the number of total components in the system, the number of chains and crosslinks in the gel and the distribution of functionalities in the gel. Similar analyses may be applied to the rest of the system components which we classify as the soluble fraction (i.e., sol fraction).

While the initial network has a single crosslink functionality, all subsequently formed network systems and gels have a distribution of functionalities. This makes the gel a heterogeneous network. Therefore besides reporting the structural features of the gel we also report quantities that are useful in describing te heterogeneity of the gel in a quantitative way. For that we rely on the Euler number of the gel, which is given by:

$$N_V = \lambda\left(1-\frac{\mu}{2}\right) \tag{2}$$

where the mean crosslink functionality μ (not to be confused with the number of crosslinks, which is also represented by the same symbol in eqn 1) is given by:

$$\mu = \sum_{k=1}^{\infty} k p_k \tag{3}$$

Equation (3) is a function of the probability p_k that an arbitrarily chosen crosslink has a functionality k. So for a model ϕ-functional network where only a single functionality is available and where the probability for that functionality to occur is always unity, the mean crosslink functionality is equal to ϕ.

Equation (2) contains the quantity λ (lambda), the mean number of crosslinks per unit volume. In the language of stochastic geometry this quantity is called the "vertex intensity". We identify the vertex intensity with the crosslink density of our network.

For us to study the heterogeneous structure of the gel we need to study the unbiased estimators for that gel. As a reminder, an estimator is a function of the observable sample data that is used to estimate an unknown population parameter (which is usually called the *estimand*).

Let W be an observation window in d-dimensional space, where both cases d = 2 and d = 3 are of practical interest. Let V denote the area (if d = 2) or volume (if d = 3) of W. In our particular case it is sufficient to set V = 1. Let n_k be the number of observed vertices of order k (i.e., crosslink functionality) in W. Let n be the total number of observed vertices (i.e., is the total number of crosslinks)

$$n = \sum_{k=0}^{\infty} n_k \tag{4}$$

As a reminder, θ1 is an unbiased estimator of θ if and only if B(θ1) = 0, for all values of θ in the parameter space or, equivalently, if and only if E(θ1) remains equal to θ regardless of the value of θ. The bias of θ is defined as B(θ1) = E(θ1)–θ. It is the distance between the average of the collection of estimates, and the single parameter being estimated.

Unbiased estimators are given by the estimator for the vertex intensity (i.e., crosslink density): (Tscheschel & Stoyan 2003)

$$\hat{\lambda} = \frac{n}{V} \tag{5}$$

As we have seen the above is essentially the crosslink functionality, i.e., total number of crosslinks per unit area (volume) in our observance window W. If the network under consideration possesses spatial heterogeneity then depending on the window's size and Euclidean dimension ("W" see above) it allows inspection of the crosslink density of that window and thus assessment of the heterogeneity of the system.

The estimator for the mean coordination number is given by:

$$\hat{\mu} = \frac{1}{n}\sum_{k=1}^{\infty} k n_k \tag{6}$$

For a perfect model ϕ-functional network the estimator for the mean functionality is equal to the functionality of the typical crosslink, in this case ϕ.

The estimator for the Euler number is given by:

$$\hat{N}_V = \hat{\lambda}\left(1 - \frac{\hat{\mu}}{2}\right) \tag{7}$$

The accuracy of the estimator can be characterized by the estimation variance. Finally we calculate the estimation variance of $\hat{N}_V$ (this is called "Poisson approximation"):

$$Var\,\hat{N}_V = \frac{\lambda}{V}\left(\frac{1}{4}\sigma^2 + \left(1 - \frac{\mu}{2}\right)^2\right) \tag{8}$$

where σ^2 is the variance of the order of the typical vertex:

$$\sigma^2 = \sum_{k=0}^{\infty}(k-\mu)^2 = \sum_{k=1}^{\infty} k^2 p_k - \mu^2 \tag{9}$$

After replacing the unknown quantities in (7) by their estimators, a simple estimator is given:

$$Estof Var\,\hat{N}_V = \frac{\hat{\lambda}}{V}\left(\frac{1}{4}s^2 + \left(1 - \frac{\hat{\mu}}{2}\right)^2\right) \tag{10}$$

with:

$$s^2 = \frac{1}{n-1}\sum_{k=1}^{\infty} n_k\left(k - \hat{\mu}\right)^2 \tag{11}$$

3 RESULTS AND DISCUSSION

The initial tetrafunctional network as constructed has 16,200 chains and 8,100 crosslinks. The normalized cycle rank per chain is 0.5. We calculate the mean functionality to be equal to four (4), as expected. The estimation variance (EV) is equivalent to zero (0), also as expected.

The initial network sets the baseline for the rest of the networks which are a result of random chain scission of that original network. We created 9 degraded networks wit an increasing number of scissions. For example the final network system (i.e. gel and sol combined) in the series has the following crosslink functionality distribution: {0,776}, {1,2375}, {2,2992}, {3,1633}, {4,324}, where the first number of each element in the list represents the functionality of the crosslink and the second number is the number of crosslinks with that functionality. Below we give summary results for all gels obtained in this simulation.

Figure 1 shows how the normalized cycle rank drops as the number of chains that are removed from the network increases. We notice that the trend is monotonic for most of the data. However the curve seems to be reaching an asymptote as the number of chains increases to 9,000; over 50% of the chains of the original network have been removed by now. At this point the cycle rank is around 0.1; the gel is a very weak structure. This asymptote is not expected to be the limiting behavior for the cycle rank, since eventually one would expect that if degradation continues the cycle rank will be zero. However this is not observed for the results reported here.

The results shown in figure 2 document the dependence of the EV on the normalized cycle rank. If one follows the degradation of the network by going from higher cycle rank values to lower ones one sees three distinct areas. First as the network degrades the EV increases. This signifies that a distribution of functionalities is being generated as a result of the network degradation. Second one sees that at around a value of the 0.3 of the cycle rank and up to around

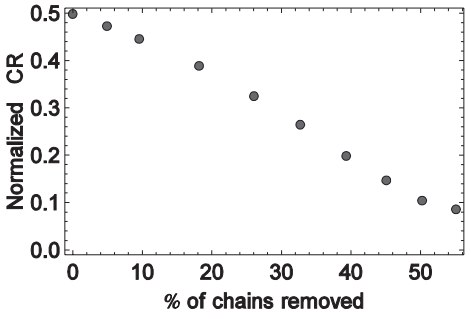

Figure 1. Dependence of normalized cycle rank on % of chains removed from the original structure.

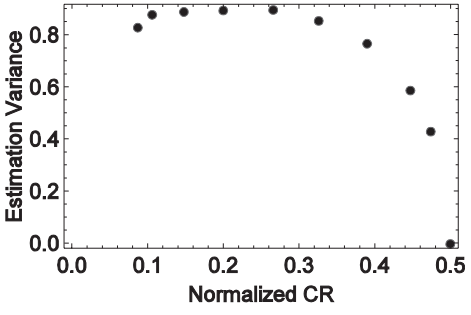

Figure 2. Correlation of estimation variance with normalized cycle rank.

0.1 the EV is more or less constant at around 0.85. The third region is blow a value of 0.1 for the cycle rank and at that point the EV starts decreasing again. This implies that the functionality distribution becomes narrower. This is a direct result of the fact that the network is so degraded that the availability of functionalities is limited.

Another way to look at the relationship of the EV to the network structure is of that shown in Figure 3. Here we plot the EV vs the number of chains removed. We see that the EV values increase rapidly at the beginning. This means that at the beginning of the degradation process the distribution of functionalities becomes broader, as would expect. Then as the number of the chains removed reaches 4,000 or so (approx 25% of the total) the standard deviation levels off until 7,000 chains or so have been removed. This signifies that the broadness of the functionalities does not change. Notice however that the actual distributions do change.

4 CONCLUSIONS

We have presented simulation results for the degradation of polymer networks. The method is based on connectivity algorithms. We find out that degraded networks are heterogeneous in

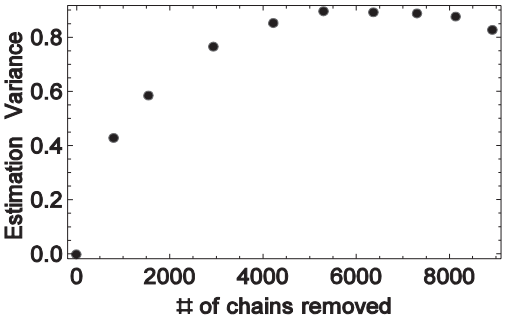

Figure 3. Estimation variance vs # of chains removed.

their functionality distribution. We present a way to quantify that heterogeneity, by relying on the Euler number and the estimation variance of the Euler number to accomplish that goal. We show here selected results from the simulation of degradation of a perfect tetrafunctional network and demonstrate the applicability of our method. We discover that during degradation the functionality distribution increases, while at the same time the cycle rank of the network decreases. As the degradation proceeds further the heterogeneity as it is measured the EV value seems to level off while at the same time the cycle rank keeps dropping. In the final stages of the simulation the heterogeneity decreases while the cycle rank falls even further.

ACKNOWLEDGEMENTS

The author is grateful to the Leibniz Institute of Polymer Research (IPF) in Dresden for their hospitality during the Fall of 2008 when this work was initiated. The author is particularly grateful to Prof. Dr. Gert Heinrich for his suggestion to explore the applicability of the Euler number in the area of elastomers and for many useful discussions on the subject.

REFERENCES

Flory, P.J. 1982. Elastic activity of imperfect networks. *Macromolecules* 15: 99–100.

Flory, P.J. 1985. Network topology and the theory of rubberlike elasticity. British Polym. J. 17(2): 96–102.

Galiatsatos, V. (ed.) 2005. *Molecular simulation methods for predicting polymer properties.* New York, NY: Wiley Interscience.

Galiatsatos, V. 1995. Computational methods for modeling polymers: An introduction. In K.B. Lipkowitz & D.B. Boyd (eds), *Reviews in Computational Chemistry*: 149–208. New York, NY: VCH Publishers, Inc.

Tscheschel, A. & Stoyan, D. 2003. On the estimation variance for the Euler-Poincaré characteristic of random networks. *Journal of Microscopy* 211: 80–88.

Constitutive Models for Rubber VI – Heinrich et al. (eds)
© 2010 Taylor & Francis Group, London, ISBN 978-0-415-56327-7

A micro-continuum-mechanical material model for failure of rubber-like materials

Hüsnü Dal & Michael Kaliske
Institut für Statik und Dynamik der Tragwerke, Technische Universität Dresden, Germany

Lutz Nasdala
Institut für Statik und Dynamik, Leibniz Universität Hannover, Germany

ABSTRACT: Conventional phenomenological hyperelastic constitutive models do not account for material softening. Consequently, the stored energy and stresses tend to infinity as stretch increases. The contribution presents a micro-mechanically motivated constitutive model for material failure. The proposed micro-continuum model is based on a serial construction of a Langevin-type spring representing the energy storage owing to conformational changes induced by deformation, to a bond potential representing the energy stored in the polymer chain due to the interatomic displacement. For the representation of the micro-macro transition, the non-affine kinematics of the micro-sphere model is used. The Morse potential is utilized for the interatomic bond, which describes the energetic contribution to rubber-like materials and governs the failure of the polymer chain in terms of bond rupture. Failure envelope predictions of the model are demonstrated in comparison to experimental data.

1 INTRODUCTION

Elastomers owe their large extensibility to long chain molecules forming the polymer network and act quite dissimilar to crystalline solids possessing regular lattice structure. The energy storage in crystalline solids and amorphous glasses is primarily due to interatomic distortion where the configurational changes in the lattice are small and, hence, entropic contributions to the overall behaviour are neglected. On the other hand, rubbery polymers well above the glass transition temperature T_g possess no intermolecular attractions and the amount of energetic distortions of the intra-molecular bonds is commonly omitted. This notion is known as ideal or strictly entropic elasticity and was based on the stress-temperature experiments of Meyer & Ferri (1935) by which they concluded that internal energy is solely a function of absolute temperature. Although the idealization of rubber elasticity and models based on Gaussian and non-Gaussian statistical mechanics proved successful results, it was later shown by Chadwick & Creasy (1984) that this idealization is too restrictive and ideally entropic elasticity excludes thermal expansion about the reference state. Alternatively, they have proposed the so-called *modified entropic elasticity* concept by which the internal energy is split into $e = e_1(\theta) + e_2(J)$ thermal and distortional parts where J denotes the volume change.

Considering the limitations of the ideal entropic elasticity models, a micromolecular model for material failure is introduced subsequently as an extension to the micro-sphere model of Miehe et al. (2004). The model is based on a serial connection of a Langevin-type spring representing the energy storage owing to conformational changes induced by deformation, to a bond potential representing the energy stored in the polymer chain due to the interatomic displacement. For the representation of the micro-macro transition in terms of non-affine kinematics, the micro-sphere model is used. The Morse potential is utilized for the interatomic bond, which describes the energetic contribution to rubber-like materials and governs the failure of the polymer chain in terms of bond rupture. Moreover, the model enables uniaxial tension, equi-biaxial tension, pure shear or pure dilatational failure modes, since it is not constructed in terms of a classical volumetric-isochoric split of the free energy function. The coupled representation in terms of the volumetric and isochoric stretches enables the definition a unified failure criterion for all deformation modes. This structure, however, does not prevent the model from showing nearly incompressible behaviour at small to moderate stretches. Unlike the compressible models introduced in the previous subsection, the proposed model attaches the volumetric part to a bond potential where the failure is attained as the

energy barrier and the peak stretch is attained. Therefore, the volumetric deformations are considered to be purely energetic. Further information and algoritmic treatment of the proposed model is documented in Dal & Kaliske (2009).

2 FINITE ELASTICITY OF A POLYMER NETWORK

This section presents a formulation of hyperelasticity within an Eulerian setting in terms of covariant Cartesian metric tensor in current configuration. After a brief summary of the basic geometric description and the constitutive equations, we describe the micro-sphere model non-affine stretch part. The topological constraints are omitted due to the minor contribution to the rubber behaviour at large stretches. The inverse Langevin statistics for a freely jointed, perfectly flexible chain is introduced. The non-affine micro-macro transition scheme of the micro-sphere model is discussed along with the previously presented network models. The interatomic bond potential of Morse (1929) will be introduced. A new energetic-entropic model which accounts for the increasing energetic contribution upon stretching will be discussed. The model consists of a serial connection of Langevin type free energy introduced in the previous section with Morse potential. A coupled volumetric-isochoric representation will be used in contrast to the traditional representations in rubber elasticity.

2.1 *Basic geometry in spatial configuration*

Let $\varphi : \boldsymbol{X} \mapsto \boldsymbol{x}$ be the deformation map at time $t \in \mathbb{R}_+$ of a body. φ maps points $\boldsymbol{X} \in \mathscr{B}$ of the reference configuration $\mathscr{B} \subset \mathbb{R}^3$ onto points $\boldsymbol{x} = \varphi(\boldsymbol{X};t) \in \mathscr{S}$ of the current configuration $\mathscr{S} \subset \mathbb{R}^3$. Let $\boldsymbol{F} := \nabla\varphi(\boldsymbol{X};t)$ with the Jacobian $J := \det \boldsymbol{F} > 0$ denote the deformation gradient. $\boldsymbol{l} := \nabla\upsilon = \dot{\boldsymbol{F}}\boldsymbol{F}^{-1}$ is the gradient of the spatial velocity $\upsilon := (\partial\varphi / \partial t) \circ \varphi^{-1}$. The boundary-value problem for a general inelastic body is governed by the balance of momentum

$$\rho\dot{\upsilon} = \mathrm{div}[\tau / J] + \gamma \tag{1}$$

along with prescribed displacement boundary conditions $\varphi = \bar{\varphi}(\boldsymbol{X};t)$ on $\partial\mathscr{B}_t$ and the traction boundary conditions $[\tau / J]\eta = \bar{\boldsymbol{t}}$ with outward normal $\boldsymbol{n}$. ρ is the density and is prescribed body force with respect to unit volume of the current configuration. Let furthermore $\boldsymbol{g} = \delta_{ab}$ denote the covariant Cartesian metric tensor or the so-called Kronecker symbol in the current configuration. Due to nearly incompressible behaviour of elastomers, the model considers the split of the elastic response into volumetric and dilatational parts

$$\bar{\boldsymbol{F}} := J^{-1/3}\boldsymbol{F}. \tag{2}$$

The macroscopic free energy is a function of the spatial metric $\boldsymbol{g}$ and the deformation gradient $\boldsymbol{F}$, i.e.

$$\Psi := \Psi(\boldsymbol{g};\boldsymbol{F}), \tag{3}$$

and satisfies the normalization conditions $\Psi(\boldsymbol{g};\boldsymbol{1}) = 0$ and $\partial_F\Psi\,\boldsymbol{g};\boldsymbol{1}) = 0$. For an elastic solid with no dissipation, the Eulerian Kirchhoff stresses and the associated spatial elasticity moduli reads

$$\tau := 2\partial_g\Psi(\boldsymbol{g};\boldsymbol{F}) \quad \text{and} \quad \mathbb{C} := 4\partial^2_{\boldsymbol{gg}}\Psi(\boldsymbol{g};\boldsymbol{F}). \tag{4}$$

The Langevin model which considers the finite extensibility of a single chain is introduced by Kuhn & Griin (1942). The free energy function of a single chain based on the Langevin model reads

$$\psi_L(\lambda) = Nk_BT\left(\lambda_r L^{-1}(\lambda_r) + \ln\left(\frac{L^{-1}(\lambda_r)}{\sinh L^{-1}(\lambda_r)}\right)\right), \tag{5}$$

where $\lambda = L/L_0$ is the stretch of the single chain and $\lambda_r = \lambda/\sqrt{N}$ is the relative stretch. L_0 is the end-to-end distance in the unstrained state. Here, $L(x) = \coth x - \dfrac{1}{x}$ is the Langevin function.

2.2 *Micro–macro transition*

Let $\boldsymbol{r}$ denote the Lagrangian orientation vector of a point on a unit sphere such that $|\boldsymbol{r}|_G := \sqrt{\boldsymbol{r}_0 \cdot \boldsymbol{r}} = 1$, where $\boldsymbol{r}_b := \boldsymbol{G}\boldsymbol{r}$ ($\boldsymbol{r}_A = \delta_{AB}\boldsymbol{r}^A$) is the co-vector of $\boldsymbol{r}$ obtained by mapping with the metric $G = \delta_{AB}$ in the reference configuration. The Eulerian counterpart of the orientation vector $\boldsymbol{r}$ is given by

$$\boldsymbol{t} := \bar{\boldsymbol{F}}\boldsymbol{r}. \tag{6}$$

Then, the macro-stretch in the given orientation direction r reads

$$\bar{\lambda} = |\boldsymbol{t}|_g := \sqrt{\boldsymbol{t}_b \times \boldsymbol{t}} \quad \text{with} \quad \boldsymbol{t}_b := \boldsymbol{g}\boldsymbol{t}. \tag{7}$$

The Cauchy-Born rule states that for crystals undergoing small deformations, each orientation stretch in the micro-scale is equivalent to the macroscopic stretch $\bar{\lambda}$. This hypothesis, however is too restrictive for rubber-like polymers, especially in the non-Gaussian region at large strains. For the transition from a molecular level towards a continuum model, there exist many approaches.

The affine full network model has been originally developed by Treloar (1946) for uniaxial deformations and elaborated by Treloar & Riding (1979) for biaxial deformations with a numerical implementation. Wu & van der Giessen (1993) advanced the theory into a generalized three-dimensional deformation state. Full network model cannot show the characteristic material behaviour of rubber which exhibits different locking stretches for different deformation modes. Miehe et al. (2004) related the non-affine micro-stretch λ and the affine macro-stretch $\bar{\lambda}$ via p-root average such that

$$\lambda = \langle \lambda \rangle_p := \left\{ \frac{1}{|\mathscr{S}|} \int_{\mathscr{S}} \bar{\lambda}^p dS \right\}^{1/p} . \tag{8}$$

Hence, p is a non-affinity parameter which relates the micro-stretch entering the Langevin free energy to the macro-stretch field on the unit-sphere. The model recovers the 8-chain model of Arruda & Boyce (1993) for $p = 2$. The macroscopic free energy takes the following representation

$$\Psi(\boldsymbol{g};\boldsymbol{F}) = \Psi_{vol}(J) + \Psi_{iso}(\boldsymbol{g};\bar{\boldsymbol{F}}), \tag{9}$$

and the dilatational part is defined as

$$\Psi_{iso}(\boldsymbol{g};\boldsymbol{F}) = n\psi_L\left(\langle \lambda \rangle_p\right), \tag{10}$$

where n is the chain density.

2.3 *Morse potential*

Gao & Klein (1998) have proposed a continuum-atomistic approach for amorphous solids by using atomic pair potentials $U(l)$ distributed over a unit-sphere. They introduced a bond distribution density function D over the unit sphere. The integration of the pair potentials over the unit-sphere then leads to the strain energy density function.

The pair potential proposed by Morse (1929) has the following form

$$\phi(r) = \hat{e}\,[\exp(-2\alpha(r - r_0)) - 2\exp(-\alpha(r - r_0))] \tag{11}$$

and is depicted in Figure 1a. Partial derivative with respect to r leads to the force displacement relation

$$f = 2\hat{e}\alpha[\exp(\alpha(r_0 - r)) - \exp(2\alpha((r_0 - r))]. \tag{12}$$

$\hat{e}$ is the dissociation energy for a given pair of atoms. For interatomic distance $r = r_0$, the atomic pair possess an energy minimum $-e$ with corresponding zero force level $f = 0$. The bond is stable until the force peak at $(r_m, f_m) = (r_0 + \ln 2/\alpha, \hat{e}\alpha/2)$ (Figure 1b). However, the energy required to reach the peak level is only $\hat{e}/4$.

2.4 *A new failure model for rubber-like materials*

We propose a new free energy function within the kinematical context of the micro-sphere model

$$\Psi(\boldsymbol{g};\boldsymbol{F}) = n\psi_\eta(\lambda_\eta) + n\,\psi_e(\gamma) \tag{13}$$

where

$$\gamma := \alpha_1(\lambda_e - 1) + \alpha_2(J - 1)^2 \tag{14}$$

and

$$\lambda_\eta \cdot \lambda_e = \lambda \quad ; \quad \lambda = \langle \lambda \rangle_p . \tag{15}$$

λ_η and λ_e denote the entropic and the energetic part of the average network stretch λ. ψ_η is given by Eq. (5) and characterizes the change in the free energy solely due to entropic effects. It is taken to be purely iso-choric. The energetic part of the free energy is given by a modified version of the Morse potential (see Eq. (11))

$$n\psi_e(\gamma) = n\hat{e}\,[\exp(-2\gamma) - 2\exp(-\gamma) + 1] \tag{16}$$

and satisfies the normalization conditions $\psi_e(0) = 0$ and $\partial_\gamma \psi_e(0) = 0$. The rheology of the model

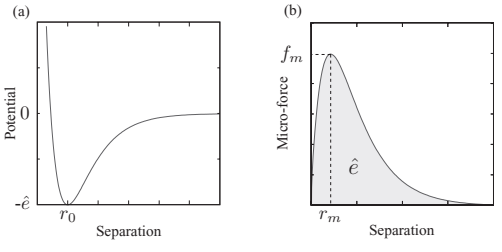

Figure 1. (a) The Morse potential and (b) the corresponding force displacement curve.

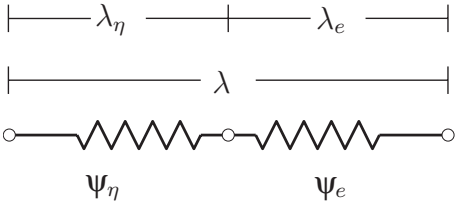

Figure 2. Rheological representation of the proposed model.

is depicted in Figure 2. The micro-forces of the entropic and energetic contributions are

$$f_\eta := \frac{\partial \psi_\eta}{\partial \lambda_\eta} = k_B T \frac{3N - \lambda_\eta^2}{N - \lambda_\eta^2} \tag{17}$$

and

$$f_e := \frac{\partial \psi_e}{\partial \lambda_e} = 2\alpha_1 e_0 (-\exp(-2\gamma) + \exp(-\gamma)), \tag{18}$$

respectively. For a given deformation state λ, the micro-forces are subject to the equilibrium constraint

$$f_\eta \lambda_\eta = f_e \lambda_e. \tag{19}$$

The proposition (19) is in line with the rheology depicted in Figure 2 under finite deformations.

3 ALGORITHMIC TREATMENT OF THE CONSTITUTIVE MODEL

In the sequel, we develop an appropriate numerical scheme for the computation of the quilibrium stresses. The algorithmic setting of the proposed model begins with equilibrium computations in order to find entropic λ_η and energetic λ_e stretches for a given micro-stretch λ. Then, the stresses expressions in the Eule-rian setting will be derived. For further information on the moduli expressions for the finite element method, we refer to Dal & Kaliske (2009).

3.1 *Equilibrium iterations at micro level*

The equilibrium condition of the serial construction depicted in Figure 2 is defined as follows: Problem: *Given λ, find λ_η and λ_e such that*

$$f_\eta \lambda_\eta - f_e \lambda_e = 0 \text{ and } \lambda_\eta . \lambda_e = \lambda.$$

For the solution of the above problem, we define the residual expression

$$r := f_\eta \lambda_\eta - f_e \lambda_e = 0. \tag{20}$$

This expression can be solved micro level. The numerical procedure involves solely scalar expressions which costs acceptable computation time. For the sake of simplicity, we demonstrate a Newton type iteration scheme outlined in Table 1.

3.2 *Kirchhoff stresses*

With micro-equilibrium at hand, the Kirchhoff stresses can be derived from Eq. (13) and Eq. (4.1). Before defining the stress expression, we take the

Table 1. Steps of local equilibrium iterations at micro-level.

1. *Set*

   $\lambda_\eta^0 = \lambda$ and $\lambda_e = \lambda / \lambda_\eta$

2. DO

   a. Residual equation

   $r := f_\eta \lambda_\eta - f_e \lambda_e = 0$

   b. Linearization

   $$\mathrm{Lin}\, r = r|_{\lambda_\eta^k} + \left.\frac{\partial r}{\partial \lambda_\eta}\right|_{\lambda_\eta^k} \Delta\lambda_\eta^{k+1} = 0$$

   c. Compute

   $$\kappa := \left.\frac{\partial r}{\partial \lambda_\eta}\right|_{\lambda_\eta^k}$$

   $$\kappa = \bar{\mathbb{C}}_\eta + \frac{\lambda}{\lambda_\eta^2} \bar{\mathbb{C}}_e$$

   where $\bar{\mathbb{C}}_\eta = f_\eta + \lambda_\eta \mathbb{C}_\eta$; $\bar{\mathbb{C}}_e = f_e + \lambda_e \mathbb{C}_e$

   $$\mathbb{C}_\eta := \frac{\partial f_\eta}{\partial \lambda_\eta} \; ; \; \mathbb{C}_e := \frac{\partial f_e}{\partial \lambda_e}$$

   d. Solve

   $\Delta\lambda_\eta^k = -k^{-1} r$

   e. Update

   $\lambda_\eta^{k+1} \leftarrow \lambda_\eta^k + \Delta\lambda_\eta^k$

WHILE $\|r\| \le TOL$

following definitions for the intermediate derivatives from Miehe et al. (2004)

$$2\partial_{\boldsymbol{g}} \lambda = \lambda^{1-p} \boldsymbol{h} \quad \text{with} \quad \boldsymbol{h} := \left\langle \bar{\lambda}^{p-2} \boldsymbol{t} \otimes \boldsymbol{t} \right\rangle. \tag{21}$$

It is however to be noted that although the energetic part of the free energy function has a coupled representation in terms of γ, the entropic part of the free energy is purely incompressible. The split of the stresses in line with this assumption then takes the form

$$\boldsymbol{\tau} := \bar{\boldsymbol{\tau}} : \mathbb{P} + \boldsymbol{\tau}^{vol}. \tag{22}$$

The volumetric part of the Kirchhoff stresses can be defined as

$$\boldsymbol{\tau}^{vol} := 2\partial_J \Psi \partial_{\boldsymbol{g}} J = p \boldsymbol{g}^{-1} \tag{23}$$

where

$$p := J\alpha_2 n \psi'_e(\gamma) \quad \text{and} \quad \psi'_e(\gamma) := \partial_\gamma \psi_e(\gamma). \tag{24}$$

The incompressible part of the Kirchhoff stresses are given by

$$\begin{aligned}\bar{\tau} &:= n[\partial_{\lambda\eta}\psi_n \partial_\lambda \lambda_\eta + \partial_{\lambda e}\psi_e \partial_\lambda \lambda_e]\, 2\partial_{\boldsymbol{g}}\lambda \\ &= n[f_\eta \partial_\lambda \lambda_\eta + f_e \partial_\lambda \lambda_e]\lambda^{1-p}\boldsymbol{h}.\end{aligned} \tag{25}$$

For the computation of partial derivatives $\partial_\lambda \lambda_\eta$ and $\partial_\lambda \lambda_e$, we refer to the residual expression (20). By using the implicit function theorem, we obtain

$$\frac{dr}{d\lambda} = \frac{\partial r}{\partial \lambda} + \frac{\partial r}{\partial \lambda_\eta}\frac{\partial \lambda_\eta}{\partial \lambda} = 0. \tag{26}$$

This leads to

$$\frac{\partial \lambda_\eta}{\partial \lambda} = \frac{\bar{\mathbb{C}}_e}{\lambda_\eta \bar{\mathbb{C}}_\eta + \lambda_e \bar{\mathbb{C}}_e};\ \frac{\partial \lambda_e}{\partial \lambda} = \frac{\bar{\mathbb{C}}_\eta}{\lambda_\eta \bar{\mathbb{C}}_\eta + \lambda_e \bar{\mathbb{C}}_e}. \tag{27}$$

Let $f := \partial_\lambda \psi$ denote the micro-force where ψ is defined in Eq. (13). With this definition at hand and by inserting Eq. (27) into Eq. (25), we get

$$f = \frac{f_\eta \bar{\mathbb{C}}_e + f_e \bar{\mathbb{C}}_\eta}{\lambda_\eta \bar{\mathbb{C}}_\eta + \lambda_e \bar{\mathbb{C}}_e}. \tag{28}$$

If Eq. (28) is examined carefully, it is seen that after some manipulations, it holds for

$$f\lambda = f_\eta \lambda_\eta = f_e \lambda_e, \tag{29}$$

which is nothing but the constraint proposed in Eq. (19). This justifies the choice of constraint for the serial construction for the rheology of materials subjected to large deformations. Then, the representation of the incompressible part of Kirchhoff stresses simplifies to

$$\bar{\tau} = nf\lambda^{1-p}\boldsymbol{h}. \tag{30}$$

This expression is identical to the one proposed by Miehe et al. (2004) if $nf : \psi'$ is derived from a single elastic potential. Although the isochoric and volumetric part of the stresses have a decoupled representation, both expressions are dependent on stretches λ and volume change J. This leads to extra terms in the moduli expressions which are not encountered in the rubber elasticity models based on the isochoric-volumetric split of the deformation gradient. Finally, the proposed model is compared with the micro-sphere model non-affine stretch part (Figure 3). The parameters are $\mu = 0.325$ MPa, $N = 22.263$, $p = 1.39$ and are identical to the ones used

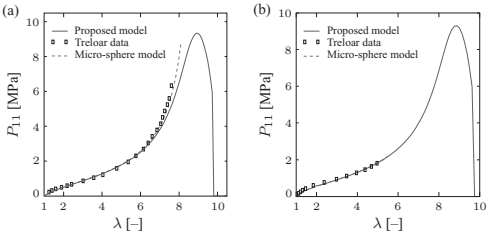

Figure 3. Comparison of the first Piola Kirchhoff stress vs. stretch for micro-sphere model non-affine stretch part, proposed approach and the experimental data from Treloar under (a) uniaxial tension and (b) pure shear.

in Miehe et al. (2004), Figure 11. The extra parameters appearing in the proposed model are $\alpha_1 = 7$, $\alpha_2 = 100$ $n\hat{e} = 22$ MPa. The parameter α_2 is taken to be high enough ($\alpha_2 \approx 5\alpha_1$) in order to enforce incompressibility up to moderate stretches. Despite the introduced free energy function in the serial form, the proposed model demonstrates nearly identical behaviour compared to the micro-sphere model. This can simply be explained by serially attached soft and hard springs. As a macroscopic deformation is applied, the initial stiffness of the Langevin spring is much less than that of the energetic part. As a consequence, the energetic part is solely responsible for enforcing the incompressibility. As the deformation increases and the $\lambda \approx \lambda_{lock}$ is approached, the slope of the Langevin spring becomes comparable to that of the energetic spring and strong coupling occurs in this range. It is to be noted that at high stretches near λ_{lock}, the material model is not incompressible anymore. Soon, the peak level is attained and the material is not stable anymore. Up to this level $\lambda = \lambda_\eta \lambda_e$ can be traced continuously. After the peak is achieved, the stress drops continuously and then discontinuously to zero. At this instant of discontinuity, a jump in λ_η and λ_e occurs at micro level and λ_η drops (the Langevin spring contracts upon failure) whereas λ_e increases drastically (bond rupture). From this moment, material failure is occurred and stress computations can be omitted. Failure information can be stored with an integer switch in the material routine. The model requires no additional history variable for deformation.

3.3 *Failure prediction under various loading states*

This section is devoted to the failure envelope prediction of the proposed model. Hamdi et al. (2006) investigated fracture stresses and elongation at break values for NR and SBR rubber under different loading conditions and proposed a phenomenological failure criterion for rubber. They performed uniaxial tension, equibiaxial tension

and biaxial tension experiments with various biaxiality ratios until fracture. The material parameters of the proposed model are fitted to the given stress strain curves (Hamdi et al. (2006), Fig. 8) for natural rubber (NR) and styrene-butadiene rubber (SBR), respectively. The fitted parameters for NR are: μ = 0.60 MPa, N = 9.02, p = 1.6, α_1 = 2.12, α_2 = 20 and $n\hat{e}$ = 144 MPa. For SBR: μ = 1.3 MPa, N = 6.68, p = 1.3, α_1 =1.54, α_2 = 20 and $n\hat{e}$ = 171 MPa. During the fitting procedure initial tangent of the stress strain curve and elongation at break values are enforced with a higher priority whereas stresses obtained from simulations at moderate stretch levels underestimate the experimental values. This is due to the fact that the data includes Mullins type damage since it gives the first loading to failure. Moreover, the constraint part of the micro-sphere model is not considered in this paper. The results of the normalized ultimate elongations and comparison with the data from Hamdi et al. (2006) are depicted in Figure 4. The failure elongations corresponding to uniaxial tension (UT), pure shear (PS) and equibiaxial tension (ET) are depicted explicitly. Simulations show good agreement for both NR and SBR with slight overestimation for SBR. It should be mentioned that for smaller p values, better fit to the failure envelope is possible. The failure envelope has an ellipsoid shape. For p = 2, the model yields a circular failure envelope. For higher values the failure envelope approaches the Kawabata's failure criterion which states that failure occurs if stretch in any principal direction approaches ultimate elongation in uniaxial tension λ_{UT}. Figure 5 compares the ultimate Cauchy stresses normalized with respect to the ultimate uniaxial tension values for NR and SBR. The model predictions give a linear envelope for failure Cauchy stresses. The results presented by the model overestimate the experimental values, especially for NR. As one observes in Figure 4a and Figure 5a, the stress results from the model predictions clearly underestimate the failure stresses for NR. One possible reason can be crystallisation. The ultimate failure properties of crystallising rubbers are known to be quite dissimilar to to non-crystallising rubber. As one observes in Figure 4b and Figure 5b, the overestimation of stresses by the proposed model is in accordance with the overestimation of the stretch value for SBR. Different test geometries used in the biaxial experiments can lead to different failure stresses. The larger the specimen, the higher is the probability of an existing defect in the microstructure. This argument holds, however, only for SBR. It is obvious that more experimental study is necessary, especially for NR and future research will be initiated on the verification of the model.

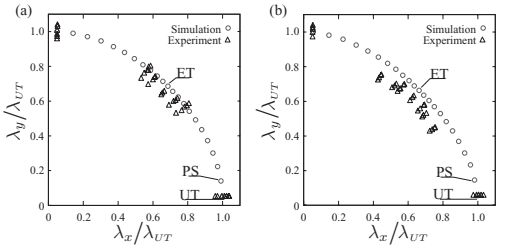

Figure 4. Ultimate stretches normalized with respect to uniaxial ultimate stretch λ_{UT} for (a) NR, (b) SBR.

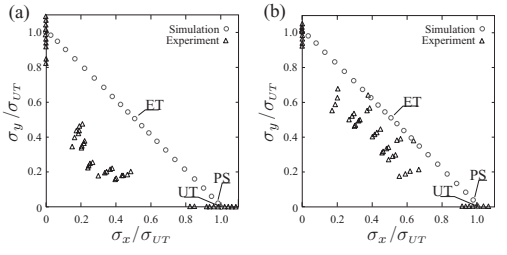

Figure 5. Ultimate Cauchy stresses normalized with respect to ultimate uniaxial Cauchy streses σ_{UT} for (a) NR, (b) SBR.

In summary, the proposed model is better suited for predicting the failure characteristics of non-crystallising rubber under biaxial deformations.

4 CONCLUSION

We proposed a new energetic-entropic model for rubber-like materials as an extension to the micro-sphere model. The theoretical aspects of the model are discussed and a novel algorithmic treatment for the serially constructed non-linear springs in the micro level is presented. This algorithm is further combined with micro-macro approach of micro-sphere model. Unlike typical rubber elasticity models, the proposed approach has a coupled representation for the free energy in terms of volumetric and isochoric parts of the deformation gradient. This scheme proves useful at large deformations near the failure limit. The proposed model can be considered as a softening hyper-elasticity model based on micromolecular considerations. Core of the model is to include fracture energy and the fracture stress as material parameters at micro-level. Material failure is interpreted as the bond rupture of a chain molecule beyond a threshold value. This enables direct implementation of the fracture relevant parameters into the constitutive model. The predictions based on the model

for different fracture models are compared to the experimental data. Reduced ultimate stretches and stresses under equi-biaxial tension can be successfully captured by the proposed model. An ellipsoidal failure envelope is obtained for normalized failure stretches, from uniaxial tension to equibiaxial tension.

ACKNOWLEDGEMENT

The financial support of the Deutsche Forschungsgemeinschaft (DFG) under grant Ka 1163/2-1 is gratefully acknowledged.

REFERENCES

Arruda, E.M. & M.C. Boyce 1993. A three-dimensional constitutive model for the large stretch behavior of rubber elastic materials. *Journal of the Mechanics and Physics of Solids 41*, 389–412.

Chadwick, P.&C.F.M. Creasy 1984. Modified entropic elasticity of rubberlike materials. *Journal of the Mechanics and Physics of Solids 32*, 337–357.

Dal, H.&M. Kaliske 2009. A micro-continuum-mechanical material model for failure of rubber-like materials: Application to ageing induced fracturing. *Journal of the Mechanics and Physics of Solids,* doi: 10.1016/j.jmps.2009.04.007.

Gao, H. & P. Klein 1998. Numerical simulation of crack growth in an isotropic solid with randomized internal cohesive bonds. *Journal of the Mechanics and Physics of Solids 46*, 187–218.

Hamdi, A., M. Nait Abdelaziz, N. Ait Hocine, P. Heuil-let & Benseddiq 2006. Fracture criterion of rubber-like materials under plane stress conditions. *Polymer Testing 25*, 994–1005.

Kuhn, W. & F. Grün 1942. Beziehungen zwis-chen elastischen konstanten und dehnungsdop-pelbrechung hochelastischer stoffe. *Kolloid-Zeitschrift 101*, 248–271.

Meyer, K.H.&C. Ferri 1935. Sur l'élasticité du caoutchouc. *Helvetica Chimica Acta 18*, 570–589.

Miehe, C., S. Göktepe, & F. Lulei 2004. A micro-macro approach to rubber-like materials, part I: The non-affine micro-sphere model of rubber elasticity. *Journal of the Mechanics and Physics of Solids 52*, 2617–2660.

Morse, P.M. 1929. Diatomic molecules to the wave mechanics. II. vibrational levels. *Physical Review 34*, 57–64.

Treloar, L.R.G. 1946. The photoelastic properties of short-chain molecular networks. *Transactions of the Faraday Society 50*, 881–896.

Treloar, L.R.G. & G. Riding 1979. A non-gaussian theory of rubber in biaxial strain, i.mechanical properties. *Proceedings of the Royal Society of London A 369*, 261–280.

Wu, P.D. & E. van der Giessen 1993. On improved network models for rubber elasticity and their applications to orientation hardening in glassy polymers. *Journal of the Mechanics and Physics of Solids 41*, 427–56.

Constitutive Models for Rubber VI – Heinrich et al. (eds)

Meso-scopic 3D-finite element analysis of filled elastomer

Keizo Akutagawa, Satoshi Hamatani & Hisashi Heguri
Bridgestone Corporation, Ogawahigashi-cho, Kodaira-shi, Tokyo, Japan

ABSTRACT: In most industrial applications the elastomers are used as reinforced materials with filler such as carbon-black and silica, but the mechanical behaviours in meso-scopic scale have not been fully understood due to the limitation of the mechanical analysis in meso-scopic scale. Combination of 3D-TEMT (Transmission Electron Micro Tomography) and 3D-FEA (Finite Element Analysis) enables us to investigate the deformation of the filled elastomer in meso-scopic scale. The polymer phase between carbon black aggregates showed a large strain concentration over 200%, even if the overall strain was only 15%[1]. Hence, a constitutive equation, which can cover the stress-strain behaviours up to higher strain region as a function of temperature, has been investigated. Since the stress-strain behaviour shows a transition to the glass-hard state at lower temperature, where the contribution of the internal energy is increased, a constitutive equation was derived from the statistical thermodynamics with Hamiltonian equations considering the change in internal energy.

1 INTRODUCTION

For tyre tread compounds the viscoelastic properties can be empirically correlated with tyre performance characteristics. It has been shown, for example, that the wet traction and the rolling resistance are best correlated with the dynamic mechanical loss properties at the temperature of around 0°C and 60°C, respectively. For tyre compound design the dynamic properties, particularly tan δ, in this range are often of major concern in reducing tyre rolling resistance with keeping the wet traction unchanged.

For tyre applications the finite element method is one of important tool to model the behaviour of tyre components stressed in a complex manner. Recently this method was applied to the nano-scopic analysis of the filled rubber and it can provide the meso-scopic stress-strain behaviour of rubber phase and filler phase separately[1]. To carry this out successfully it was also needed to develop a constitutive equation to represent the stress-strain behaviour of a rubber phase, preferably at least up to the glass transition temperature of rubber phase encountered in many tyre tread applications. The stress-strain behaviours of rubber at low temperature are largely contributed by the internal energy change of rubber[2,3]. The purpose of this study is aiming at the meso-scopic stress-strain behavious of the filled rubber at different temperatures using a constitutive equation based on the change in material energy and entropy, which represents the continuous change in elasticity from transition state to rubbery state.

2 EXPERIMENTAL

Stress-strain curves were measured using a TOYO-SEIKI tensile testing machine with temperature-controlled chamber. Rubber strip samples with ring shape were used for this study. The tests were carried out at a crosshead speed of 0.5 mm/s.

The rubber used for this study was an unfilled cross-linking styrene-butadiene rubber (SBR), which is a non-strain crystallizing, and a filled cross-linking SBR with 30 phr of carbon black.

3 RESULTS AND DISCUSSION

From the statistical thermodynamics it can be assumed that the energy function of A_α can be described by a function of the Hamiltonians, H.

$$A_\alpha = f(H_{interaction}, H_{trans}, H_{rot}) \quad (1)$$

where the Hamiltonian for the system can be assumed as a function of temperature and constrains due to stretching the chain molecules with transversal motion, H_{trans}, rotational motion, H_{rot} and molecular interaction, $H_{interaction}$. For the model of the temperature dependence of the rubber elasticity it can be thought of as two distinguishable molecules, each of which can be in either of two different strain states at different temperatures as shown in Table 1.

There has to consider the attractive energy or interaction energy term, κ, which lowers the energy of the system by κ of the two molecules. At low

Table 1. Molecular system on thermodynamic model.

	Unstretched	stretched
Lower Temp.		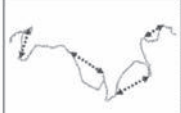
Higher Temp.		

temperature both molecules are to be found in the lower strain energy state, which is the constrain state of the rubber elasticity. As the temperature increases, the molecules will spend more time in the higher strain energy state. As the temperature continues to increase, it will reach a point where the molecules become 'un-bound'. This may be associated with the transition region of the temperature dependence of the rubber elasticity. At this region more energy can be absorbed by the system, because the molecules can move easily. Once the temperature becomes very high, the energy of the system will be constant. According to this model[2,3] the partition function, Z, can be represented by

$$Z = k \cdot T \cdot N \left[\underbrace{\lambda \cdot \Lambda \cdot \left(\frac{2 \cdot \pi \cdot m}{\beta} \right)^{\frac{3}{2}}}_{\text{transverse}} + \underbrace{\log[2\{e^{\beta\kappa} \cosh(2 \cdot \beta \cdot (I-3)) + 1\}]}_{\text{interaction}} \right] + k \cdot T \cdot N \left[\underbrace{\frac{l}{N \cdot a} \cdot \frac{a \cdot F}{k \cdot T} + \log \left[\frac{\left(\frac{a \cdot F}{k \cdot T} \right)}{\sinh \left(\frac{a \cdot F}{k \cdot T} \right)} \right]}_{\text{rotation (Langevin function)}} \right] \quad (2)$$

where k is Boltzmann constant, T is absolute temerature, N is the number of molecules, Λ is volume, m is mass of a molecule, β is 1/kT, I is the strain invariant and F is force applied to molecules. The Helmhortz free energy of the rubber elasticity, A_α, can be represented by[2,3]

$$A_\alpha = p e^{\frac{\kappa}{R\Delta T}} \frac{\kappa \cdot \cosh\left(\frac{2(I_1-3)}{R\Delta T} \right) + 2(I_1-3) \cdot \sinh\left(\frac{2(I_1-3)}{R\Delta T} \right)}{e^{\frac{\kappa}{R\Delta T}} \cdot \cosh\left(\frac{2(I_1-3)}{R\Delta T} \right) + 1} + qvRT \left[\frac{1}{2} I_1 + \frac{3}{100n}(3I_1^2 - 4I_2) + \frac{99}{12250n^2}(5I_1^3 - 12 I_1 I_2) \right] \quad (3)$$

where p = q = 1, n is the crosslink density, n is the number of statistical links between crosslinks. The first term of the equation (3) represents the internal energy change of the elasticity and the second term represents the entropy change of the rubber elasticity described by the inverse Langevin function[4]. The volume change due to stretching was ignored.

The stress-strain curves shown in Figure 1 were plotted as a function of temperature together with the fitted curves using the constitutive equation. The procedure of curve fitting was followed by Morris method[5]. The theoretical curves were fitted with a parameter of the attractive energy, κ, using the equation (3). The theoretical curves show a good agreement with the experimental plots over a wide range of temperature.

The equation (3) was applied to the element model of 3D-FEA (Finite Element Analysis), which can be reconstructed from the 3D-image taken by 3D-TEMT (Transmission Electron Micro Tomography)[6]. The size of one element is 3 nm × 3 nm × 3 nm, which is equivalent to the size of molecular chain between cross-links. The calculations of 3D-FEA were carried out at strain of 15% and temperature at 25°C and −50°C. Figure 2 shows a strain distribution in meso-scopic scale of 30 phr carbon filled rubber. Each size of the model is 150 nm × 150 nm × 150 nm. The black part is represented by the filler and the rest of it is by rubber. Highly strain region is deformed with more than 10 times larger than macro-scopic strain of 15%.

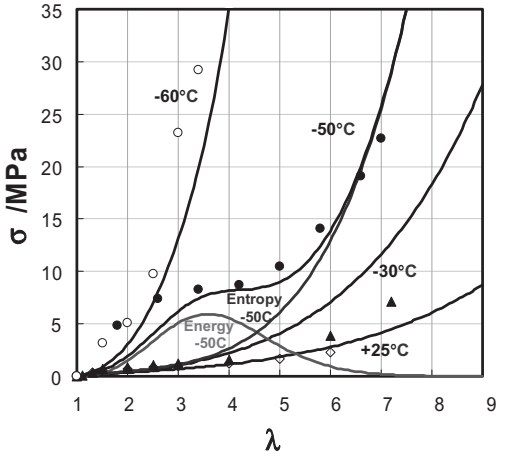

Figure 1. The stress-strain curves plotted as a function of temperature together with the fitted curves using the constitutive equation (3). A line is represented by the energy term and the entropy term of equation (3) at temperature of −50°C.

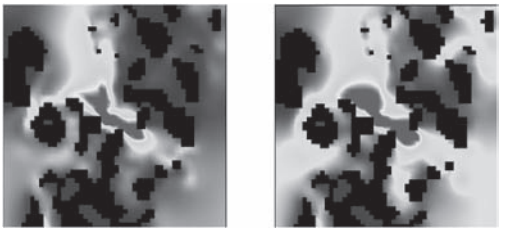

(a) 15% strain at 25°C (b) 15% strain at -50°C

Figure 2. The strain distribution in meso-scopic scale calculated by 3D-FEA at strain of 15% and temperature of 25°C (a) and –50°C.

4 CONCLUSIONS

The constitutive equation, which was derived from the statistical thermodynamics with Hamiltonian equations considering the change in internal energy, was applied to 3D-FEA in meso-scopic scale. In Figure 2 the deformed area of the rubber part at –50°C is much larger than that at 25°C, even if the model was stretched in the same strain of 15%. This will provide the useful information about the role of the rubber parts in filled rubbers, especially at transition and glassy region of temperature.

REFERENCES

1. K. Akutagawa., K. Yamaguchi., A. Yamamoto., H. Heguri., H. Jinnai., & Y. Shinbori. *Rubber Chem. Technol*., 2008, 81, 182.
2. Per-Erik Austrell., & Leif Kari. Constitutive Models for Rubber IV: Proceedings of the 4th ECCMR, Taylor & Frances, 2005, 185.
3. K. Akutagawa., S. Hamatani., & H. Heguri., Proceedings of the 8th Meeting of Fall Rubber Colloquium, 2008, 49.
4. M.C. Wang., & E. Guth. J. Chem. Phys. 1952, 20, 1144.
5. M.C. Morris., J. Appl. Polym. Sci. 1964, 8.
6. H. Jinnai., Y. Shinbori., T. Kitaoka., K. Akutagawa., N. Mashita., & T. Nishi, Macromolecules, 2007, 40, 6758.

Constitutive Models for Rubber VI – Heinrich et al. (eds)
© 2010 Taylor & Francis Group, London, ISBN 978-0-415-56327-7

Changes in the orientation state of polymer molecules in the space between filler particles

L.A. Komar & A.L. Svistkov,
Leibniz-Institut fur Polymerforschung Dresden e. V., Dresden, Germany
Institute of Continuous Media Mechanics, Ural Branch of Russian Academy of Sciences, Perm, Russia

G. Heinrich & B. Lauke
Leibniz-Institut fur Polymerforschung Dresden e. V., Dresden, Germany

ABSTRACT: For the analysis of formation of polymeric layers with particular properties that arise near filler particles in a filled elastomeric material, a mathematical model has been developed. The model is based on the hypothesis that the oriented regions of the polymer are able to influence the orientation state of neighboring regions. The periodicity cell of the elastomeric material filled with rigid spherical particles is examined. Formation of layers in the space between particles and away from it is modelled. The results of numerical simulation show that in the material near filler particles there occur regions where polymeric molecules are in uniaxial and biaxial states.

1 INTRODUCTION

The layers of 2 to 10 nm (and more) that occur near the surface of filler particles play a large part in the formation of the mechanical properties of polymer nanocomposites. Despite the longstanding efforts of scientists to elucidate the cause of formation of these layers and to understand the mechanism of their influence on the mechanical properties of the material, the problem still remains to be solved. There is no answer to the question as to why the thickness of the layers formed near the surface of filler particles is so large that it achieves several nanometers. In the current study, an attempt has been made to construct a mathematical model capable of providing the answer to this question.

2 CONTINUUM, PROBABILISTIC AND DISCRETE MODELLING

For constructing the model, it is essential to determine mathematical parameters best suited to our study. The establishment of these parameters requires information regarding the preferential orientation of polymer links. To gain it, we use the notion of the orientation tensor. However, before proceeding to the description of the oriented state of the medium, it is necessary to introduce the characteristic of the oriented state of a single link of one of the polymeric chains. Let all links of all polymer chains have a through enumeration: the first link of the first chain is designated as 1, and the last link of the last chain as N. The index j, running the values from 1 to N, takes the numbers of all links of all polymer chains.

As the orientation characteristic of the polymer chains link with number j, we use the tensor $\tau_j \otimes \tau_j$, in which τ_j denotes a unit vector defining the space orientation direction of the j-th link. Clearly, a change in the direction of the vector τ_j to the opposite produces no effect on the values of the tensor $\tau_j \otimes \tau_j$. The proposed tensor is suitable for our purpose because its averaged value can be found for all possible links of polymer chains and the result of such averaging will not be equal to a zero tensor. It gives an estimate of the oriented state of the polymer. Its eigenvectors and eigenvalues have a clear physical meaning. The eigenvectors of the averaged tensor $\tau_j \otimes \tau_j$ define the space directions along which the chain links are mainly oriented and the directions along which the links are rarely oriented. The eigenvalues of this tensor give a quantitative estimate of the degree of orientation of polymer chains in corresponding directions. We assume that the energy of interaction between the i-th and j-th links of polymer chains is represented as a potential

$$u_{ij} = u_0 w_1(r_{ij})\, w_2(\tau_i \cdot \tau_j),$$

where u_0 is the depth of the energy well, and $w_1(r_{ij})$ is the Lenard-Jones potential energy function. The dependence of the energy of interaction u_{ij} on the angle between the orientation directions of the links of polymeric chains can be written as

$$w_2(\tau_i \cdot \tau_j) = (\tau_i \cdot \tau_j)^2 - \frac{1}{3} = \tau_i \otimes \tau_i \cdot \tau_j \otimes \tau_j - \frac{1}{3}.$$

The energy of interaction of the i-th link with other links is defined as

$$\sum_{j=1, j\neq i}^{N} u_{ij} = u_0 \sum_{j=1, j\neq i}^{N} w_1(r_{ij})\, w_2(\tau_i \cdot \tau_j) = \frac{u_0}{C_N}\left(\frac{1}{3} - \tau_i \otimes \tau_i \cdot \langle \tau_j \otimes \tau_j \rangle_V\right),$$

where the value of the constant C_N is determined by the discrete normalization condition

$$C_N \sum_{j=1, j\neq i}^{N} \rho(r_{ij}) = 1,$$

where $\rho(r_{ij}) = -w_1(r_{ij})$ is the weight factor.

We use the space averaging $\langle \tau_j \otimes \tau_j \rangle_V$ which in the discrete formulation can be obtained as

$$\langle \tau_j \otimes \tau_j \rangle_V = C_N \sum_{j=1, j\neq i}^{N} \rho(r_{ij})\, \tau_j \otimes \tau_j,$$

and in the continuum formulation as

$$\langle \tau_j \otimes \tau_j \rangle_V = C_V \int_V \rho(r)\mathbf{O}\, dV.$$

Here, the value of the constant C_V is determined by the continuum normalization condition

$$C_V \int_V \rho(r)\, dV = 1.$$

We assume that there is a continuous twice differentiated tensor function $\mathbf{O}(t, \mathbf{x})$, which provides calculation of the energy of interaction of the i-th link with the remaining material, as it is usually fulfilled in the context of probability and discrete models.

It is easy to demonstrate that the requirement of equivalence of continuum averaging and discrete averaging for the arbitrary bounded doubly differentiable tensor function is fulfilled under the following condition

$$C_N \sum_{j=1, j\neq i}^{N} \rho(r_{ij})(x_k^j - x_k^i)^2 = C_V \int_V \rho(r)\Delta x_k{}^2\, dV.$$

3 MAIN CAUSES OF TIME VARIATIONS IN THE ORIENTATION TENSOR

The rate of change of the orientation tensor at the material point under consideration is defined by two factors: (a) the effect of the orientation of the neighboring points of the medium on the orientation of the examined point, and (b) the effect of the thermal motion of polymer chains, which tends to bring the material to the non-oriented state. Hence, the evolution equation of the orientation tensor $\mathbf{O}$ takes the form

$$\frac{1}{b}\frac{D\mathbf{O}}{Dt} = a\left(\langle \tau_j \otimes \tau_j \rangle_V - \mathbf{O}\right) + \left(\frac{\mathrm{I}}{3} - \mathbf{O}\right) + f_*,$$

where $D\mathbf{O}/Dt$ is the objective derivative with respect to time, $\mathbf{I}$ is the unit tensor, and b is the parameter defining the rate of orientation. The use of an additional term f_* allows us to take into account the peculiarities of the laying down of molecules at the interface between the oriented layer and the chaotic matrix. Inside the polymeric layer and the polymeric matrix, the term f_* is equal to zero. The function $a(\mathbf{O} \cdot \mathbf{O})$ is calculated using the following scheme of reasoning.

Under equilibrium conditions, the following equality is fulfilled:

$$\langle \tau_j \otimes \tau_j \rangle_V \cdot \langle \tau_i \otimes \tau_i \rangle_\Gamma = \langle \tau_j \otimes \tau_j \rangle_V \cdot \mathbf{O}.$$

With the Gibbs distribution, it is possible to calculate the average value of probability distribution for the tensor $\tau_i \otimes \tau_i$

$$\langle \tau_i \otimes \tau_i \rangle_\Gamma = \int_\Gamma \tau_i \otimes \tau_i C \exp\left\{-\frac{u_0}{c_B \theta C_V} \times \left(\frac{1}{3} - \tau_i \otimes \tau_i \cdot \langle \tau_j \otimes \tau_j \rangle_V\right)\right\} d\Gamma,$$

where c_B is the Boltzmann constant, and θ is the temperature.

Under equilibrium conditions, the evolution equation of the orientation tensor $\mathbf{O}$ is transformed into the following equation when $f_* = 0$

$$\langle \tau_j \otimes \tau_j \rangle_V = \mathbf{O} + \frac{1}{a}\left(\mathbf{O} - \frac{\mathrm{I}}{3}\right).$$

In this case value of function $a(\mathbf{O} \cdot \mathbf{O})$ should be defined from a condition

$$\left[\mathbf{O} + \frac{1}{a}\left(\mathbf{O} - \frac{\mathrm{I}}{3}\right)\right] \cdot \mathbf{O} = \left[\mathbf{O} + \frac{1}{a}\left(\mathbf{O} - \frac{\mathrm{I}}{3}\right)\right] \cdot \langle \tau_i \otimes \tau_i \rangle_\Gamma,$$

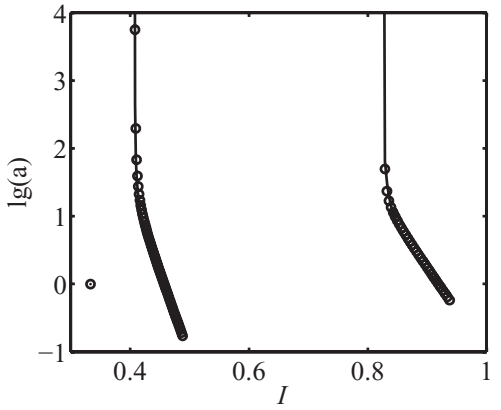

Figure 1. Dependence of the function a on the argument I for uniaxially ($I > 0.8$) and biaxially ($0.4 < I < 0.5$) oriented states, and chaos ($I = 1/3$).

which is valid for the material both inside the polymeric layer and inside the polymeric matrix. The solution of this equation is shown in Fig. 1. The parameter I is equal to $\mathbf{O} \cdot \mathbf{O}$.

Series expansion of the function $\mathbf{O}$ in the vicinity of the considered point yields

$$\langle \tau_j \otimes \tau_j \rangle_V = \mathbf{O} + C_\Delta \sum_{i=1}^{3} \frac{\partial^2 \mathbf{O}}{\partial x_i^2},$$

where

$$C_\Delta = \frac{1}{2} C_V \int_V \rho(r) \Delta x_i^2 dV.$$

Finally, the evolution equation of the orientation tensor $\mathbf{O}$ takes the form

$$\frac{1}{b} \frac{D\mathbf{O}}{Dt} = a\, C_\Delta \sum_{i=1}^{3} \frac{\partial^2 \mathbf{O}}{\partial x_i^2} + \left(\frac{\mathbf{I}}{3} - \mathbf{O} \right) + f_*.$$

4 EXAMPLES OF LAYER FORMATION

Let the term f_* have the following form

$$f_* = (f_u + f_b) \left(\mathbf{O} - \frac{\mathbf{I}}{3} \right),$$

where the functions f_u and f_b depend on the parameter I. These functions describe the formation of layers in the polymeric material, where the polymeric chains are uniaxially and biaxially oriented. In the remaining material, these functions are equal to zero.

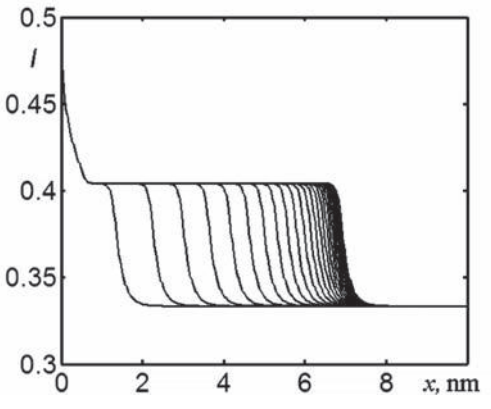

Figure 2. Layer formation near the filler surface (one-dimensional formulation of the evolution equation).

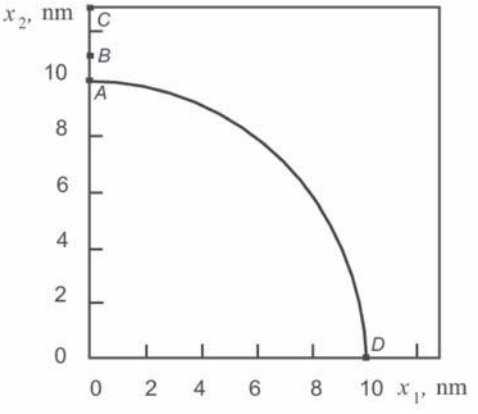

Figure 3. Filled polymer fragment (one fourth of the spherical filler particle.

The functions f_u and f_b are written as

$$f_u = g_u \left(I_u^{max} - I \right) \left(I - I_u^{min} \right), \quad I_u^{min} < I < I_u^{max},$$
$$f_b = g_b \left(I_b^{max} - I \right) \left(I - I_b^{min} \right), \quad I_b^{min} < I < I_b^{max}.$$

Here, g_u and g_b are constants. The values I_u^{max} and I_b^{max} are equal to the values of the parameter I, at which the function $a(I)$ has the minimal values for uniaxially and biaxially oriented states (Fig. 1). On the other hand, the values I_u^{min} and I_b^{min} are equal to the values of the parameter I, at which the function $a(I)$ has the maximal values for uniaxially and biaxially oriented states.

Let us assume that, in the biaxially oriented area (near the orientation source), the parameter of the rate of orientation b changes under the law

$$b = b_1 \exp(-b_2 t),$$

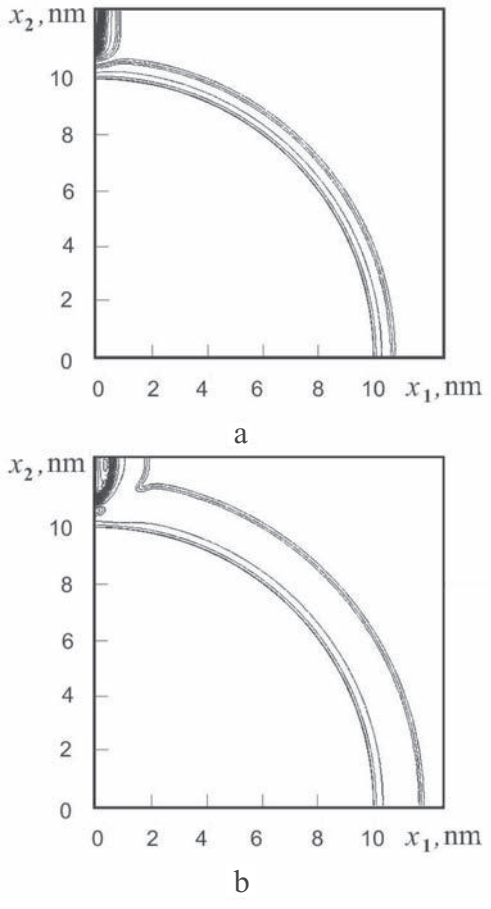

Figure 4. Layer formation in the gap between the filler particles for two moments of time: 400 s (a); 1000 s (b).

where b_1 and b_2 are constants.

The time history of layer formation in the material in the one-dimensional formulation is presented in Fig. 2. It is seen that the process of formation of layers has a frontal character. The lines illustrating the movement of the front are given with equal time steps, $\Delta t = 10$ s. The extreme left line corresponds to $t = 10$ s, and the extreme right line to $t = 300$ s. In the presence of the orientation source, the maximal layer thickness is equal to about 8 nanometers. Thus, the distinct boundary between the strictly oriented area and the area of chaotic orientation is observed.

Let us consider one more example. The evolution equation is used to model the change of the orienta-tional state of polymer molecules in the presence of two orientation sources of f_u and f_b. The first source orients the molecules in the uniaxial direction, while the second in the biaxial direction. The fragment of the filled polymer containing one fourth of the spherical filler particle is presented in Fig. 3. The radius of the particle R is equal to 10 nanometers. The thickness of the gap between the filler particles is equal to 0.5 R. Let the source f_u operate along the line BC, and the source f_b along the line AD.

The results illustrating this process are shown in Fig. 4 for two moments of time: 400 s (a); 1000 s (b).

5 CONCLUSIONS

Numerical experimentation reveals a distinct boundary between the areas of oriented and non-oriented polymer. The oriented layers formed near the active filler particles occupy large part of the volume of polymeric nanocomposite. This fact is supposed to be the main cause of significant changes in the mechanical properties of filled materials at the macroscopic level.

ACKNOWLEDGEMENT

The research was supported by the Russian Foundation for Basic Research and Perm region Department of Industry, Innovations and Science (grant 07-08-96017) and DFG-FOR 597.

Constitutive Models for Rubber VI – Heinrich et al. (eds)
© 2010 Taylor & Francis Group, London, ISBN 978-0-415-56327-7

Modelling the effects of various contents of fillers on the relaxation rate of filled rubbers

L. Laiarinandrasana, A. Jean, D. Jeulin & S. Forest
MINES ParisTech, Centre des Matériaux, CNRS UMR 7633, Evry Cedex, France

ABSTRACT: The present work is devoted to numerical investigations on viscoelasticity of filled rubbers, with the help of experimental data on stress relaxation with time. The evidence is that increasing the content of rigid particles such as fillers or even crystallization index, results in higher value of the stress relaxation rate. This peculiar result seems to indicate that higher rigid particle contents promote the macroscopic viscoelastic strain. To better understand this effect, finite element analyses are carried out on 2D axi-symmetrical unit cell as well as 3D tetracaidecaedron periodic cell.

1 INTRODUCTION

The extensive applications of elastomers in industry and civil fields nowadays motivate many investigations dealing with continuum mechanics and material science on rubbers. Usually the used rubbers are filled with active fillers like carbon black or silica. The filler-aggregates configurations are arranged in order to enhance essential properties like stiffness, strength, abrasion resistance, fatigue lifetime… Many constitutive studies focused on both Payne and Mullins' effects the main characteristic of which is the stress-softening related to nonlinearities induced by strain.

The present work is devoted to the characterisation of viscoelasticity of filled rubbers, with the help of experimental data on stress relaxation with time. In Figure 1, (Omnes, 2007) reported that increasing the content of rigid particles such as fillers results in higher value of the stress relaxation rate. This phenomenon was also encountered on crystallization during relaxation (Gent, 1998). This peculiar result seems to indicate that higher rigid particle contents promote the macroscopic viscoelastic strain whereas classical viscohyperelastic models cannot capture this effect.

The approach proposed in this work deals with an attempt to model the relaxation rate, first, with the help of computations on unit cell (cylinder with spherical particle). By changing only the amount of the particle contents, the deviation from the experimental data will be shown. Alternatively, changing the stiffness of the particle (for a given content) seems to give better results.

The extension of the unit cell into 3D microstructure is the proposed. To this end, periodic tetrakaidecaedron cells are investigated. Comparison of results between unit and periodic cell(s) is discussed.

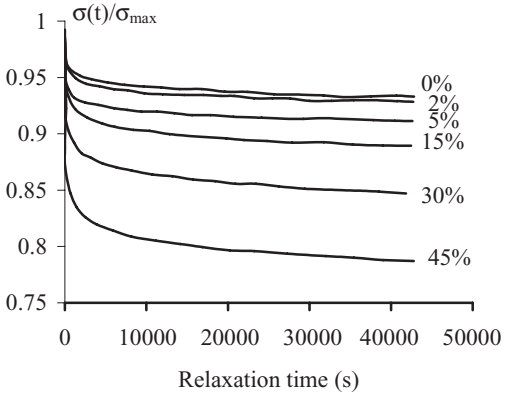

Figure 1. Evolution of the stress relaxations corresponding to four particles contents (0% w, 2% w; 5% w; 15% w; 30% w; 45 w) according to Omnes (2007).

2 NUMERICAL APPROACH ON UNIT CELL

2.1 *Axi-symmetrical unit cell*

The unit cell meshes are illustrated in Figure 2. Let f be the particle volume fraction, r, R and $2h$ respectively the radius of the particle, the radius and the height of the outer cylinder. f is expressed as follows:

$$f = \frac{\frac{4}{3}\pi r^3}{2\pi R^2 h} = \frac{2r^3}{3R^2 h} \tag{1}$$

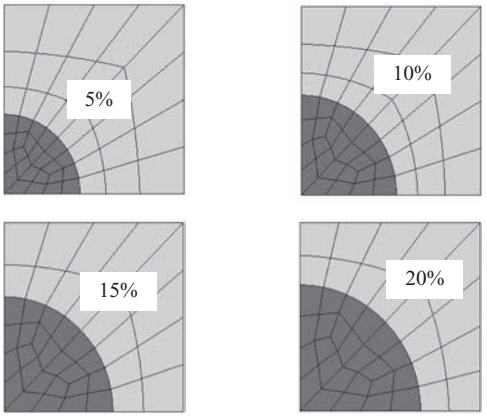

Figure 2. Axi-symmetrical unit cell meshes corresponding to four particles contents (5; 10; 15; 20%).

Since the meshing was carried out with unit length of R and h, the particle volume fraction is function of the particle radius:

$$r = \sqrt[3]{\frac{3f}{2}} \tag{2}$$

Hence the indicated particle volume fractions are obtained via Equation 2.

2.2 *Visco-hyperelastic constitutive equations, material coefficients*

The classical generalized Rivlin deformation energy $W_m = c_{10}(I_1-3) + c_{01}(I_2-3) + c_{20}(I_1-3)^2 + c_{30}(I_1-3)^3$ was used ($c_{10} = c_{01} = 0.46$ MPa; $c_{20} = 0.15$ MPa) for the matrix. The viscoelasticity is ensured by two terms Prony series $(g_1, \tau_1) = (0.3, 0.01)$ and $(g_2, \tau_2) = (0.1, 0.2)$.

For the particle, $W_p = c_{30}(I_1-3)^3$ but $c_{30} = 1$ MPa. This value will vary, in order to study the effect of the stiffness of the particle.

FE computations of uniaxial stress relaxation were done at a prescribed strain of 2. The maximum stresses corresponding to this strain increases with respect to the filler contents.

2.3 *Fillers volume fraction effects*

Figure 3 shows, for the axi-symmetrical unit cell, the first Piola Kirschoff stress relaxation ratios ($\sigma(t)/\sigma_{max}$) plotted against the relaxation time: $\sigma(t)$ is the current stress, σ_{max} is the uni-axial stress obtained at the end of the loading step and the relaxation time begins at the end the loading step. Figure 3 clearly shows that increasing the particle content results in stiffening the compound, that is decreasing the "asymptotic" stress relaxation rate. In fact this intuitive effect can

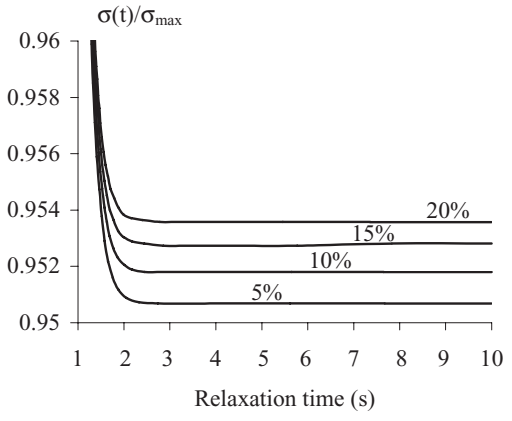

Figure 3. Relaxation rate for the axi-symmetrical unit cell.

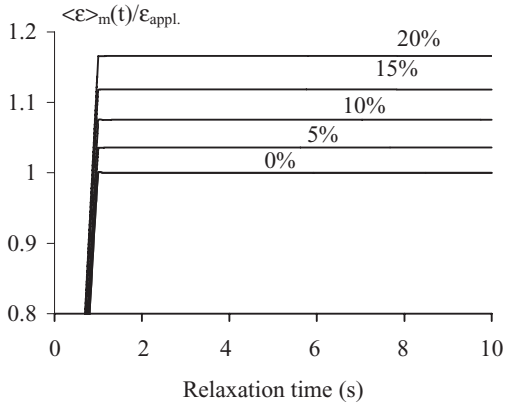

Figure 4. Strain amplification.

be easily explained by the fact that when $f = 100\%$ the stress relaxation rate should vanish.

Local analyses of the strain indicate that there is a heterogeneous state of deformation. The maximum strain is located at a small distance from the pole of the particle. Figure 4 shows the strain amplification in terms of the mean strain in the matrix, in the tensile direction, normalized by the applied strain ($\varepsilon_{appl} = 2$). It can be observed that all ratios are higher than unity, meaning that there is indeed strain amplification. Additionally, the higher the filler content, the higher the strain amplification. This effect is supposed to be due to gage length effect, regarding the maximum strain.

By plotting the Cauchy stress relaxation rate within the rubber matrix only $\langle\sigma\rangle^m(t)/\langle\sigma\rangle^m_{max}$, results are given in Figure 5. There is clearly a contrast between the trends of the first Piola Kirschoff stress relaxation rate (Figure 3) and the

matrix Cauchy stress relaxation rate (Figure 5). The latter seems to be in accordance with the experimental data (Figure 1).

2.4 *Particle stiffness effects*

Following the Rivlin deformation energy in section 2.2 for the particle, c_{30} was prescribed to respectively take the values 0.0012 MPa, 0.018 MPa, 0.118 MPa and 1 MPa. f is fixed at 20%. c_{30} values were selected such that the same maximum stresses for various filler contents as in section 2.3 were obtained.

Figure 6 shows the impact of the stiffness of the particle on the first Piola Kirschoff relaxation rate. The system tends to relax more by increasing the rigidity of the fillers. This is understandable in the case of crystallizing rubber during relaxation: the stiffness of the crystallite phase gradually increases during the crystallization process. For a specific filler, the trend in Figure 1 seems to deal with stiffness increasing with the filler content. Thus, corresponding to a filler content concentrated in the spherical particle within the unit cell, one would find an apparent stiffness that compensates the variation of stress relaxation rate.

In the same way as in section 2.3, let us plot the strain amplification in the matrix (Figure 7). The ratios are of the same order of magnitude than when increasing the filler contents.

Figure 8 illustrates the evolution of the Cauchy stress relaxation rate according to the stiffness of particle. Increasing the stiffness of particles results in the same trend in the relaxation rate in both Piola Kirschoff and matrix Cauchy stresses.

In Figures 5 and 8, it should be mentioned that the Cauchy mean stress within the matrix is uniaxial. The increasing strain amplification due to filler contents induces higher stress levels. Under visco-hyperelasticity, this presumably increases the stress relaxation rate.

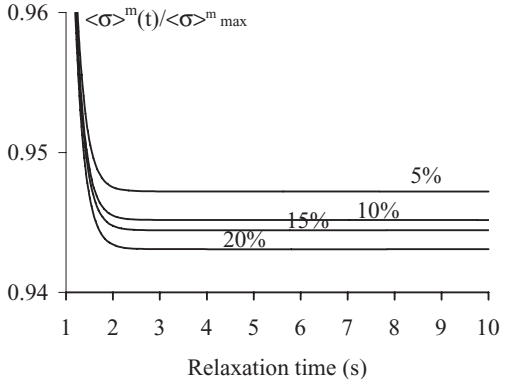

Figure 5. Matrix Cauchy stress relaxation rate for the axi-symmetrical unit cell.

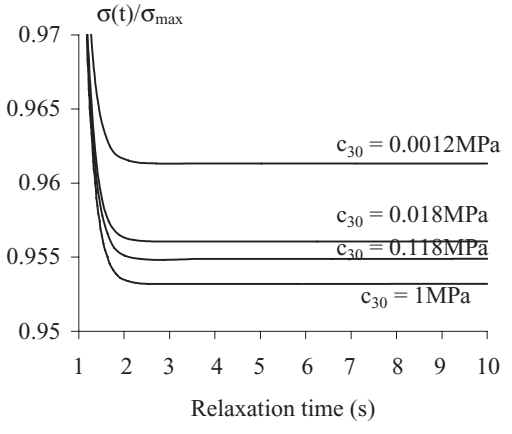

Figure 6. Particle stiffness effect.

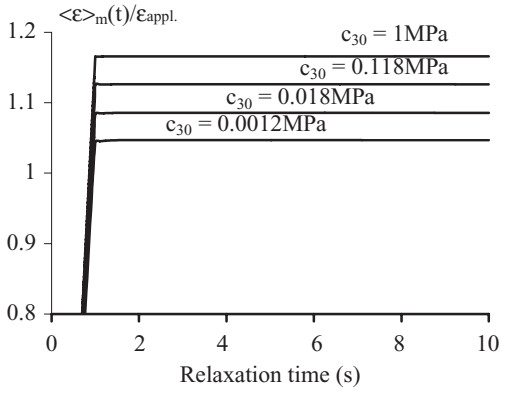

Figure 7. Strain amplification.

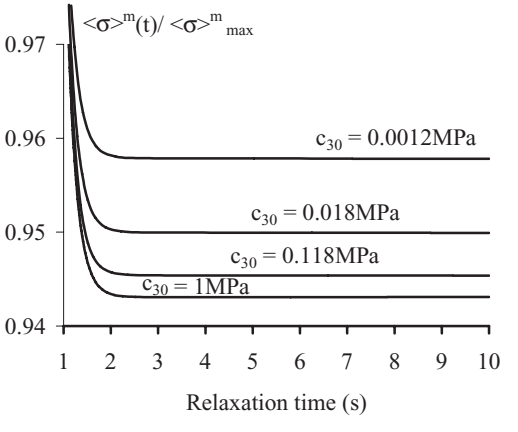

Figure 8. Matrix Cauchy stress relaxation rate for the axi-symmetrical unit cell.

3 NUMERICAL APPROACH ON PERIODIC CELLS

In fact, axi-symmetrical geometry is a too simplistic model far from the real microstructure, such that 3D effects cannot be accounted for. In her PhD work, Jean (2009) attempted to mesh real carbon black filled rubbers with various filler contents.

3.1 *Meshing of real microstructure*

By using TEM images of the microstructure, more realistic models of microstructures which take the cluster effect of fillers into account, can be attempted.

The approach consists in using morphological models like Boolean models combination (Savary et al. 1999), (Delarue, 2001), (Moreaud and Jeulin, 2005), (Jean et al. 2007). Figure 9 shows an example of simulation of microstructure. But computation on such a mesh is very huge. Therefore, in order to extend the 2D axisymmetrical case of study, a simple periodic 3D cell, called tetrakaidecaedron cell (Weaire, 2008), is proposed.

3.2 *Tetrakaidecaedron cell*

The tetrakaidecaedron cell (Figure 10) consists of eight hexagons and six squares. The geometry confers to the cell a symmetry of fifth order. The ideal microstructure is obtained by placing a spherical particle at the center of cell. The periodic symmetry leads to a centered cubic symmetry of fillers in the rubber matrix (Figure 11).

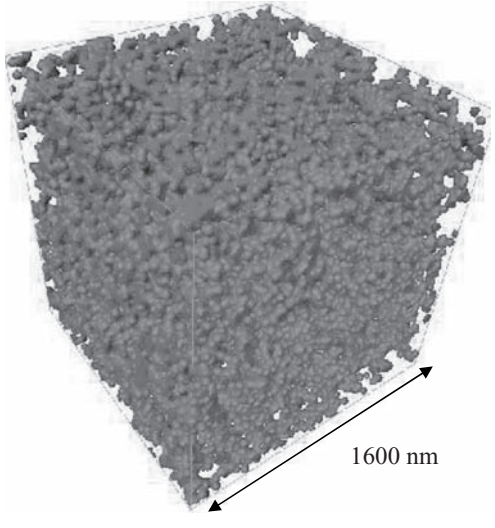

Figure 9. Example of simulation of microstructure containing 60000 spherical particles.

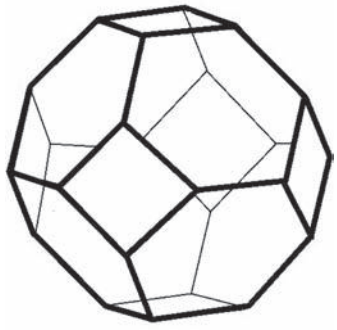

Figure 10. Tetrakaidecaedron cell.

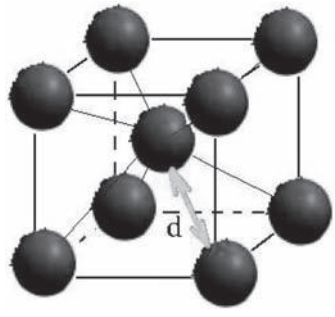

Figure 11. Periodic pattern of fillers in matrix.

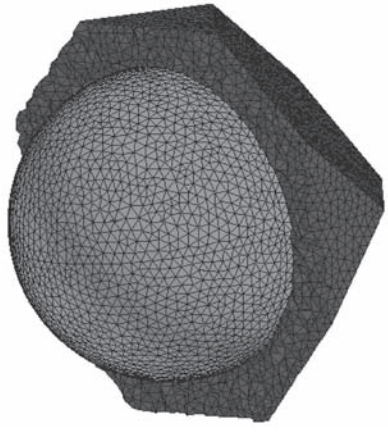

Figure 12. Mesh of tetrakaidecaedron cell containing a spherical particle inside (34268 nodes, 190380 elements).

The volume fraction is expressed as follows:

$$f = \sqrt{3}\left(2 + \frac{d}{R}\right)^{-3} \tag{3}$$

where R is the radius of a particle and d the inter-distance between particles.

By increasing the volume fraction of particles, the inter-distance *d* is decreasing. This «idealized» microstructure does not take into account the cluster effect in the sense of union of more than one particle. Figure 12 illustrates a mesh of a tetrakaidecaedron cell containing 40% of fillers. A particular meshing (GMSH, 2001) (Besson & Foerch, 1997) procedure had to be performed due to the needs of periodic mesh for the periodic computation.

3.3 *Simplified constitutive relations—material coefficients*

Due to the size of the 3D mesh, a simplified small deformation linear viscoelastic behavior was used. The particle is supposed to be linear elastic with a Young's modulus E = 80 GPa and a Poisson ratio $\nu = 0.3$.

For the matrix the bulk modulus is K = 3 GPa whereas the shear modulus is G = 1 MPa. The viscoelasticity, acting only on the shear terms, is ensured by three components of a Prony series $(g_1, \tau_1) = (0.45, 13)$; $(g_2, \tau_2) = (0.33, 455)$ and $(g_2, \tau_2) = (0.24, 1800)$.

Similarly to 2D axi-symmetrical computations, uniaxial mean stress state is ensured by the boundary conditions during the relaxation.

3.4 *Fillers volume fraction effects*

Figure 13 illustrates the case of 3D microstructure using tetrakaidecaedron cell where the volume fraction of particles is varying from 0% to 40%.

It turns out that neither the axi-symmetrical unit cell nor the 3D tetrakaidecaedron cell allow to retrieve the relaxation experimental data (see Figure 1). Indeed, in contrast with numerical results, the material tends to relax more with increasing volume fraction of fillers.

By plotting the histogram dealing with fraction of matrix against the axial strain normalized by the mean strain at the end of the calculation (Figure 14), it is observed that there is a strain heterogeneity, that is well distributed within the whole matrix. It can be seen in Figure 14 that about 14% of the matrix elements have an axial strain value similar to the applied one. The maximum value of the strain amplification is about 3.5.

Presumably, this strain amplification would not induce stress relaxation due to the used small strain viscoelastic constitutive relationships.

About the stress distribution at the end of the stress relaxation computation, Figure 15 plots the fraction of matrix elements with respect to respectively σ_{11}, σ_{22} and σ_{33} normalized by the $\langle\sigma_{11}\rangle_{tot}$ corresponding to the applied stress.

Although the applied stress is uni-axial, it turns out that within the matrix the stress state is

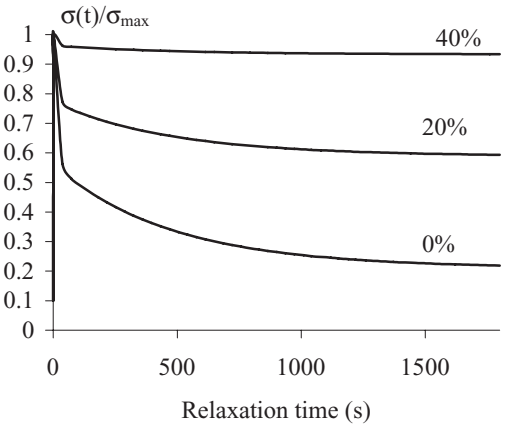

Figure 13. Relaxation rate for the periodic tetrakaidecaedron cell.

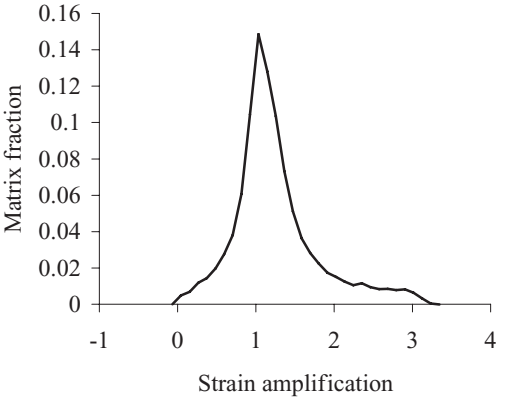

Figure 14. Fraction of matrix elements with respect to strain amplification.

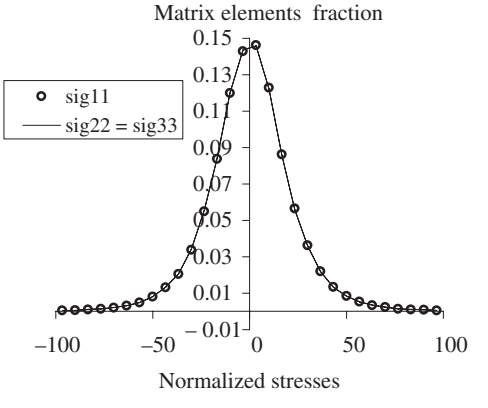

Figure 15. Fraction of matrix elements with respect to normalized σ_{11}, σ_{22} and σ_{33} stresses.

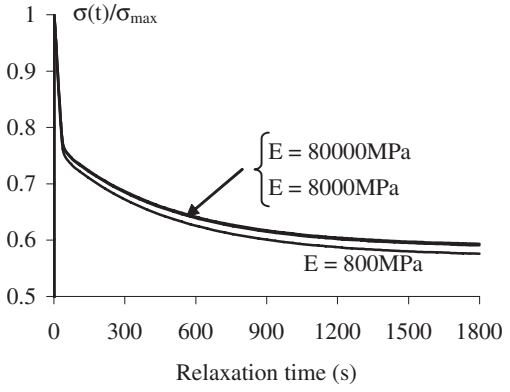

Figure 16. Normalized stress relaxation rate for the periodic tetrakaidecaedron periodic cell filled with 20% of particle and for three values of the particle Young's modulus.

tri-axial, which makes the difference regarding that of the axisymmetrical unit cell. Additionally, it should be mentioned that the curves are centered (peak values) to 1 for σ_{11} and to 0 for $\sigma_{22} = \sigma_{33}$. Further detailed investigations have to be carried out about this effect.

3.5 *Particle stiffness effects*

By using the same 3D tetracaidecaedron periodic cell, the Young's modulus of the particle (with filler content of 20%) was assigned to take three values: 80000 MPa (as in previous calculation), 8000 MPa and 800 MPa. Figure 16 shows the normalized stress relaxation rate.

In contrast with what was observed in 2D axisymmetrical unit cell, Figure 16 indicates that by increasing the stiffness of the particles, the stress relaxation rate decreases. Moreover, it is observed that a change of the Young's modulus from 80000 MPa to 8000 MPa leads to only a very slight effect on the stress relaxation rate. Again, it has to be analyzed further in order to better understand the effect of the 3D dispersed fillers.

4 CONCLUSION

The present work starts with the experimental evidence that higher rigid particle contents promote the macroscopic viscoelastic strain. Classical visco-hyperelastic models cannot capture this effect.

Numerical FE analyses were carried out on 2D axi-symmetrical unit cell, as well as 3D tetracaidecaedron periodic cell. Under 2D investigations, the experimental trend cannot be reproduced by increasing the volume fraction of the particle content but by the increase in the stiffness of the particle. Locally, the strain amplification leads to higher Cauchy stress relaxation due to non linearity in the elasticity (hyperelasticity).

3D periodic cell simulations showed that neither the increase in the particle content, nor the stiffening of the filler particle allow to capture the stress relaxation rate. FE simulations showed that strain amplification occurred within the rubber matrix. Additionally, whereas the applied stress is uniaxial, it was observed that within the matrix the stress state is tri-axial.

REFERENCES

Besson, J., and Foerch, R., 1997. *Computer Methods in Appplied Mechanics and Engineering* 142:165–187.

Delarue, A., 2001. Prévision du comportement électromagnétique de matériaux composites à partir de leur mode l'élaboration et de leur morphologie. *PhD, Mines-ParisTech*.

Gent, A.N., Kawahara, S., and Zhao, J., 1998. Crystallization and strength of natural rubber and synthetic cis-1.4-polyisoprene, *Rubber Chemistry and technology* 71:668–678.

GMSH, 2001: A three-dimensional finite element mesh generator with built-in pre- and post-processing facilities: Christophe Geuzaine and Jean-François Remacle. http://geuz.org/gmsh/

Jean, A., Jeulin, D., Forest, S., Cantournet, S., Mounoury, V., and N'Guyen, F. 2007. Rubber with carbon black fillers: Parameters identification of a multi-scale nanostructure model. *Proc. of European Conference on Constitutive Models for Rubber V*, Paris.

Jean, A. 2009. Etude d'un élastomère chargé, de la nanostructure au macro-comportement *PhD, Mines-ParisTech*.

Moreaud, M., and Jeulin, D., 2005. Multi-scale simulation of random spheres aggregates. *6th International Conference of Stereology, Spatial Statistics and Stochastic Geometry*. Prague.

Omnes, B., 2007. Modélisation micromécanique du comportement d'élastomères chargés. *PhD Université de Bretagne-Sud*.

Savary, L., Jeulin, D., and Thorel, A., 1999. Morphological analysis of carbon-polymer composite materials from thick section. *Acta stereologica* 18 (3): 297–303.

Weaire, D., 2008. Kelvin's foam structure: a commentary. *Philosophical Magazine Letters*.

Constitutive Models for Rubber VI – Heinrich et al. (eds)
© 2010 Taylor & Francis Group, London, ISBN 978-0-415-56327-7

A microstructure-based model of the stress-strain behaviour of filled elastomers

H. Lorenz & M. Klüppel
Deutsches Institut für Kautschuktechnologie e.V., Hannover, Germany

ABSTRACT: To calculate the mechanical behavior of a loaded component the engineer needs a model which describes the stress-strain-behaviour. In order to relate the properties of rubber and filler to those of a filled elastomer we use a microstructure-based approach where material parameters are physical quantities, instead of mere fit parameters. Core of the model is the hydrodynamic reinforcement of rubber elasticity (tube model) by stiff filler clusters. The deformation is concentrated at a smaller part of the total volume, resulting in an amplification of stress. Under stress, clusters can break and become soft, leading to deformation of larger parts of the volume and related stress softening. The effect is expressed as an integral over the "surviving" section of the cluster size distribution. On the other hand, cyclic breakdown an re-agglomeration of soft clusters causes hysteresis. Filled elastomers also show an inelastic set behavior. The corresponding stress contribution is modeled by a semi-empirical dependency with respect to maximum deformation. Using dumbbell specimens, we have done uniaxial stress-strain measurements in tension an compression. Parameterfits show that the model satisfactorily describes compression and tension -tests. Generally, the parameters lie in a physically reasonable range. For the first time hydrodynamic reinforcement (formulated by a reinforcement exponent) and stress softening have been implemented into FE-code. A rolling rubber wheel under load is simulated.

1 INTRODUCTION

Nanoscopic filler materials like carbon black or silica play an important role in reinforcement of elastomers. Besides making the elastomer stiffer and tougher, the incorporation of a filler brings about a non-linear dynamic-mechanical response reflected by the amplitude dependence of the dynamic moduli. This effect was investigated by several authors like Payne (Kraus 1965) and Medalia (1973). A related effect is the stress softening under quasi-static cyclic deformation, which was studied by Mullins intensively (Kraus 1965). A drop in stress usually occurs after the loading history has gone beyond the previous maximum. Most of the stress drop at a certain strain occurs in the first cycle, and in the following cycles the specimen approaches a steady state stress-strain curve. A second characteristic effect caused by fillers is the pronounced hysteresis, which leads to the dissipation of mechanical energy.

All these effects are temperature- and time-dependent and are interrelated due to their common origin, but neither the elastomer nor the powderous filler alone shows such behaviour. Where the filler itself can be treated as composed of relatively stiff particles, also the entropy elastic behaviour of the elastomer or rubber matrix is quite well understood (Heinrich et al. 1988, Klüppel & Schramm 2000).

To understand the stress-strain behaviour of filled elastomers the nanostructure of the filler particles and their interaction with the polymer are of basic significance. During the deformation history a dynamic creation and damage of filler-filler bonds, i.e. glassy polymer bridges of some nanometers in thickness (Klüppel & Schramm 2000, Klüppel & Meier 2001, Klüppel 2003, Klüppel et al. 2003, Klüppel et al. 2005), takes place. This damage of bonds is structurally reversible. A steady state stress-strain cycle results, when the same amount of bonds is damaged and recovered during a cycle (Kraus 1984).

If the filler volume fraction in a compound goes beyond a critical value, a percolated filler network is formed during the vulcanization process. But, already under low deformations this network starts to break down, and the storage modulus drops from relatively high to low values. The remaining fragments are clusters of filler particles which are still capable of reinforcing the rubber matrix (Klüppel et al. 1997, Meakin 1988, Havlin & Bunde 1991, Huber & Vilgis 1998). The principal mechanism is called hydrodynamic reinforcement. The branched clusters which are relatively stiff immobilize a certain amount of rubber. So, the deformation is concentrated in the remaining part of the matrix, the local strain is higher than the global external strain, and the measured stress is accordingly increased.

With increased loading, clusters are successively broken, and more rubber takes part in the deformation, which in turn leads to the observed stress softening. On the other hand, cyclic breakage and re-agglomeration of damaged clusters causes the observed hysteresis.

In the present report we will formulate the basic assumptions of our reinforcement theory. Then we will adapt the model equations to measured stress-strain cycles of filled elastomers, whereby compression and tension tests will be considered. The main part of the model which describes hydrodynamic reinforcement and stress softening has also been implemented into the Finite-Element-Method (FEM). As one example, a rolling rubber wheel under load will be simulated. The results will be discussed in the frame of the physically well understood material parameters obtained from the fitting procedures.

2 EXPERIMENTAL

2.1 *Sample preparation*

To identify parameter for the micromechanical model and to verify the model in further simulations, measurements were carried out with unfilled and filled rubber compounds. Carbon Black (CB) was mixed into styrene butadiene rubber (SBR, VSL 5025-0). Also, a CB-filled blend with butadiene rubber (BR, Buna CB 10) was examined which is a typical tire tread compound from industrial practice. The corresponding mass fractions in phr (per hundred rubber) are listed in table 1 which also includes the vulcanization agents, i.e. ZnO, stearic acid and a semi-efficient cross-linking system (sulfur + accelerator CBS), and anti-ageing IPPD. The compounding was prepared using an internal mixer, Werner & Pfleiderer GK 1,5E.

The whole compound was rolled for a homogeneous distribution and then allowed to rest for 2 h, before the vulcanization time t_{90} at 160°C was determined with a Monsanto vulcameter. For uniaxial testing, axial-symmetrical dumbbells were used.

2.2 *Multihysteresis measurements*

Uniaxial multi-hysteresis tests at $\dot{\varepsilon} \approx 0.01$/s and $T = 22$°C were carried out on dumbbells, 15 mm in thickness, using a Zwick 1445 universal testing machine. For strain measurement, two reflection marks were placed in a 15 mm distance. Multi-hysteresis means: at constant velocity up and down -cycles between certain minimum and maximum strains, $\varepsilon_{\min}$ and $\varepsilon_{\max}$, are carried out. This is done 5 times each step, and after every of such steps the boundaries of deformation are successively raised ($\varepsilon_{\max}$) or lowered ($\varepsilon_{\min}$), respectively. Only every 5th up and down -cycle are evaluated, which can be regarded as being steady state in a good approximation.

Table 1. Components of the investigated compounds in phr.

Compound	SBR 5025	BR CB 10	Filler N115	Filler N339	ZnO	Stearic acid	X-linking S	X-linking CBS	X-linking IPPD
S60N1	100		60		4	1	1.7	2.5	1.5
S60N3	100			60	4	1	1.7	2.5	1.5
SB6R2	85	15		60	3	1	1.7	2.5	1.5

3 THEORY

The Helmholtz free energy density of a filled elastomer constitutes the elastic material function and can be described as the sum of matrix and filler contributions (Klüppel 2003, Klüppel et al. 2005):

$$W = \left(1 - \Phi_{eff}\right) W_R + \Phi_{eff}\, W_A \tag{1}$$

where W_R is calculated for the entropy-elastic rubber phase, and W_A is the energy-elastic contribution of the fragile agglomerates (damaged clusters) of filler particles. The respective stress components are obtained as the derivatives with respect to ε. Φ_{eff} stands for the mechanical effective filler volume fraction (which is larger than the real volume fraction, because of rubber occluded in the aggregates).

To describe the hyperelastic behavior of the rubber matrix, we use the non-affine tube model with non-GAUSSian extension (Heinrich et al. 1988, Klüppel & Schramm 2000).

We can assume the presence of filler clusters dispersed in the rubber matrix. A filler cluster is thought to be composed of spherical particles (with diameter d) and to have a diameter ξ_μ in each space direction μ. The relative size x_μ is the ratio ξ_μ/d. Also, a SMOLUCHOWSKI type of cluster size distribution, $\phi_\mu(x)$, is adopted, according to the kinetics of cluster-cluster aggregation (CCA), Klüppel (2003):

$$\phi_\mu(x) = \frac{4x}{\left\langle x_\mu \right\rangle^2} e^{-2\frac{x}{\left\langle x_\mu \right\rangle}}, \tag{2}$$

where $\langle x_\mu \rangle$ stands for the average cluster size. Previously, an isotropic cluster size distribution $\langle x_1 \rangle = \langle x_2 \rangle = \langle x_3 \rangle \equiv x_0$ has been used. To account for a preconditioning of clusters under compression, we use an anisotropic cluster size distribution here as derived by Witten et al. (1993) which states that clusters deform like the specimen

as a whole. This means: $\langle x_\mu \rangle = \lambda_{\mu,\min}\, x_0$, x_0 being the initial isotropic average cluster size and $\lambda_{\mu,\min}$ the minimal deformation ratio that has occurred during the deformation history in space direction μ.

A crucial point in our approach which we call "dynamic flocculation model" are the bonds between filler particles. Under the load transferred from the matrix to the clusters the filler-filler bonds can break. The strength of damaged filler-filler bonds is reduced, compared to the virgin bonds. The following paragraph describes the stress contribution of the hydrodynamically reinforced matrix. We are mainly interested in the response to uniaxial loading in 1-direction which fulfils the symmetry conditions $\lambda \equiv \lambda_1$ and $\lambda_2 = \lambda_3 = \lambda^{-1/2}$.

3.1 *Hydrodynamic strain amplification*

Due to the presence of the filler, only parts of the material volume are deformed under an external strain ε or relative deformation $\lambda = 1 + \varepsilon$. We describe the local strain of the rubber matrix as multiplied by a factor X, and the local stretch $\kappa = 1 + X\varepsilon$.

Because of the fractal geometry of undamaged, stiff clusters, we can use a result of Huber & Vilgis 1998 for overlapping CB aggregates. They calculated an amplification factor X that is proportional to powers of filler volume fraction and relative aggregate diameter. All of the stiff clusters contribute to X. Damage of stiff clusters causes stress softening by decreasing X, which is expressed as an integral over the "surviving", hard, section of the cluster size distribution and is a function of the maximum deformation the material has been subjected to in its entire deformation history (Klüppel et al. 2005):

$$X_{\max} = X\left(\varepsilon_{\min}, \varepsilon_{\max}\right) = 1 + \frac{c}{3}\Phi_{eff}^{\frac{2}{3-d_f}} \sum_{\mu=1}^{3} \left(\int_0^{x_{\mu,\min}} x^{d_w - d_f}\, \phi_\mu(x)\,\mathrm{d}x + \int_{x_{\mu,\min}}^{\infty} \phi_\mu(x)\,\mathrm{d}x \right) \quad (3)$$

where the constant c is taken to be ≈ 2.5, the EINSTEIN coefficient for spherical inclusions. The exponent d_w stands for the anomalous diffusion exponent which amounts to ≈ 3.1 (Klüppel et al. 1997), and d_f is the fractal dimension of the filler clusters (≈ 1.8 for CCA, Meakin 1988).

To solve the integrals analytically, we make use of an approximation for the exponent $d_w - d_f = 1$. The solution of this expression can be found by inserting the cluster size distribution eq. (2) into the integrals. For an explicit evaluation of this strain amplification factor, we also have to calculate the integration limits. The tensile strength of damaged bonds s_d (which governs the amount of hysteresis) can be expressed by their failure strain $\varepsilon_{d,b}$ and elastic modulus Q_d/d^3, the same is valid for virgin bonds where we use the index "v". As depicted in Klüppel (2003), the cluster strain under a certain load rises stronger with cluster size than the failure strain does. Accordingly, with rising load, large clusters break fist followed by smaller ones. The critical size of currently breaking clusters was accordingly derived:

$$x_\mu(\varepsilon) = \frac{Q_d \varepsilon_{d,b}}{d^3 \hat{\sigma}_{\mathrm{R},\mu}(\varepsilon)} = \frac{s_\mathrm{d}}{\hat{\sigma}_{\mathrm{R},\mu}(\varepsilon)}. \quad (4)$$

The strength of virgin bonds s_v governs the strain amplification factor X, because it enters into the minimum size of damaged clusters $x_{\mu,\min}$ and consequently into the integration limit of eq. (3):

$$x_{\mu,\min} = \frac{Q_\mathrm{v} \varepsilon_{\mathrm{v,b}}}{d^3 \hat{\sigma}_{\mathrm{R},\mu}(\varepsilon_{\max})} = \frac{s_\mathrm{v}}{\hat{\sigma}_{\mathrm{R},\mu}(\varepsilon_{\max})}. \quad (5)$$

The two parameters s_d and s_v, i.e. the tensile strength of damaged and virgin filler-filler bonds can be treated as fitting parameters.

3.2 *Constance of volume*

For unfilled as well as for filled elastomeres it has been found experimentally that the volume remains more or less constant during deformation. This makes it possible to derive a uniaxial stress from $W(\varepsilon)$ as a total derivative to axial strain and to calculate mutual derivatives of strains. On the other side, the condition of volume constance has to be taken into consideration for strain amplification, if large deformations occur.

Mathematically, inner volume constance means:

$$\kappa_1\, \kappa_2\, \kappa_3 = (1 + X_1\varepsilon_1)(1 + X_2\varepsilon_2)(1 + X_3\varepsilon_3) = 1,$$

and outer volume constance means:

$$\lambda_1\, \lambda_2\, \lambda_3 = (1 + \varepsilon_1)(1 + \varepsilon_2)(1 + \varepsilon_3) = 1.$$

If for instance $X_1 = 10$, κ_1 would take on negative values for $\varepsilon_1 < -10\%$, which is not permissible, physically. Therefore, the amplification factor for space directions with negative strain has to depend on strain. For simplicity, we assume that for the direction of largest strain: $X_\mathrm{f} = \text{const.}$ (only dependant on maximum strain) and $X_\mathrm{f} = X_{\max}$ is calculated from eq. (3). Using the assumption of constant volume and uniaxial or equibiaxial symmetry conditions, the other amplification factors can be calculated.

In order to unify the calculation for all required deformation states we use an alternative formalism by introducing an amplification exponent r, equal for all space directions: $\kappa_1 = \lambda_1^r$, $\kappa_2 = \lambda_2^r$, $\kappa_3 = \lambda_3^r$.

$r = 1$ for unfilled rubbers. The formalism immediately satisfies inner volume constance, if outer

volume constance is given. The amplification exponent is dependent on X_{max} and current stretch, λ_f, in direction of maximum strain:

$$\kappa_\mu = \lambda_\mu^r, \quad r = \frac{\ln\left(1+X_{\max}\cdot(\lambda_f-1)\right)}{\ln(\lambda_f)}, \tag{6}$$

while now, for all modes of loading the same quations hold.

3.3 *Hysteresis*

The damaged clusters are softer and elastically more deformable. Cyclic stretching, breakdown (stress release) and re-agglomeration of soft clusters causes hysteresis. The stress-strain relation is formulated in main axes. Within this framework, the reversible fraction of the mechanical energy density spent at soft filler clusters is:

$$W_A(\varepsilon) = \sum_{\mu}^{\partial\varepsilon_\mu/\partial t>0} \frac{1}{2} \int_{x_\mu(\varepsilon_{\max})}^{x_\mu(\varepsilon)} G_A(x)\,\varepsilon_{A,\mu}^2 \times\left(x,\varepsilon_\mu\right)\phi_\mu(x)dx \tag{7}$$

Here, we integrate over the re-agglomerated section of the cluster size distribution $\phi_\mu(x)$, in each space direction μ where clusters are being stretched. In the directions of negative strain rate we assume that no forces shall act on soft clusters, because all of these have been broken in the preceding cycle and are now re-agglomerating. Additionally, we assume that clusters deform plastically when compressed in a certain direction. Therefore, to calculate the strain energy in the up cycle of a uniaxial tension test ($\partial\varepsilon_1/\partial t > 0$), we only consider the axial elastic cluster strains $\varepsilon_{A,1}$. To describe the down cycle ($\partial\varepsilon_2/\partial t$, $\partial\varepsilon_3/\partial t > 0$) the same isochoric state of the material shall be modeled by an equibiaxial compression test that starts at the end of the tension cycle, where still $\varepsilon_{A,2} = 0$.

$$\sigma_{A,\nu} = \frac{\partial W_A}{\partial\varepsilon_{A,\nu}} = \sum_\mu \frac{\partial W_A}{\partial\varepsilon_{A,\mu}}\frac{d\varepsilon_{A,\mu}}{d\varepsilon_{A,\nu}} = \sum_{\mu}^{\partial\varepsilon_\mu/\partial t>0} \hat{\sigma}_{R,\mu}(\varepsilon) \int_{x_\mu(\varepsilon_{\max})}^{x_\mu(\varepsilon)} \frac{d\varepsilon_{A,\mu}(x)}{d\varepsilon_{A,\nu}(x)}\phi_\mu(x)dx \tag{8}$$

The hat over $\sigma_{R,\mu}$ means the matrix stress relative to the start of the cycle. The elastic deformation of clusters is caused by this very "relative stress" which in turn depends on the hydrodynamically amplified local stretch $\kappa_1(\varepsilon)$.

The matrix stress perpendicular to the loading direction, $\sigma_{R,2} = \sigma_{R,3}$, is calculated as the stress that is needed to cause the same deformation, from equivalence of energies, we have:

$$\sigma_{R,2}(\varepsilon) = -\kappa_1(\varepsilon)^{3/2}\,\sigma_{R,1}(\varepsilon). \tag{9}$$

The integral in eq. (8) is an average of a mutual derivative of cluster strains, $d\varepsilon_{A,\mu}/d\varepsilon_{A,\nu}$, which has to be evaluated in order to calculate the down cycle. Because there is no exact solution, we use an approximation. In the uniaxial case, therefore:

$$\left\langle\frac{\partial\varepsilon_{A,2}}{\partial\varepsilon_{A,1}}\right\rangle \approx \frac{\partial\varepsilon_2}{\partial\varepsilon_1} = -\frac{1}{2}(1+\varepsilon_1)^{-3/2}. \tag{10}$$

This means, the re-agglomerated clusters, in the average, shall deform like the specimen as a whole.

3.4 *Set behaviour*

Filled elastomers also show a certain inelastic behaviour called setting which is characterized be a permanent deformation ε_{set} at released load. The corresponding stress contribution has to be described by a term separate from elastic potentials. The set stress σ_{set} is the stress required to get the material back into the un-deformed state. Because the physical mechanism of setting is not fully understood, we utilize a semi-empirical description, where σ_{set} depends on maximum deformation:

$$\sigma_{set} = s_{set,0}\cdot f(\varepsilon_{min}, \varepsilon_{max}) \tag{11}$$

In the expression there is only one free parameter, $s_{set,0}$, which stands for the setting stress at $\varepsilon_{max} = 1$.

4 RESULTS AND DISCUSSION

4.1 *CB–filled rubber in combined compression–tension test*

To identify a parameter set that describes the mechanical behaviour of the compound SB6R2, multihysteresis measurements in combined compression-tension were carried out. Fig. 1 shows the extracted 5th cycles, the set of fitted parameters is given as an inset. Some parameters can be assumed to have specified values. These parameters are recognizable from the fitting error = 0 in the right column. The setting constant $s_{set,0}$ was calculated from the evaluated setting stresses. And the modulus of topological constraints, G_e, should be equal to ≈ 1/2 G_N, the plateau value of un-cross-linked rubber which is 0.6 MPa for SBR, but only under the assumption that there are no filler-induced entanglements.

Generally, the identified parameters are physically reasonable:

- G_c (cross-link modulus) ≈ 2 MPa

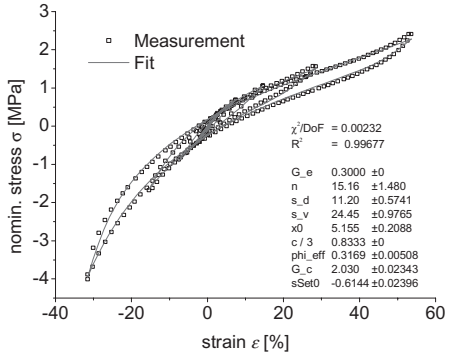

Figure 1. Uniaxial multihysteresis measurement and fit, inset shows parameter set, SB6R2.

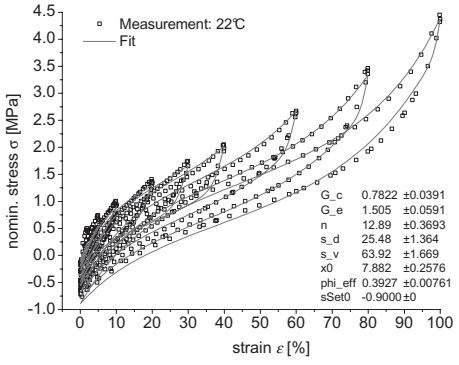

Figure 2. Uniaxial multihysteresis measurement and fit, inset shows parameter set, S60N1.

- $n \equiv n_e/T_e$ (number of chain segments between trapped entanglements) ≈ 15
- s_d and s_v amount to some 10 MPa, whereby: $s_d < s_v$
- $x_0 \approx 5$ is near a typical value of about 10 particles/cluster
- $\Phi_{eff} \approx 0.32$ is higher than the filler volume fraction, $\Phi = 0.24$, and a reasonable value for 60 phr of "structured" CB particles of the grade N339

It has been verified in previous studies that parameters fitted with the dynamic flocculation model vary systematically when the filler volume fraction is varied (Klüppel 2009).

4.2 *Variation of filler particle size*

For investigating the effect of particle size of CB, the compounds S60N1 and S60N3 were tested in a multihysteresis tension mode. The stress-strain curves (5th cycles) are depicted in Fig. 2 and Fig. 3 (symbols), where fits with the dynamic flocculation model (lines) are also shown. The fitted parameters are listed in the legend of the plots, which again appear physically reasonable. For taking into account the effect of surface induced entanglements and for getting better fitting results, in this case the topological constraints modulus, G_e, has also been treated as a fit parameter. It is found to converge at values of G_e = 1.505 MPa (S60N1) and G_e = 1.257 MPa (S60N3), respectively, which are larger than the previously used specified value G_e = 0.3 MPa of the polymer matrix. This indicates that the attractive interaction of the polymer chains with the filler surface increases the entanglement density significantly. We point out that this modification slightly affects the other parameters, but mostly the cross-link modulus G_c which is found to be reduced compared to the fits with G_e = 0.3 MPa.

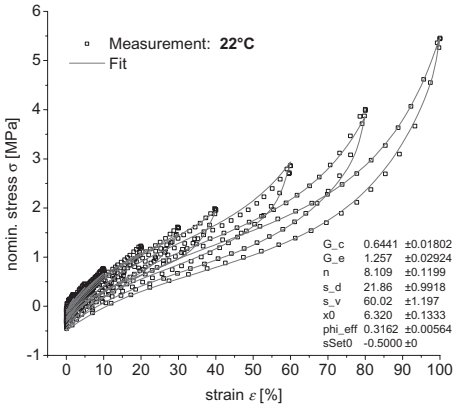

Figure 3. Uniaxial multihysteresis measurement and fit, inset shows parameter set, S60N3.

The two compounds differ in the kind of CB used: N115 (S60N1) and N339 (S60N3). The different morphology of the filler has a considerable effect on the stress-strain behaviour and accordingly on the fit parameters: N115 consists of smaller filler particles with a higher specific surface area. This results in a higher relative cluster size x_0 and Φ_{eff}, at constant Φ, compared to N339 (N115/N339: x_0 = 7.882 / 6.32, Φ_{eff} = 0.3927/0.3162).

N115 is also a more "active" filler, which apparently leads to stronger filler-filler bonds (N115/N339: s_d = 25.48/21.86 MPa, s_v = 63.92/60.02 MPa). But, the filler also affects the parameters of the polymer network: the higher filler surface area of N115 results in higher cross-linking and entanglement-densities (N115/N339: G_c = 1.505/1.257 MPa, G_e = 1.505/1.257 MPa). If more entanglements are present one would also expect a lower n (segments between trapped entanglements), but the trapping fac-

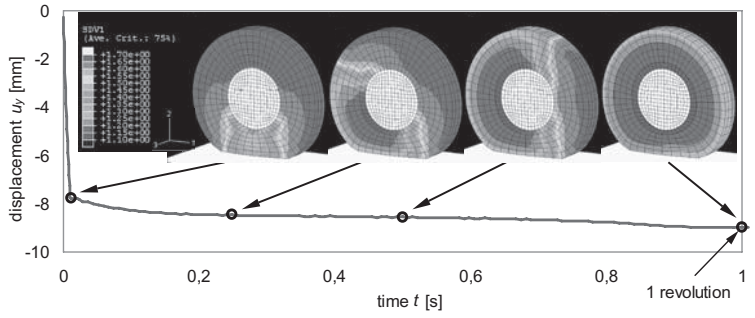

Figure 4. Rigid displacement of the GROSCH wheel found from 3-D FE simulation as a function of time; stress softening expressed by the damage variable r is depicted in the insets for chosen times.

tor, T_e, may also be reduced leading to a higher n for N115: $n = 12.89$, compared to $n = 8.109$ for N339.

4.3 *Finite–element simulation of a rolling wheel*

The main part of the flocculation model which describes hydrodynamic reinforcement and stress softening has been implemented into the Finite-Element-Method (FEM). This was done by referring to a strain amplification exponent, which has been described previously in more detail (Klauke et al. 2005). Here, we demonstrate for the first time the evolution of this damage parameter under practical conditions, i.e. for a rolling rubber wheel (known as "GROSCH wheel"), 80 mm in diameter. This 3-D model was meshed with symmetric boundary conditions in axial 3-direction.

At the beginning of time history, a compressive load of $F_{max} = 1.9$ kN in 2-direction is applied to the middle part which consists of a rigid shaft. Under the load the wheel is compressed by 7.8 mm, as can be seen in Fig. 4. In the following step the wheel rotates around the axis and rolls on the ground, frictionless. Despite the constant load, the displacement increases by 1.2 mm (between the first and last snapshot) while the wheel fulfils one complete revolution. This is due to stress softening, as can be seen from the strain amplification exponent, r. Prior to loading, r is ubiquitously equal to 1.7. It can be observed how it decreases during the test. The smallest values of 1.1 are found near the shaft where, simultaneously, the highest stresses are found. Because the decrease of r corresponds to stress softening, it can be regarded as a kind of damage variable.

REFERENCES

Edwards, S.F., & Vilgis, T.A. 1988. The tube model theory of rubber elasticity. *Rep. Prog. Phys.* 51:243.

Havlin, S., & Bunde, A. 1991. Fractals and disordered systems. Springer.

Heinrich, G., Straube, E., & Helmis G. 1988. Rubber elasticity of polymer networks: theories. *Adv. Polym. Sci.* 85:33.

Huber, G., & Vilgis, T.A. 1998. Universal Properties of Filled Rubbers: Mechanisms for Reinforcement on Different Length Scales. *Euro. Phys. J.* B3:217.

Klauke, R., Meier, J., & Klüppel, M. 2005. FE-Implementation of a constitutive model for stress softening based on hydrodynamic reinforcement. In Boukamel, Laiarinandrasana, Méo & Verron (eds), *Constitutive Models for Rubber V. London:* Taylor & Francis.

Klüppel, M., Schuster, R.H., & Heinrich G. 1997. Structure and properties of reinforcing fractal filler networks in elastomers. *Rubber Chem. Technol.* 70:243.

Klüppel, M., & Schramm, J. 2000. A generalized tube model of rubber elasticity and stress softening of filler reinforced elastomer systems. *Macromol. Theory Simul.* 9:742.

Klüppel, M., & Meier, J. 2001. Modeling of Soft Matter Viscoelasticity for FE-Applications. In D. Besdo, R. H. Schuster & J. Ihlemann (eds), *Constitutive Models for Rubber II*, Lisse: Balkema.

Klüppel, M., 2003. The Role of Disorder in Filler Reinforcement of Elastomers on Various Length Scales. *Adv. Polym. Sci.* 164:1.

Klüppel, M., Meier, J., & Heinrich, G. 2003. Impact of Pre-Strain on Dynamic-Mechanical Properties of Carbon Black an Silica Filled Rubbers. In J.J.C. Busfield & G.A.H. Muhr (eds), *Constitutive Models for Rubber III*. Lisse: Balkema.

Klüppel, M., Meier, J., & Dämgen, M. 2005. Modelling of stress softening and filler induced hysteresis of elastomer materials. In Austrell & Kari (eds), *Constitutive Models for Rubber IV*. London: Taylor & Francis.

Klüppel, M. 2009. Evaluation of viscoelastic master curves of filled elastomers and applications to fracture mechanics. *J. Phys.: Condens. Matter* 21:035104.

Kraus, G. (ed.) 1965. *Reinforcement of elastomers*. N.Y. London Sydney: Wiley, Interscience Publ.

Kraus, G. 1984. Mechanical Losses in Carbon-Black-filled Rubbers. *J. Appl. Polym. Sci., Appl. Polym. Symp.* 39:75–92.

Meakin, P. 1988. Fractal Aggregates. *Adv. Colloid Interface Sci.* 28:249.

Medalia, A.I. 1973. Elastic Modulus of Vulcanizates as related to Carbon Black Structure. *Rubber Chem. Technol*. 46:877.

Witten, T.A., Rubinstein, M., & Colby, R.H. 1993. Reinforcement of rubber by fractal aggregates. *J. Phys. II France*. 3:367–383.

Constitutive Models for Rubber VI – Heinrich et al. (eds)

A multiscale approach to model the mechanical behaviour of heterogeneous hyperelastic membranes

L. Meunier, L. Orgéas, G. Chagnon & D. Favier

In memory of Luc Meunier

CNRS/Université de Grenoble, Laboratoire Sols-Solides-Structures-Risques (3S-R), Grenoble Cedex, France

ABSTRACT: Within the framework given by the homogenisation method with multiple scale asymptotic expansions, a theoretical and numerical analysis is proposed in order to study the mesoscale behaviour of hyperelastic thin membranes exhibiting geometrical or material heterogeneities at the microscale. Results deduced from this multiscale approach are then used to analyse the mechanical behaviour of a crenellated thin membrane made up of a compressible Neo-Hookean material.

1 INTRODUCTION

Many structures and materials such as thin heterogeneous and/or fibre-reinforced elastomers structures, thin living tissues, manufactured woven or non-woven 2D textiles, behave as a first and reasonable approximation as elastic and anisotropic membranes undergoing finite strains.

In this work, we propose to estimate, from a theoretical and numerical multiscale approach, the mesoscale effective mechanical properties of such membranes, (i) starting from the description of both the microstructure and the mechanical equilibrium of the membranes at the microscale, and (ii) assuming that the involved materials at the microscale behave as hyperelastic bodies.

Firstly, the above micromechanical problem at the heterogeneity scale is upscaled by using the homogenisation method with multiple scale asymptotic expansions for periodic structures (Bensoussan et al. 1978; Sanchez-Palencia 1980; Caillerie 1984; Auriault 1991; Pruchnicki 1998). The homogenisation also provides suitable localisation problems to be solved within the Representative Elementary Volumes (REV) in order to compute the effective hyperelastic responses of the membranes.

Secondly, these boundary values problems are implemented into a Finite Elements software and the effective mesoscale properties of heterogeneous membranes are investigated quantitatively. The considered membrane is rather simple: it is made up of hyperelastic materials and it exhibits crenellated cross sections. Hence, its associated REV is subjected to meso-scopic in plane loadings (uniaxial/biaxial tensions, pure shear) and their resulting mesoscopic behaviours (stress levels, evolving anisotropy) are analysed and discussed.

2 PROBLEM STATEMENT

We consider a thin heterogeneous plate, *e.g.* that shown in figure 1(a), with an initial average thickness e_0 along the $\underline{\mathbf{e}}_3$ direction and with a characteristic in-plane initial macroscopic dimension L_0 (in $(\underline{\mathbf{e}}_1, \underline{\mathbf{e}}_2)$). The plate is made up of a periodic assembly of Representative Elementary Volumes (REV) with a characteristic in-plane initial dimension l_0. It is supposed that the thickness e_0 and the REV in-plane length l_0 are of the same order of magnitude, *i.e* $e_0/l_0 \approx \mathcal{O}(1)$, and that they are very small with respect to the in-plane size L_0 of the plate, *i.e* $e_0/L_0 \approx l_0/L_0 \approx \mathcal{O}(\varepsilon)$, the scale separation parameter ε being very small. A typical example of such REV's is shown in figure 1(b).

For a sake of simplicity, we assume here that the plate is only subjected to in quasi-static and in-plane mechanical loadings without volumetric forces. With the example shown in figure 1(b), this means that the upper Γ^+ and lower Γ^- surfaces of the REV are not loaded.

By noting respectively $\underline{\mathbf{X}}$ and $\underline{\mathbf{x}}$ the initial and current position vectors of materials points and $\mathbf{u}(\underline{\mathbf{X}}) = \underline{\mathbf{x}} - \underline{\mathbf{X}}$ the displacement vector, the first momentum balance equation corresponding to this problem and to be solved in the initial configuration is:

$$\underline{\mathrm{Div}}_X \underline{\underline{\boldsymbol{\pi}}} = \underline{\mathbf{0}}, \tag{1}$$

where Div_X is the divergence operator with respect to the initial configuration and position vectors $\underline{\mathbf{X}}$.

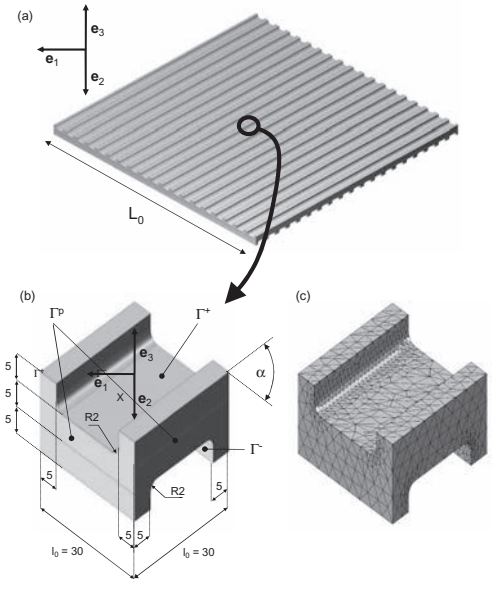

Figure 1. Typical plate which is here considered (a), geometry with $\alpha = 65°$ (b) and P2 tetrahedral FE mesh (≈ 50000 degrees of freedom) (c) of the Representative Elementary Volume of the considered membrane (dimensions in mm).

From the second momentum balance equation, the first Piola-Kirchhoff stress tensor $\underline{\underline{\pi}}$ must verify:

$$\underline{\underline{\pi}} \cdot \underline{\underline{\mathbf{F}}}^t = \underline{\underline{\mathbf{F}}} \cdot \underline{\underline{\pi}}^t. \tag{2}$$

In the last equation, $\underline{\underline{\mathbf{F}}}$ is the transformation gradient defined as:

$$\underline{\underline{\mathbf{F}}} = \underline{\underline{\delta}} + \underline{\underline{\mathbf{Grad}}}_X \underline{\mathbf{u}}, \tag{3}$$

$\underline{\underline{\delta}}$ and $\underline{\underline{\mathbf{Grad}}}_X$ being the identity tensor and the gradient operator with respect to $\underline{\mathbf{X}}$, respectively.

Besides, the plate is supposed to be made up of compressible hyperelastic materials, the characteristic stiffness of which being of the same order of magnitude. Their stress tensors $\underline{\underline{\pi}}$ can therefore be written as:

$$\underline{\underline{\pi}} = \frac{\partial W(\underline{\underline{\mathbf{F}}})}{\partial \underline{\underline{\mathbf{F}}}}, \tag{4}$$

The local strain energy function W per unit of unde-formed volume is supposed to be positive and such that $W(\underline{\underline{\delta}}) = 0$. For example, let us assume that the membrane is made up of compressible Neo-Hookean materials. In this situation, W is expressed as:

$$W = \frac{1}{2}\left(\mu(I_1 J^{-\frac{2}{3}} - 3) + k(1-J) \right), \tag{5}$$

where

$$J = \mathrm{Det}\underline{\underline{\mathbf{F}}},\ I_1 = \mathrm{Tr}(\underline{\underline{\mathbf{F}}}^t \cdot \underline{\underline{\mathbf{F}}}) \tag{6}$$

and where $\mu(\underline{\mathbf{X}})$ and $k(\underline{\mathbf{X}})$ are the shear modulus and the compressibility modulus, respectively.

3 UPSCALING

3.1 *Introduction*

In order to obtain the equivalent mesoscopic mechanical behaviour of the as-described problem, the homogenisation method with multiple scale asymptotic expansions is now used (Bensoussan et al. 1978; Sanchez-Palencia 1980; Caillerie 1984; Auriault 1991). Hence, provided a good scale separation between L_0 and l_0, the problem can be tackled by introducing two distinct and independent dimensionless space variables, *i.e.* $\underline{\tilde{\mathbf{Y}}}$ and $\underline{\mathbf{Z}}$ (the symbol "~" denotes quantities which are defined in $(\underline{\mathbf{e}}_1, \underline{\mathbf{e}}_2)$). The mesoscopic in-plane space variable $\underline{\tilde{\mathbf{Y}}} = \underline{\tilde{\mathbf{X}}} / L_0$ is defined in the $(\underline{\mathbf{e}}_1, \underline{\mathbf{e}}_2)$ plane ($Y_3 = 0$) and characterises the membrane geometry at the mesoscopic scale. The microscopic one, *i.e.* $\underline{\mathbf{Z}} = \underline{\mathbf{X}} / l_0$, characterises the membrane geometry in the REV's. Thus, any scalar function $\varphi(\underline{\mathbf{X}})$ is now written as a function of $\underline{\tilde{\mathbf{Y}}}$ and $\underline{\mathbf{Z}}$, *i.e.* $\varphi(\underline{\tilde{\mathbf{Y}}}, \underline{\mathbf{Z}})$. Therefrom, it is further assumed that the displacement field $\underline{\mathbf{u}}(\underline{\tilde{\mathbf{Y}}}, \underline{\mathbf{Z}})$ can be expressed as an asymptotic expansion in powers of ε:

$$\underline{\mathbf{u}} = \underline{\mathbf{u}}^{(0)}(\underline{\tilde{\mathbf{Y}}}, \underline{\mathbf{Z}}) + \varepsilon \underline{\mathbf{u}}^{(1)}(\underline{\tilde{\mathbf{Y}}}, \underline{\mathbf{Z}}) + \varepsilon^2 \underline{\mathbf{u}}^{(2)}(\underline{\tilde{\mathbf{Y}}}, \underline{\mathbf{Z}}) + \ldots \tag{7}$$

where the displacement fields $\underline{\mathbf{u}}^{(i)}$ are supposed to be $\underline{\mathbf{Z}}$-periodic on the lateral surface Γ^p of the REV (see figure 1(b)).

Accounting for this last assumption, the homogenisation method consists (i) in introducing the new set of space variables $\underline{\tilde{\mathbf{Y}}}$ and $\underline{\mathbf{Z}}$ together with the above asymptotic expansion (7) in the problem (1–6) and (ii) in identifying and solving the problems arising at the different ε-orders.

3.2 *Main results*

Theoretical developments are very similar to what was achieved by Pruchnicki (Pruchnicki 1998) for Saint Venant-Kirchhoff materials. We have here extended his work to a larger class of

hyperelastic materials and we have also avoided any *a priori* assumption on the first order displacement field $\underline{\mathbf{u}}^{(0)}$. The reader is referred to his work (Pruchnicki 1998) and to that of Meunier (Meunier 2009) for details about the theoretical developments. We briefly summarise hereafter the main results deduced from the approach:

- From the assumptions stated for W, it can be shown that the first order displacement field only depends on the in-plane mesoscopic space variable, *i.e.* $\underline{\mathbf{u}}^{(0)} = \underline{\mathbf{u}}^{(0)}(\underline{\tilde{\mathbf{Y}}})$.
- The mesoscopic equivalent continuum is a 2D membrane. In the $(\underline{\mathbf{e}}_1, \underline{\mathbf{e}}_2)$ plane, its first momentum balance equation in the initial configuration is expressed as:

$$\underline{\tilde{\mathbf{Div}}}_{\tilde{X}} \left\langle \tilde{\underline{\underline{\pi}}}^{(0)} \right\rangle = \underline{\tilde{\mathbf{0}}}, \tag{8}$$

where the mesoscopic first order Piola-Kirchhoff stress tensor $\left\langle \tilde{\underline{\underline{\pi}}}^{(0)} \right\rangle$ is defined as

$$\left\langle \tilde{\underline{\underline{\pi}}}^{(0)} \right\rangle = \frac{1}{V_0} \int_{\Omega_0} \tilde{\underline{\underline{\pi}}}^{(0)} \mathrm{d}V, \tag{9}$$

such a volume averaging being performed on the initial solid domain Ω_0 of the REV, of initial volume V_0. The local first order stress tensor $\tilde{\underline{\underline{\pi}}}^{(0)}$ involved in the last equation is defined from:

$$\underline{\underline{\pi}}^{(0)} = \frac{\partial W(\tilde{\underline{\underline{\mathbf{F}}}}^{(0)} + \underline{\underline{\mathbf{H}}}^{(1)})}{\partial(\tilde{\underline{\underline{\mathbf{F}}}}^{(0)} + \underline{\underline{\mathbf{H}}}^{(1)})}, \tag{10}$$

where

$$\tilde{\underline{\underline{\mathbf{F}}}}^{(0)} = \underline{\underline{\tilde{\delta}}} + \underline{\underline{\underline{\mathbf{G\tilde{r}ad}}}}_{\tilde{X}} \tilde{\underline{\mathbf{u}}}^{(0)} \tag{11}$$

and

$$\underline{\underline{\mathbf{H}}}^{(1)} = \underline{\underline{\underline{\mathbf{Grad}}}}_{X} \varepsilon \underline{\mathbf{u}}^{(1)} \tag{12}$$

From (2), it also follows that $\left\langle \tilde{\underline{\underline{\pi}}}^{(0)} \right\rangle$ verifies:

$$\left\langle \tilde{\underline{\underline{\pi}}}^{(0)} \right\rangle \cdot \tilde{\underline{\underline{\mathbf{F}}}}^{(0)t} = \tilde{\underline{\underline{\mathbf{F}}}}^{(0)} \cdot \left\langle \tilde{\underline{\underline{\pi}}}^{(0)} \right\rangle^{t}. \tag{13}$$

- The mesoscopic first order Piola-Kirchhoff stress tensor $\left\langle \tilde{\underline{\underline{\pi}}}^{(0)} \right\rangle$ is defined as the partial derivative of the mesoscopic strain energy function $\left\langle W(\tilde{\underline{\underline{\mathbf{F}}}}^{(0)}, \text{microstructure}) \right\rangle$ with respect to the first order 2D transformation gradient $\tilde{\underline{\underline{\mathbf{F}}}}^{(0)}$:

$$\left\langle \tilde{\underline{\underline{\pi}}}^{(0)} \right\rangle = \frac{\partial \left\langle W(\tilde{\underline{\underline{\mathbf{F}}}}^{(0)}, \text{microstructure}) \right\rangle}{\partial \tilde{\underline{\underline{\mathbf{F}}}}^{(0)}}, \tag{14}$$

- The first order stress tensor $\left\langle \tilde{\underline{\underline{\pi}}}^{(0)} \right\rangle$ can be obtained by solving in the REV the following boundary value problem:

$$\left\{ \begin{array}{l} \underline{\mathbf{Div}}_X \underline{\underline{\pi}}^{(0)} = \underline{\mathbf{0}} \\ \underline{\underline{\pi}}^{(0)} = \dfrac{\partial W(\tilde{\underline{\underline{\mathbf{F}}}}^{(0)} + \underline{\underline{\mathbf{H}}}^{(1)})}{\partial(\tilde{\underline{\underline{\mathbf{F}}}}^{(0)} + \underline{\underline{\mathbf{H}}}^{(1)})} \\ \underline{\underline{\mathbf{H}}}^{(1)} = \underline{\underline{\underline{\mathbf{Grad}}}}_X \varepsilon \underline{\mathbf{u}}^{(1)} \\ \underline{\underline{\pi}}^{(0)} \cdot \underline{\mathbf{N}} = \underline{\mathbf{0}} \text{ on } \Gamma^+, \Gamma^- \end{array} \right\} \quad \text{in } \Omega_0 \tag{15}$$

where the first order periodic fluctuation of the displacement field $\varepsilon \underline{\mathbf{u}}^{(1)}$ is the unknown field, $\underline{\mathbf{N}}$ is the unit vector normal to the external surfaces Γ^+ and Γ^-, and where $\tilde{\underline{\underline{\mathbf{F}}}}^{(0)}$ is given and constant within the entire REV.

4 APPLICATION TO A SIMPLE MEMBRANE

By following the previous theoretical framework, it is now possible to compute the effective properties of hyperelastic membranes.

4.1 *Considered membrane geometry and material*

For that purpose, we consider a thin plate made up of upper and lower crenellated profiles. It is shown in figure 1(a). The corresponding REV and its dimensions are given in figure 1(b). As shown from this figure, the upper and lower crenellated profiles are identical but they are not parallel: they respectively make an angle $\pm\alpha/2 = \pm 32.5°$ with respect to the $\underline{\mathbf{e}}_1$ direction.

For the sake of simplicity, the membrane is assumed to be made up of a unique material, the mechanical behaviour of which is defined from the compressible Neo-Hookean hyperelastic strain energy function (5). The constitutive parameters associated with this function, *i.e.* μ and k, are assumed to be constant in the whole REV, they were set to 1 and 1000 MPa, respectively. Hence, the considered material can be regarded as quasi-incompressible.

In order to study the mesoscopic mechanical behaviour of such an heterogeneous membrane, *i.e.* to analyse the relationship between $\left\langle \tilde{\underline{\underline{\pi}}}^{(0)} \right\rangle$, $\tilde{\underline{\underline{\mathbf{F}}}}^{(0)}$ and the membrane microstructure (see (14)), the

boundtary values problem (15) was solved on the considered REV for given values of the 2D mesoscopic transformation gradient $\underline{\underline{\tilde{\mathbf{F}}}}^{(0)}$. This allows to estimate the displacement fluctuation $\varepsilon\underline{\mathbf{u}}^{(0)}$, then the local stress tensor $\underline{\underline{\tilde{\pi}}}^{(0)}$ (from (15b), and finally the mesoscopic stress tensor $\left\langle \underline{\underline{\tilde{\pi}}}^{(0)} \right\rangle$ (from (9)).

For that purpose, the weak form of this problem was implemented into the Finite Elements (FE) code Comsol Multiphysics, and the REV was meshed using FE elements with second order polynomial form functions (P2, see figure 1(c)). Such a highly nonlinear formulation was solved incrementally, with an iterative Newton's like algorithm at each time step.

4.2 *Anisotropy*

A first type of numerical experiments was achieved in order to analyse the mechanical anisotropy of the considered membrane. Hence, the REV was subjected to a plane strain tension along the $\underline{\mathbf{e}}_1$ direction:

$$\underline{\underline{\tilde{\mathbf{F}}}}^{(0)} = \lambda_{11}\underline{\mathbf{e}}_1 \otimes \underline{\mathbf{e}}_1 \tag{16}$$

up to an axial elongation $\lambda_{11} = 2$. Then, the REV was rotated by an angle θ in the $(\underline{\mathbf{e}}_1, \underline{\mathbf{e}}_2)$ plane, and the same numerical experiment was achieved. This was repeated for various values of θ ranging from 0° to 180°. Therefrom, the dimensionless stresses components:

$$\left\langle \tilde{\pi}_{11}^{(0)} \right\rangle^* = \frac{\left\langle \tilde{\pi}_{11}^{(0)} \right\rangle(\theta)}{\left\langle \tilde{\pi}_{11}^{(0)} \right\rangle(\theta = 0)} \text{ and } \left\langle \tilde{\pi}_{22}^{(0)} \right\rangle^* = \frac{\left\langle \tilde{\pi}_{22}^{(0)} \right\rangle(\theta)}{\left\langle \tilde{\pi}_{22}^{(0)} \right\rangle(\theta = 0)} \tag{17}$$

were built and analysed as functions of the orientation angle θ. This is illustrated in figure 2, in which these dimensionless stress ratios were plotted as functions of θ, for two values of the imposed mesoscopic elongation λ_{11}:

- Even if the membrane is made up of a unique material, the architecture of the REV induces noticeable anisotropy: stresses components depend on θ. For example the dimensionless stress component $\left\langle \tilde{\pi}_{11}^{(0)} \right\rangle^*$ is approximately 25% higher when $\theta = 90°$ than when $\theta = 0°$. This trend is reversed but less pronounced for the second dimensionless stress component $\left\langle \tilde{\pi}_{22}^{(0)} \right\rangle^*$.
- The anisotropy magnitude evolves as the imposed mesoscopic elongation is increased. For example, it is approximately twice higher for $\left\langle \tilde{\pi}_{22}^{(0)} \right\rangle^*$ when λ_{11} goes from 1.25 to 2. This is much less emphasised and this trend is reversed for $\left\langle \tilde{\pi}_{11}^{(0)} \right\rangle^*$, as evident from figure 2.

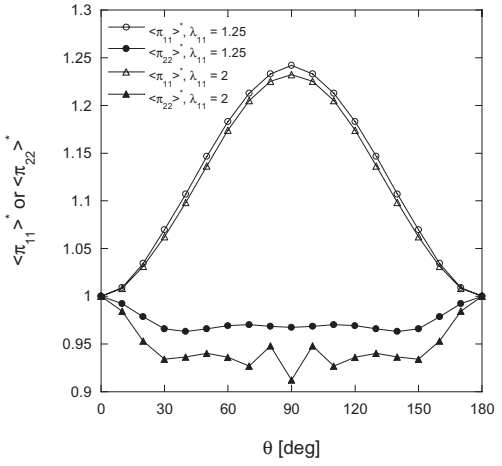

Figure 2. Evolution of the dimensionless stresses $\left\langle \tilde{\pi}_{11}^{(0)} \right\rangle^*$ and $\left\langle \tilde{\pi}_{22}^{(0)} \right\rangle^*$ as functions of the angle θ the REV is rotated from its initial configuration shown in figure 1(b). These stresses have been estimated for two imposed mesoscopic elongations λ_{11}.

- Whatever the considered elongation λ_{11}, figure 2 proves that the mesoscopic mechanical in-plane behaviour of the membrane exhibits orthotropy: stress ratios exhibit two symmetries along two orthogonal directions, *i.e.* for $\theta = 0°$ and $\theta = 90°$.

4.3 *Biaxial loadings*

We now return to the REV given in figure 1(b) in order to analyse the effect of the mechanical loading type on its behaviour. For this reason the REV was here subjected to in plane and radial biaxial loadings corresponding to the following in plane mesoscopic transformation gradient:

$$\underline{\underline{\tilde{\mathbf{F}}}}^{(0)} = \lambda_{11}(\underline{\mathbf{e}}_1 \otimes \underline{\mathbf{e}}_1 + \beta\underline{\mathbf{e}}_2 \otimes \underline{\mathbf{e}}_2) \tag{18}$$

When it was possible, the elongation λ_{11} along the $\mathbf{e}_1$ was increased until a value of 2. The positive biaxial ratio $\beta = \lambda_{22}/\lambda_{11}$ was kept constant during each loading. Various numerical experiments were achieved with the following β values : –1 (corresponding to an in-plane pure shear test), –0.5, 0 (corresponding to a plane strain tension test), 0.5 and 1 (corresponding to an equibiaxial tension test).

Numerical results have been summarised in figure 3, in which the stress-elongation diagrams $\left\langle \tilde{\pi}_{11}^{(0)} \right\rangle - \lambda_{11}$ and $\left\langle \tilde{\pi}_{22}^{(0)} \right\rangle - \lambda_{11}$ have been reported forthe different tested values of β, together with the deformed shapes of the REV at the end of

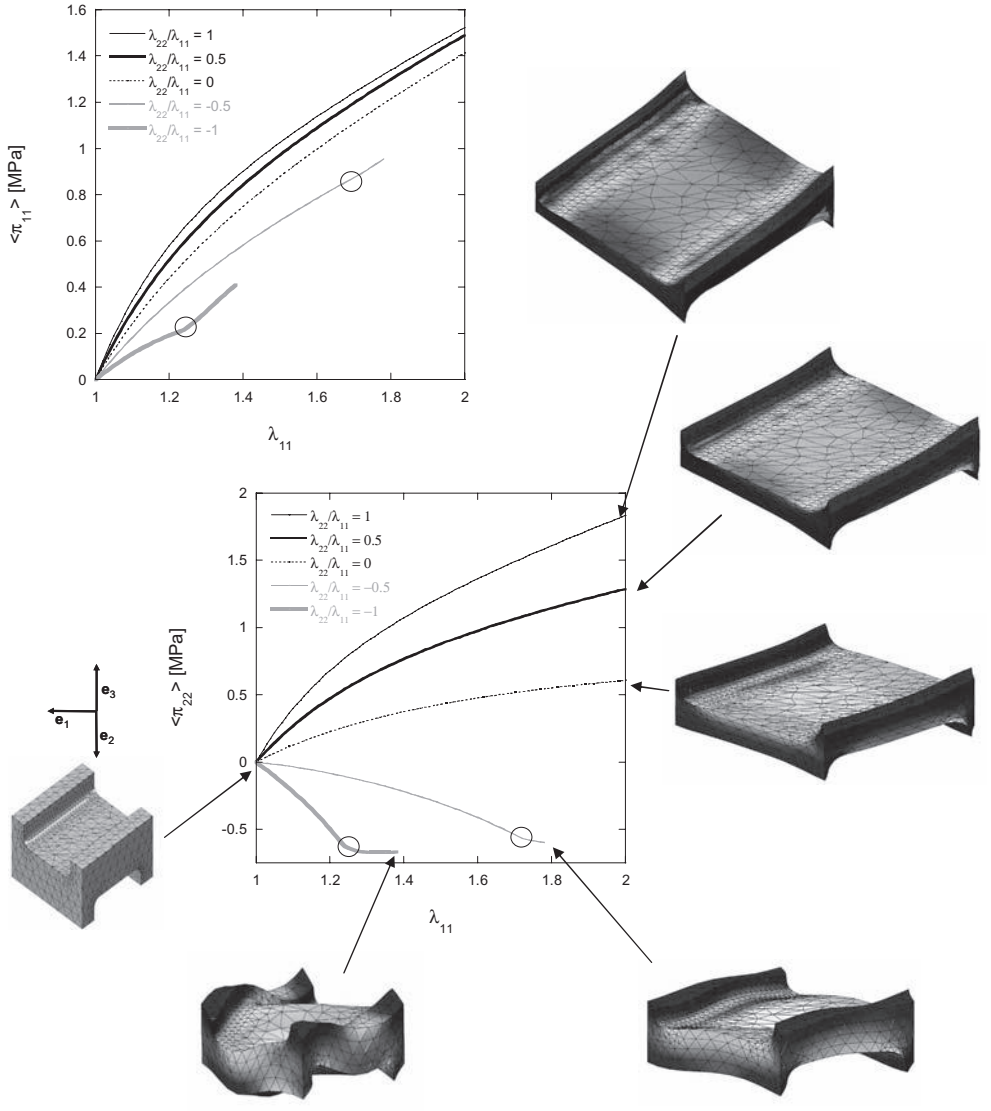

Figure 3. Biaxial loadings achieved with various elongation ratios $\beta = \lambda_{22}/\lambda_{11}$. The two graphs represent the evolution of the mesoscopic stress components $\left\langle \tilde{\pi}_{11}^{(0)} \right\rangle$ (upper graph) and $\left\langle \tilde{\pi}_{22}^{(0)} \right\rangle$ (lower graph) as functions of the imposed mesoscopic elongation λ_{11}. We have also reported the initial mesh of the REV, as well as its deformed meshes at the end of the different mechanical loadings. Colormaps shown on the deformed meshed represent the values of the Von Mises stress, ranging from its lowest value (blue) to its maximal one (red).

the mechanical loadings. This figure brings up the following comments:

- The two stress-elongation graphs emphasise the key role of the mechanical loading on the mechanical response of the membrane. Whatever the considered stress component, an increase of β yields to an increase of stress levels. Such a trend is much more pronounced with the stress component $\left\langle \tilde{\pi}_{22}^{(0)} \right\rangle$ than with $\left\langle \tilde{\pi}_{11}^{(0)} \right\rangle$.
- The anisotropy of the membrane, which was emphasised in the previous subsection, can also be observed when looking at stress-elongation curves in the case of the equibiaxial test, *i.e.* for $\beta = 1$. Indeed, the two graphs of figure 3, show

that $\left\langle \tilde{\pi}_{22}^{(0)} \right\rangle$ is higher than $\left\langle \tilde{\pi}_{11}^{(0)} \right\rangle$ (20% higher when $\lambda_{11} = 2$).

- Stress-elongation curves for $\beta \geq 0$ exhibit a curvature with a constant sign: this is directly due to the Neo-Hookean nature of the membrane material.
- Such an expected behaviour is not observed at all for stress elongation curves obtained with $\beta = -1$ and $\beta = -0.5$. Indeed, for these two mechanical loadings which involve compression stress components $\left\langle \tilde{\pi}_{22}^{(0)} \right\rangle$, the sign of the curvature suddenly change around $\lambda_{11} = 1.25$ and $\lambda_{11} = 1.75$ when $\beta = -1$ and $\beta = -0.5$, respectively (see the circles sketched in the graphs of figure 3). This change results in an anomalous increase of the strain hardening of $\left\langle \tilde{\pi}_{11}^{(0)} \right\rangle$ and in an anomalous strain softening of $\left\langle \tilde{\pi}_{22}^{(0)} \right\rangle$ By closely looking at the deformed shapes of the REV just after these transition zones (see figure 3), one can clearly see that the REV has been subjected to a local buckling along the $\underline{\mathbf{e}}_2$ direction, such a buckling being induced by the imposed meso-scopic compression elongation along this direction.

5 CONCLUSIONS

Within the framework proposed by the homogeni-sation method with multiple scale asymptotic expansions, and more precisely by pursuing the work of Pruchnicki (Pruchnicki 1998), we have proposed a method to analyse from numerical simulation the mesoscopic mechanical behaviour of heterogeneous hyperelastic membranes.

In particular, it has been shown that a membrane made up of a unique homogeneous material but with geometrical heterogeneities at the REV scale could exhibit significant anisotropy and possible microstructure instabilities such as buckling. A deeper analysis of these phenomena as functions of both the membrane geometry (*e.g.* the inclination angle α) and the imposed mesoscopic loading should be required.

The method also permits to analyse the mechanical behaviour under various mechanical loadings, thus allowing to constitute a precious and exhaustive database in order to propose relevant analytical forms of the mesoscopic law (14). This work is planned.

Before, its relevance must be proved. For that purpose, its prediction could be compared to what could be observed experimentally on similar heterogeneous membranes with a homogeneous hyperelastic material such as silicone rubber (Meunier et al. 2008). This work is also planned.

REFERENCES

Auriault, J.-L. (1991). Heterogeneous medium. is an equivalent macroscopic description possible? *Int. J. Eng. Sci. 29*(7), 785–795.

Bensoussan, A., J.-L. Lions, and G. Papanicolaou (1978). *Asymptotic Analysis for Periodic Structures*. Amsterdam: North Holland.

Caillerie, D. (1984). Thin elastic and periodic plates. *Math. Meth. Appl. Sci. 6*, 159–191.

Meunier, L. (2009). *Etude Du Comportement Mécanique de Membranes de Silicone Á Anisotropie Contrôlée: Application À la Conception de Muscles Artificiel*s. Ph.D. thesis, Univ. de Grenoble, France.

Meunier, L., G. Chagnon, D. Favier, L. Orgéas, and P. Vacher (2008). Experimental and numerical study of the mechanical behaviour of an unfilled silicone rubber. *Polym. Testing 27*, 765–777.

Pruchnicki, E. (1998). Overal properties of thin hyperelastic plate at finite strain with edge effects using asymptotic method. *Int. J. Eng. Sci. 36*, 973–1000.

Sanchez-Palencia, E. (1980). *Non-Homogeneous Media and Vibration Theory*. Lecture Notes in Physics. Berlin, Germany: Springer-Verlag.

Constitutive Models for Rubber VI – Heinrich et al. (eds)
© 2010 Taylor & Francis Group, London, ISBN 978-0-415-56327-7

Dynamic mechanical properties of strongly stretched polymer chains and networks: Different molecular models

V. Toshchevikov
Leibniz-Institut für Polymerforschung Dresden e. V., Dresden, Germany;
Institute of Macromolecular Compounds, Saint-Petersburg, Russia

G. Heinrich
Leibniz-Institut für Polymerforschung Dresden e. V., Dresden, Germany

Yu. Gotlib
Institute of Macromolecular Compounds, Saint-Petersburg, Russia

ABSTRACT: A freely-jointed-rods chain model and a modified Rouse model are used to study molecular mobility and dynamic mechanical properties of strongly stretched polymer chains and networks. Stretched polymer chains and networks are characterized by the anisotropy of dynamic mechanical properties: frequency dependent storage and loss shear moduli are different for different geometries of applying the shear gradient (parallel or perpendicular to the axis of deformation) and display several plateaus (or maxima), whose positions depend on the static strain. Theoretically calculated frequency dependences of the loss and storage moduli are in an agreement with experimental data.

1 INTRODUCTION

Investigation of the molecular mobility of polymer chains and networks under large static deformations is one of the important topics in the modern physics of rubbers. On the one hand, superposition of large static and small oscillating strains has been proposed recently as a method for studying the molecular mobility and structure of polymer networks (Bodneva, Borodin, Khazanovich 2005; Munch, Pelletier, et al. 2006). On the other hand, this topic is of importance to understand the phenomenon of crack propagation in heterogeneous rubbers under pulsed loading conditions (Horst and Heinrich 2008; see also http://www.ipfdd.de/FOR597).

To study the dynamics of strongly stretched polymer chains, several approaches have been suggested which take into account the finite extensibility of macromolecules. Among the approaches one should mention theories which used the blob chain model (Pincus 1977), the freely-jointed-rods chain model (Gotlib, Darinskii, et al. 1984; Darinskii, Gotlib, et al. 1994) and FENE potential for chain fragments (Febbo, Milchev, et al. 2008). Results of these theories were confirmed by direct comparison with the results of computer simulations (Darinskii, Gotlib, et al. 1994; Febbo, Milchev, et al. 2008). Note, however, that the above-mentioned works considered only normal modes of a polymer chain under static deformation and did not deal with the frequency dependences of the storage and the loss moduli which can be measured in dynamic mechanical experiments (Munch, Pelletier, et al. 2006).

Much progress in theoretical study of dynamic mechanical properties of highly stretched polymer chains and networks has been achieved using Gaussian approximation and a corresponding modified Rouse model (Borodin, Khazanovich 1973, 1986, 2005). The latter theories considered the frequency dependences of the loss Young modulus $E''(\omega)$ when a small tensile oscillating strain is applied along the direction of the static elongation. However, in view of recent experimental data (Munch, Pelletier, et al. 2006), it is important to calculate the moduli for other geometries of application of oscillating and static strains.

The main purpose of the present work is to study the anisotropy of the dynamic mechanical properties of strongly stretched polymer chains and networks with respect to the direction of a static elongation and to calculate the *shear* moduli for different geometries of applying the periodic shear (parallel or perpendicular to the axis of deformation). In Section 2, we consider the normal modes for a freely-jointed-rods chain model. We demonstrate that even at large static strains the relaxation times

for long-scale normal modes can be described in a good approximation by the modified Rouse model. In Sections 3 and 4, using the modified Rouse model we calculate the frequency dependences of the storage and the loss moduli for polymer chains and networks under large static strains.

2 RELAXATION TIMES OF A STRETCHED POLYMER CHAIN: FREELY-JOINTED-RODS CHAIN (FJRC) MODEL AND A MODIFIED ROUSE (MR) MODEL

The simplest model which is able to describe the effect of finite extensibility of real macromolecules is the freely-jointed-rods chain (FJRC). Let us consider a freely jointed chain composed of $N_{\rm rod}$ rigid rods having the length l and connecting $N_{\rm rod}+1$ centres of viscous resistance with the friction coefficient ζ, Figure 1a. Action of a stretching force f to the chain ends is equivalent to application of an orientation potential affecting to each segment,

$$U(\alpha) = -U_0 \cos\alpha, \tag{1}$$

where $U_0 = f\,l$ and α is the angle between the long axis of the rod and the direction of the stretching force **f**. End-to-end distance of a chain, h, is a function of the stretching force, $h/L = Lan(fl/kT)$, where $L = lN_{\rm rod}$ is the contour length of the chain and $Lan(x) = \coth(x) - x^{-1}$ is the Langevin function. Here k is the Boltzmann constant and T is the absolute temperature.

The non-linear dynamics of the FJRC affected by the potential (1) has been considered by Darinskii, Gotlib, et al. (1994). Fluctuations, $\delta\mathbf{b}_j$, of the end-to-end vectors for the rod-like segments (Figure 1a) around their average values $\langle\mathbf{b}_j\rangle$ can be presented as a superposition of the normal coordinates, $\mathbf{q}_k$:

$$\delta\mathbf{b}_j(t) = \sqrt{\frac{2}{N_{\rm rod}+1}}\sum_{k=1}^{N_{\rm rod}} \sin\left(j\psi_k\right)\mathbf{q}_k(t), \tag{2}$$

where $\psi_k = \pi k/(N_{\rm rod}+1)$ is the phase shift between neighbouring segments at excitation of the kth normal mode. Using an approximation which relates the values $\delta\mathbf{b}_j$ and $\delta\mathbf{b}_j^2$, the autocorrelation functions for the normal coordinates was shown to obey an exponential decay:

$$\left\langle q_{\xi,k}(t)q_{\xi,k}(0)\right\rangle = C\exp[-t/\tau_{\xi,k}], \tag{3}$$

where the relaxation times $\tau_{\xi,k}$ ($\xi = \|,\perp$) are different for motions parallel and perpendicular to the axis of chain deformation, $\tau_{\|,k} \neq \tau_{\perp,k}$, and have been calculated by Darinskii, Gotlib, et al. (1994).

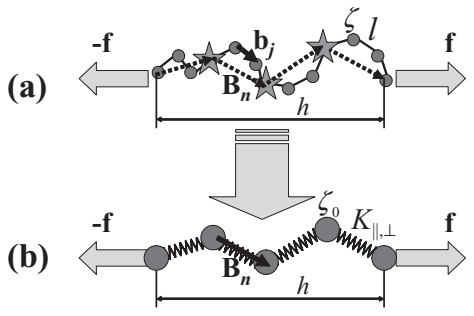

Figure 1. (a) Freely-jointed-rods chain under a static stretching force **f**. Stars show the dividing points of the chain into subchains, see text for details. (b) Modified Rouse model corresponding to the chain presented in the Figure 1a.

Although the FJRC model describes explicitly the effect of finite extensibility, it is not obvious how to use above-mentioned approximation for calculating the dynamic modulus. Therefore, we introduce here a modified Rouse (MR) model which obeys linear equations of motions and allows us to derive expression for the dynamic modulus.

We build the MR model as follows: the initial chain is divided up into N identical subunits whose end-to-end distribution is Gaussian (Gaussian subchains). In Figure 1a, the dividing points are marked by stars. In contrast to a nonstretched chain, whose shape is isotropic, the distribution of end-to-end vectors, $\mathbf{B}_n$, for the subchains in a stretched chain is anisotropic:

$$P\{\mathbf{B}_n\} = C\exp\left[-\sum_{n=1}^{N}\left(\frac{(B_{\|,n}-\bar{B}_{\|,n})^2}{2\left\langle\Delta B_{\|}^2\right\rangle} + \frac{\mathbf{B}_{\perp,n}^2}{2\left\langle\Delta B_{\perp}^2\right\rangle}\right)\right] \tag{4}$$

where $B_{\|,n}$ and $\mathbf{B}_{\perp,n}$ are the components of the vector $\mathbf{B}_n$ parallel and perpendicular to the **f**, respectively.

An anisotropic Gaussian chain can be represented by a mechanical model: the $(N+1)$ beads are considered to be connected by N harmonic springs which are characterized by two elasticity constants $K_{\|} \neq K_{\perp}$ (a *modified* Rouse model). The elasticity constants are related to the mean-square fluctuations of the end-to-end vectors, $K_{\|,\perp} = kT/\langle\Delta\mathbf{B}_{\|,\perp}{}^2\rangle$, and are the functions of the degree of chain stretching, h/L:

$$K_{\|} = K_0\frac{1}{3}\left[1-(h/l)^2 - \frac{2(h/l)}{Lan^{-1}(h/L)}\right]^{-1} \tag{5}$$

$$K_{\perp} = K_0\frac{Lan^{-1}(h/L)}{3h/L} \tag{6}$$

where $Lan^{-1}(x)$ is the inverse Langevin function and $K_0 = 3kT/nl^2$ is the elasticity constant of a non-stretched subchain (n is the number of segments in the subchain). Friction coefficient of the bead in MR model, ζ_0, is related to ζ as follows: $\zeta_0 = n\zeta$. Equations of motion for the MR model are linear and have been solved by the method of normal coordinates. The relaxation times for different normal modes (with different values of the phase shift ψ) have been calculated as a function of h/L.

Figure 2 show the dependences of the relaxation times $\tau_{\parallel,\perp}$ on the phase shift ψ for the FJRC model (filled symbols) and for the MR model (open symbols) at different values of the parameter h/L. One can see that the MR model describes in a good approximation the values of relaxation times for small ψ (i.e. for large-scale motions) where the asymptotic behavior $\tau \propto \psi^{-2}$ holds. The last result is confirmed also by the theory (Febbo, Milchev, et al. 2008). Since the MR model ignores short-scale motions, there are discrepancies between the relaxation times for the MR and FJRC models at $\psi \to \pi$.

The next problem is to calculate the dynamic moduli of a stretched polymer chain. It is a simple way now to do this using the MR model since this model obeys linear equations of motion. As long as the MR model describes correctly the large-scale (or low-frequency) dynamics of a polymer chain, one can certainly claim that it provides a true picture for low-frequency behavior of the moduli.

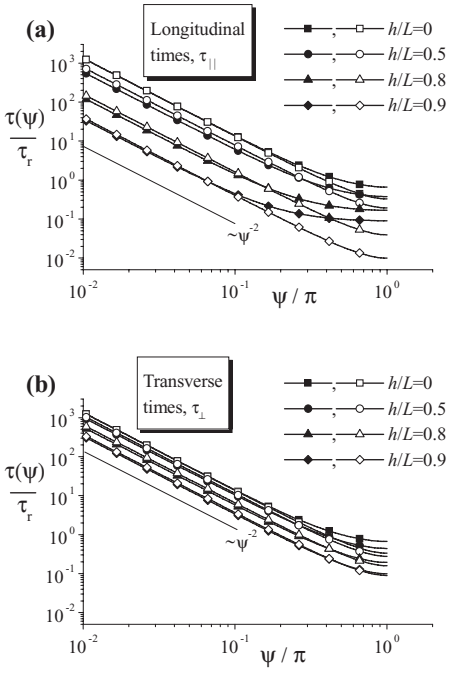

Figure 2. Relaxation times $\tau_{\parallel}$ (a) and $\tau_{\perp}$ (b) as functions of the phase shift ψ for the FJRC model (filled symbols; Darinskii et al. 1994) and for the MR model (open symbols) at different values of the parameter h/L. Here $\tau_r = \zeta l^2/4kT$.

3 SHEAR DYNAMIC MODULI OF A STRETCHED POLYMER CHAIN

In order to calculate the shear dynamic moduli of a stretched polymer chain we consider an infinitesimal periodic shear deformation applied along the x-axis. This leads to the shear flow:

$$\mathrm{v}_x(\mathbf{R},t) = \kappa(t)R_y, \mathrm{v}_y = \mathrm{v}_z = 0, \tag{7}$$

where $\mathbf{v}(\mathbf{R},t) = (\mathrm{v}_x,\mathrm{v}_y,\mathrm{v}_z)$ is the macroscopic velocity field at the point $\mathbf{R} = (R_x,R_y,R_z)$ and $\kappa(t) = \mathrm{d}\varepsilon/\mathrm{d}t$ is the shear rate. Here $\varepsilon = \delta L_x/L_y$ (Figure 3) is the relative periodic shear deformation: $\varepsilon(t) \sim e^{i\omega t}$. We consider three geometries of the shear with respect to the axis of chain stretching **f**, denoted by D (displacement), by V (vorticity) and by G (for **f** along the shear gradient), see Figure 3.

The shear deformation results in the appearance of the mechanical stress, $\delta\sigma_{xy}$. The value $\delta\sigma_{xy}$ can be calculated in terms of the end-to-end vectors of the subchains $\mathbf{B}_p$ and of the forces $\mathbf{F}_p \equiv -\partial U/\partial \mathbf{B}_p$ acting on the subchains:

$$\delta\sigma_{xy} = -\nu\sum_p \left\langle \delta F_{x,p}(\bar{B}_y + \delta B_{y,p}) \right\rangle, \tag{8}$$

where ν is the number of chains in a unit volume; $\delta\mathbf{F}_p$ and $\delta\mathbf{B}_p$ denote the deviations of the quantities $\mathbf{F}_p$ and $\mathbf{B}_p$ from their equilibrium values. Note that since mechanical stress is a quadratic function of the coordinates, it is necessary to keep not only the first term for δF ($\delta F_{x,p}^{(1)} = K_x \delta B_{x,p}$) but also the second one $\delta F_{x,p}^{(2)} \sim (\delta \mathbf{B}_p)^2$ due to the factor $\bar{B}_y$ in the right-hand side of Equation (8). However, $\bar{B}_y \neq 0$ only for G-geometry when the axis Oy is parallel to the vector **f**. For this geometry we have found for $\delta F_{\perp,p}$:

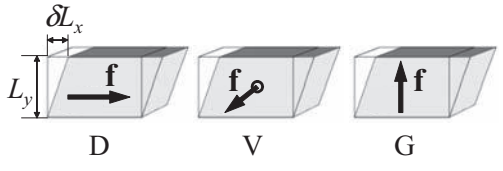

Figure 3. Three principal geometries of the shear with respect to the axis of chain stretching, **f**: D (displacement), V (vorticity) and G (for **f** along the shear gradient).

$$\delta F_{\perp,p} = K_{\perp}\delta B_{\perp,p} + \frac{K_{\parallel} - K_{\perp}}{\bar{B}_{\parallel}}\delta B_{\perp,p}\delta B_{\parallel,p}. \qquad (9)$$

Now, it is a simple way to calculate the stress $\delta\sigma_{xy}$, using Equations (8) and (9) as well as using the method of normal coordinates. For MR model, the dynamics of normal coordinates is described by linear differential equations. As a result, we obtain at small deformations ($|\varepsilon|<<1$):

$$\delta\sigma_{xy} = G^{*}_{xy}\varepsilon, \qquad (10)$$

where the complex dynamic moduli $G^{*}_{xy} = G'_{xy} + iG''_{xy}$ (here G' and G'' are the storage and loss moduli, respectively) have the following forms for the D-, V-, and G- geometries:

$$\frac{G^{*}_{D}}{\nu kT} = \frac{K_{\parallel}}{K_{\perp}}\sum_{k}\frac{\omega^2 + i\omega[\tau^{-1}_{\parallel,k} + \tau^{-1}_{\perp,k}]}{[\tau^{-1}_{\parallel,k} + \tau^{-1}_{\perp,k}]^2 + \omega^2}, \qquad (11)$$

$$\frac{G^{*}_{V}}{\nu kT} = \sum_{k}\frac{\omega^2 + i\omega[2\tau^{-1}_{\perp,k}]}{[2\tau^{-1}_{\perp,k}]^2 + \omega^2}, \qquad (12)$$

$$\frac{G^{*}_{G}}{\nu kT} = \sum_{k}\frac{\omega^2 + i\omega[\tau^{-1}_{\parallel,k} + \tau^{-1}_{\perp,k}]}{[\tau^{-1}_{\parallel,k} + \tau^{-1}_{\perp,k}]^2 + \omega^2}. \qquad (13)$$

Figures 4 and 5 show the frequency dependences of the storage and the loss moduli, respectively, for two values of the degree of chain stretching h/L = 0.4 (a) and 0.8 (b). One can see that at h/L = 0.4 the splitting of the principal moduli into three components $G^{*}_{D,V,G}$ is rather small and the moduli for a stretched chain are close to those for a non-stretched Gaussian chain. Thus, a broad region of stretching exists (h/L < 0.4) where the dynamic mechanical characteristics of a stretched chain is similar to those for nonstretched Gaussian chain (Gaussian regime). At limiting strains (h/L > 0.4) the frequency dependences $G'(\omega)$ and $G''(\omega)$ for a stretched chain are shifted to higher frequencies and a significant splitting of the moduli into three components $G^{*}_{D,V,G}$ appears.

4 SHEAR DYNAMIC MODULI OF A STRETCHED POLYMER NETWORK: THREE-CHAIN NETWORK MODEL

For describing the dynamics of a polymer network we use a regular cubic network model built from anisotropic Gaussian subchains. A cell of this network model (Figure 6) consists of three identical polymer chains whose end-to-end vectors form

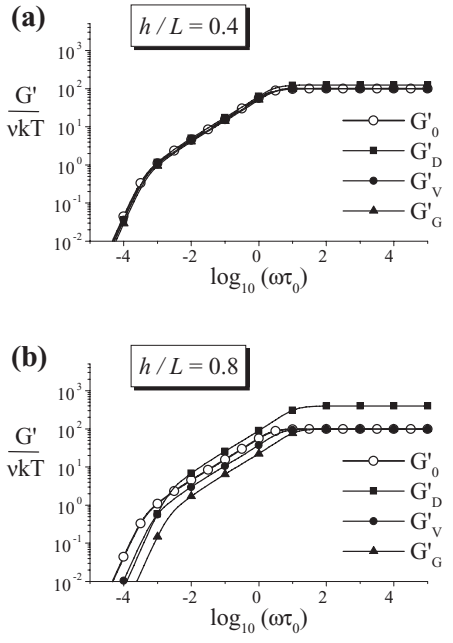

Figure 4. Three principal storage moduli $G'_{D,V,G}$ for a stretched polymer chain (filled symbols) and the storage modulus G'_0 for nonstretched Gaussian chain (open symbols) as a function of the reduced frequency ($\omega\tau_0$); $\tau_0 = \zeta_0/4K_0$. N = 100.

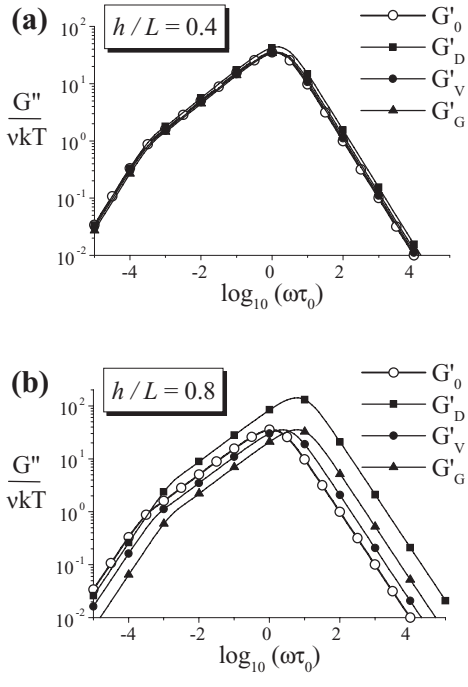

Figure 5. Same as Figure 4, but for the loss moduli G''.

a Cartesian frame of reference; so-called "three-chain network model" (Gotlib, Torchinskii and Toshchevikov V.P. 2002). As in works (Borodin, Khazanovich, et al. 1973, 1986, 2005), intrachain relaxation processes are considered here when network junctions remain immobile.

Due to the condition of constant volume for elastomers, the end-to-end distances, $h_{\|}$ and $h_{\perp}$, obey the following relations for chains, which lie parallel ($h_{\|}$) and perpendicular ($h_{\perp}$) to the axis of network elongation, $h_{\|} = h_0\lambda$ and $h_{\perp} = h_0/\lambda^{1/2}$ (Figure 6). Here λ is the elongation ratio of a network and h_0 is the end-to-end distance of chains in a nonstretched network. The value of h_0 equals the average end-to-end distance of network strands in an elastomer and can be estimated for Gaussian networks as $h_0/L \cong (N_K)^{-1/2}$, where N_K is a number of Kuhn segments in network strands (Gotlib, Torchinskii and Toshchevikov V.P. 2002).

In the framework of this network model, the relaxation spectrum of a stretched network consists of two main branches corresponding to the chains which lie parallel and perpendicular to the axis of network elongation. The former are stretched and their relaxation times decrease at network stretching, whereas the latter are uniaxially compressed and their relaxation times increases.

Using the results of the Section 3 for separate chains, we have calculated the frequency dependences of the dynamic moduli $G^*_{D,V,G}$ for three geometries of the shear applied to a stretched polymer network. Contributions of three chains in the cell to the total modulus of a polymer network have been taken into account.

For networks built from long and flexible chains ($N_K > 10$), a broad region of elongation, λ, exists where network strands are in a Gaussian regime ($h/L < 0.4$—see Section 3) and the frequency dependences of the relaxation part of the storage modulus ($G' - G_{eq}$) and of the loss modulus (G'') for a polymer network do not change with elongation and coincide with these dependences for soft Gaussian networks. For example, if $N_K \approx 100$ (as in the experiment Munch, Pelletier, et al. 2006), the initial stretching of chains is $h_0/L \cong (N_K)^{-1/2} \cong 0.1$, so that even until $\lambda = 3$ (i.e. until 200% of the static strain) we have $h_{\|}/L = \lambda(h_0/L) < 0.4$ and the frequency dependences of the loss moduli and of the relaxation part of the storage moduli for such polymer network do not change with elongation (Figures 7a and 8a). At such deformations only the low-frequency values of the storage moduli G' (i.e. the equilibrium storage moduli, G_{eq}) change with deformation. This result is in an agreement with experimental data (Munch, Pelletier, et al. 2006).

Strong effects of a static strain on the dynamic moduli of polymer networks take place at limiting elongations, when $h_{\|}/L > 0.4$. At such elongations, the contributions from network strands which lie parallel and perpendicular to the axis of network stretching lead to the broadening of the frequency dependences of storage and loss moduli, which can display several plateaus and maxima (Figures 7b and 8b). Positions of these plateaus and maxima depend on the elongation ratio, λ.

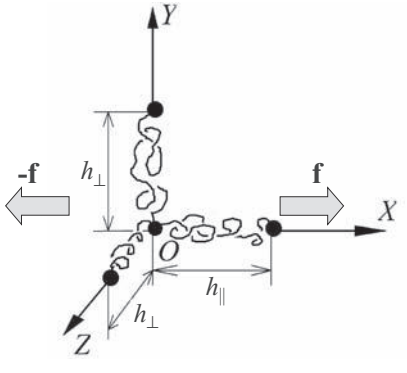

Figure 6. Cell of a regular cubic network model.

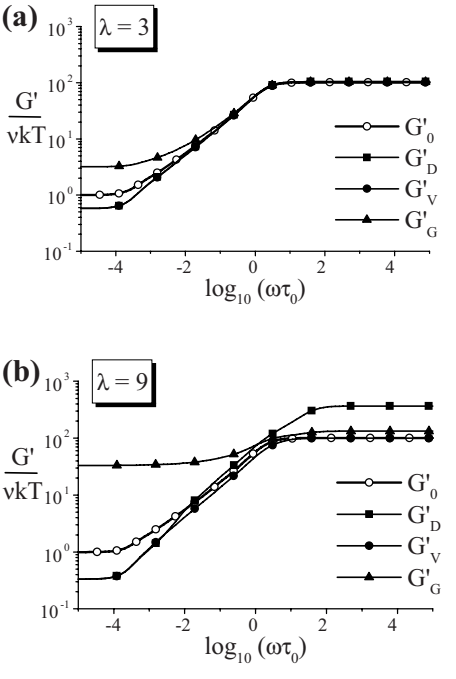

Figure 7. Three principal storage moduli $G'_{D,V,G}$ for a stretched polymer network (filled symbols) and the storage modulus G'_0 for a nonstretched Gaussian network (open symbols) as a function of the reduced frequency ($\omega\tau_0$); $\tau_0 = \zeta_0/4K_0$. A regular cubic network model is used. $N_K = 100$ (or $h_0/L = 0.1$).

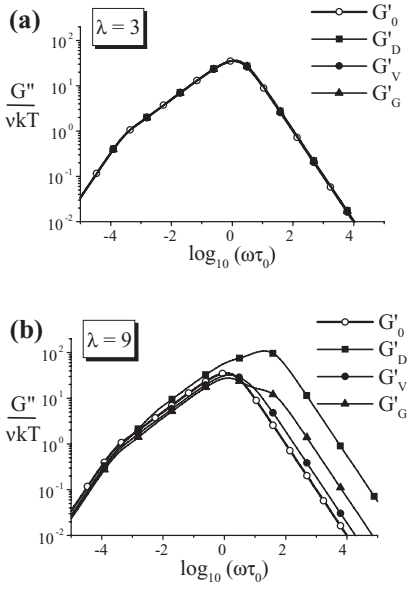

Figure 8. Same as Figure 7, but for the loss moduli G''.

5 CONCLUSIONS

A theory of molecular mobility and mechanical relaxation properties of strongly stretched polymer chains and networks has been proposed. A freely-jointed-rods chain model and a modified Rouse model have been used. The large-scale relaxation spectrum of a stretched polymer chain consisting of freely-jointed rods has been shown to be described in a good approximation by a modified Rouse model. For describing the network structure we use a regular cubic network model. In the framework of this network model the relaxation spectrum of a deformed network consists of two main branches corresponding to chains which lie parallel and perpendicular to the axis of a network deformation. The former are stretched and their relaxation times decrease at network stretching, whereas the latter are uniaxially compressed and their relaxation times increases.

We show that both stretched polymer chains and stretched polymer networks are characterized by the anisotropy of the dynamic mechanical properties: frequency dependent shear modulus is different for different geometries of applying the shear gradient (parallel or perpendicular to the axis of deformation). For all geometries of the shear, the fine structure of the relaxation spectrum leads to the broadening of the frequency dependences of the loss moduli, this result being valid both for stretched polymer chains and for stretched polymer networks. Frequency dependent storage and loss moduli for highly stretched polymer networks can display several plateau (or maxima, respectively) at strong deformations due to the contributions from the chains which lie parallel and perpendicular to the axis of a network deformation. A broad region of stretching exists (both for single chains and for polymer networks) where the storage and the loss moduli do not display the splitting with respect to the axis of deformation and behave like those for flexible Gaussian systems. The significance splitting of the storage and of the loss moduli with respect to the axis of deformation takes place at limiting values of the degree of stretching. Theoretically calculated frequency dependences of the loss and storage moduli for polymer networks are in a good agreement with experimental data.

ACKNOWLEDGEMENT

This work was supported by the Russian Foundation for Basic Research (08–03–00150).

REFERENCES

Borodin I.P., & Khazanovich T.N. 1973. Statistical derivation of equations of viscoelasticity for rubber polymers at large strains. *Vysokomol. Soed. (USSR)* 15(9): 2121–2127.

Borodin I.P., & Khazanovich T.N. 1986. The strain dependence of elastomer loss modulus: Rubber elasticity and the structure of polymer networks. *Polymer* 27: 1044–1049.

Bodneva V.L., Borodin I.P., & Khazanovich T.N. 2005. Superposition of large static and small oscillating strains as a method for studying polymer networks. *Polymer Science Ser. A* 47(4): 409–415.

Darinskii A.A., Gotlib Yu.Ya., et al. 1994. The local dynamics of a polymer chain in an external dipole field. *Polymer Science Ser. A* 36(7): 948–954.

Febbo M., Milchev A., et al. 2008. Dynamics of a stretched nonlinear polymer chain. *Journal of Chemical Physics* 129: 154908, 1–13.

Gotlib Yu.Ya., Darinskii A.A., et al. 1984. Properties of kinetic element and local mobility of polymer chains. *Acta Polymerica* 35(3): 124–129.

Gotlib Yu.Ya., Torchinskii I.A., & Toshchevikov V.P. 2002. The Estimation of Statistical Parameters Determining the Relaxation Times of Nematic Elastomers. Three-Chain Network Model. *Macromol. Theory Simul.* 11(8): 898–912.

Horst T., & Heinrich G. 2008. Crack propagation behavior in rubber materials. *Polymer Science Ser. A* 50(5): 583–590.

Munch E., Pelletier J.M., et al. 2006. Molecular mobility of crosslinked elastomers stretched above T_g *Polymer* 47: 3477–3485.

Pincus P. 1977. Dynamics of stretched polymer chains. *Macromolecules* 10(1): 210–213.

Multiphics and biomechanics

Constitutive Models for Rubber VI – Heinrich et al. (eds)
© 2010 Taylor & Francis Group, London, ISBN 978-0-415-56327-7

A direction dependent approach to the modeling of shape memory polymers

M. Böl & S. Reese
Institute of Solid Mechanics, Braunschweig University of Technology, Germany

ABSTRACT: Shape memory materials represent a promising class of multi-phase materials that have the ability to memorize a permanent shape, be manipulated and fixed to a temporary shape under specific conditions of temperature and stress, and then later relax to the original shape under a stimulus such as heat, electricity or magnetism. In this regard, the biomedical field is showing large interest in this class of materials, especially in shape memory polymers (SMPs), whose mechanical properties make them extremely attractive for many biomedical applications. However, shape memory properties of polymers can be quantified by cyclic thermo-mechanical investigations. One cycle includes the "programming" of the sample and the recovery of its permanent shape. Based on the different micro structures SMPs can be programmed direction dependent (non-isotropic behavior) of direction independent (isotropic behavior).

The first part of the paper deals with the isotropic, thermo-mechanical modeling of these materials. Aspects as the transition from entropy to energy elasticity are included. The constitutive equations are derived in the framework of large strains. In the second part of the work we extend the modeling to direction dependent SMP effect in the sense of transversal isotropic material behavior. The paper closes with representative examples such as simulation of a realistic stent structure.

1 INSTRUCTION

1.1 *Characteristic behavior of shape memory polymers*

Shape memory materials are materials that have the ability to memorize a permanent shape, be manipulated and fixed to a temporary shape under specific conditions of temperature and stress, and then later relax to the original, stress-free condition under thermal, electrical or environmental command, see e.g. Otsuka &Wayman 1998. Due to the fact that this class of materials has the capacity to remember two (Lendlein & Kelch 2002) or three (Chen et al. 2008) shapes at different conditions gives shape memory materials an increasing potential for application in the area of sensor/actuator development, for detailed reviews see e.g. Poliane et al. 2000, Lendlein & Kelch 2002, Beloshenko et al. 2005.

The most prominent shape memory materials are shape memory alloys (SMAs). Their shape memory effect arises from the existence of two stable crystallographic structures, an austenitic phase and a martensitic one. However, concerning e.g. stent implantation, SMAs show several disadvantages that limit their application, such as only moderately large recoverable strains, an inherently high stiffness, high cost and a hardly changeable transition temperature. Such limitations have provided motivation for the development of alternative materials, especially polymeric shape memory materials.

In comparison to SMA polymeric shape memory materials show the advantages of large elastic deformation (e.g. several hundred percents of strain), low cost, low density, potential biocompatibility and biodegradability. Other important properties are a broad range of application temperatures that can be well adjusted by the polymer chemist and a tunable stiffness. In addition SMPs are easily formed into a variety of complex shapes and sizes using standard processing methods such as extrusion, molding or forming that are normally used in manufacturing processes of plastics.

The mechanisms of SMPs differ dramatically from those of metal alloys. In SMAs, pseudoplastic fixing is possible through the martensitic detwinning mechanism, while recovery is triggered by the martensitic-austenitic phase transition. Thus, fixing of a temporary shape is accomplished at a single temperature and recovery occurs upon heating beyond the martensitic transformation temperature. In contrast, SMPs achieve temporary strain fixing and recovery through a variety of physical means, their extreme extensibility being derived from the intrinsic elasticity of polymeric networks. Above their glass transition temperature

Θ_t cross-linked polymers are elastic up to very large strains. The thermo-mechanical behavior is called rubber-like. In the temperature range $\Theta < \Theta_t$ polymer networks behave more stiffly than in the high temperature range. The mobility of the polymer chain segments between the cross-link points is reduced, the material behavior can be approximately described by energy elasticity, the so-called glass-like behavior.

The characteristic behavior of shape memory polymers is illustrated in Figure 1 in form of a stress-strain-temperature (σ–ε–Θ) diagram.

The guiding idea of such (mostly biodegradable) SMP strands is the application of it as suture material. The material is programmed to be laced up at high temperatures, such as the body temperature. Considering Figure 1, the thermo-mechanical cycle begins at the stress-free state at the high temperature level Θ_{high} (see point IV in Figure 1a), whereas this temperature level is in the case medical implants the body temperature. This state corresponds to the initial structure of the strand illustrated in Figure 1b (point IV). Subject to purely mechanical loading the material shows the classical rubber-like material behavior (S-shape). At a certain point I one may hold the mechanical loading fixed and decrease the temperature. Near the glass transition temperature Θ_t the material behavior changes from being rubber-like to glass-like. In particular, the deformation reached up to this point is "frozen".

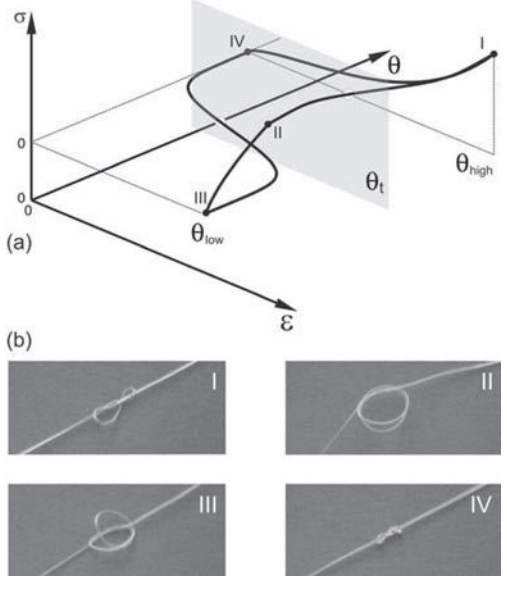

Figure 1. Typical thermo-mechanical cycle of SMP material. (a) σ–ε–Θ diagram and (b) shape memory effect, illustrated by four deformed states of a polymer strand (adopted from Lendlein & Langer 2002).

The lowest temperature Θ_{low} is reached at point II. At this point the mechanical loading is reduced until zero, see point III. In the case of an inhomogeneous stress state a redistribution of the stresses takes place. Residual stresses remain in the system. These two aspects contribute to the fact that the deformed state at point III (see Figure 1b) differs from the one at point II. Increasing the temperature again above the glass transition temperature Θ_t lets the structure "remember" its initial shape and deform back to this state, see point IV.

1.2 *Material modeling of SMPs*

Experimental investigation on the field of dual-shape SMP proved popular in the last years, see e.g. Lendlein & Kelch 2002, Lendlein & Langer 2002, Abrahamson et al. 2003, Liu et al. 2003a/b, Alteheld et al. 2005, Behl & Lendlein 2007a/b. Recent research focuses on the experimental characterization of triple-shape SMP, see e.g. Bellin et al. 2006, Bellin et al. 2007, Chen et al. 2008, Lendlein & Behl 2008. In contrast to such experimental work little effort has been realized in the modeling of such material behavior. In contrast, there has been very little effort spent on modeling SMPs.

Several authors have developed one-dimensional models, mostly based on linear viscoelasticity, which are partially valid only for small strains, see Abrahamson et al. 2003, Liu & Mather 2004, Barot & Rao 2006, Kafka 2008, Qi et al. 2008.

On the other hand, there exist only a few fully three-dimensional model approaches. The three-dimensional concept of Liu et al. 2006 incorporates the molecular mechanism of SMPs and is also based on experimental results. However, the model has been formulated in the framework of small strains which limits the range of application. The work of Diani et al. 2006 includes large strains and differs from the present approach (see also Reese et al. 2009) in several regards. For instance changes in the internal energy are fully attributed to the glassy state of the material. In contrast we apply a simple rule of mixture to indentify the energy parts of the rubbery and the glassy phase. Also the evolution of the two phases differs in the approaches and will be discussed later in this paper. The modeling approach of Barot et al. 2008 bases on earlier works of Barot & Rao 2006 and models constitutively the thermo-mechanical behavior of crystallizable shape memory polymers. The modeling is carried out using a framework that was developed for studying crystallization in polymers and is based on the theory of multiple natural configurations. The work does not include complex three-dimensional examples but shows its ability on an example of an inflated and extended

hollowed cylinder. In the present approach, see also Reese et al. 2009, we develop a three-dimensional, fully thermo-mechanical coupled model for the simulation realistic geometries like stents. To the author's knowledge, finite element-based simulations of realistic three-dimensional structures are not found in any previous publication. Especially from the aspect of direction depended shape memory effects in three-dimensional structures no modeling approaches are available.

2 SHAPE MEMORY POLYMER MODELING

2.1 *Phase transition between rubber-like and glassy-like behavior*

Fundamental properties of elastomers are so-called switch temperatures. These temperatures represent limits, where the material switches (mostly continuously) from one phase to the other. In the case of SMPs this switch temperature is the so-called glass transition temperature Θ_t which differs from one elastomer to another. Basically this means that above Θ_t the material is dominated by a rubber-like behavior, below Θ_t glass-like behavior can be observed. In the glassy state natural rubber is about magnitudes stiffer than in its rubbery state. In Figure 2 typical polymer examples are illustrated. In the energetic region the different materials are thousand-fold stiffer than in the entropic state. Between these states the glass transition area is given. The reason for the existence of a glass transition temperature can be understood in terms of the molecular structure of rubber. Above Θ_t the molecular chains are in a constant state of thermal motion (Brownian motion). As the temperature is lowered and reaches the glass transition temperature the deformed shape becomes fixed because the Brownian movements of shape.

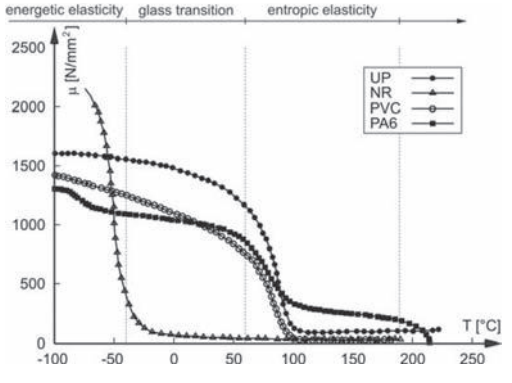

Figure 2. Transition and condition states: shear modulus μ in dependence on the temperature T for a thermoset (UP), elastomer (NR), amorphous (PVC) and for a semi-crystallized (PA6) thermoplastic.

In both, the glassy and the rubbery state, the molecular structure is amorphous. Due to the fact that at temperatures clearly below Θ_t the positions of the chain molecules are frozen a deformation of the material is achieved by an elongation of the intermolecular bonds. After unloading the molecules return to their original position. This is typical for a so-called energy elastic process. In contrast, at temperatures clearly above Θ_t the chains will always tend to assume a configuration corresponding to a state of maximum entropy, see also Böl & Reese 2006.

For the realistic description of the SMP effect as illustrated in Figure 1 we have to take following aspects into account, see also Reese et al. 2009:

(1) With decreasing temperature the Helmholtz free energy becomes more and more dominated by the internal energy.
(2) The mechanical stiffness noticeably increases with decreasing temperature.
(3) The material passes a temperature range where time-dependent effects are strongly dominant.

In the current contribution we limit our material modeling on the first two aspects.

2.2 *Isotropic two-phase model*

As already mentioned both, the rubbery and the glassy phase, are amorphous. It is therefore reasonable to assume isotropy of the Helmholtz free energy per reference volume for both material phases. For the total Helmholtz free energy we apply a simple rule of mixture

$$W(\mathbf{b}, \mathbf{b}_e, \Theta) = (1-z)W_r(\mathbf{b}, \Theta) + zW_g(\mathbf{b}_e, \Theta) \qquad (1)$$

In Equation (1) $W_r(\mathbf{b}, \Theta)$ is the free energy function of the rubber-like phase above the glass transition temperature Θ_t. It depends on

$$\mathbf{b} = \mathbf{F}\mathbf{F}^T, \qquad (2)$$

the classical left Cauchy Green tensor. Below the transition temperature the material is specified by the second contribution $W_g(\mathbf{b}_e, \Theta)$, the energy function for the glassy phase. Herein, the left Cauchy Green tensor

$$\mathbf{b}_e = \mathbf{F}\mathbf{C}_f^{-1}\mathbf{F}^T \qquad (3)$$

is extended by, $\mathbf{C}_f^{-1}$ the inverse right Cauchy Green tensor including the "frozen" deformations. Therefore, $\mathbf{b}_e$ can be seen to be analogous to the so-called "elastic" left Cauchy Green tensor in plasticity.

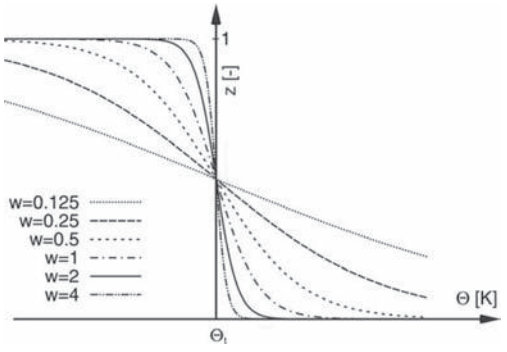

Figure 3. Transition variable z: influence of the width parameter w in dependence on the temperature.

Furthermore, in Equation (1) the two material phases are coupled via the glass transition variable z by means of the relation

$$z = \frac{1}{2}\left(1 - \frac{\exp(w\Delta\Theta) - \exp(-w\Delta\Theta)}{\exp(w\Delta\Theta) + \exp(-w\Delta\Theta)}\right) \quad (4)$$

Herein, $\Delta\Theta = \Theta - \Theta_t$ is the difference between the current temperature Θ and the glass transition temperature Θ_t. Furthermore w describes the transition width between the rubber-like and glassy-like state, see Figure 3.

Obviously, due to the fact that the material behavior in the rubber-like state is much softer than the one in the glass-like state, different sets of material parameters have to be chosen for the two phases in Equation (1).

2.3 *Transversal isotropic two-phase model*

Taking into account that SMP have a great potential in the area of sensor/actuator techniques it is obvious to cover with such SMP structures as much as possible movements. A single SMP dual-shape layer is capable of only one shape change since it exhibits only one thermal transition. Further, the programming of such layer is mostly done in an isotropic way. In order to achieve more complex movements it is necessary to program such layers in one preferred direction. The conglutination of layers programmed in *different directions* with *different thermal transitions* would lead to complex deformation states.

Due to the fact that such layers can be programmed in *one* preferred direction only, we extend the modeling approach in Section 2.2 and establish a transversal isotropic approach for the modeling of SMP effects. By introducing a unit vector $\mathbf{a}_0$, describing the direction of the material programming, we establish the fourth and fifth invariant in order to describe transversal isotropic material behavior. The Helmholtz free energy function of the rubber-like material behaves still isotropically, only the glassy-like material behaves non-isotropically, therefore Equation (1) formally changes to

$$W(\mathbf{b}, \mathbf{b}_e, \Theta, \mathbf{a}_0) = (1-z)W_r(\mathbf{b}, \Theta) + zW_g(\mathbf{b}_e, \Theta\mathbf{a}_0) \quad (5)$$

In contrast to Equation (1) here we freeze during the thermo-mechanical cycle the deformation including the preferred direction.

3 NUMERICAL EXAMPLES

This section is devoted to the assessment of modeling capabilities of the proposed model. Therefore we apply simulations on isotropic as well as on transversally isotropic SMP examples.

3.1 *Isometric behavior: Realistic stent polymer*

In order to show the potential and the robustness of the proposed modeling approach we realize a simulation on a three-dimensional stent geometry, see Figure 4.

The stent is mechanically loaded by an uniformly distributed load q = 300 N/m and an axial displacement of u = 0.035 m. The thermal load is a constant temperature at the whole stent (to be equal to the body temperature $\Theta = 310.15$ K), whereby a glass transition temperature is assumed to be $\Theta_t = 250$ K. Furthermore the stent has a length of L = 0.2 m, an inner radius of $R_i = 0.096$ m and a outer one of $R_o = 0.1$ m. The material parameters read $\mu_r = 3$ Pa, $\mu_g = 300$ Pa and $\Lambda_{r/g} = 30000$ Pa.

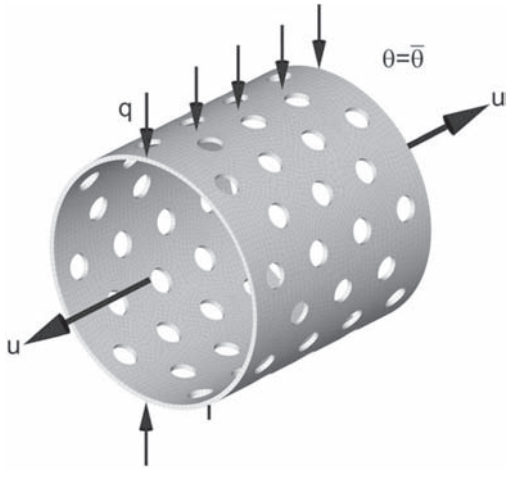

Figure 4. Geometry and boundary conditions of a realistic stent structure.

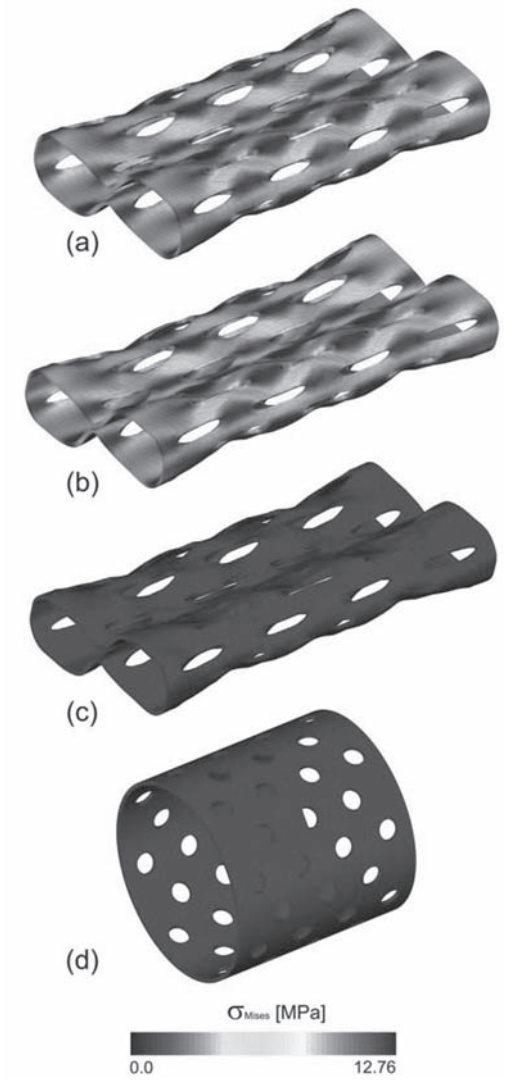

Figure 5. Typical thermo-mechanical cycle. stent (a) after mechanical loading, (b) after thermal loading, (c) after mechanical unloading and (d) after thermal unloading.

The contours in Figure 5 refer to the von Mises stress given in MPa. The state depicted in Figure 5 (a) represents the state after mechanical loading. By cooling down the stent, what is identical with the thermal loading, the stent further deforms, see (b). In the next step the mechanical load is removed (c) and the stent is now stress-free, but deformed. In this state the stent is implanted into the blood vessel. By the body temperature, the thermal unloading, the stent is heated up so that it is able to expand and hold the blood vessel open. In doing so, the stent "remembers" its old shape what is documented in Figure 5d. Here in the simulation, the stent is perfectly recovered illustrated by the original, undeformed state of the structure. This will not necessarily be the case inside the blood vessel where an interaction between the blood vessel wall and the stent takes place.

3.2 *Transversal isometric behavior: Rectangle under non-isotropic programming*

In the second example a three-dimensional rectangle is generated whereby the preferred programming direction is chosen to be a sinus-like curve, see the deformed structure in Figure 6b. The system is pressed from top and bottom by a pressure load of 3 kPa. Further the rectangle is bounded on all eight corners via springs in all directions in space.

The thermal load is a constant temperature at the whole rectangle (to be equal to $\Theta = 310.15$ K), whereby the glass transition temperature is assumed to be $\Theta_t = 250$ K. Furthermore the rectangle has a height of $H = 0.12$ m, a width of $W = 0.04$ m and a thickness of $T = 0.01$ m. The material parameters read $\mu_r = 5$ kPa, $\mu_g = 50$ Pa and $\Lambda_{r/g} = 1000$ Pa.

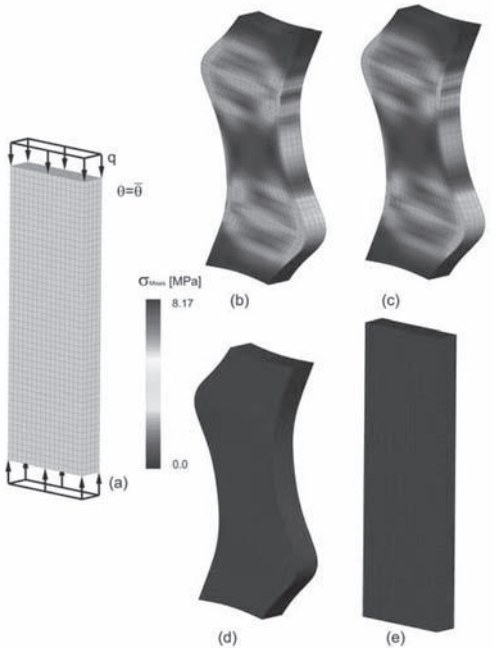

Figure 6. Finite element simulation of structure with preferred programming direction (sinus-like curve). (a) Geometry and boundary conditions, (b) deformed structure after mechanical loading, (c) after thermal loading, (d) after mechanical unloading and (e) after thermal unloading.

In a first step, the example is loaded mechanically, see Figure 6b. Then the rectangle is cooled below the glass transition temperature as illustrated in Figure 6c. Now the specimen behaves glassy-like. By removing the mechanical loading the example shows a stress-free deformed shape, see Figure 6d. The state depicted represents the so-called frozen state. In the application field of actors/sensors it is possible to position the geometry in a region where it has to expand. This situation takes place if the rectangle is heated up, see Figure 6e. In this state the system expands.

4 CONCLUSION

In this paper we present a new constitutive approach for the modeling of shape memory polymers. The focus is on the modeling of direction dependent as well as direction independent material behavior. The results show that the suggested method is a powerful tool to simulate the deformation behavior of SMPs in various situations.

Here, the development of the model is the main focus of the work, therefore we dispensed with any quantitative comparison with experimental data. It is, however, already at this point clear that the model offers enough flexibility for a satisfactory correlation with such data. This will be shown in future work.

REFERENCES

Abrahamson, E.R., M.S. Lake, N.A. Munshi & K. Gall 2003. Shape memory mechanics of an elastic memory composite resin. *Journal of the Intelligent Material Systems and Structures* 14, 623–632.

Alteheld, A., S. Feng, Y. Kelch & A. Lendlein 2005. Bioabbaubare, amorphe copolyesterurethannetzwerke mit Formgedaechtniseigenschaften. *Angewandte Chemie* 117, 1212–1216.

Barot, G. & I.J. Rao 2006. Constitutive modeling of the mechanics associated with crystallizable shape memory polymers. *Zeitschrift für Angewandte Mathematik und Physik (ZAMP)* 57 (4), 652–681.

Barot, G., I.J. Rao & K.R. Rajagopal 2008. A thermodynamic framework for the modeling of crystallizable shape memory polymers, *International Journal of Engineering Science* 46, 325–351.

Behl, M. & A. Lendlein 2007a. Actively moving polymers. *Soft Matter* 3, 58–67.

Behl, M. & A. Lendlein 2007b. Shape-memory polymers. *Materials Today* 10 (4), 20–28.

Bellin, I., S. Kelch & A. Lendlein 2007. Dual-shape properties of triple-shape polymer networks with crystallizable network segments and grafted side chains. *Journal of Materials Chemistry* 17 (28), 2885–2891.

Bellin, I., S. Kelch, R. Langer & A. Lendlein 2006. Polymeric Triple Shape Materials. *Proceedings of the National Academy of Sciences of the United States of America* 103 (48), 18043–18047.

Beloshenko, V.A., V.N. Varyukhin & Y.V. Voznyak 2005. The shape memory effect in polymers. *Russian Chemical Reviews* 74 (3), 265–283.

Böl, M. & S. Reese 2006. Finite element modelling of rubber-like polymers based on chain statistics. *International Journal of Solids and Structures* 43, 2–26.

Chen, S., J. Hu, H. Zhuo & Y. Zhu 2008. Two-way shape memory effect in polymer laminates. *Materials Letters* 62, 4088–4090.

Diani, J., Y. Liu, & K. Gall 2006. Finite strain 3d thermoviscoelastic constitutive model for shape memory polymers. *Polymer Engineering and Science* 46, 486–492.

Kafka, V. 2008. Shape memory polymers: A mesoscale model of the internal mechanism leading to the SM phenomena. *International Journal of Plasticity* 24, 1533–1548.

Lendlein, A. & M. Behl 2008. Shape-Memory Polymers for Biomedical. *Applications Advances in Science and Technology* 54, 96–102.

Lendlein, A. & S. Kelch 2002. Shape-memory polymers. *Angewandte Chemie International Edition* 41, 2034–2057.

Lendlein, A. & R. Langer 2002. Biodegradable, elastic shape memory polymers for potential biomedical applications. *Science* 296, 1673–1676.

Liu, Y., K. Gall, M.L. Dunn, A. R. Greenberg & J. Diani 2006. Thermomechanics of shape memory polymers: Uniaxial experiments and constitutive modeling. *International Journal of Plasticity* 22 (2), 279–313.

Liu, Y., K. Gall, M.L. Dunn & P. McCluskey 2003a. Thermomechanical recovery couplings of shape memory polymers in flexure. *Smart Materials and Structures* 12, 947–954.

Liu, Y., K. Gall, M.L. Dunn, P. McCluskey & R. Shandas 2003b. Shape memory polymers for medical applications. *Advanced Materials & Processes*, 31.

Liu, C. & P. Mather 2004. A shape memory polymer with improved shape recovery. *Materials Research Society Symposium Proceedings* 855, 112–117.

Otsuka, K. & C.M. Wayman 1998. *Shape Memory Materials*. New York: Cambridge University Press.

Poliane, C., P. Delobelle, C. Lexcellent, S. Hayashi & H. Tobushi 2000. Analysis of the mechanical behavior of shape memory polymer membranes by nanoindentation, bulging and point membrane deflection tests. *Thin Solid Films* 379, 156–165.

Qi, H.J., T.D. Nguyen, F. Castro, C.M. Yakacki & R. Shandas 2008. Finite deformation thermomechanical behavior of thermally induced shape memory polymers. *Journal of the Mechanics and Physics of Solids* 56, 1730–1751.

Reese, S., M. Böl & D. Christ 2009. Finite element-based multiphase modelling of shape memory polymer stents, *Computer Methods in Applied Mechanics and Engineering*, accepted.

Constitutive Models for Rubber VI – Heinrich et al. (eds)
© 2010 Taylor & Francis Group, London, ISBN 978-0-415-56327-7

Modeling of myocardial splitting due to deep penetration

Caroline Forsell & T. Christian Gasser
Department of Solid Mechanics, School of Engineering Sciences, The Royal Institute of Technology (KTH), Stockholm, Sweden

ABSTRACT: The risk for pacemaker lead perforation, a rare but serious clinical complication, is thought to be minimized by perforation resistant device design. Fracture properties of ventricular tissue play a central role in such optimization studies, however, this information is currently not provided by the open literature; even failure models for soft biological tissue in general are rare. Incompressible finite deformations, material nonlinearity and time-dependent anisotropic properties require sophisticated approaches to identify and model failure of such a material. In this study we investigated myocardial failure due to deep penetration, where previously collected data from in-vitro experiments are integrated in a non-linear Finite Element model. In details, the proposed model describes tissue splitting by a cohesive process zone, and hence, tissue failure is modeled as a gradual process, where all inelastic phenomena are accumulated and mathematically captured by a traction separation law. The cohesive zone is embedded in a fibrous bulk material thought to capture the properties of passive myocardial tissue, where a transversely isotropic hyper-elastic constitutive description proposed in the literature was utilized. The developed numerical model integrates latest experimental data and is able to replicate quantitative and qualitative data from ventricular penetration experiments.

1 INTRODUCTION

Lead perforation, acute or delayed, are rare but serious complications of pacemaker implantations (Khan, Joseph, Khaykin, Ziada, and Wilkoff 2005). This risk is thought to be minimized by appropriate lead design, where naturally the constitutive properties of ventricular tissue play a central role.

Mechanical failure of vascular tissue is a fairly unexplored field of biomechanics and only a few experiments are reported in the literature. Most commonly, uniaxial tensile tests in different directions have been proposed, which conform that vascular tissue exhibits anisotropic failure properties, see, e.g., (Mohan and Melvin 1982) (MacLean, Dudek, and Roach 1999). Apart from that, tearing (Purslow 1983), dissecting (Sommer, Gasser, Regitnig, Auer, and Holzapfel 2008) and inflation of circular specimens (Mohan and Melvin 1983) have been reported to derive failure properties from vascular tissue. For the present study, i.e. analyzing trauma due to lead perforation, the failure properties derived from deep penetration experiments (Gasser, Gudmundson, and Dohr 2009) are most relevant.

Despite experimental studies performed in the past, the failure mechanisms of ventricular tissue are poorly understood. Complex material properties like spatial inhomogeneity, nonlinearity, anisotropy, and time- dependent finite deformations require sophisticated approaches to identify and model failure of soft biological tissue. Up to date no constitutive law for damage and failure of soft biological tissue enjoys broad acceptance, however, reliable models are perquisite to enrich our current knowledge in the field of accidental biomechanics and to guide medical device development.

In the present study a finite element model has been developed to analyze mechanical trauma of myocardium (the muscular layer of the ventricular wall) due deep penetration, i.e. under mechanical circumstances applicable to lead perforation. The model has been compared and adjusted to earlier experiments (Gasser, Gudmundson, and Dohr 2009) and thought to assist lead design development.

2 METHOD

2.1 *Experiments*

To estimate the cohesive strength of myocardial tissue in cross-fiber direction uniaxial tension tests have been performed. In details, tissue from pig hearts (n = 12) was tested in physiological salt solution at 37 ± 0.5 degrees Celsius within less than four hours post mortem. Data was derived from in total 64 bone-shaped specimens and the testing was performed at a uniaxial testing machine

(Mts 305,03/30KN, Eden Prairie, Minn) with a 10N-Load cell under displacement control.

2.2 *Modeling*

Histological examinations of penetrated bovine and porcine ventricles confirmed localized tissue failure, i.e. tissue failure did not spread away from the penetration site. Likewise, the primary failure mechanism, even for flat-bottomed punches, was a splitting mode, where the crack faces were wedged open by the advancing punch (Gasser, Gudmundson, and Dohr 2009). To model this type of failure, cohesive interface elements were embedded in an otherwise anisotropic hyperelastic model for myocardial tissue.

In details, a fibrous tissue is considered and described by the transversely isotropic strain energy function

$$\Psi(\mathbf{C}, \mathbf{N}) = c_1(\alpha - 1)^2 + c_2(\alpha - 1)^3 + c_3(I_1 - 3) + c_4(I_1 - 3)(\alpha - 1) + c_5(I_1 - 3)^2,$$

as it has been derived from the myocardium of canine left ventricles (Humphrey, Strumpf, and Yin 1990b). Here, $I_1 = \mathrm{tr}\mathbf{C}$ and $\alpha^2 = I_4 = \mathbf{C}: (\mathbf{N} \otimes \mathbf{N})$ are coordinate invariant measures of tissue deformation, where the referential fiber direction $\mathbf{N}$ and the Right Cauchy Green strain $\mathbf{C} = \mathbf{F}\mathbf{F}^{\mathrm{T}}$ with the deformation gradient $\mathbf{F}$ have been introduced. Stress-like material constants $c1,\ldots, c5$, as identified from experimental data (Humphrey, Strumpf, and Yin 1990a) were used. The strain energy function $\Psi(\mathbf{C}, \mathbf{N})$ entirely renders the constitution of passive myocardium and standard arguments lead to the Second Piola Kirchhoff stress $\mathbf{S} = 2\partial\Psi/\partial\mathbf{C}$ and the associated elasticity tensor $\mathbb{C} = 2\partial\mathrm{S}/\partial\mathrm{C}$ (Ogden 1997).

In cohesive theory the separation of material surfaces is resisted by cohesive traction and the development of fracture is thought to be a gradual process. The constitution of the cohesive zone is described by traction separation law, i.e. by relating traction $\mathbf{T}$ and opening $\hat{\mathbf{u}}$ of the material surfaces. For the present study the cohesive potential

$$\psi(\hat{\mathbf{u}}, \delta) = \frac{t_0}{2\delta}\exp(-a\delta)i_1,$$

aims at modeling the fracture process, where $i_1 = \hat{\mathbf{u}} \bullet \hat{\mathbf{u}}$ and $\delta = \max[|\hat{\mathbf{u}}|]_0^t$ at time t. The cohesive strength t_0 and the material parameter a of dimension 1/Length need to be identified from experimental data. The cohesive potential $\psi(\hat{\mathbf{u}},\delta)$ entirely defines the constitution of the cohesive zone and standard arguments lead to the First Piola Kirchhoff traction $\mathbf{T} = \partial\psi/\partial\hat{\mathbf{u}}$ (Ortiz and Pandolfi 1999) and the associated cohesive stiffness $\mathbf{c} = \partial\mathbf{T}/\partial\hat{\mathbf{u}} + (\partial\mathbf{T}/\partial\delta) \otimes (\partial\delta/\partial\hat{\mathbf{u}})$ (Gasser and Holzapfel 2005).

2.3 *Myocardium penetration model*

Previous experiments (Gasser, Gudmundson, and Dohr 2009) considered ventricular tissue penetration of bi-axially stretched patches under quasi-static loading conditions. In Figure 1 the basic experimental principle is illustrated and Figure 2 summarizes the identified load displacement responses when using a punch of 1.32 mm in diameter.

In the present study a single failure site of such an experiment is numerically modeled, which allows us to investigate the induced failure mechanisms with respect to the punch design parameters. Due

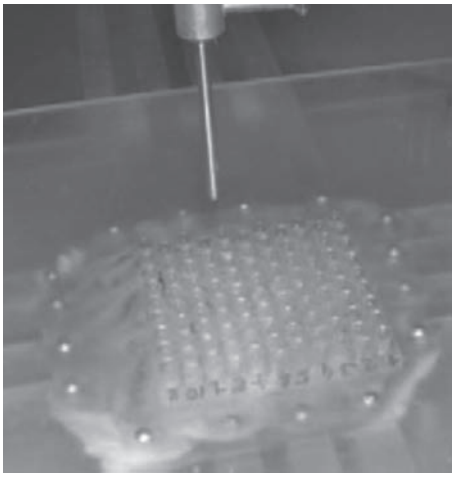

Figure 1. Penetration of bi-axially stretched ventricular heart tissue under quasi-static loading conditions (Gasser, Gudmundson, and Dohr 2009).

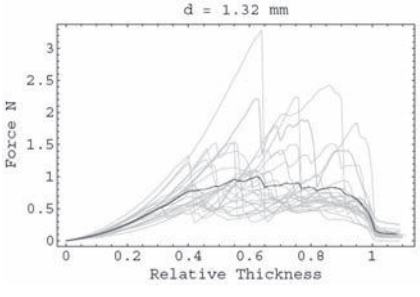

Figure 2. Load displacement response due to penetrating bi-axially stretched myocardial tissue with a punch of 1.32 mm in diameter. Gray lines denote recorded data from single penetrations, and the dark line denotes their algebraic mean.

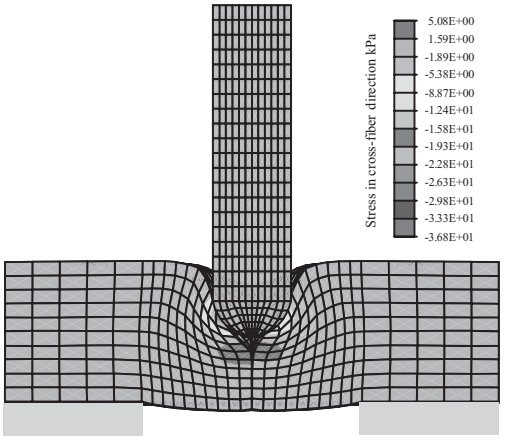

Figure 3. Numerical model of ventricular tissue penetration, where crack faces are wedged open by the advancing (rigid) punch.

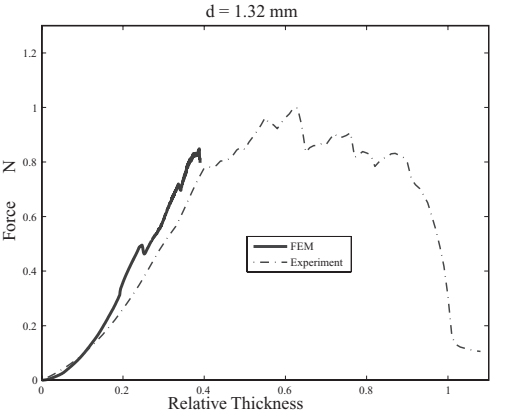

Figure 4. Comparison between predicted (solid line) and experimentally observed (dashed line) load displacement curves from deep penetration of myocardial tissue.

to symmetry conditions half of the problem was modeled and a stretch of 1.128 and 1.084 in fiber and cross-fiber directions were considered, respectively. Myocardial tissue was represented by 2500 hexahedral elements using the Q1P0 finite element formulation (Simo and Taylor 1991), where the fiber orientation **N** was in parallel to the cohesive zone. The punch was assumed rigid, with typical dimensions of pacemaker leads, and a contractor-target formulation rendered the frictionless contact problem, where the contact constraint was (approximately) enforced by the Penalty method (Wriggers 2002). The numerical problem is illustrated by the stress plot in Figure 3 and a dynamic simulation using implicit Newmark integration was followed, where nodal viscosity was added to damp out oscillations.

3 RESULTS AND CONCLUSION

Load displacement curves from uniaxial tensile tests in cross-fiber direction exhibited shape as they are typical for soft biological tissues, i.e. the stress increased progressively until rupture and irreversible (damage) mechanism could frequently be identified before reaching the ultimate load. The elastic part of the curve was quantitatively in accordance with data reported earlier (Humphrey, Strumpf, and Yin 1990a) (Humphrey, Strumpf, and Yin 1990b) and an ultimate tensile strength of 32.6(SD 15.9) kPa was identified.

Using $t_0 = 32.6$ kPa in the cohesive failure model in combination with realistic numbers for a, i.e. those causing a cohesive length in the range of 0.1 mm, overestimated severely the experimentally observed penetration force. Hence, uniaxial tensile test in cross-fiber direction might not be appropriate to identify failure properties, which in turn characterize deep penetration.

Finally the set $t_0 = 2.0$ kPa and $a = 17.0$ mm^{-1} of cohesive material parameters predicted a penetration force of about 0.9 N, i.e. that matches experimental data; Figure 4 illustrates an overlay of numerically predicted (solid line) and experimentally defined (dashed line) load displacement curves. It is emphasized that $a = 17.0$ mm^{-1} defines a realistic cohesive length, i.e. the cohesive traction is reduced by 90% at an opening of 0.135 mm and the used set of parameters defines a fracture energy of 0.118 mN mm^{-1} of tissue splitting due to deep penetration.

ACKNOWLEDGEMENT

This work has been financed by the Project Grant No. 2007-4514 from the Swedish Research Council, which is gratefully acknowledged.

REFERENCES

Gasser, D.C., P. Gudmundson., and G. Dohr (2009). Failure mechanisms of ventricular tissue due to deep penetration. *J. Biomech. 42,* 626–633.

Gasser, T.C., and G.A. Holzapfel (2005). Modeling 3D crack propagation in unreinfoced concrete using PUFEM. *Comput. Meth. Appl. Mech. Eng. 194,* 2859–2896.

Humphrey, J.D., R.K. Strumpf., and F.C.P. Yin (1990a). Determination of constitutive relation for passive myocardium—Part I and II. *J. Biomech. Eng. 112,* 333–346.

Humphrey, J.D., R.K. Strumpf., and F.C.P. Yin (1990b). Determination of constitutive relation for passive myocardium: II. Parameter estimation. *J. Biomech. Eng. 112,* 340–346.

Khan, M.N., G. Joseph., Y. Khaykin., K.M. Ziada., and B. L. Wilkoff (2005). Delayed lead perforation: a disturbing trend. *Pacing and Clinical Electrophysiology 28,* 251–253.

MacLean, N.F., N.L. Dudek., and M.R. Roach (1999). The role of radial elastic properties in the development of aortic dissections. *J. Vasc. Surg. 29*, 703–710.

Mohan, D., and J.W. Melvin (1982). Failure properties of passive human aortic tissue I—uniaxial tension tests. *J. Biomech. 15,* 887–902.

Mohan, D., and J.W. Melvin (1983). Failure properties of passive human aortic tissue II—biaxial tension tests. *J. Biomech. 16,* 31–44.

Ogden, R.W. (1997). *Non-linear Elastic Deformations.* New York: Dover.

Ortiz, M., and A. Pandolfi (1999). Finite-deformation irreversible cohesive elements for three-dimensional crack-propagation analysis. *Int. J. Numer. Meth. Eng. 44,* 1267–1282.

Purslow, P.P. (1983). Positional variations in fracture toughness, stiffness and strength of descending thoracic pig aorta. *J. Biomech. 16,* 947–953.

Simo, J.C., and R.L. Taylor (1991). Quasi-incompressible finite elasticity in principal stretches. Continuum basis and numerical algorithms. *Comput. Meth. Appl. Mech. Eng. 85,* 273–310.

Sommer, G., T.C. Gasser., P. Regitnig., M. Auer., and G.A. Holzapfel (2008). Dissection of the human aortic media: An experimental study. *J. Biomech. Eng. 130,* 12 pages.

Wriggers, P. (2002). *Computational Contact Mechanics.* Chichester: John Wiley & Sons.

Constitutive Models for Rubber VI – Heinrich et al. (eds)
© 2010 Taylor & Francis Group, London, ISBN 978-0-415-56327-7

Magnetoelastic anisotropic elastomers in a static magnetic field: Constitutive equations and FEM solutions

Hoang Sy Tuan & B. Marvalová
Technical University of Liberec, Czech Republic

ABSTRACT: In this paper we present briefly constitutive equations describing the behavior of magnetoelastic (or magneto-sensitive) anisotropic elastomers. The equations of the mechanical equilibrium and Maxwell's equations are summarized and a Helmholtz strain-energy functions for MS anisotropic elastomers is proposed in order to govern the interaction between a magnetoelastic anisotropic material and a magnetic field. Some FEM solutions are implemented in Comsol Multiphysics to illustrate a coupling of the magnetoelastic anisotropic material and the applied magnetic field.

1 INTRODUCTION

Recently a number of industrial applications of magneto-sensitive (MS) elastomers have been developed considerably owing to providing relatively simple and quiet variable-stiffness devices as rapid-response interfaces between electronic and mechanical systems including controllable membranes, controllable stiffness devices and applications for the active control of structural components.

Constitutive equations and appropriate strain-energy functions to model the magnetoelastic properties of these isotropic materials which consist of micron-sized ferrous particles dispersed randomly can be found in the recent series of papers by Dorfmann, Ogden, Brigadnov & Bustamante (2003–2007). However, in some particular cases during fabricating processing the MS materials can be embedded in a magnetic field, so that all ferrous particles are oriented in the same direction of the specified magnetic field. Therefore we have formulated constitutive equations of MS anisotropic elastomers with a single preferred direction which work in a magnetic field akin to composite materials reinforced by two families of fibers (more details see Holzapfel (2000)): one oriented in the direction of the chains of ferrous particles and one given by the direction of applied magnetic field based on the general theory of nonlinear magnetoelasticity incorporated with the theory of two fiber-reinforced composites.

The utilization of the constitutive equations of MS anisotropic elastomer into Comsol Multiphysics finite element code with supporting the Moving Mesh mode which involves large geometric changes of the domains is performed. The FE simulations of the magneto-mechanical coupling response of the magnetoelastic material are presented in which an incompressible magnetoelastic anisotropic material capable of large deformations is embedded in the uniform magnetic field and subsequently the body is subjected simultaneously by the magnetic force and the mechanical loading.

2 GOVERNING EQUATIONS

The balance equations for nonlinear magnetoelastic elastomers in a static magnetic field, as developed generally by Bridgadnov & Dorfmann (2003), Dorfmann & Ogden (2005), are summarized concisely in this section.

2.1 *Magnetic equations*

In the Eulerian description, Maxwell's equations in the absence of time dependence, free charges and free currents reduce to

$$div\mathbf{B} = 0, \qquad curl\mathbf{H} = 0 \tag{1}$$

which hold both inside and outside a magnetic material (for example, Kovetz (2000), Bridgadnov & Dorfmann (2003)), where div and curl relates to the spatial configuration.Thus, **B** and **H** can be regarded as fundamental field variables. In the vacuum, we have a basic relation between **B** and **H** as

$$\mathbf{B} = \mu_0 \mathbf{H} \tag{2}$$

where $\mu_0 = 4\pi \times 10^{-7}$ is a universal constant.

Associated with the equations (2) are the boundary continuity conditions

$$[\mathbf{B}] \cdot \mathbf{n} = 0, \qquad [\mathbf{H}] \times \mathbf{n} = \mathbf{0} \tag{3}$$

where [•] signifies a discontinutity across the boundary and **n** is its outward unit normal.

Lagrangian counterparts of **B** and **H**, denoted $\mathbf{B}_l$ and $\mathbf{H}_l$, respectively, are only considered in material domains to be given by (for example Dorfmann & Ogden (2005))

$$\mathbf{B}_l = J\mathbf{F}^{-1}\mathbf{B}, \qquad \mathbf{H}_l = \mathbf{F}^T\mathbf{H} \tag{4}$$

where the superscript $^{\mathrm{T}}$ denotes the transpose of a tensor.

And these quantities equations (1) become

$$Div\mathbf{B}_l = 0, \qquad Curl\mathbf{H}_l = \mathbf{0} \tag{5}$$

where *Div* and *Curl* are 'div' and 'curl' operators relative to the reference configuration respectively.

The boundary conditions (3) can also be expressed in Lagrangian form

$$\left(\mathbf{B}_l - J\mathbf{F}^{-1}\mathbf{B}_0\right)\cdot\mathbf{N} = 0, \qquad \left(\mathbf{H}_l - \mathbf{F}^T\mathbf{H}_0\right)\times\mathbf{N} = \mathbf{0} \tag{6}$$

in which $\mathbf{B}_0$ and $\mathbf{H}_0$ are the corresponding fields exterior to the material, but evaluated on the boundary in the reference configuration.

2.2 *Mechanical equations*

The conservation of mass equation is written simply as

$$\rho_0 = J\rho \tag{7}$$

where J is a volume ratio, $J = \det\mathbf{F}$ and **F** is the deformation gradient of the MS body.

The influence of the magnetic field on the mechanical stress in the deforming body may be incorporated through magnetic body forces or through a magnetic stress tensor (see Dorfmann & Ogden (2005)). Herein, we use the latter approach and denote the resulting total Cauchy stress tensor by $\boldsymbol{\tau}$, which has the advantage of being symmetric. In case the absence of mechanical body forces, the equilibrium equation for a magnetoelastic solid in Eulerian configuration has the form

$$div\boldsymbol{\tau} = \mathbf{0} \tag{8}$$

By using the total nominal stress tensor, here denoted **T**, which is related to $\boldsymbol{\tau}$ by

$$\mathbf{T} = J\mathbf{F}^{-1}\boldsymbol{\tau} \tag{9}$$

then the equilibrium equation (8) may be expressed in Lagrangian form as

$$Div\mathbf{T} = \mathbf{0} \tag{10}$$

The boundary condition involving the stress $\boldsymbol{\tau}$, where traction rather than displacement is specified, may be written in the form

$$[\boldsymbol{\tau}]\mathbf{n} = \mathbf{0} \tag{11}$$

and it can be noted that the traction $\boldsymbol{\tau}\mathbf{n}$ on the outer boundary includes a contribution from the (symmetric) Maxwell stress outside the material as well as any mechanical traction applied to the surface of the body.

According to Dorfmann & Ogden (2005) as well as Bustamante, Dorfmann & Ogden (2007) that the Maxwell stress outside the material, denoted $\boldsymbol{\tau}_{\mathrm{M}}$, is given by

$$\tau_M = \mathbf{H}^* \otimes \mathbf{B}^* - \frac{1}{2}\left(\mathbf{H}^*\cdot\mathbf{B}^*\right)\mathbf{I} \tag{12}$$

where **I** is the identity tensor and $\mathbf{B}^*$ and $\mathbf{H}^*$ are the corresponding fields exterior to the material evaluated on the boundary in the Lagrangian configuration, of cause $\mathbf{B}^* = \mu_0\mathbf{H}^*$.

2.3 *Constitutive equations*

For isothermal MS anisotropic materials we postulate the existence of a Helmholtz free energy function Ψ, which depends not only on a deformation gradient tensor **F** and a preferred direction of ferrous particles represented by $\mathbf{a}_0$ but also on a magnetic induction $\mathbf{B}_l$, denoted in the Lagrangian configuration, and the total free energy function is expressed as

$$\Psi = \Psi\left(\mathbf{F}, \mathbf{a}_0, \mathbf{B}_l\right) \tag{13}$$

From Clausius–Duhem inequality for electromagnetic media, see Brigadnov & Dorfmann (2003), we can derive constitutive equations which are obtained by differentiation of Ψ with respect to **F** or $\mathbf{B}_l$. The total nominal stress tensor **T** and the magnetic field $\mathbf{H}_l$ are given by the simple formulas

$$\mathbf{T} = \frac{\partial\Psi}{\partial\mathbf{F}}, \qquad \mathbf{H}_l = \frac{\partial\Psi}{\partial\mathbf{B}_l} \tag{14}$$

and for an incompressible material by

$$\mathbf{T} = \frac{\partial\Psi}{\partial\mathbf{F}} - p\mathbf{F}^{-1}, \qquad \mathbf{H}_l = \frac{\partial\Psi}{\partial\mathbf{B}_l} \tag{15}$$

where p is a Lagrange multiplier associated with the constraint $\det\mathbf{F} = 1$.

2.4 *The free energy function*

As above mentioned a MS anisotropic elastomers with one preferred direction undergoing an applied magnetic field is similar to composite materials reinforced by two fiber families (more details see Holzapfel (2000)), hence instead of only dependency of 6 invariants as for MS isotropic materials

(see Brigadnov & Dorfmann (2003), Dorfmann & Ogden (2005)) the free energy function has to depend on 10 invariants of $\mathbf{C}$, $\mathbf{a}_0$ and $\mathbf{B}_l$ that are defined as follows

$$
\begin{aligned}
&I_1(\mathbf{C}) = tr\mathbf{C}, \quad I_2(\mathbf{C}) = \frac{1}{2}[(tr\mathbf{C})^2 - tr\mathbf{C}^2] \\
&I_3(\mathbf{C}) = \det\mathbf{C} = J^2, \quad I_4(\mathbf{C},\mathbf{a}_0) = \mathbf{a}_0.\mathbf{C}\mathbf{a}_0 \\
&I_5(\mathbf{C},\mathbf{a}_0) = \mathbf{a}_0.\mathbf{C}^2\mathbf{a}_0, \quad I_6(\mathbf{B}_l) = \mathbf{B}_l.\mathbf{B}_l \\
&I_7(\mathbf{C},\mathbf{B}_l) = \mathbf{B}_l.\mathbf{C}\mathbf{B}_l, \quad I_8(\mathbf{C},\mathbf{B}_l) = \mathbf{B}_l.\mathbf{C}^2\mathbf{B}_l \\
&I_9(\mathbf{C},\mathbf{a}_0,\mathbf{B}_l) = (\mathbf{a}_0.\mathbf{B}_l)\mathbf{a}_0.\mathbf{C}\mathbf{B}_l \\
&I_{10}(\mathbf{a}_0,\mathbf{B}_l) = (\mathbf{a}_0.\mathbf{B}_l)^2
\end{aligned}
\tag{16}
$$

The free energy function can be rewritten as

$$
\Psi = \Psi\left(I_1, I_2, I_3, I_4, I_5, I_6, I_7, I_8, I_9, I_{10}\right) \tag{17}
$$

For incompressible materials, $I_3 = 1$, and the invariant I_{10} does not depend on the deformation therefore only the eight invariants I_1, I_2, I_4, …, I_9 remain. Then the total stress tensor $\boldsymbol{\tau}$ is expressed as

$$
\begin{aligned}
\tau = &-p\mathbf{I} + 2\Psi_1\mathbf{b} + 2\Psi_2(\mathrm{I}_1\mathbf{b} - \mathbf{b}^2) \\
&+ 2I_4\Psi_4\mathbf{a}\otimes\mathbf{a} + 2I_4\Psi_5(\mathbf{a}\otimes\mathbf{b}\mathbf{a} + \mathbf{b}\mathbf{a}\otimes\mathbf{a}) \\
&+ 2\Psi_7\mathbf{B}\otimes\mathbf{B} + 2\Psi_8(\mathbf{B}\otimes\mathbf{b}\mathbf{B} + \mathbf{b}\mathbf{B}\otimes\mathbf{B}) \\
&+ I_4\Psi_9(\mathbf{a}.\mathbf{b}^{-1}\mathbf{B})(\mathrm{a}\otimes\mathbf{B} + \mathbf{B}\otimes\mathbf{a})
\end{aligned}
\tag{18}
$$

where $\Psi_a = \partial\Psi/\partial I_a$, $a = 1, 2, 4, ..., 9$, and $\mathbf{b}$ is the left Cauchy-Green tensor. The total nominal stress tensor $\mathbf{T}$ is given by

$$
\begin{aligned}
\mathbf{T} = &-p\mathbf{F}^{-1} + 2\Psi_1\mathbf{F}^T + 2\Psi_2(I_1\mathbf{F}^T - \mathbf{F}^T\mathbf{b}) \\
&+ 2\Psi_4\mathbf{a}_0\otimes\mathbf{F}\mathbf{a}_0 + 2I_4\Psi_5(\mathbf{F}^{-1}\mathbf{a}\otimes\mathbf{b}\mathbf{a} + \mathbf{F}^T\mathbf{a}\otimes\mathbf{a}) \\
&+ 2\Psi_7\mathbf{B}_l\otimes\mathbf{B} + 2\Psi_8(\mathbf{B}_l\otimes\mathbf{b}\mathbf{B} + \mathbf{F}^T\mathbf{B}\otimes\mathbf{B}) \\
&+ \Psi_9(\mathbf{a}_0.\mathbf{B}_l)(\mathbf{a}_0\otimes\mathbf{B} + \mathbf{B}_l\otimes\mathbf{F}\mathbf{a}_0)
\end{aligned}
\tag{19}
$$

Finally, the magnetic field vector $\mathbf{H}_l$ is found from $(15)_2$ as

$$
\begin{aligned}
\mathbf{H}_l = &2(\Psi_6\mathbf{B}_l + \Psi_7\mathbf{C}\mathbf{B}_l + \Psi_8\mathbf{C}^2\mathbf{B}_l) \\
&+ \Psi_9((\mathbf{a}_0.\mathbf{C}\mathbf{B}_l)\mathbf{a}_0 + (\mathbf{a}_0.\mathbf{B}_l)\mathbf{C}\mathbf{a}_0)
\end{aligned}
\tag{20}
$$

and its Eulerian counterpart is

$$
\begin{aligned}
\mathbf{H} = &2(\Psi_6\mathbf{b}^{-1}\mathbf{B} + \Psi_7\mathbf{B} + \Psi_8\mathbf{b}\mathbf{B}) \\
&+ \Psi_9\left((\mathbf{a}_0.\mathbf{F}^T\mathbf{B})\mathbf{F}^{-T}\mathbf{a}_0 + (\mathbf{a}_0.\mathbf{B}_l)\mathbf{F}\mathbf{a}_0\right)
\end{aligned}
\tag{21}
$$

In order to simulate behaviors of incompressible MS anisotropic elastomers, we choose the free energy function similar to Ottenio et al.(2008)

$$
\Psi = \Psi_{iso} + \Psi_{ani} - p(J-1) \tag{22-a}
$$

$$
\Psi_{iso} = \frac{G}{4}\left[(1+\gamma)\left(\bar{I}_1 - 3\right) + (1-\gamma)\left(\bar{I}_2 - 3\right)\right] \tag{22-b}
$$

$$
\Psi_{ani} = \frac{k}{2}\left(\bar{I}_4 - 1\right)^2 + \frac{1}{\mu_0}\left(\alpha I_6 + \beta\bar{I}_7\right) \tag{22-c}
$$

where the free energy function is splitted into isotropic and anisotropic contributions that the isotropic part is the basic Mooney-Rivlin model while the anisotropic part contains both the elastic energy of ferrous particle chains and the magnetic energy. We assume that $G = G_0\left(1 + \eta_G I_6\right)$ is the shear modulus in the reference configuration, G_0 is the field independent shear modulus (or zero-field modulus) and $k = k_0\left(1 + \eta_k I_6\right)$ representes the anisotropic characteristic of MS elastomers. The material parameters α, β and γ are non-dimensional material constants and η_G and η_k are material constants involving the magnetic strength, these parameters need to be determined by coupling magnetic and mechanical experiments, and p is the hydrostatic pressure.

3 FEM SIMULATION OF MS ANISOTROPIC ELASTOMERS

3.1 *Coupling magnetic and mechanical solution*

To implement the coupled interaction of magnetic field and mechanical material we assert the magnetic field is solved in the spatial coordinates and the deformation response is computed in the reference coordinates. We also suppose that the external boundaries of the surrounding space (vacuum) are far away from the surfaces of the MS elastomer body, hence the remote magnetic field is considered to be homogeneous.

The influence of the magnetic field on the surface of magnetoelastic body is expressed via the corresponding tractions in the material coordinates by using Nanson's formula $\mathbf{n}da = J\mathbf{F}^{-T}\mathbf{N}dA$, where dA and da are the associated area elements respectively, and using equation (9) to derive as

$$
\mathbf{t}_a = J\tau_M\mathbf{F}^{-T}\mathbf{N} \tag{23}
$$

where $\boldsymbol{\tau}_\mathrm{M}$ is the Maxwell stress defined by equation (12) and $\mathbf{N}$ is a unit outer normal vector on the boundary of the undeformed body.

The stress and strain response of the body is calculated undergoing both magnetic and external forces, the displacement components are passed simultaneously into the magnetic solution by means of an advance technique as the Moving Mesh mode so that the magnetic field domain is changed in compliance with the large deformation of body. Therefore we can investigate the effect of the magnetic field to the magnetoelastic materials during the mechanical loading or vice versa.

In order to investigate the interaction of the MS anisotropic elastomers and the magnetic field we

use material parameters as listed in Table 1 for all following FEM examples.

3.2 *Compression of a block*

First we consider an MS anisotropic block with different aligned directions of ferrous particle chains embedded in a static uniform magnetic field parallel to its axis and simultaneously subjected a compressive load as a constant pressure $p_0 = 1$ MPa. A scheme sketch of the MS anisotropic block together with an applied magnetic field is depicted in figure 1.

We have obtained series of stress and strain responses of the block as well as the distribution of the magnetic field interior and exterior domains of the MS anisotropic material. In figure 2 illustrates some achieved results of deformations and equivalent stress distributions corresponding to ferrous particle orientations by 0° and 30° without and with the magnetic field applied by B = 1 T, moreover the direction of the magnetic traction vectors implies the body tends to lengthen along the direction of the applied field. In figure 3 we try to represent a distribution of the magnetic field and a magnetization of the body with the chain orientation by 30° and the magnetic flux density at

Table 1. Material parameters of a MS anisotropic composite.

G_0 [MPa]	η_G [T^{-2}]	k_0 [MPa]	η_k [T^{-2}]
1.8	0.6	5.0	0.9
α [–]	β [–]	γ [–]	
0.05	0.1	0.6	

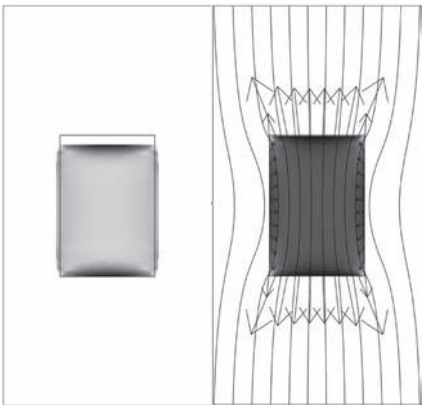

a) Orientation of particle chains: φ = 0° at B = 0T and B = 1T

b) Orientation of particle chains: φ = 30° at B = 0T and B = 1T

Figure 2. Deformation of the MS anisotropic block without and with a uniform magnetic field.

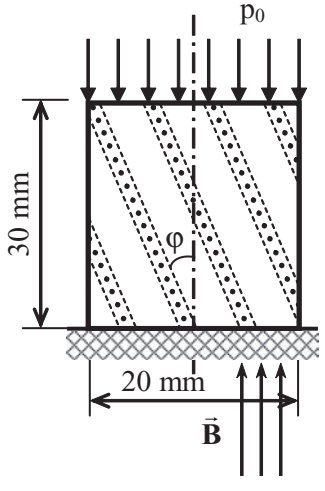

Figure 1. A scheme sketch of the compressive block in a magnetic field.

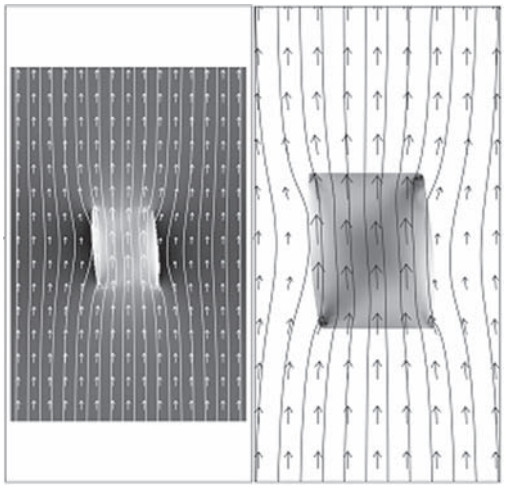

Figure 3. Distribution of the magnetic field and magnetization of the MS anisotropic material.

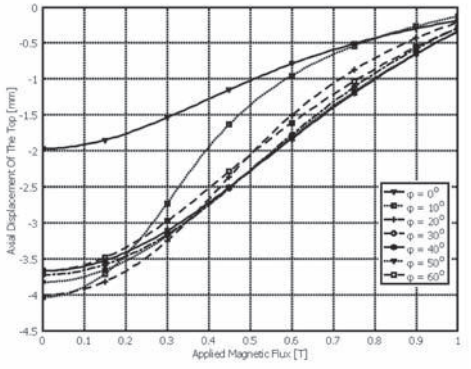

a) Vertical displacement of the top surface

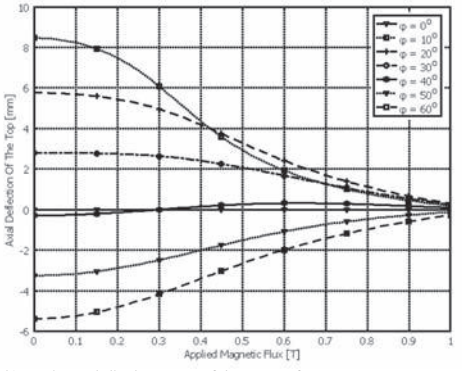

b) Horizontal displacement of the top surface

Figure 4. Displacements of the top surface of the block versus the magnetic flux density.

that time as 0.5 T, it can be seen that owing to the change of the domains induced by the deformation of the block the distribution of magnetic field does not remain to be symmetric and a strong dependency of the magnetic field on the deformation of the material is still denoted by the distribution of the magnetization inside the material.

Next dependencies of horizontal and vertical displacements of the top surface on orientations of ferrous particle chains and on an applied magnetic filed are shown as figure 4, the stiffness of the body increases fast that is demonstrated by the deformed block recovered nearly complete when the magnetic field reaches to 1 T.

3.3 *Simple shear*

In this subsection a rectangular MS anisotropic composite plate subjected a simple shear state is investigated according to altered directions of an applied magnetic. Here we assume ferrous particles are oriented in a vertical direction, only the modification of the applied magnetic field is considered. The geometry of the plate and loading conditions

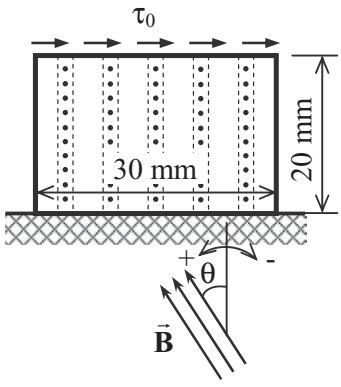

Figure 5. A geometry of a plate subjected a simple shear state is embedded in a static uniform magnetic field.

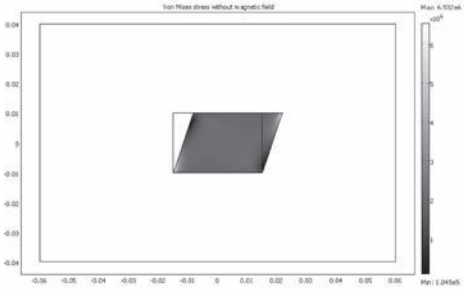

a) Shear deformation of the plate without magnetic field

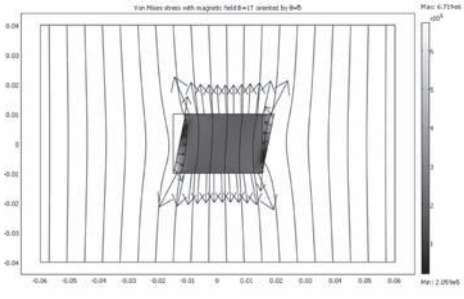

b) Magnetic field oriented in a vertical direction

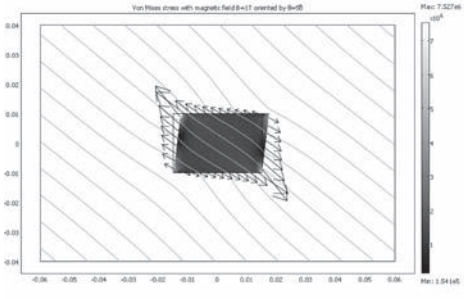

c) Magnetic orientation compared to a vertical direction θ = 50°

Figure 6. Simple shear state of the plate with different directions of the applied magnetic field.

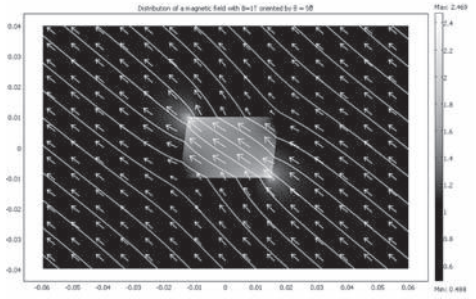

Figure 7. Distribution of the magnetic field with $\theta = 50^0$.

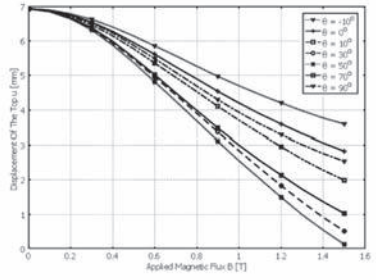

a) Displacement of the top surface versus different directions of the applied magnetic field

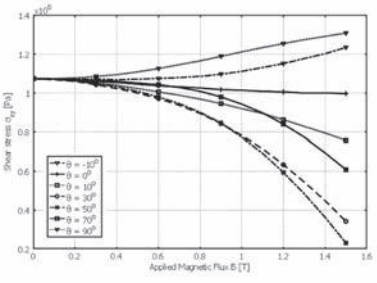

b) Shear stress at the center of the body versus different directions of the applied magnetic field

Figure 8. Dependencies of a displacement and a shear stress on the applied magnetic field.

are represented in figure 5. The direction of the magnetic field is defined by θ compared to the vertical direction. The external loading is set up by a constant traction as $\tau_0 = 1$ MPa.

In order to verify effects of the applied magnetic field on the MS body suffered a simple shear state a direction of the magnetic field is changed and some deformation results are obtained as in figure 6. It can conclude that the magnetic forces always affect towards to lengthen the MS body and enhance strongly the stiffness of the material. A high concentration and a large alteration of the magnetic field through the interface of the material and the surrounding space are shown in figure 7, of cause inside a dense material the field is distributed higher otherwise it still depends on the deformation of the body.

Dependencies of a displacement of the top surface applied by the external loading and a shear stress at the central position of the plate on the altered direction of the applied magnetic field are investigated in figure 8. Combination of both the displacement and the shear stress results state that we should apply the contrary direction of the magnetic field against the direction of the deformation in order to enhance a recovery back to the initial form of the deformed MS material.

4 CONCLUSION

We have summarized constitutive equations and shown a particular Helmholtz strain-energy function to represent an interaction between an MS anisotropic elastomer and an applied magnetic field. A coupling of the magnetic field and the mechanical problems for MS anisotropic materials are implemented successfully in Comsol Multiphysics. Reciprocal effects of MS materials and the magnetic field are examined via two standard examples: A compression and a simple shear. Achieved FEM results agree with practical experimental results and with the predictions in the mentioned papers.

ACKNOWLEDGMENT

This work was supported by the subvention from Ministry of Education of the Czech Republic under Contract Code MSM 4674788501.

REFERENCES

Brigadnov, I.A. & Dorfmann, A. 2003. Mathematical modeling of magneto-sensitive elastomers. *Int. Journal of Solids and Structures*, 40, pp. 4659–4674.

Bustamante, R., Dorfmann, A. & Ogden, R.W. 2007. A nonlinear magnetoelastic tube under extension and inflation in an axial magnetic field. *J. Eng. Math., 59*, pp. 139–153.

Dorfmann, A. & Ogden, R.W. 2003. Nonlinear magnetoelastic deformations of elastomers. *Journal Acta Mechanica*.

Dorfmann, A. & Ogden, R.W. 2005. Some problems in nonlinear magnetoelasticity. *Z. angew. Math. Phys., 56*, pp. 718–745.

Holzapfel, G.A. 2000. Nonlinear Solid Mechanics. A Continuum Approach for Engineering. *John Wiley & Son, Chichester*.

Kovetz, A. 2000. Electromagnetic theory. *Oxford Univ. Press*.

Ottenio, M., Destrade, M. & Ogden, R.W. 2008, Incremental Magnetoelastic Deformations with Application to Surface Instability, *Journal of Elasticity, Vol. 90, No. 1*, pp. 19–42.

Constitutive Models for Rubber VI – Heinrich et al. (eds)
© 2010 Taylor & Francis Group, London, ISBN 978-0-415-56327-7

Identification of strain energy function for magneto elastomer from pseudo pure shear test under the variance of magnetic field

S. Ishikawa
Mechanical Design & Analysis Corporation, Nagoya, Japan

F. Tsumori
Department of Mechanical Engineering, Faculty of Engineering, Kyushu University, Japan

H. Kotera
Department of Micro Engineering, Graduate school of Engineering, Kyoto University, Japan

ABSTRACT: Magneto elastomers are a class of smart materials whose mechanical properties may be controlled instantly by the application of an external magnetic field. Recently magneto elastomers are used in the automobile application area such as the tunable mounts and suspension devices. Such materials typically consist of micron-sized ferrous particles dispersed within an elastomeric matrix. In this present paper we performed the pseudo pure shear test for PDMS (polydimethylsiloxane) including carbonyl iron particles under the variance of magnetic field to explore the features. Furthermore we develop the governing equations for a more general form of constitutive model into the Nonlinear Finite Element Analysis program. The results, which show the stiffening of the shear modulus response with increasing magnetic field strength, are indicated on both of experimental tests and numerical analyses.

1 INTRODUCTION

Magneto elastomers can respond to an applied magnetic field with an instantaneous change in the mechanical behavior. This novel behaviour is caused by consisting of micron-sized ferrous particles dispersed within an elastomeric matrix such as rubber and polymer. Recently magneto elastomers are used in the automobile application area such as the stiffness tunable mounts and suspension devices, see for example Kordonsky (1993), Carlson & Jolly (2000), Jolly et al. (1996) and Watson (1997). On the other hand, the constitutive equations governing deformations of these materials were recently discussed on various literatures, see for Brigadnov & Dorfmann (2003), Dorfmann & Ogden (2004, 2005), Kankanala & Triantafyllidis (2004), Steigmann (2004) and Bustamante et al. (2008).

In this study, our purpose is the establishment of numerical analysis method for mechanical explication of magneto elastomer. For this purpose, we performed the pure shear experimental test for PDMS including carbonyl iron particles under the variance of magnetic field that is controlled by the distance of permanent magnets. In addition, we identify the strain energy function of magneto elastomers to analyze its nonlinear behaviour by using FEM.

The key results reveal the stiffening of the shear modulus response with increasing magnetic field strength; the results are also signified on both of experimental tests and numerical analyses. Proposed numerical method can handle the nonlinearity of magneto elastometric behaviour accurately.

2 PURE SHEAR EXPERIMENTAL TEST

2.1 *Material*

The PDMS is used as a Deformable micro structure in industrial field; for example, DMD (Digital Micro-mirror Device), acceleration sensors and etc. Recently, it is reported by Tsumori et al. (2007) that micro actuator and smart device are dispersed 50 nm sized ferromagnetic particles and driven by the exterior magnetic field. In this study, we prepared the PDMS including ferromagnetic particles by the same previous method.

The test specimens were prepared with containing 0, 1 and 2% iron by volume, on account of taking the different behavior through the volumetric density. The matrix was mixed ten parts of PDMS with one parts of curing agent.

The matrix was stirred about 10 minutes by an agitator, and degassed by vacuum equipment for one hour. The test specimen was mixed the matrix with 0, 1, and 2 volumetric percent of 50 nm sized ferromagnetic particles. Each specimen were molded and degassed for one hour, and held at 80°C for two hours in an oven to heat curing.

2.2 *Pure shear test*

Figure 1 shows the concise figure of pure shear test under the variance of magnetic field. For an incompressible material such as rubber, a state of pure shear may be achieved by the stretching of a rectangular sheet in one direction so as to produce an extension ratio λ_1, while maintaining the perpendicular or transverse dimension unchanged ($\lambda_2 = 1$), see Treloar (1944). The test specimen represents the appearance of wide strip (20 mm × 2 mm × 1 mm).

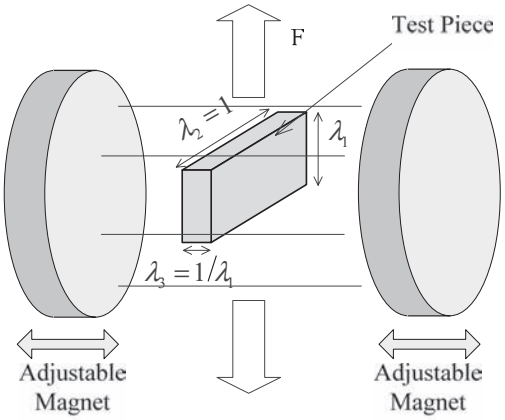

Figure 1. Concise figure of pure shear test.

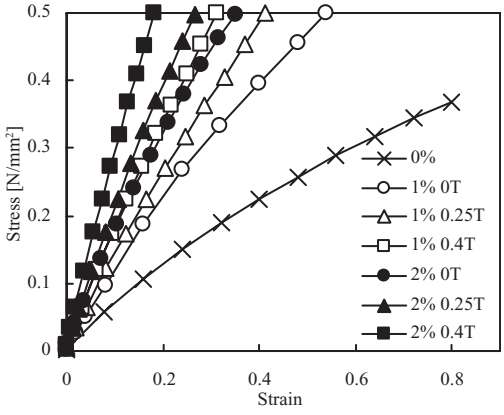

Figure 2. Experimental test of pure shear test.

There are two adjustable permanent magnets on both sides of the test specimen for applying variable magnetic field parallel to the width direction. The strength of magnetic field is controlled by the position of permanent magnets and applied to the specimen with 0, 0.25, and 0.4 Tesla.

2.3 *Result*

Figure 2 shows the stress-strain relation of pure shear test under the variance of magnetic field. It

Table 1. Grand state of elastic modulus (N/mm²).

	External magnetic field (T)		
Volume ratio (%)	0	0.25	0.4
0	0.651	0.651	0.651
1	1.096	1.309	1.645
2	1.590	1.883	2.620

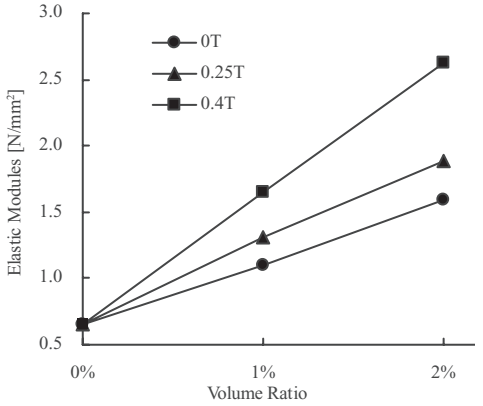

Figure 3. Elastic modulus against volume ratio.

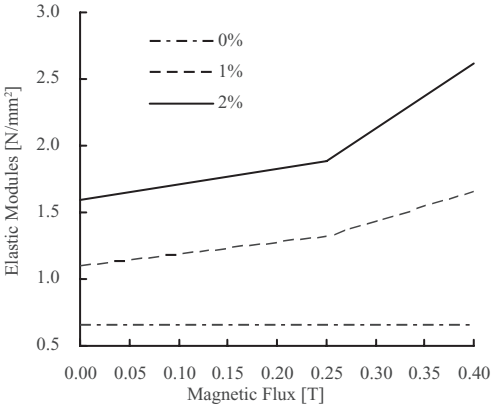

Figure 4. Elastic modulus against magnetic flux density.

can be seen that the shear stiffness varies with the volumetric particle and the external magnetic field. The grand state of elastic modulus was calculated from each stress-strain relationship (see Table 1). Figure 3 shows the elastic modulus of each external magnetic flux density against the volume ratio. Figure 4 also shows the elastic modulus of each volumetric ratio against the magnetic flux density. It can be seen the linear relationship on each external magnetic field, also the stiffness hardening by the magnetic particle volume ratio.

3 NUMERICAL ANALYSIS

3.1 *Constitutive equation*

To analyze the magneto elastomer behaviour in an applied magnetic field by the continuum mechanics, the electromagnetic equations should be coupled with mechanical deformation equations. In this study, it is assumed that the applied magnetic field is static and also the applied magnetic field does not change among the materials.

The Maxwell stress $\mathbf{T}_{\mathrm{m}}$ without electric field defined by the following equation is induced by the magnetic field in the ferromagnetic material:

$$\mathbf{T}_{\mathrm{m}} = \mathbf{B} \oplus \mathbf{H} - \mathbf{U}, \tag{1}$$

where $\mathbf{B}$ is the magnetic flux density and $\mathbf{H}$ is the magnetic field strength and $\mathbf{U}$ is magnetic energy per unit volume defined as follows:

$$\mathbf{U} = \frac{1}{2}(\mathbf{B} \cdot \mathbf{H})\mathbf{I}, \tag{2}$$

where $\mathbf{I}$ is the second order unit tensor. Magnetic flux density in the material is defined as

$$\mathbf{B} = \mu(\mathbf{H} + \mathbf{M}), \tag{3}$$

where μ is permeability of the material and $\mathbf{M}$ refers to magnetization.

In the Finite Element Analysis, the strain energy function should be used for describing the nonlinear elastometric behaviour. In this study, it is assumed that the rotation of magnetic particle in the magneto elastomer is infinitesimally, therefore, the symmetry condition covers not only the strain energy function but also the stress tensor. Therefore the Cauchy stress tensor $\mathbf{T}$ is defined in terms of the strain energy function Ψ under the symmetry condition as follows:

$$\mathbf{T} = J^{-1}\mathbf{F}\frac{\partial \Psi}{\partial \mathbf{C}}\mathbf{F}^{\mathrm{T}}, \tag{4}$$

where $J = \det\mathbf{F} > 0$ is the volume ratio, $\mathbf{F}$ is the deformation gradient, and $\mathbf{C} = \mathbf{F}^{\mathrm{T}}\mathbf{F}$ is the right Cauchy deformation tensor.

The strain energy function can be split into the mechanical strain energy of deformation and the magnetic strain energy of magnetic field as follows.

$$\Psi(\mathbf{C}, \mathbf{B}) = \Psi_{\mathrm{mech}}(\mathbf{C}) + \Psi_{\mathrm{mag}}(\mathbf{C}, \mathbf{B} \otimes \mathbf{B}). \tag{5}$$

The magnetic strain energy function has, consequently, two variables of the right Cauchy deformation tensor and the tensor dyad of the magnetic flux density.

Furthermore Equation 5 should satisfy the objectivity. Hence the strain energy function takes below six invariants according to the invariants theory of Spencer (1971).

$$I_1 = \mathrm{tr}\,\mathbf{C}, \tag{6}$$

$$I_2 = \frac{1}{2}(\mathrm{tr}\,\mathbf{C}\,\mathrm{tr}\,\mathbf{C} - \mathrm{tr}\,\mathbf{C}^2), \tag{7}$$

$$I_3 = \det\mathbf{C}, \tag{8}$$

$$I_4 = \mathbf{B} \cdot \mathbf{C} \cdot \mathbf{B} = \mathbf{C} : (\mathbf{B} \otimes \mathbf{B}), \tag{9}$$

$$I_5 = \mathbf{B} \cdot \mathbf{C}^2 \cdot \mathbf{B} = \mathbf{C}^2 : (\mathbf{B} \otimes \mathbf{B}), \tag{10}$$

$$I_6 = |\mathbf{B}|^2, \tag{11}$$

where tr is the trace of a second-order tensor. And the invariants of I_1, I_2 and I_3 are the mechanical invariant from the deformation gradient, while I_4, I_5 and I_6 are the magnetic invariant from the deformation gradient and the magnetic flux density. A slightly more general theory could accommodate direction dependence of $\mathbf{B}$, but here we restrict attention to the simpler case.

Then, the second Piola-Kirchhoff stress tensor $\mathbf{S}$, for example, is given explicitly in terms of Ψ as

$$\mathbf{S} = 2\frac{\partial \Psi(\mathbf{C}, \mathbf{B} \otimes \mathbf{B})}{\partial \mathbf{C}} = 2\sum_{a=1}^{6} \frac{\partial \Psi(\mathbf{C}, \mathbf{B} \otimes \mathbf{B})}{\partial I_a}\frac{\partial I_a}{\partial \mathbf{C}}. \tag{12}$$

By using differentiation with respect to six invariants

$$\begin{aligned}\mathbf{S} = 2\Bigg[&\left(\frac{\partial \Psi}{\partial I_1} + I_1\frac{\partial \Psi}{\partial I_2}\right)\mathbf{I} - \frac{\partial \Psi}{\partial I_2}\mathbf{C} + I_3\frac{\partial \Psi}{\partial I_3}\mathbf{C}^{-1} \\ &+ \frac{\partial \Psi}{\partial I_4}\mathbf{B} \otimes \mathbf{B} + \frac{\partial \Psi}{\partial I_5}(\mathbf{B} \otimes \mathbf{C}\mathbf{B} + \mathbf{B}\mathbf{C} \otimes \mathbf{B})\Bigg].\end{aligned} \tag{13}$$

The last two terms are contribution from magnetic field.

If the material is incompressible, so that $I_3 \equiv 1$, for isotropic magneto hyperelastic incompressible materials a suitable strain energy function is given by

$$\Psi = \Psi(I_1, I_2, I_4, I_5, I_6) + p(I_3 - 1), \tag{14}$$

where p is the negative hydrostatic pressure as an indeterminate Lagrange multiplier.

Finally, the total Cauchy stress tensor can be defined as follows:

$$\mathbf{T} = p\mathbf{I} + 2\left[\left(\frac{\partial\Psi}{\partial I_1} + I_1\frac{\partial\Psi}{\partial I_2}\right)\mathbf{b} - \frac{\partial\Psi}{\partial I_2}\mathbf{b}^2 + \mathbf{b}\frac{\partial\Psi}{\partial I_4}\mathbf{B}\otimes\mathbf{B} + \frac{\partial\Psi}{\partial I_5}\left(\mathbf{B}\otimes\mathbf{b}^2\mathbf{B} + \mathbf{B}\mathbf{b}^2\otimes\mathbf{B}\right)\right], \tag{15}$$

where $\mathbf{b} = \mathbf{F}\mathbf{F}^{\mathrm{T}}$ is the left Cauchy deformation tensor or the Finger objective tensor. This stress tensor is the same tensor as the transverse isotropic material (Holzapfel 2000; Ishikawa & Kotera 2005). Mechanical behaviour can be analyzed by substitution the magnetic flux density for the initial fiber orientation of elastic tangent as transverse isotropic material. Here, however, $\mathbf{B}$ is not a unit vector so the theory involves one more invariant I_6 than in the case for transverse isotropy.

It should also be added the relationship of magnetic field and magnetic flux density as follows:

$$\mathbf{H} = 2\left(\frac{\partial\Psi}{\partial I_4}\mathbf{B} + \frac{\partial\Psi}{\partial I_5}\mathbf{b}\mathbf{B} + \frac{\partial\Psi}{\partial I_6}\mathbf{b}^{-1}\mathbf{B}\right) = \mu_0{}^{-1}\mathbf{B} - \mathbf{M}. \tag{16}$$

3.2 *Strain energy function*

Assuming that the initial stress arisen from the magnetostriction is very small, also the magnetic flux density is uniform and same direction; we propose the following two parameter strain energy function for simplicity to analyze the mechanical behaviour of an isotropic magneto elastomer.

$$\Psi(I_1, I_6) = \frac{1}{q(I_6)}G(I_6)(I_1 - 3)^{q(I_6)/2}. \tag{17}$$

Here G is the shear modulus in the reference configuration, known from the linear theory, and $q > 2$ is the parameter of growth, which are functions of I_6 only. For $q = 2$ we obtain the classical neo Hookean model, which may be derived using concepts from the statistical theory of the elasticity of the molecular network structure of vulcanized rubber, see Treloar (1975). We assume that the shear modulus G and the growth parameter q can be written in the form

$$G(I_6) = G_0 + G_1\left[\coth(G_2 \cdot I_6) - \frac{1}{G_2 \cdot I_6}\right], \tag{18}$$

$$q(I_6) = q_0 + q_1 \cdot I_6, \tag{19}$$

where G_0 and q_0 are the field independent shear modulus and growth parameter; the others G_1, G_2 and q_1 are the field dependent parameters; G_0 and G_1 have the same unit of the stress, the others are dimensionless material parameters. The function of shear modulus G is modified from the Langevin function, since it should be able to manage the flux saturation. As a result, the strain energy function requires five material parameters for an isotropic incompressible magneto elastomer. This proposed energy function is not complicate, therefore five material parameters are easily fitted from the pure shear experimental test by using the least square methods. At first, G_0 and q_0 are determined from the stress-strain relationship from the non magnetic field result, secondly the other three parameters are computed from the results of varying magnetic field. Table 2 shows the fitted material parameters of each volume ratio test specimen from the pure shear test in Figure 2.

We implemented this strain energy function to MSC. Marc by using a user subroutine which executes the shear modulus change from the variance of magnetic field. The finite element analysis was executed to simulate the pure shear test results described previous section. The results

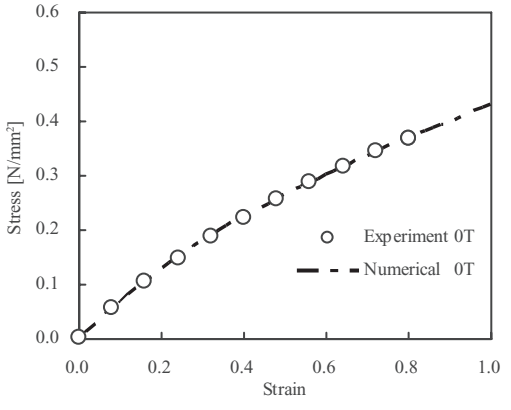

Figure 5. Pure shear test for volume ratio 0%.

Table 2. Material parameters for pure shear experimental test.

Volume ratio (%)	G_0 (N/mm²)	G_1 (N/mm²)	G_2	q_0	q_1
0	0.223	–	–	2.072	–
1	0.397	1.767	2.087	2.079	–0.059
2	0.546	2.963	1.917	2.050	–0.313

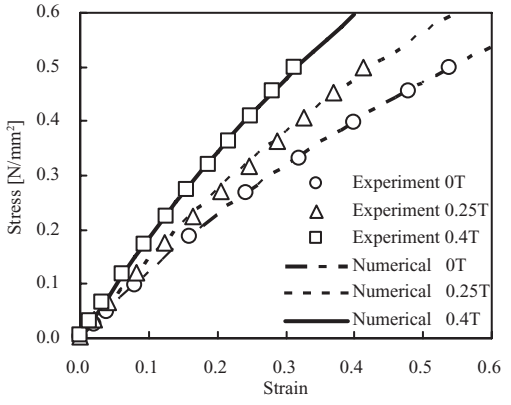

Figure 6. Pure shear test for volume ratio 1%.

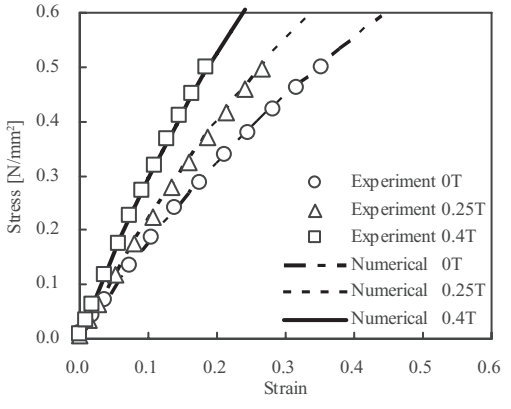

Figure 7. Pure shear test for volume ratio 2%.

of finite element analysis and experimental test appear in Figure 5, 6, and 7 on each volumetric ratio. The numerical results coincided with the experimental results in whole conditions.

4 ADDITIONAL EXAMINATION

We measured the stress strain relationship by the pure shear test under the constant magnetic field, whereas Jolly et al. (1996) measured the change in modules while varying the magnetic field.

In their study, the simple shear test was performed on the double lap specimen which was prepared in a mould using silicone oil loaded with a specified volume percent of carbonyl iron particles of a 3–4 μm mean diameter (see Figure 8). Three double lap shear specimens of MR elastomer were prepared containing 10, 20 and 30% iron by volume. The elastomer segments (shaded) are 20 mm by 7.5 mm by 1.0 mm thick and are sandwiched between an inner iron plate and two outer iron plates. The bold vertical arrow indicates the direction of applied field.

In order to verify the accuracy of our numerical model, we examined material parameter of our proposed model applying to the results of the literature. For this numerical examination, one of the non magnetic parameter G_0 is applied from nominal modulus of Jolly et al. (1996, Table 1); another non magnetic parameter q_0 is set 2.0 as same as neo Hookean material. In the later, the magnetic dependent material parameters are fitted to the experimental shear modulus change of Jolly et al. (1996, Figure.8). Table 3 shows the estimated

Table 3. Material parameters of proposed model for dual lapped shear experimental test.

Volume ratio (%)	G_0 (MPa)	G_1 (MPa)	G_2	q_0	q_1
30	1.80	0.938	4.883	2.0	0.016
20	0.74	0.411	8.052	2.0	0.013
10	0.26	0.733	3.725	2.0	0.300

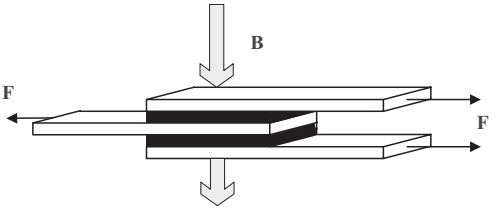

Figure 8. Double lap simple shear test.

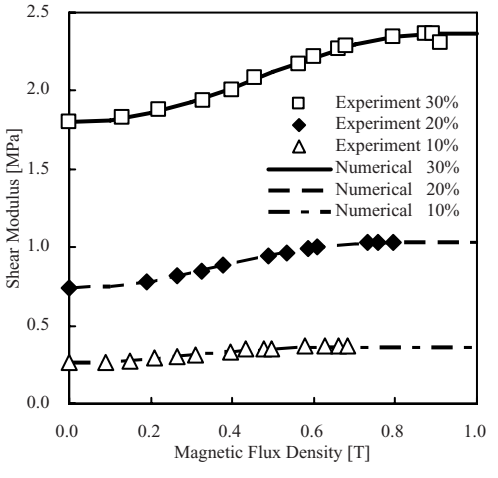

Figure 9. Variance of shear modulus by increasing the external magnetic flux density.

material parameters of our proposed model for three volume ratio specimens.

Numerical testing is carried out by Finite Element Methods with our proposed strain energy function. The symbol plots in Figure 9 denote the experimental data, and the numerical results of our method are indicated by line plot in the same figure. The calculated results agree very well with experimental ones. Especially, our model can treat accurately the no modulus change at the magnetic flux saturation plateau area.

5 CONCLUSIONS

We performed the pure shear test under the variance of magnetic flux density. The shear modulus of magneto elastomer was stiffened with increasing the external magnetic field. The stiffness change was linear through increasing the magnetic particle volume ratio.

A comparison between experimental results and FE-analysis has been conducted. The conclusion to be drawn from these results is that this proposed strain energy function accurately estimates the material testing under the magnetic flux density. In the additional examination, furthermore, our model was applied to the magnetic flux saturation plateau area.

REFERENCES

Brigadnov, I.A. & Dorfmann, A. 2003. Mathematical modeling of magneto-sensitive elastomers. *International Journal of Solids and Structures*. 40(18): 4659–4674.

Bustamante, R., Dorfmann, A. & Ogden, R.W. 2008. On Variational Formulations in Nonlinear Magnetoelastostatics. *Mathematics and Mechanics of Solids*. 13(8): 725–745.

Carlson, J.D. & Jolly, M.R. 2000. MR fluid, foam and elastomer devices. *Mechatronics*. 10: 555–569.

Dorfmann, A. & Ogden, R.W. 2004. Nonlinear Magnetoelastic Deformations. *The Quarterly Journal of Mechanics and Applied Mathematics*. 57(4): 599–622.

Dorfmann, A. & Ogden, R.W. 2005. Some problems in nonlinear magnetoelasticity. *Zeitschrift für Angewandte Mathematik und Physik*. 56(4): 718–745.

Holzapfel, G.A. 2000. *Nonlinear Solid Mechanics*. Chichester: John Wiley & Sons.

Ishikawa, S. & Kotera, H. 2005. Constitutive equations for fibre reinforced hyperelasticity. In P.-E. Austrell & L. Kari (eds.), *Constitutive Models for Rubber IV*: 619–625. Rotterdam: Balkema.

Jolly, M.R., Carlson, J.D. & Muñoz, B.C. 1996. A model of the behaviour of magnetorheological materials. *Smart materials and structures.* 5: 607–614.

Kankanala, S.V. & Triantafyllidis, N. 2004. On finitely strained magnetorheological elastomers. *Journal of the Mechanics and Physics of Solids*. 52(12): 2869–2908.

Kordonsky, W.I. 1993. Magnetorheological effect as a base of new devices and technologies, *Journal of Magnetism and Magnetic Materialsr.* 122: 395–398.

Spencer, A.J.M. 1971. Theory of invariants. In: Eringen, A.C. (eds.), *Continuum Physics*, vol. 1:239–353. Academic Press, New York.

Steigmann, D.J. 2004. Equilibrium theory for magnetic elastomers and magnetoelastic membranes, *International Journal of Non-Linear Mechanics*. 39(7): 1193–1216.

Treloar, L.R.G. 1944. Stress-strain data for vulcanized rubber under various types of deformation. *Transactions of the Faraday Society*. 40:59–70.

Treloar, L.R.G. 1975. *The Physics of Rubber Elasticity*. Oxford University Press.

Tsumori, F., Miyano, N., Fukui, A., Sagawa, K. & Kotera, H. 2007. Deformable Micro Pillar Array with Magnetic Particles and Elastic Material, IX International Conferecnce on Computational Plasticity.

Watson, J.R. 1997. US Patent. 5,609,353.

Constitutive Models for Rubber VI – Heinrich et al. (eds)
© 2010 Taylor & Francis Group, London, ISBN 978-0-415-56327-7

Experiment and material model for soft tissue materials

M. Staat, S. Sponagel & Như Huynh Nguyễn
Institute of Bioengineering, Aachen University of Applied Sciences, Jülich, Germany

ABSTRACT: The bulge test is an efficient but simple biaxial setup using only a minimum of biological material. This experiment is well suited to measure stretches in thin-walled materials such as rubber membranes, chorioamnion, bladder or intestinal tissue, etc. up to the ultimate stretch. The principal stretches are easily calculated from the experimental data, especially when the tested material shows isotropic behavior. The growth of biological tissue generates residual stresses which can be also measured with the bulge test. Tests with small specimens also permit local measurements of inhomogeneous tissues. In the paper, the small size bulge test is first developed with elastomers. For fitting of the data a modified version of the Kilian network is proposed for hyperelastic modeling of rubberlike materials. This strain-energy function represents both entropic elasticity and in addition energetic elasticity. Fitting the results shows that the proposed model, with only two material constants, can describe the behavior of rubberlike materials up to large elastic strains as accurate as the Ogden model with four or even six material constants. In a second phase the bulge test is used to test planar soft biopolymers or tissues.

1 INTRODUCTION

Biomechanics studies biological soft tissue materials (growth, remodeling) in vivo. For this objective, the detailed information of material properties must be well defined to construct reliable constitutive models. In the paper, the bulge test is carried out with elastomers in order to develop a test method. Then, application of the test for soft tissue materials is straightforward due to the similarities between elastomers with soft tissue materials as proved in Holzapfel 2005, Ogden 2009. It means, after the preliminary experiments and parameter identification with rubber materials has been setup, experiments on soft tissue materials can be similarly carried out. Elastomers have a complex behavior which strongly depends on the largest previous load cycle. For simplicity we consider only the first loading.

For elastomeric materials, experiments in multiple strain states such as simple tension, pure shear and biaxial tension may be needed to adequately define a material. The paper presents a simple equibiaxial test (bulge test) that can accompany with the tensile test to adequately define a material model. Neither sensitive to specimen's geometry (as pure shear test) nor sensitive to friction (as simple compression test), a pure state of strain can be easily attained with this equibiaxial test.

In order to estimate performance of the proposed Kilian model, fitting of experimental data based on the Ogden model is also taken into account. The Ogden model with six material parameters gives an excellent correlation with experimental data, Holzapfel 2000. The proposed Kilian model can predict the behavior of the rubberlike materials as well as the Ogden model does.

2 DESCRIPTION OF THE BULGE TEST

Many soft tissue materials, such as urinary bladder, mesentery, etc. are thin-walled and hence, can be investigated by membrane theory. The possible choices for testing membrane materials are in-plane biaxial tests and bulge (inflation) test.

This section investigates the inflation of elastomeric materials with various deformation levels. Based on relations between the internal pressure in the balloon (inflated material, i.e. in the current configuration) and the circumferential stretch λ, the material model and material parameters are identified. For isotropic materials, Ogden 2009 pointed out that only bulge tests are sufficient to fully determine the three-dimensional material properties. Compared to other biaxial tests, such as the biaxial tension test of a square specimen or the equiradial tension of a circular disk, the bulge test is the simplest one in experimental set up, see Figure 1.

In order to define the pressure-stretch relation, it is necessary to measure the pressure difference Δp and to measure geometrical data (h, L_{a1}, L_{a2}, L_b to calculate principal stretches), see (6). The side camera is used for monitoring the overall profile

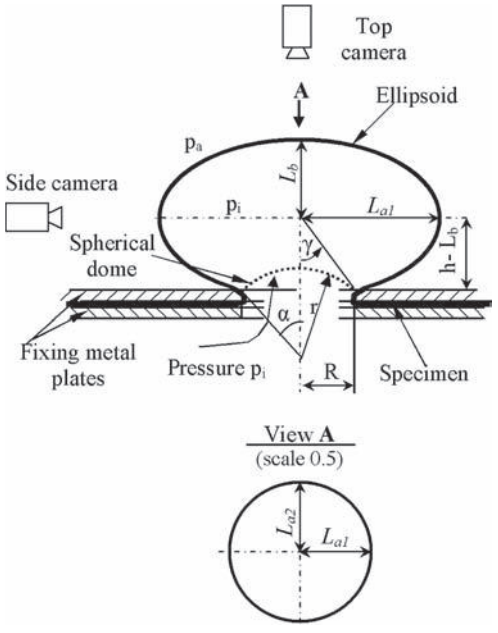

Figure 1. Schematic of bulge test.

of the specimen. The instance when the inflated specimen changes from spherical dome to ellipsoid is important because with each shape we need to use a specific formula for calculating surface area of the inflated specimen. The surface area is required to calculate the thickness stretch. The top camera is used for monitoring the semi-major axes of the ellipsoid. It is indispensable if the tested material shows some anisotropic behavior, at that time $L_{a1} \neq L_{a2}$.

2.1 *Strain calculation*

The specimen is clamped between two solid metal plates (Fig. 1). Pressurized air from one side inflates the specimen through the hole of radius R. The air pressure is increased gradually. By using a video-based system, we see that initially the specimen has a spherical dome shape. Increasing pressure, the inflated specimen will assume an ellipsoidal shape. If the material is isotropic, the ellipsoid will be rotational symmetric with two semi-major axes, which have the same length ($L_{a1} = L_{a2} = L_a$), and one semi-minor axis, which has the length L_b ($L_b < L_a$), see Figure 1. The ellipsoid with this form is named oblate spheroid.

The bulge test is considered as an equibiaxial tension with the membrane stresses:

$$\sigma_1 = \sigma_2 = \sigma \; ; \quad \sigma_3 = 0. \tag{1}$$

Consequently, the membrane stretches for the incompressible elastomer are:

$$\lambda_1 = \lambda_2 = \lambda \; ; \; \lambda_3 = \frac{1}{\lambda_1 \lambda_2} = \frac{1}{\lambda^2}. \tag{2}$$

The principal stretch λ can be calculated precisely by the formula on the basis of conservation of material volume as:

$$\lambda = \sqrt{\frac{t_0}{t}} = \sqrt{\frac{A}{\pi R^2}} \tag{3}$$

where t and t_0 are the actual and the reference thickness, respectively. A is the surface area of the spherical dome or ellipsoid, depending on the current deformation. For the spherical dome, the surface area is analytically calculated. For the ellipsoid the surface area from γ to $2(\pi-\gamma)$ (see Fig. 1) can be numerically calculated by a simple MATLAB program.

For the equibiaxial tension test, the deformation gradient $\mathbf{F}$ and the left Cauchy strain $\mathbf{B} = \boldsymbol{FF}^T$ are:

$$\mathbf{F} = \begin{pmatrix} \lambda & 0 & 0 \\ 0 & \lambda & 0 \\ 0 & 0 & \frac{1}{\lambda^2} \end{pmatrix}; \quad \mathbf{B} = \boldsymbol{FF}^T = \begin{pmatrix} \lambda^2 & 0 & 0 \\ 0 & \lambda^2 & 0 \\ 0 & 0 & \frac{1}{\lambda^4} \end{pmatrix}. \tag{4}$$

The equilibrium equations of the specimen at any stage of deformation, both the spherical dome and the ellipsoid, have the common form as:

$$\Delta p = \frac{2t}{L_a}\left(\sigma_{11} + \rho_{11}\right) \tag{5}$$

where for the spherical dome, $L_a \equiv R$ is the initial radius of the specimen; for the ellipsoid L_a is the length of the semi-major axis; ρ_{11} is the residual stress. For the sake of simplicity the relationship of equibiaxial residual stresses $\rho_{11} = \rho_{22}$ was assumed.

The above formulas are valid for isotropic materials. If the material is orthotropic, membrane stretches are directly calculated as:

$$\lambda_1 = S_1 / R \quad ; \quad \lambda_2 = S_2 / R \tag{6}$$

where S_1 is the periphery of the ellipse through the radius L_{a1} (the largest semi-major axis); S_2 is the periphery of the ellipse through the radius L_{a2} (the smallest semi-major axis).

3 HYPERELASTIC MATERIALS

We call a material Green-elastic or hyperelastic if there is an elastic potential (strain-energy function) W whose derivative with respect to a strain or deformation component determines the corresponding stress components. In the undeformed state $W = 0$

for the energy (then also the stresses) to vanish in the reference configuration. In this section a typical model that is useful for elastomeric materials and another typical model for soft tissue materials are presented. Then, a modified Kilian model is proposed. Expansion of the modified Kilian model for various tests is introduced. Later, in section 4, application of the modified Kilian model for fitting data from the bulge test is illustrated.

3.1 *Ogden model*

Most material models in commercially FEM codes allow the analyst to describe a subset of the structural properties of elastomers. The popular hyperelastic material models, such as Mooney-Rivlin or Ogden formulations, are available in almost commercial FEM codes. Ogden postulated that the strain energy is a function of the principal stretches λ_i ($i = 1, 2, 3$), see Ogden 1984, as:

$$W = W(\lambda_1, \lambda_2, \lambda_3) = \sum_{i=1}^{N} \frac{\mu_i}{\alpha_i}\left(\lambda_1^{\alpha_i} + \lambda_2^{\alpha_i} + \lambda_3^{\alpha_i} - 3\right). \quad (7)$$

The consistency condition for the model is:

$$2\mu = \sum_{i=1}^{N} \mu_i \alpha_i \quad \text{with} \quad \mu_i \alpha_i > 0 \quad (8)$$

where μ is the shear modulus of the material in the (undeformed) reference configuration.

It is suggested that three pairs of constants ($N = 3$) in (7) are enough for giving an excellent correlation with experimental data Holzapfel 2000. Applying the Ogden function (7) to calculate the membrane stresses in equibiaxial deformation for incompressible materials we have:

$$\sigma_1 = \sigma_2 = \frac{\partial W}{\partial \lambda_1} = \frac{\partial W}{\partial \lambda_2} = \sum_{i=1}^{3} \mu_i \left(\lambda^{\alpha_i} - \lambda^{-2\alpha_i}\right) \quad (9)$$

where 6 material parameters are used for fitting experimental data.

3.2 *Modified Kilian's model*

Extending the application of the van der Waals equation of state for technical polymers, Kilian proposed the stress-stretch relation in tension tests as, Kilian 1985:

$$\frac{P}{A_0} = \frac{\rho RT}{\lambda_m^2 M_m}\left(\frac{\Lambda}{1 - \frac{\Lambda}{\Lambda_m}} - a\Lambda^2\right) \quad (10)$$

where, $\Lambda(\lambda) = \lambda - 1/\lambda^2$, $\Lambda_m = \Lambda(\lambda_m)$.

Here P is the given load; A_0 is the initial cross-section of the specimen; ρ is the material density; $R = 8.31451\ \text{Jmol}^{-1}\text{K}^{-1}$ is the (general) molar gas constant; M_m is the molecular weight of the stretch-invariant basic unit. Thus $\rho = 1\ \text{gcm}^{-3}$ and $M_m = 68.11\ \text{gmol}^{-1}$ if natural rubber (C_5H_8) is considered. λ_m is a material parameter which relates to the ultimate elongation of the rubberlike material.

The formula above is derived from an energy function that only depends on the first invariant I_1. When correlating with experimental data, one sees that the Kilian model is able to represent the experimental data in the total range of stretch, Kilian 1985.

Staat et al. (2008) proposed an energy function for incompressible isotropic materials as:

$$\psi = \psi_1(J_1) + \psi_2(J_2) \quad (11)$$

where alternative invariants are defined:

$$J_1 = I_1 = tr(\mathbf{B}) \quad ; \quad J_2 = tr(\mathbf{B}^2) = I_1^2 - 2I_2. \quad (12)$$

Then the Cauchy stresses can be calculated as:

$$\boldsymbol{\sigma} + p\mathbf{I} = \rho_0\left(\frac{\partial \psi}{\partial J_1}\frac{\partial J_1}{\partial \mathbf{F}} + \frac{\partial \psi}{\partial J_2}\frac{\partial J_2}{\partial \mathbf{F}}\right)\mathbf{F}^T \quad (13a)$$

or $$\boldsymbol{\sigma} = -p\mathbf{I} + \varphi_1\mathbf{B} + \varphi_2\mathbf{B}^2 \quad (13b)$$

where, p is the hydrostatic pressure.

3.3 *Modified Kilian model for simple tension test*

Considering the simple tension test, the deformations are:

$$\mathbf{F} = \begin{pmatrix} \lambda & 0 & 0 \\ 0 & \frac{1}{\sqrt{\lambda}} & 0 \\ 0 & 0 & \frac{1}{\sqrt{\lambda}} \end{pmatrix}; \quad \mathbf{B} = \begin{pmatrix} \lambda^2 & 0 & 0 \\ 0 & \frac{1}{\lambda} & 0 \\ 0 & 0 & \frac{1}{\lambda} \end{pmatrix}. \quad (14)$$

The invariants defined in (12) are:

$$J_1 = \lambda^2 + \frac{2}{\lambda} \quad ; \quad J_2 = \lambda^4 + \frac{2}{\lambda^2}. \quad (15a, b)$$

From (13), stresses in tension test are calculated:

$$\sigma_{11} = -p + \varphi_1\lambda^2 + \varphi_2\lambda^4 \quad (16)$$

$$\sigma_{33} = \sigma_{22} = -p + \varphi_1\frac{1}{\lambda} + \varphi_2\frac{1}{\lambda^2} = 0. \quad (17)$$

Eliminating the undetermined pressure in equation (16) from (17) leads to:

$$\sigma_{11} = (\lambda^2 - \frac{1}{\lambda})\left[\varphi_1(J_1) + (\lambda^2 + \frac{1}{\lambda})\varphi_2(J_2)\right]. \quad (18)$$

Applying the model (11) for the tension test, for more details see Staat et al. 2008, leads to:

$$\frac{P}{A_0} = \sigma_{11}\frac{A}{A_0} = \frac{\sigma_{11}}{\lambda} = (\lambda - \frac{1}{\lambda^2}) \times \left[\varphi_1(J_1) + \left(\lambda^2 + \frac{1}{\lambda}\right)\varphi_2(J_2)\right] \quad (19)$$

The correlation of (10) with (19) suggests a form for the functions $\varphi_1(J_1)$ and $\varphi_2(J_2)$ as:

$$\varphi_1(J_1) = \frac{\rho RT}{\lambda_m^2 M_m}\left(\frac{1}{1 - \frac{\Lambda_1}{\Lambda_m}}\right); \qquad \varphi_2(J_2) = \frac{-a\Lambda_2}{\tilde{\lambda}_2^2(J_2) + \frac{1}{\tilde{\lambda}_2(J_2)}} \quad (20)$$

where $\Lambda_1 = \Lambda_1(\tilde{\lambda}_1)$ and $\Lambda_2 = \Lambda_2(\tilde{\lambda}_2)$; $\tilde{\lambda}_1$ is the solution of equation (15a), solved by Cardano's method and $\tilde{\lambda}_2$ is the solution of equation (15b), solved by Cardano's method, Staat et al. 2008.

For the uniaxial tension test $\tilde{\lambda}_1 = \tilde{\lambda}_2 = \lambda$. The material model proposed in (11) is different from the Kilian model because the second term of (11) is a function of the second invariant defined in (12). According to Staat et al. 2008, the first term of the energy function (11) is a representative of an entropy-elastic term (function of J_1). The second term is a representative of an energy-elastic term (function of J_2).

3.4 *Fung model*

Contrary to the hard tissues (bone, tooth, etc.), the soft tissues (skin, muscles, lung, etc.) show strongly non-linear behavior. Furthermore, because of the presence of collagen fibers distributed in soft tissues, the soft tissue materials exhibit anisotropic characteristics. Fung 1990 showed that the elastic stress for many specific soft tissues can be modeled by an exponential function of stretches. This is usually used in biomechanical applications. It is known however, that the Fung material fails to be polyconvex, Itskov et al. 2006. The strain-energy function is:

$$W(\mathbf{E}) = \frac{c}{2}[\exp(Q) - 1] \quad (21)$$

where the principal values $E_i = (\lambda_i^2 - 1)/2$ of the Lagrange strain tensor **E** are given by the principle stretches $\lambda_i (i = 1,2,3)$. Then $Q = c_1E_1^2 + c_2E_2^2 + c_3E_3^2 + 2c_4E_1E_2 + 2c_5E_2E_3 + 2c_6E_3E_1$ with the material constants $c, c_1, c_2, \ldots, c_6$. c has the dimension of an elastic modulus; $c_1, c_2, \ldots, c_6$ are dimensionless.

The associated stresses are obtained by:

$$\mathbf{S} = \frac{\partial W}{\partial \mathbf{E}}. \quad (22)$$

4 FITTING DATA FROM BULGE TEST FOR NATURAL RUBBER MATERIAL

Dimensions of the rubber specimen are $t_0 = 0.173$ mm and $R = 10$ mm. Experiments were conducted at room temperature. To define the maximum stretches, specimens are loaded until fracture.

4.1 *Fitting with the modified Kilian model*

Using (20), the functions $\varphi_1(J_1)$ and $\varphi_2(J_2)$ for natural rubber at room temperature T = 293 K the factor $\rho RT/\lambda_m^2 M_m = 35.8257\ \mathrm{Nmm^{-2}}/\lambda_m^2$ contains only the material constant λ_m.

In order to define the relation between the pressure difference Δp and the stretch λ in (5), one has to find two material parameters λ_m and a, see (10), by a least square method. Lower bounds of the material parameters λ_m and a are constrained to be positive to assure the energy function stable.

If we use expression (15) for calculating $\tilde{\lambda}_1$ and $\tilde{\lambda}_2$, and use expressions in (20) for calculating $\varphi_1(J_1)$ and $\varphi_2(J_2)$, values of the material parameters are obtained: $\lambda_m = 8.235$ and a = 0.159 N/mm^2, see Figure 2. As pointed out by Holl et al. 1990, the term λ_m is not identical to the maximum stretch λ_{max} in networks. However, there is an empirical relation $\lambda_{max} = \lambda_m + \lambda_{min}$ with $(0 \le \lambda_{min} \le 3)$. Hence, the maximal stretch of the material would be $\lambda_{max} = 8.0 \div 11.0$. This value can be attained with

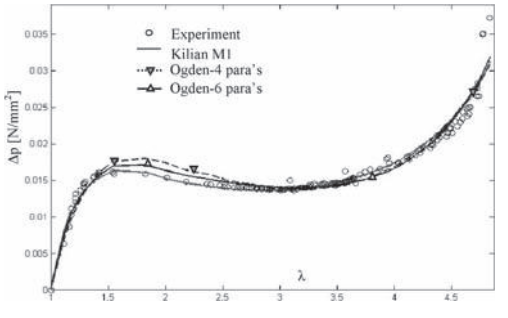

Figure 2. Curve fitting for equibiaxial test—pressure difference.

tension tests. At small stretches (λ <1.5) there is a little discrepancy between theory and experiment. This may be a consequence of using expressions (15), expressions for the tension test.

For the bulge test, curve fitting with pressure-stretch should be preferred over curve fitting with stress-stretch. In the former case values along the vertical axis are small (<0.03 N/mm^2). Hence, it is easier to check sensitive differences between experimental data and fitting curves. In the later case values along the vertical axis are larger (<60 N/mm^2). Consequently, the differences between curves are more difficult to recognize than in the later case. See Figures 4 and 5 for a comparison.

4.2 *Fitting with the Ogden model*

When $N = 2$, the curve fitting process defines material parameters of the Ogden model as below:

$$\mu_1 = -0.803 \text{ N/mm}^2 \quad ; \quad \alpha_1 = -0.902;$$
$$\mu_2 = -4.169 \cdot 10^{-5} \text{ N/mm}^2 \quad ; \quad \alpha_2 = -4.386.$$

The solutions above satisfy the consistent condition (8). As shown in Figure 2, the model of Ogden with 4 parameters does not give a good fitting. Hence, the Ogden model with more parameters should be preferred. With the same convergence criteria, when $N = 3$, the curve fitting process defines six parameters of the Ogden model as below:

$$\mu_1 = -3.828 \text{ N/mm}^2 \quad ; \quad \alpha_1 = -0.134;$$
$$\mu_2 = -1.0 \cdot 10^{-6} \text{ N/mm}^2 \quad ; \quad \alpha_2 = -5.676;$$
$$\mu_3 = 0.118 \text{ N/mm}^2 \quad ; \quad \alpha_3 = 3.263.$$

For the curve fitting process, the Kilian models satisfy the convergence criteria in 13 steps. Meanwhile using the Ogden models, the maximum iteration number was reached but the termination tolerance $1 \cdot 10^{-12}$ on the function was not reached. In fact tolerances were equal to $2.312 \cdot 10^{-4}$ and $1.746 \cdot 10^{-4}$ for Ogden models with 4 and 6 parameters, respectively.

5 VALIDATING WITH SIMPLE TENSION TEST

Objective of curve fitting is to define the necessary material parameters to input for the material model. To validate the modified Kilian model parameters which have been found with the bulge test, the identified material parameters are used to predict stresses of the simple tension test, Figure 3.

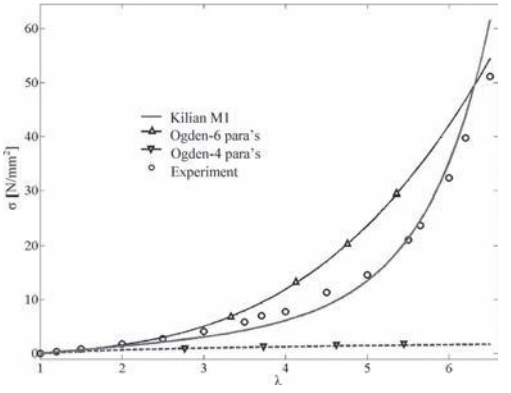

Figure 3. Uniaxial tension test prediction—Cauchy stress.

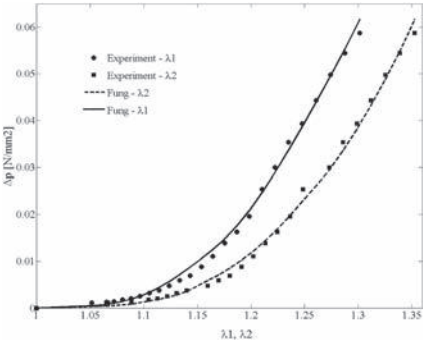

Figure 4. Curve fitting for equibiaxial test—intestine material.

In this phase, the Ogden model with six material parameters is also investigated. It was shown by Ogden et al. 2004 that by fitting the data for simple tension test (equibiaxial test) the prediction for equibiaxial tension test (simple tension test) is not good. This argument is again assured by the prediction curve of the Ogden model (6 parameters) in Figure 3. However, the modified Kilian model M1 seems to give better predictions than the Ogden model. Experimental stresses from the tension test have been used to validate the prediction results.

6 FITTING DATA FROM BULGE TEST FOR PORCINE SMALL-INTESTINE

A part of fresh, porcine small-intestine was extracted from an adult swine from a butcher's shop. Ten specimens were extracted and immersed in warm physiological saline solution (37°C). The porcine small-intestine shows orthotropic property as illustrated in Figure 4. The goal of this part is to

illustrate the application of the bulge test for soft tissue materials. The average thickness of the large-intestine is 0.065 mm.

The orthotropic samples do not inflate into a spherical cap geometry. In static equilibrium the differential pressure Δp is related to ratio between the tensions T_1, T_2, and the corresponding local radii of curvature, $L_{a1,}L_{a2}$ (Fig. 1) by the following equation (Laplace's law, see Fung 1990, section 11.7):

$$\Delta p = \frac{T_1}{L_{a1}} + \frac{T_2}{L_{a2}} = \frac{\sigma_1 h_1}{L_{a1}} + \frac{\sigma_2 h_2}{L_{a2}} \tag{23}$$

where h_1 and h_2 are thickness of the material in direction 1 (longitudinal) and 2 (circumferential direction). For the sake of simplicity, let's assume $h_1 = h_2 = h$. The equilibrium equation (23) will be applied for determining material parameters of Fung's model (21) with σ_1 and σ_2 are calculated from (22) where hydrostatic pressure is calculated from the plane stress condition ($\sigma_3 = 0$).

7 CONCLUSIONS

The paper presents a modified Kilian material model with 2 material constants for tension and biaxial. Results from curve fitting show that the modified Kilian model is able to describe the behavior of elastomeric material at large stretch ($\lambda > 4.5$) as well as the Ogden model with 6 material constants. By fitting the data for equibiaxial test the modified Kilian model is better than the Ogden model in predicting stress for the simple tension test. However, the form of the functions $\varphi_1(J_1)$ and $\varphi_2(J_2)$ is not fixed. Different choices are currently tested also in pure shear. This will be reported together with a FEM implementation of the modified Kilian model.

The paper also illustrates an application of the bulge test for soft tissue materials. Normally, soft tissue materials are orthotropic. That property can be determined by using geometrical data collected from a camera system and then the curve fitting process is carried out with (23). The mechanical characterization is important with respect to modeling aspects and medical problems such as aneurisms and PROM (premature rupture of amniotic sac before labor begins), Prévost 2006, Lindner 2006.

ACKNOWLEDGEMENT

The last author has been partially supported by the BMWi through the PRO INNO programme, project no. KF0205102SB8.

REFERENCES

Cowin, S.C. & Doty, S.B. 2007. *Tissue mechanics*. New York: Springer.

Fung, Y.C. 1990. *Biomechanics: Motions, Flow, Stress, and Growth*. New York: Springer.

Holl, B. Kilian, H.G. & Schenk, H. 1990. Crystallization in unstretched and in stretched rubber and its thermodynamic description. *Colloid & Polymer Science* 268: 205–221.

Holzapfel, G.A. 2000. *Nonlinear solid mechanics*. Chichester: John Wiley.

Holzapfel, G.A. 2005. Similarities between soft biological tissues and rubberlike materials. In Austrell P.E. and Keri L. (eds.), *Constitutive models for rubber IV*: 607–617. Leiden: A.A. Balkema.

Humphrey, J.D. 1998. Computer methods in membrane biomechanics. *Computer Methods in Biomechanics and Biomedical Engineering* 1(3): 171–210.

Itskov, M. Ehret A.E. & Mavrilas D. 2006. A polyconvex anisotropic strain-energy function for soft collagenous tissues. *Biomech Model Mechanbiol* 5(1): 17–26.

Kilian, H.G. 1985. An interpretation of the strain-invariants in largely strained networks. *Colloid & Polymer Science* 263: 30–34.

Lindner, P. 2006. *Examination of mechanical properties of human amniotic sac membranes*. Master Thesis, Aachen University of Applied Sciences.

MATLAB 7, Release 14, User guide.

Ogden, R.W. 1984. *Non-linear elastic deformations*. Mineola, New York: Dover.

Ogden, R.W. Saccomandi, G. & Sgura, I. 2004. Fitting hyperelastic models to experimental data. *Comput. Mech.* 34: 484–502.

Ogden, R.W. 2009. Anisotropy and nonlinear elasticity in arterial wall mechanics. In G.A. Holzapfel and R.W. Ogden (eds.), *Biomechanical modelling at the molecular cellular and tissue levels*: 179–258. Wien: Springer.

Prévost, T.P. 2006. *Biomechanics of the human chorio-amnion*. Master Thesis, Massachusetts Institute of Technology.

Staat, M. Baroud, G. Topcu, M. & Sponagel, S. 2008. Soft materials in technology and biology—characteristics, properties and parameter identification. In G.M. Artmann and Shu Chien (eds.), *Bioengineering in cell and tissue research*: 253–315. Berlin Heidelberg: Springer.

Reinforcement

Constitutive Models for Rubber VI – Heinrich et al. (eds)
© 2010 Taylor & Francis Group, London, ISBN 978-0-415-56327-7

Quantitative structural analysis of filled rubber by AFM

I. Morozov
Institute of Continuous Media Mechanics UB RAS, Perm, Russia
Leibniz-Institut für Polymerforschung Dresden e. V., Dresden, Germany

B. Lauke & G. Heinrich
Leibniz-Institut für Polymerforschung Dresden e. V., Dresden, Germany

ABSTRACT: The mechanical properties of carbon black reinforced rubbers, strongly depend on the uniformity of filler distribution in the material and the size of filler clusters in the finished product, i.e., on the quality of mixing of composite components. In this paper, we present methods for quantitative analysis of the structure of filled rubbers by Atomic Force Microscopy (AFM). Next microstructure characteristics as Morishita's index, cross-section area, volume, compactness and cluster size have been obtained by testing three specimens consisting of different fillers and binders. In one of these specimens, essential non-uniformities in cluster distribution and sizes have been revealed. It is shown that the density of clusters decreases with increasing size. The area and perimeter of clusters as well as their volume and size are governed by fractal mechanisms.

1 INTRODUCTION

Carbon black (CB), one of the main components of rubber composites (tires, insulators, conveyer belts, etc), is preferably delivered in the form of granules of diameter 1–2 mm. During mixing of the polymer and the fillers, the carbon granules are broken down, and the CB structures (aggregates and agglomerates) are distributed throughout the material. The more uniform the distribution of clusters is and the smaller their sizes are, the larger is the filler surface area that interacts with the binder.

Insufficient mixing and grinding of granules lead to strong filler-filler interactions. In this case, stresses are distributed non-uniformly during deformation. Breakage of large-size clusters results in an essential change in the dynamic modulus of the material, which, in turn, causes high hysteresis losses. All these factors adversely affect the mechanical properties of the end product. Hence, the deciding factor that influences the quality of filled rubbers, all other factors being equal, is the degree of filler dispersion. As the filler distribution in the material gets more uniform, the scattering in particle sizes decreases, improving thus the mechanical characteristics of the filled rubber.

Atomic force microscope provides a powerful, yet rather simple, way to study the nanostructure of materials, in particular, filled elastomers (Johnson, 2008).

This study presents methods for qualitative analysis of the structure of filled rubbers. The proposed approach includes two stages: 1) Processing of AFM images for further statistic analysis of the structure of clusters. 2) Analysis of quantitative estimates of the filler distribution in the material, its sizes, areas, volume fraction and compactness. The obtained characteristics give us insight into the microstructure of elastomeric composites.

2 EXPERIMENT

For AFM imaging, three industrial tire rubbers manufactured at the "Scientific-Research Institute of Tire Industry" (Moscow) were prepared (Table 1).

The materials were imaged in a close contact mode using DI Nanoscope IV (nominal radius of the tip <10 nm). For statistics, from each rubber 10 images of 10×10 and 3×3 μm with resolution 512×512 points in plane were obtained and analyzed by our procedures written in Matlab.

3 GENERAL ANALYSIS OF THE IMAGES

The surface structure obtained by AFM is a complex three-dimensional relief. If we observe only such part of the AFM-image that is higher as some height h above the zero level, the relief will be separated

Table 1. Materials.

No	CB	Volume fraction	Binder
1	N220	0.2	NR
2	N330	0.2	SBR
3	N339	0.2	NR

into 'islands'. As we cannot define whether this 'island' is part of CB aggregate or agglomerate any structural feature of the AFM image, whose cross-section A is larger than 0.01 μm^2, is called a cluster. The smaller objects of the surface relief are excluded from the analysis, since the probes of the microscope are unable to provide the reliable images of small (<20 nm) features in the xy-plane.

For images 10 × 10 μm, the following height dependences are constructed:

1. The average compactness (Bogaert et al. 2000) of the cluster cross-section $c(h)$:

$$c(h) = \frac{2\sqrt{\pi}}{N(h)} \sum_{k=1}^{N(h)} \frac{\sqrt{A_k(h)}}{P_k(h)}, \quad (1)$$

where $N(h)$ = number of clusters; $A_k(h)$, $P_k(h)$ are the area and perimeter of the k –th cluster cross section. Equation (1) shows how much the shape of the circle and some figure are different. For circle $c \equiv 1$, the smaller is c, the less compact is the profile of the cluster cross-section.

2. The volume fraction of clusters $\phi(h)$:

$$\phi(h) = \frac{V\Big|_h^{h+20}}{20 \cdot 10000}. \quad (2)$$

By equation (2) we calculate the volume fraction of the material in the layer 20 nm above h. To determine A and P we examine the clusters that do not intersect the image edge. Figure 1 illustrates cross-sections of the specimen with countours of separate clusters.

Figure 2 presents the dependences of c and ϕ on the relative height h/h_{max}, where h_{max} is the maximum height over the zero level.

As one can see (fig. 2) for $h = h^* \in [0.45 \ldots 0.52]h_{max}$, the compactness is minimal and volume fraction of clusters close to the filler volume fraction 0.2. At small heights we observe compact and dense clusters with high volume fraction. Such objects cannot truly represent shape of CB clusters in rubber which are known for its branchy structure (Kohjiya et al. 2006). Only from some height $h \equiv h^*$ we can suggest that the relief structure is closest to the filler geometry. Therefore, our further analysis of AFM images is concerned with the study of the upper part of the relief: $h \geq h^*$.

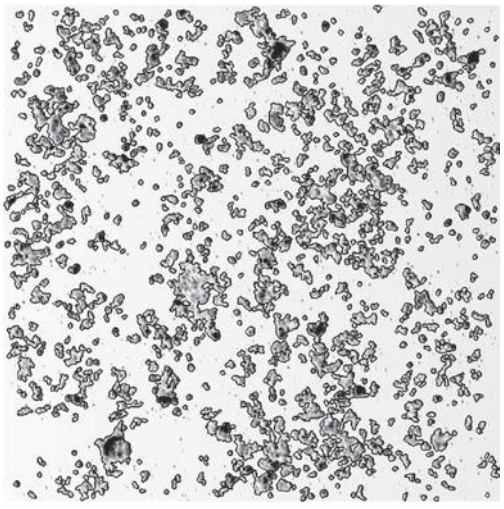

Figure 1. Upper part of one of the AFM images: $h \geq 0.5\ h_{max}$.

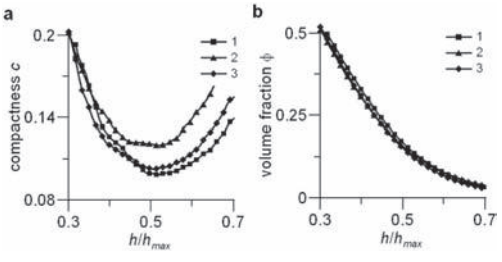

Figure 2. Example of picture obtained after cutting off the lower part of the image for $h = 0.5\ h_{max}$.

4 RESULTS

For the analysis of cluster distribution in 10 × 10 μm images, we use Morishita's index (Karasek et al. 1996):

$$I_\delta = q \sum_{i=1}^{q} n_i(n_i - 1) / \left[N(N-1)\right].$$

The image is separated into q squares, the clusters are replaced by the points coinciding with geometric center of the clusters; n_i is the number of points in the i-th square; N–total number of clusters. Obtained values of $I_\delta(q)$ are presented in Fig. 3.

The obtained dependences $I_\delta(q)$ lead to a conclusion that the largest non-uniformities in cluster distribution are observed in specimen 2, which corresponds to the case where small cluster agglomerates with uniform distribution of smaller units occure (Karasek et al. 1996). For specimens 1 and 3

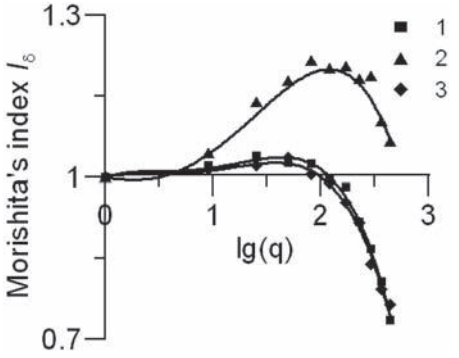

Figure 3. Morishita's index.

the cluster distribution is considered to be uniform with weakly pronounced heterogeneities.

Figure 4 gives distribution histograms for cluster cross sections at $h \equiv h^*$.

The histograms in Figure 4 show that more than 90% of clusters have an area <1 μm². However, there are also separate large-size objects of area 4…6.5 μm², which is compatible with the area of all small-size clusters. We suggest that the observed large-size clusters are parts of CB granules that have not been broken completely. The distributions for $A \le 0.5$ μm² are also given in Figure 4. For an accurate analysis of the geometry of small clusters, the 3 × 3 μm images are used. Figure 4 also shows the contribution of cluster volumes, calculated using expression (2), to their observed total volume depending on their cross-section area. It follows from measurements that from 17 (material 1) to 23% (material 2) of the total volume fractions of fillers are large-size objects ($A > 2$ μm²).

The sizes and number of large-size clusters are important mixing-quality indices. The higher are these characteristics, the smaller is the filler area wetted by the polymer, and the stronger are the filler-filler interactions.

It is known that the CB generates fractal structures in the material (Herd et al. 1992). The perimeter P_k and the cross-section area A_k of the k-th cluster are related by the fractal relationship:

$$P_k = \mu_p \left(\sqrt{A_k}\right)^{D_p},$$

where μ_p is a constant, and D_p is the fractal dimension of the perimeter. The volume V_k and diameter d_k of the cluster are related as:

$$V_k = \mu_m d_k^{D_m},$$

where μ is a constant, and D_m is the mass fractal dimension. The cluster volume above h^* is denoted by V_k. Diameter of the k-th cluster d_k calculated

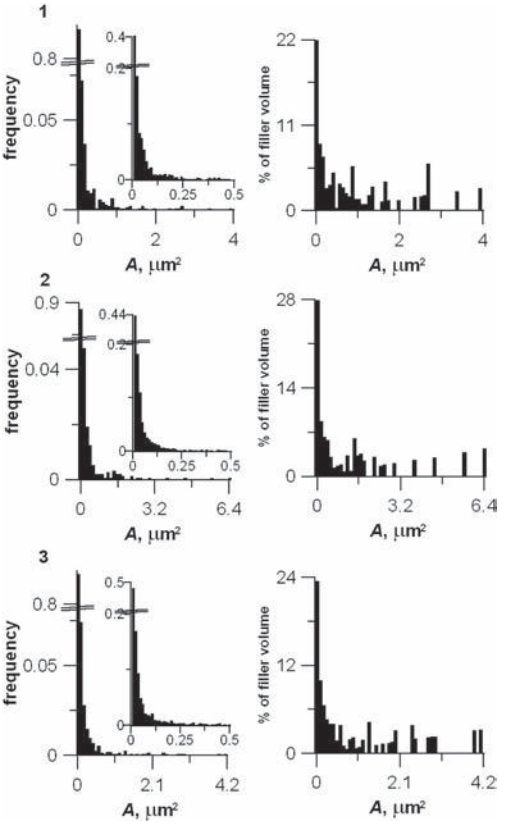

Figure 4. Distribution of cluster cross sections and contribution of clusters with respective areas to the filler volume.

as average distance between its geometrical centre and farthest point changing polar angle from 0 to 2 π with step π/16. Figure 5 presents the obtained experimental values and lines approximating these values in logarithmic coordinates.

As shown in Figure 5, the dependences $P(A)$ and $d(V)$ within the entire size scale governed by fractal relationships. For primary aggregates D_p and D_m, the values 1.28 and 2.43 (N220), 1.28 and 2.40 (N330), 1.30 and 2.40 (N339) (Herd et al. 1992) are valid. The corresponding values are supposed to be equal with accuracy to decimals. The same values have been obtained for specimens under study. Differences can be caused by many factors: agglomeration, binder layer, manufacture peculiarities, etc.

5 CONCLUSIONS

A method for analyzing filled rubber structures by AFM has been developed. Statistic treatments

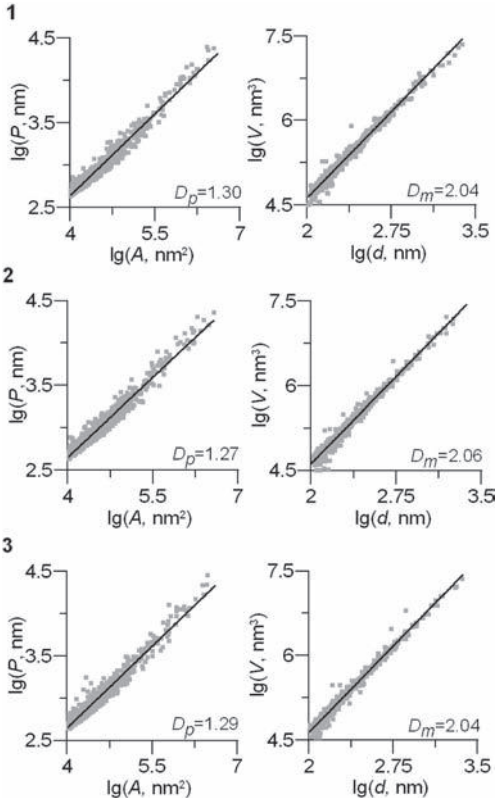

Figure 5. Fractal relationships.

of 10 × 10 and 3 × 3 μm images have been carried out for three filled rubbers (Table 1). The analysis of the cross-section of the relief has indicated that the compactness reaches its minimum and volume fraction of clusters equal to the filler fraction at the height $h^* = 0.45…0.5$ of the maximum height above the zero level. In the further analysis of the surface features, the value h^* is taken to be a zero level.

The uniformity of cluster distribution in the material has been is evaluated using Morishita's index. It is shown that the cluster distribution in materials 1 and 3 is almost uniform, while in 2 one can observe heterogeneities as agglomeration of small units. Examination of cross-sections reveals that more than 90% of clusters are relatively small (less than 2 μm^2), and the rest of clusters of area reaching 6.4 μm^2 (material 2) comprise 23% of the total filler volume fraction.

Cluster distribution and sizes are significant product-quality indices. The more non-uniform the cluster distribution is and the larger are the clusters themselves, the stronger is the filler-filler interaction, the more non-uniform is the stress field, and the greater is the amount of hysteresis losses under cyclic loading conditions. Under these aspects, the 2nd material has the worst mechanical characteristics.

ACKNOWLEDGEMENTS

Morozov thanks for support the RFBR and the Department of industry and nature-usage of Perm Region (grant 07-08-96016-r_ural_a).

REFERENCES

Bogaert J., Rousseau R., Van Hecke P. & Impens I. 2000. Alternative area-perimeter ratios for measurement of 2D shape compactness of habitats. *Applied mathematics and computation* 111(1): 71–85.

Herd C.R., McDonald G.C. & Hess W.M. 1992. Morphology of carbon-black aggregates: fractal versus euclidean geometry. *Rubber chemistry and technology* 65(1): 107–129.

Johnson, L.L. 2008. Atomic force microscopy (AFM) for rubber. *Rubber chemistry and technology* 81(3): 359–383.

Karasek L. & Sumita M. 1996. Review: characterization of dispersion state of filler and polymer-filler interactions in rubber carbon-black composites. *Journal of materials science* 31(2): 281–289.

Kohjiya S., Katoh A., Suda T., Shimanuki J. & Ikeda Y. 2006. Visualisation of carbon black networks in rubbery matrix by skeletonisation of 3D-TEM image. *Polymer* 47(10): 3298–3301.

Constitutive Models for Rubber VI – Heinrich et al. (eds)
© 2010 Taylor & Francis Group, London, ISBN 978-0-415-56327-7

Role of the interphase on reinforcement of filled rubbers: Influence of temperature, carbon black content and strain

A. Robisson & B. Chartier
Schlumberger, Cambridge, USA

ABSTRACT: We present a model that is able to describe the modulus of filled rubbers as a function of carbon black content, temperature and strain amplitude. In this model, the rubber is described as a composite of polymer, filler and the interphase between rubber and filler, the so-called bound rubber. The rubber is filled with N330 carbon black. The elastic modulus is measured using a dynamical mechanical analyzer (DMA). This modulus is measured at constant strain amplitude, sweeping temperature from 35°C to 180°C. It is also measured at constant temperature, sweeping strain amplitude from 0.015% to 15%. The modulus dependence of the composite material to carbon black content is expressed using a Guth and Gold model. The strain influence is based on Maier and Göritz model. Finally, the temperature dependence is introduced by considering the effect of temperature on bound rubber through an Arrhenius equation.

1 INTRODUCTION

Rubbers used in oilfield experience downhole oil well temperatures that can reach 180°C. Chemical behavior of those elastomers has been a very important focus of both chemical companies (DuPont, Lanxess, Solvay, etc) and end-users as Schlumberger. Their mechanical behavior at high temperature has been far less studied and understood, even though the decrease of mechanical properties with temperature has been an important concern for oilfield end-users and particularly for Schlumberger.

Some industrial elastomers exhibit a drop in modulus of more than 50% when temperature increases from 20°C to 150°C. This decrease in modulus is highly dependent on the nature and the quantity of reinforcing fillers present in the elastomer.

The reinforcing effect of carbon blacks has been found to be dependent on the filler loading (Guth, 1945) and the physical nature of the carbon black (Medalia, 1970). More specifically, it is highly correlated to the specific surface area of the filler (Göritz et al. 1999), (Göritz et al. 1999), the filler aggregate structure (Payne, 1962), (Payne et al. 1971), (Medalia, 1974), (Mele et al. 2002) and the filler structure and surface properties (Heckman, 1964), (Dannenberg, 1986), (Göritz et al. 1999). The effect of interactions between rubber and filler, driving property changes in the polymer close to the rubber filler, has also largely been discussed, referring to "occluded rubber" and "bound rubber". The occluded rubber is the immobilized rubber within aggregates. The bound rubber is the rubber modified ("immobilized" or "insolubilized") by vicinity of filler (Stickney et al. 1964), (Dessewffy, 1962), (Meissner, 1974), (Wolff et al. 1993). This bound rubber is weakly bonded to the filler surface by Van des Waals forces.

Temperatures considered here have little effect on carbon black itself, and theoretically little effect on the crosslinked polymer, but has a large effect on bound rubber properties (Dessewffy, 1962). Strain also influences both the carbon black network structure and the properties of the bound rubber (Maier et al. 1996).

This paper discusses the effect of temperature and strain amplitude on the filled rubber mechanical properties. In the first section, we present the Dynamical Mechanical Analysis (DMA) results that characterize the reinforcing ability of carbon black as a function of carbon black content, strain and temperature. Section II describes classic models of reinforcement and discussion on their limitation to predict our experimental results. In the last section, we propose a model of reinforcement that includes the effects of carbon black content, strain amplitude and temperature, and we discuss the limitations of the model.

2 EXPERIMENTAL

2.1 *Material*

The base polymer used in this study is a hydrogenated nitrile butadiene rubber (HNBR). N330

carbon black is the reinforcing filler; its content varies between 0 phr (parts per hundred of rubber, by weight) and 70 phr. The material also contains plasticizer for processing and is sulfur cured. All ingredients besides filler content are constant. Summary of tested formulations is shown in Table 1. The glass transition temperature of the vulcanized material has been measured by Differential Scanning Calorimetry and is equal to –26.5 ± 0.5°C, independent of the carbon black content.

2.2 *Coefficient of thermal expansion (CTE) measurements*

Thermal coefficient was measured using a Thermomechanical Analysis (TMA) testing setup (Q400 from TA Instrument). Sample was measured in the sheet thickness section (thickness of 2 mm) and using a constant force of 0.01 N applied by a flat-ended probe. The coefficient of thermal expansion is calculated by measuring the tangent of the sample expansion at a temperature of 100°C.

It displays non-linearity as a function of filler content as shown Figure 1.

Table 1. Carbon black content of HNBR-carbon black composite sample.

Sample name	Carbon black content (phr)	Carbon black volume fraction (Φ_{CB})
N330-0	0	0
N330-0.05	10	0.05
N330-0.10	20	0.10
N330-0.16	35	0.16
N330-0.21	50	0.21
N330-0.25	60	0.25
N330-0.28	70	0.28

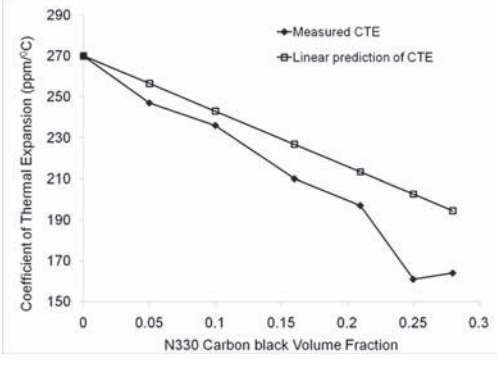

Figure 1. Coefficient of thermal expansion as a function of carbon black volume fraction.

2.3 *Dynamic Mechanical Analysis (DMA) measurements*

Uniaxial storage modulus E′ was measured under uniaxial tension, using Dynamic Mechanical Analysis (DMA) testing setup (Q800 from TA Instrument). A first set of experiments was run at constant strain amplitude (0.001 = 0.1%), at a constant frequency of 5 Hz, and sweeping temperature between 35°C and 180°C. A second set of experiments investigated the so-called Payne effect 6. Strain sweep tests were run between 0.0002 (0.02%) and 0.2 (20%) strain amplitude, at a constant frequency of 5 Hz. Four temperatures were investigated: 35°C, 80°C, 100°C and 150°C.

The modulus values are averaged over three cycles after four stabilization cycles (softening or "Mullins" effect can therefore be neglected). The error is estimated to be mainly due to dimension measurements and equal to ± 5%. The storage modulus, as measured using the DMA, is the secant modulus measured through oscillation amplitude. In the linear domain (i.e. at very small strain), this modulus is equivalent to the tangent modulus. At larger strains (observed during the strain sweep experiments), the moduli differ.

Temperature Sweep Tests—Figure 2 shows the samples' moduli plotted versus temperature. The unfilled rubber sample exhibits a quasi-constant modulus with temperature, around 3 MPa (E0 = 3 MPa in this study). Although rubber entropic elasticity does predict an increase of the modulus with temperature 20, we envision that the plasticizers present in those industrial compounds introduce an enthalpic effect that covers the entropic effect.

Filled rubber exhibit an increased modulus with increased carbon black content, as well as an important drop of modulus with temperature. For example, the sample with 0.28 volume fraction

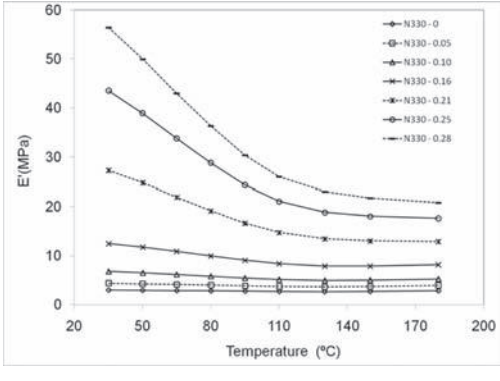

Figure 2. DMA experimental data's—storage modulus (E′) as function of temperature–HNBR rubber filled with N330 carbon black, Φ_{CB} = 0, 0.05, 0.10, 0.16, 0.21, 0.25, 0.28.

carbon blacks exhibits a modulus drop from 56 MPa at 35°C to 21 MPa at 180°C. The drop is also non-linear with temperature.

Strain Sweep Tests—Figure 3 shows moduli as a function of strain amplitude, for samples filled with 0.21 carbon black volume fraction, at temperatures of 35°C, 80°C, 110°C and 150°C. The strain amplitude is plot in logarithmic scale. The typical Payne effect is observed: The modulus is constant at very low strain, up to 0.1%, and then decreases. At 10% strain amplitude, the decrease has not stabilized yet, but it seems all temperature plots are converging. Curves are very similar for all other samples and are not displayed here. Figure 4 shows the modulus as a function of strain sweep for all samples, at a temperature of 80°C. Not surprisingly, the Payne effect is not observed for unfilled sample and its effect increases for increasing carbon black content.

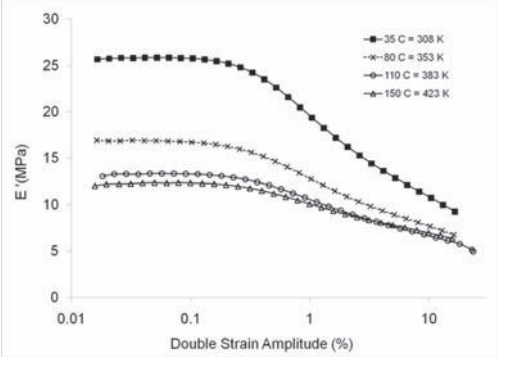

Figure 3. DMA experimental data's—storage modulus (E′) as function of Double Strain Amplitude (DSA)—HNBR rubber filled with 0.21 volume fraction N330 carbon black at four temperatures, T = 35°C, 80°C, 110°C, 150°C.

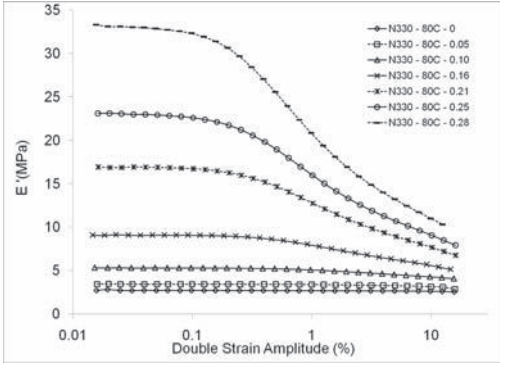

Figure 4. DMA experimental data's—storage Modulus (E′) as function of Double Strain Amplitude (DSA)—HNBR rubber filled with different volume fractions of N330 carbon black at temperature T = 80°C, Φ_{CB} = 0, 0.05, 0.10, 0.16, 0.21, 0.25, 0.28.

2.4 *Uniaxial tensile tests to failure*

Dumbbell specimen were cut out of the rubber sheets and stretched until failure, following ASTM D412 Standard. Crosshead speed was 50 mm/min. Engineering strain was measured in the straight area of the sample using a video-extensometer. Engineering stress was measured using a load cell and the initial cross-section of the sample. Three tests were performed at each condition and representative results are displayed here.

At room temperature, the elongation at break decreases and the tensile strength increases when the carbon black content increases, Figure 5. The reinforcing effect seems to plateau above 0.21 carbon black volume fraction. At 175°C, carbon blacks are favorable for both elongation at break and tensile strength, with an optimized composition around 0.25 carbon black volume content, Figure 6.

Those test results will not be used to develop the constitutive equation but for qualitative comments.

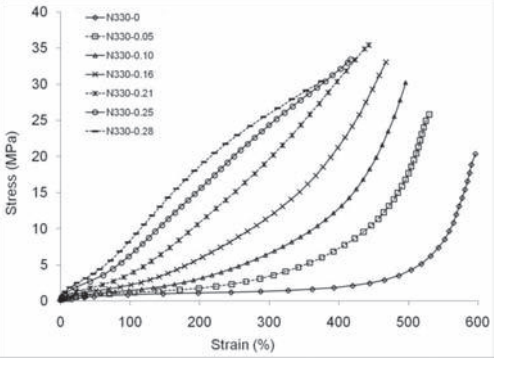

Figure 5. Uniaxial tensile tests to failure—room temperature—HNBR rubber filled with different volume fractions of N330 carbon black.

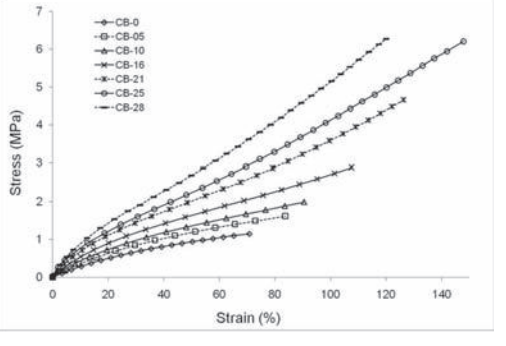

Figure 6. Uniaxial tensile tests to failure—175°C—HNBR rubber filled with different volume fractions of N330 carbon black.

3 CLASSIC MODELS OF REINFORCEMENT

3.1 *Reinforcement as a function of filler content*

Reinforcement (R) is described in this paper as the ratio between the filled rubber uniaxial storage modulus (E′) and the unfilled rubber uniaxial storage modulus (E'_0).

$$R = \frac{E'}{E'_0} \tag{1}$$

Reinforcement has mainly been described in literature as a function of carbon black volume fraction (Φ_{CB}). Guth and Gold used Smallwood-Einstein developments on fluids filled with spherical particles to describe filled rubber reinforcement (R) as a function of carbon black content (Φ_{CB}) (Guth et al. 1938):

$$R = \frac{E'}{E'_0} = 1 + 2.5\,\Phi_{CB} + 14.1\,\Phi_{CB}^2 \tag{2}$$

The first term of the equation ($2.5\Phi_{CB}$) is linear and describes a hydrodynamic reinforcement. The second term on the series ($14.1\Phi^2_{CB}$) was introduced by Guth and Gold to account for the interactions between particles, or filler networking. The equation is still widely used today.

Guth observed that modulus of rubbers with carbon black concentration above 10% exhibited "accelerated stiffening". He associated this effect with the formation of rodlike filler particles. He therefore suggested a modified equation taking into account a shape factor f.

$$R = \frac{E'}{E'_0} = 1 + 0.67\,f.\Phi_{CB} + 1.62\,f^2.\Phi_{CB}^2 \tag{3}$$

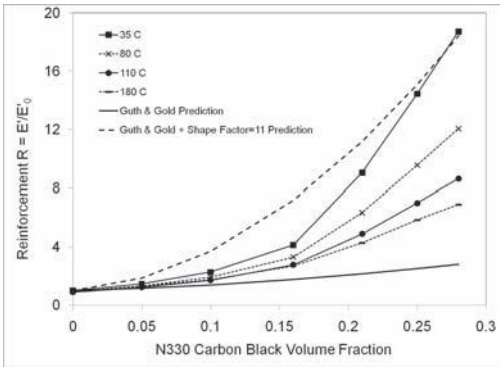

Figure 7. Carbon black content dependence of reinforcement (R = E′/E′0) for HNBR rubber filled with N330 carbon black at different temperatures, T = 35°C, 80°C, 110°C, 180°C—Experimental data's and Guth and Gold model predictions.

Figure 7 illustrates both those models, as well as the previously shown experimental data's, with yet another angle: The reinforcement is plot as a function of carbon black content. Experiments clearly show that reinforcement varies non-linearly with carbon black content, as predicted by Guth and Gold. Nevertheless, the original model (Equation 2) greatly underestimates the modulus. Above 10% carbon black content, the shape factor, identified on the experimental data's at 35°C (shape factor = 11), improves the prediction but is still not satisfactorily. More importantly, the temperature effect is not described.

3.2 *Bound rubber and occluded rubber concepts*

The Guth and Gold shape factor being unsuccessful to describe accurately the reinforcing effect of filler, bound rubber concept was introduced in the late 1930's by Fielding (1937). Bound rubber results of an adsorption of the polymer chains on the filler surface. Those adsorbed polymeric chains have restricted mobility and the resulting phase is therefore stiffer than the "free" rubber (un-bound polymer composing the matrix). Bound rubber would then participate in the reinforcement.

The phenomenon was also described as a "salvation" (Guth, 1945): the rubber would bind on the carbon black particles, or as an "insolubilization" (Meissner, 1974). Practically, bound rubber is the rubber portion that cannot be removed when the raw rubber is put in a good solvent. Authors mention several factors as the origin of this filler-rubber interaction: Adsorption effects (Van der Waals) or chemical process (reaction between rubber and functional groups on the filler surface) (Stickney et al. 1964), (Wolff, 1996), (Dannenberg, 1986), (Litvinov et al. 1999).

The bound rubber layer thickness was measured to be 4 to 8 nm for seventeen different carbon blacks using solvent methods (Wolff, 1993).

Meissner (1974) described the bound rubber content (Φ_{BR}) as a function of carbon black content (Φ_{CB}) and other physical parameters, Equation (4):

$$\Phi_{BR} = \Phi_{CB}\frac{M_W P}{N_A\,A_0} \tag{4}$$

where M_w is the weight average molecular weight of the polymer, P the specific surface area, N_A the Avogadro number, A_0 the filler surface area for reactive site (adjustable parameter).

In case of M_w = 300,000 g/mol, P = 78 m²/g and A_0 = 104 as recommended by Meissner, the bound rubber content is calculated to be

$$\Phi_{BR} = 0.39\,\Phi_{CB} \tag{5}$$

Medalia (1974) introduced the concept of "occluded rubber". He defined the occluded rubber as a geometrical concept: It is the rubber trapped within the filler aggregates. This rubber is not contributing to the deformation, and therefore contributes to the rubber stiffening. Medalia proposes an "effective" filler fraction (Φ_{eff}) as being the volumetric fraction which does not participate to the strain. In other terms, both the carbon black and the "occluded" rubber are infinitely stiff.

$$\Phi_{eff} = \Phi_{CB} \frac{(1 + 0.02139\ DBPA)}{1.46} \tag{6}$$

where DBPA is the dibutyl phthalate absorption (Oil Absorption Number, ASTM D241; gives information on the carbon black structure).

Wolff, Wang & Tan (1993) also used Equation (6) to describe the bound rubber content.

In the case of N330 Carbon Black, DBPA value is 102 $cm^3/(100\ g)$ (Medalia, 1974), the volumetric effective filler content (Φ_{eff}) or the volumetric bound rubber content (Φ_{BR}) are then

$$\Phi_{eff} = 2.18\ \Phi_{CB} \quad or \quad \Phi_{BR} = 1.18\ \Phi_{CB} \tag{7}$$

Guth and Gold equation then becomes:

$$R = \frac{E'}{E'_0} = 1 + 2.5\Phi_{eff} + 14.1\ \Phi^2_{eff},$$

$$\text{with } \Phi_{eff} = \Phi_{CB} + \Phi_{BR} \tag{8}$$

If we assume that the Guth and Gold model is valid, we can use Equation 7 to identify the bound rubber content as a function of carbon black content, using experimental results from Figure 7. The positive root of the Guth and Gold quadratic equation is solved at every data point, i.e. for every carbon black content and for every temperature, using the experimental reinforcement value. The calculated root is equal to the effective filler fraction, from which we calculate the bound rubber fraction. The bound rubber fraction is then plotted as a function of carbon black content at four temperatures, see Figure 8.

The linear relationship proposed by Medalia (Equation 8) is plotted as well. Medalia's equation largely underestimates the amount of bound rubber at 35°C for carbon black volume fraction above 0.1. Also, it does not account for the non-linearity between bound rubber content and carbon black content, nor does it for temperature effect.

We should note that the highest bound rubber content, occurring for sample with 28% carbon black content at room temperature, is equal to 0.76, which is higher than the available rubber volume fraction equal to (1–0.28) = 0.72. The Guth and Gold equation does therefore slightly underestimate

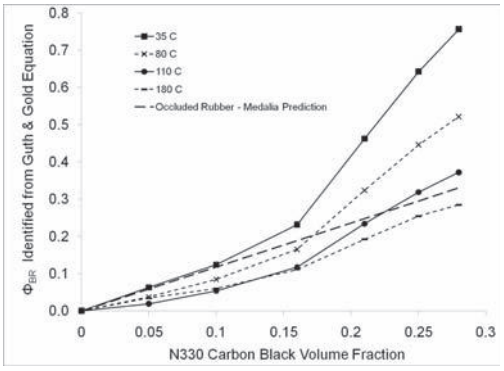

Figure 8. Bound rubber (BR) content as a function of carbon black content for HNBR rubber filled with N330 carbon black at different temperatures, T = 35°C, 80°C, 110°C, 180°C—experimental data's and Medalia prediction.

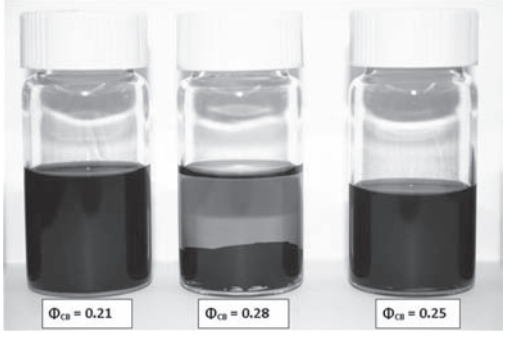

Figure 9. Raw filled rubber samples after 2 days in acetone (picture)-samples with carbon black volume fraction of 0.28 do not dissolve.

the reinforcing ability of the effective filler content but we consider this result as acceptable. Indeed, the prediction is consistent with observations that show that the sample containing 28% of carbon black content does not contain any free rubber matrix but only bound rubber. Figure 9 shows raw samples after two days exposure to acetone. Samples containing 21 and 25% of carbon blacks dissolve: the free-rubber matrix dissolves and a suspension of carbon black fillers covered with bound rubber remains. The sample with 28% carbon blacks remains bulk, indicating that none of the rubber could dissolve (no free rubber) and therefore that the whole rubber fraction is bound rubber, or that the bound rubber phases are interconnected at large scale, as described in Leblanc (2002) extensive paper.

Also, from the volumetric bound rubber content identified from Guth and Gold equation (Figure 8), we can calculate the bound rubber shell

thickness, assuming all bound rubber is due to chain adsorption on filler surface (no occluded rubber), a perfect dispersion of carbon black (bound rubber is all around the spherical filler, filler/filler contact surface area is negligible), and a monodisperse size distribution of carbon black particles. We make this calculation for effective filler fraction below 52% (fraction where the effective filler sphere diameter is equal to the matrix cubic cell edge), as above this value, interference between bound rubber spheres occurs. With these assumptions, the bound rubber would be a perfect uniform and stiff shell around perfectly spherical stiff filler. Those assumptions are far too simple but the goal is to give an order of magnitude of the rubber shell thickness.

First, carbon black filler radius is estimated. Knowing that N330 has a nitrogen surface area (NSA) of 78 m^2/g (ASTM D1765) and assuming a density of 1.8 for carbon black, we can estimate a carbon black filler radius of 21.4 nm. The bound rubber thickness can then be estimated using bound rubber fraction. It is calculated using results from Figure 8 for every carbon black content and every temperature. Our results indicate shell thickness varying between 1.5 and 8 nm depending on temperature and carbon black content. Those values are similar to the ones measured using solvent methods and NMR: 4–8 nm as measured by Wolff, Wang & Tan (1993) and in the order of nm as measured by Litvinov & Steeman (1999). We think our estimation might be underestimated, considering that the model assumes an infinitively stiff bound rubber (it does not participate in the strain), whereas the bound rubber is probably still compliant. To reach the same values of reinforcement, the fraction of bond rubber would need to be higher and therefore the shell would be thicker. Indeed, the bound rubber shell is probably not in a glassy state, as no consistent change in glass transition temperature has been observed in all samples, measured by Differential Scanning Calorimetry (DSC).

3.3 *Temperature influence on bound rubber content*

Bound rubber fraction was measured in past studies by exposing uncured samples to a good solvent at different temperatures. The bound rubber content decreases when exposure temperature increases, and it was found to follow a Maxwell–Boltzmann distribution (Dessewffy, 1962), (Wolff et al. 1993), (Göritz et al. 1999) as shown in Equation (9). Physically, the bound rubber is resulting from equilibrium between absorption and desorption of polymer chains on carbon blacks and the process is thermally activated (Maier et al. 1996).

$$\ln(\Phi_{BR}) = E_0 + \frac{E}{RT} \tag{9}$$

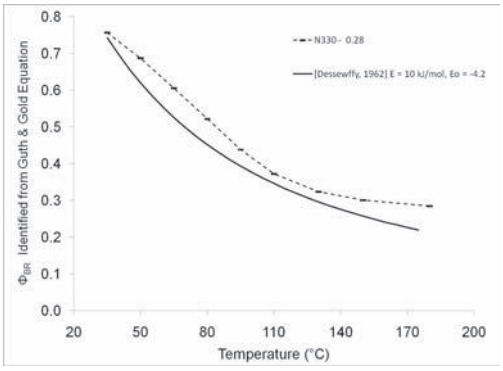

Figure 10. Bound rubber content (Φ_{BR}) as a function of temperature for HNBR rubber filled with N330 carbon black, Φ_{CB} = 0.28—experimental data's and prediction using Dessewffy equation.

where E_0 is a constant and E is the adsorption energy, R is the gas constant, T is the temperature.

From measurements on carbon black filled natural rubber exposed to benzene between 20°C and 90°C, and from using Equation (9), Dessewffy (1962) calculated adsorption energies in the range of 7.5 and 17.6 kJ/mol (resp. 0.08 eV and 0.18 eV) depending on carbon black nature and content. Göritz, Raab & Fröhlich (1999) mentioned very similar values of 17.6 kJ/mol (0.18 eV) for SBR (styrene butadiene rubber) and 14.6 kJ/mol (0.15 eV) for NR (natural rubber).

Equation (9) was used to identify the two parameters E and E_0 using Figure 7 data's for a constant carbon black content of 0.28. Results are displayed Figure 10. The equation is able to capture the bound rubber drop. This bound rubber drop can therefore explain the modulus drop with increasing temperature.

3.4 *Strain amplitude effect on reinforcement*

Payne attributed the modulus drop with strain to the breakdown of the three dimensional agglomerates of carbon blacks (Payne, 1962). Maier and Göritz proposed a molecular interpretation of this effect (Maier et al. 1996). In their model, the number of polymer chains weakly bonded to the filler surface by Van des Waals forces participate to the shear modulus G′, and this equilibrium between adsorbed and desorbed chains depends on the shear strain ϒ following Equation 10.

$$G' = (N_C + N_{St} + \frac{N_{I0}}{1 + c\gamma}).\, k_B T \tag{10}$$

where N_c is the density of chemically crosslinked chains, N_{St} the number of polymer chains tightly

bound to the active filler surface, independently of strain, N_{I0} the maximum number of possible adsorbed chains, c a constant, T the temperature and k_B the Boltzman constant.

Maier and Göritz identified those parameters for different carbon black contents at every temperature.

4 PROPOSED MODEL TO PREDICT REINFORCEMENT AS A FUNCTION OF CARBON BLACK CONTENT, TEMPERATURE AND STRAIN

Temperature influence on rubber moduli is usually studied around the glass transition temperature (T_g), where a 3-orders of magnitude drop in modulus is observed. After T_g, i.e. on the rubbery plateau, pure rubbers (no filler, no plasticizer, no additives) have their modulus increasing linearly with temperature, due to entropic elasticity 20. This increase if often neglected and the rubbery region is considered as a "plateau", i.e. the modulus is constant with temperature. Current results confirm this result: Temperatures investigated have no effect on the unfilled rubber (Figure 2, curve N330 = 0).

However, filled rubbers studied here do not exhibit constant modulus with temperature (Figure 2, curves N330 = 0.05 to 0.28). For example, the sample filled with 0.28 carbon black content shows a 60% drop in storage modulus between 35°C and 180°C.

Models described previously are not able to describe the drop in filled rubber moduli with temperature. We propose here to complement those models and introduce the bound rubber shell concept to predict the modulus drop with temperature.

The steps to build such a model include:

- Identification of the effective filler fraction using the Guth and Gold model
- Identification of the bound rubber fraction change with temperature using an Arrhenius equation
- Unification with Maier and Göritz model to build a model that predicts the effect of carbon black content, temperature and strain.

This work proposes a reinforcement model that is able to predict the elastic modulus of filled rubber as a function of filler content, strain amplitude and temperature using bound rubber concept.

The bases of the model are the observations and hypothesis previously described:

1. The Guth and Gold model is valid
2. The bound rubber is infinitively stiff when compared to matrix rubber
3. The bound rubber varies non-linearly with carbon black content (Figure 6)
4. The bound rubber content decreases with temperature and follows an Arrhenius equation
5. Maier and Göritz description of weakly bonded chains and their dependence on strain amplitude is valid

Those assumptions translate into equations 11 to 15

1. $$R = 1 + 2.5\,\Phi_{eff} + 14.1\,\Phi_{eff}^2 \tag{11}$$

2. $$\Phi_{eff} = \Phi_{CB} + \Phi_{BR} \tag{12}$$

3. $$\Phi_{BR}(\Phi_{CB}) = \Phi_{CB}.(A_o + B_o.\Phi_{CB}) \quad , \tag{13}$$

at constant temperature

4. $$\Phi_{BR}(T) = \Phi_{CB}.(A_o + B_o.\Phi_{CB}) \exp\left(\frac{E}{RT}\right) \tag{14}$$

5. $$E'(\varepsilon) = \frac{\Phi_{CB}}{1 + c\varepsilon} \tag{15}$$

Finally, the model we propose is

$$R = \frac{E'}{E'_0} = 1 + 2.5\,\Phi_{eff} + 14.1\,\Phi_{eff}^2 \tag{16}$$

$$\text{with, } \Phi_{eff} = \Phi_{CB} + \frac{\Phi_{CB}.(A_o + B_o.\Phi_{CB})}{1 + c.\varepsilon} \exp\left(\frac{E}{RT}\right)$$

where ε is the strain amplitude, A_0, B_0 and c constants, E the adsorption energy, R the gas constant (8.31 $JK^{-1}{\cdot}mol^{-1}$) and T the temperature (K).

A_0, B_0, c and E are the four parameters to identify. Those parameters were identified using a Matlab routine for all strain sweep tests, where strain amplitude was swept between 0.0002 and 0.2, at a constant frequency of 5 Hz, and at four investigated temperatures: 35ºC, 80ºC, 100ºC and 150ºC.

Table 2 shows the four identified parameters. Figures 11 to 14 show the experimental results and numerical results from identification, at temperature respectively of 35ºC, 80ºC, 110ºC, 150ºC.

The identified adsorption energy is close to the values identified by Dessewffy and Göritz Raab & Fröhlich using solvent desorption, and are within the range of Van des Waals interactions. Note that activation energies related to glass transition are much higher than values mentioned here. For example, Cerveny, Ghilarducci, Salva & Marzocca (2000) calculated the activation energy

Table 2. Fitted parameters on proposed model—data are identified from strain sweep tetss (Fig. 4 and 5).

E (kJ/mol)	A0	B0	c
8.43	0.0167	0.308	62.6

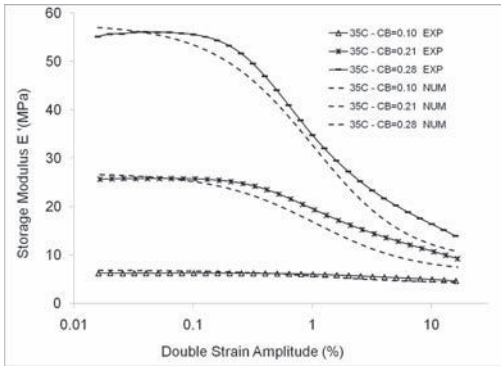

Figure 11. Model identification result-T = 35°C—dotted lines are experimental data's, dashed lines result from numerical simulation.

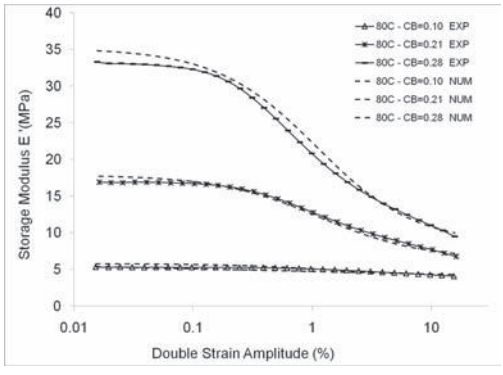

Figure 12. Model identification result-T = 80°C—dotted lines are experimental data's, dashed lines result from numerical simulation.

for the glass transition of an SBR (styrene butadiene rubber) and found a value of 294 kJ/mol. This corroborates the assumption that most part of bound/adsorbed rubber has restricted mobility but is not in a glassy state. This was discussed by Robertson, Lin, Rackaitis & Roland (2008) and was confirmed here by DSC results.

Figures 15 and 16 display the results given by the above model on temperature sweep tests using parameters identified on strain sweep tests. The curves show very good agreement between model prediction and experimental data's.

In conclusion of this paragraph, we consider, in this simple empirical model, a uniform bound rubber layer around filler which thickness varies with strain and temperature. This bound rubber phase exhibits a higher modulus (or slower relaxation times) because adsorption prevents molecular mobility, and the adsorbed chains composing the interphase experience desorption when temperature

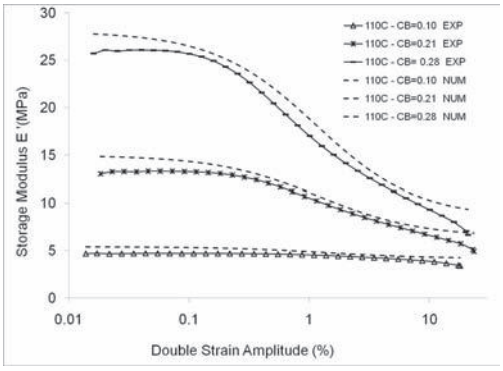

Figure 13. Model identification result-T = 110°C—dotted lines are experimental data's, dashed lines result from numerical simulation.

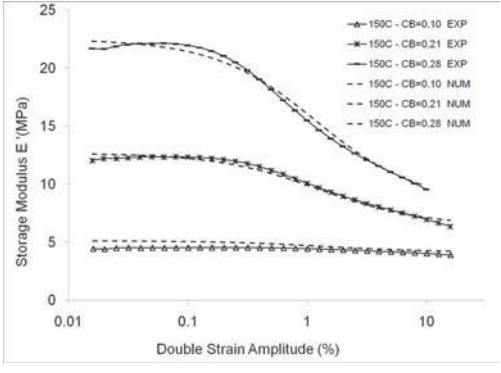

Figure 14. Model identification result-T = 150°C—dotted lines are experimental data's, dashed lines result from numerical simulation.

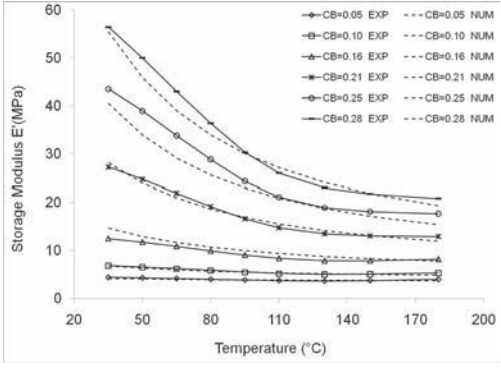

Figure 15. Model validation–dotted lines are experimental data's, dashed lines result from numerical simulation.

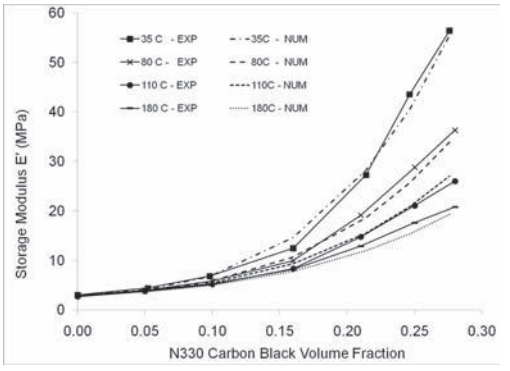

Figure 16. Model validation—dotted lines are experimental data's, dashed lines result from numerical simulation.

increases. The quality of the prediction seems to confirm that the modulus drop with increasing temperature can be explained by the disappearance (or transition) of this stiffer phase (bound rubber) in polymer. We should also note that the activation energy of desorption is at least one order of magnitude lower that the activation energy of glass transition. Therefore, the adsorbed layer observed here is mostly still elastomeric and not glassy.

5 DISCUSSION

The model empirically takes into account carbon black content, temperature and strain amplitude. It does not consider the effect of static strain or stress that can be superposed to a strain amplitude, and that arises from swelling, thermal expansion or mechanical pre-loading.

This effect has largely been discussed, beginning with Payne (1962) himself. The following paragraphs discuss the effects of particle agglomeration and static loading, considering particle/particle and particle/matrix interactions.

5.1 *Particle agglomeration effect on reinforcement*

Numerous papers discuss about the particle/particle versus particle/polymer interaction. It has been historically difficult to de-correlate those effects as particle dispersion is very difficult to achieve in polymer and rubber compound. Recently, Yanagioka, Toney & Frank (2009) could compare ordered silica hydrogel with random silica hydrogel using the polymerized crystalline colloidal array (PCCA) developed by Asher, Holtz, Liu & Wu, (1994). They determined three typical relaxation behaviors: short time (≈0.5 s) for the particle/particle relaxation time, medium time (≈10 s) for the polymer/filler relaxation time and long time (2,000 s) for the polymer/polymer relaxation time. They measured a thickness of the adsorbed layer in the swollen hydrogel around 15–20 nm depending on the filler type and above a critical concentration of polymer in water.

From DMA tests, they also conclude that the tan δ is highly dependent on the filler/polymer interaction and related to the adsorption/desorption process of chains around particles.

5.2 *Static strain or static stress effect on reinforcement*

The role played by adsorbed rubber chains onto filler surface has been discussed by Maier and Göritz. To our knowledge, this is the only micromechanical model describing the Payne effect in an accurate manner. In their model, both strain amplitude and temperature change the chain adsorption/desorption equilibrium towards more desorption and are therefore both qualitatively equivalent: they reduce the physical crosslink density.

Göritz, Raab & Fröhlich (1999) also show that the static strain has no effect on the Payne effect: the storage moduli are superposed for pre-strain varying from 0 to 8.6%.

In order to qualitatively differentiate the strain amplitude effect, from the static strain or stress effect and from the temperature effect, we conducted several DMA experiments, in addition to the series presented earlier in the paper: (1) strain sweep tests with preloads of 5 N and 10 N, (2) time sweep test on a sample swollen in acetone and drying during the test. Figures 17 and 18 gather those results combined with results previously described, displaying respectively storage modulus E′ and tan δ. The strain on the x-axis is the maximum strain seen by the sample. It is the addition of the static strain due to pre-loading, temperature,

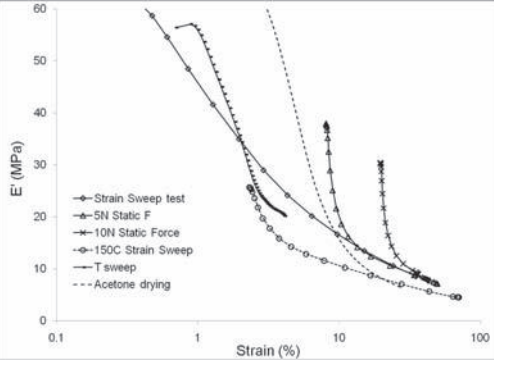

Figure 17. DMA experimental data's—storage modulus (E′) as a function of total strain—HNBR rubber filled with 0.28 volume fraction N330 carbon black.

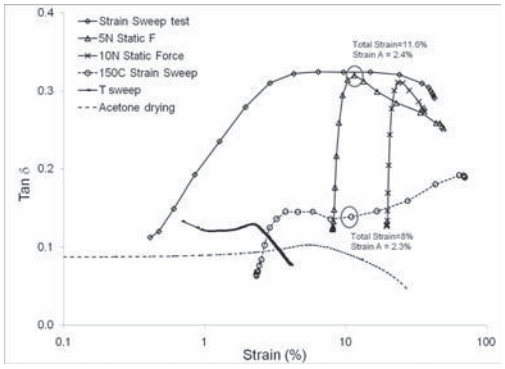

Figure 18. DMA experimental data's—tangent delta as a function of total strain—HNBR rubber filled with 0.28 volume fraction N330 carbon black.

or swelling, and the cyclic strain amplitude. The moduli are pre-treated by the TA Instruments software: the elastic modulus is calculated from the stress and strain amplitude; the tan δ is calculated from the phase angle between stress and strain.

Storage modulus results show a strong correlation between the elastic modulus and the total strain in three cases: the 30°C strain sweep test, the 150°C strain sweep and the temperature sweep test. On the other hand, when a static load is superimposed to the cyclic strain, the storage moduli diverges and there is no good correlation with the total strain. Also, during solvent drying, a large increase of elastic modulus is observed as well.

The tan δ results are more difficult to conclude from as the strain amplitude varies from one point to another. Two data point can be compared though: they are shown on Figure 18. At those points, both samples are approximately being at the same state of strain: sample A (30°C) is at 11.6% static strain (due to pre-loading) and 2.4% cyclic strain amplitude; sample B (150°C) is at 8% static strain (due to thermal expansion) and 2.4% cyclic strain amplitude. The filler networks ion A and B should therefore be at a comparable state of aggregation. At those particular points, sample A exhibits an elastic modulus of 16 MPa and sample B of 12 MPa. Those values are comparable. On the other hand, the tan δ values are respectively 0.32 and 0.14. The sample tested at 30°C is therefore twice as much dissipative. From this we conclude that the dissipation is not related to a network cyclic breakdown and re-aggregation of filler/filler bonds but to an adsorption/desorption phenomenon of chains on the filler surface, as described by Maier and Göritz.

The same conclusion seems to arise from the CTE measures. At 100°C, the filler network is disrupted. The non-linearity with carbon black content therefore tends to show that the adsorbed layer of polymer does exist and restricts the thermal expansion.

Along the same lines, tensile test to failure also show a very important effect of temperature on elongation at break and tensile strength. At room temperature, carbon black content increase goes along with a decrease in elongation at break and an increase in tensile strength. That can be explained by adsorbed chains on the filler surface that are not going through a desorption process despite the important strain. However, at 175°C, both elongation at break and tensile strength increase with carbon black content. At those temperature, more chains are undergoing desorption but still need to disentangle from adsorbed chains, increasing the overall elongation at break. Fukahori (2007) describe his interesting view on the role of filler in rubber failure.

6 CONCLUSION

Experimental data's presented in this paper underline a dependence of filled rubber moduli to filler content, strain amplitude and temperature. Elastic moduli increase with carbon black content, and decrease with strain amplitude and temperature. The last two effects can be related to the interphase that forms between the rubber and the filler, also called bound rubber, i.e. the layer of rubber with restricted mobility (adsorbed) on the filler surface. In this paper, the modulus of filled elastomers is therefore described using the three composite components: the polymer, the filler and the bound rubber.

The model we propose is based on a Guth and Gold model that fits the modulus changes with filler content and a Maier and Göritz model that accounts for the strain dependence. The temperature dependence follows an Arrhenius equation that applies on the bound rubber phase.

The model requires identification of four parameters and is able to quantitatively describe the elastic modulus of the rubber composite as a function of carbon black content, strain and temperature.

The model does not take into account the static strain effect and could be improved by considering not only the adsorbed polymer on filler surface but also the networking of such entities.

This work also emphasizes the importance of controlling the interface and interphase between the polymer and the rubber, especially when the composite rubber is used at high temperature.

ACKNOWLEDGEMENT

This work has been supported by Schlumberger. We gratefully acknowledge their support and permission to publish.

REFERENCES

Asher, S.A. Holtz, J. Liu, L. & Wu, Z. 1994. J. Am. Chem. Soc., 116, 4997–4998.

Cerveny, S. Ghilarducci, A. Salva & H. Marzocca, A.J. 2000. Polymer 41, 2227.

Dannenberg, E.M. 1986. Rubber Chem. Technol. 59, 512.

Dessewffy, O. 1962. Rubber Chem. Technol. 35, 611.

Fielding, J.H. 1937. Ind. Eng. Chem. 29, 8, 880.

Flory, P.J. 1953. "Principles of Polymer Chemistry", Cornell University Press.

Fukahori, Y. 2007. Rubber Chemistry and Technology, Vol. 80, p. 701–725.

Göritz, D. Raab, H. Fröhlich, J. & Maier, P.G. 1999. Rubber Chem. Technol. 72, 929 (1999).

Guth, E. & Gold, O. 1938. Phys. Rev. 53, 322.

Guth, E. 1945. J. App. Phys. 16, 1.

Heckman, F.A. 1964. Rubber Chem. Technol. 37, 1245.

Leblanc, J.L. 2002. Prog. Polym. Sci. 27, 627–687.

Litvinov, V. M. & Steeman, P. A. 1999. M. Macromolecules 32, 25, 8476.

Maier, P.G. & Göritz, D. 1996. Kautsch. Gummi Kunstst. 49, 18.

Medalia, A.I. 1970. J. Colloid Interface Sci. 32, 115.

Medalia, A.I. 1974. Rubber Chem. Technol. 47, 41.

Meissner, B. 1974 J. App. Polymer Sci. 18, 2483.

Mele, P. Marceaua, S. Browna, D. De Puy Y. & Alberola N.D. 2002. Polymer 43, 5577.

Payne, A.R. 1962. J. App. Polymer Sci. 6, 57.

Payne, A.R. & Whittaker, R.E. 1971. Rubber Chem. Technol. 44, 440.

Rehner, J. 1943. J. App. Phys. 14, 638.

Robertson, C.G. Lin, C.J. Rackaitis, M. & Roland, C.M. 2008. Macromolecules, 41, 2727–2731.

Stickney, P.B. & Falb, R.T. 1964. Rubber Chem. Technol. 37, 1299.

Wang, M.J. 1998. Rubber Chem. Technol. 71, 520.

Wolff, S. Wang, M.J. & Tan, E.H. 1993. Rubber Chem. Technol. 66, 163.

Wolff, S. 1996. Rubber Chem. Technol. 69, 325.

Yanagioka, M. Toney, M.F. & Frank, C.W. 2009 Macromolecules, 42 (4), pp. 1331–1343.

Constitutive Models for Rubber VI – Heinrich et al. (eds)

Non-linear elastic behavior of carbon black filler aggregates in rubber-like elastomers

Roozbeh Dargazany & Mikhail Itskov
Department of Continuum Mechanics, RWTH Aachen University, Germany

ABSTRACT: Mechanical properties of filled rubbers depend to a large extend on the behavior of carbon black aggregates inside them. In turn, the density and distribution of the aggregates is influenced by the aggregation process while their elastic modulus is determined by the nature and strength of the interparticle interaction. Moreover, the initial topology and its deformation induced evolution play an important role. In this contribution, a micro-mechanical model is proposed which describes the non-linear behavior of aggregated structures at large strains. To this end, the directional stress paths inside the aggregates are simulated by a backbone chain model. In contrast to previous works, the topology of the backbone chain during deformation is described by angular distribution pattern of chain segments. Extending the Kantor-Webman model, angular averaging concept is proposed which predicts the deformation induced evolution in the aggregate geometry. This concept enables to express the elastic modulus of the aggregate in terms of central and non-central inter-particle forces. The model predictions are in accord with the broad range of experimental observations.

1 INTRODUCTION

Earlier experimental studies of the quasi-static mechanical behavior of filled rubberlike materials demonstrated significant softening in each loading cycle. The softening has the highest value in the first cycle which is referred to as Mullins effect and reduces in the subsequent cycles till it reaches a stabilized value generally related to hysteresis. According to the experimental results, stress softening at the same strain level decisively depends on the filler concentration in the rubber network (see e.g. Rault, 2006). In unfilled elastomers, softening is negligible but becomes very pronounced in rubbers with a high filler concentration.

The influence of the filler network on the Mullins effect has been studied in detail by many authors (see e.g. Dargazany & Itskov, 2009), but so far the influence of the filler network on the hysteresis is not sufficiently understood.

From the micro-mechanical point of view, in order to obtain a proper prediction of the mechanical response of the filler network, both the mechanical behavior of a single aggregate and interaggregate interactions should be taken into account.

The elastic modulus of the aggregates depends sensitively on their geometry, deformation history and moreover, on the nature and the strength of the interparticle interactions. The attractive forces between colloidal particles are the main reason for the formation of aggregated structures. The nature of interparticle bonds of carbon black (CB) fillers in polymers is still not quite clear, but it can result from entropic depletion forces (W.C.K. Poon, 2002) or van der Waals forces (Derjaguin, 1989). Due to the strong attractive interactions between particles, an aggregate can form even at very low particle fractions.

Generally, aggregates appear in complex geometrical structures and are identified by three parameters: aggregate correlation length ζ generally known as aggregate length, the fractal dimension d_f and the particle diameter l (see Fig. 2). Aggregates are considered to be fractal on length scales up to ζ. The fractal dimension d_f is smaller than the Euclidean dimension d. This implies a volume-filling structure which means that as the aggregate size increases, its density reduces. The values of the fractal dimension d_f for different aggregation mechanisms are well established from experimental observations (see e.g. Herd et al., 1992).

With a yet further increase in the filler concentration, the particulate aggregates start to touch each other, thereby forming an electrically conductive body in the polymer matrix. Such a concentration range is known as the "percolation threshold".

The elasticity of aggregates is inherently much more complex than the geometry of them, but it can also be understood within statistical mechanics framework. In order to describe the mechanical behavior of filler networks, a number of approaches based on percolation theory are developed

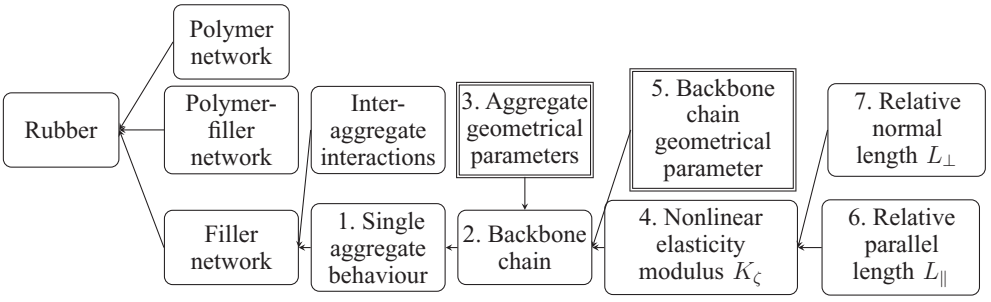

Figure 1. Flowchart of the mathematical approach, rounded rectangles are the deformation dependent coefficients and sharp cornered rectangles are constant coefficients.

(see e.g. Rueb et al., 1999) which do not consider the fractality of the particle structures.

A generic observation on mechanical behavior of aggregates confirms the appearance of apparent power law dependences of the elastic modulus and yield stress on the interparticle forces and correlation lengths. Thus, the mechanical behavior of fractal aggregates at small deformation regimes was described by scaling power law approaches (see e.g. De Rooij et al., 1994), in which a phenomenological formula is fitted to a set of experimental results.

Our goal in this study is to develop an analytical model which can explain and accurately simulate the nonlinear behavior of a single aggregate. An outline of this contribution is schematically shown in Figure 1. In order to simulate the mechanical response of filler network inside the rubber, the behavior of a single aggregate should necessarily be understood. To this end, the concept of backbone chain (BB chain) is further developed and implemented. In order to model a backbone chain, it suffices to determine the deformation dependent elastic modulus of it K_ζ. The influence of geometry on K_ζ is described by two geometric parameters, relative normal length $L_\perp$ and relative parallel length $L_\parallel$. Thus, one can write

$$K_\zeta = K(L_\perp, L_\parallel), \tag{1}$$

where deformation induced changes of $L_\perp$, $L_\parallel$ are taken into account by expressing these values in terms of the averaged bond correlations. These averaged coefficients can be obtained by means of exact angular distribution discussed in the following.

2 PRINCIPLES AND ASSUMPTIONS

A backbone is a single chain of particles through which an external stress is transmitted. The path and shape of this chain is highly dependent on the aggregation process and load direction. In

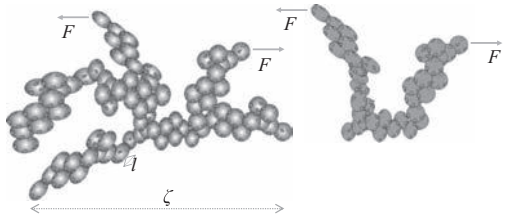

Figure 2. Schematic view of an aggregate subjected to force and the resulting BB chain.

Figure 2, an aggregate subjected to load ***F*** at two points and the stress transmission path inside the sample are depicted. This path is considered as a BB chain which transmits the main portion of load. The rest of the aggregate is supposed to be stress-free. In the following, we assume that BB chains are formed for all aggregate sizes ζ and at any stressed state.

The bonds between particles within a BB chain are simulated by elastic elements with a spring constant Q and an averaged bending-rotational stiffness $\bar{G}$ (see Fig. 3). The latter constant takes into account different kinds of angular deformation (Lin & Lee, 1996; Klüppel, 2003).

Our model is based on the following assumptions:

1. All particles in one chain have the same mass and diameter l.
2. In the virgin state, adjacent particles are assumed to be placed close to each other, thus the distance between their centers can be approximated by l.
3. In the deformed state, the average distance between centers of adjacent particles (bond length) is denoted by $\bar{l}$. Note that in the case of uniaxial tension $\bar{l} > l$.
4. In aggregates with the same values of ζ, d_f and l, BB chains can form with different conformations, where the term conformation denotes a unique configuration of particle locations. Thus, the chain

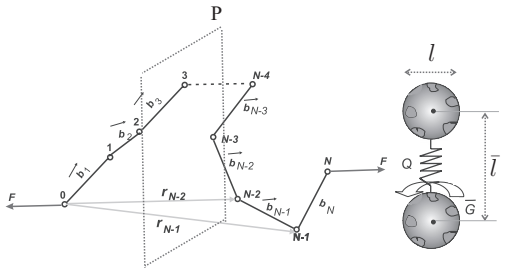

Figure 3. A BB chain with N bonds and a symbolic representation of interparticle forces.

conformation used in the further calculations, is the average of all possible configurations.

5. The chain center of gravity is located on the reflection plane of two ends of the chain denoted by P in Figure 3.

Let $\boldsymbol{b}_i$ ($i = 1, 2,\ldots, N$) be vectors connecting the centers of adjacent particles of a BB chain. The chain is subjected to a force $\boldsymbol{F}$ at its two ends as shown in Figure 3. Then, a vector $\boldsymbol{r}_i$ connecting the first particle with the ith particle is expressed by

$$\boldsymbol{r}_i = \sum_{j=1}^{i} \boldsymbol{b}_j. \tag{2}$$

Thus, the chain end-to-end distance can be written as

$$\|\boldsymbol{r}_N\| = \|\boldsymbol{L}\|. \tag{3}$$

Note that the parameters ζ and L represent the BB chain end-to-end distance in the virgin and deformed state, respectively. Thus, in the virgin state, it holds $\|\boldsymbol{r}_N\| = \|\boldsymbol{L}\| = \zeta$. The number of particles N in a BB chain is related to its end-to-end distance by

$$N = \left(\frac{\zeta}{l}\right)^{d_b}, \tag{4}$$

where the exponent d_b is called the bond dimension and has a lower bound of 1 to provide a closed path. An upperbound to d_b is given by min [d_f, 5/3], where the value of 5/3 corresponds to the dimension of chains simulated by self-avoiding walk (SAW).

2.1 *Deformation states*

In view of eq. (4), the contour length of a BB chain denoted by L_C is expected to scale with its end-to-end distance by

$$L_C = Nl \sim \zeta^{d_b} \quad \Rightarrow vd = 1, \tag{5}$$
$$N^v = \frac{\zeta}{l}$$

where v is an universal exponent. Eq. (5) just holds for the stress-free state after production denoted here as mechanically initial state (MIS). The bond dimension and some other geometrical properties of aggregates at MIS have been well studied in numerous experimental observations (i.e. Dinsmore & Weitz, 2002).

For a BB chain in MIS, d_b lies between 1.2 to 1.35 (Fixman, 1962), and so the value of v is about 0.83 which results from the correlations of orientations between near-neighbor particles along the chain.

In polymer models, one can assume a very idealized case where there is no correlation between the bond angles, which is generally referred to as unperturbed state. The value of d in unperturbed state is 2, which is specific for highly coiled chains.

Now, let us assume that the BB chains in MIS has some residual stretch inside and have already been elongated from unperturbed state. Thus, an initial unperturbed state (IIS) for all BB chains is imagined in which the spatial distribution of bonds along the chains is homogeneous, and the angular probability distributions have a constant value. IIS will further be used in order to formulate a boundary condition for differential equations governing the geometrical changes of the aggregate structure.

Considering that in transition from IIS to MIS, the major changes of the chain topology is due to the bond rotations rather than bond stretching, one can assume that the bond lengths remain constant in this transition.

In view of eq. (5), one obtains the end-to-end distance of a BB chain as

$$L_0^2 = Nl^2, \;\; \zeta^2 = N^{2v} l^2 \tag{6}$$

in IIS and MIS, respectively. Thus, the amount of residual stretch required for transition of a BB chain from IIS to MIS can be expressed by

$$\lambda_{res} = \frac{\zeta}{L_0} = N^{v-\frac{1}{2}}. \tag{7}$$

Now, let us denote the micro-mechanical stretch applied on the virgin sample by λ_ζ (see Fig. 4).

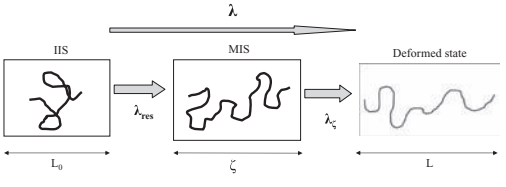

Figure 4. Conceptual representation of the deformation states and corresponding stretches.

Then with λ_{res} at hand, a pseudo stretch λ is introduced by the following identity

$$\lambda = \lambda_{res}\lambda_{\zeta} = \frac{L}{L_0}. \tag{8}$$

2.2 *Affine deformation condition*

The end-to-end length of a BB chain is written by

$$\boldsymbol{L} = \sum_{i=1}^{N} \boldsymbol{b_i}. \tag{9}$$

Then, $L = \|\boldsymbol{L}\|$ results from

$$\begin{aligned} L^2 &= \sum_{i=1}^{N} \boldsymbol{b_i} \cdot \sum_{j=1}^{N} \boldsymbol{b_j} \\ &= \sum_{i=1}^{N} \boldsymbol{b_i} \cdot \boldsymbol{b_i} + 2\sum_{i=1}^{N-1} \sum_{j=i+1}^{N} \boldsymbol{b_i} \cdot \boldsymbol{b_j} \\ &= N\bar{l}^2 + 2\bar{l}^2 \sum_{i=1}^{N-1} \sum_{j=i+1}^{N} \cos(\phi_{ij}), \end{aligned} \tag{10}$$

where ϕ_{ij} is the angle between two bond vectors of the chain $\boldsymbol{b_i}$ and $\boldsymbol{b_j}$. To obtain the accurate result, the term $\cos(\phi_{ij})$ should be evaluated. Considering the current chain geometry as an averaged conformation, one can write the mean square end-to-end length $\langle L^2 \rangle$ as

$$\langle L^2 \rangle = \sum_{i=1}^{N} \boldsymbol{b_i} \cdot \boldsymbol{b_i} + 2\bar{l}^2 \sum_{i=1}^{N-1} \sum_{j=i+1}^{N} \langle \cos(\phi) \rangle, \tag{11}$$

where $\langle \cos(\phi) \rangle$ is interpreted as an ensemble average of $\cos(\phi_{ij})$ over all segments of the BB chains distributed in the three dimensional space.

The ensemble average of an arbitrary function $F(\phi)$ is calculated by

$$\langle F(\phi) \rangle = \int_0^{\pi} F(\phi) P(\phi, \lambda) \frac{\sin(\phi)}{g} d\phi, \tag{12}$$

where g stands for a normalization factor and $P(\phi,\lambda)$ represents the angular distribution function.

In view of eq. (12), when the BB chain is in the unperturbed state

$$\langle \cos(\phi) \rangle = 0, \tag{13}$$

due to the fact that all bond directions are equally probable. In addition, in the case of a fully stretched chain

$$\langle \cos(\phi) \rangle = 1. \tag{14}$$

Further, $L^2 \alpha N$ when bonds are uncorrelated, and $L^2 \alpha N^2$ when bonds are perfectly correlated. Thus, a partial correlation between bonds can be assumed which leads to a dependence of L^2 on N in form of a power function with the exponent between 1 and 2.

For illustration, we consider a model in which bonds have a weak angular correlation just between first neighbors. In this case, $\langle \boldsymbol{b_i} \cdot \boldsymbol{b_{i+1}} \rangle = l^2 \langle \cos(\phi) \rangle$, where $\langle \cos(\phi) \rangle$ is a positive constant. There are no correlations beyond the first neighbors so that $\langle \boldsymbol{b_i} \cdot \boldsymbol{b_j} \rangle = 0$ if $|i - j| \geq 2$. Hence, for large N, one can deduce from eq. (11) that

$$\langle L^2 \rangle = \bar{l}^2 \; N + 2\bar{l}^2 \; Nb = C_N N\bar{l}^2, \tag{15}$$

where $b = \langle \cos(\phi) \rangle$ and the multiplicative coefficient C_N is called the characteristic ratio.

In order to obtain the end-to-end distance of a BB chain, two different methods can be applied. First method is based on angular correlations and directional distributions of bonds. The resulting value is denoted by L_m and is calculated by

$$\langle {L_m}^2 \rangle = N\bar{l}^2 \; \big(1 + (N-1)\, b\big) = C_{Nm} N\bar{l}^2. \tag{16}$$

In the second method, we obtain the chain end-to-end distance by means of chain initial length and deformation history. The resulting value is specified by L_M and is calculated by

$$\langle L_M^2 \rangle = \lambda^2 N l^2 = C_{N_M} N\bar{l}^2. \tag{17}$$

Bearing in mind that $L_M = L_m$, we get by virtue of eqs. (16) and (17)

$$\lambda^2 = \left(\frac{\bar{l}}{l} \right)^2 \big(1 + (N-1)b\big). \tag{18}$$

Thus in view of eq. (12), the probability function should be defined in a way that it satisfies eqs. (13), (14) and (18).

3 ANGULAR DISTRIBUTION FUNCTION

The concept of angular averaging is based on the replacement of bond correlations by their averaged values which are calculated by the distribution function of bond angles. Let us suppose that the angular distribution of bonds in a BB chain can be described by the von Mises density function. This function with respect to angle x is written as

$$f(x \mid \mu, V) = \frac{e^{V\cos(x-\mu)}}{2\pi I_0(V)}, \tag{19}$$

where $I_0(V)$ is the modified Bessel function of the order 0. Furthermore, the measure of location μ

and the concentration measure V are both functions of λ and N.

In the case of uniaxial tension, the maximum of the distribution is always located at $x = 0$, so that

$$\mu(\lambda, N) = 0. \tag{20}$$

Normalizing the distribution function to the range of availability of the angle ϕ which is $[0..\pi]$ we obtain

$$P(\phi,\lambda) = 2f(\phi|0, V). \tag{21}$$

Expanding eq. (18) gives

$$\lambda^2 = \left(\frac{\bar{l}}{l}\right)^2 \left(1 + (N-1)\int_0^{\pi} P(\phi,\lambda)\frac{\sin(2\phi)}{2g}d\phi\right). \tag{22}$$

The distribution function $P(\phi, \lambda)$ is uniform at unperturbed state. Thus, we can write

$$P(x, 1) = \frac{1}{\pi}. \tag{23}$$

Furthermore, all the bond angles in a fully stretched chain are 0. Hence, the distribution function is only non-zero at the angle 0 which yields

$$P(x,\sqrt{N}) = \delta(x|0). \tag{24}$$

Now, it remains to find a concentration meausre $V(\lambda, N)$ for the distribution function $P(x, N)$ such that it satisfies the affine motion constraint (22) and the boundary conditions represented by eqs. (23) and (24).

In view of eq. (18), finding an analytical solution for V is not tractable. Thus, we begin with the evaluation of V by minimizing the functional given in terms of the residual error. Regarding the constraint of affine deformation (18), a residual error R can be defined as

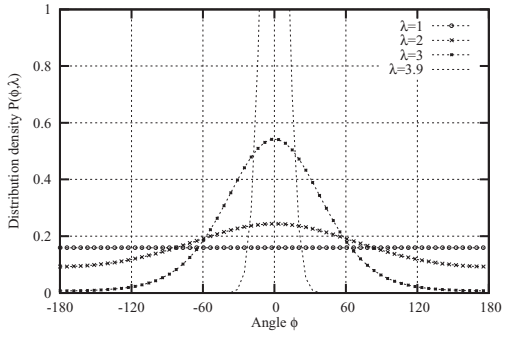

Figure 5. Evolution of normal angular distribution with deformation.

$$R = C_{N_M} - C_{N_m}. \tag{25}$$

With the aid of eqs. (12), (19) and (21), one can represent the residual error by

$$R = \left(\frac{\bar{l}}{l}\right)^2 \frac{(N-1)}{2g\pi I_0(V)}\int_0^{\pi} e^{V\cos(\phi)}\sin(2\phi)d\phi + 1 - \lambda^2. \tag{26}$$

Furthermore, the square error functional is given by

$$\Pi = \int_1^{N_{max}}\int_1^{\sqrt{N}} R^2 d\lambda dN, \tag{27}$$

where N_{max} is the maximum available size of the aggregate inside the network. In order to obtain V, the boundary conditions (23) and (24) are rewritten as

$$V(1, N) = 0,\ V(\lambda_f, N) = \infty. \tag{28}$$

We require stationarity of functional (26) over a special range of functions $\hat{V}$ given by

$$V \approx \hat{V} = \frac{1}{1 - \frac{\lambda}{\sqrt{N}}}\sum_i a_i N_i(\lambda, N), \tag{29}$$

where the trial functions N_i are defined by

$$N_i(\lambda, N) = \frac{(\lambda-1)^{\alpha_i}}{(N-1)^{\beta_i}}. \tag{30}$$

In this contribution, the function V is approximated by the first two terms of eq. (29). To this end, the square error function (27) is minimized with respect to variables a_i, α_i and $\beta_i (i = 1, 2)$ by means of the Levenberg-Marquardt algorithm. For example, we consider aggregates with the mean size of 100 nm. The so-obtaine d variables of the representations (29) and (30) are given in Table 1. The micro and exact end-to-end lengths of the BB chain obtained on the basis of eqs. (16) and (17), respectively, are plotted and compared in Figure 6. Accordingly, the predicted lengths L_m for different aggregate sizes fit well with the exact deformed lengths L_M as far as the BB chains are not fully stretched.

In the vicinity of the fully stretched state, the deviations become stronger and more terms of the series (29) have to be considered. However, BB

Table 1. Parameters of the representations (29) and (30).

a_1	α_1	β_1	a_2	α_2	β_2
1.028	1.001	0.574	0.306	0.585	1.787

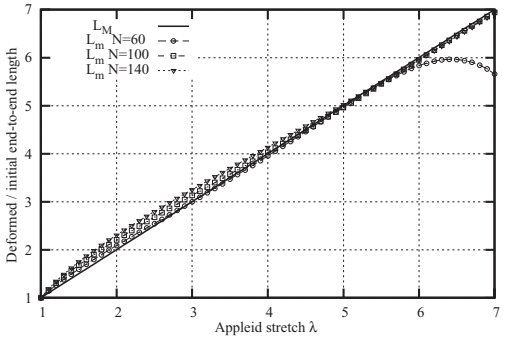

Figure 6. A comparison between the predicted and the exact end-to-end distance calculated by (17) and (16), respectively.

chains are ruptured far before reaching their fully stretched state.

By means of $P(\phi, \lambda)$, the average values of $L_{\perp}$, $L_{\parallel}$ in each state of deformation are obtained by calculating $\langle L_{\perp} \rangle, \langle L_{\parallel} \rangle$ using eq. (12). Then, by inserting $\langle L_{\perp} \rangle, \langle L_{\parallel} \rangle$ into eq. (1), we obtain the nonlinear elasticity modulus. Taking the initial geometry of the BB chain into account, we can further predict the mechanical behavior of the BB chain which is supposed to be identical to the mechanical behavior of the whole aggregate.

ACKNOWLEDGMENT

The authors thank the German Research Foundation (DFG) for the financial support of this work.

REFERENCES

Dargazany, R. and Itskov, M., 2009. A network evolution model for the anisotropic Mullins effect in carbon black filled rubbers. *Int. J. Solid Struct.*, doi:10.1016/j.ijsolstr.2009.03.022.

Derjaguin, B.V., 1989. *Theory of Stability of Colloids and Thin Films.* New York: Consultant Bureau.

De Rooij, R., Van Den Ende, D., Duits, M.H.G. and Mellema, J., 1994. Elasticity of Weakly Aggregating Polystyrene Latex Dispersions. *Phys. Rev. E* 49: 3038–3049.

Dinsmore, A.D. and Weitz, D.A., 2002. Direct Imaging of Three-Dimensional Structure and Topology of Colloidal Gels. *J. Phys.- Condens. Matt.* 14: 7581–7597.

Fixman, M.J., 1962. Radius of gyration of polymer chains. *J. Chem. Phys.* 36: 306–310.

Herd, C.R., McDonald, G.C. and Hess, W.M., 1992. Morphology of carbon-black aggregates—fractal versus Euclidean geometry. *Rubber Chem. Technol.* 65: 107–129.

Lin, R. and Lee, Y.D., 1996. Strain-dependent dynamic properties of filled rubber network systems. *Macromol. Theory Simulations* 5: 1075–1104.

Kantor, Y. and Webman, I., 1984. Elastic Properties of Random Percolating Systems. *Phys. Rev. Letters* 52: 1891–1894.

Klüppel, M., 2003. The Role of Disorder in Filler Reinforcement of Elastomers on Various Length Scales. *Adv Polym Sci.* 164: 1–86.

Poon, W.C.K, 2002. The physics of a model colloid-polymer mixture. *J. Phys. Condens. Matter* 14: R859–R880.

Rault, J., Marchal, J., Judeinstein, P., and Albouy, P.A., 2006. Stress-induced crystallization and reinforcement in filled natural rubbers: H-2 NMR study. *Macromolecules* 39: 8356–8368.

Rueb, C.J. and Zukoski, C.F., 1997. Viscoelastic properties of colloidal gels. *Rheol, J.* 41: 197–218.

Stress softening

Constitutive Models for Rubber VI – Heinrich et al. (eds)
© 2010 Taylor & Francis Group, London, ISBN 978-0-415-56327-7

Temperature dependence of Mullins softening-healing phenomena: An outline for theoretical description based on experiments

A.F.M.S. Amin
Civil Engineering Department, Bangladesh University of Engineering and Technology, Dhaka, Bangladesh

A. Lion
Institute of Mechanics, Faculty of Aerospace Engineering, University of Federal Armed Forces Munich, Neubiberg, Germany

ABSTRACT: The influence of the temperature on the Mullins softening effect and its recovery behavior (known as the *healing phenomena*) is experimentally investigated using a rubber blend. To study the influence of low temperatures and large deformations on the Mullins effect, cyclic strain-controlled processes are applied under different temperatures. Experimental results show that low temperature increases both the hysteresis properties and the Mullins effect. The softened specimens are then subjected to a sequence of heating, cooling and conditioning processes in order to study the influence of the temperature on healing phenomena. The results indicate the existence of a threshold temperature: if the specimen temperature is larger than this threshold, a nearly complete recovery of the material occurs within finite time, while any temperature below this limit will be too small for healing. In order to take the temperature dependences of softening-healing effects and their reversibility into account, the paper attempts to outline a thermodynamically consistent theoretical framework to describe these experimentally observed phenomena. In order to preserve the reversible character of the softening effect, fraction of free energy that is dissipated during softening process are described as a function of both temperature and an internal variable. Subsequent derivations lead to the constitutive relations in integral form.

1 INTRODUCTION

1.1 *General*

The Filler-reinforced vulcanized rubber and its blends are frequently-used for engineering applications, e.g. tires, base isolation bearings, air springs, acoustic coatings, tunnel linings for over a century (cf. Morawetz 2000, Amin et al. 2002, 2006). To shape the geometry of these products, geometric nonlinearities need to be considered together with the mechanical properties. The application of a numerical procedure which considers an adequate constitutive model founded on nonlinear continuum mechanics and the principles of thermodynamics (c.f. Haupt 2000) can bring realistic sophistication to a computer aided design and manufacturing process.

The mechanical behavior of filler-reinforced rubber originates from a network of macromolecules containing chemical and physical crosslinks, entanglements and filler particles. The macromolecular network of filler-reinforced rubber exhibits rate-dependent behavior, hysteresis and energy dissipation during monotonic and cyclic deformations. Therefore, the stress response of this material depends strongly on the applied deformation history (Treloar 1973). Lion (1996, 1997a,b) provided experiments and a constitutive model which also consider the temperature. On the other hand, macromolecular networks can change their microstructure at temperatures much higher than cryogenic temperatures (200 K). Such processes are possible in two different ways: 1) the healing of Mullins effect (c.f. Bueche 1961 and Figure 1) and 2) the crystallization process (c.f. Wood and Roth 1944; Wood and Bekkedahl 1946; Gent 1954; Stevenson 1983; Gent and Zhang 2001; Fuller et al. 2004). Both the temperature and the deformation history are the determining factors for the duration needed to complete these changes. The time-, temperature- and deformation-dependent changes in the macromolecular network, however, influence the mechanical material behavior of rubber. Thus, there exists an obvious necessity to extend the experimental knowledgebase of the material over the practical deformation and temperature

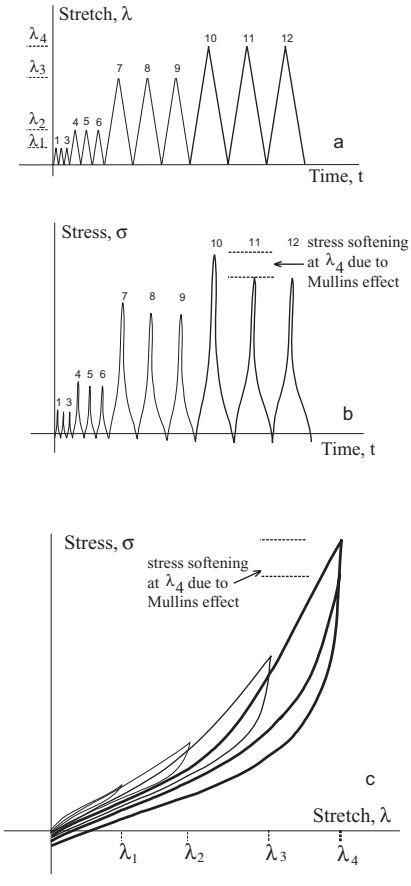

Figure 1. Mullins effect. When a virgin specimen is subjected to a cyclic process with different maximum stretches λ_1, λ_2, λ_3 and λ_4, respectively. The softening, occurring between cycles 10 and 11 in a virgin rubber at the stretch level λ_4, is illustrated in Figs. 1b and 1c. It increases progressively when the material experiences larger stretch amplitudes e.g. $\lambda_1 < \lambda_2 < \lambda_3 < \lambda_4$. At any amplitude lower than the past maximum amplitude, the material exhibits a repeatable stress-strain response with a very little softening in the successive cycles (Lion 1996, Gentot et al. 2004).

ranges such that motivations for founding more general constitutive models can be obtained. This paper examines temperature history dependence of Mullins softening-healing phenomena through experiments and outlines a theory to narrate the experimental facts.

2 EXPERIMENTS

2.1 *Experimental scheme*

We study the thermomechanical behavior of a NR/BR blend. The specimens are tested under

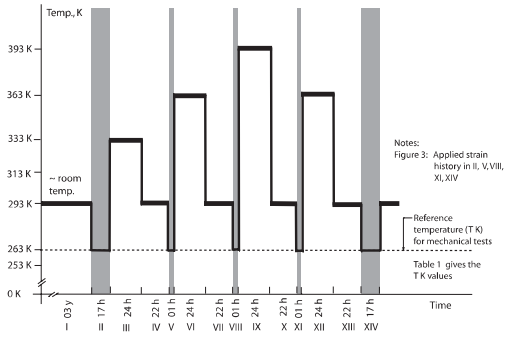

Figure 2. Temperature histories applied to specimens. The figure is to be read in conjunction with Figure 3 and Table 1.

Table 1. Reference temperatures (Figure 2) for mechanical tests.

Sl. no.	Reference temperatures T K
1	253 K
2	263 K
3	293 K
4	313 K
5	333 K

Note: The table is to be read in conjunction with Figs 2 and 3.

tension to understand the effect of the temperature on the mechanical behavior of the blend. In this course, we apply a specified deformation history (Figure 2) on a virgin specimen at a reference temperature and reapply the same deformation history at that reference temperature for a few more times, but also after subjecting the specimens to various temperature histories. By this sequence of events, an insight into the thermorheological processes which occur in the material can be obtained. In this way, the temperature history dependences of the Mullins effect and its healing are investigated under five reference temperatures (Table 1).

2.2 *Temperature dependence of Mullins effect*

Figure 4a shows the effect of the specimen temperature on the first loading cycles (Cycle 1, 3, 5, 7; Fig. 3), while Fig. 4b shows the same effect observed in the second loading cycles (Cycle 2, 4, 6, 8; Fig. 3). The stress amplitudes recorded in the second loading cycles (Fig. 4b) are lesser than those in the first cycles (Fig. 4a). These reductions can be interpreted as the Mullins effect. However, it should be noted that a specimen at a lower temperature may contain a larger crystallinity and a

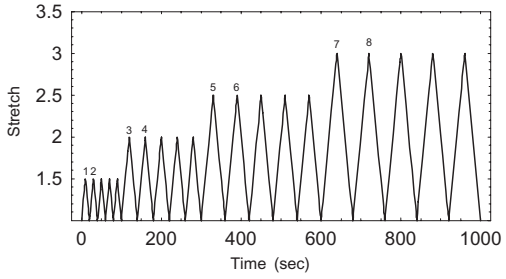

Figure 3. Deformation history applied in specimens at different thermal equilibriums. The figure is to be read in conjunction with Figure 2 and Tables 1. At XIV deformation history was applied only up to 600 s.

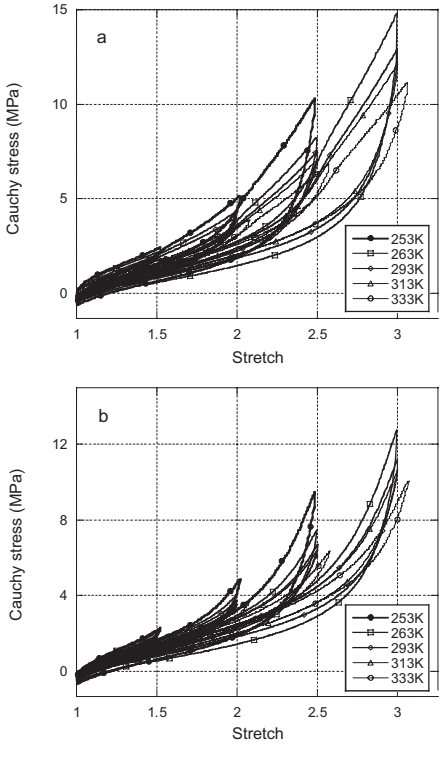

Figure 4. Mullins effect characterized by stretch amplitude dependent softening phenomena at different temperatures. All observations are made 0.05/s stretch rate as per the experimental scheme shown in Figs. 2–3. (a) The first cycles (1, 3, 5, 7); (b) The second cycles (2, 4, 6, 8).

lower amorphicity. In addition, it should have a lower molecular mobility and a larger rate dependence. By taking these points as background, we note that the energy absorption, represented by the areas of the stress-stretch curves of a cycle, is much

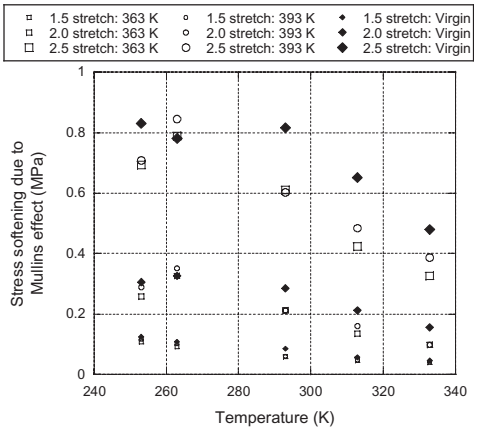

Figure 5. Mullins softening effect is viewed as the difference in stress amplitude over the first and second cycle (stress softening effect). Stress amplitudes at first cycles (1, 3, 5, 7) are deducted from those recorded at second cycles (2, 4, 6, 8) and plotted as a function of temperature. The results from the virgin specimens (at T K) are compared with those after tempering at 363 K and 393 K (Figs. 2–3).

larger at low temperatures and it decreases with the increase of temperature.

In Figure 5, the maximum stresses recorded in cycles 1, 3, 5, 7 (Figs. 2–3) are compared with those belonging to the cycles 2, 4, 6, 8 (Figs. 2–3) and are plotted as a function of temperature (T K). The plot shows that the softening increases with increasing stretch amplitude and decreasing temperature. A change is observed at temperature levels below 263 K: in comparison with the softening observed at 253 K, the softening is quite small at 333 K. The stress responses of virgin specimens recorded in the tests at 263 K are presented in Figure 6 as functions of time. A diminishing trend of the softening at each stretch amplitude is noted after the second cycles (cycles 2, 4, 6, 8). In addition, the peaks of the stress response clearly depict the deformation dependence of the Mullins effect: the higher the applied stretch the higher is the softening effect. At the end of each cycle, the applied stretch was set to zero (Fig. 2–3). This causes that the stress changes its sign due to viscosity-induced strain rate effects. The stress responses belonging to the other temperatures lead to the same conclusions and are skipped for brevity. These observations (Figure 6) are consistent with the earlier work at room temperature (Lion 1996).

2.3 *Effect of heat treatment temperature on the healing behavior*

The consequences of successive temperature increases during the heat treatment (from 333 K

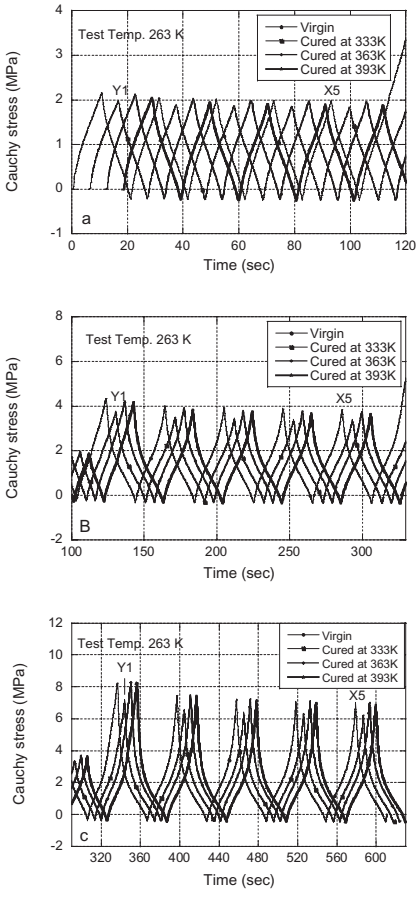

Figure 6. Stress histories obtained from virgin specimen and specimens tempered at different temperatures. The mechanical processes (Figs. 2–3) were applied at 263 K in each of the tests. For the purpose of understandable illustration, the stress histories have been separated from each other by 6 sec. In reporting the stress history for virgin specimen, records only up to first 600 seconds are plotted.

to 393 K; Figure 2, Steps *III, VI, IX*) on the healing behavior of the Mullins effect are also presented in Figure 6. They show different segments of the stress responses corresponding to the different stretch amplitudes. The parameter in these tests is the temperature during the heat treatment which was 24 hours in duration. In performing the mechanical tests, the specimen temperature was held constant at 263 K and the stretch rate was set to 0.05/s. Due to the same stretch rate in all tests, strain-rate effects are not considered. The virgin specimen and tempered specimens were deformed with the stretch history as shown in Fig. 3. During the first 600 seconds both histories are equal. In order to point out the relevant effects in Fig. 6, the stress histories of the tempered specimens have been shifted by 6, 12 and 18 seconds relative to the response of the virgin specimen.

The comparison of the stress peaks of the virgin specimen at 263 K and that tempered at 333 K (Fig. 2, Segment *III*) and tested at 263 K shows an interesting trend: even the fifth peak (marked *X5*) of the virgin specimen lies at a higher value than the first peak (*Y1*) produced by the specimen after tempering at 333 K (Fig. 2, Segment *III*). This amplitude reduction is the result of the application of the further deformation process which the specimen observed before experiencing the heat treatment (Gentot et al. 2004). The effect of the temperature treatment at 333 K is small. But after tempering the specimen at 363 K for 24 hours, the stress peaks become comparable to those of the virgin specimen. The heat treatment at a higher temperature facilitates molecular motions and increases the rate of reconstruction of ruptured bonds between the filler aggregates and the rubber molecules. However, from the current measurements it is not clear whether the bonds reconstructed upon applying temperature are physical or chemical in nature. The experimental data and its interpretation obtained from mechanical tests call for the necessity of measuring the amount of heat which is absorbed or dissipated by the specimens during the heat treatment. Precise measurement of the heat exchange in a DSC device provides more information in this context. After the heat treatment, the specimen was cooled down to room temperature and then to 263 K for performing the mechanical tests. During this cooling process, it was perhaps possible to completely or partially regenerate the crystalline structure. Finally, the stress-stretch responses of the virgin specimen and those of the specimen tempered at 363 K for 24 hours are compared (Segments *II* and *VIII*, Figure 2) in Figure 7: the match is nearly perfect.

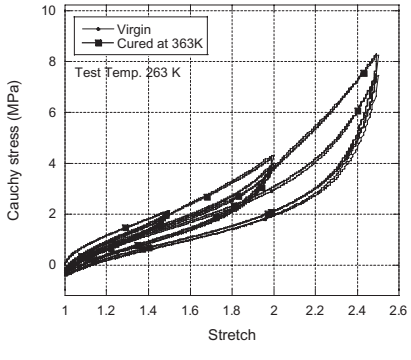

Figure 7. Comparison between the stress-stretch response from virgin specimen and that from the specimen after tempering at 363 K (Figure 2, Segment VI).

A tempering of the specimen at a higher level of 393 K (Figure 2, Segment *IX* and Figure 10) was not found to cause an appreciable increase in the stress amplitude. This observation also demonstrates the existence of a threshold temperature for attaining the virgin material behavior through thermally-activated healing processes. The comparison of the stress responses obtained after tempering the specimen at 333 K, 363 K and 393 K does not suggest any stretch history effect. The significant role of the temperature on the appearance of healing within a specific time interval can thus be recognized.

3 THEORETICAL CONSIDERATIONS

In order to formulate a constitutive theory for the softening-healing phenomena that we observed in experiments, we start with the fundamental laws of thermodynamics in their one-dimensional version. The first law of thermodynamics reads as

$$\rho\dot{e} = \sigma\,\dot{\varepsilon} - \frac{\partial q}{\partial z} + \rho r \tag{1}$$

The constant ρ is the mass density of the material, e is the specific internal energy density per unit mass, σ is the stress, ε is the strain, $q(z,t)$ is the heat flux in z-direction and r is the heat supply per unit mass. The second law of thermodynamics reads as

$$\rho\theta\gamma = -\rho\dot{\psi} + \sigma\dot{\varepsilon} - \rho s\dot{\theta} - \frac{1}{\theta}q\frac{\partial\theta}{\partial z} \tag{2}$$

where ψ is the free energy density, s is the specific entropy, θ the thermodynamic temperature and γ the internal entropy production which is caused by irreversible processes. The principle of irreversibility states that

$$\gamma \geq 0 \tag{3}$$

for arbitrary thermomechanical changes. To combine both thermodynamical laws, the relation between the internal energy, the free energy and the entropy is needed:

$$e = \psi + s\theta \tag{4}$$

The mechanical part of the free energy function of an unsoftened or virgin nonlinear viscoelastic elastomer can be written as

$$\rho\psi_{mech} = w_{eq}(\varepsilon) + \sum_{k=1}^{n} w_{ovk}(\varepsilon_{ek}). \tag{5}$$

Its equilibrium part $w_{eq}(\varepsilon)$ depends on the total deformation ε and its non-equilibrium part $\sum w_{ovk}(\varepsilon_{ek})$ on the elastic strains of a series of Maxwell elements in parallel. The variables ε_{ek} are the elastic strains of the springs and the ε_{ink} are the inelastic strains belonging to the damping elements:

$$\varepsilon = \varepsilon_{ek} + \varepsilon_{ink} \tag{6}$$

To represent the Mullins effect, we introduce an additional internal variable $0 \leq D \leq 1$ describing the softening behaviour and assume that the loss in the mechanical free energy is not completely dissipated into heat but stored in a different manner in the material:

$$\rho\psi = (1-D)\left(w_{eq}(\varepsilon) + \sum_{k=1}^{n} w_{ovk}(\varepsilon_{ek})\right) + \delta(D,\theta) \tag{7}$$

The function $\delta(D,\theta)$ is that part of the free energy that is released during softening but not dissipated into heat. It has the properties $\delta(0,\theta) = 0$ and $\partial\delta/\partial D \geq 0$. In order to evaluate the second law of thermodynamics, we differentiate the free energy (7) with respect to time

$$\begin{aligned}\rho\dot{\psi} = (1-D)\left\{\frac{\partial w_{eq}}{\partial\varepsilon} + \sum_{k=1}^{n}\frac{\partial w_{ovk}}{\partial\varepsilon_{ek}}\right\}\dot{\varepsilon} - (1-D)\sum_{k=1}^{n}\frac{\partial w_{ovk}}{\partial\varepsilon_{ek}}\,\dot{\varepsilon}_{ink} \\ + \frac{\partial\delta}{\partial\theta}\dot{\theta} - \left\{w_{eq}(\varepsilon) + \sum_{k=1}^{n} w_{ovk}(\varepsilon_{ek}) - \frac{\partial\delta}{\partial D}\right\}\dot{D}\end{aligned} \tag{8a}$$

and insert it into (2):

$$\begin{aligned}\rho\theta\gamma = &\left(\sigma - (1-D)\left\{\frac{\partial w_{eq}}{\partial\varepsilon} + \sum_{k=1}^{n}\frac{\partial w_{ovk}}{\partial\varepsilon_{ek}}\right\}\right)\dot{\varepsilon} \\ &+ (1-D)\sum_{k=1}^{n}\frac{\partial w_{ovk}}{\partial\varepsilon_{ek}}\,\dot{\varepsilon}_{ink} \\ &- \left(\rho s + \frac{\partial\delta}{\partial\theta}\right)\dot{\theta} - \frac{1}{\theta}q\frac{\partial\theta}{\partial z} \\ &+ \left\{w_{eq}(\varepsilon) + \sum_{k=1}^{n} w_{ovk}(\varepsilon_{ek}) - \frac{\partial\delta}{\partial D}\right\}\dot{D}\end{aligned} \tag{8b}$$

In order to satisfy the non-negativity of the specific dissipation $\rho\theta\gamma \geq 0$ for arbitrary thermomechanical processes, i.e. numerical values of the temperature- and strain rates, we obtain the following potential relations for the stress and the entropy:

$$\sigma = (1-D)\left(\frac{\partial w_{eq}}{\partial\varepsilon} + \sum_{k=1}^{n}\frac{\partial w_{ovk}}{\partial\varepsilon_{ek}}\right) \tag{9}$$

$$\rho s = -\frac{\partial\delta}{\partial\theta} \tag{10}$$

The evolution laws for the inelastic deformations and the heat flux are assumed to be

$$\dot{\varepsilon}_{ink} = \frac{(1-D)}{\eta_k} \frac{\partial w_{ovk}}{\partial \varepsilon_{ek}} \,, \tag{11}$$

$$q = -\lambda \frac{\partial \theta}{\partial z} \,, \tag{12}$$

which are sufficient conditions for the non-negativity of the corresponding terms in (9). The heat conductivity λ and the viscosities η_k are non-negative constants or functions which have to be determined experimentally. A similar argumentation leads the differential equation

$$\dot{D} = \mu (1-D) \left(w_{eq}(\varepsilon) + \sum_{k=1}^{n} w_{ovk}(\varepsilon_{ek}) - \frac{\partial \delta}{\partial D} \right) \tag{13}$$

modelling the evolution of the internal variable D. The material function μ is non-negative as well and has to be determined on the basis of experimental data. The factor $(1-D)$ has been introduced in (14) in order to constrain $D \le 1$ The driving force for the evolution of the variable D is the mechanically-stored free energy and the limiting term in (14) is the partial derivative of the function $\delta(D,\theta)$. The simplest constitutive assumption for this derivative is

$$\frac{\partial \delta}{\partial D} = \alpha(\theta) D, \tag{14}$$

where the function $\alpha(\theta)$ describes the temperature dependence of the limiting term. If the mechanical part of the free energy is zero, i.e. $w_{eq}(\varepsilon) + \sum w_{ovk}(\varepsilon_{ek}) = 0$, the material is in mechanical equilibrium. In this case, the rate of the softening variable is negative

$$\dot{D} = -\mu (1-D) \alpha(\theta) D \tag{15}$$

such that the developed constitutive model can represent the temperature-dependent healing of the Mullins effect. Integration of (15) leads to the function

$$\delta = \frac{1}{2} \alpha(\theta) D^2 + h(\theta) \tag{16}$$

and with (11) to the expression

$$\rho s = -\left(\frac{1}{2} \alpha'(\theta) D^2 + h'(\theta) \right) \tag{17}$$

for the entropy. Differentiating (4) with respect to time leads to

$$\rho \dot{e} = \rho \dot{\psi} + \rho s \dot{\theta} + \rho \dot{s} \theta. \tag{18}$$

Considering (8) in combination with (10)–(14) the relation

$$\rho \dot{\psi} = \sigma \dot{\varepsilon} - \sum_{k=1}^{n} \eta_k \dot{\varepsilon}_{ink}^2 - \rho s \dot{\theta} - \frac{\dot{D}^2}{\mu} \tag{19}$$

is obtained for the time rate of the free energy. Inserting this into (19), the expression

$$\rho \dot{e} = \sigma \dot{\varepsilon} - \sum_{k=1}^{n} \eta_k \dot{\varepsilon}_{ink}^2 - \frac{\dot{D}^2}{\mu} + \rho \dot{s} \theta \tag{20}$$

follows for the rate of the internal energy. To derive the equation of heat conduction, we replace $\rho \dot{e}$ in the first law of thermodynamics (1) by (21) and obtain

$$\begin{aligned} -\theta \frac{d}{dt} \left(\frac{1}{2} \alpha'(\theta) D^2 + h'(\theta) \right) &= \lambda \frac{\partial^2 \theta}{\partial z^2} \\ &+ \sum_{k=1}^{n} \eta_k \dot{\varepsilon}_{ink}^2 + \frac{\dot{D}^2}{\mu} + \rho r \end{aligned} \tag{21}$$

which leads to

$$\begin{aligned} -\theta \left(\frac{\alpha''(\theta)}{2} D^2 + h''(\theta) \right) \dot{\theta} &= \lambda \frac{\partial^2 \theta}{\partial z^2} + \sum_{k=1}^{n} \eta_k \dot{\varepsilon}_{ink}^2 \\ &+ \frac{\dot{D}^2}{\mu} + \theta \frac{\alpha'(\theta) D}{2} \dot{D} + \rho r \end{aligned} \tag{22}$$

after rearranging the terms. The factor of the temperature rate on the left-hand side is the specific heat capacity of the material which depends on both the temperature and the internal variable D. The material function $h(\theta)$ can be determined if the specific heat capacity $c_0(\theta)$ of the on the virgin or unsoftened material is known. Integration of

$$-\theta h''(\theta) = c_0(\theta) \tag{23}$$

leads to the expression

$$h(\theta) = h(\theta_0) + (\theta - \theta_0) h'(\theta_0) - \int_{\theta_0}^{\theta} \left(\int_{\theta_0}^{y} \frac{c_0(x)}{x} dx \right) dy \tag{24}$$

for this constitutive function.

4 CONCLUSIONS

Experimental results show that a decrease in the specimen temperature leads to more pronounced hysteresis properties together with an increased softening effect. This observation is rather general in nature and may have a relation to the amount of crystallinity present in the material. Tempering of the softened specimens leads to healing such that the Mullins effect can be observed once again. A comparison of the results obtained from the virgin and the tempered specimens tested at different

temperatures suggests that the Mullins effect shown by the virgin can be healed due heat treatment. However, the tempering of the specimens at elevated temperatures for a specific time showed the existence of a threshold temperature which is necessary to completely heal the specimens.

From our point of view, the experimental data provided in this essay appears to be useful for the future development of physically-based thermo-mechanical material models for filler-reinforced rubber. We have seen that the material behavior of the NR/BR rubber blend does not depend only on the deformation history and the current thermodynamic temperature, but also on the entire temperature history. In addition, healing does occur. To this end, we have presented a thermodynamically consistent phenomenological formulation that has the potential to describe the softening-healing phenomena.

ACKNOWLEDGEMENTS

Dr. A.F.M.S. Amin is grateful to the Alexander von Humboldt foundation for granting a Georg Forster fellowship that enabled him to stay at the Institute of Mechanics, Faculty of Aerospace Engineering, University of the Federal Armed Forces Munich during February 2007–July 2007 to conduct this Joint Collaborative Research. The authors are also much grateful to Mr. P. Höfer for assistance in measurements.

REFERENCES

Amin, A.F.M.S., Alam, M.S., & Okui, Y., 2002. An improved hyperelasticity relation in modelling viscoelasticity response of natural and high damping rubbers in compression: experiments, parameter identification and numerical verification, *Mech. Mater.*, 34, 75–95.

Amin, A.F.M.S., Lion, A., Sekita, S., & Okui, Y., 2006. Nonlinear dependence of viscosity in modeling the rate-dependent response of natural and high damping rubbers in compression and shear: Experimental identification and numerical verification, *Int. J. Plast.*, 22, 1610–1657.

Bueche, F., 1961. Mullins effect and rubber-filler interaction, *J. Appl. Polym. Sci.*, 5, 271–281.

Fuller, K.N.G., Gough, J., & Thomas, A.G. 2004. The effect of low temperature crystallization on the mechanical behavior of rubber, *J. Polymer Science, Part B: Polymer Physics*, 42, 2181–2190.

Gent, A.N., 1954. Crystallization and the relaxation of stress in stretched natural rubber vulcanizates, *Trans. Faraday Soc.*, 50, 521–533.

Gent, A.N., & Zhang, L.Q., 2002. Strain-induced crystallization and strength of rubber, *Rubber Chem. Technology*, 75, 923–933.

Gentot, L., Brieu, M., & Mesmacque, G., 2004. Modeling of stress-softening for elastomeric materials, *Rubber Chem. Technology*, 77, 759–775.

Haupt, P., 2000. Continuum Mechnanics and Theory of Materials, Springer-Verlag, Berlin.

Lion, A., 1996. A constitutive model for carbon black filled rubber: Experimental investigations and mathematical representation, *Continuum Mech. Thermodyn.*, 8, 153–169.

Lion, A., 1997a. A physically based method to represent the thermo-mechanical behavior of elastomers, *Acta Mechanica*, 123, 1–25.

Lion, A., 1997b. On the large deformation behavior of reinforced rubber at different temperatures, *J. Mech. Phys. Solids*, 45, 1805–1834.

Morawetz, H., 2000. History of rubber research, *Rubber Chem. Technology*, 73, 405–426.

Stevenson, A., 1983. The influence of low-temperature crystallization on the tensile elastic modulus of natural rubber, *J. Polymer Science*, 21, 553–572.

Treloar, L.R.G., 1973. The elasticity and related properties of rubbers, *Rep. Prog. Phys.*, 36, 755–826.

Wood, L.A., & Bekkedahl, N., 1946. Crystallization of unvulcanized rubber at different temperatures, *J. Appl. Physics*, 17, 362–375.

Wood, L.A., & Roth, F.L., 1944. Stress-temperature relations in a pure gum vulcanizate of natural rubber, *J. Appl. Physics*, 15, 781–789.

Constitutive Models for Rubber VI – Heinrich et al. (eds)

A micro-mechanical model for the anisotropic Mullins effect in filled rubber-like elastomers

Roozbeh Dargazany, Mikhail Itskov & Georg Weinhold
Department of Continuum Mechanics, RWTH Aachen University, Germany

ABSTRACT: In this contribution, a micro-mechanical model for the anisotropic Mullins effect is proposed for carbon black filled rubbers. The model describe both the deformation induced anisotropy and permanent set. Damage of the polymer-filler network is considered as a consequence of chain sliding on or debonding from aggregates. In contrast to previous works on anisotropy of the Mullins effect, no phenomenological damage function is introduced. Damage in different directions is governed by a network evolution concept which describes changes in the inter-aggregate distribution of polymer chains. The model includes a few number of physically motivated material constants and demonstrates good agreement with own experimental data on subsequent uniaxial tensions in two orthogonal directions.

1 INTRODUCTION

One of the important mechanical characteristics of rubber is stress softening after the first loading cycle which is referred to as the Mullins effect. It was experimentally observed and reported along with deformation induced anisotropy and time-independent residual strains generally known as permanent set. According to experimental results, stress softening at the same strain level decisively depends on the filler concentration in the rubber network. In unfilled elastomers softening is negligible but becomes very pronounced in rubbers with high filler concentrations.

Although slight stress softening does occur in unfilled rubbers as well, its mechanism differs fundamentally from that one underlying softening in filled rubbers. This motivated a class of theories in which damage was considered as an effect of filler contribution. Bueche (1960) developed a physically based model considering consequent debonding of chains from fillers during the primary loading. He supposed that chains with different lengths are distributed within the rubber network and employed statistical mechanics in order to describe the Mullins effect.

Govindjee & Simo (1991) proposed a three-dimensional model of the chain network evolution which included three new features. First, polymer chain distribution inside the rubber matrix was implemented. Second, consequent debonding as a direct result of network elongation was taken into account and, finally, the concept of network decomposition was applied in which the rubber network is decomposed into elastic rubber (CC) and polymer-filler (PP) networks. Although the resulting three-dimensional model was obtained by summation over principal strain directions, its numerical implementation was solely applied to the one-dimensional case. In order to improve the model, the same authors (Govindjee & Simo, 1992) further proposed a phenomenological concept based on the previous assumptions. This concept was easily implemented into a finite element code and showed good agreement with experimental data. Like the previous formulations this model was isotropic and did not describe permanent set.

Quite recently, Göktepe & Miehe (2005) proposed an anisotropic extension of the theory by Govindjee & Simo (1992). The CC network was considered to be purely elastic and its strain energy is formulated by applying a concept of non-affine micro-macro transition to the tube model. Damage was attributed to the PP-network and described by an approach proposed by Govindjee & Simo (1992). The model was able to take into account permanent set and deformation induced anisotropy which represents a clear advantage in comparison to previous models. However, the model was not compared to experimental data on anisotropy of the Mullins effect while softening was simulated by means of a phenomenological damage function.

Another model by Diani et al. (2006) was obtained as an extension of the network alteration theory. In order to predict induced anisotropy and permanent set the model utilizes a phenomenological damage function. It demonstrates good agreement with experiments for the unloading in the first direction but suffers from an unrealistic stress upturn in the prediction of the loading branches.

In the present paper, we pursue the concept of network decomposition by Govindjee & Simo (1991) and propose a new micro-mechanical model for the polymer-filler network where softening of the equilibrium stress-stretch behavior is based an evolution of the polymer chain network suspended between carbon black aggregates. Finally, the model is compared with own experimental data on subsequent uniaxial tensions in **two orthogonal directions** in order to validate its behavior both with respect to the anisotropic Mullins effect and permanent set.

2 STATISTICAL MECHANICS OF POLYMERS

Due to energy barriers, adjacent monomers in a polymer chain keep a certain angle between each other generally referred to as valence angle. Considering the valence angle as a material parameter, we apply the freely rotating chain (FRC) concept in order to model polymer molecules. Within this concept, a chain is defined as the whole or a part of a polymer molecule limited between two constrained segments, each of them might be either bonded to the aggregate surface or cross-linked with other chains. Now, consider a FRC with n segments each of length l. Let $\boldsymbol{R}$ be a vector connecting two ends of this chain. The length of this vector r is referred to as end-to-end distance. Using the abbreviation

$$\alpha = \left(\frac{1-\cos\theta}{1+\cos\theta}\right)^2, \tag{1}$$

where θ denotes the supplement of the valence angle and following the lead of Govindjee & Simo (1991), the probability density function for a FRC is obtained as

$$p(r)dr = \sqrt{\frac{3\alpha}{2\pi n l^2}}\, e^{-\frac{3\alpha r^2}{2nl^2}} dr. \tag{2}$$

The above function shows a better agreement with the exact chain distribution than a non-Gaussian one (see, e.g., Treloar, 1975), although the latter one is still advantageous in application to the calculation of the entropy and the resulting free energy. For this reason, the non-Gaussian distribution will be used in the next section for the derivation of the free energy of the FRC.

Let A be the total area of active adsorption sites inside the rubber matrix and N be the number of bonded segments of polymer chains per unit volume. Then, one defines the average area of active adsorption sites available for the formation of a bond with one structural segment of a polymer chain as $\kappa = A/N$.

We consider further a set of chains in a particular direction $\boldsymbol{d} = \boldsymbol{R}/r$ both ends of which are connected to two aggregate surfaces. Moreover, we consider r as the average interaggregate distance (Fig. 1).

We assume that none of segments between the number 1 and n is joined to aggregate surfaces. Considering $\bar{r} = r/l$ as relative distance, the probability of this state is expressed as (cf. Govindjee & Simo, 1991)

$$P(n, \bar{r}) = \sqrt{\frac{3\alpha\kappa^2}{2\pi n}}\, e^B, \tag{3}$$

where B depends on α, κ, n, $\bar{r}$ (see Dargazany & Itskov, 2009).

The number n and length l of segments of a FRC are related to those of the so-called freely jointed chain, n_i and l_i, respectively by

$$l_i = al, \quad n_i = bn, \tag{4}$$

where the coefficients a and b are calculated by (Treloar, 1975)

$$a = \frac{1}{\cos\left(\frac{\theta}{2}\right)\sqrt{\alpha}}, \quad b = \cos^2\left(\frac{\theta}{2}\right)\sqrt{\alpha}. \tag{5}$$

In order to estimate the entropic energy of a single chain one assumes that all chains are initially in the unperturbed state. Thus, one can write

$$r = \lambda\sqrt{\frac{nl^2}{\sqrt{\alpha}}}, \quad \bar{r} = \lambda\sqrt{\frac{n}{\sqrt{\alpha}}}, \tag{6}$$

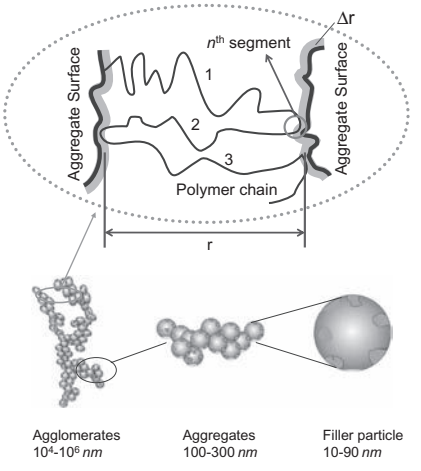

Figure 1. Hierarchical structure of filler reinforcement with polymer chain bonds to aggregate surfaces.

where λ is the chain stretch. Thus, the entropic energy of single chain can be written as

$$\psi(n,\lambda) = KT\left(\lambda\sqrt{bn}\beta + \ln\frac{\beta}{\sinh\beta}\right), \tag{7}$$

where $\beta = \mathcal{L}^{-1}(\lambda/\sqrt{bn})$ and $\mathcal{L}^{-1}$ denotes the inverse-Langevin function. Finally, T stands for the temperature (isothermal condition is assumed) and K is Boltzmann's constant. The free energy function (7) resulting from the FRC concept will further be implemented for all polymeric chains in the rubber matrix.

3 NETWORK DECOMPOSITION

The rubber matrix is decomposed into a pure rubber network and a polymer-filler network which act parallel to each other. In line with this assumption, the free energy of the rubber matrix Ψ_M can be represented by

$$\Psi_M = \Psi_{cc} + \Psi_{pp}, \tag{8}$$

where Ψ_{cc} and Ψ_{pp} denote the free energies of chains in pure rubber network and chains distributed between filler aggregates, respectively. By this means, one assumes that there is no interaction between both networks. The network decomposition concept is illustrated in Figure 2.

3.1 *Pure rubber network*

Although stress softening has also been observed in unfilled rubbers, its magnitude can be neglected in comparison to that one occurring in filled elastomers. For this reason, in the present study, the pure rubber network will be considered as a perfectly elastic component. In addition, the cross-link motion in the direction $\boldsymbol{d}$ is affine with the macro-stretch in that direction.

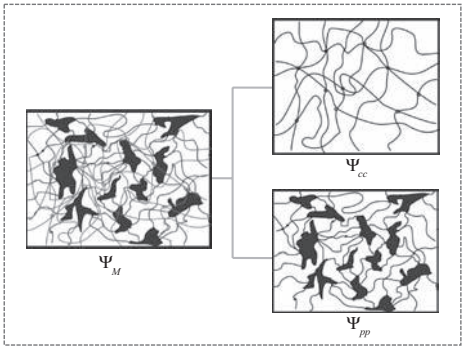

Figure 2. Network decomposition concept.

In order to obtain the free energy of this network one then substitutes n by the average number of segments in one chain n_c, multiplies (7) by the average number of chains N_c in the direction $\boldsymbol{d}$ and finally integrates over the unit sphere (see Sect. 5.2).

3.2 *Polymer-filler network*

The evolution of the polymer-filler network is assumed to be responsible for the already mentioned stress softening. Let $N(n,\bar{r})$be the number of chains with the number of segments (relative length) n, the relative end-to-end distance $\bar{r}$ and the end-to-end direction $\boldsymbol{d}$. Integration over the whole set D_A of relative chain lengths n available in the direction $\boldsymbol{d}$ further yields the free energy of chains in this direction as

$$\overset{d}{\Psi} = \int_{D_A} N(n,\bar{r})\psi\left(\overset{d}{\lambda}\right)dn. \tag{9}$$

In the following, the network evolution is understood to be an interaction of two simultaneous processes referred to as aggregate-polymer debonding and network rearrangement.

4 NETWORK EVOLUTION

4.1 *Aggregate-polymer debonding*

In the course of deformation, the polymer chains begin to slide on or debond from the aggregates. This debonding starts with the shortest chain and gradually involves longer and longer chains.

The strength of monomer bonds within polymer chains is far higher than that of polymer-filler bonds. Thus, polymer chains do not break but rather slide from their bonding sites on the aggregate surface. During consequent unloadings, the debonded chains do not reattach back to the aggregates active sites.

The debonding or the sliding takes place if the force magnitude exceeds the effective interaction strength of polymer-filler bonds. Thus, the parameter υ is introduced such that the chains with the contour length $L < \upsilon\lambda_m r_0$ are assumed to be debonded. Here, r_0 denotes the initial interaggregate distance. Then, by means of (5), the set of available relative lengths of chains bounded to aggregates in the direction $\boldsymbol{d}$ can be expressed by

$$D_A\left(\overset{d}{\lambda}_m\right) = \left\{ n \,\middle|\, \upsilon\frac{\overset{d}{\lambda}_m \bar{r}_0}{ab} \le n \le n_{\max} \right\}, \tag{10}$$

where $\overset{d}{\lambda}_m$ denotes the maximal micro-stretch reached in this direction. By means of this value

the loading history influences the material behavior in the direction ***d***.

Note that the set (10) is defined for freely rotating chains and is direction dependent. Thus, it can be considered as a three-dimensional extension of the one-dimensional domain proposed by Govindjee & Simo (1991) for freely jointed chains. Besides, eq. (10) includes the upperbound parameter $n_{\max}$ which restricts the number of active segments to a finite number.

4.2 *Network rearrangement*

The concept of chain rearrangement in rubber network as a result of deformation has recently been explored (see, e.g., Diani et al., 2006). It is usually assumed that after debonding chains do not contribute to the network entropic energy any more and their energy is thus lost. This concept considers molecular chains bonded to aggregates only at two points which might be, indeed, well justified for relatively short chains. However, longer molecular chains are usually bonded at different places to aggregates and have numerous cross-linkages with each other. Thus, the actual status of a polymer molecule with many linkages to aggregates should be taken into account in the network modeling.

Detachment of chains from the aggregate surface does not necessarily result in the complete loss of their role in the network entropic energy. Vice versa, the debonding can even lead to the recruiting of some new active segments. Indeed, we can imagine three simultaneously happening competitive processes accompanying debonding (see Fig. 3):

1. Deactivation of some segments
2. Activation of some segments
3. No effect on number of active segments

Note also that with increasing interaggregate distance one of these processes triggers another one and so on. All in all, one can assume that the total number of active segments remains constant.

Since the integration will be carried out only over the set available chains DA· a normalization function $g(\lambda_m^d)$ is introduced such that

$$\int\limits_{D_A\left(\lambda_m^d\right)} g\left(\lambda_m^d\right) P(n,\bar{r}_0)\, dn = 1. \tag{11}$$

The amplification of the probability distribution caused by the function g is illustrated in Figure 4.

Multiplying then the term $P(n,\bar{r}_0)g(\lambda_m^d)$ by the total number of active chains $N_c(\bar{r})$, and taking further into account that this distribution may change only during primary loading, where $\lambda = \lambda_m^d$, yields

$$N(n,\bar{r}) = \widehat{N}_p\left(\lambda_m^d\right)\widehat{P}(n), \tag{12}$$

where the abbreviations

$$\widehat{N}_p\left(\lambda_m^d\right) = N_c\left(\lambda_m^d \bar{r}_0\right) g\left(\lambda_m^d\right), \widehat{P}(n) = P(n,\bar{r}_0) \tag{13}$$

are used. The earlier assumption of a constant number of active segments leads to the condition

$$\widehat{N}_p\left(\lambda_m^d\right) = N_0 \Phi\left(\lambda_m^d\right), \tag{14}$$

where

$$N_0 = \widehat{N}_p(1), \quad \Phi\left(\lambda_m^d\right) = \frac{\int\limits_{D_A(1)} \widehat{P}(n) n dn}{\int\limits_{D_A\left(\lambda_m^d\right)} \widehat{P}(n) n dn}. \tag{15}$$

The variable N_0 represents the number of active chains per unit undeformed volume. It depends on

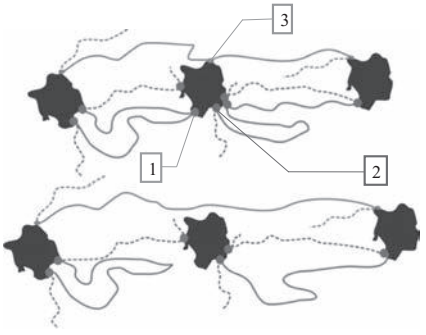

Figure 3. Effect of chain detachment on the number of active segments.

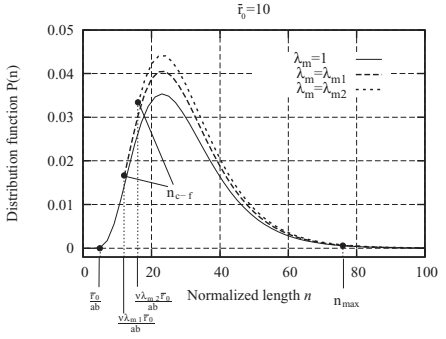

Figure 4. Effect of normalization factor on the probability distribution.

the molecular mass of segments and density of the polymer network. For this reason, N_0 can and will be considered in the following as a material parameter.

Finally, inserting (14) into (9), we obtain

$$\overset{d}{\Psi} = \int_{D_A(\overset{d}{\lambda}_m)} N_0 \Phi\left(\overset{d}{\lambda}_m\right) \widehat{P}(n) \psi\left(n, \overset{d}{\lambda}\right) dn. \tag{16}$$

5 TRANSITION TO MACRO-MODEL

5.1 *3D generalization*

It is generally assumed that the virgin rubber network is initially homogeneous and isotropic and the macroscopic free energy is regarded as the sum of microscopic strain energies of all active chains available within the network which can be calculated by integration over the unit sphere. Applying the isotropic space distribution (chains are spread equally in all directions), we can write

$$\Psi_{cc} = \frac{1}{4\pi} \int_s N_c \psi\left(n, \overset{d}{\chi}\right) d\overset{d}{u}, \; \Psi_{pp} = \frac{1}{4\pi} \int_s \overset{d}{\Psi} d\overset{d}{u}, \tag{17}$$

where S denotes the unit sphere. The integration is carried out numerically by

$$\Psi_{cc} \cong \sum_{i=1}^{k} N_c \Psi\left(n, \chi^{d_i}\right) w_i, \Psi_{pp} \cong \sum_{i=1}^{k} \overset{d_i}{\Psi} w_i, \tag{18}$$

where w_i are weight factors corresponding to the collocation directions $\boldsymbol{d}_i$ (see, Bažant & Oh, 1986).

5.2 *Strain amplification*

The strain amplification concept is based on the fact that the filler aggregates are considerably stiffer than polymer chains connecting them. This inhomogeneity of the material motivates the assumption of non-affine deformation. Accordingly, the amplification function X establishing arelationship between the microstretch $\overset{d}{\lambda}$ and the macrostretch $\overset{d}{\chi}$ in the direction $\boldsymbol{d}$ is defined by

$$\overset{d}{\lambda} = X\left(\overset{d}{\chi}\right) = \frac{\overset{d}{\chi} - C^x}{1 - C^x}, \tag{19}$$

where $C \in (0,1)$ represents the volume fraction of filler ($C < 0.3$ in most studies). The exponent x depends on the structure of the filler network. For example, Bueche (1961) showed that $x = 1/3$ in the case of statistically homogeneous distribution of spherical particles.

5.3 *Final formulation*

Now, the total strain energy of the network can be obtained by inserting (18) into (8). Taking the incompressibility condition

$$\det \mathbf{F} = 1 \tag{20}$$

into account the constitutive equation for the first-Piola Kirchhoff stress tensor $\mathbf{T}$ can be written by

$$\mathbf{T} = \frac{\partial \Psi_M}{\partial \mathbf{F}} - p\mathbf{F}^{-T} = \frac{\partial \Psi_{cc}}{\partial \mathbf{F}} + \frac{\partial \Psi_{pp}}{\partial \mathbf{F}} - p\mathbf{F}^{-T}, \tag{21}$$

where $\mathbf{F}$ denotes the deformation gradient and p stands for an arbitrary scalar parameter which can be defined according to a particular boundary value problem.

6 COMPARISON WITH OWN EXPERIMENTAL DATA

In this experimental study, a cross-shaped specimen made from 50 phr carbon black filled ($C = 0.2$) polychloroprene rubber (CR) was used. In order to obtain a nearly homogenous state of uniaxial tension, the four arms of cruciform specimens were multiply slitted parallel to the side.

The experimental procedure was as follows. First, the virgin specimen was subject to loading-unloading cycles of uniaxial tension (x-direction) with the increasing stretch amplitudes. After unloading to the stress-free state, the sample was unclamped and clamped again for the consequent loading in the orthogonal direction (y-direction). Thus, residual strains accumulated in the specimen are included in the new reference configuration. Then, the above described loading procedure was repeated in y-direction.

In the case of elongation in x-direction, the classical Mullins effect and permanent set are observed after the first loading cycle. In y-direction, stress-stretch diagrams reveal the Mullins effect as a strongly anisotropic phenomenon and also show considerable permanent set (see Fig. 5).

By means of the seven material parameters (Table 1) the model was fitted to the above presented experimental data. For the fitting, only the loading cycle corresponding to the stretch amplitude 1.6 in x-direction is used. Thus, good agreement with other unloading curves in x-direction and all loading-unloading curves in y-direction is obtained automatically (Fig. 5).

7 CONCLUSION

The motivating key for this work was the absence of micro-mechanical models that can describe

experimental data on the anisotropic Mullins effect of filled rubber-like materials without using empirical damage functions. Thus, we have proposed in the present paper a purely micro-mechanical network evolution theory granting a new insight into the damage mechanism which takes place inside the rubber network. Without using a damage function, the constitutive formulation is obtained based on partial energy dissipation of debonded chains and orientational changes in inter-aggregate chain distribution.

A simple structure combined with the low number of material parameters makes the model suitable for a finite element implementation. The excellent performance of the model was illustrated by comparing to a new set of own experimental data particularly designed to reveal the anisotropic Mullins effect and permanent set. To this end, the material parameters were evaluated by fitting only to one loading cycle. Good agreement with the all other experimental curves is obtained automatically.

Table 1. Material parameters for CR-50 phr.

κ	ν	$\bar{r}_0$	$n_{\max}$	n_c	N_0KT	N_cKT
4.1	1.001	8.216	100	100	0.80 MPa	0.87 MPa

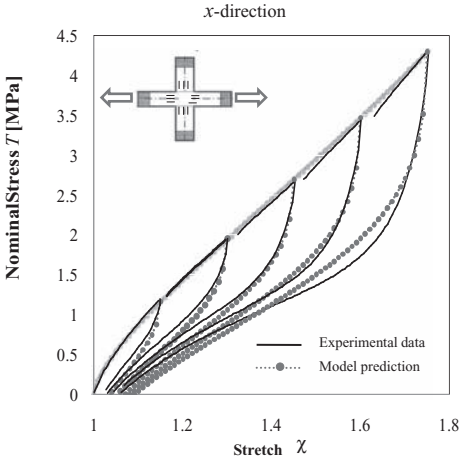

Figure 5. The nominal stress-stretch curves for the uniaxial tension test in x-direction.

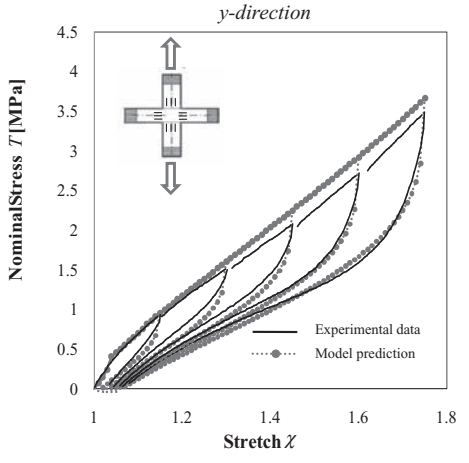

Figure 6. The nominal stress-stretch curves for the uniaxial tension test in y-direction.

ACKNOWLEDGEMENT

The authors thank the German Research Foundation (DFG) for the financial support of this work. The experimental part of this study is a result of cooperation with Professor E. Haberstroh (Institute of Rubber Technology, RWTH Aachen University) whose contribution is also gratefully acknowledged.

REFERENCES

Bueche, F., 1960. Molecular basis for the Mullins effect. *J. Appl. Polymer Sci.* 4: 107–114.

Bueche, F., 1961. Mullins effect and rubber-filler interaction. *J. Appl. Polymer Sci.* 5: 271–281.

Bažant, Z.P. & Oh, B.H., 1986. Efficient numerical integration on the surface of a sphere. *Z. Angew. Math. Mech.* 66: 37–49.

Dargazany, R. & Itskov, M., 2009. A network evolution model for the anisotropic Mullins effect in carbon black filled rubbers. *Int. J. Solid Struct.,* doi:10.1016/j.ijsolstr.2009.03.022.

Diani. J., Brieu. M. & Vacherand. J.M., 2006. A damage directional constitutive model for Mullins effect with permanent set and induced anisotropy. *Eur. J. Mech. A/Solids* 25: 483–496.

Govindjee, S. & Simo, J., 1991. A micromechanically based continuum damage model for carbon black filled rubbers incorporating Mullins effect. *J. Mech. Phy. Solids* 39: 87–112.

Govindjee, S. & Simo, J.C., 1992. Transition from micromechanics to computationally efficient phenomenology: Carbon black-filled rubbers incorporating Mullins effect. *J. Mech. Phys. Solids* 40: 213–233.

Göktepe, S. & Miehe, C., 2005. Micro-macro approach to rubber-like materials. Part III: The microsphere model of anisotropic Mullins-type damage. *J. Mech. Phys. Solids* 53: 2259–2283.

Puso, M., 2003. *Mechanistic Constitutive Models for Rubber Elasticity and Viscoelasticity.* Doctoral dissertation, University of California, Davis.

Treloar, L.R.G., 1975. *The Physics of Rubber Elasticity, 3rd Edition.* Oxford: Clarendon Press.

Constitutive Models for Rubber VI – Heinrich et al. (eds)
© 2010 Taylor & Francis Group, London, ISBN 978-0-415-56327-7

Experimental observation of induced anisotropy of the Mullins effect in particle-reinforced silicone rubber

G. Machado, G. Chagnon & D. Favier
Université de Grenoble/CNRS, Laboratoire 3S-R, Grenoble, France

ABSTRACT: This study is concerned with the experimental observation of anisotropy induced by the Mullins effect in a particle-reinforced silicone rubber. Like many filled rubber-like materials, filled silicone exhibits highly nonlinear mechanical behavior. This nonlinearity is characterized by large strain levels under static conditions, a non-linear stress-strain response and strain rate dependence. However, experimental data concerning the influence of tensile loading cycles in one direction on the stress-softening in other tension directions is quite scarce. In this scope several tension cyclic tests were carried, using a filled silicone rubber material, in order to evidence the anisotropy of the stress-softening phenomenon. The results lead to the conclusion that tensile cycles in one direction practically do not cause the Mullins effect in tension in the perpendicular direction. Nevertheless, the level of influence of the Mullins effect developed in one tension direction on tension behavior for intermediate directions could be measured with respect the different angles in plane. Thus, the anisotropy of the Mullins effect becomes clearly evident.

1 INTRODUCTION

Like many filled rubber-like materials, as well as soft biological tissues and other biomaterials, filled silicones exhibit highly non-linear mechanical behavior. This non-linearity is commonly characterized by large strain levels under static conditions, a non-linear stress-strain response and strain rate dependence. Finally, under cyclic loading conditions, hysteresis and stress-softening behaviors are observed on both filled and unfilled elastomers. For the last half century all these cyclic phenomena were evidenced and modeled to support the most widely engineering applications. However, their microscopic mechanisms (breaking of weak chains, breaking of links, desabsorption of chains, etc.) explanation remains non-unanimous.

Hysteresis is rather related to the dissipative nature of material, i.e., related with viscoelasticity Bergstrom (2000) and viscoplasticity Miehe (2000) behaviors. It is characterized as the difference between loading and unloading paths during a stabilized cycle. On the other hand the stress-softening phenomenon, also called the Mullins effect (see Mullins (1969)), can be described as a softer behavior of the second loading after a first loading. It can be idealized as an instantaneous and irreversible softening of the stress-strain curve, due to rearrangements in the microstructure of the material that occurs whenever the load increases beyond its prior all-time maximum stretch value. At times when the load is less than a prior maximum, nonlinear elastic behavior prevails. One time the previous maximum stretch is reached the loading path turns up and follows the primary curve again up to a new maximum.

Through the years, the Mullins effect has experimentally been observed in different deformation states and numerous models have been proposed, but experimental data concerning the influence of loading cycles in one direction on the stress-softening in other directions are quite scarce.

Mullins (1947) has alluded that the degree of softening was not the same in all directions for natural rubber samples cut both along and perpendicular to the direction of the previous preconditioning stretch; and thus some anisotropic stress-strain properties were developed. This evidence, for example, can be found in a homogeneous plane-strain compression experiment by Pawelski (2001) and in a simple shear experiment performed by Muhr (1999) where simple shear loadings in different directions produce different responses. Other experimental results can be seen in Laraba (2003) using a carbon-black filled natural rubber, Diani (2006) for the commercial elastomer filled black (EPDM) and Itskov (2006) for carbon-black filled acrylate rubber (ACM). All these experimental results point out the strain-induced anisotropy in orthogonal directions due to some in-plane preconditioning test procedure.

Within that context, the aims of this work are to characterize and understand the mechanical behavior of a filled silicone. The objective is to

focus on the strain-induced anisotropy by studying the influence of loading direction on the Mullins effect.

2 EXPERIMENTAL SETUP

2.1 *Preparation of the silicone specimens*

The samples used in the experiments were made of a filled silicone rubber called Rhodorsil®RTV3428 supplied as two liquid components: the uncured silicone and the curing agent. The final material is produced by a polyaddition, curing at room temperature. The liquid mixture is injected in a mold to obtain a sheet with constant thickness.

Specimens used for each of the experiments were made using the same protocol of elaboration, in order to obtain specimens with reproducible mechanical properties, as follow: (i) mixing the components with a 10/1 mass ratio, (ii) putting the mixture under vacuum for 20 minutes in order to eliminate undesirable entrapped air bubbles, (iii) sheet molding injection, (iv) putting mold inside an oven at 70ºC for 4 hours in order to accelerate the curing process and assure a sufficient cross-linking density; (v) sheet demolding after 1 hour exposed at ambient temperature.

Finally, the external surface of the molded plate was coated with a stochastic silicone paint pattern. Made of small speckles, the pattern is necessary for the digital image correlation (DIC) field measurement. Note that the quality of the coated pattern (size, density and gray contrast level) is a critical point to obtain an accurate strain field measurement.

2.2 *Testing procedures*

All the quasi-static experiments were conducted on a MTS 4M universal testing machine with an Entran ELPM-T2 ± 250 N load cell. The images were recorded at 0.5 Hz with a Jai TM-4200GE CCD camera using a reduced scan of 2048 × 1000 pixels. Figure 1 presents the experimental setup. Simple tensile tests were performed on rectangular samples having an initial gauge length $l_o = 40$ mm, width $w_o = 13$ mm and a thickness $e_o = 2$ mm. Since the experiment was not intended to fail the specimen, there was no need to use a dumbbell shaped specimen commonly used to prevent specimen failure nearby the clamps. But knowing that the effects of clamps create an indeterminate state of stress and strain in the region surrounding the clamps, due to the process of gripping, the initial gauge length was adopted as being less than the real physical size of the samples. Figure 2 presents the tensile test specimen together with the grid used by the DIC software to estimate strain fields in the gauge region. For all tests, homogeneity of strain fields in the gauge region has been verified and elongations are averaged values.

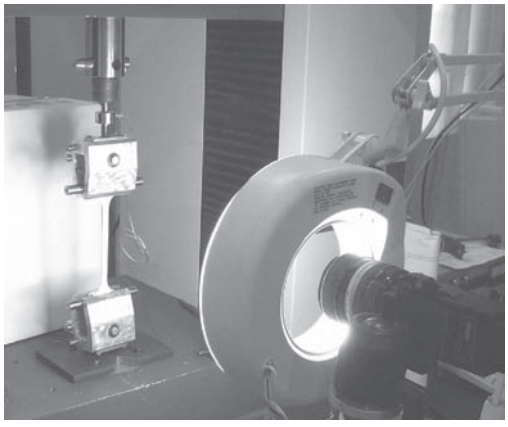

Figure 1. Testing machine with tensile test specimen, load cell and CCD camera.

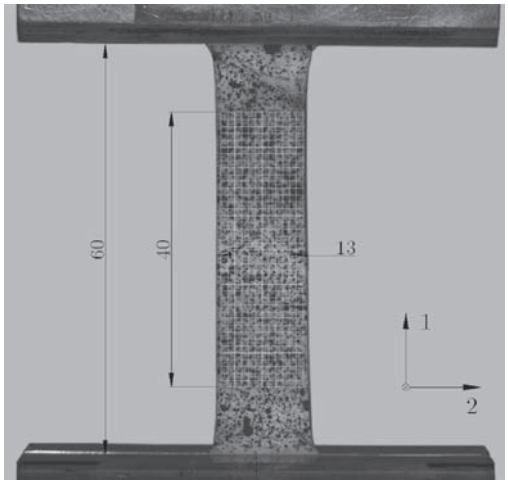

Figure 2. Uniaxial test specimen dimensions and the homogeneous gauge zone.

2.3 *Strain field measurement*

The DIC technique like a non-contact method is often used to characterize rubber-like materials, see for example Meunier (2008) and Sasso (2008). At each testing time step, one image of the sample deformation was recorded using a CCD camera. The DIC technique allows surface reconstruction of the deformed samples and determination of the full-field surface displacements. For the in-plane

displacement an accuracy of 10^{-2} pixels or better can be reached. For point-to-point strain, the accuracy value lies around 10^{-4}. The DIC method is preferred because there is no change in sample stiffness resulting from the presence of an attached sensor (classical extensiometry) and for being insensitive to ambient vibrations and rigid body motions (speckle pattern interferometry). Moreover the method is able to deal with high strain levels, what is a very desirable feature given the high strain level experienced by the tested material. Also the DIC allows demonstrating and measuring a heterogeneous deformation field. See Sutton (2008) for further explanation about digital image correlation method.

3 RESULTS

3.1 *Simple tensile strain state*

During the test, using an elongation rate of $\lambda' = 1.60 \times 10^{-2}$ s^{-1}, the nominal stress tensor **P** (First Piola-Kirchhoff stress tensor) is assumed to be homogeneous within the gauge region as well as the deformation gradient tensor **F**.

Since the actual thickness is not measured, the material is assumed to be incompressible, i.e., $\det(\mathbf{F}) = 1$ for convenience. In the central zone, the deformation gradient, considering that the direction 1 is the tensile loading one, is given by

$$\mathbf{F} = \lambda\left(\mathbf{e}_1 \otimes \mathbf{E}_1\right) + \lambda^{-1/2}\left(\mathbf{e}_2 \otimes \mathbf{E}_2 + \mathbf{e}_3 \otimes \mathbf{E}_3\right) \quad (1)$$

and the nominal stress tensor

$$\mathbf{P} = P_{11}\left(\mathrm{e}_1 \otimes \mathrm{E}_1\right) \quad (2)$$

where $(\mathbf{E}_1, \mathbf{E}_2, \mathbf{E}_3)$ and $(\mathbf{e}_1, \mathbf{e}_2, \mathbf{e}_3)$ are the orthonormal basis used for the initial and current configurations, respectively.

In a second time, a tensile specimen has been subjected to a load/unload sequence at different elongation rates $\lambda' = 25 \times 10^{-4}$ s^{-1} to $\lambda' = 125 \times 10^{-2}$ s^{-1} in order to verify the rate-dependence influence. No noticeable difference between stress-strain responses was observed at the considered strain rate range. Consequently the RTV3428 behavior can be assumed independent of the rate of deformation for the observed ranges.

A cyclic tensile loading test was realized, the results are presented in Figure 3. Different phenomena are highlighted, first a large Mullins effect appears by comparing the two first loadings at each strain level, but with very little residual elongation. Moreover, a little hysteresis (difference between second and subsequent loadings and unloadings) is observed.

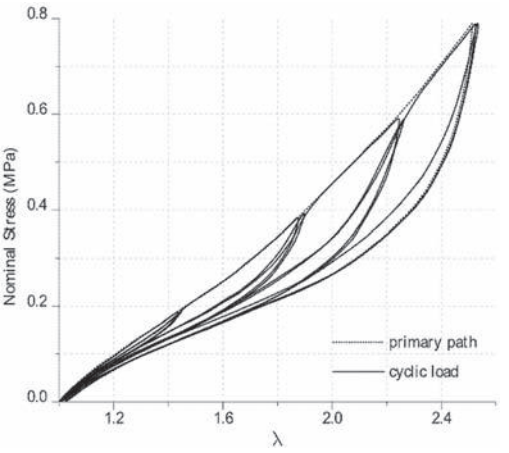

Figure 3. Cyclic loading-unloading tensile test with increasing maximum stress: 0.2, 0.4. 0.6 and 0.8 MPa at $\lambda' = 1.60 \times 10^{-2}$ s^{-1}.

3.2 *Directional influence*

In order to study the anisotropy induced by the Mullins effect, two identical large specimens $l_o = 100$ mm, width $w_o = 70$ mm and $e_o = 2$ mm of thickness were submitted to one cycle of stretch, at $\lambda = 2.45$ in uniaxial tension along a principal direction referred to 0°. Then, a set of smaller specimens was cut from each of these preconditioned large samples along four different directions 0° (first loading direction), 30°, 45° and 90° (orthogonal direction). An illustration is presented in Figure 4. All the cut specimens have been submitted to the same initial strain state (this has been verified thanks to the DIC measures). Figure 5 presents the second loading and unloading curves for the different cut specimens.

It clearly appears that all these second loading curves come back on the first loading curve at the same maximum elongation. Moreover, the subsequent unloading curves are almost independent of the history. The main difference is the shape of the second loading curve, the amount of stress-softening can be relied to the angle between the two loading directions.

As represented by Shariff (2006) and Diani (2006b), Figure 6 shows the stress ratio between the first virgin load curve and the set of sub-samples orientated at 0°, 30°, 45° and 90° directions. The curves highlight that there is no proportionality between the different curves, moreover there is no easy link between the second loading curves.

Figure 7 presents the evolution of the loss energy by Mullins effect according to the loading angle.

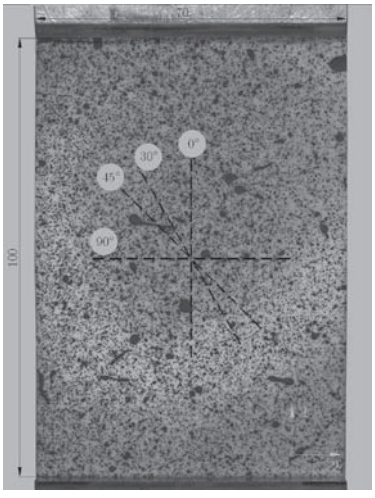

Figure 4. The large preconditioned sample and the different observed orientations.

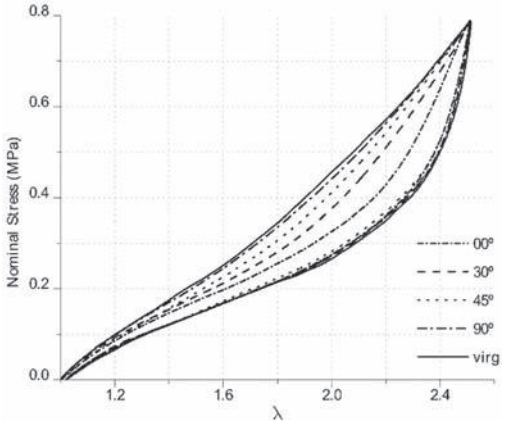

Figure 5. Anisotropy induced by Mullins effect of a filled silicone RTV3428, superposed uniaxial stress-strain responses (load-unload).

Experimental points are fitted using the periodic function given by

$$Wr = a_o + a_1 \cos(\alpha\omega) + a_2 \cos(2\alpha\omega) \qquad (3)$$

where $a_o = 0.460$, $a_1 = 0.440$, $a_2 = 0.093$ and $\omega = 2.0$.

It appears that the function evolves from a maximum of stress-softening, when the two loadings are in the same direction and a minimum, close to zero, when the directions are orthogonal. That means that, at least, two parameters are necessary to describe the Mullins effect: the maximum stretch criteria and the angle between the first and second loading.

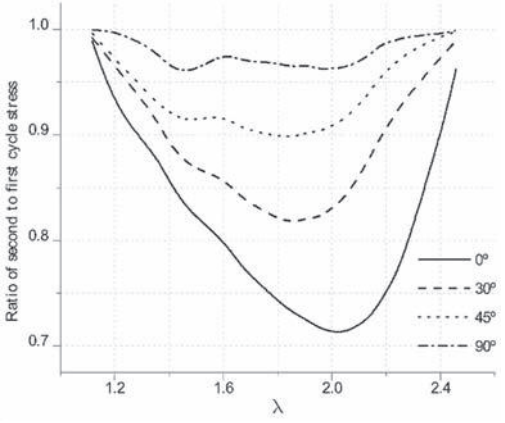

Figure 6. Stress ratio between the first virgin load curve and the set of sub-samples, for sub-samples orientated at 0°, 30°, 45° and 90° (perpendicular) directions.

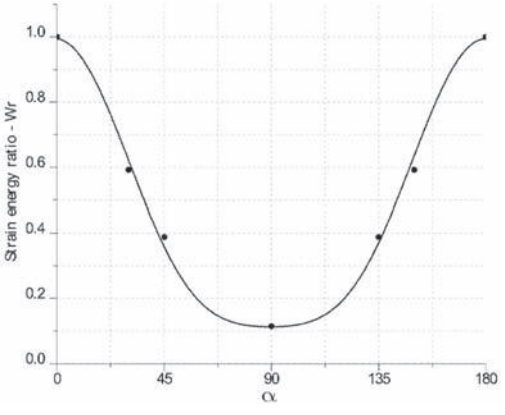

Figure 7. Ratio of energy loss according to the difference of angle loading.

4 CONCLUSION

In the present work we have conducted an experimental campaign to build evidence showing that the Mullins effect in filled silicone rubbers is, in general, non-isotropic. The reproducibility and accuracy of measurements were evaluated through several successive tests. Results have shown that our protocol to manufacture the silicone specimens without any pre-existent anisotropy and our experimental methodology work well and provide a precise experimental characterization of softening phenomena.

Using the DIC method as a non-contact full-field optical measurement, a large strain level was achieved. The results have shown that tensile cycles in one direction hardly cause any softening in the perpendicular direction. In addition, the results with respect to the influence of Mullins effect in the intermediate directions provide valuable information for testing and calibrating numerical models.

Finally, the anisotropy of the Mullins effect becomes clearly evident and should be taken into account in the constitutive modeling of filled elastomers.

ACKNOWLEDGEMENTS

We would like to thank the French ANR for supporting this work through the project RAAMO ("Robot Anguille Autonome pour Milieux Opaques").

REFERENCES

Bergstrom J.S., & Boyce M.C. 2000. Large strain time-dependent behaviour of filled elastomers, Mechanics of Materials, 32(11) pp. 627–644.

Chagnon G., Verron E., Gornet L., Marckmann G., & Charrier P. 2004. On the relevance of continuum damage mechanics as applied to the Mullins effect in elastomers, J. Mech. Phys. Solids, 52, pp. 1627–1650.

Chagnon G., Verron E., Marckmann G., & Gornet L. 2006. Development of new constitutive equations for the Mullins effect in rubber using the network alteration theory, Int J Solids Struct, 43, pp. 6817–6831.

Diani J., Brieu M., & Gilormini P. 2006. Observation and modeling of the anisotropic visco-hyperelastic behaviour of a rubberlike material. Int J Solids Struct, 43 -10:3044–3056.

Diani J., Brieu M., & Vacherand J.M. 2006. A damage directional constitutive model for Mullins effect with permanent set and induced anisotropy, European journal of mechanics. A. Solids, 25(3), 483–496.

Itskov M., Haberstroh E., Ehret A.E., & Vohringer M.C. 2006. Experimental observation of the deformation induced anisotropy of the Mullins effect in rubber, Kautschuk Gummi Kunststoffe, Volume 59, Issue 3, Pages 93–96.

Laraba-Abbes F., Ienny P., & Piques R. 2003. A new Taylor-made' methodology for the mechanical behaviour analysis of rubberlike materials: II. Application to the hyperelastic behaviour characterization of a carbon-black filled natural rubber vulcanizate. Polymer, 44 (3), 821–840.

Marckmann G., Verron E., Gornet L., ChagnonG., Charrier P., & Fort P. 2002. A theory of network alteration for the Mullins effect, J. Mech. Phys. Solids, 50, pp. 2011–2028.

Meunier L., Chagnon G., Favier D., Orgeas L., & Vacher P. 2008. Mechanical experimental characterisation and numerical modelling of an unfilled silicone rubber, Polymer Testing, 27(6), pp. 765–777.

Meunier L., Chagnon G., Favier D., & Orgeas L. 2008. Experimental and numerical study of the mechanical behaviour of an unfilled silicone rubber, Cosntitutive Models for Rubber V, Pages 35–40.

Miehe C., & Keck J. 2000. Superimposed finite elastic-viscoelastic-plastoelastic stress response with damage in filled rubbery polymers. Experiments, modelling and algorithmic implementation. J. Mech. Phys. Solids, 48, 323–365.

Muhr A.H., Gough J., & Gregory I.H. Experimental determination of model for liquid silicone rubber. In: Muhr A, Dorfmann A (eds) Constitutive models for rubber. A.A. Balkema, Rotterdam, pp. 181–187.

Mullins L. 1947. Effect of stretching on the properties of rubber. J. Rubber Res, 16(12), 275–289.

Mullins L. 1969. Softening of rubber by deformation. Rubber Chem. Technol, 42, 339–362.

Pawelski H. Softening behaviour of elastomeric media after loading in changing directions. In: Besdo D, Schuster RH, Ihlemann J (eds) Constitutive models for rubber II. A.A. Balkema Lisse, The Netherlands, pp. 27–36.

Sasso M., Palmieri G., Chiappini G., & Amodio D. 2008. Characterization of hyperelastic rubber-like materials by biaxial and uniaxial stretching tests based on optical methods. Polymer Testing, 27(8), pp. 995–1004.

Shariff, M.H.B.M. 2006. An anisotropic model of the Mullins effect, Journal of Engineering Mathematics, Springer Netherlands, vol. 56, no. 4, pp. 415–435.

Sutton M.A. 2008. Digital Image Correlation for Shape and Deformation Measurements, Springer Handbook of Experimental Solid Mechanics—PartC, Pages 565–600.

Constitutive Models for Rubber VI – Heinrich et al. (eds)
© 2010 Taylor & Francis Group, London, ISBN 978-0-415-56327-7

Author index

In a wide range of technical applications, constitutive models are needed to represent the material properties of filler-reinforced elastomers under quasistatic or dynamic, infinitesimal or finite thermomechanical deformations. Elastomers are used for products like tyres, engine and suspension mounts, seals or shock absorbers, to name a few. In industrial development processes, for example, it is profitable to simulate the behaviour of these parts under realistic operating conditions. This challenge necessitates detailed experimental investigations, the development of constitutive models representing the material behaviour in combination with techniques to identify the material parameters and efficient numerical methods. The interest in modelling the quasistatic stress-strain behaviour or the Mullins effect was dominant in the past but nowadays, the interests also include the influences of environmental conditions on the material characteristics and estimations of the product lifetime.

The most recent developments in order to represent the material behaviour of filler-reinforced elastomers under realistic operating conditions are collected in the present volume. Special topics are finite element simulations and methods, dynamic material properties, experimental characterization, lifetime prediction, friction, multiphysics and biomechanics, reinforcement, ageing, fracture and fatigue as well as micro- and macromechanical approaches. **Constitutive Models for Rubber VI** is of interest to research and development engineers in the industry, and to postgraduates and researchers in all disciplines of engineering and materials science.

CRC Press
Taylor & Francis Group
an **informa** business
www.crcpress.com

6000 Broken Sound Parkway, NW
Suite 300, Boca Raton, FL 33487
Schipholweg 107C
2316 XC Leiden, NL
2 Park Square, Milton Park
Abingdon, Oxon OX14 4RN, UK

an **informa** business